

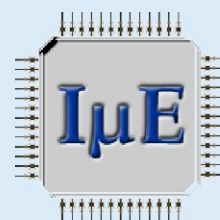
# *11th International Workshop on Computational Electronics*

## *Book of Abstracts*

Wien, 25-27 May 2006



(Eds.) Hans Kosina  
Siegfried Selberherr



*11th International Workshop on  
Computational Electronics*

*Book of Abstracts*

(Eds.) Hans Kosina  
Siegfried Selberherr

Hans Kosina  
Siegfried Selberherr

© 2006 Technische Universität Wien (TU Wien), Institute for Microelectronics  
A full journal publication of extended abstracts contained in this book will be  
published in the *Journal of Computational Electronics*.

Cover: St. Charles Church, located next to TU Wien  
Typesetting: Camera ready by authors  
Printing: Firma Ing. Christian Janetschek, A-3860 Heidenreichstein, Austria

ISBN 3-901578-16-1

## Editorial

This volume contains the extended abstracts of the 11th International Workshop on Computational Electronics, IWCE-11, held at TU Wien on May 25–27, 2006. Over the years the workshop has become the main international forum for discussions on the current trends and future directions for computational electronics. The workshop continues a series of events initiated in 1992, when the first IWCE was organized by the Beckmann Institute of the University of Illinois. The following events were held at the University of Leeds, UK (August 1993), Portland, Oregon, USA (May 1994), Arizona State University, Tempe, USA (November 1995), University of Notre Dame, South Bend, USA (May 1997), Osaka University, Japan (September 1998), University of Glasgow, UK (May 2000), University of Illinois, Urbana, USA (October 2001), University of Rome, Monte Porzio Catone, Italy (May 2003), and Purdue University, West Lafayette, USA (October 2004). Additional information can be found on the web site <http://www.iwce.org>.

The scientific program of IWCE-11 is organized in a single-session format and comprises 8 invited lectures, 43 contributed talks, and 135 poster presentations. The program covers traditional topics of Technology CAD, Monte Carlo and molecular dynamics methods, optical processes, quantum transport as well as emerging areas of molecular and organic electronics, nano-bio electronics, and alternative computing architectures.

The distribution of the abstracts reflects the international nature of the workshop: 43 from the USA, 26 from Italy, 22 from Austria, 18 from Germany, 10 from France, Spain, and the United Kingdom, 8 from Japan, 6 from China, 4 from Korea and Switzerland, 2 from Canada, Greece, Hungary, India, Lithuania, Mexico, and Taiwan, and 1 from Algeria, Argentina, Belgium, Czech Republic, Ireland, New Zealand, Poland, Slovakia, Sweden, and The Netherlands.

A companion workshop on Modeling of Reliability Issues is held on the day before IWCE-11. A special focus is put on bias temperature instability (NBTI and PBTI), a topic on which 11 invited speakers summarize their findings.

The book of abstracts is printed from camera-ready manuscripts provided by the authors. The editors are not responsible for any inaccuracies, comments, or opinions given in the extended abstracts.

We would like to express our sincere appreciation to the authors for their effort to provide high-quality contributions and respecting the abstract preparation guidelines.

We thank the International Advisory Committee for the nomination of the invited speakers and the Program Committee for careful evaluation of the submitted abstracts.

Hans Kosina  
Siegfried Selberherr

Institute for Microelectronics  
TU Wien, May 2006

## Conference Organization

H. Kosina	TU Wien	Austria
S. Selberherr	TU Wien	Austria

## Advisory Committee

J. Barker	University of Glasgow	United Kingdom
A. Di Carlo	University of Rome Tor Vergata	Italy
D. Ferry	Arizona State University	USA
M. Fischetti	University of Massachusetts	USA
C. Hamaguchi	Osaka University	Japan
J. Jerome	Northwestern University	USA
G. Klimeck	Purdue University	USA
W. Porod	University of Notre Dame	USA
M. Saraniti	Illinois Institute of Technology	USA
C. Stanton	University of Florida	USA
M. Strosio	University of Illinois	USA
H. Tsuchiya	Kobe University	Japan
P. Vogl	TU Munich	Germany

## Program Committee

S. Aboud	Worcester Polytechnic Institute	USA
M. Anantram	NASA Ames Research Center	USA
A. Asenov	University of Glasgow	United Kingdom
P. Gamiz	University of Granada	Spain
S. Goodnick	Arizona State University	USA
T. Grasser	TU Wien	Austria
G. Iannaccone	University of Pisa	Italy
C. Jungemann	Bundeswehr University	Germany
S. Laux	IBM T.J. Watson Research Center	USA
Y. Li	National Chiao Tung University	Taiwan
P. Lugli	TU Munich	Germany
M. Lundstrom	Purdue University	USA
W. Porod	University of Notre Dame	USA
N. Sano	University of Tsukuba	Japan
A. Schenk	ETH Zürich	Switzerland
M. Stettler	Intel Corporation	USA

## Supporting Organizations

austriamicrosystems AG  
Austrian Research Centers  
Infineon Technologies Austria AG  
Gesellschaft für Mikro- und Nanoelektronik

IWCE-11 receives technical co-sponsorship from the IEEE Electron Devices Society.

# **PROGRAM**

## **International Workshop on Computational Electronics (IWCE-11)**

---

### **Wednesday, 24 May 2006**

---

09:00 - 17:10    Companion Workshop: **Modeling of Reliability Issues**

---

### **Thursday, 25 May 2006**

---

08:30 - 10:15    Session 1: **Technology CAD**

10:45 - 12:30    Session 2: **Monte Carlo 1**

14:30 - 16:00    Session 3: **Monte Carlo 2**

16:15 - 18:15    Poster Session 1: **TCAD, Monte Carlo, Molecular Devices, Biological Systems**

---

### **Friday, 26 May 2006**

---

08:30 - 10:15    Session 4: **Quantum Transport 1**

10:45 - 12:30    Session 5: **Quantum Transport 2**

14:30 - 16:00    Session 6: **Optoelectronic Devices**

16:15 - 18:15    Poster Session 2: **Quantum Transport, Optoelectronic Devices**

---

### **Saturday, 27 May 2006**

---

08:30 - 10:15    Session 7: **Nanotubes and Nanowires**

10:45 - 12:30    Session 8: **Molecular Devices and Ab-Initio Methods**

14:30 - 16:00    Session 9: **Biological Systems**



# TABLE OF CONTENTS

## International Workshop on Computational Electronics (IWCE-11)

---

Thursday, 25 May 2006

---

### Session 1: Technology CAD

Chairperson: S. Goodnick

08:30	<b>Welcome</b> H. Kosina and S. Selberherr	
08:45	<b>Calculating Future CMOS and CMOS Future – Where Industry Needs Academia</b> (Invited) ..... 1 T. Skotnicki and H. Jaouen STMicroelectronics, France	1
09:15	<b>A Novel Approach to Three-Dimensional Semiconductor Process Simulation: Application to Thermal Oxidation</b> ..... 3 V. Suvorov, A. Hössinger, and Z. Djuric Silvaco Technology Center, United Kingdom	3
09:30	<b>A 3D Moving Grid Algorithm for Process Simulation</b> ..... 5 N. Strecker and D. Richards Synopsys Inc., USA	5
09:45	<b>Kinetic-Energy Transport Equation for the Modeling of Ballistic MOSFETs</b> ..... 7 T.-W. Tang and P. Samra University of Massachusetts at Amherst, USA	7
10:00	<b>Multi-Dimensional Semiconductor Tunneling in Density-Gradient Theory</b> ..... 9 M. Ancona Naval Research Laboratory, USA	9

### Session 2: Monte Carlo 1

Chairperson: M. Fischetti

10:45	<b>Particle-Based Simulation: An Algorithmic Perspective</b> (Invited) ..... 11 M. Saraniti, S. Aboud, and S. Goodnick	11
11:15	<b>A Linear Response Monte Carlo Algorithm for Inversion Layers and Magnetotransport</b> ..... 13 C. Jungemann, A. Pham, and B. Meinerzhagen TU Braunschweig, Germany	13
11:30	<b>Global Modeling of High-Frequency Devices</b> ..... 15 J. Ayubi-Moak, S. Goodnick, and M. Saraniti <sup>1</sup> Arizona State University, USA <sup>1</sup> Illinois Institute of Technology, USA	15

11:45	<b>Introducing Energy Broadening in Semiclassical Monte Carlo Simulations</b> .....	17
	G. Ferrari, C. Jacoboni <sup>1</sup> , M. Nedjalkov <sup>2</sup> , and A. Asenov University of Glasgow, United Kingdom <sup>1</sup> University of Modena, Italy <sup>2</sup> TU Wien, Austria	
12:00	<b>Schrödinger/Luttinger Approach to Scaled MOS Transport for Various Crystal Orientations and its Experimental Verifications</b> .....	19
	T. Okada and H. Yoshimura Toshiba Corporation, Japan	
12:15	<b>Joule Heating and Phonon Transport in Silicon MOSFETs</b> .....	21
	Z. Aksamija and U. Ravaioli University of Illinois at Urbana, USA	

### **Session 3: Monte Carlo 2**

**Chairperson: C. Jungemann**

14:30	<b>First Self-Consistent Full-Band-2D Monte Carlo-2D Poisson Device Solver for Modeling SiGe Heterojunction p-Channel Devices</b> .....	23
	S. Krishnan, D. Vasileska, and M. Fischetti <sup>1</sup> Arizona State University, USA <sup>1</sup> University of Massachusetts at Amherst, USA	
14:45	<b>Monte Carlo Simulation of Double Gate MOSFET Including Multi Sub-Band Description</b> .....	25
	J. Saint-Martin, A. Bournel, F. Monsef, C. Chassat, and P. Dollfus Universite Paris Sud, France	
15:00	<b>An Improved Wigner Monte Carlo Technique for the Self-Consistent Simulation of RTDs</b> .....	27
	D. Querlioz, P. Dollfus, V.-L. Do, and V.-L. Nguyen <sup>1</sup> Universite Paris Sud, France <sup>1</sup> VAST, Vietnam	
15:15	<b>Scattering and Space-Charge Effects in Wigner Monte Carlo Simulations of Single and Double Barrier Devices</b> .....	29
	V. Sverdlov, T. Grasser, H. Kosina, and S. Selberherr TU Wien, Austria	
15:30	<b>Kinetic Monte Carlo Simulations of Germanium Epitaxial Growth on Silicon</b> .....	31
	R. Akis and D. Ferry Arizona State University, USA	
15:45	<b>Self-Consistent Ion Transport Simulation in Carbon Nanotube Channels</b> .....	33
	J. Eschermann, Y. Li <sup>1</sup> , T. A. Van der Straaten <sup>1</sup> , and U. Ravaioli <sup>1</sup> TU Munich, Germany <sup>1</sup> University of Illinois at Urbana, USA	

## Poster Session 1 (16:15-18:15)

### Technology CAD

P1	<b>Power-Delay Product in COSMOS Logic Circuits</b> .....	35
	A. Al-Ahmadi and S. Kaya Ohio University, USA	
P2	<b>A 3D Finite Element Parallel Simulator for Studying Fluctuations in Advanced MOSFETs</b> .....	37
	M. Aldegunde, A. Garcia-Loureiro, K. Kalna <sup>1</sup> , and A. Asenov <sup>1</sup> University of Santiago de Compostela, Spain <sup>1</sup> University of Glasgow, United Kingdom	
P3	<b>Calibration of the Density-Gradient Model by Using the Multidimensional Effective-Mass Schrödinger Equation</b> .....	39
	P. Andrei Florida State University and Florida A&M University, USA	
P4	<b>Random Dopant Fluctuation Analysis for Scaling Multi-Gate Device Structures</b> .....	41
	Y. Ashizawa, R. Tanabe, and H. Oka Fujitsu Laboratories, Japan	
P5	<b>Study of Piezoresistivity Effect in FET</b> .....	43
	M. Auf der Maur, M. Povolotskyi, F. Sacconi, and A. Di Carlo University of Rome Tor Vergata, Italy	
P6	<b>Influences of Grain Structure on Thermally Induced Stresses in 3D-IC Inter-Wafer Vias</b> .....	45
	D. Bentz, M. Bloomfield, J.-Q Lu, R. Gutmann, and T. Cale Rensselaer Polytechnic Institute, USA	
P7	<b>TCAD-Assisted Development of Technology-Independent Device Models</b> .....	47
	P. Blakey, S. Bates, and U. Yahya Northern Arizona University, USA	
P8	<b>Intrinsic Parameter Fluctuations due to Random Grain Orientations in High-k Gate Stacks</b> .....	49
	A. Brown, J. Watling, and A. Asenov University of Glasgow, United Kingdom	
P9	<b>Gummel Iterations for Inverse Dopant Profiling of Semiconductor Devices</b> .....	51
	M. Burger Johannes Kepler University, Austria	
P10	<b>An Evolution Algorithm for Noise Modeling of HEMT's down to Cryogenic Temperatures</b> .....	53
	A. Caddemi, F. Catalfamo, and N. Donato University of Messina, Italy	
P11	<b>Combined Line-Width-Roughness (LWR) and Local Critical Dimension (CD) Variation Effects on Sub-65nm MOSFET Current-Voltage Characteristics: From Lithography to Metrology to Device Simulation</b> .....	55
	V. Constantoudis, G. Patsis, and E. Gogolides NCSR Demokritos, Greece	

P12	<b>TCAD Simulation of OTFT Small-Signal Parameters</b> .....	57
	C. Erlen, P. Lugli, B. Nickel <sup>1</sup> , and M. Fiebig <sup>1</sup>	
	TU Munich, Germany	
	<sup>1</sup> LMU Munich, Germany	
P13	<b>Semiconductor Transport Modeling for the Analysis of Nanoscaled CMOS Circuits</b> ...	59
	F. Felgenhauer, M. Begoin, J. Bremer, and W. Mathis	
	University of Hannover, Germany	
P14	<b>A Novel Framework for Distributing Computations</b> .....	61
	T. Fühner, S. Popp <sup>1</sup> , and T. Jung	
	Fraunhofer IISB, Germany	
	<sup>1</sup> University of Applied Science Regensburg, Germany	
P15	<b>Efficient Full-Flow Process Simulation for 3D Structures including Stress Modeling</b> ...	63
	A. Gencer, A. Lebedev <sup>1</sup> , and P. Pfäffli <sup>1</sup>	
	Synopsys GmbH, Germany	
	<sup>1</sup> Synopsys Switzerland LLC, Switzerland	
P16	<b>Simulation of Slow Current Transients and Current Compression in AlGaAs/GaAs HFETs</b> .....	65
	H. Ikarashi, K. Kitamura, N. Kurosawa, and K. Horio	
	Shibaura Institute of Technology, Japan	
P17	<b>Compact Model for Schottky-Barrier CNT-FETs</b> .....	67
	D. Jimenez, X. Cartoixa, E. Miranda, J. Sune, and S. Roche <sup>1</sup>	
	Universitat Autònoma de Barcelona, Spain	
	<sup>1</sup> Commissariat à l'Énergie Atomique, France	
P18	<b>A Simulation-Based Evolutionary Technique for Inverse Problems of Sub-65nm CMOS Devices</b> .....	69
	Y. Li, S.-M. Yu, and C.-K. Chen	
	National Chiao Tung University, Taiwan	
P19	<b>Numerical Simulation of Electrical Characteristics on Uniaxial Strained Bulk and SOI FinFETs</b> .....	71
	Y. Li and W.-H. Chen	
	National Chiao Tung University, Taiwan	
P20	<b>Strain Engineering with Si<sub>1-y</sub>C<sub>y</sub> Source and Drain Stressors</b> .....	73
	C. Maiti and A. Saha	
	IIT Kharagpur, India	
P21	<b>Hot Electron Distribution Function for the Boltzmann Equation with Analytic Bands</b> .	75
	O. Muscato	
	University of Catania, Italy	
P22	<b>Computer Simulation Experiment on Prospects of ZnS as Novel Material for High mm-Wave Power/Low Noise Generation in Impatt Mode</b> .....	77
	S. Pati and P. Tripathy	
	Sambalpur University, India	

P23	<b>Accurate Extraction of Maximum Current Densities from the Layout</b> .....	79
	A. Seidl, T. Schnattinger <sup>1</sup> , A. Erdmann <sup>1</sup> , H. Hartmann <sup>2</sup> , and A. Petrashenko <sup>2</sup>	
	Hochschule Magdeburg-Stendal, Germany	
	<sup>1</sup> Fraunhofer IISB, Germany	
	<sup>2</sup> Software and System Solutions GbR, Germany	
P24	<b>A 3D Parallel Simulation of the Effect of Interface Charge Fluctuations in HEMTs</b> ..	81
	N. Seoane, A. Garcia-Loureiro, K. Kalna <sup>1</sup> , and A. Asenov <sup>1</sup>	
	University of Santiago de Compostela, Spain	
	<sup>1</sup> University of Glasgow, United Kingdom	
P25	<b>Negative Gate-Overlap in Nanoscaled DG-MOSFETs with Asymmetric Gate Bias</b> ....	83
	X. Shao and Z. Yu	
	Tsinghua University, China	
P26	<b>Human Body Model ESD Simulation Including Self Heating Effect</b> .....	85
	T. Takani and T. Toyabe	
	Toyo University, Japan	
P27	<b>Quantum Correction for DG MOSFETs</b> .....	87
	M. Wagner, M. Karner, T. Grasser, and H. Kosina	
	TU Wien, Austria	
P28	<b>Weak Accumulation of Gate Polysilicon</b> .....	89
	H. Watanabe, K. Matsuo, T. Kobayashi, K. Nakajima, and T. Saitoh	
	Toshiba Corporation, Japan	
P29	<b>Numerical Analysis of a DAR IMPATT Diode</b> .....	91
	A. Zemliak and S. Cabrera	
	Puebla Autonomous University, Mexico	
<b>Monte Carlo and Molecular Dynamics Methods</b>		
P30	<b>Meshless Solution of the 3-D Semiconductor Poisson Equation</b> .....	93
	Z. Aksamija and U. Ravaioli	
	University of Illinois at Urbana, USA	
P31	<b>Particle-Based Simulations of Phonon Transport in Silicon</b> .....	95
	A. Asokan and R. Kelsall	
	University of Leeds, United Kingdom	
P32	<b>Neutral and Negatively Charged Interstitial Oxygen in Silicon</b> .....	97
	P. Ballo, D. Donoval, and L. Harmatha	
	Slovak University of Technology, Slovakia	
P33	<b>Model Plasma Dispersion Functions for SO Phonon Scattering in Monte Carlo Simulations of High-k Dielectric MOSFETs</b> .....	99
	J. Barker and J. Watling	
	University of Glasgow, United Kingdom	
P34	<b>On a Simple and Accurate Quantum Correction for Monte Carlo Simulation</b> .....	101
	F. Bufler <sup>1,2</sup> , R. Hude <sup>1</sup> , and A. Erlebach <sup>1</sup>	
	<sup>1</sup> ETH Zürich, Switzerland	
	<sup>2</sup> Synopsys Schweiz GmbH, Switzerland	

P35	<b>DSMC versus WENO-BTE: A Double Gate MOSFET Example</b> .....	103
	M. Caceres, J. Carrillo <sup>1</sup> , I. Gamba <sup>2</sup> , A. Majorana <sup>3</sup> , and C.-W. Shu <sup>4</sup>	
	Universidad de Granada, Spain	
	<sup>1</sup> Universitat Autònoma de Barcelona, Italy	
	<sup>2</sup> University of Texas at Austin, USA	
	<sup>3</sup> University of Catania, Italy	
	<sup>4</sup> Brown University, USA	
P36	<b>Electronic Noise in Semiconductor Systems: A Monte Carlo Simulation under Mixed Fields</b> .....	105
	M. Capizzo, D. Persano Adorno, and M. Zarcone	
	University of Palermo, Italy	
P37	<b>Thermal Noise in Nanometric DG-MOSFET</b> .....	107
	P. Dollfus, A. Bournel, and J. Velazquez <sup>1</sup>	
	Universite Paris-Sud, France	
	<sup>1</sup> Universidad de Salamanca, Spain	
P38	<b>Full-Band Particle-Based Simulation of 85 nm AlInSb/InSb Quantum Well Transistors</b> .....	109
	N. Faralli, J. Branlard, S. Goodnick <sup>1</sup> , D. Ferry <sup>1</sup> , and M. Saraniti	
	Illinois Institute of Technology, USA	
	<sup>1</sup> Arizona State University, USA	
P39	<b>On the Impact of High-k Gate Stacks on Mobility: A Monte Carlo Study Including Coupled SO Phonon-Plasmon Scattering</b> .....	111
	G. Ferrari, J. Watling, S. Roy, J. Barker, P. Zeitoff <sup>1</sup> , G. Bersuker <sup>1</sup> , and A. Asenov	
	University of Glasgow, United Kingdom	
	<sup>1</sup> SEMATECH, USA	
P40	<b>Electron Injection Model for the Particle-Simulation of 3D, 2D and 1D Nanoscale FET</b>	113
	E. Fernandez-Diaz and X. Oriols	
	Universitat Autònoma de Barcelona, Spain	
P41	<b>Free-Carrier Grating due to the Optical Phonon Emission in InP n+nn+ Structures</b> ..	115
	V. Gruzinskis, E. Starikov, and P. Shiktorov	
	Semiconductor Physics Institute, Lithuania	
P42	<b>3D Monte Carlo Device Simulations Using an Effective Quantum Potential Including Electron-Electron Interactions</b> .....	117
	C. Heitzinger, C. Ringhofer, S. Ahmed, and D. Vasileska	
	Arizona State University, USA	
P43	<b>Pearson versus Gaussian Effective Potentials for Quantum Corrected Monte Carlo Simulation</b> .....	119
	M. Jaud <sup>1,2,3</sup> , S. Barraud <sup>1</sup> , P. Dollfus <sup>3</sup> , H. Jaouen <sup>2</sup> , and G. Le Carval <sup>1</sup>	
	<sup>1</sup> CEA-LETI, France	
	<sup>2</sup> STMicroelectronics, France	
	<sup>3</sup> CNRS-UPS, France	
P44	<b>Atomistic Modeling for Boron Up-Hill Diffusion After Ge Pre-Amorphization</b> .....	121
	J.-S. Kim and T. Won	
	Inha University, Korea	

P45	<b>Threshold Energy and Impact Ionization Scattering Rate Calculations for Strained Silicon</b> .....	123
	C. May <sup>1,2</sup> and F. Bufler <sup>1,3</sup>	
	<sup>1</sup> ETH Zürich, Switzerland	
	<sup>2</sup> University of Tuebingen, Germany	
	<sup>3</sup> Synopsys Schweiz GmbH, Switzerland	
P46	<b>Monte Carlo Calculation of Voltage-Current Nonlinearity and High-Order Harmonic Generation in GaAs Microstructures</b> .....	125
	D. Persano Adorno, M. Capizzo, and M. Zarcone	
	University of Palermo, Italy	
P47	<b>Static-Electric-Field Effects on Harmonic Generation in Gallium Arsenide Bulk Exposed to Intense Sub-THz Radiation</b> .....	127
	D. Persano Adorno, M. Zarcone, and G. Ferrante	
	University of Palermo, Italy	
P48	<b>Transport in Silicon Nanowires: Surface Roughness and Confined Phonons</b> .....	129
	E. Ramayya, D. Vasileska <sup>1</sup> , S. Goodnick <sup>1</sup> , and I. Knezevic	
	University of Wisconsin at Madison, USA	
	<sup>1</sup> Arizona State University, USA	
P49	<b>Electrothermal Monte Carlo Simulation of Submicron Wurtzite GaN/AlGaIn HEMTs</b> .	131
	T. Sadi, R. Kelsall, and N. Pilgrim <sup>1</sup>	
	University of Leeds, United Kingdom	
	<sup>1</sup> University of Aberdeen, United Kingdom	
P50	<b>Quantum Ensemble Monte Carlo Simulation of Silicon-Based Nanodevices</b> .....	133
	C. Sampedro, F. Gamiz, A. Godoy, and F. Jimenez-Molinoz	
	Universidad de Granada, Spain	
P51	<b>Monte Carlo Simulation of 2D TASER</b> .....	135
	E. Starikov, P. Shiktorov, V. Gruzinskis, A. Dubinov <sup>1</sup>	
	V. Aleshkin <sup>1</sup> , L. Varani <sup>2</sup> , C. Palermo <sup>2</sup> , and L. Reggiani <sup>3</sup>	
	Semiconductor Physics Institute, Lithuania	
	<sup>1</sup> Institute for Physics of Microstructures, Russia	
	<sup>2</sup> CEM2, France	
	<sup>3</sup> INFM-National Nanotechnology Laboratory, Italy	
P52	<b>Analysis of Nano-Scale MOSFET Including Uniaxial and Biaxial Strain</b> .....	137
	R. Tanabe, T. Yamasaki, Y. Ashizawa, and H. Oka	
	Fujitsu Laboratories, Japan	
P53	<b>Study of the Cutoff Frequency of Optimized SOI MESFETs</b> .....	139
	K. Tarik, D. Vasileska, and T. Thornton	
	Arizona State University, USA	
P54	<b>Physical Modeling of Electron Mobility Enhancement for Arbitrarily Strained Silicon</b>	141
	E. Ungersböck, S. Dhar, G. Karlowatz, H. Kosina, and S. Selberherr	
	TU Wien, Austria	
P55	<b>Simulation of Tri-Gate MOSFET Using 3D Monte Carlo Method Based on the Quantum Boltzmann Equation</b> .....	143
	J. Wang, Z. Xia, G. Du, X. Liu, and R. Han	
	Peking University, China	

P56	<b>Electron Transport in Self-Switching Nano-Diode</b> .....	145
	K.-Y. Xu, A.-M Song <sup>1</sup> , and G. Wang	
	Sun Yat-sen University, China	
	<sup>1</sup> University of Manchester, United Kingdom	
P57	<b>Molecular Dynamic Simulation on Boron Cluster Implantation for Shallow Junction Formation</b> .....	147
	L. Yuan, W. Li, M. Yu, H. Ji, K. Zhan, R. Huang,	
	X. Zhang, Y. Wang, J. Zhang <sup>1</sup> , and H. Oka <sup>2</sup>	
	Peking University, China	
	<sup>1</sup> Fujitsu R&D Center, China	
	<sup>2</sup> Fujitsu Laboratories, Japan	
P58	<b>Physical Modeling of Hole Mobility in Silicon Inversion Layers under Uniaxial Stress</b> .....	149
	J. Zhao, J. Zou, and Z. Yu	
	Tsinghua University, China	
<b>Molecular Devices and Ab-Initio Methods</b>		
P59	<b>Reduced Backscattering in Potassium Doped Nanotubes</b> .....	151
	C. Adessi, S. Roche <sup>1,2</sup> , and X. Blase	
	Universite Claude Bernard Lyon, France	
	<sup>1</sup> CEA-DSM, France	
	<sup>2</sup> CEA-DRT, France	
P60	<b>Scaling Of Molecular Electronics Devices</b> .....	153
	A. Boudjella <sup>1,2,3</sup> and K. Mokhtar <sup>4</sup>	
	<sup>1</sup> Queen's College, Mississauga, Canada	
	<sup>2</sup> Alpha Toronto, Canada	
	<sup>3</sup> Conseil Scolaire de District du centre-Sud-ouest, Canada	
	<sup>4</sup> Honeywell-Engines, Canada	
P61	<b>Computation of the I-V Characteristics of a Molecular Switch</b> .....	155
	I. Cacelli <sup>1</sup> , A. Ferretti <sup>2</sup> , M. Girlanda <sup>1,2</sup> , and M. Macucci <sup>1</sup>	
	<sup>1</sup> University of Pisa, Italy	
	<sup>2</sup> CNR, Italy	
P62	<b>Simulations of Correlated Electronic Transport Across Molecular Junctions</b> .....	157
	G. Fagas, P. Delaney <sup>1</sup> , and J. Greer	
	Tyndall National Institute, Ireland	
	<sup>1</sup> Queen's University Belfast, Ireland	
P63	<b>Numerical Simulation of Organic Field-Effect-Transistors</b> .....	159
	W. Klix, R. Stenzel, T. Herrmann, and E. Mehler	
	University of Applied Sciences Dresden, Germany	
P64	<b>Percolation Current in Organic Semiconductors</b> .....	161
	L. Li, G. Meller, and H. Kosina	
	TU Wien, Austria	
P65	<b>Ferromagnetism in Tetrahedrally Coordinated Compounds of I/II-V Elements: Ab-Initio Calculations</b> .....	163
	M. Sieberer, J. Redinger, S. Khmelevskiy, and P. Mohn	
	TU Wien, Austria	

P66	<b>Ab-Initio Calculations for Indium Migration in Silicon Substrate</b> .....	165
	K.-S. Yoon, C.-O. Hwang <sup>1</sup> , and T. Won	
	Inha University, Korea	
	<sup>1</sup> Soongsil University, Korea	
<b>Biological Systems</b>		
P67	<b>Electrostatic Modeling of Ion Motive Sodium Pump</b> .....	167
	J. Fonseca, R. Rakowski, and S. Kaya	
	Ohio University, USA	
P68	<b>Numerical Aspects of the Three-Dimensional Feature-Scale Simulation of Silicon-Nanowire Field-Effect Sensors for DNA Detection</b> .....	169
	C. Heitzinger and G. Klimeck	
	Purdue University, USA	
P69	<b>Shot Noise in Single Open Ion Channels: A Computational Approach Based on Atomistic Simulations</b> .....	171
	E. Piccinini, R. Brunetti, F. Affinito, C. Jacoboni, and M. Rudan <sup>1</sup>	
	University of Modena, Italy	
	<sup>1</sup> University of Bologna, Italy	

---

**Friday, 26 May 2006**

---

## **Session 4: Quantum Transport 1**

**Chairperson: D. Ferry**

- 8:30 **The 3D Nanometer Device Project nextnano<sup>3</sup>: Concepts, Methods, Results** (Invited) . 173  
A. Trellakis, T. Zibold, T. Andlauer, S. Birner, K. Smith, R. Morschl, and P. Vogl  
TU Munich, Germany
- 9:00 **Conductance of Winding Wires** ..... 175  
E. Cancellieri, M. Rosini<sup>1</sup>, A. Bertoni, G. Ferrari<sup>2</sup>, and C. Jacoboni  
University of Modena, Italy  
<sup>1</sup>Universita of Lecce, Italy  
<sup>2</sup>University of Glasgow, United Kingdom
- 9:15 **Determination of the Many-Body Conductance of a Fully Interacting System of Electrons** ..... 177  
M. Gilbert and J. Shumway<sup>1</sup>  
University of Texas at Austin, USA  
<sup>1</sup>Arizona State University, USA
- 9:30 **Self-Consistent Treatment of Quantum Transport in 10-nm FinFET Devices Using CBR Method** ..... 179  
H. Khan, D. Mamaluy, and D. Vasileska  
Arizona State University, USA
- 9:45 **Electron Mobility in Silicon and Germanium Inversion Layers** ..... 181  
T. O'Regan and M. Fischetti  
University of Massachusetts, USA
- 10:00 **First-Principles Calculations of Mobilities in Ultrathin Double-Gate MOSFETs** ..... 183  
M. Evans<sup>1</sup>, M. Caussanel<sup>1</sup>, R. Schrimpf<sup>1</sup>, and S. Pantelides<sup>1,2</sup>  
<sup>1</sup>Vanderbilt University, USA  
<sup>2</sup>Oak Ridge National Laboratory, USA

## **Session 5: Quantum Transport 2**

**Chairperson: W. Porod**

- 10:45 **Perspectives on Solid-States Flying Qubits** (Invited) ..... 185  
A. Bertoni  
CNR-INFN, Italy
- 11:15 **Simulation of the Entanglement Creation for Identical Particles Scattering in a 2D System** ..... 187  
F. Buscemi, P. Bordone, and A. Bertoni<sup>1</sup>  
University of Modena, Italy  
<sup>1</sup>CNR-INFN, Italy

11:30	<b>Classical and Quantum Mechanical Transport Simulations in Open Quantum Dots</b> .	189
	R. Brunner, R. Meisels, F. Kuchar, J. Bird <sup>1</sup> , R. Akis <sup>2</sup> , and D. Ferry <sup>2</sup>	
	Montanuniversität Leoben, Austria	
	<sup>1</sup> University at Buffalo SUNY, USA	
	<sup>2</sup> Arizona State University, USA	
11:45	<b>Simulation of Quantum-Ballistic Nanoswitches</b> .....	191
	A. Heigl and G. Wachutka	
	TU Munich, Germany	
12:00	<b>The Rashba Effect and Non-Abelian Phase in Quantum Wire Devices</b> .....	193
	A. Cummings, R. Akis, and D. Ferry	
	Arizona State University, USA	
12:15	<b>Circuit Modeling of Flux Qubits Interacting with Superconducting Waveguides</b> .....	195
	G. Csaba, Z. Fahem, F. Peretti, and P. Lugli	
	TU Munich, Germany	

## **Session 6: Optoelectronic Devices**

**Chairperson: P. Vogl**

14:30	<b>Carbon Nanotube Electronics and Optoelectronics (Invited)</b> .....	197
	P. Avouris	
	IBM TJ Watson Research Center, USA	
15:00	<b>Single-Mode Performance Analysis for VCSELs</b> .....	199
	S. Odermatt, B. Witzigmann, and S. Eitel <sup>1</sup>	
	ETH Zürich, Switzerland	
	<sup>1</sup> Avalon Photonics, Switzerland	
15:15	<b>MC Simulation of THz Quantum Cascade Lasers</b> .....	201
	C. Jiruschek, M. Manenti <sup>1</sup> , G. Scarpa, P. Lugli	
	TU Munich, Germany	
	<sup>1</sup> University of Rome Tor Vergata, Italy	
15:30	<b>The Driven Two-Level System as an Inverse Problem</b> .....	203
	M. Wenin and W. Pötz	
	University of Graz, Austria	
15:45	<b>DEPFET Sensors, a Test Case to Study 3D Effects</b> .....	205
	K. Gärtner	
	WIAS, Germany	

## Poster Session 2 (16:15-18:15)

### Quantum Transport

- P71 **Shot Noise in Transport Through Quantum Dots: Clean versus Disordered Samples** . 207  
F. Aigner, S. Rotter, and J. Burgdörfer  
TU Wien, Austria
- P72 **Effect of Elastic Processes and Ballistic Recovery in Silicon Nanowire Transistors** .... 209  
D. Basu, M. Gilbert, and S. Banerjee  
University of Texas at Austin, USA
- P73 **A Hierarchy of Quantum-Classical Transport Models in the Framework of the SDM Method** ..... 211  
N. Ben Abdallah, A. Domaingo, M. Mouis<sup>1</sup>, C. Negulescu, and N. Vauchelet  
Universite Paul Sabatier, France  
<sup>1</sup>IMEP, CNRS, France
- P74 **Channel Length Dependence of Tunnel FET Subthreshold Swing** ..... 213  
K. Bhuiwarka, M. Born, M. Schindler, and I. Eisele  
Universität der Bundeswehr, Germany
- P75 **Quantum Corrections to Semiclassical Transport in Nanoscale Devices using Entropy Principles** ..... 215  
J. Bourgade<sup>1</sup>, P. Degond<sup>2</sup>, N. Mauser<sup>1</sup>, and C. Ringhofer<sup>1,3</sup>  
<sup>1</sup>University of Vienna, Austria  
<sup>2</sup>Universite Paul Sabatier, France  
<sup>3</sup>Arizona State University, USA
- P76 **Micromagnetic Simulation of Current-Driven Domain Wall Propagation** ..... 217  
G. Csaba, P. Lugli, L. Ji<sup>1</sup>, and W. Porod<sup>1</sup>  
TU Munich, Germany  
<sup>1</sup>University of Notre Dame, USA
- P77 **Shot Noise in Resonant Tunneling Structures Using Non-Equilibrium Green's Function Calculation** ..... 219  
V.-N. Do, P. Dollfus, and V.-L. Nguyen<sup>1</sup>  
Universite Paris Sud, France  
<sup>1</sup>VAST, Vietnam
- P78 **Inelastic Cotunneling Through an Interacting Quantum Dot with a Quantum Langevin Equation Approach** ..... 221  
B. Dong and H.-L. Cui<sup>1</sup>  
Shanghai Jiaotong University, China  
<sup>1</sup>Stevens Institute of Technology, USA
- P79 **Quantum Transport Using Parallel Computing Techniques** ..... 223  
P. Drouvelis<sup>1,2</sup>, P. Schmelcher<sup>1</sup>, and P. Bastian<sup>2</sup>  
<sup>1</sup>University of Heidelberg, Germany  
<sup>2</sup>Interdisziplinäres Zentrum für Wissenschaftliches Rechnen, Germany
- P80 **Simulation of a Resonant Tunneling Diode Using an Entropic Quantum Drift-Diffusion Model** ..... 225  
P. Degond, S. Gallego, and F. Mehats  
Universite Paul Sabatier, France

P81	<b>Quantum Transport through Nano-Wires with One-Sided Surface Roughness</b> .....	227
	J. Feist, A. Bäcker <sup>1</sup> , R. Ketzmerick <sup>1</sup> , S. Rotter, B. Huckestein <sup>2</sup> , and J. Burgdörfer	
	TU Wien, Austria	
	<sup>1</sup> TU Dresden, Germany	
	<sup>2</sup> Ruhr University, Bochum	
P82	<b>Coupled Mode Space versus Real Space Approach for the Simulation of CNT-FETs</b> .	229
	G. Fiori, G. Iannaccone, and G. Klimeck <sup>1</sup>	
	University of Pisa, Italy	
	<sup>1</sup> Purdue University, USA	
P83	<b>Scattering-Dependence of Bias Dependent Magnetization Switching in Ferromagnetic Resonant Tunneling Diode</b> .....	231
	S. Ganguly, A. MacDonald, L. Register, and S. Banerjee	
	University of Texas at Austin, USA	
P84	<b>Numerical Simulations of Propagation of SCWs in Strained Si/SiGe Heterostructure at 4.2 and 77 K</b> .....	233
	A. Garcia, V. Grimalsky, and E. Gutierrez <sup>1</sup>	
	INAOE, Mexico	
	<sup>1</sup> INTEL SRCM, Mexico	
P85	<b>Phonon Exacerbated Quantum Interference Effects in III-V Nanowire Transistors</b> ...	235
	M. Gilbert	
	University of Texas at Austin, USA	
P86	<b>Quantum-Mechanical Simulation of Multiple-Gate MOSFETs</b> .....	237
	A. Godoy, A. Ruiz-Gallardo, C. Sampedro, and F. Gamiz	
	Universidad de Granada, Spain	
P87	<b>Effects of Non-Parabolicity in Si Quantum Wires</b> .....	239
	F. Gomez-Campos, S. Rodriguez-Bolivar, and J. Carceller	
	Universidad de Granada, Spain	
P88	<b>Boundary Condition at the Junction</b> .....	241
	M. Harmer, B. Pavlov <sup>1</sup> , and A. Yafyasov <sup>2</sup>	
	Massey University Albany, New Zealand	
	<sup>1</sup> The University of Auckland, New Zealand	
	<sup>2</sup> St-Petersburg University, Russia	
P89	<b>Time-Dependent Carrier Transport in Quantum-Dot Array Using NEGF</b> .....	243
	Y. He, D. Hou, X. Liu, G. Du, J. Kang, J. Chen <sup>1</sup> , and R. Han	
	Peking University, China	
	<sup>1</sup> National Institute of Nanotechnology and University of Alberta, Canada	
P90	<b>Investigation of the Nonlinearity Properties of the DC I-V Characteristics of Metal-Insulator-Metal (MIM) Tunnel Diodes with Double-Layer Insulators</b> .....	245
	B. Hegyi, A. Csurgay, and W. Prod <sup>1</sup>	
	Peter Pazmany Catholic University, Hungary	
	<sup>1</sup> University of Notre Dame, USA	
P91	<b>Interband Tunneling Description of Holes in Wurtzite GaN at High Electric Fields</b> ..	247
	M. Hjelm, A. Martinez <sup>1</sup> , H. Nilsson, and U. Lindefelt	
	Mid Sweden University, Sweden	
	<sup>1</sup> University of Glasgow, United Kingdom	

P92	<b>Control of Fano Resonances and the Transmission Phase of a Multi-Terminal Aharonov-Bohm Ring with Three Embedded Quantum Dots</b> .....	249
	E. Hedin, A. Satanin <sup>1</sup> , and Y. Joe	
	Ball State University, USA	
	<sup>1</sup> RAS, Russia	
P93	<b>Indirect Optimal Control of a Qubit</b> .....	251
	H. Jirari and W. Pötz	
	University of Graz, Austria	
P94	<b>Real-Performance Modeling of Carbon Nanotube FETs</b> .....	253
	D. John and D. Pulfrey	
	University of British Columbia, Canada	
P95	<b>VSP – A Multi-Purpose Schrödinger-Poisson Solver for TCAD Applications</b> .....	255
	M. Karner, A. Gehring <sup>1</sup> , S. Holzer, M. Pourfath, M. Wagner, H. Kosina, T. Grasser, and S. Selberherr	
	TU Wien, Austria	
	<sup>1</sup> AMD Saxony, Germany	
P96	<b>Self-Consistent Quantum Transport Theory: Applications and Assessment of Approximate Models</b> .....	257
	T. Kubis and P. Vogl	
	TU Munich, Germany	
P97	<b>Fast Inverse using Nested Dissection for the Non-Equilibrium Green's Function</b> .....	259
	S. Li and E. Darve	
	Stanford University, USA	
P98	<b>3D Simulation of a Silicon Quantum Dot in a Magnetic Field Based on Current Spin Density Functional Theory</b> .....	261
	M. Lisieri, G. Fiori, and G. Iannaccone	
	University of Pisa, Italy	
P99	<b>Comparing Models of Many-Electron Quantum Dynamics</b> .....	263
	M. Lohwasser and N. Mauser	
	University of Vienna, Austria	
P100	<b>Eigenstate Fitting in the k·p Method</b> .....	265
	H. Lopez, A. Chantis <sup>1</sup> , J. Sune, and X. Cartoixa	
	Universitat Autònoma de Barcelona, Spain	
	<sup>1</sup> Arizona State University, USA	
P101	<b>Transport Calculation of Semiconductor Nanowires Coupled to Quantum Well Reservoirs</b> .....	267
	M. Luisier, G. Klimeck <sup>1</sup> , A. Schenk, and W. Fichtner	
	ETH Zürich, Switzerland	
	<sup>1</sup> Purdue University, USA	
P102	<b>Tunneling Enhancement through a Barrier Surrounded by a Mesoscopic Cavity</b> .....	269
	M. Macucci and P. Marconcini	
	University of Pisa, Italy	
P103	<b>Modeling the Inelastic Scattering Effect on the Resonant Tunneling Current</b> .....	271
	B. Majkusiak	
	Warsaw University of Technology, Poland	

P104	<b>Tight-Binding and k-p Methods in Carbon Nanotubes: Comparison, Results, and Improvements</b> .....	273
	P.Marconcini and M. Macucci University of Pisa, Italy	
P105	<b>Developing a Full 3D NEGF Simulator with Random Dopant and Interface Roughness</b>	275
	A. Martinez, J. Barker, M. Anantram <sup>1</sup> , A. Svizhenko <sup>1</sup> , and A. Asenov University of Glasgow, United Kingdom <sup>1</sup> NASA Ames Research Center, USA	
P106	<b>Simulation of High-Field Magnetotransport in Non-Planar 2D Electron Systems</b> .....	277
	G. Meyer and I. Knezevic University of Wisconsin at Madison, USA	
P107	<b>Numerical Simulation of Hole Transport in Silicon Nanostructures</b> .....	279
	H. Minari, H. Takeda, M. Okamoto, and N. Mori Osaka University, Japan	
P108	<b>Energy Dispersion Relations for Holes in Silicon Quantum Wells and Quantum Wires</b>	281
	V. Mitin, N. Vagidov, M. Luisier <sup>1</sup> , and G. Klimeck <sup>2</sup> University at Buffalo SUNY, USA <sup>1</sup> ETH Zürich, Switzerland <sup>2</sup> Purdue University, USA	
P109	<b>Simulation of the Rashba Effect in a Multiband Quantum Structure</b> .....	283
	O. Morandi and L. Demeio <sup>1</sup> University of Florence, Italy <sup>1</sup> Universita Politecnica delle Marche, Italy	
P110	<b>Ultrafast Wigner Transport in Quantum Wires</b> .....	285
	M. Nedjalkov, D. Vasileska <sup>1</sup> , E. Atanassov <sup>2</sup> , and V. Palankovski TU Wien, Austria <sup>1</sup> Arizona State University, USA <sup>2</sup> Bulgarian Academy of Sciences, Bulgaria	
P111	<b>A Many-Particle Quantum-Trajectory Approach for Modeling Electron Transport and its Correlations in Nanoscale Devices</b> .....	287
	X. Oriols Universitat Autònoma de Barcelona, Spain	
P112	<b>Computational Study of the Schottky Barrier at the Metal-Carbon Nanotube Contact</b>	289
	N. Park and S. Hong <sup>1</sup> Dankook University, Korea <sup>1</sup> Sejong University, Korea	
P113	<b>Tunneling-CNTFETs</b> .....	291
	M. Pourfath, H. Kosina, and S. Selberherr TU Wien, Austria	
P114	<b>Conductance of Nanowires</b> .....	293
	A. Raichura, M. Stroschio, and M. Dutta University of Illinois at Chicago, USA	
P115	<b>Extension of the <math>R</math>-<math>\Sigma</math> Method to Any Order</b> .....	295
	M. Rudan, E. Gnani, S. Reggiani, and G. Baccarani University of Bologna, Italy	

P116	<b>Quantum Simulation of Silicon Nanowire FETs: Ballistic Transport and Corner Effects</b> .....	297
	M. Shin Information and Communications University, Korea	
P117	<b>Quantized Conductance Without Reservoirs: Method of the Non-Equilibrium Statistical Operator</b> .....	299
	B. Soree and W. Magnus IMEC, Belgium	
P118	<b>Validity of the Effective Mass Approximation in Silicon and Germanium Inversion Layers</b> .....	301
	J. Van der Steen <sup>1</sup> , D. Esseni, P. Palestri, and L. Selmi University of Udine, Italy <sup>1</sup> University of Twente, The Netherlands	
P119	<b>Simulation of Magnetization Reversal and Domainwall Trapping in Submicron NiFe Wires with Different Wire Geometries</b> .....	303
	E. Varga <sup>1</sup> , A. Imre, L. Ji, and W. Porod Pazmany Peter Catholic University, Hungary <sup>1</sup> University of Notre Dame, USA	
P120	<b>The NEGF Simulation of the RTD Bistability</b> .....	305
	J. Voves, T. Trebicky, and R. Jackiv The Czech Technical University, Czech Republic	
P121	<b>I-V Characteristics and Nonclassical Behavior in Networks of Small Metal Clusters</b> ..	307
	H. Zhang, D. Mautes, and U. Hartmann University of Saarbrücken, Germany	
<b>Optoelectronic Devices</b>		
P122	<b>Perimeter Recombination in Thin Film Solar Cells</b> .....	309
	A. Belghachi University of Bechar, Algeria	
P123	<b>Study of the Light Intensity Threshold for Simulated PIN Photodiode under Proton Radiation</b> .....	311
	M. Cappelletti <sup>1</sup> , E. Peltzer y Blanca <sup>1,2</sup> <sup>1</sup> Universidad Nacional de La Plata, Argentina <sup>2</sup> IFLYSIB, Argentina	
P124	<b>Determination of Single Mode Condition for Rib Waveguides with Large Cross Section by Finite Element Analysis</b> .....	313
	M. De Laurentis, A. Irace, and G. Breglio Universita degli Studi di Napoli "Federico II", Italy	
P125	<b>Improved Simulation of VCSEL Distributed Bragg Reflectors</b> .....	315
	F. De Leonardis, V. Passaro, and F. Magno Politecnico di Bari, Italy	
P126	<b>Scattering Effect in Optical Microring Resonators</b> .....	317
	F. De Leonardis and V. Passaro Politecnico di Bari, Italy	

P127	<b>Simulation of a High Speed Interferometer Optical Modulator in Polymer Materials</b> .	319
	F. Dell’Olio, V. Passaro, and F. De Leonardis Politecnico di Bari, Italy	
P128	<b>Blinking of Colloidal Semiconductor Quantum Dots: Blinking Mechanisms</b> .....	321
	M. Dutta, M. Stroschio, and B. West <sup>1</sup> University of Illinois at Chicago, USA <sup>1</sup> Army Research Office, USA	
P129	<b>Monte Carlo Modeling of the X-Valley Leakage in Quantum Cascade Lasers</b> .....	323
	X. Gao, D. Botez, and I. Knezevic University of Wisconsin at Madison, USA	
P130	<b>A Parallel MCTDHF Code for Few-Electron Systems with Time-Dependent External Field</b> .....	325
	G. Jordan, J. Caillat, V. Putz, C. Ede, and A. Scrinzi TU Wien, Austria	
P131	<b>Input and Intrinsic Device Modeling of VCSELs</b> .....	327
	K. Minoglou <sup>1</sup> , E. Kyriakis-Bitaros <sup>1,2</sup> , D. Syvridis <sup>3</sup> , and G. Halkias <sup>1</sup> <sup>1</sup> NCSR Demokritos, Greece <sup>2</sup> TEI of Pieraus, Greece <sup>3</sup> University of Athens, Greece	
P132	<b>A Two Dimensional Analytical Model for Finger Photodiodes</b> .....	329
	T. Naeve and P. Seegebrecht Christian-Albrechts University of Kiel, Germany	
P133	<b>Atomistic Modeling of GaN Based Nanowires</b> .....	331
	L. Prokopova, M. Persson, M. Povolotskyi, M. Auf Der Maur, and A. Di Carlo University of Rome Tor Vergata, Italy	
P134	<b>Plasma Effects in Lateral Schottky Junction Terahertz Detector: Models and Characteristics</b> .....	333
	V. Ryzhii, A. Satou, and M. Shur <sup>1</sup> University of Aizu, Japan <sup>1</sup> Rensselaer Polytechnic Institute, USA	
P135	<b>New Scales: Properties of Nanostructures in the Femtosecond Regime</b> .....	335
	A. Vernes and P. Weinberger TU Wien, Austria	
P136	<b>Spontaneous Polarization Effects in Nanoscale Wurtzite Structures</b> .....	337
	T. Yamanaka, M. Dutta, and M. Stroschio University of Illinois at Chicago, USA	

---

**Saturday, 27 May 2006**

---

## **Session 7: Nanotubes and Nanowires**

**Chairperson: S. Laux**

- 8:30 **Modeling and Numerical Challenges in Nanoscale Device Engineering** (Invited) ..... 339  
E. Polizzi  
University of Massachusetts at Amherst, USA
- 9:00 **Electronic Transport Properties of CNT Fibers** ..... 341  
H. Mehrez and M. Anantram  
NASA Ames Research Center, USA
- 9:15 **Non-Equilibrium Green's Function (NEGF) Simulation of Metallic Carbon Nanotube Transistors: Impact of Vacancy Defect** ..... 343  
N. Neophytou, S. Ahmed, and G. Klimeck  
Purdue University, USA
- 9:30 **Dissipative Transport in CNTFETs** ..... 345  
M. Pourfath, H. Kosina, and S. Selberherr  
TU Wien, Austria
- 9:45 **Influence of Hot Phonons on the Transport Properties of Single-Wall Carbon Nanotubes** ..... 347  
C. Auer, C. Ertler, and F. Schürer  
TU Graz, Austria
- 10:00 **Electronic and Transport Properties of Silicon Nanowires** ..... 349  
F. Sacconi, M. Persson, M. Povolotskyi, L. Latessa, A. Pecchia, B. Aradi<sup>1</sup>, T. Frauenheim<sup>1,2</sup>, and A. Di Carlo, A. Gagliardi<sup>1</sup>,  
University of Rome, Italy  
<sup>1</sup>University of Paderborn, Germany  
<sup>2</sup>University of Bremen, Germany

## **Session 8: Molecular Devices and Ab-Initio Methods**

**Chairperson: P. Lugli**

- 10:45 **Beyond the Local Density Approximation** (Invited) ..... 351  
G. Kresse and J. Hafner  
University of Vienna, Austria
- 11:15 **Heat Dissipation and Non-Equilibrium Phonon Distributions in Molecular Devices** .. 353  
A. Pecchia, A. Gagliardi<sup>1</sup>, T. Frauenheim<sup>1</sup>, and A. Di Carlo  
University of Rome Tor Vergata, Italy  
<sup>1</sup>University of Paderborn, Germany

11:30	<b>Tight-Binding Calculations of Ge-Nanowire Bandstructures</b> .....	355
	M. Bescond <sup>1</sup> , N. Cavassilas, K. Nehari, and M. Lannoo L2MP, CNRS, France <sup>1</sup> IMEP, CNRS, France	
11:45	<b>GW Corrections of Energy Bandgaps for Coherent Transport Across Molecular Junctions</b> .....	357
	A. Pecchia, A. Gagliardi <sup>1</sup> , T. Niehaus <sup>1</sup> , T. Frauenheim <sup>1</sup> , and A. Di Carlo University of Rome Tor Vergata, Italy <sup>1</sup> University of Paderborn, Germany	
12:00	<b>Multi-Scale Approaches in Computational Materials Science</b> .....	359
	P. Weinberger TU Wien, Austria	
12:15	<b>Convergence of Density Functional Iterative Procedures with a Newton-Raphson Algorithm</b> .....	361
	J. Jerome, L. Ye, P. Sievert, I. Kim, and A. Freeman Northwestern University, USA	

## Session 9: Biological Systems

Chairperson: M. Saraniti

14:30	<b>Simulating Biological Ion Channels using Computational Electronics Methods</b> (Invited) .....	363
	K. Hess University of Illinois at Urbana, USA	
15:00	<b>Shockley-Ramo Theorem Measures Conformation Changes of Ion Channels and Proteins</b> .....	365
	B. Eisenberg <sup>1,2</sup> and W. Nonner <sup>1</sup> <sup>1</sup> Rush University and Argonne National Lab, USA <sup>2</sup> University of Miami, USA	
15:15	<b>Continuum versus Particle Simulation of Model Nano-Pores</b> .....	367
	C. Millar, S. Roy, O. Beckstein <sup>1</sup> , M. Sansom <sup>1</sup> , and A. Asenov University of Glasgow, United Kingdom <sup>1</sup> University of Oxford, United Kingdom	
15:30	<b>Exploring Free Energy Profiles Through Ion Channels: Comparison on a Test Case</b>	369
	E. Piccinini, M. Ceccarelli <sup>1</sup> , F. Affinito, R. Brunetti, and C. Jacoboni CNR-INFN, Italy <sup>1</sup> University of Cagliari, Italy	
15:45	<b>Improving the Efficiency of BD Algorithms for Biological Systems Simulations</b> .....	371
	D. Marreiro <sup>1</sup> , Y. Tang <sup>2</sup> , S. Aboud <sup>1</sup> , E. Jakobsson <sup>2,3</sup> , and M. Saraniti <sup>1,3</sup> <sup>1</sup> Illinois Institute of Technology, USA <sup>2</sup> University of Illinois at Urbana, USA <sup>3</sup> National Center for Design of Biometric Nanoconductors, USA	

# TABLE OF CONTENTS

## Companion Workshop: Modeling of Reliability Issues

---

Wednesday, 24 May 2006

---

09:00	<b>Welcome</b> T. Grasser	
09:05	<b>Negative Bias Temperature Instability: What Is It and Why Is It a Problem?</b> .....	373
	D. Schroder; Arizona State University, USA	
09:40	<b>On Prospects of Computational Modeling of Reliability Phenomena</b> .....	375
	M. Alam; Purdue University, USA	
10:15	<b>Probing Negative Bias Temperature Instability using a Continuum Numerical Framework: Physics to Real World Operation</b> .....	377
	S. Chakravarthi; Texas Instruments, USA	
11:10	<b>NBTI Product Level Reliability Challenges</b> .....	379
	H. Puchner; Cypress Semiconductors, USA	
11:45	<b>Negative Bias Temperature Instabilities in HfSiO(N)-Based MOSFETs: Electrical Characterization and Modeling</b> .....	381
	M. Houssa; IMEC, Belgium	
12:20	<b>Physical Modeling of Negative Bias Temperature Instabilities for Predictive Extrapolation</b> .....	383
	V. Huard; Philips Semiconductors, Crolles, France	
14:00	<b>Reliability Issues in Power MOSFETs</b> .....	385
	M. Pölzl; Infineon Technologies, Villach, Austria	
14:35	<b>Deep Level Defects Involved in MOS Device Instabilities</b> .....	387
	P. Lenahan; Pennsylvania State University, USA	
15:10	<b>Hydrogen Transport in Doped and Undoped Disordered Silicon</b> .....	389
	N. Nickel; Hahn-Meitner-Institut, Berlin, Germany	
16:00	<b>First-Principles Approach to the Reliability Issues of MOS Gate Oxides</b> .....	391
	T. Maruizumi; Musashi Institute of Technology, Tokyo, Japan	
16:35	<b>Hydrogen in MOSFETs – The Good, the Bad, and the Ugly</b> .....	393
	S. Pantelides; Vanderbilt University, USA	
	<b>Author Index</b> .....	395

---

# Calculating Future CMOS and CMOS Future - - Where Industry Needs Academia

T. Skotnicki & H. Jaouen  
STMicroelectronics, 850 rue Jean Monnet, 38926 Crolles, France  
e-mail: thomas.skotnicki@st.com

## INTRODUCTION

During the last 30 years the number of transistors per chip has increased X100 000, that is even more (10 times) than the predictions of Moore's laws, see Fig. 1. The transistor has decreased X320, bringing its feature dimensions close to the atomic resolution scale, see Fig. 2. Consequently, the now-a-day circuits present a tremendous complexity of NANO-objects, in the order of  $1e9$  per chip. All of those objects (mainly transistors) are governed to large extend by quantum solid-state physics. Their fabrication to be controlled also requires the more and more sophisticated models and tools. In this paper we will review the main issues and needs the IC industry encounters with this respect.

## FUTURE CMOS

The time constant for introduction of new technologies in CMOS industry may go up to 10 years, especially if development of specific equipment is involved. Therefore, the CMOS Technology Roadmap is a key element permitting the entire industry anticipation and consequently a smooth pursuit of the Moore's laws. Predictive modelling and simulation are the main instruments for the conception of the Roadmap. However, the challenge for being predictive is very high today. This is because after 40 years of domination of the planar bulk transistor structure, starting from years 2000 a multitude of non-classical structures, non-classical materials, and non-classical technologies has come to play, Fig. 3. In addition, the physics governing the functioning of these devices changes. The device electrostatics changes (due to smallness of geometry), transport becomes ballistic or semi-ballistic, the quantum and confinement effects grow, mobility is strongly affected by mechanical strain (intentional or non-intentional), etc, etc. All these phenomena, being long time objects of academic studies, now become an engineer every-day task. Therefore, we not only need reliable and

sophisticated models but we also need the models to be simple and implemented in a very different to traditional environment. An example of such can be the MASTAR [1] tool that in spite of having implemented sophisticated transport models, see Fig. 4, as well as confinement and strain physics, guaranties a push-button solutions to process and device engineers. Thanks to that hundreds of hypothesis and options could have been quickly evaluated with MASTAR when designing the ITRS CMOS roadmap.

## CMOS FUTURE – BEYOND CMOS ?

The continuous scaling of CMOS transistors hits atomic resolution, thus menacing the CMOS future. As illustrated in Fig. 5, in an 8nm transistor (already scheduled in the ITRS roadmap) merely a few dopants will be present under the gate. This will expose the transistor characteristics to large statistical fluctuations. The impact of the latter is simulated in Fig. 6, showing disappearing SNM (static noise margin) of SRAM cells. More generally, phenomena that used to be well described by continuum statistical models, exhibit more and more random and singular character. Still another issue arises from the fact that scaling reduces the volume of the materials constituting the active device body. Device properties thus become dominated by interfaces. Electrochemical properties of interfaces being different from volume ones, new models and new simulation approaches are needed. Whereas in the past continuum models used to satisfy process as well as electrical simulations, today MonteCarlo, Molecular Dynamics and Ab-initio calculations have to enter industrial R&D labs, see Fig. 9.

## CONCLUSION

The demand for modeling and simulation is today growing exponentially and could also be qualified as a Moore's law.

REFERENCES

[1] MASTAR tool is freely available from the ITRS 2005 web site, <http://public.itrs.net/HomeStart.htm#Models>

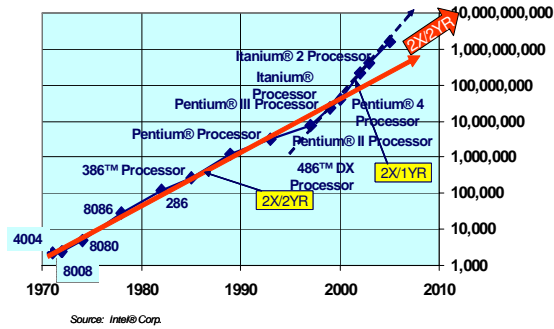


Fig. 1 Experimental CMOS transistors are hitting atomic resolution. Background graph copied from ITRS 2003.

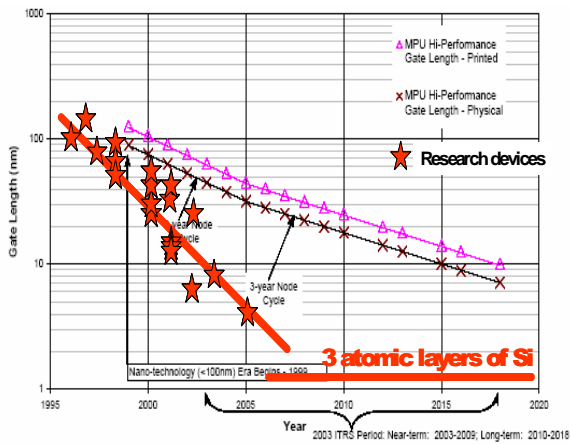


Fig. 2. Experimental CMOS transistors are hitting atomic resolution. Background graph copied from ITRS 2003.

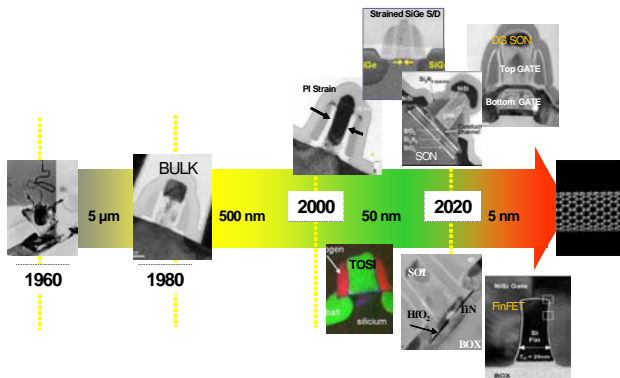


Fig. 3. Burst of non-classical CMOS device structures.

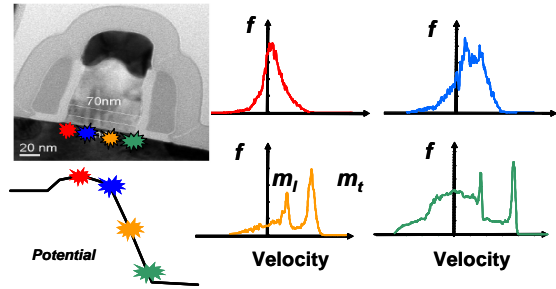


Fig. 4. Ballistic and semi-ballistic transport model by E. Fuchs, implemented in MASTAR.

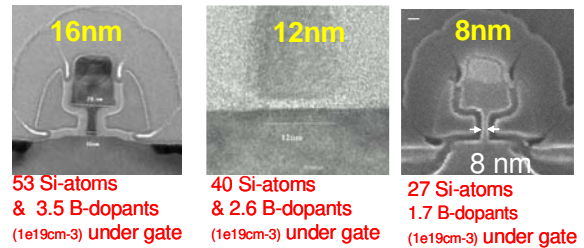


Fig. 5. Continues scaling reveals granularity of the matter.

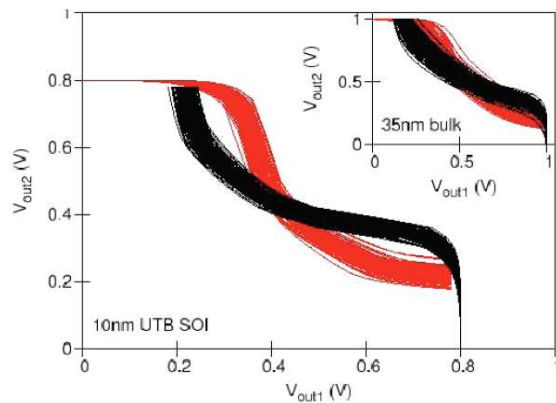


Fig. 6. Vanishing SRAM functionality with 35nm Bulk technology, and its recovering with UTB SOI, A. Asenov, SINANO Summer School, Glasgow 2005.

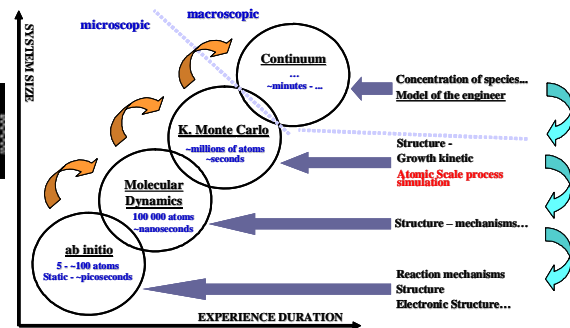


Fig. 7. Evolution of models used in IC industrial R&D.

# A Novel Approach to Three-Dimensional Semiconductor Process Simulation: Application to Thermal Oxidation

Vasily Suvorov, Andreas Hoessinger and Zoran Djurić  
Silvaco Technology Center, Compass Point, St Ives, Cambridgeshire, PE27 5JL, UK.

## INTRODUCTION

One of the major issues in three-dimensional semiconductor processes simulation is the problem of moving interfaces. The standard approach involves very complex and often unstable mesh generation algorithms. Alternatively, we applied the level set method on fixed Cartesian meshes [1], where the meshing algorithms are not needed, and all differential equations can be solved by the standard finite-difference methods.

However, there are two problems associated with this methodology: approximating of general-type boundary conditions near the interface and handling of a big scale ratio of sizes in complex structures. In the last decades a considerable progress has been achieved in resolving both issues (e.g. [2], [3], [4]). In our development we use our original in-house numerical method, the method described in [3] and the concept of Adaptive Mesh Refinement (AMR) [4]. The above principles are cornerstones of a software package Victory, Silvaco's three-dimensional process simulation framework. In this work we demonstrate Victory's capability to simulate numerically the most demanding process, namely thermal oxidation.

## MODELLING OF THERMAL OXIDATION

Three different processes occur simultaneously during the thermal oxidation: diffusion of oxygen, a chemical reaction at oxide/silicon interface and a volume expansion of the newly formed oxide. The aim of the modelling and simulation is to explain and predict the resulting shape of oxide and mechanical stresses developed in a structure during the process. Our physical model assumes Newtonian viscous constitutive model for oxide and nitride (valid for relatively high temperatures).

The mathematical model comprises three different sets of equations: i) equation for level-set function to track moving interfaces; ii) diffusion equation to describe oxidant behaviour; iii) the system for incompressible Navier-Stokes equations for creeping flow. The first set also constitutes a core of the etching/deposition module.

For illustration purposes we have modeled three typical oxidation process steps: locos, polysilicon oxidation and trench oxidation. Figures 4 and 5 demonstrate two different types of 3D bird's beak effects obtained by rather long time oxidation which is the numerically most critical application.

Moreover Fig. 6 shows iso-surfaces of compressive (blue) and tensile (red) mechanical stresses near the silicon surface obtained during trench oxidation. The stresses resulting from locos and reoxidation will be presented in a full version of the paper.

## CONCLUSION

The state-of-the-art finite-difference methods for the simulation of thermal oxidation is presented which can handle arbitrary complex geometries. This enables us to design a new generation process modelling tool that avoids meshing/re-meshing procedures.

## REFERENCES

- [1] J. A. Sethian, *Level set methods and fast marching methods*, Cambridge University Press (1999).
- [2] S. Deng, K. Ito, and Z. Li, *Three-dimensional elliptic solvers for interface problems and applications*, J. Comp. Phys. **184**, 215 (2003).
- [3] M. Sussman, P. Smereka, and S. Osher, *A level set approach for computing solutions to incompressible two-phase flow*, J. Comp. Phys. **114**, 146 (1994).
- [4] P. Colella et al. *Chombo software package for AMR applications: design document*, available at <http://seesar.lbl.gov/anag/chombo/>.

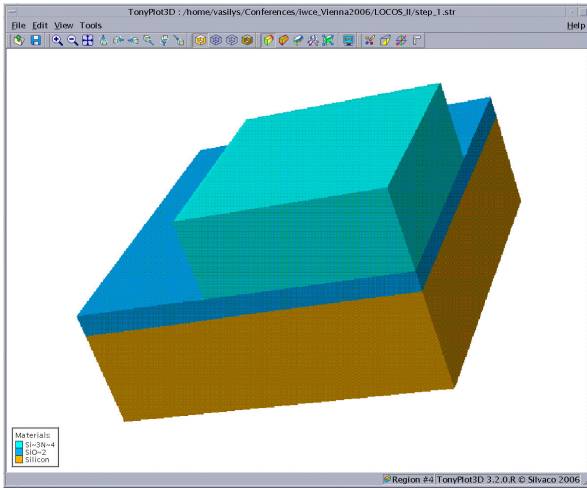


Fig. 1. Input structure for the locos process built by Victory's etching/deposition module

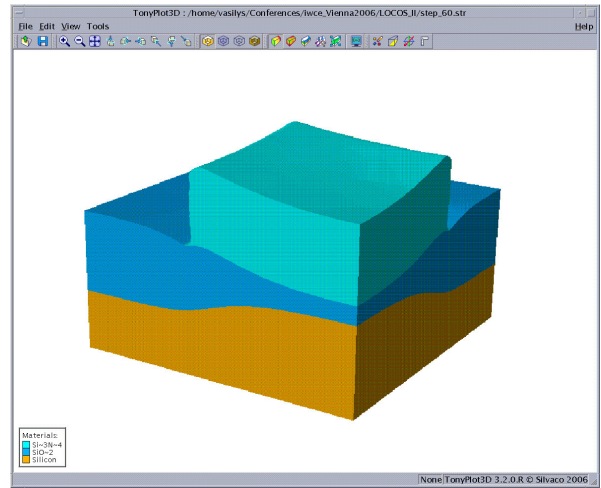


Fig. 4. Locos structure after 10 min wet oxidation at  $T=1000^{\circ}\text{C}$

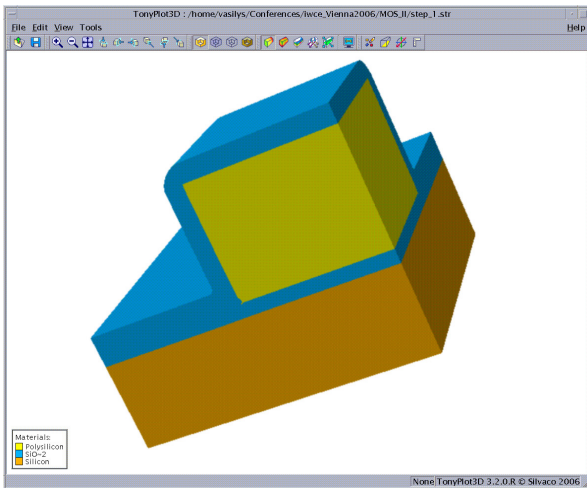


Fig. 2. Input structure for reoxidation of two oxidizable regions

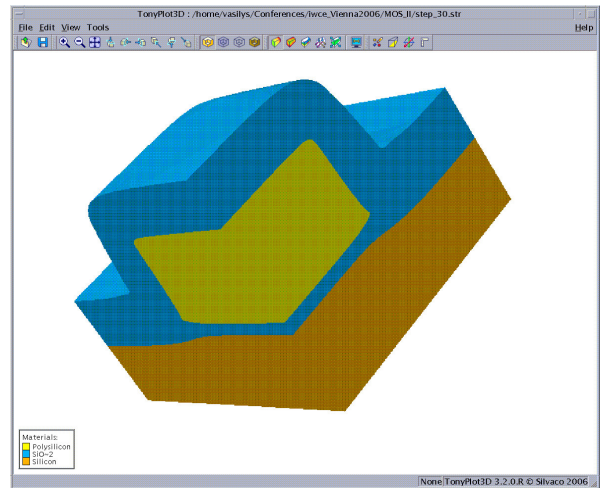


Fig. 5. Shape of the device after 5 min reoxidation of the polysilicon and the silicon substrate

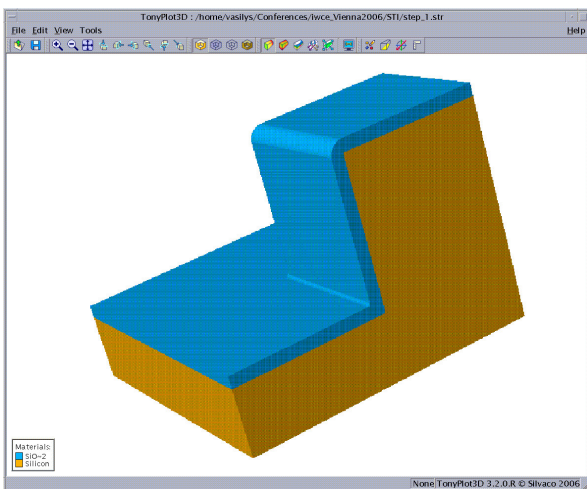


Fig. 3. Input structure for trench oxidation generated by the etching/deposition module

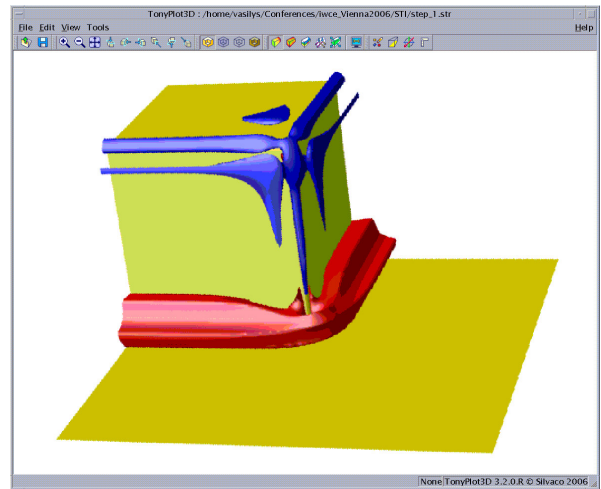


Fig. 6. Iso-surfaces of compressive pressure  $P = -5400$  MPa (blue) and tensile one  $P = 13200$  MPa (red) in oxide. Yellow surface is the oxide/silicon interface in the trench

# A 3D Moving Grid Algorithm for Process Simulation

N. Strecker, D. Richards

Synopsys Inc., 700 E. Middlefield Road, Mountain View, CA 94043  
e-mail: norbert.strecker@synopsys.com, david.richards@synopsys.com

During the simulation of 3D oxidation and similar processes computation of geometry and topology changes requires construction of a valid 3D mesh at every time step.

During the past year significant progress has been made to improve the moving grid algorithm used in Synopsys' Sentaurus Process.

For each oxidation time step the oxygen diffusion/reaction and stress equations are solved in the appropriate regions of a static boundary fitted all-tetrahedron mesh.

The equations for the point defect and dopant diffusion are solved on a moving grid, using several smaller time steps if necessary. The displacements computed from the stress equations are used to deform the mesh elements and the geometry.

For each mesh element a cubic equation is solved to determine the time when the element degenerates. The minimum of these times for all mesh elements is used as grid limited step for the grid update and for solution of the diffusion equations. The box weights for the old and new positions of the mesh points are computed and used for the solution of the diffusion equations. During the diffusion step the mesh topology remains fixed.

This approach, which is very similar to the one used in the 2D simulator TSUPREM-IV eliminates the need for convective terms in the equations and only requires accounting for the discontinuous velocities at the reaction front.

At the end of each time step, a grid cleanup step is performed. Short edges and poorly shaped or small volume elements are removed. Several methods to remove such elements have been implemented:

- Face swapping
- Moving one node to the location of another
- Removing elements by breaking edges or faces for the degenerate cases of a node close to an edge or face and the case of two

edges crossing at close proximity

- Re-assigning volume elements to another region.
- Local Laplacean smoothing

After removing poorly shaped mesh elements and too short edges, a refinement algorithm is used that checks for long edges "perpendicular" to a material interface.

With the given set of methods it is still not always possible to eliminate all elements of poor shape or small volume. As a backup method for these cases a global Delaunay reconnection algorithm is used, that allows constructing a new mesh from the set of all triangles on the material interfaces and the external surface and from the cloud of all (displaced) internal points that do not belong to a "bad" tetrahedron.

While the performance and robustness of the moving grid algorithm has been enhanced sufficiently during the past year, current and future work will be focused on the reduction of the geometric noise near moving ridges and corners and on maintaining a "nice" tessellation where an initially sharp ridge or corner becomes rounded e.g., along one axis. The identification of the root cause for such problems has been difficult due to the complex interaction of mesh element quality, computation method of box weights, iterative solution of large systems of equations, displacement of mesh points and local removal of "bad" elements. Test cases simulating isotropic deposition and etching with the same moving grid algorithm have been used to study the evolution and movement of such ridges and corners in the presence of "ideal" analytic velocity fields.

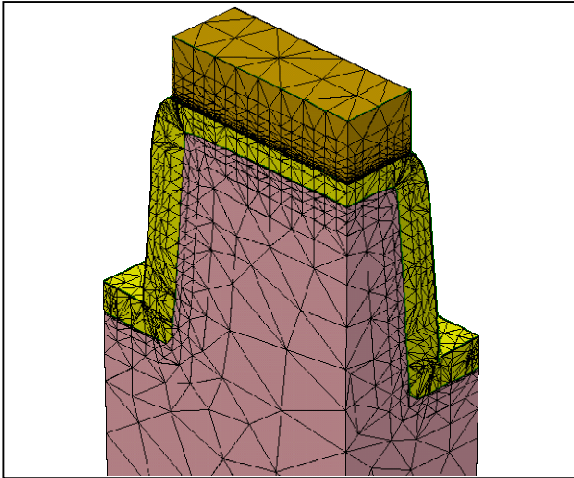


Fig. 1. Final mesh and structure after STI liner oxidation

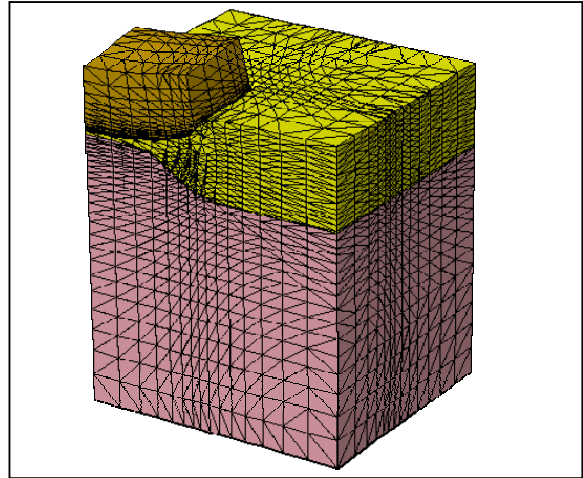


Fig. 4. Final mesh after long, conventional Locos simulation

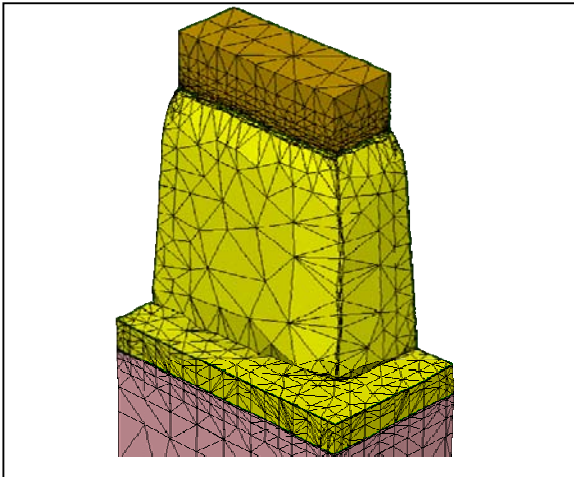


Fig. 2. 3D STI liner oxidation (opposite view)

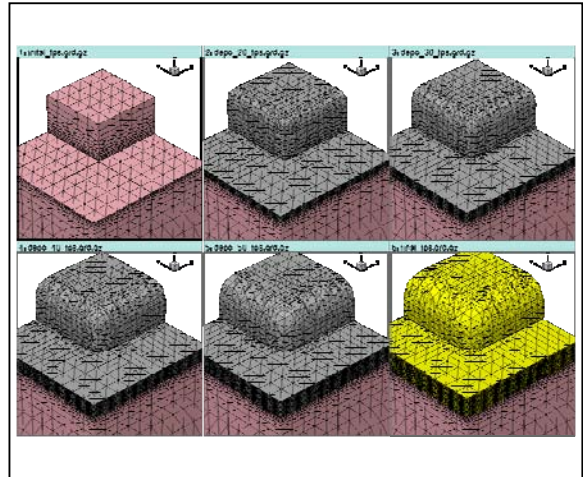


Fig. 5. Simulation of 3D isotropic deposition – test case

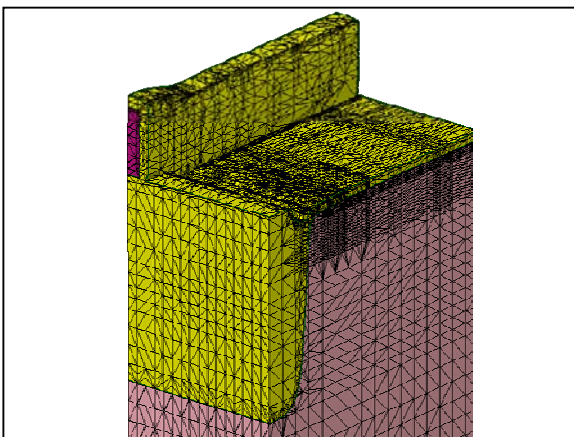


Fig. 3. Final mesh after 3D Poly gate re-oxidation

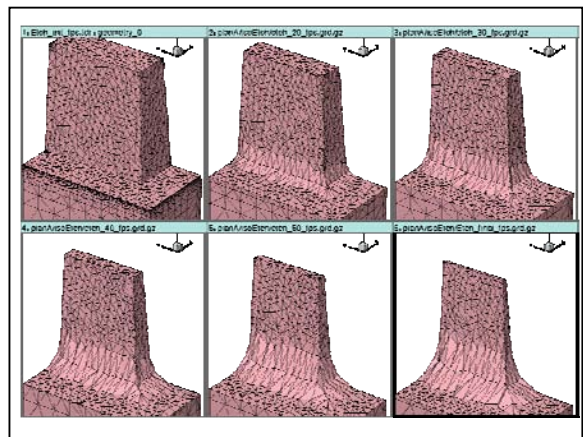


Fig. 6. Simulation of 3D isotropic etching – test case

# Kinetic-Energy Transport Equation for the Modeling of Ballistic MOSFETs

Ting-wei Tang and Parmijit Samra  
 Dept. of ECE, University of Massachusetts, Amherst  
 Amherst, Massachusetts 01003 USA  
 e-mail: ttang@ecs.umass.edu

## INTRODUCTION

As MOS devices are scaled down to the sub-30nm regime, carrier transport may approach the ballistic limit. It has long been recognized that ballistic transport is limited by the barrier height [1]. Natori [2] has applied Landauer's transmission method to simulate ballistic MOSFETs by assuming a Fermi-Dirac energy distribution function. The Purdue group has extended McKelvey's one-flux method to include accelerating fields and obtained a ballistic drift-diffusion equation [3]. Here, we present yet another method of describing pure ballistic transport in nanoscale MOSFETs.

## KINETIC-ENERGY TRANSPORT EQUATION

We utilize the first two moment equations of the collisionless Boltzmann transport equation in one-dimension, namely,

$$\frac{d}{dx}(nv_x) = 0, \quad (1)$$

and

$$\frac{d}{dx}(nU_{xx}) + nq\mathcal{E}_x = 0, \quad (2)$$

where the stress tensor  $U_{xx}$  for parabolic bands is assumed to be given by  $\gamma k_B T + m^* v_x^2$ , and  $\gamma$  is a dimensionless parameter. From (1) and (2) one can obtain

$$n = \text{const.} \exp\left(-\frac{E_c + \eta}{\gamma k_B T}\right) \quad (3)$$

and

$$\left[1 - \frac{\gamma}{2(\eta/k_B T)}\right] \frac{d}{dx} \left(\frac{\eta}{k_B T}\right) + \frac{1}{k_B T} \frac{dE_c}{dx} = 0, \quad (4)$$

where  $\eta = \frac{1}{2} m^* v_x^2$  represents the kinetic energy (K.E.) and  $E_c$  represents the conduction band edge.

The transport equation (4) for  $\eta$  has two solutions,  $\eta_+$  and  $\eta_-$ , representing the two-stream K.E. of the carriers injected from the source and the drain, respectively. The corresponding carrier density in (3) is determined by the boundary conditions at the source and drain contacts.

## SIMULATION RESULTS AND DISCUSSION

We have applied the above K.E. transport equation to the simulation of a cylindrical gate-all-around (G-A-A) SOI MOSFET, shown in Fig. 1. Fig. 2 shows the potential barrier for  $\gamma = 2/\pi$ ,  $V_{gs} = 1.5V$  and  $V_{ds} = 1.0V$ . The negative of kinetic energies,  $\eta_+$  and  $\eta_-$ , are shown in Fig. 3. Fig. 4 shows the velocity of carriers injected from the source ( $v^+$ ) and drain ( $v^-$ ), as well as the average velocity of the carriers. Shown in Fig. 5 are the corresponding carrier densities. In Fig. 6, I-V curves of the ballistic G-A-A SOI MOSFET with  $\gamma = 2/\pi$  and  $\gamma = 1$  are compared to that of drift-diffusion transport. Furthermore, underlying approximations and limitations of this approach will be discussed and compared with that of [3].

## CONCLUSION

The two-stream K.E. transport equation can be used to model ballistic MOSFETs. The drain current in pure ballistic transport is increased by a factor of more than 50%, in agreement with most published results.

## REFERENCES

- [1] W. Frensley, IEEE Trans. ED, **30**, 1619 (1983).
- [2] K. Natori, J. Appl. Phys. **76**, 4879 (1994).
- [3] J. Rhew and M. Lundstrom, J. Appl. Phys. **92**, 5196 (2002).

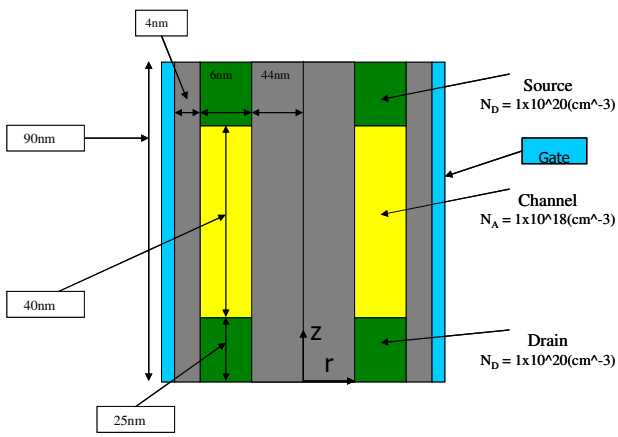


Fig. 1. Cross-section of cylindrical G-A-A SOI MOSFET

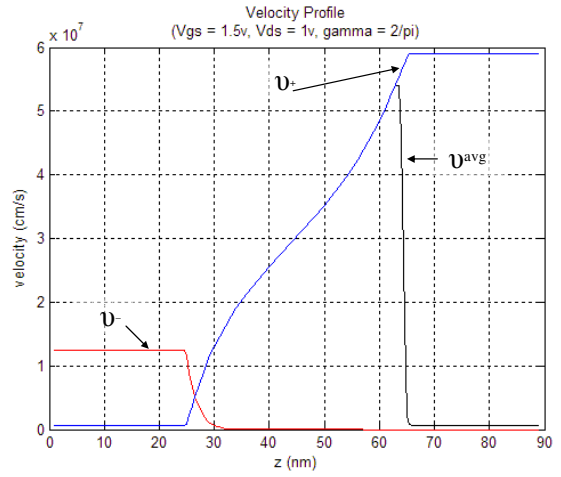


Fig. 4. Two-stream velocities for G-A-A SOI MOSFET

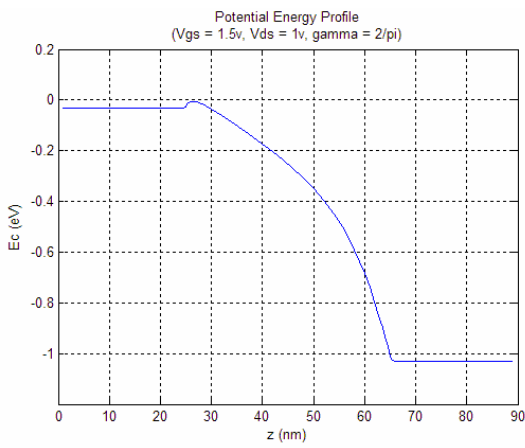


Fig. 2. Potential Energy barrier for G-A-A SOI MOSFET

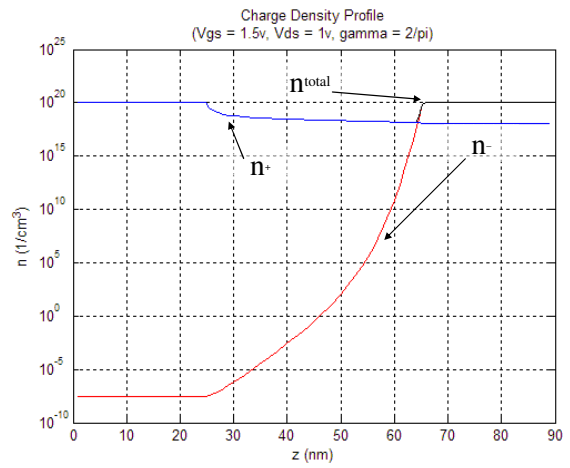


Fig. 5. Two-stream charge densities for G-A-A SOI MOSFET

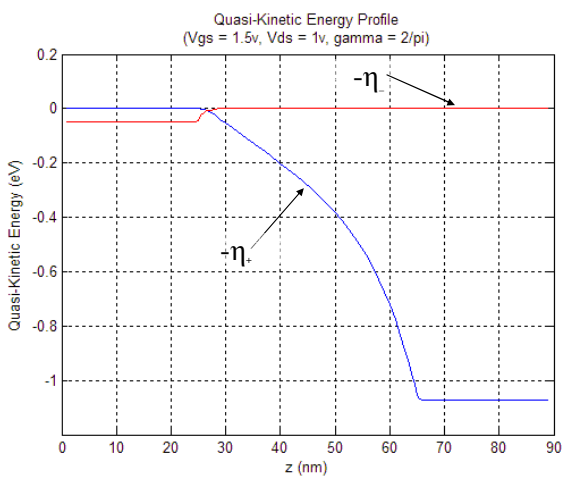


Fig. 3. Two-stream kinetic energies for G-A-A SOI MOSFET

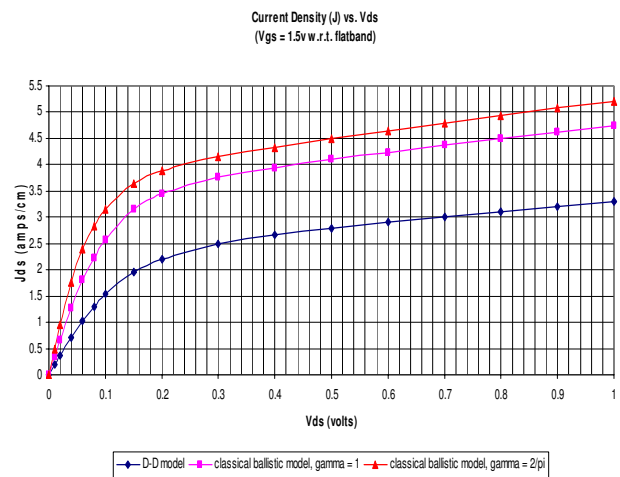


Fig. 6. I-V curves for G-A-A SOI MOSFET

# Multi-Dimensional Semiconductor Tunneling in Density-Gradient Theory

M.G. Ancona

Code 6876, Naval Research Laboratory, Washington, DC, USA  
[ancona@estd.nrl.navy.mil](mailto:ancona@estd.nrl.navy.mil)

Density-gradient (DG) theory has come into wide use as a physically well-founded approximate treatment of quantum confinement effects that is well suited for engineering-oriented applications including in multi-dimensions. DG theory has also been applied successfully to quantum mechanical tunneling [1], however, this application has received far less attention in part because it has been studied mostly in one dimension where direct quantum mechanical methods (e.g., using the Keldysh formalism) are a realistic alternative. At the last IWCE workshop I presented a DG treatment of multi-dimensional tunneling from ideal metals [2]. This research direction is continued here with a first DG analysis of direct, elastic tunneling from semiconductors in multi-dimensions.

The previous DG treatment of multi-dimensional tunneling from ideal metals [2] was simplified by the fact that, with the solution in the metal known, one could focus entirely on the electron transport in the barrier. The case of semiconductor tunneling is harder of course because one must analyze the transport in the semiconductors as well as in the barrier. In this regard, an important aspect of the approximate DG approach is its unified character: Essentially the same basic partial differential equations are applied inside the semiconductors and in the barrier, and these equations are solved simultaneously without involving eigenvalue problems or self-consistency iterations. The chief differences between the transport equations in the semiconductors and in the barrier arise from the relative importance of scattering. In the semiconductors the transport can be regarded as dominated by scattering so that the electron population tends to act as a single gas obeying a quantum-corrected drift-diffusion-like description, whereas in the barrier scattering is neglected ("elastic" tunneling) and, among other things, this implies that carrier populations emitted from different electrodes will not mix and must be treated separately. All of these features were present in the one-dimensional treatment presented in [1]. Also entirely analogous to the 1-D treatment are the boundary conditions, including the tunneling recombination velocity conditions [1] and the bandgap blocking effect depicted in Fig. 1 [3]. As in [2], the primary new ingredient in multi-dimensions enters through the steady-state continuity equation  $\nabla \cdot (n\mathbf{v}_n) = 0$  that, unlike in one-dimension, cannot be integrated analytically. As a result, it becomes necessary to solve it for the velocity field in the barrier in order to find out where the electrons go, and obviously this equation must be solved simultaneously with the other governing

equations. These equations, various useful transformations of them, and their numerical solution will all be given brief coverage in the presentation.

Although quantitative verification of the DG description of tunneling (and of descriptions of tunneling in devices generally) is an important topic [1-3], as a practical matter it tends not to be that critical because of the exponential dependence of the calculated tunneling currents on various physical parameters that are rarely known with much accuracy, e.g., the precise geometry, tunneling effective masses or barrier heights. For this reason, in this work the focus is on solutions of the DG equations, and on understanding their qualitative meaning and implications. As a first such solution, in Fig. 2 the importance of the bandgap blocking effect (Fig. 1) is explored in 1D by simulating a Si-SiO<sub>2</sub>-Si tunnel diode with asymmetrical doping. As seen, the bandgap blocking effect is essential for getting the correct built-in voltage and the necessarily zero current at zero voltage (at least to good approximation). The kink seen near 0.1V is associated with the fact that for biases below the built-in voltage it is the forward current that is blocked by the bandgap. Representative conduction band and density profiles for the diode (with electron flow from left to right) are shown in Fig. 3; evident is the downstream depletion layer that, as it grows, causes the bandgap blocking effect to diminish with bias as seen in Fig. 2. Illustrating the use of the same DG equations (with bandgap blocking) in multi-dimensions, Fig. 4 shows a 2-D contour plot of the electron density in an n-channel SOI transistor with  $V_{SD} = 0$  and  $V_G = 0.5V$ . This FET has a gate length of 50nm and an oxide thickness that varies from 3nm at the source and drain to 1.5nm at the center of the device (i.e., an "oxide smile"). In this plot as well as in the plots of current density in Figs. 5 and 6, the expected dominance of tunneling at the center where the oxide is thinnest is evident. These and other results illustrating the power and also the limitations of the DG approach for modeling devices that involve multi-dimensional semiconductor tunneling will be discussed in the presentation.

## ACKNOWLEDGEMENT

The author thanks ONR for funding support.

## REFERENCES

1. M.G. Ancona, *Phys. Rev.* **B42**, 1222 (1990).
2. M.G. Ancona *et al.*, *J. Comp. Elect.* **3**, 189 (2004).
3. M.G. Ancona, *et al.*, *IEEE Trans. Elect. Dev.* **47**, 2310 (2000).

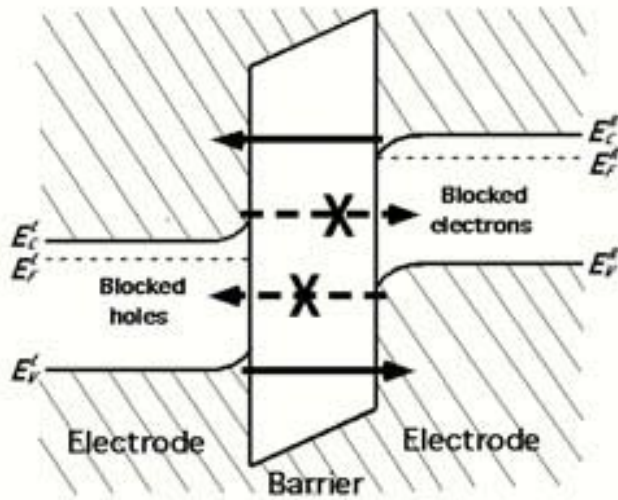


Fig. 1. Band diagram depicting the bandgap blocking effect in semiconductor tunneling.

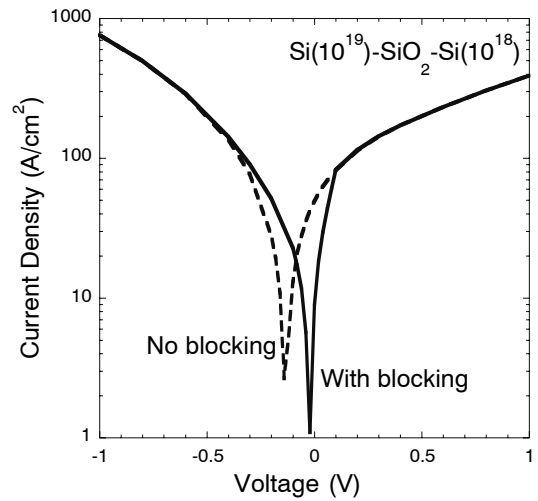


Fig. 2. Calculated J-V characteristic in an SIS diode showing the essential contribution of bandgap blocking at low voltage.

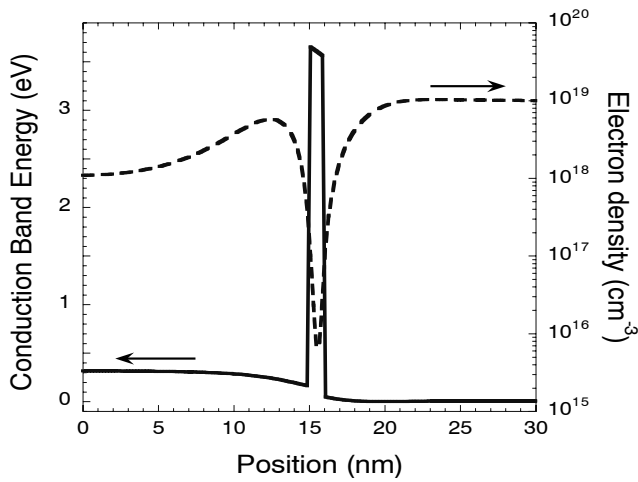


Fig. 3. Conduction band barrier and electron density in an asymmetrically doped SIS tunnel diode with  $V = -0.25V$ .

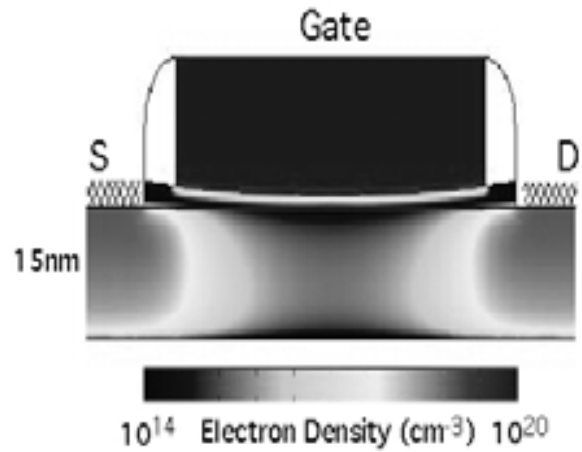


Fig. 4. Electron density contour plot in a 50nm gate length SOI FET with a non-uniform gate oxide.

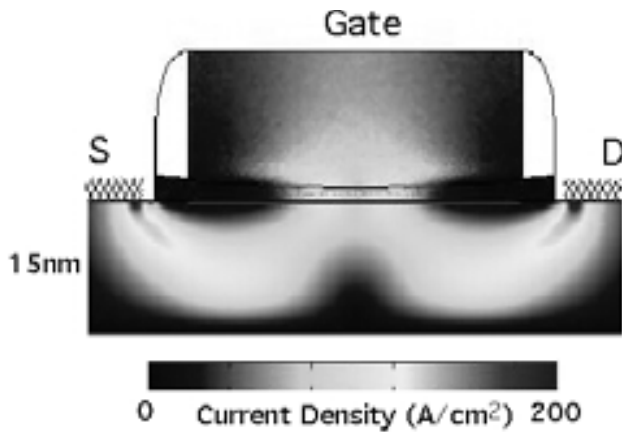


Fig. 5. Current density contour plot in a 50nm gate length n-channel SOI FET with a non-uniform gate oxide,  $V_G = -0.5$  and  $V_{SD} = 0V$ .

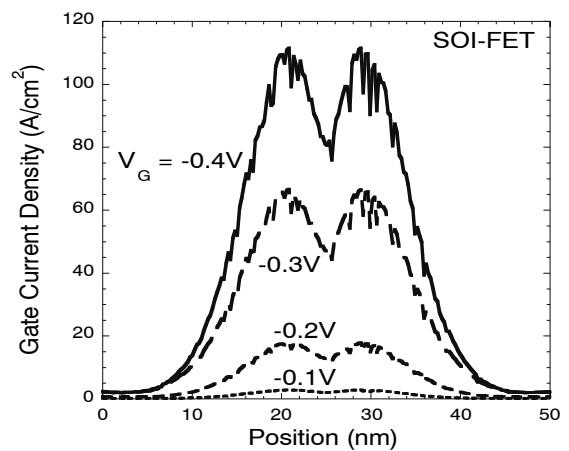


Fig. 6. Gate current density in the n-channel SOI FET with  $V_{SD} = 0V$  and  $V_G$  a parameter.

# Particle-Based Simulation: An Algorithmic Perspective

M. Saraniti, S.Aboud, and S.M. Goodnick\*

ECE Department, IIT, 3301 S. Dearborn, Chicago, IL 60616, U.S.A.

\*EE Department, ASU, Tempe, AZ 85287, U.S.A.

e-mail: saraniti@iit.edu

## INTRODUCTION

This talk reviews some of the latest advances of the algorithmic aspects of particle-based methods for the simulation of both solid-state devices and biological systems. After a brief historical introduction, a discussion will be offered about the recent evolution of numerical methods used by both Full-Band Ensemble Monte Carlo (EMC) and Molecular Dynamics (MD) algorithms. A discussion of some relevant applications of both simulative approaches will be accompanied by a critical analysis of the main limitations of the methods. Several needed improvement will be discussed as well, and the potential of the algorithms for modelling systems of higher complexity.

## FULL-BAND SIMULATION

The idea of using a k-space tabulated representation of the electronic structure and scattering rates of a semiconductor material rather than an analytical representation of portions of the first Brillouin Zone (BZ1) was introduced by K. Hess and co-workers in 1981 [1], [2]. The subsequent work of M. Fischetti and S. Laux [3] set the algorithmic standard for EMC simulation in 1988. In 2000, M. Saraniti and S. Goodnick revised the basic EMC algorithm by introducing the Cellular Monte Carlo (CMC) method [4], based on the tabulation of the probability of transition between different regions of BZ1, rather than the probability of scattering out of an initial momentum “state”. The growing availability of large amounts of fast storage (RAM) and the introduction of efficient data compression techniques allowed the extremely fast CMC to reach accuracy comparable to the traditional EMC. From the viewpoint of force-field schemes, the implementation of state-of-the-art Poisson solvers [5], [6],

[7] allowed longer simulation times and extremely complex (and large) 3D devices [8]. The self-consistent coupling of the charge transport simulation with time-domain Maxwell solvers [9] allowed the resolution of the radiation field generated by a device. As a consequence of these improvements, the characterization of the dynamic behavior of devices, as well as study of device noise became realistic. The recent introduction in the consumer market of fast 64bit processors based on dedicated memory bus architecture extended dramatically the addressable memory space and its efficiency, and allowed the implementation of more sophisticated physical models in particle-based full-band simulation codes. Recent applications of such algorithmic improvements will be discussed, such as the simulation of spin transport and the modeling of self-consistent non-equilibrium electron-phonon interactions.

## MOLECULAR DYNAMICS

The evolution of the computing hardware discussed above had an even more dramatic impact on the application of molecular dynamics algorithms to the simulation of complex biological systems. Basing on simulation tools developed by the whole community [10], [11] and on the intensive use of parallel computing, MD algorithms made possible the atomistic simulation of macromolecules [12] and even small viruses [13]. While these advances are extremely encouraging, much work needs to be done on the algorithmic development of the force-fields schemes [14], [15] used in MD. The talk will review some state-of-the-art algorithms for polarizable force-fields [16], [17], and will discuss their development. Applications to the simulation of

both solid- and liquid-state systems will be shown as well.

#### ACKNOWLEDGMENT

This work has been partially supported by Grant Number PHS 2 PN2 EY016570B from the National Institutes of Health through the NIH Roadmap for Medical Research.

#### REFERENCES

- [1] H. Shichijo and K. Hess, "Band-structure-dependent transport and impact ionization in GaAs," *Physical Review B*, vol. 23, no. 8, pp. 4197–4207, Apr 1981.
- [2] J. Tang and K. Hess, "Impact ionization of electrons in silicon (steady state)," *Journal of Applied Physics*, vol. 54, no. 9, pp. 5139–5144, Sep 1983.
- [3] M. Fischetti and S. Laux, "Monte Carlo analysis of electron transport in small semiconductor devices including band-structure and space-charge effects," *Physical Review B*, vol. 38, no. 14, pp. 9721–9745, Nov. 1988.
- [4] M. Saraniti and S. Goodnick, "Hybrid full-band Cellular Automaton/Monte Carlo approach for fast simulation of charge transport in semiconductors," *IEEE Transactions on Electron Devices*, vol. 47, no. 10, pp. 1909–1915, October 2000.
- [5] M. Saraniti, A. Rein, G. Zandler, P. Vogl, and P. Lugli, "An efficient multigrid poisson solver for device simulations," *IEEE Transaction on Computer-aided Design of Integrated Circuits and Systems*, vol. 15, no. 2, pp. 141–150, Feb. 1996.
- [6] S. Wigger, "Three dimensional multigrid poisson solver for use in semiconductor device modeling," Master's thesis, Arizona State University, Tempe, AZ, Aug 1998.
- [7] J. Ayubi-Moak, S. Wigger, S. Goodnick, and M. Saraniti, "3D biconjugate gradient-multi grid coupling schemes for field equations in semiconductor device simulation," in *Proceedings of 2002 International Conference on Modeling and Simulation of Microsystems - MSM2002*, April 2002, accepted for poster presentation.
- [8] P. Chiney, J. Branlard, S. Aboud, M. Saraniti, and S. Goodnick, "Full-band particle-based analysis of device scaling for 3D tri-gate FETs," *Journal of Computational Electronics*, vol. 4, no. 1-2, pp. 45–49, Apr 2005.
- [9] J. Ayubi-Moak, S. Wigger, S. Goodnick, and M. Saraniti, "Coupling maxwell's equations to full-band particle-based simulators," *Journal of Computational Electronics*, vol. 2, pp. 183–190, 2003.
- [10] H. Berendsen, D. van der Spoel, and R. van Drunen, "Gromacs: A message-passing parallel molecular dynamics implementation," *Comp. Phys. Comm.*, vol. 91, pp. 43–56, 1995.
- [11] B. Brooks, R. Bruccoleri, B. Olafsson, D. States, S. Swaminathan, and M. Karplus, "CHARMM: a program for macromolecular energy, minimization and dynamics calculations," *Journal of Computational Chemistry*, vol. 4, pp. 187–217, 1983.
- [12] I. H. Shrivastava and M. S. P. Sansom, "Simulations of Ion Permeation Through a Potassium Channel: Molecular Dynamics of KcsA in a Phospholipid Bilayer," *Biophysical Journal*, vol. 78, no. 2, pp. 557–570, 2000.
- [13] P. Freddolino, A. Arkhipov, S. Larson, A. McPherson, and K. Schulten, "Molecular dynamics simulation of the complete satellite tobacco mosaic virus," *Structure*, vol. 14, no. 3, pp. 437–449, March 2006.
- [14] B. Roux and S. Bernèche, "On the Potential Functions used in Molecular Dynamics Simulations of Ion Channels," *Biophysical Journal*, vol. 82, no. 3, pp. 1681–1684, 2002.
- [15] M. Saraniti, S. Aboud, and R. Eisenberg, *The Simulation of Ionic Charge Transport in Biological Ion Channels: an Introduction to Numerical Methods*, ser. Reviews in Computational Chemistry. Wiley, February 2006, vol. 22, pp. 229–284.
- [16] T. Halgren and W. Damm, "Polarizable force fields," *Current Opinion in Structural Biology*, vol. 11, no. 2, pp. 236–242, 2001.
- [17] G. Lamoreux, A. MacKerell, and B. Roux, "A simple polarizable model of water based on classical drude oscillators," *Journal of Chemical Physics*, vol. 119, no. 10, pp. 5185–5197, Sep 2003.

# A Linear Response Monte Carlo Algorithm for Inversion Layers and Magnetotransport

C. Jungemann, A. T. Pham, and B. Meinerzhagen  
BST, TU Braunschweig, Postfach 33 29, 38023 Braunschweig, Germany  
e-mail: Jungemann@ieee.org

## INTRODUCTION

Simulation of deca nanometer MOSFETs requires at least Monte Carlo (MC) models. Since no first principles scattering model for inversion layers exists, semiempirical models have to be used. Parameters of these models are determined by matching low-field measurements. Such simulations are extremely CPU intensive. We present a new linear response MC algorithm for electrons and holes in inversion layers and under the influence of an arbitrary magnetic field, which works even in the case of full band structures.

## THEORY

The Boltzmann equation is linearized around equilibrium with respect to the driving electric field. In the case of an inversion layer this is the electric field in channel direction. Due to the symmetry of the problem the response of even expected values of the distribution function is quadratic in the driving field, and the first order response of the particle temperature or density and therewith of the electrostatic potential vanishes. Thus, a “frozen” electric field can be used at equilibrium. The linear response term in the Boltzmann equation is treated as a particle source, where only the positive part is considered due to symmetry at equilibrium. The approach is equivalent to a fluctuation dissipation theorem, where the integral over the conditional velocity is evaluated by an MC method.

## RESULTS

All simulations are based on full band structures calculated by the nonlocal empirical pseudo potential method [1]. In Figs. 1,2 longitudinal ( $\mu_{yy}$ ) and transverse ( $\mu_{zy}$ ) hole mobilities are shown for strained and relaxed bulk Si as a function of the magnetic field, which is in one case applied parallel to the growth direction along the  $x$ -axis and in the

other parallel to the driving field in  $y$ -direction. In the strained case the nonquadratic dependence of the mobility on the magnetic field is clearly visible. Moreover, the second order magnetotransport coefficient ( $\alpha_{yy}^x = \sqrt{-1/\mu_{yy}} \partial^2 \mu_{yy} / \partial B_x^2 |_{B_x=0}$ ) is about twice the drift mobility. Thus the simple approximation of equating  $\alpha$  and the drift mobility fails for holes. In strained Si for parallel electric and magnetic fields the longitudinal magnetotransport effect almost completely vanishes due to the less warped band structure. CPU times are about 30 CPU seconds per bias point, where the longitudinal mobility is accurate within 0.3%. In Figs. 3,4 effective hole mobilities for inversion layers are shown. The parameters of the surface scattering model were determined by matching experimental data. The CPU time per bias point is about 1 CPU minute for a stochastic error of 1%. Without the CPU efficient MC algorithm determination of the model parameters would have not been possible, because the CPU time would have been at least three orders of magnitude larger.

## CONCLUSION

We have presented a novel linear response MC algorithm, which is many orders of magnitude faster than the conventional one, and works in the case of magnetotransport and inversion layers.

## REFERENCES

- [1] M. M. Rieger and P. Vogl, “Electronic-band parameters in strained  $\text{Si}_{1-x}\text{Ge}_x$  alloys on  $\text{Si}_{1-y}\text{Ge}_y$  substrates,” *Phys. Rev. B*, vol. 48, pp. 14 276–14 287, 1993.
- [2] S. Takagi, A. Toriumi, M. Iwase, and H. Tango, “On the universality of inversion layer mobility in Si MOSFET’s: Part I—Effects of substrate impurity concentration,” *IEEE Trans. Electron Devices*, vol. 41, pp. 2357–2362, 1994.
- [3] M. T. Currie, C. W. Leitz, T. A. Langdo, G. Taraschi, and E. A. Fitzgerald, “Carrier mobilities and process stability of strained Si n- and p-MOSFETs on SiGe virtual substrates,” *J. Vac. Sci. Technol. B*, vol. 19, no. 6, pp. 2268–2279, 2001.

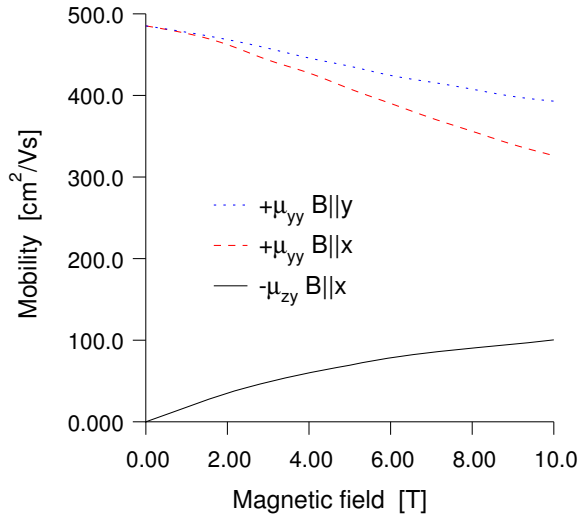


Fig. 1. Longitudinal and transverse mobilities for holes in undoped relaxed Si at room temperature for magnetic fields in  $x$  and  $y$  direction.

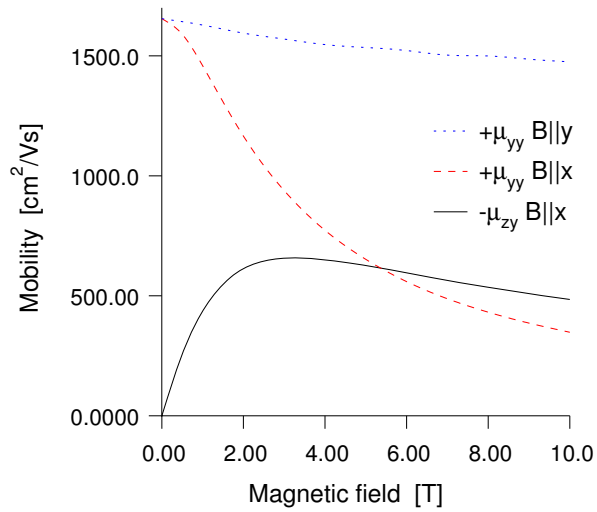


Fig. 2. Longitudinal and transverse mobilities for holes in undoped strained Si on  $\text{Si}_{0.7}\text{Ge}_{0.3}$  at room temperature for magnetic fields in  $x$  and  $y$  direction.

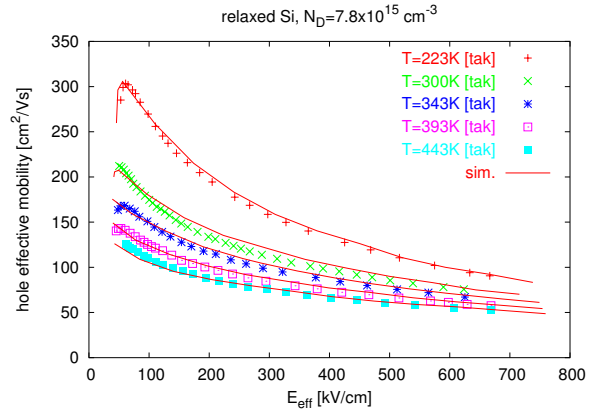


Fig. 3. Simulated effective hole mobility for a silicon inversion layer and measurements [2].

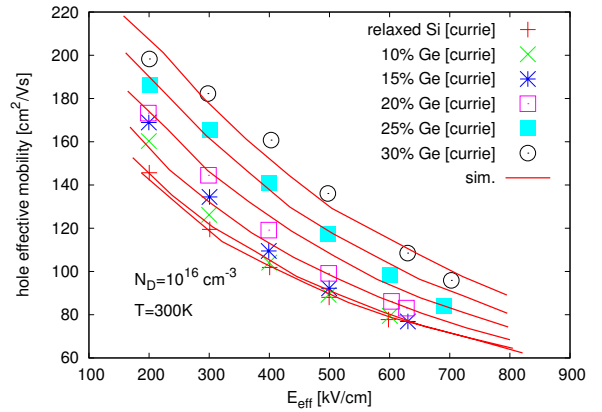


Fig. 4. Simulated effective hole mobility for a strained silicon inversion layer on relaxed  $\text{Si}_{1-y}\text{Ge}_y$  and measurements [3].

# Global Modeling of High-Frequency Devices

J. S. Ayubi-Moak<sup>\*</sup>, S. M. Goodnick<sup>\*</sup> and M. Saraniti<sup>\*\*</sup>

<sup>\*</sup>Department of Electrical Engineering, Arizona State University, USA

<sup>\*\*</sup>Department of Computer and Electrical Engineering, Illinois Institute of Technology, USA

e-mail: [jason.ayubi-moak@asu.edu](mailto:jason.ayubi-moak@asu.edu)

## ABSTRACT

In this work, we utilize the Finite-Difference Time Domain (FDTD) Method coupled to a full band, Cellular Monte Carlo simulator to model high-frequency devices. Replacing the traditional Poisson solver with a more robust electromagnetic (EM) solver provides a complete solution of the Lorentz force resulting in a more accurate model for determining the small-signal response of microwave transistors and various other high-frequency devices.

## INTRODUCTION

We have improved upon a previously developed and reported on simulator [1][2] extending its capability to accurately model high-frequency devices. In particular, we have improved the performance of the employed perfectly matched layer (PML) absorbing boundary conditions (ABC) and are now able to simulate electric, magnetic, and current excitation sources within the full-wave module of the simulation tool. This new feature extends the most recent simulation work performed in this area within our group [3][4] providing a more accurate method for (i) modelling the high-field transport in semiconductor devices and (ii) calculating the characteristic figures of merit such as the cutoff frequency and the maximum frequency of oscillation often used to measure performance characteristics of electron devices.

In extending the development of this new simulator, particular emphasis has been placed upon both the implementation and testing of Berenger's PML [5] and the self-consistent coupling of the particle-based section to the full-wave solver. Furthermore, the new EM solver has been extensively tested and benchmarked against established work [6] and more recent results [7] in the current EM literature providing a high level of confidence in its ability to accurately calculate the time-varying EM fields within a given device

structure of interest.

Another critical challenge faced when solving Maxwell's equations involves the maximum timestep over which the resulting finite-difference expressions can be resolved. The inherent stability limit, known as the Courant-Frederichs-Levy (CFL) criterion [8], severely limits the timestep for precisely the submicron scale dimensions we are interested in investigating and thus dramatically increases the number of simulation timesteps required. We have, therefore, developed a 3D FDTD algorithm based upon the recently developed ADI-FDTD method [9][10]. This new formulation relaxes the above CFL criterion allowing one to solve Maxwell's equations using timesteps several orders of magnitude greater than that dictated by the conventional limit. Finally, we are enhancing our simulator's internal architecture by including the standard MPI protocol providing it with the capability of being run on a large cluster of parallel nodes providing a further decrease in the overall simulation time required.

## SIMULATION AND MODELING

Monochromatic sinusoidal excitation and Fourier decomposition are being used to study the small signal response of high-frequency electron devices and to investigate the overall performance of the latter including metal semiconductor field-effect transistors (MESFETs), and high electron mobility transistors (HEMTs). In particular, a 3D MESFET device shown in Fig. 1 is currently being tested via sinusoidal source excitation.

Using this technique, a high-frequency, sinusoidal perturbation of 80GHz is applied to either the gate or drain electrode after the device has reached a certain, steady-state DC bias point as shown in Fig. 2. A sampling of the subsequent time-domain fields computed by the full-wave solver then allows one to determine the time-varying electric potentials (as shown in Fig. 3), currents, and the frequency-dependant Y-parameters (i.e.

transconductance, output resistance, and the open-circuit voltage gain.) used to characterize the device performance.

### CONCLUSIONS

A more detailed description of the simulation tools, the device structures investigated, and the resulting figures of merit for various excitation schemes will be provided during the presentation format selected for this work.

### ACKNOWLEDGEMENT

This work has been supported by a grant from the Department of Defense High Performance Computing Modernization Program (HPCMP).

### REFERENCES

- [1] M. Saraniti, and S. M. Goodnick, "Hybrid full-band cellular automaton/Monte Carlo approach for fast simulation of charge transport in semiconductors," *IEEE Transactions on Electron Devices*, **47**(10), 1909 (2000).
- [2] J. S. Ayubi-Moak, S. M. Goodnick, S. J. Aboud, M. Saraniti, and S. El-Ghazaly, "Coupling Maxwell's Equations to Full Band Particle-Based Simulators," *Journal of Computational Electronics*, vol. 2, pp. 183-190, 2003.
- [3] J. Branlard, S. Aboud, S. Goodnick, and M. Saraniti, "Frequency analysis of 3D GaAs MESFET structures using full-band particle-based simulations," *Journal of Computational Electronics*, vol. 2, Issue 2-4, pp. 213-217, 2003.
- [4] J. Branlard, S. Aboud, P. Osuch, S. Goodnick, and M. Saraniti, "Frequency analysis of semiconductor devices using full-band Cellular Monte Carlo simulations," *Monte Carlo Methods and Applications, Special Issue*, 2004.
- [5] J. P. Bérenger, "Three-dimensional perfectly matched layer for the absorption of electromagnetic waves," *J. Comput. Phys.*, **127**, 363 (1996).
- [6] D. M. Sheen and S. M. Ali, "Application of the Three-Dimensional Finite-Difference Time-Domain Method to the Analysis of Planar Microstrip Circuits," *IEEE MTT*, vol. 38, no. 7, July 1990.
- [7] G. Liu and S. D. Gedney, "Perfectly Matched Layer Media for an Unconditionally Stable Three-Dimensional ADI-FDTD Method," *IEEE Microwave Guided Wave Lett.*, vol. 9, pp. 441-443, Nov. 1999.
- [8] R. Courant, K. Frederichs, and H. Lewy, "On the partial difference equations of mathematical physics," *IBM Journal* 215 (1967).
- [9] T. Namiki, "A New FDTD Algorithm Based on Alternating-Direction Implicit Method," *IEEE MTT*, vol. 47, no. 10, Oct. 1999.
- [10] F. Zheng, Z. Chen, and J. Zhang, "A Finite-Difference Time-Domain Method Without the Courant Stability Conditions," *IEEE Microwave Guided Wave Lett.*, vol. 9, no. 11, Nov. 1999.

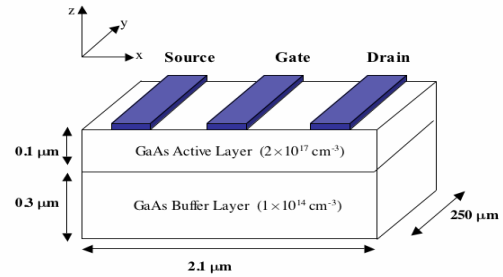


Fig. 1. 3D MESFET device currently being investigated

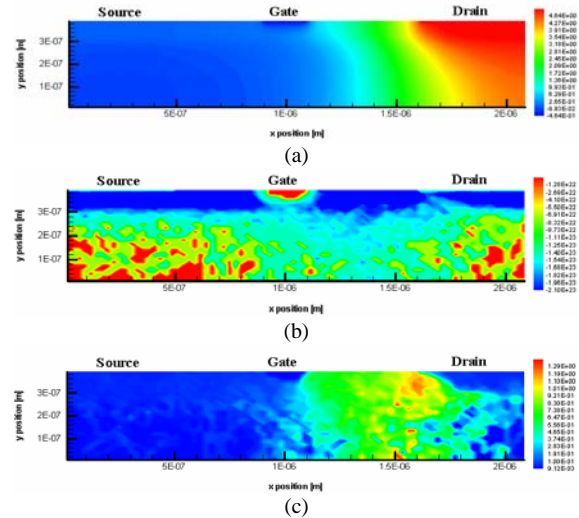


Fig. 2. Contour plots of (a) electric potential, (b) average electron concentration [ $\text{m}^{-3}$ ], and (c) average electron energy [eV] for DC bias point:  $V_{\text{Source}} = 0\text{V}$ ,  $V_{\text{Gate}} = -0.5\text{V}$ , and  $V_{\text{Drain}} = 5.0\text{V}$ .

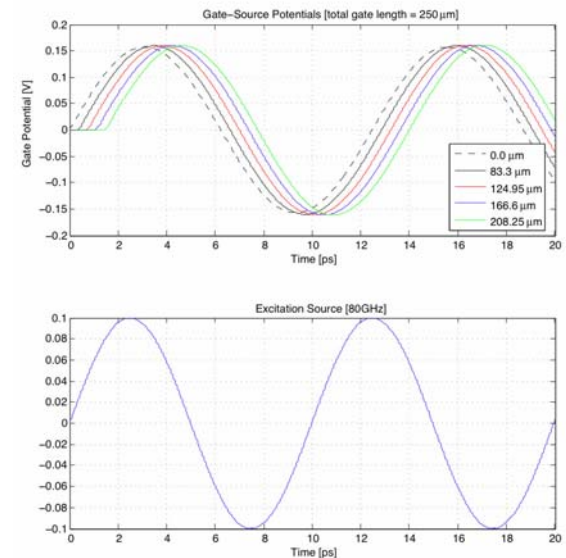


Fig. 3. Propagation of applied small-signal perturbation between gate and source electrodes in the 3D MESFET structure shown in Fig.1.

# Introducing Energy Broadening in Semiclassical Monte Carlo Simulations

G. Ferrari\*, C. Jacoboni†, M. Nedjalkov‡, and A. Asenov\*

\*Device Modelling Group, Dept. Electronics & Electrical Engineering, University of Glasgow  
 G12 8LT Glasgow, United Kingdom. E-mail: G.Ferrari@elec.gla.ac.uk

†National Research Center S3, INFN-CNR and Dipartimento di Fisica

Università di Modena e Reggio Emilia, Via Campi 213/A, I-41100 Modena, Italy.

‡AMADEA Group, Inst. for Microelectronics, TU Wien, Gußhausstr. 27-29/E360, 1040 Wien, Austria.

In the past, several attempts have been made to introduce collisional broadening in semiclassical electron transport Monte Carlo (MC) simulations [1, 2]. The inclusion of energy non-conservation at each scattering event has produced non-physical instabilities. In this work we propose an algorithm which overcomes the difficulties encountered in previous approaches. Moreover, it is suitable for a direct implementation in device modelling, since it can be easily introduced in existing MC simulators. The scaling of device architecture will shortly require this effect to be taken into account in simulations.

In order to include energy broadening without losing long term energy conservation, one must consider the following:

1. That the overall energy in transport is conserved because the Hamiltonian for the total system of the electron(s) and phonons is time independent.
2. In an electron-phonon interaction the crystal-momentum conservation, in a homogeneous system, is guaranteed by the matrix elements.
3. An electron can be scattered to a state with an energy not given by the simple balance between the energy before scattering and the energy of the involved phonon. This is due to the fact that the final state, considered in transition, is an eigenstate of the unperturbed Hamiltonian, which is not a state of well defined energy in the total interacting system.

Therefore we may assume that the energy is conserved at each scattering event. In fact, in the two-time Wigner-function approach a frequency contribution is transferred to the electron equal to the frequency of the phonon [3]. But, we have to distinguish the true “frequency energy”

of the electron  $E$  from the “momentum energy”  $E'$ :

$$E' = \frac{p^2}{2m} \quad (1)$$

Because of collisions, the energy-momentum relation is no longer given by equation (1), but it broadens.

In this type of MC simulation, it is necessary to keep track of both  $E$  and  $E'$ . The energy exchanged at each scattering event is determined by the phonon frequency  $\omega_{ph}$ , and the momentum exchanged is determined by the phonon wave-vector  $q$ . But, the final electron energy and electron momentum are not necessarily related by (1).

The energy spreading is related to the time between collisions via the Heisenberg uncertainty relation:

$$\sigma_{Ei} \approx \frac{\hbar}{t_i - t_{(i-1)}} \quad (2)$$

Where  $t_i$  is the time at which the  $i$ -th scattering event takes place.

The MC algorithm will then proceed as follows.

Initial state:

The semiclassical simulation starts at time  $t = t_0$ ; the initial momentum  $p_0$  is generated according to the thermal distribution, the initial energy  $E_0$  is calculated according to (1).

Flights:

The duration  $(t_i - t_{(i-1)})$  of the flights is determined, in a traditional way, according to the scattering probabilities, including self-scattering. The value of the momentum at the end of the flights is  $p_{ib}$  (where  $b$  stands for “before” the scattering event) and is determined classically. Starting from the value  $p_{(i-1)a}$  “after” the previous scattering, the variation in the momentum can be calculated classically:

$$\Delta p_i = eF(t_i - t_{(i-1)}) \quad (3)$$

Where  $F$  is the field (assumed to be constant and uniform within the flight) acting on the system. Under the action of the electric field, the variation  $\Delta_f E_i$  of the energy during the  $i$ -th flight is determined by the distance  $\Delta z$  covered by the electron:

$$\Delta z_i = \frac{P_{(i-1)a}}{m}(t_i - t_{(i-1)}) + \frac{1}{2} \frac{eF}{m}(t_i - t_{(i-1)})^2 \quad (4)$$

The energy variation is therefore:

$$\Delta_f E_i = eF \Delta z_i \quad (5)$$

The energies at the end of each flight can be easily calculated from the above equation:

$$E_{ib} = E_{(i-1)a} + \Delta_f E_i \quad (6)$$

Scattering events:

Firstly, for simplicity, we limit ourselves to the case of scattering from non-polar optical and acoustic phonons, within the elastic approximation, and with deformation potential interaction.

At the time  $t_i$  a scattering event occurs. Before each scattering event the position can be calculated from equation (4), allowing a relatively simple implementation of this algorithm in a device simulation. At the scattering time  $t_i$ , a new energy  $E'_{ib}$  is defined, taking into account the energy broadening  $\delta E_i$ . This is chosen from a distribution determined using the standard deviation given by equation (2):

$$E'_{ib} = E_{ib} + \delta E_i \quad (7)$$

The new value of  $E'_{ib}$  is calculated based on the value of the true electron energy  $E_{ib}$ . The type of scattering is determined using the probabilities  $P(E'_{ib})$ . Applying this approach, the energy non conservation due to the flight duration is taken into account, affecting the type of process chosen as scattering. If self scattering is chosen, then the flight continues. If true scattering is chosen, the new values for the electron energy and momentum are determined as follows:

$$E_{ia} = E_{ib} \pm \hbar \omega_0 \quad (8)$$

$$E'_{ia} = E'_{ib} \pm \hbar \omega_0 \quad (9)$$

$$p_{ia} = \sqrt{\frac{E'_{ia}}{2m}} \quad (10)$$

The orientation of the momentum is chosen from an isotropic distribution; once  $p_{ia}$  is calculated then the  $q$  of the phonon is determined. The sign  $\pm$  corresponds to an absorption or emission process.

The new energy  $E'_{ib}$  is calculated based on the value of the true electron energy  $E_{ib}$ , not on the previous  $E'_{ib}$ ,

so that the energy broadening is not propagated from one scattering event to the following ones. Moreover, no memory of the energy broadening that occurred in the previous scattering event is retained. The energy spreading given by equation (2) is calculated according to the time interval  $(t_i - t_{(i-1)})$ . With this approach, a physical collisional broadening is accounted for. This influences threshold processes, such as impact ionisation or oxide penetration. The overall energy conservation is, however, guaranteed and the stability of the system is achieved.

Initially this algorithm has been tested on bulk semiconductors, in order to understand the effect on threshold processes, before application to realistic device models.

#### REFERENCES

- [1] Y.-C. Chang, D.Z.Y. Ting, J.Y. Tang and K. Hess, Applied Physics Letters **42**, 76 (1983).
- [2] L. Reggiani, P. Lugli and A.-P. Jauho, Journal of Applied Physics **64**, 3072 (1988).
- [3] C. Jacoboni and P. Bordone, Reports on Progress in Physics **67**, 1033 (2004).

# Schrödinger/Luttinger Approach to Scaled MOS Transport for Various Crystal Orientations and its Experimental Verifications

Takako Okada and Hisao Yoshimura\*

Corporate Research & Development Center, Toshiba Corporation, Kawasaki 212-8582, Japan

\*System LSI Division, Semiconductor Company, Toshiba Corporation, Yokohama, Japan

e-mail: [t-okada@amc.toshiba.co.jp](mailto:t-okada@amc.toshiba.co.jp)

## INTRODUCTION

In scaled device designing for the 40 nm regime and beyond, deeper physical insight into channel transport will be required than previously. A Schrödinger/Luttinger approach to scaled MOS transport was applied for the first time to various crystal orientations, channel directions, applied voltages and mechanical stresses together with experimental verifications. Typical findings obtained in this work are as follows: (1)marked variations of inversion carrier distributions have been calculated among (110), (111), (112), (120) and (100) surfaces, (2)significant differences in channel conductivities of p-channel MOS have been simulated between triode and pentode regions, and (3)effective mass characteristics have been output as functions of germanium concentration.

## SCHRÖDINGER/LUTTINGER BASED APPROACHES

Newly developed Schrödinger/Luttinger prototype codes are composed of (1)extended Luttinger<sup>[1][2][3]</sup> equations with stress/strain tensor and matrix solvers, (2)Poisson solver<sup>[4]</sup>, and (3)Monte Carlo parts<sup>[5]</sup> with anisotropic subband energy and scattering rates linked with each other as shown in Figs.1 and 2. Typical subband structures for p-channel inversion layers, band diagrams of (110) Si and inversion charge distribution are presented in Figs.3, 4 and 5, respectively. It should be noted that distinctive variations of hole inversion band scheme were calculated for the first time among (110), (111), (120), and (100) surfaces in terms of external stress, and significant differences in channel carriers of p-channel MOS have been simulated among Si/Si/Ge and Ge substrates. Figure 6 shows energy dependence of scattering rate results for carrier transports. Real-time snapshots of carrier distributions and drift mobility are demonstrated in Figs.7, 8 and 9. From the above results, it is first clarified quantitatively that (1)stress sensitivities of effective masses in Si/Ge and Ge substrate have been simulated and (2)the mobility advantage of [110] hole carriers on strained

(100)Si is simulated to be smeared in high electric field. In order to verify the modes and simulated results, MOS cantilever experiment have been conducted as shown in Fig.10. Drain currents were measured upon application of external uniaxial stress. The amounts of additional strain  $\Delta\varepsilon_{ij}$  were calculated by means of the following equation:

$$\Delta\varepsilon_{ij} = (3Z \times b \times \Delta h) / L^3,$$

where  $\Delta h$ ,  $Z$  and  $L$  are indicated in Fig.10 and  $b$  is a half of the wafer thickness.  $\Delta h$  was measured using a micrometer head. In the case of [110] Si p-channel on (100) Si, measurement reveals that drain current gain decreases with compressive strain  $\Delta\varepsilon_{ij}$  in the pentode region contrarily to the triode region, which is consistent with the results in Fig3.

## SUMMARY

A Schrödinger/Luttinger approach to scaled MOS transport was applied for the first time to various kinds of crystal orientations, channel directions, applied voltages and mechanical stress together with experimental verifications. Through intensive analysis, it has been determined that Si/Ge and Ge are promising materials from the view-point of scaled CMOS drivability in conjunction with mechanical stress and crystal orientations. Details of mathematical derivations in Schrödinger/Luttinger part and scattering rate procedures will also be reported with calling upon current references<sup>[6][7]</sup> at the IWCE conference.

## REFERENCES

- [1] J. M. Luttinger and W. Kohn, Phys. Rev. **97**, 869 (1955).
- [2] S. Rodriguez, J. A. Lopez-Villanueva, I. Melchor and J. E. Carceller, J. Appl. Phys. **86**, 438 (1999).
- [3] D. A. Broido and L. J. Sham, Phys. Rev.B. **31**, 31888 (1985).
- [4] F. Stern, J. Computational Phys. **6**, 56 (1970).
- [5] J.E.Dijkstra and W. Th. Wenckebech, J. Appl. Phys. **81**, 259 (1997).
- [6] M. V. Fischetti and S. E. Laux, Phys. Rev.B **48**, 2244 (1993).
- [7] M. V. Fischetti et al., J. Appl. Phys. **92**, 7320 (2002).

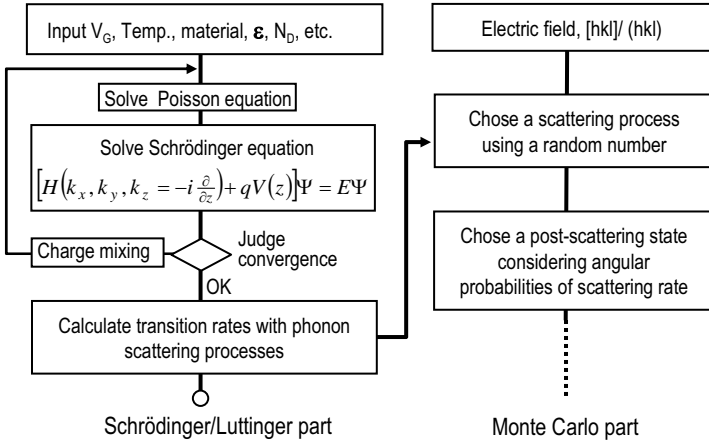


Fig.1 Block diagram and flows of our newly developed Schrödinger/Luttinger based codes.

$$H = \begin{pmatrix} P+Q & S & R & 0 & -iS/\sqrt{2} & i\sqrt{2}R \\ S^* & P-Q & 0 & R & i\sqrt{2}Q & -i\sqrt{3}/2S \\ R^* & 0 & P-Q & -S & i\sqrt{3}/2S^* & i\sqrt{2}Q \\ 0 & R^* & -S^* & P+Q & i\sqrt{2}R^* & iS^*/\sqrt{2} \\ iS^*/\sqrt{2} & -i\sqrt{2}Q^* & -i\sqrt{3}/2S & -i\sqrt{2}R & P-\Delta & 0 \\ -i\sqrt{2}R^* & i\sqrt{3}/2S^* & -i\sqrt{2}Q^* & -iS/\sqrt{2} & 0 & P-\Delta \end{pmatrix}$$

$$P = -\frac{\hbar^2}{2m_0} \gamma_1 (k_x^2 + k_y^2 + k_z^2) + a(\varepsilon_{xx} + \varepsilon_{yy} + \varepsilon_{zz})$$

$$Q = \frac{\hbar^2}{2m_0} \left\{ \left( \frac{\gamma_2}{2} - \frac{3\gamma_3}{2} \right) k_x^2 - \gamma_2 k_y^2 + \left( \frac{\gamma_2}{2} + \frac{3\gamma_3}{2} \right) k_z^2 \right\} + \left( -\frac{b}{4} \right) (\varepsilon_{xx} + \varepsilon_{yy}) + \left( \frac{b}{2} \right) \varepsilon_{zz} - \frac{\sqrt{3}}{2} d \varepsilon_{xy}$$

$$R = \frac{\hbar^2}{2m_0} \left( -\frac{\sqrt{3}}{2} \gamma_2 \right) (k_x^2 - 2k_y^2 + k_z^2) + \frac{\hbar^2}{2m_0} \left( -\frac{\sqrt{3}}{2} \gamma_3 \right) (k_x^2 - k_z^2) + \frac{\hbar^2}{2m_0} (-i2\sqrt{3}\gamma_3) k_x k_y + \frac{\sqrt{3}}{4} b (\varepsilon_{xx} + \varepsilon_{yy} - 2\varepsilon_{zz}) - d \left\{ \frac{1}{2} \varepsilon_{xy} + \frac{i}{\sqrt{2}} (\varepsilon_{xz} - \varepsilon_{yz}) \right\}$$

$$S = \frac{\hbar^2}{2m_0} i \left( -2\sqrt{3} \right) \gamma_2 \left( k_x + i \frac{\gamma_3}{\gamma_2} k_y \right) k_z + i \frac{\sqrt{3}}{2} b (-\varepsilon_{xx} + \varepsilon_{yy}) - \frac{d}{\sqrt{2}} (\varepsilon_{xz} + \varepsilon_{yz})$$

Fig.2 Outline of typical  $6 \times 6$  Luttinger Hamiltonian for Si(110). Some of notation here are consulted on Ref [2].

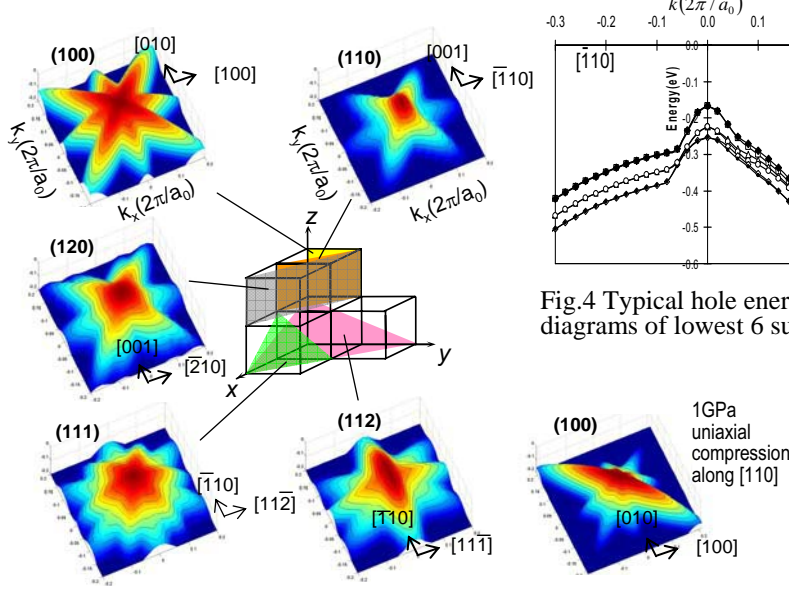


Fig.3 Typical perspective plot of hole lowest subbands of Si in terms of surface orientation. Interval of contours is 20meV.

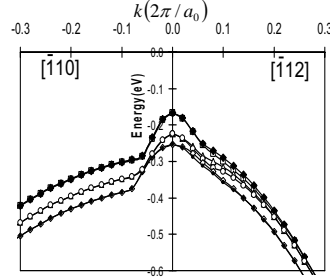


Fig.4 Typical hole energy diagrams of lowest 6 subbands.

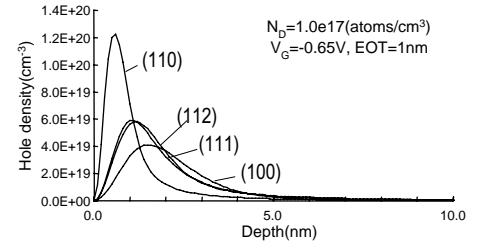


Fig.5 In-depth profiles of carrier density.

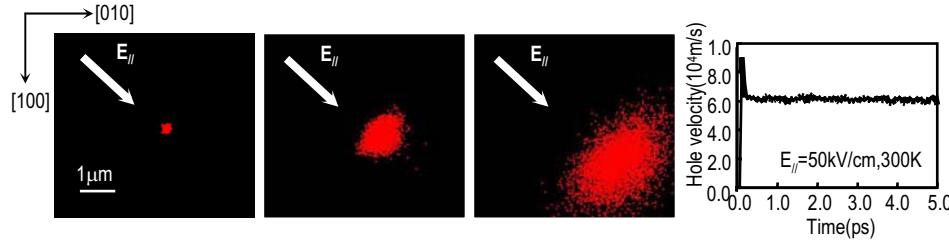


Fig.7 Typical snapshots of hole distribution in electric field. Lateral electric field  $E_{||}$  is 50kV/cm.

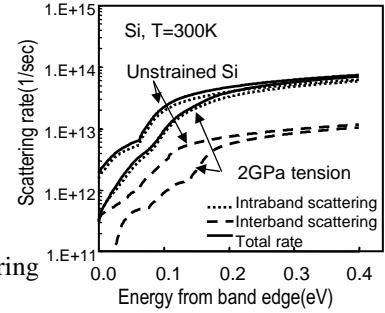


Fig.6 Scattering rate.

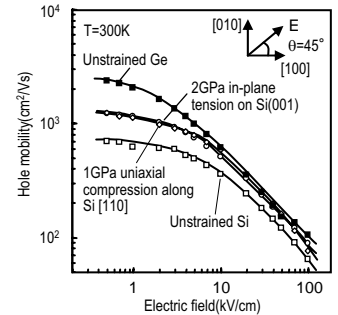


Fig.8 Hole mobility as a function of the lateral electric field.

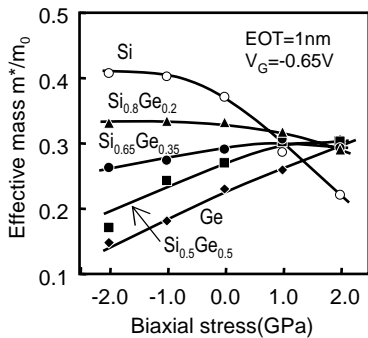


Fig.9 Hole effective mass of lowest subband in Ge and  $Si_{1-x}Ge_x$  as a function of biaxial stress and material composition.

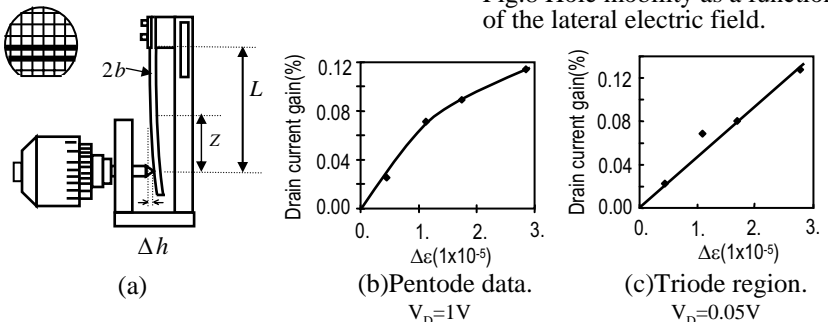


Fig.10 MOS cantilever experimental setup(a) and experimental results(b)(c). Dimensions of the specimen are as followed;  $L=39.08\text{mm}$ ,  $Z=9.60\text{mm}$  and  $2b=0.70\text{mm}$ . S/D is located on transversal to the beam, and generated strain is compressive on the S/D direction.

# Joule Heating and Phonon Transport in Silicon MOSFETs

Z. Aksamija, and U. Ravaioli

Beckman Institute, University of Illinois, 405 N. Mathews, 61801 Urbana IL., U.S.A.

e-mail: aksamija@uiuc.edu

## INTRODUCTION

Joule heating is caused by emission of phonons as electrons traverse through a semiconductor device. In silicon MOSFETs, most of the emission is concentrated in the small region where the channel meets the drain. It has been noted in the literature that this causes a hot-spot in the device where strong non-equilibrium conditions exist [1]. The emission of phonons has previously been examined, but the resulting non-equilibrium temperature conditions in a typical device have never been established. This work aims at using full-band Monte Carlo simulation coupled with phonon transport to quantify the extent and the location of Joule heating in a silicon MOSFET.

## NUMERICAL APPROACHES

Data on scattering events in a device can be obtained from a Monte Carlo simulation. In this work we use a three-dimensional full-band simulator with a self-consistent non-linear Poisson solver. In order to insure accuracy of results for phonon events, a full phonon dispersion is included. It is calculated from an Adiabatic Bond Charge model and tabulated for lookup [2]. An iterative algorithm was devised in order to make all scattering events involving phonons energy and momentum conserving with the full phonon dispersion relationship. This gives us a more accurate value for the phonon momentum and energy.

Once the simulation run is complete, data on all phonon events that occurred is tabulated. Then phonon velocity is looked up from the dispersion relationship for each phonon, and each phonon is allowed to move without scattering until the end of the simulation time-frame. Finally, the entire simulation region is divided into small cubes, and the total phonon energy in each cube is computed.

A curve relating lattice energy  $U(T)$  and temperature  $T$  is pre-computed by integrating the phonon density-of-states (DOS)  $D(\omega)$  with the phonon occupation probability  $\langle n(\omega) \rangle$ , as given by (1).

$$U(T) = \int d\omega D(\omega) \langle n(\omega) \rangle \hbar\omega \quad (1)$$

The phonon DOS is calculated numerically from tabulated dispersion data using the algorithm proposed in [3]. Using these results, the non-equilibrium temperature in each location of the device can be found.

## RESULTS

The computed phonon DOS is shown in Fig. 1. It was found that transitions between opposite equivalent valleys dominate the scattering statistics, as shown in Fig. 2. The reduced momenta of the phonons resulting from such transitions are near the Brillouin zone edge and rest on the longitudinal optical branch. The direction of propagation of these phonons is perpendicular to the energy isosurface, shown in Fig. 3, so most of the phonons emitted continue to travel in the direction of the flow of electrons. This means very little heat actually flows towards the substrate, as in Fig. 4. Future work is planned to enable coupled electro-thermal simulation in order to probe this process in more detail.

## REFERENCES

- [1] S. Sinha, P. K. Shelling, S. R. Phillpot, and K. E. Goodson, *Scattering of g-process longitudinal optical phonons at hotspots in silicon*, Journal of Applied Physics **97**, 023702 (2005).
- [2] W. Weber, *Adiabatic bond charge model for the phonons in diamond, Si, Ge and  $\alpha$ -Sn*, Physical Review B **15**, 10 (1977).
- [3] G. Gilat and L. J. Raubenheimer, *Accurate Numerical Method for Calculating Frequency-Distribution Functions in Solids*, Physical Review **144**, 2 (1966).

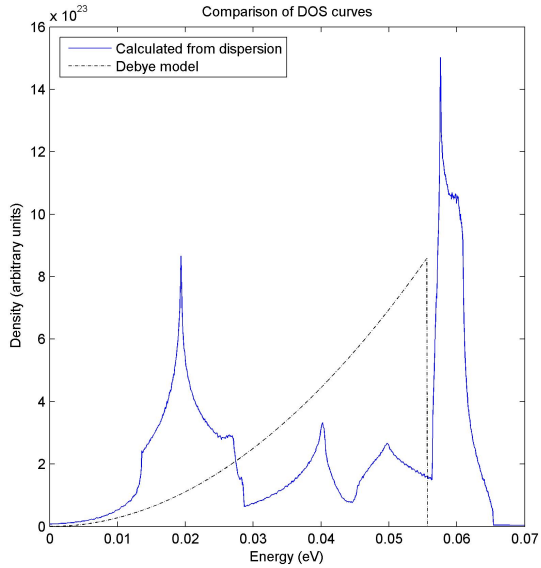


Fig. 1. Phonon DOS computed numerically. The dashed line is the standard Debye approximation, for comparison.

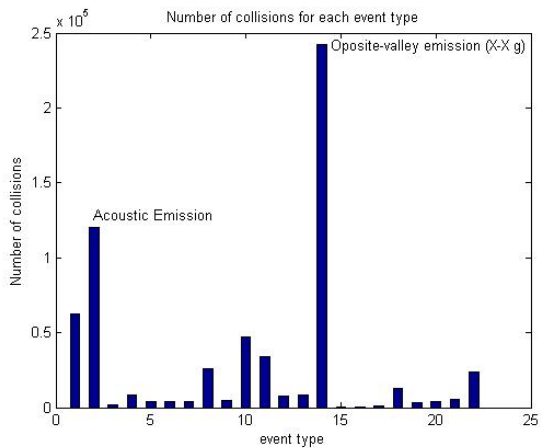


Fig. 2. Number of phonons emitted for each event type. Opposite equivalent valley and acoustic intravalley transitions are marked. Opposite equivalent valley transitions dominate.

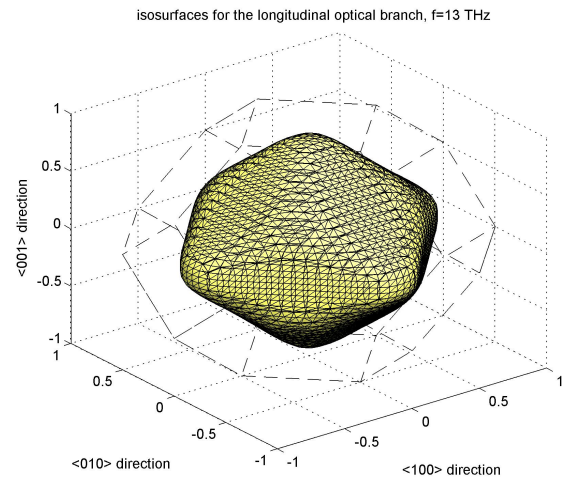


Fig. 3. Surface of equal phonon energy in momentum space for the longitudinal optical branch. Direction of phonon propagation is perpendicular to this surface.

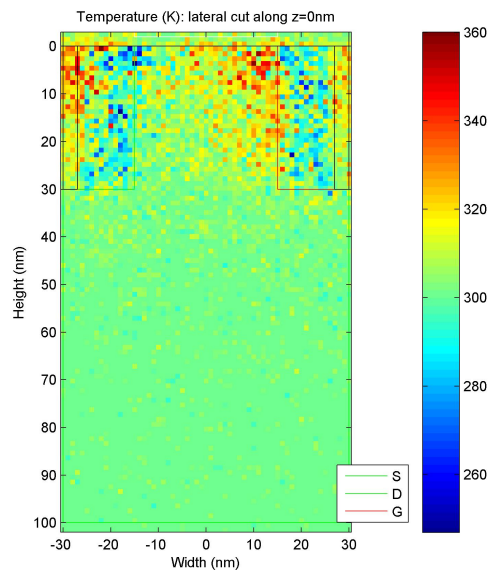


Fig. 4. Map of temperature distribution in an example short channel MOSFET device after 20ps. The clouds of elevated temperature have moved to the left of the source and drain regions.

# First Self-Consistent Full-Band – 2D Monte Carlo – 2D Poisson Device Solver for Modeling SiGe Heterojunction p-Channel Devices

S. Krishnan<sup>1</sup>, D. Vasileska<sup>1</sup>, M. Fischetti<sup>2</sup>

<sup>1</sup>Arizona State University, Tempe AZ, <sup>2</sup>University of Massachusetts, Amherst, MA  
e-mail: vasileska@asu.edu, skrish2@imap2.asu.edu, fischett@ecs.umass.edu

Though their necessity is still perhaps few years out, alternative MOSFET structures shown in Fig. 1 appear to deliver the technologies that will scale CMOS further than ever anticipated. Regarding the performance of SiGe p-channel devices, it is necessary to investigate a variety of issues that require atomic scale electronic structure and transport calculations. These include investigations of the role of alloy scattering, the thickness of the cap Si layer, the role of strain-induced interface roughness (that depends upon the temperature growth conditions), the presence of a parallel channel at the interface and how it affects the device performance. To determine the effect of thickness variations, one needs to evaluate the associated fluctuations in the electrostatic potential at the Si/SiGe interface using self-consistent solution of the Poisson equation coupled with the Schrödinger equation which utilizes the effective masses derived from k.p calculations. Another issue is the strain-splitting of the heavy-hole and the light-hole bands and the role played by quantum-mechanical size-quantization effects at the source end of the channel on the overall device performance.

To incorporate band-structure effects like warping, anisotropy and non-parabolicity in the description of carrier transport, our device simulator couples a 2D Poisson solver with a discretized 6×6 k.p Hamiltonian solver that includes the effect of the confining potential and provides the subband structure in the channel region. Strain effects in buried channel strained-SiGe MOSFET simulations are included by employing the 6×6 Bir-Pikus strain Hamiltonian perturbatively. Having calculated the hole band-structure in the contacts (3D) and the subband structure (2D) in the active device region i.e. under the gate self-consistently with the 2D

Poisson equation, the quantum mechanical hole density in the channel is then calculated by weighing the sheet density of each subband with the probability density corresponding to that subband along the device depth and then summing over all subbands of each of the six bands. The initialization of carriers in real space is based on the local 3D carrier density for holes in the reservoirs. In the channel region the carriers are assigned to subbands in a probabilistic manner that reflects the contribution to the hole sheet density from different subbands.

We use an Ensemble Monte Carlo (EMC) particle based simulator to handle the transport of holes. After the carriers are initialized, a bias is applied on the drain contact and the Monte Carlo algorithm takes over the hole transport, performing the drift and scattering of carriers. As the simulation time evolves in steps of 0.1 fs, and the carriers drift under the influence of the electric field, the confining potential changes along the channel from the source end to the drain end, and this, in turn, changes the hole subband structure in the channel. As a result, the hole subband structure and subsequently the scattering rates must be updated frequently during the simulation to reflect these changes.

The density of states for 2D confined carriers in the channel for the case of a triangular test potential is shown in Fig. 2; the left panel is for Si inversion layer, while the right panel is indicative of the same for strained SiGe inversion layer.. The drain current enhancement ratio of the strained SiGe MOSFET over the conventional Si MOSFET as a function of the applied drain bias for different gate voltages is shown in the right panel of Fig. 3. At the conference we will discuss the method we have used to eliminate the subband crossings.

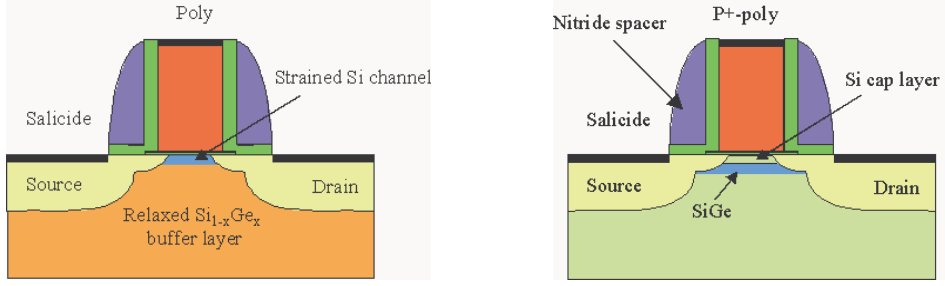


Fig. 1. Alternative device structures in SiGe technology. Left panel - Both pMOS and nMOS enhanced carrier mobility can be achieved. Critical issue is the fabrication of the buffer and strained layers. Doping further degrades the mobility. Right panel - This device structure is used to boost the pMOS behavior by introducing a quantum well beneath the Si layer. The alloy disorder scattering and the parallel transport channel is a problem.

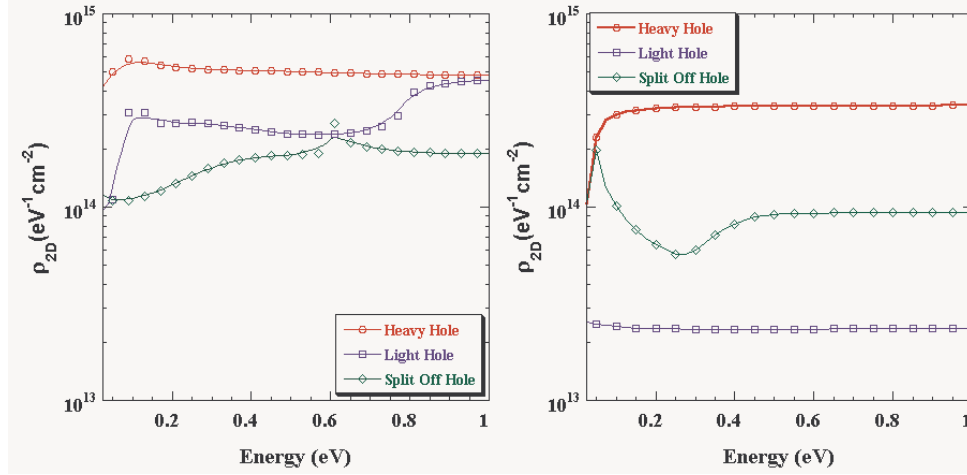


Fig. 2. The density of states for 2D confined carriers in the channel for the case of a triangular test potential; the left panel is for Si inversion layer, and the right panel is indicative of the same for strained SiGe inversion layer. Considering the left panel: (a) The deviation of the 2D density of states obtained by a full band calculation from a regular step-like profile expected out of an effective-mass type approximation is clearly seen in the case of the light hole and split off bands. (b) Subband crossings are seen in the case of light hole and split off subbands, where these subbands cross into higher lying heavy hole subbands, resulting in spikes in the density of states. For the case of the right panel: (c) The heavy and light hole subbands have a clear density of states with no subband crossings, (d) The split off band actually follows the heavy hole subband density of states and there is a subband crossing from split off subband into the heavy hole subband. The crossover then changes shape and the density of states consequently drops and settles down to a constant value at higher energies.

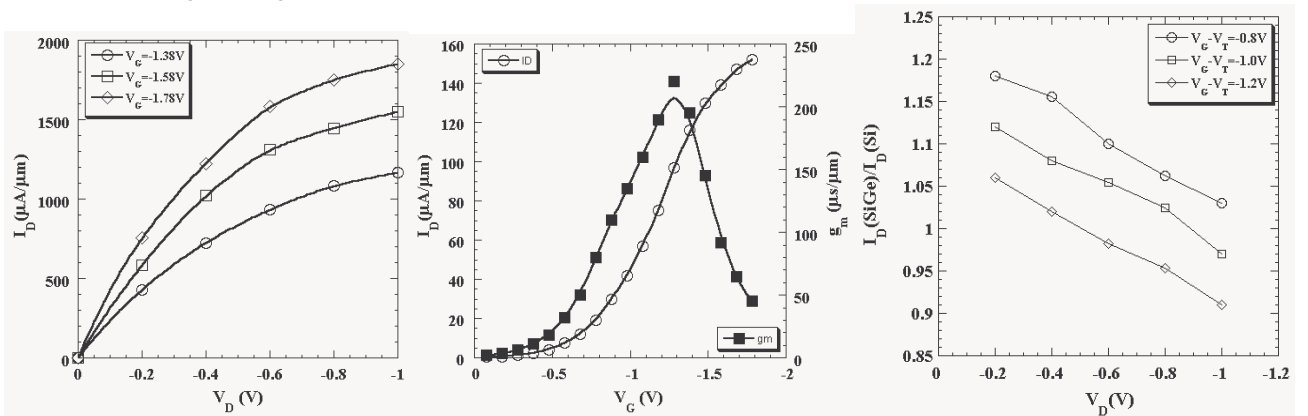


Fig. 3. Left panel - Output characteristics of the 25 nm p-channel strained SiGe MOSFET. Central Panel - Transfer characteristics of the 25 nm p-channel strained SiGe MOSFET. The device exhibits a peak transconductance of  $\sim 220 \mu\text{S}/\mu\text{m}$ . Thus, the enhancement in transconductance of the strained SiGe MOSFET over the Si MOSFET is about 26%. Right panel - Drain current enhancement of the strained SiGe MOSFET over the conventional Si MOSFET. It is seen that the SiGe MOSFET clearly performs better than the conventional Si MOSFET at low values of applied drain bias (low field regime) and moderate values of the gate voltage. This is the regime in which the hole mobility enhancement is predicted for device structures using a strained SiGe layer as the active layer for carrier transport.

# Monte Carlo Simulation of Double Gate MOSFET Including Multi Sub-Band Description

J. Saint-Martin, A. Bournel, F. Monsef, C. Chassat and P. Dollfus

Institut d'Electronique Fondamentale, CNRS UMR 8622, Université Paris Sud, Bât. 220, F 91405 Orsay cedex, France,

E-mail: jerome.saint-martin@ief.u-psud.fr

## INTRODUCTION

Double gate (DG) structures are promising architectures likely to overcome short channel effects in nanometer scaled MOSFET. In sub 50 nm MOSFETs,  $T_{Si}$  (Si body thickness) should be typically less than 10 nm to obtain good performances in both off and on states [1]. In order to accurately describe these transistors, quantum effects in the transverse direction and also quasi-ballistic carrier transports need to be taken into account.

## MODEL

Inspired by the mode-space approach of quantum transport [2] and the MC technique developed in ref. [3], our Monte Carlo simulations of DG MOSFET are self consistently coupled with 1D Schrödinger equation (cf. Fig 1 and Fig 2). Then, the x-axis, along which the carrier movement is supposed to be semi-classical, is separated from the z axis along which the energy is quantized (energies  $E_n$  and wavefunctions  $\xi_n(z)$  associated with the sub-bands 'n').

2D scattering mechanisms included in the simulation are bulk phonon and impurity scatterings, taking non parabolic and ellipsoidal band structures into account [4]. Roughness scattering treatment is underway and is not included in these preliminary results.

## RESULTS

The simulated 15 nm-long DGMOS device is described in Fig. 1. Fig. 3 presents the evolution of the quantized energies in the structures and the square of wave function associated with the first sub-band. In accordance with the mode space approach [2], the profile of this wavefunction does not significantly depend on x, even in the high electric field region (drain end). Fig. 4 clearly indicates that the electrons are moved away from

the Si/SiO<sub>2</sub> interface due to quantum repulsion in the whole structure.

As the velocities in this 15 nm long channel, shown in Fig. 5, are much higher than the stationary saturation velocity (about 10<sup>5</sup> m/s), the carrier transport is far from equilibrium. Moreover, Fig. 5 exhibits hot electron transfer from the lowest energy sub-band to higher sub-bands, in particular near the drain region. As a consequence, the sub-band occupation in the channel strongly differs from that obtained with a 1D Schrödinger-Poisson algorithm in which equilibrium distribution is assumed.

At last, Fig. 6 presents the drain current as a function of the gate voltage for both classical (3Dk) and multi sub-band (2Dk) simulations. The current is only softly modified by quantization effects.

## CONCLUSION

Multi sub-band description allows us to properly include the effects of quasi-ballistic transport and scattering on sub-band occupancy in nanoscale devices. With the price of a large increase of computation time, it gives a more accurate description of density profile and carrier transport than quantum correction approach. A detailed investigation of transport, ballisticity and I-V characteristics including the roughness influence will be presented at the conference.

## REFERENCES

- [1] Saint-Martin J. et al., *Comparison of multiple-gate MOSFET architectures using Monte Carlo simulation*, Solid State Electronics, in Press.
- [2] Venugopal R. et al., *Simulating Quantum Transport in Nanoscale MOSFETs: Real vs. Mode Space Approaches*, J. Appl. Phys. **92**, 3730 (2002).
- [3] Fischetti M.V., Laux S.E. *Monte Carlo study of electron transport in silicon inversion layers*, Phys. Rev. B **48**, 2244 (1993).
- [4] Monsef F. et al., *Electron transport in Si/SiGe modulation-doped heterostructures using Monte Carlo simulation*, J. Appl Phys. **95**, 35870 (2004).

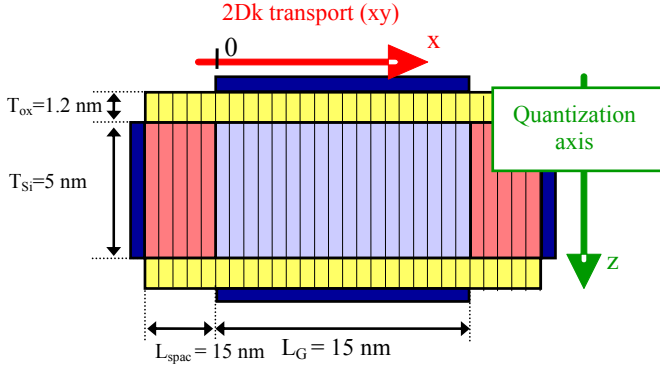


Fig. 1. Schematic of DG MOS structure

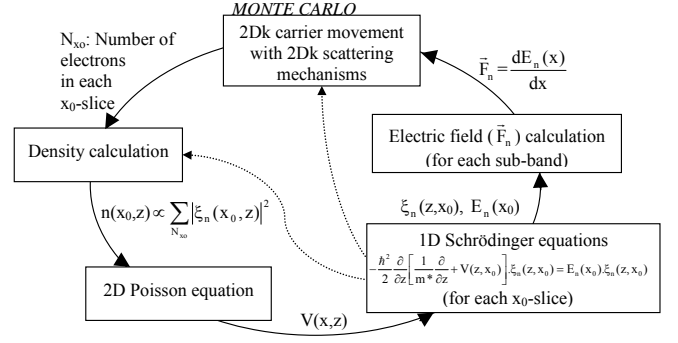


Fig. 2. Multi sub-band Monte-Carlo algorithm

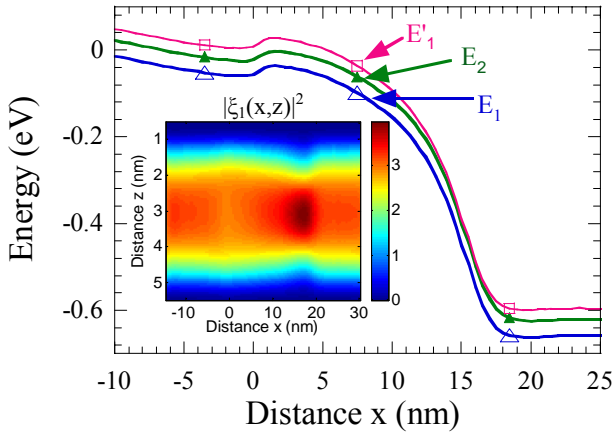


Fig. 3. Quantized energy evolutions along  $x$  axis. Inset: 2D cartography of square wavefunction of the first sub-band. NB: nonprime and prime sub-bands have a quantization mass of  $0.916.m_0$  and  $0.19.m_0$ , respectively

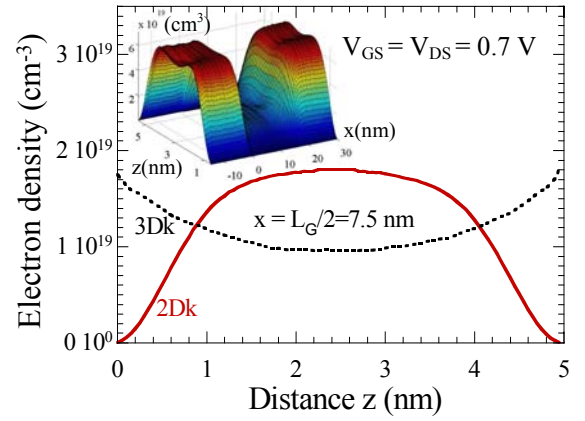


Fig. 4. Electron density versus distance  $z$  by including 2Dk (continuous lines) or not 3Dk (dashed lines) quantization effects. Inset: 2D cartography of electron density

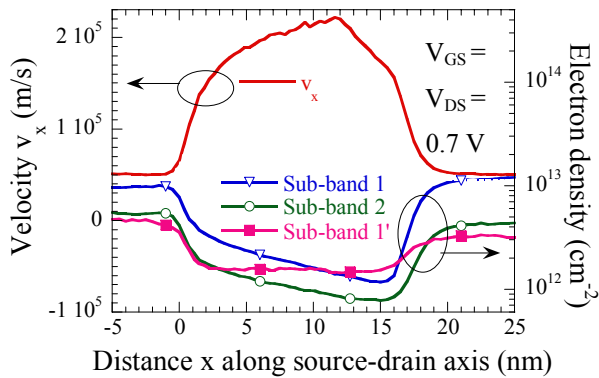


Fig. 5. Average velocity  $v_x$  and sheet density of first sub-bands versus distance  $x$ . N.B:  $E_1' > E_2 > E_1$ .

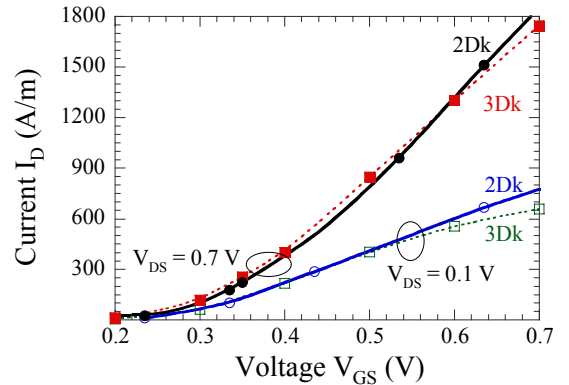


Fig. 6. Drain current  $I_D$  versus Gate voltage  $V_{GS}$  by including 2Dk (continuous lines) or not 3Dk (dashed lines) quantization effects.

# An Improved Wigner Monte-Carlo Technique for the Self-Consistent Simulation of RTDs

D. Querlioz, P. Dollfus, V. Nam Do, and V. Lien Nguyen\*

Institut d'Electronique Fondamentale, UMR CNRS 8622, Univ. Paris Sud, 91405 Orsay cedex, France

\*Theoretical Dept., Institute of Physics, VAST, P.O. Box 429 Bo Ho, Hanoi 10000, Vietnam

e-mail: damien.querlioz@ief.u-psud.fr

## INTRODUCTION

We present an original approach to include quantum transport in classical Ensemble Monte Carlo (EMC) simulations. The method is fully self-consistent, and includes scattering according to the Fermi Golden rule. The method is inspired by an approach suggested by Shifren and Ferry [1], with some major improvements that make possible successful comparison with other simulation techniques and experiments.

## BASICS OF THE METHOD

The method takes advantage of a pseudo-particle interpretation of the Wigner function formalism. The Wigner quasi-distribution function can indeed be seen as a sum of pseudo-particles whose real and reciprocal space coordinates evolve as classical particles, and whose magnitudes (affinities) evolve according to a quantum evolution term

$$Qf_w(x, k) = \frac{1}{2\pi\hbar} \int dk' V_w(x, k') f_w(x, k + k')$$
$$V_w(x, k) = \int dx' \sin(kx') \left[ V\left(x + \frac{x'}{2}\right) - V\left(x - \frac{x'}{2}\right) \right]. \quad (1)$$

Such pseudo-particles are scattered as classical particles and it is possible to build an EMC-like method for quantum-transport simulation. In such a method, however, injection and boundary conditions are different from that used in classical EMC simulations. In this paper we propose an original solution for this issue that seems more suitable than Shifren's initial suggestion. Note that the pseudo-particles interpretation of this method strongly differs from Nedjalkov's [2].

## RESULTS

On Fig. 1, we show J/V characteristics we got for a GaAs Resonant Tunneling Diode (RTD), for

simulations with scattering activated and deactivated. On Fig. 2, the simulation with scattering deactivated is first compared with a fully self-consistent NEGF simulation and very good agreement is obtained, except for the peak current which is a little higher in the Wigner simulation. This is the first step to validate quantum mechanics handling implemented in our method.

Figs. 3 and 4 show the Wigner functions for a resonant and a non-resonant state. The population of the quasi-bound state of the RTD quantum well is clearly seen. Fig 5 shows the self-consistent potential profile for these two situations.

## COMPARISON WITH EXPERIMENTS

To validate our approach of scattering handling, we compare on Table 1 peak to valley ratios of experimental RTDs [3] with values extracted from our simulations. These first results are encouraging, and more comparisons are underway.

## CONCLUSION

We have developed a model that seems very promising to incorporate quantum mechanics effects into traditional EMC simulations. Self-consistence and scattering are included, and the method is fully compatible with classical EMC simulations.

## ACKNOWLEDGEMENT

This work was partially supported by the EC 6th FP (NoE SINANO, contract no 506844).

## REFERENCES

- [1] L. Shifren, C. Ringhofer, and D. K. Ferry, IEEE Trans. Electron Devices **50**, 769 (2003).
- [2] M. Nedjalkov, H. Kosina, S. Selberherr, C. Ringhofer, and D. K. Ferry, Phys. Rev. B **70**, 115319 (2004).
- [3] T. J. Shewchuk, P. C. Chapin, P. D. Coleman, W. Kopp, R. Fischer, and H. Morkoc, Appl. Phys. Lett. **46**, 508 (1985).

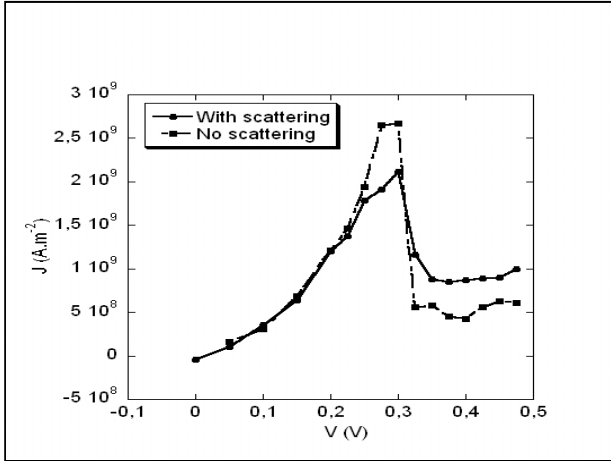


Fig. 1.  $J/V$  characteristic of a 300K GaAs RTD, with scattering activated and deactivated

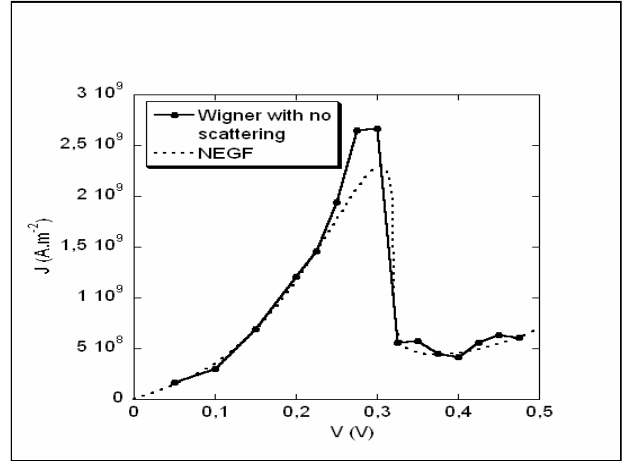


Fig. 4. Comparison of the characteristic of the RTD with scattering deactivated with a fully self-consistent ballistic NEGF calculation

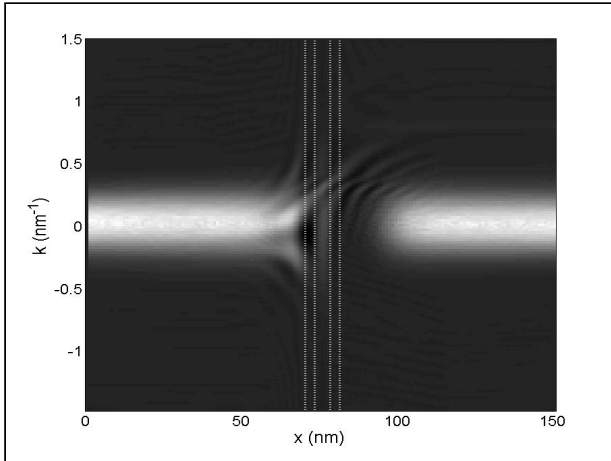


Fig. 2. Wigner function for an on-resonant state ( $V=0.3V$ )

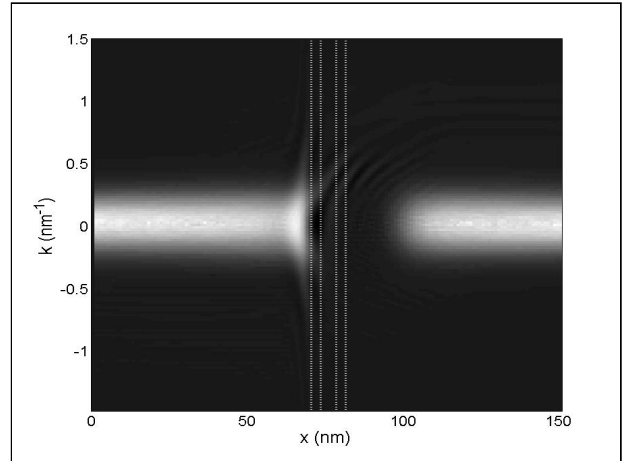


Fig. 5. Wigner function for an off-resonant state ( $V=0.475V$ )

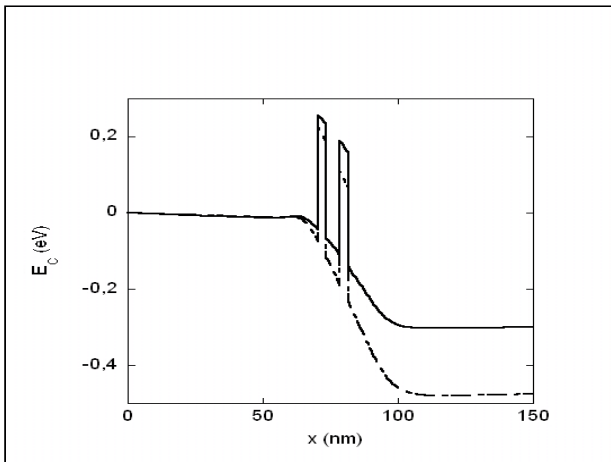


Fig. 3 Self-Consistent potential profiles of the RTD for  $V=0.3$  (plain line) and  $V=0.475V$  (dotted line)

	Exp	Simu
	$\frac{I_{peak}}{I_{valley}}$	$\frac{I_{peak}}{I_{valley}}$
Device [3] 300K	1.3	1.25
Device [3] 77K	4.0	3.8

Table 1. Comparison of simulations and experimental results

# Scattering and Space-Charge Effects in Wigner Monte Carlo Simulations of Single and Double Barrier Devices

V. Sverdlov, T. Grasser, H. Kosina, and S. Selberherr

Institute for Microelectronics, TU Wien, Gußhausstraße 27–29/E360, 1040 Wien, Austria  
e-mail: sverdlov@iue.tuwien.ac.at

Due to the aggressive downscaling of MOSFETs the channel length  $L$  is rapidly approaching 25 nm and is expected to be further reduced. At these channel lengths quantum effects such as direct source-to-drain tunneling start affecting the device characteristics. At the same time, scattering still controls the current in decananometer devices [1]. An accurate theory of MOSFETs near the scaling limit must therefore properly account for the interplay between coherent quantum and dissipative scattering effects. This mixed transport regime can be treated by the Wigner function formalism which allows for a seamless link between classical and quantum device regions [2]. Early numerical solutions of the Wigner equation were obtained by the finite difference method, assuming simplified scattering models based on the relaxation time approximation [3]. However, for realistic device simulations comprehensive scattering models are required. The Wigner equation including realistic scattering mechanisms can be solved by means of Monte Carlo (MC) techniques [2]. Due to the non-positive kernel, however, Wigner MC simulations require significantly longer computation times than classical MC simulations do.

In this work we demonstrate the role of scattering and space charge effects on the electrical characteristics of single and double barrier devices. Single barrier  $n-i-n$  structures, double gate field-effect transistors (FET), and resonant tunneling diodes (RTD) are considered. Several numerical methods have been improved to render the Wigner MC technique more robust, including the separation of a classical force, discretization of the Wigner potential, and a particle annihilation algorithm. A self-consistent iteration scheme with the Poisson equation was introduced.

For the lowest sub-band profile of a 10 nm gate length double-gate FET we have compared the quantum ballistic currents computed using Wigner MC and a numerical Schrödinger solver. Fig.1 demonstrates good quantitative agreement and also shows the classical ballistic current for comparison. The quantum ballistic current is higher than the classical one due to carriers tunneling through the potential barrier.

Self-consistent (SC) potentials for  $n-i-n$  Si diodes with a length  $W$  of the intrinsic region ranging from 20 nm down to 2.5 nm have been calculated by Wigner and classical MC simulations (Fig.2.) The transition regions of the doping profile have length  $W$ . Electron-phonon and ionized impurity scattering are included. As expected, for a thick barrier the classical and quantum calculations yield the same result ( $W = 20$  nm). For  $W = 2.5$  nm, the additional space charge of electrons tunneling through the barrier results in an increase of the barrier height. Despite the increased barrier, the current  $I_{\text{WTE}}$  is nearly 20% higher than the classical value  $I_{\text{BTE}}$  (Fig.3,  $W = 2.5$  nm). The relative difference between  $I_{\text{WTE}}$  and  $I_{\text{BALL}}$  for a "ballistic" device with scattering inside the intrinsic and transition regions turned off is shown in Fig.3. For  $W = 2.5$  nm the relative differences due to quantum effects and scattering in the barrier area still in the order of 25% and cannot be neglected.

Self-consistent carrier concentration profiles for a double-barrier GaAs RTD are shown in Fig.4. Before the barrier, an accumulation layer forms, depending on the applied voltage. The result is an additional voltage shift of the resonance peak of the I/V characteristics as demonstrated in Fig.5.

In conclusion, the importance of both scattering and quantum interference effects for simulations of decananometer devices at room temperature is

demonstrated. Space charge effects cannot be neglected, as tunneling currents would be overestimated otherwise.

The work was supported by FWF project P17285-N02 (Austria).

### REFERENCES

- [1] P. Palestri *et al.*, "Understanding Quasi-Ballistic Transport in Nano-MOSFETs: Part I-Scattering in the Channel and in the Drain", *IEEE T-ED* **52**, 2727 (2005).
- [2] H. Kosina *et al.*, "A Monte Carlo Method Seamlessly Linking Quantum and Classical Transport Calculations", *J. Computational Electronics* **2**, 147 (2003).
- [3] W.R Frensley, "Boundary Conditions for Open Quantum Systems Driven far from Equilibrium", *Rev.Mod.Phys.*, **62**, 745 (1990).

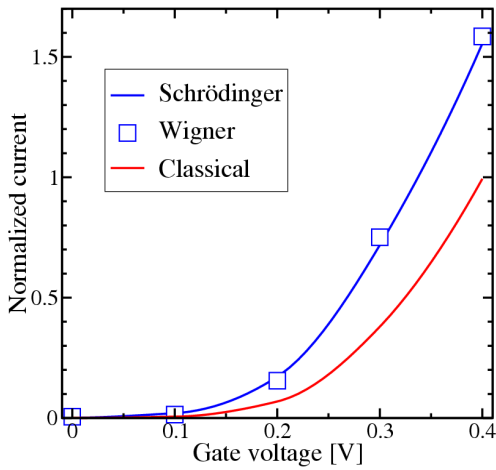


Fig. 1. Relative ballistic currents calculated classically (red) and quantum mechanically (blue). Wigner MC results are shown with open squares.

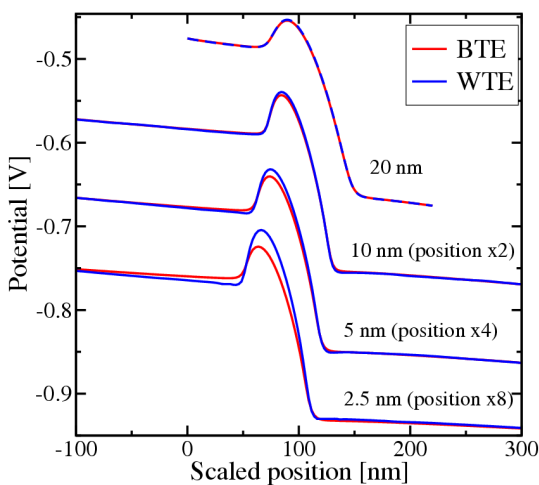


Fig. 2. Initial and self-consistent potential profiles calculated with Wigner (blue) and Boltzmann (red) MC.

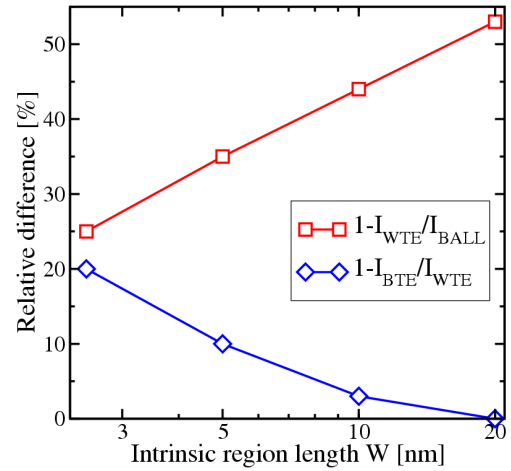


Fig. 3. Relative difference between currents calculated with Wigner and Boltzmann Monte Carlo methods (blue) and with and without scattering in the intrinsic region of *n-i-n* structure.

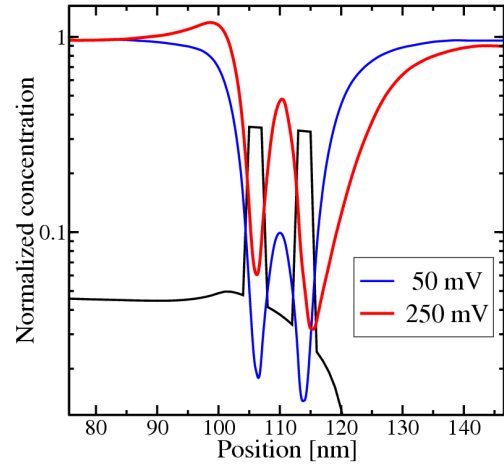


Fig. 4. Normalized electron concentration off-resonance (blue) and at resonance (red) in double-barrier structure. Space charge accumulation is seen at the cathode side of resonant tunneling diode.

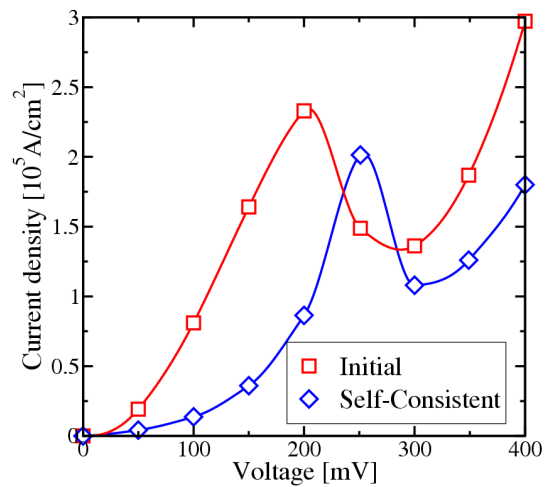


Fig. 5. Space charge accumulation at the cathode leads to significant shift of the resonance peak.

# Kinetic Monte Carlo Simulations of Germanium Epitaxial Growth on Silicon

R. Akis and D. K. Ferry

Center for Solid State Electronics Research and Department of Electrical Engineering  
Arizona State University, Tempe, AZ 85287-5706 USA  
e-mail: richard.akis@asu.edu

Due to its importance for microelectronic and optoelectronic device applications, there is great interest in gaining a detailed understanding in the processes involved in the epitaxial growth of Ge films and structures such as quantum dots and wires on the Si surface. Experimentally, a technique known as “atom tracking” has been employed using scanning tunneling microscopes to study the diffusion of Ge adatoms and ad-dimers [1-3]. The information about the surface kinetics extracted from these measurements provide a starting point for meaningful Kinetic Lattice Monte Carlo (KLMC) simulations, which we have implemented. As shown in Fig. 1, in this approach, atoms sit at discrete lattice sites in potential wells. The rate of hopping from site to site via a mechanism  $q$  is governed by an Arrhenius law,  $r_q = \nu_q \exp(-B_{ij}/k_b T)$ , where  $\nu_q$  is the attempt frequency. In our simulations, we also take into account the effects of surface reconstruction on the Si (100) surface. As shown in Fig. 2, this leads to the formation of rows and troughs which lead to anisotropy in the barriers for adatom and ad-dimer motion.

Importantly, studies [4,5] have indicated that there is intermixing in the layers adjacent to the interface so that the Si-Ge interface is not generally abrupt. We have used two inter-mixing mechanisms to account for this in our simulator. The first, illustrated in Fig. 3, is the dimer exchange mechanism, whereby Ge-Ge ad-dimers become Si-Ge ad-dimers when Si atoms are promoted from the substrate. The second involves the exchange of Si and Ge atoms below the surface to relieve misfit strain [5], which dominates what occurs beyond one monolayer of coverage, and generates a highly non-uniform interface between Ge and Si regions, but with a tendency for Ge and Si atoms to be

segregated depending on whether they are under a row or a trough.

One method of controlling what structures result from the growth process is to use a pre-patterned substrate (see, for example, Ref. [7]). We shall present the results of simulations on patterned substrates. An example is shown in Fig. 4, where the starting surface features a grid pattern. Here, the indentation is only 3 atomic layers deep with step edges. As shown in Figs. 5 and 6, our KLMC simulations in this case yield growth upon the surface, rather than in the pits. This gives Ge-Si stripes, that result largely from the anisotropy generated from the surface reconstruction. Some growth in the pits also occurs, but the major effect is on the surface.

## REFERENCES

- [1] X. R. Qin, B. S. Swartzentruber, and M. G. Lagally, *Diffusional Kinetics of SiGe Dimers on Si(100) Using Atom-Tracking Scanning Tunneling Microscopy*, Phys. Rev. Lett. **85**, 3660 (2000).
- [2] Z.-Y. Lu, Feng Liu, C.-Z. Wang, X. R. Qin, B. S. Swartzentruber, M. G. Lagally, and K.-M. Ho, *Unique Dynamic Appearance of a Ge-Si Ad-dimer on Si(001)*, Phys. Rev. Lett. **85**, 5603 (2000).
- [3] D.-S. Lin, J.-L. Wu, S.-Y. Pan, and T.-C. Chiang, *Atomistics of Ge Deposition on Si(100) by Atomic Layer Epitaxy*, Phys. Rev. Lett. **90**, 046102 (2003).
- [4] H. W. Yeom, J. W. Kim, K. Tono, I. Matsuda, and T. Ohta, *Electronic structure of monolayer and double-layer Ge on Si(001)*, Phys. Rev. B **67** (2003).
- [5] L. Nurminen, F. Tavazza, D. P. Landau, A. Kuronen, and K. Kaski, *Reconstruction and intermixing in thin Ge layers on Si(001)*, Phys. Rev. B **68**, 085326 (2003).
- [6] Y.-J. Ko, K.-H. Park, J. S. Ha, and W. S. Yun, *Ab Initio study of the mixed dimer formation in Ge growth on Si(100)*, Phys. Rev. Lett., **85**, 3660 (2000).
- [7] Z.Y. Zhong, A. Halilovic, M. Muhlberger, F. Schaffler, and G. Bauer, *Positioning of self-assembled Ge islands on stripe-patterned Si(001) substrates*, J. App. Phys. **93**, 6258 (2003).

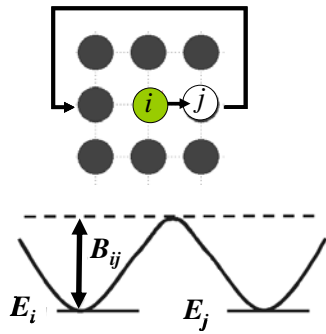


Fig. 1 In the KLMC approach, each adatom on the surface sits at a lattice site, coincident with a local potential minimum, as shown above. The bottom inset illustrates the potential energy landscape for two adjacent lattice sites,  $i$  and  $j$ , which are separated by an activation energy  $B_{ij}$ . When  $B_{ij} \gg k_B T$  ( $k_B$  is Boltzmann's constant and  $T$  is temperature), the transition rate,  $r_{ij}^q$ , of going from site  $i$  to site  $j$  via a process  $q$  is determined by an Arrhenius law.

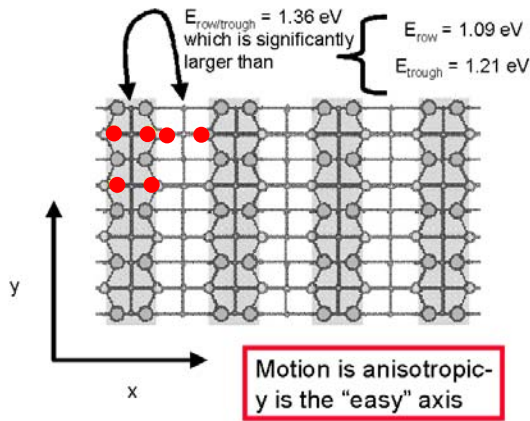


Fig. 2 The A top view of the reconstructed Si (100) surface. The diffusion of adatoms and ad-dimers across the reconstructed surface is anisotropic, with activation energies depending on whether the diffusion is  $\perp$  or  $\parallel$  to the dimer rows.

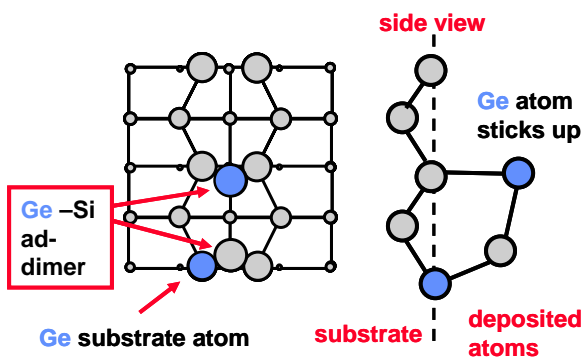


Fig. 3 Illustration of the surface dimer exchange mechanism. When two Ge adatoms meet on the surface, they form a dimer. However, it then becomes energetically favorable for one Ge atom to exchange places with a Si atom in the the substrate, resulting in a mixed dimer on the surface.

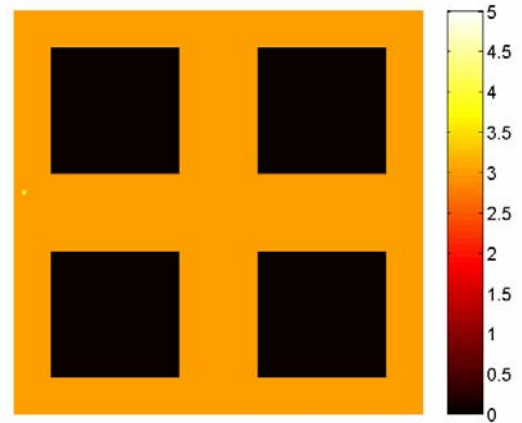


Fig. 4 The Si surface after a single Ge adatom has been deposited. Color indicates the number of atomic layers. The initial substrate has been patterned so that there is a Si grid, three atomic layers high and square voids.

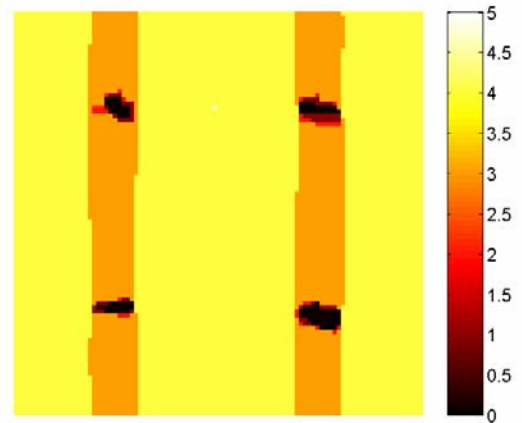


Fig. 5 As above, but after after two monolayers of Ge have been deposited at 470 K. The initial grid combined with the anisotropic hopping barriers have led to the formation of Ge/Si stripes on the surface.

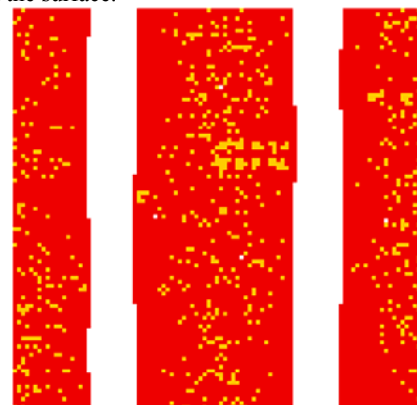


Fig. 6 The fourth atomic layer after deposition, with red corresponding to where there are Ge atoms and orange to Si. The Si atoms have been promoted from the substrate mainly via the exchange mechanism illustrated in Fig. 3.

# Self-Consistent Ion Transport Simulation in Carbon Nanotube Channels

Jan F. Eschermann\*, Yan Li†, Trudy A. Van der Straaten†, and Umberto Ravaioli†

\*Technical University of Munich

Institute for Nanoelectronics, Arcisstrasse 21, 80333 München, Germany

†Beckman Institute for Advanced Science and Technology

University of Illinois, 405 N. Matthews Ave., Urbana, IL 61801

**Abstract**— We propose a method to self-consistently deal with polarisation effects in Monte Carlo particle simulation of charge transport. The systems of interest were membrane structures with a narrow (4-8 Å) carbon nanotube (CNT) channel in an aqueous environment. Due to computational limitations for Molecular Dynamics (MD) computations we extended the Transport Monte Carlo known from semiconductor simulations to ionic transport in water as a background medium [1]. This method has been used successfully to compute transport rates of ions in biological channels but polarization effects on protein walls cannot be easily included self-consistently, due to the complexity of the structure. Since CNTs have a regular structure, it is instead practical to include a self-consistent scheme that accounts for the charge redistribution on the channel wall when an external bias is applied or when the electrical field of a passing ion is screened out. Previous work has shown that this is necessary and the computationally efficient tight-binding (TB) approach developed there [2] is coupled to transport Monte Carlo simulation in this work.

## I. INTRODUCTION

In recent years both the fields of CNT and ion channel research have been very active. While CNTs are promising in many respects because of their mechanical and electronic properties [3], biological ion channels on the other hand have received considerable attention both because they behave like nanoscale devices and because the causes of many diseases are linked to them. This makes them very interesting to develop new applications in bioengineering so that a better understanding of the transport mechanisms is required for the development of more efficient drugs or the development of highly specific biosensors. In this respect, CNTs are useful prototypes for biomimetic applications in artificial membranes due to their simple structure [4], [5]. What makes them even more interesting is the possibility to produce functionalized CNTs which are biocompatible and selective to certain types of ions [6], [7].

## II. TRANSPORT MONTE CARLO FOR ION CHANNEL SIMULATIONS

Because of the vast number of degrees of freedom when an ion channel structure is fully considered including water molecules and ion charges, it is only possible to simulate transport on the nanosecond scale with MD methods on computers available today. This, however, is not enough to fully understand the statistical properties of biological systems.

Our group has adapted its experience from semiconductor device simulations to develop implicit water transport Monte Carlo methodologies that may be applied to ion channel simulations [1]. Figure 1 shows the flow chart of this method. So far, this approach showed good agreement with experimental data and makes it possible to simulate the transport up to microsecond or millisecond scale, yielding results with high statistical significance.

As the Poisson solver requires the permittivities of each part of the domain, in previous calculations bulk dielectric constants were used. This, of course, does not account for the fact that single molecules in the system exhibit different behavior than bulk and becomes even more problematic for pore walls realized with CNTs, where the delocalized electrons can move along the tube easily.

In order to account for this effect a quantum mechanical treatment of the electronic structure becomes necessary. As the self-consistent charge distribution on the CNT has to be recalculated frequently a fast method is required. The semi-empirical TB approach fulfills this requirement [8]. In this proof of concept, a single orbital, nearest neighbor scheme has been integrated into the Monte Carlo code. One of the obtained trajectories is shown in figure 3.

Various comparisons between old and new model have been performed. The average fields like showed in Fig. 4 exhibit large differences and the transport rates changed by up to 50%. Results for different biases and ion types, were qualitatively the same for CNTs of different sizes.

We identified the solution of the Poisson equation as a computational bottleneck and work is in progress to parallelize this part of the code. This might allow highly precise simulations with even smaller time steps and mesh spacing. In the long term, our goal is to realize a platform for bioelectronics simulations comparable to the known tools for the design of semiconductor devices.

This work was supported by the NSF Network for Computational Nanotechnology and the German students exchange council (DAAD).

## REFERENCES

- [1] T.A. Van der Straaten, G. Kathawala, A. Trelakis, R.S. Eisenberg, and U. Ravaioli, *BioMOCA - a Boltzman transport Monte Carlo model for ion channel simulation*, Mol. Simulation **31**(2-3), 151-171 (2005).

- [2] D. Lu, Y. Li, U. Ravaioli, and K. Schulten, *Empirical Nanotube Model for Biological Applications*, J. Phys. Chem. B **109**, 11461-11467 (2005).
- [3] R. Saito, G. Dresselhaus, and M.S. Dresselhaus *Physical Properties of Carbon Nanotubes*, Imperial College Press, London (1998).
- [4] B.R. Azamian, J.J. Davis, K.S. Coleman, C.B. Bagshaw, and M.L.H. Green, *Biochemical single-walled carbon nanotubes*, J. An. Chem. Soc. **124**, 12664-12665 (2002).
- [5] F. Zhu, and K. Schulten, *Water and Proton Conduction through Carbon Nanotubes as Models for Biological Channels*, Biophysical J. **85**, 236-244 (2003).
- [6] M. Shim, N.W.S. Kam, R.J. Chen, Y. Li, and H. Dai, *Functionalisation of carbon nanotubes for biocompatibility and biomolecular recognition*, Nano Lett. **2**, 285-288 (2002).
- [7] S. Joseph, R.J. Mashl, E. Jakobsson, and N.R. Aluru, *Electrolytic Transport in Modified Carbon Nanotubes*, Nanoletters, **3**(10), 1399-1403 (2003).
- [8] K. Esfarjani, and Y. Kawazoe, *Self-consistent tight-binding formalism for charged systems*, J. Phys. C **10**, 8257-8267 (1998).

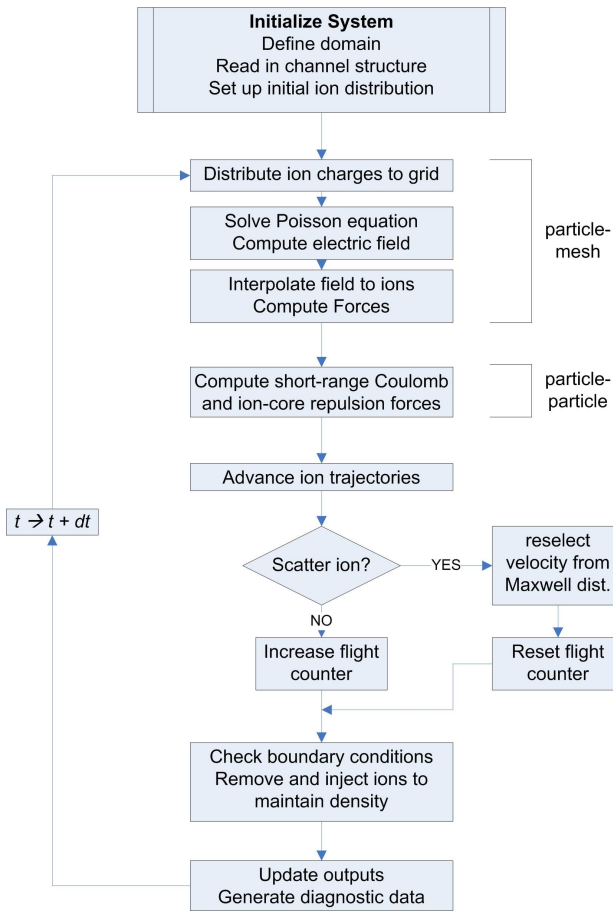


Fig. 1. Boltzman transport Monte Carlo.

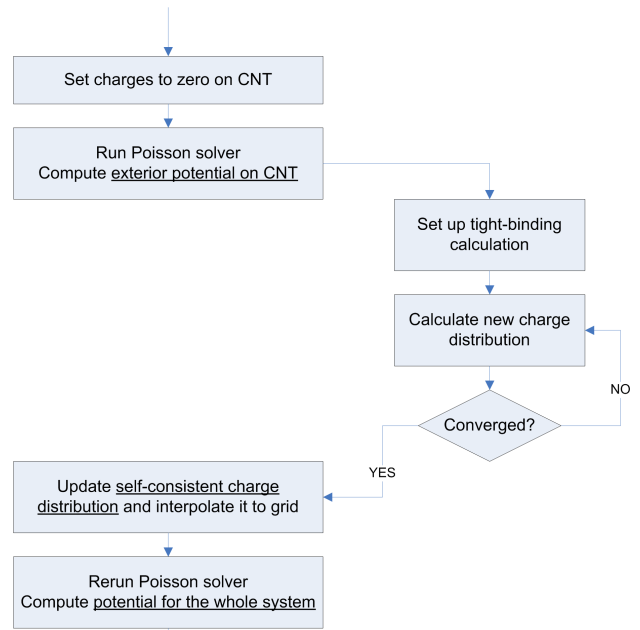


Fig. 2. Integration of the TB solver.

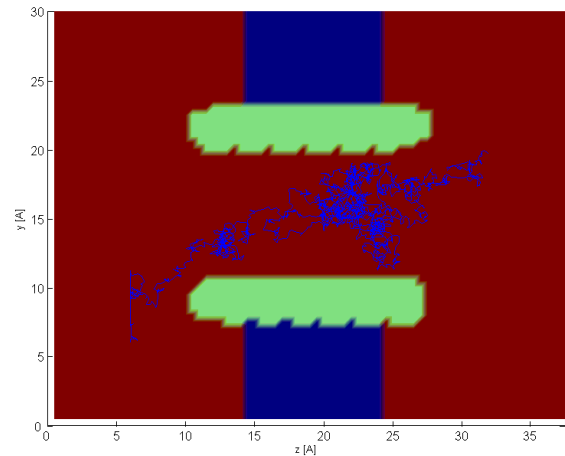


Fig. 3. Sample trajectory of a sodium ion passing through a (8,8) CNT.

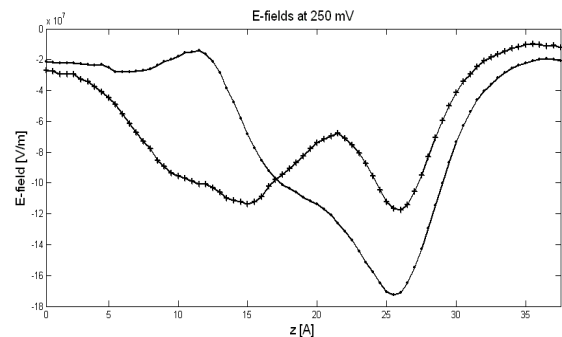


Fig. 4. Average electrical fields along the axis. Self-consistent solution is marked with (+).

# Power•Delay Product in COSMOS Logic Circuits

Ahmad Al-Ahmadi and Savas Kaya

SEECs, Russ College of Engineering & Technology, Ohio University, Athens, OH 45701, USA  
e-mail:kaya@ohio.edu, fax:1-740-593-0007

As CMOS devices explores its fundamental scaling limits, there is a clear consensus that planar MOSFET architecture will be replaced with novel SOI devices incorporating one or more of performance enhancing features such as strain engineering, multiple-gates, heterostructure channels and contacts [1,2]. In accordance with this trend, we have recently purposed a unique CMOS device pair called COSMOS that integrates *n*- and *p*-type MOSFETs both vertically and laterally in an orthogonal layout using strained Si/SiGe on SOI technology [2,3]. Previously, we have shown that COSMOS devices are especially suitable for low-voltage and area-tight designs, due to its inherent reduction in active area and parasitics [4,5]. However, these analyses were based on a simple inverter circuit and did not consider power•delay product, which is the focus of this work.

Fig.1 shows the 3D perspective view of a COSMOS inverter gate. The COSMOS architecture relies for operation on several important structural modifications. For the transport, a thin silicon layer (electron channel) must be grown atop a strained SiGe hole channel. Alternatively, flip-bond on SOI may be used to this end [6-8]. To facilitate threshold tuning, reduce parallel conduction and eliminate need for doping, Ge concentration in the strained channel must be high. In accordance, the gate material may be a mid-gap metal, poly-SiGe alloy or polySi, depending on the choice of Ge concentration. For a layer structure with a 3nm strained-Si<sub>0.3</sub>Ge<sub>0.7</sub> hole channel and 2nm Si electron channel under a mid-gap metal gate, 3D TCAD simulations indicate that symmetric MOSFET characteristics (Fig.2) can be obtained using only a single gate. Typically we can achieve a threshold  $|V_T|=0.4\pm 0.2$  V.

To demonstrate the usefulness of COSMOS for digital circuits, the simulated transient response of a 40nm COSMOS NOT gate to an input pulse is provided in Fig.3. Note that there is no additional manufacturing steps or structures needed for the NOT gate except a *short* metallization layer, hence reducing total RC losses considerably. Clearly, the single gate COSMOS inverter is operational with acceptable noise margins and delay (~100ps).

In the present work, we report the result of 3D simulations to analyze and optimize the temporal response of larger COSMOS circuits such as the NOR gate shown in Fig.4. All our simulations are carried out using ISE TCAD suite [9], which allows accurate 3D meshes and advanced transport models to be incorporated. The transient response of the NOR gate (Fig.5) confirms that output remains low except the '00' input to the gates for a rail-to-rail ( $V_{DD}+|V_{SS}|$ ) voltage of 0.6V. Further simulations at higher voltages (Figs.6&7) indicate that, while the NOR gate is operational, its leakage performance and noise margin deteriorate rapidly above  $V_{DD}+|V_{SS}|=0.8V$ . At the same time, however, the delay improves rapidly, indicating the importance of optimizing power•delay product in COSMOS circuits.

At the heart of the power versus delay trade-off in COSMOS circuit is the static leakage stemming from the intrinsic formation of 90°-bent *p-i-n* diode between the  $V_{DD}$  and  $V_{SS}$  contacts. Since the number of such contacts in close proximity increases in logic gates with multiple inputs, large-scale COSMOS circuits can radically benefit from identification of power•delay 'sweet spots' being explored in this work. Furthermore it is possible to reduce the static leakage by i) raising the  $V_T$  above 0.3V in the present circuits, for instance by relaxing oxide thickness slightly, which can be tolerated in such ultra-thin channels, ii) adding an extra stop etch beneath the top Si electron channel as opposed to a single etch used in the original COSMOS design [4], and iii) optimizing the device layout by way of shifting the center of the COSMOS cross [10].

We focus on the implementation and comparison of above approaches in choosing suitable power•delay products in large-scale COSMOS circuits. Therefore the present work will assess and explore COSMOS designs in more realistic settings.

- [1] SIA Silicon Roadmap, 2005 Ed., <http://public.itrs.net/>
- [2] H-S P Wong, *IBM J Res & Dev.*, vol.46, pp.133, 2002.
- [3] J.-S-Rieh *et al.*, *IEDM Tech Dig.*, p771, 2002.
- [4] S Kaya, Proc. Si Nanoelectronic Workshop, p.7, 2004
- [5] A AlAhmadi and S. Kaya, Proc. SISPAD, p.263, 2005
- [6] T Numata *et al.*, *IEEE SOI Conference*, p.119, 2003,
- [7] T Mizuno *et al.*, *IEDM Tech Dig.*, p.809, 2003.
- [8] S Harrison *et al.*, *IEDM Tech Dig.*, p.449, 2003.
- [9] ISE TCAD 8.0, <http://www.ise.com/>
- [10] A AlAhmadi and S. Kaya, *Sol-State Elec.*, submitted

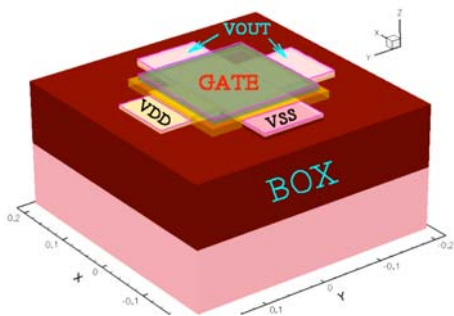


FIGURE 1: 3D view of the COSMOS device ( $L=200\text{nm}$ ) and the 3D simulation domain.

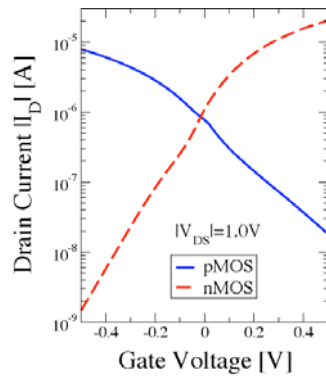


FIGURE 2: Simulated I-V plot in 3D. QM corrections are omitted in this case to save time, e- and h+ mobility are unequal

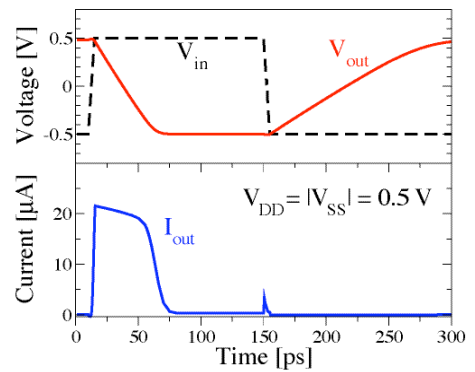


FIGURE 3: Output response of a 40 nm COSMOS inverter to high and low logic inputs of  $\pm 0.5\text{V}$ , illustrating logic functionality using a single gate

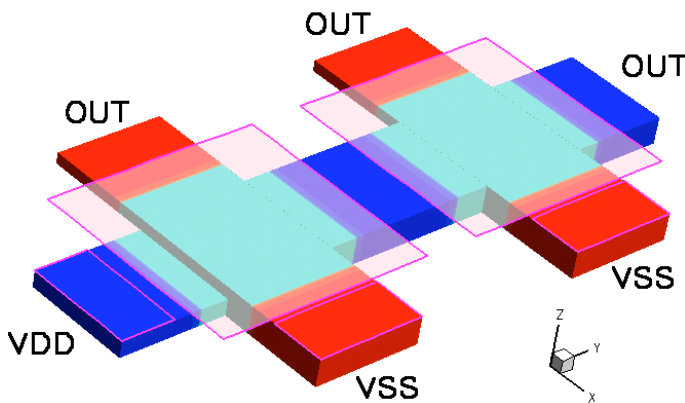


FIGURE 4: The 3D view of a two-input NOR circuit using only two COSMOS gates. All contacts and gates are shown in semi-transparent fashion to aid the reader. Note that the two nMOSFETs are aligned in parallel while the two p-MOSFETs are in series.

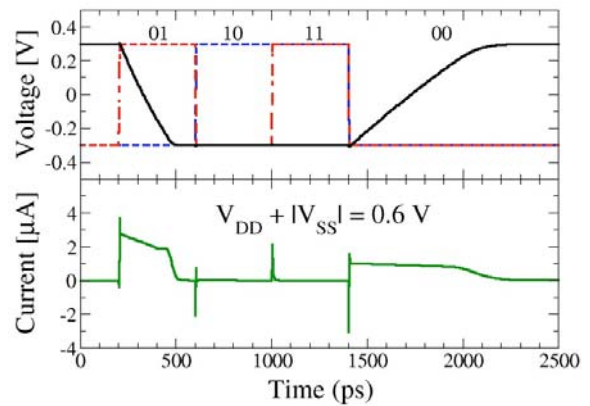


FIGURE 5: The transient response of output voltage (top) and total supply current (bottom) in the COSMOS NOR gate with 40nm gates (see Fig.4). The top figure also includes the input waveforms to the two gates. Only '00' input produces a high output.

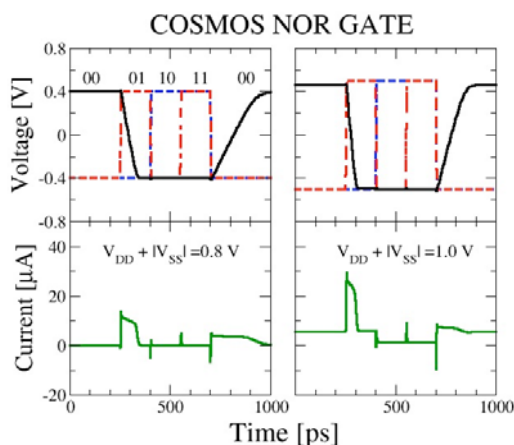


FIGURE 6: Similar to Fig.5 except at higher rail-to-rail voltages. At larger bias conditions the static leakage through the of  $90^\circ$ -bent  $p$ - $i$ - $n$  diode becomes visible as well as the deterioration of the noise margins.

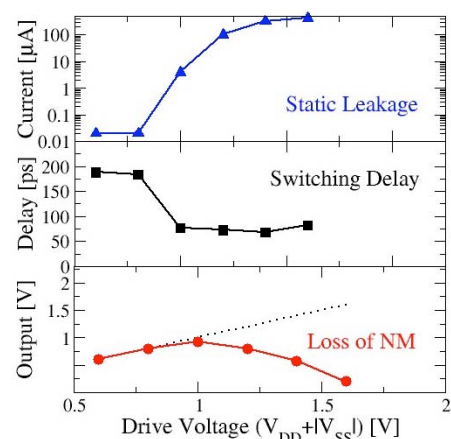


FIGURE 7: Summary of major performance figures for the COSMOS NOR gates driven at different rail-to-rail voltages. Note that optimum power\*delay product is likely to be between 0.8 to 1.0V in this circuit.

# A 3D Finite Element Parallel Simulator for Studying Fluctuations in Advanced MOSFETs

M. Aldegunde\*, A. J. García-Loureiro\*, K. Kalna†, and A. Asenov†

\*Department of Electronics and Computer Science, University of Santiago de Compostela,  
15782 Santiago de Compostela, Spain. E-mail: maldegunde@dec.usc.es

†Device Modelling Group, Department of Electronics & Electrical Engineering,  
University of Glasgow, Glasgow G12 8LT, United Kingdom

Polysilicon gates and high- $\kappa$  dielectrics used in today's MOSFETs are a serious source of intrinsic parameter fluctuations in addition to the random dopants in the channel, source and drain, the line edge, and interface roughness [1]. Limits in doping activation in the polysilicon gate and the doping depletion near the interface result in an unwanted poly depletion effect [2]. The grain structure of the polysilicon is one of the main contributors to the fluctuations, leading to a mismatch in the threshold voltage of sub-100 nm MOSFETs.

Most of the high- $\kappa$  dielectrics exhibit a thermal instability which leads to local crystallisation of the initially amorphous layer. Regions with different dielectric constant appear which contribute to the intrinsic parameter fluctuations in a device.

In this work, we investigate intrinsic parameter fluctuations introduced by the polysilicon gate and the high- $\kappa$  dielectric layer using a 3D parallel device simulator. The simulator employs the finite element discretisation in a drift-diffusion (D-D) approximation for the electron transport and runs in parallel employing MPI standard library. We have developed an efficient tetrahedral unstructured mesh generator designed to deal with complicated geometry appearing in sub-100 nm advanced Si MOSFETs in the presence of fluctuations. The mesh is refined close to the boundaries between different regions of the transistor and the zones with the highest variations in the electrostatic potential resulting in a mesh illustrated in Fig. 1. This meshing is also suitable for an accurate description of the polysilicon grain boundaries illustrated in Fig. 2. The simulation domain is partitioned into sub-domains shown in Fig. 3 and assigned to individual processors.

The 3D parallel D-D MOSFET simulator has

been calibrated with respect to an  $n$ -type 67 nm effective gate length Si MOSFET [3]. Fig. 4 compares  $I_D$ - $V_G$  characteristics obtained from the 3D D-D parallel simulator with experimental data. It also shows results obtained when the  $\text{SiO}_2$  gate dielectric is replaced with a high- $\kappa$  one with a dielectric constant of 20 ( $\text{HfO}_2$ ), and results when considering an interfacial layer of  $\text{SiO}_2$  together with relatively large polycrystalline islands of different dielectric constants in the gate dielectric. Finally, the results obtained assuming a Gaussian distribution of different dielectric constants with a correlation length of 3 nm mimicking fine grains of different orientations in the high- $\kappa$  gate dielectric layer are presented as well. Fig. 5 shows a semilogarithmic plot of electron density in the 67 nm MOSFET. The effect of intrinsic parameter fluctuations in the polysilicon gate and in the high- $\kappa$  dielectric layer will be also studied in a template 25 nm gate length bulk MOSFET. As an example, in Fig. 6, we show the electron density right below the semiconductor-insulator interface in the case when the dielectric layer consists of two regions with different dielectric constant separated by a plane  $y = 0$ .

## REFERENCES

- [1] A. Asenov and S. Saini, *Polysilicon gate enhancement of the random dopant induced threshold voltage fluctuations in sub-100 nm MOSFETs with ultrathin gate oxide*, IEEE Trans. Electron Devices **47**, 805 (2000).
- [2] P. R. Suresh, P. Venugopal, S. T. Selvam and S. Potla, *Combined Effect of Grain Boundary Depletion and PolySi/Oxide Interface Depletion on Drain Characteristics of a p-MOSFET*, Proc. IEEE Int. Conf. VLSI Design, 156 (1996).
- [3] K. Rim et al., *Strained Si NMOSFETs for high performance CMOS technology*, Symp. VLSI Technol., Dig. Tech. Pap., 59 (2001).

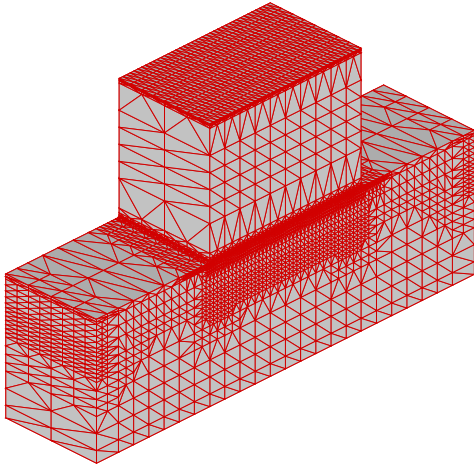


Fig. 1. Finite element mesh for simulation of the 67 nm effective gate length Si MOSFET with a polysilicon gate.

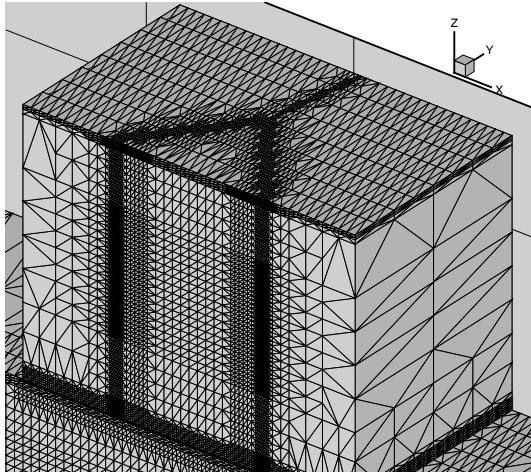


Fig. 2. Detail of a gate meshed for the simulation of three grains in polysilicon.

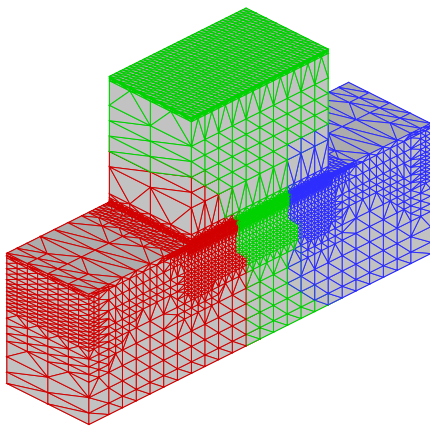


Fig. 3. Partition of the finite element mesh in three subdomains.

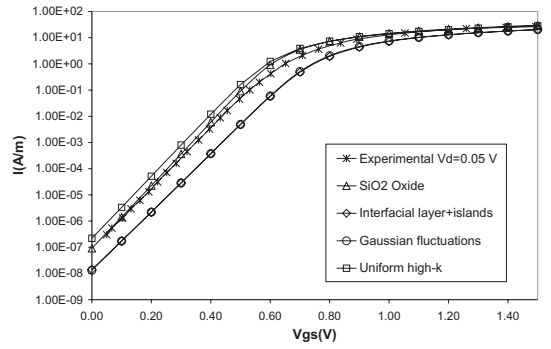


Fig. 4.  $I_D - V_G$  characteristics obtained from the 3D D-D parallel simulator compared with experimental data for the 67 nm effective gate length Si MOSFET.

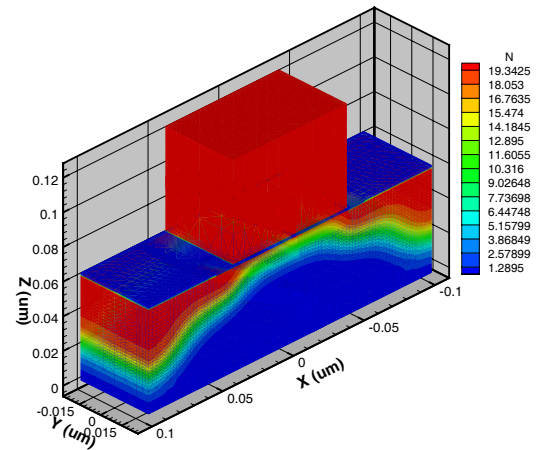


Fig. 5. Electron density on log scale in the 67 nm effective gate length Si MOSFET at  $V_G = 0.5V$  and  $V_D = 0.05V$ .

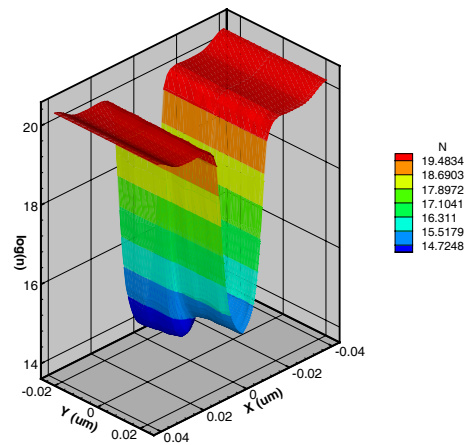


Fig. 6. Electron density at equilibrium beneath a dielectric layer with two different dielectric constants of 7 ( $Si_3N_4$ ) and 5 in the template 25 nm gate length bulk MOSFET.

# Calibration of the Density-Gradient Model by Using the Multidimensional Effective-Mass Schrödinger Equation

Petru Andrei

ECE Department, Florida State University and Florida A&M University  
Tallahassee, Florida, USA  
e-mail: pandrei@eng.fsu.edu

## INTRODUCTION

The calibration of phenomenological models of semiconductors is one of the most important tasks in the modeling and analysis of an electronic device. Before a model is used to analyze a semiconductor device, the model parameters should be carefully identified by using more elaborate physical models. In the case of the Density-Gradient model (DGM), the electron and hole effective masses should be computed by using self-consistent Poisson-Schrödinger computations.

The existing methods for the computation of electron and hole effective masses are based on the comparison of the model with 1D Poisson-Schrödinger computations. While this approach is appropriate for devices in which the carriers are confined in only one direction, it is not appropriate for devices in which the carriers are confined in more than one direction, such as short-channel MOSFETs, SOI devices, Fin-FETs, etc. In this article we calibrate the DGM against 2- and 3-dimensional Schrödinger computations. We focus mainly on the computation of electron effective mass, since it enters directly in the equations of the electron current density in n-channel transistors, which are widely used in integrated circuits.

## TECHNICAL APPROACH AND DISCUSSION

In the framework of the DGM, the electron concentration at thermal equilibrium can be computed by using the following partial differential equation [1]:

$$\frac{\hbar^2}{12q} \frac{2\nabla \cdot \left( m_{eff,n}^{-1} \nabla \sqrt{n} \right)}{\sqrt{n}} + \varphi - \Phi_n(T) = 0, \quad (1)$$

where  $\Phi_n(T)$  is some function that depends on the nature of electron statistics used,  $m_{eff,n}$  is the electron effective mass, and all other notations have their usual meaning. Due to the low-order approximations involved in the derivation of (1) it is unrealistic to use the experimental value of  $m_{eff,n}$  and the electron effective mass in (1) should be treated as a fitting parameter.

It should be noted that there is no unanimous agreement on the values of  $m_{eff,n}$  presented in the literature and the results obtained vary from  $0.175m_0$  in [2] to  $0.278m_0$  in [3]. The common feature of the existing identification techniques is that  $m_{eff,n}$  is calibrated against results obtained by solving the 1D Schrödinger equation in the direction perpendicular to the oxide layer of MOS devices. In this way, it is tacitly assumed that the motion of electrons and holes is quantized only in the direction perpendicular to the oxide and it is described by classical statistics in the other two directions. In the following we present a technique based on the multidimensional effective-mass Schrödinger equation that overcomes the limitations of the existing methods. To simplify numerical computations, let us consider that the electrostatic potential is given a-priori and we can compute the electron concentration by using the effective-mass Schrödinger equation. The electron effective mass can then be computed either by integrating equation (1) or by fitting the electron concentration obtained from (1) to the electron concentration obtained from the Schrödinger equation. This approach has the advantage that it avoids expensive Poisson-

Schrödinger computations. Moreover, for particular shapes of the quantum region the eigenvalues and eigenfunctions of the Hamiltonian can be computed analytically and solving the Schrödinger equation numerically can be completely avoided. For example, if we consider a 2D quantum box with infinite walls (see Fig. 1), the electron effective mass depends of the spatial coordinates as in Fig. 2. For a  $10 \times 20$  nm quantum box in which the electrostatic potential is increasing exponentially, the electron concentration is presented in Fig. 3 for various potential profiles. In these computations  $m_{eff,n}$  is assumed constant and it is found by fitting the results obtained by the Schrödinger equation to equation (1).

In Fig. 4 we present the values of the electron effective mass computed for different sizes and shapes of the quantum box. We clearly observe that  $m_{eff,n}$  changes from  $0.14m_0$  in the case when  $L_x \gg L_z$ , to  $0.24m_0$  for  $L_x \ll L_z$ . In numerical simulations one should use the value of the electron effective mass which corresponds to the approximate size of the quantum region. In the case of short channel MOSFET devices,  $m_{eff,n}$  lies between  $0.14m_0$  and  $0.24m_0$ , depending on the values of  $W_{eff}/L_{eff}$  (the effective width divided by the effective length of the conduction channel), as well as on the epitaxial cut of the silicon crystal. For short-channel MOSFET devices,  $m_{eff,n}$  is either  $0.15m_0$  or  $0.24m_0$ , depending on whether the x-axis is along or perpendicular to the conduction channel. Our analysis also suggests that the existing discrepancies in the literature on the values of  $m_{eff,n}$  originate from the different sizes of the quantum regions used in simulations.

#### REFERENCES

- [1] M. G. Ancona and G. J. Iafrate, *Quantum correction to the equation of state of an electron gas in a semiconductor*, Phys. Rev. B **39**, 9536 (1989).
- [2] A. Asenov, S. Slavcheva, A. R. Brown, J. H. Davies, and S. Saini, *Increase in the random dopant induced threshold fluctuations and lowering in sub-100 nm MOSFETs due to quantum effects: A 3-D Density-Gradient simulation study*, IEEE Trans. Electron Devices **48**, 722 (2001).
- [3] A. Wettstein, A. Schenk, and W. Fichtner, *Quantum device-simulation using the density-gradient model on unstructured grids*, IEEE Trans. Electron Devices **48**, 279 (2001).

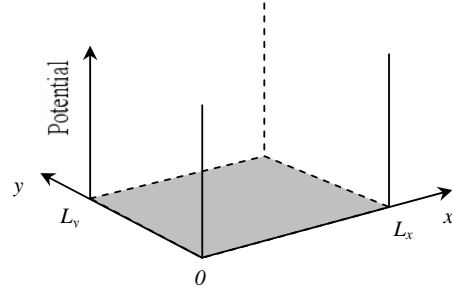


Fig. 1. 2D quantum box with infinite walls.

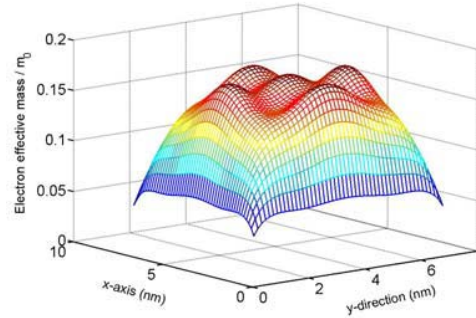


Fig. 2. Electron effective mass computed by integrating eq. (1), in which  $n$  was obtained by solving Schrödinger eq. for Si(100).

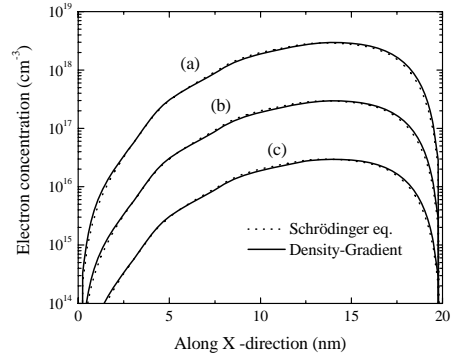


Fig. 3. Electron concentration cross-sections through the middle plane of a  $10 \times 20$  nm rectangular quantum box.

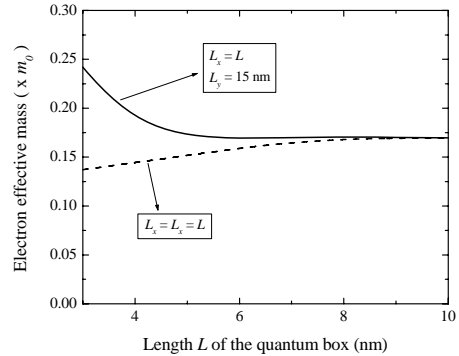


Fig. 4. Electron effective mass that gives the best agreement between the electron concentration computed by using the 2D Schrödinger equation and the 2D Density-Gradient model, respectively, for a rectangular quantum box. The dimensions of the box are indicated on the abscissa.

# Random Dopant Fluctuation Analysis for Scaling Multi-Gate Device Structures

Yoshio Ashizawa, Ryo Tanabe, and Hideki Oka  
Fujitsu Laboratories Ltd., 50 Fuchigami, Akiruno, Tokyo, 197-0833, Japan  
e-mail: ashizawa.yoshio@jp.fujitsu.com

## INTRODUCTION

Multi-gate devices are extensively examined and expected to be one of the promising device structures beyond bulk MOSFETs. We have investigated basic characteristics of random dopant fluctuation for novel device structures, such as SG (Single Gate) SOI, DG (Double Gate) and tri-gate, by giving discrete dopant distribution[1] to the substrate. Moreover, we have calculated SNM (Static Noise Margin) for 6T-SRAM cell from hp45 to hp22 by a device simulator directly.

## BASIC CHARACTERISTICS

Fig. 1 shows device parameters to see basic characteristics for hp45 SG, DG and tri-gate devices. Discrete dopant is distributed only in the substrate by an atomistic process simulator while SD regions are assumed to be uniform box profiles analytically. As for DG structures, thinner DG (A) devices fluctuate less than thicker DG (C). However, DG (A) devices are almost a half of SG at the same body thickness,  $T_{si}$ , because of symmetrical layout of gates. Tri-gate devices with lower aspect ratios fluctuate much more than DG or tri-gate with higher aspect ratios. Table 1 shows device parameters to compare DG with bulk structures. Fig. 2 summarizes device characteristics fluctuation by  $\sigma V_{th}$  and sub-threshold factors. As for both DG and bulk structures,  $\sigma V_{th}$  will decrease with narrowing  $T_{si}$  or junction depth  $X_j$  for bulk structures. However, DG structures reduce  $\sigma V_{th}$  remarkably with narrowing  $T_{si}$ . As for sub-threshold factors, this is the same trend as  $\sigma V_{th}$ . This difference comes from floating body effect for DG or SG SOI.

## SENSITIVITY TO PROCESS VARIATIONS

Assuming uniform dopant profiles, we have studied sensitivity to process variations. Fig. 3 shows device parameters to scale hp45 and hp22 technologies.  $V_{th}$  is calculated for these structures

with process parameters ranging from  $-20\%$  to  $+20\%$ . However, continuous variation for  $T_{si}$  is not acceptable because it varies by lattice constant, 0.54 nm, for Si.

Now  $V_{th}$  shift is calculated at the process variation by lattice constant for  $L_g$ ,  $T_{si}$  and  $T_{fin}$  (Fig.4). It is becoming very important to control  $T_{si}$  for DG structures as well as  $L_g$  for future scaling. It is found that thinner  $T_{si}$  and uniform thickness are key factors as well as  $L_g$  to control characteristics fluctuation.

## 6T SRAM WITH RANDOM DOPANT FLUCTUATION

We have modeled SRAM with 6 DG transistors and calculated SNM from hp45 to hp22. Fig. 5 shows bird's-eye view and boron concentration for this SRAM. In this calculation, discrete dopant distribution is applied to channel regions only. SNM distribution width is getting narrower with scaling because body thickness becomes thinner. However, SNM is observed to shift lower value. To keep SNM high, optimizations of device structure and cell layout should be done in the future devices.

## CONCLUSION

We have investigated basic device characteristics fluctuation for novel device structures. DG structures are more sensitive to  $T_{si}$  thickness than  $X_j$  for bulk structures and multi-gate devices with thinner  $T_{si}$  and higher aspect ratios show less characteristics fluctuation. This finding suggests that multi-gate devices with thinner  $T_{si}$  should be one of the preferable candidates in the view of characteristics fluctuation.

## REFERENCES

- [1] N. Sano, K. Matsuzawa, M. Mukai, and N. Nakayama, *Role of Long-Range and Short-Range Coulomb Potentials in Threshold Characteristics under Discrete Dopants in Sub-0.1 $\mu$ m Si-MOSFETs*, IEDM Tech. Dig., pp.275-278, 2000.

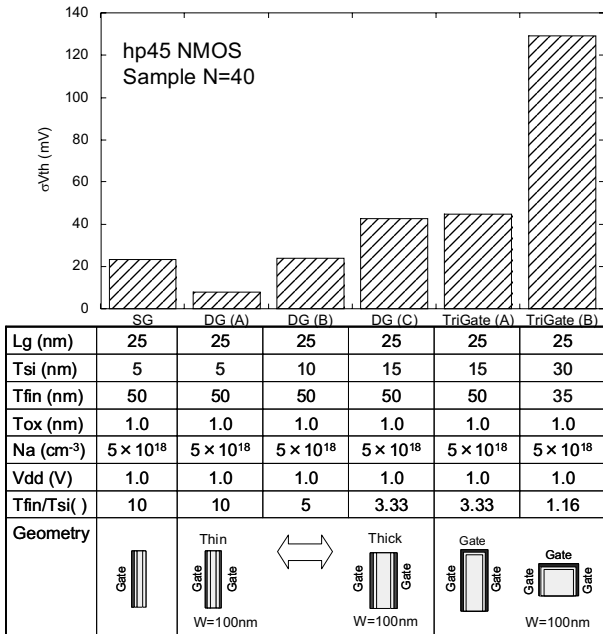


Fig. 1. Device parameters and  $\sigma V_{th}$  with random dopant fluctuation in the Si body.

Table 1. Device parameters to compare DG, SG and bulk structures.

hp45	DG (C)	DG (D)	SG (D)	Bulk (A)	Bulk (B)
Lg (nm)	25	25	25	25	25
Tox (nm)	1.0	1.0	1.0	1.0	1.0
H (nm)				60	60
Tsi/Xj (nm)	15	8	8	15	8
W (nm)	100	100	50	50	50
N <sub>xj</sub> (cm <sup>-3</sup> )	10 <sup>20</sup>	10 <sup>20</sup>	10 <sup>20</sup>	5 × 10 <sup>19</sup>	5 × 10 <sup>19</sup>
N <sub>SD</sub> (cm <sup>-3</sup> )	10 <sup>20</sup>				
N <sub>s</sub> (cm <sup>-3</sup> )	5 × 10 <sup>18</sup>				
Vdd (V)	1.0	1.0	1.0	1.0	1.0

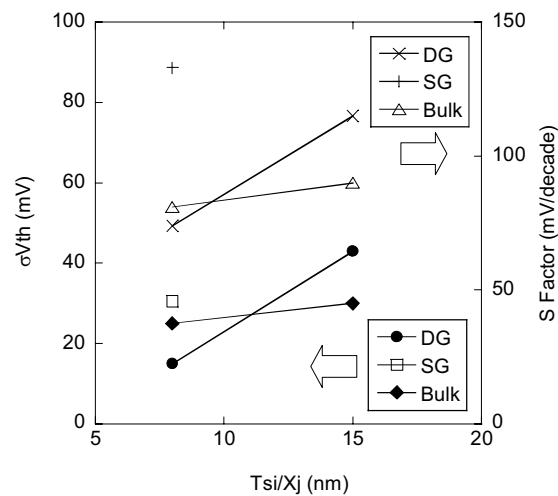


Fig. 2.  $\sigma V_{th}$  and S factors for various device structures.

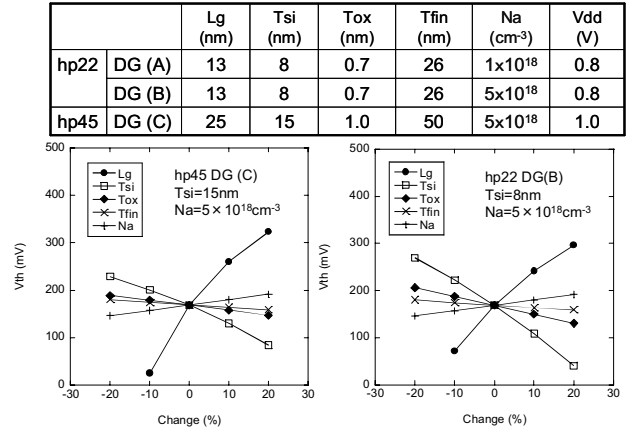


Fig. 3. Sensitivity analysis by giving process variations and channel dopant concentration for hp45 and hp22 technologies.

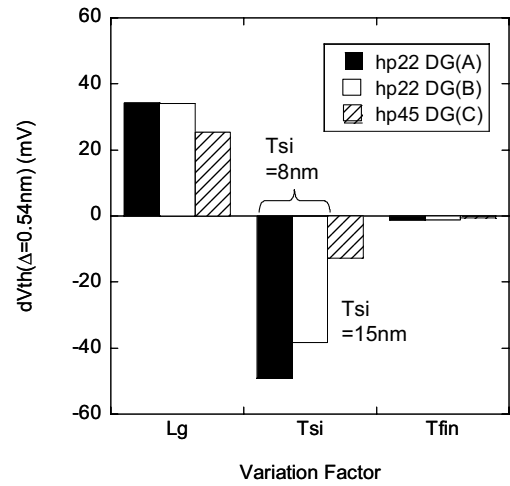


Fig. 4.  $V_{th}$  shift with process variations by lattice constant.

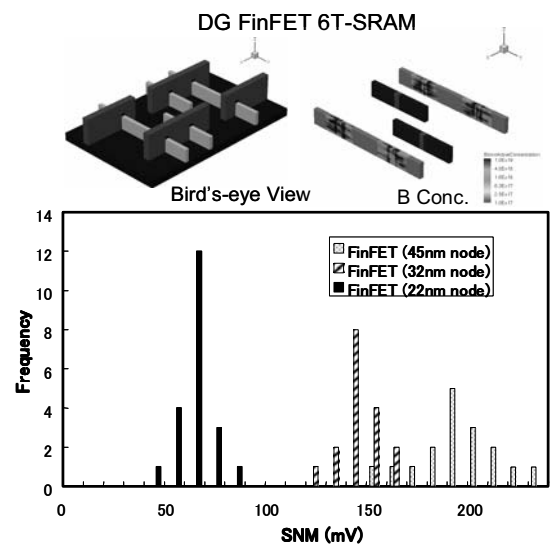


Fig. 5. SNM frequency distribution for DG 6T-SRAM with scaling.

# Study of Piezoresistivity Effect in FET

M. Auf der Maur,\* M. Povolotskyi, F. Sacconi, and A. Di Carlo  
MINAS Lab, University of Rome “Tor Vergata”, Italy

\*Department of electronic engineering, Via del Politecnico 1, 00133 Rome, Italy  
e-mail: auf.der.maur@ing.uniroma2.it

## INTRODUCTION

Piezoelectric effect is very important for the functionality of FET based on GaN/AlGaN heterostructures. Such systems were realized and characterized experimentally. The measurements of piezoresistivity of nitride-based heterostructures were also reported [1]. In this study we model the effect of an external mechanical force applied to a transistor. We describe a theoretical model, numerical methods and application for different structures such as GaN/AlGaN HFETs and GaAs/InGaAs HEMTs grown on (N11)-oriented substrates [2]. These systems are chosen because they exhibit a strong piezoelectric effect and therefore change their electrical characteristics due to applied stress.

## THEORETICAL MODEL

Mechanical deformation of transistors are studied in the framework of continuous media theory. Strain is a result of both lattice mismatch between the constituent materials of the structure and external mechanical forces applied at the surface of the device. We assume perfect crystallographic interfaces between materials and a linear relationship between stress and deformation. Computed strain enables us to calculate piezo- and pyroelectric polarization ( $\mathbf{P}^{pz}$  and  $\mathbf{P}^{py}$ ) and the deformation potentials of conduction and valence bands. The built-in potential  $\varphi$  is calculated by solving the nonlinear Poisson equation

$$\nabla(\varepsilon\nabla\varphi + \mathbf{P}^{py} + \mathbf{P}^{pz}) = -\rho(\varphi), \quad (1)$$

assuming Fermi-Dirac distribution of the free charge density  $\rho(\varphi)$ . The electrical characteristics are simulated by means of a drift-diffusion approximation considering both constant and field-dependent mobilities.

The numerical model for the above equations is based on the finite element method. We performed

2D simulations on a mesh that is automatically refined in the regions of interest such as regions near interfaces and stressed surfaces. Poisson and current equations are solved as a coupled nonlinear system, while the mechanical strain equation is solved separately. A Gummel iteration scheme is used for coupling strain and current equations in order to study the converse piezoelectric effect.

## APPLICATION EXAMPLE

We show an InAs/GaAs HEMT (see Fig. 1) grown on a (411) InAs substrate. The y-component of the piezopolarization induced by an external mechanical force is shown in Fig. 3. The applied pressure is equal to 0.5 GPa over a band with width of 0.5  $\mu\text{m}$ . In Fig. 2 we show the equilibrium band diagrams calculated for the device with and without pressure applied. One can see that pressure results in additional bending of the bands. This is similar to applying a negative voltage to the gate as demonstrated in the output characteristic (Fig. 5). Fig. 4 shows the electron density in the channel with and without external pressure. One can observe a partial depletion of the channel caused by piezoelectric effect.

## ACKNOWLEDGMENT

We acknowledge the Marie Curie Research Training Network (CLERMONT2 project, contract nr. MRTN-CT-2003-503677) and ESA (ATHENA contract 14205/00/NL/PA) for financial support.

## REFERENCES

- [1] T. Eickhoff, O. Ambacher, G. Krötz and M. Stutzmann *Piezoresistivity of  $\text{Al}_x\text{Ga}_{1-x}\text{N}$  layers and  $\text{Al}_x\text{Ga}_{1-x}\text{N}/\text{GaN}$  heterostructures*, Journal of Applied Physics **90**, 3383 (2001).
- [2] L. Bouzaïene, S. Rekaya, H. Sghaier, L. Sfaxi and H. Maaref *Piezoelectric field effects on electron density in a  $\delta$ -doped  $\text{AlGaAs}/\text{In}_y\text{Ga}_{1-y}\text{As}/\text{GaAs}$  pseudomorphic HEMT*, Applied Physics A **80**, 295 (2005).

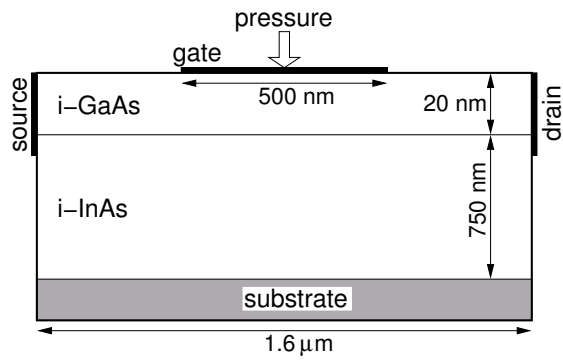


Fig. 1. Sketch of the considered HEMT structure

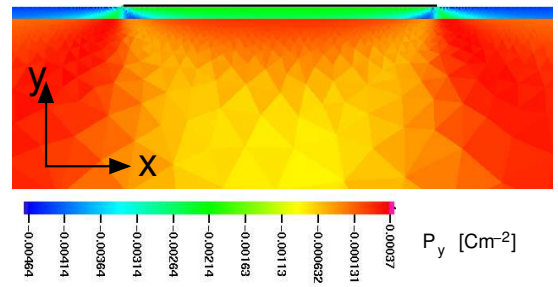
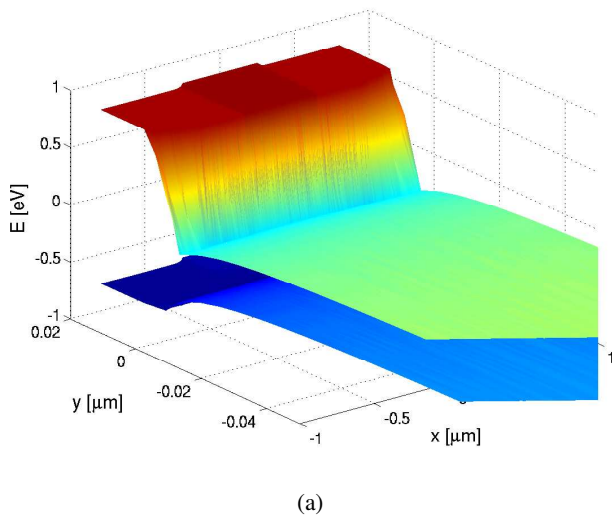
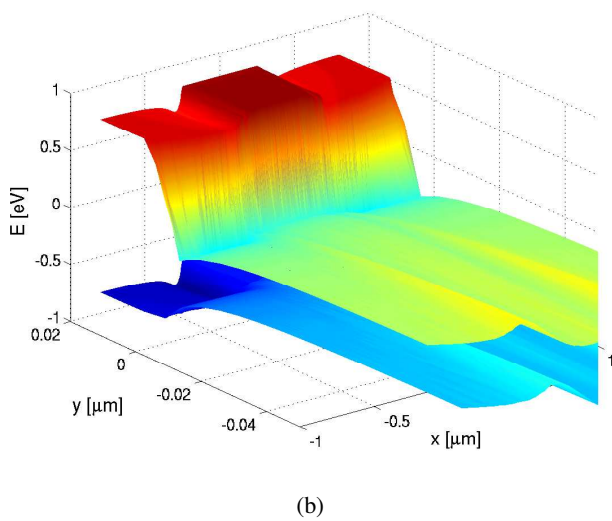


Fig. 3.  $y$ -component of the piezopolarization with applied pressure on top of the gate



(a)



(b)

Fig. 2. Lowest conduction and highest valence band without (a) and with (b) applied pressure

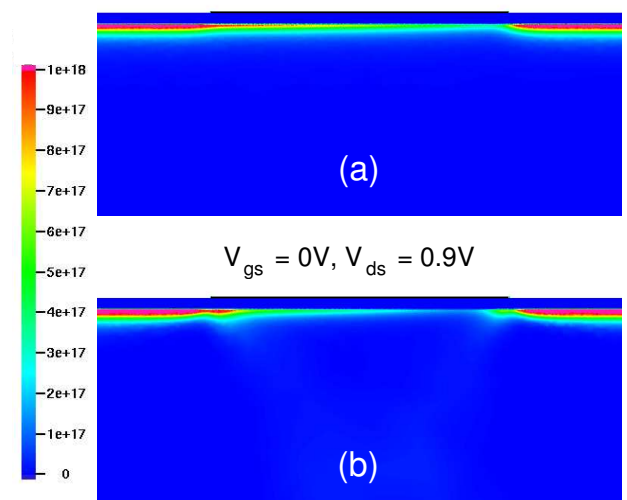


Fig. 4. Electron density without (a) and with (b) pressure

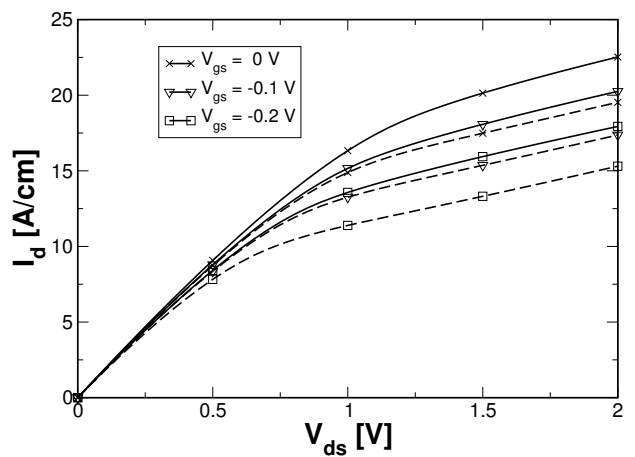


Fig. 5. Output characteristic with (dashed lines) and without (solid lines) pressure

# Influences of Grain Structure on Thermally Induced Stresses in 3D-IC Inter-Wafer Vias

D.N. Bentz, M.O. Bloomfield, J.-Q Lu, R. J. Gutmann, T.S. Cale  
Focus Center- New York, Rensselaer: Interconnects for Gigascale Integration  
Rensselaer Polytechnic Institute, Troy, NY, USA 12180-3590  
e-mail: calet@rpi.edu

We discuss the status of our thermo-mechanical modeling effort to provide parameters for the design and fabrication of 3D ICs based on benzocyclobutene (BCB) bonding (see Fig. 1). Broadly speaking, the stability concerns for inter-wafer Cu vias in 3D ICs are the same as for Cu-based MLM structures. For 3D ICs, a major reliability concern is the stability of the vias, which pass through several materials/layers. We are studying thermo-mechanical issues in these structures to help understand potential failure mechanisms.

In previous reports [2, 3], we describe our use of FEMLAB (COMSOL [4]) in thermo-mechanical modeling of inter-wafer Cu vias. Fig. 2 shows a schematic of a via through multiple layers; for details, see Refs. 2 and 3. The Cu was treated as a homogeneous material; the impact of grain size was introduced via correlations to copper yield stress, per Hall-Petch. We concluded that the inter-wafer Cu vias may fail due to the high stresses generated, depending upon details such as the diameter and pitch of the vias, and the BCB thickness. Our approach was validated by comparing results to data from reliability studies of Cu via structures in SiCOH and SiLK [5,6], and XRD studies of damascene-patterned Cu lines [7]. Because our results indicate that stresses will limit design space, it is important to refine our computations to improve our predicted design parameters.

Our thermo-mechanical modeling results show large gradients in the principle stresses (*e.g.*, see Fig. 3). These stresses provide driving forces for Cu migration and failure, and motivates including Cu grain structure in the models. We have developed a finite element model (FEM) that includes the grain structure of the Cu vias. We use anisotropic elastic constants, taken from the literature, of individual Cu

grains in via structures. We have generated randomly textured 3D grain structures, for demonstration purposes, and used COMSOL to perform thermo-mechanical modeling (see Fig. 4). The materials' properties and other model details can be found in Refs. 2 and 3. Stresses are those induced by a temperature change from a stress-free state at 523 K to 298 K.

We wrap up with a discussion of how PLENTE [8, 9], the code we use to represent and track grain structures, is combined with COMSOL. PLENTE uses level sets on finite elements to track the motion of multiple materials or multiple phases/grains in a 3D environment (see Fig. 5). Evolution can be due to deposition, etch, annealing processes, and/or be stress-induced and/or current-induced migration. In this study, PLENTE provides 3D grain structures to COMSOL, and COMSOL computes the forces acting on the grains. These forces are converted into grain boundary motion. PLENTE then updates the grain structure and the cycle is repeated. We will detail a novel method to extract a consistent structure for finite element analysis, after evolution.

## REFERENCES

- [1] J.-Q. Lu et al., in Proc. 2002 IITC, IEEE, 2002, p. 78.
- [2] J. Zhang et al., *Microelect. Eng.* **82**, 534 (2005).
- [3] D. N. Bentz et al., in Proc. 22<sup>nd</sup> VMIC, IMIC, 2005, p. 89.
- [4] "COMSOL-Multiphysics", <http://www.comsol.com>
- [5] R. G. Filippi et al., in Proc. 2004 IRPS, IEEE, 2004, p. 316.
- [6] D. Edelstein et al., in Proc. 2004 IRPS, IEEE, 2004, p. 61.
- [7] S.-H. Rhee et al., *J. Appl. Phys.*, **93**, 3926 (2003).
- [8] M.O. Bloomfield et al., *Phil. Mag.* **83**, 3549 (2003).
- [9] M.O. Bloomfield and T.S. Cale, *Microelectron. Eng.* **76**, 195 (2004).

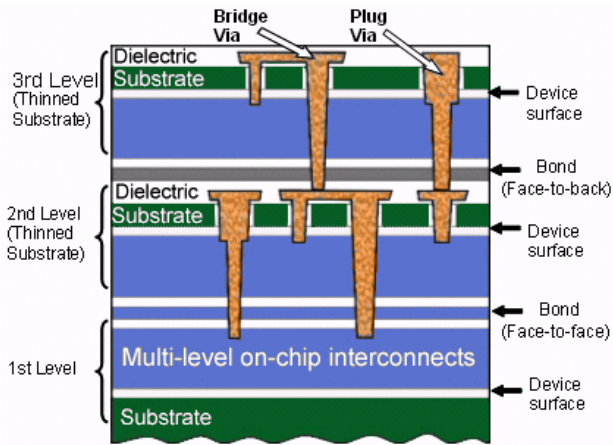


Fig. 1. 3D chip cross-sectional structure using “face-to-face” BCB bonding [1]. This schematic shows three wafers (2 BCB bond layers).

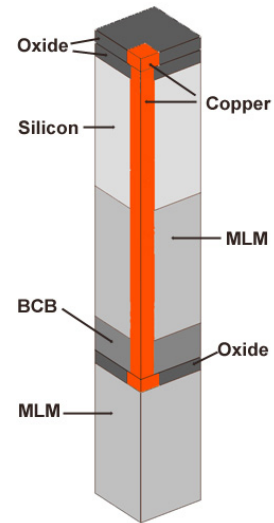


Fig. 2. Schematic of representative simulation cell, constructed using periodic boundary conditions. Horizontal expansion is controlled by the underlying silicon layer. The MLM is treated as a homogenous mixture of 30% Cu and 70% SiO<sub>2</sub> [2, 3]

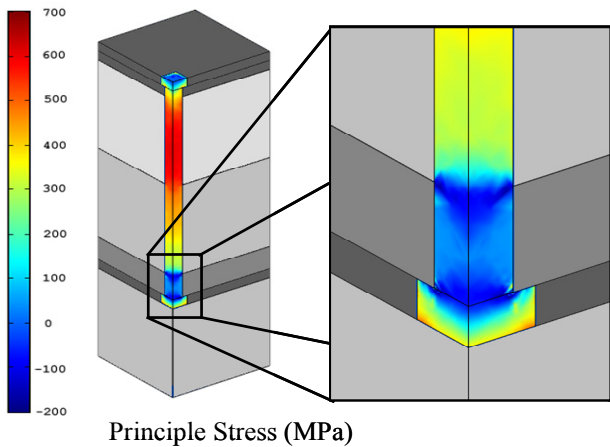


Fig. 3. First principal stresses in a 3D IC via due to a change in temperature from a stress free state at 523 K to 298 K. For clarity, the stress distribution is only shown in the Cu. Stresses are close to or exceed the Cu yield strength; migration and failure are concerns.

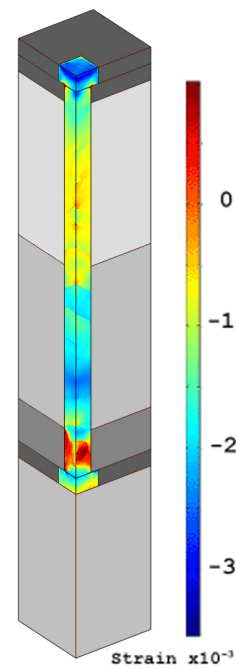


Fig. 4. First principal strains in the Cu 3D IC via due to a change in temperature from 523 K to 298 K, accounting for the internal grain structure using a grain-continuum model. The texture is random and anisotropic materials properties are used. Significant deviations from the continuum results are observed.

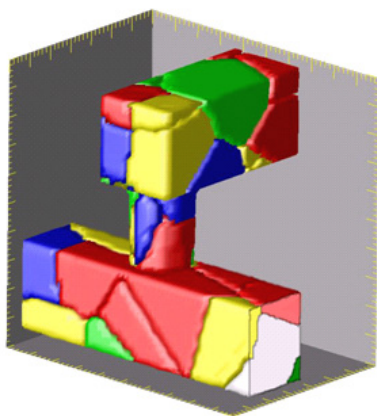


Fig. 5. Example grain structure in a Cu interconnect, developed using PLENTE with random nucleation followed by an isotropic deposition model.

# TCAD-Assisted Development of Technology-Independent Device Models

P. Blakey, S. Bates and U. Yahya

Department of Electrical Engineering, Northern Arizona University, Flagstaff, AZ 86011  
e-mail: peter.blakey@nau.edu

## BACKGROUND

Circuit simulators use device models that provide a compact representation of electrical behaviour. The parameters associated with compact models are normally extracted from experimental measurements. The parameters can also be extracted from the results of device simulation. The extraction of compact device models from simulated electrical behaviour provides an important bridge between TCAD and circuit design.

There are many different approaches to the development of compact device models. For example, models can be specialized for DC or small-signal AC conditions, and can be physics-based or empirical. Within the overall spectrum of approaches, there is considerable interest in *technology-independent* device models that associate voltage-dependent current and charge functions  $I_i$  and  $Q_i$  with each device terminal. A good description of the basic technique has been given by Corbella et. al. [1].

The label *technology-independent* is misleading. A more accurate description would be “applicable to any well-behaved FET technology when used at sufficiently low frequencies.” Extensions are required to handle bipolar technologies, frequencies that are not small with respect to the unity current gain cut-off frequency of the device and the presence of surface or bulk traps.

Industrial practice has shown the need to use pulsed I-V measurements, rather than DC I-V characteristics, to determine the terminal current functions. The device temperature (T) then becomes an explicit variable of the model. Non-quasi-static effects can be described by associating delay times

$\tau_i$  with the evolution of the charge functions (see, e.g. [2].) Measurement-based extraction of the parameters of  $IQ(T,\tau)$  models requires pulsed measurements of small-signal s-parameters as a function of frequency, up to the region of the unity current gain cut-off frequency. Such measurements are difficult and expensive. These problems can be overcome by the judicious use of TCAD.

## APPROACH

This paper describes the use of TCAD in the implementation of a computer-controlled  $IQ(T,\tau)$  model development and parameter extraction system. The system uses experimental pulsed I-V measurements to determine the  $I(T)$  functions, TCAD simulation to determine the  $Q(T,\tau)$  functions, and low-frequency small-signal AC measurements to calibrate the TCAD results. This hybrid approach provides an excellent trade-off between accuracy, generality, simplicity, and ease of use.

Fig. 1 shows the experimental set up used to determine the  $I(T)$  functions. Fig. 2 depicts a test of whether trap effects are negligible. Figs. 3 and 4 show examples of charge surfaces extracted from simulated results. Fig. 5 shows the ability of the model to reproduce several breakpoints in the frequency-dependent roll-off of  $y_{21}$ .

The role of TCAD will expand in the future as it is used for additional purposes, e.g.:

- As a test reference to evaluate alternative non-quasi-static model formulations
- As a test reference to evaluate and extract parameters for bipolar extensions
- As a test reference to evaluate and extract parameters for trap-related extensions.

### ACKNOWLEDGEMENT

We thank Accent Optical Technologies for providing a pulsed I-V measurement instrument and for funding the development of the thermal measurement system.

### REFERENCES

- [1] I. Corbella, J. M. Legido and G. Naval, "Instantaneous Model of a MESFET for use in Linear and Nonlinear Circuit Simulations," IEEE Trans. Microwave Theory and Techniques, vol. 40, pp. 1410-1421, 1992
- [2] R.R. Daniles, A. T. Yang and J. P. Harrang, "A Universal Large/Small Signal 3-Terminal FET Model Using a Nonquasi-Static Charge-Based Approach," IEEE Trans. Electron Devices., vol. 40, pp. 1723-1729, 1993



Fig. 1. The experimental I(T) modeling system incorporates a computer-controlled pulsed I-V instrument and thermal chuck.

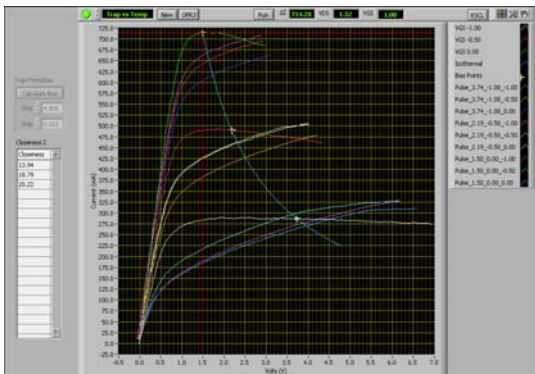


Fig. 2. The system software can test for the impact of traps. This data shows that traps are significant for a CLY5 MESFET.

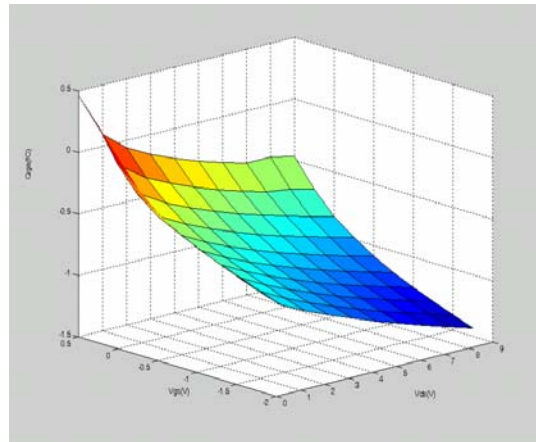


Figure 3: A simulated isothermal gate charge surface calculated as a function of gate and drain bias.

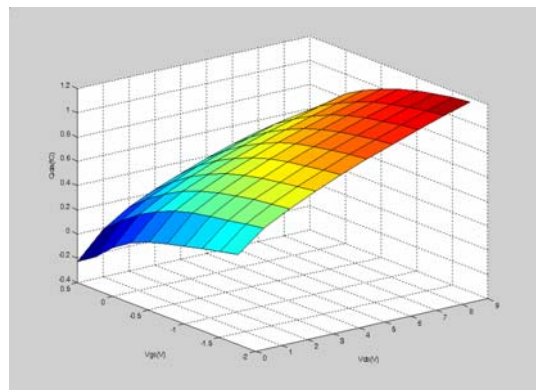


Figure 4: A simulated isothermal drain charge surface calculated as a function of gate and drain bias.

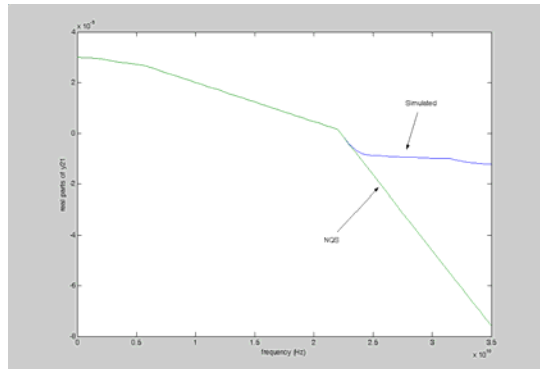


Fig. 5: Data for  $y_{21}$  shows how the model handles frequency-dependent break points.

# Intrinsic Parameter Fluctuations due to Random Grain Orientations in High- $\kappa$ Gate Stacks

A. R. Brown, J. R. Watling and A. Asenov  
Device Modelling Group, Dept. of Electronics & Electrical Engineering,  
University of Glasgow, Glasgow G12 8LT, UK  
e-mail: A.Brown@elec.gla.ac.uk

As the scaling of MOSFETs continues the requirement to maintain electrostatic integrity dictates an aggressive reduction of the oxide thickness below 1 nm, introducing intolerably high gate leakage [1]. This has led to the introduction of high- $\kappa$  materials in the gate stack offering the required SiO<sub>2</sub> equivalent oxide thickness at increased physical thickness and reduced gate leakage. There are many technological issues [2] associated with the use of high- $\kappa$  material in the MOSFET gate stack leading to mobility degradation. Some of these factors [3] will also introduce intrinsic parameter fluctuations in the corresponding MOSFETs, similar to the fluctuations introduced by random discrete dopants and oxide thickness variations. We recently reported an investigation of intrinsic parameter fluctuations in decanometre MOSFETs introduced by non-uniformity of the dielectric properties of the high- $\kappa$  material due to *phase separation* of Hf and Si oxides [4]. Here we present a simulation study of another source of non-uniformity, also due to the polycrystalline nature of the high- $\kappa$  dielectric material, which is *random grain orientation*. Each crystalline grain within the gate stack can have a random orientation which, due to anisotropy in the dielectric constant, leads to localised variations in gate-to-channel capacitance. This results in local fluctuations in the MOSFET surface potential leading to variations in characteristics from one device to the next. The possible granular nature of a high- $\kappa$  film structure is illustrated in Fig 1 which shows a plan-view TEM image of a polycrystalline HfO<sub>2</sub> film, with different grain orientations.

The simulations were carried out with the Glasgow 'atomistic' device simulator, which has been modified to include a polycrystalline high- $\kappa$  gate stack with variations in dielectric constant for

different grains. In order to introduce a realistic grain structure a large AFM image of polycrystalline grains [5] has been used as a template. The grain boundaries in this image were traced in Adobe Illustrator and each grain was coloured to allow differentiation, as shown in Fig. 2. The image was scaled so that the grain diameters are in the range of 2-10nm (see Fig. 3), typical for a high- $\kappa$  film [6].

The simulator imports a random (in both location and orientation) section of the grain template which corresponds to the dimensions of the device, and for each different grain assigns a dielectric constant chosen randomly from within a given range. An example is shown in Fig. 4. The resultant fluctuations in surface potential are shown in Fig. 5.

Fig. 6 shows the fluctuations in threshold voltage,  $\sigma V_T$ , for bulk MOSFETs scaled from 50nm to 15nm. The gate stack for each device consists of a 0.5nm interfacial SiO<sub>2</sub> layer with the polycrystalline high- $\kappa$  dielectric above. One would expect that as the device dimensions are reduced the magnitude of the fluctuations would increase, however this is tempered by the necessary scaling of oxide thickness which reduces the capacitive contribution of the high- $\kappa$  relative to the interfacial layer, limiting the effect of the dielectric fluctuations.

## REFERENCES.

- [1] International Technology Roadmap for Semiconductors
- [2] G. D. Wilk, *et al.*, J. Appl. Phys., **89**, 5243 (2001)
- [3] G. Bersuker, *et al.*, Mat. Res. Soc. Symp. Proc. **811**, 31, 2004
- [4] A. R. Brown, *et al.*, Proc. SISPAD, 27 (2005)
- [5] S. Uma, *et al.*, International Journal of Thermophysics, **22**, 605 (2001)
- [6] G. Bersuker, Sematech, *personal communication*

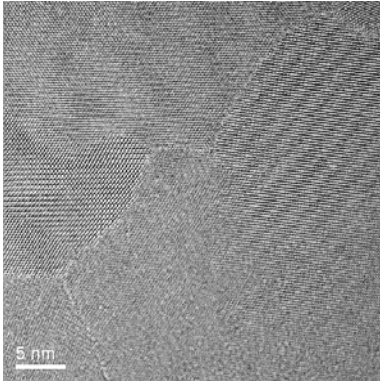


Figure 1. Top view TEM image of a HfO<sub>2</sub> film showing different polycrystalline grains each with different crystalline orientation.

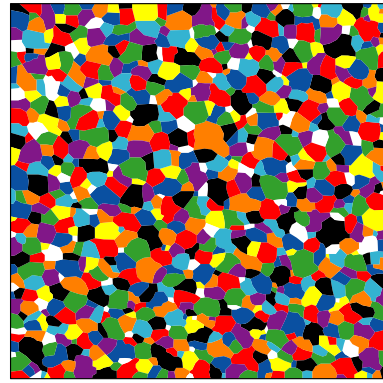


Figure 2. An AFM image is used as a template in Adobe Illustrator where the grain boundaries are traced and filled with colours. It is important to note that the colours used in this image are purely to allow the simulator to differentiate between different grains and bear no relation to the dielectric constant assigned to that grain by the simulator.

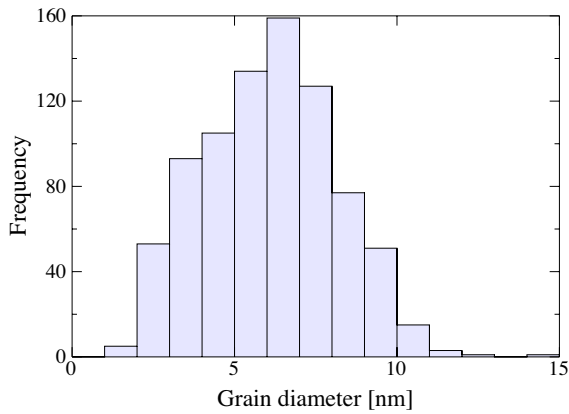


Figure 3. The grain image is scaled so that the grain diameters are between 2 and 10 nm [6]. The diameter is calculated from the area of the grain assuming a circular grain shape. The image file is then written in a format readable by the simulator at a particular resolution, e.g. 1 pixel/nm.

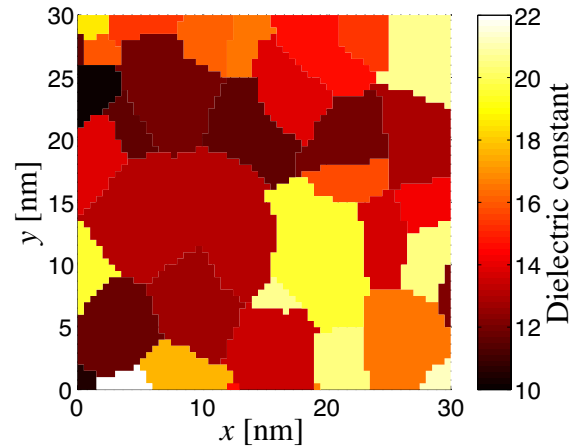


Figure 4. Once a randomly selected region of the grain image is imported to the simulator a recursive spatial search algorithm is used to identify every grid node within a particular grain and assign the dielectric constant for that grain to all those nodes. The dielectric constant is chosen randomly from within a given range. Here is shown an example for a 30×30nm channel MOSFET.

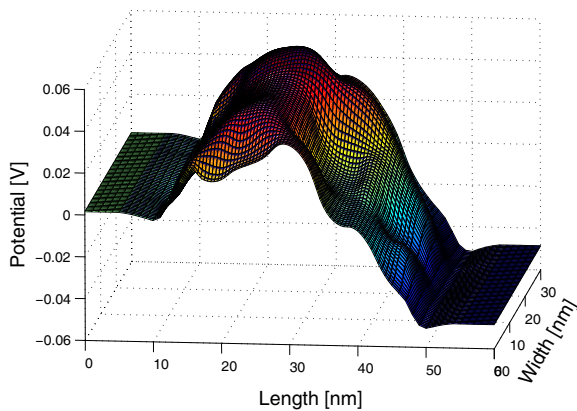


Figure 5. Surface potential in a 30×30nm MOSFET demonstrating the fluctuations induced by variations in dielectric constant.

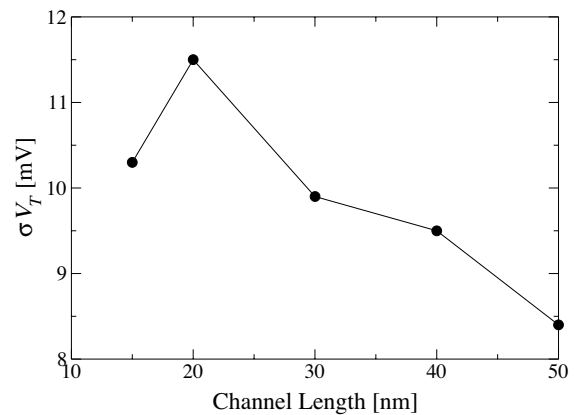


Figure 6.  $\sigma V_T$  for bulk MOSFETs scaled from 50nm to 15nm. Simulations of 200 devices with unique grain pattern and associated dielectric constants were performed for each channel length.

# Gummel Iterations for Inverse Dopant Profiling of Semiconductor Devices

M. Burger\*

Institut für Industriemathematik, Johannes Kepler Universität, Altenbergerstr. 59, A 4040 Linz, Austria  
e-mail: martin.burger@jku.at

## INTRODUCTION

Optimal dopant profiling of semiconductor devices is an interesting and challenging task in modern microelectronics (cf. [1], [2]), which is nowadays treated by a combination of mathematical optimization and numerical simulation techniques. Such optimizations of doping profiles involves a high computational effort since a high number of forward simulations have to be carried out in the optimization process. Here we discuss a more efficient approach to the solution of the optimization problem, which is based on a Gummel-type iteration for the optimality system.

## MACROSCOPIC DEVICE MODELS

Macroscopic models for semiconductor devices such as the frequently used *drift-diffusion model* (cf. [3]) can be written schematically in the form

$$\lambda^2 \Delta V = Q(\rho) - N, \quad C(\rho, V) = 0, \quad (1)$$

where  $V$  denotes the electric potential,  $\rho$  a vector of densities (for electrons and holes), and  $N$  the (scaled) doping profile. The first equation is the Poisson equation for the electrical field with scaled Debye length  $\lambda$  and  $Q(\rho)$  is the charge generated by the electrons and holes. The equation symbolizes by  $C = 0$  is a set of continuity equations, e.g. Nernst-Planck equations for electron and hole densities.

Optimal dopant profiling can be formulated as an optimization problem on top of such a model, namely as a minimization task

$$F(\rho, V, N) \rightarrow \min_{(\rho, V, N)} \quad \text{subject to (1)}. \quad (2)$$

## EFFICIENT OPTIMIZATION

A disadvantage of the optimization model (2) is the strong coupling of the Poisson and continuity equations, which implies a strong coupling of all

variables in the first-order optimality system. In order to avoid this problem we use an approach proposed in [4], namely to replace the doping profile by the total charge density  $q := Q(\rho) - N$  as the unknown in the optimization. In this way the state equations have a triangular form, the densities do not further appear in the Poisson equation. As a consequence, the optimality system for the minimization of a functional  $G(\rho, V, q) = F(\rho, V, N)$  considerably simplifies and one can construct a simple Gummel iteration for this system (based on alternating solution of Poisson and continuity equations), which turns out to be globally convergent and rather efficient.

## OPTIMIZATION RESULTS

We illustrate the optimization for the drift-diffusion model, with an objective functional of the form

$$G(\rho, V, q) = (I - I^*)^2 + \epsilon \int (q - q^*)^2 dx, \quad (3)$$

where  $I$  is the current flowing out over a contact and  $I^*$  a reference value to be achieved. The second term in the objective avoids to large deviations from a reference configuration modeled by  $q^*$

Results of the optimization for a PNP-Diode are shown in Figures and 1. Figure shows a comparison of the reference state and the optimal doping profile, and Figure 1 displays the current-voltage curves obtained with these doping profiles.

For a Metal-electron field effect transistor (MES-FET), the result of the optimization on an adaptive mesh is shown in Figure 2. Finally, Figure 3 illustrates the convergence history of the optimization method, one observes that the result of the optimization is obtained after few Gummel iterations for the optimality system.

## CONCLUSION

We have derived an efficient Gummel iteration for optimal inverse dopant profiling, which is easy to implement and globally convergent. With this approach the effort for optimization only doubles the one for simulation.

## ACKNOWLEDGMENT

Supported by the Austrian National Science Foundation (FWF) through project SFB F 013 / 08.

## REFERENCES

- [1] R. Plasun, M. Stockinger, R. Strasser, S. Selberherr, *Simulation based optimization environment and its application to semiconductor devices*, in: Proceedings IASTED Intl. Conf. on Applied Modelling and Simulation, 1998, pp. 313-316.
- [2] M. Hinze, R. Pinnau, *An optimal control approach to semiconductor design*, Math. Mod. Meth. Appl. Sci., **12** (2002), 89-107.
- [3] S. Selberherr, *Analysis and Simulation of Semiconductor Devices*, Springer, New York, 1984.
- [4] M. Burger, R. Pinnau, *Fast optimal design of semiconductor devices*, SIAM J. Appl. Math. **64** (2003), 108-126.

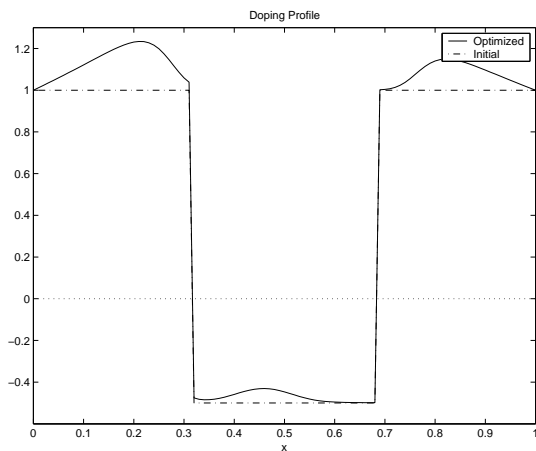


Fig. 1. Optimized Doping Profile of an NPN-Diode.

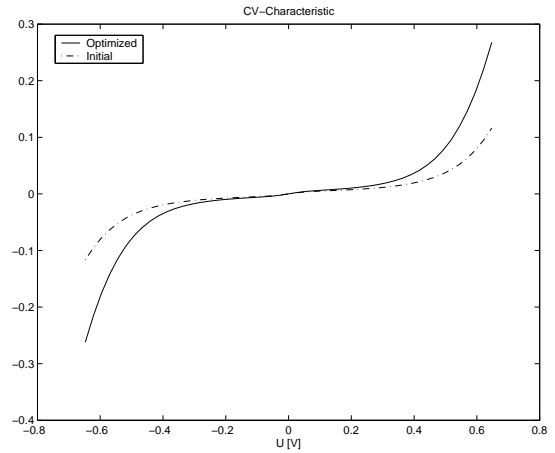


Fig. 2. CV-curve of the NPN-Diode before and after optimization.

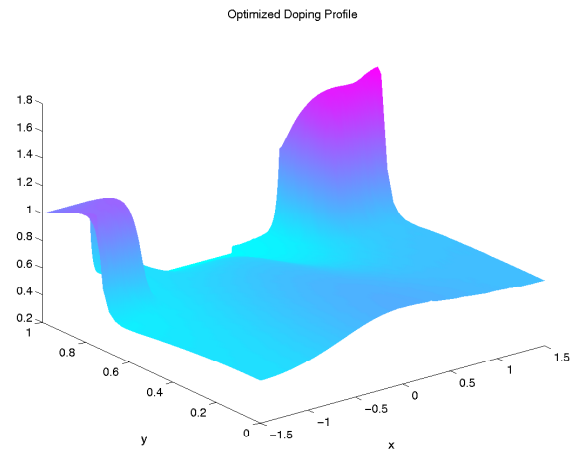


Fig. 3. Optimized Doping Profile of a MESFET.

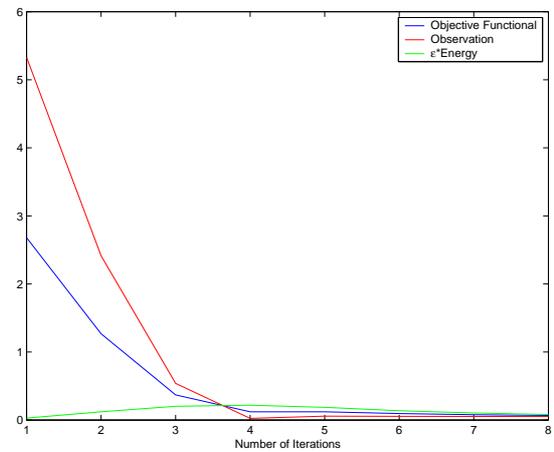


Fig. 4. Convergence History of the Optimization Method

# An Evolution Algorithm for Noise Modeling of HEMTs down to Cryogenic Temperatures

A. Caddemi, F. Catalfamo, and N. Donato

Dipartimento di Fisica della Materia e Tecnologie Fisiche Avanzate, University of Messina,  
Salita Sperone 31, - 98166 S. Agata, Messina, Italy - Phone: +39 090 3977378; fax: +39 090 3977468;  
e-mail: fcatalfamo@ingegneria.unime.it

## INTRODUCTION

The implementation of an evolution algorithm (EA) for the cryogenic noise modeling of microwave devices has been the object of the present work. The characterization of advanced microwave devices, like High Electron Mobility Transistors (HEMT), in terms of the noise parameters results in a set of time consuming measurements to be performed with very expensive instrumentation [1 – 3]. A complete noise characterization is required for an accurate design of low-noise front-ends for high-sensitivity cryogenic receivers, wireless telecommunication circuits, nuclear and aero-spatial instrumentation.

## NOISE PARAMETERS

The Noise Parameters (NP), together with the Scattering (S-) parameters, provide a full small-signal characterization (i.e., a *black-box* model) of any device dependent on the frequency, the bias conditions and the operating temperature. The four NP's here employed are the minimum noise figure ( $F_{\min}$ ), the noise resistance ( $R_n$ ), the magnitude and phase of the optimum noise source reflection coefficient ( $\Gamma_{opt}$ ). The NP's are related to the global noise figure  $F(\Gamma_S)$  as reported in the following expression, where  $Z_0$  is the normalization impedance, typically 50  $\Omega$ :

$$F(\Gamma_S) = F_{\min} + \frac{4R_n}{Z_0} \cdot \frac{|\Gamma_S - \Gamma_{opt}|^2}{|1 + \Gamma_{opt}|^2 \cdot (1 - |\Gamma_S|^2)} \quad (1)$$

The eq. (1) represents a parabolic-like surface on the Smith Chart.

## IMPLEMENTATION OF THE EVOLUTION ALGORITHM

EA's are adaptive procedures that are mostly used for optimization and research problems [4]. These procedures are conceptually based on the principles of the natural evolution of the species. Living organisms consist of many cells and each cell contains one or more chromosomes that can be divided in genes. Each gene codifies a specified feature of the living organism. From the point of view of the information theory, the chromosome refers to a candidate solution.

In our analysis, an eight base function set constitutes the collection of the chromosomes, namely the initial population. The main program of the EA assigns a set of suitable coefficients to the base functions. Subsequently, these functions combine with each other. The high number of the potential solutions obtained ensures the generation of an optimum solution that exhibits the lowest error compared to the maximum fixed threshold. The "fitness" is warranted by a continuous comparison between the candidate solution and the measured value of each NP. The comparison ends when a chosen threshold for the fitness is reached. A convergence procedure is also carried out to refine the generated solutions by exploring its neighbor regions. The selection is achieved by successive "mutation" steps.

The obtained analytical equations thus provide an estimation of the behavior of the NP's down to cryogenic temperatures and also outside the frequency range under observation. This approach is original and very flexible because it does not require a training procedure like in the Artificial Neural Networks (ANNs) – based systems [5, 6]. Moreover, the performance of this EA technique

shows to be independent from the particular device typology.

## RESULTS

By the procedure here presented we have obtained a complete set of the NP's for a commercial super low-noise pseudomorphic HEMT (MGF4319 by Mitsubishi Semiconductors). This transistor was previously measured in our laboratory and a complete noise characterization was performed vs. frequency and temperature. Therefore, the EA performance for the noise modeling of the device under test (DUT) has been checked by using these experimental data in the 6-18 GHz frequency range and down to cryogenic temperatures. The comparison between measured data and EA simulation of the NP's vs. frequency and temperature (290-90 K, step 50 K) for the chosen DUT was performed and the results are reported in Figs. 1-3. Finally, a thorough analysis of these plots allows us to establish that application of the EA technique produces reasonably good values of the NP's down to cryogenic temperatures for the DUT.

## CONCLUSION

In this work, an evolution algorithm was implemented for estimating to a good accuracy extent the behavior of the NP's for a low-noise HEMT down to cryogenic temperatures. By this original procedure, we have also obtained the analytical expressions of the derived curves whose coefficient behavior vs. temperature is currently under analysis.

## REFERENCES

- [1] G. Martines, M. Sannino, *The determination of the noise, gain and scattering parameters of microwave transistors (HEMTs) using only an automatic noise figure test-set*, IEEE Trans. Microwave Theory Tech. **42**, 7 (1994).
- [2] A. Cappy, *Noise Modeling and Measurement Techniques*, IEEE Trans. Microwave Theory Tech., **36**, 1 (1988).
- [3] M. Pospieszalski, *Modeling of noise parameters of MESFET's and MODFET's and their frequency and temperature dependence*, IEEE Trans. Microwave Theory Tech., **37**, 9 (1989).
- [4] H.-Y. Chen, G.-W. Huang, K.-M. Chen, and C.-Y. Chang, *Noise Parameters Computation of Microwave Devices Using Genetic Algorithms*, IEICE Trans. Electron., **E88-C**, 7 (2005).
- [5] A. Caddemi, F. Catalfamo and N. Donato, *Cryogenic HEMT Noise Modeling by Artificial Neural Networks*, Fluctuation and Noise Letters **5**, 3 (2005).

- [6] A. Caddemi, F. Catalfamo, and N. Donato, *Simulating Noise Performance of Advanced Devices down to Cryogenic Temperatures*, AIP Conf. Proc. **800**, 480 (2005).

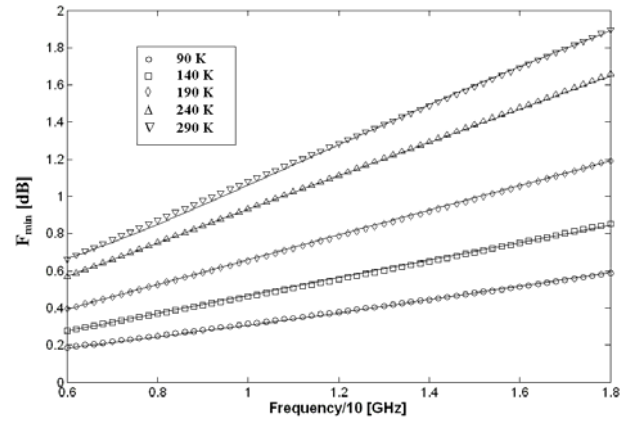


Fig. 1. Comparison between experimental data and EA simulation of the minimum noise figure  $F_{\min}$  vs. frequency and temperature for the MGF4319 device.

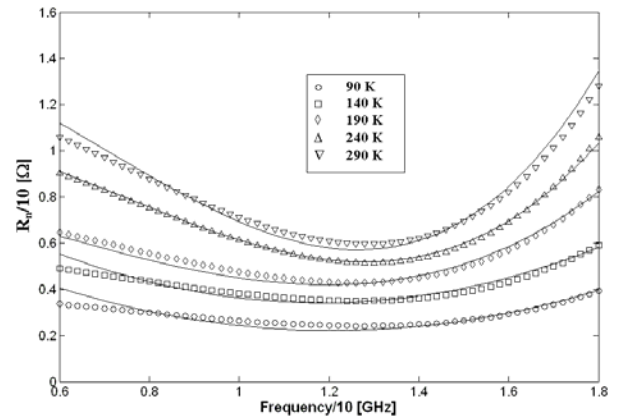


Fig. 2. Comparison between experimental data and EA simulation of the noise resistance  $R_n$  vs. frequency and temperature for the MGF4319 device.

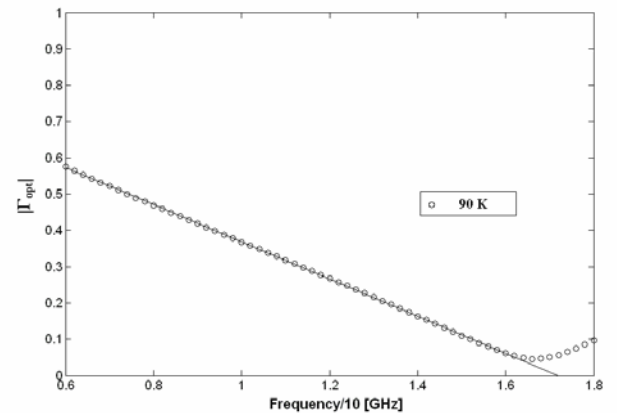


Fig. 3. Comparison between experimental data and EA simulation of the magnitude of the optimum noise reflection coefficient  $\Gamma_{\text{opt}}$  vs. frequency for the MGF4319 device at 90 K.

# Combined Line-Width-Roughness (LWR) and Local Critical Dimension (CD) Variation Effects on Sub-65nm MOSFET Current – Voltage Characteristics: From Lithography to Metrology to Device Simulation

V. Constantoudis, G. Patsis, and E. Gogolides

Institute of Microelectronics (IMEL), NCSR “Demokritos”, P.O. Box 60228, 15310, Aghia Paraskevi, Attiki,  
Greece

e-mail: gpatsis@imel.demokritos.gr

## INTRODUCTION

Various characterization methods and lithography technologies using new resist materials and advanced gate patterning processes to reduce line-edge roughness (LER) have been developed, but the aggressively continuing progress in CMOS technology calls for more detailed understanding, quantification and estimation of LER/LWR effects on the electrical behavior of future scaled MOS transistors. Simple statistical analysis has shown that the gate patterns without the appropriate LWR control may cause severe fluctuations in device parameters and performance, especially in the nanometer scaled MOSFET technologies, resulting in a negative average threshold voltage shift, a sub-threshold slope degradation, an unrealistic effective channel length extraction and an exponential increase in off-state leakage current [1],[2].

Our metrological work has shown that LWR is not a value but a function of the width of the transistor [4]. LWR increases with transistor width and saturates at large (“infinite”) widths on the order of  $2\mu\text{m}$ . For smaller widths LWR is not independent but it is coupled to local CD variation. LWR is reduced at small widths while CD variation increases keeping the sum of their squares constant (this value is termed sigma “infinite”). The interplay between LWR and CD variation depends on the LWR spectrum, i.e. the correlation length  $\xi$  and the roughness exponent  $\alpha$  (related to the fractal dimension of the transistor edges). Thus LWR is a function described with three parameters namely

“sigma infinite”, correlation length  $\xi$ , and roughness exponent  $\alpha$ .

## WORK DESCRIPTION

This work has two goals: First, using simple analytic models to examine the effect of combined LWR and CD variation on transistor operation, and the relevant importance of each effect. In addition we explore how the transistor operation is influenced by the triad of the LWR parameters, hence from the whole LWR spectrum. This part of our work connects LWR metrology to device operation. In order to evaluate LWR effects on device current behavior we follow an analogous approach as is described in [2].

Specifically, the total gate width  $W$  is divided into  $N$  segments with no LWR and with a certain characteristic width  $\Delta W=1\text{-}5\text{nm}$  (Fig. 1). The drain current of the whole gate is calculated by summing the  $N$  gate segments in parallel. The drain current of each segment is given by simple or more complicated analytical formulas including short channel and narrow width effects. By the drain current vs. gate voltage curve, the threshold voltage shift of the total gate can be estimated. The calculation is repeated for a large number of gates with specific LWR parameters so that sufficient statistics is obtained. First results for the dependence of these shifts on the spatial LWR parameters ( $\alpha, \xi$ ) are shown in Fig.2. The standard deviation of these values as well as the off-current for the whole spectrum of ( $\alpha, \xi$ ) will be also presented in the work. Furthermore, the effects of

the gate width  $W$  and length on these dependencies will be also examined.

Second we connect the lithography process and material architecture to the device operation. Here, LWR is introduced through the explicit stochastic simulation of the processes leading to the development of photoresist lines (Fig.3), and assuming that LWR introduced in the final transistor gate will be a modulation of this initial photopolymer LWR, after silicon etching, doping, and annealing [3]. Then LWR effects on device operation are evaluated as above (Fig. 1), where  $\Delta W$  now indicates the photopolymer chain monomer size. The result of this second part of our work is to connect the LWR effects on the device to photoresist molecular weight and polymer chain architecture, for both conventional and chemically amplified photopolymers. The effects of transistor width will be also investigated.

#### ACKNOWLEDGEMENT

Financial support from the European project “More Moore” and is kindly acknowledged.

#### REFERENCES

- [1] Diaz, C. H.; Tao, H. J.; Ku, Y. C.; Yen, A.; Young, K. IEEE Electron Device Letters 2001, 22, 287-289.
- [2] Kim, H. W.; Lee, J. Y.; Shin, J.; Woo, S. G.; Cho, H. K.; Moon, J. T. IEEE Transactions On Electron Devices 2004, 51, 1984-1988.
- [3] Xiong, S. Y.; Bokor, J. IEEE Transactions on Electron Devices 2004, 51, 228-232.
- [4] Constantoudis, V.; Patsis, G. R.; Gogolides, E. Journal of Microlithography Microfabrication and Microsystems 2004, 3, 429-435.

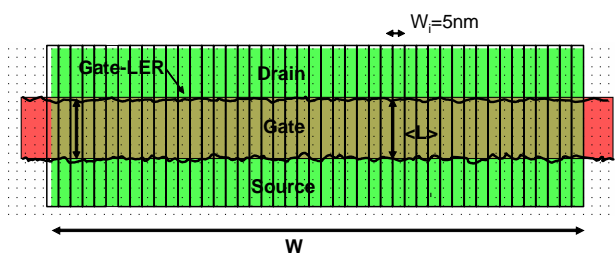


Fig. 1. The transistor is divided into sub-transistors.

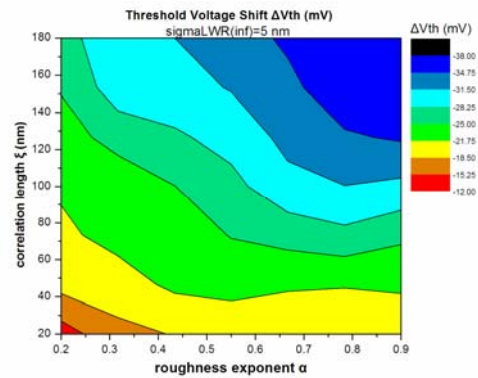


Fig. 2. Effect of correlation length and roughness exponent on threshold voltage shift for  $W=135\text{nm}$ ,  $\Delta W=5\text{nm}$  and  $CD\text{ nominal}=45\text{nm}$ .

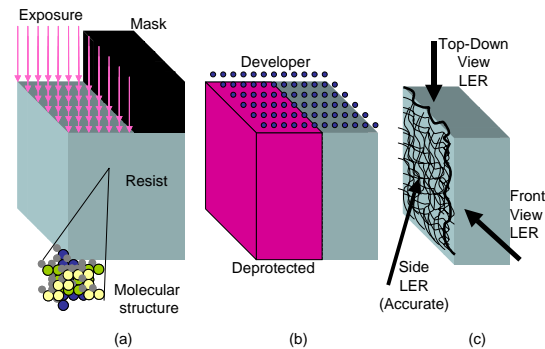


Fig. 3. Qualitative picture of process simulation. (a) Material placement in lattice, and exposure. (b). Acid-diffusion simulation and creation of deprotection sites. Beginning of development. (c). Measurement of edge roughness.

# TCAD Simulation of OTFT Small-Signal Parameters

C. Erlen, P. Lugli, B. Nickel\*, M. Fiebig\*

Institute for Nanoelectronics, TU München, Arcisstr. 21, 80333 München, Germany

\*Department für Physik, LMU München, Germany

e-mail: erlen@tum.de

## INTRODUCTION

Advances in fabrication techniques have led to organic thin-film transistors (OTFTs), which are increasingly interesting for electronic applications. The associated design of organic circuits results in the need for a solid modeling of device behavior.

Up to now, research has mainly targeted the modeling of static IV characteristics [1][2][3][4]. In the following, we report simulations of OTFT small-signal parameters, which are important for the dynamic performance.

## SIMULATION ENVIRONMENT

The work is based on the commercial device simulator ISETCAD that we modified to account for the special nature of organic semiconductors according to Refs. [1][2]. Input variables are the device geometry, material properties, and the nature of the interfaces.

## DEVICE LAYOUT

Figure 1 shows the layout of the simulated pentacene OTFT. The device has a channel length of 20  $\mu\text{m}$ , a channel width of 100  $\mu\text{m}$ , and an oxide thickness of 190 nm. Figure 2 shows the finite element mesh used for the numeric computations.

## STATIC OFET CHARACTERISTICS

The simulation of static output and transfer characteristics can be employed to extract valuable knowledge from experimental IV data. By fitting the threshold voltage and the sub threshold region (Figure 3 and Figure 4), one can quantify the properties of fixed charges and traps at the insulator-semiconductor interface [3][4]. Typical values are reported in Ref. [4] with a trap concentration of  $N_t = 1 \times 10^{12} \text{ cm}^{-2}$  at a level 0.15 eV above the valence band. The analysis of pentacene OTFTs fabricated by the group of B. Nickel has led to values of  $8 \times 10^{11} \text{ cm}^{-2}$  at 0.16 eV (Figure 4).

The measured devices have an excellent mobility in the order of  $\mu = 2 \text{ cm}^2/\text{Vs}$ .

## SIMULATION OF AC SMALL-SIGNAL OTFT PARAMETERS

Small-signal parameters are vital for modeling the transient behavior of transistors. We have set up an environment in ISETCAD which is able to simulate these parameters for different OTFT layouts and material combinations.

Figure 5 shows the low-frequency source gate CV characteristic of the pentacene OTFT and illustrates the influence of interface traps and charges. Figure 6 reports the simulated AC small-signal transconductance  $g_m$ , the output conductance  $g_d$ , and the source gate capacity  $C_{sg}$  at a frequency of 2 kHz. By fitting small-signal measurements, it is possible to extract transistor properties such as trap release times, which govern the dynamic device behavior.

## CONCLUSION

In conclusion, we have shown that the ISETCAD method allows for an effective simulation of OTFT small-signal parameters. Based on these results, transient simulations of organic inverter circuits and ring oscillators can be performed. We plan to present further results at the conference in May.

## ACKNOWLEDGEMENT

We thankfully acknowledge the funding of this project by the DFG in the scope of the SPP 1121.

## REFERENCES

- [1] M. A. Alam, A. Dodabalapur, and M. R. Pinto, *A two-dimensional simulation of organic transistors*, IEEE Trans. El. Dev. **44**, 1332 (1997).
- [2] A. Bolognesi, M. Berliocchi, and M. Manenti, *Effects of grain boundaries, field dependent mobility and interface trap states on the electrical characteristics of pentacene thin film transistors*, IEEE Trans. El. Dev. **51**, 1997 (2004).

[3] S. Scheinert, G. Paasch, and M. Schrodner, *Subthreshold characteristics of field effect transistors based on poly(3-dodecylthiophene) and an organic insulator*, J. Appl. Phys. **92**, 330 (2002).

[4] A. Bolognesi and A. Di Carlo, *Influence of carrier mobility and interface trap states on the transfer and output characteristics of organic thin film transistors*, J. Comp. Elec. **2**, 297 (2003).

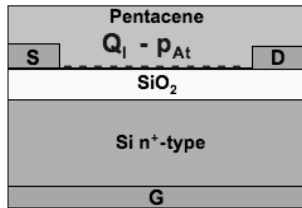


Fig. 1. Layout of simulated pentacene OTFT with channel length of 20  $\mu\text{m}$ , width of 100  $\mu\text{m}$ , and oxide thickness of 190 nm.

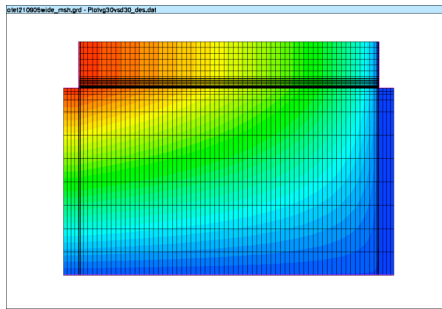


Fig. 2. Numeric mesh and simulated potential for  $V_g = -30$  V and  $V_{sd} = -30$  V.

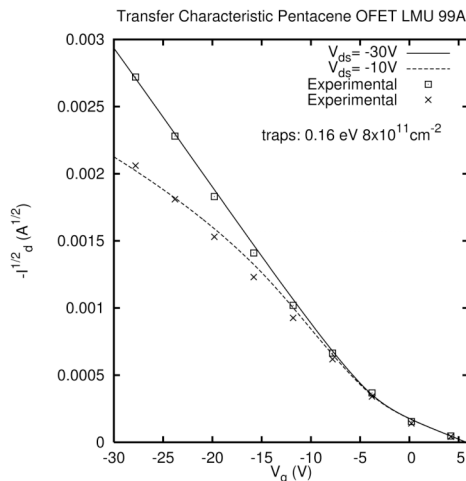


Fig. 3. Simulated and experimental OTFT transfer characteristics with an extracted mobility of  $\mu_p = 2.0$   $\text{cm}^2/\text{Vs}$ .

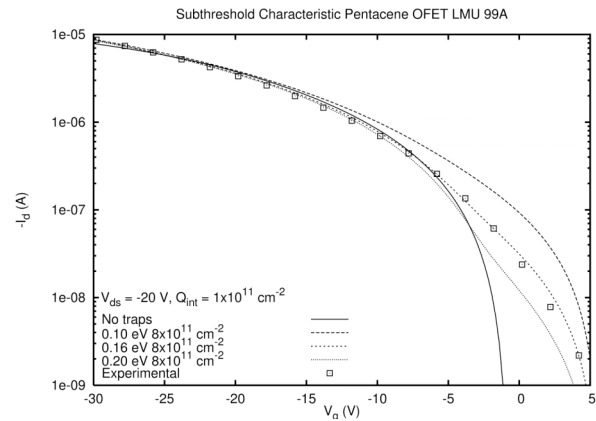


Fig. 4. Extraction of the trap energy by fitting the experimental data with ISETCAD.

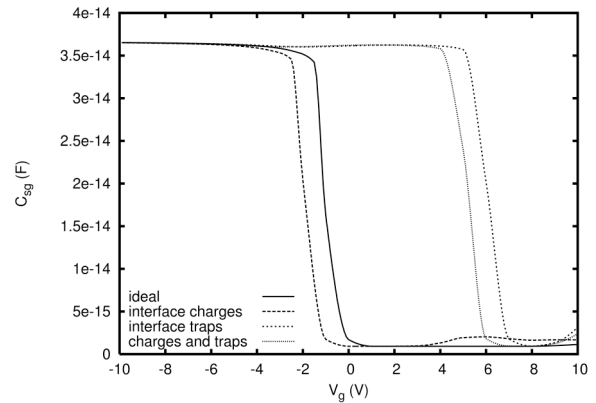


Fig. 5. Simulation of the low-frequency CV characteristics of  $C_{sg}$  showing the influence of interface charges ( $1 \times 10^{11} \text{ cm}^{-2}$ ) and interface traps ( $8 \times 10^{11} \text{ cm}^{-2}$ , 0.16 eV above valence band).

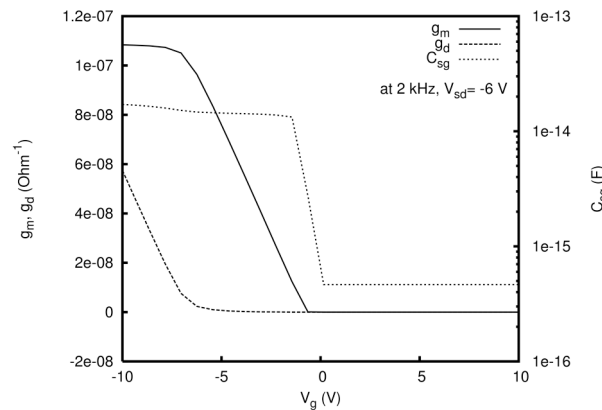


Fig. 6. Simulated AC small-signal parameters  $g_m$ ,  $g_d$  and  $C_{sg}$  at 2 kHz and  $V_{sd} = -6$  V.

# Semiconductor Transport Modeling for the Analysis of Nanoscaled CMOS Circuits

F. Felgenhauer, M. Begoin, J.-K. Bremer, and W. Mathis

Institute for Theoretical Electrical Engineering, Uni Hannover, Appelstr., 9A Hannover, Germany  
 e-mail: felgenhauer@tet.uni-hannover.de

**Abstract**—We discuss the influence of quantum effects in highly scaled CMOS circuits. On the base of 1-d numerical simulations for transport in mesoscopic systems, we set up Spice circuit models. With this Spice models rebuilding the influence of quantum effects, the functionality of classical circuit concepts can be 'tested' in their robustness against these effects. A few circuit examples will be given.

## DISCUSSION

The most important quantum effects for MOS devices in the sub 100nm regime are direct tunneling currents (edge-direct and channel-direct tunneling), charge quantization in the inverted channel and quasi-ballistic transport in very short channel devices. All these effects are pure parasitics influencing or significantly disturbing the device performance. Since CMOS is dominating the semiconductor industry it is very important to ensure that conventional circuit concepts are still applicable when the devices are scaled into the sub 100nm regime. Instead of developing complete new device models we restrict ourselves on the quantum-mechanical description of transport problems, which cause parasitic noise in MOS devices and analyse CMOS circuits under the direct influence of quantum effects. The quantum transport is described in terms of the Schrödinger equation with spatial dependent mass

$$\left[ -\frac{\hbar^2}{2} \frac{d}{dx} \frac{1}{m^*(x)} \frac{d}{dx} + v_{\text{eff}}(\mathbf{k}_t, x) \right] \psi(x) = \varepsilon_x^L \psi(x) \quad (1)$$

with

$$v_{\text{eff}}(\mathbf{k}_t, x) = v_{\text{coul}}(x) + E_c(x) + \frac{\hbar^2 k_t^2}{2m_L^*} \left( 1 - \frac{m_L^*}{m^*(x)} \right).$$

With the restriction to pure Coulomb interaction, the solution of (1) is coupled with the Poisson equation

$$\frac{d}{dx} \epsilon(x) \frac{d}{dx} v_{\text{coul}}(x) = -q^2 [n(x) - N_D^+(x) + N_A^-(x)] \quad (2)$$

according to the Hartree approximation. For more details please see [1]. We implemented a 1-d numerical self-consistent solver (see figure 1,2,3), whereby we use the NEGF formalism for the Schrödinger equation and the Newton-Raphson method for the Poisson equation. The primary goal we want to achieve with the quantum transport calculation is the estimation of tunneling currents for circuit applications, as we already emphasized in the beginning. The advantage of the use of the NEGF formalism, is that it intrinsically enables the inclusion of more sophisticated interactions in devices. Thus we are able to calculate more parasitic quantum effects, which is our future goal.

Using the numerical simulations we build Spice circuit models to include influence in circuit simulations. One example to show a functionality breakdown in a dynamic logic circuit caused by tunneling currents is the Domino-AND-2-gate (suggested by Choi et al. [2]). We simulated this circuit (see figure 4) using a corresponding Spice model for edge-direct tunneling in transistor M2. For the input signal sequence shown in figure 5 the circuit is producing two logic errors at the output (figure 6).

## REFERENCES

- [1] F. Felgenhauer Maik Begoin and Wolfgang Mathis. *Transistor Level Modeling for Analog/RF IC Design*, chapter On Incorporating Parasitic Quantum Effects in Classical Circuit Simulations. Springer Verlag, to be published in 2006.
- [2] Choi CH, Nam KY, Yu Z, Dutton RW. Impact of gate direct tunneling current on circuit performance: a simulation study. *IEEE Transactions on Electron Devices* 2001; **48**(12):2823–2829.

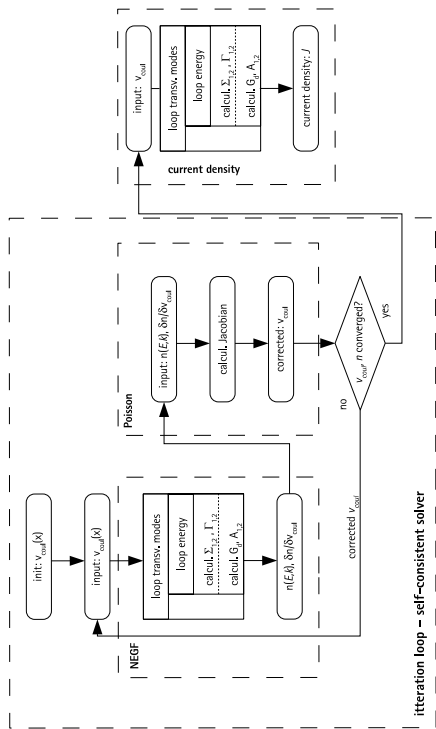


Fig. 1. Flowchart self-consistent solution

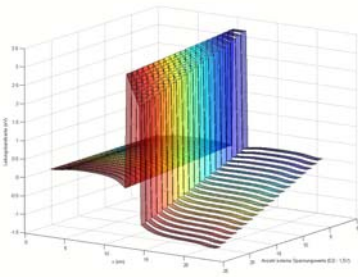


Fig. 2. Potential profile for 1.8nm SiO<sub>2</sub> barrier

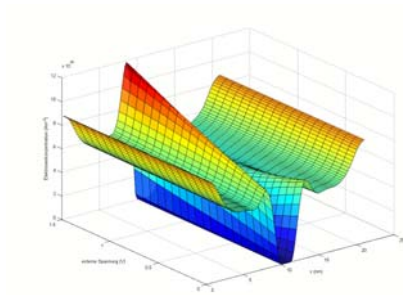


Fig. 3. Charge concentration profile for 1.8nm SiO<sub>2</sub> barrier

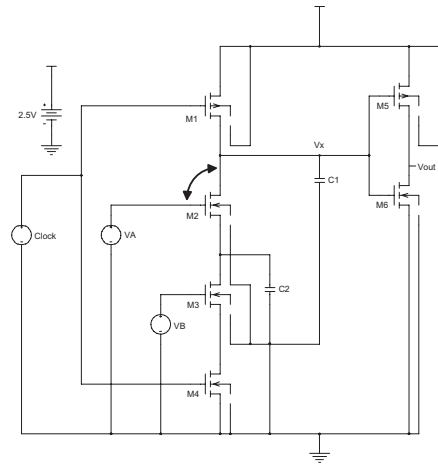


Fig. 4. Domino AND 2 Gate

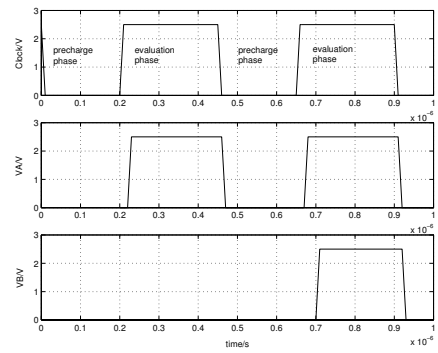


Fig. 5. Input signals for Domino AND 2 Gate

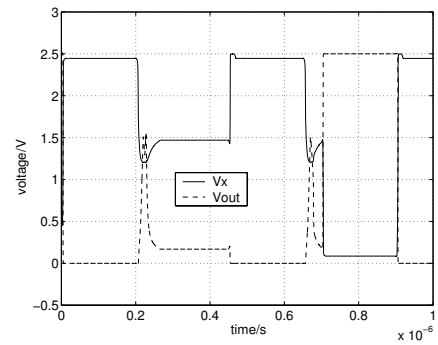


Fig. 6. Output signals for Domino AND 2 Gate

# A Novel Framework for Distributing Computations

T. Fühner, S. Popp\*, and T. Jung

Fraunhofer Institute of Integrated Systems and Device Technology,  
Schottkystrasse 10, 91058 Erlangen, Germany, fuehner@iisb.fraunhofer.de

\* University of Applied Science Regensburg, Department of Computer Science and Mathematics,  
Universitaetsstrasse 31, 93053 Regensburg, Germany, st.popp@gmx.de

## I. INTRODUCTION

Decreasing costs and increasing performance characteristics of desktop-style computers lead to a significant displacement of traditional supercomputers. Nowadays, many of the high-performing computer systems are based on networks of standard PC computers (clusters) [1]. In order to efficiently make use of those distributed systems, sophisticated parallel programming techniques are required.

There is large number of programming frameworks that deal with this. Among them are:

- *Message Passing Interface (MPI)*: A communication framework which provides a high-level interface for parallelization tasks on distributed memory systems [2]. Including fault-tolerance and load-balancing mechanisms has to be specially tailored per application. In addition, there is a number of different MPI implementations, many of which are not compatible to each other.

- *Parallel Virtual Machine (PVM)*: This approach uses a virtual machine in which a network of heterogeneous hosts is represented as one parallel computer to the application [3]. In contrast to MPI, PVM provides a basic mechanism for fault tolerance: The failure of one node will not lead to a crash of the entire multi-node/-process application. As a drawback, compared to MPI PVM lacks a feature-rich communication interface (an often stated shortcoming is the lack of non-blocking operations).

## II. DISPYTE

In this work we propose a new concept: A Dispatchable Python Tasks Environment (DisPyTE), implemented in the free, efficient, and increasingly popular interpreter language Python [4]. The main design and implementation goals of this framework are fault-tolerance and an easy-to-use load-

balancing mechanism. Another important criterion was to achieve a maximum facility in both application and implementation.

The result is a requester/worker type implementation (see Fig. 1). The main components of DisPyTE are:

- *Worker*: *Workers* are realized as processes residing on any computers within the network. They are connected to by the requesters' administrator. Once a *Worker* receives a task, it will be computed, and the result is sent back to the administrator.

- *Proxy Factory*: The factory checks whether new *Workers* are available, generating a proxy for each of them. Proxies are made available to the *Admin*. Additionally, failures of *Workers* are communicated to the *Admin*.

- *Admin*: This module manages the actual distribution process. It keeps track of the state of the *Workers* and distributes the tasks accordingly.

- *Producer*: The *Producer* generates *Tasks*. A task is conferred on the *Admin*, which assigns it to the next idle *Worker* (using the corresponding *Proxy*). Once a *Worker* has completed a task, the result is transferred to the *Requester* using a callback routine.

The *Proxy Factory*, the *Admin*, and the *Producer* are within the scope of the same process. No extra programs such as schedulers are required. An *implicit* load-balancing mechanism is inherent, since the *Admin* is assigning tasks only to idle *Workers*. Thus, for example, a *Worker* that is twice as fast as another one, will in general be assigned twice as many tasks. The proposed approach is also fault-tolerant: If a *Worker* fails, the pending task is re-assigned to a different *Worker*. Even in case no *Workers* are available (any longer), the *Admin* will wait for new computing entities to attach.

DisPyTE does not depend on a specific inter-process communication (IPC) mechanism. As a first implementation the Python package Twisted proved an ideal framework [5]. It provides a wide range of protocols and is freely available for all platforms that support Python.

### III. APPLICATION EXAMPLE: GENETIC ALGORITHM

A genetic algorithm (GA) is a heuristic global optimization routine, which is well suited for optimization tasks that exhibit little information on the search space [6]. Each GA iteration consists of the following two steps: (1) evaluation of the (current) set of solutions and (2) recombination of these solutions. The implicitly parallel behavior of GAs can be exploited in a straightforward manner using a distributed system (see Fig. 2).

In order to use DisPyTE as the underlying distribution layer, following steps are required:

- *Producer* implementation: The GA “produces” a set of solutions per iteration. Instead of directly evaluating these solutions, they act as tasks of a DisPyTE *Producer* and are hence distributed to available *Workers*.

- *Worker* implementation: A *Worker*’s job in the context of a GA is to compute the merit of a specific parameter set. As DisPyTE is using a callback mechanism, the only adjustment that has to be made is to have the DisPyTE *Worker* call the object function.

### IV. CONCLUSIONS

The proposed DisPyTE framework proved very reliable and well suited for the described task. Especially in the regime of heavily loaded desktop computers, the fault-tolerance and the implicit load-balancing mechanisms payed off well. A very moderate implementation effort had to be made in order to use DisPyTE for the parallelization of the genetic algorithm. The concept has already been successfully applied to the optimization of crystal growth and lithography simulation processes (for a discussion on these applications see [7] and [8], resp.). Future work on DisPyTE will be focused on the integration of explicit load-balancing mechanisms. Moreover, as this design seems well suited for other parallelization tasks, it is also planned

to adapt additional applications such that they can make use of DisPyTE.

### REFERENCES

- [1] TOP500 Supercomputer Sites. [www.top500.org](http://www.top500.org).
- [2] W. Gropp, E. Lusk, and A. Skjellum. *Portable Parallel Programming with the Message Passing Interface*. MIT Press, Cambridge, MA, 1999.
- [3] A. Geist, A. Beguelin, J. Dongarra, W. Jiang, R. Manchek, and V. Sunderam. *PVM: Parallel Virtual Machine*. MIT press, 1994.
- [4] Programming Language Python Homepage. [www.python.org](http://www.python.org).
- [5] A. Fetting. *Twisted Network Programming Essentials*. O’Reilly, Sebastopol, CA, 2005.
- [6] D. E. Goldberg. *Genetic Algorithms in Search, Optimization, and Machine Learning*. Addison-Wesley, Reading, MA, 1989.
- [7] T. Fühner and T. Jung. Use of genetic algorithms for the development and optimization of crystal growth processes. *Journal of Crystal Growth*, 266(1-3):229–238, 2004.
- [8] T. Fühner, A. Erdmann, R. Farkas, B. Tollkühn, and G. Kókai. Genetic algorithms to improve mask and illumination geometries in lithographic imaging systems. In Raidl et al., editor, *EvoWorkshops 2004*, pages 208–217, 2004.

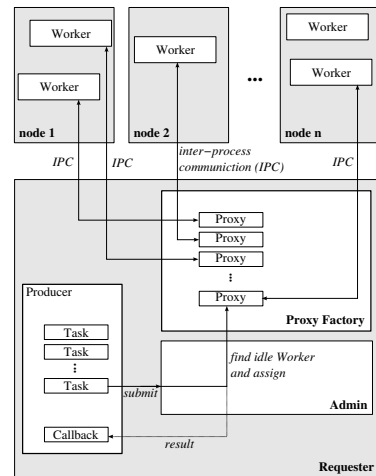


Fig. 1. Main components and call scheme of DisPyTE.

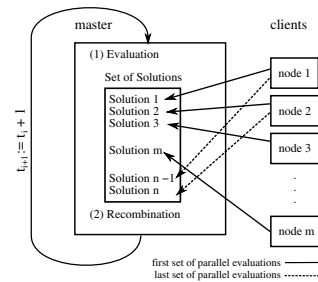


Fig. 2. Distributed computations in the GA regime.

# Efficient Full-Flow Process Simulation for 3D Structures including Stress Modeling

A. H. Gencer, A. Lebedev<sup>\*</sup>, and P. Pfäffli<sup>\*</sup>

Synopsys GmbH, Karl-Hammerschmidtstr. 34, 85609 Aschheim, Germany

<sup>\*</sup>Synopsys Switzerland LLC, Zurich, Switzerland

e-mail: alp.gencer@synopsys.com

## MOTIVATION

As silicon based devices become smaller in size, conventional simulation methods using 2D structures become insufficient. Many effects, such as narrow width effect and line edge roughness require 3D simulation. Moreover, many new devices such as FinFET are 3D by nature. Also, many modern devices are built using stress engineering, which requires 3D stress modeling to predict device performance.

However, 3D process simulation is by its nature more complicated than 2D simulation and even with modern computers it requires a long simulation time. New methods are needed to perform 3D full-flow simulation in a reasonable amount of time.

## HYBRID APPROACH

3D geometry modifications such as deposition, etch, oxidation and epitaxy, present a big challenge to traditional TCAD tools when performed with methodologies such as string algorithm or level-set movement, as these methodologies work only on a mesh. The most efficient method for performing such steps is using a solid modeling. However, solid modeling tools cannot perform process simulation steps, such as diffusion or implantation. A hybrid method, where etching, deposition and epitaxy steps are performed with a solid modeling tool, such as Synopsys' Sentaurus Structure Editor (SDE) and the diffusion and implantation steps are performed by a process simulator, such as Sentaurus Process (Sprocess) had been devised previously [1].

The hybrid method requires of segregation of the input flow into an SDE flow and Sprocess flow, which need to be manually intertwined. A new input flow definition strategy has been developed, which allows for keeping the process flow in one single file, and letting the interpreter to do the necessary book keeping while switching between the tools.

The methodology works in two modes of meshing strategy, called remesh every switch and paint by number. In the former, entirely new mesh is built at every switch. In the latter case, all steps from the full flow are combined into one structure and the merged regions are assigned numbers. The mesh is built once on the merged structure and regions indicated by numbers change material type to obtain the structure at a particular step.

## STRESS MODELING

Solving for stress-strain equations concurrently with diffusion equations slows down simulation time considerably. To avoid this, we run the process simulation twice: Once solving only for implantation steps and diffusion equations and a second time only solving the mechanical equations. The second run is extremely fast compared to the first one, since the simulator can choose large time steps. The results are then combined to perform device simulation including stress effects on band gap and mobility.

## CONCLUSION

The methods described have been applied to several 3D process flows, including a FinFET [2], a CMOS image sensor, a PMOS device with raised SiGe S/D and other structures. The simulation times are about an order of magnitude faster than using a process simulator with a mesh to perform the topography modification steps. This makes 3D simulation feasible for everyday use.

## REFERENCES

- [1] "More Efficient Process Flow for 3D NMOS Transistors", Synopsys TCAD News, October 2004.  
[http://www.synopsys.com/products/tcad/pdfs/news\\_oct04.pdf](http://www.synopsys.com/products/tcad/pdfs/news_oct04.pdf)
- [2] M. Nawaz, P. Haibach, E. Landgraf, W. Rösner, M. Städle, H. Luyken and A.H. Gencer "Full 3D Process and Device Simulation for FinFET Optimization", ISDRS 2005.

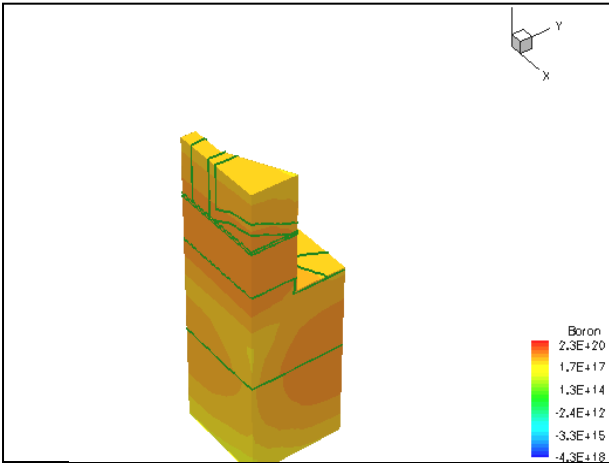


Fig. 1a. FinFET structure after fin formation. Note region boundaries from the merged structure.

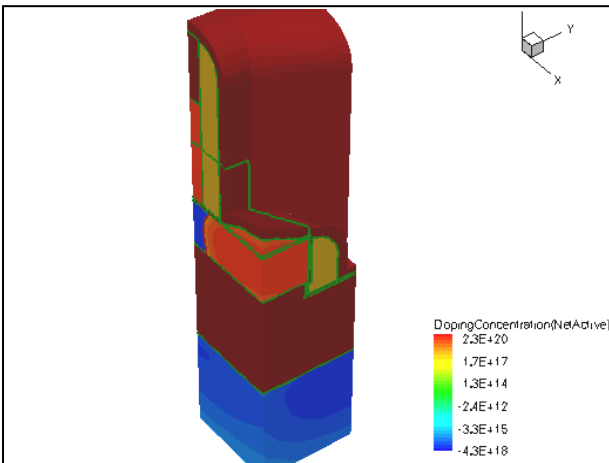


Fig. 1b. Final FinFET structure. Only one quarter of the FinFET was simulated to take advantage of symmetry.

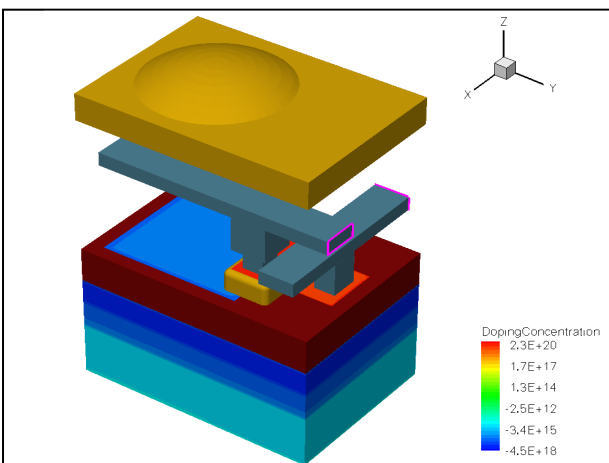


Fig. 2. Final topography for the CMOS image sensor

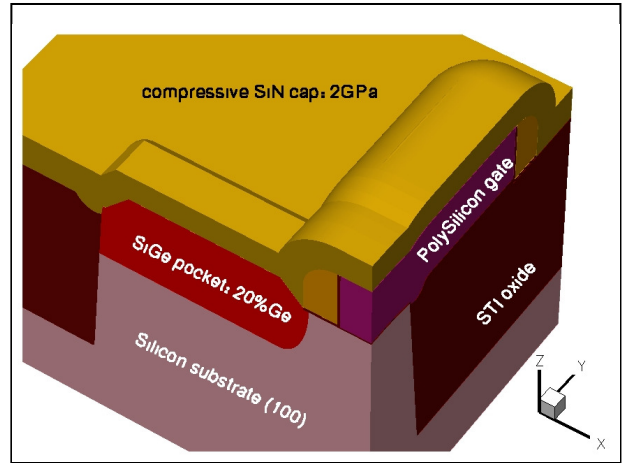


Fig. 3a. Final topography for SiGe raised S/D PMOS

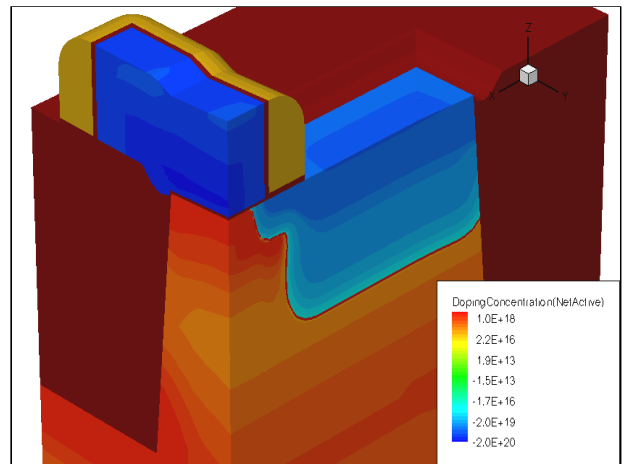


Fig. 3b. Final doping distribution for the 3D PMOS

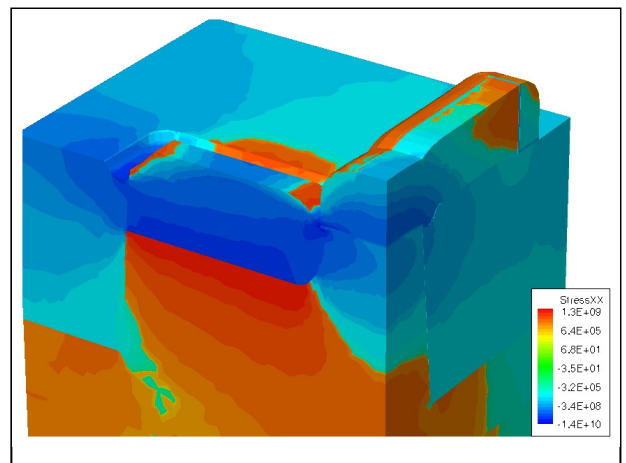


Fig. 3c. Final stress distribution for the 3D PMOS

# Simulation of Slow Current Transients and Current Compression in AlGaAs/GaAs HFETs

H. Ikarashi, K. Kitamura, N. Kurosawa and K. Horio

Shibaura Institute of Technology, 307 Fukasaku, Minuma-ku, Saitama 337-8570, Japan

## INTRODUCTION

Compound semiconductor FETs, such as GaAs MESFETs, HFETs and GaN-based FETs, are very important devices for microwave power devices and ICs that are now receiving great attention, particularly for mobile communication applications. However, slow current transients are often observed even if the drain voltage  $V_D$  or gate voltage  $V_G$  is changed abruptly. This is called drain lag or gate lag [1]. Hence the dc  $I$ - $V$  curves and ac  $I$ - $V$  curves become quite different, resulting in lower ac power available than that expected from dc operation. This is called power (current) compression [2,3]. These are serious problems and there are many experimental works reported on these phenomena, but only a few theoretical works are reported for HFETs [4], although several numerical analyses were made for MESFETs [5,6]. Also, the lag phenomena were studied by changing only  $V_D$  or  $V_G$ . But both voltages should be changed during turn-on or RF drive. Therefore, in this work, we have made transient simulations of AlGaAs/GaAs HFETs, and particularly calculated cases when both  $V_D$  and  $V_G$  are changed abruptly, and derived quasi-pulsed  $I$ - $V$  curves. As a result, we have clearly shown that the current compression could occur both due to substrate traps and surface states.

## PHYSICAL MODEL

Fig.1 shows a modeled AlGaAs/GaAs HFET. As a substrate, we consider undoped semi-insulating GaAs where deep donors "EL2" ( $N_{EL2}$ ) compensate shallow acceptors ( $N_{Ai}$ ) [5]. As a surface state, we consider an acceptor-type state, and vary its energy level  $E_{SA}$  as a parameter because the detailed information is not obtained for AlGaAs surface. Basic equations are Poisson's equation including ionized deep-level terms, continuity equations for electrons and holes which include carrier loss rates via the deep levels, and rate equations for the deep levels.

## SUBSTRATE-TRAP EFFECTS

Fig.2 shows calculated drain-current responses of the AlGaAs/GaAs HFET when  $V_D$  is changed abruptly from 0 V ( $V_{Dini}$ ) to  $V_{Dfin}$  while keeping  $V_G$  at 0 V. Here, surface states are not included. The drain currents overshoot the steady-state values, because electrons are injected into the substrate, and the substrate trap (EL2) needs certain time to capture these electrons. Fig.3 shows the case when  $V_D$  is lowered abruptly from 5V to  $V_{Dfin}$  while keeping  $V_G$  at 0 V. The drain currents remain at low values for some period, and begin to increase slowly, showing drain-lag behavior. It is

understood that the drain current begin to increase when the deep donors begin to emit electrons.

We have next calculated a case when both  $V_D$  and  $V_G$  are changed from an off point. Fig.4 shows calculated turn-on characteristics when  $V_G$  is changed from the threshold voltage  $V_{th}$  to 0 V. The off-state drain voltage  $V_{Doff}$  is 5 V, and the parameter is an on-state drain voltage  $V_{Don}$ . The characteristics are similar to Fig.3, and hence the change of  $V_D$  (drain lag) is essential in this case, although slight transients are seen when only  $V_G$  is changed ( $V_{Don} = 5$  V in Fig.4). Fig.5 shows  $I_D$ - $V_D$  curves. Here, we plot by point (x) the drain current at  $10^{-6}$  s after  $V_G$  is switched on. This is obtained from Fig.4, and this curve corresponds to a quasi-pulsed  $I$ - $V$  curve with pulse width of  $10^{-6}$  s. (For reference, we also plot other quasi-pulsed  $I$ - $V$  curves when only  $V_D$  is changed, which reflect the overshoot and undershoot). The drain currents in the pulsed  $I$ - $V$  curve are rather lower than those in the steady state. This clearly indicates that the current compression could occur due to the substrate-trap effects, and it occurs due to drain lag in this case.

## SURFACE-STATE EFFECTS

Next we have calculated a case when only the surface states are included. It is found that the lags are not seen when the energy level of deep-acceptor surface state  $E_{SA}$  is far from the valence band and it acts as an electron trap. The lags become important when the deep acceptor acts as a hole trap. Fig.6 shows calculated  $I_D$ - $V_D$  curves for such a case. The current compression is significant, as shown by point (x), and it occurs mainly due to the change of  $V_G$  (gate lag) in this case.

## COMBINED EFFECTS OF SUBSTRATE AND SURFACE

Finally, we have studied the case when both the substrate traps and surface states are included. Fig.7 shows an example of calculated  $I_D$ - $V_D$  curves. It is seen that the lags (overshoot and undershoot) and current compression are very pronounced when comparing with Figs.5 and 6. This significant combined effect is an interesting feature which has not been pointed out.

## REFERENCES

- [1] S. C. Binari, P. B. Klein and T. E. Kazior, Proc. IEEE, vol.90, pp.1048-1058 (2002)
- [2] R. E. Leoni et al., IEEE Trans. Electron Devices, vol.47, pp.498-506 (2000).
- [3] U. K. Mishra, P. Parikh and Y.-F. Wu, Proc. IEEE, vol.90, pp.1022-1031 (2002).
- [4] G. Verzellesi et al., IEEE Trans. Electron Devices, vol.50, pp.1733-1740 (2003).
- [5] Y. Kazami, D. Kasai and K. Horio, IEEE Trans. Electron Devices, vol.51, pp.1760-1764 (2004).
- [6] K. Horio et al., J. Appl. Phys., vol.98, no.12 (2005).

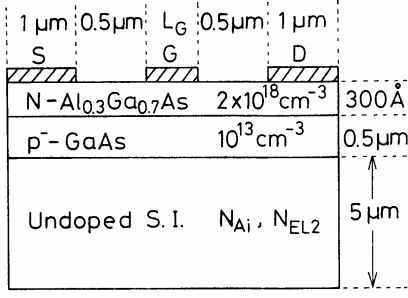


Fig.1. Device structure analyzed in this study

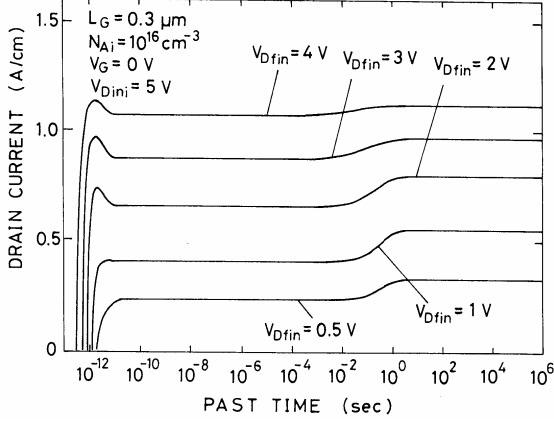


Fig.3. Calculated drain-current responses of AlGaAs/GaAs HFET when  $V_D$  is lowered from 5 V to  $V_{Dfin}$ .  $V_G$  is kept 0 V.

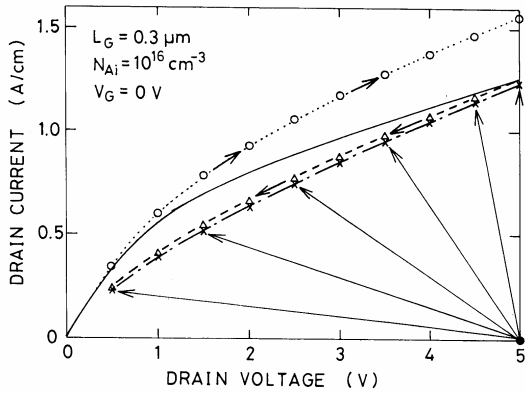


Fig.5. Steady-state  $I_D$ - $V_D$  curve (solid line) and quasi-pulsed  $I$ - $V$  curves of AlGaAs/GaAs HFET with a semi-insulating substrate. (x):  $V_{Goff} = V_{th}$  and  $V_{Doff} = 5$  V ( $t = 10^{-6}$  s; Fig.4), (o):  $V_{Dini} = 0$  V and  $V_G = 0$  V ( $t = 10^{-9}$  s; Fig.2), (Δ):  $V_{Dini} = 5$  V and  $V_G = 0$  V ( $t = 10^{-6}$  s; Fig.3).

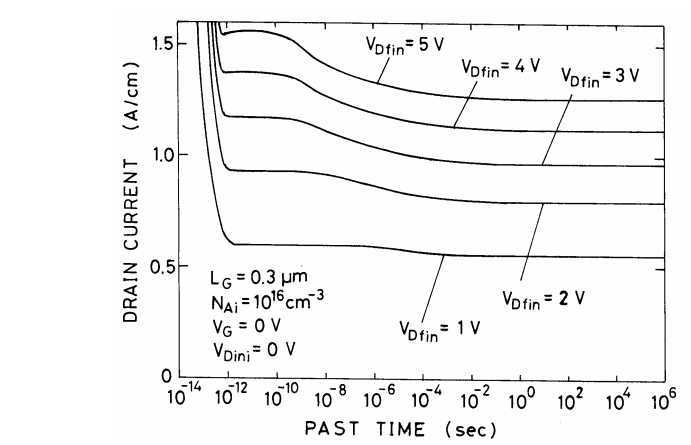
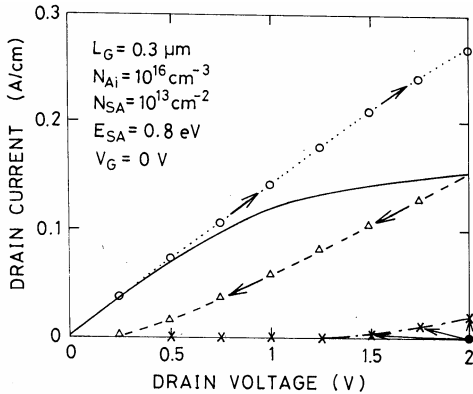


Fig.2. Calculated drain-current responses of AlGaAs/GaAs HFET when  $V_D$  is raised from 0 V to  $V_{Dfin}$ .  $V_G$  is kept 0 V.

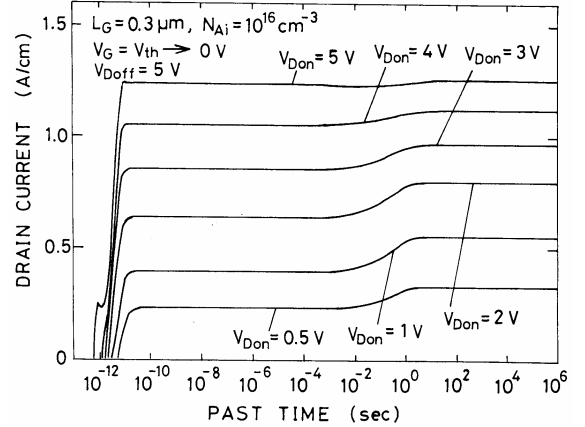


Fig.4. Calculated turn-on characteristics of AlGaAs/GaAs HFET when  $V_G$  is changed from  $V_{th}$  to 0 V.  $V_D$  is also changed from 5 V to  $V_{Don}$ .

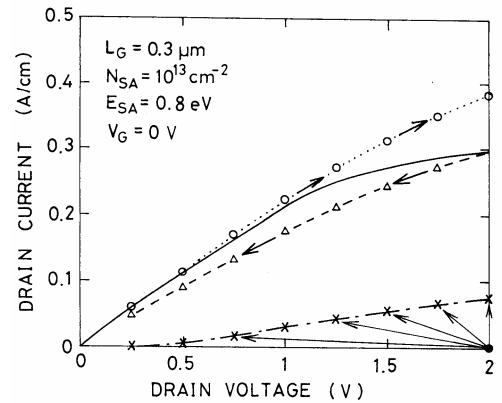


Fig.6. Steady-state  $I_D$ - $V_D$  curve (solid line) and quasi-pulsed  $I$ - $V$  curves (pulse width of  $10^{-6}$  s) of AlGaAs/GaAs HFET with surface states but without substrate traps. (x):  $V_{Goff} = V_{th}$  and  $V_{Doff} = 5$  V, (o):  $V_{Dini} = 0$  V and  $V_G = 0$  V, (Δ):  $V_{Dini} = 5$  V and  $V_G = 0$  V.

Fig.7. Steady-state  $I_D$ - $V_D$  curve (solid line) and quasi-pulsed  $I$ - $V$  curves (pulse width of  $10^{-6}$  s) of AlGaAs/GaAs HFET with both surface states and substrate traps. (x):  $V_{Goff} = V_{th}$  and  $V_{Doff} = 5$  V, (o):  $V_{Dini} = 0$  V and  $V_G = 0$  V, (Δ):  $V_{Dini} = 5$  V and  $V_G = 0$  V.

# Compact Model for Schottky-Barrier CNT-FETs

D. Jiménez, X. Cartoixà, E. Miranda, J. Suñé, and S. Roche\*

Departament d'Enginyeria Electrònica, Universitat Autònoma de Barcelona, Spain

\*DSM/DRFMC/SPSMS, Commissariat à l'Énergie Atomique, France

e-mail: david.jimenez@uab.es

## ABSTRACT

Carbon nanotube field-effect transistors (CNT-FETs) are being the subject of very intense research as promising devices for future electronic applications. This research is motivated by the technical and economic difficulties in further miniaturizing silicon-based transistors with the current fabrication technologies.

At present, an important issue is to dispose of compact models describing the interplay between the observed phenomenology in CNT-FETs. These models are intended to serve as guidelines for understanding the experimental work at this early stage of development, and for design and projection purposes. In this work we develop a physics-based compact model for the current-voltage (I-V) characteristics of Schottky-barrier CNT-FETs (Fig. 1). The model captures a number of features exhibited by Schottky barrier CNT-FETs: (a) thermionic and tunnel emission [1]; (b) ambipolar conduction [2]; (c) ballistic transport [3]; (d) multimode propagation [4]; and (e) electrostatics dominated by the nanotube capacitance [5].

In the proposed model, the spatial band diagram along the nanotube consists of three distinctive regions: two injecting barriers at the ends of the nanotube and an intermediate region where ballistic transport occurs (Fig. 2). This latter region is approximated by a flat band structure, its energetic level being essentially determined by the nanotube capacitance, which is supposed to dominate over the insulator capacitance (operating conditions close to the quantum capacitance limit). The energetic diagram at the two injecting barriers can be analytically calculated solving Laplace's equation along the transport direction. A coaxial gate geometry is considered. The current is calculated by means of the Landauer formula for one-dimensional systems contacted with infinite reservoirs. The key information to compute the current is the transmission probability for all energies, which is calculated using the WKB formalism.

We have taken into account that multiple reflections can arise between both Schottky barriers at the interfaces, in the same way as a Fabry-Pérot resonator [6]. The proposed model is compared with accurate self-consistent quantum mechanical simulations based on the Non-Equilibrium Green's Functions (NEGF) [7]. Specifically, the test consist in the comparison of the I-V characteristics showing the effect of power supply voltage scaling (Fig. 3), nanotube diameter scaling (Fig. 4), and barrier height (Fig. 5). Notice the good agreement between our model and NEGF's simulations. The compact model is valid as long as the CNT-FET operates at the quantum capacitance limit (see Fig. 6).

## ACKNOWLEDGEMENT

This work was supported by the MCyT under project TIC2003-08213-C02-01 and the European Commission under Contract 506653 ("EUROSOI").

## REFERENCES

- [1] J. Appenzeller, M. Radosavljevic, J. Knoch, and Ph. Avouris, *Tunneling versus thermionic emission in one-dimensional semiconductors*, Phys. Rev. Lett. **92**, no. 4 (2004).
- [2] R. Martel, V. Derycke, C. Lavoie, J. Appenzeller, K. K. Chan, J. Tersoff, and Ph. Avouris, *Ambipolar electrical transport in semiconducting single-wall carbon nanotubes*, Phys. Rev. Lett. **87**, no. 25 (2001).
- [3] C. T. White, and T. N. Todorov, *Carbon nanotubes as long ballistic conductors*, Nature **393**, 240 (1998).
- [4] J. Appenzeller, J. Knoch, M. Radosavljevic, and Ph. Avouris, *Multimode transport in Schottky barrier carbon-nanotube field-effect transistors*, Phys. Rev. Lett. **92**, no. 22 (2004).
- [5] D. L. John, L. C. Castro, and D. L. Pulfrey, *Quantum capacitance in nanoscale device modeling*, J. Appl. Phys. **96**, 5180 (2004).
- [6] W. Liang, M. Bockrath, D. Bozovic, J. H. Hafner, M. Tinkham, and H. Park, *Fabry-Perot interference in a nanotube electron waveguide*, Nature **411**, 665 (2001).
- [7] J. Guo, S. Datta, and M. Lundstrom, *A numerical study of scaling issues for Schottky-barrier carbon nanotube transistors*, IEEE Trans. Electron Devices **51**, 172 (2004).

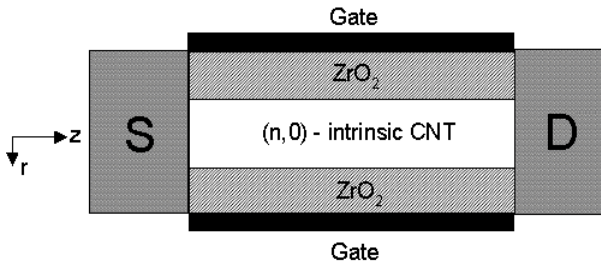


Fig. 1. CNT-FET cross-section. The electrodes are assumed to be metallic and the body is an intrinsic (n,0) semiconductor nanotube.

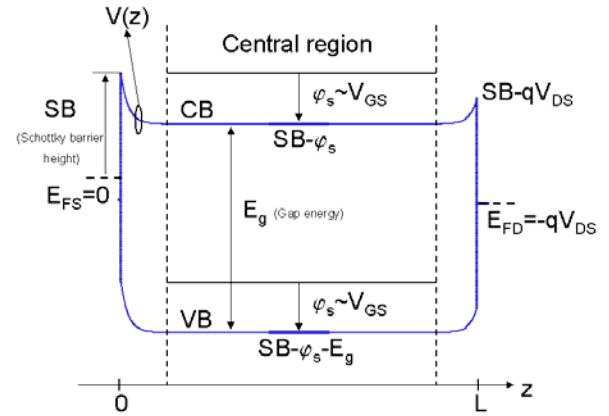


Fig. 2. Spatial band diagram scheme (along the transport direction).

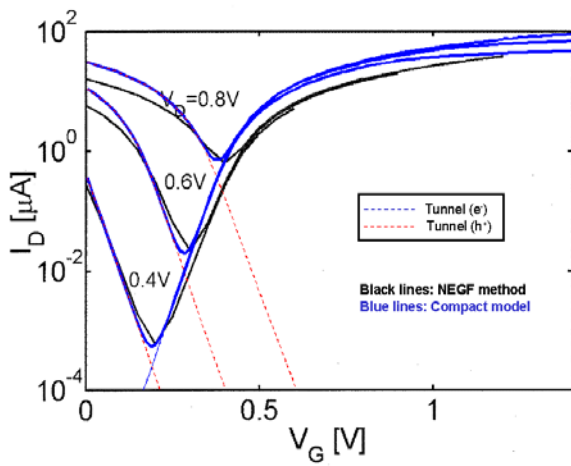


Fig. 3. Transfer characteristics: effect of the power supply voltage scaling.

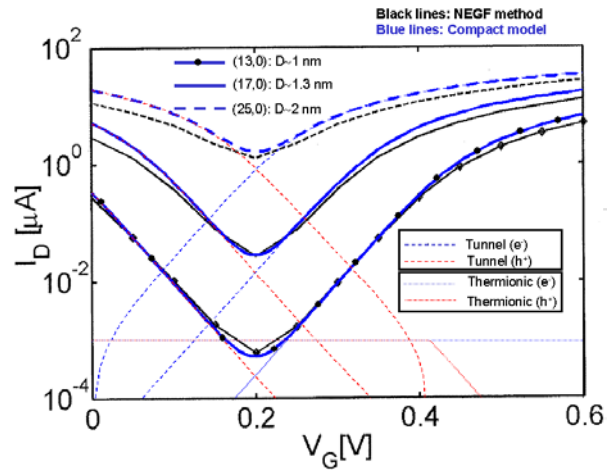


Fig. 4. Transfer characteristics: effect of the nanotube diameter scaling.

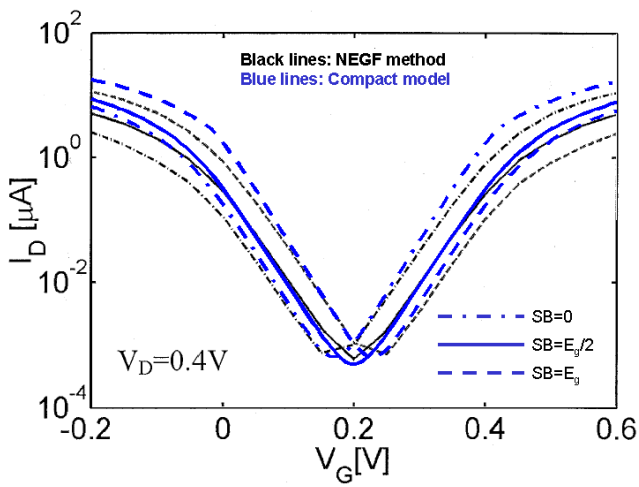


Fig. 5. Transfer characteristics: effect of the barrier height.

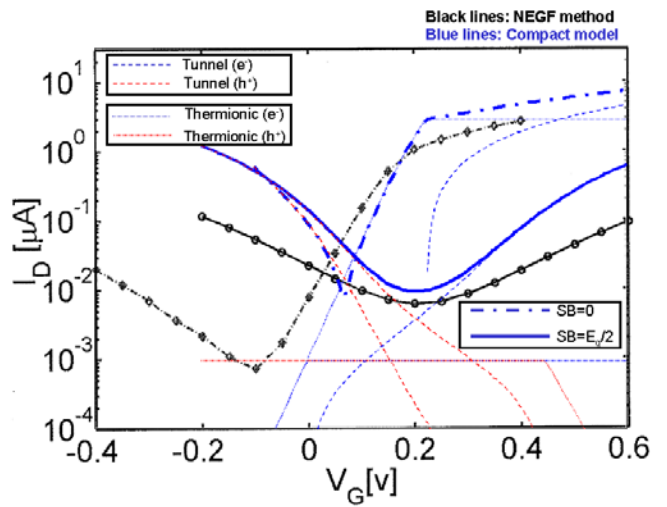


Fig. 6. Transfer characteristics for a thick oxide thickness (40 nm) CNT-FET, not working at the quantum capacitance limit.

# A Simulation-Based Evolutionary Technique for Inverse Problems of Sub-65nm CMOS Devices

Yiming Li<sup>\*</sup>, Shao-Ming Yu<sup>1</sup>, and Cheng-Kai Chen<sup>1</sup>

Department of Communication Engineering, National Chiao Tung University

<sup>1</sup> Department of Computer Science, National Chiao Tung University

<sup>\*</sup> Corresponding author. Address: P.O. Box 25-178, 1001 Ta-Hsueh Rd., Hsinchu 300, TAIWAN  
TEL: +886-930330766; FAX: +886-3-5726639; and Email: ymli@faculty.nctu.edu.tw

## ABSTRACT

In this paper, we utilize an evolutionary technique for inverse modeling problems of scaled-down 65 nm CMOS devices. The approach mainly bases upon the process and device simulations, evolutionary strategy, and empirical knowledge. For a set of given measured I-V curves of 65nm CMOS, a developed prototype performs the optimization task to automatically calibrate and inversely find out, for example the doping recipe and device physical model parameters. It benefits the development of fabrication technology and can be used for the performance diagnosis.

## INTRODUCTION

The technology computer-aided design (TCAD) simulation has widely been used for the analysis of semiconductor devices [1]. For a set of given device's I-V curves, finding out the associated optimal configurations forms an inverse problem [2]. It nowadays plays an important approach to technology development as well as the performance diagnosis due to significant characteristic fluctuation of sub-65nm CMOS devices.

In this work, a simulation-based evolutionary system is developed for inverse problem of sub-65nm N- and P-MOSFET. Compared to realistic experimental process recipe, the achieved results demonstrate good extraction capability of the proposed method.

## METHODOLOGY AND EXTRACTED RESULTS

Figure 1a shows the computational flowchart of the TCAD simulation-based inverse modeling problem. The developed system, shown in Fig. 1b, is mainly relying on a hybrid genetic algorithm (GA) [3] incorporating with other optimization techniques. Inset of Fig. 2 is a 2D cross-section view of the simulated 65 nm MOSFET with LDD doping profile. Table 1 shows the partial list of LDD profile

parameters for process simulation, and physical model parameters for device simulation. Figure 2 shows the target I-V curves to be optimized and several most concerned physical quantities empirically. Figure 3 depicts the performance of three different calibration strategies. The single optimization approach is limited and can not improve the accuracy of extraction. It is necessary to perform process and device simulation simultaneously. The extracted curves are shown in Fig. 4 for both N- and P- MOSFETs, where Fig. 5 illustrates the inversely calibrated doping profile for the 65nm MOSFETs. A set of inversely optimized results is shown in Table 1.

## CONCLUSIONS

We have presented an evolutionary system for inverse problem and tested on 65nm CMOS devices. Process and device parameters have been obtained according to realistic device data. The proposed system is now under developed to explore asymmetric transport phenomena due to fluctuation of source and drain implantations.

## ACKNOWLEDGEMENT

This work was supported in part by Taiwan National Science Council (NSC) under Contract NSC-94-2215-E-009-084 and Contract NSC-94-2752-E-009-003-PAE, by the Ministry of Economic Affairs, Taiwan under Contract 93-EC-17-A-07-S1-0011, and by the TSMC under a 2005-2006 grant.

## REFERENCES

- [1] S. Selberherr, *Analysis and Simulation of Semiconductor Devices*, New York: Springer-Verlag, 1984
- [2] T. Binder *et al.*, *A Study on Global and Local Optimization Techniques for TCAD Analysis Tasks*, IEEE T CAD, **23**, 6 (2004).
- [3] Y. Li *et al.*, *Intelligent BSIM4 Model Parameter Extraction for Sub-100 nm MOSFET Era*, Jpn. JAP, **43**, 1717 (2004).
- [4] A. Schenk, *Rigorous theory and simplified model of the band-to-band tunneling in Silicon*, Solid-State Elec., **36**, 19 (1993).
- [5] C. Lombardi *et al.*, *A Physically Based Mobility Model for Numerical Simulation of Nonplanar Devices*, IEEE T CAD, **7**, 1164 (1988).

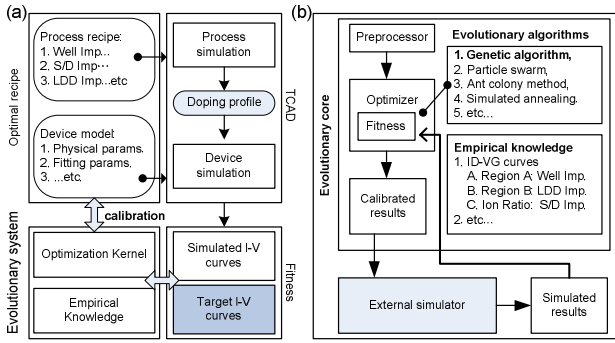


Fig. 1. (a) A flowchart of the proposed optimization system to solve the device inverse modeling problem. (b) An architecture of the developed system. The system has its built-in 2D/3D device and process simulation programs; it also interfaces to well-known TCAD tools.

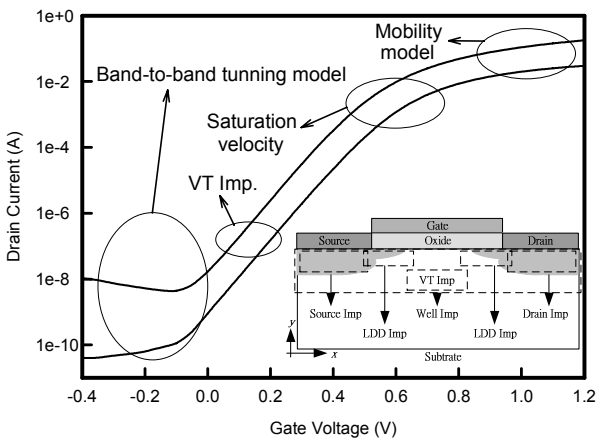


Fig. 2. An illustration of the target I-V curves to be extracted and empirical knowledge. The inset plot is a 2D cross-section view of the simulated MOSFET with LDD doping profile.

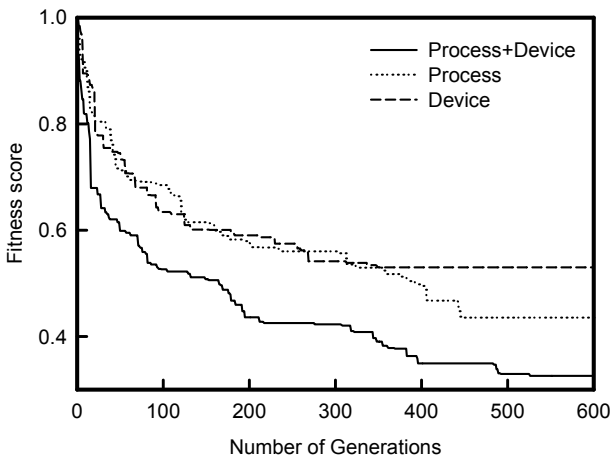


Fig. 3. The performance comparisons among three different evolutionary strategies. There are totally 31 process and device parameters to be optimized in the case of process and device simulations. The total time is about 70 hours on a PC-based Linux cluster with 16 CPUs.

Table 1. A partial list of process and device's parameters to be extracted for the explored 65nm N- and P-MOSFETs. The Schenk model [4] is adopted to describe the band-to-band tunneling. The enhanced Lombardi model [5] is selected as a mobility model.

Process Recipe	Parameter Range	Calibrated Result	
		N-MOS	P-MOS
Well Imp.	Energy: 300~500 KeV	462	276
	Dose: 5e12~5e13 cm <sup>-2</sup>	2.6e13	3.1e13
LDD Imp.	Energy: 10~50 KeV	30	25
	Dose: 5e12~5e13 cm <sup>-2</sup>	3.7e13	2.1e13
S/D Imp.	Energy: 20~80 KeV	17	11
	Dose: 1e13~1e14 cm <sup>-2</sup>	2.1e13	1.5e13
Device Model	Parameter Range	Calibrated Result	
Mobility model	B(cm/s): 2e7~8e7	462	276
	C(cm <sup>5/3</sup> /V <sup>2/3</sup> s): 1e2~5e2	2.6e13	3.1e13
Velocity saturation model	Vsat 0(cm/s): 1e6~1e8	9e6	8.1e6
	Vsat exp: 0.5~1.0	0.81	0.94

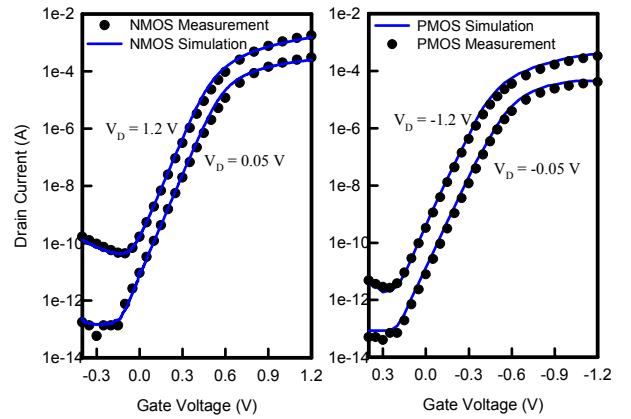


Fig. 4. The achieved accuracy of the extracted I-V curves for N- and P-MOSFETs, where gate length  $L = 65\text{nm}$  and device width  $W = 1\mu\text{m}$ . Results are simultaneously obtained with considering device and process configurations. Symbols are measured data and lines are eventually optimized result.

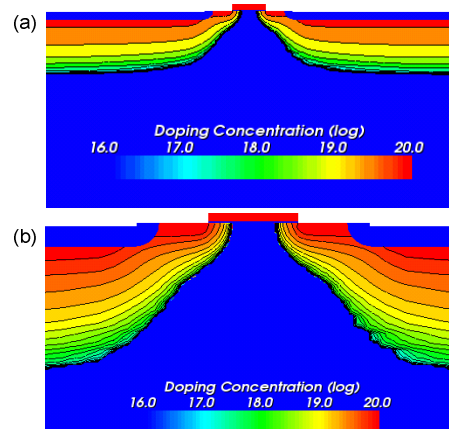


Fig. 5. The extracted 65nm (a) N-MOSFET doping profile and (b) a zoom-in plot of the profile. Similar results are obtained for the P-MOSFET. These results are corresponding to the optimized I-V curves shown in Fig. 4. We note that simulations are performed with 2D process and device structures.

# Numerical Simulation of Electrical Characteristics on Uniaxial Strained Bulk and SOI FinFETs

Yiming Li\* and Wei-Hsin Chen<sup>1</sup>

Department of Communication Engineering, National Chiao Tung University

<sup>1</sup> Department of Electrophysics, National Chiao Tung University

\* Corresponding author. Address: P.O. Box 25-178, 1001 Ta-Hsueh Rd., Hsinchu 300, TAIWAN  
TEL: +886-930330766; FAX: +886-3-5726639; and Email: ymli@faculty.nctu.edu.tw

## ABSTRACTS

In this paper, electrical characteristics of fin-typed metal-oxide-semiconductor field effect transistor (MOSFET) with oxide nitride stacked capping layer is numerically studied. Compared the simulation results between strained bulk FinFET and strained SOI one, the strained bulk FinFET shows promising characteristics, and therefore the strained bulk FinFET may play an important role in the trend of scaling by the advantage of a much lower cost of fabrication for the electronic industry.

## INTRODUCTION

Single gate FETs strained with diverse materials are very popular and have been investigated in decades [1]. Strained FETs are possible candidates for next generation high performance devices. Higher speed is due to higher carrier mobility which comes from the mismatch between two different lattice constants and the conduction energy band bending, leading to a smaller effective mass of the electron in the channel region in contrast with pure silicon (Si) MOSFETs. On the other hand, the advantages of SOI technology are high speed, less leakage current and high density [2]. SOI structure, however, has some fatal drawbacks, e.g., floating-body effect and self-heating effect. By the Body effect, the threshold voltage is changed and the device will be operated in the incorrect region.

In this paper, we computationally explore electrical characteristics of bulk and SOI FinFETs with an oxide nitride stacked capping layer. Strained impacts on their performance are examined with 3D.

## COMPUTATIONAL MODEL AND RESULTS

As shown in Fig. 1, Si bulk and SOI substrates are examined for a 25 nm FinFET, where the oxide thickness is fixed at 1.4 nm. A 3D density-gradient simulation is performed to explore these electrical characteristics. The 3D hydrodynamic and density-gradient equations are solved with the adaptive

finite volume and the monotone iterative methods [3]. To valid the simulation, mobility with considering strained effect, band bending, for example, should be adjusted carefully.

Figures 2 and 3 show the doping profile and electrostatic potential of the strained bulk FinFET and SOI one. The oxide layer of SOI one leads to a different distribution of doping conditions and electrostatic potential, which changes the grounded substrate to a floating body. From Fig. 4, we observe the stress distribution of cross-section of the FinFET with face perpendicular to the direction from source to drain, which is resulted from the oxide nitride capping layer. Therefore, Si channel is strained to make the electron having a higher mobility. The IdVd and IdVg curves, shown in Fig. 5, indicate that the strained bulk FinFET and SOI one have almost matched characteristics. The IdVd values of SOI are not more than 3.79% than bulk one. Table 1 indicates the bulk one has a smaller SS and DIBL values than SOI one.

## CONCLUSIONS

Our preliminary investigation has shown that the strained bulk FinFET posses acceptable electrical properties compared with SOI one. Due to a significant advantage of less cost of fabrication, the strained bulk FinFET is a candidate for the scaling of VLSI devices in the near future.

## ACKNOWLEDGEMENT

This work was supported in part by Taiwan National Science Council (NSC) under Contract NSC-94-2215-E-009-084 and Contract NSC-94-2752-E-009-003-PAE, by the Ministry of Economic Affairs, Taiwan under Contract 93-EC-17-A-07-S1-0011, and by the TSMC under a 2005-2006 grant.

## REFERENCES

- [1] Scott E. Thompson *et al.*, *A Logic Nanotechnology Featuring Strained-Silicon*, IEEE EDL, **25**, 191 (2004).
- [2] W.K. Yeh *et al.*, *High Performance 0.1 um Partially Depleted SOI CMOSFET*, IEEE Int. SOI Conf, 68 (2000).
- [3] Y. Li, *et al.*, *Investigation of Electrical Characteristics on Surrounding-Gate and Omega-Shaped-Gate Nanowire FinFETs*, IEEE T Nanotech, **4**, 510 (2005).

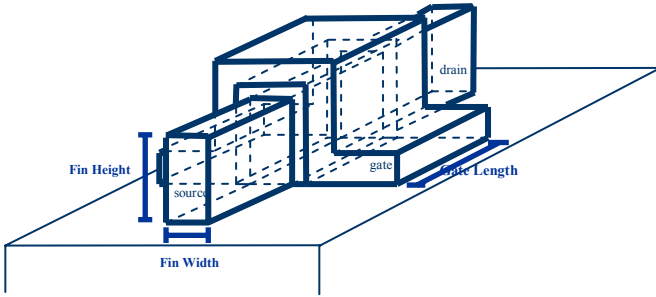


Fig. 1. The FinFET structure used for the 3D simulation.

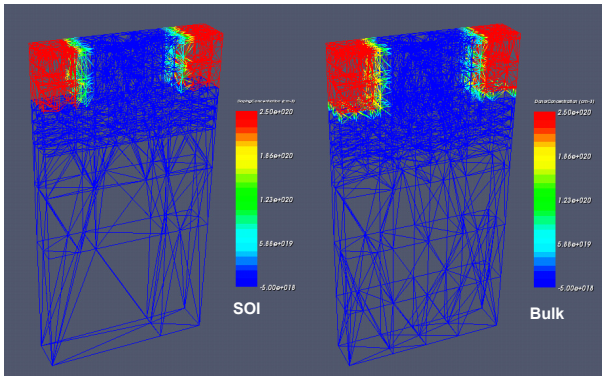


Fig. 2. The 3D doping distribution of the strained bulk FinFET (the right plot) and strained SOI one (the left one).

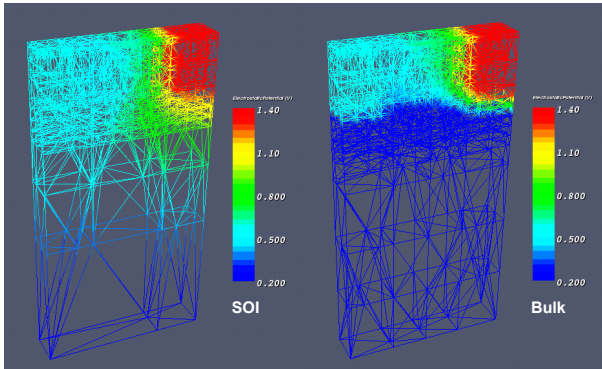


Fig. 3. The 3D electrostatic potential distribution of the strained bulk FinFET (the right plot) and strained SOI one (the left one).

Table 1. Comparison of the extracted subthreshold swing (SS) and drain induced barrier height lowering (DIBL) between the strained bulk FinFET and strained SOI one.

	SOI	Bulk
S.S. (mV)	75.82	64.75
DIBL (mV)	89.20	56.08

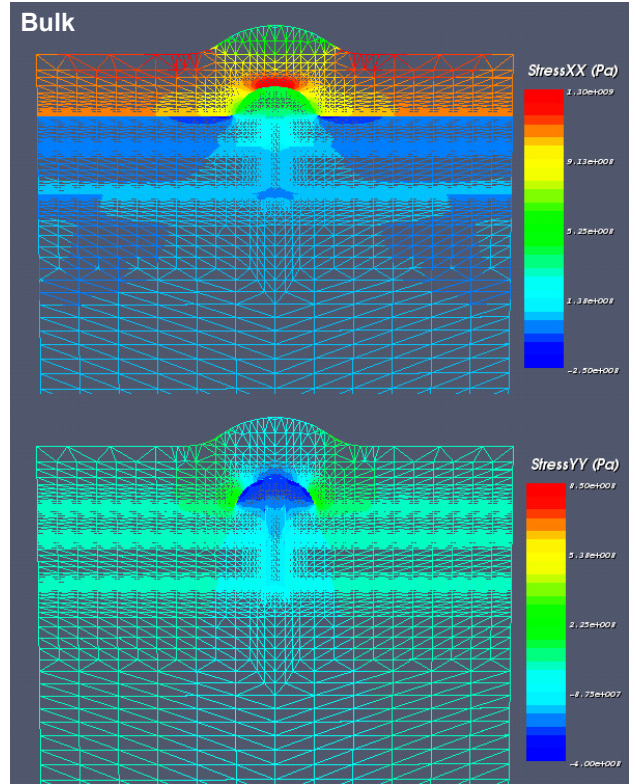


Fig. 4. The stress distribution of the cross-section of the FinFET with face perpendicular to the direction from source to drain.

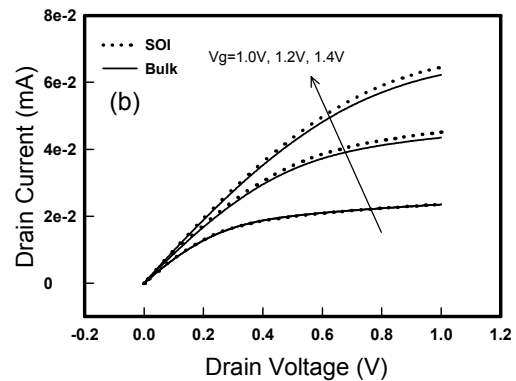
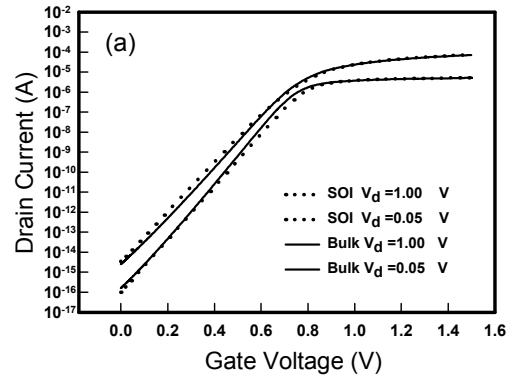


Fig. 5. The simulated (a)  $I_d/V_g$  and (b)  $I_d/V_d$  characteristics of the strained bulk FinFET and strained SOI one.

# Strain Engineering with $\text{Si}_{1-y}\text{C}_y$ Source and Drain Stressors

C. K. Maiti, and A. R. Saha\*

Indian Institute of Technology, Kharagpur, Kharagpur-721302, INDIA

\*e-mail: ars.iitkgp@gmail.com

## INTRODUCTION

To improve the Si-MOSFET performance, one attractive approach is to enhance carrier mobility and transistor drive current by using strain-induced effects. Recently, group IV alloys such as  $\text{Si}_{1-x}\text{Ge}_x$  and  $\text{Si}_{1-y}\text{C}_y$  have attracted great attention as new materials for introducing band gap engineering in Si technology. It has been shown that hole and electron mobility is considerably enhanced in a MOSFET by employing silicon-germanium (SiGe) stressors in the source and drain regions and nitride cap layer. Recently, a novel 50 nm gate length strained-Si n-MOSFET comprising  $\text{Si}_{1-y}\text{C}_y$  S/D regions, metal gate and high-k gate dielectric has been demonstrated [1].

There is no experimental investigation on the lattice strain distribution in such a transistor structures. Understanding the strain distribution and its effect on the device performance will be important for channel strain engineering in CMOS transistors. In this paper, technology CAD (TCAD) approach is taken to explore the stress management in the SiC (S/D region) and the distribution of local strain components in the channel region. Some of the issues affecting the MOSFETs DC and AC characteristics due to the SiC induced strain in the channel has been studied using SILVACO VWF-simulation suite.

## SIMULATION METHODOLOGY

SiGe source and drain stressors lead to lateral compressive strain and vertical tensile strain in the Si channel [2]. On the other hand, the SiC source and drain stressors give rise to lateral tensile strain and vertical compressive strain in the Si channel, an effect complementary to that of SiGe source/drain stressors and will enhance electron mobility in n-channel transistors. This gives rise to the SiC-

strained-Si heterojunction which enables increased electron injection velocity at the source end.

The ATHENA process simulation framework from SILVACO was used for the process simulation by implementing preceding ideas. Typical device structures for process-induced strained-Si MOSFETs (with SiC in S/D) and subsequent stress contour, generated from the process simulation, is shown in Fig. 1a and 1b.

## RESULTS AND DISCUSSION

To explore the device design parameters space for advance MOSFETs with elevated SiC S/D structure, Silvaco ATLAS device simulation tools was used. C-interpreter function has also been used to incorporate the mobility enhancement, SiC material parameter and strain mismatch models. Fig. 2 shows the simulated DC output characteristics of a n-MOSFET with SiC in S/D, at room temperature for a gate voltage variation from 0.5 to 2.5V. The sub-threshold characteristics simulated at 10, 50 and 100 mV is also shown in Fig. 3. A sub-threshold slope (SS) of 81.6mV/dec and  $V_{th} \sim 0.52$  V is obtained from simulation. The frequency response of the SiC embedded (PSS) n-MOSFET was simulated in the common source configuration and the necessary figures of merit are calculated from the simulated S-parameter data. Fig. 4 shows the magnitude of current gain ( $|h_{21}|$  in dB) versus frequency for PSS n-MOSFETs with 10/0.1  $\mu\text{m}$  device, at nominal  $V_{gs} \sim 1\text{V}$ . The extrapolation of the plots displays an  $f_T$  of about 98 GHz and  $f_{max} \sim 470$  GHz.

## CONCLUSION

In conclusion, local lattice strain in transistor structures with SiC stressors in the S/D regions was investigated. This work will be useful for channel

strain engineering in complementary metal-oxide-semiconductor transistors.

REFERENCES

- [1] K. W. Ang, K. J. Chui, V. Blimetsov, A. Du, N. Balasubramanian, M. F. Li, G. Samudra, and Y.-C. Yeo, *Enhanced Performance in 50 nm N-MOSFETs with Silicon-Carbon Source/Drain Regions*, Review of Modern Physics IEEE IEDM 1069 (2004).
- [2] A. R. Saha, S. S. Mahato, S. Chattopadhyay, and C. K. Maiti, *Process-Induced Strain Engineering Beyond 90 nm Technology Node*, IWPSD-2005, New Delhi, India, 2005

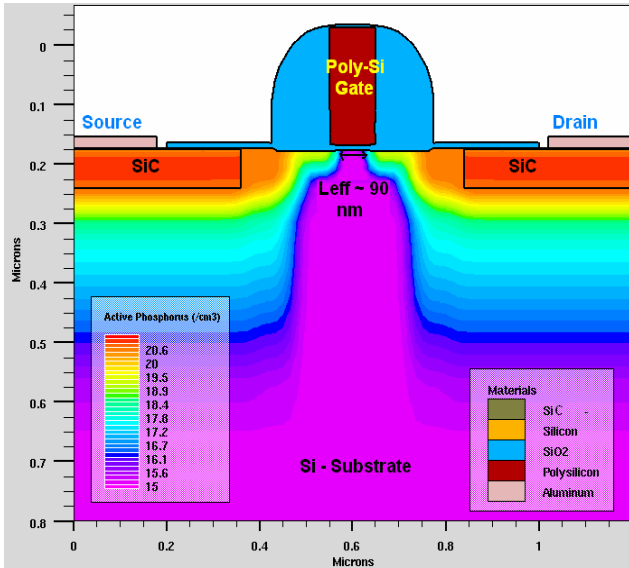


Fig. 1a. ATHENA simulated device structure

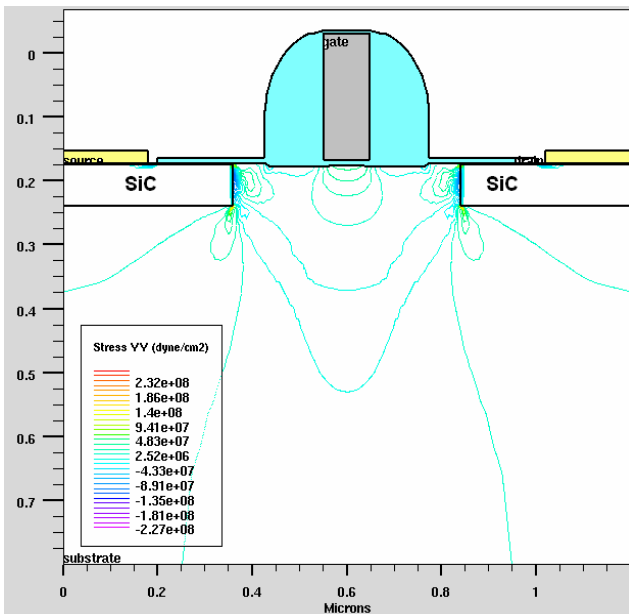


Fig. 1b. 2D Tensile Stress contours: indicating SiC induced strain

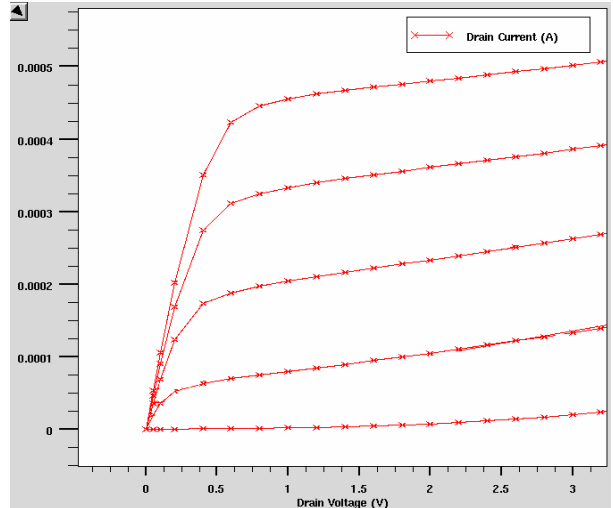


Fig. 2. Simulated DC output characteristics of SiC embedded (PSS) n-MOSFET structure with gate length ( $L_g \sim 0.1 \mu m$ ).

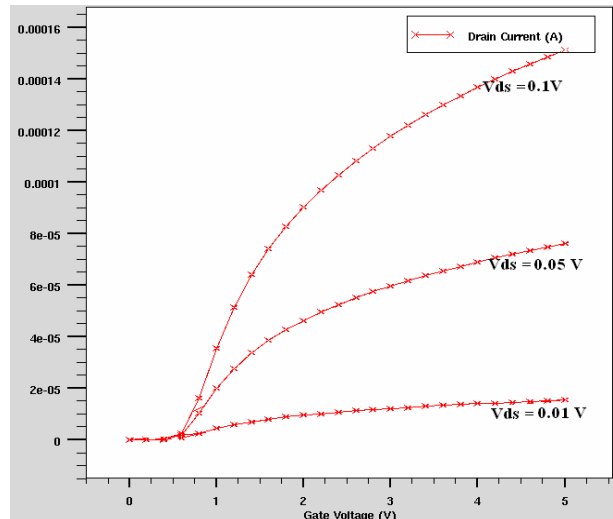


Fig. 3. Sub-threshold characteristics at different drain voltage.

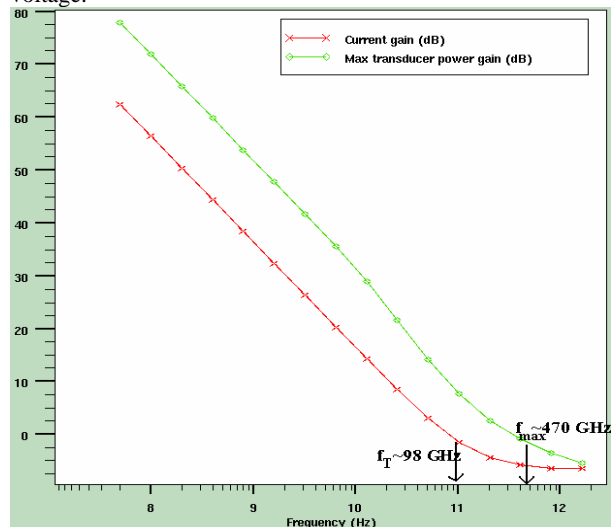


Fig. 4. Simulated Current Gain Vs frequency plot to extract the ac figure of merit.

# Hot Electron Distribution Function for the Boltzmann Equation with Analytic Bands

Orazio Muscato

Dipartimento di Matematica e Informatica, Viale A. Doria 6 ,95125 Catania, Italy  
 e-mail: muscato@dmi.unict.it

MANUSCRIPT SUBMISSION

The shape of the electron energy distribution (EED) is of paramount importance in order to predict disruptive phenomena in semiconductor devices. Monte Carlo simulations with parabolic bands prove that the EED tail is maxwellian [1], [2], and several analytic euristic models have been introduced for modeling the EED in the bulk case [3], [4]. Starting form the Boltzmann transport equation in the bulk case, with quasi parabolic band, scattering with impurities, acoustic and optical phonons, we prove analytically that its EED, for large values of the energy  $\varepsilon$ , is of the following type

$$f(\varepsilon) \simeq \exp \left[ -r(2\varepsilon)^{\frac{s}{2}} \right] \quad (1)$$

where  $r$  and  $s$  are some positive constants. In order to obtain this result, we introduce the functionals

$$\mathcal{F}_{r,s}(f) = \int_{\mathbb{R}^3} f(\mathbf{k}) \exp \left[ r(2\varepsilon)^{\frac{s}{2}} \right] d\mathbf{k} \quad (2)$$

which indicate that the solution of the BTE have high-energy tails given by eq.(1). By expanding the exponential function in (2) into Taylor series we obtain (formally):

$$\begin{aligned} \mathcal{F}_{r,s}(f) &= \int_{\mathbb{R}^3} f(\mathbf{k}) \left( \sum_{n=0}^{\infty} \frac{r^n}{n!} (2\varepsilon)^{\frac{sn}{2}} \right) d\mathbf{k} = \\ &= \sum_{n=0}^{\infty} \frac{m_p^{sn}}{n!} r^n \end{aligned} \quad (3)$$

where  $m_p$  are the *symmetric moments* of the distribution function. The maximum value  $r_s^*$  of  $r$ , for which the power series (3) converges, is its radius of convergence, and the order of the tail  $s$  is the value for which the series has a positive and nite radius of convergence. By using suitable moments estimate based on the BTE, we are able to prove that  $r_s^*$  is nite, for some  $s \geq 1$ . However this method

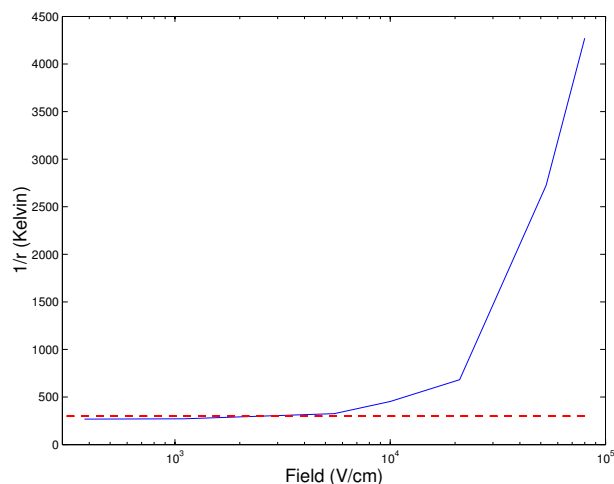


Fig. 1. The parameter  $1/r$  in eq.(1) with  $s=2$ , as function of the electric eld, in the parabolic band approximation. The dashed straight line indicates the lattice temperature 300 K .

does not give any information about the numerical values of  $r$  and  $s$ , which could be determined by MC simulations. These simulations show that the high-energy tail depends on the band structure. In fact in the parabolic band approximation the tail is maxwellian (i.e.  $s = 2$  ) where  $1/r_s^*$  is not the lattice temperature, but a function of the electric eld, as shown in gure 1. In the quasi parabolic case, MC simulations show that  $s$  is not a constant but a function of the electric eld, as well as  $1/r_s^*$ .

## REFERENCES

- [1] A. Abramo, C. Fiegna, J. Appl. Phys. **80** , 889–893, (1996)
- [2] C.C.C. Leung, P.A. Childs, Appl. Phys. Lett., **66**(2), 162–164, (1995)
- [3] D. Cassi and B. Riccò, IEEE Trans. Elec. Dev., **37**, 1512,(1990)
- [4] T. Grasser, H. Kosina, C. Heitzinger and S. Selberherr, J. Appl. Phys., **91**, 3869,(2002)



# Computer Simulation Experiment on Prospects of ZnS as Novel Material for High mm-Wave Power /Low Noise Generation in Impatt Mode

S. P. Pati and P. R. Tripathy

Department of Physics, Sambalpur University, Jyoti Vihar-768 019, Sambalpur, Orissa

Email: [patispsu@sancharnet.in](mailto:patispsu@sancharnet.in)

Impatt Devices have been identified as premier class of Solid State Electronics Device for stable rf power generation used for present day e-communication systems with the added advantage that any form of p-n junction fabricated from any semiconductor material, can exhibit Impatt action based on combined physical phenomena of transit time delay and avalanche phase delay. Studies on new materials are being carried out by several groups spreading over the globe to enhance the rf power/efficiency and reduce the avalanche noise in this class of devices even at far mm-wave frequencies. Recent report [1] presents ionization rate and other material parameters in ZnS which is also high band gap semiconductor. The reported high ionization rate at high field with nose dive fall with lowering of electric field provided intuition for ZnS becoming a novel material for Impatt devices. The authors carried out computer simulation experiment to compute microwave characteristics of ZnS Impatt through use of a sophisticated three phase computer algorithm.

At the outset, the extracting the values of electron ionization rate ( $\alpha$ ) at different electric field values, an usual exponential as well as high order polynomial form of equations for  $\alpha \sim E$ , are framed and used following curve fitting technique ensuring the correspondence to reported plot. Double Iterative Computer method incorporating drift, diffusion and tunnel currents, for DC analysis solving Poisson, Carrier Continuity and Space Charge equations simultaneously, is framed to compute breakdown electric field/voltage ( $E_m/V_b$ ), normalized avalanche zone ( $x_a/W$ ), qualitative value of efficiency ( $\eta$ ) etc. from the final solution. In the second phase of analysis, another double iterative computer method is framed for high frequency analysis of ZnS Impatts solving simultaneous integrated second order device equations on diode resistance (R) and susceptance (X) subject to fulfillment of usual boundary conditions to compute rf properties of diode like BW showing exhibition of (-) rf negative conductance (G), the values of negative resistance (r), r(x) profile, avalanche phase delay ( $\theta_a$ ) etc. The third complicated iterative computer

software is developed to solve second order integrated equations on noise complex field for determination of avalanche noise and noise measure considering noise element progressively at individual space step and then integrating over space for particular noise element separately and then for all noise elements. All the computer programs are designed for quick convergence towards satisfying the usual boundary conditions.

The ZnS p-n junctions are then designed for various frequencies of operation specially for atmospheric window frequencies ( 12 and 35 GHz ) and optimized for current density, diode doping/width, punch through factor to ensure the lowest avalanche zone, closest location of  $E_m$  to junction plane and  $\theta_a \approx 90$  degree. The optimized diodes have been analyzed through use of the three phase computer method and DC; microwave and noise characteristics have been computed and presented in table 1 and figures 1 & 2. The results indicated some favourable features for ZnS Impatts.

The material has very high band gap energy of 3.68 eV. Thus as seen from the table, the ZnS junction would provide very high break down voltage, 661 V for X-band as against 105 V for corresponding Silicon Impatt. The nose dive fall of ionization rate below  $1.6 \times 10^8$  V/m, causes very thin avalanche zone ( $x_a/W=8\%$  as against 45% for Si). This factor would enable the ZnS Impatt diode to give an efficiency of 28.5 % as against 13 % for Si. It may be mentioned that the theoretical optimum efficiency based on 50% rf modulation is only around 30%. Thus it may be possible to achieve the theoretical optimum efficiency for ZnS. The Frequency-negative conductance plots for 12 and 35 GHz optimum frequencies are shown in figure 1. Further the negative conductance and resistance values for ZnS X-band devices are higher by nearly two times compared to Silicon Impatt. Figure 2 shows the mean square noise voltage at different frequencies. The most important result that can be seen from table and figure 2 is that the ms noise voltage associated in ZnS Impatt diode is  $1.87 \times 10^{-17}$  V<sup>2</sup>.s at 12 GHz as against  $70.6 \times 10^{-17}$  V<sup>2</sup>.s for 12 GHz Si diode. For 35 GHz similar results could also

be noticed.

The high value of  $V_b$  would provide high input power and the efficiency being high, ZnS diode is expected to give high rf power. The high value of negative conductance and resistance would help to increase rf power further. The avalanche noise which is an evil factor of Impatt diode in general would be only 3% for ZnS X-band diodes compared to corresponding Silicon diode. Thus possible high power generation at high efficiency and low noise may make ZnS a novel material for m/mm-wave generation

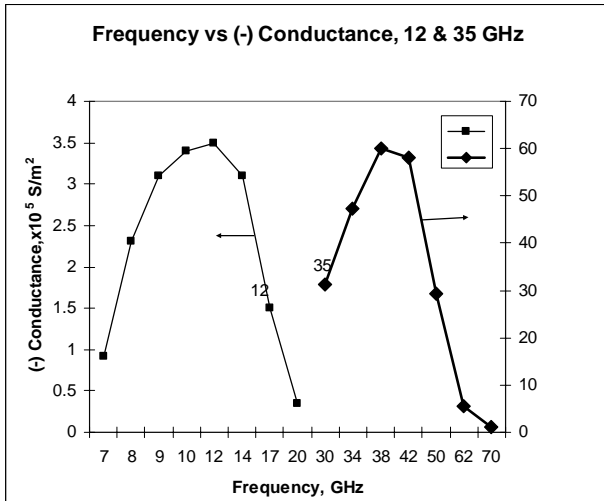


Fig. 1. Frequency-(-) Conductance plots for ZnS Impatt Diodes

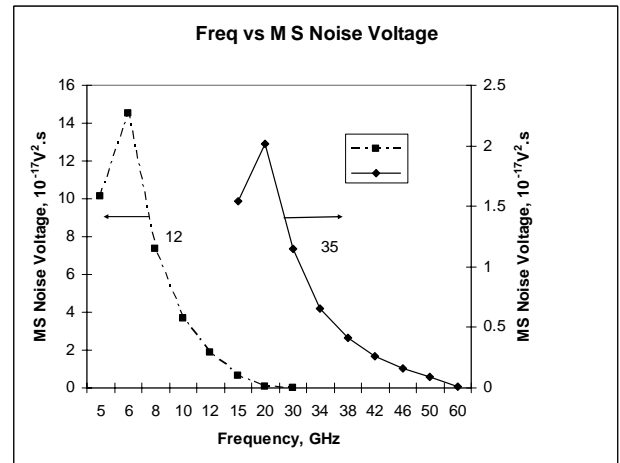


Fig. 2. Frequency-Mean Square Voltage for ZnS Impatt diodes

	ZnS		Si	
	12GHz	35GHz	12 GHz	35 GHz
$E_m, 10^7 \text{ V/m}$	17.95	18.52	3.65	4.77
$V_b, \text{ V}$	661	301	105	41.1
$X_a/W, \%$	8.12	12.1	45.8	47.1
$\eta, \%$	28.1	26.0	13.0	12.1
$-G, \times 10^3 \text{ S/m}^2$	3.47	60	2.6	32.0
$-R, \times 10^{-6} \Omega \cdot \text{m}^2$	7.01	5.16	0.209	0.0275
$\langle V^2 \rangle / df, \text{ at fp}$ $10^{-17} \text{ V}^2 \cdot \text{s}$	1.87	0.413	70.6	3.99

Fig. 3. Some properties of ZnS and Silicon IMPATT Diodes at 12 & 35 GHz.

# Accurate Extraction of Maximum Current Densities from the Layout

A. Seidl<sup>1)</sup>, T. Schnattinger<sup>2)</sup>, A. Erdmann<sup>2)</sup>, H. Hartmann<sup>3)</sup>, A. Petrashenko<sup>3)</sup>

<sup>1)</sup>Hochschule Magdeburg-Stendal, Breitscheidstraße 2, 39114 Magdeburg, Germany

<sup>2)</sup>Fraunhofer IISB, Schottkystraße 10, 91058 Erlangen, Germany

<sup>3)</sup>Software & System Solutions GbR, Sollachweg 9, 82234 Wessling, Germany  
e-mail: albert.seidl@elektrotechnik.hs-magdeburg.de

## SUMMARY

A module for efficient extraction of maximum current densities from the layout has been developed and implemented within the CAD package PARIS. A parameterized model for corner-rounding dependence on technology parameters, such as numerical aperture (NA) and acid/base diffusion, was developed. A combination of classical and meshless FEM was used to obtain accurate results taking realistic shapes of the corners into account.

## PIN CURRENT CALCULATION AND EXTRACTION OF NET LAYOUTS

Electromigration as well as yield and performance loss of chips are among others caused by high current-density stress in the metallization levels. Simulation of the current density distribution within all stressed metal patterns and/or vias is important for the assessment of the reliability. Our approach for the calculation of the current density distribution is based on three main steps. The first step provides the pin current values inside the chip using a standard net list circuit simulator. The simulation stimuli include the entire range of possible input values and worst case conditions. The second step provides the layout geometry of complete nets combined with the calculated pin current values, which are determined via circuit simulation. Third, the current density distribution is calculated for critical parts of the layout by solving the electrical field equation using the finite element method. Input data are the relevant technology parameters, like wire thickness, resistivity, and pin current values combined with the extracted net layout graphs.

## COMPUTATION OF REALISTIC CORNER ROUNDING

The necessary profile geometry is obtained from the

IISB lithography simulation software Dr.LiTHO. A sample profile is shown in Fig. 1. The corner is approximated by a circular arc with best fitting radius. NA of the lithographic projector lens and the acid/base diffusion lengths of the resist were varied to get the radii for different process conditions. The calculated radii can then be stored in a database. Thus the simulations have to be done only once for each set of process parameters and layout pattern.

## SOLUTION OF FIELD EQUATIONS

A combination of classical FEM with meshless methods, namely Element-Free Galerkin (EFG) [1] has been used to obtain accurate results in the corners of the layout. For the application addressed in this work a mesh-refinement of up to 3-4 orders of magnitude was necessary while maintaining relatively coarse meshes in the non-critical region. A quadtree strategy was used for mesh/point-set generation in order to achieve appropriate refinement in the corners. Heuristics were used for local error estimates. The geometry of a ground connection with local refinement (at critical corners only) is shown in Fig. 2 and 3.

## CONCLUSION

For accurate values of the current density, the actual corner rounding effects have to be considered instead of idealized sharp corners. Otherwise errors can be in the order of 100% (Fig. 4). The problem of high peak field strengths will aggravate as advanced lithography techniques will allow further reduction of curve radii in the future.

## REFERENCES

- [1] T. Belytschko, Y. Y. Lu, and L. Gu, *Element-Free Galerkin Methods*, International Journal for Numerical Methods in Engineering, vol. 37, 1994, pp. 229-256

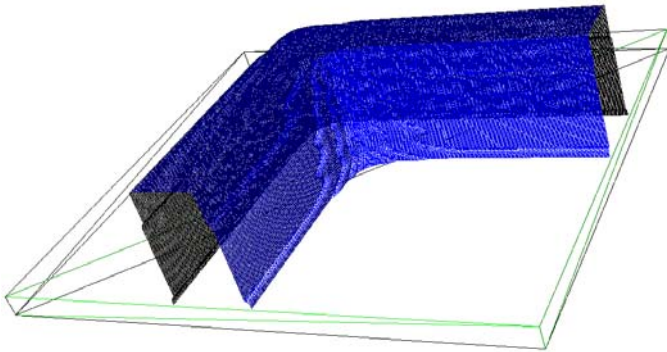


Fig. 1. Simulated resist profile with a linewidth of 120 nm used for determining the curvature radius. The process was simulated with a NA of 0.8 and an acid and base diffusion length of 20 nm and 80 nm, respectively.

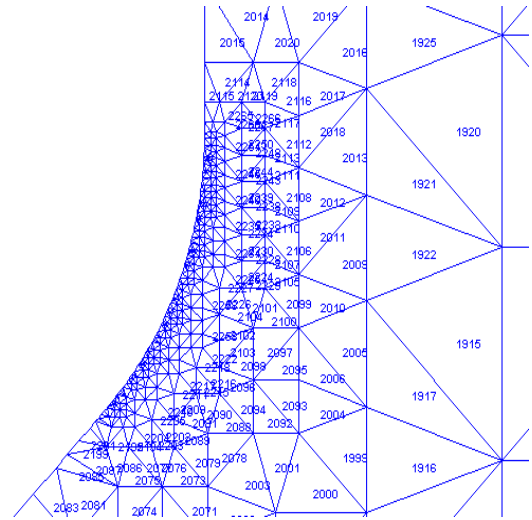


Fig. 3. Zoom from Fig. 2 of the local refinement at a critical corner.

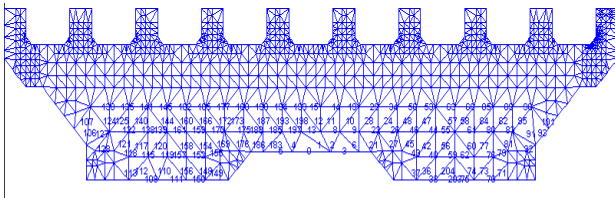


Fig. 2. Entire structure of the ground connection with different refinement levels. A zoom of the local refinement at a critical corner is shown in Fig. 3.

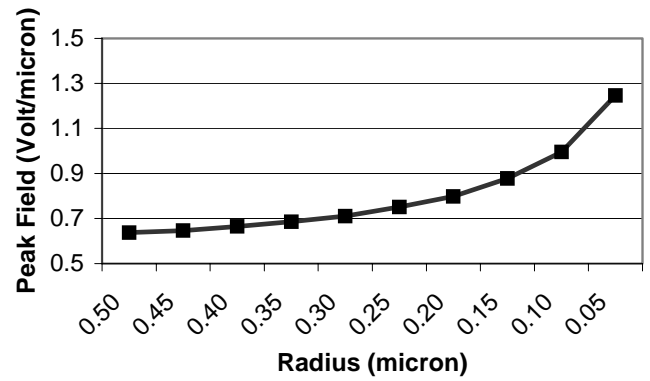


Fig. 4. Dependency of computed peak field-strength on radius of curvature of a critical corner for a given structure.

# A 3D Parallel Simulation of the Effect of Interface Charge Fluctuations in HEMTs

N. Seoane\*, A. J. Garc'a-Loureiro\*, K. Kalna†, and A. Asenov†

\*Department of Electronics and Computer Engineering, Univ. Santiago de Compostela  
15782 Santiago de Compostela, Spain. E-mail: natalia@dec.usc.es

†Device Modelling Group, Dept. Electronics & Electrical Engineering, University of Glasgow  
G12 8LT Glasgow, United Kingdom

A 3D parallel device simulator is employed to study the impact of charge fluctuations in the recess region of nanometre scale HEMTs. The simulator [1] is based on a drift-diffusion (D-D) approach using finite element discretisation on an unstructured tetrahedral mesh [2]. In order to reduce computational time, the simulator is parallelised via the MPI library. Fig. 1 shows the parallel efficiency obtained using the 3D D-D device simulator for the solution of Poisson's equation at equilibrium using a mesh with 76500 nodes.

The intrinsic parameter fluctuations are expected to affect the RF performance and the matching of submicron HEMTs [3]. Random variations in the Si  $\delta$ -doping and In content of the channel ternary alloy will induce significant parameter fluctuations in  $I_D$ - $V_G$  characteristics of 50 nm gate length InP HEMTs [3]. In this work we study the effect of interface charge fluctuations in the recess regions of HEMTs on device characteristics and compare it with the effect induced by charge fluctuations in the  $\delta$ -doping layer and by variations in the ternary alloy content. Fig. 2 shows the difference between the electron densities at equilibrium for a 120 nm pseudomorphic HEMT (PHEMT) with and without interface charge. The electron density is plotted along a plane in the middle of the channel. We have assumed uniformly distributed interfacial charge of  $-2 \times 10^{12} \text{cm}^{-2}$  at the recess region surface.

The effect of the interface charge is studied in two different HEMTs: (i) a 120 nm gate length PHEMT with an  $\text{In}_{0.2}\text{Ga}_{0.8}\text{As}$  channel on GaAs substrate and (ii) a 50 nm gate length InP HEMT with an  $\text{In}_{0.7}\text{Ga}_{0.3}\text{As}$  channel. The  $I_D$ - $V_G$  characteristics of the transistors have been calibrated at low and high drain biases. The calibration was carried out in comparison with the measured data obtained from real devices fabricated at Glasgow and with data obtained from Monte Carlo (MC) device simulations [4,5]. Note that the external resistances associated with the contacts have to be included in simulated I-V characteristics [6] for a fair comparison with measured data. Figs. 3 and 4 compare simulated and measured  $I_D$ - $V_G$  characteristics for the 120 nm PHEMT at drain biases of 0.1 and 1.0 V respectively. The results

obtained from the 3D parallel D-D simulator with the presence of interface charge in the recess regions (at the source and drain sides of the device) are also shown. The results of the MC simulations, which have only been carried out without interface charge, are presented for comparison. The interface charge lowers the drive current and the lowering increases at  $V_D = 1.0$  V. Similar calibration and simulations are carried out for the 50 nm InP HEMT. Figs. 5 and 6 compare  $I_D$ - $V_G$  characteristics at drain biases of 0.1 and 0.8 V respectively, for the 50 nm transistor. The effect of interface charge is smaller compared to the effect in the 120 nm PHEMT but the qualitative behaviour is similar. A statistical study of the effect of fluctuations in the discrete interface charge in the recess regions on the characteristics of both HEMTs will be reported at the conference.

## REFERENCES

- [1] A. J. Garc'a-Loureiro, K. Kalna and A. Asenov, *Efficient three-dimensional parallel simulations of PHEMTs*, Int. J. Numer. Model.-Electron. Netw. Device Fields **18**, 327-340 (2005).
- [2] P. A. Markowich, *The stationary semiconductor device equations*, Computational Microelectronics, Springer-Verlag (1986).
- [3] N. Seoane, A. J. Garc'a-Loureiro, K. Kalna and A. Asenov, *Discrete doping fluctuations in the delta layer of a 50 nm InP HEMT*, in Proc. Workshop on Modeling and Simulation of Electron Devices, ed. by A. Campera, G. Fiori, G. Iannaccone, and M. Macucci, (Pisa, Italy, 2005) 78-79.
- [4] K. Kalna, S. Roy, A. Asenov, K. Elgaid and I. Thayne, *Scaling of pseudomorphic high electron mobility transistors to decanano dimensions*, Solid-State Electron. **46**, 631-638 (2002).
- [5] K. Kalna, K. Elgaid, I. Thayne and A. Asenov, *Modelling of InP HEMTs with high Indium content channels*, Proc. Indium Phosphide and Related Materials, 61-65 (2005)
- [6] S. Babiker, A. Asenov, N. Cameron and S. P. Beaumont, *A simple approach to include external resistances in the Monte Carlo simulation of MESFETs and HEMTs*, IEEE Trans. Electron Devices **43**, 2032-2034 (1996).

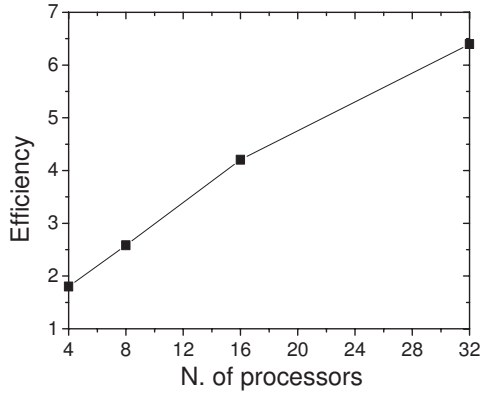


Fig. 1. Parallel efficiency for the solution of Poisson's equation at equilibrium using a 76500 node mesh.

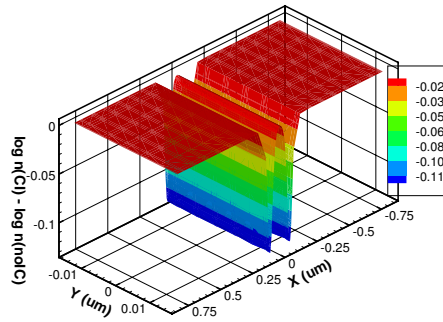


Fig. 2. Difference in electron density at equilibrium between a device with an interface charge of  $-2 \times 10^{12} \text{cm}^{-2}$  in the recess layer and a device without the interface charge, in a plane along the 120 nm PHEMT InGaAs channel. The x-axis is along the device with the zero set in the middle of the gate and the y-axis is along the device width.

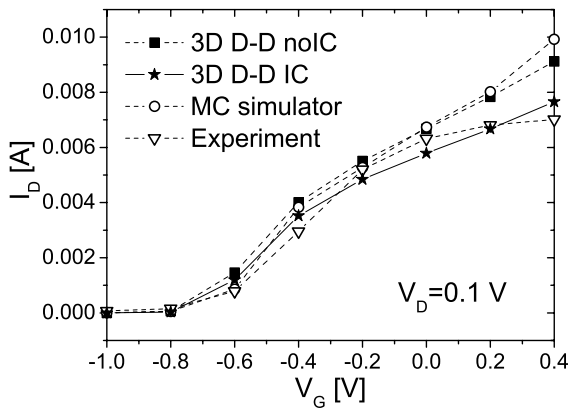


Fig. 3.  $I_D$ - $V_G$  characteristics at  $V_D=0.1$  V for the 120 nm PHEMT. Full squares are for 3D D-D simulations with excluded interface charge and stars are for 3D D-D simulations with included interface charge. All simulations, including MC results, represent an intrinsic device. Experimental data are also shown for a comparison.

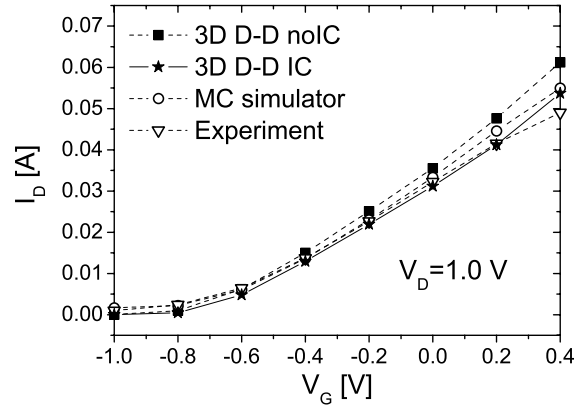


Fig. 4.  $I_D$ - $V_G$  characteristics at  $V_D=1.0$  V for the 120 nm PHEMT. The symbols have the same meaning as in Fig. 3.

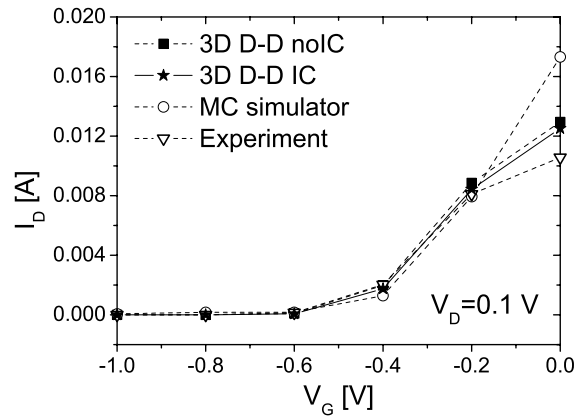


Fig. 5.  $I_D$ - $V_G$  characteristics at a low drain bias of 0.1 V for the 50 nm InP HEMT. The results obtained from the 3D D-D simulator with interface charge excluded (full squares) and included (stars), and MC results are shown, all for an intrinsic device. Experimental data given by open triangles are presented for a comparison.

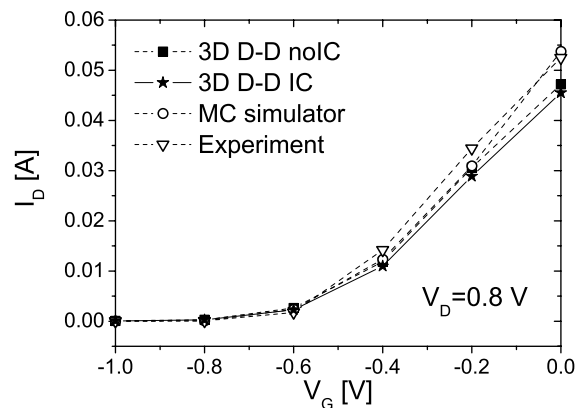


Fig. 6.  $I_D$ - $V_G$  characteristics for the 50 nm InP HEMT. The same data from 3D D-D and MC device simulators as in Fig. 5 are shown but at a high drain voltage of 0.8 V.

# Negative Gate-Overlap in Nanoscaled DG-MOSFETs with Asymmetric Gate Bias

Xue Shao and Zhiping Yu

Institute for Microelectronics, Tsinghua University, Beijing 100084, China

E-mail: shaox97@mails.tsinghua.edu.cn

## ABSTRACT

The transfer characteristics of double-gate (DG) MOSFETs are numerically simulated with 2D quantum drift-diffusion (QDD) model. Negative gate-overlap is introduced in devices to optimize the dynamic capacitance characteristics to get the best speed performance. Separate controlling of the back gate to vary the threshold voltage is investigated.

## INTRODUCTION

DG-MOSFETs/FinFETs with ultra thin bodies are the way to suppress the DIBL and drain leakage when devices are scaled down below 50nm. Negative gate-overlap (Fig. 1) has been conceived to suppress drain leakage in literature [1-2]. But no dynamic performance has been studied. In this work, QDD model [3] (or density gradient model) is used to calculate the effects of quantum mechanics. A complete gate-S/D alignment can suppress short-channel effects (SCE) most but the gate capacitance is also the largest for fixed channel length and width. Applying an appropriate negative gate-overlap can optimize the device for best speed performance.

## MODEL DESCRIPTION

A 2D numerical simulator Taurus-PMEI [4] was used to implement our simulation. All devices in this work are  $L_{ch}=10\text{nm}$ ,  $W_{ch}=3\text{nm}$  and  $T_{ox}=2\text{nm}$  nMOSFET. S/D doping of device is  $2.0e20/\text{cm}^3$  and channel p-type doping is  $1.0e17/\text{cm}^3$ . QDD model with Scharffeter-Gummel approach [5] was used. Constant carrier mobility is assumed. Fig. 2 plots the electron and current density distribution within the device from using both DD and QDD models. Apparently, electrons peak away from the Si/SiO<sub>2</sub> interface because of the quantum effects.

## NEGATIVE GATE-OVERLAP

Negative gate-overlap weakens the gate control and increases the resistance under gate at on-state,

but it reduces the gate capacitance. So there is a tradeoff between SCE control and device dynamic performance. Fig. 3 shows the I-V curves for different length of gate-overlap and Fig. 4 for C-V curves. The quantum effects affect not only the distribution of carrier and current densities but also capacitance. QM effects decrease capacitance and increase threshold voltage, especially for nanoscaled devices. To predict the speed performance of devices, we extract the  $I_{on}$ ,  $I_{off}$  and dynamic capacitance using both DD and QDD models. Using the following delay time for characterizing the circuit speed,

$$t \approx \bar{C}_g V_{dd} / I_{on} \quad (1)$$

Fig. 5. shows the trend of  $t$  vs.  $L_{overlap}$ . The device speed will increase about 20% when the gate-overlap changed from zero to -1.0nm.

## BACK GATE CONTROL

Compared to the simultaneous control of front and back gates, it is more flexible to bias the back gate separately. Fig. 6 shows I-V curves for different  $V_{gb}$  bias. With higher  $V_{gb}$ , device works with lower threshold voltage. So the circuit speed is boosted benefited from the higher drain current. Lower  $V_{gb}$  makes the threshold voltage of devices higher. This decreases  $I_{on}$  and  $I_{off}$  greatly. So the circuit works with low-power dissipation. The results in Table 1 verified this prediction with QDD model. Note that, the power dissipation (PD) of the switching state refers to the average PD caused by gate charging/discharging current at 1GHz. And the PD of On/Off state refers to the PD caused by channel current when the device switches between on/off states.

## CONCLUSIONS

An appropriate negative gate-overlap improves circuit speed performance and also decreases power dissipation. Controlling the back gate separately is an appropriate way to make circuits adaptive for more versatile applications.

## REFERENCES

- [1] R. S. Shenoy, *Optimization of Extrinsic Source/Drain Resistance in Ultrathin body Double-Gate FETs*, IEEE Trans. Nanotechnology, p.265, Dec. (2003).
- [2] V. P. Trivedi, *Nanoscale FinFETs with Gate-Source/Drain Underlap*, IEEE Trans. Electron Devices, p.56, Jan. (2005).
- [3] M.G. Ancona and G.J. Iafrate, *Quantum correction to the equation of state of an electron gas in a semiconductor*, Physical Review B, pp.9536-9540, 39 (1989).
- [4] *Taurus-2004.9 Users Manual*, Synopsys, (2004)
- [5] D.L. Scharfetter and H.K. Gummel, *Large signal analysis of a silicon Read diode oscillator*, IEEE Trans. Electron Devices, pp.64-77, 116 (1969).

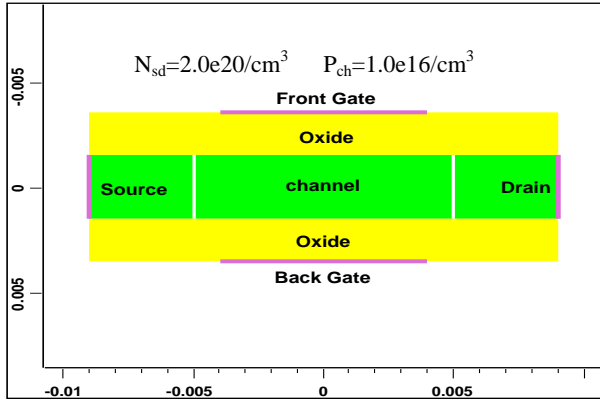


Fig. 1 Negative gate overlap DG-MOSFET structure

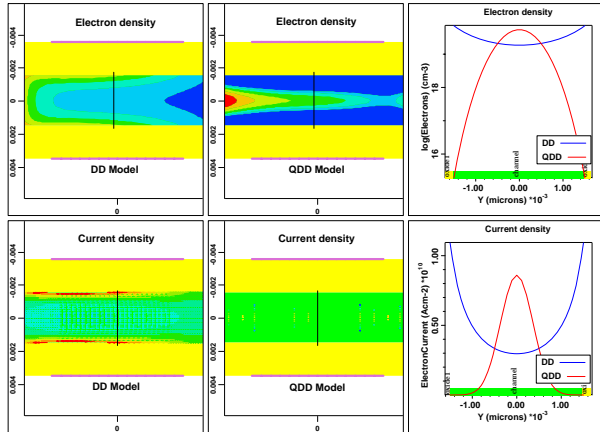


Fig. 2 Electron and current density in channel ( $V_{gs}=V_{ds}=1V$ )

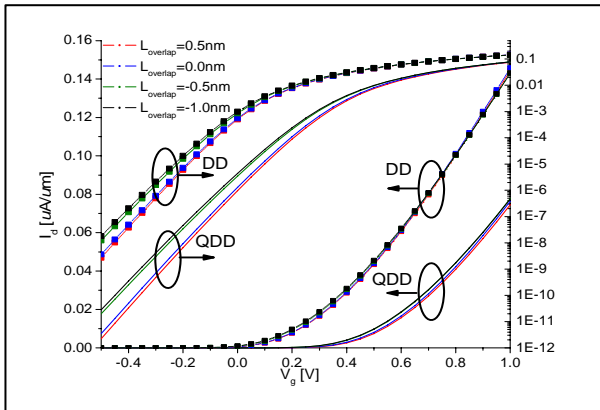


Fig. 3 I-V curves for 10nm-channel DG-MOSFETs ( $V_{ds}=1.0V$ )

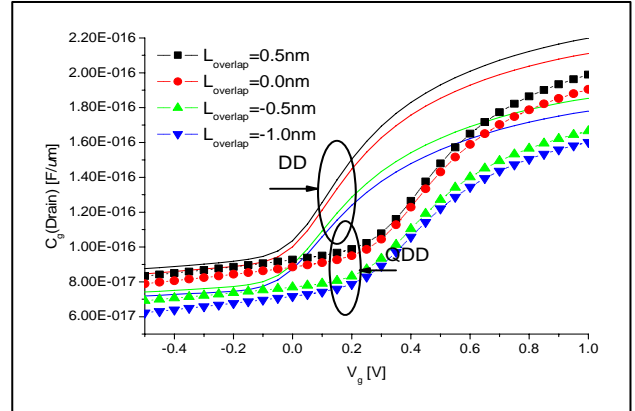


Fig. 4 C-V curves for 10nm-channel DG-MOSFETs ( $V_{ds}=1.0V$ )

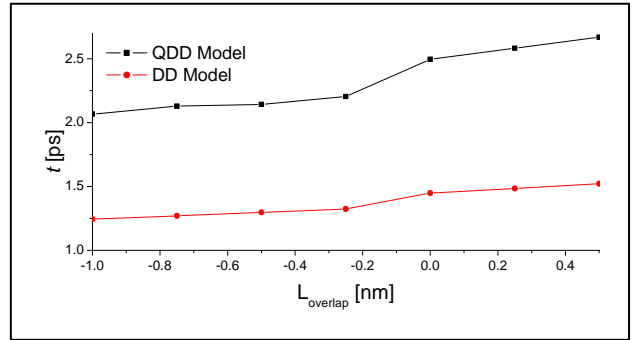


Fig. 5 Delay time of devices with different  $L_{overlap}$

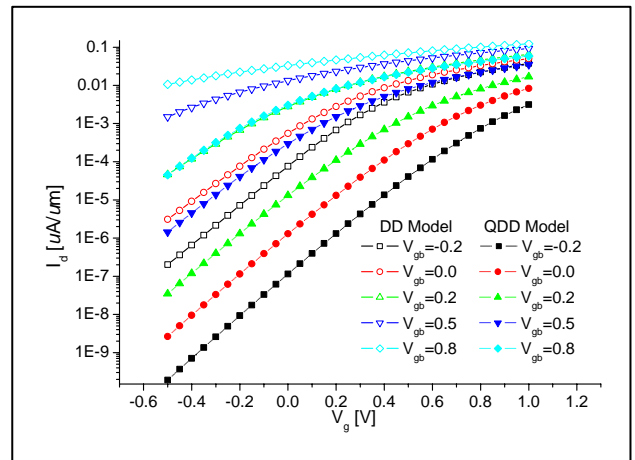


Fig. 6 I-V curves for 10nm-channel DG-MOSFET (fixed  $V_{gb}$ )

$V_{gb}$ (V)	Device parameter			Power dissipation ( $\mu W/\mu m$ )		
	$V_{th}$ (V)	$S_{sub}$ (mV/dec)	Delay (ps)	On state	Off state	Switch state*
-0.5	0.87	170	144	3.4e-4	2.7e-9	5.0e-2
-0.2	0.82	176	20	3.1e-3	1.2e-7	6.2e-2
0.0	0.75	181	8.6	8.4e-3	1.3e-6	7.2e-2
0.2	0.66	186	4.7	1.7e-2	1.3e-5	8.0e-2
0.5	0.50	198	2.5	3.5e-2	2.9e-4	8.7e-2
0.8	0.31	225	1.6	5.8e-2	3.0e-3	9.2e-2

Table 1 Device characteristics at 1GHz ( $V_{ds}=1.0V$ , QDD model)

# Human Body Model ESD Simulation Including Self Heating Effect

T. Takani, and T. Toyabe

Toyo Univ. Bio-Nano Electronics Research Center, Kawagoe, Saitama, 350-8585 Japan

e-mail: t\_toya@cs.toyo.ac.jp

## INTRODUCTION

Electrostatic discharge (ESD) is an important issue in LSI design and fabrication. One category of ESD pulses is known as the human body model (HBM) which represents a charged human discharging into an integrated circuit. In this paper we present transient characteristics simulation of NMOSFETs for which ESD pulses of HBM are applied. The temperature rise owing to the self heating effect is included in the simulation, which is naturally an important aspect in high current phenomenon such as ESD.

## MODELING

A setup for HBM ESD simulation is shown in Fig.1. A capacitance  $C$  of 100pF is charged by high voltage  $V_0$  of several hundreds Volt closing a switch a, and then the capacitance is connected with a resistance  $R$  of 1.5kOhm [1] and a MOSFET opening the switch a and closing the switch b. In the actual transient simulation  $V_I$  is raised from zero to a high voltage equal to  $V_0$  in a very short time (0.1ps), and then  $C$  is connected with  $R$ . The charge on  $C$  is discharged through  $R$  and the MOSFET. The temperature rise  $\Delta T$  in time  $\Delta t$  is given by (1),

$$\Delta T = \frac{I_D V_D}{c \rho V_a} \Delta t \quad (1)$$

where  $c$  is the specific heat of Si (0.7J/gK),  $\rho$  the density (2.33g/cm<sup>3</sup>) and  $V_a$  is the volume of the device. The conduction of heat is ignored in driving (1) considering that the phenomenon is slow compared with ESD process. It takes microseconds for heat to diffuse in Si by ten micrometers much larger than the device size.

The temperature dependent models of carrier mobility and impact-ionization coefficients which are measured in [2] are included in the simulation. Robustness of the convergence computation is

attained by including Jacobian of the impact-ionization coefficients.

## RESULTS AND DISCUSSION

First, DC  $I_d$ - $V_d$  curves having snapback characteristics are shown in Fig.2 for temperatures 300K-900K. Transient  $I_d$ - $V_d$  trajectories in HBM ESD with self heating effect are shown in Fig.3 for initial voltages on  $C$ ,  $V_0$  of 100V-500V. On the  $I_d$ - $V_d$  trajectory for 500V, several time points are shown by symbols, which shows that the time scale of ESD is of the order of  $RC$  time constant (=0.15  $\mu$ s). Drain current changes in time are shown in Fig.4. The drain current in the early stage is equal to  $V_0/R$ . The changes of internal drain voltage and the voltage on  $C$ ,  $V_I$  in time are shown in Fig.5. The internal drain voltage changes largely in the time range of 100ps, while  $V_I$  is constant and equal to  $V_0$  up to 1ns and decreases to zero in 1 $\mu$ s. Finally the temperature rises vs. time are shown in Fig.6(left). For  $V_0$  of 500V, temperature rises to 1100K. At such a high temperature  $I_d$  is high as seen in Fig.3. Maximum temperatures  $T_{max}$  caused by ESD pulses are shown in Fig.6(right). It should be noted that the results are obtained for the case of the channel width,  $W=100\mu$ m, and the wider the channel, the lower  $T_{max}$  is.

## CONCLUSIONS

HBM ESD transient simulation is successfully carried out including self heating effect. Transient  $I_d$ - $V_d$  trajectories and temperature rise in time can be obtained for various high voltages on discharging  $C$ .

## REFERENCES

- [1] S. Dabral and T. J. Maloney, Basic ESD and I/O Design, John Wiley & Sons, Inc.1998.
- [2] S.Reggiani, E.Gnani, M.Rudan, G.Baccarani, C.Corvasce, D.Barlini, M.Ciappa, W.Fichtner, M.Denison, N.Jensen, G.Groos, and M.Stecher, IEEE Trans. Electron Devices **52**, 2290 (2005).

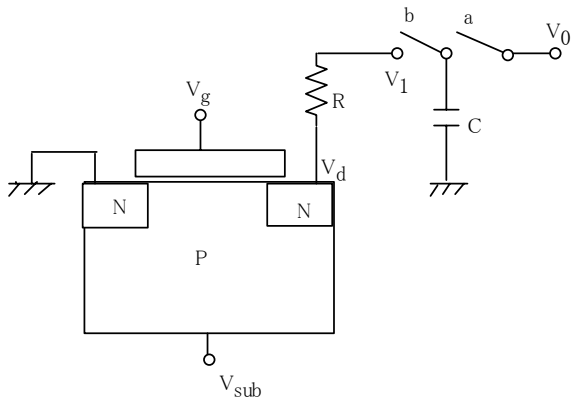


Fig. 1. A setup for HBM ESD simulation.  $C=100\text{pF}$ ,  $R=1.5\text{k}\Omega$ .

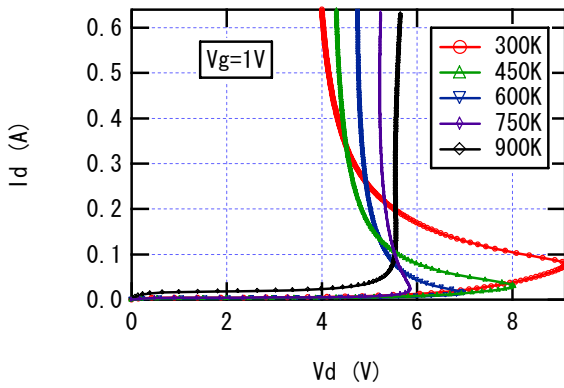


Fig. 2. DC drain current characteristics for various temperatures. Channel length,  $1\mu\text{m}$ , and width,  $100\mu\text{m}$ .

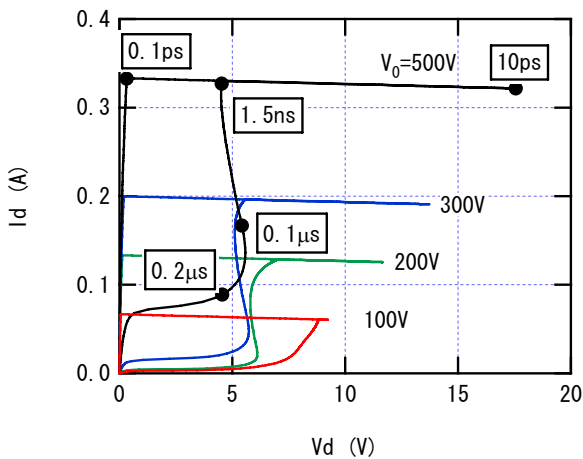


Fig. 3. Transient drain current characteristics with self heating effect.

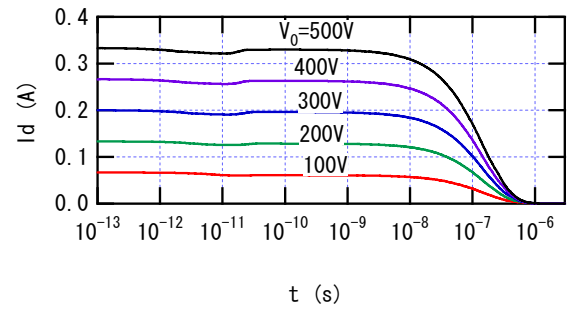


Fig. 4. Drain current vs. time. for  $V_0$  of 100V-500V.

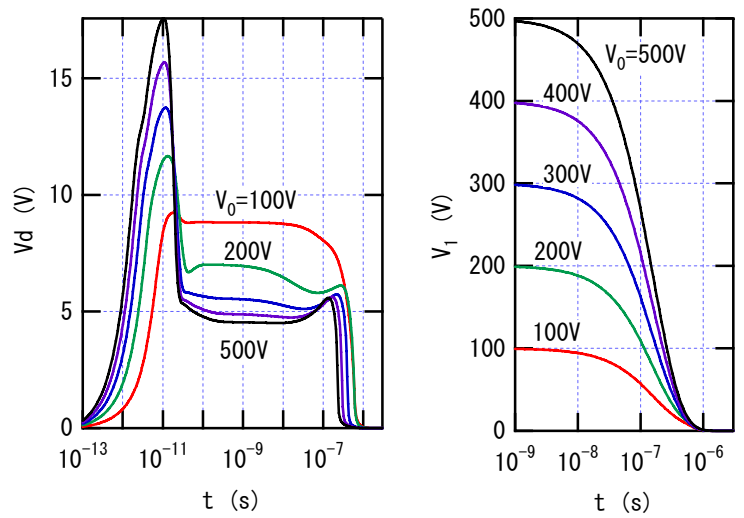


Fig. 5. Internal drain voltage  $V_d$  vs. time, and  $V_1$  vs. time.

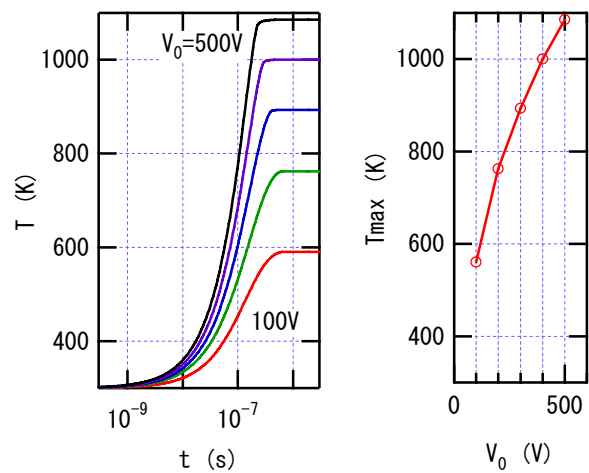


Fig. 6. Temperature vs. time(left) and  $T_{\text{max}}$  vs.  $V_0$ (right)

# Quantum Correction for DG MOSFETs

M. Wagner, M. Karner, T. Grasser, and H. Kosina

Institute for Microelectronics, TU Wien, Gußhausstraße 27–29/E360, 1040 Wien, Austria

e-mail: mwagner@iue.tuwien.ac.at

## INTRODUCTION

Due to the strong impact of quantum mechanical effects on the characteristics of today's semiconductor devices, purely classical device simulation is no longer sufficient to provide proper results.

Schrödinger Poisson (SP) solvers, delivering a self consistent solution of the quantum mechanical carrier concentration and the Poisson equation, accurately determine quantum confinement, but they are computationally demanding. In order to obtain proper results at significantly reduced CPU time, several quantum correction models for classical simulations have been proposed [1–5]. However, some of these corrections are based on empirical fits with numerous parameters [3,4]. In some other models, the dependence on the electrical field adversely affects the convergence behavior [2]. Practically, the model proposed in [1] has to be recalibrated for each device. A comprehensive comparison of these models can be found in [5]. In addition, none of these models is suitable for highly scaled DG MOSFETs in the deca nanometer regime where two coupled inversion regions occur. In this work, we present a new, physically based, and more specific approach for state-of-the-art DG MOSFETs.

## APPROACH

The value of the classical carrier concentration with quantum confinement correction is adjusted to be equal to the quantum mechanically calculated carrier concentration by introducing the quantum correction potential  $\varphi_{\text{corr}}$  as

$$n_{\text{cl,corr}} = N_{\text{C}} \exp\left(-\frac{E_{\text{c}} - q\varphi_{\text{corr}} - E_{\text{f}}}{k_{\text{B}}T}\right)$$

$$n_{\text{qm}} = N_{\text{C1}} \sum_n |\Psi_n(x)|^2 \exp\left(-\frac{E_n - E_{\text{f}}}{k_{\text{B}}T}\right).$$

Here,  $N_{\text{C}}$  and  $N_{\text{C1}}$  denote the effective density of states for classical and the quantum mechanical carrier concentration, respectively,  $\varphi_{\text{corr}}$  the quantum

correction potential,  $E_{\text{c}}$  the conduction band edge energy, and  $E_{\text{f}}$  the Fermi energy.

This approach requires the knowledge of the energy levels  $E_n$  and the wavefunctions  $\Psi_n(x)$  of the quantized states. To avoid the computationally expensive solution of the Schrödinger equation, we tabulate the solutions for a parabolic shaped conduction band edge,  $E_{\text{c}}(x) = E_{\text{max}} - a(d/2 - x)^2$ , as displayed in Fig. 1. Input parameters are the film thickness  $d$  and the curvature  $a$  which is derived from an initial classical simulation. The wave functions are expanded as

$$\Psi_n(x) = \sum_k \xi_{n,k} \sqrt{\frac{2}{d}} \sin\left(\frac{\pi}{d} kx\right).$$

Hence, the offset of the energy levels  $\epsilon_n$  and the expansion coefficients of the wavefunctions  $\xi_{n,k}$  can be found by interpolation of tabulated values. This allows one to estimate a correction potential  $\varphi_{\text{corr}}$  such that the corrected classical carrier concentration is consistent with the SP solution

$$\exp\left(-\frac{q\varphi_{\text{corr}}}{k_{\text{B}}T}\right) = \exp\left(-\frac{a(d/2 - x)^2}{k_{\text{B}}T}\right)$$

$$\times \sum_m \frac{N_{\text{C1},m}}{N_{\text{C}}} \sum_n |\Psi_{m,n}(x)|^2 \exp\left(-\frac{\epsilon_{m,n} - E_{\text{f}}}{k_{\text{B}}T}\right).$$

Here,  $m$  denotes the summation over the different valley sorts (three for silicon) [6].

## RESULTS

We implemented this model in the general purpose device simulator MINIMOS-NT [7]. Our SP simulator VSP was used to derive the reference QM curves. Fig. 2 and Fig. 3 show the electron concentration at different bias points for DG MOSFETs with 5 nm and 10 nm film thickness. Outstanding agreement between the QM and the corrected classical curves (DGTab) is achieved. Both the inversion charge and the gate capacitance shown in Fig. 4 and Fig. 5 demonstrate excellent agreement for a wide range of gate voltages and relevant film thicknesses.

## CONCLUSION

We derived a physically based quantum correction model which accurately reproduces both carrier concentrations and gate capacitance characteristics even for extremely scaled DG MOSFET devices. Due to its computational efficiency the model is well suited for TCAD simulation environments.

## REFERENCES

- [1] W. Hänsch et al., SSE, vol. 32, pp. 839–849 (1991).
- [2] M. Van Dort et al., SSE, Vol. 37, no. 3, pp. 411–414 (1994).
- [3] C. Jungemann et al., Proc. MSM, pp. 458–461 (2001).
- [4] C. Nguyen et al., Proc. NSTI-Nanotech, vol. 3, pp. 33–36 (2005).
- [5] M. Wagner et al., Proc. IWPSD, Vol. 1 458–461 (2005).
- [6] F. Stern, Phys.Rev. B Vol. 5 4891 - 4899 (1972).
- [7] IuE, MINIMOS-NT 2.1 User's Guide, TU Wien, <http://www.iue.tuwien.ac.at/software/minimos-nt> (2004).

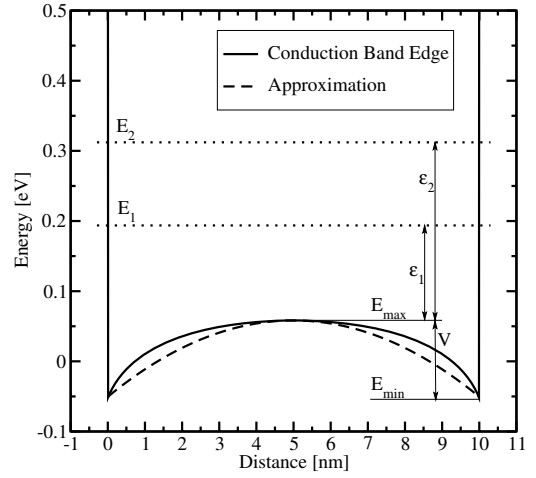


Fig. 1. Conduction band edge energy approximation and eigenenergies

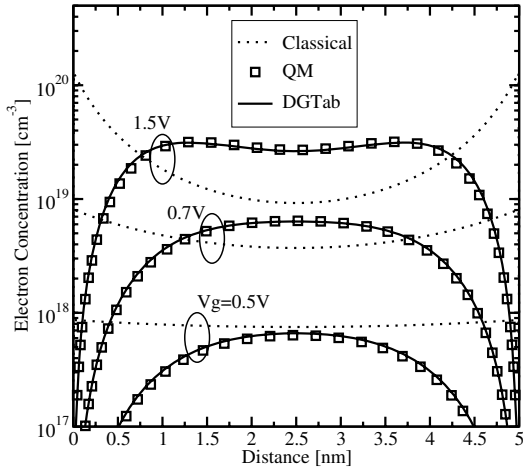


Fig. 2. Electron concentrations for a 5 nm DG MOSFET

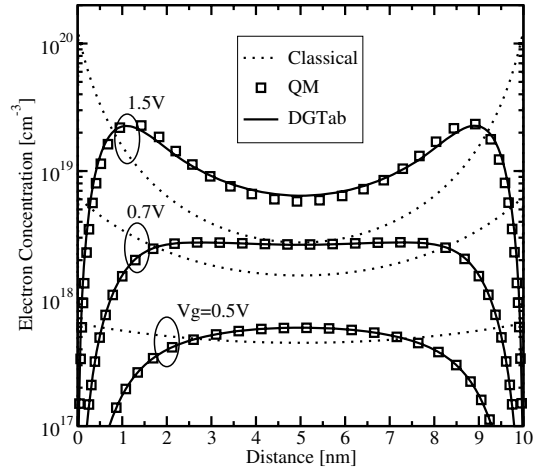


Fig. 3. Electron concentrations for a 10 nm DG MOSFET

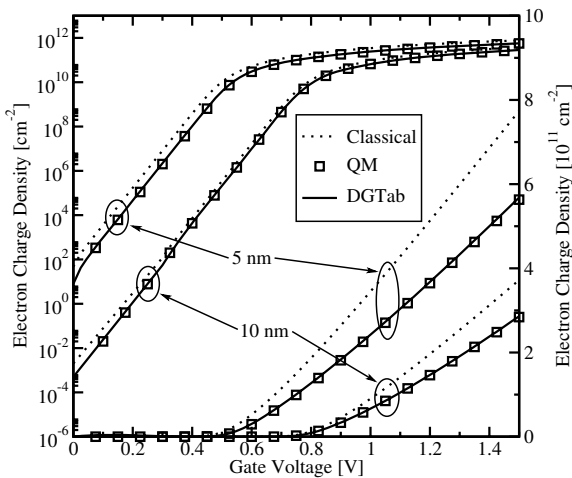


Fig. 4. Electron charge density per unit area. Logarithmic scale in the upper left part, linear scale in the lower right part.

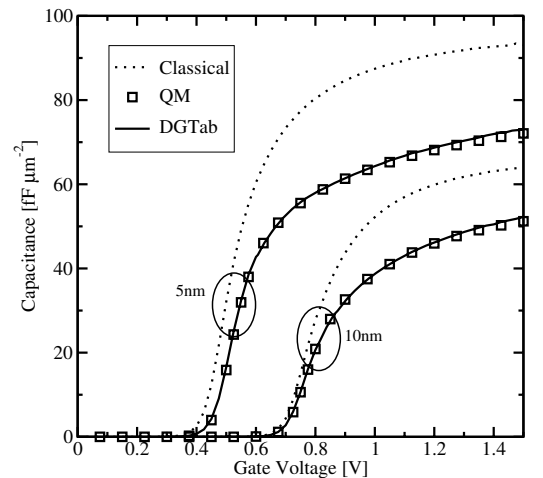


Fig. 5. Gate capacitance per unit area versus gate voltage

# Weak Accumulation of Gate Polysilicon

H. Watanabe, K. Matsuo\*, T. Kobayashi\*, K. Nakajima\*, and T. Saitoh\*

Adv. LSI Tech. Lab., Toshiba Corp., Isogo, Yokohama, 235-8522, Japan

\*Proc. & Man. Eng. Center, Semiconductor Company, Toshiba Corp., Isogo, Yokohama, 235-8522, Japan

E-mail: [pierre.watanabe@toshiba.co.jp](mailto:pierre.watanabe@toshiba.co.jp)

## INTRODUCTION

To suppress depletion effect of gate polysilicon in MOSFETs, fully-silicided (FUSI) gate has been extensively studied these several years [1-3]. One of left fundamental issues is that capacitance of FUSI gate MOSFETs is larger than that of polygate MOSFETs having the same oxide thickness ( $T_{OX}$ ) as the FUSI gate having in a case of negative gate voltage ( $V_G$ ) [1, 3]. We regarded this difference as ascribed to weak accumulation layer (WAL), and then carried out the one-dimensional exact calculation. As a result, the measured CV characteristics of polygate and FUSI gate MOSFETs are excellently reproduced [4].

In this work, we will propose an approximation method to be implemented into general-use three-dimensional device simulators, and then discuss the influence of WAL on simulation of programming non-volatile memory cell.

## WEAK ACCUMULATION [4]

The accumulation layer of polygate has been neglected since the band bending is quite small at the surface of degenerate polysilicon, assuming that the charge density is increased exponentially with the surface potential in terms of classical physics. However, expansion of electron wave is larger than width of accumulation layer which is too narrow for electrons to be confined there. Electrons are accordingly excited up to the three-dimensional conduction band at the surface. In this case, the density-of-states (DOS) becomes larger than in classical case (no accumulation layer) with a square-root function of surface potential ( $\psi_s$ ), as shown in Fig. 1. To confirm this effect, we compare CV characteristics of the FUSI gate in which WAL can be neglected and the polygate including WAL, between the measurements and the exact calculation, as shown in Fig. 2. The excellent agreement strongly supports the WAL due the quantum repulsion effect. Since the CV characteristics are agreed between neglecting the WAL and considering it with 4Å thinner oxides, as shown in Fig. 3, the width of WAL is found to be 4Å.

## METHOD and RESULTS

Considering that the DOS is increased in the square-root manner, we can solve the Poisson equation to obtain the surface charge density at the interface of polysilicon ( $Q_s$ ):

$$Q_s = \alpha \times \epsilon_F^{1/2} \cdot \psi_s^{3/4} \quad (1),$$

where  $\epsilon_F$  is the Fermi energy calculated in the bulk of the polysilicon, considering many-body interactions of carrier-carrier and carrier-ion, incomplete ionization of donors and

acceptors, and the Fermi-Dirac statistics [5, 6]. The increased density of electrons in WAL ( $\delta n_{QM}$ ) is obtained:

$$\delta n_{QM} = \frac{\alpha^2}{2q^{3/2} \epsilon_{Si}} \times \left\{ \sqrt{\epsilon_F + q\psi} \cdot \epsilon_F - \frac{\epsilon_F^2}{\sqrt{\epsilon_F + q\psi}} \right\} \quad (2),$$

where  $\psi$  is a local potential in the WAL,  $\epsilon_{Si}$  is the silicon permittivity and  $q$  is the elementary charge. The  $\alpha$  can be written as a function of polysilicon material constants (the effective density-of-states mass, the permittivity, and the number of conduction valleys). However, since these constants are ambiguous as long as considering the influence of grains in polysilicon, we may regard  $\alpha$  as a fitting parameter. To extract  $\alpha$ , we compare  $Q_s$  and  $\psi_s$  that are calculated using Eqs. (1) and (2), and are exactly calculated while the donor density in polysilicon ( $N_D$ ) is  $1 \times 10^{20} \text{cm}^{-3}$ , as shown in Fig. 4. The agreement is obtained if we set  $\alpha = 1 \times 10^5 (\text{C}^{1/2} \text{V}^{-5/4} \text{cm}^{-2})$ , while the classical calculation gives us the overestimated  $Q_s$  and the underestimated  $\psi_s$ . The CV characteristics are agreed using the same value of  $\alpha$  regardless of  $T_{OX}$ , as shown in Fig. 5, which indicates that  $\alpha$  is independent of  $T_{OX}$ . On the other hand, the extracted  $\alpha$  is decreased as  $N_D$  is increased, as shown in Fig. 6. This is due to the decrease of WAL width.

## DISCUSSION

The present method is applicable to simulation of programming non-volatile memory, since WAL appears at the interface between floating gate (FG) and inter-poly dielectric (IPD) film. Note that  $\Psi_s$  degrades the tunnel barrier height ( $\phi_B$ ) although electric field across the IPD layer ( $E_{IPD}$ ) is unchanged. This increases the tunneling from FG to traps in IPD film and from the traps to control gate, which degrades the programming efficiency. Then, if the WAL was neglected, then the tunnel mass of the IPD film would be increased from that of the tunnel oxide film by:

$$1 + 3q\psi_s \cdot \frac{\phi_B^{1/2} - (\phi_B - E_{IPD} \cdot T_{IPD})^{1/2}}{\phi_B^{3/2} - (\phi_B - E_{IPD} \cdot T_{IPD})^{3/2}},$$

where  $T_{IPD}$  is the IPD thickness, and  $\phi_B$  is the barrier height. Since this increase of tunnel mass causes the calibration to be complicated, the present method using Eqs. (1) and (2) is quite useful.

## CONCLUSION

An approximation method for calculating the effect of WAL is proposed. The influence of the WAL on simulation of programming non-volatile memory is discussed.

## REFERENCES

- [1] B. Tavel, et al., IEDM Tech. Dig. 825 (2001)
- [2] J. Kedzierski, et al., IEDM Tech. Dig., 247 (2002)
- [3] T. Aoyama et al., IEDM Tech. Dig. 95 (2004)
- [4] H. Watanabe, et al., Ext. Abs. SSDM, 504 (2005)
- [5] H. Watanabe and S. Takagi, J. Appl. Phys. **90**, 1600 (2001)
- [6] H. Watanabe, IEEE Trans. ED. **52**, 3265 (2005)

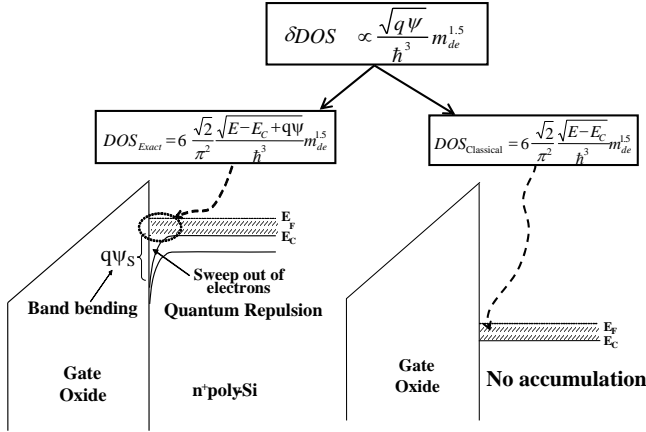


Fig. 1 Scheme of the weak accumulation: The  $m_{de}$  is the effective density-of-states mass of electron in polysilicon

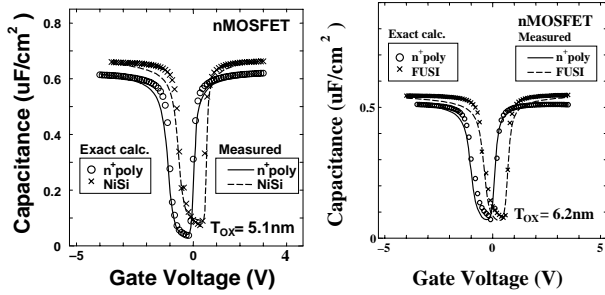


Fig. 2 Exact calculation and measurement of CV characteristics: The oxide thicknesses of the FUSI gate and the polygate MOSFETs are regarded as equivalent, since the same processes were carried out before fabricating the gates [4].

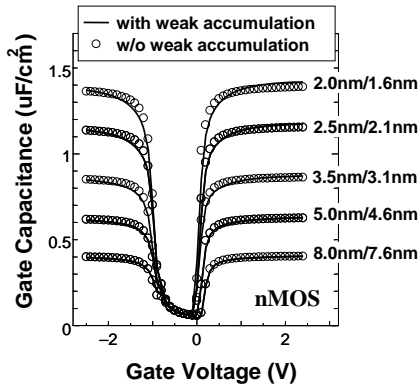


Fig. 3 CV characteristics calculated neglecting the polysilicon band bending (i.e., neglecting both WAL and incomplete depletion layer [6]) and considering it with 4Å thinner oxides, while  $N_D$  is fixed  $1 \times 10^{20} \text{cm}^{-3}$ . The width of WAL and the incomplete depletion layer are almost same.

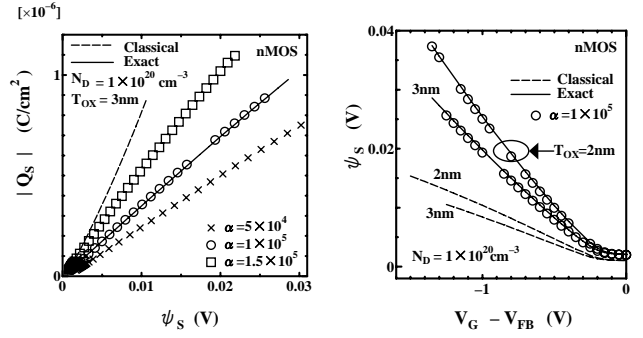


Fig. 4 Calculated surface charge density and surface potential: The dashed line depicts the data classically calculated neglecting the weak accumulation. The bulk line depicts the data exactly calculated considering the weak accumulation. The marks (circles) depict the present data calculated using Eqs. (1) and (2). Not-converged data are removed. The present and the exact data are excellently agreed in both figures while the classical calculation gives us the overestimated  $Q_S$  and the underestimated  $\psi_s$ . The  $V_{FB}$  is flat band potential. The unit of  $\alpha$  is  $(\text{C}^{1/2} \text{V}^{-5/4} \text{cm}^{-2})$ .

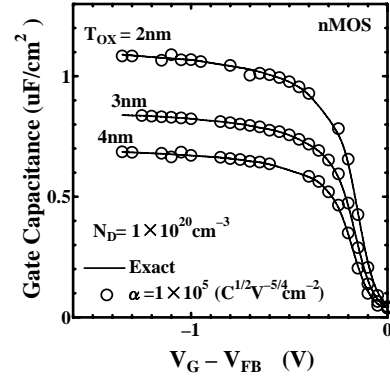


Fig. 5 Calculated CV characteristics: The bulk line depicts the data exactly calculated considering the weak accumulation. The marks (circles) depict the present data calculated using Eqs. (1) and (2) and  $\alpha = 1 \times 10^5 (\text{C}^{1/2} \text{V}^{-5/4} \text{cm}^{-2})$ . Not-converged data are removed. The  $V_{FB}$  is flat band potential. The present and the exact data are excellently agreed regardless of  $T_{OX}$  while  $N_D$  is  $1 \times 10^{20} \text{cm}^{-3}$ .

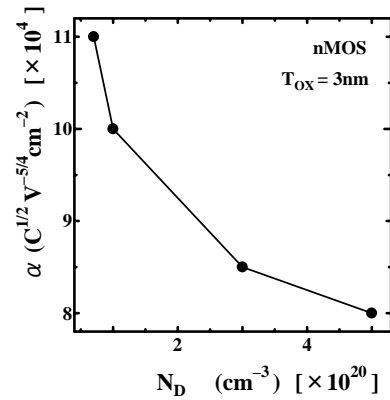


Fig. 6 The extracted  $\alpha$ : The value of  $\alpha$  is decreased as  $N_D$  is increased, since the WAL width is decreased with the increase of  $N_D$  while  $\psi_s$  is fixed.

# Numerical Analysis of a DAR IMPATT Diode

A. M. Zemliak, and S. Cabrera

Puebla Autonomous University, Av. San Claudio y 18 Sur, C.U., Puebla, 72570, Mexico  
azemliak@fcfm.buap.mx

## PROBLEM FORMULATION

The analysis of the  $n^+pvnp^+$  avalanche diode structure (Fig. 1) has been realized on the basis of the nonlinear model. This type of the diode that was named as Double Avalanche Region (DAR) IMPATT diode includes two avalanche regions inside the diode. The phase delay which was produced by means of the two avalanche regions and the drift region  $v$  is sufficient to obtain the negative resistance for the wide frequency band. The drift-diffusion model which is used for the analysis of the internal diode structure describes all important physical phenomena of the semiconductor device. This model is based on the system of two continuity equations for the electrons and holes, the Poisson equation for the potential distribution and necessary boundary conditions as for continuity equations and for the Poisson equation [1]. The dependences of the ionization coefficients  $\alpha_n, \alpha_p$  on field and temperature have been approximated using the approach described in [2]. This physical model adequately describes processes in the IMPATT diode in a wide frequency band. However, numerical solution of this system of equations is very difficult due to existing of a sharp dependence of equation coefficients on electric field. The non-evident modified Crank-Nicholson numerical scheme was used to improve numerical stability. Computational efficiency and numerical algorithm accuracy are improved by applying the space and the time coordinates symmetric approximation.

## DISCUSSION

The analysis showed that the active properties of the diode practically are not displayed for more or less significant width of the region  $v$  (Fig. 2). The negative diode admittance appears for three different frequency bands when the region  $v$  less than  $0.4 \mu\text{m}$  (Fig. 3). However these characteristics are not optimal. The possible optimization of the diode internal structure for selected frequency band can improve the power characteristics.

The DAR diode internal structure optimization has been provided below for the second frequency band near 220 GHz. The optimization algorithm is combined by one kind of direct method and a gradient method. The cost function of the optimization process was selected as output power for frequency 220 GHz. It means that the energy characteristics for the first and the third frequency bands have been obtained as functions of a secondary interest without a special improvement.

The small signal characteristics of the optimized diode structure are shown in Fig. 4 for all possible frequency bands and three values of feeding current.

The characteristics obtained for 220 GHz under the large signal serve as the main result of the optimization process. The amplitude characteristics for this frequency and for three values of feeding current density are shown in Fig. 5.

The output power dependencies as a function of first harmonic amplitude  $U_1$  for  $f = 220$  GHz and for three values of feeding current are shown in Fig. 6.

## CONCLUSION

The numerical scheme that has been developed for the analysis of the different types of IMPATT diodes is suitable for the DAR complex doping profile investigation. Some new features of the DAR diode were obtained by the analysis on the basis of nonlinear model. The diode structure optimization gives the possibility to increase the output power level for the high frequency bands.

## ACKNOWLEDGEMENT

This work was supported by the Mexican National Council of Science and Technology CONACYT, under project SEP-2004-C01-46510.

## REFERENCES

- [1] A. Zemliak, S. Khotiaintsev, and C. Celaya, Complex nonlinear model for the pulsed-mode IMPATT diode. *Instrumentation and Development*, **3**, 8, 45 (1997).
- [2] W.N. Grant, Electron and hole ionization rates in epitaxial silicon at high electric fields. *Solid-State Electron*, **16**, 1189 (1973).

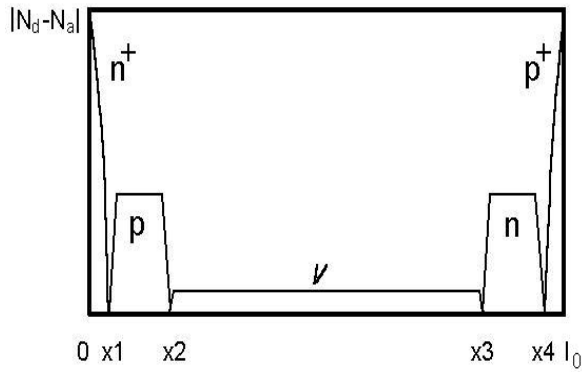


Fig. 1. Doping profile for DAR IMPATT diode.

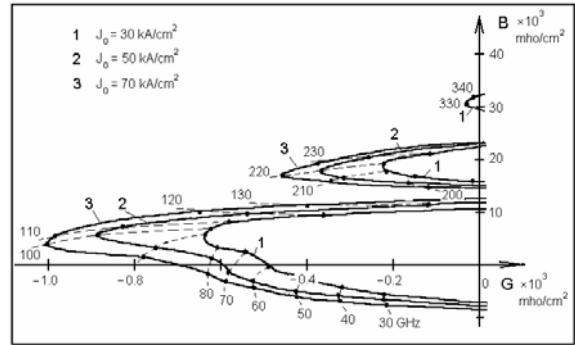


Fig. 4. Complex small signal DAR diode admittance optimized for second frequency band for different value of feeding current density.

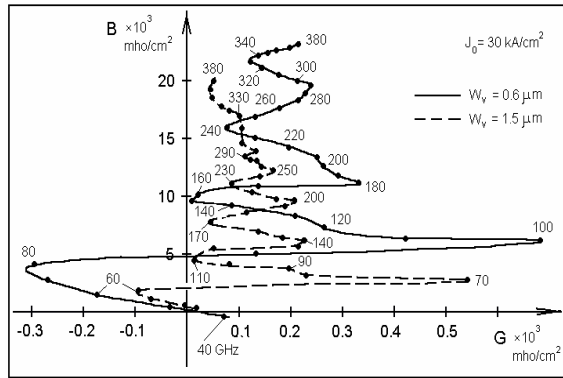


Fig. 2. Complex small signal DAR diode admittance (conductance  $G$  versus susceptance  $B$ ) for different frequencies and two values of drift layer widths  $W_v$ .

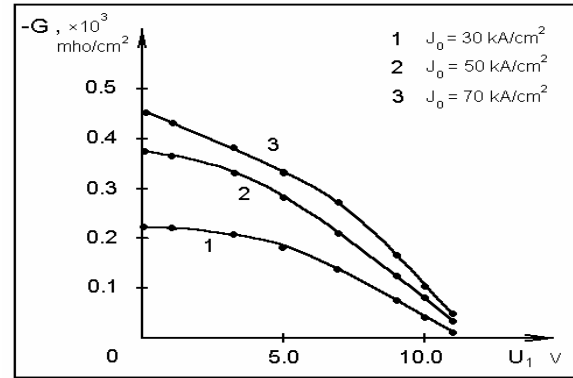


Fig. 5. Conductance  $G$  dependency as functions of first harmonic amplitude  $U_1$  for  $f = 220$  GHz and for three values of feeding current density.

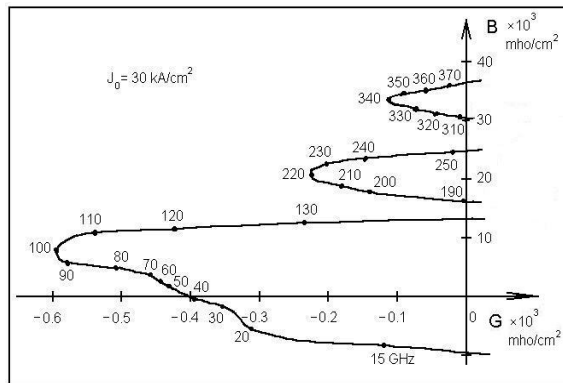


Fig. 3. Complex small signal DAR diode admittance (conductance  $G$  versus susceptance  $B$ ) for different frequencies and  $W_v = 0.32 \mu\text{m}$ .

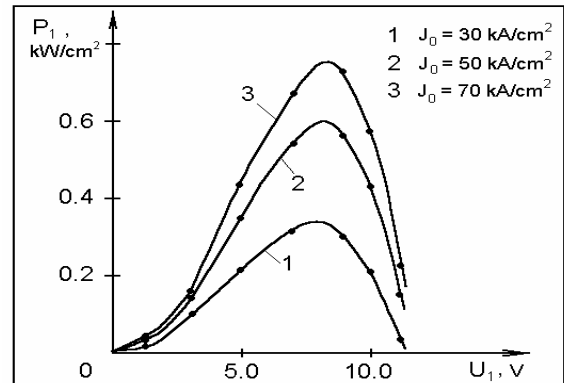


Fig. 6. Output generated power  $P$  dependency as functions of first harmonic amplitude  $U_1$  for  $f = 220$  GHz and for three values of feeding current density.

# Meshless Solution of the 3-D Semiconductor Poisson Equation

Z. Aksamija, and U. Ravaioli

Beckman Institute, University of Illinois, 405 N. Mathews, 61801 Urbana IL., U.S.A.

e-mail: aksamija@uiuc.edu

## INTRODUCTION

The Poisson equation arises frequently from problems in applied physics, fluid dynamics and electrical engineering. We solve the Poisson equation in order to obtain the electric potential in a semiconductor device and find the electric field for electronic simulation. Finding a suitable solution mesh is complicated by the fact that there is usually a large region at the bottom of the device which has few particles and is of little interest. On the other hand, the channel region at the top of the device is small but the detailed solution in it is important. There are also numerous problems arising from assigning charge to a regular mesh [1], [2]. Therefore a regular rectangular mesh is the least desirable solution. An alternative approach is to treat each individual particle as a mesh point. Meshless methods have been proposed in the past [3], [4]. This work starts with a series expansion and aims at reaching a solution which is continuous and infinitely differentiable, and optimal in the least squares sense.

## NUMERICAL APPROACH

In order to seek a solution, we expand the potential into sinusoidal components. Since we have fixed boundary conditions (the voltage at the edges/contacts is given), we know all solutions must be a super-position of sinusoidal harmonics, so we write the solution as in (1), where  $L_x$ ,  $L_y$  and  $L_z$  are the lengths of the solution domain in each respective direction.

$$V(x, y, z) = \sum_{l=1}^{N_l} \sum_{m=1}^{N_m} \sum_{n=1}^{N_n} \Phi(l, m, n) \sin\left(\frac{\pi l}{L_x} x\right) \sin\left(\frac{\pi m}{L_y} y\right) \sin\left(\frac{\pi n}{L_z} z\right) \quad (1)$$

Now the Laplacian operator can be applied analytically to each of the terms above. This produces one equation for each particle. Taken together, we have a system of equations with  $N_l \times N_m \times N_n$  terms in each row, and  $P$  rows, where  $N_l$ ,  $N_m$ , and  $N_n$  is the number of harmonic components in each direction and  $P$  is the total number of particles. This algebraic system can be expressed in matrix form as  $A\Phi = \rho \setminus \epsilon$  and solved for  $\Phi$ . In order to obtain an overdetermined system of equations, we must have more points than harmonic components. Then the system can be solved by standard least-squares techniques or by fast iterative methods [5].

## RESULTS

A test was performed by solving the system above for a rectangular region with zero boundary conditions and uniformly randomly distributed charges. The 3-D results in Fig. 2 shows good smoothness and precision. Fig. 3 compares the numerical solution to the analytical one we would expect from a uniform charge distribution.

## REFERENCES

- [1] S. E. Laux, *On Particle-Mesh Coupling in Monte Carlo Semiconductor Device Simulation*, IEEE Transactions on Computer-Aided Design of Integrated Circuits and Systems **15**, 10 (1996).
- [2] R. W. Hockney and J. W. Eastwood, *Computer Simulation using Particles*, New York: Adam Hilger, (1988).
- [3] C. J. Wordelman, N. R. Aluru, and U. Ravaioli, *A Meshless Method for the Numerical Solution of the 2- and 3-D Semiconductor Poisson Equation*, Computer Modeling in Engineering and Sciences **1**, 1 (2000).
- [4] G. Pöplau and D. Potts, *Fast Poisson solvers on nonequid-spaced grids: Multigrid and Fourier methods compared*, in: Proceedings of SPIE: Advanced Signal Processing Algorithms, Architectures and Implementations XIII, F.T. Luk (Ed.) **5205**, (2003).
- [5] D. S. Watkins, *Fundamentals of Matrix Computations*, New York: Wiley-Interscience, (2002).

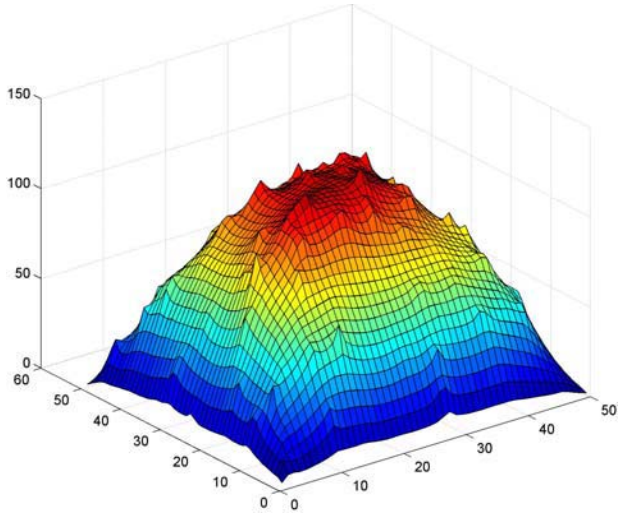


Fig. 1. Solution obtained finite differences with a CIC charge assignment. Only a horizontal cut through the 3-D computational domain is shown.

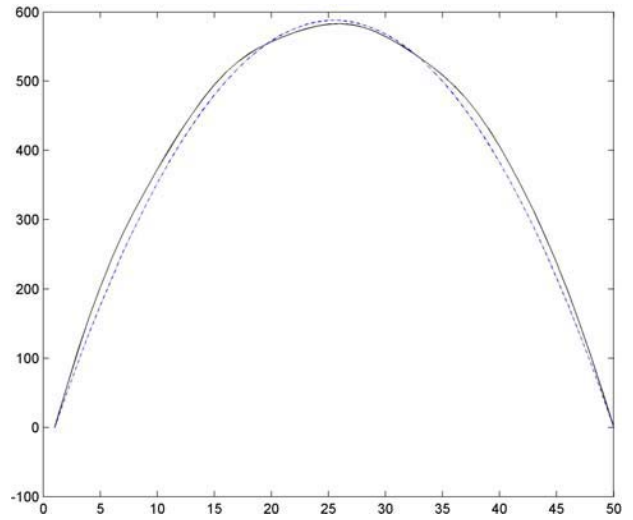


Fig. 3. Comparison of solutions. The solid line is the numerically computed solution, and the dashed line is the analytical quadratic solution which assumes a uniform distribution. The agreement is excellent and the small discrepancy is due to the random assignment of charge locations.

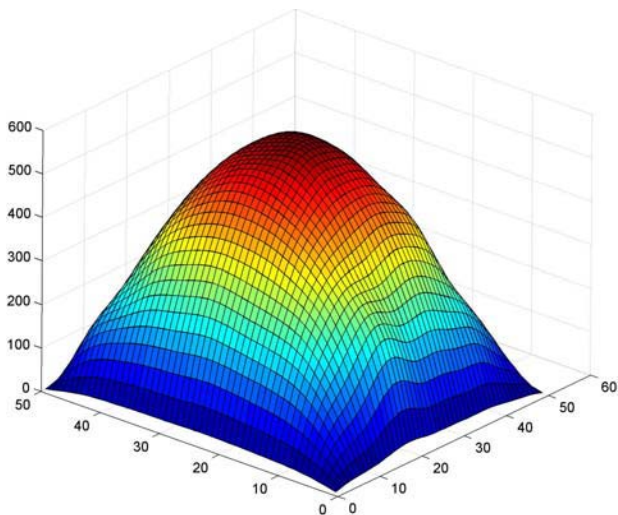


Fig. 2. Solution obtained from the meshless approach. Only a horizontal cut through the 3-D computational domain is shown.

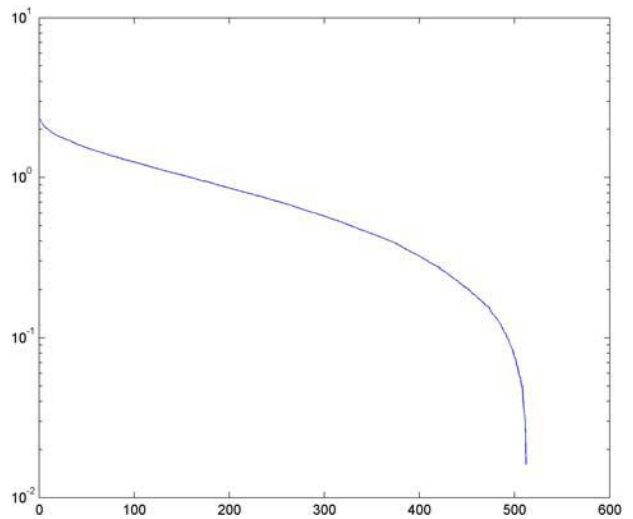


Fig. 4. Logarithmic plot of the singular values of the matrix  $A$ . The ratio of the largest to the smallest singular value is around 100, meaning that the solution is sufficiently well conditioned. Experience has shown that increasing the number of harmonics  $N$  beyond the number of points  $P$  drastically increases the condition number and makes the solution ill-conditioned.

# Particle-based simulations of phonon transport in Silicon

A. M. Asokan, and R. W. Kelsall  
Institute of Microwaves and Photonics,  
School of Electronic and Electrical Engineering,  
University of Leeds, U.K.  
e-mail: een9ama@leeds.ac.uk

## INTRODUCTION

Thermal management is one of the main issues which must be overcome in order to maintain the continued reduction of feature sizes in silicon microelectronics. Developments in size and structure of silicon devices has led to ever increasing power levels (currently  $\approx 100\text{W}$  per chip), the power dissipation is predicted to rise exponentially and will reach catastrophic levels in the near future. New materials and device architectures, such as silicon-on-insulator and strain silicon/silicon-germanium devices being used to achieve better performance have had a detrimental effect on thermal management due to higher thermal resistances and additional thermal interfaces. As a result thermal modelling is becoming increasingly important for understanding device properties. Current thermal models, based on diffusive continuum flow, are inaccurate at the nanoscale and a model which considers the microscopic nature of heat generation and heat transport must be used.

## RESEARCH

In this paper we describe the development of thermal transport model for small semiconductor structures. On the microscale, heat transport can be described by the Boltzmann transport equation for phonons. The complexity and quantity of the phonon anharmonic interactions make a direct numerical solution difficult without numerous approximations. We have developed a Monte Carlo simulation approach to this problem, modeling phonon trajectories and three phonon scattering events.

The simulation domain is subdivided into cells and a discretized phonon distribution is monitored in every cell. The relaxation time for each phonon is

calculated using third order elastic constants [1] [2] and used to simulate the anharmonic three-phonon processes (both 'absorption' and 'emission' type) for acoustic phonon modes in silicon. Phonon-phonon absorption events are performed by selecting a 'partner' phonon from within the same real space cell that satisfies momentum and energy conservation, similarly to the algorithms used for electron-electron scattering. The difference between phonon and electron transport is the necessity, in the latter case, of simulating the Umklapp processes, since these are essential in defining the thermal conductivity. Whereas in previous derivations of analytical approximations for phonon lifetimes and thermal conductivities, it has been difficult to determine the relative contribution of Normal and Umklapp processes in phonon-phonon interactions, in principle, this information can be extracted directly from the Monte Carlo simulation.

## REFERENCES

- [1] R. Orbach, and L. A. Vredevoe, *The Attenuation of High Frequency Phonons at Low Temperatures*, Physics **1**, 91 (1964).
- [2] Shin-ichiro Tamura, *Spontaneous decay rates of LA phonons in quasi-isotropic solids*, Phys. Rev. B **31**, 2574 (1985).



# Neutral and Negatively Charged Interstitial Oxygen in Silicon

P.Ballo, D.Donoval\* and L.Harmatha\*

Department of Physics,  
\*Department of Microelectronics,  
Faculty of Electrical Engineering and Information Technology,  
Slovak University of Technology, Ilkovičova 3, 812 19 Bratislava, Slovak Republic  
e-mail: [peter.ballo@stuba.sk](mailto:peter.ballo@stuba.sk)

## INTRODUCTION

Being the predominant impurity in Czochralski-grown silicon, oxygen has been extensively studied since the early years of semiconductor research by a multitude of experimental [1] and theoretical [2] techniques. The generally accepted model shows the oxygen atom 'squeezed' between two neighboring lattice atoms. It is believed that oxygen breaks the silicon-silicon bond and forms a Si-O-Si bridge. The interaction between the neighbors forms a Si-O-Si virtual molecule with  $C_{2v}$  symmetry. The defect is electrically neutral and induces a shallow donor level at  $E_v+0.07$  eV. Advent of highly powerful computers offers a chance to shed light on the essential features of the physics behind the charge distribution during the filling period. The problem of the charge distribution has been solved using the translational symmetry of the system [3]. It appeared to be more than a good idea. Using this technique, the equilibrium structure of the oxygen defect in silicon has been extensively studied. Cluster approach with the hydrogen-saturated surface coupled with the Hartree-Fock (HF) techniques [4] developed mostly for quantum chemistry could give advantages in the simulation. Methods based on HF technique usually reduce the time of computation and neglect some computationally expensive procedures but the performance in silicon-oxygen systems is less convincing giving very poor results for Si-O-Si geometry. To solve this problem, we optimized the adjustable parameters for oxygen by fitting the geometrical data to the *ab initio* values. The set of parameters, which is refer to as "new

oxygen parametrization" (NOP), was presented recently [5]. The aim of this paper is to report a study on the oxygen defect in various charge states using NOP combined with cluster approach.

## METODOLOGY

In our study, we use a cluster of 66 silicon atoms. The lattice constant is set to the experimental value of 5.43 Å [6]. The disconnected bonds to the remaining crystal are terminated with hydrogen. The optimized Si-H bond distance corresponding with the total energy minimum was found to be 1.48 Å. The interstitial oxygen was positioned at the center of Si-Si bond. The final cluster configuration is  $Si_{66}H_{58}O$ . The Si-O-Si complex was positioned in the cluster center, surrounded by five shells of silicon atoms. All atoms positioned in first two shells around the oxygen were relaxed by Broyden-Fletcher-Goldfarb-Shanno (BFGS) technique. This corresponds to a fixed lattice outside a flexible core region. In Fig. 1 is shown the Si-O-Si complex after relaxation. To simulate the negative charge state either one or two extra electrons were introduced in the Si-O-Si system. The broadened eigenvalue spectrum (DOS function) for the oxygen defect in various charge states is shown in Fig.4.

## CONCLUSIONS

The calculations performed in combination with the cluster technique and NOP model have proved to be successful. The main structural features of the oxygen defect in silicon are found in good agreement with the experiment. We confirmed that

the large lattice relaxation is provided by the bridging oxygen atom. The neutral oxygen produces two resonance states in the valence band and a shallow donor level positioned in the gap. Application of HF technique to a charged cluster allows calculate the charge distribution for one or two extra electrons.

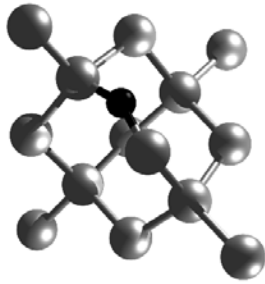


Fig.1. Structure of the oxygen defect in silicon after relaxation. The relaxed structure shows on  $C_{2v}$  symmetry. Light gray spheres represent silicon atoms, black sphere interstitial oxygen atom.

Our calculations show that an extra electron trapped on the oxygen defect induces a small change in lattice distortion and push up the donor level in the gap. This state is unstable with a high emission rate of extra electron. DLTS transient controlled by this emission gives the right position of the donor level at  $E_v+0.07\text{eV}$ . The emission rate of the second extra electron is low in comparison with the previous charge state. A lesson from the present study is that MNDO technique in combination with the NOP is accurate enough to have, at least, predictive power and is fast enough to allow to study large systems.

#### ACKNOWLEDGMENTS

We are pleased to acknowledge helpful discussions with Professor P. Deák and Dr. J. Breza. This research was supported through the Slovak Grant Agency under Grant No. 1/2041/05.

#### REFERENCES

- [1] R.C.Newman, *J.Phys.:Condens.Matter* **12**, R335 (2000).  
 [2] D.J.Chadi, *Phys.Rev.Lett.* **77**, 861 (1996).

- [3] S.G.Louie, M.Schlüter, J.R.Chelikowsky, and M.L.Cohen, *Phys.Rev.B* **13**, 1654 (1976).  
 [4] J.C.Inkson, in *Many-Body Theory of Solids* (Plenum Press, New York, 1984).  
 [5] P.Ballo and L.Harmatha, *Phys.Rev.B* **68**, 153201 (2003).  
 [6] Ch. Kittel, in *Introduction to Solid State Physics* (John Wiley & Sons, New York, 1996).

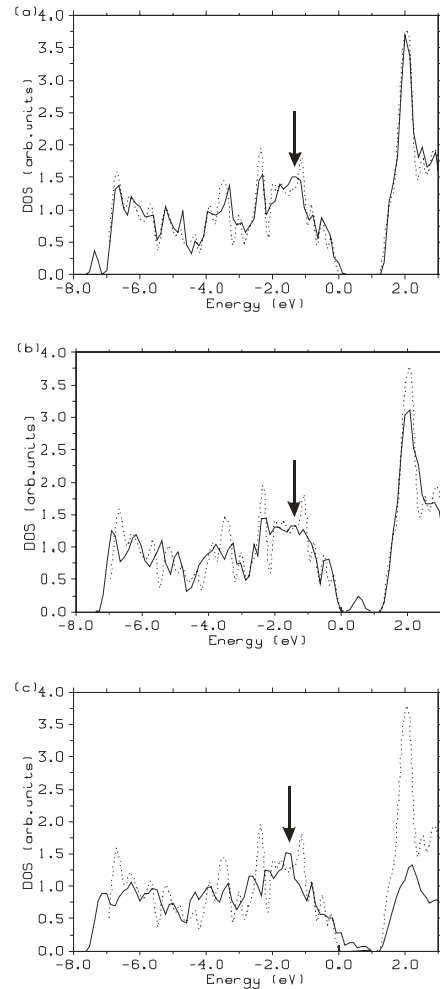


Fig. 2: Computed electronic density of states (DOS) of an interstitial oxygen defect in silicon in various charge states: (a) neutral; (b) negatively charged; (c) double negatively charged. Solid line represents silicon crystal with the oxygen; dashed line represents a perfect silicon crystal. The eigenvalue spectra were broadened by convolution with a Gaussian function.  $E=0$  corresponds to the top of the valence band. The arrows point at the resonance induced by  $sp^3 2p$  bond

# Model Plasma Dispersion Functions for SO Phonon Scattering in Monte Carlo Simulations of High- $\kappa$ Dielectric MOSFETs

J. R. Barker, J.R. Watling

Dept. of Electronics and Electrical Engineering, University of Glasgow, Glasgow G12 8LT, UK  
e-mail:jbarker@elec.gla.ac.uk

The recent interest in high- $\kappa$  dielectric MOSFETs to overcome gate leakage problems has raised a number of problems for accurate Monte Carlo based device simulation of such devices. The problem is caused by carrier scattering on soft surface optic (SO) phonons. It leads to a strong degradation of effective mobility. A precise quantification of the mobility degradation requires us to compute the electron-phonon scattering rates as a function of position within the channel, the dependence on local carrier concentration  $n$  and carrier temperature  $T_e$ , the gate stack layer thickness variations and inhomogeneities within the dielectric regions. The situation is exacerbated by the role of plasmons in the channel and gate regions [1]. The core problem for implementing Monte Carlo simulation with SO phonon scattering is the development of fast algorithms for the dynamically-screened position-dependent scattering rates. Unfortunately, the re-normalised coupling of the phonons and plasmons is sensitive to the gate stack inhomogeneities and the variation in  $n(\mathbf{r})$  and  $T_e(\mathbf{r})$  along the channel. In the present work we significantly extend earlier studies [1] that utilised the simple plasmon-pole approximation for the electronic dielectric functions  $\epsilon(q, \omega)$  in the gate and channel plasmas. We proceed by evaluating the Lindhard function for the gate and channel carrier assemblies so as to include dynamic screening and Landau damping. For example in the Si channel,

$$\epsilon_e(q, \omega) = \epsilon_{Si} - \frac{e^2 m^2 * k_B T_e}{2\pi^{3/2} \hbar^3 q^3} \{Z(W^+) - Z(W^-)\} \quad (1)$$

At the heart of the calculation is the plasma dispersion function  $Z$ , that depends upon the energy distribution function  $f_0$  which is Maxwell-Boltzmann for non-degenerate systems and Fermi-Dirac for degenerate systems.

$$Z(z) = \frac{1}{\sqrt{\pi}} \int_{-\infty}^{\infty} \frac{f_0(u^2)}{u - z} du; (u^2 \equiv E/k_B T_e) \quad (2)$$

$$W_{\pm} = \left( \frac{2m^* k_B T_e}{\hbar^2} \right)^{-1/2} \left( \frac{m^* \omega}{\hbar q} \pm \frac{q}{2} + i\eta \right). \quad (3)$$

In principle the scattering-out rate  $\lambda(\mathbf{k})$  at a position  $\mathbf{r}$  may be expressed in the Born approximation in terms of an angular frequency integral over the complex dielectric permittivity:

$$\lambda(\mathbf{k}) = \int_{-\infty}^{\infty} d(\hbar\omega) \pi^{-1} \{1 + f_{BE}(\omega)\} \sum_{\mathbf{q}} \{1 - f(\mathbf{k} + \mathbf{q})\} \frac{2\pi}{\hbar} |V(\mathbf{q})|^2 \text{Im}\left\{-\frac{1}{\epsilon(q, \omega)}\right\} \delta(\epsilon_{\mathbf{k}+\mathbf{q}} - \epsilon_{\mathbf{k}} + \hbar\omega). \quad (4)$$

In the present paper we present new analytical models for the non-degenerate and degenerate plasma dispersion functions  $Z$  based on rational fractions of low order polynomials in angular frequency  $\omega$ . With such a formulation the problem of computing the re-normalised phonon and plasmon energies together with scattering strengths as functions of wave vector is considerably simplified. Figures (1-3) compare the analytical approximations with direct numerical computation of the dispersion functions. A second new development reported here is the evaluation of the final scattering state from (4) using importance sampling with applications to realistic MOSFETs.

## REFERENCES

- [1] M.V. Fischetti, D. A. Neumayer and E. A. Cartier, J. App. Phys. **90**,4587-4607 (2001).

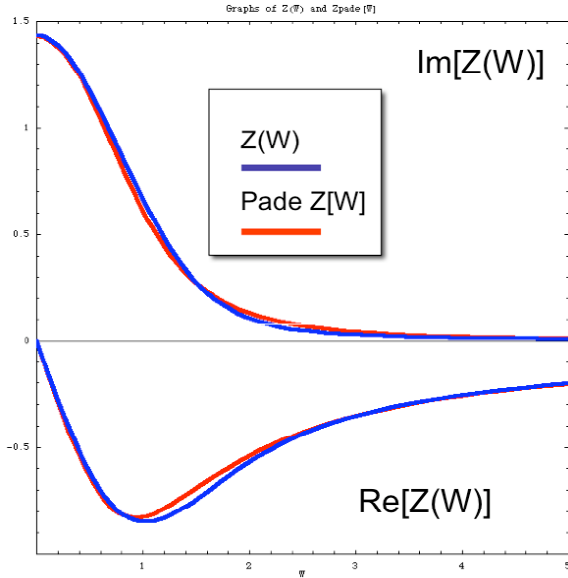


Fig. 1. The real and imaginary part of the dispersion function  $Z$  for non- degenerate systems with  $T = 300K$ , and zero collisional damping . The figure compares the numerically computed result  $Z(W)$  with the analytical Padé approximant model.

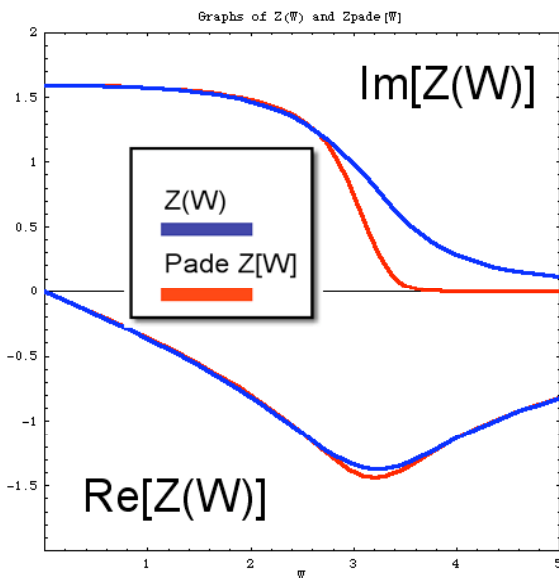


Fig. 2. The real and imaginary part of the dispersion function  $Z$  for strongly collision damped degenerate systems with  $\epsilon_F - \epsilon_c = 10 k_B T$ ;  $T = 300K$ , and damping factor  $\Gamma/k_B T = 0.25$ .

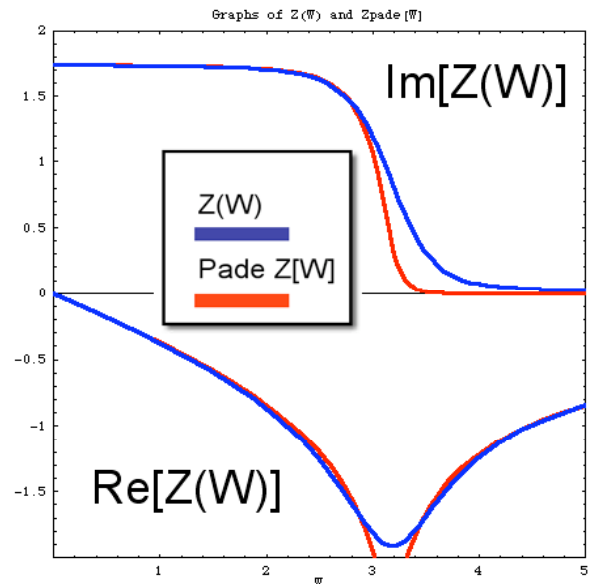


Fig. 3. The real and imaginary part of the dispersion function  $Z$  for weakly collision damped degenerate systems with  $\epsilon_F - \epsilon_c = 10 k_B T$ ;  $T = 300K$ , and damping factor  $\Gamma/k_B T = 0.01$ .

# On a Simple and Accurate Quantum Correction for Monte Carlo Simulation

F.M. Bufler\*<sup>†</sup>, R. Hudé<sup>†</sup>, and A. Erlebach<sup>†</sup>

\*Institut für Integrierte Systeme, ETH Zürich, Gloriastrasse 35, CH-8092 Zürich, Switzerland

<sup>†</sup>Synopsys Schweiz GmbH, Affolternstrasse 52, CH-8050 Zürich, Switzerland

## INTRODUCTION

Usual quantum corrections to Monte Carlo simulation feature an electron density profile, which tends to vanish at the interface. However, the corresponding formulation of surface roughness scattering and/or the application to realistic MOSFETs is problematic. Using directly or indirectly the Schrödinger equation involves an arbitrary choice of the transition point between bulk and quantization region both in space and in energy, and requires for computational reasons analytical band structure descriptions. The model for surface roughness scattering based on the surface roughness root mean square and correlation length still involves in the full-band versions [1], [2] an effective mass and requires strain-dependent calibration to measurements [1]. In contrast, a combination of specular and diffusive scattering at the interface explicitly involves the strain-dependence via the conservation of energy and parallel-momentum in the specular part. However, this approach necessitates a classical density profile allowing electrons to hit the surface. A possibility to combine this surface scattering model with quantum effects is to use a modification of oxide thickness and work function as obtained from quantum mechanics [3]. It is the aim of this paper to generalize this method to a completely numerical approach, to demonstrate its accuracy and to apply it to process-simulated p- and n-MOSFETs of a 65 nm technology.

## APPROACH AND DISCUSSION

Our quantum-correction method consists of reproducing density-gradient (DG) simulations below and around the threshold by a classical drift-diffusion (DD) simulation with modified work function and oxide thickness and to employ these modified values subsequently in full-band Monte

Carlo (MC) simulation. First, the increase of the effective oxide thickness in the on-state is computed according to  $\Delta t_{\text{ox}} = (X_{\text{qm}} - X_{\text{cl}}) \epsilon_{\text{ox}}/\epsilon_{\text{Si}}$ . In a 2nd classical DD simulation using this  $\Delta t_{\text{ox}}$ , the remaining threshold voltage shift to the DG simulation is extracted and considered as a modified work function in the 3rd DD simulation as well as in the MC simulation.

For the example illustrated by the geometry in Fig. 1 and the roll-off curves in Fig. 2, the logarithmic and linear plots of the transfer characteristics are shown in Figs. 3 and 4. In the subthreshold regime, i.e. in weak inversion, changing only  $t_{\text{ox}}$  is not sufficient while considering only the threshold voltage shift matches the DG result, whereas both modifications are still significantly away from DG for higher  $V_{\text{GS}}$ . Only the combined correction reproduces DG up to far above threshold (compare also Fig. 5). In Fig. 6, the results of the different corrections when used in MC simulation are shown for the on-current scaling of n- and p-MOSFET. It can be seen that considering only the total threshold shift still involves a significant difference to the final result based upon the combined correction.

## CONCLUSION

We have presented a quantum-correction scheme for full-band MC simulation which considers the quantum mechanical increase of effective oxide thickness and threshold voltage. In a TCAD environment, this method can be used fully automatical in a workbench project and allows to use consistently diffusive and specular surface roughness scattering and the corresponding stress-dependence.

## REFERENCES

- [1] A. T. Pham *et al.*, in *Proc. ESSDERC*, pp. 293–296 (2005).
- [2] X.-F. Fan *et al.*, *IEEE Trans. Electron Dev.* **51**, 962 (2004).
- [3] R. Hudé *et al.*, *Proc. ULIS*, pp. 159–162 (2005).

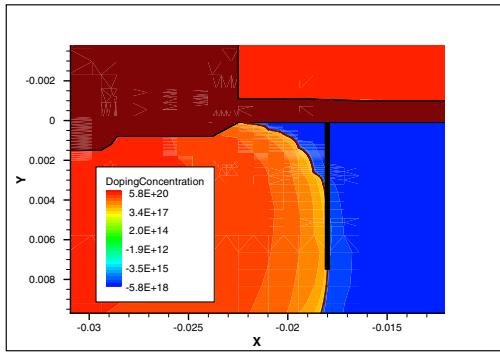


Fig. 1. Cross section of the source side of the channel in a 45 nm nMOSFET. The bold vertical bar shows the position where the charge centroids are calculated from the electron density profiles.

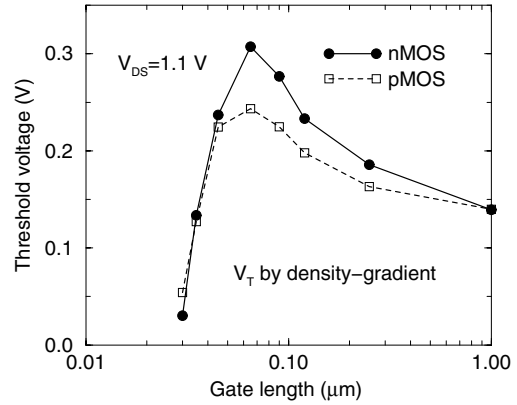


Fig. 2. Saturation threshold voltage roll-off curves of nMOSFET and pMOSFET for a 65 nm node technology according to density-gradient simulations.

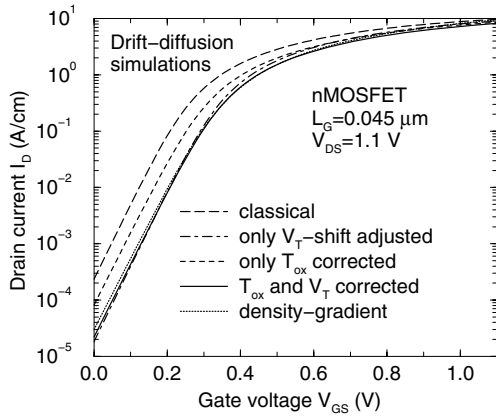


Fig. 3. Logarithmic plot of the transfer characteristics of the 45 nm nMOSFET showing the results of different quantum corrections employed in drift-diffusion simulations.

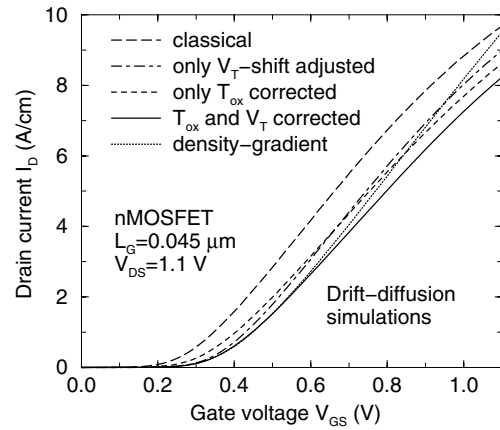


Fig. 4. Linear plot of the transfer characteristics of the 45 nm nMOSFET showing the results of different quantum corrections employed in drift-diffusion simulations.

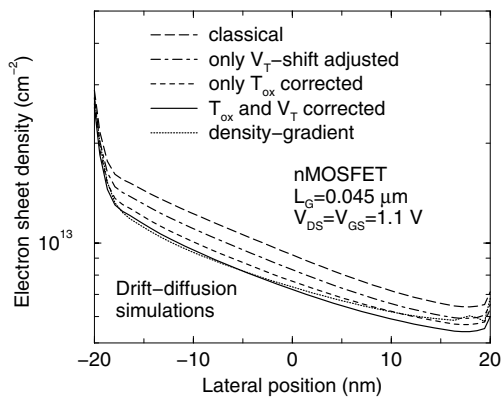


Fig. 5. Electron sheet densities along the channel in the 45 nm nMOSFET as present for different quantum corrections within drift-diffusion simulations.

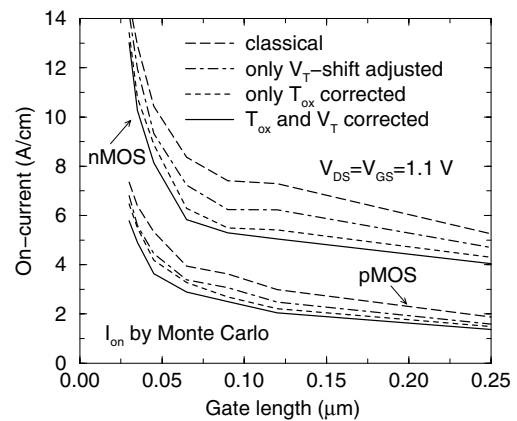


Fig. 6. On-current scaling according to full-band Monte Carlo simulations of nMOSFETs and pMOSFETs using different quantum corrections.

# DSMC versus WENO-BTE: a double gate MOSFET example.

M.J. Caceres<sup>¶</sup>, J.A. Carrillo<sup>\*</sup>, I.M. Gamba<sup>†</sup>, A. Majorana<sup>‡</sup> and C.-W. Shu<sup>§</sup>

<sup>¶</sup> Departamento de Matematica Aplicada, Universidad de Granada, 18071 Granada, Spain.

<sup>\*</sup> ICREA - Department de Matemàtiques, Universitat Autònoma de Barcelona, E-08193 Bellaterra, Spain

<sup>†</sup> Department of Mathematics and TICAM, The University of Texas at Austin, USA

<sup>‡</sup> Dipartimento di Matematica e Informatica, Università di Catania, Catania, Italy

<sup>§</sup> Division of Applied Mathematics, Brown University, Providence, RI 02912, USA

## ABSTRACT

In modern highly integrated devices, a consistent description of the dynamics of carriers is essential for a deeper understanding of the observed transport properties. The semi-classical Boltzmann equation

$$\frac{\partial f}{\partial t} + \frac{1}{\hbar} \nabla_{\mathbf{k}} \varepsilon \cdot \nabla_{\mathbf{x}} f - \frac{q}{\hbar} \mathbf{E} \cdot \nabla_{\mathbf{k}} f = Q(f). \quad (1)$$

coupled with the Poisson equation

$$\nabla_{\mathbf{x}} [\varepsilon_r(\mathbf{x}) \mathbf{E}] = - \frac{q}{\epsilon_0} [\rho(t, \mathbf{x}) - N_D(\mathbf{x})], \quad (2)$$

provides a general theoretical framework for modeling electron transport. Moreover, time-dependent solutions of the Boltzmann equation contain all the information on the evolution of the carrier distribution. In Eq. (1),  $f$  represents the electron probability density function in phase space  $\mathbf{k}$  at the physical location  $\mathbf{x}$  and time  $t$ .  $\mathbf{E}$  is the electric field,  $Q(f)$  denotes the collision operator, which describes electron-phonon interactions and  $\varepsilon$  is the energy-band function. Physical constants  $\hbar$  and  $q$  are the Planck constant divided by  $2\pi$  and the positive electric charge, respectively. In Eq. (2),  $\epsilon_0$  is the dielectric constant in a vacuum,  $\varepsilon_r(\mathbf{x})$  labels the relative dielectric function depending on the material,  $\rho(t, \mathbf{x})$  is the electron density, and  $N_D(\mathbf{x})$  is the doping. Very recently, deterministic solvers to the Boltzmann-Poisson system (1)-(2) for two-dimensional devices were proposed [1]-[4]. These methods provide accurate results which, in general, agree well with those obtained from Monte Carlo simulations. In this paper, we consider a double gate MOSFET device [5] (Fig. 1) and compare numerical solutions, by means of the use of WENO schemes, of Eqs. (1)-(2) and results given by DSMC. Figs. 2-3

show charge density and electrical potential profiles, obtained by solving Eqs. (1)-(2), in the stationary state. Since the symmetric geometry and the boundary conditions, only the  $y \geq 0$  domain is considered. In Figs. 4-6 we show a comparison between BTE solutions and DSMC. For a fixed value of  $y$  coordinate, we consider the charge density and the velocity. In our opinion, deterministic solutions might improve algorithms of DSMC, as, in particular, the charge assignment to the mesh, the treatment of the boundary conditions and the free flight duration, where well accepted rules do not exist.

## REFERENCES

- [1] J.A. Carrillo, I.M. Gamba, A. Majorana, and C.-W. Shu, *A direct solver for 2D non-stationary Boltzmann-Poisson systems for semiconductor devices: a MESFET simulation by WENO-Boltzmann schemes*, J. Comput. Electron., **2**, 375 (2003).
- [2] J.A. Carrillo, I.M. Gamba, A. Majorana, and C.-W. Shu, *2D semiconductor device simulations by WENO-Boltzmann schemes: efficiency, boundary conditions and comparison to Monte Carlo methods*, to appear in J. Comput. Phys. (2005)
- [3] M. Galler, *Multigroup Equations for the description of the Particle Transport in Semiconductors*, Series on Advances in Mathematics for Applied Sciences - Vol. 70, World Scientific Publishing (2005).
- [4] M. Galler, and A. Majorana, *Deterministic and stochastic simulation of electron transport in semiconductors*, to appear in Transp. Th. and Stat. Phys., 6th MAFPD (Kyoto) special issue (2005).
- [5] F.M. Bufler, A. Schenk and W. Fichtner, *Monte Carlo, Hydrodynamic and Drift-Diffusion Simulation of Scaled Double-Gate MOSFETs*, J. Comput. Electron., **2**, 81 (2003).

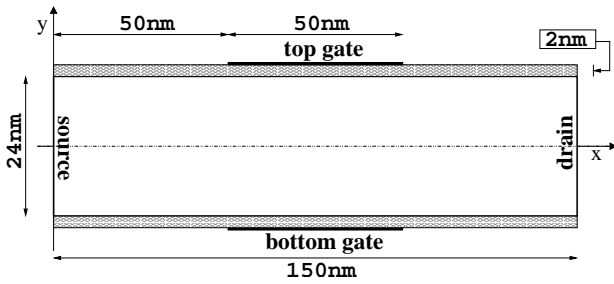


Fig. 1. A double gate MOSFET structure.

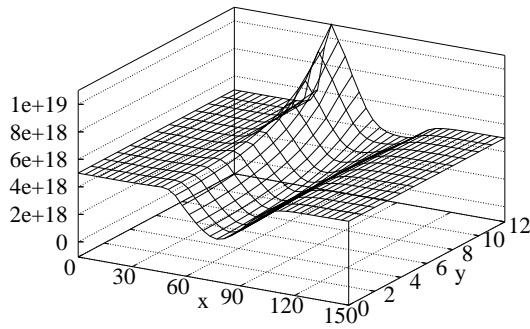


Fig. 2. Charge density. Units: x (nm), y (nm), density ( $\text{cm}^{-3}$ ).

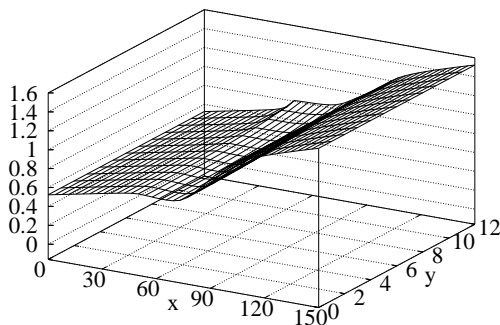


Fig. 3. Electric potential. Units: x (nm), y (nm), potential (Volt).

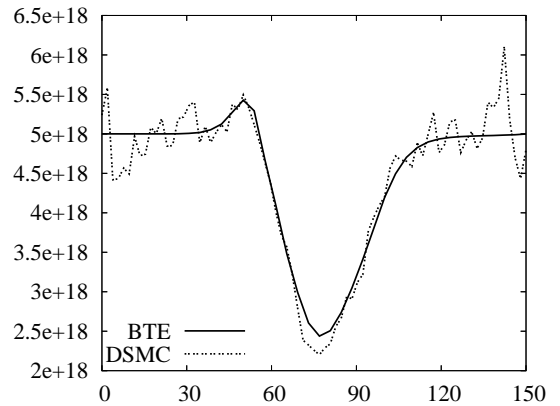


Fig. 4. Charge density at  $y = 6$ . Units: x (nm), density ( $\text{cm}^{-3}$ ).

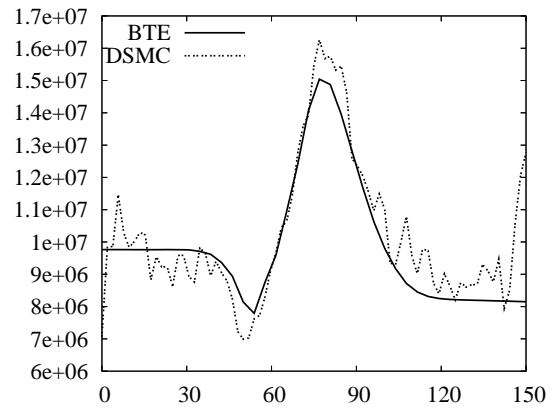


Fig. 5. x-component of the velocity at  $y = 6$ . Units: x (nm), velocity (cm/s).

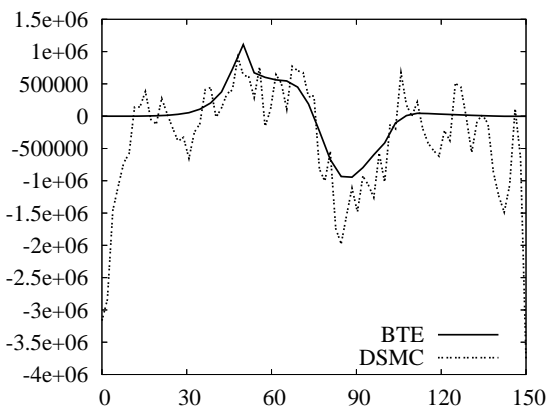


Fig. 6. y-component of the velocity at  $y = 6$ . Units: x (nm), velocity (cm/s).

# Electronic Noise in Semiconductor Systems: A Monte Carlo Simulation under Mixed Fields

M.C. Capizzo, D. Persano Adorno and M. Zarcone

Dipartimento di Fisica e Tecnologie Relative, Viale delle Scienze, Ed. 18, Palermo (Italy)  
 e-mail: capizzo@difter.unipa.it

## INTRODUCTION

Progress in telecommunications systems has been made possible by computer simulation techniques and physical modelling of semiconductor structures. The level of noise in semiconductor components limits the successful design of any low noise electronic system. Therefore, characterization of the semiconductor behaviour under dynamic operation condition could help to predict the sensitivity of semiconductor based devices. The generation of electronic noise in bulk semiconductor is due to the strong nonlinear behaviour at microscopic level.

For these reasons, the Monte Carlo (MC) method has been used for the simulation since it includes at a microscopic level, the sources of the nonlinearities (hot carriers, velocity overshoot, intervalley transfer, etc) taking place in electronic devices operating under large-signal conditions. In particular, the electronic transport in the bulk semiconductor driven by two a.c. mixed electric fields has been performed and the noise response has been analysed.

Recently, an analysis of electronic noise under large-signal conditions has been developed for the case of bulk semiconductor and simple devices [1,2,3,4]. However, to the best of our knowledge, these effects have not been investigated in the presence of a mixing of coherent electromagnetic radiations of commensurate frequencies.

In the last years we have investigated high-order harmonic generation and frequency mixing effects in low-doped bulk semiconductors subject to far-infrared intense electric field [5,6]. It has been shown that the wave mixing can produce an enhancement of the harmonic generation. However, the extraction of these harmonics is limited by the

intrinsic high-frequency noise of the nonlinear medium, which can mask the generated high-order harmonics. Therefore, under cyclostationary conditions, these dynamical effects have to be considered and nonlinear analysis of noise must be performed.

However, a physical understanding of noise sources and a full theory for nonlinear noise modelling is still under development.

## PHYSICAL MODEL AND NOISE CALCULATION

In this study we investigate electronic noise in bulk GaAs operating under two mixed large-amplitude periodic electric fields. The microscopic modelling of system is the same of Ref. [5].

To analyze the noise present in the carrier velocity, the autocorrelation function approach has been used [4]. The two times autocorrelation function is defined as:

$$C_{\delta v, \delta v}(t, \tau) = \left\langle v\left(t - \frac{\tau}{2}\right)v\left(t + \frac{\tau}{2}\right) \right\rangle - \left\langle v\left(t - \frac{\tau}{2}\right) \right\rangle \left\langle v\left(t + \frac{\tau}{2}\right) \right\rangle \quad (1)$$

By averaging over the whole set of values of  $t$  during the period  $T_f$ , the longer period of excitation mixed fields, one obtain the autocorrelation function as:

$$C_{\delta v, \delta v}(\tau) = \frac{1}{T_f} \int_0^{T_f} C_{\delta v, \delta v}(t, \tau) dt \quad (2)$$

Finally, the mean spectral density is defined as:

$$S_{\delta v, \delta v}(t, \nu) = \int_{-\infty}^{\infty} C_{\delta v, \delta v}(t, \tau) e^{i2\pi\nu\tau} d\tau \quad (3)$$

## RESULTS

Figure 1 and 2 illustrate the autocorrelation function of velocity fluctuations and the mean spectral density for a GaAs bulk with doping level of  $n=10^{13} \text{ cm}^{-3}$ , temperature  $T=80 \text{ K}$ , amplitude of excitation signal  $E_1= 7 \text{ kV/cm}$ ,  $E_2= 15 \text{ kV/cm}$  and

different frequencies. The autocorrelation curves show oscillations becoming more pronounced at higher mixed fields frequencies. The whole relaxation process becomes the longer the higher is the mixed fields frequencies.

For mixed fields frequencies  $\nu_1 < 400$  GHz and  $\nu_2 < 800$  GHz, the spectral density have the shape typical for the hot carrier conditions under the steady-state operation and the peak maximum slightly shift to higher frequencies. The frequency of the peak value of the spectral density has no direct relations with mixed fields frequencies. In contrast, at higher mixed frequencies the “steady-state” peak is replaced by two resonant peaks appearing at the mixed fields frequencies. For fixed frequencies, the amplitude of the resonant peaks are related to the amplitude of the excitation signal.

### CONCLUSION

This study reports some interesting results for bulk semiconductor under two large amplitude mixed electric fields. Our results indicated that, the intensities and the frequencies of the mixed fields can play an important role in the noise enhancement or suppression. Future work could be oriented to the investigation of the influence of different polarization of mixed fields in the noise behaviour in both bulk materials and submicron structures.

### REFERENCES

- [1] P. Shiktorov, E. Starikov, V. Gružinskis, L. Reggiani, L. Varani, J. C. Vaissière, *Monte Carlo calculation of electronic noise under high-order harmonic generation*, Appl. Phys. Letters **80**, 4759 (2002).
- [2] S. Perez, T. Gonzalez, *Monte Carlo analysis of voltage in sub-micrometre semiconductor structures under large-signal regime*, Semiconductor Science Technology **17**, 696 (2002).
- [3] P. Shiktorov, E. Starikov, V. Gružinskis, L. Reggiani, L. Varani, J. C. Vaissière, S. Perez, T. Gonzalez, *Monte Carlo simulation of electronic noise in semiconductor materials and devices operating under Cyclostationary conditions*, Journal of Computational Electronics **2**, 455 (2003).
- [4] P. Shiktorov, E. Starikov, V. Gružinskis, L. Reggiani, L. Varani, J. C. Vaissière, M. Zarcone, D. Persano Adorno, G. Ferrante, *Monte Carlo simulation of electronic noise under large-signal operation*, in *Noise in Physical systems and 1/f fluctuations*, Ed. Gijs Bosman, World Scientific, 677 (2001).
- [5] D. Persano Adorno, M. Zarcone and G. Ferrante, *High harmonic generation by two color field-mixing in n-type low-doped GaAs*, Phys. Status Solidi C **0**, 1488 (2003).
- [6] D. Persano Adorno, M. Zarcone and G. Ferrante, *High-Order Harmonic Emission from Mixed Fields in n-Type Low-Doped Silicon*, Laser Phys. **13**, 270 (2003).

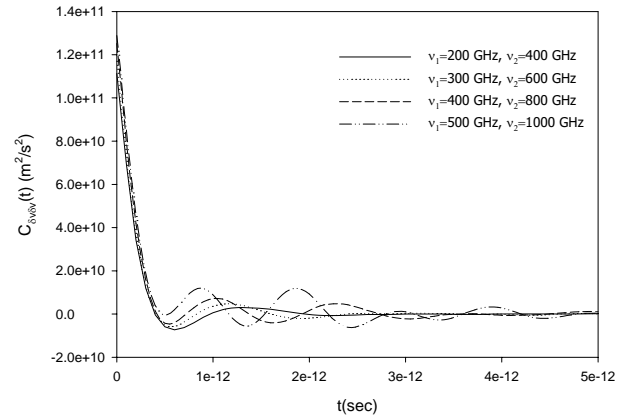


Fig. 1. Autocorrelation function of velocity fluctuations for a GaAs bulk with doping level of  $n=10^{13}$  cm<sup>-3</sup>, temperature  $T=80$  K, amplitude of excitation signal  $E_1=7$  kV/cm,  $E_2=15$  kV/cm and different frequencies

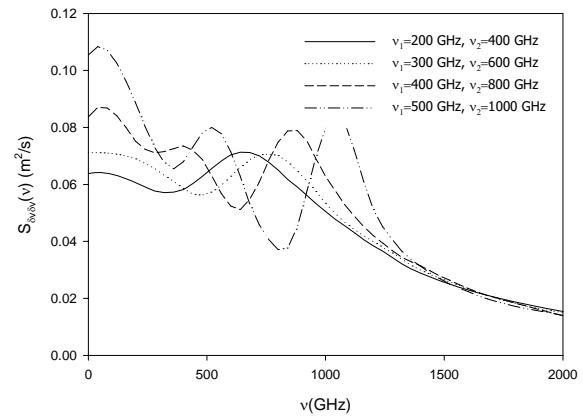


Fig. 2. Spectral density for the same case as in fig. 1

# Thermal Noise in Nanometric DG-MOSFET

P. Dollfus, A. Bournel, and J.E. Velázquez\*

Institut d'Electronique Fondamentale, CNRS UMR 8622, Université Paris-Sud 11, F-91405 Orsay, France

\*Dept. Física Aplicada, Universidad de Salamanca, E-37008 Salamanca, Spain

e-mail: js@usal.es

## DESCRIPTION OF DEVICES AND MODEL

In nano-scale FETs, the fluctuations in the number and position of dopants in the channel makes necessary the use of a transport model including the atomistic nature of ionized impurities and 3D Poisson solver. These fluctuations induce spreading in overall device performance and should be reflected on noise characteristics. The present work deals with the study of thermal noise in Single-Gate Fully-Depleted SOI (SG) and Double-Gate (DG) MOSFET using self-consistent 3D Monte Carlo simulation including the effect of discrete impurities in the channel.

The atomistic approach describing the electron-ion interaction in the presence of discrete impurities was presented in [1]. This model has been successfully used to study the effect of impurity position in the channel of 50 nm bulk-MOSFETs [2]. The influence of atomistic doping on noise in nano-resistors has been tackled in [3].

The simulated devices (Figs.1 and 2, where values  $L_G=25\text{nm}$ ,  $L_{ch}=17\text{nm}$ ,  $T_{Si}=5\text{nm}$ ,  $T_{OX}=1.1\text{nm}$ , and  $W=15\text{nm}$  apply to both structures) consist of ultra-thin SG and DG transistors (denoted as SG1 and DG1, respectively). They operate at  $V_{DD}=1\text{V}$ . Source/channel and channel/drain junctions are assumed to be abrupt with continuous doping of  $5 \times 10^{19}\text{cm}^{-3}$  in S/D regions. We consider the possible presence of a single residual P type impurity in the channel of DGMOS.

## RESULTS

Figures 3a and 3b show the typical effect of the presence of a single residual impurity on the transfer characteristics of both SG and DG MOSFET. We compare the case of channel without impurity (solid line) to the case of channel with one impurity in  $X_1=5.25\text{nm}$  (dashed line). In the case without impurity, the  $I_{on}$  current in DG1 ( $26\mu\text{A}$ ) is only 40% higher than in SG1 ( $I_{on}=18.5\mu\text{A}$ ). This apparently good result for SG is only due to strong short-channel effects which induce high output

conductance and also poor subthreshold behavior. The presence of a single impurity in the channel (dashed lines) perceptibly shifts the transfer characteristics and degrades  $I_{on}$ . This effect seems stronger in SG than in DG which is confirmed by Fig. 3b where the relative variation of  $I_{on}$  is plotted as a function of impurity position between  $X=0$  and  $X=17\text{nm}$ . The  $I_{on}$  degradation reaches 6% for DG and 10.5% for SG if the impurity is located near the source-end. An impurity located near the drain-end of the channel has a much smaller impact.

In order to evaluate the noise performance of both SG and DG transistors we first studied the current fluctuations for the same gate overdrive ( $V_{GS}=V_{DS}=V_{DD}$ ). We considered three structures: SG1, DG1 and a DG with one P-type residual impurity located near the source (DG2 from now on). From Fig. 4 it follows that for the same gate overdrive the spectral density of the gate current ( $S_{igig}(f)$ ) is considerably larger in SG1 than in both DG1 and DG2. In all the structures  $S_{igig}(f)$  exhibits the typical  $f^2$  dependence and the slower increase with frequency for the DG structures must be attributed to a partial cancellation of the fluctuations due to the double gate topology. On the contrary, the SG exhibits the lowest value of the spectral density of the drain current ( $S_{idid}(f)$ ) (Fig. 5). Preliminary calculations of noise figures point out a reduction of this key parameter in DG structures, in agreement with the observed behaviour of  $S_{igig}(f)$  and only little impact of the residual impurity (DG2). Further work is needed in order to extend the calculations to other regimes and fully establish if DG can effectively guarantee lower noise operation than SG ones and the weight of residual impurities in the channel.

## REFERENCES

- [1] S. Barraud, P. Dollfus, S. Galdin, P. Hesto, Solid-State Electron., **46**, 1061 (2002)
- [2] P. Dollfus, A. Bournel, S. Galdin-Retailleau, S. Barraud, P. Hesto, IEEE Trans. Electron Dev., **51**, 749 (2004)
- [3] P. Dollfus, J.E. Velázquez, A. Bournel, S. Retailleau, Proc. IWCE-10, J. Comput. Electron., **3**, 311 (2004)

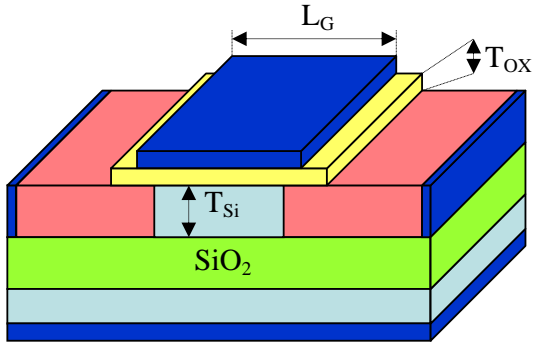
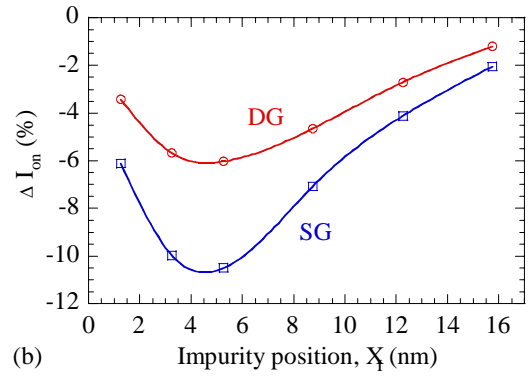


Fig. 1.a Schematic picture of the simulated SGMOS



(b)  $I_{on}$  versus lateral position  $X_I$  of a single impurity in the channel with respect to SG1 and DG1.

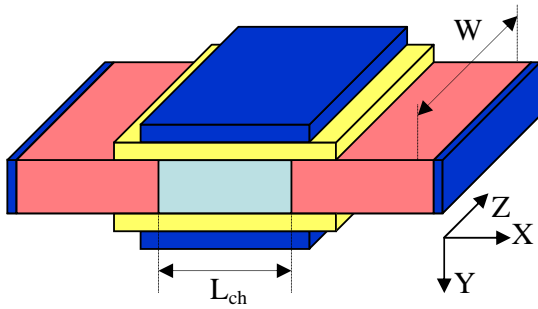


Fig. 2. Schematic picture of the simulated DGMOS

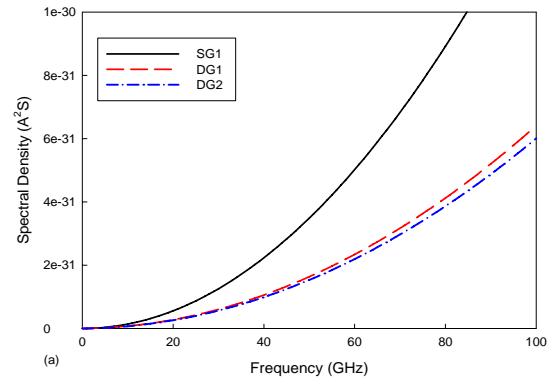


Fig. 4.  $S_{igig}(f)$  at the same value of the gate overdrive

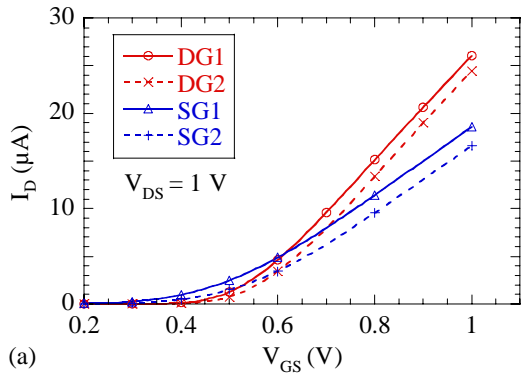


Fig. 3a.  $I_D$ - $V_{GS}$  characteristics of SG and DG MOS.

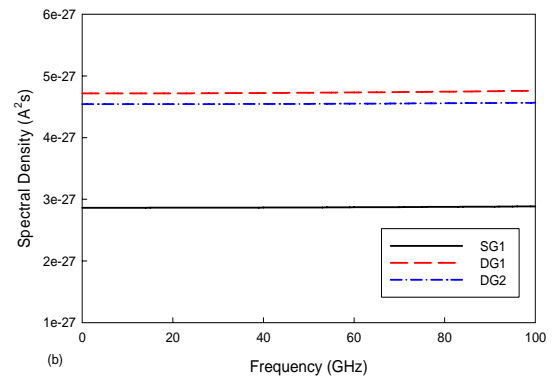


Fig. 5.  $S_{idid}(f)$  at the same value of the gate overdrive

# Full-Band Particle-Based Simulation of 85 nm AlInSb/InSb Quantum Well Transistors

N. Faralli<sup>1</sup>, J. Branlard<sup>1</sup>, S.M. Goodnick<sup>2</sup>, D.K. Ferry<sup>2</sup>, M. Saraniti<sup>1</sup>

<sup>1</sup>Illinois Institute of Technology, Chicago, IL 60616

<sup>2</sup>Arizona State University, Tempe, AZ 85287

email: faranic@iit.edu

## ABSTRACT

Due to its high electron mobility at room temperature and its narrow band gap of 0.17 eV, Indium Antimonide (InSb) has a great potential for very low power and extremely high frequency applications. Previous simulations [1] on a high-speed 200 nm quantum well transistor described in [2] predicted very good performance in terms of cut-off frequency and bias requirements. However, the need for high integration scale implies smaller transistors, such as the sub 50 nm SOI MOSFETs demonstrated by Intel [3]. The design of such devices requires the implementation of efficient and accurate CAD tools.

In this work, we model and simulate an 85 nm AlInSb/InSb quantum well transistor by using a particle-based, full-band simulator based on the Cellular Monte Carlo (CMC) method [4], [5]. The geometry and doping profile of the simulated transistor are shown in Fig.1. The layout consists of a 160 nm unintentionally doped Al<sub>0.2</sub>In<sub>0.8</sub>Sb substrate, a 20 nm thick InSb channel, a 5 nm thick spacer and a 45 nm thick Al<sub>0.2</sub>In<sub>0.8</sub>Sb barrier. A  $\delta$ -doped donor layer ( $1.3 \times 10^{12} \text{ cm}^{-2}$ ) is located between the spacer and the barrier to increase the electron mobility. The transistor has an 85 nm gate length and a source to drain separation of 750 nm. Fig.2 shows the conduction band profile obtained with this layout. The quantum well where the charge transport occurs can be easily seen in the channel.

The InSb electronic band structure (Fig.3) used for the simulations is computed using the empirical pseudopotential method [6]. Momentum-dependant

scattering rates are computed according to the work of Fischetti and Laux [7], and tabulated within the CMC framework, while the full phonon spectra are obtained with the 14-parameter empirical shell model [9]. Quantization effects are accounted for by using the effective potential technique [10].

The complete static and dynamic characterization of the simulated quantum well transistor as well as the noise analysis will be presented. The static and dynamic parameters, such as I-V curves or cutoff frequency ( $f_t$ ) will be extracted showing all the advantages of the Indium Antimonide technology; the cutoff frequency will be compared with traditional Si MOSFET, technology and a comparison with recently published experiments [11] will be shown as well.

## REFERENCES

- [1] J. Branlard, N. Faralli, T. Dutta-Roy, S.M. Goodnick, D.K. Ferry and M. Saraniti, *Springer Proceedings in Physics Series, in press*, (2006)
- [2] T. Ashley *et al.*, *Novel InSb-based Quantum Well Transistors for Ultra-High Speed, Low Power Logic Applications* IEEE, (2004).
- [3] R. Chau *et al.*, *IEDM Technical Digest*, 621, (2001).
- [4] M. Saraniti and S.M. Goodnick *IEEE Transactions on Electron Devices*, **47**, 1909, (2000).
- [5] M. Saraniti, J. Tang, S.M. Goodnick and S.J. Wigger *Mathematics and Computers in Simulations*, (2002)
- [6] J.R. Chelikowsky and M.L. Cohen, *Physical Review B*, **14**, 556, (1976).
- [7] M.V. Fischetti and S.E. Laux *Physical Review B*, **38**, 9721, (1988).
- [8] G. Gilat and L.J. Raubenheimer, *Physical Review*, **144**, 390, (1966).
- [9] M.V. Fischetti, N. Sano, S.E. Laux and K. Natori, *Proc SISPAD'96*, (1996).
- [10] D.K. Ferry, *Superlattices and Microstructures*, **27**, 61, (2000)
- [11] S. Datta *et al.*, in *International Electron Devices Meeting Conference*. IEEE, (2005)

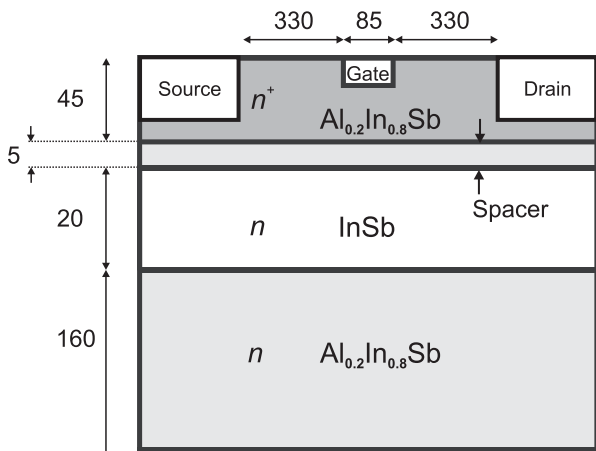


Fig. 1. Schematic layout of the simulated quantum well transistor. The dimensions are indicated in nm.

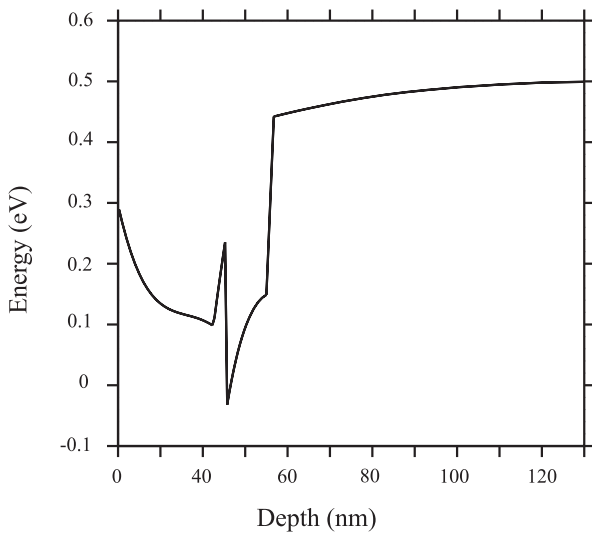


Fig. 2. Profile of the conduction band underneath the gate.

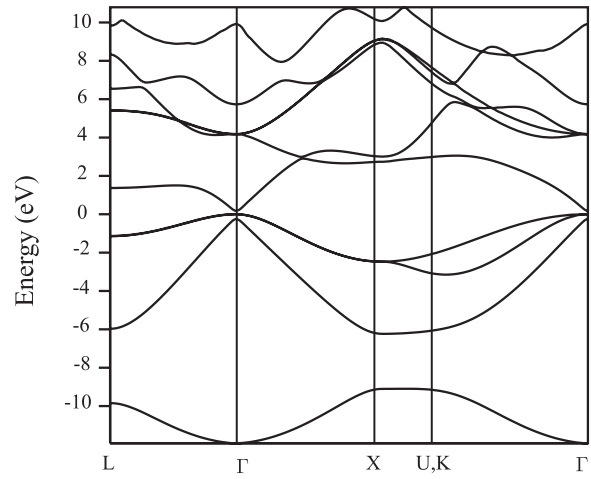


Fig. 3. Band structure of InSb computed using the empirical pseudopotential method.

# On the Impact of High- $\kappa$ Gate Stacks on Mobility: A Monte Carlo Study Including Coupled SO Phonon-Plasmon Scattering

G. Ferrari\*, J.R. Watling\*, S. Roy\*, J.R. Barker\*, P. Zeitoff†, G. Bersuker†, and A. Asenov\*

\*Device Modelling Group, Dept. Electronics & Electrical Engineering, University of Glasgow  
G12 8LT Glasgow, United Kingdom. E-mail: G.Ferrari@elec.gla.ac.uk

†SEMATECH, 2706 Montopolis Drive, Austin, Texas 78741, USA.

The scaling of MOSFET architecture, as dictated by the International Technology Road Map for Semiconductors, is reaching its limit. A major problem is the requirement for extremely thin gate oxides and high channel doping, the consequence being low device performance and high-gate leakage. The fulfilment of the next generation technology requires changes in terms of both new materials and architectures.

HfO<sub>2</sub> based high- $\kappa$  oxide materials have been identified as the most promising candidates to replace SiO<sub>2</sub> as insulators. A thickness of about  $t_{ox} \approx 0.7nm$  is required for SiO<sub>2</sub> gate oxides to obtain the required gate capacitance. The introduction of high- $\kappa$  dielectrics allow a physically thicker oxide, while maintaining the gate capacitance, to reduce the gate leakage current.

Our Monte Carlo (MC) simulator includes all the relevant scattering mechanisms necessary for the accurate modelling of electron transport in Silicon. In Fig.1 we show the results for the universal mobility curve in the case of SiO<sub>2</sub> as insulator.

It is well known [1, 2] that high- $\kappa$  materials lead to a mobility degradation due to the coupling of carriers in the channel to surface soft-optical (SO) phonons in the vicinity of the dielectric interface. These SO modes are induced by the longitudinal-optical (LO) phonons in the insulator. The coupling of LO phonons through long range polarisation fields to the free-carrier system gives rise to collective plasma modes and electron excitations. These hybrid modes (polarons) are affected by Landau damping [1].

We have introduced the new scattering mechanisms relevant for high- $\kappa$  dielectrics in our MC simulator. Landau damping is taken into account and plays an effective role at high momentum transfer, as shown in Fig.2. A comparison has been performed between the mobility of SiO<sub>2</sub> and HfO<sub>2</sub>. We have obtained the universal mobility curve for HfO<sub>2</sub> and the results are presented in Fig.3: the severe degradation in

mobility is evident.

The gate-stack system is further complicated by the presence of an interfacial layer at the interface between the channel and the insulator. The effect of this layer is twofold: on the one hand it will effectively mitigate the strong interaction with the SO phonon modes of the high- $\kappa$  dielectric, resulting in a higher mobility; on the other hand the introduction of a layer with a lower- $\kappa$  value lowers the total effective capacitance of the gate oxide. We have simulated a system with an interfacial layer of pure SiO<sub>2</sub>, obtaining the results presented in Fig.4. In Fig.5 we present a surface plot of our results for the mobility as a function of both the interfacial layer thickness and of the perpendicular field applied. The mobility increases when the SiO<sub>2</sub> layer becomes thicker, having as a limit the mobility of SiO<sub>2</sub>; moreover the agreement with the experimental data [3] is qualitatively and quantitatively excellent. The slight discrepancy that we observe at low interfacial layer thicknesses may result from the interfacial layer composition, being SiO<sub>x</sub> in nature rather than the SiO<sub>2</sub> at these thicknesses.

The composition of the interfacial layer is still to be understood. It may be an SiO<sub>2</sub> layer with oxygen deficiency, resulting in an SiO<sub>x</sub> layer, or an SiO<sub>2</sub> layer enriched by Hf [4], thus to be an Si<sub>1-x</sub>Hf<sub>x</sub>O<sub>2</sub> layer. We have performed simulations for the first case based on the experimental values of  $\kappa$  of the interfacial layer [3]. To understand the second case, we have simulated the universal mobility with an alloy of Si<sub>1-x</sub>Hf<sub>x</sub>O<sub>2</sub> as dielectric, and the results are presented in Fig.6.

## REFERENCES

- [1] M.V. Fischetti, S.E. Laux, J. Appl. Phys. **89**, 1205 (2001).
- [2] J.R. Watling, L. Yang, A. Asenov, J.R. Barker, S. Roy, IEEE Trans. Dev.& Mats Rel. **5**, 103 (2005).
- [3] G. Bersuker, private communication (2005).
- [4] M.H. Evans, M. Caussanel, R.D. Schrimpf, S.T. Pantelides, IEDM Tech. Dig., 611 (2005).
- [5] S. Takagi, A. Toriumi, M. Iwase, H. Tango, IEEE Trans. on Elec. Dev. **41**, 2357 (1994).

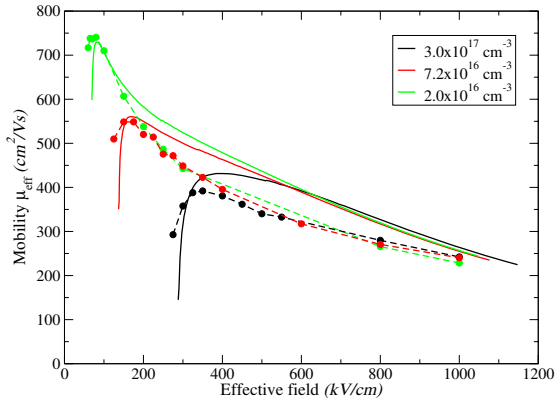


Fig. 1. Electron mobility in the inversion layer at 300 K versus effective field  $E_{eff}$ . The results are shown for three values of substrate doping concentration, as given in the legend. The solid lines are the experimental results from reference [5], and the dashed lines are the results obtained via the Monte Carlo simulator.

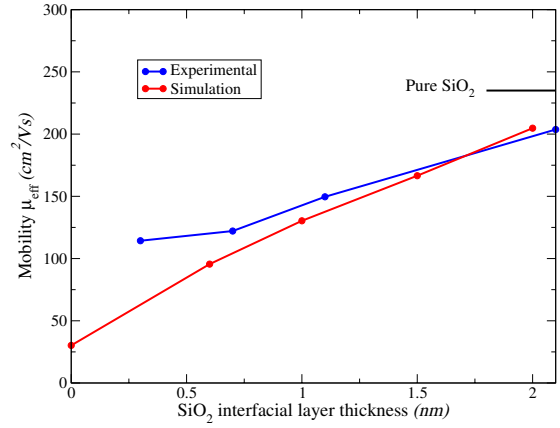


Fig. 4. Electron mobility in the inversion layer at 300 K as a function of the  $\text{SiO}_2$  interfacial layer thickness, for a field  $E_{eff}=1000 \text{ kV cm}^{-1}$ . As comparison is reported also the value for the mobility for pure  $\text{HfO}_2$ , corresponding to 0 nm layer thickness, and for pure  $\text{SiO}_2$ .

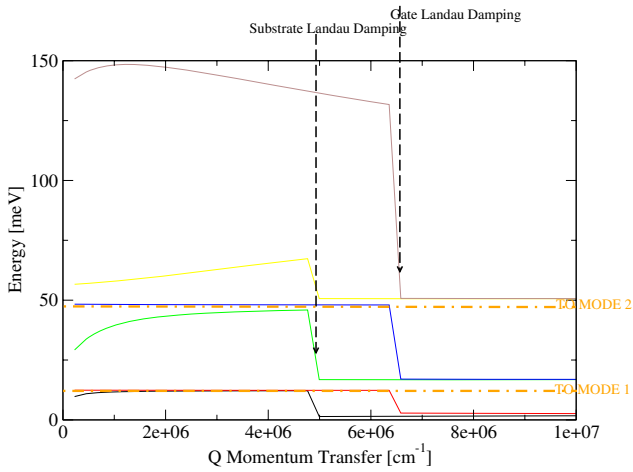


Fig. 2. Polaron dispersions considering Landau damping for the substrate and for the gate. The gate Landau damping is effective for higher momentum transfer since the doping is higher in that region.

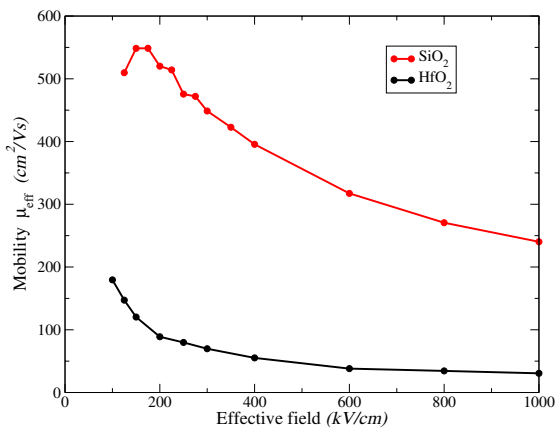


Fig. 3. Electron mobility in the inversion layer at 300 K versus effective field  $E_{eff}$ . The results reported are for  $\text{HfO}_2$  and  $\text{SiO}_2$ , as shown in the legend.

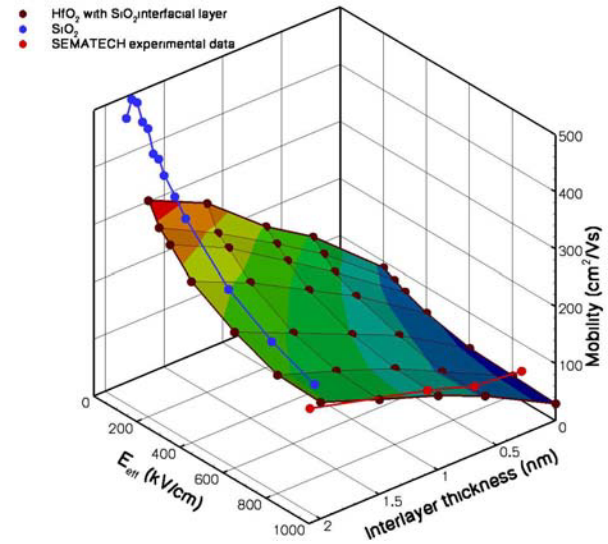


Fig. 5. Electron mobility in the inversion layer at 300 K for  $\text{HfO}_2$  versus effective field  $E_{eff}$  and the  $\text{SiO}_2$  interfacial layer thickness. The mobility for pure  $\text{SiO}_2$  and the experimental results [3] are also reported.

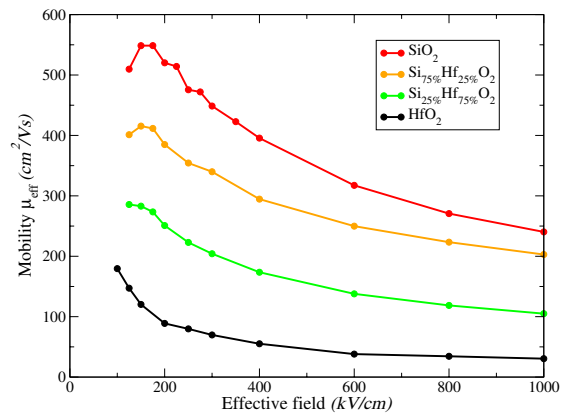


Fig. 6. Electron mobility in the inversion layer at 300 K versus effective field  $E_{eff}$  for an alloy of  $\text{Si}_{1-x}\text{Hf}_x\text{O}_2$  as given in the legend.

# Electron Injection Model for the Particle-Simulation of 3D, 2D and 1D Nanoscale FETs

E. Fernández-Díaz and X. Oriols

Departament d'Enginyeria Electrònica, Universitat Autònoma de Barcelona, Catalonia, Spain

e-mail: Xavier.Oriols@uab.es

## ABSTRACT

In nanoscale systems, electron transport becomes ballistic and the current and its fluctuations are mainly determined by the injection process. We present an electron injection model suitable for the semi-classical (or the quantum) Monte Carlo simulation of nanoscale field effect transistors (FET) with or without electron confinement. As an application, we show that the signal-to-noise ratio and the bit-error are drastically degraded because of electron confinement.

## INJECTION MODEL

For ballistic devices, the average current,  $\bar{I}$ , and the power spectral density at zero frequency of the current fluctuations,  $S(0)$ , are determined from the Binomial probability  $P(N, \tau)$  that  $N$  electrons ( $e^-$ ) are injected during a time interval  $\tau$  [1, 2]:

$$P(N, \tau) = \frac{M_\tau!}{N!(M_\tau - N)!} f(E)^N (1 - f(E))^{M_\tau - N} \quad (1)$$

where  $M_\tau = \tau/t_0$  is the number of attempts of injecting an  $e^-$  during  $\tau$  and  $f(E)$  is the contact Fermi distribution function. The time  $t_0$  between two successive injection attempts is [1, 3]:

$$t_0(y, z, k_x, k_y, k_z) \Big|_{3D} = \left( \frac{\hbar k_x \Delta y \Delta z \Delta k_x \Delta k_y \Delta k_z}{4\pi^3 m} \right)^{-1}$$

$$t_0(y, k_x, k_y) \Big|_{2D} = \left( \frac{\hbar k_x \Delta y \Delta k_x \Delta k_y}{2\pi^2 m} \right)^{-1} \quad (2)$$

$$t_0(k_x) \Big|_{1D} = \left( \frac{\hbar k_x \Delta k_x}{\pi m} \right)^{-1}$$

in 3D, 2D and 1D system, respectively. A mesh in the phase-space is defined (see Fig. 1). We assume that the electrons at the contact are only correlated with those electrons in the same contact due to the Pauli exclusion principle. As a test, we show that the one-channel Landauer current [4] and the general Büttiker noise expression [4] are exactly recovered with our particle-injection model.

## EFFECT OF ELECTRON CONFINEMENT ON THE CURRENT AND NOISE PROPERTIES OF ANALOG AND DIGITAL APPLICATIONS

The injection model, defined in (1) and (2), can be used to directly determine the current and noise of ballistic FETs with different dimensionality. The Fano factor  $F$  ( $S(0) = F \cdot 2 \cdot e \cdot \bar{I}$ ) is the standard parameter to classify shot noise [1, 7]. In fig. 2, we compute the Fano factors for three FET geometries as a function of the contact Fermi level. In Fig. 3, we show that  $e^-$  confinement can cause the output signal-to-noise ratio,  $P_S / P_N = \bar{I}^2 / (S(0) \cdot \Delta f)$ , to decrease because of the reduction in the number of states available for electron transport. The  $P_S / P_N$  of 3D (Bulk-) and 1D (quantum wire-) FETs can differ by 40 dB with  $\Delta f = 1$  MHz. Smaller devices are noisier.

In Fig. 4, the noise performance of a CMOS inverter is quantified by the bit error probability (BER). For any input logic level, one of the transistors is on opened-channel conditions with zero averaged current but with thermal noise. The BER of 3D (Bulk-) and 1D (quantum wire-) FETs can differ by more than 25 dB (see fig. 4). These results, which only consider the unavoidable thermal and shot-noise that are present in expression (1) and (2), predict important drawbacks for noise properties of 2D (quantum well-) or 1D (quantum wire-) FETs.

## CONCLUSION

A general electron injection model for the device simulation of the transport properties of FETs with and without electron confinement has been presented. Our injection model generalizes previous works of Gonzalez *et al.* [5] and Oriols *et al.* [6, 7]. The model exactly reproduces the (Landauer) average current and the (Büttiker) shot-noise. We have shown that for ballistic nanoscale FETs the signal-to-noise ratio and the bit-error can be drastically affected by electron confinement, which indicates drawbacks for aggressively scaled FETs.

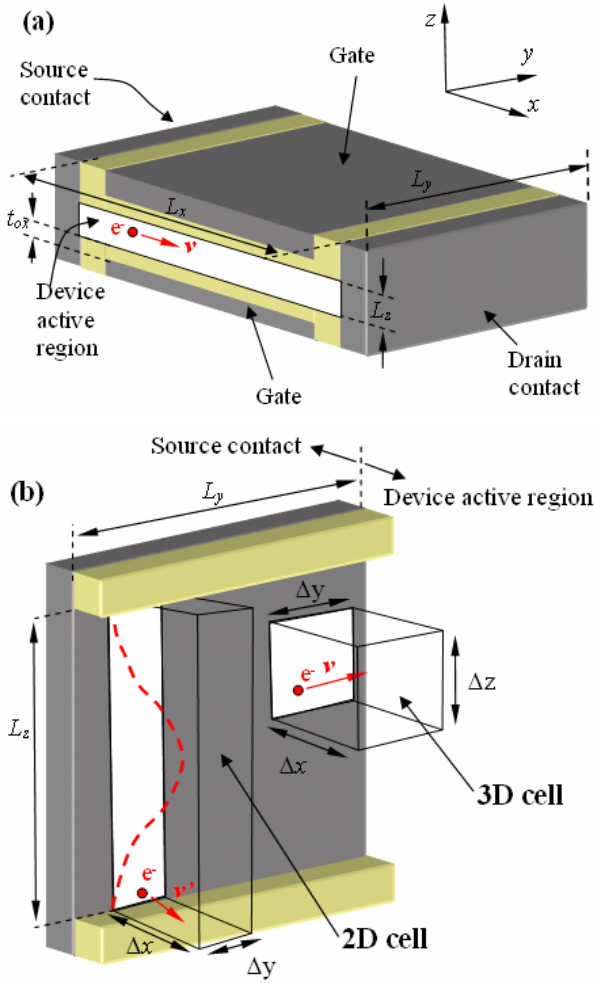


Fig. 1. (a) Schematic representation of a nanoscale double gate FET. The transversal dimensions  $L_y$  and  $L_z$  of the active region determine electron confinement. (b) Schematic representation of the 3D cell and the 2D cell used in the text (equation 2) to describe the injection of electrons through the  $L_y \cdot L_z$  surface. In dashed line, for a 2D cell, schematic representation of the distribution of electrons in the direction  $z$  due to confinement

#### REFERENCES

- [1] E. Fernández-Díaz and X. Oriols (submitted).
- [2] V.Sverdlov, X.Oriols and K.Likharev, IEEE transactions on Nanotechnology, 2(N1), 59 (2003).
- [3] X.Oriols, Nanotechnology, 15, S167 (2004).
- [4] Ya. M. Blanter and M. Büttiker, Phys. Rep. 336, 1 (2000).
- [5] T. González, D. Pardo, Solid-State Electr. 39, 555 (1996).
- [6] X.Oriols, IEEE Trans. on Elect. Devices, 50 1830 (2003).
- [7] X. Oriols, A. Trois and G. Blouin, Appl. Phys. Lett., 85 3596 (2004).

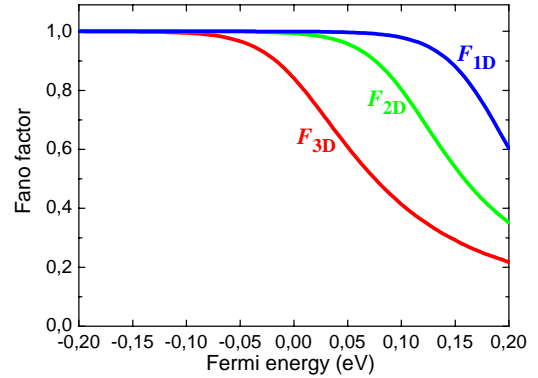


Fig. 2. Fano factors,  $F$ , for the 3D, 2D and 1D nanoscale FETs considered in this work. The transistor volumes are  $15 \text{ nm} \times 10 \text{ nm} \times 8 \text{ nm}$ ,  $15 \text{ nm} \times 10 \text{ nm} \times 2 \text{ nm}$  and  $15 \text{ nm} \times 5 \text{ nm} \times 2 \text{ nm}$  for the 3D (Bulk-), 2D (quantum well-) and 1D (quantum wire-) device active regions, respectively

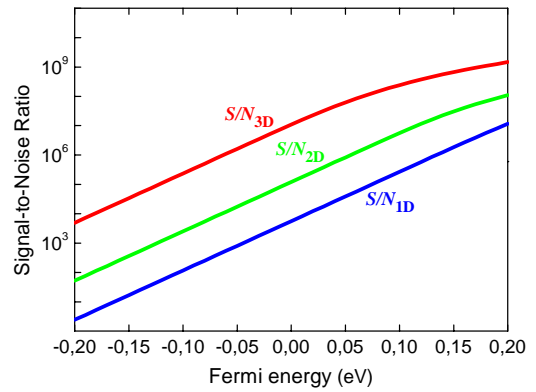


Fig. 3. Signal-to-noise ratios,  $P_S / P_N$ , for the 3D, 2D and 1D nanoscale transistors of Fig. 2.

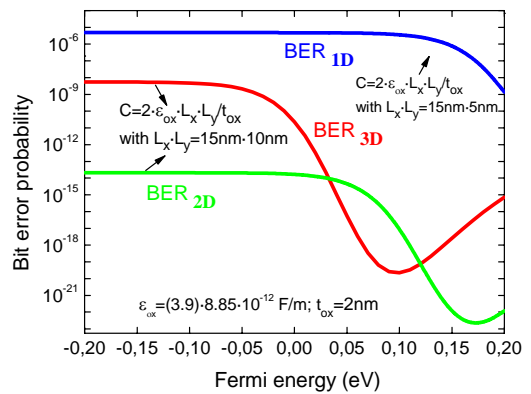


Fig. 4. Bit-error probabilities, BER, for the 3D, 2D and 1D nanoscale FETs mentioned in figure 2.

# Free-Carrier Grating due to the Optical Phonon Emission in InP $n^+nn^+$ Structures

V. Gružinskis, E. Starikov, P. Shiktorov,  
Semiconductor Physics Institute, A. Goštauto 11, LT 01108 Vilnius, Lithuania  
e-mail: viktor@pav.pfi.lt

The scattering by optical phonons takes a special place in hierarchy of scattering mechanisms in semiconductors. At low temperatures when the optical phonon energy  $\hbar\omega_0$  considerably exceeds the carrier thermal energy the scattering by optical phonons is mainly accompanied by optical phonon emission. Due to the constant value of energy  $\hbar\omega_0$  the optical phonon emission rate dependence on energy has a threshold. At such conditions the periodic motion of carrier ensemble in momentum space is possible. This motion can lead to the microwave power generation as it was shown for bulk InP theoretically and confirmed experimentally (see, e.g. [1] and references therein). Recently the modelling of electron transport in indium nitride based  $n^+nn^+$  structures when optical phonon emission is dominating scattering mechanism shows the possibility of the cyclic real-space motion of carrier ensemble which leads to the formation of the free-carrier grating (FCG) in the n-region of the structure [2]. The aim of this report is to simulate the electron transport in InP  $n^+nn^+$  structures in the conditions when FCG formation can be expected [2].

The calculations of electron transport in  $n^+nn^+$  InP structures are performed by simultaneous solution of coupled Boltzmann and Poisson equations by Monte Carlo particle (MCP) technique [3]. The InP band and material parameters of a spherically symmetric nonparabolic conduction band are taken from [3]. The doping of simulated 0.02-5.00-0.02  $\mu\text{m}$   $n^+nn^+$  InP structures is  $n = 10^{15} \text{ cm}^{-3}$  and  $n^+ = 10^{17} \text{ cm}^{-3}$ . All the calculations are made at 10 K and applied voltage  $U = 0.3 \text{ V}$  to the structure with the n-region length  $L = 5 \mu\text{m}$ .

Figures from 1 to 4 demonstrate the FCG in real space due to periodic motion of electrons under low temperature optical phonon emission in n-region. A low energy electron injected from cathode

contact is accelerated by field up to optical phonon energy and loose the energy and velocity after optical phonon emission. The process is repeated until the electron leaves the n-region through the anode contact. So the electron trajectory consists of flight and stop, where electron emits optical phonon, regions. The stop regions coincide with the concentration maxima. The number of stop regions is integer part of  $eU/\hbar\omega_0$ , where  $e$  is electron charge. The impedance  $Z(f)$  of InP structure is calculated simulating by MCP technique the current response to periodic voltage. The frequency behaviour of the real and imaginary parts of impedance,  $\text{Re}Z$  and  $\text{Im}Z$ , respectively, is demonstrated in Fig. 5. For comparison, Fig. 5 also shows  $Z(f) = [en\mu(f)/L + i2\pi fC_L]^{-1}$  obtained for the considered diode with the length  $L$  and geometrical capacitance  $C_L$  from small-signal mobility  $\mu(f)$  calculated by MC simulation of bulk material subjected to the electric field equal to  $U/L$  in the n-region (i.e. without the grating).

In Fig. 6 the spectral density of current fluctuations (noise) in InP structure at a constant voltage  $U$  is shown. The noise peak at 0.345 THz frequency coincides with the high frequency edge of negative  $\text{Re}Z$  values (see Fig. 5).

## REFERENCES

- [1] L. Varani, J. C. Vaissiere, E. Starikov, P. Shiktorov, V. Gružinskis, L. Reggiani, and J. H. Zhao., *Monte Carlo Calculations of THz Generation in Nitrides*, physica status solidi (a) **190**, 247 (2002).
- [2] V. Gružinskis, P. Shiktorov, E. Starikov, L. Reggiani, L. Varani and J. C. Vaissiere., *Free-carrier grating and terahertz generation from InN  $n^+nn^+$  structures under streaming plasma instability*, Semiconductor Science and Technology **19**, s173 (2004).
- [3] V. Mitin, V. Gruzinskis, E. Starikov, and P. Shiktorov, *Submillimeter wave generation and noise in InP diodes*, Journal of Applied Physics **75**, 935 (1994).

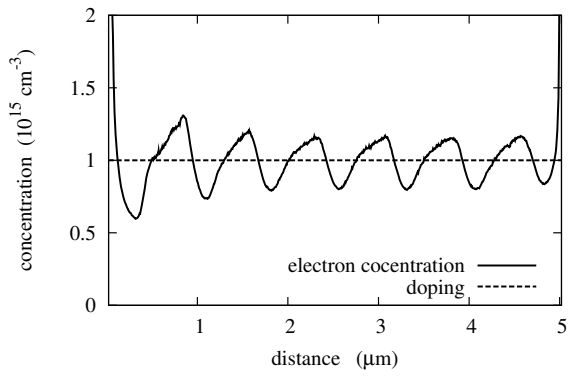


Fig. 1. Electron concentration profile in n-region of simulated InP  $n^+nn^+$  structure.

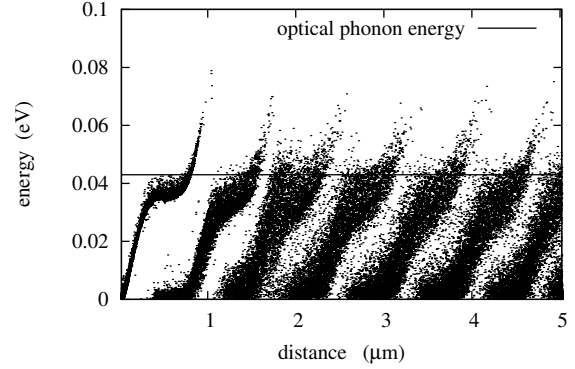


Fig. 4. Positions of simulated particles in energy - coordinate plane in n-region of InP  $n^+nn^+$  structure.

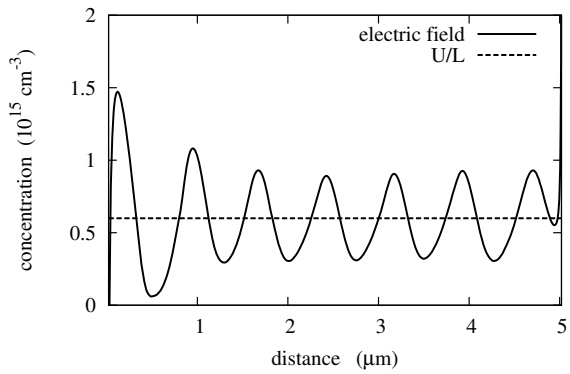


Fig. 2. Electric field profile in n-region of simulated InP  $n^+nn^+$  structure.

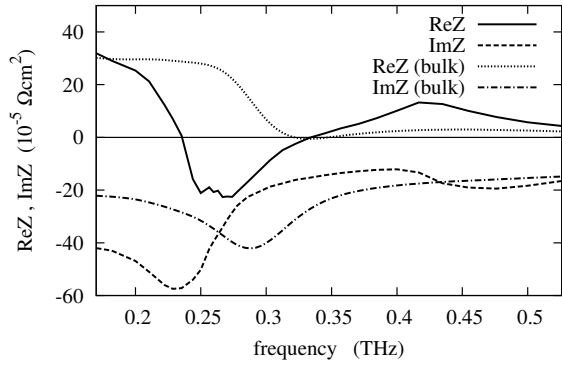


Fig. 5. Impedance real  $ReZ$  and imaginary  $ImZ$  part spectra of simulated InP  $n^+nn^+$  structure. For comparison MC results for bulk InP are presented.

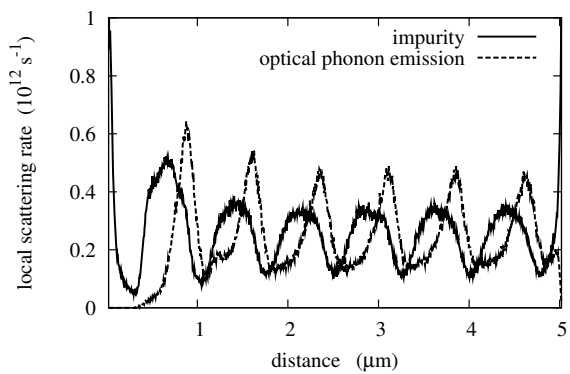


Fig. 3. Impurity and optical phonon emission local scattering rate profiles in n-region of simulated InP  $n^+nn^+$  structure.

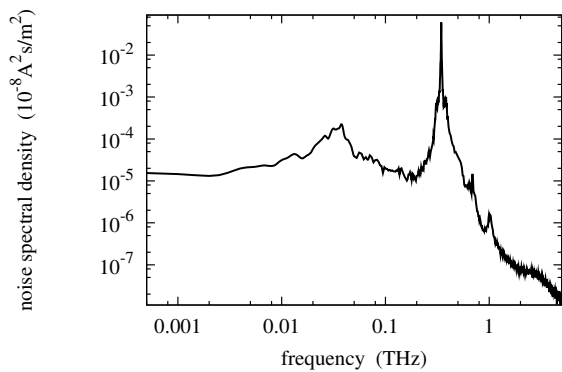


Fig. 6. Spectral density of current fluctuations (noise) in simulated InP  $n^+nn^+$  structure at applied constant voltage.

# 3D Monte-Carlo Device Simulations Using an Effective Quantum Potential Including Electron-Electron Interactions

Clemens Heitzinger, Christian Ringhofer, Shaikh Ahmed\*, and Dragica Vasileska\*  
Department of Mathematics, Arizona State University, Tempe, AZ 85287, USA

\*Department of Electrical Engineering, Arizona State University, Tempe, AZ 85287, USA  
E-mail: Clemens.Heitzinger@asu.edu

## THE EFFECTIVE QUANTUM POTENTIAL

As device sizes decrease, the standard mean-field theory for the treatment of electron-electron forces becomes less applicable. Motivated by this fact, effective quantum potentials have been established as a proven way to include quantum-mechanical effects into Monte-Carlo (MC) device simulations. The pseudo-differential operator for the effective quantum potential we build on here is based on a perturbation theory around thermal equilibrium [1], [2] and was first derived in [3]. The approach was generalized in [4] to the general  $N$ -body problem, i.e., particle-particle interactions. In this work we present 3D MC device simulation results obtained from this formulation.

## SIMULATION RESULTS AND DISCUSSION

The effective quantum potential is shown in Fig. 1 and Fig. 2. The SOI device used here (Fig. 3) has the following specifications: gate length is 10nm, the source/drain length is 15nm each, the thickness of the silicon on insulator (SOI) layer is 7nm, with p-region width of 10nm makes it a fully-depleted device under normal operating conditions, the gate oxide thickness is 0.8nm, the box oxide thickness is 140nm, the channel doping is uniform at  $1.45 \cdot 10^{10} \text{cm}^{-3}$  (intrinsic/undoped), the doping of the source/drain regions equals  $5 \cdot 10^{19} \text{cm}^{-3}$ , and the gate is assumed to be a metal gate with a work-function adjusted to 4.188. The device is designed in order to achieve the ITRS performance specifications for the year 2016.

The distribution function (Fig. 4) shows that inclusion of quantum potential leads to an increase

of the high energy tail of the electron distributions at the transition from channel to drain.

The simulated output characteristics are shown in Fig. 5 with an applied gate bias of 0.4V. Noticeable is the reduced short-channel effects even with an extremely low channel doping density. Inclusion of quantum potential significantly reduces the drive current and transconductance and increases the device threshold voltage as observed from the slope of the linear region. One can also see that the impact of quantization effects reduces as the drain voltage increases (increase in energy) because of the growing bulk nature of the channel electrons.

## CONCLUSION

We showed the applicability of a novel effective quantum potential not using any fitting parameters for the  $N$ -body problem to 3D MC device simulations. The inclusion of particle-particle interactions, as opposed to the classical Coulomb potential, shows a notable difference in the current-voltage characteristics.

## ACKNOWLEDGMENT

The authors acknowledge support by the Austrian Science Fund (Fonds zur Förderung der wissenschaftlichen Forschung, FWF) and through National Science Foundation grant DECS-0218008.

## REFERENCES

- [1] I. Gasser and A. Jünger. *Z. Angew. Math. Phys.*, 48:45–59, 1997.
- [2] C.L. Gardner and C. Ringhofer. *Physical Review*, E53:157–167, 1996.
- [3] C. Ringhofer, C. Gardner, and D. Vasileska. *Inter. J. on High Speed Electronics and Systems*, 13(3):771–801, 2003.
- [4] C. Heitzinger and C. Ringhofer. *Journal of Computational Electronics*, 2005. (Submitted for publication).

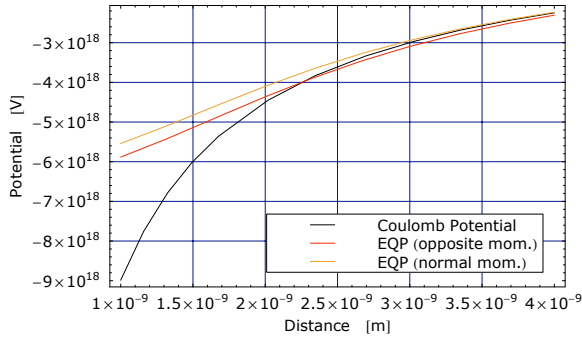


Fig. 1. The effective quantum potential (EQP) compared the Coulomb potential. For the EQP the momentum vectors are  $(p,0,0)$  and  $(-p,0,0)$  for the opposite momentum curve and  $(p,0,0)$  and  $(0,p,0)$  for the normal momentum case where  $p := 5.40275 \cdot 10^{-26}$ .

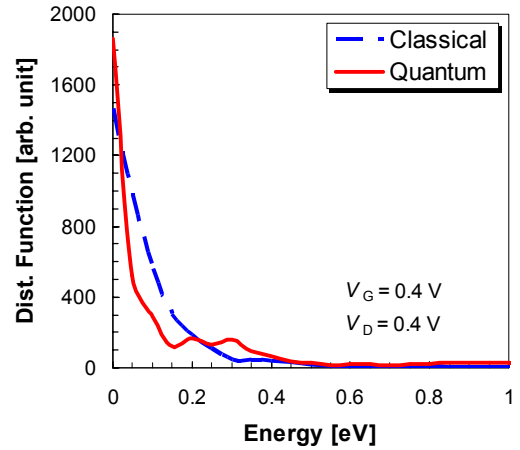


Fig. 4. Distribution function.

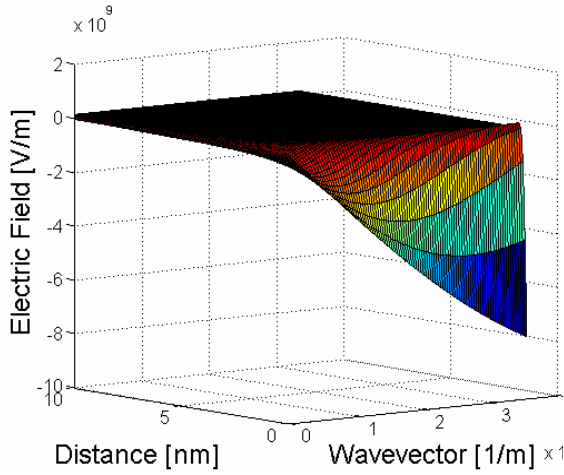


Fig. 2. The effective quantum potential due to the barrier.

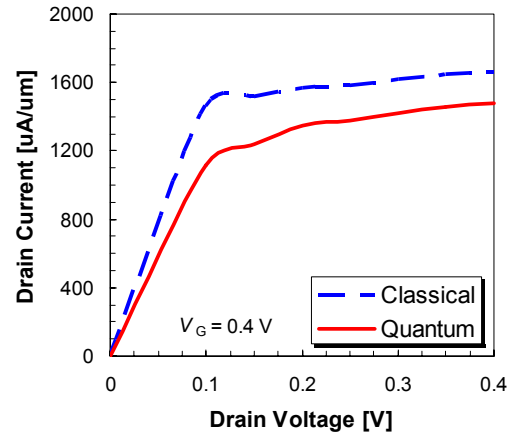


Fig. 5. Current-voltage characteristics for a gate bias of 0.4V.

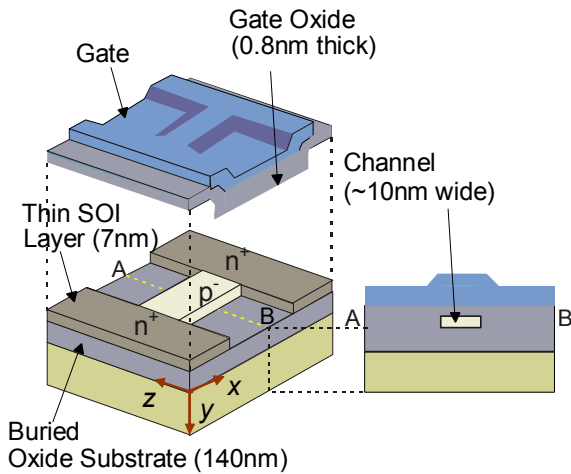


Fig. 3. The structure of the simulated 3D device.

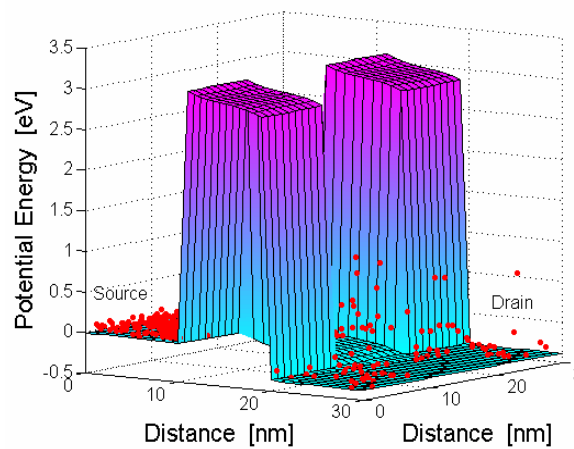


Fig. 6. The electron distribution in the device during the simulation.

# Pearson versus Gaussian Effective Potentials for quantum corrected Monte-Carlo simulation

M.-A. Jaud<sup>1,2,3</sup>, S. Barraud<sup>1</sup>, P. Dollfus<sup>3</sup>, H. Jaouen<sup>2</sup>, G. Le Carval<sup>1</sup>

<sup>1</sup>CEA-LETI/D2NT/LSCDP, 17 rue des Martyrs, 38059 Grenoble, France

<sup>2</sup>STMICROELECTRONICS, 38926 Crolles, France, <sup>3</sup>IEF, CNRS-UPS, 91405 Orsay, France

E-mail : marie-anne.jaud@cea.fr

These last years, the Gaussian Effective Potential (GEP) has become a very attractive approach for assessing the impact of quantum effects on the classical potential. This formalism was already used for including quantum effects into the simulation of ultra-short channel MOSFETs [1-4]. However, discussions on the validity limit of this method have been recently reported [3-4]. They highlight that, even if the GEP model is able to conserve the Schrödinger-Poisson (SP) inversion charge, the Gaussian function is unsuitable for reproducing the carrier density profile. Our motivation is here to demonstrate the ability of a more general concept based on the Pearson Effective Potential (PEP) to accurately reproduce both the SP electron density profile and the inversion charge.

The GEP induces an overestimation of the carrier repulsion at SiO<sub>2</sub>/Si interfaces [1-4], which is due to the fact that the electron presence probability is represented by a Gaussian function all along the silicon film thickness [4]. At SiO<sub>2</sub>/Si interfaces, this description is not realistic with regard to SP. This preliminary study leads us to propose a new Effective Potential formulation using a function inspired by the shape of the SP wave functions. As the GEP formalism, our PEP formalism is based on the convolution of the Poisson potential by a function representing the non zero-size of the electron wave-packet [1]. Our 1D PEP is defined as:

$$\text{PEP}(x, y) = \int_{-T_{\text{ox}}}^{T_{\text{Si}}+T_{\text{ox}}} \left[ V_p(x', y) * \text{Pearson IV}(E_{x,y}, T_{\text{Si}}, x') \right] dx'$$

where  $V_p(x', y)$  is the potential energy,  $T_{\text{Si}}$  and  $T_{\text{ox}}$  are the silicon film and oxide thicknesses,  $E_{x,y}$  is the local electrical field in the confinement direction. The first four moments of the Pearson IV distribution are then calculated as a function of  $T_{\text{Si}}$  and  $E_{x,y}$  so as to qualitatively follow the evolution of

squared modulus of the first level Schrödinger's wave function. Figure 1 compares the Gaussian and Pearson IV distributions for different carrier positions in the confinement direction of a double-gate device. The shape of the Pearson IV distribution close to the SiO<sub>2</sub>/Si interfaces is more realistic than that observed with the Gaussian one.

To validate our PEP formalism, a long double-gate nMOSFET has been simulated with  $N_A = 10^{16} \text{ cm}^{-3}$ ,  $0.5 \text{ nm} \leq T_{\text{ox}} \leq 2 \text{ nm}$  and  $5 \text{ nm} \leq T_{\text{Si}} \leq 10 \text{ nm}$ . Simulations have been performed for a large range of effective field ( $10^5 \text{ V.cm}^{-1} \leq E_{\text{eff}} \leq 10^6 \text{ V.cm}^{-1}$ ). Figures 2 to 5 show the electron density profiles calculated for two different effective fields in various double-gate devices. In all the cases, an excellent agreement is obtained between SP and PEP results with an average error on the inversion charge of about 3.2%. As the SP electron density profile is accurately reproduced, the Poisson potential is now correct. Figure 6 shows the Poisson potential resulting from semi-classical Monte-Carlo, SP, PEP simulations and the Effective Potential for  $T_{\text{Si}} = 10 \text{ nm}$  and  $E_{\text{eff}} = 10^6 \text{ V.cm}^{-1}$ .

To conclude, we demonstrate that our PEP approach is able to accurately reproduce the SP electrostatic confinement effects in various double-gate MOSFETs. The calculated potential inside the silicon film is correct and can be used for improved quantum corrected Monte-Carlo simulation. The extension of the PEP model for  $T_{\text{Si}} = 20 \text{ nm}$  is currently underway.

- [1] D. K. Ferry, R. Akis, D. Vasileska, IEDM, 287-290 (2000)
- [2] J.R. Watling, A.R. Brown, A. Asenov, D.K. Ferry, Proc. SISPAD (2001)
- [3] P. Palestri, S. Eminent, D. Esseni, C. Fiegna, E. Sangiorgi, L. Selmi, Solid-State-Electronics, 49, pp.727-732, (2005)
- [4] M.-A. Jaud, S. Barraud, P. Dollfus, H. Jaouen, F. De Crecy, G. Le Carval, accepted for publication in JCE (2005)

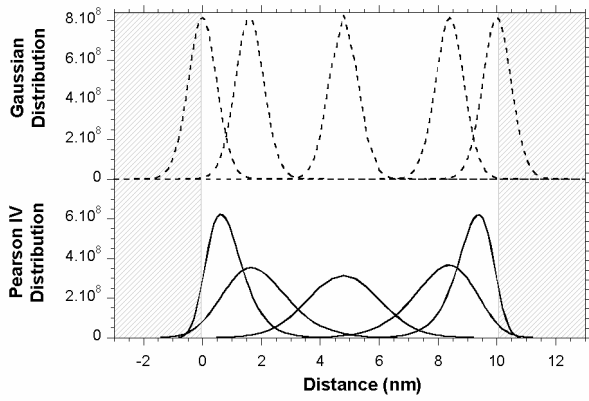


Fig. 1. Gaussian and Pearson IV distributions for different carrier positions in a double-gate device with  $T_{Si} = 10$  nm.

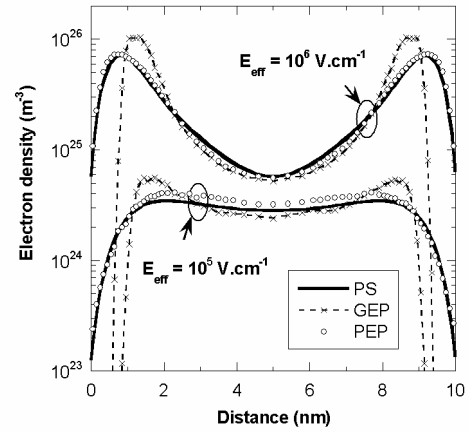


Fig. 4. Electron density in a double-gate nMOSFET with  $T_{Si} = 10$  nm and  $T_{ox} = 0.5$  nm using SP, GEP and our PEP.

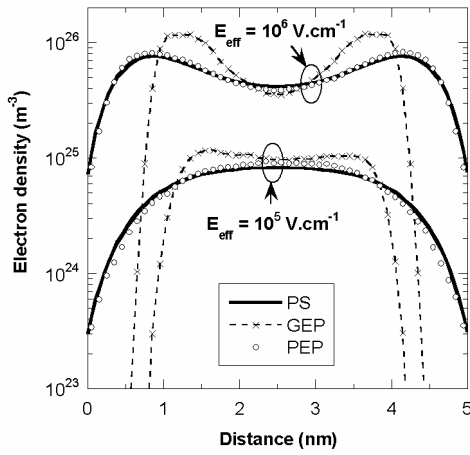


Fig. 2. Electron density in a double-gate nMOSFET with  $T_{Si} = 5$  nm and  $T_{ox} = 1$  nm using SP, GEP and our PEP.

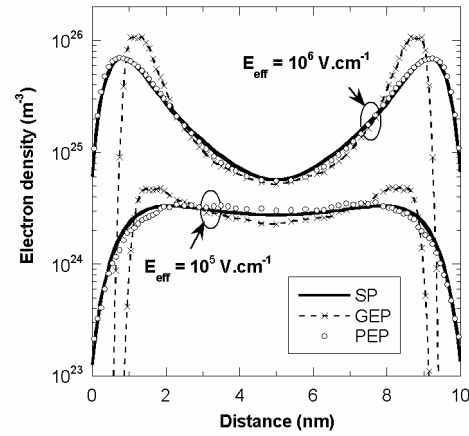


Fig. 5. Electron density in a double-gate nMOSFET with  $T_{Si} = 10$  nm and  $T_{ox} = 2$  nm using SP, GEP and our PEP.

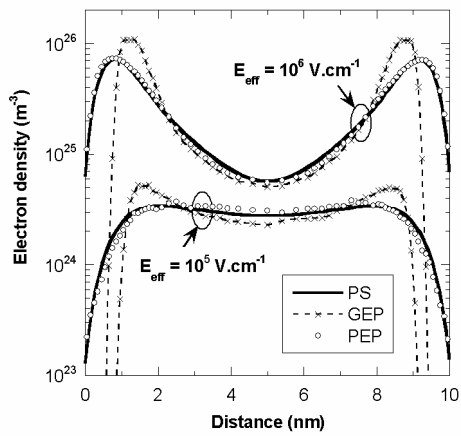


Fig. 3. Electron density in a double-gate nMOSFET with  $T_{Si} = 10$  nm and  $T_{ox} = 1$  nm using SP, GEP and our PEP.

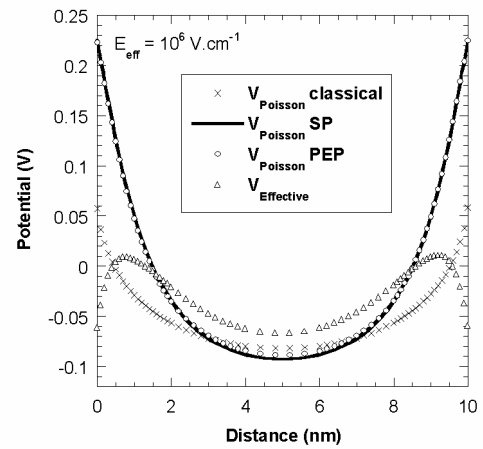


Fig. 6. Poisson Potential resulting from semi-classical Monte-Carlo, SP, PEP simulations and Effective Potential in a double-gate device with  $T_{Si} = 10$  nm,  $T_{ox} = 1$  nm.

# Atomistic Modeling for Boron Up-Hill Diffusion After Ge Pre-Amorphization

Joong - sik Kim and Taeyoung Won

Department of Electrical Engineering, School of Engineering, Inha University

National IT Research Center for Computational Electronics

253 Yonghyun-dong, Nam-gu, Incheon 402-751, Korea

Phone: +82-32-875-7436 Fax: +82-32-862-1350 E-mail: {kjs, [twon@hseel.inha.ac.kr](mailto:twon@hseel.inha.ac.kr)}

## INTRODUCTION

Pre-amorphizing implants (PAI) are a promising option for forming highly doped B ultra shallow junctions [1]. With increasingly stringent requirement on source/drain extension junction depth scaling in CMOS devices, pre-amorphization has also been used prior to low energy implant to generate shallower junction depth [2].

In this work, we investigated the effect of Ge pre-amorphization on low energy B implant and up-hill diffusion mechanism due to excess interstitials at EOR using Kinetic Monte Carlo (KMC) for the first time

## RESULTS and DISCUSSTION

For investigating Ge PAI effect, Ge implantation is performed with dosage varying from  $5 \times 10^{12}$  to  $5 \times 10^{15}/\text{cm}^2$  and with an implantation energy varying from 10 to 50 keV. Further, B implantation is performed with dosage of  $1 \times 10^{15}/\text{cm}^2$  and implantation energy 0.5 and 1.5 keV.

Figure 1 shows the comparison KMC data with SIMS data for accounting the Ge PAI effect. In this figure, diffusion profiles are in good agreement with experimental data. Figure 2 shows the diffusion profile with varying Ge implantation energy. We can see that implantation energy of Ge does negligible influence on the uphill-diffusion of boron. In addition, figure 3 shows the diffusion profile with varying dose of Ge. With increasing the dose of Ge  $5 \times 10^{12}$  to  $5 \times 10^{15}/\text{cm}^2$ , uphill-diffusion effect also increases.

One of the up-hill diffusion mechanisms in PAI silicon is the flux of self-interstitials from the EOR defect band. During thermal annealing, point defects vanish from amorphous region by I-V

recombination. As a consequence, interstitial flux to the surface occurs and this phenomenon is an important effect of "up-hill" diffusion which reduces boron TED and minimizes the junction depth [1]. Figure 4 explains this mechanism. In order to confirm this mechanism, we simulate self-interstitials in terms of very low time scale. Figure 5 shows the interstitial profile without Ge PAI and figure 6 shows the interstitial profile with Ge PAI. In figure 6, we can see the difference of surface density of interstitials with bulk density of interstitials, but not in figure 5. Therefore, the flux of interstitials towards surface is observed in the Ge PAI.

In our KMC simulations, the parameters were obtained either from *ab-initio calculation* or from experimental data. Figure 7 shows the migration and binding energies employed in this study. [3, 4].

## CONCLUSION

In this work, the boron diffusion in the Ge pre-amorphized silicon was simulated in the atomistic scale. Our KMC simulation profiles of boron in PAI silicon were compared with experimental data and excellent agreement was confirmed. Also we can see the key mechanism of uphill diffusion through simulating interstitials using KMC method. Furthermore, we also confirmed that boron TED could be reduced from using the Ge PAI. These techniques are useful for reducing boron TED and thus seem to be very effective for obtaining the ultra shallow junction for PMOS devices.

## ACKNOWLEDGEMENT

This work was supported partly by the Korean Ministry of Information & Communication (MIC) through the Information Technology Research

Center (ITRC) Program supervised by IITA, and partly by the Korean Ministry of Science and Technology (MOST) through the International cooperative research program by KISTEP.

REFERENCES

[1] N.E.B. Cowern, et al., Proceeding MRS Symposium on CMOS Front-End Materials and Process Technology (2003) 21~25.  
 [2] H.-J. Li, et al., IEEE Electron Device Lett. 23 (2002) 646~648.  
 [3] S. K. Thesis, et al., Thin Solid Films. (2000) 219~230  
 [4] N. E. B. Cowern, et al., Phys. Rev. Lett. 82 (1999) 4460~4463.

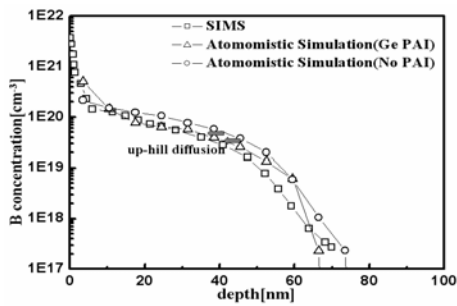


Fig. 1. Comparison with SIMS data and up-hill diffusion effect; boron 0.5 keV,  $1 \times 10^{15}/\text{cm}^2$ , germanium 10 keV,  $1 \times 10^{15}/\text{cm}^2$  and 1000 °C 10s (RTA).

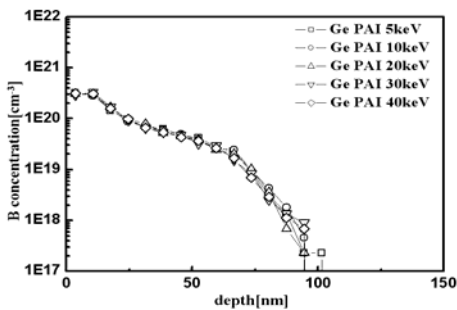


Fig. 2. Boron profiles are compared with Ge PAI wherein energy varies from 5 keV ~ 40 keV ; boron 1.5 keV,  $1 \times 10^{15}/\text{cm}^2$  and 1000 °C 10s (RTA).

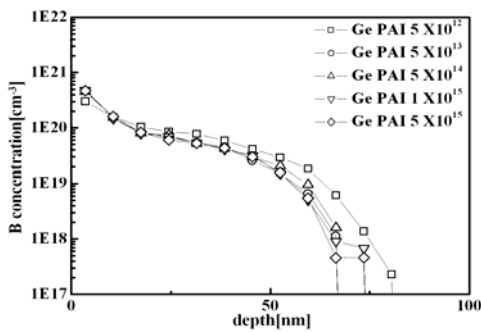


Fig. 3. Boron profiles are compared with Ge PAI wherein dosage of Ge varies from  $5 \times 10^{12}/\text{cm}^2 \sim 5 \times 10^{15}/\text{cm}^2$ ; boron

0.5 keV,  $1 \times 10^{15}/\text{cm}^2$  and 1000 °C 10s (RTA).

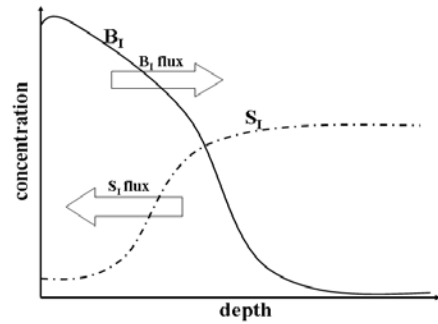


Fig. 4. This figure shows “up-hill” diffusion mechanism

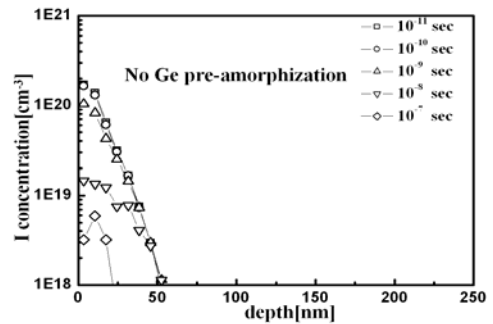


Fig. 5. Interstitial profiles in terms of very low time scale with no Ge PAI

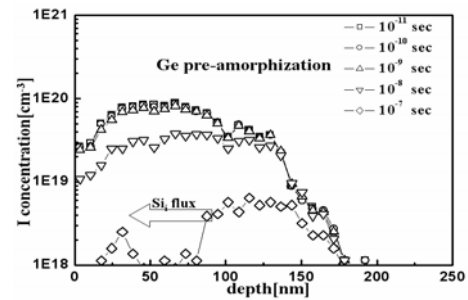


Fig. 6. Interstitial profiles in terms of very low time scale with Ge PAI

	$B_2I_3$	$B_3I_3$	$B_4I_3$
	=-6.0	=-8.0	=-8.5
$BI_2$	$B_2I_2$	$B_3I_2$	$B_4I_2$
=-3.3	=-4.6	=-6.0	=-6.5
$B_2I$	$B_3I$	$B_4I$	
=-1.6	=-3.6	=-4.0	
$B_2$	$B_3$	$B_4$	
=0.8	=0.8	=0.8	

Fig. 7. Migration and binding energies of  $B_mI_n$  clusters use in this work.

# Threshold Energy and Impact Ionization Scattering Rate Calculations for Strained Silicon

C. May\*<sup>†</sup> and F.M. Bufler\*<sup>§</sup>

\*Institut für Integrierte Systeme, ETH Zürich, Gloriastrasse 35, CH-8092 Zürich, Switzerland

<sup>†</sup>Universität Tübingen, Physikalisches Institut, A. d. Morgenstelle 10, D-72076 Tübingen, Germany

<sup>§</sup>Synopsys Schweiz GmbH, Affolternstrasse 52, CH-8050 Zürich, Switzerland

## MOTIVATION

Impact ionization is an important scattering process in semiconductors where a high-energetic particle creates an electron-hole pair. This concerns e.g. device reliability where the substrate current in MOSFETs serves as a monitor for hot electrons, which are responsible for oxide degradation, or avalanche breakdown which destroys the device. More recently, it is also relevant for the operation of partially-depleted silicon-on-insulator (PD-SOI) MOSFETs where the generated holes give rise to the floating-body effect (cf. [1]). On the other hand, strained silicon has now become indispensable for further performance improvement of CMOS technology. From a simulation viewpoint, this requires knowledge of the stress-dependence of all transport parameters. While impact ionization has already been studied extensively in unstrained Si (e.g. [2], [3]), transport parameter calculations for strained Si have so far been restricted to drift velocity and mobility (e.g. [4]).

## METHODOLOGY AND RESULTS

Our algorithm obtains threshold energies of impact ionization by means of numerical optimization using full-band structure information and energy- and momentum conservation. Results for strained Si are presented in Tab. 1 and are used as a starting point for the impact ionization rate integration. We observe that the threshold energy is lowered with increasing Ge content by a smaller amount than the band gap is reduced, which can be explained by the availability of fewer possibilities to fulfill both momentum and energy conservation simultaneously.

Performing the so-called Random- $\mathbf{k}$  (e.g. [3]) approximation yields a nine-dimensional integral

which is also known in terms of the DOS. Therefore, it can be used as a test case for impact ionization rate integration approaches. A modified Lorentz profile with optimized cutoff and half-width parameters serving as a delta distribution approximation and a Monte-Carlo integration algorithm was found to show excellent agreement.

Some of the comparisons of different delta distribution approximations and integration methods are illustrated in Fig. 2. We have then used this method to obtain the momentum-conserving energy-averaged impact ionization rate

$$R(E) = \frac{\sum_v \int d^3\mathbf{k}_v \delta(E - E_v(\mathbf{k}_v)) S_{II}(v, \mathbf{k}_v)}{\sum_v \int d^3\mathbf{k}_v \delta(E - E_v(\mathbf{k}_v))}.$$

Fig. 4 – 6 show the results of our fitting to a generalized Keldysh formula. We observe that steep steps in the impact ionization rate are due to the number of allowed processes times the DOS (cf. Fig. 3). The dimensionless matrix element has been set to unity and has to be matched to impact ionization coefficient measurements. For example, for electrons in unstrained Si, we obtain  $|M|^2 = 0.14$ . In conclusion, we have presented a new comprehensive method for the calculation of impact ionization scattering rates. The method can be applied to any semiconductor, especially also to uniaxially-stressed silicon. Thus a sound basis has been given for the inclusion of impact ionization in the simulation especially of strained-Si devices. We thank A. Erlebach for support of this work.

## REFERENCES

- [1] G. G. Shahidi, IBM J. Res. & Dev. **46**, No. 2/3, 121 (2002)
- [2] E. Cartier, M. V. Fischetti, E. A. Eklund, and F. R. McFeely, Appl. Phys. Lett. **62**, 3339 (1993)
- [3] M. V. Fischetti, N. Sano, S. E. Laux, and K. Natori, IEEE J. TCAD **3** (1997)
- [4] F. M. Bufler, Ph.D. thesis, U. of Bremen (1998)

Ge content [%]	Band gap [eV]	$E_{th}^{(e^-)}$ [eV]	$E_{th}^{(h^+)}$ [eV]
0	1.12	1.140	1.367
10	1.063	1.091	1.337
20	1.003	1.036	1.314

Fig. 1. Threshold energies for electron and hole initiated impact ionization in silicon under biaxial tensile strain with different substrate germanium content.

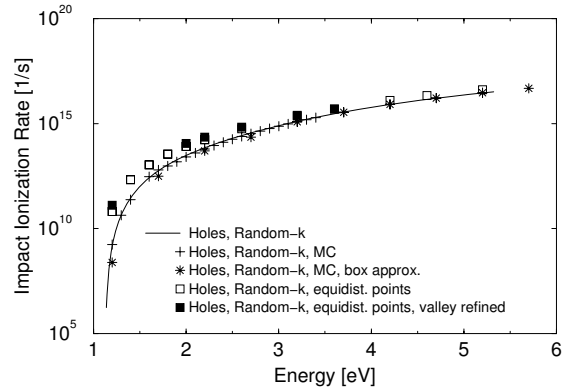


Fig. 2. Delta distribution and integration method comparison for the random-k method.

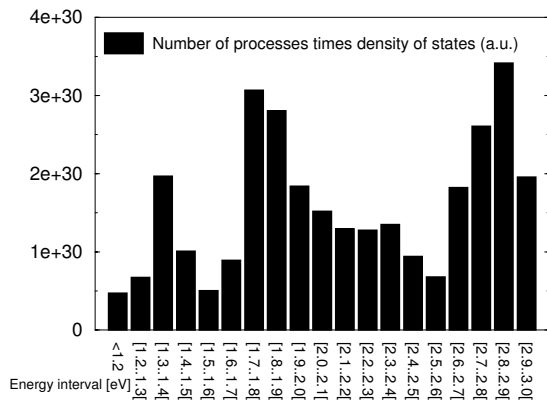


Fig. 3. Density of states times number of processes (a. u.) starting to be accessible per energy interval in eV for electron initiated impact ionization in Si.

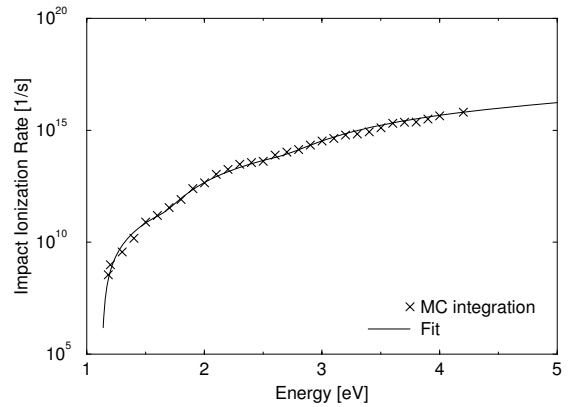


Fig. 4. Electron initiated impact ionization rate in Si.

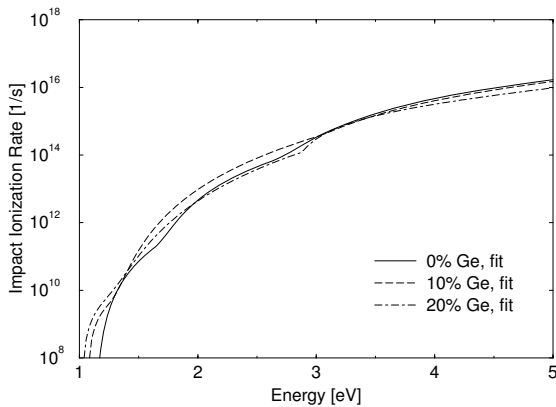


Fig. 5. Electron initiated impact ionization rates in strained silicon.

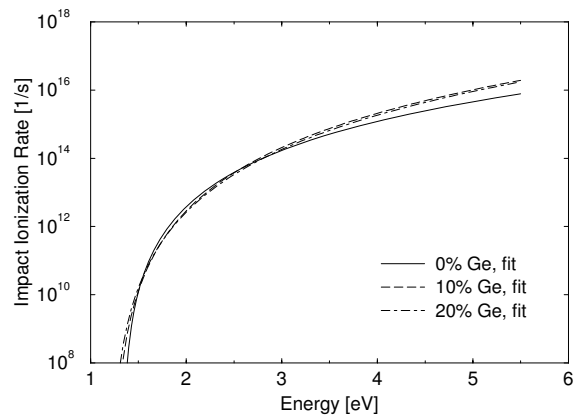


Fig. 6. Hole initiated impact ionization rates in strained silicon.

# Monte Carlo Calculation of Voltage-Current Nonlinearity and High-Order Harmonic Generation in GaAs Microstructures

D. Persano Adorno, M.C. Capizzo and M. Zarcone

Dipartimento di Fisica e Tecnologie Relative, Viale delle Scienze, Ed. 18, Palermo (Italy)  
e-mail: dpersano@unipa.it

## INTRODUCTION

The use of semiconductor systems for broadband telecommunication stimulates a more accurate knowledge of both their low and high frequency electric response. Recent advances in electronics pushes the devices to achieve higher output power and efficiency at very high frequencies around the THz region. The miniaturization of integrated circuits implies that even at moderate applied voltages these systems are typically exposed to very intense electric fields.

For these reasons, nonlinear processes involving dynamical effects and high-order harmonic generation in semiconductor structures exposed to intense radiation are attracting increasing attention. Furthermore, the understanding of such processes in semiconductors exposed to far-infrared radiation can be fruitfully exploited for implementing coherent sources in the THz region. Both experimental and theoretical analysis have shown high conversion efficiency for the third and fifth harmonics in low-doped Si, GaAs and InP crystals in the frequency range 30-500 GHz and temperature range 80-400 K, due to the nonlinearity of the velocity-field relation [1-4]. The problem of nonlinear processes in the sub-terahertz region has been recently investigated by considering the nonlinearity of the I-V characteristic, the harmonic generation and the electronic noise behavior in a nanometric n+n metal GaAs Schottky-barrier diode [3]. In the Schottky diode the behavior of high-order harmonic intensity is similar to that exhibited by bulk materials. The hysteresis-like behavior of the curve  $\langle I(V) \rangle$  is accompanied by a rapid increase

with the frequency  $f$  of the amplitude of the higher order harmonics.

The aim of this work is to study and discuss the dependence of the voltage-current hysteresis cycle and the high-order harmonic efficiency in GaAs n+nn+ structures operating under sub-terahertz signals by the frequency and the intensity of the excitation signal. These structures have been chosen because they form the basis for various high-frequency semiconductor devices.

## MODEL AND CALCULATIONS

Using a multiparticles Monte Carlo (MC) code, self-consistently coupled with a one-dimensional Poisson solver, we simulate the nonlinear carrier dynamics in GaAs n+nn+ structures operating under large-amplitude periodic signals. In order to compare the results with those obtained in a previous analysis of GaAs bulk [4], we analyse a symmetric GaAs n+nn+ structure with doping levels of  $n_+=10^{17} \text{ cm}^{-3}$  and  $n_-=10^{15} \text{ cm}^{-3}$ . The spatial length of the n+ region is 0.15  $\mu\text{m}$  and 1  $\mu\text{m}$  for the n region. All calculations are performed at lattice temperature  $T=300 \text{ K}$ . We simulate electronic transport in the structure driven by a periodic voltage  $V(t)=V_0\sin(2\pi ft)$ , with amplitude  $V_0$  and frequency  $f$ . To solve the Poisson equation the self-consistent electric field is updated every 10 fs and the structure is meshed by cells of  $10^{-8} \text{ m}$  length. The total simulated history duration is greater than 100 periods of the frequency of the applied voltage. We set  $10^3$  particles in the whole diode.

The algorithm of MC simulation of the electron motion in the alternating electric field used involves the nonparabolicity of the band structure and the

intervalley and intravalley scattering of electrons in multiple energy valleys. We assume field-independent scattering probabilities; accordingly, the external fields may alter them only indirectly through the field-modified electron velocities [2]. Electron scatterings due to ionized impurities, acoustic and polar optical phonons in each valley as well as all intervalley transitions between the equivalent and non-equivalent valleys are taken into account. The parameters of the band structure and the modelling for harmonic generation are taken from Ref. [3]. The adopted impurity concentration is  $10^{13} \text{ cm}^{-3}$ .

#### NUMERICAL RESULTS

At sufficiently low frequencies dynamical relations recover those of the static case. However, when the applied signal frequency increases the inertia of carrier transport and the heating/cooling processes significantly modify the static J-V relation. Figure 1 presents the instantaneous total current density  $\langle J \rangle$  as a function of the instantaneous periodic voltage  $V(t)$  applied to the diode, with  $V_0=4 \text{ V}$  and different frequencies. The inertia effect into the current response is nearly absent up to  $f \approx 20 \text{ GHz}$ . Here the  $\langle J(V) \rangle$  diagram follows practically the static J-V relation. For  $f > 20 \text{ GHz}$ , the instantaneous  $\langle J(V) \rangle$  characteristic begins to be significantly different with respect to the static case. In figure 2 we show the harmonic spectra of the current density obtained for some values of frequency. A strong reduction of harmonic emission is clearly evident for  $f=62.5 \text{ GHz}$ , which is the frequency value in which the J-V curve changes its shape.

#### CONCLUSION

We have studied the nonlinear behavior of a n+nn+ junction. Our results show that: (i) for  $f > 100 \text{ GHz}$ , the hysteresis-like behaviour of  $\langle J(V) \rangle$  produces a similar increasing of the amplitude of the high order harmonics with  $f$  observed in bulk samples. This increasing ends only for very high values of frequency ( $f > 600 \text{ GHz}$ ); (ii) in the n+nn+ structure some peculiar mechanism is present and produces a significant reduction in the harmonic emission rate in a very low frequency range. This is a very interesting result, not expected in bulk or in other structures, as the Schottky diode, and remains an open problem.

#### REFERENCES

- [1] R. Brazis, R. Ragoutis, and M. R. Siegrist, *Suitability of drift nonlinearity in Si, GaAs, and InP for high-power frequency converters with a 1 THz radiation output*, J. Appl. Phys. **84**, 3474 (1998).
- [2] D. Persano Adorno, M. Zarcone, and G. Ferrante, *Far-Infrared Harmonic Generation in Semiconductors: A Monte Carlo Simulation*, Laser Physics **10**, 310 (2000).
- [3] D. Persano Adorno, M. Zarcone, G. Ferrante, P. Shiktorov, E. Starikov, V. Gružinskis, S. Perez, T. Gonzalez, L. Reggiani, L. Varani, and J. C. Vaissière, *Monte Carlo simulation of high-order harmonics generation in bulk semiconductors and submicron structures*, Phys. stat. sol. (c) **1**, 1367 (2004).
- [4] D. Persano Adorno, PhD Thesis, Palermo University (2005)

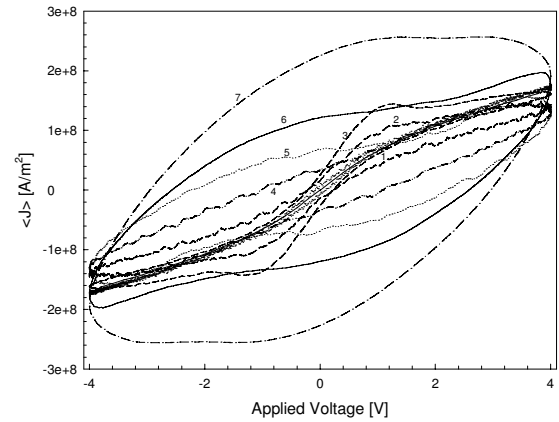


Fig.1 Instantaneous total current density  $\langle J \rangle$  as a function of the instantaneous periodic voltage  $V(t)$  applied to the n+nn+ junction and frequencies  $f=10, 20, 50, 62.5, 100, 200, 400 \text{ GHz}$  (curves 1 to 7, respectively). The thick solid line shows the dc behaviour of the structure, drawn for comparison.

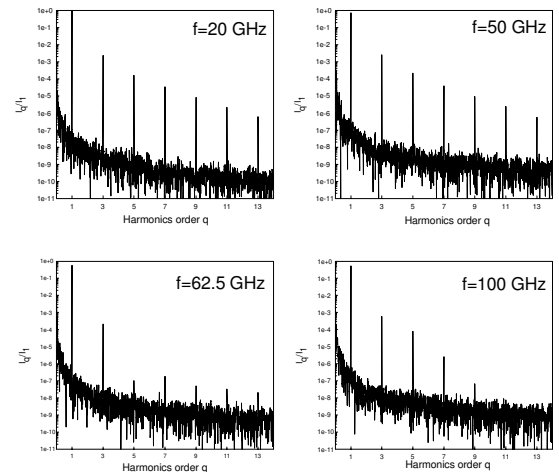


Fig.2 Harmonics generation efficiency versus their order.  $V_0=4 \text{ V}$  and  $f=20, 50, 62.5$  and  $100 \text{ GHz}$ .

# Static-Electric-Field Effects on Harmonic Generation in Gallium Arsenide Bulk Exposed to Intense Sub-THz Radiation

D. Persano Adorno, M. Zarccone and G. Ferrante

Dipartimento di Fisica e Tecnologie Relative, Viale delle Scienze, Ed. 18, Palermo (Italy)  
e-mail: [dpersano@unipa.it](mailto:dpersano@unipa.it)

## INTRODUCTION

The process of high order harmonic generation in semiconductors driven by intense radiation fields having sub-terahertz frequencies has been widely investigated in recent years [1-3]. This field of research represents a useful mean for the general understanding of several features of the highly non linear processes of carrier transport in doped semiconductors. Moreover a possible way to achieve high-power and high-frequency radiation sources is given by the efficient frequency conversion of high-power gyrotron radiation in nonlinear materials.

Harmonics generation in the presence of an additional static field has been addressed by several authors [4-5]. Among others, Bao and Starace have experimentally found that in H<sup>-</sup> and in Ar the addition of a static field, having an amplitude less than 2% of that of the laser field, produces very intense even harmonics. Furthermore, they have shown that the intensities of odd harmonics near the low-order end of the plateau increase by orders of magnitude. A static field thus appears to have a very sensitive role for controlling the emission rates of both even and odd high harmonics [4].

In this paper we report and discuss the static-electric-field effects on harmonic generation in a GaAs bulk driven by an intense alternating field. To the best of our knowledge this subject in semiconductors has never been addressed before.

## PHYSICAL MODEL AND CALCULATIONS

We assume that our GaAs sample is acted by an oscillating electric field and a static field having the components:

$$\begin{aligned} E_x &= E_0 + E_1 \cos \varphi \cos (2\pi\nu_1 t - k_1 z) \\ E_y &= E_1 \sin \varphi \cos (2\pi\nu_1 t - k_1 z) \end{aligned}$$

where  $\varphi$  is the angle between the polarization of the static field  $E_0$  and the oscillating field  $E_1$ .

The theory of harmonic generation in semiconductors has been derived in a previous paper [2] and it is based on the Maxwell equation for the propagation of an electromagnetic wave in a medium along a given direction. Our analysis is referred to a thin sample and for this reason we do not consider the complex form of the dielectric function  $\epsilon(\nu)$  in our calculations and neglect the field-dependent absorption. Within these assumptions, the efficiency of the harmonic generation at frequency  $\nu$ , normalized to the fundamental one ( $\nu_1$ ), is given by:

$$\eta_\nu = \frac{I_\nu}{I_{\nu_1}} = \frac{V_1^2 u_\nu^2}{\nu^2 u_{\nu_1}^2} \quad (1)$$

where  $u_\nu$  is the Fourier transform of the electron drift velocity, obtained via a multiparticles Monte Carlo (MC) simulation of the electron motion in the semiconductor. The spectra of emitted radiation are reconstructed by the analysis of the velocity Fourier components. The algorithm for MC simulation of the electron motion in the alternating electric field used in this work follows the standard procedure. It takes into account the nonparabolicity of the band structure and the intervalley and intravalley scattering of electrons in multiple energy valleys. Since the far-infrared frequencies are below the absorption threshold, in our model we consider the

electrons in the conduction band as the only source of nonlinearity. We assume field-independent scattering probabilities; accordingly, the influence of the external fields is only indirect through the field-modified electron velocities. All the results are obtained in a stationary regime, just after a transient time of a few ps.

The conduction bands of GaAs are represented by the  $\Gamma$  valley, the four equivalent L-valleys and the three equivalent X-valleys. Our harmonic spectra have been obtained in GaAs by adopting a free electrons concentration of  $n=10^{13}\text{cm}^{-3}$  and a lattice temperature  $T=80$  K. For a complete set of n-type GaAs parameters used in our calculations, see Ref. [4].

#### NUMERICAL RESULTS

The process of harmonic generation has been analyzed for different geometries of the linear polarization of the two incident fields. In all cases we have assumed  $E_0=3$  kV/cm,  $E_1=30$  kV/cm and  $\nu_1=200$  GHz.

Also if the intensity of the static field  $E_0$  is only 1/10 of the amplitude of the oscillating one, we have found even harmonics having efficiency comparable with those of the odd ones. In order to study the effect of the static field on the spectrum by varying the angle  $\varphi$  between the two electric fields, we have computed the intensity spectra of the electromagnetic waves polarized along the x axis and the y axis. The spectrum along the x axis when  $\varphi=0^\circ$  shows, as expected, odd and even harmonics, while along the y axis we have only noise. The situation is very different when the oscillating electric field has a component also along y, i.e. when  $\varphi \neq 0^\circ$ . In fact in this case we find that the spectrum along the y axis contains also the even harmonics due to the static field  $E_0$  although along the y direction is present only the pump field  $E_1$  at frequency  $\nu_1$ . When  $\varphi=90^\circ$  only the static field  $E_0$  is present along the x axis and the spectrum shows the even harmonics of an oscillating field direct along the y-axis, while along the y direction the spectrum contains only the odd harmonics.

Figure 1 shows the efficiency of the second harmonic as a function of the angle  $\varphi$  between  $E_0$  and  $E_1$ , along the x and y directions. The intensity of  $\eta_2$  is constant along the x-axis, while it is a function of the angle  $\varphi$  along the y-axis.

#### CONCLUSIONS

The most significant results of our investigation may be summarized as follows:

1) When the only alternating field is applied no even harmonics are present. The presence of a static field, lowering the symmetry of the system, produces the generation of even harmonics, with amplitudes increasing with the intensity of the static field.

2) In GaAs bulk the spectra contain also the even harmonics at angles  $\varphi$  different from zero although the static electric field  $E_0$  has no component along that direction.

3) As compared to the case in which only the oscillating field is present, (for  $\nu=200$  GHz and for the studied intensities), two-field calculations show that the addition of the static field does not enhance the efficiency of the odd harmonic.

#### REFERENCES

- [1] R. Brazis, R. Ragoutis, and M. R. Siegrist, *Suitability of drift nonlinearity in Si, GaAs, and InP for high-power frequency converters with a 1 THz radiation output*, J. Appl. Phys. **84**, 3474 (1998).
- [2] D. Persano Adorno, M. Zarcone, and G. Ferrante, *Far-Infrared Harmonic Generation in Semiconductors: A Monte Carlo Simulation*, Laser Physics **10**, 310 (2000).
- [3] P. Shiktorov, E. Starikov, V. Gružinskis, M. Zarcone, D. Persano Adorno, G. Ferrante, L. Reggiani, L. Varani, and J. C. Vaissière, *Monte Carlo Analysis of the Efficiency of Tera-Hertz Harmonic Generation in Semiconductor Nitrides*, Phys. stat. sol. (a) **190**, 271 (2002).
- [4] M. Bao and A. F. Starace, *Static electric field effects on high harmonic generation*, Phys. Rev. A **53**, R3723 (1996).
- [5] B. Wang, X. Li and P. Fu, *The effects of a static electric field on high-order harmonic generation*, J. Phys. B: At. Mol. Opt. Phys. **31**, 1961 (1998)

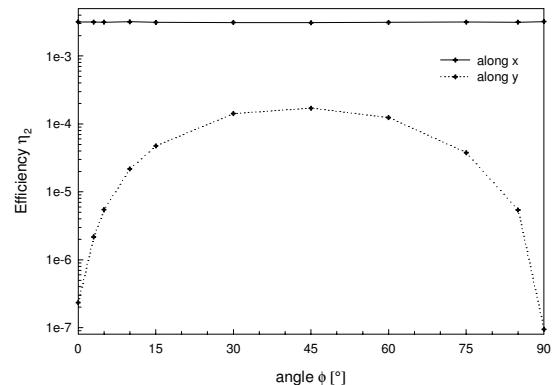


Fig.1 Efficiency of 2nd harmonic generated by the GaAs bulk as a function of the angle  $\varphi$  formed by the polarization of the a.c. electric field and the static one.

# Transport in Silicon Nanowires: Surface Roughness and Confined Phonons

E.B. Ramayya<sup>1</sup>, D.Vasileska<sup>2</sup>, S.M. Goodnick<sup>2</sup>, and I. Knezevic<sup>1</sup>

<sup>1</sup>Department of Electrical and Computer Engineering, University of Wisconsin-Madison,  
Madison, WI 53706, USA

<sup>2</sup>Department of Electrical Engineering, Arizona State University, Tempe, AZ-85281, USA  
e-mail: ramayya@wisc.edu, knezevic@enr.wisc.edu

Nanostructures with spatial confinement along two directions are termed nanowires. It has been experimentally shown [1] that, besides the channel thickness, the channel width can also be reduced down to nanometer scale. The resulting quasi-one-dimensional nanostructures are expected to play a key role in future nanotechnology, as well as to provide model systems to demonstrate quantum size effects. Silicon nanowires (SiNWs) in particular are potentially very attractive, given the central role of Si in the semiconductor industry and the existing set of known fabrication technologies.

In our recent work [2], we investigated the mobility of electrons in a rectangular SiNW, by taking into account the major scattering mechanisms, namely acoustic phonon scattering, non-polar optical phonon scattering and surface roughness scattering. Surface roughness scattering was modeled using Ando's model [3], and the phonons were treated in the bulk mode approximation. The effect of impurity scattering was not included, since the channel was very lightly doped. Fig. 1 shows the schematic of the ultrathin-body SOI (UTBSOI) device considered in the work, and the potential profile along the cutline CC', which was obtained by solving 3D Poisson and 2D Schrödinger equations self-consistently.

The device of width 30 nm [at this width electrons in the channel feel very weak spatial confinement along the width and hence behave like a two-dimensional electron gas (2DEG)] was used to compare the mobility results obtained from our simulator with the experimental data of Koga *et al.* [4] for a 2DEG of the same thickness. Fig. 2 shows the calculated low-field electron mobility. Although there is a good agreement with the experimental data, we find that the simulator overestimates the mobility in moderate effective field region, where

phonon scattering dominates. This discrepancy is due to assuming bulk phonons in the calculation of the phonon scattering rates. Fig. 3 shows the field-dependent mobility for different SiNW thicknesses. Phonon-limited mobility is found to decrease with decreasing width, because the overlap between the phonon and electron wavefunctions is larger in narrower wires. In contrast, surface-roughness scattering mobility increases with decreasing wire width, because electrons in narrow (1D) wires are located near the wire center, as opposed to near the side interfaces in wide (2D) wires.

Presently, we are investigating the effect of confined phonons on the phonon scattering, and the variation of mobility for SOI thickness and width below 8 nm, and the results of these computations will be presented at the conference. Modification of the phonon spectrum due to the spatial confinement is expected to enhance the overlap of the electron and confined phonon wave function [5], thereby increasing the electron-phonon scattering rates. For SiNWs narrower than 5 nm, we expect the effect of surface roughness to be more detrimental to the mobility, because the average distance of the carriers from the interfaces would be just 2.5 nm or less, even though they are located near the wire center.

This work has been funded by Wisconsin Alumni Research Foundation and Intel Corporation.

- [1] H. Majima, H. Ishikuro, and T. Hiramoto, IEEE Electron Dev. Lett. **21**, 396 (2000).
- [2] E.B. Ramayya, MS Thesis, Arizona State University, Nov. 2005; E.B. Ramayya, D.Vasileska, S.M. Goodnick, and I. Knezevic, J. Appl. Phys., *submitted*.
- [3] T. Ando, A. Fowler, and F. Stern, Rev. Mod. Phys. **54**, 437 (1982).
- [4] J. Koga, S. Takagi, and A. Toriumi, IEEE Trans. Electron Devices **49**, 1042 (2002).
- [5] M. A. Stroscio, K. W. Kim, S. Yu, and A. Ballato, J. Appl. Phys. **76**, 4670 (1994).

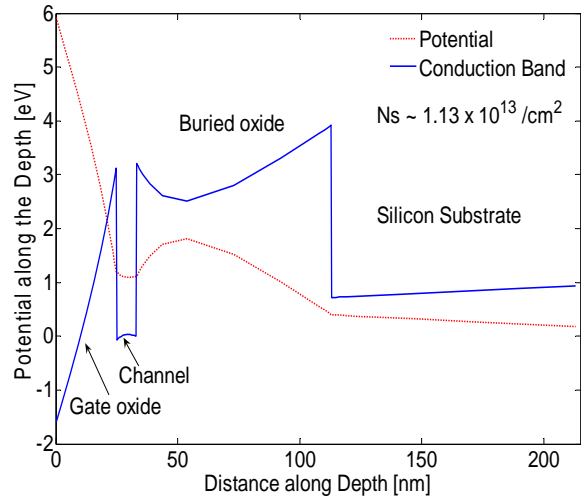
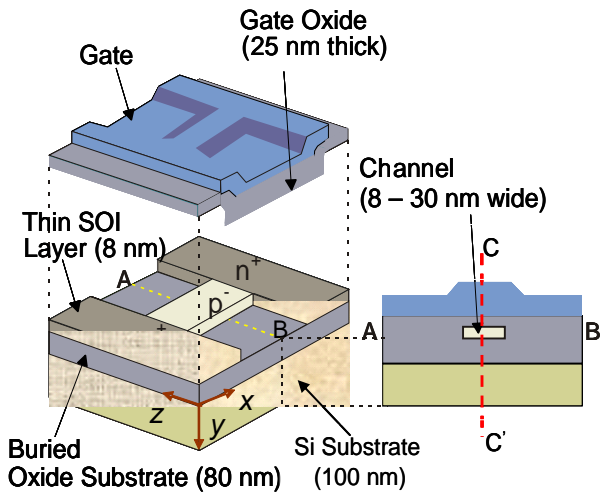


Fig. 1. Left panel: Schematic of the simulated SiNW on ultrathin SOI. The conduction band profile depicted in the right panel is taken along the red cutline CC' from the left panel.

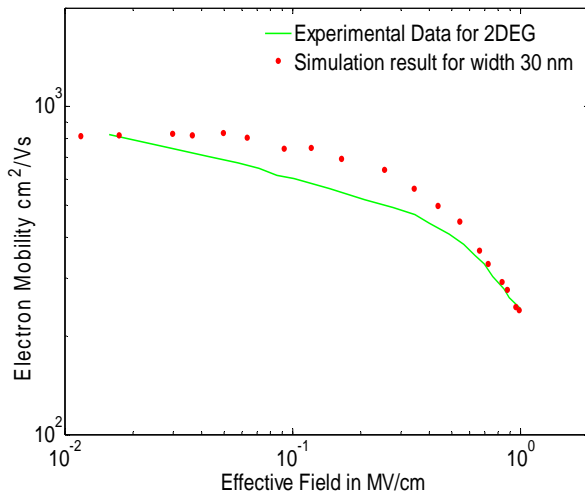


Fig. 2. Low-field mobility of 30 nm wide SiNWs as a function of the effective transverse field, as obtained from the calculation (solid line) and the experiment by Koga *et al.* [4] (circles). Overestimation of the mobility at moderate fields is due to the assumed bulk phonon scattering, and should be remedied by the incorporation of confined phonons.

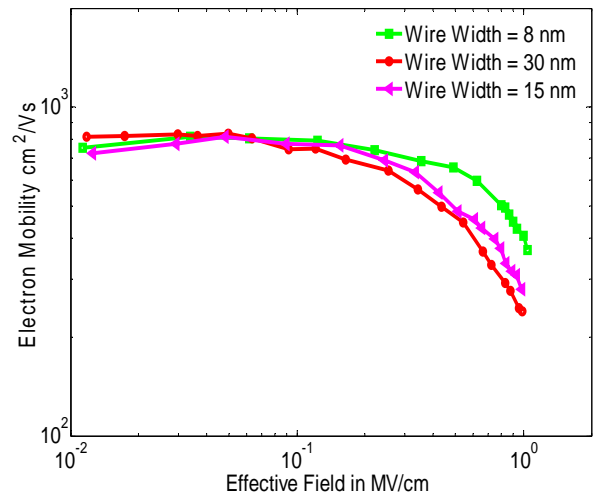


Fig. 3. Variation of the field-dependent mobility with varying SiNW thickness [3].

# Electrothermal Monte Carlo Simulation of Submicron Wurtzite GaN/AlGaN HEMTs

T. Sadi, R. W. Kelsall, and N. J. Pilgrim\*

School of Electronic and Electrical Engineering, The University of Leeds, Leeds LS2 9JT, UK

\*The Department of Physics, The University of Aberdeen, Aberdeen AB24 3UE, UK

e-mail: eents@leeds.ac.uk

The miniaturisation of device features has been accompanied by an exponential increase of the heat generated within the devices. As a result, the development of electrothermal models is necessary to study the effect of self-heating on the performance of submicron devices. This paper presents results from the application of an electrothermal Monte Carlo (MC) simulator to submicron wurtzite GaN/Al<sub>0.15</sub>Ga<sub>0.85</sub>N High Electron Mobility Transistors (HEMTs). The simulator iteratively couples a MC electronic trajectory simulation with a fast Fourier series solution of the Heat Diffusion Equation (HDE). The simulator models the effect of acoustic and optical phonons mediating intravalley electronic transitions, and phonons mediating intervalley electronic transitions. Ionised impurities, alloy disorder, electron-electron and impact ionisation scatterings, and the effect of electron degeneracy are also included in the simulations. The simulator uses a simple five-valley spherical non-parabolic model of the bandstructures of GaN and AlGaN, as this work focuses on the coupling of electronic and thermal transport. The simulations are performed self-consistently, by solving Poisson's equation in two dimensions every 1.0 fs. Polarisation induced charge at the GaN/AlGaN interface is modelled as a sheet of ionised donors placed at the interface. Polarisation effects also induce a net negative charge at the top surface of the AlGaN layer, a feature which is included in the simulations. The simulator extracts the power density distribution within the simulated region (see Fig. 1) using the net phonon emission approach [1]. The generated distribution is fed to the HDE solver to determine the temperature distribution. The HDE is solved in two dimensions using an analytical thermal resistance matrix technique [2], which solves for the temperature over the

simulated region while considering the conditions at the boundaries of the semiconductor die (see Fig. 2). The subsequent MC iteration is performed with the updated temperature distribution characterising the lattice temperature in the simulated region.

Preliminary results are shown in Fig. 3, which are obtained using a SiC substrate. The electrothermal device  $I_{ds}$ - $V_{ds}$  characteristics, shown in Fig. 3(a), demonstrate the thermal droop effect, which is known to be caused by device self-heating. Fig. 3(b) illustrates how the temperature distribution is non-uniform with a peak value occurring at the top of the device between the drain end of the gate and the start of the drain region. Fig. 3(c) demonstrates how the value of the peak temperature depends on the applied bias. The substrate material type plays an important role in the device thermal management, and thus the effect of using different substrate materials is investigated. More results have been generated using Si, GaN and single crystal sapphire substrates. Under the same biasing conditions, the use of a SiC substrate is shown to provide the lowest peak temperature and the lowest current reduction (upon the inclusion thermal self-consistency). The use of a sapphire substrate gives the worst thermal performance, as it is a poor thermal conductor. A reduction in the device die length is observed to raise the peak temperature in the simulated region and increase the extent of the thermal droop. The effect of introducing a negative polarisation charge of different concentrations at the top surface of the device is also examined. The presence of the surface charge modifies the electric potential distribution in the simulated region, and thus affects the values of the source-drain current and the peak temperature.

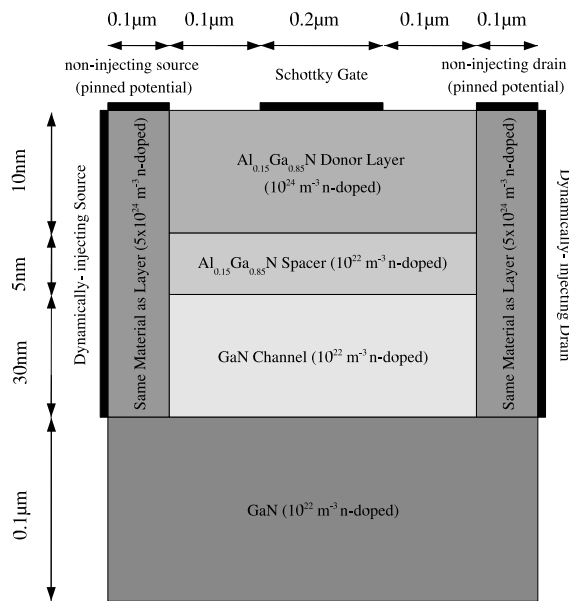


Fig. 1. The electronically simulated region of the GaN/AlGaIn HEMT.

Monte Carlo Domain

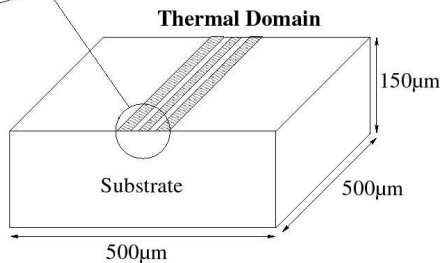
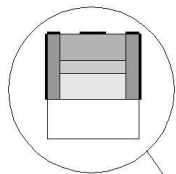
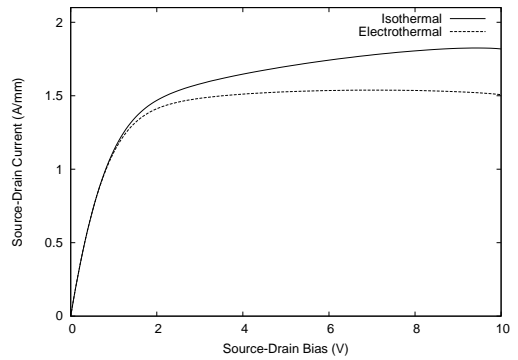


Fig. 2. The electronic MC and the thermal simulation domains.

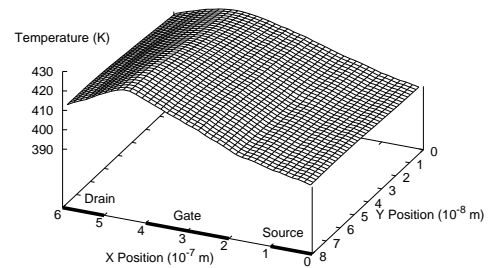
REFERENCES

[1] C. Moglestue, F. A. Buot, and W. T. Anderson, "Ensemble Monte Carlo particle investigation of hot electron induced source-drain burnout characteristics of GaAs field-effect transistors," *J. Appl. Phys.*, vol. 78, no. 4, pp. 2343–2348, 1995.

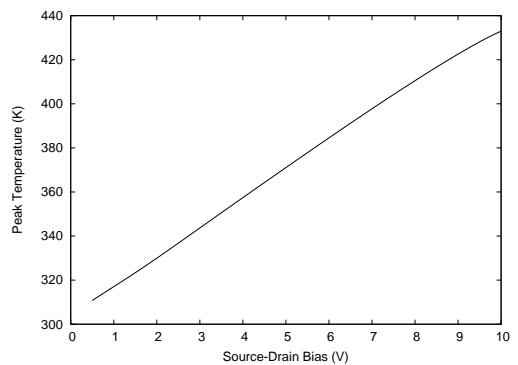
[2] W. Batty, C. E. Christoffersen, A. J. Pranks, S. David, C. M. Snowden, and M. B. Steer, "Electrothermal CAD of power devices and circuits with fully physical time-dependent compact thermal modeling of complex nonlinear 3-D systems," *IEEE Trans. Comp. Packag. Technol.*, vol. 24, no. 4, pp. 566–590, 2001.



(a)



(b)



(c)

Fig. 3. (a)  $I_{ds}$ - $V_{ds}$  characteristics of the HEMT at a source-gate bias of 1.0 V; isothermal simulations are performed at 300 K. (b) Temperature distribution at a source-gate bias of 1.0 V and a source-drain bias of 10.0 V;  $x = 0$  is the start of the source region,  $x = 6 \times 10^{-7}$  m is the end of the drain region,  $y = 8 \times 10^{-8}$  m is the device top surface. (c) Variation of the peak temperature with the source-drain bias at a source-gate bias of 1.0 V.

# Quantum Ensemble Monte Carlo Simulation of Silicon-Based Nanodevices

C. Sampedro, F. Gámiz A. Godoy and F. Jiménez-Molinos  
Dept. Electrónica y Tecnología de Computadores, University of Granada  
Campus Fuentenueva 18071, Granada, Spain.  
Phone: +34 958 240490, Fax: +34 958 243230 e-mail: [csampe@ugr.es](mailto:csampe@ugr.es)

## ABSTRACT

A Quantum Ensemble Monte Carlo (QEMC) simulator is used to calculate electrical characteristics and transient response of actual nanotransistors: both sub-50nm CMOS N-MOSFETs and ultrathin double gate SOI transistors, have been deeply studied. Doping profiles and oxide thickness have been selected to cope with the available specifications of the ITRS Roadmap and have been tuned in order to comply with the specification for the maximum leakage drain current in OFF state. The Quantum Ensemble Monte Carlo simulator QEMC has been used to self-consistently solve the Boltzmann Transport and Poisson equations in actual devices. Quantum effects are included through a multivalley version of the Effective Conduction Band Edge (ECBE) model, and new approaches for phonon and surface roughness scattering have been developed to include the effects of carrier quantization. ).

## MULTI-VALLEY EFFECTIVE CONDUCTION BAND EDGE METHOD

It is possible to include quantum effects in nanotransistors without solving the Schrödinger equation by adding a correction term to the electrostatic potential [1-2]. Thus, it is possible to reproduce the carrier density given by the full quantum solution. In drift-diffusion simulations Density Gradient (DG) model [1] has been widely used. However, this correction cannot be implemented easily in Monte Carlo simulations due to the fact that the driving force depends on the third derivative of the electron concentration which is a very noisy magnitude. To avoid this problem, the quantum correction should be expressed in terms of the electrostatic potential. The Effective Conduction Band Edge (ECBE) method explodes this idea[2]. Starting from the DG and assuming an exponential

relation between the electron concentration and the potential, the effective potential can be evaluated. Independent calculations for each valley are included to avoid mass fitting. The developed simulator is 2D real-space and 3D k-space where time is also considered as an independent variable to perform transient simulations. Phonon, surface roughness and Coulomb scattering are taken into account. Surface roughness scattering has been implemented using a three dimensional version of the model proposed by Gamiz et al [3], for two-dimensional electron gases. In addition, to take into account the effect of quantization on phonon scattering, a new phonon scattering model has been developed. Figure 1 compares the electron mobility obtained with a one-particle Monte Carlo simulator (where quantum effects are taking into account by solving Schroedinger equation) and the electron mobility obtained with the QEMC simulator, for a DGSOI device ( $T_{Si}=12\text{nm}$ ).

## SIMULATION RESULTS

Different structures have been studied with the QEMC simulator developed here. Figure 2 shows the results for a 25nm channel length MOSFET with HALO implants. Oxide thickness was considered to be 8.9 nm, and the doping profiles (shown in Figure 2-b) were selected to reduce short channel effects. Fig.2-c and 2-d show the averaged electron velocity along the channel and the averaged drift electric field along the channel. Fig.2-a shows the actual carrier distribution in the device when quantum corrections are taken into account. As can be observed, the maximum of the distribution is not anymore at the interface and its position corresponds to the predicted by the solution of the Schrödinger equation. Fig. 3 shows the results for a DGSOI transistor. The silicon thickness was considered to be 7nm (a-c) and 12nm in Fig.3-b. The channel length is 25nm, and the oxide thickness

$T_{ox}=8.9\text{nm}$  for the two gates. Fig.3-a shows the electron distribution when the two gates are biased at  $V_{GS}=1\text{V}$ , and  $V_{DS}=0.5\text{ V}$ . Note once more how carriers are pushed out of the interfaces because of quantum effects. Fig.3-c shows that quantization breaks down the degeneracy of the Si conduction band minima, and as a consequence the population of the valleys with longitudinal effective mass perpendicular to the interface (Valley 1) is higher than the population of the valleys showing the transverse effective mass perpendicular to the interface. Finally, this simulator allows us to calculate the electrical characteristics of these nanodevices both in transient and stationary regimes (Fig.4).

### CONCLUSIONS

A quantum corrected QEMC simulator using the multi-valley version of the ECBE method has been presented. This method can be used in MC studies due to the fact that the problems derived from the noisy electron distribution are avoided. This simulator allows us to study actual devices, and evaluate their electrical characteristics (both transient and stationary responses).

### ACKNOWLEDGMENTS

This work has been supported in part by the EU (Network of Excellence SINANO and EUROSIOI project) and by the Spanish Government project FIS-2005-6832).

### REFERENCES

- [1] M. G. Ancona G. J. Iafrate, *Quantum Correction to the equation of state of an electron gas in a semiconductor* Phys. Rev. B, **39**,9536 (1989)
- [2] TW Tang B Wu, *Quantum correction for the Monte Carlo simulation via the effective conduction-band edge equation* Semicond. Sci. Technol., **19**, 54 (2004)
- [3] F. Gámiz, et al., *Surface Roughness at the Si-SiO2 Interfaces in Fully Depleted Silicon-On-Insulator Inversion Layers* J. Appl. Phys., **86**, 6854 (1999)

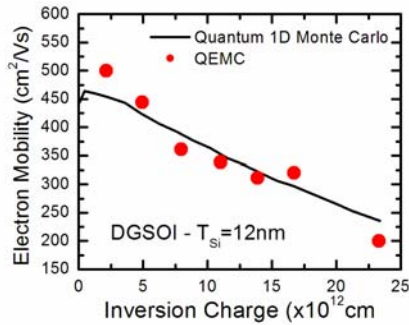


Fig.1: Comparison of the electron mobility in a DGSOI MOSFET evaluated using a one-particle Monte Carlo simulator and the QEMC simulator.

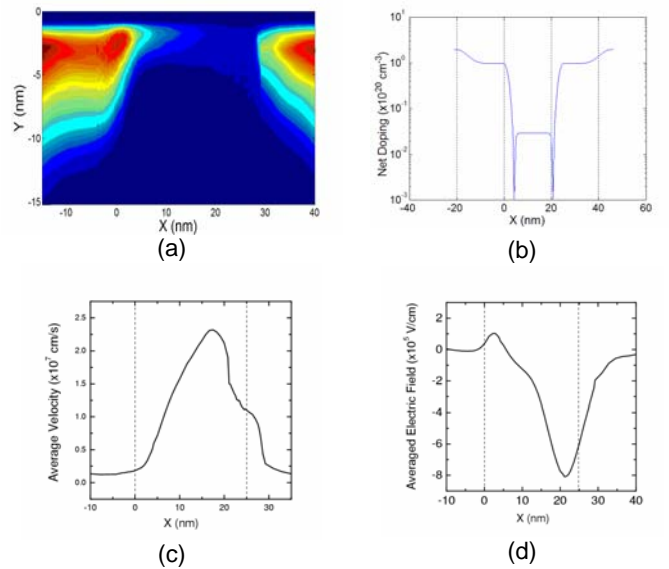


Fig.2: QEMC simulation of a 25-nm NMOSFET with HALO implants: a) charge distribution with  $V_{GS}=V_{DS}=1\text{V}$ ; b) Net doping profile along the channel; c,d) Averaged drift velocity and averaged electric field along the channel.

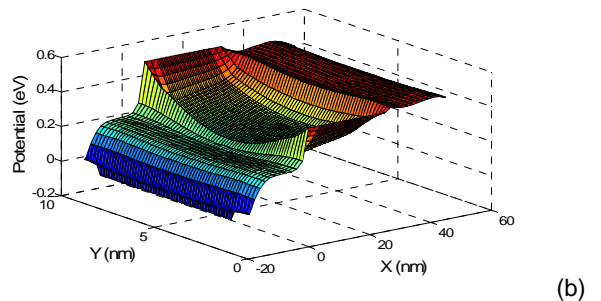
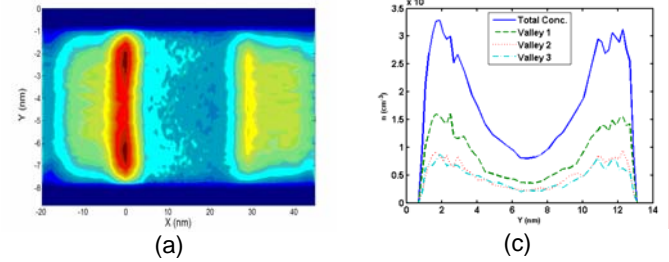


Fig.3: QEMC simulation of a 25-nm DGSOI MOSFET: Electron distribution (a) and potential distribution (b) with  $V_{GS}=1\text{V}$ ,  $V_{DS}=0.5\text{V}$ ; c) Total electron distribution along the direction perpendicular at the interfaces, and contribution of each valley.

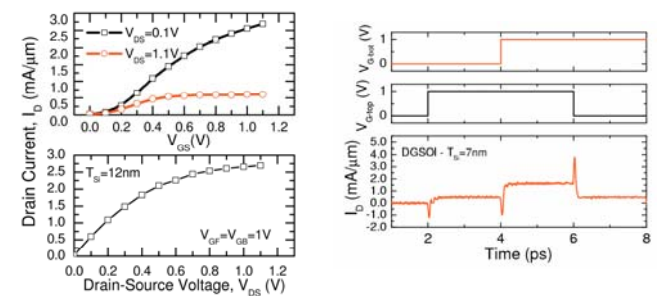


Fig.4: (a) Calculated I-V characteristics of a 25nm channel length DGSOI MOSFET. (b) Transient simulation.

# Monte Carlo Simulation of 2D TASER

E. Starikov, P. Shiktorov, V. Gružinskis, A.A. Dubinov\*, V.Ya. Aleshkin\*,  
L. Varani†, C. Palermo†, and L. Reggiani‡

Semiconductor Physics Institute, A. Goštauto 11, LT 01108 Vilnius, Lithuania

\*Institute for Physics of Microstructures, Nizhny Novgorod, GSP-105 603950, Russia

†CEM2 - (CNRS UMR 5507), Université Montpellier II, 34095 Montpellier Cedex 5, France

‡INFN - National Nanotechnology Laboratory, Via Arnesano s/n, 73100 Lecce, Italy,  
e-mail: jane@pav.pfi.lt

## INTRODUCTION

To develop THz-frequency range micro- and nano-structures the modern strategy widely uses 2D carrier transport in real space, where the third dimension is quantized (see, e.g. [1] and references therein). From one hand, this allows to avoid strong impurity scattering since carriers move in practically undoped 2D channels. From another hand, the transition from a 3D to a 2D transport leads to sharper behaviors of the phonon emission probability at the optical threshold energy and of carrier transfer to upper valleys. Both these reasons can lead to a considerable extension of the lattice temperature and frequency ranges where THz radiation generation related with transit-time effects in momentum space or intervalley transfer is possible. To investigate various quantum wells (QW) a general model of electron transport, which allows a quick comparison among different materials, QW widths  $d$ , etc. is of great importance.

The aim of this communication is to present such a model that is based on Monte Carlo (MC) simulations of 2D electron transport and noise at low lattice temperatures and to investigate the so-called optical-phonon-assisted transit-time resonance (OPTTR) of electrons favorable for THz radiation generation [2,3].

## MODEL

The model includes the deformation acoustic and polar optical phonon emission (POPE) scatterings in deep QW as described in [4]. Fig. 1 shows the energy dependence of the corresponding scattering rates for 2D-GaN QW of  $d = 5\text{nm}$  in comparison with those of 3D-GaN. By choosing the angle  $\phi$

after POPE through a random number  $r$  the dependence of  $\phi(P)$  on the corresponding probability  $P = r$  is presented in Fig. 2.

## RESULTS

The spectral density of velocity fluctuations,  $S_{vv}(\nu)$ , and the real part of the differential mobility,  $Re[\mu(\nu)]$ , calculated by the MC method [2] for the 2D-GaN QW are shown in Figs. 3 and 4, respectively. In the frequency regions, where  $Re[\mu(\nu)] < 0$  the amplification and generation of the radiation are possible. By comparing Figs. 3 and 4, we conclude that near these regions there also appear spikes in  $S_{vv}(\nu)$ , which should be considered as precursors of the generation. The frequency regions for THz generation in 2D-GaN and 2D-InP 5 nm QW are displayed in Figs. 5 and 6, respectively, and compared with the 3D case. Results show a considerable extension of the frequency region for TASER (Terahertz-Amplification-by-the-Stimulated-Emission-of-Radiation) when going from 3D to 2D.

## REFERENCES

- [1] T. Ando, A. Fowler, and F. Stern, *Electronic properties of two-dimensional systems*, Review of Modern Physics **54**, 437 (1982).
- [2] E. Starikov et al., *Monte Carlo simulation of the generation of terahertz radiation in GaN*, Journal of Applied Physics **89**, 1161 (2001).
- [3] J.T. Lu and J.C. Cao, *Monte Carlo study of terahertz generation from streaming distribution of two-dimensional electrons in a GaN quantum well*, Semiconductor Science and Technology **20**, 829 (2005).
- [4] P.J. Price, *Polar-optical-mode scattering for an ideal quantum-well heterostructure*, Physical Review B **30**, 2234 (1984).
- [5] L.E. Vorob'ev et al., *Generation of millimeter radiation due to electric-field-induced electron-transit-time resonance in indium phosphide*, JETP Letters **73**, 219 (2001).

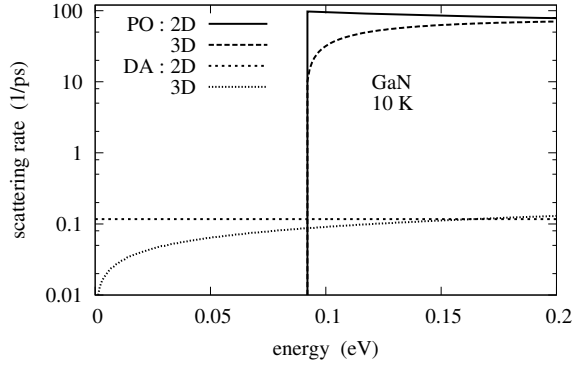


Fig. 1. Scattering rates for polar-optical phonon emission (PO) and deformation acoustic (DA) scatterings in bulk GaN (3D) and 5 nm GaN superlattice (2D)

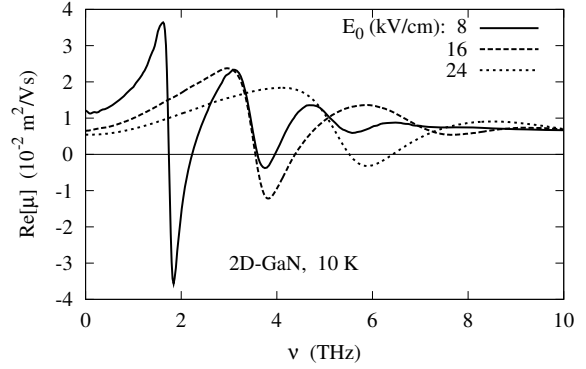


Fig. 4. Frequency dependence of real part of differential mobility calculated by MC method for 2D-GaN

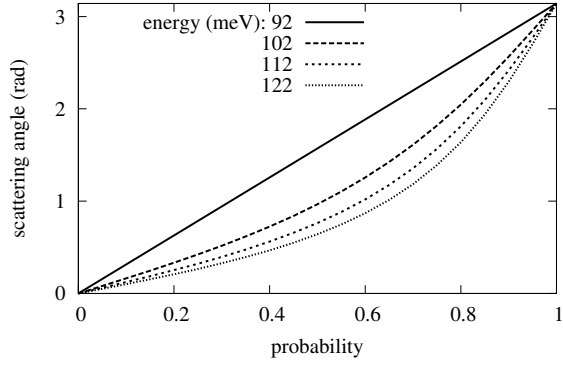


Fig. 2. Dependence of scattering angle for POPE on probability  $0 < P < 1$  for different electron energy

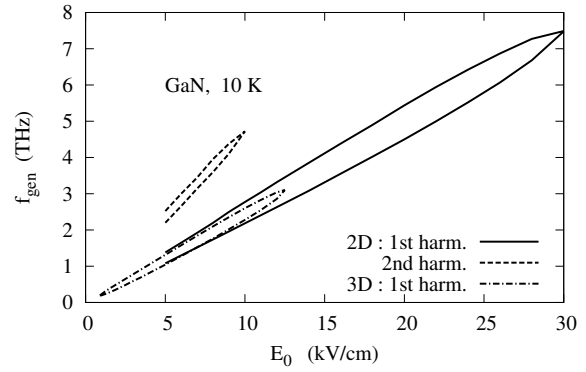


Fig. 5. Contour plot of the dynamic negative differential mobility in the  $E - f$  plane for 2D-GaN. For comparison dot-dashed line reports MC results of bulk GaN.

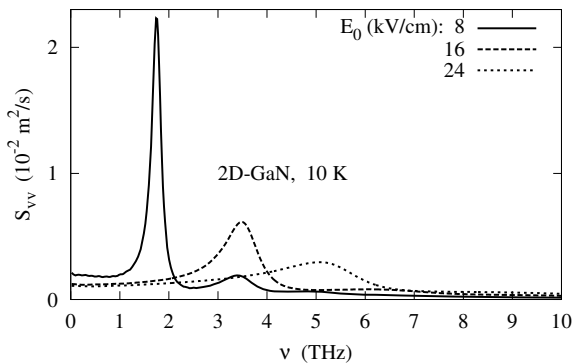


Fig. 3. Spectral density of velocity fluctuations calculated by MC method for 2D-GaN at different values of the applied constant field  $E_0$

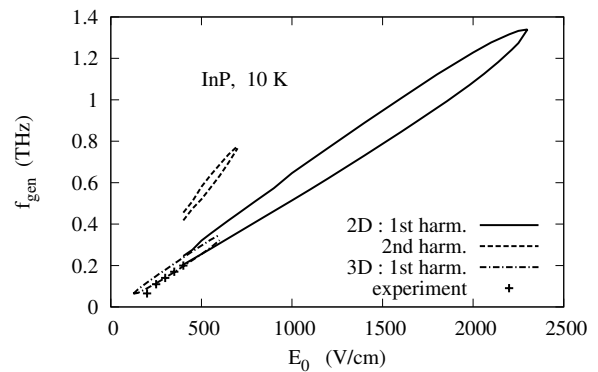


Fig. 6. Contour plot of the dynamic negative differential mobility in the  $E - f$  plane for 2D-InP. For comparison dot-dashed line reports MC results of bulk InP and symbols show experimental data [5].

# Analysis of Nano-Scale MOSFET Including Uniaxial and Biaxial Strain

Ryo Tanabe, Takahiro Yamasaki, Yoshio Ashizawa, and Hideki Oka  
Fujitsu Laboratories Ltd., 50 Fuchigami, Akiruno, Tokyo, 197-0833, Japan  
e-mail: tanabe.ryou@jp.fujitsu.com

## INTRODUCTION

The mobility improvement technology using strained channel is being actively researched for further scaling. Mainly, two methods have been discussed. One method is that we use biaxial strained Si which is formed on the SiGe buffer layer. The other method is that we use uniaxial strained Si. For example, SiN Cap film, SiGe-SD and SiC-SD. In addition, several surface orientations and channel directions have been considered to use best performance in strained Si.

In this paper, we focus uniaxial and biaxial strain technologies, and an optimum combination of strain method and channel direction is studied.

## UNIAXIAL STRAIN CHARACTERISTICS

First of all, uniaxial strain characteristics are studied. The states of the strained Si band are calculated by using the first principles pseudo-potential band calculation program PHASE [1]. The transport analysis was discussed by Fujitsu Full Band Monte Carlo Simulator FALCON.

In Fig.1, calculated double gate (DG) structure is shown. Fig.2 shows the results of uniaxial characteristics. We calculated the state of strain from -2.0%(compressive) to +2.0%(tensile). We considered two channel directions,  $\langle 100 \rangle$  and  $\langle 110 \rangle$ . As shown in Fig.2, for NMOS,  $I_{on}$  increases by tensile strain and decreases by compressive strain respectively. It is the almost same tendency for both directions, but  $\langle 100 \rangle$  direction has larger merit than  $\langle 110 \rangle$ . On the other hand, for PMOS, the dependency for strain is small for  $\langle 100 \rangle$ .  $\langle 110 \rangle$  direction has large dependency for strain. Current increases by compressive strain largely.

Next, we will discuss the difference of  $\langle 100 \rangle$  and  $\langle 110 \rangle$  for NMOS. In Fig. 3 and 4, we show the valley energy and population for both directions. Although for  $\langle 110 \rangle$  uniaxial, all  $\Delta 4$ fold valleys are isotropic,  $\Delta 4$ fold valleys show anisotropic property for  $\langle 100 \rangle$  uniaxial strain. As pointed out in [2], additional electron population leads smaller conductivity mass.

## BIAXIAL STRAIN CHARACTERISTICS

Next, we will show the results of biaxial strain. In Fig.5, the  $I_{on}$  improvement ratios are shown as a

function of strain. In biaxial strain condition, for NMOS,  $I_{on}$  increases by tensile strain, and decreases by compressive strain respectively. For PMOS,  $I_{on}$  increases by both tensile and compressive strain. Fig.6 shows the dependencies of current direction. 0 deg is  $\langle 110 \rangle$  direction and 45 deg is  $\langle 100 \rangle$  direction. For electron, current improvement ratio is almost the same for any angle in unstrained state, but electron has anisotropic property in strained state.  $\langle 100 \rangle$  direction has maximum merit of strain. For hole,  $\langle 100 \rangle$  direction has maximum merit for both unstrained and strained states. Finally we will show the relationship between scaling and ballistic ratio in Fig.7 and 8.  $I_{on}$  improvement ratio decreases as gate length scaled down. But, the merit of strain will be kept to 5nm gate length especially for  $\langle 100 \rangle$  direction. Ballistic ratio in  $\langle 100 \rangle$  direction is also higher than that of  $\langle 110 \rangle$  direction. This is because of effective mass differences between  $\langle 100 \rangle$  and  $\langle 110 \rangle$  direction.

## DISCUSSION

In Table 1, each  $I_{on}$  improvement ratio is summarized for both uniaxial and biaxial ( $L_g=30\text{nm}$ ). The combination of biaxial tensile strain and  $\langle 100 \rangle$  current for NMOS, and compressive uniaxial strain and  $\langle 110 \rangle$  channel for PMOS are optimum methods for current enhancement. However, for technological difficulties and process cost, the way that we use uniaxial tensile strain and  $\langle 100 \rangle$  channel direction for NMOS and uniaxial compressive strain and  $\langle 110 \rangle$  channel direction for PMOS is one of candidate method.

## CONCLUSION

We focused both uniaxial and biaxial strain technologies, and an optimum combination of strain method and channel direction was studied. The way that we use biaxial tensile strain and  $\langle 100 \rangle$  channel direction for NMOS and uniaxial compressive strain and  $\langle 110 \rangle$  channel direction for PMOS is considered to be the most realizable combination.

## REFERENCES

- [1] <http://www.fsis.iis.u-tokyo.ac.jp/theme/nanoscal/software/>
- [2] H. Irie et al., IEDM Tech. Dig., pp.225 (2004).

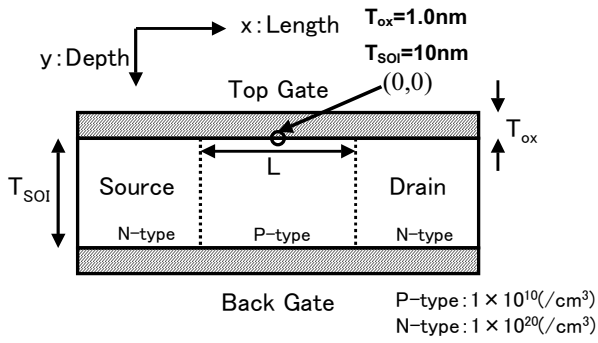


Fig. 1. Calculated DG structure

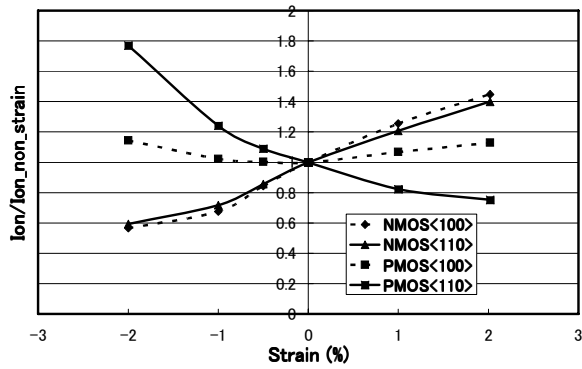


Fig. 2. Uniaxial strain characteristics for both <100> and <110> direction

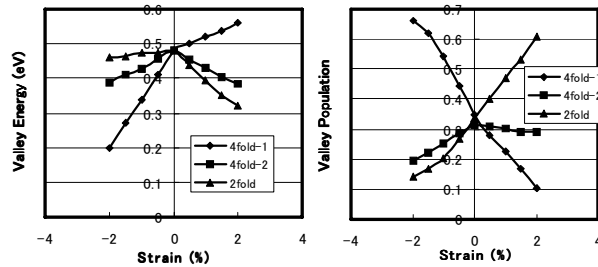


Fig. 3. Valley energy and valley population for <100> uniaxial strain

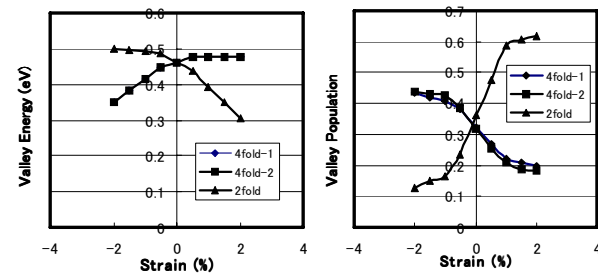


Fig. 4. Valley energy and valley population for <110> uniaxial strain

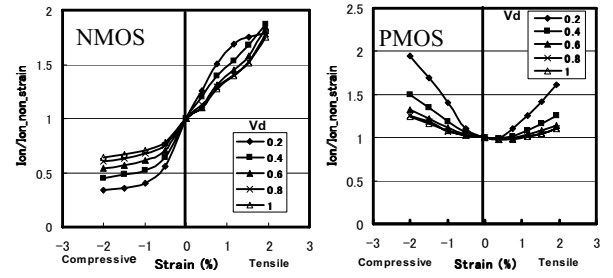


Fig. 5. Biaxial strain characteristics for <110> direction

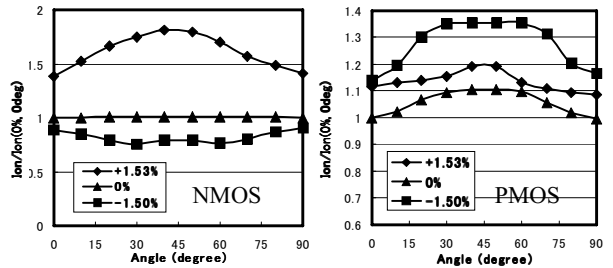


Fig. 6. The dependencies of current direction

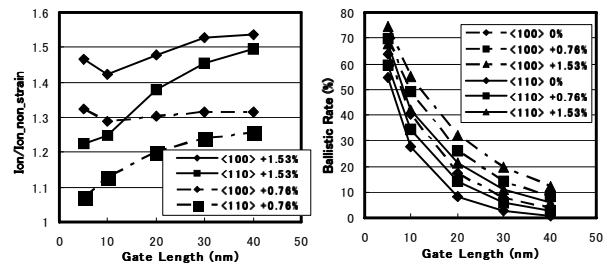


Fig. 7.  $I_{on}$  improvement and ballistic rate with scaling (NMOS)

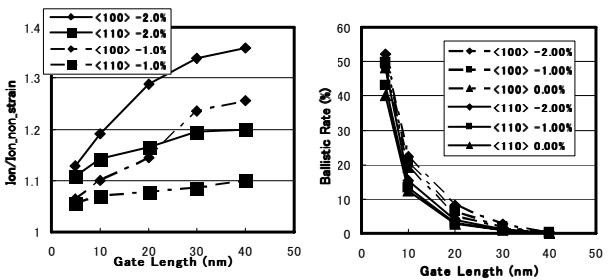


Fig. 8.  $I_{on}$  improvement and ballistic rate with scaling (PMOS)

Table 1. Summary of  $I_{on}$  improvement ratios for several strain and current conditions ( $L_g=30nm$ )

	Channel	NMOS	PMOS
Uniaxial	<100>	1.47(tens.)	1.16(comp.)
	<110>	1.38(tens.)	1.80(comp.)
Biaxial	<100>	1.72(tens.)	1.34(comp.)
	<110>	1.65(tens.)	1.20(comp.)

# Study of the Cutoff Frequency of Optimized SOI MESFETs

K. Tarik, D. Vasileska, and T. J. Thornton  
Arizona State University, Tempe, AZ, 85287-5706, USA  
Fax: (480) 965-8058, Phone: (480) 727-7522  
[ktk@asu.edu](mailto:ktk@asu.edu), [vasileska@asu.edu](mailto:vasileska@asu.edu), [t.thornton@asu.edu](mailto:t.thornton@asu.edu)

The Schottky Junction Transistor (SJT) [1] is a novel device suitable for micropower circuits applications due to its high mobility values with respect to its conventional counterpart - the silicon MOSFET. Since the mobility of the SJT or SOI MESFET is higher than that of SOI MOSFET in subthreshold and the on state regime, obviously the cutoff frequency should be higher as well for SJT [2]. Even though the SJT device offers higher  $f_T$ , there is no guarantee that the same device will also offer optimum performance in terms of the voltage gain.

To calculate the cutoff frequency and to determine optimized device dimensions, we have developed a transport model, based on the solution of the Boltzmann Transport Equation, for modeling  $n$ -channel silicon-on-insulator (SOI) MESFETs using the Ensemble Monte Carlo technique. All relevant scattering mechanisms for the silicon material system have been included in the model [3]. Major modifications in the existing device simulator have been made in the description of the carrier flow from the gate contact to the conduction channel (as shown in Fig. 1) which takes place mainly by tunneling through the Schottky barrier at the silicon/CoSi<sub>2</sub> interface. The tunneling probability is calculated using the transfer matrix approach for piece-wise linear potentials[4]. To optimize the performance of the device structure in terms of figures of merit, like cutoff frequency and voltage gain, different devices have been simulated for different doping densities, various SOI layer thickness and with different gate lengths. Then, a mathematical model is employed to identify which device shows optimum performance.

A prototypical transfer character for a device with gate length  $L_g=50\text{nm}$  is shown in Fig. 2 and is used in calculating the cut off frequency  $f_T$ . More precisely, the cut-off frequency  $f_T$  is extracted by using  $f_T=g_m/2\pi C_g$ , where  $g_m$  is the transconductance

and  $C_g$  is the gate capacitance of the device under consideration. A sample extracted value for the cut-off frequency is 83.6GHz, as shown in Fig. 3 for a device with  $L_g=50\text{nm}$  and  $t_{si}=25\text{nm}$ , which is quite high with respect to the cutoff frequency of an equivalent MOSFET device. These data are also compared with projected experimental values derived from experimental results of  $0.6\mu\text{m}$  gate length SJT that are shown in Fig. 3. Similarly, the voltage gain is found from the transconductance and the output conductance for the same device dimension which is shown in Fig. 5. Then, the mathematical model is employed where the product of the cutoff frequency and voltage gain is determined for a particular device dimension and the device which has maximum product is chosen to be the optimum one.

From this simple model it is found that the device with a gate length 90nm, silicon film thickness of 20nm and doping density in the channel of  $5\times 10^{17}\text{cm}^{-3}$  is the optimum one (see Fig. 6) and exhibits 33.3GHz cutoff frequency and 25.3 voltage gain. Due to this enhanced cutoff frequency and voltage gain, we can conclude that the SOI MESFET device is a suitable candidate for application in r.f. micropower circuit design for both digital and analog applications.

## REFERENCES

- [1] T. J. Thornton "Physics and Applications of the Schottky Junction Transistor", *IEEE Trans. Electron Devices*, 48, 2421 (2002).
- [2] K. Tarik, S. Ahmed, D. Vasileska, T. Thornton, "Subthreshold mobility modeling of SOI MESFETs", *Journal of Computational Electronics*, Volume 3, Numbers 3-4 Pages: 243 - 246 2005.
- [3] M. V. Fischetti et al., "Long-Range Coulomb Interactions in Small Silicon Devices. Part I: Performance and Reliability" *J. Appl. Phys.*, 89, 1205(2001).
- [4] B. Winstead and U. Ravaioli, "Simulation of Schottky barrier MOSFETs with coupled quantum injection/ Monte Carlo technique", *IEEE TED* 47, 1241 (2000).

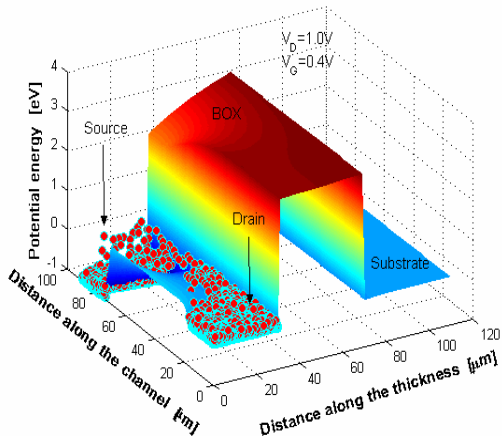


Fig. 1. Two dimensional potential profiles where electrons are flowing interacting with the top interface of the BOX layer and few of them are tunneling through the schottky barrier.

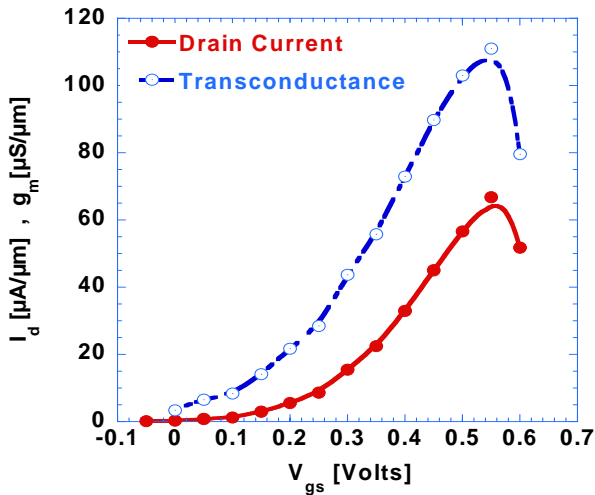


Fig. 2. Transfer characteristics and variation of transconductance with gate voltage at  $V_d = 0.1V$ .

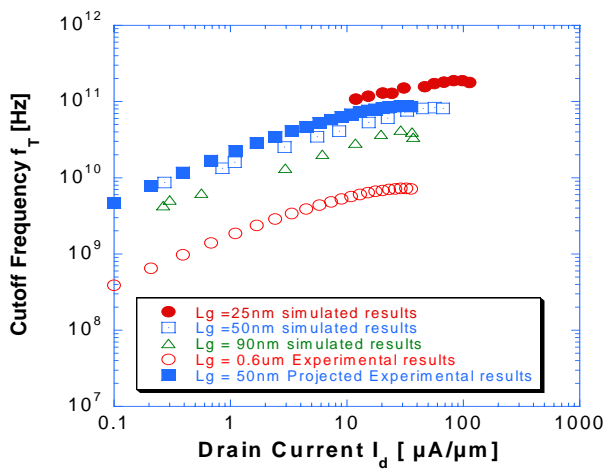


Fig. 3. Simulated and experimentally obtained cutoff frequency

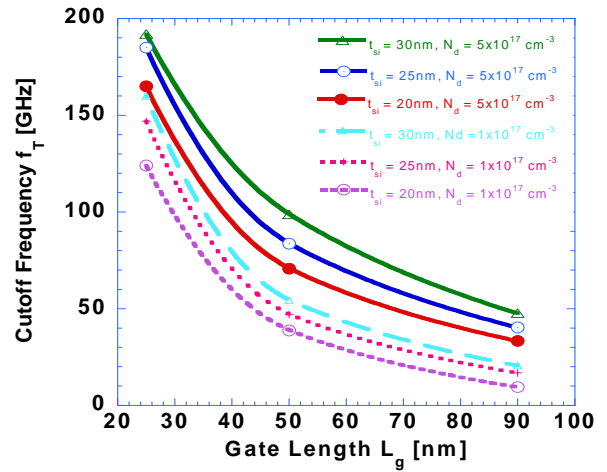


Fig. 4. Variations of cutoff frequency for different device dimensions to find the optimized dimension.

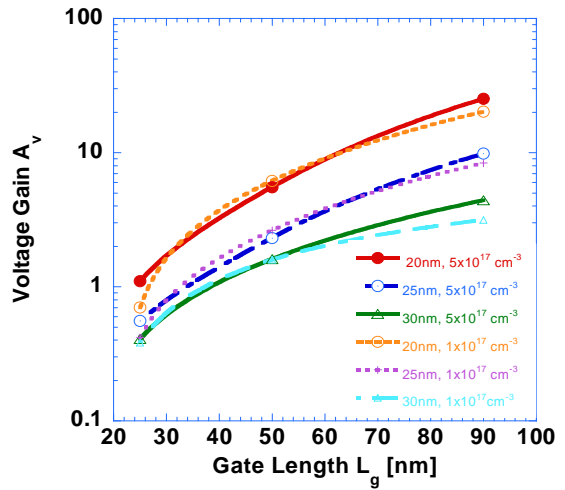


Fig. 5. Variations of voltage gain for different device dimensions to find the optimized dimension.

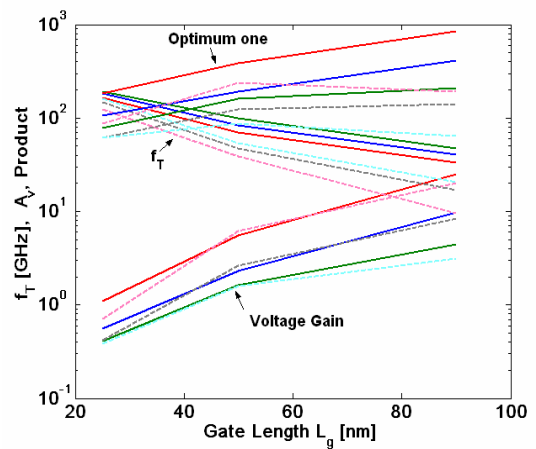


Fig. 6. Determination of the optimized device dimension.

# Physical Modeling of Electron Mobility Enhancement for Arbitrarily Strained Silicon

E. Ungersboeck, S. Dhar, G. Karlowatz, H. Kosina, and S. Selberherr  
Institute for Microelectronics, TU Wien, Gußhausstraße 27–29/E360, 1040 Wien, Austria  
e-mail: ungersboeck@iue.tuwien.ac.at

## ABSTRACT

The band structure (BS) of Si with arbitrary stress/strain conditions has been calculated using the empirical non-local pseudopotential method (EPM). It is shown that the change of the effective masses cannot be neglected for general stress conditions and how this effect together with the strain induced splitting of the conduction bands can be used to optimize electron mobility enhancement  $\Delta\mu_n$ . The new findings have been incorporated into an existing low-field mobility model.

## BAND STRUCTURE CALCULATIONS

Strain effects on the electronic BS of Si are often described using deformation potential theory, which allows the determination of the strain induced splitting of the conduction bands. However, experiments [1] have shown that the mobility enhancement  $\Delta\mu_n$  cannot solely be attributed to this effect, and a recent study has shown that a stress along the  $\langle 110 \rangle$  direction leads to a change of the effective mass  $\Delta m^*$  [2].

In this work, the effect of general strain conditions on the BS is studied by means of EPM calculations. The number of symmetry elements  $P(\Gamma)$  at the center of the Brillouin zone of the strained lattice determines the volume of the irreducible wedge via  $\Omega_{\text{irred}} = \Omega_{\text{BZ}}/P(\Gamma)$ . For stress along  $\langle 100 \rangle$ ,  $\langle 111 \rangle$ , and  $\langle 110 \rangle$ , as shown in Fig. 1,  $P(\Gamma)$  is 16, 12, and 8, respectively, while for stress along other directions the lattice is invariant only to inversion, thus  $P(\Gamma) = 2$ .

## MOBILITY ENHANCEMENT

Bulk mobility was calculated by means of Monte Carlo simulations [3]. In Fig. 2 the strain induced valley splitting is shown for biaxially strained and uniaxially stressed Si (along  $\langle 110 \rangle$  and  $\langle 120 \rangle$ ). It

can be seen that biaxial tension is more effective in splitting the conduction bands than uniaxial tension in  $\langle 110 \rangle$  and  $\langle 120 \rangle$ . Note that for  $\langle 120 \rangle$  stress the conduction bands split into three two-fold degenerate pairs. The in-plane effective masses of the lowest valley were extracted from EPM calculations. Fig. 3 shows how uniaxial tensile stress along  $\langle 110 \rangle$  yields a pronounced  $\Delta m_t$ , whereas the effect is smaller for stress along  $\langle 120 \rangle$  stress and negligible for biaxial tensile strain. The direction of stress in turn leads to a pronounced anisotropy of the mobility in the transport plane. In Fig. 4 the anisotropy of  $\Delta\mu_n$  is compared for different stress directions. It can be clearly seen that  $\Delta m_t$  cannot be neglected for  $\langle 110 \rangle$  uniaxial stress.

The two beneficial effects on the mobility arising from  $\Delta m_t$  and the valley splitting can be combined to yield the highest mobility enhancement in a system with in plane biaxial tension and uniaxial stress along  $\langle 110 \rangle$ . In Fig. 5 the in-plane mobilities parallel and perpendicular to  $[110]$  are shown.

The physically based low-field mobility model in [4] was extended to take into account the stress induced effective mass change of the lowest  $\Delta_2$  valley. For  $\langle 110 \rangle$  stress the effective mass tensor becomes non-diagonal, with  $m_c/2(m_{t,\parallel}^{-1} + m_{t,\perp}^{-1})$  in the diagonal and  $m_c/2(m_{t,\parallel}^{-1} - m_{t,\perp}^{-1})$  in the off-diagonal. Good agreement between Monte Carlo simulation and the analytical model is observed (Fig. 5).

This work has been partly supported by the Austrian Science Fund (FWF), project 17285-N02.

## REFERENCES

- [1] K. Uchida et al., IEDM, pp. 229–232 (2004).
- [2] K. Uchida et al., IEDM, pp. 135–138 (2005).
- [3] Institute for Microelectronics, VMC 1.0 User's Guide, TU Wien, <http://www.iue.tuwien.ac.at/software/vmc> (2004).
- [4] S. Dhar et al., TED, vol. 52, pp. 527–533 (2005).

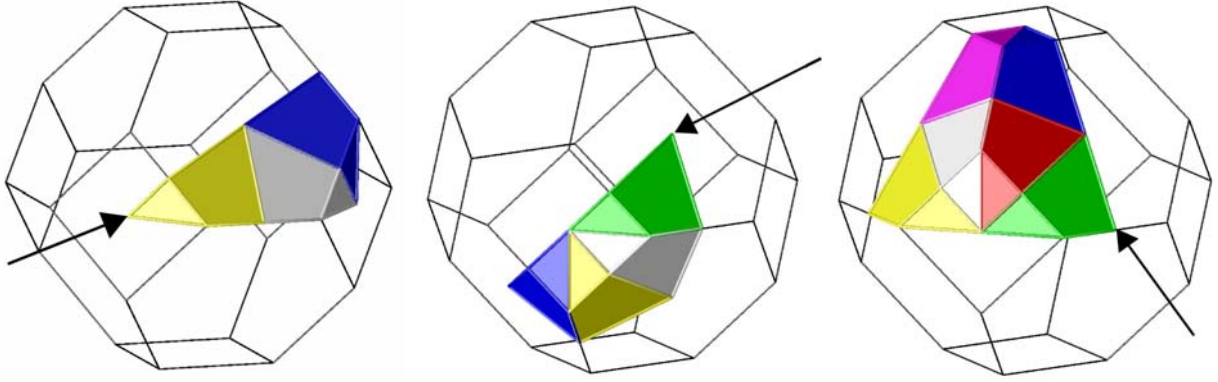


Fig. 1. Irreducible wedge for stress applied in  $[100]$ ,  $[111]$ , and  $[110]$  direction.

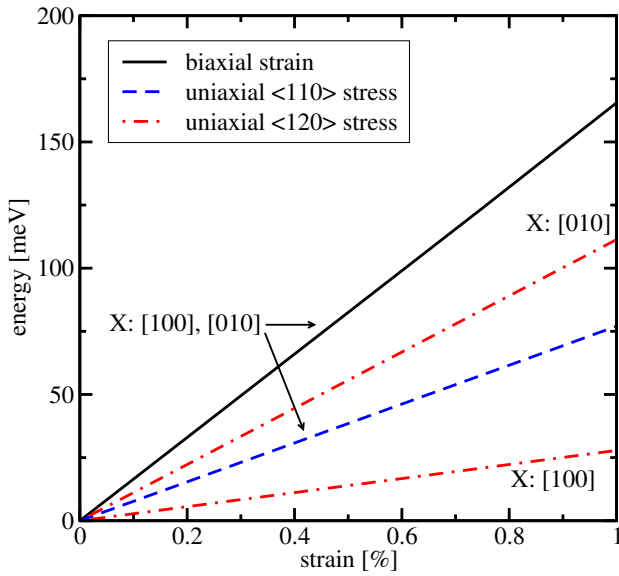


Fig. 2. Effect of biaxial tensile strain and uniaxial  $\langle 110 \rangle$  and  $\langle 120 \rangle$  tensile stress on valley splitting. Strain component in the stressed direction is plotted.

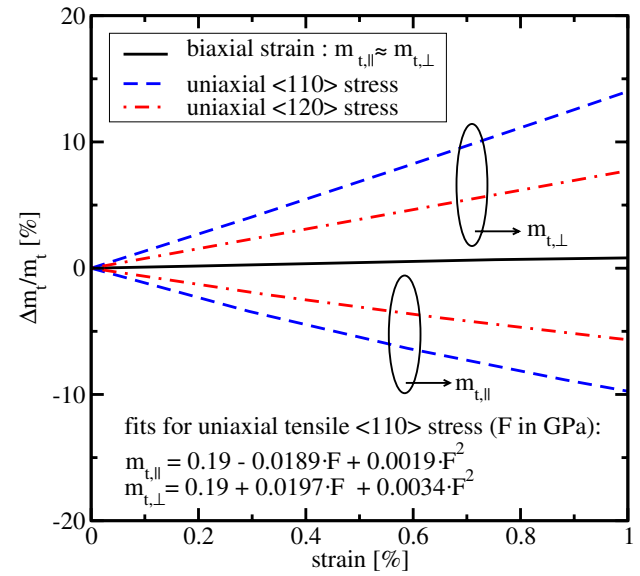


Fig. 3. Effect of biaxial tensile strain and uniaxial  $\langle 110 \rangle$  and  $\langle 120 \rangle$  tensile stress on the in-plane masses of the lowest valley.

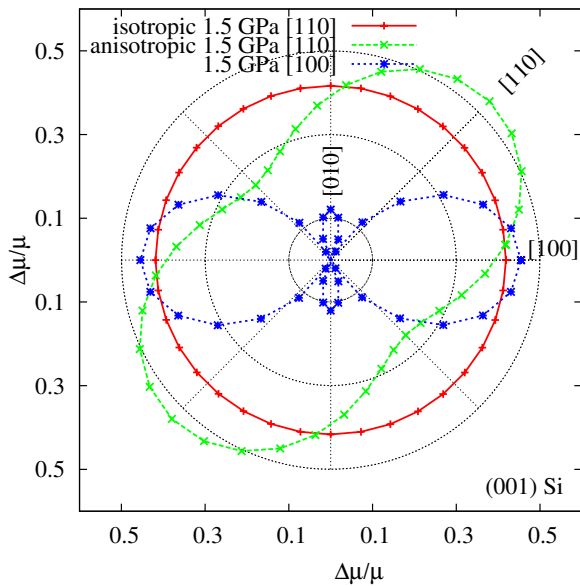


Fig. 4. Mobility enhancement for uniaxial  $\langle 110 \rangle$  tensile and  $\langle 001 \rangle$  compressive stress (equivalent to biaxial in-plane strain). The red line shows  $\Delta\mu_n$  without the mass corrections.

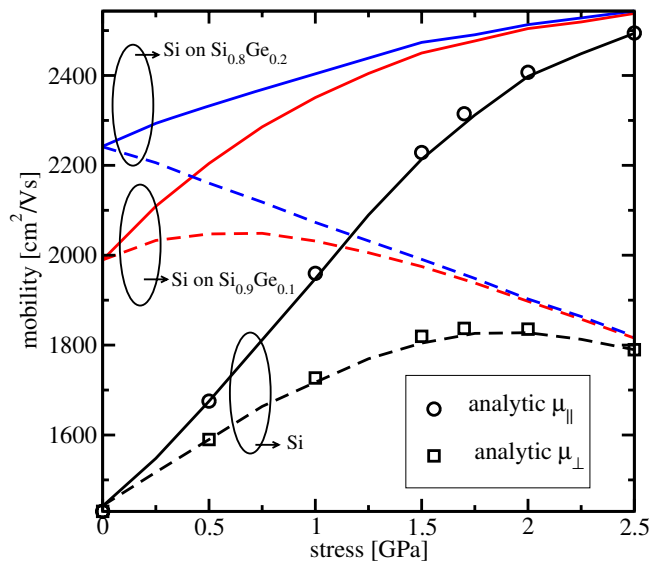


Fig. 5. Simulated bulk mobility for systems combining uniaxial  $\langle 110 \rangle$  tensile stress and biaxial tensile strain in  $[110]$  (solid lines) and  $\bar{1}10$  (dashed lines) direction. The symbols show the mobility calculated from the analytic mobility model [4].

# Simulation of Tri-Gate MOSFET Using 3D Monte Carlo Method Based on the Quantum Boltzmann Equation

Jian Wang, Zhiliang Xia, Gang Du, Xiaoyan Liu, Ruqi Han  
Institute of Microelectronics, Peking University, Beijing 100871, P.R.China  
E-mail: Gang\_Du@ime.pku.edu.cn

The progress in CMOS technologies has resulted in scaling down devices to nano-scale where quantum mechanical (QM) effects in carrier transportation become crucial for the device performance and simulation in three dimension of real space is necessary especially for the non-planar MOSFET such as double-gate MOSFET, tri-gate MOSFET and omega MOSFET. In this paper, a self-consistent full-band Monte Carlo method to solve quantum Boltzmann equation (QBE) three-dimensional both in real space and in K space is developed. The property of a 25nm tri-gate MOSFET is investigated by this method to verify the 3D MC program.

The quantum Boltzmann equation (QBE) obtained from quantum kinetics equation and Wigner distribution function can be used to describe the QM effect [1-4]. Comparing to semi-classical Boltzmann equation (BTE), quantum potential[2,4] and collision broadening [2,5,6] are two key QM effects in QBE that describe the quantum effect in real space and K space respectively.

In Monte Carlo method, the quantum potential correction gives an additional driving force while the carriers are free-flying and is self-consistently calculated every time step just like Poisson potential. As for collision broadening, the selection of the final energy after scattering has to be changed. The final energy is not only given by the initial energy and phonon energy as in the classical method. An additional random number is used to select the final state energy according to the joint spectral function. The joint spectral function for each scattering process is calculated and stored in a table to save CPU time.

The band structure of Si is obtained from empirical pseudo potential calculation. Four conduction bands and three valence bands are used. The acoustic and optical phonon scattering, the ionized impurity scattering, and the impact ionization scattering are also taken into account.

PETSC[7] is employed as 3D Poisson equation solver.

The tri-gate MOSFET we used in the simulation is shown in Fig.1, with  $L=25\text{nm}$ ,  $H=25\text{nm}$ ,  $W=20\text{nm}$ , and gate-oxide thickness  $T_{ox}=2\text{nm}$ . The channel p-doping is  $10^{16}\text{cm}^{-3}$  and the source/drain n-doping is  $10^{20}\text{cm}^{-3}$ . Fig.2 plots the output characteristics with and without quantum effect (QM). The electron density distribution without QM along five sections of the channel is plotted in Fig.3 where the top-gate is on top of each color map, front-gate on the right and back gate on the left. To compare with classical case, Fig.4 shows the electron density distribution with QM along the same five sections. The quantum effects on the electron drift velocity are shown in Fig.5 and Fig.6. Both figures are plotted along the same L-W plane which cuts H-axis approximately in the middle. Fig.3-6 are all plotted when  $V_{gs}=V_{ds}=1.0\text{V}$ .

Simulation results indicate that the quantum effects both in real space and momentum space are obvious in nano-scale device. The device I-V characters, distributions of carrier density, and the drift velocity are all strongly affected by the quantum confinement in 3D.

## References

- [1]Gang Du, Xiaoyan Liu, Computational Electronics, 2004. IWCE-10 2004. Abstracts. Pages:186-187
- [2]H. Haug, A.-p. Jauho *Quantum Kinetics in Transport and Optics of Semiconductors*. Springer 1998.
- [3]W.Hansch *The Drift Diffusion Equation and Its Applications in MOSFET Modeling*. Springer 1991.
- [4] Hideaki Tsuchiya and Tanroku Miyoshi. *IEICE TRANS.ELECTRON*. VOL.E82-C (1999) p.880.
- [5]Antti-Pekka Jauho and Lino Reggiani. *SSE* Vol.31, No.3/4, pp.535-538, 1988
- [6]Leonard F. Register and Karl Hess. *Microelectronic Engineering* Vol.47, 1999 p353
- [7] S. Balay, et.al "PETSc Users Manual," Argonne National Lab., Argonne, IL, Tech. Rep. ANL-95/11—Revision.1.5,2002.

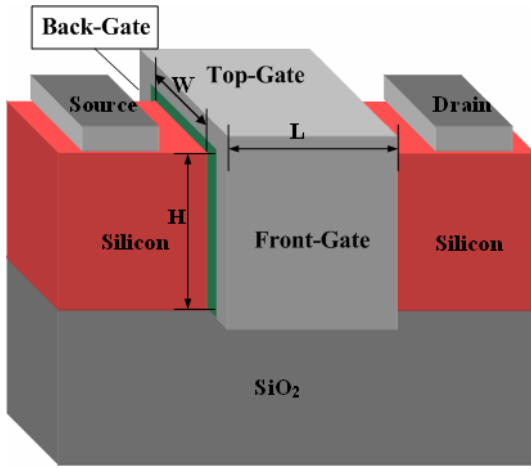


Fig. 1. Device Structure

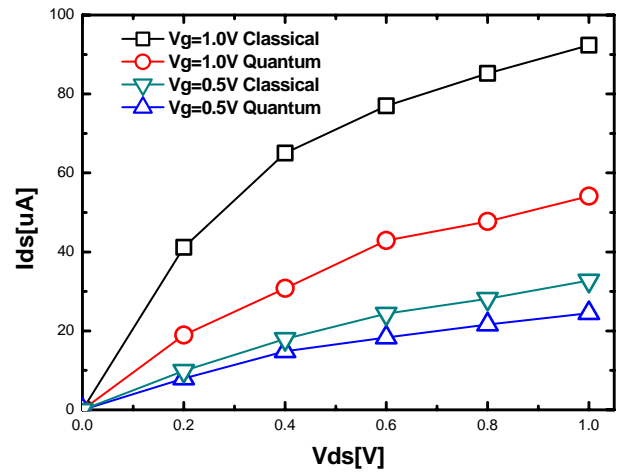


Fig. 2. Ids vs. Vds curves with and without QM

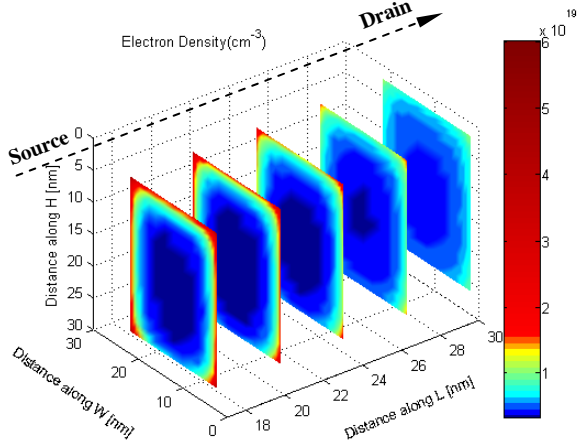


Fig. 3. Charge distribution without QM along five sections of the channel. The Source is on the left while Drain on the right.

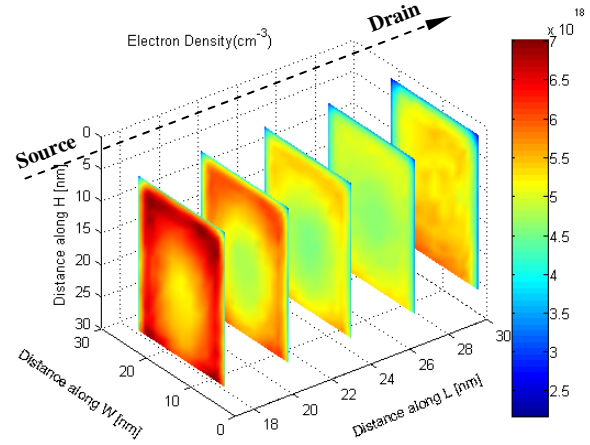


Fig. 4. Charge distribution with QM along the same five sections of the channel as in Fig.3

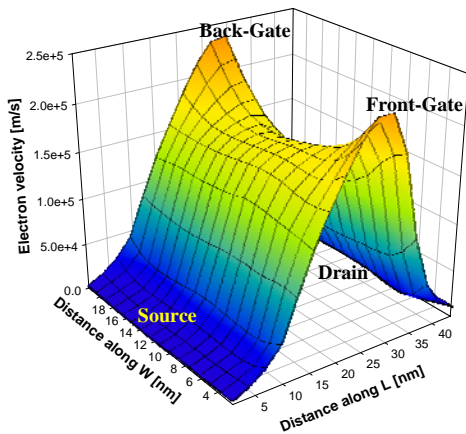


Fig. 5. Electron drift velocity without QM along L-W plane which cuts H-axis approximately in the middle

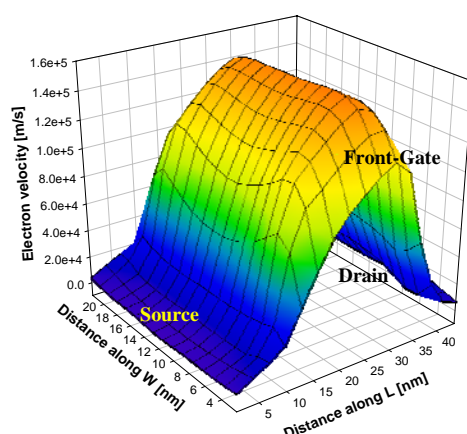


Fig. 6. Electron drift velocity with QM along the same L-W plane as in Fig.5.

# Electron Transport in Self-Switching Nano-Diode

K. Y. Xu, A. M Song\*, and G. Wang

State key Laboratory of Optoelectronic Materials and Technologies/Institute of Optoelectronic and Functional Composite Materials/School of Physics and Engineering, Sun Yat-sen University, Guangzhou 510275, China

\*School of Electrical and Electronic Engineering, University of Manchester, Manchester, UK  
e-mail: stswangg@zsu.edu.cn

## INTRODUCTION

Self-switching Diode (SSD) is a new type of planar nano-diode, which is based on a nano-channel with a broken geometric symmetry [1]. It has been shown to operate in the Terahertz regime at room temperature. In this work, Monte Carlo (MC) simulations were performed and the mechanism of the diode-like characteristics and the existence of threshold voltages were explained.

## MONTE CARLO MODEL

An SSD with the geometry shown in Fig. 1 is considered here and a semi-classical ensemble MC method, self-consistently coupled with Poisson equation, is used [2]. For simplicity, not all layers in the InGaAs/InAlAs heterostructure are included in the simulation. The 2D MC simulation is carried out only on the InGaAs layer which contains the two-dimensional electron gas and hence determines the characteristic of the device. In order to take into account the effect of carriers injection from the  $\delta$ -doped layer, a virtual doping (without impurity scattering),  $N_v=10^{17}\text{cm}^{-3}$ , is assigned to the InGaAs layer. For comparison, the effect of the surface states at the semiconductor-air interfaces originated by the etching process is ignored initially and then added in the simulations.

## RESULT AND DISCUSSION

Figs. 2&3 show the electron distributions inside the SSD at applied voltages  $V=-2.0\text{V}$  and  $+2.0\text{V}$ , respectively. As expected, the electron density inside the channel increases for  $V=+2.0\text{V}$  and decreases for  $V=-2.0\text{V}$ . In these two cases, the average velocities of the electrons in the channel are similar because of the same voltage drop, yet the currents are very different, resulting in the diode-like characteristic in Fig. 5(a). The different electron densities in the channel come from the different electron distributions outside the channel. As shown

in Figs. 2&3, the asymmetric boundary induces electron accumulation and depletion on the left and right sides, respectively, for  $V=+2.0\text{V}$  and inversely for  $V=-2.0\text{V}$ . The different distributions cause a different transverse electric potential (see Fig. 4) which eventually yields different electron densities. At low biases, the above difference can be ignored, so the device works like an ohmic resistance with no threshold voltage (see Fig. 5(a)). In a more realistic case, a negative surface charge density,  $\sigma$ , is assigned to the semiconductor-air interfaces to simulate the effect of surface states. Fig. 6 shows the distributions of electric potential inside the SSD with  $\sigma=0.3 \times 10^{12}\text{cm}^{-2}$  for  $V=+2.0\text{V}$ ,  $0.0\text{V}$  and  $-2.0\text{V}$ , which are similar to those in the references [3, 4]. Comparing Figs. 4&6, one can find that the electric potential in the vicinity of the channel is reduced by the surface states and a barrier of a height of about 1V arises. Such a barrier yields a threshold voltage of about 1.2V (see Fig. 5(b)).

## CONCLUSION

The diode-like characteristics of SSD are simulated based on the different electron distributions caused by asymmetric boundary. The existence of the threshold voltage is found to be a result of the lateral depletion by the surface states at the semiconductor-air interfaces.

## REFERENCES

- [1] A. M. Song, M. Missous, P. Omling, A.R. Peaker, L. Samuelson and W. Seifert, *Unidirectional electron flow in a nanometer-scale semiconductor channel: A self-switching device*, Applied Physics Letters **83**, 1881 (2003).
- [2] T. Kazutaka, *Numerical Simulation of Submicron Semiconductor Devices*, London: Artech House (1993).
- [3] J. Mateos, B. G. Vasallo, D. Pardo, and T. González, *Operation and high-frequency performance of nanoscale unipolar rectifying diodes*, Applied Physics Letters **86**, 212103 (2005).
- [4] J. Mateos, A.M. Song, B.G. Vasallo, D. Pardo, and T. González, *THz operation of self-switching nano-diodes and nano-transistors*, Proceedings of SPIE **5838**, 145 (2005).

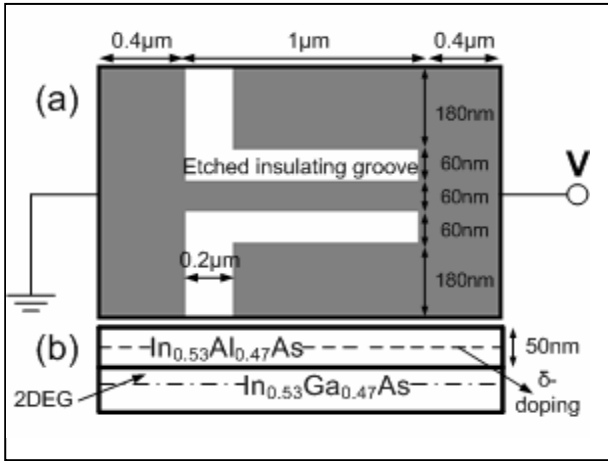


Fig.1. Top view of the simulated SSD (a) and lateral view of a real structure (b).

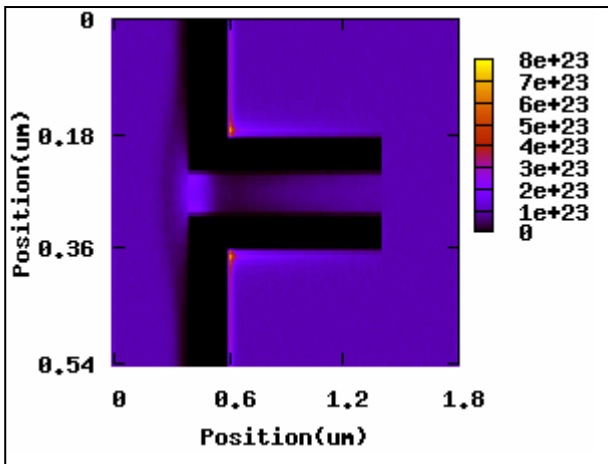


Fig.2. Spatial distribution of the electron density inside the SSD assuming no surface states for  $V= -2$  V.

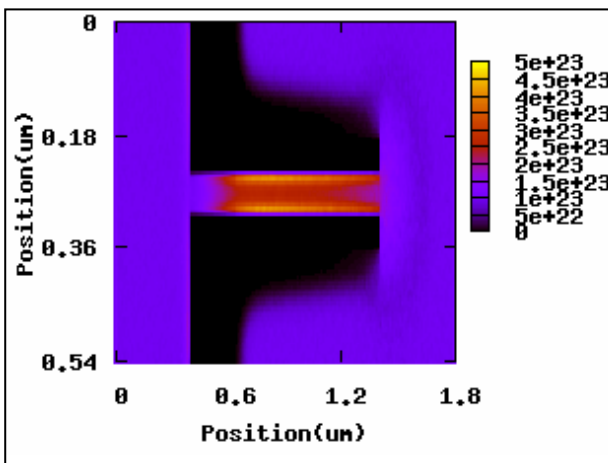


Fig.3. Spatial distribution of the electron density inside the SSD at  $V=+2$  V assuming no surface states.

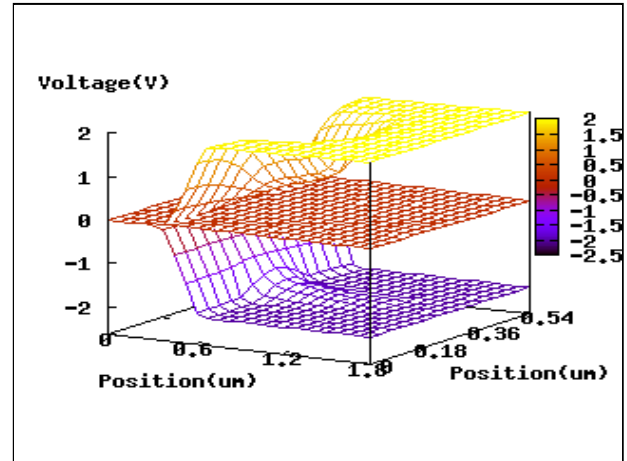


Fig.4. Distribution of electric potential inside the SSD assuming no surface states for  $V=+2.0$  V, 0.0 V and -2.0 V

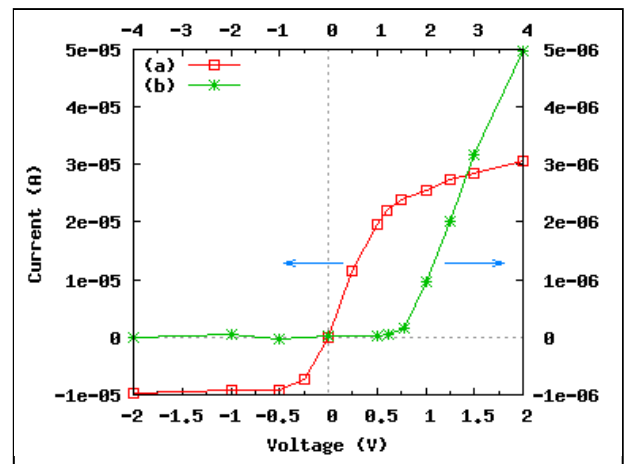


Fig.5. I-V characteristics of the SSD assuming no surface states (a) and with surface states density  $\sigma=0.3 \times 10^{-12} \text{ cm}^{-2}$  (b)

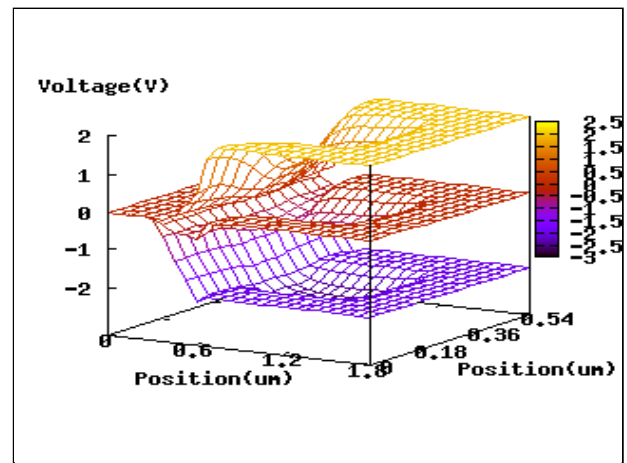


Fig.6. Distribution of electric potential inside the SSD with  $\sigma=0.3 \times 10^{-12} \text{ cm}^{-2}$  for  $V=+2.0$  V, 0.0 V and -2.0 V.

# Molecular Dynamic Simulation on Boron Cluster Implantation for Shallow Junction Formation

Li Yuan<sup>a</sup>, Wei Li<sup>a</sup>, Min Yu<sup>\*a</sup>, Huihui Ji<sup>a</sup>, Kai Zhan<sup>a</sup>, Ru Huang<sup>a</sup>, Xing Zhang<sup>a</sup>, Yangyuan Wang<sup>a</sup>,  
Jinyu Zhang<sup>b</sup> and Hideki Oka<sup>c</sup>

<sup>a</sup> Institute of Microelectronics, Peking University, China 100871,

<sup>b</sup> Fujitsu R&D Center Co. LTD, Room B1003, Eagle Run Plaza No.26 Xiaoyun Road Chaoyang District  
Beijing, China,

<sup>c</sup> Fujitsu Laboratories LTD, 10-1 Morinosato-Wakamiya, Atsugi 243-0197, Japan

\* Email: [yum@ime.pku.edu.cn](mailto:yum@ime.pku.edu.cn)

## INTRODUCTION

Boron cluster ion implantation is a potential technology for shallow junction formation in integrated circuits manufacture [1]. By cluster implantation, space-charge blow up of the beam can be minimized and more B atoms are implanted at the same beam current. Another advantage of using clusters is that it generates more defects to reduce channeling effect [2]. With the technology becoming more practicable, capability of simulating it for shallow junction formation becomes necessary, which is still difficult for full MD method. A localized molecular dynamic method [3] for simulating cluster implantation at normal dose, e.g.  $10^{15} \text{ cm}^{-2}$ , aimed at microelectronics application, is presented in this paper.

## MODEL

In our MD simulation, a moving simulation box [3], composing of  $3 \times 3 \times 3$  unit cells (about 200 atoms), is applied to save computing time. Accurate geometry structures of boron clusters [4] are considered in the model by described accurate position of both B and H atoms as is illustrated in Fig. 1. In order to describe interactions between atoms in boron clusters, potential function in which the repulsive action term is ZBL potential function and attractive term has the form of SW [5] potential function is applied.

## RESULTS

Simulation examples of  $\text{B}_{10}\text{H}_{14}$  and  $\text{B}_{18}\text{H}_{22}$  are performed. The snapshot of cluster implantation is shown in Fig. 2. Simulation results are shown in Fig. 3~6. It can be seen that range profiles from simulation agree well with the SIMS data. Specially, agreement of H profile is also shown for  $\text{B}_{18}\text{H}_{22}$

implantation, where obvious deviation at near surface region exists maybe due to uncertainty of SIMS measurements at such shallow region. Simulation and SIMS data of B monomer implantation at equivalent energy and dose is also shown in Fig. 3 and 5 as comparison. It shows cluster implantation tends to generate shallower distribution profile. It is notable that with cluster model presented, the simulation can reproduce that difference well.

Fig.4, 6 also show that cluster implantation induces more Si interstitial defects than B monomer. These results agree with reference [2].

## ACKNOWLEDGEMENT

This paper is supported by the National Natural Science Fund (No. 90207004)

## REFERENCES

- [1] Takayuki Aoyama, Masatoshi Fukuda, Yasuo Nara, Ext. Abs. the 5th International Workshop on Junction Technology (2005) S2-2
- [2] Aoki T., Matsuo J., Takaoka G., Ion Implantation Technology. 2002. Proceedings of the 14th International Conference (2002) P560 - 563
- [3] K. Norlund, Comput. Mater. Sci. 3 (1995) P448
- [4] A.F. Wells, Structure Inorganic Chemistry Fourth Edition 870
- [5] Paul B. Rasband, Paulette Clancy, Bruce W. Roberts, Journal Applied. Physics, V.84, P.2471 (1998)
- [6] M. Ishibashi, Y. Kawasaki, K. Horita, Ext. Abs. the 5th International Workshop on Junction Technology (2005) S2-3
- [7] Tanjyo M., Hamamoto N., Umisedo S., Solid-State and Integrated Circuits Technology, 7th International Conference (2004) V1 P434 - 438

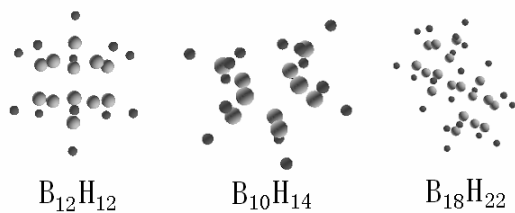


Fig. 1. The schematic representation of boron clusters ( $B_{12}H_{12}$ ,  $B_{10}H_{14}$  and  $B_{18}H_{22}$ ). Structure of  $B_{10}H_{14}$  and  $B_{18}H_{22}$  is described based on that of  $B_{12}H_{12}$ .

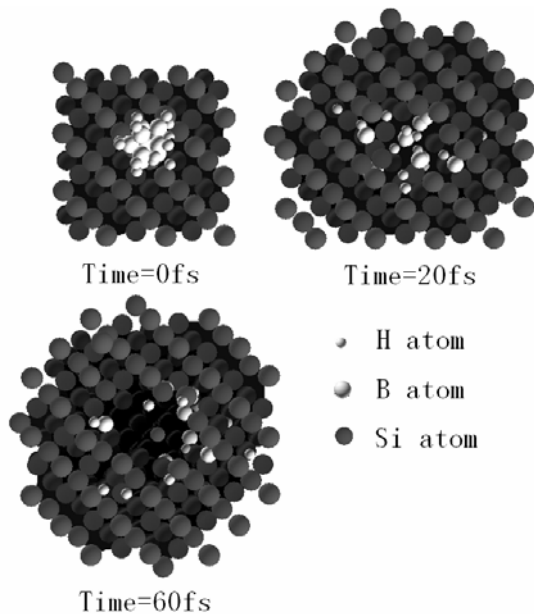


Fig. 2. Snapshots of  $B_{10}H_{14}$  implantation at 1keV/molecular

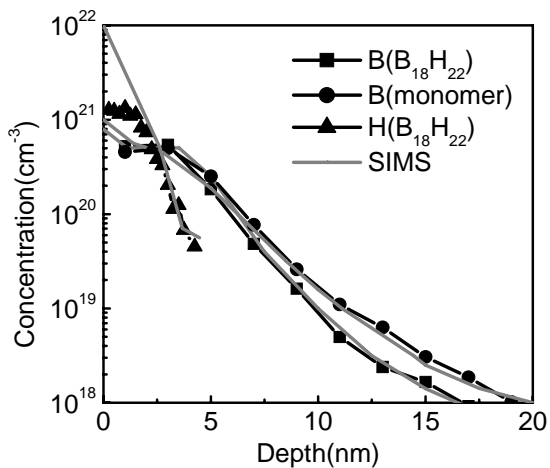


Fig.3 Concentration profiles of B atoms and H atoms for  $B_{18}H_{22}$  implantation at 10keV/molecular and B monomer atom implantation at 0.5keV/atom. (Dose  $3e14B/cm^2$ )The SIMS data is from Ref. [6]

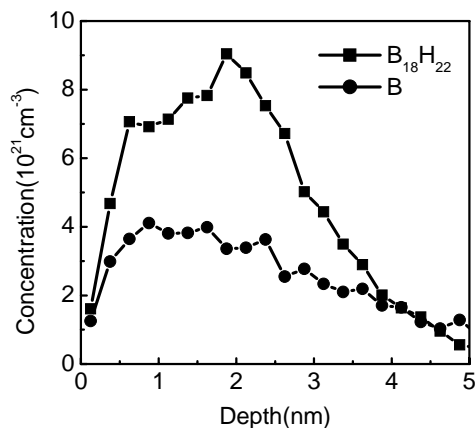


Fig.4 Concentration profiles of Si interstitials for  $B_{18}H_{22}$  implantation at 10keV/molecular and B monomer atom implantation at 0.5keV/atom. (Dose  $3e14B/cm^2$ )

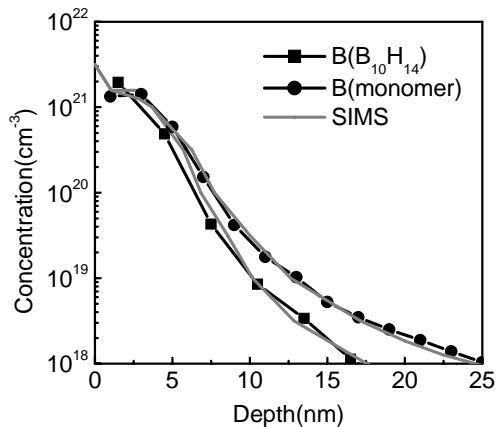


Fig.5 Concentration profiles of B atoms for  $B_{10}H_{14}$  implantation (Dose  $8.3e14B/cm^2$ ) at 5keV/molecular and B monomer atom implantation at 0.5keV/atom (Dose  $8.1e14B/cm^2$ ). The SIMS data is from Ref. [7]

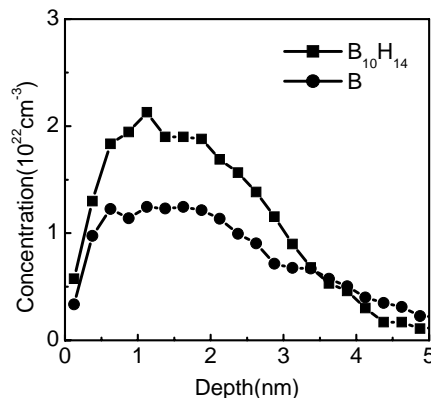


Fig.6 Concentration profiles of Si interstitials for  $B_{10}H_{14}$  implantation (Dose  $8.3e14B/cm^2$ ) at 5keV/molecular and B monomer atom implantation at 0.5keV/atom (Dose  $8.1e14B/cm^2$ ).

# Physical Modeling of Hole Mobility in Silicon Inversion Layers under Uniaxial Stress

Ji Zhao, Jianping Zou, and Zhiping Yu

Institute of Microelectronics, Tsinghua University, Beijing, 100084, China

E-mail: zhaoji03@mails.tsinghua.edu.cn

## ABSTRACT

A physical model for hole mobility under both biaxial and uniaxial stress has been developed. The six-band  $k \cdot p$  theory is used to obtain the bandstructure with stress-dependent Hamiltonian. The hole mobility in the silicon inversion layer is studied in details using Monte Carlo method. A numerically robust method has been applied to achieve self-consistent solution of Poisson's and Schrödinger equations.

## INTRODUCTION

The uniaxial compressive stress has been used as an important technology for enhancing hole mobility. The theoretical models of hole mobility under biaxial stress have been studied [1,2]. Wang [3] has also discussed hole transport in inversion layers under arbitrary stress. This work is focused on hole mobility modeling under uniaxial stress of different orientation.

## BANDSTRUCTURE AND MOBILITY CALCULATIONS

We applied the six-band stress dependent  $k \cdot p$  theory to assemble the Hamiltonian in one-dimensional (1D) Schrödinger equation. We used self-consistent solution of Poisson's and Schrödinger equations to achieve the electronic structure in strained Si inversion layers. The self-consistency is achieved by applying a numerically efficient Newton-Broyden's method. The Monte Carlo procedure is used to evaluate the carrier transport under constant electric field and considering the scattering mechanisms of hole-phonon interaction, interface roughness, and Coulomb scattering.

## RESULTS AND DISCUSSION

First, we compare the convergence behavior of several different numerical, iterative methods in Fig. 1. It can be seen that the improved Newton-Broyden method has the best performance compared to the

standard Newton and standard Newton-Broyden methods. The calculated hole mobility vs. the effective electric field under unstrained Si, biaxial stress, and uniaxial stress are shown in Fig. 2 together with the experimental data for unstrained channel. Fig. 3 gives the first subband energy contours under unstrained and uniaxial compressive stress along the [110] direction with an effective field of 0.8MV/cm. Due to the effect of uniaxial stress the energy of regions K and L is lifted relative to the other regions M and N. More holes redistribute to the regions M and N with a low effective mass along the [110] direction. So, under uniaxial stress the mobility enhancement originates from an effective mass change and scattering suppression due to the splitting of band. The biaxial tensile stress, on the other hand, enhances mobility only through scattering suppression [3]. Fig. 4 shows the hole mobility under [110] and [100] uniaxial stress, respectively, and it is apparent that the hole mobility is larger in [110] than in [100] direction. Figs. 5-6 show the effective mass for the above two orientations and the mobility gain with the change in composition of Ge in SiGe.

## CONCLUSIONS

The effective mass and scattering suppression play the important roles in mobility enhancement. Uniaxial compressive stress along [110] direction enhances the hole mobility much more than in any other crystalline orientation. The physical model shows good agreement with experiment data.

## REFERENCES

- [1] M. Fischetti, *et al.*, "Six-band  $k \cdot p$  calculation of the hole mobility in silicon inversion layers: Dependence on surface orientation, strain, and silicon thickness," *J. Appl. Phys.* 94(2), 1079(2003)
- [2] R. Oberhuber, G. Zandler, and P. Vogl, "Subband structure and mobility of two-dimensional holes in strained Si/SiGe MOSFET's," *Phys. Rev. B*, 58(15), 9941(1998)
- [3] E. Wang, *et al.*, "Quantum mechanical calculation of hole mobility in silicon inversion layers under arbitrary stress," *IEDM Digest*, 2004

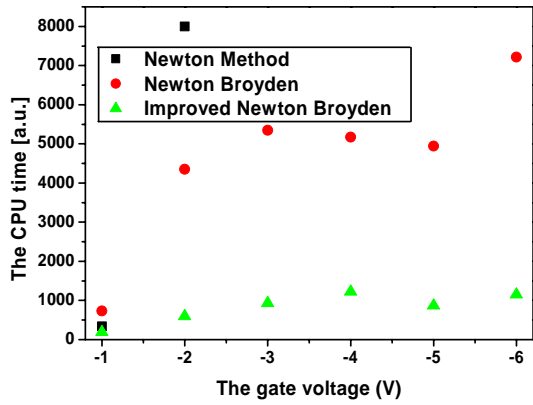


Fig. 1: The CPU time to achieve the consistent solution to 1D Schrödinger and Poisson's eqs. with various numerical method.

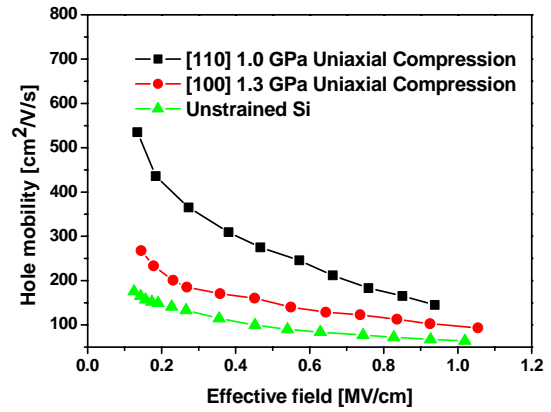


Fig. 4: The hole mobility in pMOS under unstrained and uniaxial compressive stress along the [110] and [100] direction, respectively, as a function of the effective electric field.

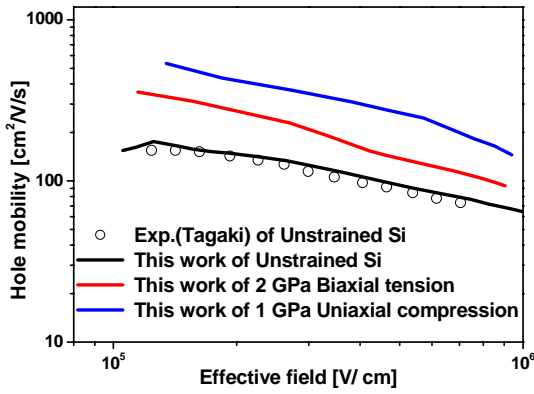


Fig. 2: Calculated hole mobility of pMOS under unstrained, biaxial tension and uniaxial compression as a function of the effective electric field.

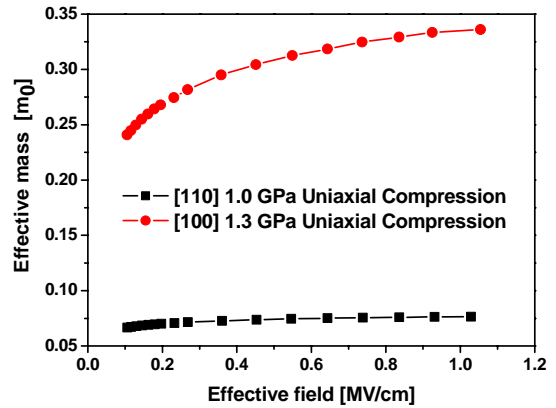


Fig. 5: The first subband hole effective mass of pMOS under uniaxial compressive stress along the [110] and [100] direction as a function of the effective electric field.

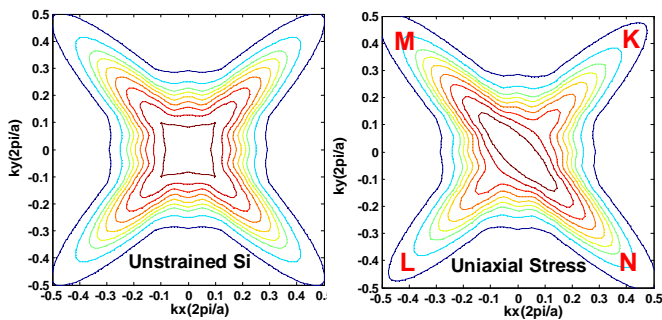


Fig. 3: First subband energy contours for valence band with an effective field of 0.8MV/cm under no stress and 1 GPa uniaxial compressive stress along [110].

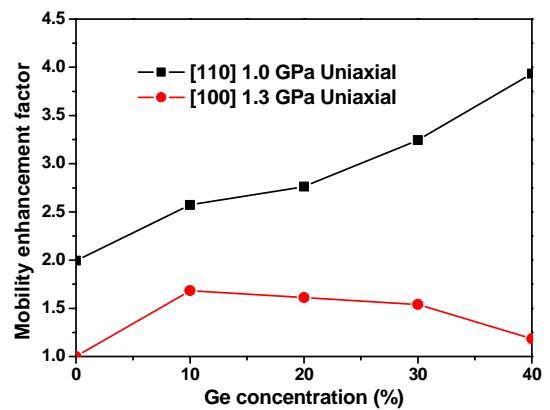


Fig. 6: The hole mobility enhancement factor of pMOS under uniaxial compressive stress along the [110] and [100] direction as a function of the Ge mole fraction in SiGe.

# Reduced Backscattering in Potassium Doped Nanotubes

Ch. Adessi, Stephan Roche\*<sup>†</sup>, and X. Blase

Laboratoire de Physique de la Matière Condensée et des Nanostructures (LPMCN),  
CNRS and Université Claude Bernard Lyon I, UMR 5586,  
Bâtiment Brillouin, 43 Bd du 11 Novembre 1918,  
69622 Villeurbanne Cedex, France.

\*CEA-DSM/DRFMC/SPSMS/GT, 17 avenue des Martyrs, 38054 Grenoble, France.

<sup>†</sup>CEA-DRT/D2NT, 17 avenue des Martyrs, 38054 Grenoble, France.

e-mail: christophe.adessi@lpmcn.univ-lyon1.fr

## INTRODUCTION

The integration of carbon nanotubes (CNTs) in electronic devices such as field-effect transistors (CNFETs) [1] has generated much experimental and theoretical work to understand the basic phenomena controlling the device performances. As a crucial ingredient, the doping of the semiconducting canal has been achieved following different strategies.

While substitutional doping certainly increases the carrier density in the CNTs, it also induces significant backscattering that can reduce the charge transmission capability of a given conduction channel [2], [3]. We study the conductance of metallic and semiconducting tubes doped either by K in adsorption or N in substitution.

## THEORETICAL FRAMEWORK

A  $O(N)$  *ab initio* method is used to precisely compute the effect of isolated defects on the Landauer transmission. Our *ab initio* results are further used to construct an accurate  $\pi - \pi^*$  effective model which allows to access, within the Kubo formalism, the conductance and elastic mean free path of tubes randomly doped over micron scales.

## DISCUSSION

The case of a metallic C(6,6) and semiconducting C(7,0) nanotubes are considered (Fig. 1). In the case of K-doping, an important outcome of the present study is *the complete disappearance of the broad structure associated with the low energy (more bound) resonance state*. This is a clear indication that K-doped tubes, as compared to the N-doped

systems, will display a ballistic-like behavior on a much larger gate-voltage range and for longer propagation length of charge carriers.

We also investigate more realistic cases of micrometers long nanotubes doped by a random distribution of scatterers. Such calculations have been carried on doped (10,10) CNTs (Fig. 2). The MFP of the K-doped nanotube ( $\ell_e \sim 24\mu\text{m}$ ) is found to be four times larger than the N-doped tube at  $E_F \sim 0.5\text{eV}$  (energy of the deeper N quasibound state), and at the same impurity density.

## CONCLUSION

On the basis of *ab initio* conductance calculations, K-impurities have been shown to induce much less backscattering as compared to nitrogen substitutions. By mapping the *ab initio* Hamiltonian onto a reduced  $\pi - \pi^*$  model, the conductance and mean-free path of randomly doped micrometers long tubes was investigated within the Kubo formalism, confirming that K-doping leads to much longer mean free paths.

## REFERENCES

- [1] A. Bachtold, P. Hadley, T. Nakanishi, and C. Dekker, *Science* **294**, 1317 (2001).
- [2] S. Latil, S. Roche, D. Mayou, and J.-C. Charlier, *Phys. Rev. Lett.* **92**, 256805 (2004)
- [3] H.J. Choi, J. Ihm, S.G. Louie, and M.L. Cohen, *Phys. Rev. Lett.* **84**, 2917 (2000).

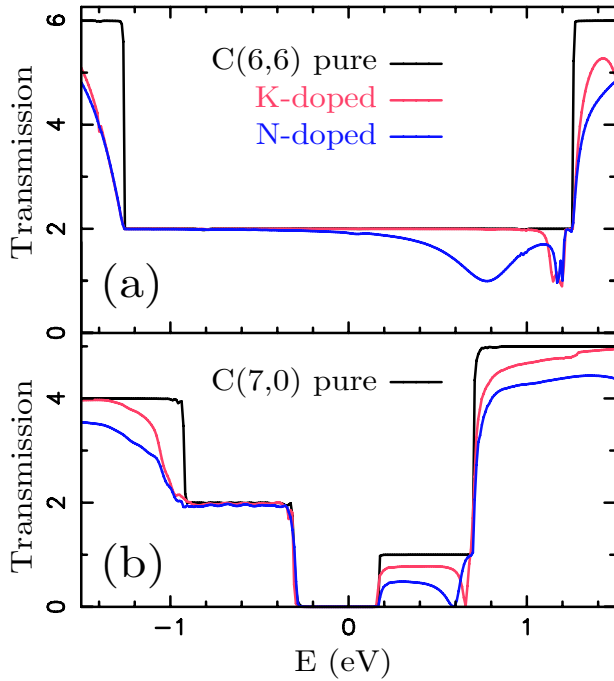


Fig. 1. Transmission for (a) a C(6,6) and (b) a C(7,0) nanotube. Undoped (black), nitrogen-doped (blue) and potassium-doped (red) tubes are considered.

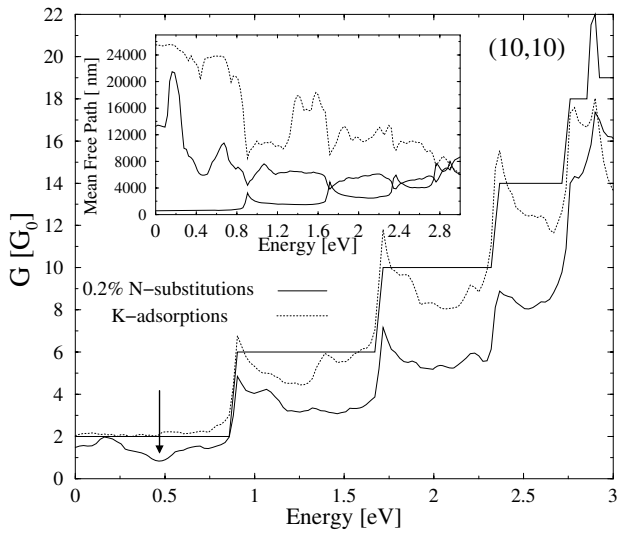


Fig. 2. Main frame: Conductance for the (10,10) nanotube with 0.2% of randomly substituted N-impurities (bold) or physisorbed K-impurities (dotted line). The number of quantum channels is also reported (solid line). Inset: Corresponding mean free paths together with the rescaled density of states (solid line).

# Scaling of Molecular Electronics Devices

Aissa Boudjella <sup>1, 2, 3)</sup> Kamli Mokhtar <sup>4)</sup>

<sup>1)</sup>Queen's College, Mississauga <sup>2)</sup>Alpha Toronto <sup>3)</sup>Conseil Scolaire de District du Centre Sud Ouest, Toronto, Canada

<sup>4)</sup>Honeywell - Engines, Mississauga, Toronto, Canada~

## 1 characterization procedure

Here, we use Poisson equation<sup>1)</sup> to examine the electric field distribution in the simplified device structure shown schematically in figure 1. We study different oxide thickness and present all results for both thin ( $T_{ox}=1\text{ nm}$ ) and thick dielectric ( $T_{ox}=100\text{ nm}$ ). The gap distance between the drain and source is  $1$  or  $4\text{ nm}$ , and contains 4-thioacetylphenil or PDT material. These molecules are modeled as rigid dielectric material with suitable relative permittivity  $2$  [ref. 2] or  $6.3$  [ref. 3]. We performed simulations using TCAD tools<sup>1)</sup>. The set of simulations were run under GENESISe. The tool flow starts with the two dimensional editor MDRAW (mesh generator/device). DESSIS was used to perform the device simulation. The results, e.g. the electric field distributions inside the device structure are visualized with the plotting and extraction tool Tecplot. Since TCAD tools do not normally allow device dimensions as small as those considered in this research, a possible approach is to scale voltages and dimensions. For example, a classical method to maintain the short channel MOSFETs behavior is to reduce all dimensions and voltages of larger device by a scaling factor  $\kappa (>1)$ , so that the internal electric fields are the same as those of a long channel FET. This widely used approach is called constant field scaling<sup>4)</sup>. Based on the fundamental limits, it may be possible to scale the FETs down to very small dimensions such as  $10\text{nm}$  of channel length or smaller<sup>5)</sup>. We use the scaling relations at constant field to determine all dimensions and voltages of nanoscale FETs<sup>4, 6)</sup>. Nanoscaled SAMFET circuit parameters are scaled up by a factor  $\kappa=1000$  to produce larger FET with similar internal electric fields behavior.

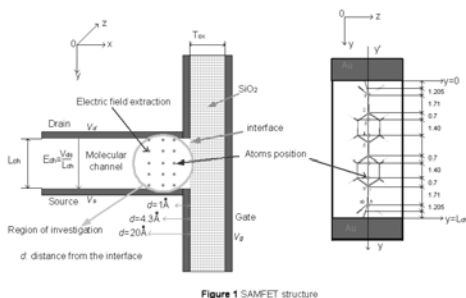


Figure 1 SAMFET structure

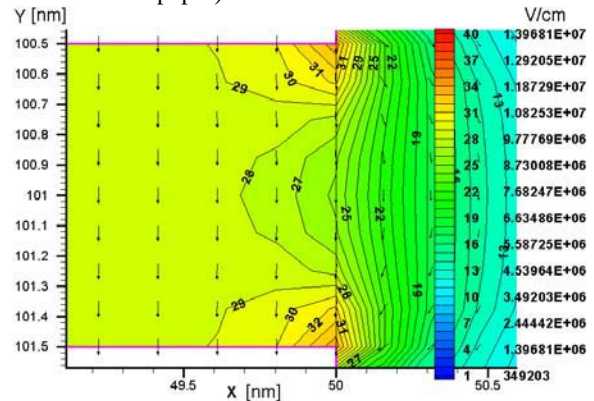
Figure 1 cross section view of molecular field effect

## 2 Simulation Results

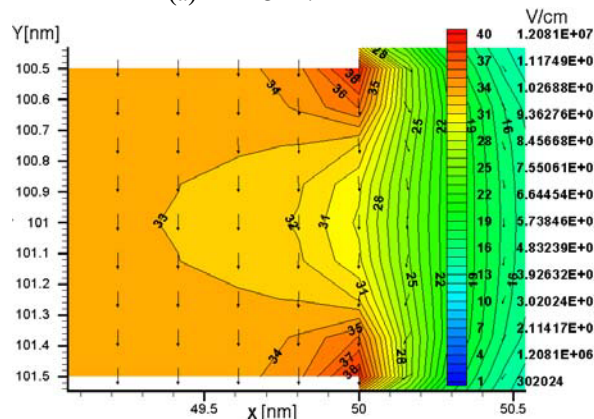
Fig. 2 and 3 show the fields distribution for  $T_{ox}/L_{ch} = 5$  and  $15$  respectively with the dielectric constant  $\epsilon=2$  and  $6.3$ . Near the drain or source electrode, from the interface, the non-uniform field region penetrates the molecular channel for  $4\text{\AA}$  (fig.2) and  $3\text{\AA}$  (fig.3). At mid distance between drain and source, the electric field penetration from the

interface is about  $3\text{\AA}$  for fig. 2 and  $6\text{\AA}$  for fig. 3. By comparison with the results in fig.2 and 3, a typical representative of the region where  $T_{ox}/L_{ch}$  is increased from  $15$  to  $50$  (not shown in here), the gate field seems to have little effect on the fields inside the molecular structure.

In order to compare the electric field distribution inside the active region along the molecular channel at atoms position, fig. 4 and 5 show the variation of channel electric field versus the gap distance at different distances  $d$  from the interface  $1, 2, 2, 4$  or  $5\text{\AA}$ . The drain electrode is located at  $y=0$  and the source at  $y=L_{ch}$ . Certain points in the y-axis correspond to the atoms positions. The details are reported by the author in ref.7. The electric field distribution is completely symmetrical with respect to a horizontal line at mid-distance between drain and source. High field are near the source or drain electrode. The field becomes larger when  $d$  decreases. Low fields are observed in the middle of the drain and source electrode. The same symmetry (not shown in this paper) was observed for  $\epsilon=6.3$ .



(a)  $\epsilon = 2.$



(b)  $\epsilon = 6.3.$

Figure 2 Electric field distribution for  $T_{ox}/L_{ch} = 5$  with  $V_d=1\text{ V}$ ,  $V_g=1\text{ V}$ ,  $T_{ox}=5\text{nm}$ ,  $L_{ch}=1\text{ nm}$ ,  $V_d/L_{ch}= 0.1\text{ Kv/A}$ .

## 3 Conclusion

Calculations of electric field distribution on FETs molecular channel is carried out on the range of  $T_{ox}/L_{ch} = [0.2-50]$  under different dielectric constant of the molecular environment. Based on numerical simulations, to evaluate the voltage gate effect on the molecular channel, three regions can coarsely be defined as follows: 1) strong gate effect,  $T_{ox}/L_{ch} = [0.2-0.66]$ , 2) significant gate effect,  $T_{ox}/L_{ch} = [0.66-5]$  and 3) limited gate effect,  $T_{ox}/L_{ch} > 5$ . For  $T_{ox}/L_{ch}$  of the order of 5,  $V_g$  has a limited impact on the channel field. A high  $T_{ox}/L_{ch}$  limits this effect. When  $T_{ox}/L_{ch}$  is too large,  $V_g$  does not have much effect on the channel field distribution. The difference of the dielectric constant seems has no effect on modifying the channel field distribution.

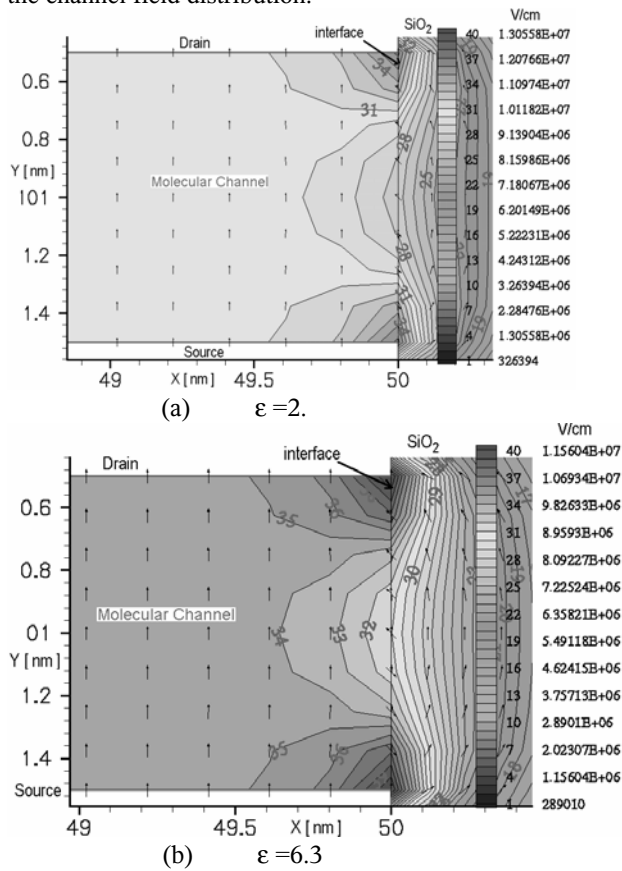


**Figure 3** Electric field distribution for  $T_{ox}/L_{ch} = 15$  with  $V_d = -1V, V_g = -0.5V, T_{ox} = 15nm, L_{ch} = 1nm, V_d/L_{ch} = 0.1Kv/\text{\AA}$

### Reference

- [1] Integrated Systems Engineering (ISE) of Technology Computed Aided Design (TCAD) software. Simulation structure in our paper is 2D dimensional.
- [2] P. Damle et al.: IEEE Trans. Nanotechnol. 1 (2002) 145.
- [3] C. Zhou et al.: Tour: Appl. Phys. Lett. 71 (1997) 611.
- [4] R. H. Dennard et al.: IEEE J. Solid State Circuits SC-9 (1974) 256. [5] J. Frank et al.: Proc. IEEE. 89 (2000) 259.
- [6] H. S. P. Wong et al.: Proc. IEEE. 87 (1999) 537.
- [7] A. Boudjella et al.: Japanese Journal of Applied Physics. Vol. 43, 8B, 2004.

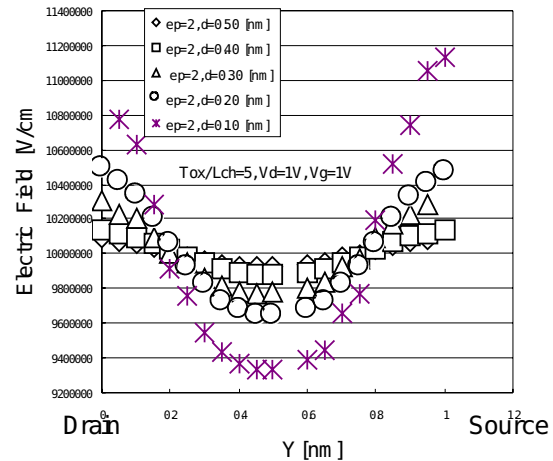
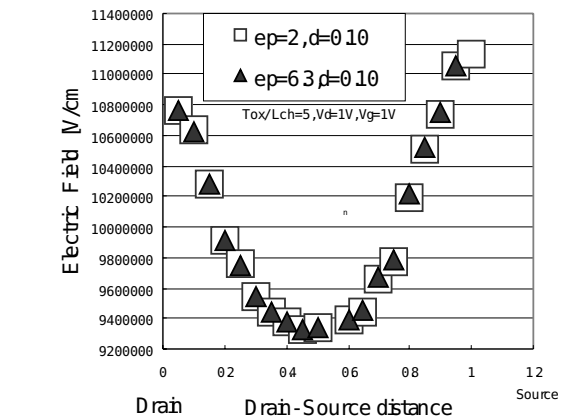
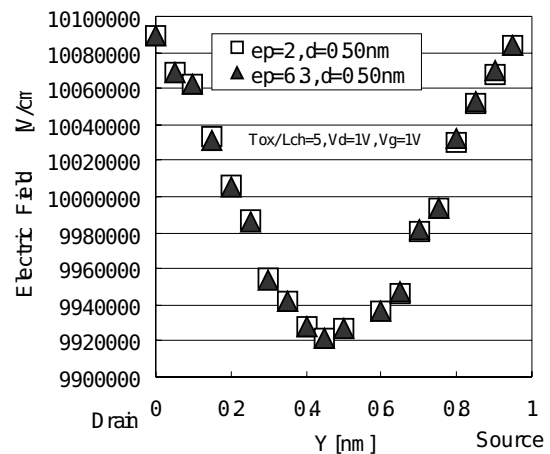


**Figure 4** Electric field versus gap distance.  $d = 1, 2, 3,$  and  $5\text{\AA}$ .  $L_{ch} = 10\text{\AA}, T_{ox}/L_{ch} = 5, V_d = 1V, V_g = 1V$  and  $\epsilon = \epsilon_p = 2$



(a)



(b)

**Figure 5** Electric field versus gap distance.  $L_{ch} = 10\text{\AA}, T_{ox}/L_{ch} = 5$  with  $V_d = 1V, V_g = 1V, \epsilon = \epsilon_p = 2$  and  $6.3$ .

# Computation of the $I$ - $V$ Characteristics of a Molecular Switch

I. Cacelli\*, A. Ferretti<sup>†</sup>, M. Girlanda\*<sup>†‡</sup>, M. Macucci<sup>‡</sup>

\*Dip. di Chimica e Chimica Industriale, Università di Pisa, via Risorgimento 35, I-56126 Pisa, Italy

<sup>†</sup>Istituto per i Processi Chimico-Fisici del CNR, via G. Moruzzi 1, I-56010 Pisa, Italy

<sup>‡</sup> Dipartimento di Ingegneria dell'Informazione, Università di Pisa, via Caruso 2, I-56122 Pisa, Italy  
e-mail: macucci@mercurio.iet.unipi.it

## INTRODUCTION

We study the single molecule conduction properties of a class of molecular torsional switches whose conformation is sensitive to the electric field perpendicular to the molecular plane and affects the possibility of charge transport from one end of the molecule to the other. In particular, we present a calculation of the current as a function of the internal configuration of the molecule.

## MOLECULAR DEVICE AND COMPUTATIONAL METHOD

The molecular switch we are analyzing is made up of two benzene rings (each with two electron withdrawing chemical groups) connected by an acetylene bridge. A terminal thiol group is placed at each molecular end to act as a clip between the molecule and the gold electrodes (see Fig. 1). The switching functionality in such a class of molecules has already been extensively investigated [1], [2]. The principle of operation is that, under the action of an electric field of appropriate intensity and perpendicular to the ring-ring axis, the two rings counter-rotate: this leads to a disappearance of the conjugation of the molecular  $\pi$  orbitals, resulting in charge localization. Thus the conductance of the molecule is expected to drop significantly when the rings reach the mutually perpendicular position.

The  $I - V$  characteristics of the molecular structure, with the rings coplanar or perpendicular, have been computed using a method developed from the approach recently proposed by Gonzalez *et al.* [3]. Within the framework of the combined Density Functional Theory and Green's function formalisms, the molecule-electrode coupling contributing to the self-energy is taken to be proportional to

the projection of the molecular orbitals onto the terminal thiol fragment. The proportionality constant determines the strength of the molecule-electrode coupling and reflects the physical evidence that strongly coupled molecule and lead result, in the contact region, into spatially extended orbitals. With respect to the method of Ref. [3], we consider only the thiol as a terminal fragment and evaluate the true projection of the molecular orbitals onto the thiol orbitals, thus taking into account the effects of a non-diagonal overlap matrix.

In Fig. 2 we report the transmission function and the molecular projections obtained with our approximate computational method. The transmission function, if determined with the assumption of a diagonal Green's function, is non-zero for both coplanar and perpendicular rings, but in the latter case interference effects that are introduced by the off-diagonal terms do cancel the diagonal contribution, thereby resulting in current suppression. Such a cancellation does not occur for coplanar rings, which leads to a net current flowing through the molecule. The on-off ratio and the  $I - V$  characteristic for the molecular switch are reported in Fig. 3, as computed from the results of Fig. 2 via the Landauer-Büttiker formula.

## REFERENCES

- [1] A. W. Ghosh, T. Rakshit, S. Datta, Nano Lett. **4**, 565 (2004).
- [2] I. Cacelli, A. Ferretti, M. Girlanda, M. Macucci, Chem. Phys. **320**, 84 (2006).
- [3] C. Gonzales, Y. Simon-Manso, J. Batteas, M. Marquez, M. Ratner, M., V. J. Mujica, Phys. Chem. B **108**, 18414 (2004).

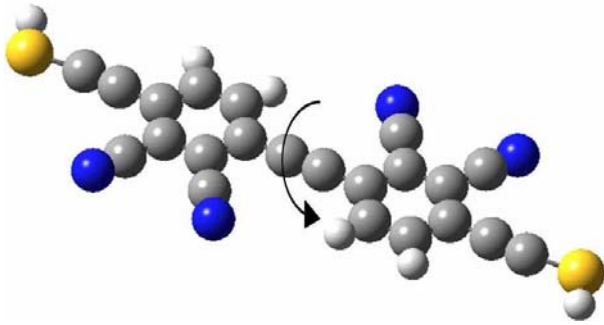


Fig. 1. Sketch of the molecular switch

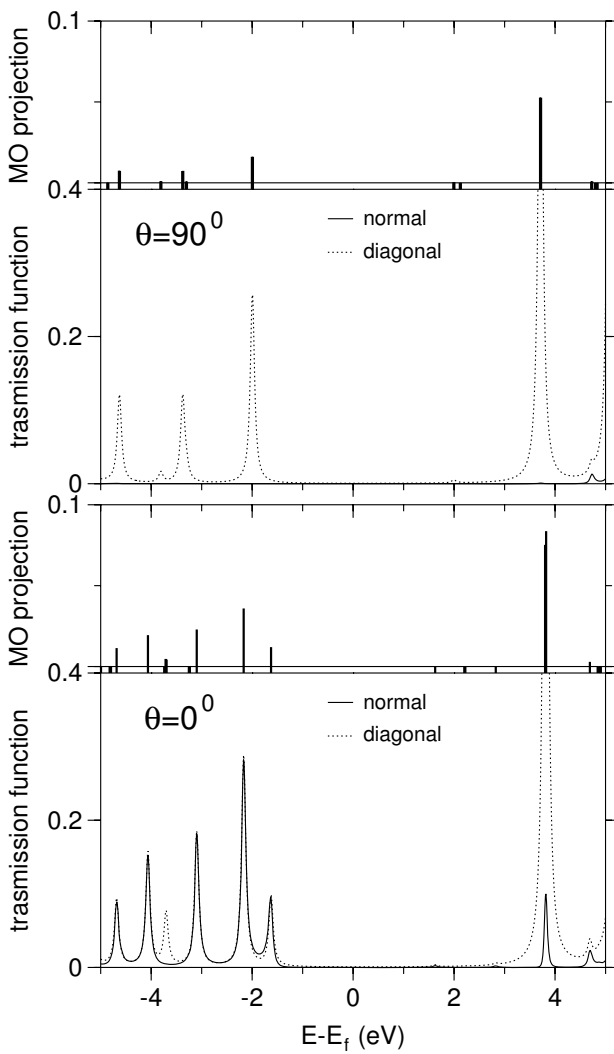


Fig. 2. Molecular orbital projections and transmission function for the configurations with perpendicular and parallel rings.

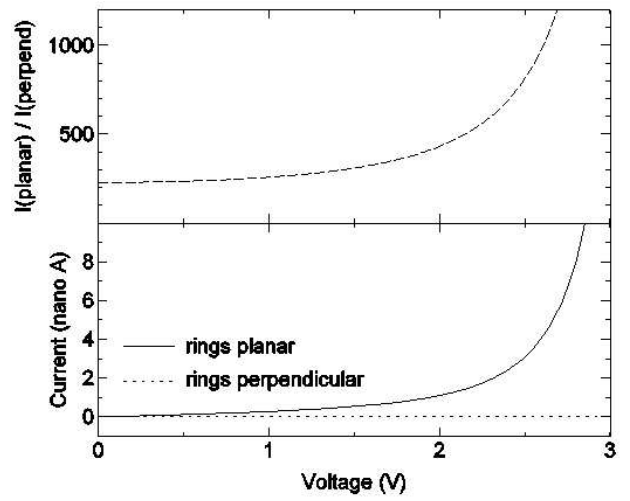


Fig. 3. Computed on-off ratio vs. applied longitudinal bias and  $I - V$  characteristic.

# Simulations of Correlated Electronic Transport Across Molecular Junctions

Giorgos Fagas, Paul Delaney\*, and Jim Greer

Tyndall National Institute, Lee Maltings, Prospect Row, Cork, Ireland

\* School of Mathematics and Physics, Queen's University Belfast, Belfast BT7 1NN, UK  
gfagas@tyndall.ie

## INTRODUCTION

Measurement and theoretical prediction of current-voltage (IV) characteristics for molecular-scale electronic devices remains a challenge. A physical scheme for transport at the many-body level and its implementation leading to calculation of IV curves for molecular scale systems is presented. Open boundary conditions are applied to a many-body wavefunction calculated by the configuration interaction (CI) technique. Our aim is to remove as many approximations from the calculation of the current carrying many-body wavefunction as possible, and to allow for a systematic treatment of electron correlation.

## METHOD

A constraint *Ansatz* is made to incorporate open-system boundary conditions for the calculation of the subsystem reduced density matrix that describes the device region (typically the molecule plus part of the electrodes) at each value of applied voltage. The  $N$ -body reduced density matrix operator for the device region is written  $\hat{\gamma}_N = |\Psi\rangle\langle\Psi|$ , where  $|\Psi\rangle$  is the best approximation to an  $N$ -body wavefunction of the subsystem with constraints.

However, application of scattering boundary conditions is not conceptually tractable. For example, what is meant by incoming electrons on the left (or right)? All electrons are indistinguishable, and there is no localization of a single electron beyond the one-body density  $\rho(\mathbf{r})$  yielding the probability of finding *any* electron at position  $\mathbf{r}$ . To this end, our approach relies on the use of the first order Wigner function  $f(\mathbf{q}, \mathbf{p})$ , which is the Wigner-Weyl transform of  $\rho(\mathbf{r})$ , in order to fix the incoming electron momentum distributions.

Finally,  $|\Psi\rangle$  is represented by a CI expansion written as a sum of spin-projected Slater determinants. This enables us to adjust the electronic correlations between the HF exact-exchange level and improve to approach the in principle exact treatment of full CI limit.

## DISCUSSION

We review the method and discuss our most recent results for correlated electron transport in nanoscale systems (see Fig. 1 and 2). Application of our many-body formalism to the study of transport across single aromatic molecules like benzene dithiol( Fig. 3), short oligomer chains of alkanes and point contacts all lead to results that compare well to the best experimental data available. In particular, we discuss the influence of electron-electron interactions on tunneling through molecular junctions and determine the validity of independent particle models for tunneling quantifying respective deviations of tunneling currents magnitudes. To this end, we thoroughly examine the properties of the one-particle reduced density matrix and its corresponding eigenvalues and eigenvectors.

## ACKNOWLEDGMENT

This work was funded by Science Foundation Ireland.

## REFERENCES

- [1] *Introducing Molecular Electronics*, edited by G. Cuniberti, G. Fagas, and K. Richter (Springer, Berlin, 2005).
- [2] P. Delaney and J. C. Greer, Phys. Rev. Lett. **93**, 036805 (2004); P. Delaney and J. C. Greer, Int. J. Quant. Chem. **100**, 1163 (2004).
- [3] G. Fagas, P. Delaney, and J. C. Greer, *preprint*.

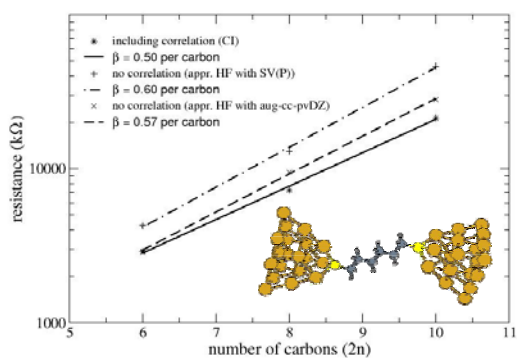


Fig. 1. Resistance-increase exponential law at different levels of theory. Inset: Typical geometry of the studied  $\text{Au}_{\text{tip}}\text{-S-(C}_2\text{H}_4)_n\text{-S-Au}_{\text{tip}}$  molecular junctions ( $n = 3$ ).

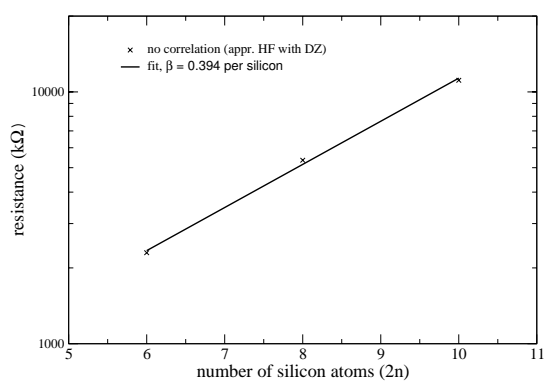


Fig. 2. Resistance-increase exponential law for silicon hydrate molecular junctions ( $\text{Au}_{\text{tip}}\text{-S-(Si}_2\text{H}_4)_n\text{-S-Au}_{\text{tip}}$ ). Note that  $\beta(\text{\AA}^{-1}) \approx 0.2$  much smaller than that of alkanes  $\beta(\text{\AA}^{-1}) \approx 0.45$ .

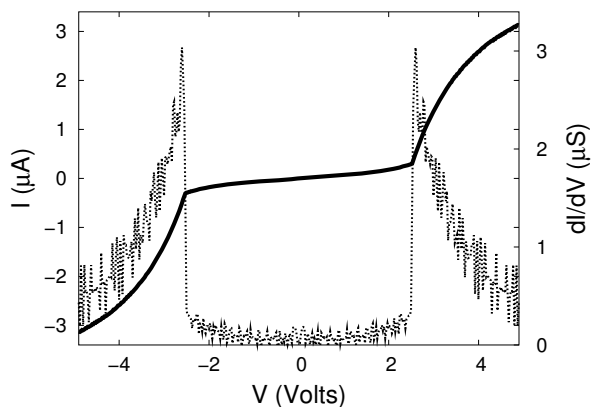


Fig. 3. Predicted current voltage characteristics of benzene dithiol attached to Au electrodes.

# Numerical Simulation of Organic Field-Effect-Transistors

W. Klix, R. Stenzel, T. Herrmann, E. Mehler

Department of Electrical Engineering, University of Applied Sciences Dresden,  
Friedrich-List-Platz 1, D-01069 Dresden, Germany  
e-mail: klix@et.htw-dresden.de

## INTRODUCTION

Organic field effect transistors (OFET's) have been gaining attention over the past years for different applications including organic displays and all-polymer integrated circuits. To understand the basic device operation and to optimize the device structure, analytical models [3] or numerical simulations [1], [2], [4], [5] will be used increasingly. In this paper we have been evaluated physical and numerical models regarding the simulation of OFET's. Our simulation results will be compared with other simulations and with measurements.

## NUMERICAL MODEL

For the simulations of organic field effect transistors we have used our 2D/3D simulation program SIMBA whereas only the conventional drift-diffusion-model was taken into consideration. The basic equations Poisson equation, continuity equations and the transport equations are solved numerically by using a box method for the discretization [6]. Beneath these equations, some special models for organic semiconductors must be used. The carrier mobility is either assumed to be constant or modeled by the following equation

$$\mu_{p,n}(E, T) = \mu_0 \cdot \exp \left( c \cdot \left( \left( \frac{\sigma}{kT} \right)^2 - 2.25 \right) \cdot \sqrt{E} \right), \quad (1)$$

where  $\sigma$  means the width of the density of states (DOS) and  $c$  is a fitting parameter [4].

## SIMULATION RESULTS

Several simulations have been carried out to calculate the behaviour of OFET's. As an example we present some results for a pentacene OFET from [5]. For our simulations we have used constant mobilities. In Figure 1 the schematic view of the

device is illustrated. In Figure 2 the simulated output characteristics are shown. They agree very well with the simulation results from the program ATLAS and with measurements from [5]. The calculated hole density at  $V_{DS} = -100V$  and  $V_{GS} = -40V$  is shown in Figure 3.

Many other simulations have been carried out to test several mobility models and to calculate the influence of material and device parameters. Output characteristics and drain current as a function of doping are shown in Figures 4 and 5.

Simulation results for different Wide/Length ratios ( $w/L$ ) in comparison with measurements are shown in Figure 6.

## CONCLUSION

The simulations have demonstrated that a drift-diffusion model can be used as a first step to describe the behaviour of organic field effect transistors with numerical simulations.

Further investigations must be done, especially to include trap models to get a better accordance with measurements.

## REFERENCES

- [1] S. Scheinert, G. Paasch, *Fabrication and analysis of polymer field-effect transistors*, Phys. Stat. Sol. (a) 201, No. 6, pp. 1263-1301 (2004)
- [2] S. Scheinert, G. Paasch, et.al, *Subthreshold characteristics of field effect transistors based on poly(3-dodecylthiophene) and an organic insulator*, Journ. of Appl. Phys., Vol. 92, No. 1, July 2002, pp. 330-337.
- [3] E. Calvetti, L. Colalongo, Zs.M. Kovacs-Vajna, *Organic thin film transistors: a DC/dynamic analytical model*, Solid State Electronics, 49 (2005), pp. 567-577.
- [4] Y. Roichman, Y. Preezant, N. Tessler, *Analysis and modelling of organic devices*, Phys. Stat. Sol. (a), 201, No. 6, pp. 1246-1262, 2004.
- [5] Silvaco International, *Simulation Standard*, Vol. 12, 2, (2003).
- [6] W. Klix, R. Stenzel, *Program System SIMBA, Models and Solution Methods*.  
<http://www.htw-dresden.de/~klix/simba/welcome.html>.

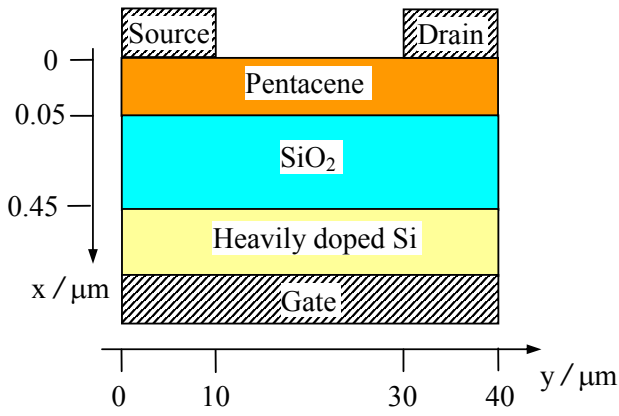


Fig. 1. Schematic view of the device, used for simulations [5], channel wide: 220  $\mu\text{m}$ , doping:  $N_A = 2.09 \cdot 10^{17} \text{ cm}^{-3}$ .

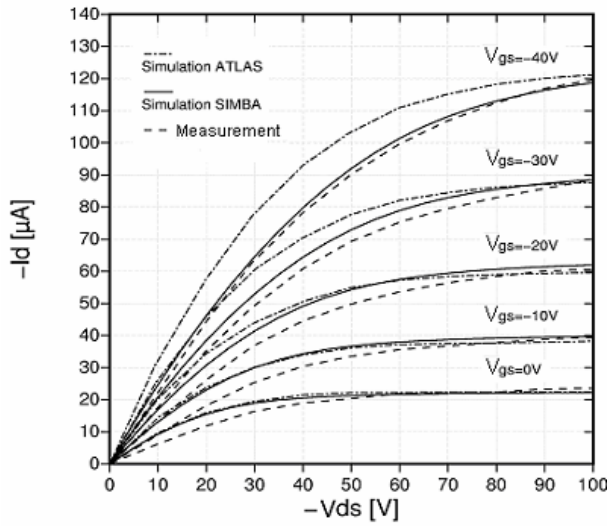


Fig. 2. Measured and simulated output characteristics (with constant mobility) for the example from [5]

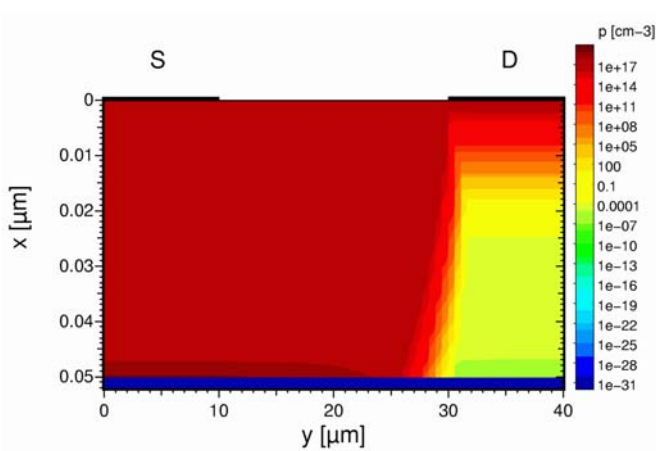


Fig. 3. Simulated hole density at  $V_{DS} = -100\text{V}$  and  $V_{GS} = -40\text{V}$

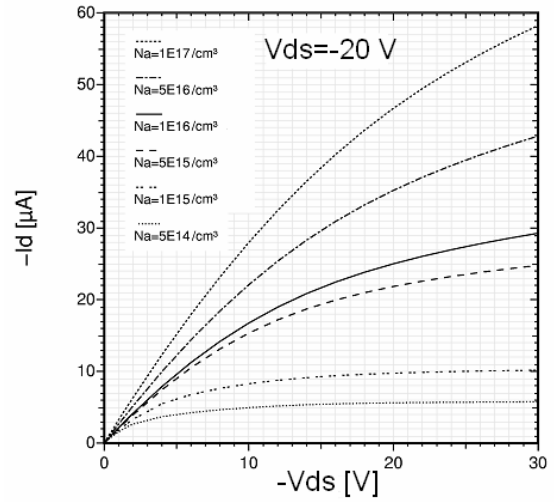


Fig. 4. Simulated output characteristics for different doping density for a P3DDT-OFET

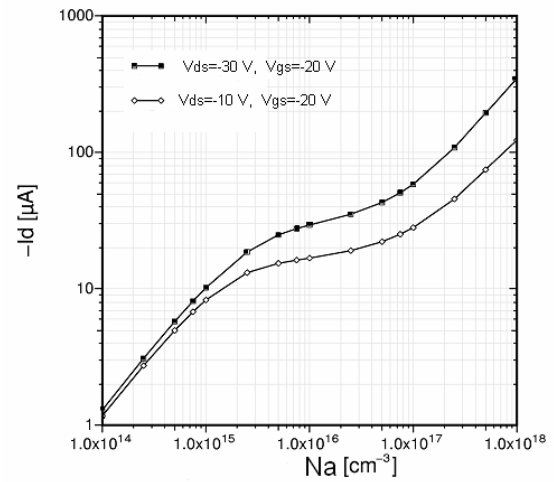


Fig. 5. Simulated drain current as a function of doping density ( $N_a$ ) for a P3DDT-OFET

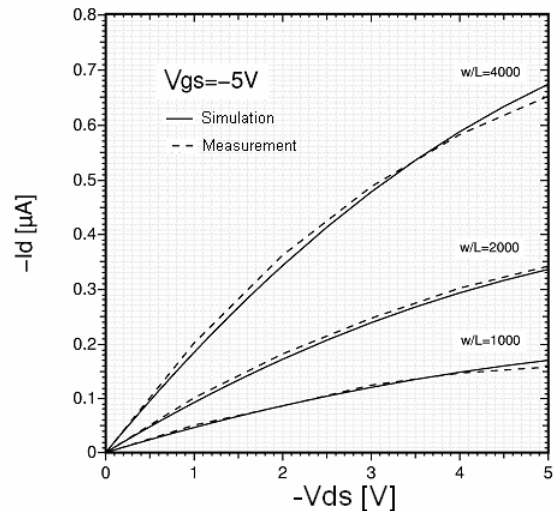


Fig. 6. Simulated output characteristics for different  $w/L$ -ratio and measurements from [1] for a P3HT-OFET

# Percolation Current in Organic Semiconductors

L. Li, G. Meller, and H. Kosina

Institute for Microelectronics, TU Wien, Gußhausstraße 27–29/E360, 1040 Wien, Austria  
e-mail: ling.li@iue.tuwien.ac.at

## INTRODUCTION

After the discovery of electroluminescence in the conjugated polymer PPV [1] and its derivatives, much effort has been devoted to the study of the (opto)electronic and electrical transport properties. Understanding the carrier transport properties in these organic materials is of crucial importance to design and synthesize better materials and to improve device performances. The electrical transport in organic semiconductors has been widely investigated for several decades in theoretical as well as experimental studies [2], [3], [4], [5]. For the important concept of variable range hopping (VRH) [6] it is difficult to account for the electric field characteristics observed by experiments. In this work, we extend VRH theory for organic semiconductors to include percolation theory [7]. The developed model shows good agreement with Mott's formalism at high electric field.

## MODEL

For a disordered organic semiconductor system, when an electric field  $F$  exists, the transition rate of a carrier hopping from site  $i$  with energy  $E_i$  to site  $j$  with energy  $E_j$  is described as [8]

$$\omega_{ij} = \gamma \exp \left[ - (2\alpha + \beta \cos \theta) R_{ij} - \frac{E_j - E_i}{k_B T} \right] \quad (E_j \geq E_i + \beta \cos \theta R_{ij})$$

and

$$\omega_{ij} = \gamma \exp (-2\alpha R_{ij}) \quad (E_j \leq E_i + \beta \cos \theta R_{ij})$$

where  $\gamma$  is dependent on the phonons spectrum,  $\alpha^{-1}$  is the Bohr radius of the localized wave function,  $k_B$  is the Boltzmann constant,  $\beta = eF/(k_B T)$ ,  $e$  is the electrons charge,  $R_{ij}$  is the distance between the two sites  $i$  and  $j$ , and  $\theta$  is the angle between  $F$  and  $R_{ij}$ . Assuming no correlation between occupation

probability of different localized states, the current between the two sites is given by

$$I_{ij} = \gamma \exp \left[ - (2\alpha + \beta \cos \theta) R_{ij} - \frac{|E_j - E_i|}{2k_B T} \right] \zeta \quad (1)$$

where

$$\zeta = \sinh \left( \frac{\mu_j - \mu_i}{2k_B T} \right) \times \left[ \cosh \left( \frac{E_i - \mu_i}{2k_B T} \right) \cosh \left( \frac{E_j - \mu_j}{2k_B T} \right) \right]^{-1}$$

In this model, it is assumed that both the backbone of the percolation cluster and the threshold current do not alter upon rearranging the site potentials. At the same time, the redistribution of the charge seems negligible due to the large spread in  $I_{ij}$  at the high electric field.

We consider a network of sites connected with impedances proportional to  $I_{ij}^{-1}$ . According to general percolation theory, the critical percolation cluster of sites would comprise a current carrying backbone with at least one site-to-site current equal to the threshold value. As shown in [9], optimization of the current is obtained when the site potentials are altered in such a way that the single hopping event with smallest tunneling probability is optimized. With these assumptions, we can get the equation

$$B_c \approx N_t \frac{2\pi k_B T \xi}{3qF\delta} S_c^3 \eta \quad (2)$$

with

$$\xi = 1 - \frac{\delta}{\Gamma(1 - T/T_0) \Gamma(1 + T/T_0)}$$

$$\eta = \left( 2\alpha - \frac{eF}{2k_B T} \right)^{-2} - \left( 2\alpha + \frac{eF}{2k_B T} \right)^{-2}$$

$B_c$  is the critical number of bonds per site,  $\Gamma$  is gamma function,  $\delta$  is carrier occupation [10],  $N_t$  is the number of states per unit volume,  $S_c$  is

the exponent of the critical percolation current  $I = I_0 \exp(-S_c)$ , and  $T_0$  is the width of the exponential density of states. This yields an expression for the current in organic semiconductors as a function of the electric field

$$I = I_0 I_t = I_0 \exp \left[ - \left( \frac{3eFB_c}{N_t \pi k_B T \xi \eta} \right)^{1/3} \right] \quad (3)$$

where  $I_0$  is a prefactor and  $I_t$  is the critical current.

## RESULTS AND DISCUSSION

We use the present model to calculate the electric field characteristic of the percolation current in organic semiconductors, as shown in Fig.1. Clearly, the expected dependence that  $\log I \sim F^{-1/4}$  is observed at high electric field, the comparison with Mott formalism

$$I_t \sim \exp \left( - \left( C_F \alpha^4 / e N_t F \right)^{1/4} \right)$$

is also provided, Mott formalism can be seen as the asymptote of our model. The input parameters are  $N_t = 10^{19} \text{cm}^{-3}$  and  $T_0 = 380 \text{ K}$ . In Fig.2 we provide the temperature dependence of the percolation current. It can be seen that temperature plays a minor role in high electric field current.

## CONCLUSION

We developed an analytic model of high electric field current applicable for organic semiconductors. This model is shown to agree with Mott's formalism. We also discussed the temperature characteristics of this model.

## ACKNOWLEDGMENT

We acknowledge financial support from the Austria Science Fund, project P16862-N02.

## REFERENCES

- [1] J. H. Burroughes, D. Bradley, A. Brown, R. Friend, P. Burn, and A. Holmers, "Point defects and dopant diffusion in silicon," *Nature*, vol. 347, pp. 539–541, 1990.
- [2] P. M. W. Blom, M. J. M. de Jong, and M. G. van Munster, "Electric-field and temperature dependence of the hole mobility (p-phenylene vinylene)," *Phys. Rev. B*, vol. 55, no. 2, pp. 656–659, 1997.
- [3] W. D. Gill, "Drift mobilities in amorphous charge-transfer complexes of trinitrofluorenone and poly-n-vinylcarbazole," *J. Appl. Phys.*, vol. 43, no. 12, pp. 5033–5040, 1972.
- [4] A. Miller and E. Abrahams, "Impurity conduction at low concentrations," *Phys. Rev.*, vol. 120, no. 3, pp. 745–755, 1960.

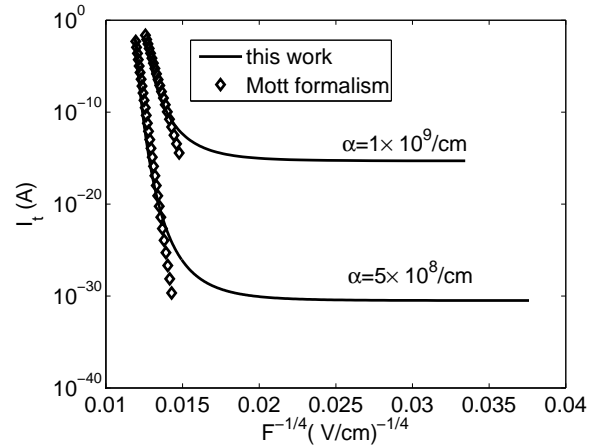


Fig. 1. Electric field dependence of percolation current in a network of localized states.

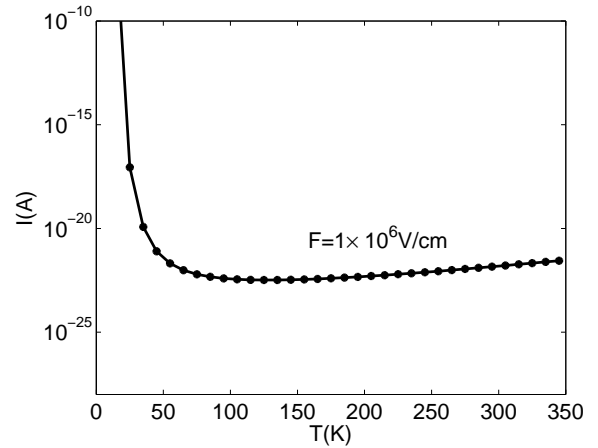


Fig. 2. Temperature dependence of percolation current in a network of localized states in the high electric field regime.

- [5] P. M. Anderson, "Absence of diffusion in certain random lattices," *Phys. Rev.*, vol. 109, pp. 1492–1505, 1958.
- [6] N. F. Mott, "Conduction in noncrystalline materials. iii localized states in pseudogap and near extremities of conduction and valence bands," *Philos. Mag.*, vol. 19, pp. 835–852, 1969.
- [7] V. Ambegokar, "Hopping conductivity in disordered system," *Phys. Rev. B*, vol. 4, no. 8, pp. 2612–2620, 1971.
- [8] M. Pollak and I. Riess, "A percolation treatment of high-field hopping transport," *J. Phys. C*, vol. 9, pp. 2239–2352, 1976.
- [9] J. van Hapert, *Hopping conduction and chemical structure: a study on silicon suboxides*. PhD thesis, University Utrecht, Netherlands, 2002.
- [10] M. C. J. M. Vissenberg and M. Matters, "Theory of the field-effect mobility in amorphous organic transistors," *Phys. Rev. B*, vol. 57, no. 20, pp. 12964–12967, 1998.

# Ferromagnetism in Tetrahedrally Coordinated Compounds of I/II-V Elements: *Ab Initio* Calculations

M. Sieberer, J. Redinger, S. Khmelevskiy, and P. Mohn  
Center for Computational Materials Science, Vienna University of Technology,  
Getreidemarkt 9/134, A-1060 Vienna, Austria  
e-mail: ms@cms.tuwien.ac.at

## INTRODUCTION

Recently Kusakabe et al. [1] proposed magnetic zinc-blende CaAs as a possible material for spintronics application. Their proposal was motivated by the need for half metallic ferromagnets (HMF) in spintronic devices [2], which are seen as key ingredients. However, apart from the technological application the magnetic I/II-V compounds represent a new class of ferromagnetic materials where magnetic order is carried by the anion p-electrons without any direct involvement of d-electrons as in the magnetic transition metals and their compounds. The p-electron magnetism in CaAs and the other I/II-V systems appears in the fully ordered stoichiometric compounds and their magnetic order is intrinsic and not triggered by the presence of crystal defects of various kinds.

## TOTAL ENERGY

By applying density functional theory (DFT) within the generalized gradient approximation of Perdew, Burke and Ernzerhof [3] using the FLAIR [4] code, an implementation of the full potential linearized augmented plane wave method (FLAPW) [5], we first investigated the stability of CaAs, the prototype of the so-called half-metallic-ferromagnets (HMF) of this type. In Fig. 1 the total energy is plotted over the volume per formula unit for various crystal structures including zinc-blende (ZB), wurtzite (WZ), sodium chloride (NaCl) and the experimentally found structure NaO (P62m). Our calculated lattice constants for the true ground state (NaO) with  $a=15.03$  bohr and  $a/c=1.326$  (red) are in good agreement with the experimental values of  $a=14.84(2)$  and  $c=11.19$  [6]. Furthermore we

found out that the ground state of CaAs found experimentally is energetically rather far away from the structures which are expected to exhibit HMF ( $\approx 1.4$  eV/f.u.). However, since e.g. CrAs and CrSb have already been prepared successfully in the ZB structure even though it is not their equilibrium crystal structure, also for CaAs a preparation as a thin film on a substrate may be possible.

## ELECTRONIC PROPERTIES

All ZB compounds composed of group I/II elements as cations and group V elements as anions investigated combine two key features, namely a relatively wide band-gap of approximately 2 eV present in both spin channels (in an LSDA approximation), and a ferromagnetic ground state with an integer magnetic moment obeying a simple  $|8 - n|$  rule,  $n$  being the total number of valence electrons. The large difference in electronegativity between the constituent elements leads to a charge transfer causing a gap between occupied bands having predominantly p-character and empty bands with s and/or d character. The band structure for CaAs as one representative is plotted in Fig. 2, most interesting is the uppermost occupied band being almost dispersionless. This flatness is caused - amongst others - by the relatively large lattice constant of these compounds (between 9.15 bohr for MgN and 15.37 bohr for BaSb). For the representatives having cations with empty d-bands in the energetic proximity of the Fermi energy (e.g. Ca, Sr, Ba), additionally a curious anion-p - cation-d hybridization occurs, which further reduces the dispersion of the so-called flat band.

All compounds investigated exhibit a well localized

magnetic moment proportional to the number of holes in the almost atomiclike anion p-band. A systematic study of these compounds showed that the origin of this p-electron magnetism can be understood in terms of the Stoner-criterion, which predicts instabilities towards magnetism due to the high density of states at the Fermi energy in the hypothetical nonmagnetic state caused by the at band.

Comparisons of the total energy between a ferromagnetic (FM) and an antiferromagnetic (AFM) ground state - including augmented spherical wave (ASW) [7] calculations that allow for the set up of so-called spin-spirals - in all cases showed relatively large energy gains (between 50 meV and 220 meV) for the system to adopt the FM ground state (see Fig. 3). In a mean el d approximation also the paramagnetic Curie temperature has been estimated, resulting in a value of 680 K for CaAs, which would be well suited for technological application.

#### CONCLUSION

We nd that half metallicity is very common among ionic compounds composed of alkaline earth/alkali metals and group V elements if a tetrahedrally coordinated crystal structure like the ZB or WZ structure is assumed. Despite the fact that CaAs exists as bulk phase at best in metastable form, however, its highly interesting magnetic properties including p-electron magnetism, the occurrence of an extremely at band being of interest in the context of the Hubbard model, and a reasonably high Curie temperature will warrant also experimental efforts to stabilize these materials in a fourfold coordinated structure such as ZB or WZ (e.g. via vacuum laser deposition) on suitable substrates.

#### REFERENCES

- [1] K. Kusakabe, M. Geshi, H. Tsukamoto, and N. Suzuki, *J.Phys.: Condens. Mater* **16**, 5639 (2004).
- [2] J.-H. Park, E. Vescovo, H.-J. Kim, C. Kwon, R. Ramesch, and T. Venkatesan, *Nature* **392**, 794 (1998).
- [3] J. Perdew, K. Burke, and M. Ernzerhof, *Phys. Rev. Lett.* **77**, 3865 (1996).
- [4] <http://www.uwm.edu/~weinert/air.html>.
- [5] E. Wimmer, H. Krakauer, M. Weinert, and A. J. Freeman, *Phys. Rev. B* **24**, 864 (1981).
- [6] P. L'Haridon, J. Guyader, and M. Hamon, *Revue de Chimie minerale* **13**, 185 (1976).
- [7] A. R. Williams, J. Kübler, and C. D. Gelatt Jr., *Phys. Rev. B* **19**, 6094, (1979).

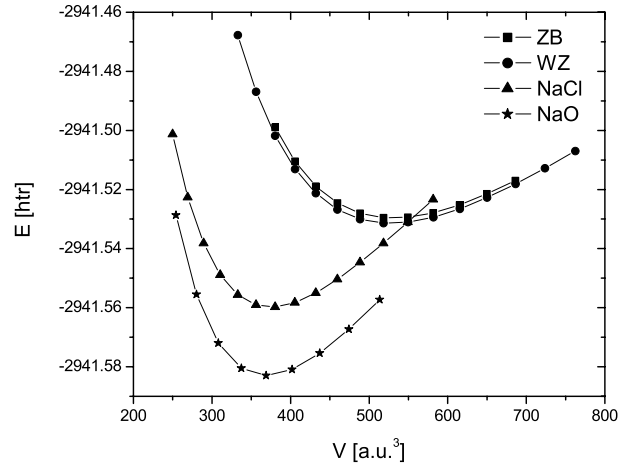


Fig. 1. Total energy for CaAs in different crystal structures. Energies and volumes are given per formula unit.

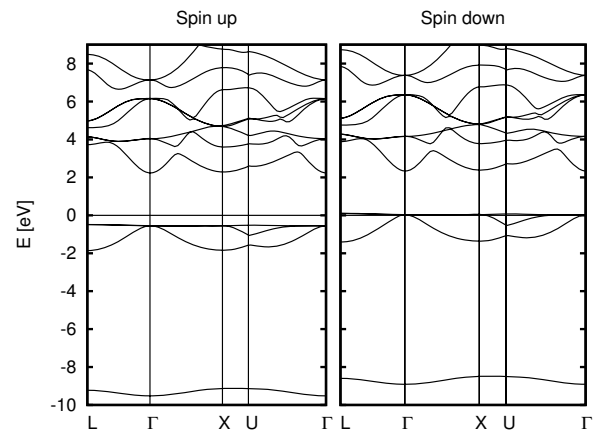


Fig. 2. Band structure of ZB-CaAs for both spin channels. A half filled, extremely at band is present at the Fermi energy.

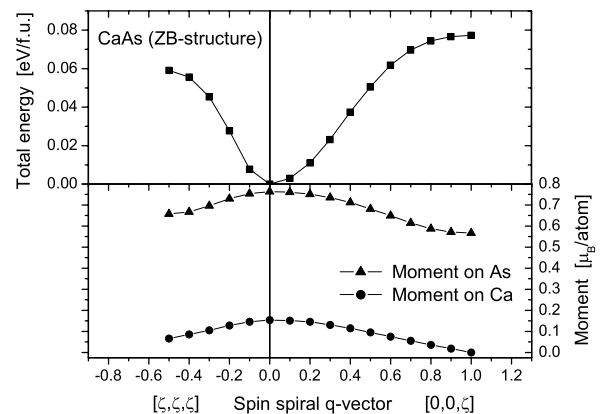


Fig. 3. Upper panel: total energy as a function of the spin spiral in  $[\zeta, \zeta, \zeta]$  and  $[0, 0, \zeta]$  direction, respectively. The spin spiral propagation vector  $\mathbf{q}$  is given in multiples of  $2\pi/a$ . Lower panel: magnetic moment of Ca and As.

# *Ab-Initio* Calculations for Indium Migration in Silicon Substrate

Kwan-Sun Yoon, Chi-Ok Hwang\*, and Taeyoung Won

Department of Electrical Engineering, National IT Research Center for Computational Electronics  
Inha University, Incheon 402-751

\*Computer Aided Molecular Design Research Center, Soongsil University  
e-mail: yks@hsel.inha.ac.kr

## INTRODUCTION

Recently, indium has been employed in the fabrication of retrograde p-tub and halo region for n-channel in CMOS. Since its heavier mass, indium is utilized as an alternative to boron in silicon substrate, in order to achieve shallower and steeper profiles required by ultra-large-scale integration technology. It is known that indium diffuses mainly through the interstitial-mediated mechanism during the thermal annealing process. Recently, Kinetic Monte Carlo (KMC) method has been widely employed for the modeling of thermal annealing process for nano-CMOS devices [1]. The input parameters of a migration event, one of the main events in thermal annealing, are given either from experiments or from *ab-initio* calculations.

In this work, we investigated the atom-scale characterizations and MEP of indium diffusion in silicon by *ab-initio* calculations and transition state theory tools.

## NUMERICAL CALCULATIONS

First of all, we performed a defect structure calculation in a cubic super-cell, comprising 216 silicon atoms with a single neutral indium atom. In Fig. 1 is shown a schematic diagram illustrating the atomic structures comprising an indium atom in the silicon lattice. The *ab-initio* calculations were implemented within density functional theory (DFT) with VASP (Vienna *Ab-initio* Simulation Package) [2] which combines ultrasoft pseudopotentials and generalized gradient approximation (GGA) in the Perdew and Wang formulation.

Relative energy values of each defect configuration are shown in Table 1. The energy landscape, calculated by VASP for Si:In, indicates

that the lowest-energy structure ( $\text{In}_s + \text{Si}_i^{\text{Td}}$ ) consists of indium sitting on a substitutional site stabilizing a silicon self-interstitial in a nearby tetrahedral position [Fig. 2(a)]. The second lowest-energy structure is  $\text{In}_i^{\text{Td}}$ , the interstitial indium in the tetrahedral position [Fig. 2(b)]. The energy difference between the two defect configurations is 0.43 eV.

In the prior investigation, we found that the initial state is  $\text{In}_s + \text{Si}_i^{\text{Td}}$  while the final state is  $\text{In}_i^{\text{Td}}$ . Repeating the transitions between those two states, the neutral indium diffuses in silicon. Consequently, we can now obtain the energy barrier for indium migration if we investigate the MEP from the initial state to the final state.

In order to search for the MEP, we performed the climbing image nudged elastic band (CINEB) [3] calculation which is a kind of TST. Figure 3 is a diagram illustrating the calculated minimum energy path for indium via the CINEB method with four intermediate images. The initial intermediate images, denoted with triangles, are linearly interpolated between the initial and final images. The Migration energy is estimated as an energy difference to move from a local energy minimum state to another local minimum along the diffusion path. We find that the migration energy of In-interstitial defect is 0.79 eV in Fig. 3, which is in agreement with previous estimation [4].

## CONCLUSION

In order to decide the migration energy for the diffusion of indium, it is essential to find out the migration path of the interstitial-mediated mechanism. *Ab-initio* study in this work comprises steps of performing the electronic structure relaxation and obtaining its total energy at the local

minimum. We could come up with the atomistic configurations and migration energy during indium diffusion in silicon, wherein we tried to find out saddle points from a minimum and reaction pathway between those two stable states by using TST. After we found the transition state, we tried to get the energy barrier for diffusing the particle through the calculation of the exact total energy at the transition state. These *ab-initio* results of indium diffusion in silicon are essential in obtaining an exact modeling of the experimental profiles.

#### ACKNOWLEDGEMENT

This work was supported partly by the Korean Ministry of Information & Communication (MIC) through Information Technology Research Center (ITRC) Program. The authors would like to express special thanks to the Korea Institute of Science and Technology Information (KISTI) for the support under ‘The Seventh Strategic Supercomputing Applications Support Program’.

#### REFERENCES

- [1] K. A. Fichthorn and W. H. Weinberg, *Theoretical foundations of dynamical Monte Carlo simulations*, J. Chem. Phys. **95**, 1090 (1991).
- [2] G. Kresse and J. Hafner, *Ab initio molecular dynamics for liquid metals*, Phys. Rev. B **47**, 558 (1993).
- [3] Vasp TST Tools: [http:// theory.cm.utexas.edu/vtsttools/](http://theory.cm.utexas.edu/vtsttools/)
- [4] P. Alippi, A. L. Magna, S. Scalese, and V. Privitera, *Energetics and diffusivity of indium-related defects in silicon*, Phys. Rev. B **69**, 5213 (2004).

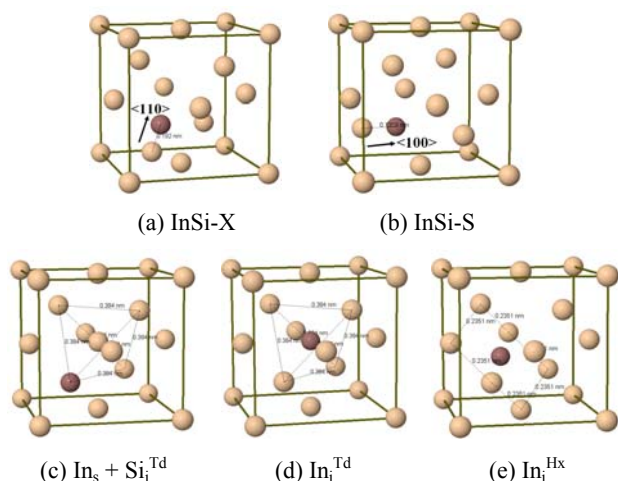


Fig. 1. Atomic structures illustrating the configurations of indium in silicon: Indium atom is depicted as dark-colored and silicon atoms are depicted as light colored for each configuration. The InSi-X consists of silicon self-interstitial with an indium atom sharing the same lattice site, with the Si-

indium dimer lying in the  $\langle 110 \rangle$  direction. If the direction is  $\langle 100 \rangle$  with the same configuration, the structure is referred to as InSi-S. The  $\text{In}_s + \text{Si}_i^{\text{Td}}$  configuration means the case when indium atom sits on a substitutional site and stabilizes a silicon self-interstitial in a nearby tetrahedral position. The  $\text{In}_i^{\text{Td}}$  and  $\text{In}_i^{\text{Hx}}$  structures are the interstitial indium atom respectively in the tetrahedral position and in the hexagonal position.

Table 1. A table showing the calculated energies of the Si:In defect configuration: the listed energies are relative energies with reference to the ground-state configuration.

Configuration (In)	Relative energy [eV]
InSi-X	46.11
InSi-S	58.09
$\text{In}_i^{\text{Td}}$	0.43
$\text{In}_s + \text{Si}_i^{\text{Td}}$	0.00
$\text{In}_i^{\text{Hx}}$	1.63

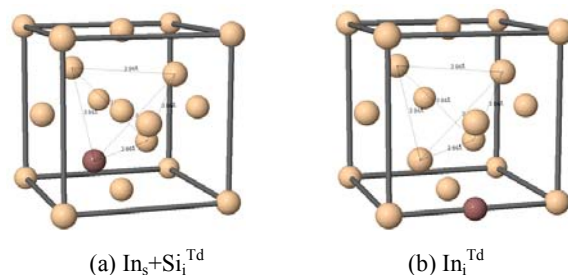


Fig. 2. Plots illustrating defect configurations: In atom (dark-colored), Si self-interstitial (light-colored) are shown over the underlying diamond lattice. The  $\text{In}_s + \text{Si}_i^{\text{Td}}$  (a) and the interstitial In at the tetrahedral position,  $\text{In}_i^{\text{Td}}$  (b) are also shown.

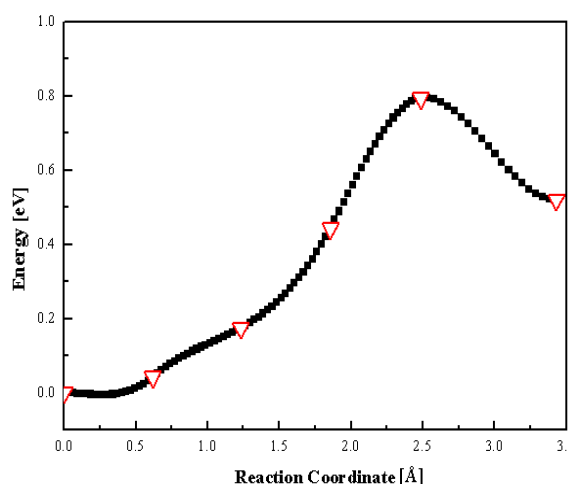


Fig. 3. The relative energy along the MEP of Si:In from  $\text{In}_s + \text{Si}_i^{\text{Td}}$  to  $\text{In}_i^{\text{Td}}$  by the climbing image nudged elastic band method. The triangles indicate the simulation images and the squares are the interpolation by using the force parallel to the band.

# Electrostatic Modeling of Ion Motive Sodium Pump

J. Fonseca, R. F. Rakowski\*, and S. Kaya

School of EECS, Russ College of Eng & Tech, Ohio University, Athens, OH 45701, USA

\* Dept. of Biological Sciences, Ohio University, Athens, OH 45701, USA

e-mail:kaya@ohio.edu, fax: (740) 593-0007

## INTRODUCTION

An ongoing convergence of bio and nano engineering has focused interest on ion transport through trans-membrane proteins. Ion transport takes place either through *passive* (ion channels) or *active* (ion pumps) proteins, which have innate properties such as selectivity and gating that allow them to be classified as bioelectric devices. Contrary to ion channels that have attracted attention from the device community recently [1,2] ion-motive pumps are still largely unexplored [3].

The Na<sup>+</sup>/K<sup>+</sup>-ATPase, or sodium pump, is a voltage-gated membrane transport protein found in most higher order eukaryotic cells and is essential for life. The sodium pump is vital to maintaining a transmembrane voltage and regulating cellular volume. Electrophysiological studies have yielded a wealth of information on the sodium pump's function in recent years [4,5]. Yet, many aspects regarding the structure-function nature of the pump such as ion binding, permeation and gating remain elusive.

The sodium pump functions by using the Gibbs free energy from the hydrolysis of adenosine triphosphate (ATP) to exchange three intracellular sodium ions for two extracellular potassium ions (Fig.1). Sodium ions are moved against a strong electrochemical gradient and the pump can also be operated in the reverse mode. This functionality is believed to incorporate a dual-gating action that allows ions to bind to the protein on only one side of the membrane, followed by an occluded state where both gates are closed, and continuing with a gated release of the ions to the opposite side of the membrane. Movement of ions against a strong electrochemical gradient, the hallmark of ion pumps, is thought to accompany large changes in protein structure, allowing this ping-pong exchange to occur. We seek to use a variety of modeling and simulation tools to investigate the effects of electrostatic and steric changes on the properties of ion binding sites as well as ion and water pathways [3].

## HOMOLOGY MODELING

Recent successes in crystallography by Toyoshima and others have given structures [6] of different conformations of the calcium pump, SERCA, which has a relatively degree of similarity with the sodium pump. Due to this similarity between the genomic sequences of these proteins, aligning the genomic sequence of Na<sup>+</sup>/K<sup>+</sup>-ATPase with SERCA gives reliable homology models. The software Modeller [7] improves this alignment with the secondary and tertiary structure of SERCA to determine reliable models of the sodium pump (Fig.2). After inclusion of the model in an lipid

bilayer, calculated electrostatic maps and pathways determined from the molecular surface can be combined with molecular dynamics simulations to investigate regions in which ion binding and permeation is believed to occur.

## ELECTROSTATICS

The electrostatic maps generated by APBS [8] can be augmented with protein surface/cavity calculations to show possible binding locations as well ion/water permeation pathways between these sites and the exterior of the protein (Fig.3&4). Traditionally, protein electrostatic investigations have mostly considered surface-mapped potentials. However, isopotential profiles in the protein's cavities yield information about the ions' environment, and allows the calculation of ion binding affinities. In the present work, we explore how electrostatic analysis can be coupled with molecular cavity data to refine ion and water pathways. We also show how the deployment of efficient 3D solvers originally developed for electrical devices may facilitate modeling and analysis of biomolecules and biodevices not yet explored.

## WATER ACCESSIBILITY

The molecular dynamics (MD) packages, such as GROMACS [9], can be used to explore water and ion accessibility and permeation pathways through simulations of the >500,000 atom protein-lipid-water-ions system. This is the first attempt to perform molecular dynamics simulations of a sodium pump and bilayer system, a task which has been considered only for H<sup>+</sup>-K<sup>+</sup> ATPase previously [10]. MD trajectories can be evaluated to test water permeation pathways, and to test the relationship between the binding sites and water accessibility.

The present work establishes a unique framework for the simulation study of ion-motive pumps in general and Na<sup>+</sup>/K<sup>+</sup> pump in particular. We shall discuss the implications of electrostatic analysis and MD simulations for the structure-function relationship of Na<sup>+</sup>/K<sup>+</sup> ATPase.

- [1] T. Van Der Straaten et al., *Mol Simulation*. **31**, 151 (2005).
- [2] C Millar, A Aseonov and S Roy, *J Comp. Electron*. **12**, 56 (2005).
- [3] R. Rakowski, S. Kaya, J. Fonseca, *J Comp. Electron*. **4**, 189 (2005).
- [4] R. Rakowski and S. Sagar, *News Physiol Sci* **18**, 164 (2003).
- [5] P. Artigas and D. Gadsby, *Proc. Natl. Acad. Sci. USA* **100**, 501 (2003).
- [6] C. Toyoshima, H. Nomura, T. Tsuda, *Nature* **432**, 361 (2004).
- [7] M.A. Marti-Renom et al., *Annu. Rev. Biophys. Biomol. Struct.* **29**, 291 (2000).
- [8] N.A. Baker et al., *Proc. Natl. Acad. Sci. USA* **98**, 10037 (2001).
- [9] H. J. C. Berendsen, D. van der Spoel, R. van Drunen, *Comp. Phys. Comm.* **91**, 43 (1995).
- [10] K. Munson, R. Garcia, G. Sachs, *Biochemistry* **44(14)**, 5267, (2005).

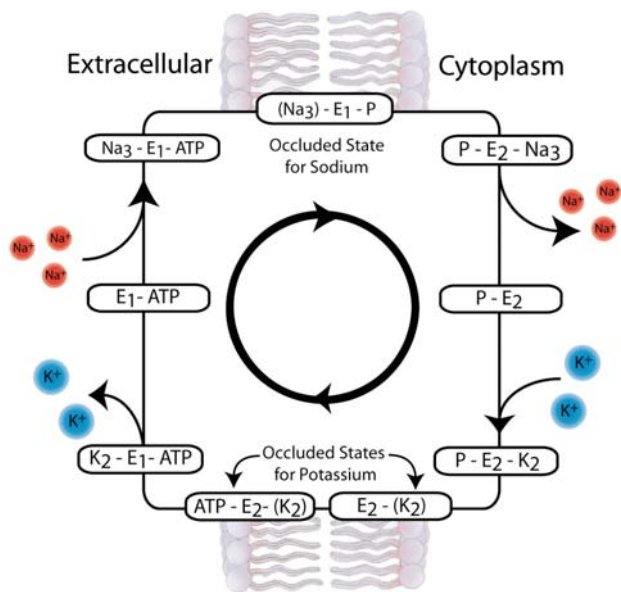


Fig.1: The Post-Albers cycle above indicates the main stages of conformational changes ( $E_1$ - $E_2$ ), ion binding, release and occlusion, and ATP hydrolysis. Potassium is released and sodium bound on the intracellular side and this process is reversed on the extracellular side. The arrows indicate the forward pump cycle.

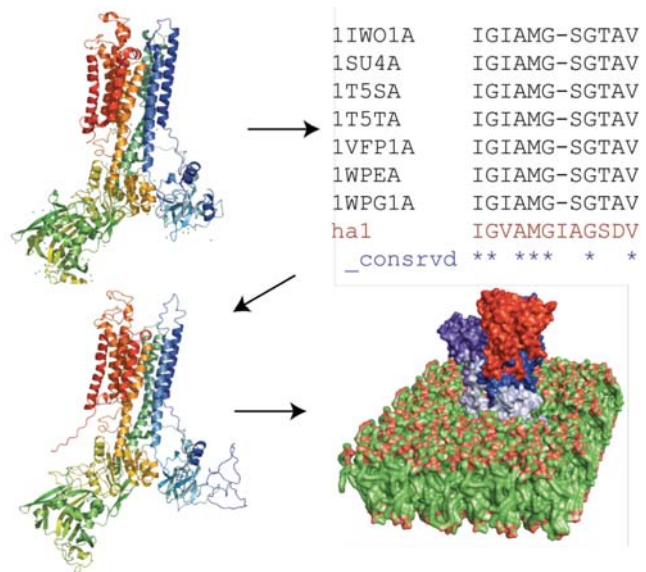


Fig.2: An overview of the homology process. From the seven available SERCA structures (top left), an alignment of the genomic sequences is made with the human  $\alpha$ -1 isoform (hal) of the sodium pump. The alignment and coordinates of the structure file are combined to provide the homology model (lower left). At the lower right is a frame from a MD simulation that shows the model embedded in a lipid bilayer.

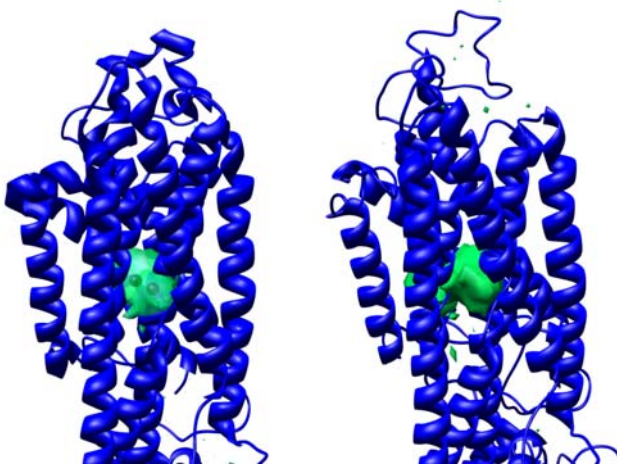


Fig.3: Transmembrane regions of the  $E_2$  state of a SERCA (PDB: 1WPG) structure (left) and homology based model, each with a negative isopotential surface (green) indicating a high-affinity region for cations. Two bound  $Ca^{2+}$  ions can be seen inside the isopotential surface in the SERCA structure. Electrostatic investigations based on homologues can yield information on putative binding sites in the Na/K pump.

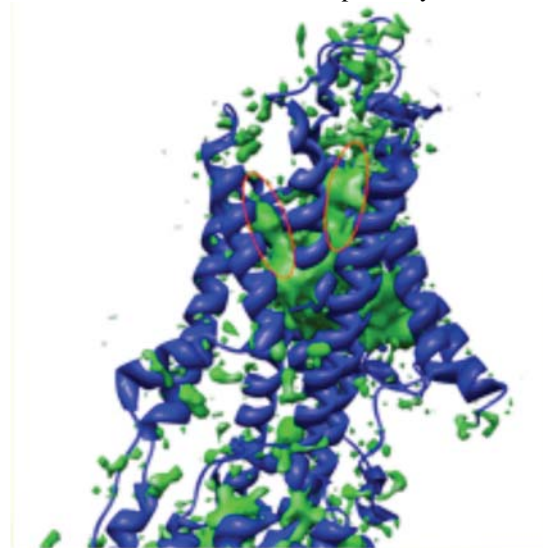


Fig.4: At smaller negative potentials, the isosurface expands towards the extracellular side (at left) of the model. The orange ovals indicate regions of negative potential that may provide a pathway conducive to ion movement between the lumen and the binding sites. Created with Chimera and electrostatic data from APBS.

# Numerical Aspects of the Three-Dimensional Feature-Scale Simulation of Silicon-Nanowire Field-Effect Sensors for DNA Detection

Clemens Heitzinger and Gerhard Klimeck

Network for Computational Nanotechnology, School of Electrical and Computer Engineering,  
Purdue University, West Lafayette, IN 47907, USA

E-mail: ClemensH@Purdue.edu

## INTRODUCTION AND MOTIVATION

In recent months experimental silicon-nanowire field-effect biosensors were built and their functioning was verified [1], [2]. These devices consist of a silicon-nanowire core, an enveloping silicon-oxide, and a surface receptor molecule (cf. Fig. 1). When a biomolecule attaches to the surface receptor and this attachment results in a sufficiently different charge distribution, the change in current flow through the nanowire enables detection.

These sensors provide perfect selectivity since the possibility of a binding being established between two biomolecules (a protein and an antibody, for example) is equivalent to having a biological function. Furthermore extremely high detection sensitivity in the pg/ml regime has been reported [1]. It seems feasible that these devices can sense a huge array of biomolecules, and notable application areas are the detection of cancer markers and DNA fragments.

## SIMULATION METHOD

In this work we investigate the numerical aspects and challenges of three-dimensional feature-scale simulations at the example of three states of a nanoscale DNA sensor in aqueous solution. In the first state nothing is attached, in the second state one chain of the DNA fragment (5'-D(CGTGAATTCACG)-3') is attached, and in the third state the whole dodecamer is attached (see Fig. 1, Fig. 2, Fig. 3).

After determining the partial charges on the DNA fragment, their distribution was used to obtain the electrostatic potential by solving the 3D Poisson equation. Charge transport was simulated using a 3D self-consistent NEGF simulator [3].

## RESULTS AND CONCLUSIONS

Simulator timings are shown in Fig. 4, the current-voltage characteristics in Fig. 5, and the potential in Fig. 6. The characteristics imply that the differences in current between the three states allow to discern if a functional device was produced (i.e., a single-stranded fragment is attached) and if a second strand is attached to the first.

The simulations show that the length of the linker is a critical device parameter. The detection of larger and only moderately charged molecules will be correspondingly more difficult.

The calculation of the electrostatic potential around the molecules and in the nanowire necessitates the use of sparse-matrix representations and algorithms to achieve good resolution within modest memory requirements. Transport simulations using the NEGF formalism benefit from parallelization.

(Readers will be able to run simulations on various structures online at <http://www.nanohub.org>.)

## ACKNOWLEDGMENT

This material is based upon work supported by the National Science Foundation under Grant No. EEC-0228390, the Indiana 21st Century fund, and the Semiconductor Research Corporation.

## REFERENCES

- [1] G. Zheng, F. Patolsky, Y. Cui, W.U. Wang, and C.M. Lieber. *Nature Biotechnology*, 23:1294–1301, October 2005.
- [2] C. Yang, Z. Zhong, and C.M. Lieber. *Science*, 310:1304–1307, November 2005.
- [3] J. Wang, E. Polizzi, and M. Lundstrom. In *IEDM 2003*, pages 695–698, Washington DC, USA, December 2003.

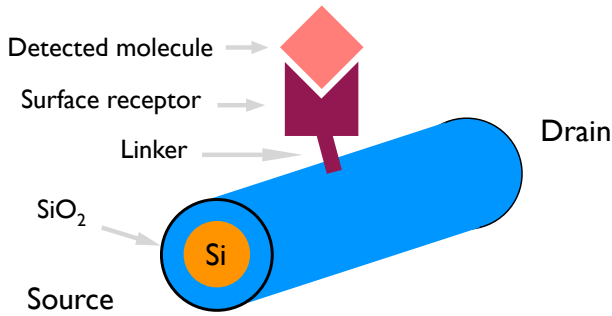


Fig. 1. The structure of a silicon nanowire biosensor. In the simulations the length of the wire is 10nm with a doped region of 4nm in the middle. The diameters of the silicon core and the outer oxide cylinder are 3nm and 5nm, respectively.

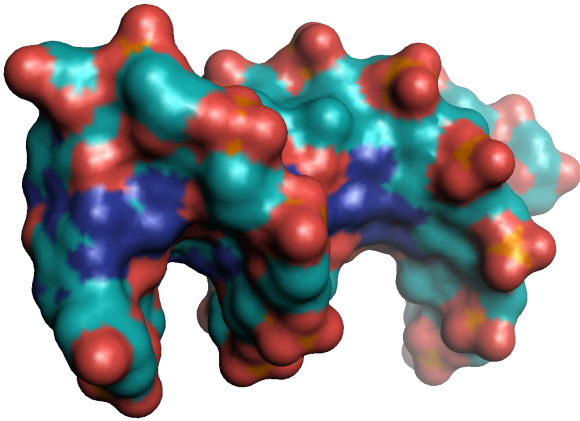


Fig. 2. The double-stranded dodecamer (5'-D(CGTGAATTCACG)-3'). It carries a total of  $-41.74$  positron charges. Its size is approximately  $2\text{nm} \times 2\text{nm} \times 4\text{nm}$ .

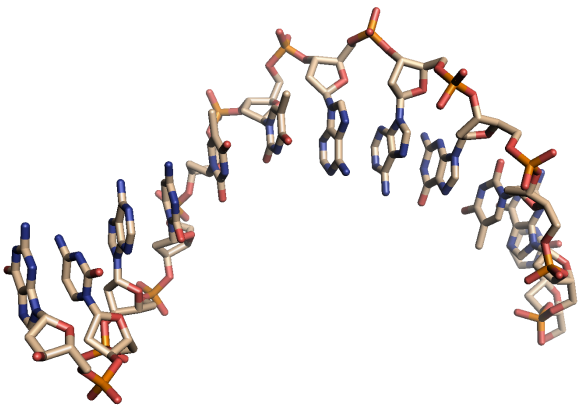


Fig. 3. Chain A of the structure shown in Fig. 2 only. It carries half as many charges, namely  $-20.87$  positron charges.

Schrödinger equation	2.5s
Charge transport (NEGF)	40s
Poisson equation	4.0s

Fig. 4. This table shows the duration of the three parts of the self-consistent loop of the charge transport simulations. A grid spacing of 0.2nm was used in the transport direction which gives 51 slices for the device length of 10nm. The Schrödinger equation was solved for each slice in parallel on 51 processors. In the directions normal to charge transport a grid with 562 nodes, 1611 edges, and 1050 elements was used. In total 28 100 nodes were used for the 3D Poisson solution.

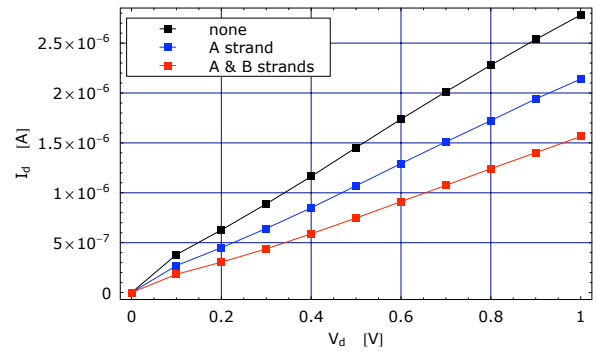


Fig. 5. The current-voltage characteristics for source-drain voltages from 0.0V to 1.0V. The upper most curve corresponds to no molecule attached, the middle curve to single-stranded DNA, and the lower most curve to double-stranded DNA. The addition of each set of charged molecules reduces the current by  $\approx 25\%$ .

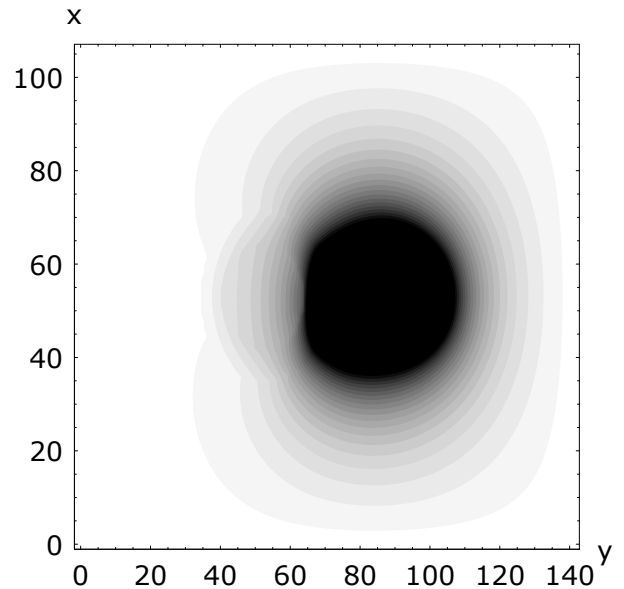


Fig. 6. The potential in a plane normal to the nanowire through the middle of the double-stranded DNA fragment. The shape of the nanowire can be recognized in the left part of the picture.

# Shot Noise in Single Open Ion Channels: A Computational Approach Based on Atomistic Simulations

E. Piccinini<sup>1</sup>, R. Brunetti<sup>1</sup>, F. Affinito<sup>1</sup>, C. Jacoboni<sup>1</sup> and M. Rudan<sup>2</sup>

<sup>1</sup>Nat. Res. Center S3, INFN-CNR and Dipartimento di Fisica, Università di Modena e Reggio Emilia, Italy

<sup>2</sup>ARCES and Dip. di Ingegneria Elettronica, Informatica e Sistemistica, Università di Bologna, Italy

## SOURCES OF NOISE IN ION CHANNELS

Ion channels are nanometric macromolecular pores in the cell membranes which exhibit ion selectivity and gating properties. The transport of ions through a channel protein has been traditionally described as a sequence of discrete transitions over various energy barriers. In the last years X-ray crystallographic structures obtained with atomic resolution [1] confirmed this picture, but suggested that ion motion is highly correlated in the narrow segments of the pore, so that a realistic model for the permeation process is obtained considering transitions between different ion occupancy configurations along given paths on the free-energy landscape as a function of a number of specified process coordinates. Current fluctuations are expected to arise from the discrete nature of the current flow, producing a shot noise, as it is observed in electronic devices. An additional source of noise is associated with fluctuations of the energy barriers due to thermal structural fluctuations of the protein [2]. Another major source of noise is associated with the gating process of the channel. The characteristic time scales of the three fluctuations discussed above are different: ns for shot noise, ps to ns for thermal structural fluctuations, ms for gating. Noise spectra in the frequency domain of the last two processes above have been experimentally obtained and studied in the past [2,3]. The noise spectrum in the frequency domain of the shot noise is still difficult to be measured and has not been studied yet. A theoretical analysis of the time-dependent ion current fluctuations in these nanometric biological conductors is feasible through the implementation

of advanced atomistic approaches. This is actually the subject of the present paper.

## ATOMISTIC MODELS FOR ION CHANNELS

The tremendous advancement in the atomistic knowledge of some prototype channel proteins produced a number of computational approaches which range from the solution of coupled macroscopic equations to molecular-dynamics (MD) [4]. Even though MD provides a simulation of the dynamical motion of all atoms of the protein as a function of time, given the microscopic forces that enter the Newton's equation, the method is limited in its capability to quantitatively characterize the electrical properties of ionic flux through selective channels due to the long time scale involved in the physiological process (ms). Computational approaches able to calculate ion fluxes and including as much as possible the molecular information inside the protein in the input parameters and in the model are today one of the main challenges in computational studies of ion channels. A combined Monte Carlo-Molecular Dynamic approach [5] has been used in the present paper in order to calculate ion conduction properties.

## COMBINED MONTE CARLO MOLECULAR DYNAMICS APPROACH

In selective ion channels the permeation process along the selectivity filter of the protein takes place as a single-file concerted motion of ions. Both current and its noise have been obtained from a Monte Carlo simulation of a single channel under open-gate conditions. A multi-ion model is used, where the ion binding sites around and inside the

protein, the allowed transitions between different occupancy states and the associated rate constants are obtained from the atomic structure and atomistic MD simulations. We focused our attention on the KcsA+ channel. For such a protein recent results from MD simulations have been consistent with what is suggested from the atomic structure at high resolution of this system and provide the necessary microscopic physical input for the statistical model [6]. Six binding sites have been included in the model and the transition rates are evaluated by means of free-energy profiles for the possible ion-occupancy configurations of the channel [5].

## RESULTS

In order to identify what is the frequency domain of current fluctuations produced by the discreteness of the charge carried by the permeating ions we evaluated from the simulation the distribution of time intervals between two successive ion exits. An example for a bias of 100 mV and an ion concentration of 100mM is shown in Fig. 1. The average time  $\langle T_{exit} \rangle$  between two successive ion exits is estimated to be approximately  $9 \times 10^{-9}$  s, while the most frequent time between two consecutive exits is  $5.5 \times 10^{-9}$  s. An example of calculated noise power spectrum as a function of frequency is shown in Fig.2. White noise is found until about  $2 \times 10^7$  Hz with a Fano factor of about 0.75, clearly indicating that a correlation between consecutive ion exits from the channel exists, reducing the noise spectrum with respect to the Poissonian shot-noise value. At frequencies larger than  $1/\langle T_{exit} \rangle$  (corresponding to times much shorter than the current collection time) an increase of the spectrum is observed towards a plateau which corresponds to the spectrum structure of the delta-like ion current spikes. How this correlation is sensitive to the physiological operating conditions of the channel will be discussed in the paper.

## REFERENCES

- [1] Y. Zhou, J. Morais-Cabral, A. Kaufman, and R. MacKinnon, *Chemistry of ion coordination and hydration revealed by a K+ channel-fab complex at 2.0 Å resolution*, Nature **414**, 43 (2001).  
 [2] S.H. Heinemann and F. Sigworth, *Open channel noise V*

*Fluctuating barriers to ion entry in gramicidin A channels*, Biophys. J., **57**, 499-514 (1990).

[3] Le Masurier M., Heginbotham L., and C. Miller, *KcsA: It's a potassium channel*, J. Gen. Physiol., **118**, 303-313 (2001)

[4] For a review see, e.g.: B. Roux, *Theoretical and computational models of ion channels*, Curr. Opin. Struct. Biol. **12**, 182-189 (2002)

[5] Piccinini E., Affinito F., Brunetti R., Jacoboni C., and Rudan M., *Physical mechanisms for ion-current levelling off in the KcsA channel through combined Monte Carlo/Molecular Dynamics simulations*, Proc. XIV Int. Conf. On Nonequilibrium carrier Dynamics in Semiconductors, in press.

[6] M. Compoin, P. Carloni, C. Ramseyer, C. Girardet, *Molecular Dynamics study of the KcsA channel at 2.0 Å resolution: stability and concerted motion within the pore*, Biochim. Biophys. Acta, **1661**, 26 (2004)

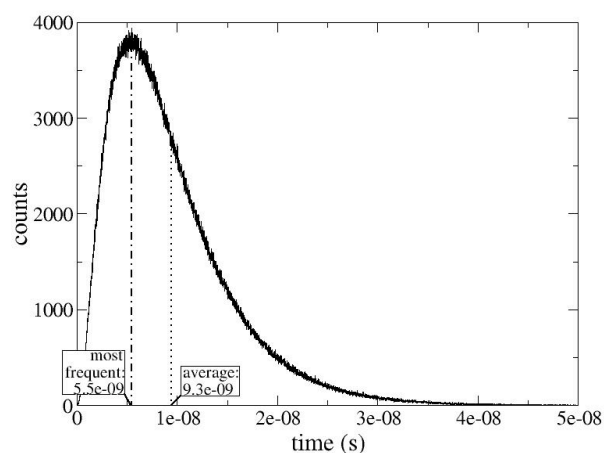


Fig. 1. Number of ion exits as a function of the time interval between two successive ion exits as obtained from the simulation (see text). A current collection time of  $10^{-6}$  s has been used

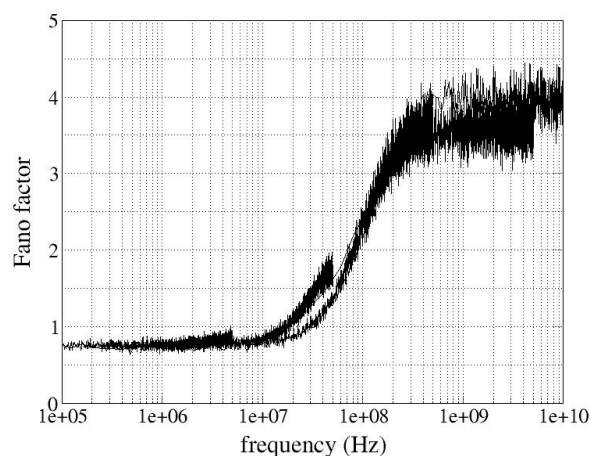


Fig. 2. Power spectrum of the current fluctuations as a function of frequency (see text) Several curves, simulated with different current collection times, have been combined together to explore a wide frequency range.

# The 3D Nanometer Device Project nextnano<sup>3</sup>: Concepts, Methods, Results

A. Trellakis, T. Zibold, T. Andlauer, S. Birner, K. Smith, R. Morschl, P. Vogl  
Walter Schottky Institute, Technische Universität München, 85748 Garching, Germany  
e-mail: vogl@wsi.tum.de

## INTRODUCTION

nextnano<sup>3</sup> is a versatile software for the simulation of nanometer-scale quantum structures and devices. With this simulator, we can calculate the strain and the associated piezoelectric and pyroelectric charges, the electronic structure in external electric and magnetic fields, optical properties such as excitonic energies and transition matrix elements, or also carrier densities and currents. Almost arbitrary device geometries and material compositions consisting of the zincblende or wurtzite crystal systems are supported [1].

In this paper, we will outline some of the basic physical concepts and numerical methods that have been developed for nextnano<sup>3</sup> or are being developed for the ongoing nextnano++ project, an international collaborative effort involving many physicists, mathematicians, and programmers. In addition, we will present a few application examples.

## ELECTRONIC STRUCTURE AND DISCRETIZATION

The electronic structure is calculated in terms of envelope function in the oneband or multiband  $\mathbf{k}\cdot\mathbf{p}$  equations. For the latter it is well established that discretization on a grid may result in spurious energy solutions and discontinuities in the wave functions. For this reason, we have developed a new dimension independent box discretization scheme of the multi-band  $\mathbf{k}\cdot\mathbf{p}$  Hamiltonian that virtually eliminates these problems. Within this method, an artificial diffusion term similar to upwinding schemes [2] is added to the Hamiltonian in order to stabilize the discretization. In addition, the operator ordering employed here avoids singularities in the wave functions.

Another barely recognized problem is that it is numerically extremely difficult to find the correct

solution of Schrödinger's equation in the presence of an external magnetic field. Since the magnetic vector potential is spatially unbounded, every naive discretization of the standard minimal coupling Hamiltonian violate the inherent gauge invariance and consequently leads to huge errors in the numerically obtained solutions. We have developed a gauge invariant discretization scheme of the multiband  $\mathbf{k}\cdot\mathbf{p}$  Hamiltonian that is based on Wilson's formulation of lattice gauge theories. This allows us to calculate the electronic structure and the carrier transport even in the quantum Hall regime.

## NUMERICAL CONCEPTS

We have developed and implemented various numerical algorithms to improve the performance and stability of the coupled Poisson-Schrödinger system. For example, the extremal eigenvalues of the  $\mathbf{k}\cdot\mathbf{p}$  Hamiltonian are calculated using ARPACK in conjunction with a spectral transformation based on Chebyshev polynomials in order to emphasize all relevant eigenstates and to suppress all others.

For 8-band calculations, the interior eigenvalues and wave functions are needed. In this case we employ a block variation of the Rayleigh quotient iteration. An efficient and stable block preconditioner, which approximately decouples the electronic components from the spatial variations, is then used to invert the resultant indefinite linear system of equations.

Finally, in order to solve the coupled Poisson-Schrödinger system, we employ an approximate quantum charge density inside of Poisson's equation in order to estimate the dependence of the density on the potential through Schrödinger's equation. Using this estimator the coupling between both equations is much decreased and rapid convergence is achieved. Recently, we have refined this

technique further by projecting the Hamiltonian into the subspace spanned by all already known eigenvectors, and then diagonalizing this small subspace matrix. With this method only half as much work is needed to obtain the correct solution.

#### CARRIER TRANSPORT

Carrier transport is currently calculated either as ballistic current using the contact block reduction (CBR) method [3] or in terms of an empirical quantum drift-diffusion method. We are currently working on a generalized CBR method that includes scattering within a Büttiker probe model.

#### SOFTWARE DESIGN AND SPEED

In order to achieve a high degree of code reuse we heavily rely on object-orientated programming techniques. An inheritance based class hierarchy combined with the widespread use of C++ templates results into a very efficient and compact implementation without code duplication.

All input files use a powerful hierarchical syntax that can easily describe even complicated device geometries. These input files are then parsed using a BISON generated parser module and validated for errors using an approach similar to the one used for validating XML files.

A self-consistent and fully quantum mechanical 3D electronic structure calculation of a HEMT-type AlGaAs/GaAs device with a total of  $4 \times 10^5$  grid points requires about an hour on a standard PC with 2 GB RAM.

#### APPLICATIONS

We are using `nextnano3` extensively to model devices and quantum structures in the Si-SiGe and III-V material systems. Examples for such applications are for instance strained p-channel inversion layers, double gate and wrap-gate MOSFETs, or also strain-induced T-shaped InAlAs quantum wires, InGaAs/GaAs quantum dot molecules, and GaN based ISFETs for biosensing applications.

Worldwide, `nextnano3` is downloaded about 5-10 times per day. In addition to the already extensive documentation tutorials on our website; consulting services are available through Stefan Birner's company `nextnano` [1].

#### ACKNOWLEDGEMENTS

Financial support by the Deutsche Forschungsgemeinschaft (SFB 631), the Österreichische FWF (Projekt IR-ON F025), and the Office of Naval Research under Contract No. N00014-01-1-0242 is acknowledged.

#### REFERENCES

- [1] See <http://www.wsi.tum.de/nextnano3> for executables and documentation and <http://www.nextnano.de> for consulting services.
- [2] R. E. Bank, J. F. Bürgler, W. Fichtner, and R. K. Smith, "Some Upwinding Techniques for Finite Element Approximations of Convection Diffusion Equations", *Numerische Mathematik*, pp 185-202, 1990
- [3] D. Mamaluy, D. Vasileska, M. Sabathil, T. Zibold, and P. Vogl, *Phys. Rev. B* 71, 245321 (2005), "Contact block reduction method for ballistic transport and carrier densities of open nanostructures", *Phys. Rev. B* 71, 245321 (2005)

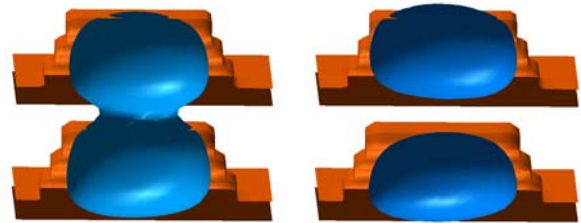


Figure 1: Isosurface of bonding and antibonding electron wave functions in two adjacent InGaAs/GaAs quantum dots 6 nm apart from each other.

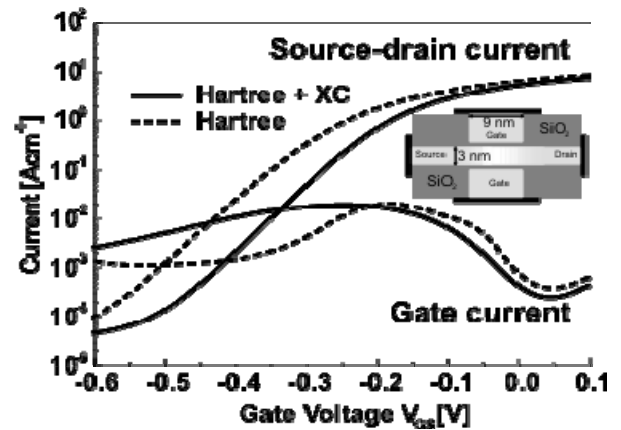


Figure 2: Currents in a 9 nm gate DGFET device as depicted in the inset. Results from a pure Hartree calculation (dashed line) and one including exchange and correlation within the local density framework (full line) are shown.

# Conductance of Winding Wires

E. Cancellieri, M. Rosini\*, A. Bertoni, G. Ferrari<sup>†</sup> and C. Jacoboni

Dipartimento di Fisica Università di Modena e Reggio Emilia and  
CNR-INFM S3 National Research Center, via Campi 213/a, 41100 Modena (Italy)

\* Dipartimento di Ingegneria dell'innovazione, Università degli studi di Lecce

<sup>†</sup> Device Modelling Group, Dept. Electronics & Electrical Engineering, University of Glasgow  
e-mail: ecancellieri@unimo.it

## INTRODUCTION

In the past years a strong attention has been focused on the optical and transport properties of semiconductor heterostructures due to the possibility of tailoring material parameters such as the electron effective mass, and the band gap, by changing the structure parameters.

Recent experimental results on  $\text{In}_x\text{Ga}_{1-x}\text{As}$  structures [1], [2] can not be explained in the framework of standard theoretical and simulative approach for the description of carrier transport in quantum wells. While the values of the experimental mobility can be fitted using existing theories [3], [4], [5] in terms of background impurities scattering and alloy disorder scattering, a variation with respect to the transport direction seems to be explained only by the different surface roughness (SR) experimentally observed along two orthogonal lattice directions. However, according to the theory, its effect should be negligible.

Since the effect of the SR on the conductance may depend upon resonances and localized states, the traditional approach, based on the scattering perturbation theory, is questionable.

In order to get a better insight on the effect of the SR on the conductance, we have considered winding quantum wires (QWRs) and have computed the coherent transport characteristics by means of the Landauer approach and a numerical solution of the open-boundary two dimensional Schrödinger equation.

## THE METHOD

The profile of the QWRs analyzed in the present work are shown in figures 1 and 2. The distance between the boundary walls of the simulated wires

is constant since the roughness profile of the considered structures is mainly due to the profile of the substrate. The numerical approach we adopted is based on the Landauer formula and the needed transmission coefficient  $T(E)$  is obtained from the solution of the two-dimensional Schrödinger equation for the winding wire 20 nm wide. The open-boundary Schrödinger equation is solved making use of the Quantum Transmitting Boundary Method [6]. In particular we are able to introduce in the model a realistic potential profile taken directly from the experiments [1], [2].

In this way we are able to calculate the transmission coefficient, the coherent component of the current flowing through the device and the ohmic conductance, without any free parameter.

## RESULTS

From preliminary results, it turns out that for specific values of the carrier energy the winding profile of the wire can generate resonances as shown in figs 3 and 4. This explains the behavior transmission coefficient  $T(E)$  curve of fig. 5: for smoother winding the  $T(E)$  reaches the unity at lower energy. We believe that this effect can explain the different values of the mobility measured along two orthogonal lattice directions characterized by two different periodicities of the substrate SR.

## REFERENCES

- [1] F. Capotondi et. al., Thin Solid Films **484**, 400 (2005)
- [2] F. Capotondi et. al., J. Crystal Growth **278**, 538 (2005)
- [3] A. Gold, Phys. Rev. B **35**, 723 (1987)
- [4] A. Gold, Phys. Rev. B **38**, 10798 (1988)
- [5] T. Ando, A. Fowler, and F. Stern, Rev. of Mod. Phys. **54**, 437 (1982).
- [6] C. S. Lent et. al., J. Appl. Phys. **67**, 6353 (1990)

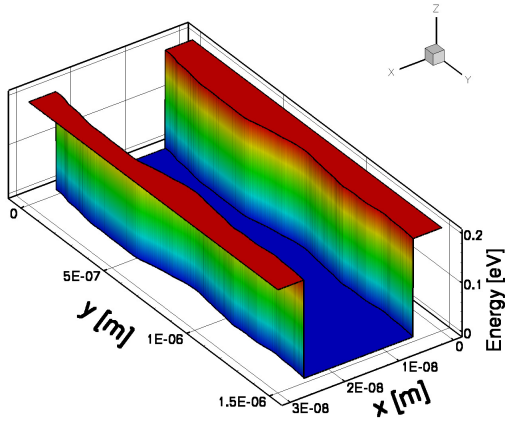


Fig. 1. This potential profile is characterized by a root mean square height of 2-3 nm and a periodicity of about  $0.9 \pm 0.3 \mu\text{m}$ .

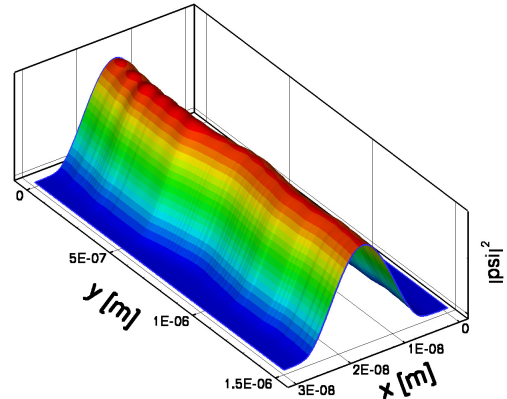


Fig. 3. Example of a scattering state of the system of fig. 1. The longitudinal energy of the incoming electrons is about 0.41 meV.

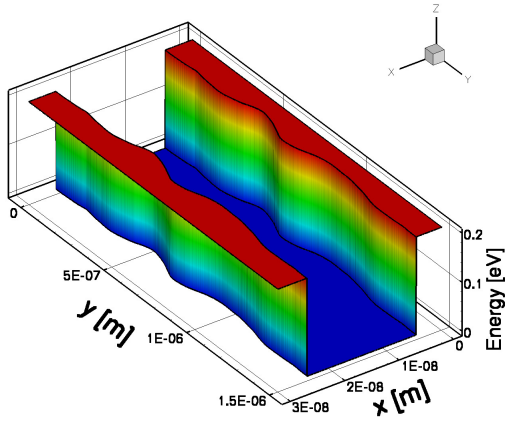


Fig. 2. This potential profile is characterized by a root mean square height of 2-3 nm and a periodicity of about  $0.28 \pm 0.09 \mu\text{m}$ .

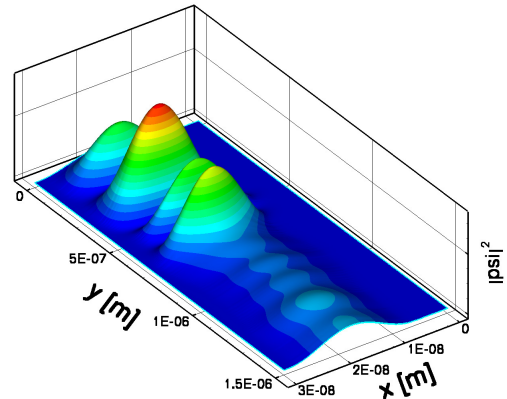


Fig. 4. Example of a scattering state of the system of fig. 2. The longitudinal energy of the incoming electrons is about 0.13 meV.

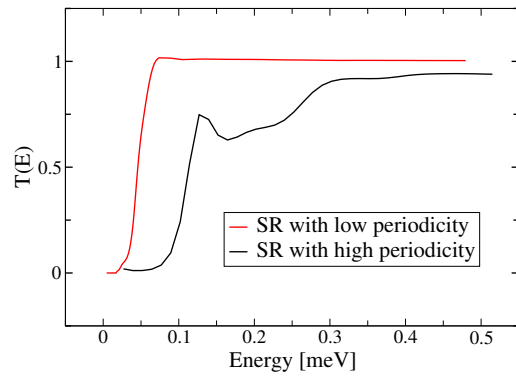


Fig. 5. Transmission coefficients as a function of the longitudinal energy of the injected electron in the case of the two QWRs shown in figures 1 and 2.

# Determination of the Many-Body Conductance of A Fully Interacting System of Electrons

M.J. Gilbert and J. Shumway\*

Microelectronics Research Center, University of Texas at Austin, Austin, TX 78758-9900

\*Department of Physics and Astronomy, Arizona State University, Tempe, AZ 85287-1504

e-mail: mgilbert@mer.utexas.edu

## Abstract

New simulation tools are required to correctly capture the physics of strongly interacting systems. Here, we present results of a new technique for extracting the many-body conductance for interacting systems in two or three dimensions. Our approach is to extend many-body path integral Monte Carlo (PIMC) simulations, which we have used for small quantum dots [1], to much larger, two-dimensional, simulations of several different quantum point contact (QPC). In each QPC, we simulate up to two hundred fully interacting electrons in a fully quantum many-body framework. This technique allows the seamless simulation of both the dense 2DEG in the contacts and a low-density, quasi-1D correlated electron distribution in the device, as illustrated in Fig. 1.

## Estimating the Conductance

To estimate the DC conductance, we collect the current-current correlation function, which we measure in imaginary time (illustrated in Fig. 2),

$$\Pi(x, x'; i\tau) = \langle j_x(x; 0) j_x(x'; i\tau) \rangle_{\beta} \quad (1)$$

The Fourier transform is a set of real amplitudes at the bosonic Matsubara frequencies,  $\omega_n = \frac{2n\pi}{\beta}$ ,

$$\Pi(x, x'; i\omega_n) = \sum_{m=0}^{\infty} e^{i\omega_n m\tau} \Pi(x, x'; im\tau) \quad (2)$$

The conductivity is then given by the Kubo formula,

$$\sigma(x, x'; \omega) = \frac{i}{\omega} \left[ \Pi(x, x'; \omega) + \frac{ne^2}{m} \right] \quad (3)$$

To obtain  $\Pi(x, x'; \omega)$  requires analytic continuation from the Matsubara frequencies, formally denoted as  $i\omega_n \rightarrow \omega + i\delta$ . The  $i\delta$  part of the notation

dictates that for the retarded Green's functions, the real frequency axis must be approached in the upper-half plane. Therefore, we must use the collected data for the Matsubara frequencies in the upper-half plane and analytically continue them to small real-valued frequencies. Once the conductivity is then fit to a Drude formula based model and the DC conductance is extracted.

## QPC with Several Hundred Electrons

Here we take a simple analytic expression [2] for a split-gate QPC that is 200 nm in length and 50 nm in width containing 200 total electrons (100 spin up and 100 spin down). We obtain the current-current correlation functions, as described in the previous section, as well as the electron density and correlation functions. In Fig. 3, we plot the conductivity at the first Matsubara frequency for  $V_g = -0.3$  V. We find that it is essentially diagonal and that the conductivity is suppressed within the channel and that the transport is purely local in nature. In Fig. 4, we plot the DC conductance for  $V_g = -0.3$  V. We solve for the conductance in the steady-state limit using an N-point Padé approximation. Here we see that the conductance is also suppressed in the channel corresponding to the high negative gate bias. While the conductance is low, the conductance is still higher than in the case of the non-interacting electrons as the interactions force the electrons to higher energies.

Further, we will show that our new method yields the same conductance values as that of Green's functions in the non-interacting system and analyze the resultant Kondo behavior near pinch-off.

\* Work supported in part by the NRI, SRC, AMRC, and NSF.

[1] M. Harowitz, D. Shin, and J. Shumway, *J. of Low Temp. Phys.* **140**, 211-226 (2005).

[2] G. Timp, *Semicond. and Semimetals* **35**, 113 (1992).

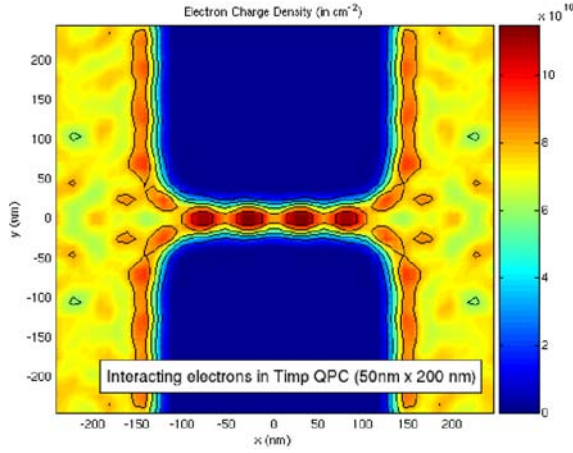


Fig. 1. Example of charge density in and around a model QPC, as calculated with our new many-body PIMC technique. The method seamlessly includes both the dense 2DEG outside the channel and the highly-correlated, quasi-1D electron ordering within the device.

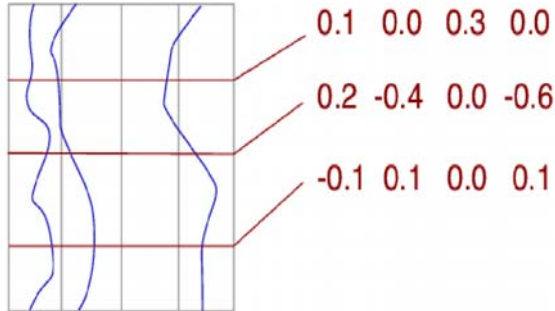


Fig. 2. A schematic illustration of collecting charge current density information from the PIMC. We set up discrete real-space bins, then histogram the location and velocities of discretized beads. We then use an FFT to convolve the data for the relative time separations and collect the current-current correlation functions over many path configurations.

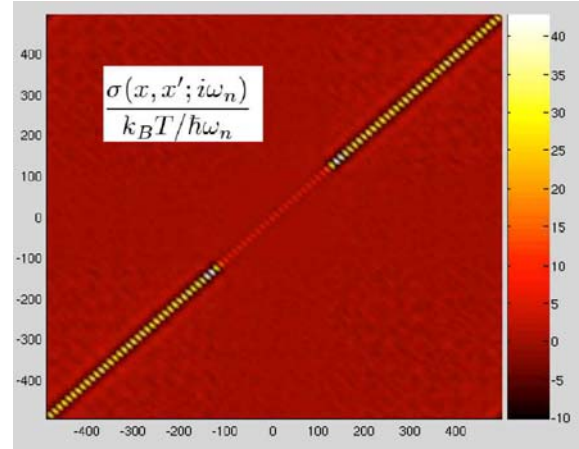


Fig. 3. The conductivity at the first Matsubara frequency, as calculated by sampling the current-current correlation function for 200 interacting electrons at  $V_g = -0.3$  V. The device is in the range  $-100$  nm  $< x < 100$  nm and is coupled to wide leads, which display much higher conductivity.

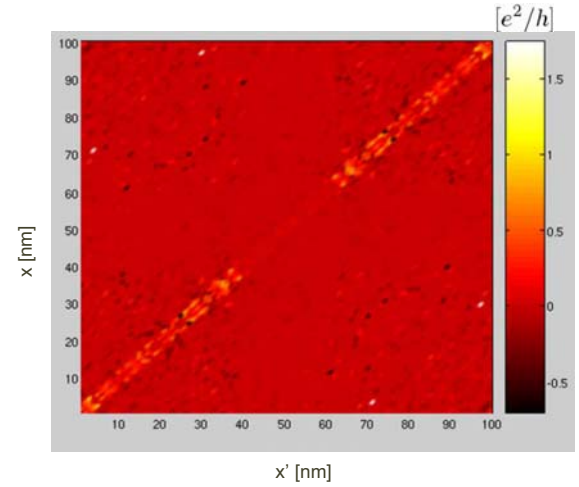


Fig. 4. DC conductivity as extrapolated using an N-point Padé approximation at  $V_g = -0.3$  V. While the conductance is quite clear, the off-diagonal values represent statistical noise in our simulation which may be reduced with longer Monte Carlo runs.

# Self-Consistent Treatment of Quantum Transport in 10-nm FinFET Devices Using CBR Method

H. Khan, D. Mamaluy, D. Vasileska

Department of Electrical Engineering, Ira A. Fulton School of Engineering,  
Arizona State University, Tempe, AZ 85287,  
email: [mamaluy@asu.edu](mailto:mamaluy@asu.edu)

In order to investigate quantum transport properties in open 3D systems in sub-nanometer regime, a highly efficient numerical approach is essential. We have utilized the Contact Block Reduction (CBR) method [1-3] to simulate a variety of nano-scale FinFET devices self-consistently.

In this work the band-structure has been modeled by a single parabolic band with anisotropic effective mass for silicon and a spherical mass for the oxide. The exchange-correlation potential has been taken into account via the local density approximation. Real-space treatment of surface roughness and the effect of scattering (via a simple phenomenological model) have also been included. The self-consistent potential and current are obtained as converged solutions of the open-system Schrödinger equation coupled with the Poisson equation. This is achieved by employing the CBR method based on the Green's functions formalism, and a predictor-corrector approach, which has been modified for a superior convergence rate for open quantum systems. In the latest version of our CBR code, the appropriate number of eigenstates and lead modes used in the calculation is determined dynamically for each iteration, which helps to further reduce the computational time and makes it easier to simulate devices of arbitrary structure and with any number of leads.

Several FinFET devices shown in Fig. 1 with varying fin width have been simulated. Gate lengths of 10 nm and oxide thickness of 1.75 nm have been used in all the simulations. The fin is assumed to be lightly doped with a thickness varying from 6 nm to 12 nm. For the 12 nm fin width our simulation shows the formation of a distinct channel on each side of the fin (Fig. 2, left panel). As fin width decreases gradually from 12 nm towards 8 nm, inversion layer formed adjacent to both gates merge into a single channel as shown in Fig. 2 (middle and right panel).

The transfer characteristics for different fin widths are shown in Fig. 3, left panel. The data for 12nm fin width near subthreshold regime is in good correspondence to the experimental data [4]. We found that the effect of the fin width variation is more important for the subthreshold device behavior than for higher gate voltages (the linear scale is not shown here).

The device turn-off behavior has been examined by extracting sub-threshold slope for different fin widths. The corresponding data are shown on Fig. 3, right panel. It has been found that as the fin width decreases, the gate control improves *linearly* up to the fin width of 8 nm and then saturates with the further decreasing of the fin width. For 12 nm fin width the calculated value of the subthreshold slope is 126 mV/dec, as compared to 125mV/dec experimental value in Ref. [4].

The fully quantum mechanical approach utilized in the CBR method enables one to calculate the gate leakage with no additional computational costs, which might be impossible or difficult using other approaches. While the precise values of the gate currents are naturally very sensitive to the oxide thickness and the quality of Si/SiO<sub>2</sub> interface (simulated using an adjustable surface roughness parameter in the code), the trend of the simulated gate current matches closely the experimental data.

## REFERENCES

- [1] D. Mamaluy, M. Sabathil, P. Vogl, J. Appl. Phys. **93**, 4628 (2003).
- [2] D. Mamaluy, A. Mannargudi, D. Vasileska, J. Comp. El. **3**, 45 (2004).
- [3] D. Mamaluy, M. Sabathil, T. Zibold, D. Vasileska, P. Vogl, Phys. Rev. B **71**, 245321 (2005).
- [4] Bin Yu, Leland Chang, Shibly Ahmed et al., IEDM, pp. 251-254 (2002).

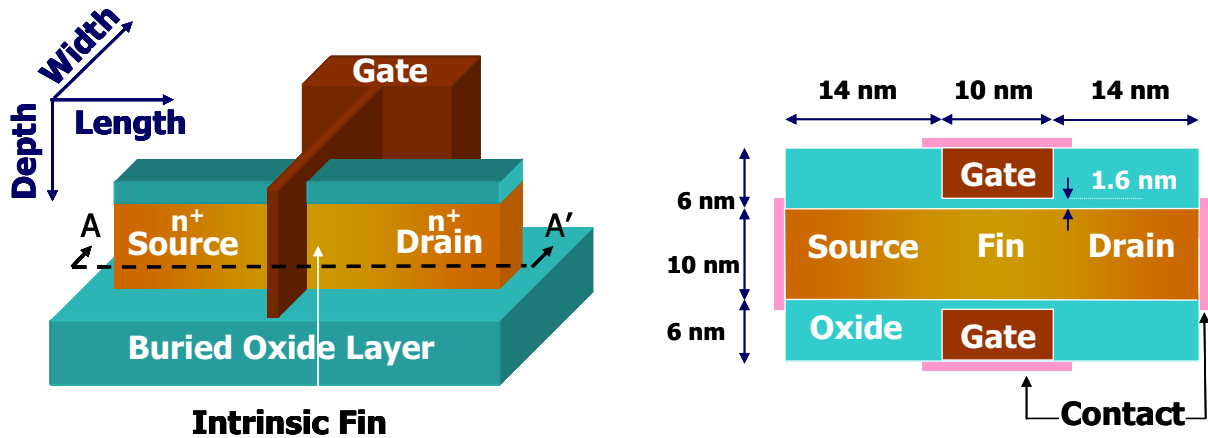


Figure 1. Left panel – 3D schematic view. Right panel – top view along A-A' cross section.

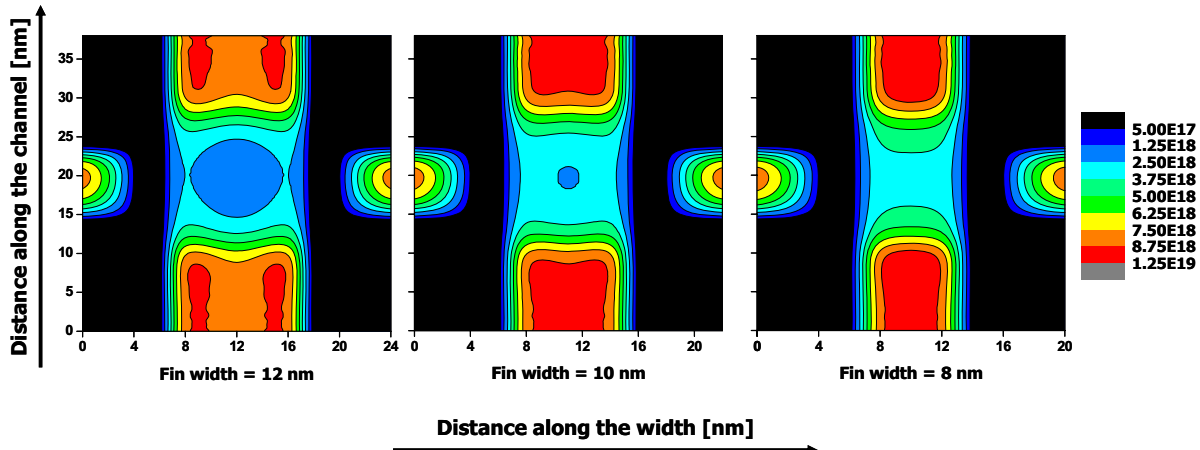


Figure 2. Electron density along A-A' cross section. Left panel: fin width=12nm, middle panel: fin width=10nm, right panel: fin width=8nm.

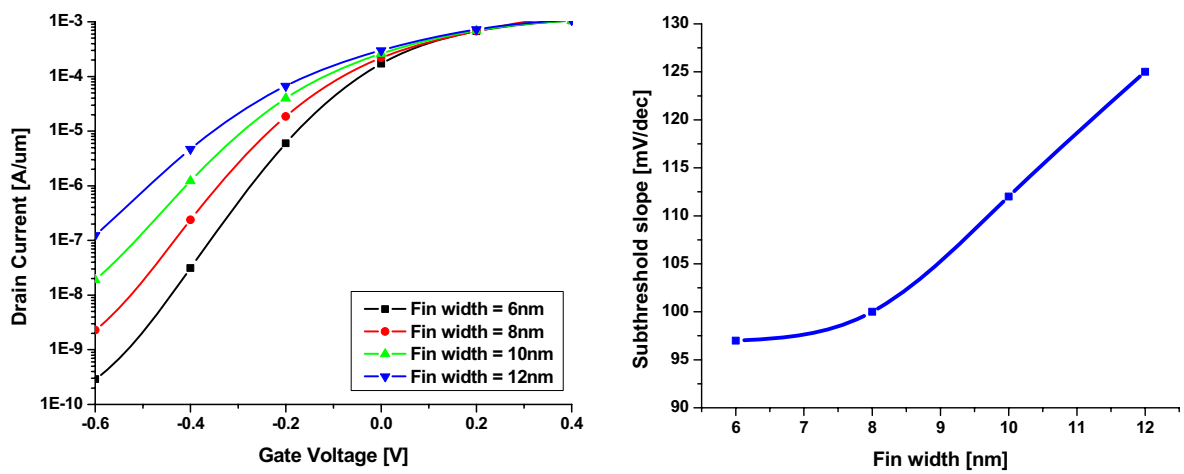


Figure 3. Left panel - transfer characteristics,  $V_D = 0.1V$ . Right panel – subthreshold slope vs. fin width.

# Electron Mobility in Silicon and Germanium Inversion Layers

T. P. O'Regan, and M. V. Fischetti  
Department of Electrical and Computer Engineering  
University of Massachusetts  
Amherst MA 01003, USA  
e-mail: toregan@ecs.umass.edu

The perception that conventional scaling of Si MOSFETs is approaching its limits is forcing us to look at alternative ways to increase device performance, such as alternative crystal orientations, channel materials, and high- $\kappa$  insulators. In this work we focus on calculating electron mobility in Si and Ge inversion layers on various crystal and channel orientations, and with high- $\kappa$  insulators.

The calculation utilizes a self-consistent 1-D Schrödinger-Poisson solver with non-parabolic corrections. The mobility is then computed using the Kubo-Greenwood formula accounting for intravalley phonon scattering (described in the elastic approximation by an anisotropic model using the deformation potential obtained by Herring and Vogt [1]), intervalley phonon scattering [2], and scattering with surface roughness, accounted for following Ando's approach and by computing the screening matrix with the appropriate Green's function [3]. Scattering with gate plasmons and with interface optical phonons associated with several high- $\kappa$  dielectrics are also included by solving for the dispersion of the interface modes. This is given by the solution of the secular equation associated with the dielectric function [1].

In the figures we show the electron mobility in Si and Ge inversion layers on the (100) and (111) surfaces with the channel along the [011] and  $[1\bar{1}0]$  directions, respectively with an equivalent oxide thickness of 1.5 nm. As expected, Ge has a higher mobility than Si for both the phonon limited case in Fig. 1 and when surface roughness is included in Fig. 4. For Ge, the (111) surface is best at lower densities, while the (001) is better at higher densities due to surface roughness scattering. For Si, the (001) surface exhibits a higher mobility than

the (111) surface, primarily due to the effect of bulk phonons. Figures 2. and 5. show the mobilities for Si and Ge including scattering with high- $\kappa$  phonons. The dielectrics included are silicon dioxide and hafnium oxide. The mobility is degraded significantly by the presence of HfO<sub>2</sub> for both Si and Ge. Unfortunately, this is the result of the "soft phonons" responsible for the high dielectric constant itself [1]. Note that the electron mobility in Ge is depressed significantly more by scattering with the insulator phonons (also SiO<sub>2</sub>) than Si in general. This is simply because the bulk-phonon-limited mobility in Ge is quite large and so is very sensitive to the presence of any additional scattering process. Figures 3. and 6. show the contributions of each scattering process for the (001) surface in Si and Ge respectively. Surface roughness is most important at high densities because the wavefunctions are "squeezed" tightly to the dielectric/substrate interface. Scattering with high- $\kappa$  phonons has a decreasing effect at high densities, thanks to the increasing dielectric screening by the electrons in the channel.

We shall also present results related to additional surface and channel orientations, semiconductors, and high- $\kappa$  dielectrics.

## ACKNOWLEDGMENT

This work is supported by the Semiconductor Research Corporation (Task ID: 1373.001)

## REFERENCES

- [1] M.V. Fischetti, J. of Applied Phys. **89**, 1232 (2001).
- [2] C. Jacoboni and L. Reggiani, Rev. Mod. Phys. **55**, 645 (1983).
- [3] M.V. Fischetti and S.E. Laux, Phys. Rev. B **48**, 2244 (1993).

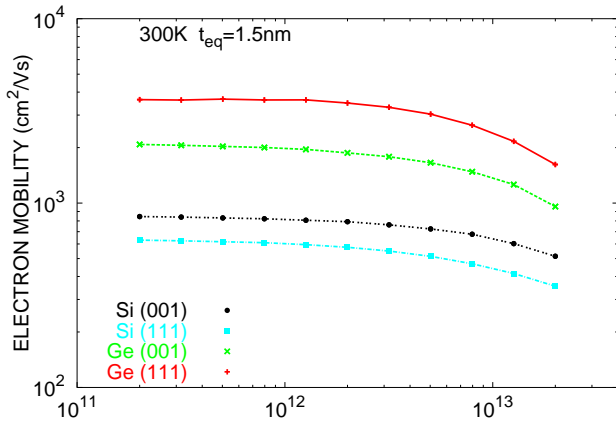


Fig. 1. Calculated phonon limited electron mobility in Si and Ge inversion layers as a function of electron sheet density.

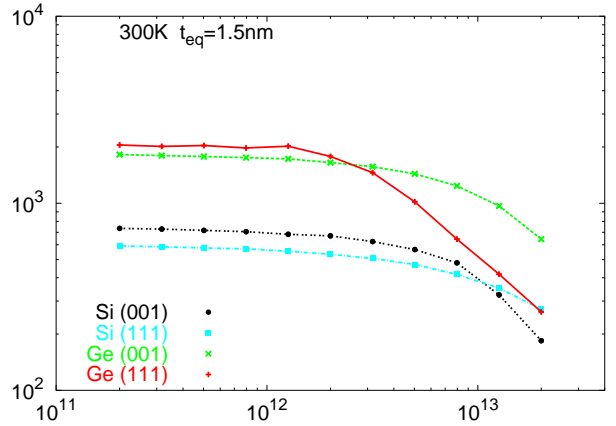


Fig. 4. As in Fig. 1, but with surface roughness included.

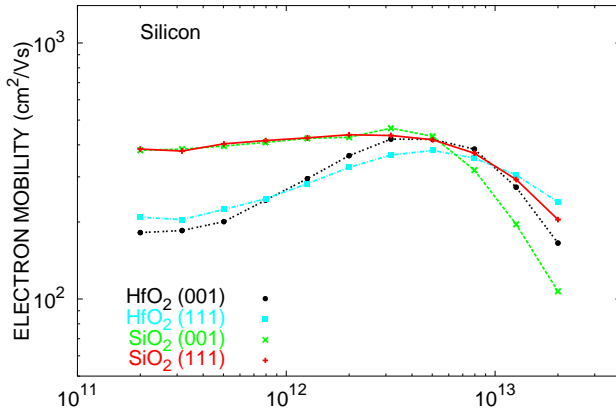


Fig. 2. Total calculated mobility, including scattering with bulk phonons, surface roughness and high- $\kappa$  phonons (Si only), as a function of electron sheet density.

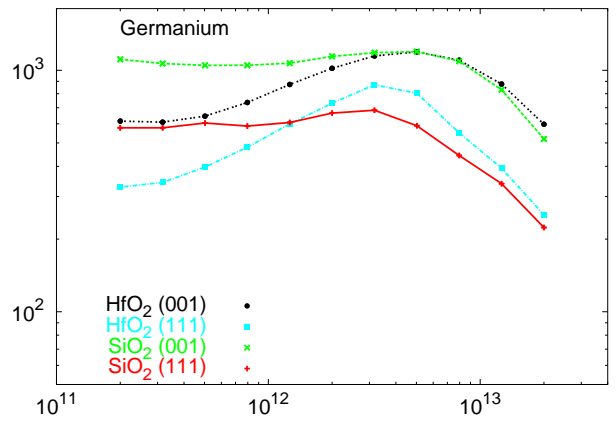


Fig. 5. As in Fig. 2, but for Ge.

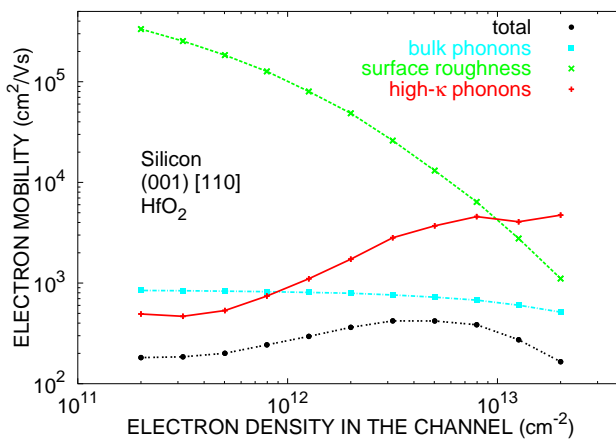


Fig. 3. Calculated contributions to the total mobility.

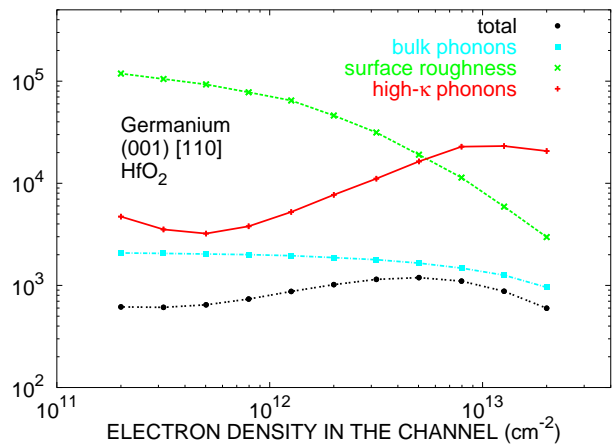


Fig. 6. As in Fig. 3, but for Ge.

# First-Principles Calculations of Mobilities in Ultrathin Double-Gate MOSFETs

M. H. Evans,<sup>1</sup> M. Caussanel,<sup>2</sup> and R. D. Schrimpf,<sup>2</sup> and S. T. Pantelides,<sup>1,3</sup>

<sup>1</sup>Department of Physics and Astronomy, Vanderbilt University, Nashville, TN USA

<sup>2</sup>Department of Electrical Engineering and Computer Science, Vanderbilt University, Nashville, TN USA

<sup>3</sup>Condensed Matter Sciences Division, Oak Ridge National Laboratory, Oak Ridge, TN USA

e-mail: pantelides@vanderbilt.edu

Methods for modeling mobilities in MOSFETs rely on empirical models for various scattering mechanisms and generally treat the Si-SiO<sub>2</sub> interface as an infinite potential barrier, confining electrons in the Si channel. The underlying atomic structure in the channel is suppressed and its effects are captured either in effective masses or via the energy bands of the bulk crystal. Despite their success in modeling the “universal mobility curve” and other cases, the models are reaching their limits as new materials are being introduced (e.g., strained Si, alternate dielectrics) and devices have nanoscale dimensions (ultrathin double-gate devices have been fabricated with channels only ~2 nm thick[1]).

We recently published a first-principles, quantum-mechanical) method for calculating mobilities in double-gate devices using atomic-scale models with no empirical parameters. Scattering potentials are extracted from the calculations and include all atomic relaxations and self-consistent electrostatic screening. Wave function penetration into the gate dielectric is automatically included (Fig. 1). The initial applications examined the effect of atomic-scale interface roughness[2] in the form of suboxide bonds (Si-Si bonds on the SiO<sub>2</sub> side of the interface) and O protrusion (Si-O-Si bonds on the Si side of the interface). Here we will present our latest applications, including the following:

Calculations of mobilities in ultrathin double-gate devices with a strained-Si channel: Experiments using strained-Si channels in conventional MOSFETs found significantly enhanced mobilities.[3] Fischetti et al.[4] were able to

reproduce the data only by introducing an *ad hoc* large reduction of interface roughness. Here we show that enhanced mobility arises from the fact that, in strained Si, the strain fields produced by atomic-scale roughness are reduced significantly (Fig. 2).

Atomically-resolved images of Si-SiO<sub>2</sub>-HfO<sub>2</sub> alternate-dielectric structures recently obtained by van Benthem and Pennycook (Fig. 3) revealed the presence of “stray” individual Hf atoms in the thin SiO<sub>2</sub> interlayer. Density-functional calculations were used to obtain relaxed structures of such Hf atoms near the interface. Mobility calculations find a significant reduction caused by scattering from neutral Hf atoms, in agreement with measured mobilities in such structures.

Applications to other scattering mechanisms are in progress and available results will be reported at the conference.

Finally, we compare our first-principles method with the Density-Gradient (DG) method,[5] which includes quantum mechanical effects in an approximate way in device modeling (Fig. 4). The DG method reproduces the overall shape of the electron-density spatial distribution, but underestimates carrier penetration into the oxide. The results of first-principles calculations can be used to optimize the range of applicability and accuracy of the DG method for device modeling.

This work was supported in part by the National Science Foundation grant No. ECS-0524655 and by the Air Force Office of Scientific Research MURI program. We would like to thank K. van Benthem for the Z-contrast image of Fig. 4.

REFERENCES

- [1] K. Uchida *et al.*, *IEDM Tech. Dig.*, 805 (2003); D. Esseni *et al.*, *IEEE T. Electron Dev.*, **50**, 802 (2003).
- [2] R. Buczko, S. Pennycook, and S. T. Pantelides, *Phys. Rev. Lett.*, **84**, 943 (2000).
- [3] J. Welser *et al.*, *IEDM Tech. Dig.*, 373 (1994); K. Rim *et al.* *IEDM Tech. Dig.*, 707 (1998).
- [4] M. V. Fischetti, *J. Appl. Phys.* **92**, 7320 (2002).
- [5] M. G. Ancona and H.F. Tiersten, *Phys. Rev. B* **35**, 7959 (1987).

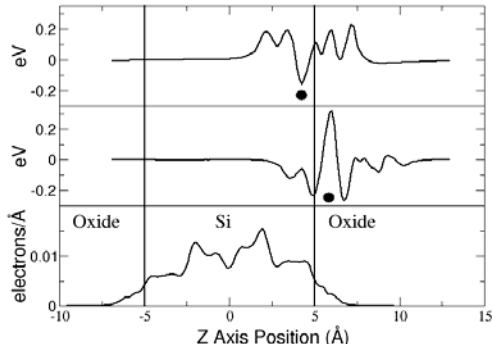


Fig. 1 Scattering potentials and carrier electron density (bottom) for oxygen protrusion (top) and suboxide bond (middle) defects. Black dots indicate defect centers. Penetration of the channel electron density is evident.

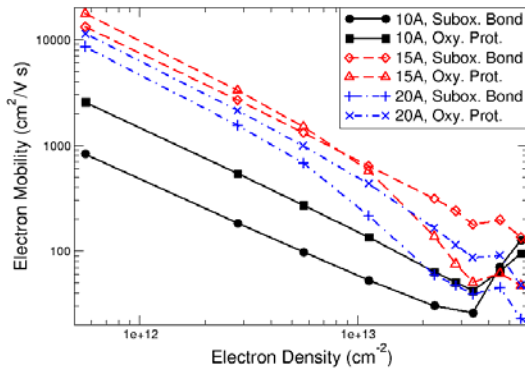


Fig. 2 Calculated mobilities for oxygen protrusions and suboxide bonds in 10Å-20Å channels. Defect density is  $5.6 \times 10^{11} \text{ cm}^{-2}$ . No other scattering mechanisms are included.

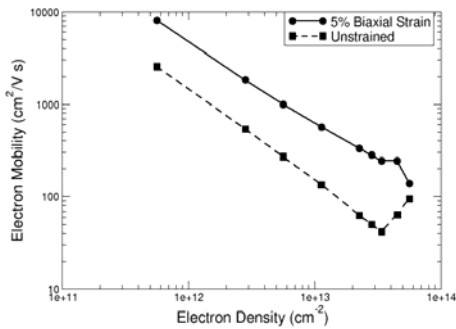


Fig. 3 Calculated mobilities for oxygen protrusions in unstrained and 5% biaxially-strained (001) channels in double-gate channels. Defect density is  $5.6 \times 10^{11} \text{ cm}^{-2}$ . No other scattering mechanisms are included.

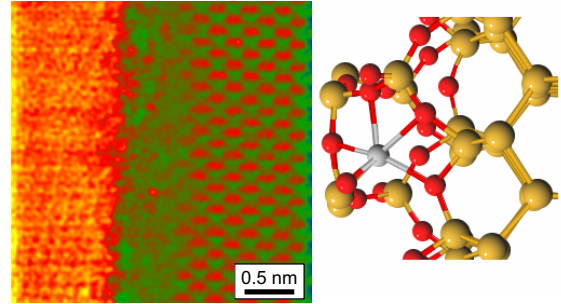


Fig. 4 Left: Z-contrast STEM image of Si-SiO<sub>2</sub>/HfO<sub>2</sub> interface. The arrow highlights a stray Hf atom in the SiO<sub>2</sub> interlayer (K. Van Benthem and S. J. Pennycook, unpublished); right: schematic of the stray Hf atom and its neighbors

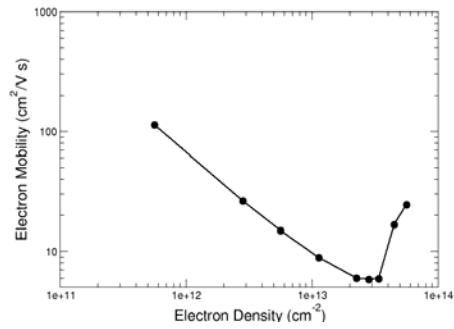


Fig. 5 Calculated mobility due to a neutral Hf defect as shown in Fig. 4. Hf sheet density is  $10^{12} \text{ cm}^{-2}$ . No other scattering mechanisms are included.

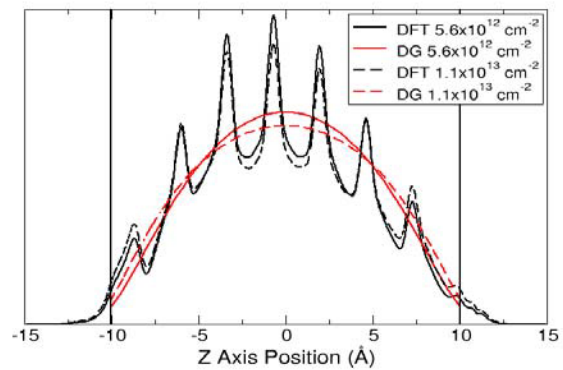


Fig. 6 Conduction electron densities in a 20Å-thick UTSOI channel, calculated from first-principles and the Density Gradient model (DG). Densities are scaled to common, arbitrary units. As carrier density increases (black to red), charge shifts from the center of the channel to the interfaces.

# Perspectives on Solid-State Flying Qubits

A. Bertoni

National Research Center on nanoStructures and bioSystems at Surfaces (S3), INFM-CNR  
via Campi 213/A, 41100 Modena  
e-mail: bertoni.andrea@unimore.it

## SOLID STATE FLYING QUBITS

The quest for quantum-computing capable architectures has recently focused on solid-state implementations, since they seem more prone to meet the required criteria [1] of scalability and integrability than alternative approaches like the ones based on nuclear magnetic resonance, ion traps or quantum electrodynamics techniques [2].

In many proposals different components of a quantum-computing system are dedicated to different quantum transformations. As a consequence at each stage the outputs of these transformations, i.e. the state of a qubit register, must be moved to the inputs of other quantum gates. This process, overlooked in the early times of quantum information processing research, results to be critical in viable practical realizations [3], so that the celebrated Di Vincenzo checklist has been recently extended with two extra issues [4], namely (a) the ability to interconvert stationary and flying qubits, and (b) the ability to faithfully transmit flying qubits between specific locations. However these new requirements are redundant for proposals in which the logical operation is performed on the flying qubit itself. The present contribution will review the recent efforts towards the numerical modeling (and eventually the experimental realization) of prototypes of one- and two-qubit quantum gates (Fig. 1) based on electron transport in single and coupled quantum wires (QWRs) [5].

## ELECTRON STATES IN QUANTUM WIRES

Two alternative possibilities for the qubit definition have been considered in literature: the charge localization of electrons transmitted through a couple of QWRs [6] (or, equivalently, the current states in an electron interferometer [7]), and the spin orientation of the carriers [8]. In both cases the theoretical feasibility of a universal set of quantum gates has been demonstrated. Furthermore it has

been proposed to use surface acoustic waves as a highly controllable mean to inject and drive electrons in the QWRs [8,9]. We showed by numerical simulations that the introduction of the new time-dependent potential, while altering the dynamics of the quantum gates, preserves the logical transformation on the qubit [10] (Fig. 2).

## ENTANGLEMENT AND DECOHERENCE

Quantum entanglement is the key-resource for quantum information processing but it represents a detriment when it couples the qubit state with some “external” degree of freedom (environment), leading to the well-known phenomenon of decoherence. If the modeling of the qubit system includes the quantum state of the environment, the quantitative evaluation of entanglement dynamics (and consequently of decoherence) can be obtained (Fig. 3), together with the few-particle effects originating from quantum correlation. A numerical approach will be presented to include few-particle dynamics in the calculation of scattering states in the framework of coherent transport through a QWR with localized states.

## REFERENCES

- [1] D. DiVincenzo, *The physical implementation of quantum computation*, quant-ph/0002077 (2000).
- [2] J. A. Jones et al., *J. Mag. Res.* 135, 353 (1998).  
L.M.K. Vandersypen et al., *Nature* 414, 883 (2001). C. A. Sackett et al., *Nature* 404, 256 (2000). V. Giovannetti et al., *Phys. Rev. A* 62, 32306 (2000).
- [3] D. V. Khveshchenko, *Phys. Rev. B* 70, 92407 (2004). Y. L. Lim et al., *Phys. Rev. A* 73, 12304 (2006).
- [4] *Quantum Computation Roadmap*, ARDA, <http://qist.lanl.gov> (2004).
- [5] A. Bertoni et al., *Phys. Rev. Lett.* 84, 5912 (2000). R. Ionicioiu et al., *Int. J. Mod. Phys. B* 15, 125 (2001) quant-ph/9907043.
- [6] A. Bertoni et al., *J. Mod. Optics* 49, 1219 (2002).
- [7] T. Zibold et al., *Proc. 14<sup>th</sup> HCIS Conference*, to appear (2006).
- [8] C.H.W. Barnes et al., *Phys. Rev. B* 62, 8410 (2000).
- [9] R. Rodriguez et al., *Phys. Rev. B* 72, 085329 (2005).
- [10] A. Bertoni and al., *Proc. 32nd ESSDERC Conf.* (2002).

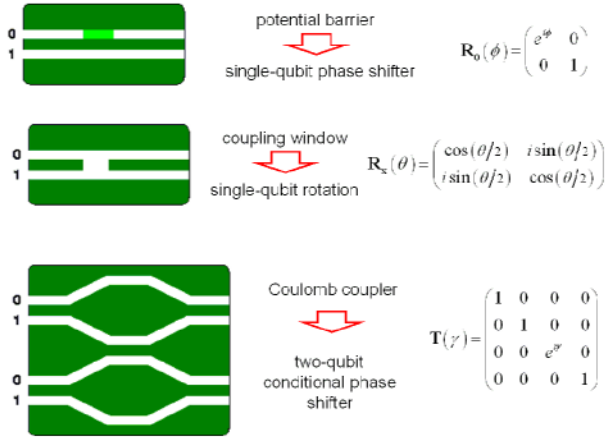


Fig. 1. Schematic representation of a universal set of quantum gates. [6]

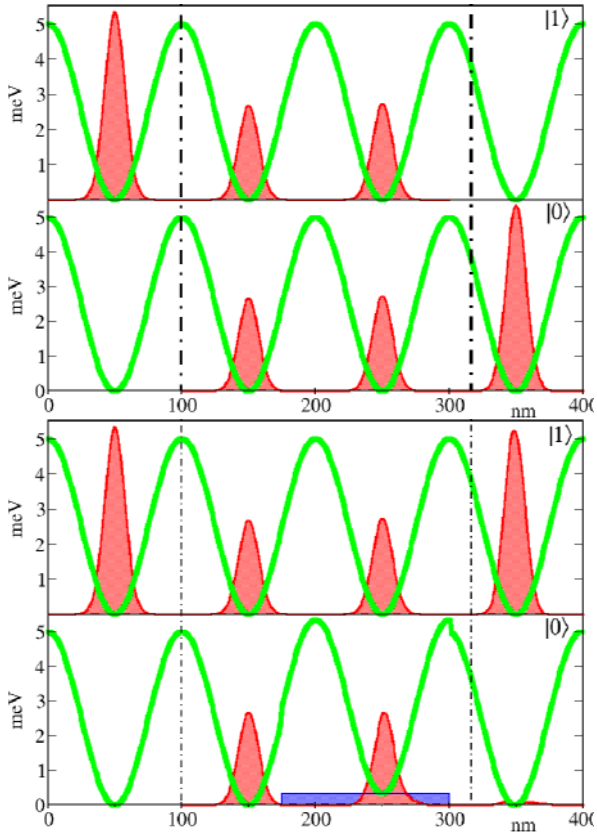


Fig. 2. One-dimensional time-dependent simulation of an electron wave function (red) trapped inside a minimum of a surface acoustic wave (green) propagating (from the left to the right) along a coupled-wire device with two single-qubit rotations  $R_x(\pi/2)$  (represented by dashed-dotted lines). In the lower graph a phase shifter (blue) is inserted in the wire 0 between the rotations, leading to a different final state of the qubit. [10]

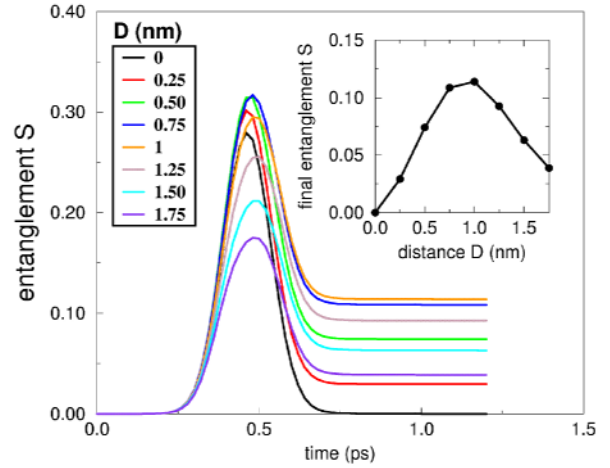


Fig. 3. Entanglement, as a function of time, of two electrons propagating in opposite directions along two parallel single-mode quantum wires.  $D$  represents the distance between the wires. The entanglement is computed from the von Neumann entropy  $S(\rho) = -Tr_1((Tr_2\rho)\log_2(Tr_2\rho))$ , where  $\rho$  is the two-particle density matrix and  $Tr_n$  is the trace operation on the position variable of particle  $n$ . The inset show that the dependence on  $D$  of the final value of  $S$  is non monotonic.

# Simulation of the entanglement creation for identical particles scattering in a 2D system

F. Buscemi \*, P. Bordone and A. Bertoni

CNR-INFM S3 Research Center, via Campi 213/A,I-41100 Modena, Italy and Dipartimento di Fisica, Università di Modena e Reggio Emilia, Modena, Italy

\* e-mail:buscemi.fabrizio@unimore.it

We study, by means of a time-dependent numerical analysis, the entanglement between an electron freely propagating in a 2D system and another electron bound to a specific site by a harmonic potential. This physical system can be used as guideline to analyze the entanglement formation in the case of a carrier-impurity scattering event in bulk semiconductors. The dynamics of the bound particle in the harmonic potential is coupled to the incoming particle through a screened Coulomb potential.

The above model has been already studied for a system of two distinguishable particles[2]. The aim of this work is to overcome this restriction taking into account the issues arising from the indistinguishability of the particles. Some theoretical questions about the notion and the evaluation of the entanglement between indistinguishable particles are addressed. In the present work we use a criterion, given by Schliemann, based on the Schmidt decomposition theorem for the state  $|\Psi_F\rangle$  of two fermionic particles [3], [4]. Through an unitary transformation the antisymmetric wavefunction is expressed into a basis of  $N$  Slater determinants with a minimum number of non vanishing coefficients  $z_i$ . This number, the Slater rank, gives the measure of the entanglement that can still be equivalently expressed as the von Neumann entropy of the one particle reduced density operator  $\rho^f$  as:

$$\varepsilon = -\text{Tr}[\rho^f \ln \rho^f] = \ln 2 - 2 \sum_{i=1}^N |z_i|^2 \ln 2|z_i|^2 \quad (1)$$

with

$$\rho_{\mu\nu}^f = \frac{\text{Tr}[\rho_F f_\nu^\dagger f_\mu]}{\text{Tr}[\rho_F \sum_\mu f_\mu^\dagger f_\mu]} \quad (2)$$

where  $\rho_F$  is two particles density matrix  $\rho_F = |\Psi_F\rangle\langle\Psi_F|$  and  $2N$  is the dimension of the single particle Hilbert space and corresponds, in the present case, to 2 times the number of discretization points in the space degree of freedom.

In our approach we solve numerically the time-dependent Schroedinger equation for the wavefunction of the system by means of a Crank-Nicholson finite difference scheme. From such wavefunction we calculate the one-particle reduced density matrix, related to each initial state, at different time steps. In order to calculate at any time, the entanglement by means of the von Neumann entropy from (1), we need to diagonalize the one-particle reduced density matrix  $\rho^f$ . This procedure turns out to be extremely demanding from the point of view of the numerical calculation. In fact these matrices are dense and typically of the order of  $10^{10}$  complex elements. Such a numerical problem has been faced by resorting to a parallel algorithms for matrices diagonalization. As a reference, a typical a simulation runs for 8 hours on 128 CPUs on a IBM-SP5 machine. As an example in Fig. 1 we show the evolution of the entanglement for the state with two electrons having same spin at three different values of the incoming electron initial energy, namely 10, 20, 30 meV, when the harmonic trap energy is  $\hbar\omega = 2meV$ . As the particles get closer their quantum correlation builds up and entanglement reaches a stationary value once scattering event is completed. From the square modulus of the two-particle space wavefunction before and after the scattering event (Fig. 2), we can evaluate the role played in entanglement creation by the correlations between the spatial degrees of freedom.

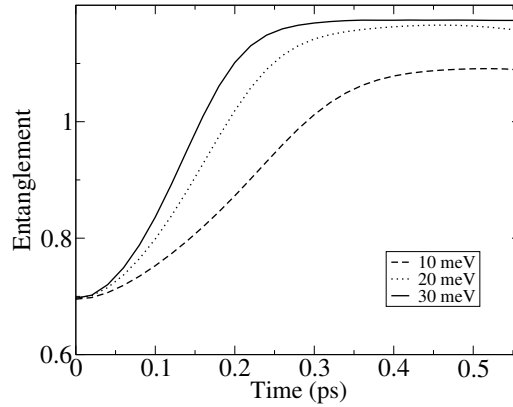


Fig. 1. The time evolution of entanglement for the state  $|\Psi_F\rangle$  at three different values of the incoming electron initial energy when the harmonic oscillator energy is  $\hbar\omega = 2meV$

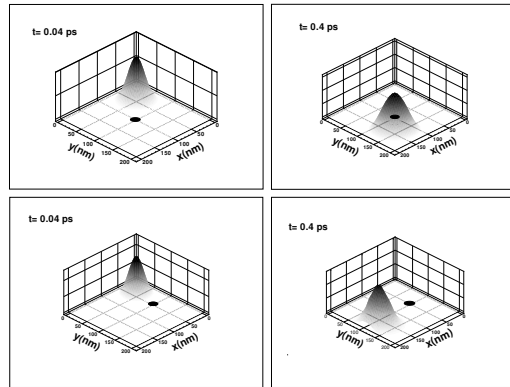


Fig. 2. Square modulus of the two-particle antisymmetrized wavefunction  $\psi(\mathbf{r})\phi(\mathbf{R}) - \phi(\mathbf{R})\psi(\mathbf{r})$  for  $|\Psi\rangle$  at two different times before ( $t = 0.04$  ps) and after ( $t = 0.4$  ps) scattering, calculated keeping fixed at a specific value  $\mathbf{R}$  (black spot) the position of one of the two particles. In the two upper graphs  $\mathbf{R}=(100$  nm, $100$  nm), while in the two lower graphs  $\mathbf{R}=(50$  nm, $150$  nm)

## REFERENCES

- [1] D.Giulini et al. *Decoherence and the Appearance of a Classical World in Quantum theory* (Springer, Berlin 1996)
- [2] P. Bordone and A. Bertoni *J.Comp.Elec.*, **3**: 407 2004; P. Bordone and A. Bertoni *Simulation of Entanglement Creation for Carrier-Impurity Scattering in a 2D*, (to be published on the Proceedings of 14-th International Conference on ‘ Non Equilibrium carrier dynamics semiconductors’ - HCIS 14 - Chicago, July 24-29, 2005)
- [3] J.Schliemann, J.I.Cirac, M. Kus, M.Lewenstein and D. Loss *Phys. Rev. A*, **64**:022303, 2001.
- [4] G. Ghirardi and L.Marinatto *Phys. Rev. A*, **70**:012109, 2004.

# Classical and Quantum Mechanical Transport Simulations in Open Quantum Dots

R. Brunner<sup>1</sup>, R. Meisels<sup>1</sup>, F. Kuchar<sup>1</sup>, J. P. Bird<sup>2</sup>, R. Akis<sup>3</sup>, D.K.Ferry<sup>3</sup>

<sup>1</sup>Institute of Physics, University of Leoben, Austria

<sup>2</sup>Dept. of Electrical Engineering, University at Buffalo, The State University of New York, USA

<sup>3</sup>Dept. of Electrical Engineering, Arizona State University, USA

email: Roland.Brunner@unileoben.ac.at

In order to apply quantum dots as electronic devices in the near future, a quantitative understanding of the details of electron transport in the dots is required. *Open* quantum dots [1], considered here, consist of small cavities connected to two-dimensional regions of electron gas (2DEG) by narrow constrictions which allow several modes to propagate. An interesting aspect of open quantum dots is the interplay of regular, quasi-regular and chaotic behavior of the electron transport, where one is concerned with the correspondence of classical and quantum mechanical behavior [2].

In this work we focus on the transport in open quantum-dot arrays regarding the correspondence of classical and quantum-mechanical treatments. We analyze, in particular, a prominent peak that was recently reported in the low-field magneto-resistance, MR, of a single dot and arrays with different numbers of dots [3,4]. Certain details of the behavior of this MR peak can be interpreted in the classical treatment only by additionally assuming phase-space tunneling. In the quantum-mechanical interpretation an important result is the opening of gaps in the (complex) band structure and the decay of the wave function along the dot array and its dependence on the energetic position in the gap.

The quantum-mechanical calculation is performed by discretizing the Schrödinger equation onto a finite-difference mesh and using it in its discrete form to set up a numerically stabilized variant of the transfer matrix [5,6] approach. By imposing an electron flux from the left, one obtains the transmission coefficient that enters the Landauer-Buttiker formula to give the conductance. For obtaining the band structure periodic boundary conditions are assumed at the ends of a single dot. The confinement is modeled by a smooth potential.

In the classical treatment this is approximated by a parabolic potential. It allows us solving the equation of motion analytically. Choosing certain initial conditions (position and velocity) the further path of the electron can be calculated in closed form; reflected (backscattered to the entrance constriction) and transmitted trajectories can be distinguished. The weighting of the direction of the initial velocity  $v_0$  is chosen to be Lambert like, i.e. it

depends as  $\cos \alpha$  on the entrance angle.

Electrons are counted as transmitted if they hit the part of the boundary corresponding to the exit constriction. They are counted as backscattered if they hit the entrance constriction.

Finally, the conductance is obtained as

$$G(B) = \langle G(B, \alpha) \cos \alpha \rangle_{\alpha} = \frac{\int_{-\pi/2}^{\pi/2} G(B, \alpha) \cos \alpha d\alpha}{\int_{-\pi/2}^{\pi/2} \cos \alpha d\alpha} \quad (1)$$

In order to visualize the electron dynamics in the phase space of the array we also compute Poincaré sections.

The Poincaré sections provide a useful numerical tool for testing the phase space for different magnetic fields. We get a mixed phase space for the open dot array. At the MR peak the phase space consists of periodic and chaotic orbits whereas by moving the magnetic field away from the peak position the phase space shows quasi-periodic and chaotic orbits. Quasi periodic and periodic orbits emerge due certain initial conditions within the dot and are classically inaccessible. In the literature these closed orbits are referred to as Kalmogorov-Arnol'd-Moser (KAM) islands [2].

The quantum-mechanically computed band structure shows, in contrast to the zero field case, band gaps at the MR peak. For an energy situated within the gap the probability density,  $|\psi(x,y)|^2$ , (Fig.1), shows a fast exponential decay which indicates tunneling through the array. The  $|\psi(x,y)|^2$  in the first dot corresponds in shape to the backscattered trajectory of the classical calculation. When positioning the considered energy near the bottom of the gap we reveal a probability density which is peaked in the 3<sup>rd</sup> dot (Fig.2). The decay of  $|\psi(x,y)|^2$  is now weaker than in Fig.1. Again the  $|\psi(x,y)|^2$  in the 3<sup>rd</sup> dot can be described by a combination of two classically calculated trajectory with starting angle  $\alpha_1=227^\circ$  (red) and  $\alpha_2=47^\circ$  (green). Identifying the orbits as closed we argue that the transmission through the array is based on tunneling between these closed orbits. In order to

describe the transmission through the dot the classically inaccessible regions existing in the mixed phase space have to be taken into account. This is only possible by assuming phase space tunneling introduced above.

#### REFERENCES

- [1] J.R. Barker and D.K.Ferry, *Solid-State Electron.* **23**, 531 (1980).
- [2] M. C. Gutzwiller, *Chaos in Classical and Quantum Mechanics*, Springer Verlag (1990).
- [3] M. Elhassan *et al.*, *Phys. Rev. B* **70**, 205341 (2004)
- [4] R. Brunner *et al.*, *Physica E* **21**, 491 (2004)
- [5] T. Usuki, M. Saito, M. Takatsu, R. A. Kiehl, and N. Yokoyama, *Phys. Rev. B* **52**, 8244 (1995).
- [6] R. Akis, J. P. Bird, D. Vasileska, D. K. Ferry, A. P. S. de Moura, and Y.-C. Lai, in *Electron Transport in Quantum Dots* (Kluwer, Boston, 2003), chapter 6.

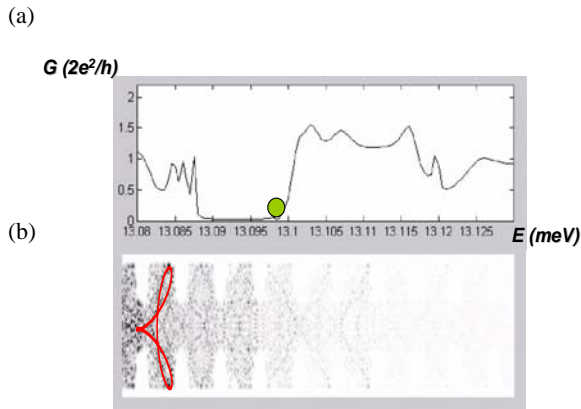


**Fig. 1.** (a) The calculated conductance as a function of energy at the magnetic field position of the MR peak. The Green point indicates the energy position for the calculated  $|\psi(x,y)|^2$ . (b)  $|\psi(x,y)|^2$  looks like an *open, backscattered* trajectory of the classical calculation (superimposed in red in the 1st dot).

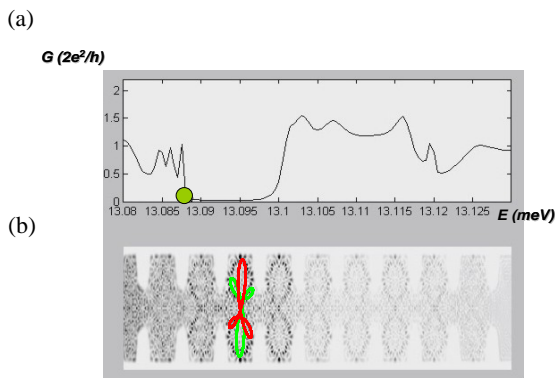


**Fig. 2** (a) The calculated conductance as a function of energy at the magnetic field position above the MR peak. The green point indicates the energy position for the calculated  $|\psi(x,y)|^2$ . (b) The  $|\psi(x,y)|^2$  in the 3<sup>rd</sup> resembles two *closed* trajectories (red and green) that are classically inaccessible from the outside, indicating that conductance is only possible by assuming phase space tunnelling.

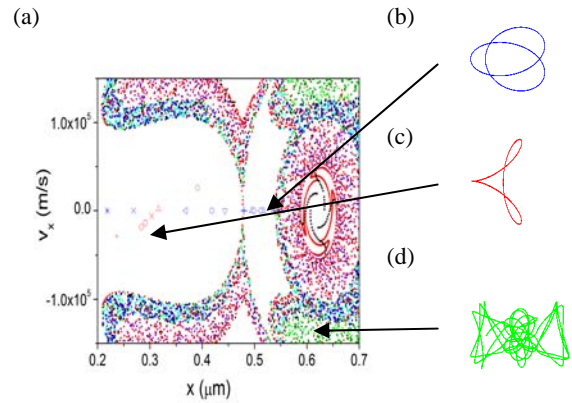


**Fig. 3.** (a) Poincaré section at the MR peak. (b) A periodic orbit (blue open symbols), (c) backscattered trajectory (red open symbols) (d) chaotic trajectory (green points). The arrows mark points representing  $v_x$  and  $x$  at  $y=0$  on the trajectories shown.

# Simulation of Quantum-Ballistic Nanoswitches

A. Heigl and G. Wachutka

Institute for Physics of Electrotechnology, TU Munich, Arcisstraße 21, 80333 Munich, Germany  
 e-mail: heigl@tep.ei.tum.de

## INTRODUCTION

We study quantum-ballistic transport processes in nanoswitches realized by the use of modulation doped heterostructures such as GaAs/AlGaAs layers. These structures have been modelled on the basis of a direct Schrödinger-Poisson approach taking into account also their non-linear behavior.

## MODELLING

The electric current through a two-port structure is represented as quantum-ballistic current density

$$J = 2 \sum_{t \in T} \int j_{\varepsilon,t}(r) (f(\varepsilon, \mu_1) - f(\varepsilon, \mu_2)) d\varepsilon \quad (1)$$

This formula is actually the non-linear version of the well-known Landauer-Büttiker formula. Here, it is assumed that the ports are connected - via ideal electron waveguides - with charge reservoirs which are kept in thermodynamic equilibrium. This means that  $f(\varepsilon, \mu)$  can be modelled as Fermi-Dirac distribution with  $\mu$  as the electrochemical potential of the respective contact (Fig. 1).

The wavefunctions in the active area of the device are determined as solutions of the Schrödinger equation in effective-mass formulation

$$\left[ -\frac{\hbar^2}{2} \nabla \frac{1}{m^*} \nabla + V_h - e\varphi + V_{xc}[n] - \varepsilon \right] \psi_{j,\varepsilon} = 0 \quad (2)$$

with the electrostatic potential  $\varphi$ , the exchange-correlation potential  $V_{xc}$  and the step potential of the heterostructure  $V_h$ . At the contacts, scattering boundary conditions are assumed. This yields an energy-dependent transmission probability for the scattering states. The resulting wavefunctions are self-consistently coupled to the Poisson equation by the temperature-dependent electron density

$$\rho(r) = \int \sum_j g(\varepsilon) f_j(\varepsilon) |\psi_{j,\varepsilon}(r)|^2 d\varepsilon \quad (3)$$

The electrostatic potential is calculated using the Green's function method. Practically this approach

is equivalent to adding the convolution  $G \star \rho$  to the electronic potential without the electrostatic Coulomb potential according to

$$V(r) = V_h(r) + V_{xc}[n](r) - eG(r) \star \rho(r) \quad (4)$$

The assumption that the top surface is metallized leads to the following Green's function:

$$G(r) = \frac{1}{4\pi\varepsilon} \left( \frac{1}{|r|} - \frac{1}{|r-d|} \right) \quad (5)$$

Another modification of the electronic potential originates from the gate-voltages. These will change the number of occupied states of the 2D electron gas at the heterojunction.

## RESULTS

The simulations were performed using the 3D simulator SIMNAD [1] and a new non-linear version of the simulator HIGHBIAS [2]. As a first test problem we considered a quantum-wire fabricated and characterized at the University of Würzburg [3]. This structure is built from 40 nm deep and 80 nm wide trenches forming a 100 nm quantum-wire. At a depth of 40 nm underneath the surface a 2D electron gas is easily recognized (Figs. 2, 3).

The influence of the gate voltage is demonstrated by the output characteristics displayed in Fig. 5. We obtain a fairly good agreement between simulation and measurement (Fig. 6) proving the quality of our approach.

## ACKNOWLEDGMENT

This project is funded by the Bavarian Science Foundation within the research consortium for nanoelectronics FORNEL.

## REFERENCES

- [1] F.O. Heinz, *Simulation approaches for nanoscale semiconductor devices*, Dissertation, ETH Zürich (2004).
- [2] E. Forsberg and J.O.J. Weström, *Self-consistent simulations of mesoscopic devices operating under a finite bias*, Sol. State Electronics **48**, 1147 (2004).
- [3] L. Worschech and D. Hartmann, *Private communication*.

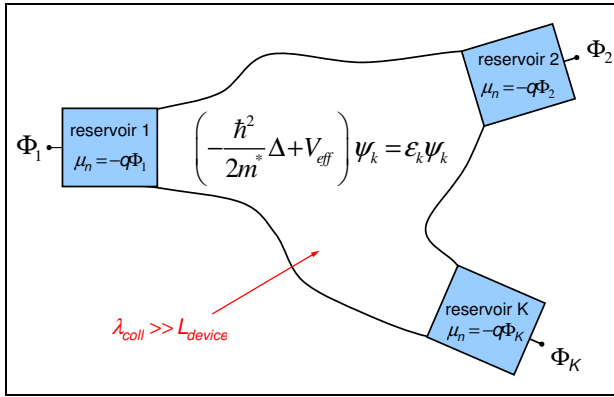


Fig. 1. Basic scheme of simulation domain and boundary conditions (within the active region of the device there are no inelastic scattering processes; only potential-scattering at  $V_{eff}$ )

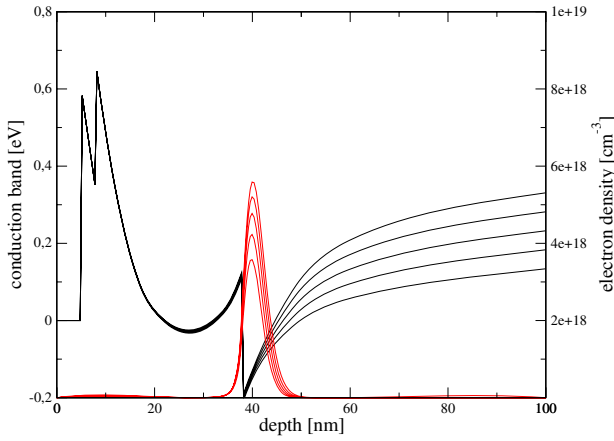


Fig. 2. Conduction band energy and electron density along a vertical cut at different gate voltages (see cut-line in Fig.4)

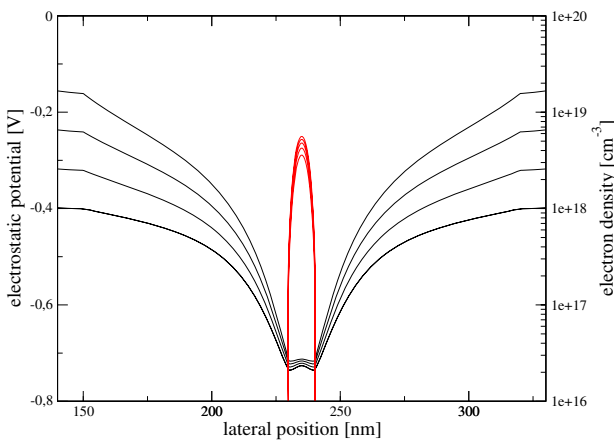


Fig. 3. Electron density and electrostatic potential along a lateral cut at different gate voltages (see cut-line in Fig.4)

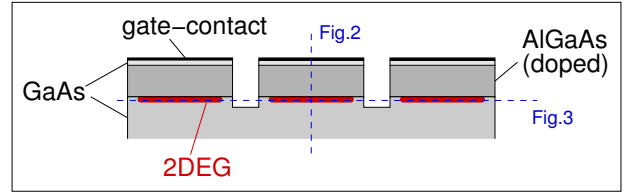


Fig. 4. Schematic view of the trench-controlled 2D quantum-wire structure (lateral cross section)

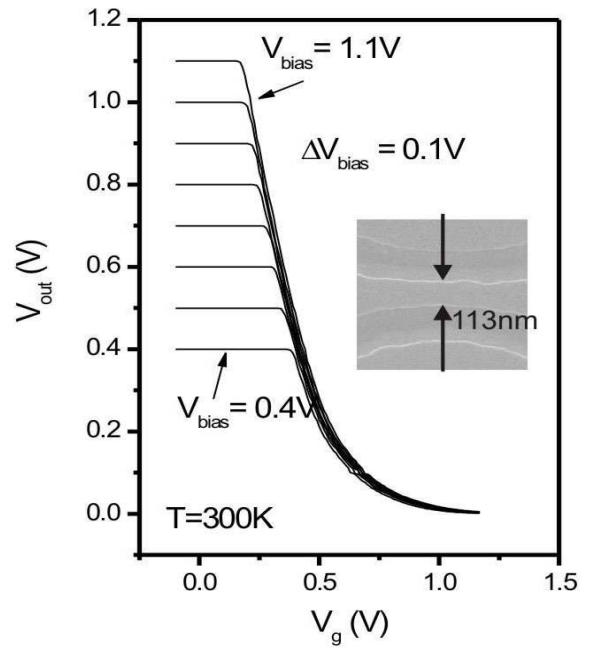


Fig. 5. Measured output characteristics of a quantum-wire structure (obtained from the University of Würzburg) [3]

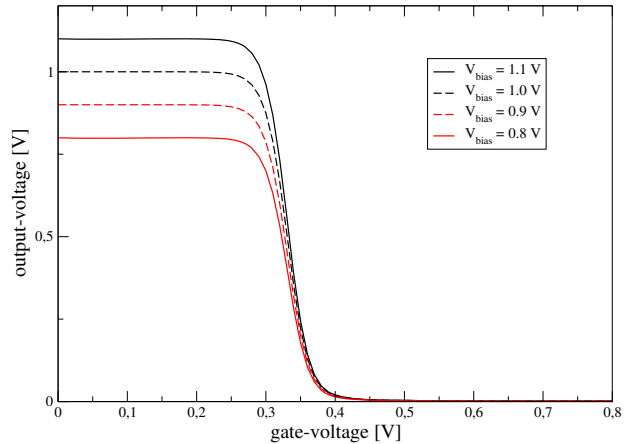


Fig. 6. Simulated output characteristics of a quantum-wire as calculated by SIMNAD

# The Rashba Effect and Non-Abelian Phase in Quantum Wire Devices

A. Cummings, R. Akis, and D. K. Ferry

Center for Solid State Electronics Research and Department of Electrical Engineering  
Arizona State University, Tempe, AZ 85287-5706 USA  
e-mail: aron.cummings@asu.edu

The study of the phase acquired by propagation in a mesoscopic device can be important for determining the presence/absence of phase interference in re-entrant geometries. While the study of the Aharonov-Bohm phase, due to a magnetic flux, has been studied for some time, it only recently has been realized that an additional geometric (topological) phase can be introduced through the presence of the Rashba spin-orbit interaction in a heterostructure [1,2]. In the presence of both fields, a more complicated behavior can be present [3]. It is still somewhat controversial as to whether the spin dynamics follows the orbital motion adiabatically or even whether the geometrical phase can be detected in interference experiments. Nevertheless, the phase shifts introduced by the spin-orbit interactions produce non-Abelian phases in the network, and the general use of non-Abelian statistics has become of interest for quantum computation [4,5].

In this paper, we report the results of simulations of quantum wire networks present at the interface of a GaAs/AlGaAs heterostructure. The spin-orbit interaction appears through the interfacial electric field (normal to the interface) and is assumed to be modulated through the use of surface gates. This leads to an additional term in the Hamiltonian. We solve the transport problem through the use of a recursive scattering matrix formulation for the total wave function [6]. The quantum wire network is assumed to be defined by a set of surface gates, as shown in Fig. 1. Illustration of the spin precession in a straight quantum wire is shown in Fig. 2. The  $z$ -field couples via the  $y$ -component of momentum to the  $s_x$  spin matrix, giving spin precession around the  $s_x$  axis. This rotation of the spin vector around the Bloch sphere is illustrated in Fig. 3 for this configuration. Here, an applied electric field has

been used to introduce the spin-orbit phase shifts necessary for the spin precession.

We consider a ring of radius 100 nm, with wires that have width of 100 nm, as shown in Fig. 1. The magneto-conductance of this ring is shown in Fig. 4, with no Rashba term present. Here, we see normal Aharonov-Bohm interference for transport around the ring. The Rashba term is characterized by the factor  $\alpha \cong ehE_z/4\pi m^*$  (in appropriate units). In Fig. 5, we plot the variation of the conductance through the ring as the electric field is varied, with no magnetic field. Now, we see resonances in the transmission due to the geometrical phase introduced by the Rashba effect. In Fig. 6, we plot how the magneto-conductance changes for a Rashba field giving  $\alpha = 6.25 \mu\text{eV}\cdot\mu\text{m}$ . The conductance is now more complicated due to the contributions from both phase factors. The two sharp drops in conductance near  $|B| = 0.3 \text{ T}$  are due to localization resonances where the ring connects to the wires.

## REFERENCES

- [1] Y. Aharonov and A. Casher, *Topological quantum effects for neutral particles*, Phys. Rev. Lett. **53**, 319 (1984).
- [2] D. Bercioux, M. Governale, V. Cataudella, and V. M. Ragaglia, *Rashba effect in quantum networks*, Phys. Rev. B **72**, 075305 (2005).
- [3] R. Capozza, D. Giuliano, P. Lucignano, and A. Tagliacozzo, *Quantum interference of electrons in a ring: Tuning of the geometrical phase*, Phys. Rev. Lett. **95**, 226803 (2005).
- [4] M. H. Freedman, M. Larsen, and Z. Wang, *A Modular Functor Which is Universal for Quantum Computation*, Commun. Math. Phys. **227**, 605 (2002).
- [5] S. Das Sarma, M. Freedman, and C. Nayak, *Topologically protected qubits from a possible non-Abelian fractional Quantum Hall state*, Phys. Rev. Lett. **94**, 166802 (2005).
- [6] R. Akis, D. K. Ferry, and J. P. Bird, *Magnetotransport fluctuations in regular semiconductor ballistic quantum dots*, Phys. Rev. B **54**, 17705 (1996).

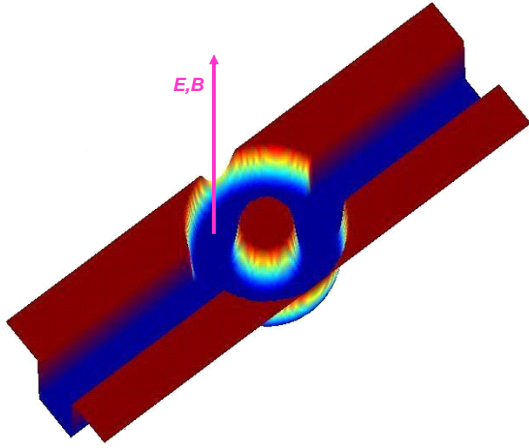


Fig. 1. Structure of the quantum wire network, which is assumed to exist at the interface of a GaAs/AlGaAs heterostructures. The ring radius and wire width are both 100 nm.

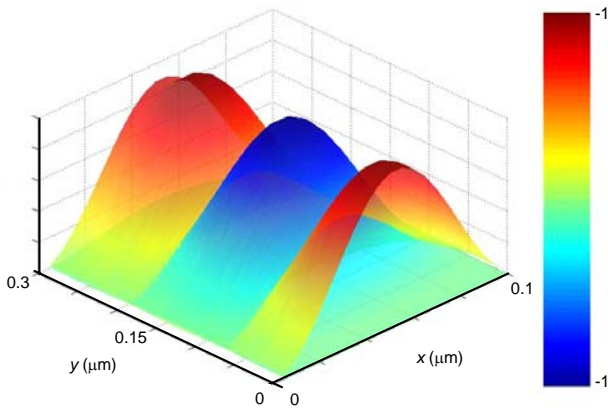


Fig. 2. Propagation in a single quantum wire. The color coding gives the spin orientation, which is in the z-direction.

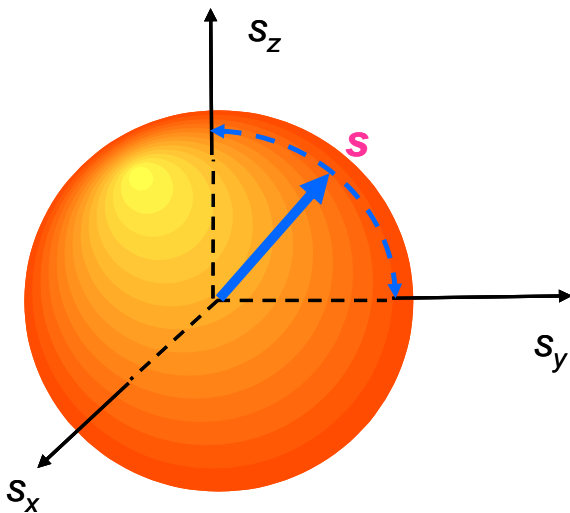


Fig. 3. Rotation of the spin vector around the Bloch sphere for the case shown in Fig. 2.

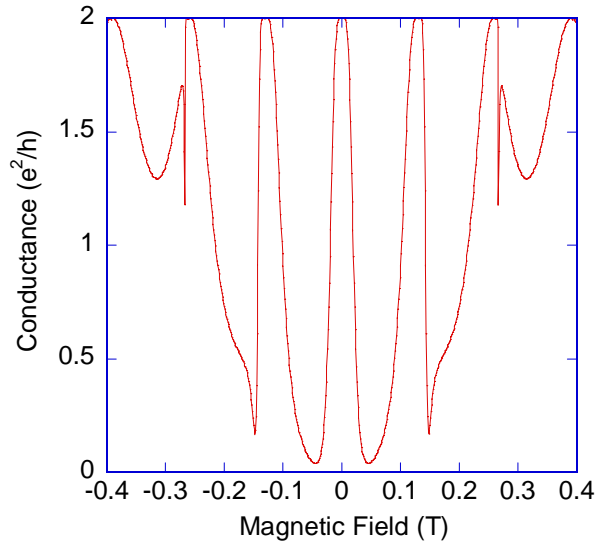


Fig. 4. Ring conductance as a function of the magnetic field, with no Rashba electric field applied.

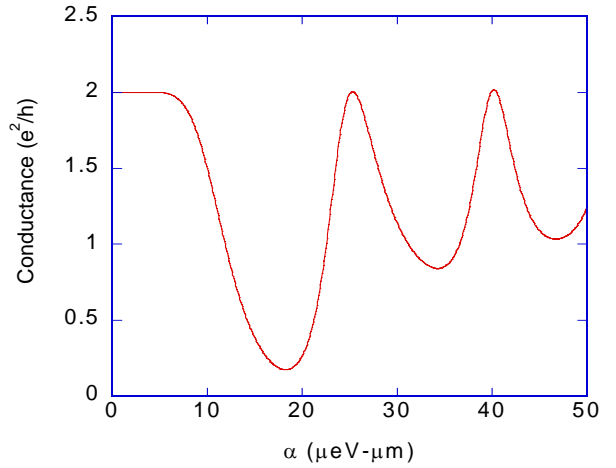


Fig. 5. Ring conductance as a function of the Rashba coupling term, with no magnetic field.

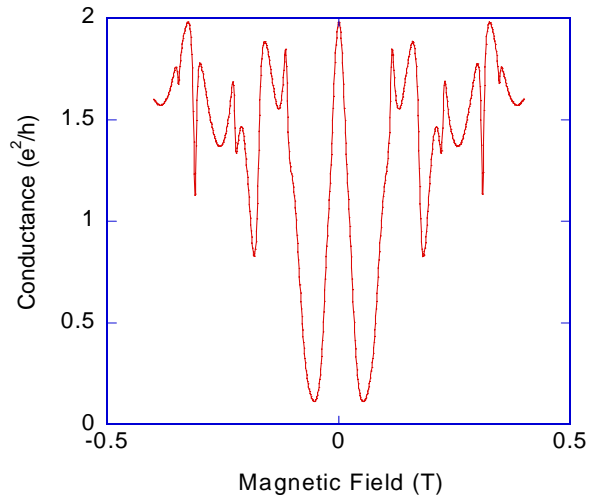


Fig. 6. Ring conductance as a function of magnetic field for the Rashba coupling term equal to 6.25  $\mu\text{eV}\cdot\mu\text{m}$ .

# Circuit Modeling of Flux Qubits Interacting with Superconducting Waveguides

G. Csaba, Z. Fahem, F. Peretti, and P. Lugli

*Institute for Nanoelectronics, Technical University of Munich, Arcisstrasse 21, D-80333 Munich, Germany*  
csaba@ei.tum.de

## MOTIVATION

Superconducting quantum circuits emerged as a promising candidate for quantum computer ‘hardware’, mainly because their quantum behavior can be engineered by the appropriate choice of their circuit parameters. In the implementation outlined in [1], the interrogation of the qubit is obtained via coupling to a one-dimensional cavity. Since such electromagnetic environment has a decisive role in the quantum dynamics of the qubit, it is crucial to simulate a qubit together with the write-in and read-out circuitry. This is a complex task, which requires different levels of modeling: quantum-mechanical simulations for the qubit itself, classical and quantum electrodynamics for the cavity around the qubit and extensive microwave simulations of the read-out apparatus.

## DESCRIPTION OF WORK

Equivalent circuit construction is a promising approach to simulate different physical phenomena in a unified environment. As earlier work [2][3] has demonstrated, simple few state quantum systems can be numerically simulated in a standard circuit simulator such as SPICE, using an equivalent circuit shown in Fig 1. A ‘modes-to-nodes’ conversion is used to construct equivalent lumped circuits of microwave components and state of the art electromagnetic simulators (such as the HFSS code by Ansoft [4]) perform this conversion automatically. To understand the electromagnetic behavior of superconducting components, we employ the Comsol Multiphysics software suite [5] which allows us to couple Maxwell’s equations to London’s equations that describe superconducting materials. Lumped superconducting circuits (with Josephson junctions) could also be simulated by their equivalent circuits (see Fig. 2).

Once all circuit models are built and verified separately, they are interconnected in SPICE, which simulates the mixed quantum-classical dynamics of the entire measurement apparatus. The results are directly comparable with experiments.

## RESULTS

We concentrate on the structure proposed by [6], and sketched in Fig 3. We investigate the dynamic behavior of this circuit, optimize its circuit parameters and geometry and investigate how the noise of the electromagnetic environment influences decoherence of the qubit. Detailed results will be presented at the conference.

Modeling of the interaction between quantum systems and their (classical) electromagnetic environment is a fundamental point of nanoelectronics and quantum technology – we hope this work brings us closer to the understanding of such structures.

## ACKNOWLEDGEMENTS

This work is done in close collaboration with the Nanotechnology group of the Walther Meissner Institute for Low Temperature Physics (Bavarian Academy of Sciences and Technical University of Munich). We are grateful to Prof. R. Gross, Dr. A. Marx and M. Mariani for the stimulating discussions and initiating the project. The concept of circuit modeling in nanoelectronics was pioneered by Prof. A. Csurgay and Prof. Wolfgang Porod of the University of Notre Dame, USA. This work was made possible by financial support from DFG SFB 631 ‘Solid-state quantum information processing’.

## REFERENCES

- [1] A. Blais, R. S. Huang, A. Wallraff, S. M. Girvin, and R. J. Schoelkopf: Cavity quantum electrodynamics for superconducting electrical circuits: An architecture for quantum computation Phys. Rev A 69 062320, 2004
- [2] Á. Csurgay, W. Porod: Equivalent circuit representation of arrays composed of Coulomb-coupled nanoscale devices: modelling, simulation and realizability nt. J. Circ. Theor. Appl. 29, Issue 1, 2001, 3-35
- [3] G. Csaba, A. Csurgay, W. Porod: Computing architecture composed of next-neighbor coupled, optically pumped nanodevices, Int. J. Circ. Theor. Appl., 2001 29 73
- [4] <http://www.ansoft.com/products/hf/hfss/>
- [5] <http://www.comsol.com/>
- [6] M. Mariani, M. J. Storcz, F. K. Wilhelm, W. D. Oliver, A. Emmert, A. Marx, R. Gross, H. Christ, E. Solano: Generation of Microwave Single Photons and Homodyne Tomography on a Chip. cond-mat/0509737

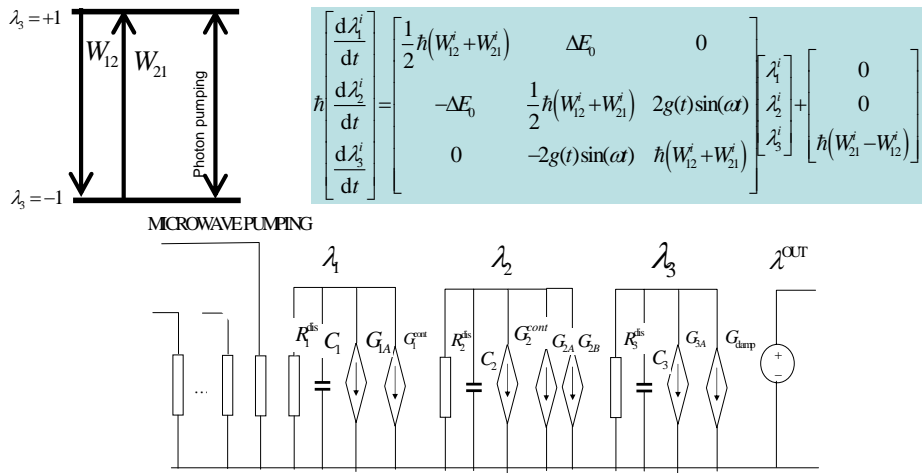


Figure 1. The Bloch equations (a dynamical model of a two-state quantum system, sketched in part a)) can be modeled by the equivalent circuit shown above. The voltages of the capacitors exhibit the same dynamic behavior as the components of the coherence vector for the two-state quantum system. This makes it possible to simulate quantum mechanics in circuit simulators.

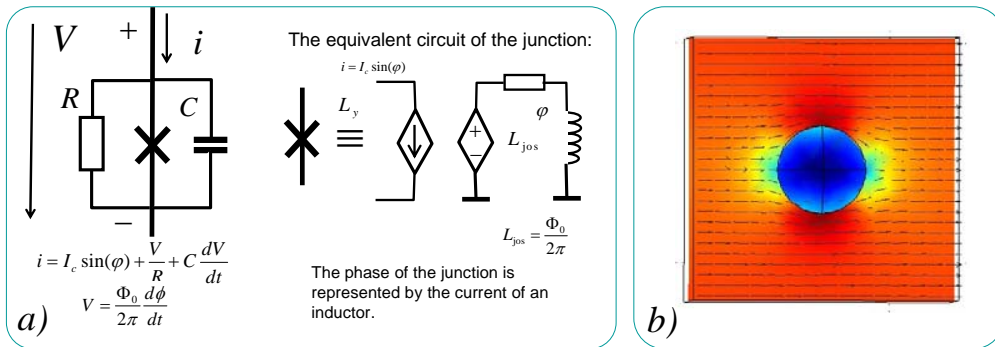


Figure 2. Non-linear classical circuits, built from Josephson junctions are modeled by the equivalent circuit shown in part a). Part b) illustrates the textbook example of magnetic field distribution around a superconducting sphere. This figure was made by Comsol Multiphysics, in which we implemented the models of superconducting electrodynamics.

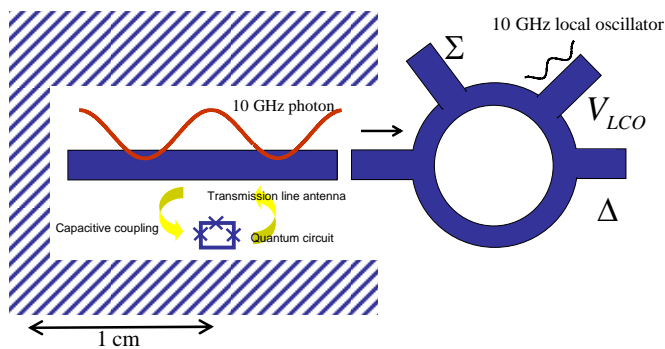


Figure 3. Sketch of the experimental setup of a qubit interacting with a microwave read-out circuitry [6]. The quantum circuit is coupled to a transmission line resonator, which is capacitively connected to a microwave hybrid. We will demonstrate our simulation approach on this circuit.

# Carbon Nanotube Electronics and Optoelectronics

Phaedon Avouris,

*IBM Research Division, T.J. Watson Research Center, Yorktown Heights, NY 10598, USA*

Carbon nanotubes (CNTs) have properties that strongly recommend them for applications in both nano- and opto-electronics. [1] Although a variety of different electronic devices based on CNTs have been demonstrated, most of the emphasis has been placed on CNT field-effect transistors (CNTFETs). These devices have in many respects characteristics superior to conventional devices. However, they also pose a set of new challenges. These include understanding the new 1D transport physics, the increased electrical noise [2], the Schottky barriers at CNT-metal contacts [3], their ambipolar character [4], the new scaling laws [5], and finding technical solutions [6] to these problems. Both single nanotube devices and multi-component single nanotube circuits [7] will be discussed. Our initial efforts to self-assemble CNTFET devices will also be discussed [8]. We are also evaluating CNTFETs as electro-optical devices. We have used ambipolar (a-) CNTFETs to simultaneously inject electrons and holes from the opposite terminal of the FET. A fraction of these recombines radiatively to produce an electrically-excited, single nanotube molecule light source [9]. Unlike conventional p-n diodes, a-CNTFETs are not doped and there is no fixed p-n interface. Thus, the emitting region can be translated at will along a CNT channel by varying the FET gate voltage [10]. We have found that much stronger localized electroluminescence can be generated at defects or inhomogeneities that introduce potential drops [11]. The emission is the result of intra-molecular impact excitation of electron-hole pairs by the hot carriers. Localized electroluminescence provides a high brightness IR source and a novel probe of defects, charging, and inhomogeneities which are otherwise difficult to observe. The reverse process

of recombination, i.e. the photogeneration of carriers in a single nanotube CNTFET channel [12], will also be discussed.

## REFERENCES

- [1] For reviews see: Ph. Avouris, MRS Bulletin 29, 403 (2004); Proc. IEEE 91, 1772 (2003); P.L. McEuen, et al., IEEE Trans. Nanotechnol. 1, 78 (2002).
- [2] P. G. Collins, et al. Appl. Phys. Lett. 76, 894 (2000); Y.-M. Lin et al. Nano Lett., to be published.
- [3] Z. Chen et al., Nano Lett. 5, 1497 (2005); S. Heinze, et al., Phys. Rev. Lett. 89, 106801 (2002); J. Appenzeller, et al., Phys. Rev. Lett. 89, 126801 (2002); S. Wind et al. Appl. Phys. Lett. 80, 3817 (2002); M. Radosavljevic, et al., Appl. Phys. Lett. 83, 2435 (2003); J. Appenzeller, et al., Phys. Rev. Lett. 92, 048301 (2003); Y.-M. Lin et al. A. Javey et al. Nano Lett. 4, 1319 (2004).
- [4] R. Martel, et al., Phys. Rev. Lett. 87, 256805 (2001); Y.-M. Lin et al. Nano Letters 4, 947 (2004); M. Radosavljevic, S. Heinze, J. Tersoff and Ph. Avouris, Appl. Phys. Lett. 83, 2435 (2003).
- [5] S. Heinze, M. Radosavljevic, J. Tersoff, Ph. Avouris, Phys. Rev. B 68, 235418 (2003); S. Wind, J. Appenzeller, Ph. Avouris, Phys. Rev. Lett. 91, 058301 (2003); M. Radosavljevic, S. Heinze, J. Tersoff and Ph. Avouris, Appl. Phys. Lett. 83, 2435 (2003).
- [6] Y.-M. Lin et al. IEEE Trans. Nanotech. 4, 481 (2005); J. Chen et al. Appl. Phys. Lett. 86, 123108 (2005).
- [7] Z. Chen et al., Science, submitted (2005).
- [8] J.B. Hannon, A. Afzali, C. Klinke and Ph. Avouris, Langmuir 21, 8569 (2005); C. Klinke et al., Nano Lett., submitted (2005).
- [9] J. A. Misewich, et al., Science 300, 783 (2003); M. Freitag et al. Nano Lett. 4, 1063 (2004)
- [10] M. Freitag, et al., Phys. Rev. Lett. 93, 076807 (2004); J. Tersoff et al. Appl. Phys. Lett. 86, 263108 (2005).
- [11] J. Chen et al. Science 310, 1171 (2005); M. Freitag et al., to be published.
- [12] M. Freitag et al. Nano Lett. 3, 1067 (2003); X. Qiu et al. Nano Lett. 5, 749 (2005).



# Single-Mode Performance Analysis for VCSELs

Stefan Odermatt\*, Bernd Witzigmann\*, and Sven Eitel†

\*Integrated Systems Laboratory, ETH Zurich, CH-8092 Zürich, Switzerland; Email: bernd@iis.ee.ethz.ch

† Avalon Photonics Ltd., CH-8048 Zürich, Switzerland

## INTRODUCTION

In this work, the simulation of the single-mode stability in vertical-cavity surface-emitting lasers (VCSELs) is presented using a microscopic electro-opto-thermal model [1]. Experimental data for oxide-confined VCSELs emitting at 850 nm with different contact metal designs are also available. It is shown that detailed models for the optical losses in the cavity consisting of out-coupling and absorption are required in order to explain the experiments. The role of cavity losses in the nonlinear electro-opto-thermal simulation framework will be discussed in a quantitative manner.

The fundamentals of the electro-opto-thermal simulation models are described in [1], [2] and only a summary and update with respect to new models is given. The optical modes of a VCSEL are modeled by solving Maxwell's vectorial wave equation using a finite element method and absorbing boundary conditions. Cavity losses consist of optical out-coupling, scattering, metallic absorption, and free-carrier absorption. The electro-thermal description comprises a Poisson equation, a drift-diffusion model for carrier transport and a continuity equation for the heat flux. Gain is modelled by the microscopic polarization based on Heisenberg's equation of motion in the second Born approximation [3]. The quantum well bandstructure is calculated by an 8-band k-p method. In general, the simulator can be used to calculate the stationary, transient, small-signal, large-signal and noise characteristics of VCSEL devices in a 2-D and 3-D [4] setup.

## RESULTS

Besides reliability properties, the maximum single-mode power is one of the most important performance criteria in industrial VCSEL design. A straight forward approach is the use of a narrow ( $<3\mu\text{m}$ ) oxide aperture diameter in order to feed the

carriers to the center of the  $HE_{11}$  mode, however this results in a higher differential resistance and tends to degrade the reliability. Other approaches introduce mode selective losses, either by surface reliefs or by narrowing the aperture of the contact metallization.

Here, the impact of the contact metallization aperture on the single-mode behavior of an 850 nm AlGaAs/GaAs VCSEL is analyzed. The basics of a similar structure are discussed in [2]. Figs. 1(a) and 1(b) show the first two optical modes of a design with a top metal radius  $R_m < 3.5 \mu\text{m}$ . The losses are obtained by the dissipation rates of the optical field vectors. Simulation shows that the losses increase with decreasing metal radius. Concurrently, the net out-coupling losses also decrease, which results in a reduced slope efficiency. On the other hand, the threshold for the onset of the higher order mode is decreased with larger metal radius. Therefore, a trade-off between partition of the contact metallization and the current confinement to the active region has to be found for high single-mode power. Fig. 2 shows the power-current characteristics from simulation and measurement, which are in excellent agreement. A detailed interpretation will be given in the presentation.

In conclusion, this contribution aims to simulate 850 nm oxide-confined VCSELs with the aid of microscopic simulation. In particular, the single-mode behaviour is determined by a complicated interplay of electrical (current confinement), thermal (self-heating) and optical (losses) processes.

## REFERENCES

- [1] Synopsys Inc., Mountain View, USA, *Synopsys Sentaurus Device User Manual*, 1995-2005.
- [2] M. Streiff *et al.* *IEEE JSTQE*, Vol. 9, pp. 879-891, 2003.
- [3] B. Witzigmann *et al.*, *Journal of Comp. Elect.*, Vol. 4, pp. 7-10, 2005.
- [4] B. Witzigmann *et al.*, *Proc. of NUSOD*, pp. 23-24, 2005.

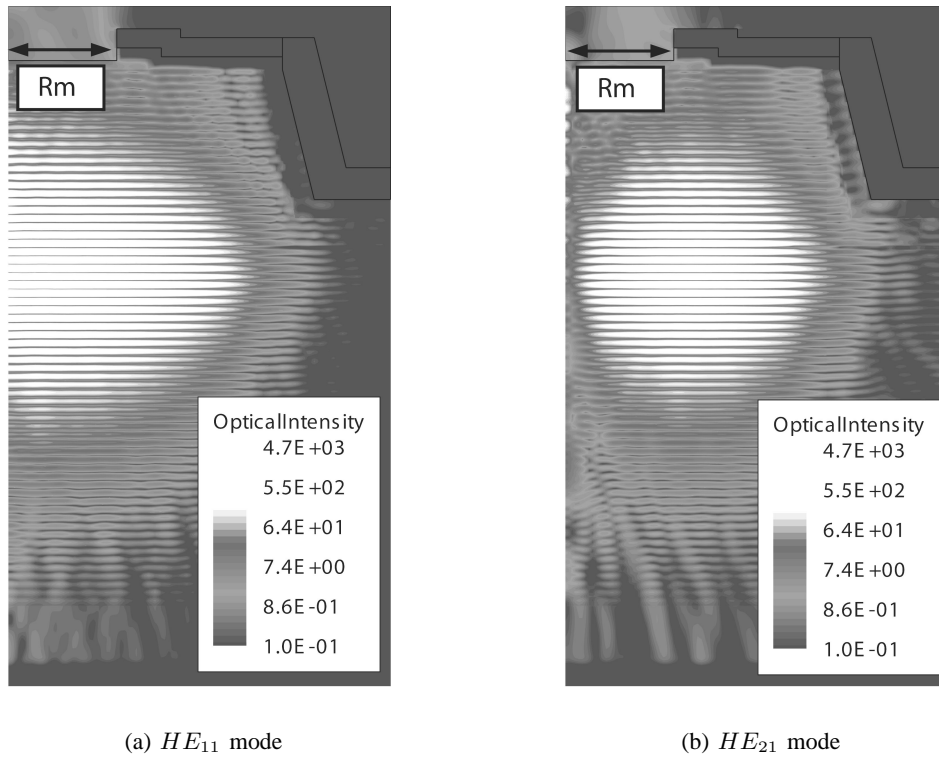


Fig. 1. Normalized optical intensity for a VCSEL with metal aperture radius  $R_m < 3.5 \mu\text{m}$ . Due to absorption in the metal, the total losses for the  $HE_{21}$  mode are significantly higher than for the fundamental  $HE_{11}$  mode. This results in an improved single-mode behaviour.

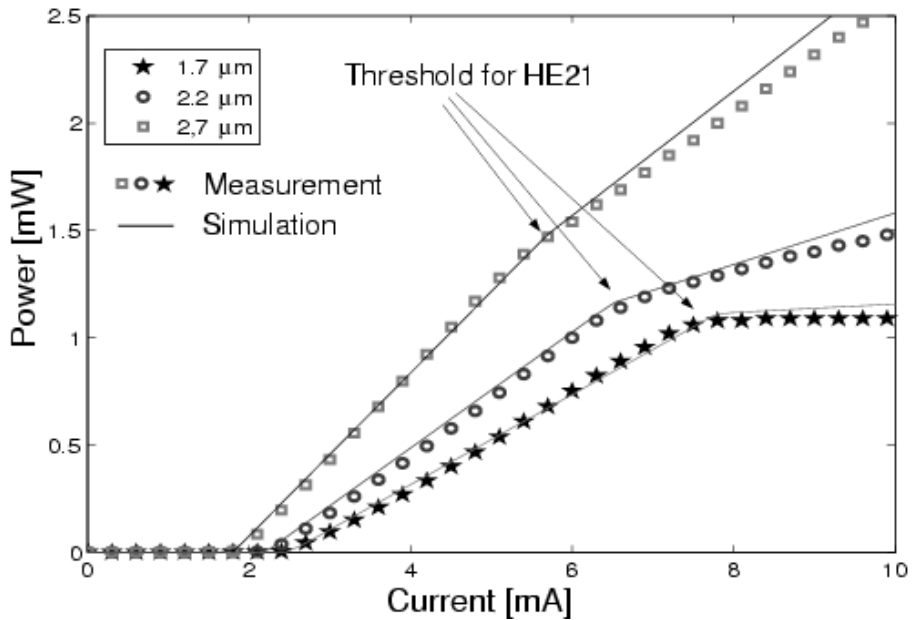


Fig. 2. Simulated (solid lines) and measured power-current characteristics of VCSEL designs with different metal aperture radii at  $T = 303 \text{ K}$ . With decreasing metal aperture, the threshold currents for the fundamental and higher order modes increase due the higher absorption in the metal. Concurrently, the slope efficiency decreases since the power generated in the device is absorbed in the metal, too.

# MC Simulation of THz Quantum Cascade Lasers

C. Jirauschek, M. Manenti<sup>\*</sup>, G. Scarpa, and P. Lugli

Institute for Nanoelectronics, TU München, Arcisstraße 21, 80333 München, Germany

<sup>\*</sup>Dept. Electronic Engineering, Università Roma "Tor Vergata", Italy

e-mail: jirauschek@mytum.de

## INTRODUCTION

In the following, we show simulation results for two types of THz quantum cascade lasers (QCLs), GaAs-based QCLs and Si/SiGe QCLs, which have enormous potential as compact and efficient THz sources.

Our simulator includes the following feature: Solution of the coupled Schrödinger-Poisson equation to determine the band diagram and the subband energies and wavefunctions; simulation of electron dynamics including all essential scattering mechanisms (electron-electron, electron-LO phonon, electron-acoustic phonon); coupling of the Schrödinger-Poisson solver to the MC simulation; calculation of gain spectra; determination of the subband electronic temperature.

## GAAS/ALGAAS THZ QCL

We report on Monte Carlo (MC) simulations aimed at the design and optimization of GaAs-based THz quantum cascade lasers operating between 2 and 4 THz, and at the modeling of their operation. We have focused our analysis on a series of QCL structures operating in the range of 3.2 – 3.8 THz reported in Refs. [1]-[3]. The results have been positively compared with experimental results [4]. Positive gain has been demonstrated in the simulation, and indeed lasing has been achieved on these reported fabricated structures. The electron temperatures agree well with the experimental ones [4].

The MC simulation allows the identification of the processes responsible for the non ideal laser performance (high threshold currents and low operation temperatures). Figure 1 shows the band diagram and subband wavefunctions for the laser structure operating at 3.2 THz, the calculated gain spectrum at two different temperatures is shown in Figure 2.

## SI/SIGE THZ QCL

THz QCLs based on Si/SiGe have the potential to operate at room temperature due to the absence of polar phonon scattering. However, no lasing in such structures has been observed up to date. Simulations are necessary to identify the reasons and help develop a working design. In order to simulate the hole-based Si/SiGe QCLs, we have modified the MC program described above to account for both light and heavy hole bands and for the proper phonon scattering active in silicon-based materials. We still use an envelope function description of the subbands, fitting the effective mass to those obtained from a k.p calculation. Improvements of the method will be presented at the conference. We have simulated a QCL structure which is also based on the phonon depopulation principle of the GaAs laser discussed above. Figure 3 shows the band diagram and subband wavefunctions of a Si/SiGe QCL, and Figure 4 displays the corresponding hole distribution functions for a lattice temperature of 150 K. The corresponding effective temperatures range from 185 K to 220 K.

## CONCLUSION

In conclusion, we have shown that the Monte Carlo simulation allows an effective design of QCLs for THz applications. Improvement of the model to include a k.p description of the hole subbands for the p-type structures will be presented at the conference.

## REFERENCES

- [1] B. S. Williams, S. Kumar, H. Callebaut, Q. Hu and J.L.Reno, *Terahertz quantum-cascade laser operating up to 137 K*, Appl. Phys. Lett. **83**, 5142 (2003).
- [2] B. S. Williams, S. Kumar, H. Callebaut, Q. Hu and J.L.Reno, *3.4-THz quantum cascade laser based on longitudinal-optical-phonon scattering for depopulation*, Appl. Phys. Lett. **82**, 1015 (2003).
- [3] S. Kumar, B. S. Williams, S. Kohen, Q. Hu and J. L.Reno, *Continuous-wave operation of terahertz quantum-cascade*

lasers above liquid-nitrogen temperature, Appl. Phys. Lett. **84**, 2494 (2004).

- [4] M. S. Vitiello, G. Scamarcio, V. Spagnolo, B. S. Williams, S. Kumar, Q. Hu and J. L. Reno, *Measurement of subband electronic temperatures and population inversion in THz quantum-cascade lasers*, Appl. Phys. Lett. **86**, 111115 (2005).

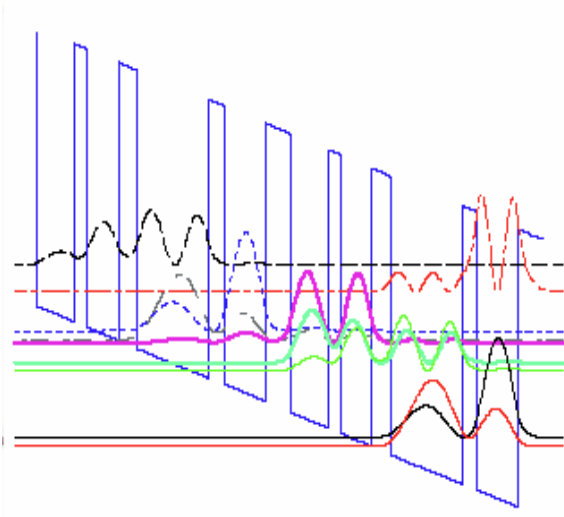


Fig. 1: Band diagram and subband wavefunctions of GaAs-based QCL.

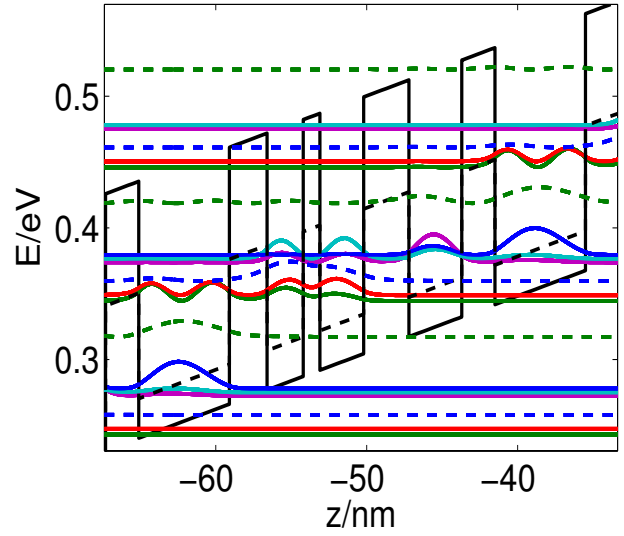


Fig. 3: Band diagram and subband wavefunctions of Si/SiGe QCL for light hole (dashed lines) and heavy holes (solid lines) band.

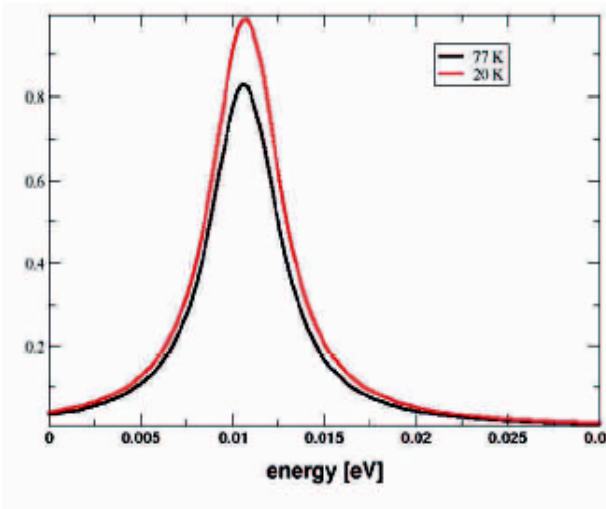


Fig. 2: Calculated gain spectrum for a lattice temperature of 20 K (red) and 77 K (black).

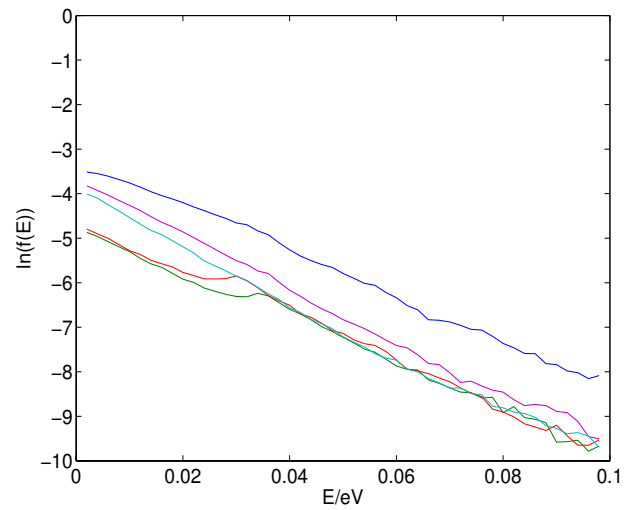


Fig. 4: Heavy hole distribution functions for a lattice temperature of 150 K for the levels shown in Fig. 4 (same color coding).

# The Driven Two–Level System as an Inverse Problem

M. Wenin, and W. Pötz\*

\*Institut für Physik, Fachbereich Theorie, Karl-Franzens-Universität Graz, Universitätsplatz 5, 8010 Graz, Austria  
 e-mail: markus.wenin@uni-graz.at

We use direct approximate inversion of the time evolution of a dissipative two–level system to identify optimal control fields. The equations of motion are formulated within the density matrix formalism, assuming weak coupling to a phonon bath. We show that the problem can be solved exactly for the isolated driven two–level system. The solution is not unique. This strategy serves to identify approximate solutions for the coupled case which may subsequently be optimized by conventional techniques.

## INTRODUCTION

In semiconductor physics recent research has concentrated on nanostructures like quantum dots (QD) or quantum wells. Electrons confined in such QD can be manipulated by external fields, as provided by lasers, but they also interact with their environment, in particular with phonons, leading to dissipation. This interaction is one of the crucial problems which prevent complete controllability of electronic quantum states and their temporal evolution in QD's [1].

In this paper we present an (approximate) solution to the inverse problem of finding an optimum control field to coherently steer a dissipative quantum system.

## THE ISOLATED TWO–LEVEL SYSTEM

As a starting point for our investigations we consider an isolated 2-level quantum system, described by the von Neumann equation  $i\hbar\dot{\rho}(t) = [H(t), \rho(t)]$ . We assume a given  $\rho(t)$  and  $\dot{\rho}(t)$  and seek a time dependent Hamiltonian  $H(t)$ , that produce this  $\rho(t)$ . Setting

$$\rho(t) = \begin{pmatrix} \rho_{11}(t) & a(t) + ib(t) \\ a(t) - ib(t) & 1 - \rho_{11}(t) \end{pmatrix}, \quad (1)$$

and using  $\frac{d}{dt}Tr\{\rho(t)^2\} = 0$ , the Hamiltonian achieving this quantum evolution is

$$H(t) = \begin{pmatrix} \hbar \frac{\dot{a}(t)}{b(t)} & -\hbar \frac{\dot{\rho}_{11}(t)}{2b(t)} \\ -\hbar \frac{\dot{\rho}_{11}(t)}{2b(t)} & 0 \end{pmatrix}. \quad (2)$$

Here  $b(t) = \sqrt{\rho_{11}(t) - \rho_{11}(t)^2 - a(t)^2 - C}$ , where  $0 \leq C \leq 1/4$  is a constant. In particular,  $C = 0$  corresponds to pure states.  $a(t)$  and  $b(t)$  are real. Clearly the solution is not unique, as follows immediately from inspection of the homogeneous equation  $[H(t), \rho(t)] = 0$ , which gives  $H = F(\rho)$ , for arbitrary function  $F$ . We note that to completely control an isolated 2-level system two independent fields are needed.

## DISSIPATIVE TWO–LEVEL SYSTEM

In this case where the situation is more complicated, we derive a non–Markovian density matrix equation. Our calculations are based on a perturbation theory in the electron–phonon–interaction up to second order [2]. We take the continuum limit for the phonon modes to obtain a realistic dissipative model. The density matrix equation has the structure

$$i\hbar\dot{\rho}(t) = [H(t), \rho(t)] + \int_0^t K(\rho(t'), U(t'), t') dt', \quad (3)$$

where the evolution operator  $U(t)$  is obeys

$$i\hbar\dot{U}(t) = -H(t)U(t). \quad (4)$$

The dissipation part (the integral term in (3)) not only depends on the phonon spectral density and the temperature of the phonon bath [3], but also on the time dependent system Hamiltonian  $H(t)$  containing the electric field in a dipole– interaction (DI).

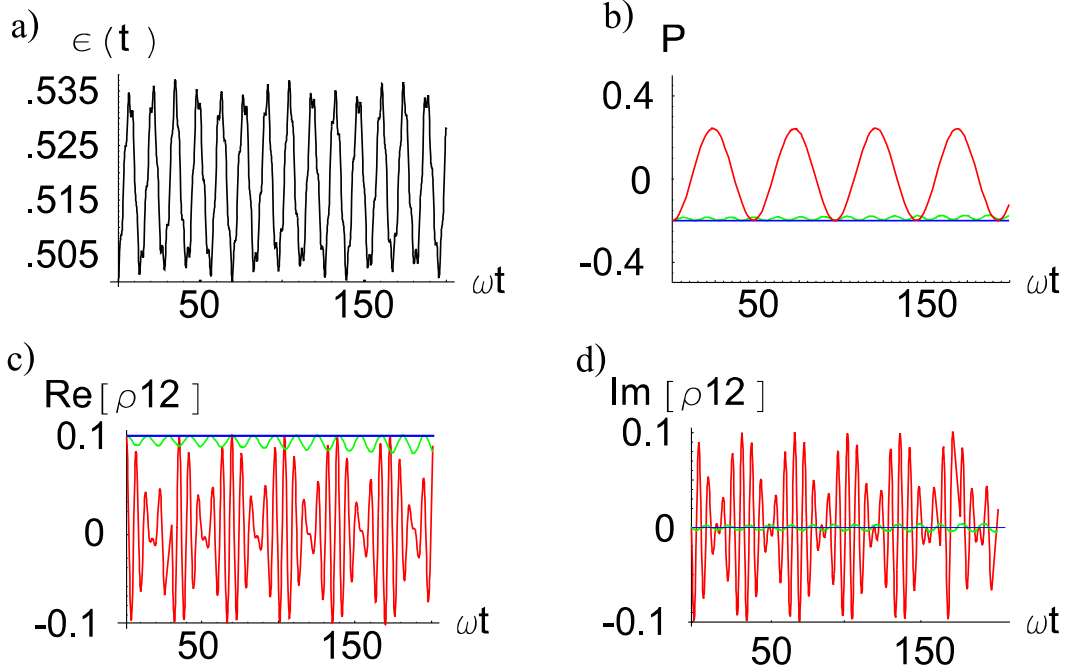


Fig. 1. Numerical results for state trapping for a simple phonon system, which contains only one resonant frequency  $\omega$ . a) The optimal field founded by inversion of the density matrix equation, b) shows  $P = \langle \sigma_z \rangle = \rho_{11} - \rho_{22}$  versus time, c) and d) the real- and imaginary part of the off-diagonal element of the system density operator. The red lines show the free evolution, the evolution with field is shown by the green lines, the target (trap) state is indicated by the blue lines. The occupation number of the phonons is  $n = 10$ , and the electron-phonon coupling strength is  $M/\hbar\omega = 1/50$ .

Since the inversion is performed analytically, we can identify more stable regions and less stable regions in the Hilbert space or, in this case equivalently, the Bloch sphere. For example, for an electron-phonon coupling which is proportional to  $\sigma_x$ , we find an optimal solution for a DI to trap the state in  $\sigma_x$  direction. This is done by an "inversion" of the density matrix equations. We set

$$H(t) = H_0 + \epsilon(t)\sigma_x, \quad (5)$$

where  $H_0$  is the (diagonalised) system Hamiltonian,  $\epsilon(t)$  is the control field, and "solve" (3) with

$$\epsilon(s) = -\frac{1}{4}Tr(\{C^{-1}, R\}). \quad (6)$$

Here  $C$  denotes the matrix  $[\sigma_x, \rho]$ , which we will assume as invertible.  $R$  contains all the remaining terms contained in (3).  $\{.,.\}$  denotes the anti-commutator. This expression is put into (4), which we solve numerically.

A simple example is shown in Fig. 1 where we seek to trap the two-level system coupled resonantly to a single phonon mode in an excited state. It

is seen that the control field can largely suppress the oscillation in the density matrix elements and stabilize them in the vicinity of the constant target state.

Further optimization of the control field obtained by direct inversion is performed by standard techniques, such as a conjugate gradient method (see [4]) and/or a genetic algorithm.

#### ACKNOWLEDGMENT

We wish to acknowledge financial support of this work by FWF, project number P16317-N08.

#### REFERENCES

- [1] L. Jacak, J. Krasnyj, W. Jacak, R. Gonczarek, and P. Machnikowski, Phys. Rev. B, Vol. **72**, 245309 (2005).
- [2] F. Rossi, T. Kuhn, Rev. of Mod. Phys., Vol. **74**, July 2002.
- [3] T. Dittrich, P. Hänggi, G.-L. Ingold, B. Kramer, G. Schn, W. Zwerger, *Quantum Transport and Dissipation*, Wiley-VCH, 1997.
- [4] H. Jirari, W. Pötz, Phys. Rev. A, Vol. **72**, 013409 (2005).

# DEPFET sensors, a test case to study 3d effects

K. Gärtner

Weierstrass Institute for Applied Analysis and Stochastics, Mohrenstr. 39, 10117 Berlin, Germany

e-mail: gaertner@wias-berlin.de

DEPFET sensors (comp. [1]) are a well suited example to study algorithms for solving the 3d drift-diffusion equations and to improve the understanding of critical design issues.

Properties of the classical drift-diffusion equations

$$-\nabla \cdot \epsilon \nabla \psi = f - n + p, \quad (1)$$

$$\frac{\partial n}{\partial t} + \nabla \cdot \mu_n n \nabla \phi_n = R, \quad (2)$$

$$\frac{\partial p}{\partial t} - \nabla \cdot \mu_p p \nabla \phi_p = R, \quad (3)$$

discretized on boundary conforming Delaunay simplex grids are discussed. The discretization allows the introduction of 'test functions', related adjoint equations for functionals describing quantities of interest, for instance the contact currents. With some assumptions one can get properties like weak discrete maximum principle for the quasi Fermi potentials and the dissipativity of the discrete equations (see [2]). Using the related discrete adjoint solutions for computing contact currents ( $J = J(\psi, n, p)$ ), with  $\psi = \psi^* + \delta\psi$ ,  $n = n^* + \delta n$ ,  $p = p^* + \delta p$ ,  $u_i^*$ ,  $\delta u_i$  denote the solution components, sufficiently small errors fulfilling homogeneous boundary conditions, respectively) yields  $J(\psi, n, p) = J(\psi^*, n^*, p^*) + O(\delta^2 u_i)$  due to the orthogonality properties of the test functions. The analog of partial integration avoids the use of second differences and replaces these expressions by products of first differences. This reduces rounding, hence it is of interest in case of small other errors. The technique adds almost no effort and should be applied. It is of special value in the study of small effects, differences, and large problems, where minimal numerical noise is crucial (typical relative current balance errors are  $10^{-12}$  or better).

In the DEPFET case one follows typically 1600 electrons generated by some X-ray of specific energy in the depleted sensor bulk. One is interested in a sensor design with low power, large amplification, low noise (goal: max. 2 electrons are lost from the cloud for different starting positions), reasonable readout frequency, and stable operation over years in a astro-physics satellite.

A DEPFET (see Figure 5) collects the generated electrons in an internal gate. The internal potential distribution resulting from applied potentials and the dopant distribution has to guarantee: electrons starting from any point below the upper  $2\mu m$  of the device arrive in the internal gate. After a collection time the MOSFET (SOURCE, GATE, DRAIN) above the internal gate is used to compare the present current with the reference current defined by an empty internal gate (computation of a current difference). After this 'read out' process the internal gate is cleared by moving the electrons to the CLEAR contact applying a voltage pulse at CLEAR.

The time scales are given by: a) the creation of the electron-hole cloud (maximum generation rate at  $25ps$  in the computations), b) the drift time from bottom to top (roughly  $1ns$ ), c) the drift and diffusion time below the surface (it is strongly influenced by small electric fields, compare Figure 3) and d) the time defined by thermal recombination processes for adding the typical noise level of 2 electrons in the internal gate. Depending on the carrier life times a steady state after the clear process is reached after 1 to  $100s$ . Hence computing the influence of the electron cloud (with the MOSFET in the on state to check the time evolution of the SOURCE-current), starts at  $1fs$  and ends at around  $100\mu s$  (the typical measurement time), if the time for reaching the steady state is not checked (Figure 6).

The simulations added more and more features of the device, the grids grew from 120 000 to 150 000 nodes. A 4 CPU SMP allowed the evaluation of a new design within 4 days.

The author has to thank R. Richter (HLL of the MPI in Munich) for the fruitful collaboration regarding this problem of next generation X-ray astronomy sensors.

## REFERENCES

- [1] J. Kemmer, G. Lutz, *New detector concepts*, Nucl. Instr. and Meth. A **253**, 356 (1987).
- [2] H. Gajewski, K. Gärtner, *On the discretization of van Roosbroeck's equations with magnetic field*, ZAMM **76**, 247 (1996).

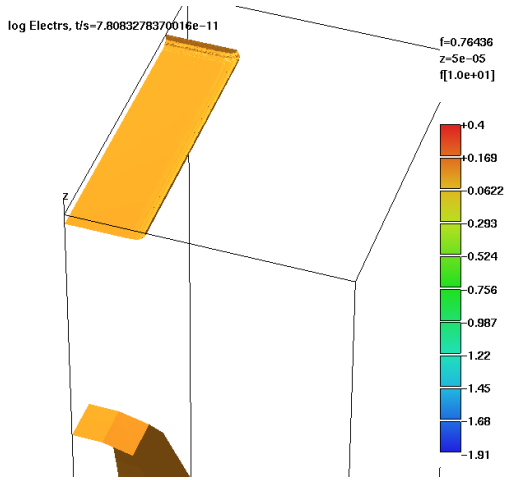


Fig. 1. Electrons start at the lower south west (SW) corner (shown is the position of the  $n = 7.6n_i$  iso-surface), time  $78ps$

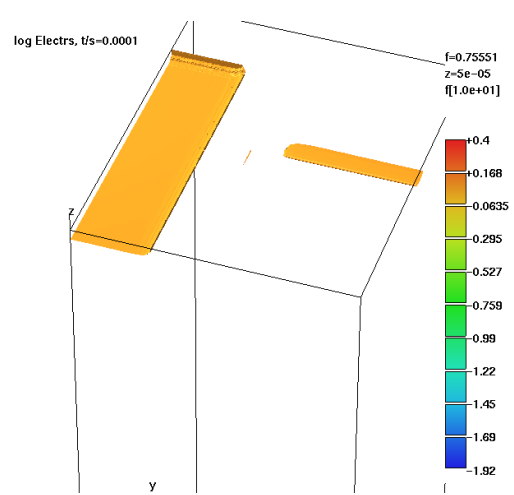


Fig. 4. Finally most electrons arrived in the internal gate ( $100\mu s$ )

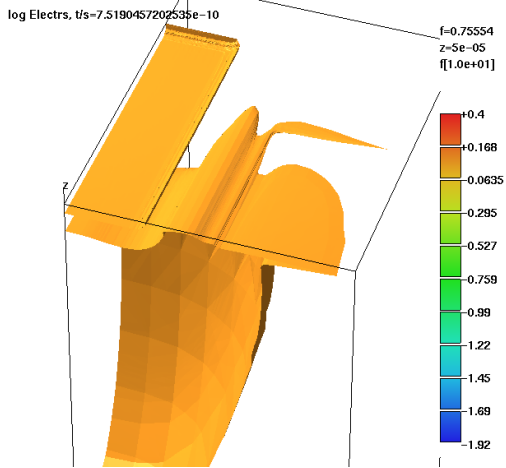


Fig. 2. The first electrons reached the top layer ( $0.75ns$ )

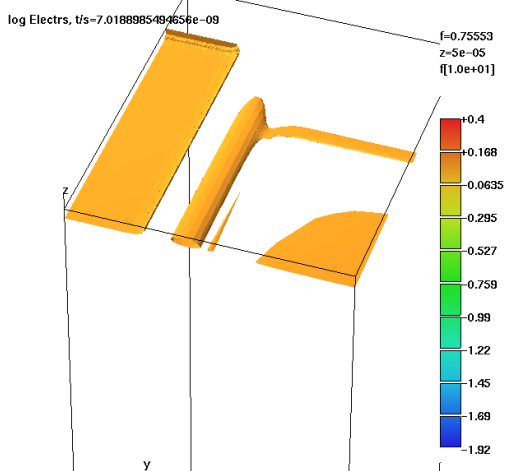


Fig. 3. Slow horizontal movement follows ( $7ns$ )

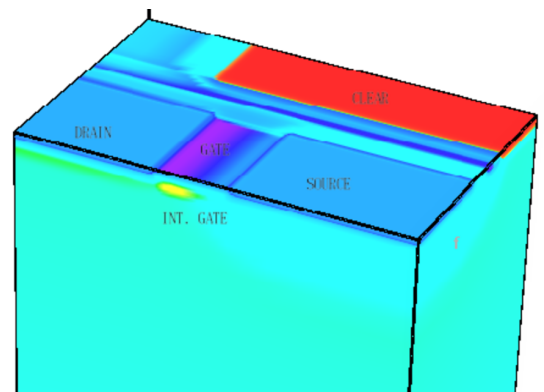


Fig. 5. Essential contacts on top of a  $50 \times 22 \times 18\mu m^3$  sensor, the internal gate stores electrons (yellow spot)

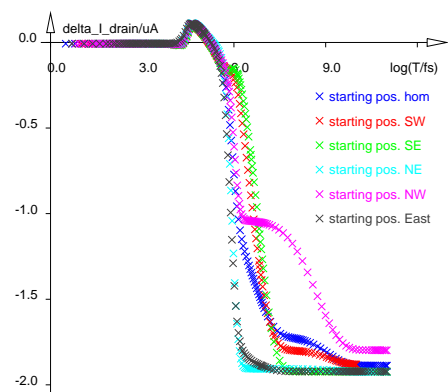


Fig. 6. Typical computed time dependent drain current differences (the reference current is  $241.4\mu A$ )

# Shot Noise in Transport Through Quantum Dots: Clean versus Disordered Samples

F. Aigner, S. Rotter, and J. Burgdörfer

Institute for Theoretical Physics, Vienna University of Technology,  
Wiedner Hauptstrasse 8-10, A-1040 Vienna, Austria, EU  
e-mail: aigner@concord.itp.tuwien.ac.at

The noise induced by the discreteness of the electron charge (“shot noise”) has become one of the central issues in the field of mesoscopic transport [1]. The correlations of electrons in quantum transport experiments lead to a suppression of shot noise,  $S$ , relative to the Poissonian value of uncorrelated electrons,  $S_P$ . This suppression is customarily expressed in terms of the Fano factor,  $F = S/S_P < 1$ .

For phase-coherent quantum transport through fully chaotic or stochastic cavities, random matrix theory predicts a universal value for the Fano factor,  $F = 1/4$ . However, in the quantum-to-classical crossover of high Fermi energies ( $E_F \rightarrow \infty$ ) or short dwell times in the cavity ( $\tau_D \rightarrow 0$ ) the Fano factor is reduced to the classical value of fully deterministic transport,  $F = 0$ .

Motivated by recent experiments [2], we numerically investigate shot noise in cavities with tunable openings that allow to vary the dwell time  $\tau_D$  [3]. Employing the modular recursive Green’s functions method [4], we reach the regime of short electron wavelengths where many open lead modes contribute to transport. We include a random bulk disorder potential inside the cavity. Varying the strength of this disorder potential we investigate the regular-to-disordered crossover of shot noise explicitly. We find the Fano factor to be very close to the RMT-result ( $F = 1/4$ ), even in regular systems without disorder, for which RMT is not expected to hold (for an independent verification of this assessment see [5]). We argue that in the case of regular dynamics in the cavity, diffraction at the lead openings is the dominant source of shot noise. To quantify this conjecture, we develop a quasi-classical transport model for shot noise suppression which agrees with the numerical data. Furthermore

our model accurately predicts the amount of shot noise suppression for stadium-shaped, rectangular, and circular billiards which are prototypical for chaotic and regular classical motion, respectively. These examples demonstrate that the chaotic-to-regular crossover in  $F$  can be correctly described, provided that diffractive scattering in the cavity is properly accounted for.

We also investigate the presence of the previously predicted “noiseless scattering states” [6] and their influence on the transport characteristics [7]. Our numerical data indeed display clear signatures of these classical (i.e. fully deterministic) states which contribute to transmission but not to the noise. We confirm previous studies [8] predicting a strong suppression of such noiseless states due to stochastic scattering resulting from a bulk disorder.

## ACKNOWLEDGMENTS

We thank E. Sukhorukov for helpful discussions. Support by the Austrian Science Foundation (Grants No. FWF-SFB016 and No. FWF-P17359) is gratefully acknowledged.

## REFERENCES

- [1] Ya. M. Blanter and M. Büttiker, *Phys. Rep.* **336**, 1 (2000).
- [2] S. Oberholzer, E. V. Sukhorukov and Ch. Schönberger, *Nature* **415**, 765 (2002).
- [3] F. Aigner, S. Rotter, and J. Burgdörfer, *Phys. Rev. Lett.* **94**, 216801 (2005).
- [4] S. Rotter et. al., *Phys. Rev. B* **62**, 1950 (2000).
- [5] P. Marconcini, M. Macucci, G. Iannaccone, B. Pellegrini, G. Marola, cond-mat/0411691 (2004).
- [6] P. G. Silvestrov, M. C. Goorden, and C. W. J. Beenakker, *Phys. Rev. B* **67**, 241301(R) (2003).
- [7] Ph. Jacquod and E. V. Sukhorukov, *Phys. Rev. Lett.* **92**, 116801 (2004).
- [8] E. V. Sukhorukov and O. M. Bulashenko, *Phys. Rev. Lett.* **94**, 116803 (2005).

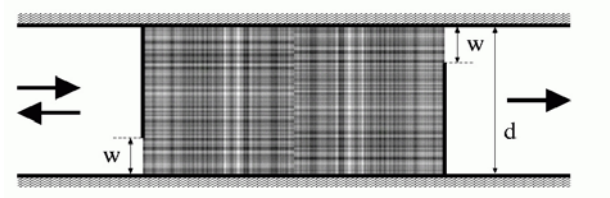


Fig. 1. Rectangular quantum billiard with shutters and disorder potential (gray shaded area). Tuning the opening of the shutters and the strength of the disorder potential the onset of the crossover from quantum-to-classical and disorder-to-regular scattering can be investigated.

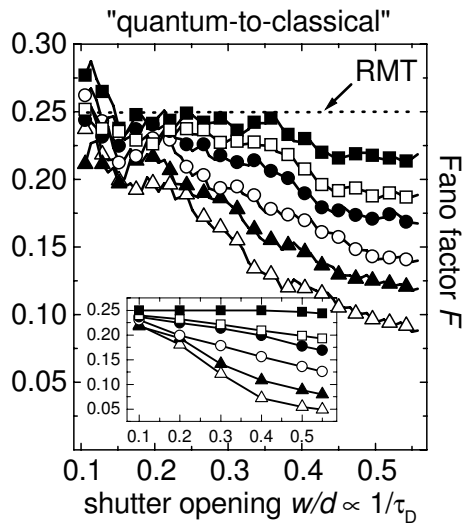


Fig. 2. Fano factor  $F$  as a function of the shutter opening ratio  $w/d$ . Curves for different disorder amplitudes:  $V_0/E_F = 0.1$  (■),  $0.07$  (□),  $0.05$  (●),  $0.03$  (○),  $0.015$  (▲),  $0$  (△). Inset: The fit parameter free prediction (quasi-classical model) with diffractive corrections.

# Effect of Elastic Processes and Ballistic Recovery in Silicon Nanowire Transistors

D. Basu, M. J. Gilbert, and S. K. Banerjee

Microelectronic Research Center, University of Texas at Austin, Austin, TX 78758 USA.

e-mail: mgilbert@mer.utexas.edu

## INTRODUCTION

Scaling of silicon devices is approaching a limit where a single gate may fail to retain effective control over the channel region. Silicon nanowire transistors (SNWT) show great promise, in terms of scalability, performance, and ease of fabrication. Here we present results of self-consistent, fully 3D quantum mechanical simulations of SNWTs using recursive scattering matrices [1]. We find that the addition of surface roughness (SR), in conjunction with the presence of impurity scattering, causes additional quantum interference which forces the SNWT operational parameters to increase their variation. However, we find that the quantum interference and elastic processes can be overcome to obtain nearly ballistic behavior in devices with preferential dopant configurations.

## DEVICE SIMULATION

In Fig. 1, we show a schematic of the device geometry we consider. The *p*-type channel is undoped. Its dimensions are 9.8 nm in length, and 8.1 nm in width. The source and drain regions, 18.47 nm wide, 10.47 nm long. The silicon film thickness is a uniform 6.51 nm high. The source and drain regions are *n*-type and doped  $10^{20}$  cm<sup>-3</sup>. Fig. 2 shows a typical interface for the devices studied. SR scattering is included by using a non-uniform mesh, with mesh spacing down to 0.36 nm at the interface. In this study, we model the Si-SiO<sub>2</sub> interface roughness using an exponential auto-correlation function, with r.m.s. roughness 0.3 nm and correlation length 1.3 nm which is consistent with experimental values [2].

## RESULTS AND DISCUSSION

Fig. 3 shows  $I_D$ - $V_G$  results for the quantum wire transistor for four different SR patterns, keeping the same dopant distribution. The SR causes a reduction of  $I_D$  while threshold voltage ( $V_T$ ) increases. We also find that the subthreshold slope (SS) remains

nearly constant, while the  $I_{on}/I_{off}$  ratio increases. This is due to the fact that SR scattering is more effective for carriers in the low field regime. These findings are summarized in Tab. 1. At high  $V_G$ , higher  $I_D$  in rough devices indicates that SR causes interference with the carriers in the channel. This not only shifts the longitudinal states in the channel, but, under constructive situations, can increase  $I_D$ .

Fig. 4. shows  $I_D$ - $V_G$  results for the SNWT for four random dopant distributions, neglecting SR. Wide variations in  $I_D$  result from different location of the dopants. Stronger reflections are caused by shallow dopants located near the source-channel interface. Such a device turns on later than others (circles in Fig.4). On the other hand, a device that has few dopants close to the source-channel interface shows nearly ballistic behaviour (square markers). In the remaining devices, there are dopants close to the source-channel interface, but buried deeper in the device, causing  $I_D$ - $V_G$  characteristics to lie between the extremes.

In Fig. 5, we show the same set of devices with a fixed SR included. The increased spread in the SNWT parameters due to SR is evident from Tab. 1. The deviation of  $I_D$  from that of the smooth device is particularly large for one particular device ( $\circ$  markers in Fig. 5), where the shallow dopant ions are also happen to be in close proximity to a rough section of the top gate-oxide-channel interface. The carriers scattered from the interface get trapped in the potential field of the dopants. As gate bias increases,  $I_D$  approaches the smooth device values since the carrier energies is now enough to overcome the quantum interference.

## REFERENCES

- [1] M. J. Gilbert and D. K. Ferry, J. App. Phys. **95**, 7954 (2004).
- [2] S. M. Goodnick, D. K. Ferry, et. al., Phys. Rev. B **32**, 8171 (1985).

Parameters	$V_T$	$\Delta V_T$	SS	$\Delta SS$	$I_{on}/I_{off}$	$\Delta I_{on}/I_{off}$
Units	(mV)		(mV/decade)			
No SR. Fixed dop. dist.	99	—	67.71	—	897	—
Diff. SR. Fixed dop. dist.	144.9	2.5	68.79	0.39	1119	43.66
No SR. Diff. dop. dist.	95.1	8.4	68.66	1.98	735.96	72.15
Fixed SR. Diff. dop. dist.	127.5	19.1	70.33	2.43	741.38	145.24

Table 1. Mean parameter values for various simulations.

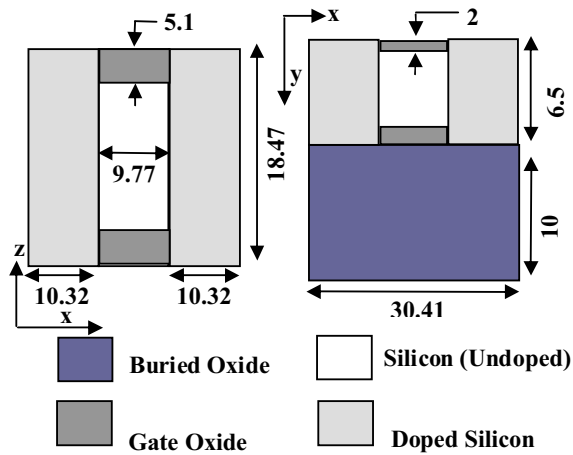


Fig. 1. Schematic of the simulated device, showing – in left, the device from top, and in right, a vertical cross-section through the middle of the device. All dimensions are in nm.

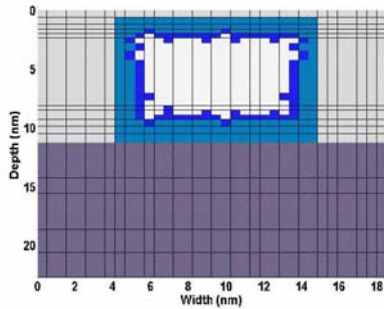


Fig. 2. A typical cross-section of the simulated nanowire, showing irregularities at the Si-SiO<sub>2</sub> interface due to SR.

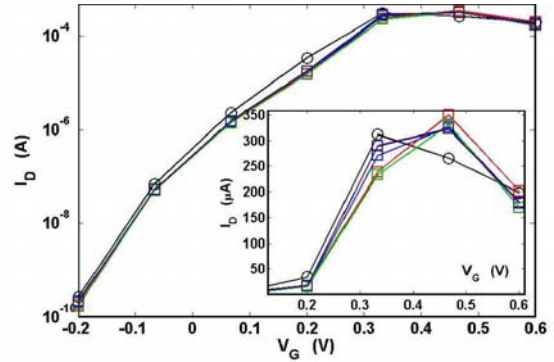


Fig. 3.  $I_D - V_G$  for four different SR patterns, keeping the dopant distribution same at  $V_D = 0.6$  V. Square markers ( $\square$ ) denote  $I_D$  including SR, circles ( $\circ$ ) imply without SR. Inset: linear scale.

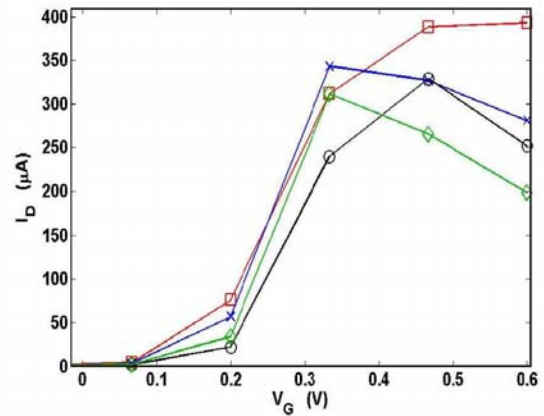


Fig. 4.  $I_D - V_G$  for four different random dopant distributions, without roughness at the Si-SiO<sub>2</sub> interface at  $V_D = 0.6$  V.

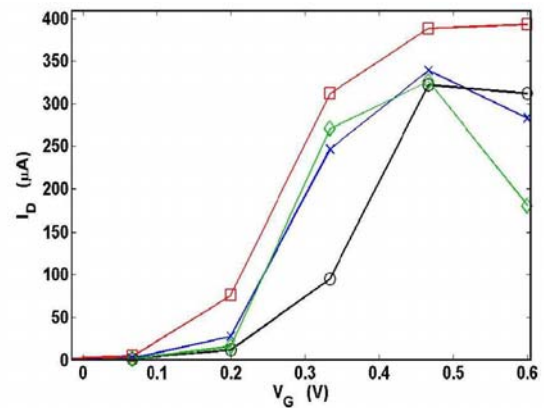


Fig. 5.  $I_D - V_G$  for same four discrete dopant distributions of Fig. 4. SR is considered and an identical pattern is used for all the simulations. The drain voltage is held constant at 0.6 V.

# A Hierarchy of Quantum-Classical Transport Models in the Framework of the SDM Method

N. Ben Abdallah\*, A. Domaingo\*, M. Mouis†, C. Negulescu\* and N. Vauchelet\*

\* MIP, Université Paul Sabatier, 118 route de Narbonne, F-31062 Toulouse Cedex 4, FRANCE

† IMEP, (UMR CNRS/INPG/UJF), 23 rue des Martyrs, BP 257, F-38016 Grenoble Cedex, FRANCE

{naoufel,domaingo,negulesc,vauchel}@mip.ups-tlse.fr, mouis@enserg.fr

## INTRODUCTION

As the channel of semiconductor devices approaches the 10 nm length-scale, quantum effects like confinement, tunneling and interference effects must be taken into account when simulating such small devices. Fully quantum models provide an accurate description in these cases, but at the expense of high computational effort [1]. An alternative approach is to treat only certain regions in the device in a quantum mechanical manner, while the rest is dealt with by classical models [2]. The advantages of these hybrid methods are low computational effort in zones where less sophisticated models are applied and high accuracy in the quantum regions.

## THE SUBBAND DECOMPOSITION METHOD (SDM)

We consider the splitting-up of the device into confinement and transport directions by applying the subband decomposition approach [3]. The electron evolution in the confinement direction  $z$  is governed by the 1D Schrödinger equation

$$-\frac{\hbar^2}{2} \frac{\partial}{\partial z} \left( \frac{1}{m_z} \frac{\partial \chi_p}{\partial z} \right) - q\Phi \chi_p = \epsilon_p \chi_p,$$

where  $\chi_p$  are the transversal wave functions and  $\epsilon_p$  the eigenvalues (energy subbands). The total energy reads  $E_p = \epsilon_p + \epsilon_p^{\text{kin}}$ . The electron evolution in the transport direction  $x$  is described by the following hierarchy of quantum, kinetic or fluid models:

- In the stationary completely quantum case, the 2D wave functions are decomposed into the transversal wave functions  $\chi_p$  and the longitudinal functions  $\varphi^p$ , which are given by a coupled system of 1D Schrödinger equations in the transport direction  $x$ . The electron density reads then

$$n(x, z) = \sum_p \int f_{FD}(E_p) \left| \sum_j \varphi_E^j(x) \chi_j(x, z) \right|^2 \frac{dk}{2\pi}.$$

An efficient method combining the SDM method with the WKB approximation permits to obtain accurate results with reduced simulation costs [4].

- A kinetic description for the electron distribution function is given by the Boltzmann equation

$$\frac{\partial f_p}{\partial t} + \frac{1}{\hbar} [\nabla_x (f_p \nabla_k E_p) - \nabla_k (f_p \nabla_x E_p)] = \mathcal{Q},$$

where  $\mathcal{Q}$  accounts for electron-phonon collisions.

The electron density is written as

$$n(x, z, t) = \sum_p \rho_p(x, t) |\chi_p(z; x, t)|^2,$$

where  $\rho_p(x, t) = (2\pi^2)^{-1} \int f_p(x, k, t) dk$ . The numerical treatment is realized similar as in [5] by applying shock capturing algorithms.

- In a fluid description [6], the density of electrons remains the same, but for the Boltzmann statistics the occupation factor is

$$\rho_p(x, t) = \frac{n_s(x, t)}{\sum_p e^{-\epsilon_p(x, t)}}.$$

The surface density  $n_s$  satisfies the Drift-Diffusion equation

$$\frac{\partial n_s}{\partial t} - \nabla_x \cdot (D(\nabla_x n_s + n_s \nabla_x U_s)) = 0,$$

where the effective energy  $U_s$  generated by the electrons itself is given by

$$U_s(x, t) = -\log\left(\sum_p e^{-\epsilon_p(x, t)}\right),$$

These models are self-consistently coupled with the Poisson equation for the electrostatic potential. Numerical results and comparisons of the different models will be presented. Each model accounts for other specific physical phenomena, where the interest of such a comparison.

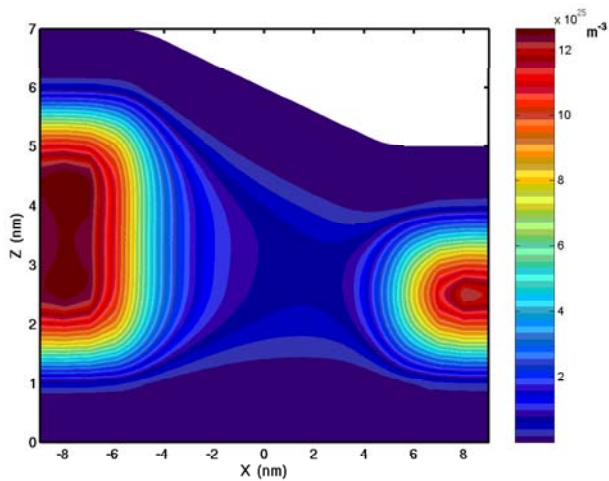


Fig. 1. Electron density for a trapezoidal MOSFET device in the quantum case for  $V_{DS} = 0.2$  V and  $V_{GS} = 0.1$  V.

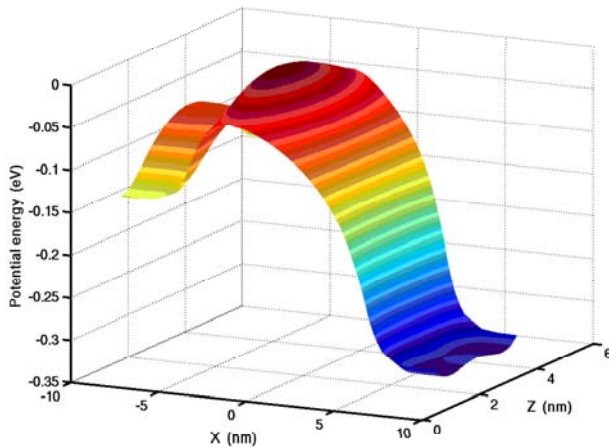


Fig. 2. Potential energy for a trapezoidal MOSFET device in the quantum case for  $V_{DS} = 0.2$  V and  $V_{GS} = 0.1$  V.

#### ACKNOWLEDGEMENTS

This work has been supported by the ACI Nouvelles Interfaces des Mathématiques MOQUA (ACINIM 176-2004), funded by the French Ministry of Research.

#### REFERENCES

- [1] E. Polizzi and N. Ben Abdallah, *Self-consistent three-dimensional models for quantum ballistic transport in open systems*, Phys. Rev. B **66**, 245301 (2002).
- [2] M. Baro, N. Ben Abdallah, P. Degond, and A. Al Ayyadi, *A 1D coupled Schrödinger drift-diffusion model including collisions*, J. Comput. Phys. **203**, 129 (2005).
- [3] E. Polizzi and N. Ben Abdallah, *Subband decomposition approach for the simulation of quantum electron transport in nanostructures*, J. Comput. Phys. **202**, 150 (2005).

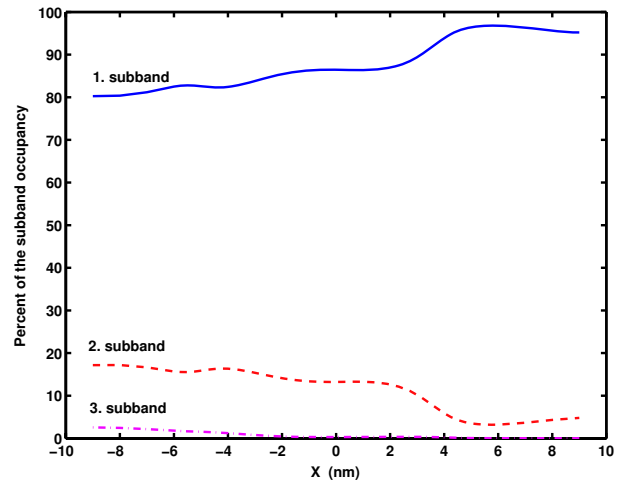


Fig. 3. Percentage of the subband occupancy for the considered trapezoidal device in the quantum case for  $V_{DS} = 0.2$  V and  $V_{GS} = 0.1$  V.

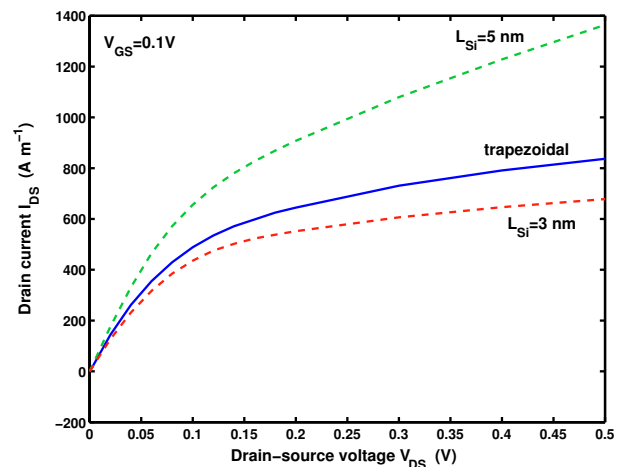


Fig. 4. Comparison of the current versus drain-source voltage characteristics in the quantum case for  $V_{GS} = 0.1$  V for different device designs: rectangular MOSFETs (5 nm and 3 nm channel width) and a trapezoidal one.

- [4] N. Ben Abdallah, M. Mouis, and C. Negulescu, *An accelerated algorithm for 2D simulations of the quantum ballistic transport in nanoscale MOSFETs*, J. Comp. Phys. **submitted**, (2005).
- [5] M. Galler and A. Majorana, *Deterministic and stochastic simulations of electron transport in semiconductors*, Transport Theor. Stat. **in press**, (2005).
- [6] N. Ben Abdallah, F. Méhats, P. Pietra and N. Vauchelet *A Drift-Diffusion subband model for the Double-Gate MOSFET*, IEEE conference on Nanotechnology, (2005).

# Channel Length Dependence of Tunnel FET Subthreshold Swing

Krishna K Bhuwalka, Mathias Born, Markus Schindler, and Ignaz Eisele  
 Institut für Physik, Universität der Bundeswehr, Munich 85577 Neubiberg, Germany  
 Tel: +49 89 6004 4043, Fax: +49 89 6004 3877, e-mail: Krishna.K.Bhuwalka@UniBw.de

## I. INTRODUCTION

Unlike conventional MOSFETs, the gated p-i-n diode [1] tunnel FETs [2]–[6] have tunneling currents for both the subthreshold as well as on-region of operation. The  $I - V$  characteristics show a weak positive temperature coefficient over a wide temperature range [7]. Thus, the subthreshold swing  $S$ , can be scaled to below the  $kT/q$  diffusion limit of conventional MOSFETs [8], [9]. In principle,  $S$  can be vanishingly small within a small range of gate bias  $V_{GS}$  [10], [11]. However, even with a 40mV/dec swing extremely low on-currents were observed in tunneling carbon nanotube MOSFETs [12]. Using a band-diagram approach we show that the subthreshold swing for tunnel FETs is not a constant but is strongly dependent on the tunneling barrier width,  $\omega$ , and hence  $V_{GS}$ .

## II. BAND DIAGRAM APPROACH

Fig. 1, shows the simulated band-diagrams for a tunnel FET ( $L = 100$  nm,  $t_{ox} = 2$  nm) as a function of  $V_{GS}$  for constant  $V_{DS}$ . The energy contours between source and drain are depicted close to the Si-SiO<sub>2</sub> interface. To a first approximation we assume constant tunneling barrier height (bandgap  $W_g$ ) and effective mass  $m_o$  (it does not vary with applied bias). In this case the drain current  $I_{DS}$  depends exponentially on the barrier width,  $\omega$ . From the band-diagrams in the saturation region [6]  $\omega$  nearly independent of  $V_{DS}$  [10]. We then can write:

$$I_{DS}(\omega) \sim e^{-\omega} \text{ and } 1/\omega \sim V_{GS} \quad (1)$$

Thus, taking a derivative of  $\omega$  with respect to  $\ln(I_{DS})$  and  $V_{GS}$ , we get

$$d\ln(I_{DS}(\omega)) \sim -d\omega, \text{ and} \quad (2)$$

$$d\omega \sim -\omega^2 \cdot dV_{GS} \quad (3)$$

This implies that the *smaller*  $\omega$  gets, the more difficult it becomes to *further* lower it for a *constant*  $dV_{GS}$ . Thus, from (2) and (3)

$$S(\omega) = \frac{dV_{GS} \cdot \ln 10}{d\ln(I_{DS})} \sim \frac{dV_{GS}}{-d\omega} \sim \frac{1}{\omega^2} \quad (4)$$

which is a strong non-linear function of  $\omega$ , and hence  $V_{GS}$ . It is degrading with increasing  $V_{GS}$ , and hence limits  $I_{on}$ . This is confirmed by experimental results as shown in Fig. 2, where we have plotted ‘spot’ swing as function of  $V_{GS}$  (data from [7]). Furthermore (4) also implies that  $I_{DS}$  is decaying *faster* than exponentially and ideally, for  $\omega \rightarrow \infty$ ,  $S \rightarrow 0$ , consistent with simulation predictions [10]. Thus, in principle, with a proper choice of device geometry parameters, for example with pseudomorphically strained  $\delta p^+$ SiGe layer [8], [10],  $I_{DS}$  can increase *several orders of magnitude* within a small range of  $V_{GS}$ .

## III. RESULTS AND DISCUSSION

We now look at the impact of channel length  $L$  scaling on  $S$ . For a fully depleted channel and heavily doped source and drain regions,  $\omega_o$  at  $V_{GS} = 0$  V (assuming flat-band and constant  $V_{DS}$ ) is limited by  $L$ . As  $L$  is scaled,  $\omega_o$  is lowered. Thus, from (4),  $S$  is expected to *degrade* with  $L$  scaling into the ultra short channel length regime. However, as  $I_{on}$  is determined by the channel in inversion ( $\omega < 5$  nm),  $L$  scaling is not expected to affect  $I_{on}$ . This is confirmed by both experimental (Fig. 3) as well as 2-D device simulations (Fig. 4) where we show the transfer characteristics as a function of  $L$ . As  $L$  is scaled,  $S$  is clearly seen to degrade at turn-off voltages while  $I_{on}$  remains almost

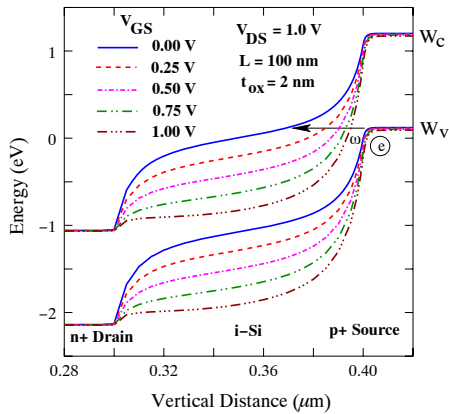


Fig. 1. Simulated band-diagrams for a tunnel FET close to the Si-SiO<sub>2</sub> interface, as a function of  $V_{GS}$ .  $\omega$  lowers with increasing  $V_{GS}$ .

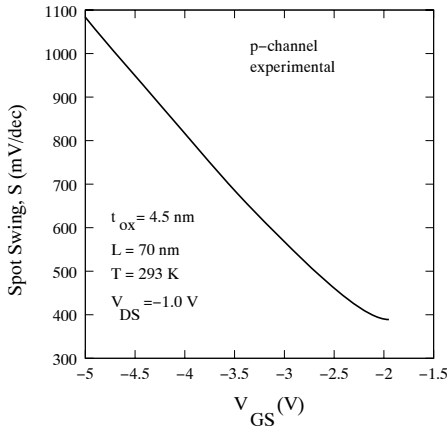


Fig. 2. Experimental 'spot'  $S$  as a function of  $V_{GS}$  (p-channel).  $S$  is seen to degrade with increasing  $V_{GS}$ . Note that the high value of spot ' $S$ ' is due to a thick oxide and doping smear-out effects.

independent of  $L$  scaling. Thus, while the characteristics of the tunnel FETs is nearly independent of channel length,  $L$  [13], [14], even for sharp and abrupt tunnel junctions,  $S$  starts to degrade with  $L$  scaling into the ultra short-channel regime. This is confirmed by both experimental as well as simulation results.

## REFERENCES

- [1] J. J. Quinn, G. Kawamoto, and B. D. McCombe, *Surface Science*, vol. 73, pp. 190-196, May 1978.
- [2] T. Baba, *Jpn. J. Appl. Phys.*, vol. 31, pp. L455-L457, 1992.
- [3] W. M. Reddick, G. A. J. Amaratunga, *Appl. Phys. Lett.*, vol. 67, no. 4, pp. 494-497, 1995.
- [4] J. Koga and A. Toriumi, *Electron Device Letters*, vol. 20, no. 10, pp. 529-531, 1999.
- [5] W. Hansch, C. Fink, J. Schulze, and I. Eisele, *Thin Solid Films*, vol. 369, pp. 387-389, 2000.

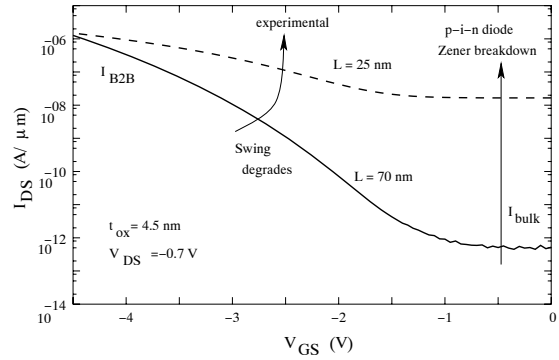


Fig. 3. Experimental p-channel transfer characteristics for  $L = 25$  nm and 70 nm [7]. It should be noted that the doping profile also plays a critical role in determining  $S$ .

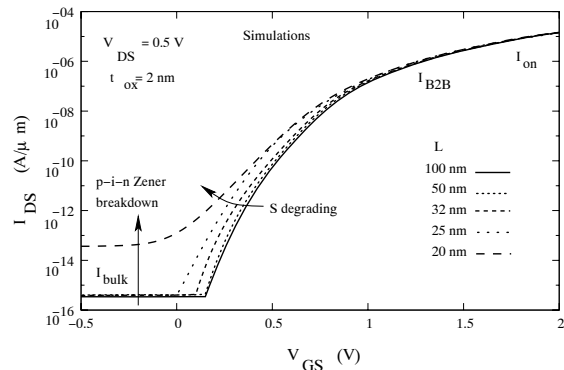


Fig. 4. Simulated n-channel transfer characteristics as a function of  $L$ . At ultra short channel lengths,  $S$  is seen to degrade with  $L$  scaling.

- [6] K. K. Bhuwarka, S. Sedlmaier, A. Ludsteck, C. Tolksdorf, J. Schulze, and I. Eisele, *IEEE Trans. Electron Devices*, vol. 51, no. 2, pp. 279-282, 2004.
- [7] K. K. Bhuwarka, M. Born, M. Schindler, M. Schmidt, T. Sulima, and I. Eisele *Int. Conf. Solid State Devices and Materials*, Kobe, Japan, 2005, pp. 288-289.
- [8] K. K. Bhuwarka, J. Schulze, and I. Eisele, *Jpn. J. Appl. Phys.*, vol. 43, no. 7A, pp. 4073-4078, 2004.
- [9] J. Appenzeller, Y.-M. Lin, J. Knoch, Z. Chen, and Ph. Avouris, to be published, *IEEE Trans. Electron Devices*, vol. 52, no. 12, 2005.
- [10] K. K. Bhuwarka, J. Schulze, and I. Eisele, *IEEE Trans. Electron Devices*, vol. 52, no. 7, pp. 1541-1547, 2005.
- [11] Q. Zhang, W. Zhao, and A. Seabaugh, *63rd Device Research Conf. Dig.*, Santa Barbara, CA, pp. 161-162, June 2005.
- [12] J. Appenzeller, Y.-M. Lin, J. Knoch, and Ph. Avouris, *Phys. Rev. Letts*, vol. 93, pp. 196805, 2004.
- [13] C. Aydin, A. Zaslavsky, S. Luryi, S. Cristoloveanu, D. Mariolle, D. Fraboulet, and S. Deleonibus, *Appl. Phys. Letters*, vol. 84, pp. 1780-1782, 2004.
- [14] K. K. Bhuwarka, J. Schulze, and I. Eisele, *IEEE Trans. Electron Devices*, vol. 52, no. 5, pp. 909-917, 2005.

# Quantum Corrections to Semiclassical Transport in Nanoscale Devices using Entropy Principles

J. P. Bourgade\*, P. Degond,<sup>†</sup> N. Mauser\* and C. Ringhofer\*<sup>‡</sup>

\* Wolfgang Pauli Institut c/o Fak. f. Math., Uni. Wien, A 1090 Wien

<sup>†</sup> MIP, UMR 5640 Université Paul Sabatier 118, route de Narbonne, 31062 TOULOUSE, FRANCE

<sup>‡</sup> Department of Mathematics, Arizona State University, Tempe, Arizona 85287-1804, USA

email: bourgade@mip.ups-tlse.fr, degond@mip.ups-tlse.fr, Norbert.Mauser@univie.ac.at, ringhofer@asu.edu

## I. BACKGROUND

The simulation of nanoscale devices requires, at least rudimentarily, the inclusion of quantum effects. Quite a lot of attention has been paid to the quantum mechanical modelling of free (collisionless) transport. Efforts here include the direct solution of the Schrödinger equation [2], [11], macroscopic moment equations (quantum hydrodynamic models) [9], [10], and extensions of semiclassical Monte Carlo methods, either directly [13], [8] or via effective potential approaches [6], [1], [12]. Comparably little work has been done on the inclusion of quantum effects into collision operators. Collisions can be treated quite rigorously using Green's functions or by Wigner function methods for the phonon system [7]. Using classical collision operators in collision with quantum corrected transport models has the disadvantage that equilibrium solutions of the resulting system do not correspond to admissible quantum mechanical states, since the semiclassical phonon collision operator increases the classical entropy and not the correct quantum mechanical entropy, given by  $S = Tr[\rho(\ln \rho - 1)]$ , where  $\rho$  denotes the density matrix of the mixed state.

## II. QUANTUM ENTROPY PRINCIPLES

In recent work [3], [4], [5] we have developed the framework to extend semiclassical transport equations, like the Boltzmann equation, to a quantum mechanical setting via the local maximization of the quantum entropy. This results in a modification of the semiclassical phonon collision operator. The resulting operator dissipates the quantum entropy, while maintaining the local conservation properties of the semiclassical collision operator. In the

Wigner picture, i.e. in terms of the Wigner function  $f_w(\mathbf{r}, \mathbf{k})$ , for a given potential  $V(\mathbf{r})$  it is of the form

$$Q[f_w](\mathbf{r}, \mathbf{k}) = \quad (1)$$

$$\int K(\mathbf{r}, V, \mathbf{k}, \mathbf{k}') \phi(\mathbf{r}, \mathbf{k}') d\mathbf{k}' - \kappa(\mathbf{r}, \mathbf{k}, V) \phi(\mathbf{r}, \mathbf{k}) ,$$

where  $\phi(\mathbf{r}, \mathbf{k})$  is the quantum mechanical entropy variable, i.e. a generalization of the quasi-Fermi function. The relation between the Wigner function  $f_w$  and the entropy variable  $\phi$  is given by a nonlocal, potential dependent, integral relation of the form

$$f_w(\mathbf{r}, \mathbf{k}) = \int A(V, \mathbf{r}, \mathbf{k}, \mathbf{r}', \mathbf{k}') \phi(\mathbf{r}', \mathbf{k}') d\mathbf{r}' d\mathbf{k}' . \quad (2)$$

The quantum corrected collision operator acts like a classical collision operator on the entropy variable  $\phi$ , but is nonlocal in space because of the nonlocal relation (2) between  $f_w$  and  $\phi$ . The resulting collision operator dissipates the quantum entropy and drives the system to a quantum mechanically correct equilibrium. It maintains the local conservation properties, i.e. a collision event results in the exchange of an amount  $\hbar\omega$  of energy with the lattice. The operator  $Q$  in (1) is amenable to Monte Carlo discretizations as well as series expansion methods. We will present preliminary results for a tunneling diode using a spherical harmonics expansion method of the resulting Wigner - Boltzmann equation. Figures 1-4 show the relation between the Wigner function  $f_w$  and the entropy variable  $\phi$ , which would classically be given by  $f_w = e^{-H} \phi$ , for a potential barrier. Figure 1 shows the potential and Figure 2 shows the Wigner function  $f_w$  for a constant entropy variable  $\phi$ . Figures 3 and 4 show

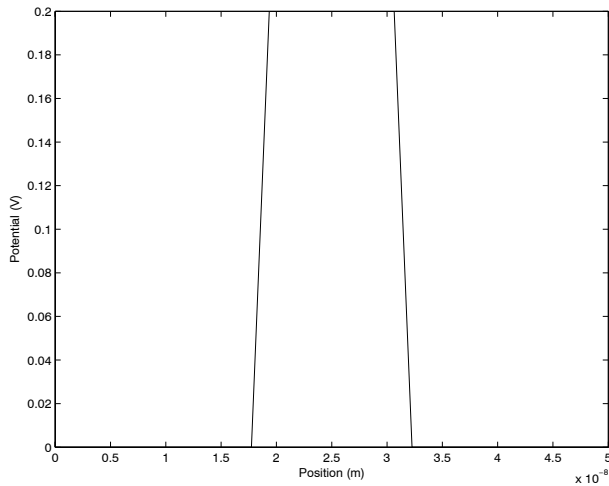


Fig. 1. Potential

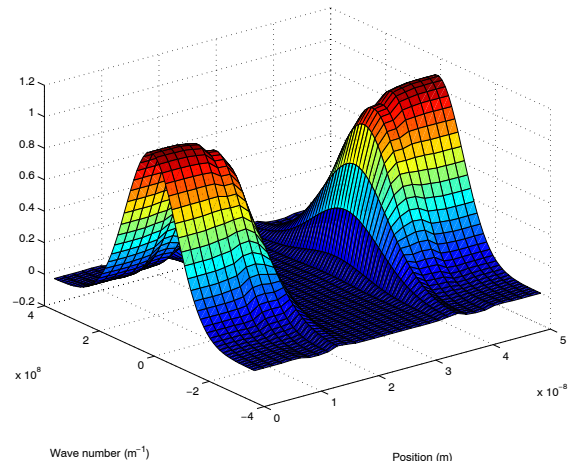


Fig. 2. Wigner function  $f_w$  for a constant entropy variable  $\phi$

the corresponding relations for an entropy variable  $\phi$  which is concentrated inside the potential barrier.

#### ACKNOWLEDGEMENT

*This work was supported by the Austrian Ministry of Science (BM:BWK) via its grant for the WPI and by the Austrian Science Foundation (FWF) via the START Project (Y-137-TEC) of N.J.M.*

#### REFERENCES

- [1] S. Ahmed, C. Ringhofer, D. Vasileska, *Journal of Computational Electronics* **2** 113 (2003).
- [2] N Ben Abdallah, *Journal of Statistical Physics* **90** 3-4 (1998).
- [3] J.-P. Bourgade, P. Degond, F. Mehats, C. Ringhofer *On quantum extensions to classical Spherical Harmonics Expansion / Fokker-Planck models*, to appear, *Journal of Mathematical Physics* (2006).
- [4] P. Degond, C. Ringhofer, *Journal Stat. Phys.* **112** (3): 587-628 (2003).
- [5] P. Degond, F. Mehats, C. Ringhofer, *Journal Stat. Phys.* **118** 625-667 (2005).
- [6] D. Ferry, H. Grubin, *Solid State Physics* 49:283 (1995).
- [7] C. Jacoboni, A. Bertoni, P. Bordone, R. Brunetti, *Math. Comp. Simul* **55** 67 (2001).
- [8] L. Shifren, C. Ringhofer, D. Ferry, *IEEE Trans. Electron Devices* **50** (3):769-773 (2002).
- [9] C. Gardner, C. Ringhofer, *Phys. Rev E* **58** 780 (1998).
- [10] I. Gasser, A. Jüngel, *Zeitschrift für Angewandte Mathematik und Physik* **48** 45 (1997).
- [11] C. Lent, D. Kirkner, *J. Applied Physics* **67** (10) 6353 (1990).
- [12] C. Ringhofer, C. Gardner, D. Vasileska, *Inter. J. on High Speed Electronics and Systems* **13** 771-803 (2003).
- [13] R. Wyatt, *Journal Chem. Phys.* **111** 4406 (1999).

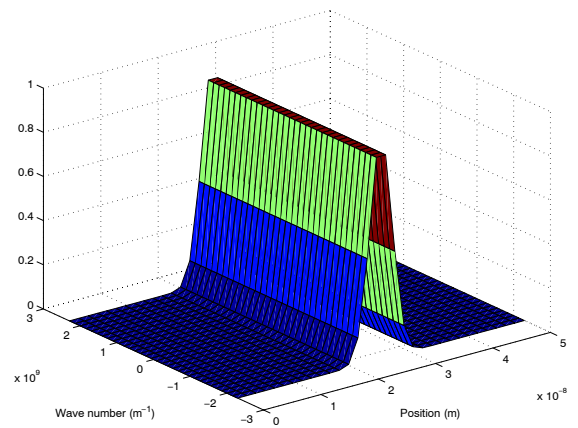


Fig. 3.  $\phi$  concentrated inside the barrier

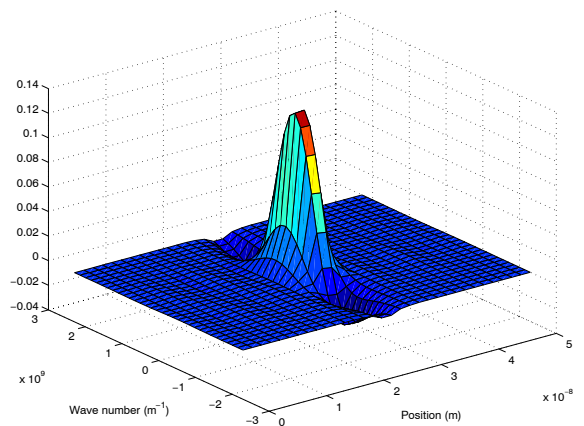


Fig. 4. Wigner function  $f_w$  corresponding to  $\phi$  in Figure 3

# Micromagnetic Simulation of Current-Driven Domain Wall Propagation

G. Csaba\*, P. Lugli\*, L. Ji\*\* and W. Porod\*\*

\**Institute for Nanoelectronics, Technical University of Munich, Arcisstrasse 21, D-80333 Munich, Germany*

\*\**Center for Nano Science and Technology, Department of Electrical Engineering, University of Notre Dame, 275 Fitzpatrick Hall, Notre Dame, IN 46556, USA:*

csaba@ei.tum.de

## MOTIVATION

In the recent years ideas of ‘magnetic computing’ emerged such magnetic field-coupling [1] or computing with domain walls [2]. Proposed spintronic devices also use the magnetic degree of freedom for information processing.

Any implementation of magnetic information processing is plagued by the difficulty of creating localized and strong magnetic fields which can be switched rapidly as well. Magnetic fields created by current-carrying wires are relatively weak and dispersed; coils are bulky, slow and dissipate a large amount of power.

Direct control of magnetic domain structures by electricity could eliminate the need for externally applied magnetic fields and bring magnetic computing close to real-world, practical applications. That is why the subject of current-driven domain wall propagation received considerable attention recently [3].

## DESCRIPTION OF WORK

We introduce an effective-field approach to simulate the interaction of currents with a localized domain wall. This current-induced effective field is superposed over the other effective field terms (such as the external and dipole magnetic fields, anisotropy fields, etc.) and can move the domain wall. The physics of the interaction between domain walls and currents is complex and not yet completely understood. For thick walls in metallic nanowires the spin (angular momentum) transfer is dominant [4] and we focus on its modeling. The current-induced effective field distribution (resulting from the spin transfer effect) is illustrated in Fig. 1 for a particular wall structure.

Our effective-field approach can be extended to include momentum transfer and parasitic effects, such as the magnetic field generated by the current. We will demonstrate how these new field components can be implemented in the OOMMF program, which is a widely-used micromagnetic simulator [5].

While this effective-field approach does not contain new physics compared to already used methods (such as adding a diffusive term to the Landau-Lifshitz equation [6]), it fits better into the framework of micromagnetics and easier to implement in existing codes.

## RESULTS

We will simulate current-induced domain wall propagation in nanowires with different shape, surface roughness and notches. We examine how domain walls can be pinned at and released from artificially created notches, as it is illustrated in Fig. 2. Our model gives relatively low spin transfer efficiencies, in accordance with experimental results [3]. Most of the recent studies are dealing with idealized domain structures – we will point out the importance to treat the micromagnetic problem accurately. We will also discuss the prospects of using current-driven domain walls in field-coupled computing devices.

## REFERENCES

- [1] A. Imre, G. Csaba, L. Ji, A. Orlov, G. H. Bernstein, W. Porod: Majority Logic Gate for Magnetic Quantum-Dot Cellular Automata SCIENCE VOL 311 13 JANUARY 2
- [2] D. A. Allwood, Gang Xiong, M. D. Cooke, C. C. Faulkner, D. Atkinson, N. Vernier, R. P. Cowburn: Submicrometer Ferromagnetic NOT Gate and Shift Register Science 14 June 2002 296: 2003-2006
- [3] A. Yamaguchi, T. Ono, and S. Nasu, K. Miyake, K. Mibu, T. Shinjo: Real-Space Observation of Current-Driven Domain Wall Motion in Submicron Magnetic Wires Phys. Rev. Lett, 92 7
- [4] L. Berger: Exchange interaction between ferromagnetic domain wall and electric current in very thin metallic films J. Appl. Phys, 55 6 1984
- [5] <http://math.nist.gov/oommf/>
- [6] A. Thiaville, Y. Nakatani, J. Miltat, N. Vernier: Domain wall motion by spin-polarized current: a micromagnetic study J. Appl. Phys., 95, 11

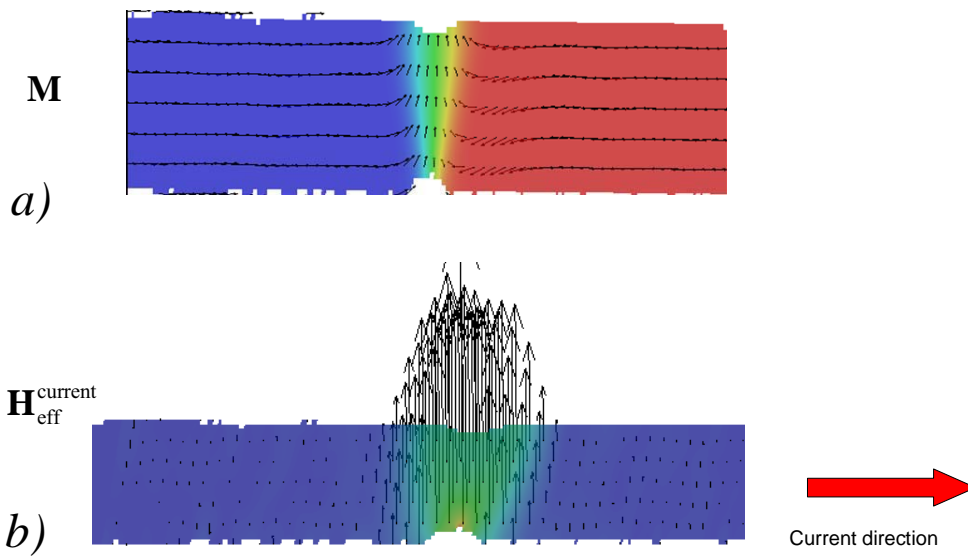


Figure 1. Part a) shows the magnetization distribution for a particular domain wall in a permalloy wire. Arrows indicate magnetization direction and the coloring indicates the strength of magnetization component parallel to the current direction. Transport currents interact with the fixed spins of the wire and generate an effective field, as it is shown in part b). If the current is sufficiently strong, it can displace the wall.

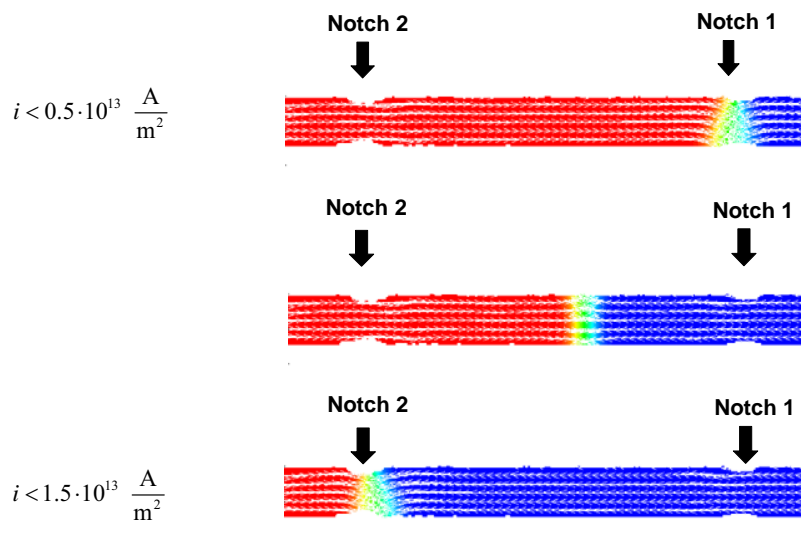


Figure 2. Domain walls can be pinned and released in a controlled way in a nanomagnet wire with notches of different depth. The figure shows snapshots of a time-dependent simulation. A domain wall, propagating from right is pinned at the right notch. When the current density exceeds  $i = 0.5 \cdot 10^{13} \text{ A/m}^2$ , the wall leaves the right notch and quickly (with a speed of few hundred meters per seconds) propagates to the left. The notch at the left side is deeper and represents a stronger pinning potential. A current density exceeding  $i = 1.5 \cdot 10^{13} \text{ A/m}^2$  is required to de-pin the wall from this position.

# Shot Noise in Resonant Tunneling Structures using Non-Equilibrium Green's Function Calculation

V. Nam Do, Philippe Dollfus, and V. Lien Nguyen\*

Institut d'Electronique Fondamentale, UMS CNRS 8622, Univ. Paris-Sud, 91405 Orsay Cedex, France

\*Theoretical Dept., Institute of Physics, VAST, P.O. Box 429 Bo Ho, Hanoi 10000, Vietnam

e-mail: van-nam.do@ief.u-psud.fr

## INTRODUCTION

The non-equilibrium Green's function (NEGF) method has been applied to simulate the electronic transport in nano-hetero semiconductor devices such as the resonant tunneling structures (RTS). Any quantity characterizing the transport are calculated once a self-consistent solution of the Poisson and transport equations is achieved. Particularly, the characteristics of shot noise have been extracted using two different formulas, one derived from the scattering method[1] and another one from the master equation[2]. The result has confirmed the experimental data and shown the complicated behavior of charges in such structure.

## BASICS OF METHOD

To simulate transport in nano-hetero semiconductor devices it is convenient to use the NEGF method. The heart of the formalism is a system of four Green's functions which completely describe the system including both the electronic structure and the statistical properties.

The equations to be solved for calculating the transport in devices are formally

$$\rho(\mathbf{r}) = -i\frac{e}{\pi} \int dE G^<(\mathbf{r}, \mathbf{r}, E) \quad (1)$$

$$\nabla[\epsilon \nabla U] = (\rho + \rho_0), \quad (2)$$

where  $\rho, \rho_0$  are the charge densities of carriers and the bath, respectively;  $G^<$  is one of the four functions, referred to as the lesser-Green function; and  $U$  is the electrostatic energy. Of course one needs more equations for the other Green's functions to compute  $G^<$ . To solve these equations our technique is to consider them as a single one and

to use the Newton-Raphson method to reduce the computation time.

## NUMERICAL RESULTS

Once the self-consistent solution is achieved, any desired quantity is computed (all concerned formulas are given Ref.[3]). We present four figures providing the transport information for a specific RTS, denoted as S[3/5/3] meaning that the thicknesses of both barriers and the well are 3 nm and 5 nm, respectively. Fig.1 is the conduction band at different values of bias. Fig.2 shows the I-V characteristics at two temperatures. The evolution of the resonant level is shown in that of the transmission coefficient plotted in Fig.3. The last figure presents the sub-poissonian (the inset) and super-poissonian noise extracted from our calculation according to the noise expressions used. The super-poissonian noise in the negative differential conductance (NDC) regime is in agreement with experimental data. The results suggest that the transport is essentially controlled by coherent tunneling under low bias and by sequential tunneling near and beyond resonance.

## ACKNOWLEDGMENT

This work was partially supported by the EC 6<sup>th</sup> FP (NoE SINANO, contract no 506844).

## REFERENCES

- [1] Ya. Blanter, M. Büttiker, Phys. Rep., 336 (2000) 1-166
- [2] G. Iannaccone, G. Lombardi, M. Marcucci, and P. Pellegrini, Phys. Rev. Lett. **80**, 1054 (1998)
- [3] V. Nam Do, Philippe Dollfus, and V. Lien Nguyen, J. Appl. Phys. (submitted decembre, 2005)

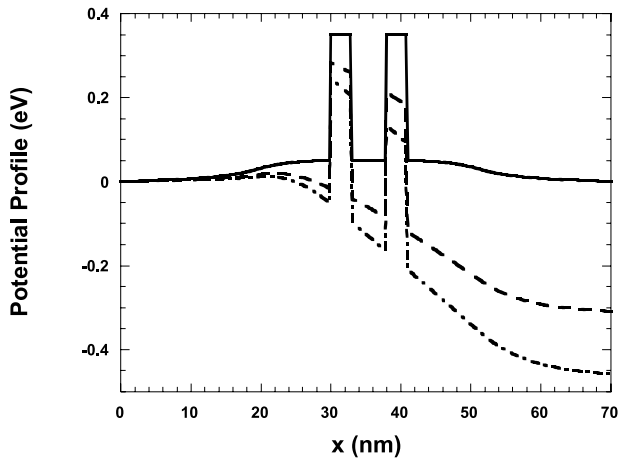


Fig. 1. Conduction band plotted at 0V (solid line), 0.31V (close to the resonance, dashed line), and 0.46V (above the resonance, dot-dashed line). Temperature: 300K.

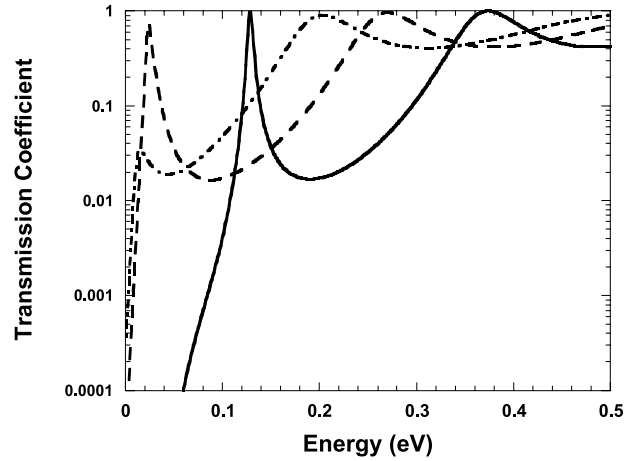


Fig. 3. The transmission evolution versus energy at different bias: 0V (solid line), 0.31V (dashed line), and 0.46V (dot-dashed line) (in the logarithmic scale).

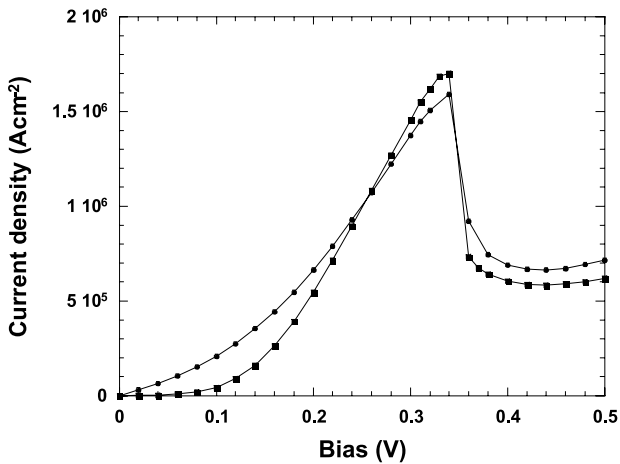


Fig. 2. The temperature effect on the current: 300K (circle) and 77K (square).

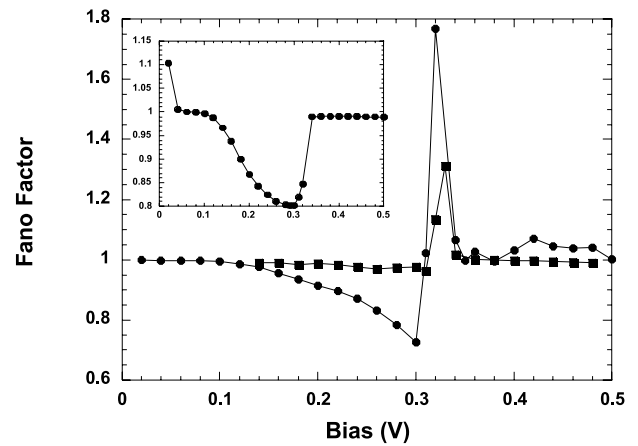


Fig. 4. The dominance of Fano factor in the NDC regime of current is reproduced at  $T=300\text{K}$  (square) and  $77\text{K}$  (circle) using the Iannacone's formula. The inset shows the Fano factor calculated from the Buttiker's formalism for the structure  $S[3/5/3]$  at  $77\text{K}$ .

# Inelastic cotunneling through an interacting quantum dot with a quantum Langevin equation approach

Bing Dong, H.L. Cui\*

Department of Physics, Shanghai Jiaotong University, 1954 Huashan Road, Shanghai 200030, China

\*Department of Physics and Engineering Physics, Stevens Institute of Technology,

Hoboken, New Jersey 07030, USA

e-mail: bdong@sjtu.edu.cn

In recent years, there has been great interest in investigation of electronic transport through semiconductor nanoscale devices. It is well known that tunneling through a quantum dot (QD) includes two distinct mechanisms: sequential (first-order) tunneling if the QD level is in resonance with the Fermi levels of the electrodes, and higher-order coherence tunneling (cotunneling)[1] when the QD level is far removed from resonance, with sequential tunneling exponentially suppressed. This kind of higher-order processes involves the simultaneous tunneling of two or more electrons through the device, which defines a primary limitation to the accuracy of quantum manipulation of single-electron devices. Therefore, it is desirable to develop a unified and effective theoretical approach for thorough examination nonequilibrium inelastic cotunneling through a single-level QD subject to a finite magnetic field in the strong Coulomb blockade regime, in the weak tunneling limit.

For this purpose, we have recently proposed a generic quantum Langevin equation approach[2] to establish a set of quantum Bloch-type dynamical equations describing inelastic cotunneling phenomenology modeled by the Kondo Hamiltonian[3] at arbitrary bias-voltage and temperature. In our formulation, the operators of the QD spin and the reservoirs were first expressed formally by integration of their Heisenberg equations of motion, exactly to all orders in the tunnel coupling constants. Next, under the assumption that the time scale of the decay processes is much slower than that of free evolution, we replaced the time-dependent operators involved in the integrands of these equations

of motion approximately in terms of their free evolution. Thirdly, these equations of motion were expanded in powers of the tunnel-coupling constants to second order (linear response theory). On the basis of these consideration, jointly with normal ordering, we developed the Bloch-type equations describing the time evolution of the spin variables of the QD explicitly and compactly in terms of the response and the correlation functions of the free reservoir variables, which not only provides explicit analytic expressions for the relaxation and decoherence in the QD spin induced by cotunneling, but also facilitates the derivation of the nonequilibrium magnetization of the QD. Employing this resulting QD magnetization and performing linear response calculation, we can also derive closed-form expressions for the spin-resolved currents and their fluctuation, which facilitated our calculation of both the charge current [Fig. 1(a)] and the spin current (Fig. 2), as well as their frequency-independent auto- and cross-shot noises [Fig. 1(b) and Fig. 3].

## ACKNOWLEDGMENT

This work was supported by the DURINT Program administered by the US Army Research Office, DAAD Grant No.19-01-1-0592.

## REFERENCES

- [1] D.V. Averin and Yu.V. Nazarov, *Phys. Rev. Lett.* **65**, 2446 (1990).
- [2] B. Dong, N.J.M. Horing, and H.L. Cui, *Phys. Rev. B* **72**, 165326 (2005).
- [3] K.A. Matveev, *Zh. Eksp. Teor. Fiz.* **99**, 1598 (1991) [*Sov. Phys. JETP* **72**, 892 (1991)]; A. Furusaki and K.A. Matveev, *Phys. Rev. B* **52**, 16676 (1995).

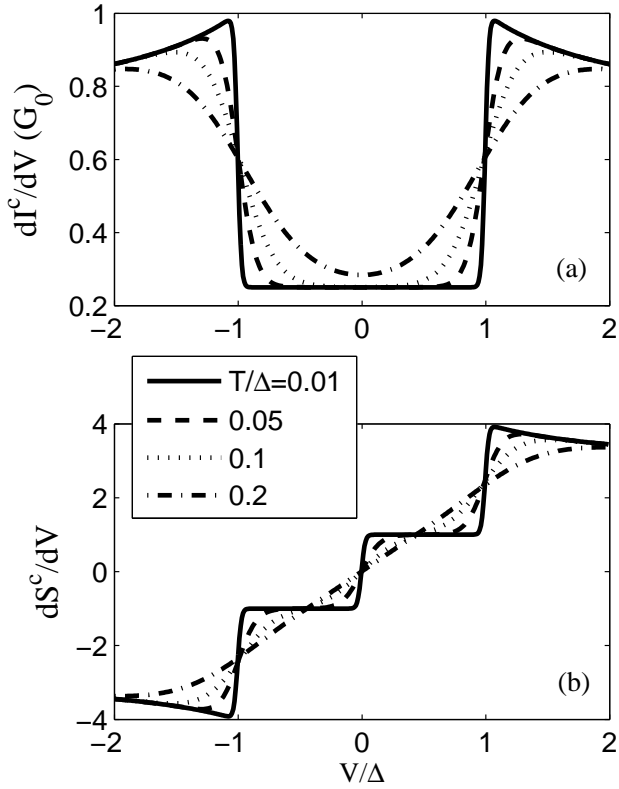


Fig. 1. (a) The calculated differential conductance  $dI^c/dV$  vs. bias-voltage  $V/\Delta$  for several temperatures at nonzero magnetic field in units of  $G_0 = 4\pi J_{LR}^2 \rho_L \rho_R$  (linear conductance at zero magnetic field); (b) The differential auto-shot noise  $dS^c_{LL}/dV$  vs. bias-voltage. The parameters we used in calculation are:  $J_{LL}\rho_L = J_{RR}\rho_R = J_{LR}\sqrt{\rho_L\rho_R} = 0.02$ .

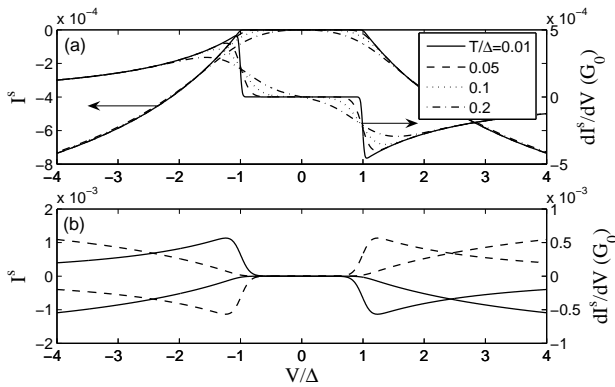


Fig. 2. The calculated spin current,  $I^s$ , and its differential conductance,  $dI^s/dV$ , as functions of bias-voltage  $V/\Delta$ , at nonzero magnetic field. (a) exhibits results for several temperatures and  $J_{RR}/J_{LL} = 4.0$ ,  $J_{LL} = 0.02$ . (b) plots the results for  $J_{RR}/J_{LL} = 5.0$  ( $J_{LL} = 0.02$ ) as solid lines, and for  $J_{LL}/J_{RR} = 5.0$  ( $J_{RR} = 0.02$ ) as dashed lines.

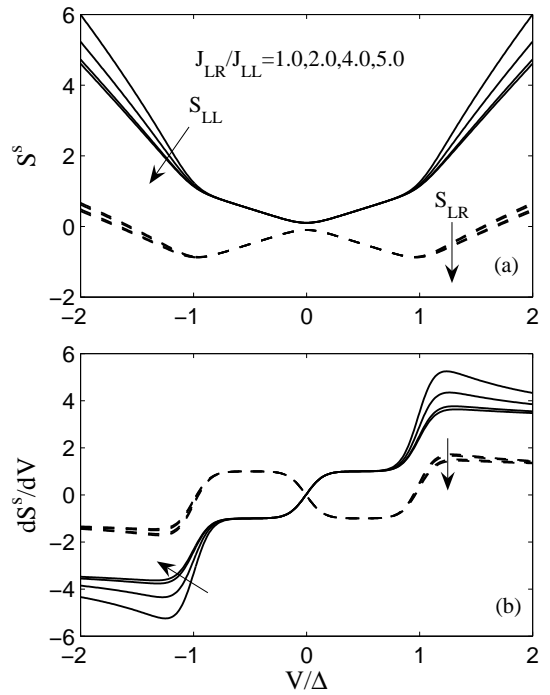


Fig. 3. (a) The calculated auto- (the solid lines) and cross-shot noises (the dashed lines) for spin current,  $S^s$ , and (b) the differential shot noise,  $dS^s/dV$ , as functions of bias-voltage  $V/\Delta$  at the temperature  $T = 0.05$  and various  $J_{RR}/J_{LL}$  ( $J_{LL} = 0.02$ ).

# Quantum transport using parallel computing techniques

P.S. Drouvelis\*<sup>†§</sup>, P. Schmelcher\*<sup>‡</sup> and P. Bastian<sup>†</sup>

\*Theoretische Chemie, Universität Heidelberg, Im Neuenheimer Feld 229, D-69120 Heidelberg, Germany

<sup>†</sup>Interdisziplinäres Zentrum für Wissenschaftliches Rechnen, Im Neuenheimer Feld 368, D-69120 Heidelberg, Germany

<sup>‡</sup>Physikalisches Institut, Philosophenweg 12, Universität Heidelberg, D-69120 Heidelberg, Germany

<sup>§</sup> e-mail: panos@tc.pci.uni-heidelberg.de

## INTRODUCTION

In this contribution quantum transmission properties will be calculated using a parallel implementation of the recursive Green's function method.

## COMPUTATIONAL METHOD

The computational method is based on an implementation of the recursive Green's function (RGF) method [1] on a parallel architecture of processors. The algorithm goes beyond the (straightforward) parallelization with respect to the external parameters of the scattering problem, such as e.g. Fermi energy or magnetic field, and proceeds with the scatterer's domain decomposition in internal independent domains which are linked via interface blocks. The latter are reordered and collected in a virtual block  $\mathbf{A}^{\Gamma\Gamma}$ . Fig. 1 shows the reordered matrix  $\mathbf{A} = E\mathbf{I} - \mathbf{H}_S - \Sigma_{\mathbf{R}}(E) - \Sigma_{\mathbf{L}}(E)$  due to processor subdivision after row and column permutations.  $\mathbf{H}_S$  is the tight-binding Hamiltonian matrix and  $\Sigma_{\mathbf{K}}(E) = \mathbf{V}_{\mathbf{K}}^\dagger \mathbf{G}_{\mathbf{K}}(E) \mathbf{V}_{\mathbf{K}}$  the self-energy matrices due to the left ( $\mathbf{K} = \mathbf{L}$ ) and right ( $\mathbf{K} = \mathbf{R}$ ) reservoir. Then a parallel block Gaussian elimination is performed to calculate the Schur's complement  $\mathbf{S} = \mathbf{A}^{\Gamma\Gamma} - \mathbf{A}^{\Gamma\mathbf{I}}(\mathbf{A}^{\mathbf{II}})^{-1}\mathbf{A}^{\mathbf{II}\Gamma}$  and the final required Green's function is evaluated by using a cyclic reduction algorithm. In ref. [2] we formulate the parallel RGF algorithm.

## PERFORMANCE ANALYSIS

In this section a performance analysis of our algorithm will be presented with respect to a rectangular billiard, as the one shown in Fig. 2. The efficiency  $F$  of the parallel algorithm will be the ratio of the

cost of simulating the parallel algorithm on a single processor over the cost of the sequential algorithm, i.e.,

$$F = \frac{7NM^3}{p \left( 7\frac{N}{p}M^3 + 5 \log_2(p)M^3 \right)} \quad (1)$$

The cost of the parallel algorithm is defined by the dominant numerical operations of matrix multiplications and inversions and is attributed to the algorithms of the parallel block Gaussian elimination and cyclic reduction. Fig. 3 shows the efficiency for the rectangular billiard of Fig. 2 discretized on a  $400 \times 250$  lattice. To do the measurements we have kept the size of the lattice fixed and increase the number of processors. We observe that the measurements agree very well with the model of equation (1). At this point we would like to remark that the setup addressed here corresponds to a perfectly load balanced problem since the total numerical cost is distributed equally to each processor.

## ACKNOWLEDGMENTS

P.S.D. acknowledges financial support from DFG in the framework of the International Graduiertenkolleg IGK 710 "Complex processes: Modeling, Simulation and Optimization".

## REFERENCES

- [1] S. Datta, *Electronic Transport in Mesoscopic Systems*, Cambridge University Press (1995).
- [2] P.S. Drouvelis, P. Schmelcher and P. Bastian, *Parallel implementation of the recursive Green's function method*, acc. f. publication to the Journal of Computational Physics, available from <arXiv:cond-mat/0507415>

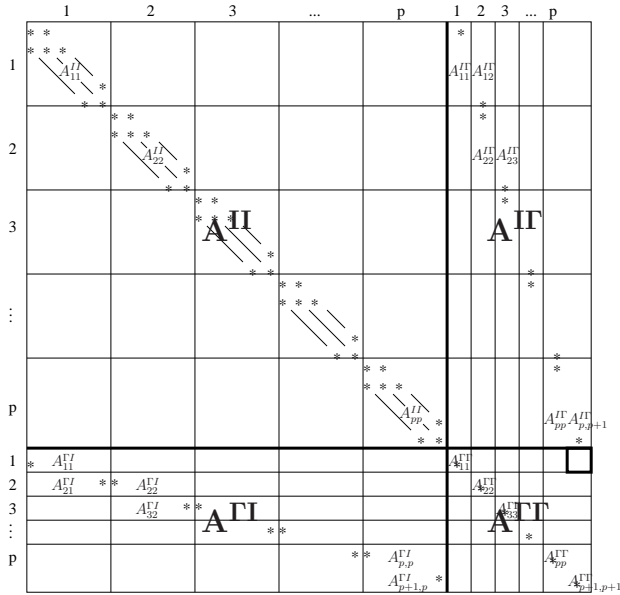


Fig. 1. Reordered matrix  $\mathbf{A} = E\mathbf{I} - \mathbf{H}_S - \Sigma_R(E) - \Sigma_L(E)$  due to processor subdivision after row and column permutations.

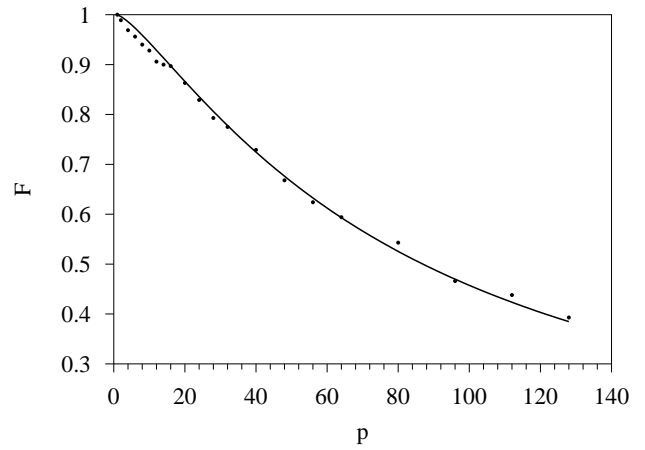


Fig. 3. Efficiency  $F$  as a function of the number  $p$  of processors. The dots correspond to the measured efficiency and the solid curve to the theoretical model employed by equation (1).

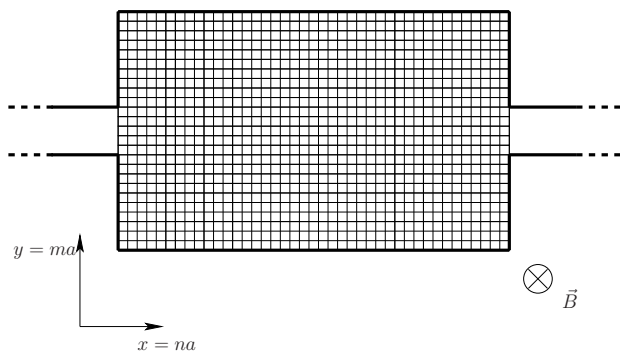


Fig. 2. Setup of a rectangular billiard attached to two reservoirs, discretized on a lattice with  $n = 0, 1, \dots, N - 1$  slices of  $m = 0, 1, \dots, M - 1$  sites each. The ratio of the two dimensions is  $\frac{N}{M} = \frac{8}{5}$ .

# Simulation of a Resonant Tunneling Diode using an Entropic Quantum Drift-Diffusion Model

P. Degond, \*S. Gallego and F. Méhats

MIP, Université Paul Sabatier, 118 Route de Narbonne, 31062 Toulouse Cedex 4 (France)

\*email : gallego@mip.ups-tlse.fr

## PRESENTATION OF THE MODEL

We present a new quantum diffusive model derived in [1], [2] and studied in [3]: the entropic Quantum Drift-Diffusion model (eQDD) is a quantum fluid model describing the evolution of the electron density  $n(t, x)$  subject to the electrical potential  $V(t, x)$  and interacting with a thermal bath of fixed temperature  $T$ . The first equation is the equation of mass conservation and reads:

$$e\partial_t n - \operatorname{div} j = 0, \quad (1)$$

where  $e$  is the positive electron charge and  $j$  is the current defined as follows:

$$j = e\mu n \nabla(A - V). \quad (2)$$

In this equation,  $\mu$  is the electron mobility. We call  $A(t, x)$  the quantum chemical potential which is linked to the density of electrons by a relation which is non local in space and which is the key of this quantum model:

$$n[A] = \sum_{p \geq 1} \exp\left(-\frac{\lambda_p[A]}{k_B T}\right) |\psi_p[A]|^2. \quad (3)$$

Here  $k_B$  is the Boltzmann constant and  $(\lambda_p, \psi_p)_{p \geq 1}$  are the eigenvalues and the normalized eigenfunctions of the following modified Hamiltonian:

$$H[A] = -\frac{\hbar^2}{2} \operatorname{div} \left( \frac{1}{m(x)} \nabla \right) - eA, \quad (4)$$

where  $\hbar$  is the Planck constant and  $m$  is the effective mass of an electron.

We show in the presentation some formal links between the eQDD model and several other models. Indeed, the limit of the eQDD model as the dimensionless Planck constant goes to zero is the Classical Drift-Diffusion model, while the leading order correction term is the Bohm potential appearing in the Density-Gradient model.

## NUMERICAL RESULTS

The 1D transient eQDD model coupled to the Poisson equation is discretized in time using a semi-implicit Euler scheme and we discretize the space variable using finite-differences. This scheme is solved with the Newton algorithm and we check that we can capture some well known features of the resonant tunneling diode: fig.1 shows the time evolution of the density from the peak to the valley. To obtain this figure, we apply a voltage of  $0.25V$  and wait for the electrons to achieve the stationary state. Then we suddenly change the value of the applied bias to  $0.29V$  and we record the evolution of the density. As expected, the density inside the well grows significantly. Fig.2 shows the evolution of the current density at the left contact and we can observe one oscillation before the stationary state is achieved.

Fig.3 shows the influence of the effective mass on the current voltage characteristics. As noted for the Density-Gradient model, this parameter must be artificially increased to obtain resonance but this figure shows also the importance of the effective mass inside the barriers, where the notion of effective mass is questionable.

We also show in the presentation some qualitative and quantitative comparisons with the Density-Gradient model and some interesting and unexpected differences are pointed out.

## REFERENCES

- [1] P. Degond, F. Méhats and C. Ringhofer, *Quantum Energy-Transport and Drift-Diffusion models*, J. Stat. Phys., **118**, 3/4 (2005)
- [2] P. Degond, F. Méhats and C. Ringhofer, *Quantum hydrodynamic models derived from the entropy principle*, Contemporary Mathematics, **371** (2005)
- [3] S. Gallego and F. Méhats, *Entropic discretization of a Quantum drift-diffusion model*, SIAM journal on numerical analysis, **43**, 5 (2005)

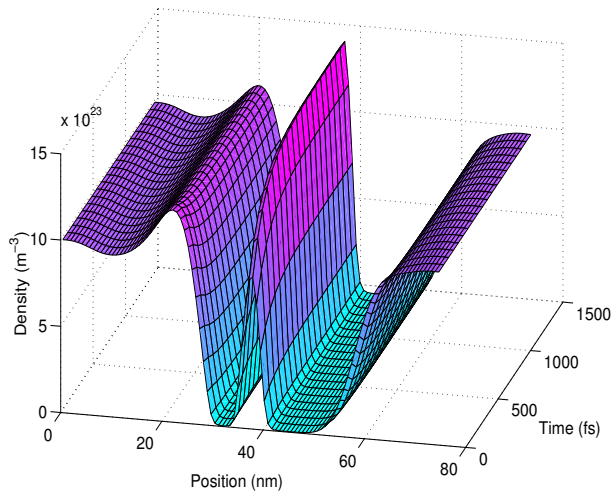


Fig. 1. Evolution of the density from the peak to the valley.

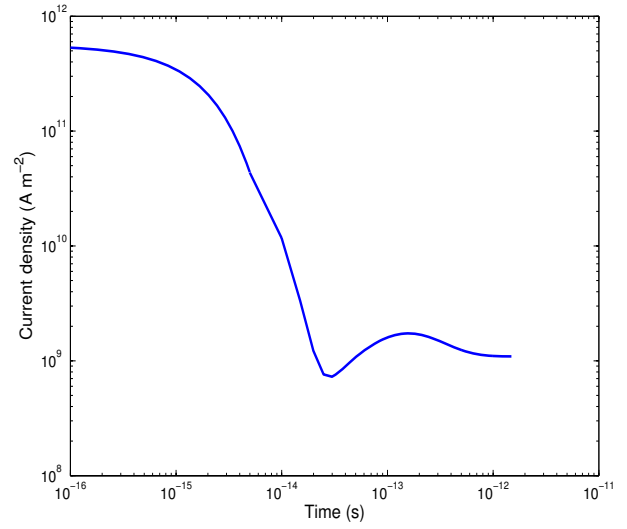


Fig. 2. Evolution of the current density at the left contact

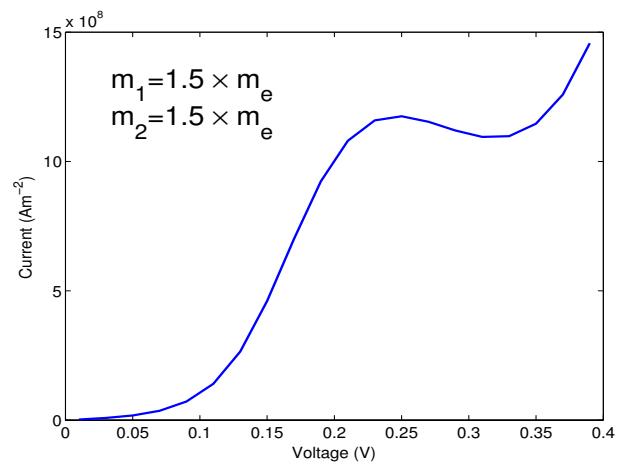
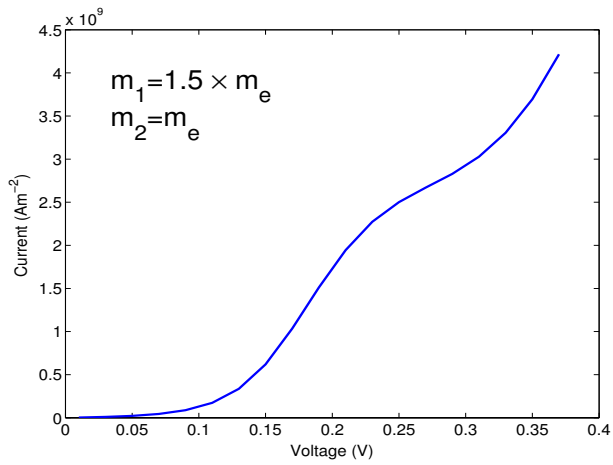
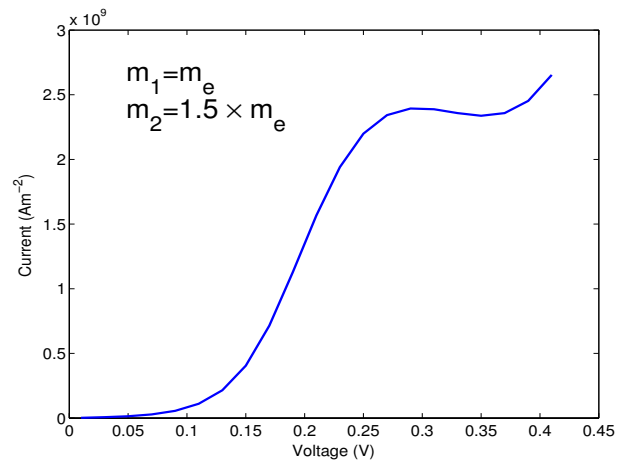
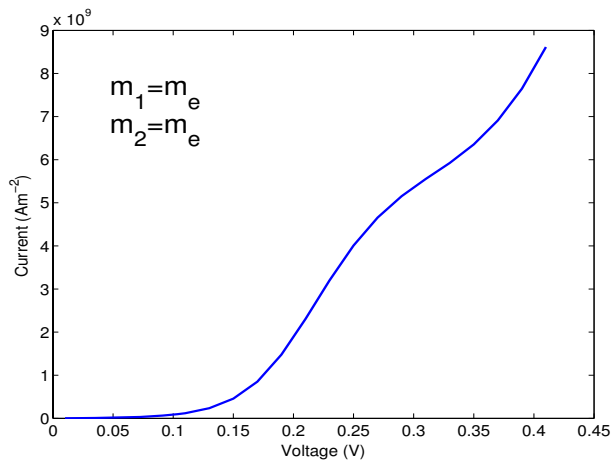


Fig. 3. Influence of the effective mass on the IV curve,  $m_1$  being the mass outside the barriers and  $m_2$  the mass inside.

# Quantum Transport Through Nano-Wires with One-Sided Surface Roughness

J. Feist,<sup>\*</sup> A. Bäcker,<sup>†</sup> R. Ketzmerick,<sup>†</sup> S. Rotter,<sup>\*</sup> B. Huckestein,<sup>‡</sup> and J. Burgdörfer<sup>\*</sup>

<sup>\*</sup>Institute for Theoretical Physics, TU-Vienna, A-1040 Vienna, Austria

<sup>†</sup>Institute for Theoretical Physics, TU-Dresden, D-01062 Dresden, Germany

<sup>‡</sup>Institute for Theoretical Physics III, Ruhr-University Bochum, D-44780 Bochum, Germany

e-mail: feist@concord.itp.tuwien.ac.at

Disordered media and their transport properties are a central issue in solid state physics, as they are the root of numerous applications in electronics and optics [1], [2]. New experimental possibilities to investigate this field in the 'mesoscopic' regime have led to an increased interest in the classical-to-quantum crossover regime of transport where a whole new class of interesting phenomena has meanwhile been discussed [3].

In most investigations a static disorder is assumed to be present in the *bulk* of a material. The theoretical analysis of bulk disordered systems typically employs random matrix theory (RMT) [4], which has proven to be a very successful description. The formation of ballistic, diffusive, and localized transport regimes, as well as any dependence on the density of scatterers and the wire length can be studied. Reduction of system sizes leads, however, to an increased surface-to-volume ratio in nano-devices, such that *surface roughness* can be the dominant source of disorder scattering. The application of RMT to systems with surface disorder is, however, not straightforward, as different transport regimes can coexist with each other, depending on the angle (mode number) of the injected particle (wave) [5].

Using the modular recursive Green's function method [6], we numerically study electronic quantum transport through extremely long nano-wires in the presence of a one-sided surface roughness and a magnetic field. We demonstrate how these two effects conspire to keep the conductance at a high value throughout vast length scales of the wire. In the quantum-to-classical crossover of high Fermi energies ( $E_F \rightarrow \infty$ ) this effect leads to exponentially diverging localization lengths.

Complementing previous investigations [7] we

argue that the giant localization length found numerically falls clearly outside the scope of RMT predictions, but can be well understood in terms of the underlying mixed regular-chaotic classical motion which electrons are subject to in such a system. As we demonstrate by an analytical calculation, this effect can quantitatively be accounted for by dynamical tunneling between the transporting regular and chaotic parts of the underlying mixed classical phase space [9], [10]. We thereby establish a direct link between experimentally accessible transport quantities like the conductance and "dynamical tunneling".

## ACKNOWLEDGMENTS

Support by the Austrian Science Foundation (Grants No. FWF-SFB016 and No. FWF-P17359) is gratefully acknowledged.

## REFERENCES

- [1] P. Sheng, *Introduction to Wave Scattering, Localization and Mesoscopic Phenomena* (Academic, New York, 1995).
- [2] P. A. Lee and T. V. Ramakrishnan, *Rev. Mod. Phys.* **57**, 287 (1985).
- [3] D. K. Ferry and S. M. Goodnick, *Transport in Nanostructures* (Cambridge University Press, Cambridge, 1997).
- [4] C. Beenakker, *Rev. Mod. Phys.* **69**, 731 (1997).
- [5] J. A. Sanchez-Gil, V. Freilikher, I. Yurkevich, and A. A. Maradudin, *Phys. Rev. Lett.* **80**, 948 (1998).
- [6] S. Rotter, B. Weingartner, N. Rohringer, and J. Burgdörfer, *Phys. Rev. B* **68**, 165302 (2003).
- [7] A. García-Martín, M. Governale, and P. Wölfle, *Phys. Rev. B* **66**, 233307 (2002).
- [8] H. Schanz, M. F. Otto, R. Ketzmerick, and T. Dittrich, *Phys. Rev. Lett.* **87**, 070601 (2001).
- [9] L. Hufnagel, R. Ketzmerick, M.-F. Otto, and H. Schanz, *Phys. Rev. Lett.* **89**, 154101 (2002).
- [10] A. Bäcker, R. Ketzmerick, and A. G. Monastera, *Phys. Rev. Lett.* **94**, 054102 (2005).

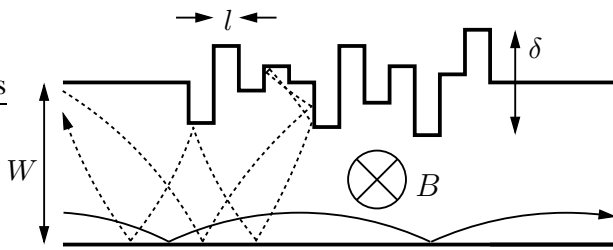


Fig. 1. Wire with one-sided surface disorder (top wall) in a magnetic field  $B$ . The strength of the disorder is governed by  $\delta/W$ . Two typical (classical) electron trajectories are shown: A trajectory injected at a low angle (solid line) skips along the lower boundary and, avoiding contact with the disorder, gets transmitted. Injection at a steeper angle (dashed line) leads to disorder scattering and reflection.

# Coupled Mode Space versus Real Space Approach for the Simulation of CNT-FETs

G. Fiori, G. Iannaccone, and G. Klimeck \*

Dipartimento di Ingegneria dell'Informazione, Università di Pisa, 56100 Pisa, Italy

\*School of Electrical Engineering, Purdue University, West Lafayette, IN USA.

Carbon Nanotube Field Effect Transistors (CNT-FETs) are considered a promising alternative to CMOS technology at end of the ITRS Roadmap [1]. Fabrication technology still poses serious challenges, such as the selection of semiconducting CNTs, the poor control of the contacts and the large CNT diameter dispersion. As with silicon technology, device simulation tools capable to address very general structures with limited computational resources, can represent a precious tool to explore device architectures, and provide fabrication guidelines. In this work, we present a three-dimensional code that can deal with general architectures, based on the self-consistent solution of the Poisson and Schrödinger equations, within the NEGF formalism, using a tight-binding Hamiltonian with an atomistic ( $p_z$ -orbitals) basis set both in the real [2] and in the mode space, by means of the Recursive Green's Functions method. In particular, the mode space approach is based on the reduction of the order of the real space Hamiltonian matrix, by means of a simple basis transformation. Compared to other mode space approaches, the one we propose intrinsically includes intersubband scattering, which is present when the coaxial symmetry of the potential is broken.

The simulated device has the structure depicted in Fig. 1 : the CNT is embedded in  $\text{SiO}_2$ , and  $n$ -doped CNT extensions at the source and drain ends are considered. In Fig. 2 we show the transfer characteristics of a (10,0) CNT with oxide thickness  $t_{ox} = 1$  nm and channel length  $L = 10$  nm, computed with the real (solid line) and the mode space approach considering only 2 modes (circles). As can be noticed, for this kind of structure, the results obtained with the two different approaches give the same results, since only the first two subbands contribute to electron transport. In Fig. 3 the time required to solve the Schrödinger equation with

NEGF for 1684 values of energy on a 1.8 GHz AMD Athlon 64 bit processor is shown. The mode space approach with an analytical expression for the self-energy [3] is 5 times faster than the real space approach (analytical self-energy) when 2 modes are considered, whereas it is slower when 10 modes are considered, due to the additional operation required by the basis transformation. As can be seen, when iterative methods [4] are used for the calculation of the self-energy, the computing time is much larger. For the real space we have for example encountered a speed enhancement of almost a factor of 4. In Fig 4, the transfer characteristics of a (25,0)  $L = 7$  nm CNT computed with the real space and mode space (4 modes) approach are compared. Here, the advance in terms of computing time is more significant, as shown in Fig. 5 since the number of atoms in the carbon ring (which determines the complexity of the problem) is much larger than the number of modes.

In conclusion, the coupled mode space approach results to be an efficient and accurate approach for the investigation of CNT device architectures with reduced computational cost. The authors gratefully acknowledge Prof. Mark Lundstrom for his support during this work. We also gratefully acknowledge support from the EU through the Network of Excellence SINANO (EC Contract n. 506844), and NSF grant # EEC-0228390.

## REFERENCES

- [1] International Technology Roadmap for Semiconductor 2005. Available : <http://public.itrs.net>.
- [2] G. Fiori, G. Iannaccone and G. Klimeck, *Performance of Carbon Nanotube Field Effect Transistors with doped source and drain extensions and arbitrary geometry*, IEDM Tech. Dig., (2005).
- [3] Neophytos Neophytou, *private communications*.
- [4] M. P. Lopez and L. Rubio, *Highly convergent schemes for the calculation of bulk and surface green function*, J. Phys. F., **15**, 851, (1985).

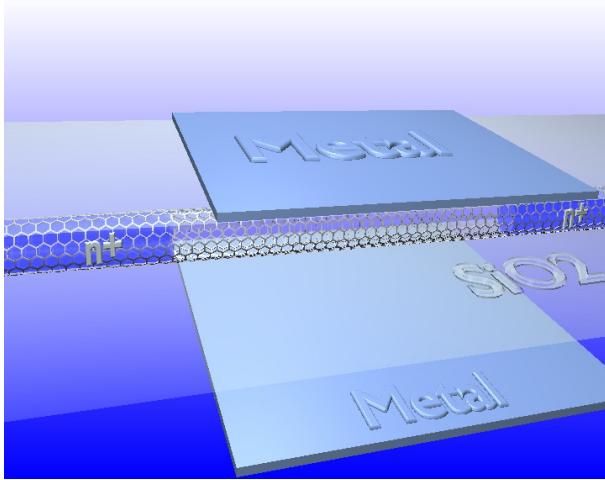


Fig. 1. Simulated device architecture: double gate CNT FET with  $\text{SiO}_2$  dielectric and metal gates,  $n$ -doped source and drain extensions.

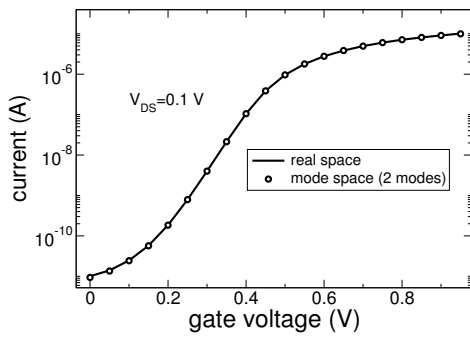


Fig. 2. Transfer characteristics for a (10,0) CNT with  $t_{ox} = 1$  nm and  $L = 10$  nm computed with the real space and mode space approach (two modes).

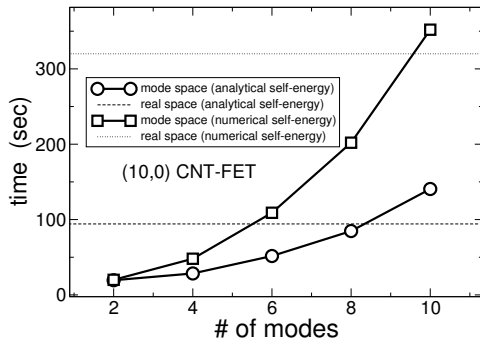


Fig. 3. Time required to solve the Schrödinger equation with NEGF in a CNT with 10 atoms per ring, 280 rings, on a 1.8 GHz AMD Athlon 64 bit processor, as a function of the number of modes with analytical self-energy (circles) and numerical self-energy (squares). The dashed line represents the time required with the real space approach.

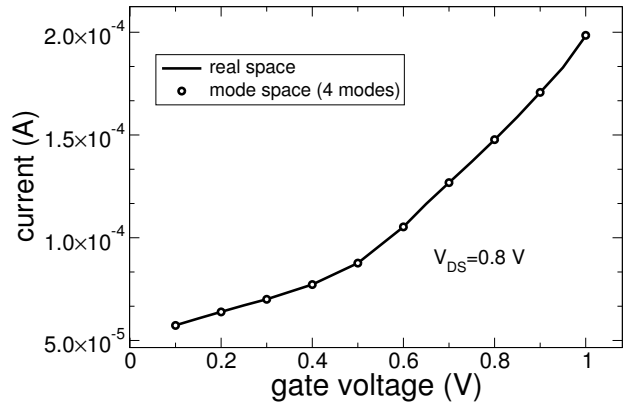


Fig. 4. Transfer characteristics of a  $L = 7$  nm (25,0) CNT-FET computed with the real space and the mode space approaches (four modes).  $V_{DS} = 0.8$  V.

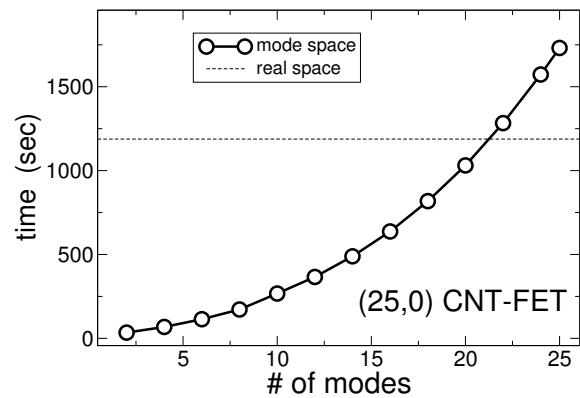


Fig. 5. Time required to solve the Schrödinger equation in a CNT with 25 atoms per ring, and 358 rings, on a 1.8 GHz AMD Athlon 64 bit processor, as a function of number of modes. The dashed line represents the computing time required by the real space approach.

# Scattering-Dependence of Bias-Dependent-Magnetization-Switching in Ferromagnetic Resonant Tunneling Diodes

Swaroop Ganguly, A.H.MacDonald,\* L.F.Register, and S.K.Banerjee  
Microelectronics Research Center, University of Texas at Austin, TX 78758, USA.  
Department of Physics, University of Texas at Austin, TX 78712, USA.  
Email: swaroop@ece.utexas.edu

It has been predicted on the basis of ballistic quantum transport theory and simulation that the Curie temperature ( $T_C$ ) of a ferromagnetic resonant tunneling diode (FRTD) – i.e. an RTD with a dilute ferromagnetic semiconductor (DFS) well – will switch with increasing bias voltage ( $V$ ) from its equilibrium value to nearly zero in two steps [1]. Here we study the effect of scattering on the magnetization switching in this system. Quantum transport in the Keldysh formalism, including the phenomenological Buttiker probe scattering model, is simulated self-consistently with the Poisson equation for electrostatics; together with the mean-field description of ferromagnetism in DFS materials, this yields the  $T_C - V$  characteristics of an FRTD.

The scattering strength is varied and its effect on the  $T_C - V$  and  $I - V$  characteristics shown in Fig. 1 and Fig. 2 respectively. Transport in an RTD can be classified into three regimes by scattering strength [2]. The first is the ‘coherent transport’ regime where the broadening of the transmission peak due to the left and right barriers, shown in Fig. 3, is much greater than the broadening due to scattering. This corresponds to the least scattering and the sharpest  $T_C - V$  profile. When the broadening due to scattering is greater than the ‘coherent broadening’, we have the ‘sequential transport’ regime. We see that, in this case, the steps are smoothed out but discernible. At still stronger scattering, one enters the regime where the resonance in the well is completely

destroyed, as evidenced by the disappearance of the negative differential resistance (NDR) region in the  $I - V$  curve and the steps in the  $T_C - V$ . It is seen from Fig. 1 that the first step in the  $T_C - V$  is almost completely washed out somewhere between the second and third regimes – the relative robustness of the second transition can be explained on the basis of the asymmetry in the barriers at non-zero bias. The decrease in the equilibrium  $T_C$  with scattering is seen to be specific to our choice of device parameters; the broadening of the density of states (DOS) moves more of it outside the range of filled states, and decreases the contribution to the spin susceptibility, as seen from Fig. 4.

Finally, by correlating the scattering time to a bulk mobility, we see that it would require much larger than typical [3] scattering for the device to enter the sequential regime. This augurs well for the experimental observability of the magnetization switching effect.

<sup>1</sup> Swaroop Ganguly, L.F. Register, S. Banerjee and A.H. MacDonald, *Phys. Rev. B* **71**, 245306 (2005).

<sup>2</sup> S. Datta, *Electronic Transport in Mesoscopic Systems* (Cambridge University Press, 1995); Chapter 6.

<sup>3</sup> B.D. McCombe, X.Liu *et al.*, [http://mccombe.physics.buffalo.edu/miscdoc/GaAs-Mn\\_Transport.pdf](http://mccombe.physics.buffalo.edu/miscdoc/GaAs-Mn_Transport.pdf), (2004). A typical measured mobility is  $2700\text{cm}^2\text{V}^{-1}\text{s}^{-1}$ , with the measured effective mass having the heavy hole mass value.

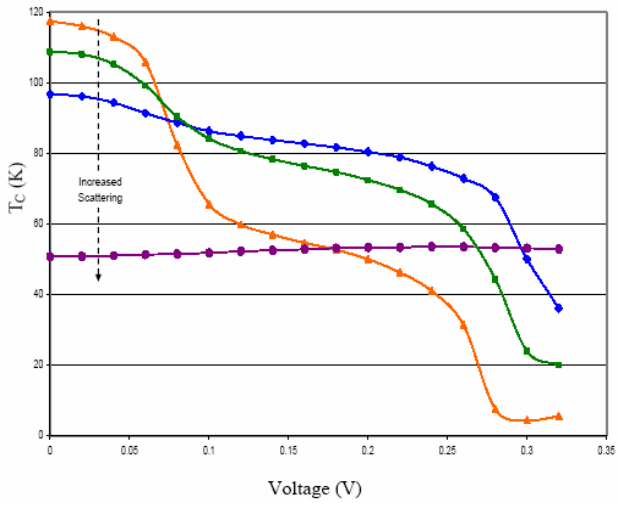


Fig. 1.  $T_C$ -V curve for ferromagnetic RTD in the presence of scattering. Scattering is modeled with Buttiker probes with associated lifetime  $\tau = \infty$  (orange triangles) - coherent, 41fs (green squares) - sequential, 16.4fs (blue diamonds), and 2.5fs (violet discs) - no resonance. Note that the first step in the  $T_C$ -V is much more broadened out than the second.

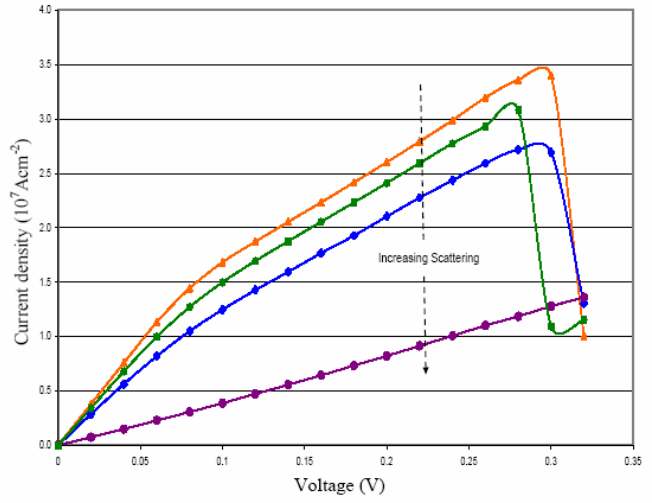


Fig. 3. I-V curve for ferromagnetic RTD in the paramagnetic regime in the presence of scattering. Scattering is modeled with Buttiker probes with associated lifetime  $\tau = \infty$  (orange triangles), 41fs (green squares), 16.4fs (blue diamonds), and 2.5fs (violet discs).

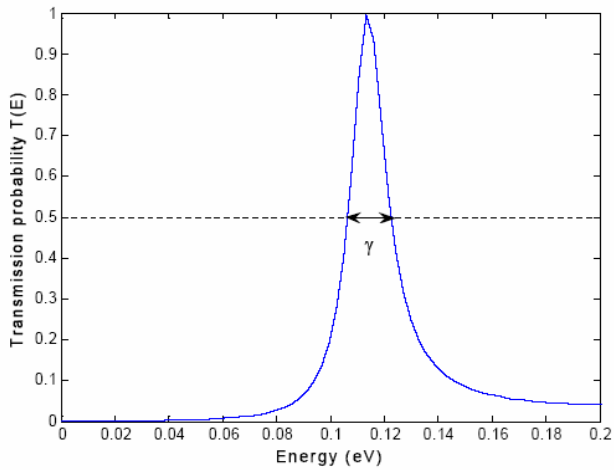


Fig. 2. Transmission probability vs. energy for the RTD in equilibrium in the absence of scattering. This is used to calculate the 'coherent broadening'  $\gamma$  - that due to the barriers - as shown.

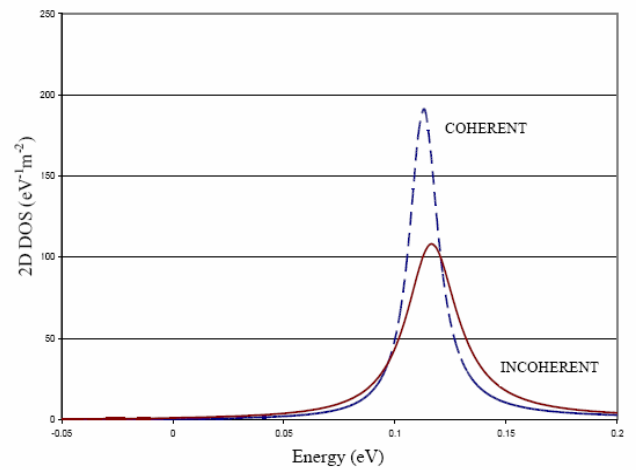


Fig. 4. Equilibrium 2D DOS vs. energy in the well region of the RTD with and without scattering. A large fraction of the DOS in the coherent case (broken blue) is seen to be within the chemical potential  $\mu=0.15$ eV than in the incoherent or sequential case (solid red). This gives a larger spin density, and hence  $T_C$  in equilibrium for the coherent case.

# Numerical Simulations of Propagation of SCWs in Strained Si/SiGe Heterostructure at 4.2 and 77 K

Abel Garcia-B<sup>1</sup>, Volodymyr Grimalsky<sup>1</sup>, and Edmundo Gutierrez-D<sup>2</sup>  
<sup>1</sup>Electronics Department, INAOE, P.O. Box 51 and 216, Puebla, Pue., Mexico  
<sup>2</sup>INTEL-SRCM, Guadalajara, Mexico  
e-mail: agarciab@inaoep.mx

## ABSTRACT

The propagation and amplification of space charge waves (SCWs) in a strained Si/SiGe heterostructure at 4.2 and 77 K has been studied by means numerical simulations, using the negative differential conductance phenomenon. The results indicate the possibility of a major amplification of SCWs on the surface of this heterostructure at 4.2 K, until frequencies  $f < 44$  GHz at 4.2 K and  $f < 40$  GHz at 77 K.

## INTRODUCTION

High-speed heterostructure device is a new topic to high speed semiconductor devices, but how almost all modern technology is Si-based, the high-speed heterostructure also need to be compatible with Si. In this paper, we present 2D simulations of propagation and amplification of space charge waves in a strained Si/SiGe heterostructure at 4.2 and 77 K, using the negative differential conductance phenomenon described in [1]. The two-dimensional electron gas is in a strained Si (100) layer on relaxed SiGe substrate. We have used the quasi-hydrodynamic model added by the Poisson's equation to describe non-stationary carrier transport, which incorporates the population transfer between two different valleys, the lower and upper valleys. The model used is two-valley model, which is described in [2]. It uses two-dimensional electron gas model and with numerical simulations based on solving a set of nonlinear partial differential equations for non-local carrier transport and the Poisson's equation for electric field can be simulated the propagation of space charge waves. These results are very import because they explain the physical and mathematical models of space charge wave excitation, propagation, interaction and reception in such heterostructure.

## ELECTRON TRANSPORT

Fig. 1 shows the strained Si/SiGe heterostructure. The excitation of space charge waves takes place in the input coupling element (input antenna, 1) at a frequency of the microwave range and the amplified space charge waves are received in the output coupling element (output antenna, 2) on the plane of strained Si/SiGe layer.

The following parameters have been chosen: 2D concentration of electrons in the film is  $n_0 \approx 10^{12}$  cm<sup>-2</sup>, the initial uniform drift velocity of electrons is  $V_0 \approx 1.7 \times 10^7$  cm/s ( $E_0 = 10$  to 11.7 kV/cm), the length of the film is  $L = 10$   $\mu$ m, the thickness of the film is  $2h = 0.5$   $\mu$ m.

Fig. 2 shows the calculated steady-state drift velocity as a function of electric field at 4.2 and 77 K, where negative differential conductivity appears beyond 10 kV/cm. This is due to the transition of electrons from twofold valley to the fourfold valley where the effective mass is heavier.

## DISCUSSION AND RESULTS

In [3] we showed the possibility of amplification of space charge waves in a strained Si/SiGe heterostructure at 77 K with all details, but now we make analysis at 4.2 K too. Fig. 3 and fig. 4 show the typical output spectrum of the electromagnetic signal at 77 and at 4.2 K, respectively. It happens when a small microwave electric signal  $E_{ext} = E_m \cdot \sin(\omega t) \cdot \exp(-((t-t_1)/t_0)^2) \cdot \exp(-(z-z_1)/z_0)^2$  is applied in the input antenna and the excitation of space charge waves in 2D electron gas takes place. The input carrier frequency is  $\omega = 8 \times 10^{10}$  rad/s. The amplitude of the input electric microwave signal is  $E_m = 0.025$  kV/cm. Here  $z_1$  is a position of the input antenna,  $z_0$  is its half-width, therefore, the parameter  $2t_0$  determines the duration of the input electric pulse. In our simulations the duration of the input

pulse is  $2t_0 = 2.5$  ns. The maximum of the input pulse occurs at  $t_1 = 2.5$  ns. One can see both the amplified signal at the first harmonic of the input signal and the second harmonic of the input signal, which is generated due to nonlinearity of space charge waves.

Fig. 5 shows the alternative part of the electron concentration  $\tilde{n}/n_0$ , where  $n_0$  is the concentration in equilibrium  $n_0 \approx 10^{12}$  cm<sup>-2</sup>. The maximum variation is in the output coupling element.

### CONCLUSION

We show the propagation and amplification of space charge waves in a strained Si/SiGe heterostructure at 4.2 and 77 K by numerical simulations. We have a major amplification at 4.2 K, it is due to the dynamic range in the negative differential conductance. Furthermore, the scope of space charge waves applications is not limited to the device here described, but can be useful to monolithic phase shifters, delay lines, as well as analog blocks for microwave signals.

### ACKNOWLEDGEMENT

The authors wish to acknowledge the support of this work by CONACyT Mexico in the frame of their research projects and by the PhD's scholarship #165390.

### REFERENCES

- [1] Kazuo Miyatsuji, Daisuke Ueda and Kazuo Masaki, "High-field transport of hot electrons in strained Si/SiGe heterostructures", *Semicond. Sci. Technol.* 9 (1994) 772-774.
- [2] Roblin Patrick and Rohdin Hans, "High-Speed Heterostructure Devices" Cambridge University, UK, 2002.
- [3] Abel Garcia-B, Volodymir Grimalsky, Edmundo Gutierrez, "Amplification of Space Charge Waves in a Strained Si/SiGe Heterostructure at 77 K". In *Proc. IEEE-CONIELECOMP2006*, in press.

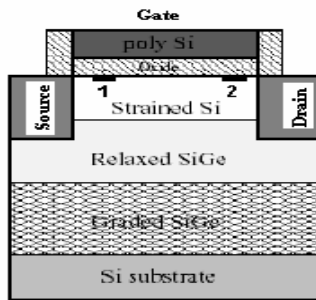


Fig. 1. Cross-section of the strained Si/SiGe heterostructure, 1 and 2 are input and output antenna respectively.

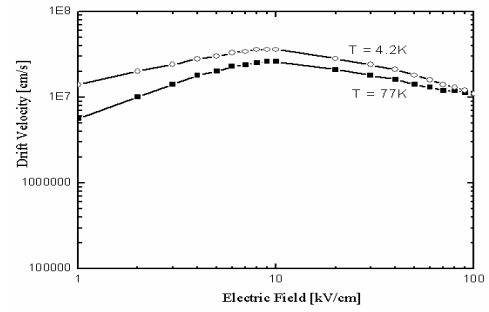


Fig. 2. Steady-state drift velocity as a function of electric field in strained Si/SiGe heterostructure at 4.2 and 77 K.

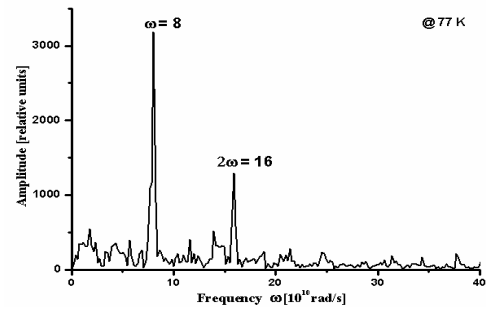


Fig. 3. Spectral components of the electric field of space charge wave at the output antenna with an excitation input signal ( $\omega = 8 \times 10^{10}$  rad/s) at 77 K.

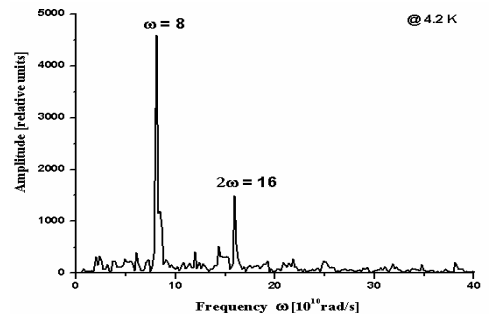


Fig. 4. Spectral components of the electric field of space charge wave at the output antenna with an excitation input signal ( $\omega = 8 \times 10^{10}$  rad/s) at 4.2 K.

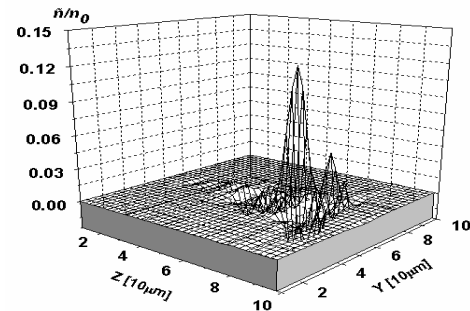


Fig. 5. The spatial distribution of the alternative part of the electron concentration  $\tilde{n}$ .

# Phonon Exacerbated Quantum Interference Effects in III-V Nanowire Transistors

M.J. Gilbert

Microelectronics Research Center, University of Texas at Austin, Austin, TX 78758  
e-mail: mgilbert@mer.utexas.edu

## Abstract

In recent years, a great deal of attention has been focused on the development of quantum wire transistors [1,2] as a means of extending Moore's Law. Here we present, results of fully three-dimensional, self-consistent quantum mechanical device simulations of InAs tri-gate quantum wire transistors. The effects of inelastic scattering have been included as real-space self-energy terms [3]. We find that the position of dopant atoms in these devices can lead to significant departures in performance when inelastic processes are considered.

## Device Structure

In Fig. 1, we show a schematic of the device geometry under consideration. Here the exact device dimensions (multiples of the lattice constant) have been included in this simulation to aid in the inclusion of the discrete dopants. In each device that we consider, the channel length is 9.69 nm, the thickness of the InAs layer is 9.09 nm, and the channel width is 8.5 nm. The source and drain of the device are *n*-type with a doping density of  $6 \times 10^{18} \text{ cm}^{-3}$ , while the channel of the device is considered to be *p*-type, but undoped. The gate material is assumed to be platinum and the gate oxide on each side is composed of 1 nm of hafnium oxide ( $\text{HfO}_2$ ). Underneath the device, we have assumed a generic insulating substrate.

## Results and Discussion

In Fig. 2, we plot the  $I_d$ - $V_g$  characteristics for an InAs quantum wire transistor both in the case of only impurity scattering and with the effects of polar optical phonons, intervalley ( $\Gamma \rightarrow X$  and  $\Gamma \rightarrow L$ ) phonons and acoustic deformation potential scattering. Here, we see that the current is not too terribly degraded from the elastic case to including

inelastic processes. Speaking strictly from a device standpoint, the devices with inelastic process included tended to have better subthreshold swing and  $I_{\text{on}}/I_{\text{off}}$  ratios than did the devices with elastic processes. This is due to the fact that the scattering in the source is relatively weak thereby producing reductions  $I_{\text{off}}$  but not significantly limiting  $I_{\text{on}}$ .

In Fig. 3, we plot where several dopants in the source of the device lie in the middle of the semiconductor close to the channel entrance. As a result, the carriers entering the channel of the device have their incident energy significantly altered. The carriers now see a significant increase in the amount of scattering they undergo before entering the channel causing a major reduction in current.

In Fig. 4(a) and (b) we plot the electron density in the middle of the device for the elastic and inelastic cases respectively. Clearly as a result of the increased scattering, the electrons begin to pile up in the source around the potential spikes near the channel entrance in the inelastic case. Furthermore, we also see a reduced electron density in the channel and the drain of the device as a result of the backscattering near the channel entrance.

We confirm this assertion in Fig. 5, where we plot the difference in potential between the elastic and inelastic cases of this device. We find that charge density increases of  $\sim 0.38 k_B T$  in the source of the device and decreases of  $0.38 k_B T$  in the channel and drain corresponding to increases or decreases in charge density of one-half order of magnitude.

\*This work is supported by NRI, Intel Corporation, SRC, ONR, and AMRC

## REFERENCES

- [1] R. Chau *et al.*, IEEE Trans. Nano. **4**, 153 (2005).
- [2] M.J. Gilbert and D.K. Ferry, J. Appl. Phys, Accepted for publication.
- [3] M.J. Gilbert, R. Akis, and D.K. Ferry, J. Appl. Phys. **98**, 094303 (2005).

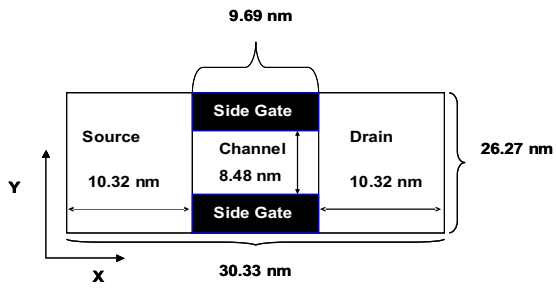


Fig. 1. Schematic of the device geometry in the  $x$ - $y$  plane

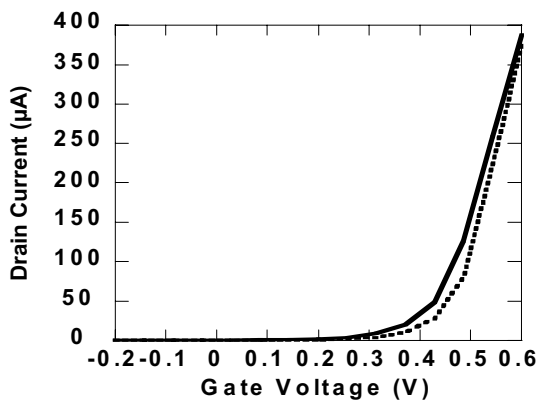


Fig. 2.  $I_d$ - $V_g$  curves for an InAs tri-gate quantum wire transistor with elastic (solid) and inelastic (dotted) scattering included.

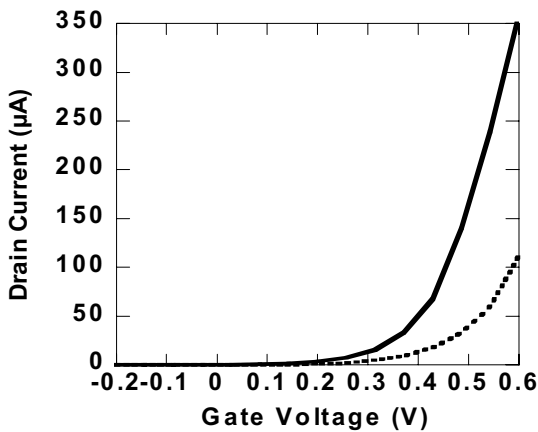


Fig. 3. Sample  $I_d$ - $V_g$  curves for an InAs tri-gate quantum wire transistor with elastic (solid) and inelastic (dotted) scattering included. Here the dopants reside close to the channel entrance.

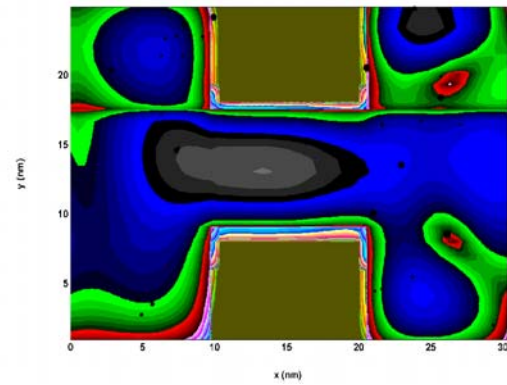


Fig. 4(a). Electron density at  $V_g = 0.6$  V and  $V_d = 0.6$  V taken at a depth of 7 nm into the device with only elastic processes included.

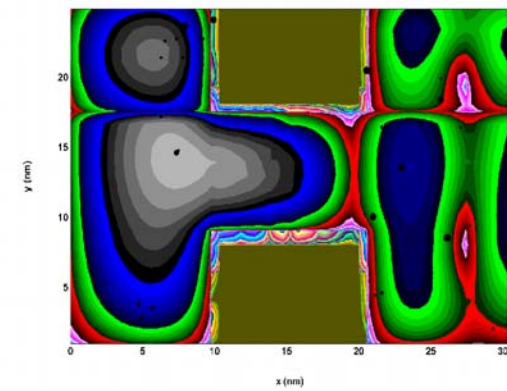


Fig. 5. Electron density at  $V_g = 0.6$  V and  $V_d = 0.6$  V taken at a depth of 7 nm into the device with elastic and inelastic processes included.

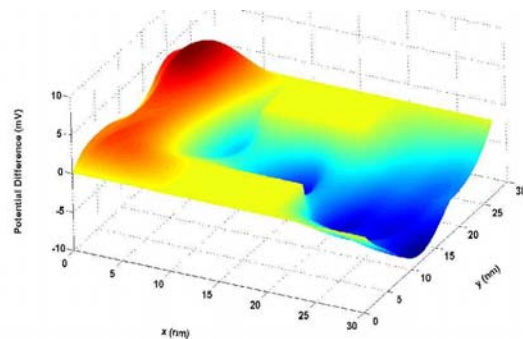


Fig. 6. Potential change at  $V_g = 0.6$  V and  $V_d = 0.6$  V taken at a depth of 7 nm between only elastic and combined processes.

# Quantum-Mechanical Simulation of Multiple-Gate MOSFETs

A. Godoy, A. Ruiz-Gallardo, C. Sampedro, and F. Gámiz  
Universidad de Granada. Departamento de Electrónica y Tecnología de Computadores  
Avda. Fuentenueva s/n, 18071 Granada, Spain  
e-mail: [agodoy@ugr.es](mailto:agodoy@ugr.es)

## ABSTRACT

A self-consistent solution of the 2D Schrödinger-Poisson equations is used to analyze Multiple-gate MOSFETs. Classical simulations overestimate the peak density compared to quantum simulations and therefore the importance of the corner effects. The impact of the corner rounding on the electron distribution has also been analyzed.

## INTRODUCTION

In order to shrink channel lengths into the nanometric range it is necessary to prevent the short channel effects since they degrade the device performance. The use of several gates has demonstrated a good electrostatic control of the channel and therefore the possibility of a higher reduction of the channel length compared to traditional bulk MOSFETs. Structures such as FinFETs, Trigates, Gate All Around (GAA), Pi and Omega-gate MOSFETs are included into the category of Multiple-gate MOSFETs.

## DEVICE SIMULATION

To get a fast convergence, the 2D Schrödinger and Poisson equations have been self-consistently solved using the predictor-corrector scheme proposed by Trellakis et al [1]. This algorithm has been proved as reliable and robust as far as enough number of eigenvalues and eigenfunctions are included in the calculations. In all the simulated devices we have considered an undoped substrate and a metal gate workfunction of  $\phi_m=4.63\text{eV}$ . Fig. 1 shows the classical electron distribution (CED) corresponding to a Trigate MOSFET with silicon height ( $H_{\text{Si}}$ ) and width ( $W_{\text{Si}}$ ) of 10nm, gate oxide thickness ( $T_{\text{ox}}$ ) of 2nm and gate voltage ( $V_G$ ) 1V. Fig. 2 shows the QED for the same structure. Important differences are observed between both figures. The CED is concentrated at the Si-SiO<sub>2</sub>

interface with a maximum at the corner of  $n_{\text{max}}=2\times 10^{20}\text{cm}^{-3}$ . This value is eight times the maximum obtained including quantum effects:  $n_{\text{max}}=2.5\times 10^{19}\text{cm}^{-3}$ . To get these results, the simulator computes a sufficiently high number of energy levels and wave functions. These results could also be applied to evaluate the transport properties of the device. The simulator offers the possibility of specifying the curvature of the silicon substrate corners, and of the surrounding oxide, independently. This fact allows us to study the behaviour of a great amount of geometries, and evaluate the influence of the corner effects. These effects are produced by the coupling between different gates which originates an favourable area for the flow of carriers [2]. This simulator is able to deal with rounded geometries since it employs finite elements. In a first step, a low-resolution mesh is used to compute a preliminary solution. We use this solution to identify the device regions where the mesh has to be refined, and where the mesh could be less dense. This allows us to greatly reduce computational costs. Fig. 3 shows the QED obtained in a Trigate MOSFET with square cross section and  $H_{\text{Si}}=W_{\text{Si}}=20\text{nm}$ ,  $T_{\text{ox}}=2\text{nm}$  and  $V_G=1\text{V}$ . The electron density's maximum is close to the corners. Fig. 4 shows the QED in the same Trigate MOSFET where the upper corners of the silicon slab have been rounded with a curvature radius of 10nm. Now, the electron distribution is more uniform along the Si-SiO<sub>2</sub> interface. Fig. 5 shows the electric field in both devices. For the square cross section a peak is observed in the corners originating a maximum in the electron density.

## CONCLUSIONS

A 2D Schrödinger-Poisson solver applicable to a wide variety of Multiple-gate MOSFET geometries has been developed. Classical simulations clearly

overestimate the peak electron density and the corner effects. We have also shown that corner effects are greatly diminished by the rounding of the substrate corners.

#### ACKNOWLEDGEMENT

This work has been supported in part by the EU (Network of Excellence SINANO and EUROSIOI project) and by the Spanish Government under project FIS2005-06832.

#### REFERENCES

- [1] A. Trellakis, A.T. Galick, A. Pacelli, U. Ravaioli, *Iteration scheme for the solution of the two-dimensional Schrödinger-Poisson equations in quantum structures*, Journal of Applied Physics, **81**(12), 7880-7884, 1997.
- [2] R. Ritzenthaler, O. Faynot, C. Jahan, S. Cristoloveanu, *Corner and Coupling Effects in Multiple-Gate FETs*, Proceedings of the Electrochemical Society, 283-288, 2005.

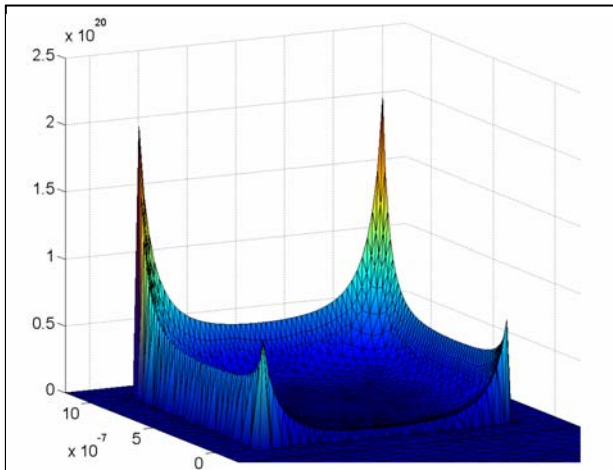


Fig. 1. CED in a Trigate MOS structure with  $H_{Si}=W_{Si}=10\text{nm}$ ,  $T_{ox}=2\text{nm}$  and  $V_G=1\text{V}$ .

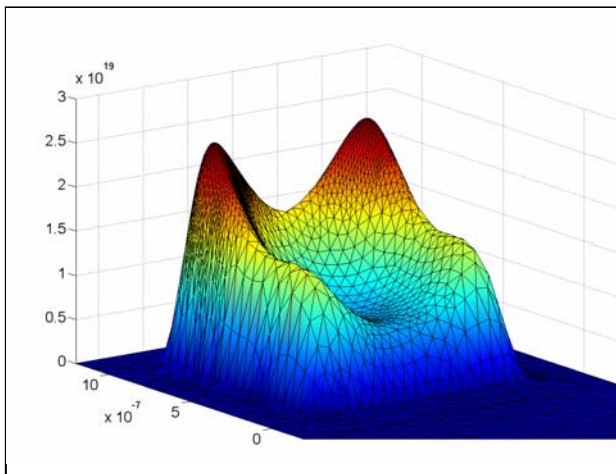


Fig. 2. QED in a Trigate MOS structure with  $H_{Si}=W_{Si}=10\text{nm}$ ,  $T_{ox}=2\text{nm}$  and  $V_G=1\text{V}$ .

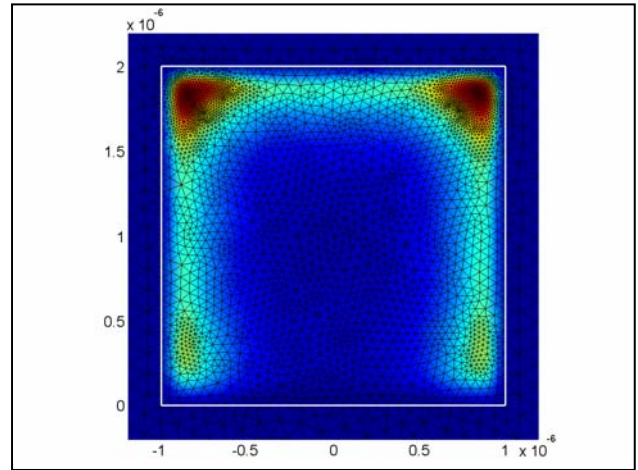


Fig. 3. QED in a Trigate MOSFET with  $H_{Si}=W_{Si}=20\text{nm}$ ,  $T_{ox}=2\text{nm}$  and  $V_G=1\text{V}$ . Note the different resolution of the mesh in different regions of the structure.

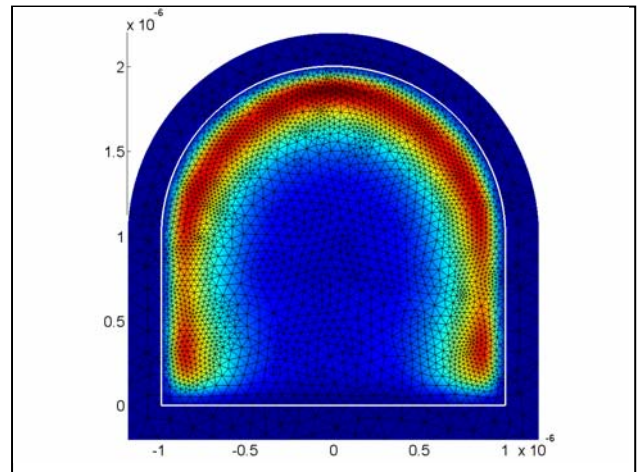


Fig. 4. QED in a Trigate MOSFET with  $H_{Si}=W_{Si}=20\text{nm}$ ,  $T_{ox}=2\text{nm}$  and  $V_G=1\text{V}$ .

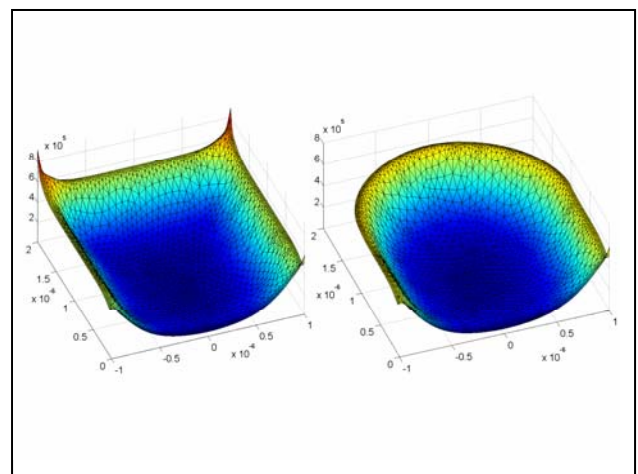


Fig. 5. Electric field in a Trigate MOSFET with square and rounded cross sections.

# Effects of Non Parabolicity in Si Quantum Wires

F. M. Gómez-Campos, S. Rodríguez-Bolívar, J. E. Carceller  
Departamento de Electrónica y Tecnología de los Computadores, Facultad de Ciencias,  
Universidad de Granada, 18071, Granada, SPAIN  
e-mail: fmgomez@ugr.es

## INTRODUCTION

Semiconductor nanostructures such as quantum wells, quantum wires and quantum dots have interesting properties which could be used for the future development of nanodevices. Since the quantum confinement in these structures removes the subband edges several tenths of meV from the bulk band edges, a good model of the bands should be used to investigate the subband structures. This model will determine not only the energy of the subband edges but also the shape of the dispersion relations. In this work we present a method for solving the Schrödinger equation in quantum wires, considering a general isotropic and a non-parabolic band. We apply it to calculate the subband structure in a squared Si 10 nm×10 nm quantum wire. We examine the curvatures of the subband edges and comment on the results.

## THEORETICAL TREATMENT

Any isotropic and non-parabolic dispersion relation,  $\varepsilon(\vec{k})$  could be expanded in power series on  $k^2$  in the following manner:

$$\varepsilon(\vec{k}) = \sum_{n=0}^{\infty} b_n k^{2n} \quad (1)$$

The  $b_n$  terms can be calculated using the Taylor theorem. The  $n=0$  term appears for bands where there is a certain energy for  $k = 0$ , i.e. the split-off band in the valence band. Following the Effective Mass Theorem, we performed the substitution  $\vec{k} \rightarrow -i\nabla$  in Eq.(1) and obtained the operator  $\varepsilon(-i\nabla)$

$$\varepsilon(-i\nabla) = \sum_{n=0}^{\infty} \left[ b_n \times (-\nabla^2)^n \right] \quad (2)$$

Thus, the effective mass Schrödinger equation of the problem can be written as

$$\left[ \sum_{n=0}^{\infty} \left[ b_n \times (-\nabla^2)^n \right] + V(x, z) \right] \psi(\vec{r}) = E \psi(\vec{r}) \quad (3)$$

where  $y$  is considered as the transport direction in the wire. In the case of a constant potential inside the wire,  $V(x, z) = V_0$ , the envelope functions of the hole states are known to be

$$\psi(\vec{r}) = e^{ik_y y} \sin(k_x x) \sin(k_z z) \quad (4)$$

where  $k_x = n_x \pi / L_x$ ,  $k_z = n_z \pi / L_z$ . Combining Eq. (3) and (4) we obtained

$$\varepsilon(k_x^2 + k_y^2 + k_z^2) = E - V_0 \quad (5)$$

Using the valence band model presented in a previous work [1], the condition of Eq. (5) is fulfilled when

$$\frac{E - V_0}{\chi_{H,L}(E - V_0)} = \frac{\hbar^2}{2m_{H,L}} \left[ \frac{n_x^2 \pi^2}{L_x^2} + \frac{n_z^2 \pi^2}{L_z^2} + k_y^2 \right]$$

$$\frac{E - V_0 - \Delta_{so}}{\chi_S(E - V_0 - \Delta_{so})} = \frac{\hbar^2}{2m_{so}} \left[ \frac{n_x^2 \pi^2}{L_x^2} + \frac{n_z^2 \pi^2}{L_z^2} + k_y^2 \right] \quad (6)$$

Where  $m_{H,L,so}$  and  $\chi_{H,L,S}(\varepsilon)$  are the effective mass values and the functions that describe the non-parabolicity of the band for the heavy, light and split-off holes respectively, and  $\Delta_{so}$  is the split-off energy. Varying the value of  $k_y$  it is possible to obtain the  $E(k_y)$  relation of each subband.

## RESULTS AND CONCLUSIONS

The results in Fig. 1 indicate the effective mass value at the edge of each subband obtained by using both a non-parabolic and a parabolic band model. In conclusion, our work suggests that non-parabolicity plays a very important role in the determination of the hole subband structure in quantum wires. In addition, the method demonstrated could be a good tool to carry out investigations on these devices.

## REFERENCES

- [1] S. Rodríguez-Bolívar, F. M. Gómez Campos, J. E. Carceller, *Simple analytical valence band structure including warping and non-parabolicity to investigate hole transport in Si and Ge*, Semiconductor Science and Technology, **20**, 16 (2005).

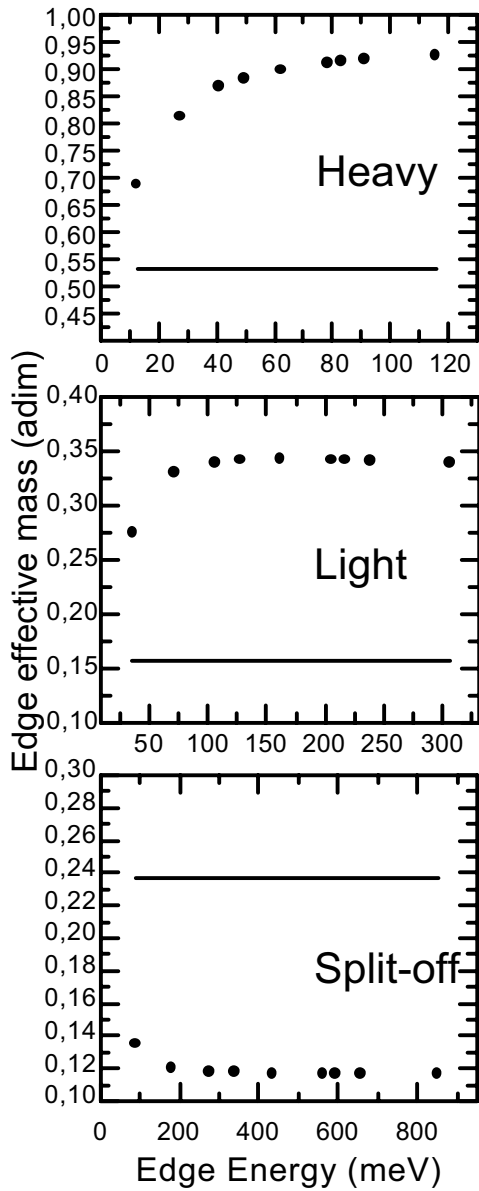


Fig. 1. Effective masses at the edges of the nine lowest subbands of heavy (a), light (b) and split-off (c) holes in a Si  $10\text{ nm}\times 10\text{ nm}$  quantum wire obtained by means of the method shown in this work (points) and by means of a parabolic model (solid line). The effective masses at the subband edges increase for higher subbands in heavy and light hole subbands, and decrease for higher subbands in split-off hole subbands. Important differences between our results and the parabolic model are observed.

# Boundary Conditions at the Junction

Mark Harmer, m.s.harmer@massey.ac.nz,  
 Inst. of Inf. and Math Sciences, Massey Univ. Albany, New Zealand  
 Boris Pavlov, pavlov@math.auckland.ac.nz  
 Dept. of Math. the University of Auckland, New Zealand  
 Adil Yafyasov, yafyasov@pobox.spbu.ru  
 Institute for Physics, St-Petersbutg University, Russia

## ABSTRACT

Practical calculation of transport properties of quantum networks is often reduced to the scattering problem for a one-dimensional differential operator on a quantum graph, see for instance [1], [2], [3], [4], [5]. Quantum graph plays a role of a solvable model for a two-dimensional network, see [6], [7], [8]. Basic detail of the model is a star-shape element with a self-adjoint boundary condition at the node. It was commonly expected that the realistic boundary condition is defined by the local geometry of the graph, that is by the angles between the wires at the node. For instance the boundary conditions for the T-junction, [1], is presented in terms of limit values of the wave-function on the wires  $\{\psi_i\}_{i=1}^3$  and the values of the corresponding outward derivative  $\{\psi'_i\}_{i=1}^3$  at the node:

$$\beta^{-1}\psi_1 = \psi_2 = \psi_3, \quad \beta\psi'_1 + \psi'_2 + \psi'_3 = 0. \quad (1)$$

Here  $\beta$  is a free parameter which describes “the strength of the coupling” between the leg and the bar of the T-junction. These boundary conditions can be represented, see [9], in the form

$$P_0^\perp \bar{\psi} = 0, \quad P_0 \bar{\psi}' = 0 \quad (2)$$

where  $\bar{\psi}$  and  $\bar{\psi}'$  are vectors of values of the wave-function at the vertex, with the projection

$$P_0 = \frac{1}{\beta^2 + 2} \begin{pmatrix} \beta^2 & \beta & \beta \\ \beta & 1 & 1 \\ \beta & 1 & 1 \end{pmatrix}.$$

The scattering matrix of such a junction is  $S = I - 2P_0$ , see [1], [4], [10]. In [11] the condition (2) is used for analysis of spin-dependent transmission across the quantum ring. In fact the projection  $P_0 = P_0(\beta)$  can also play a role of the free parameter of the model junction.

In our talk we extend, based on [12], the above boundary condition (2) to any junction of equivalent wires and interpret the corresponding free parameter  $P_0$ . Consider the junction  $\Omega$  formed by few 2-d semi-infinite wires  $\Omega_j$ ,  $j = 1, 2, \dots, n$ , attached to the quantum well  $\Omega_{int}$  via the orthogonal bottom sections  $\Gamma_j$ . The transport properties of  $\Omega$  are defined by the one-electron scattering in  $\Omega$ . We consider the resonance case when the scaled Fermi level  $E_F$  coincides with the resonance eigenvalue  $\hbar^{-2}2mE_F = \lambda_0$  of the corresponding Schrödinger operator in  $L_2(\Omega)$ , with effective mass  $m$  and “partial” Dirichlet boundary condition at  $\partial\Omega_{int}$ . We will show that the parameter  $P_0$  is defined by the shape of the resonance eigenfunction  $\Psi_0$ , but not by the angles between the wires at the node, as an example shows.

Assume that all wires have the same width  $\delta$ , the potential on the vires vanishes, and the Fermi level is situated on the first spectral band  $[\pi^2 \delta^{-2}, 4\pi^2 \delta^{-2}] := [\mu_1, \mu_2]$ . The cross-section eigenfunctions in the first (open) channel are  $\sin \frac{\pi y_j}{\delta} = e_j$ . Denote by  $E_+ := \bigvee_{j=1}^n e_j$  the subspace spanned by cross-section eigenfunctions of the open channel, and introduce the boundary current  $\vec{\phi}_0 = P_+ \frac{\partial \Psi_0}{\partial n} |_\Gamma$  of the normalized resonance eigenfunction  $\Psi_0$  via projection  $P_+ : L_2(\Gamma) \rightarrow E_+$  on the union  $\Gamma = \cup_j \Gamma_j$  of the bottom sections. If the network is relatively thin on Fermi level,  $\delta \max_{s=1,2} |\lambda_0 - \mu_s| \ll 1$ , the temperature is low,  $2m\kappa T \ll \hbar^2 \min_{s=1,2} |\lambda_0 - \mu_s|$ , and there exist only one simple resonance eigenvalue  $\lambda_0$  of the Schrödinger operator on the well on the essential spectral interval  $\Delta_T := [\lambda_0 - 2\hbar^{-2}m\kappa T \leq \lambda \leq \lambda_0 - 2\hbar^{-2}m\kappa T] \subset [\mu_1, \mu_2]$ , then we are able to derive, based on [12], an approximate expression

for the scattering matrix on  $\Delta_T$  :

$$S_{approx}(\lambda) = \left[ i\sqrt{\lambda - \mu_1}I + \frac{\vec{\phi}_0 \rangle \langle \vec{\phi}_0}{\lambda_0 - \lambda} \right] \times \left[ i\sqrt{\lambda - \mu_1}I - \frac{\vec{\phi}_0 \rangle \langle \vec{\phi}_0}{\lambda_0 - \lambda} \right]^{-1}. \quad (3)$$

The corresponding energy-dependent boundary condition at the node of the model graph is written down in terms of the limit values of the wave function and the outward derivatives,  $\vec{\psi} = (\psi_1(0), \psi_2(0), \dots, \psi_n(0))$ ,  $\vec{\psi}' = (\psi'_1(0), \psi'_2(0), \dots, \psi'_n(0))$  at the node:

$$i\sqrt{\lambda - \mu_1}[I - S_{approx}(\lambda)]\vec{\psi} = [I + S_{approx}(\lambda)]\vec{\psi}'. \quad (4)$$

The polar terms in the numerator and in the denominator of (3) have the dimension  $cm^{-1}$  and can be represented via the relevant one-dimensional orthogonal projection  $P_0 := \vec{e}_0 \rangle \langle \vec{e}_0$  with  $\vec{e}_0 := (e_0^1, e_0^2, \dots, e_0^n) = \|\vec{\phi}_0\|^{-1} \vec{\phi}_0 := \alpha^{-1} \vec{\phi}_0$ . Then  $\vec{\phi}_0 \rangle \langle \vec{\phi}_0 (\lambda - \lambda_0)^{-1} = \alpha^2 (\lambda - \lambda_0)^{-1} P_0$ . Denoting by  $P_0^\perp$  the complementary projection  $I - P_0$  in  $L_2(\Gamma)$ , we obtain

$$S_{approx}(\lambda) = P_0^\perp + \left[ \frac{i\sqrt{\lambda - \mu_1}(\lambda - \lambda_0) + \alpha^2}{i\sqrt{\lambda - \mu_1}(\lambda - \lambda_0) - \alpha^2} \right] P_0 \equiv P_0^\perp + \Theta(\lambda) P_0. \quad (5)$$

In particular, for *even lower* temperature and appropriate  $\alpha$  the factor  $\Theta$  in front of  $P_0$  is estimated on  $\Delta_T$  as  $|\Theta(\lambda) + 1| \ll 4\kappa T m \sqrt{\lambda_0 - \mu_1} \alpha^{-2} \hbar^{-2}$ . Then, in first approximation, the corresponding boundary condition (4) is reduced on  $\Delta_T$  to  $iP_0^\perp \psi - P_0 \psi' \approx 0$ , or, due to orthogonality of  $P_0, P_0^\perp$ , to  $P_0^\perp \vec{\psi} \approx 0$ ;  $P_0 \vec{\psi}' \approx 0$ . The results are applied to design of the resonance quantum switch and spin-filter based on standing waves in a 2-d quantum well.

## REFERENCES

- [1] S. Datta. *Electronic Transport in Mesoscopic systems*. Cambridge University Press, Cambridge, 1995.
- [2] F. Meijer, A. Morpurgo, and T. Klapwijk. One-dimensional ring in the presence of Rashba spin-orbit interaction: derivation of the correct Hamiltonian. *Phys. Rev. B*, 66:033107, 2002.
- [3] J. Nitta, F. E. Meijer, and H. Takayanagi. Spin-interference device. *Appl. Phys. Lett.*, 75:695–697, 1999.
- [4] I. A. Shelykh, N. G. Galkin, and N. T. Bagraev. Rashba spin-controlled quantum splitter. preprint.
- [5] J. Splettstoesser, M. Governale, and U. Zülicke. Persistent current in ballistic mesoscopic rings with Rashba spin-orbit coupling. *Phys. Rev. B*, 68:165341, 2003.
- [6] P. Kuchment *Graph models for waves in thin structures* Waves in Periodic and Random Media, 12,1 (2002)
- [7] V. Kostrykin and R. Schrader. The generalized star product and the factorization of scattering matrices on graphs. *J. Math. Phys.*, 42:1563–1598, 2001.
- [8] V. Kostrykin and R. Schrader. Quantum wires with magnetic fluxes. *Commun. Math. Phys.*, 237:161–179, 2003.
- [9] M. Harmer. Hermitian symplectic geometry and extension theory. *Journal of Physics A: Mathematical and General*, 33:9193–9203, 2000.
- [10] T. Taniguchi and M. Büttiker. Friedel phases and phases of transmission amplitudes in quantum scattering systems. *Phys. Rev. B*, 60:13814, 1999.
- [11] M. Harmer. The Rashba Ring. Subm. to Journal of Physics A: Mathematical and General.
- [12] N. Bagraev, A. Mikhailova, B. S. Pavlov, L. V. Prokhorov, and A. Yafyasov. Parameter regime of a resonance quantum switch. *Phys. Rev. B*, 71:165308, 2005.

## Time-Dependent Carrier Transport in Quantum-Dot Array Using NEGF

Yuhui He, Danqiong Hou, Xiaoyan Liu, Gang Du, Jinfeng Kang, Jie Chen\* and Ruqi Han  
Institute of Microelectronics, Peking University, Beijing, 100871, China

\* National Institute of Nanotechnology and Univeristy of Alberta, Canada  
e-mail: xyliu@ime.pku.edu.cn

### INTRODUCTION

Understanding time-dependent electron transport in mesoscopic systems is a very interesting research topic, which has drawn a great deal of research interest. [1-3] Here, we present a novel method to handle time-dependent transport in low-dimensional systems by jointly solving the nonequilibrium Green's functions (NEGF) in the time-domain and the real-space in a recursive fashion. In this way, we obtain electrical current densities in response to time-variant voltage signals.

### METHODOLOGY

Our time-domain recursively solving NEGF approach is based on the time-domain decomposition (TDD) technique [4]. This approach does not need to use the wideband limit approximation for electrodes. Thus electrodes with an arbitrary-shaped density of state (DOS) can be handled. According to the electron lifetime inside the devices, we cutoff the negative infinity limit in the integral equations of the NEGF. In the simulations, we utilize a dynamically allocated data-structure, which enables us to compute current densities in response to input signals of any time duration. Another challenge when we calculate the time-dependent transport characteristics is to handle an arbitrary-length conductor between the electrodes in low-dimensional systems. We handle this problem by combining the real-space recursively solving NEGF approach with the time-domain recursive approach. With this recursive algorithm, we can get numerical solutions by using  $O(\log_2 N)$  computation steps for a system with  $N$  principle layers in the central conductor.

### DISCUSSION

We apply this method to explore the transient and AC transport properties of a 1D quantum-dot array system, which can be used to emulate switches and interconnections made of low-dimensional materials. The electrical current densities in response to various pulses and sinusoid waveforms are simulated. The delay and distortion information is obtained, and how the hopping energy and the length of a quantum-dot array affect the transport behavior is further discussed.

The electron lifetime is extracted from the decay of equilibrium Green's functions  $G_N^r(\tau)$  [Fig. 1]. It gets larger when the number of dots increases, due to the

fact that it is inversely proportional to the probability of the electron escaping into the electrodes. Fig. 2 and Fig. 3 show the injection current densities (flow from the electrode where input signals are applied to the central conductor) and response current densities (flow from the central conductor to the other electrode) driven by the pulse waveform and sinusoid voltage signals, as the functions of time and the number of the quantum dots on the array. The injection current densities are almost the same for various dot numbers. The delay of response current densities is proportional to the array-length, which can be explained by the ballistic transport theory. In Fig. 3, the amplitude of the response current density of the 10-dot array is largest among the three response current densities. It is worth noticing that abrupt negative peaks exist at the beginning of the calculated injection current density curves. The amplitude of this transient overshoot is significantly attenuated as the electrons pass through the barrier between the conductor and electrode, so the response current densities at the right electrode are much smoother compared to the injection current densities. The influence of the hopping energy between neighboring quantum dots on the current densities is shown in Fig. 4. Larger hopping energy can suppress the peaks of the injection and response current densities at the barrier between the electrodes and conductor.

### CONCLUSION

A novel method to handle time-dependent transport in low-dimensional systems has been proposed and applied to one-dimensional quantum-dot arrays. Interesting results are presented and discussed.

ACKNOWLEDGEMENT: The authors would like to thank Dr. Chun Fan and Aidong Sun for their help in our numerical calculations. All simulations were performed on IBM RS/6000 SP3 at the CCSE at Peking University. This work was supported by the NBRF of China (Grant 2000036502) and the US NSF (Grant CCF 0304284).

REFERENCES: [1] A.-P. Jauho, N. S. Wingreen and Y. Meir, *Time-dependent transport in interacting and noninteracting resonant-tunneling systems*, Phys. Rev. B **50**, 5528 (1994). [2] Supriyo Datta, *Electronic Transport in Mesoscopic Systems*, Cambridge Univ. Press (1995). [3] Baigeng Wang, Jian Wang, and Hong Guo, *Current Partition: A Nonequilibrium Green's Function Approach*, Phys. Rev. Lett. **82**, 398 (1999). [4] Yu Zhu, Joseph Maciejko, Tao Ji, Hong Guo, and Jian Wang, *Time-dependent quantum transport: Direct analysis in the time domain*, Phys. Rev. B **71**, 075317 (2005).

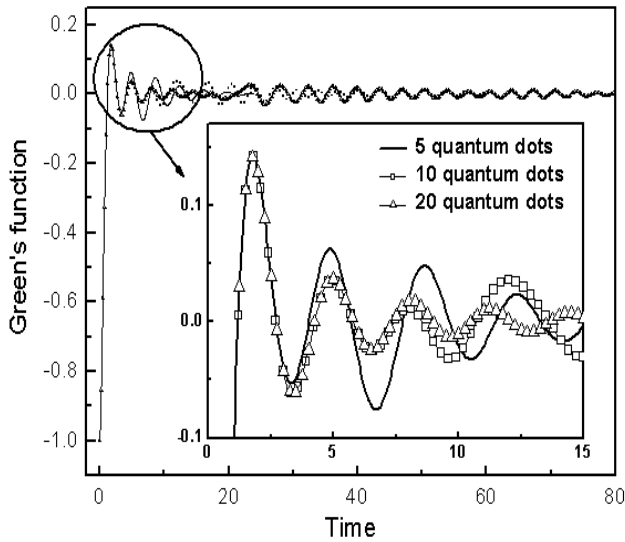


Fig. 1. Extraction of the electron lifetime from the decays of equilibrium Green's functions  $G_N(\tau)$ . Here, the numbers of dots on the quantum-dot arrays are 5, 10 and 20, respectively. The hopping energy between the neighboring dots is set to be one.

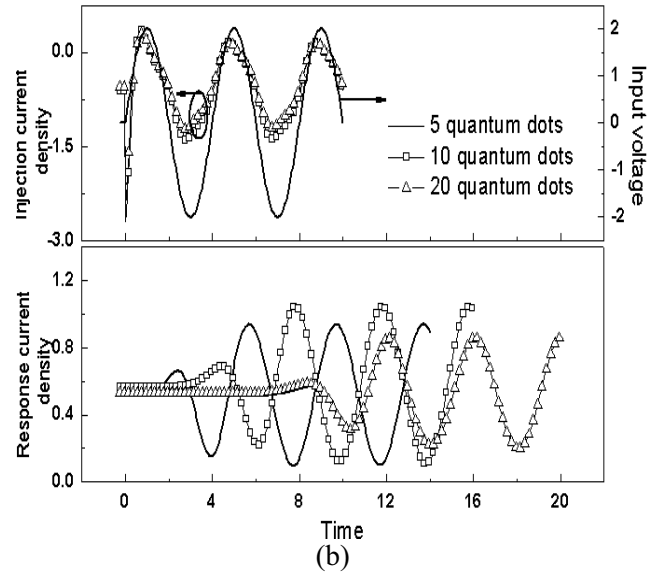


Fig. 3. Injection and response current densities driven by the sinusoid voltage signal  $V=2\sin(\pi t)$ , for 1D 5-, 10- and 20- quantum-dot arrays, respectively. The hopping energy between the neighboring dots is set to be one. A bias voltage of -2V is applied to the system.

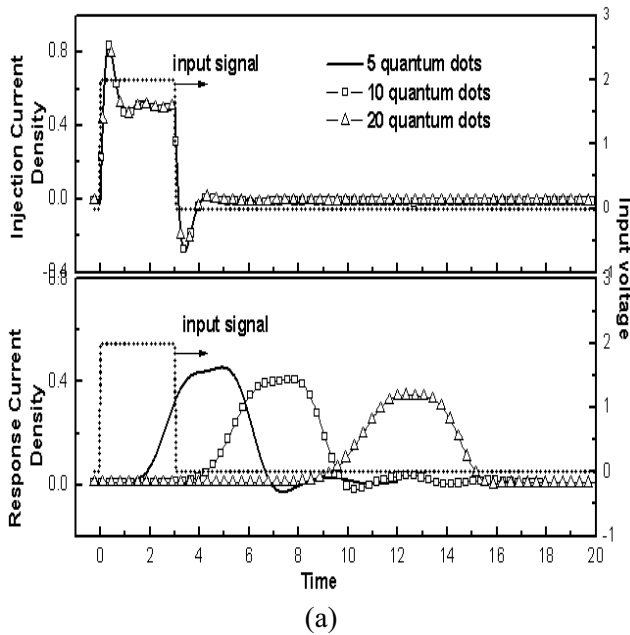


Fig. 2. Injection and response current densities driven by the pulse waveform, for 1D 5-, 10- and 20- quantum-dot arrays, respectively. The hopping energy between the neighboring dots is set to be one.

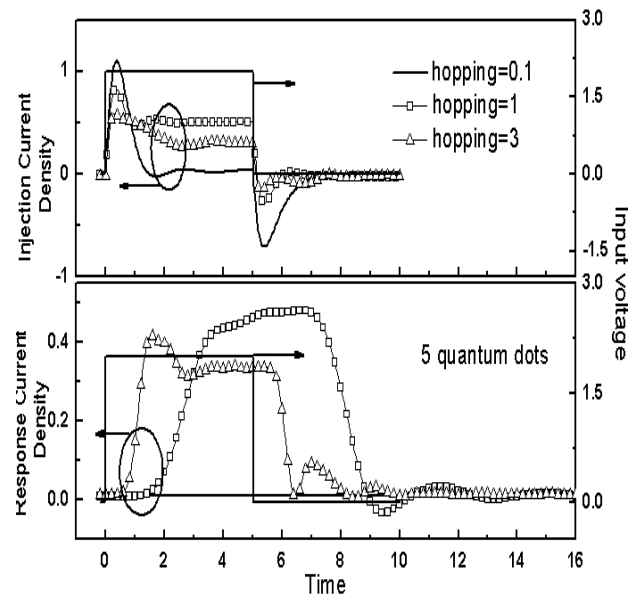


Fig. 4. Input pulse waveform and the corresponding injection and response current densities for a 1D 5-dot array. The hopping energies are 0.1, 1 and 3, respectively.

# Investigation of the Nonlinearity Properties of the DC I-V Characteristics of Metal- Insulator-Metal (MIM) Tunnel Diodes with Double-Layer Insulators

B. Hegyi, A. Csurgay, and W. Porod\*

Faculty of Information Technology, Péter Pázmány Catholic University, Budapest, Hungary

\*Center for Nano Science and Technology, University of Notre Dame, Notre Dame, IN, USA

e-mail: Hegyi.Barnabas@itk.pkke.hu

## INTRODUCTION

Metal-insulator-metal (MIM) diodes may play an important role in the future CMOS-compatible, high-speed infrared sensor applications. The different properties of the I-V curve are of great interest in these uses.

The DC I-V curve of single-insulator-layer MIM diodes is treated in several theoretical papers in the literature [1-2]. There exist also numerous experimental studies on the DC I-V curve of single-insulator-layer MIM diodes [2, 5-6].

Up to now, there have been neither numerical results nor experimental papers published on double-insulator-layer MIM diodes yet. The present paper reports and discusses simulation results on the DC I-V curve of MIM diodes with double insulator layer.

## PROBLEM FORMULATION AND SIMULATION ALGORITHM

The assumed potential profile of the double-insulator-layer MIM diode without applied voltage is depicted in Fig. 1. The value of the current density for a given value of the external voltage is then determined using the algorithm described in [3]. This very simple quantum transport model is based on the scattering of the electron wave function by a spatially varying potential. The tunneling probability of the electrons is determined by solving a space-discretized single-electron Schrödinger equation. The so called Quantum Transmitting Boundary Method (QTBM) [4] is applied when solving the equation.

## SIMULATION RESULTS AND DISCUSSION

The  $R_D$  resistance and the  $2m$  quality factor of the diode are examined as a function of five diode

parameters. These quantities can be obtained from the different derivatives of the DC I-V curve.

The diode parameters are the total thickness of the insulator layers ( $L$ ), the ratio of the thickness of the first insulator layer to the total thickness ( $r_d$ ), the ratio of the relative dielectric constants ( $r_e$ ), the average work function ( $\phi_0$ ) and the asymmetry factor of the work functions ( $\alpha$ ).

The simulation results are shown in Fig. 2-6. In each of the diagrams, three of the five diode parameters are kept constant, while the other two are considered as independent variables.

## ACKNOWLEDGEMENT

The support of the Hungarian National Research Fund (OTKA T-38345) is gratefully acknowledged. The work at the University of Notre Dame was supported by an ONR MURI grant.

## REFERENCES

- [1] J. G. Simmons, *Generalized Formula for the Electric Tunnel Effect between Similar Electrodes Separated by a Thin Insulating Film*, Journal of Applied Physics **34**, 1793 (1963).
- [2] A. Sanchez, C. F. Davis, Jr., K. C. Liu, and A. Javan, *The MOM Tunneling Diode: Theoretical Estimate of its Performance at Microwave and Infrared Frequencies*, Journal of Applied Physics **49**, 5270 (1978).
- [3] W.R. Frensley, *Heterostructures and Quantum Devices* (Academic Press, San Diego, 1994), Ch. 9 (Quantum Transport)
- [4] C. S. Lent, D. J. Kirkner, *The quantum transmitting boundary method*, Journal of Applied Physics **67**, 6353 (1990).
- [5] I. Codreanu, F. J. Gonzalez, G. D. Boreman, *Detection mechanisms in microstrip dipole antenna-coupled infrared detectors*, Infrared Physics & Technology **44**, 155 (2003).
- [6] C. Fumeaux, W. Herrmann, F.K. Kneubuhl, H. Rothuizen, *Nanometer thin-film Ni-NiO-Ni diodes for detection and mixing of 30 THz radiation*, Infrared Physics & Technology **39**, 123 (1998).

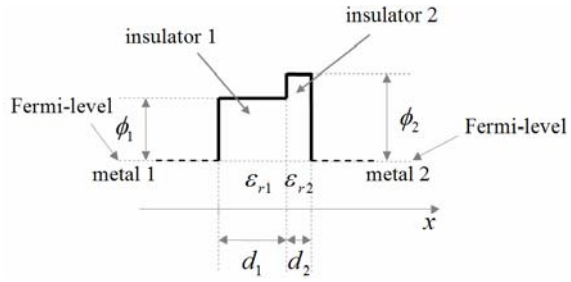


Fig. 1. Potential profile of the double-insulator-layer MIM diode without applied voltage

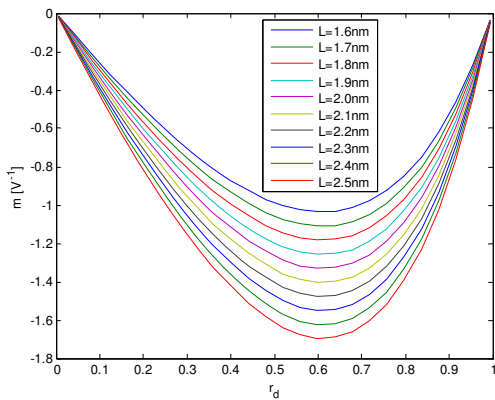


Fig. 2.  $m$  as a function of the thickness ratio  $r_d$  and the total thickness  $L$

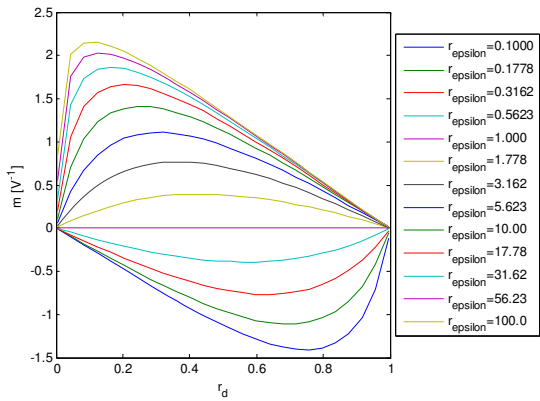


Fig. 3.  $m$  as a function of the thickness ratio  $r_d$  and the dielectric constant ratio  $r_\epsilon$

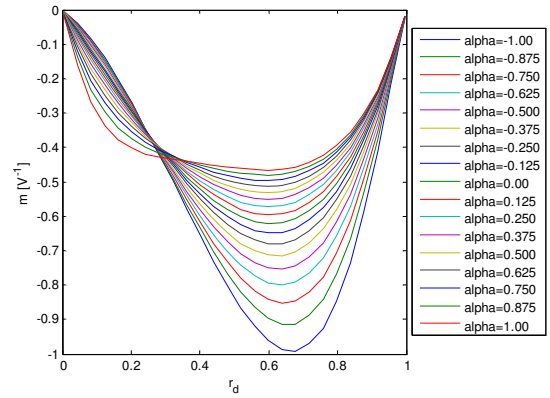


Fig. 4.  $m$  as a function of the thickness ratio  $r_d$  and the  $\alpha$  asymmetry factor of the work functions

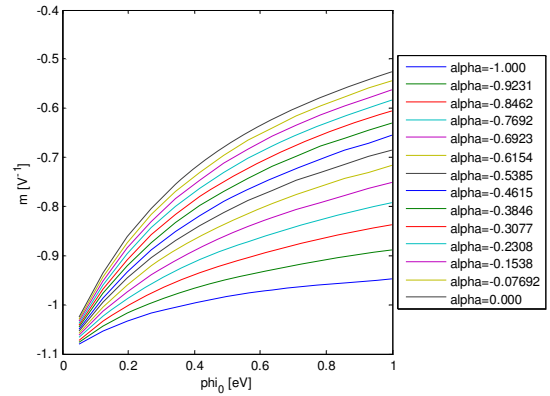


Fig. 5.  $m$  as a function of the average work function  $\phi_0$  and the  $\alpha$  asymmetry factor of the work functions

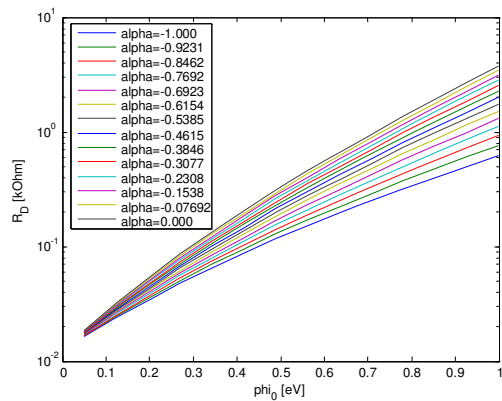


Fig. 6.  $R_D$  as a function of the average work function  $\phi_0$  and the  $\alpha$  asymmetry factor of the work functions

# Interband Tunneling Description of Holes in Wurtzite GaN at High Electric Fields

M. Hjelm, A. Martinez\*, H.-E. Nilsson, and U. Lindelfelt

Department of Information Technology and Media, Mid Sweden University, SE 851 70 Sundsvall, Sweden

\* Department of Electronics and Electrical Engineering, University of Glasgow, Glasgow G12 8LT, UK  
e-mail: mats.hjelm@miun.se

## INTRODUCTION

For semiconductors with hexagonal crystal geometry, like *4H* and *6H*-SiC, as well as GaN, the number of atoms in the unit cell is relatively large, resulting in complicated band structures with a large number of bands. Due to this large number of bands, there are several regions in the Brillouin zone with small energy distances between the bands. The small differences make it necessary to consider band-to-band tunneling (interband transitions) in studies of charge transport at high and even at moderately high fields [1]. This implies that a multi-band description of the quantum state of the charge carrier has to be used. Monte Carlo (MC) simulations of *4H*-SiC show a considerable increase of the impact ionization coefficients compared with simulations not considering tunneling [2]. However, the interference in the carrier velocity has not been considered for an ensemble. This study investigates the effect of interference on hole velocity in wurtzite GaN using a density matrix approach.

## FUNDAMENTAL EQUATIONS

The Krieger-Iafate (KI) equations, which can be derived from the single particle Schrödinger equation in the presence of an electric field, can be written as [1,3,4,5]:

$$-i\hbar \frac{\partial C_n^{\mathbf{k}_0}}{\partial t} = \varepsilon_n[\mathbf{k}(t)]C_n^{\mathbf{k}_0}(t) - \sum_{n'} q\mathbf{E} \cdot \mathbf{X}_{nn'}[\mathbf{k}(t)]C_n^{\mathbf{k}_0}(t), \quad (1a)$$

where  $C_n^{\mathbf{k}_0}$  is the probability amplitude that the a particle starting with the initial wave vector  $\mathbf{k}_0$ , with wave vector  $\mathbf{k}(t)$  ( $\dot{\mathbf{k}}(t) = q\mathbf{E}/\hbar$ ), and  $\varepsilon_n$  the

energy in band  $n$ .  $\mathbf{X}_{nn'}$  is the coupling between the bands  $n$  and  $n'$  and is given by:

$$\mathbf{X}_{nn'}[\mathbf{k}(t)] = -\frac{i}{\Omega_{cell}} \int_{cell} u_n^*[\mathbf{k}(t), \mathbf{r}] \nabla_{\mathbf{k}} u_n[\mathbf{k}(t), \mathbf{r}] d^3r, \quad (1b)$$

where  $u_n[\mathbf{k}(t), \mathbf{r}]$  is the periodic part of the Bloch function and the integration is performed over one unit cell with the volume  $\Omega_{cell}$ .

The expectation value of the carrier velocity is given by:

$$\mathbf{V}_{\mathbf{k}_0}(t) = \sum_n |C_n^{\mathbf{k}_0}(t)|^2 \frac{1}{\hbar} \nabla_{\mathbf{k}(t)}[\mathbf{k}(t)] + \sum_{n>n'} \sum_{n'} \frac{2\hbar}{m_0} \text{Im}(C_{n'}^{\mathbf{k}_0*} C_n^{\mathbf{k}_0}) \times \int_{cell} u_{n'}^*[\mathbf{k}(t), \mathbf{r}] \nabla_{\mathbf{k}} u_n[\mathbf{k}(t), \mathbf{r}] d^3r. \quad (2)$$

Equation (2) determines the trajectory of the Bloch charge carriers during the free flight between the scattering events. The first term is a mean value of the group velocity while the second term, which we call the interference term, is a quantum correction depending on the relative phase of the expansion coefficients  $C_n^{\mathbf{k}_0}$ .

## SIMULATIONS AND RESULTS

In Fig. 1 the band structure for the uppermost 6 valence bands of GaN is shown for a segment parallel to the  $\Gamma A$  direction (crystal axis) starting at a point in the  $\Gamma MK$  plane. The x-axis scale corresponds to an electric field of 0.4 MV/cm. This field is applied (parallel to  $\Gamma A$  direction) to the ensemble of holes in equilibrium. The carriers move and tunnel between different bands, which is numerically calculated according to Eq. 1. From the resulting probabilities the average energy and velocity of the

ensemble is calculated. We have considered the cases of two field strengths 0.4 and 4 MV/cm.

Fig. 2 shows the mean energy of the ensemble, both with and without tunneling. After studying Fig. 1, it may be believed that the holes tunnel from band 3 to band 4, but the contrary is actually the case, which is shown in Fig. 3. The increase of energy shown in Fig. 2 is explained by tunneling from band 1 to 2, which is more important because of the larger number of holes initially in band 1. In Fig. 4 the expectation value of the velocity is shown calculated according to Eq. 3, the classical velocity (Eq. 3 except interference), and the band velocity, i.e. the holes are assumed to stay in the same band.

### CONCLUSIONS

In this work we present average energy calculated with the KI equation, i.e. considering band-to-band tunnelling, for an ensemble of holes and compare it with the energy without tunnelling. Additionally, the velocity is calculated considering interference and compared with the velocity not considering interference and without tunnelling. At the workshop results will be shown for 4 MV/cm and a density matrix formulation of the KI equations will be given.

### REFERENCES

- [1] A. Martinez, U. Lindelfelt, and H-E. Nilsson, *J. Appl. Phys.* **93**, 9784 (2003).
- [2] H-E. Nilsson, A. Martinez, U. Sannemo, M. Hjelm, E. Bellotti, and K. Brennan, *Physica B* **314** 68 (2002).
- [3] J.B. Krieger and G. J. Iafrate, *Phys. B* **33**, 5494 (1986).
- [4] L. V. Keldysh, *Sov. Phys. JEPT* **6**, 763 (1958).
- [5] J. Rotvig *et al.*, *Phys. Rev. B* **54**, 17961 (1996).

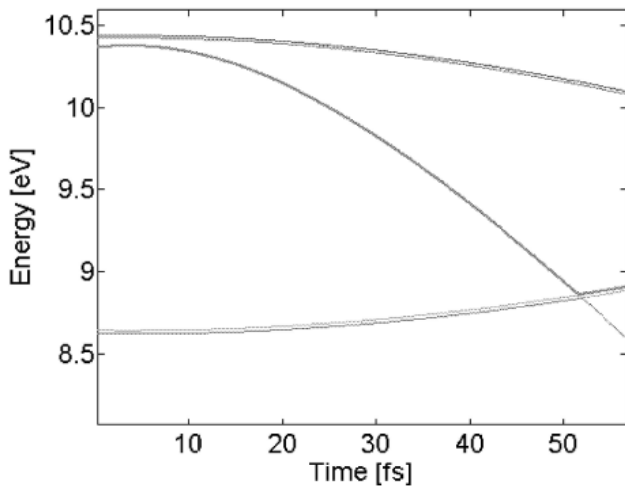


Fig. 1. Band structure in the  $\Gamma A$  direction for wurtzite GaN,  $E=0.4$  MV/cm.

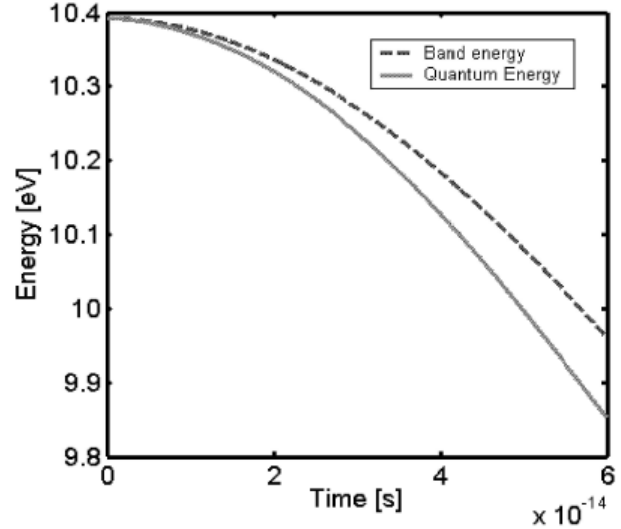


Fig. 2. Quantum energy (tunneling considered) and band energy (no tunneling) of the ensemble for 0.4 MV/cm.

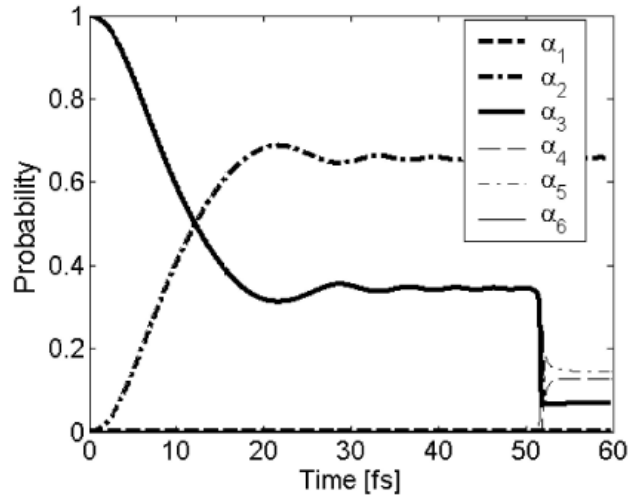


Fig. 3. The probability distribution between bands for a hole initially in the third band for 0.4 MV/cm.

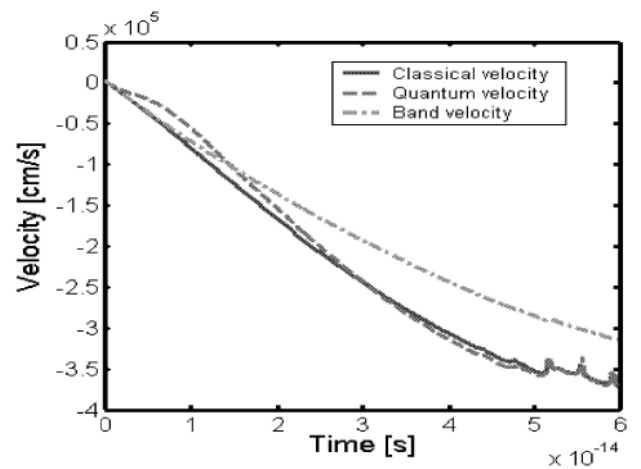


Fig. 4. Simulated velocity considering tunneling including interference (quantum velocity), tunneling not including interference (classical velocity), and without tunneling (band velocity).

# Control of Fano Resonances and the Transmission Phase of a Multi-Terminal Aharonov-Bohm Ring with Three Embedded Quantum Dots

Eric R. Hedin<sup>1</sup>, Arkady M. Satanin<sup>2</sup>, and Yong S. Joe<sup>1</sup>

<sup>1</sup>Center for Computational Nanoscience, Department of Physics and Astronomy, Ball State University, Muncie, IN 47306, USA

<sup>2</sup>Institute for Physics of Microstructures, RAS, GSP-105, Nizhny Novgorod, 603950 Russia  
e-mail: [erhedin@bsu.edu](mailto:erhedin@bsu.edu)

In order to fully characterize the transport properties of mesoscopic electronic devices, such as quantum dots (QD's) and rings, information on both the transmission coefficient (obtained experimentally from the conductance) and the phase are necessary. Phase measurements of the transmission can in principle be obtained through the interference effects produced in an Aharonov-Bohm (AB) ring with one or more embedded QD's. Transmission through the QD has been shown to be coherent, maintaining the phase information of the electron wave, through the observed oscillatory AB-effect which is periodic with the flux quantum,  $\Phi_0 = h/e$ .

In a two-terminal device, current conservation and time-reversal symmetry require that the transmission is of the form,  $T_{LR}(\Phi_0) = T_{LR}(-\Phi_0)$ , which forces the phase of the AB oscillations to be either 0 or  $\pi$ . An abrupt jump in phase of magnitude  $\pi$  is seen at the maxima of the resonant transmission peaks. In a multi-terminal device, however, this phase rigidity is relaxed, and it becomes possible to determine the intrinsic phase shift produced by the QD by measuring the phase of the AB-oscillations at different energy values across the transmission peak.<sup>1</sup>

In this work, we study a four-terminal AB-ring with three QD's embedded in one arm (Fig. 1). A tight-binding model is employed to analytically obtain the transmission through the system. Results show that the magnitude and sharpness of the resonant peak phase-jumps diminish as a function of the degree of coupling to the extra terminals. Fano resonances, produced by interference between the resonant states of the QD's and the continuum path through the reference arm of the AB-ring, are shown to have their zeros lift off the real energy axis into the complex energy plane by opening the

transmission through the ring, with coupling to the extra terminals by allowing  $V_d$  (see Fig. 1) to be non-zero. A simple analytical model of the Fano resonances shows naturally how the phase transition across the resonance peak will soften in the case where the transmission zero energy is no longer real, but complex.

Contour plots of the transmission in the complex energy plane also show that for this device with three embedded QD's it is possible to vary the coupling between the dots to obtain either three Fano dipole pairs, or to merge two of the dipoles into a Fano quadrupole (see Fig.'s 2 and 3). The Fano quadrupole behaves as a coupled object in which the two transmission peaks are preserved, but the zeros first merge and then move into the complex energy plane. As a function of magnetic flux through the ring, the zeros of the quadrupole orbit through the complex energy plane around the pair of poles corresponding to their transmission peaks.<sup>2</sup> With this device, the unique behavior of both the Fano quadrupole and the Fano dipole are exhibited simultaneously for proper ranges of the coupling parameters.

The enhanced degrees of control available with such a device give new possibilities for controlling and investigating the transmission and phase as a function of magnetic flux and inter-dot coupling.

## ACKNOWLEDGEMENT

This work is supported by the Indiana 21st Century Research and Technology Fund. One of the authors (E. R. H.) is partially supported by a grant from the Center for Energy Research, Education, and Service at Ball State University.

## REFERENCES

- [1] R. Schuster *et al.*, Nature **385**, 417 (1997).
- [2] A. M. Satanin, E. R. Hedin, and Y. S. Joe, Phys. Lett. A, **349**, 45 (2006).

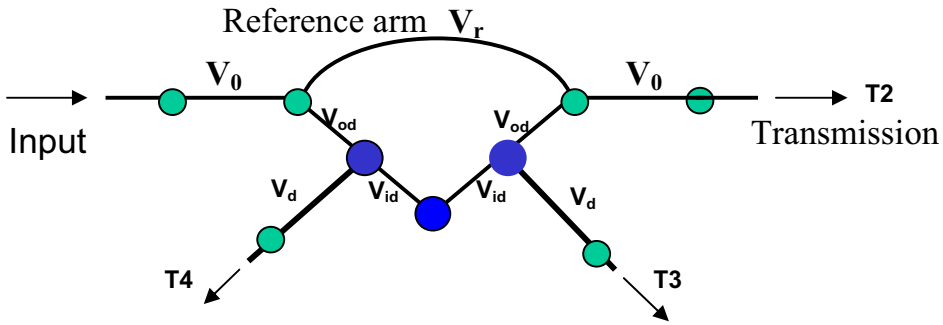


Fig. 1. Schematic of the four-terminal AB-ring with three embedded QD's in lower arm.

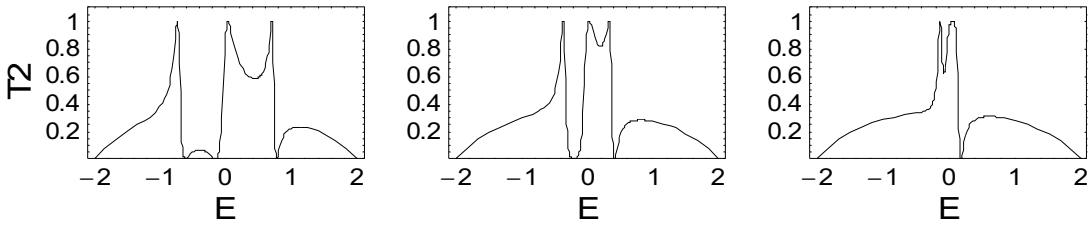


Fig. 2. Transmission plots showing the merging of the Fano zeros as inter-dot coupling,  $V_{id}$ , is decreased.  $V_{id} = 0.5, 0.25,$  and  $0.10$  (left to right). Coupling between outer dots and ring,  $V_{od}=0.3$ ; coupling through reference arm,  $V_r=0.3$ , and  $V_0=1.0$  in the leads.

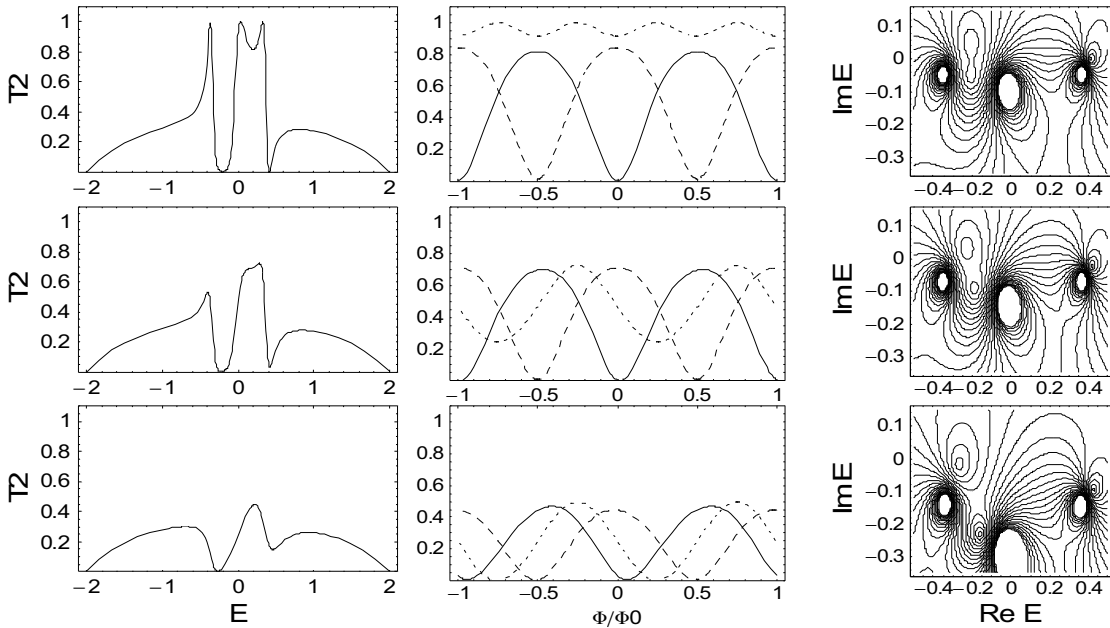


Fig. 3. Transmission vs. energy ( $\Phi/\Phi_0=0$ ) and flux ( $E = -0.2, 0, 0.25$ , for solid, dotted, and dashed lines, respectively), and transmission contour plots showing Fano zero-pole pairs, for varying degrees of openness of the ring:  $V_d=0, 0.2,$  and  $0.4$  (top to bottom).

# Indirect Optimal Control of a Qubit

H. Jirari and W. Pötz

Institut für Physik, Theory Division, Karl-Franzens-Universität Graz, Universitätsplatz 5, 8010 Graz, Austria

e-mail: walter.poetz@uni-graz.at

An indirect optimization scheme for the dynamic control of open quantum system is presented. It is demonstrated at the example of a spin 1/2 system which strongly couples to a bath of phonons. It reveals the possibility of control of the effective system-bath coupling, provided that the system is addressed in the quantum regime. The method is compared to direct algorithms, such as the genetic algorithm.

## INTRODUCTION

The fundamental principle of quantum interference between competing interactions has been seen as a potential principle of operation for electronic and electro-optic nanoscale devices of the future. Unlike optical interference effects, electronic or spin-based quantum interference effects in solids are generally difficult to establish and to maintain.[1] The fundamental reason is the generally strong coupling of the electron to its environment - other electrons and lattice ions. Nevertheless, due to the well developed semiconductor industry, there has been considerable research effort in the development of electron (electron spin) based quantum devices, such as single-electron devices, resonant-tunneling-based devices, and qubits based on the spin degree of freedom or point defects with a discrete spectrum in the main energy gap.

A key issue in ones ability to dynamically control (elementary) quantum systems along a desired quantum trajectory is the control of its interaction with the environment. Ideally one would wish to be able to eliminate the system-environment interaction altogether. Next best would be to minimize loss of coherence. This leads us directly to an optimization problem (inverse problem) in which optimal control fields are sought which, in general, stabilize coherence of a quantum system. A related

task is the optimization of control fields to maximize induced quantum interference effects. Best results can be expected when one is able to address the system on a time scale where its full quantum nature can be utilized.

## THE INDIRECT METHOD

In this contribution we present an indirect optimal control scheme for dissipative quantum systems which we apply to a study of a qubit which couples strongly to a phonon bath. For this purpose, the physical objective is formulated within a cost functional  $J(\varepsilon, \rho, t)$  where  $\rho(t)$  is the density operator of the (sub) system obeying a general kinetic equation of the form

$$\dot{\rho}(t) = \int_0^t dt' K(t, t'; \rho(t'), \varepsilon(t')), \quad \rho(0) = \rho_o,$$

for  $t \in [0, T[$ , whereby the kernel  $K(t, t'; \rho(t'), \varepsilon(t'))$  depends on the history of the system  $\rho(t')$ , as well as the real-valued external control  $\varepsilon(t')$  ( $\in \mathcal{L}^2[0, T]$ ) for  $t' \leq t$ , whereby causality is observed. This kinetic equation serves as a holonomic constraint to the cost functional in form of a non-Markovian set of differential equations in the density matrix elements. The cost function may be used to drive the system from a given initial state to a given final state, to trap it in a quantum state, or to optimize absorption, photocurrent yield, etc. An optimum control field is one which minimizes the cost functional, whereby  $\rho(t)$  plays the role of a dependent variable.

Here, this inverse problem is solved using an indirect method based on the concept of a co-state.[2] The latter may be viewed as a time-dependent Lagrangean multiplier which is used to eliminate variations with respect to the dependent variable

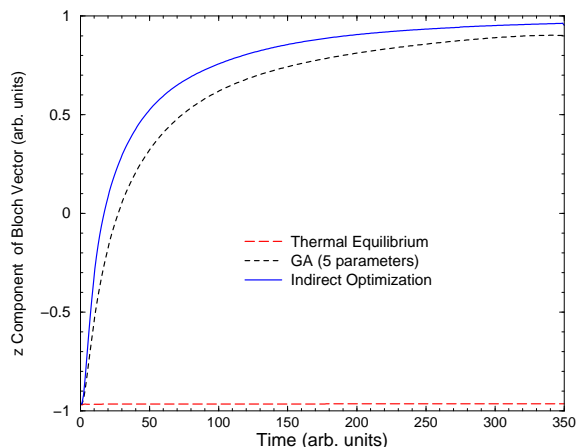


Fig. 1. Driving a qubit from its ground state into the "up" state at given target time: long dashed line: ground state (control field=0); dotted line: genetic algorithm (Gaussian pulse); solid line: indirect method.

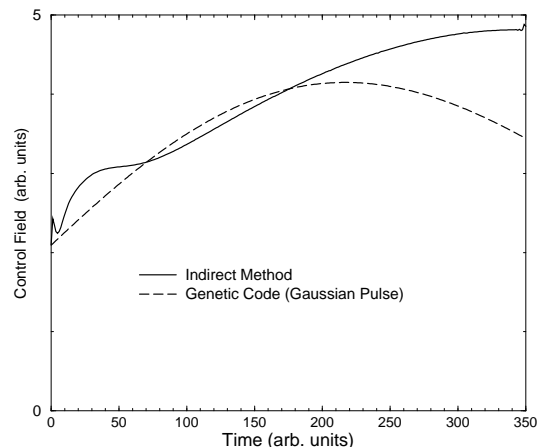


Fig. 2. Control field for driving a qubit from its ground state into the "up" state at given target time: solid line: indirect method; dotted line: genetic algorithm (Gaussian pulse).

$\rho(t)$ , or, as the canonical momentum associated with the variable  $\rho$  when following the Euler–Hamilton variation principle.[3] This procedure leads to a generalization of Hamilton’s equations of motion to non–Markovian systems.

Motivated by the current interest in the control of qubits, we demonstrate this approach for a qubit (spin-1/2 system, two–level system) which is coupled to a bath of phonons within a driven spin–boson model with strong electron–phonon coupling.[4], [6] When one is able to address the system on a time scale where it reveals its non–Markovian quantum nature, there is generally a better chance to control the system–bath interaction than when one is in a time regime where the latter behaves classically.[5] The difference can be attributed to quantum interference.

As an example, Fig. 1 gives the results for driving a qubit from its thermal ground state ( $z \approx -0.96$ ) to  $z=1$  at target time 350 (arb. units). This task is challenging since the target time is short compared to the characteristic relaxation time of the system. For comparison, the result for a Gaussian pulse which was optimized using a genetic code is given also. Fig. 2 gives the selected control fields for the two cases. Details will be presented in the full paper.

#### ACKNOWLEDGMENT

We wish to acknowledge financial support of this work by FWF, project number P16317-N08.

#### REFERENCES

- [1] H. P. Breuer and F. Petruccione, *The Theory of Open Quantum Systems*. Oxford University Press 2002.
- [2] V. F. Krotov, *Global Methods in Optimal Control Theory* (Dekker, New York, 1996).
- [3] See, for example, W. Greiner, *Classical Mechanics*, (Springer, New York, 2003).
- [4] M. A. Nielsen and I. L. Chuang, *Quantum Computation and Quantum Information*, (Cambridge Press, Cambridge, 2002).
- [5] H. Jirari and W. P’otz, *Phys. Rev. A*, **72**, 013409 (2005).
- [6] A. J. Leggett, S. Chakravarty, A. T. Dorsey, M. P. A. Fisher, A. Garg and W. Zwerger, *Rev.Mod.Phys* **59**, 1 (1987).

# “Real-Performance” Modeling of Carbon Nanotube FETs

D.L. John and D.L. Pulfrey

Department of Electrical and Computer Engineering,  
University of British Columbia, Vancouver, BC V6T1Z4, Canada  
e-mail: pulfrey@ece.ubc.ca

## Introduction

The first phase of modeling carbon nanotube field-effect transistors (CNFETs) can be considered to be over: simplifying assumptions about the geometry (coaxial), transport (ballistic), the potential distribution (azimuthally invariant), and the gate-metal thickness (zero), have allowed “ultimate-performance” predictions to be made for both DC and AC operation. Researchers are now examining these assumptions to determine whether they are appropriate for models intended to predict, and analyze, the performance of more realistic devices. In this work we focus on the azimuthal potential distribution and on the gate-metal thickness in non-coaxial structures. We self-consistently solve the equations of Poisson and Schrödinger: the latter gives the local density of states from a  $p_z$ -tight-binding Hamiltonian using a Non-Equilibrium Green’s Function formalism, within which the self-energies for the semi-infinite leads are computed by solving a quadratic matrix equation [1]. We consider two structures: the semicylindrical-gate geometry shown in Fig. 1, which may be a realizable tri-gate-like structure, and an asymmetrical, double-gate geometry shown in Fig. 2, which has recently been used to study doped-contact CNFETs [2].

## Azimuthal Potential Distribution

Equilibrium results for the azimuthal potential at mid-tube for our two structures are shown in Fig. 3. The variation in potential can be appreciable. The effects of this on the electrical characteristics of the CNFETs are under investigation; results will be presented in the full paper.

## Gate-metal Thickness

In Schottky-barrier CNFETs the gate and end-contact electrodes are inevitably close together, resulting in large, gate-thickness-dependent parasitic capacitances that significantly affect the AC performance [3]. In doped-contact CNFETs the electrode separations may be larger, but the gate-metal thickness  $T_G$  will still influence the electrostatics. The latter devices are of particular interest because of the suppression of ambipolar effects [4], and the possibility of exceptional sub-threshold slopes [5]. Solutions to Poisson’s Equation for our two structures, using null-Neumann boundary conditions to define the length  $L_{SD}$  of semi-infinite, doped lead within the simulation space [6], are shown in Figs. 4 and 5. For a self-consistent solution the potential must become flat well before the imposition of the null-Neumann boundary condition. For the case of  $L_{SD} = 20$  nm considered here, it is clear that this does not happen even for  $T_G$  as small as 2 nm in the semicylindrical-gate case, but does happen up to  $T_G \approx 10$  nm in the double-gate case. The implications of this for the electrical characteristics will be discussed in the full paper.

## References

- [1] D.L. John and D.L. Pulfrey, Phys. Stat. Solidi B, in press.
- [2] G. Fiori et al., Tech. Digest IEDM, 529 (2005).
- [3] D.L. Pulfrey et al., Proc. Intl. Wkshop. Phys. Semicond. Dev., Delhi, 7 (2005).
- [4] J. Guo et al., Intl. J. High Speed Electron. Syst., in press.
- [5] J. Appenzeller et al., IEEE Trans. Elec. Dev. 52, 2568 (2005).
- [6] S. Datta, Superlattices and Microstructures 28, 253 (2000).

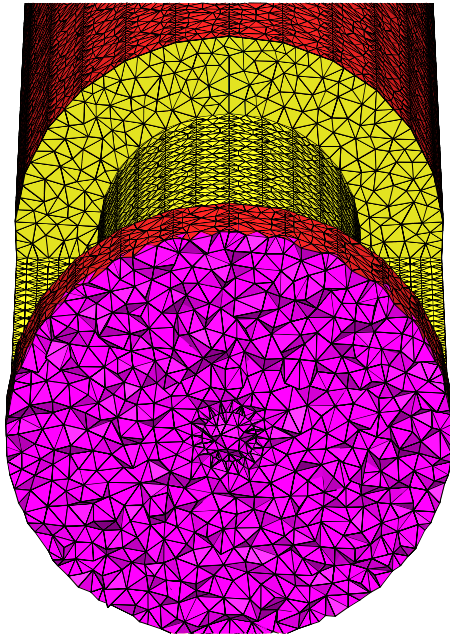


Fig. 1. Mesh for the semicylindrical-gate structure. The yellow facets are the gate surface. The results to follow are for an (11,0) tube, with an intrinsic, gated length of 7 nm and doped leads of 20 nm.

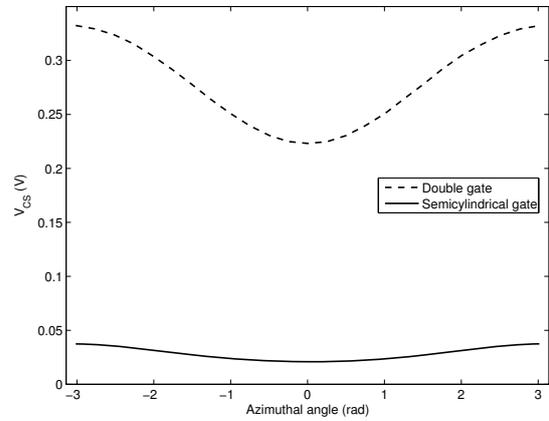


Fig. 3. Azimuthal variation of surface potential at mid-length of the nanotube for both structures.

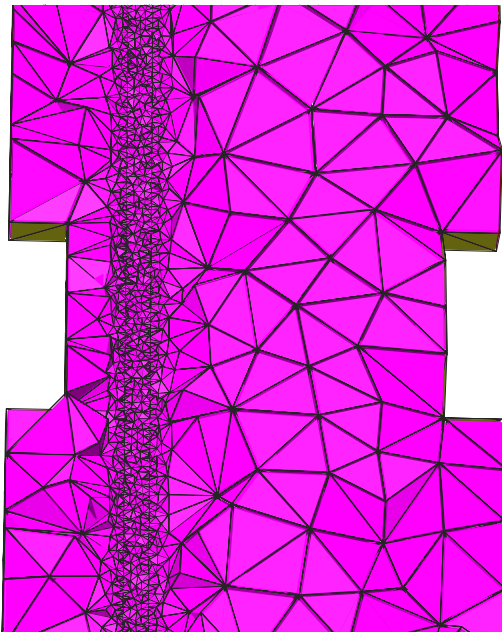
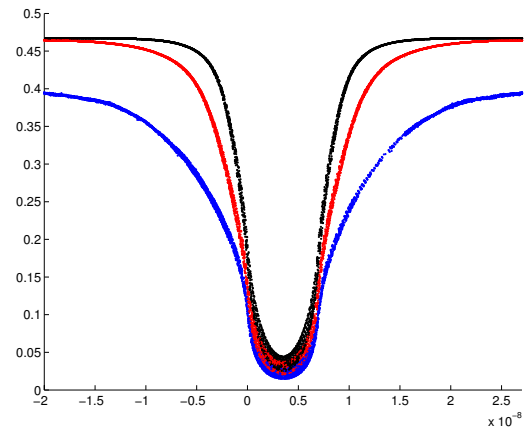


Fig. 2. Mesh for the planar, asymmetrical, double-gate structure. The gates are the cut-out regions. The results to follow are for an (11,0) tube, with an intrinsic, gated length of 7 nm, doped leads of 20 nm, oxide thicknesses of 2 nm (left) and 10 nm (right).



# VSP - A Multi-Purpose Schrödinger-Poisson Solver for TCAD Applications

M. Karner, A. Gehring\*, S. Holzer, M. Pourfath, M. Wagner,  
H. Kosina, T. Grasser, and S. Selberherr

Institute for Microelectronics, TU Wien, Gußhausstraße 27–29/E360, 1040 Wien, Austria

\*AMD Saxony, Wilschdorfer Landstrasse 101, D-01109 Dresden, Germany

e-mail: karner@iue.tuwien.ac.at

## INTRODUCTION

Numerous technological innovations, including material and process changes such as high- $k$  gate dielectrics and metal gate electrodes, are investigated to meet the upcoming scaling requirements. Furthermore, novel structures such as ultra-thin body and multiple-gate MOSFETs are expected to be introduced to suppress short-channel effects [1]. To overcome the technological problems, further theoretical and experimental research is needed which requires an extensive use of computer simulation.

## CAPABILITIES

We present the Vienna Schrödinger Poisson solver (VSP) which uses a quantum mechanical transport mode for closed as well as open boundary problems. The thereby calculated carrier concentration is used in the Poisson equation in a self consistent manner. The band structure for electrons and holes is given by an arbitrary number of valley sorts, defined by an anisotropic effective mass and a band edge energy. In this way a wide range of materials can be treated. Also, the effects of substrate orientation as well as strain on the band structure is taken into account.

For investigations of MOS inversion layers, a closed boundary solver using a predictor corrector scheme [2] is applied. VSP includes models for interface traps and bulk traps in arbitrarily stacked gate dielectrics. For the estimation of leakage currents, carriers in quasi bound states (QBS) as well as free carriers are considered [3]. Therefore, direct tunneling and trap assisted tunneling are taken properly into account [4]. These calculations are performed in a post processing step since they have

a negligible influence on the electrostatics device behavior. In addition, novel device designs like DG-MOS structures can be investigated.

For systems which are dominated by transport phenomena, like resonant tunneling diodes (RTD), an open boundary solver using the non equilibrium Green's function formalism [5] is available. We use an adaptive method to generate a nonuniform mesh for the energy-space. Very narrow resonances are resolved, while the total number of grid points is kept low, thus delivering stable results at reasonable simulation times [6].

Some typical applications are described in the captions of Fig. 1, Fig. 2 and Fig. 3 respectively.

## SOFTWARE TECHNIQUES

The software is written in C++ using state-of-the-art software design techniques. Critical numerical calculations are performed with stable and powerful numerical libraries Blas, Lapack, and Arpack. VSP holds a graphical user interface written in Java, as well as a text based interface. Furthermore, VSP has an open software application interface (API) for the use inside third party simulation environments. These features are used to perform tasks like parameter identification and model calibration, e.g for CV-curves and gate stack optimizations [7].

## CONCLUSIONS

We developed a fast and efficient multi-purpose quantum mechanical solver with the aim to aid theoretical as well as experimental research on nanoscale electronic devices. Binaries are available for Linux, Windows, IBM AIX, and MacOs on request.

This work has been supported by the Austrian Science Fund, contract SFB F25.

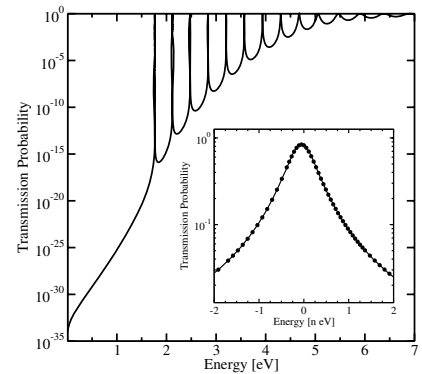
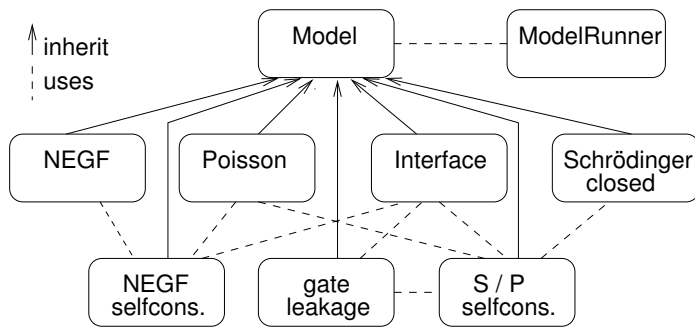


Fig. 1. a) VSP is structured into several models having a common interface. New models can be added easily. b) The transmission probability of carriers through a barrier over an energy range of 7 eV. The inset shows the first resonance in more detail. The width of the first resonance is only a few neV.

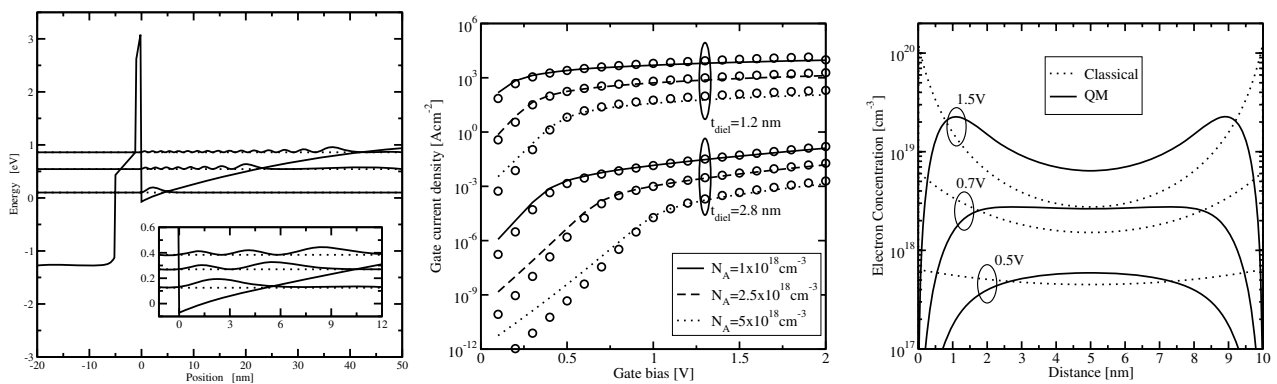


Fig. 2. a) The band edge energy of a MOS-structure with a stacked gate dielectric under inversion conditions. In addition, the wavefunctions and energy levels of some QBS are displayed. b) The estimated leakage current for several MOS-structures based on open-bound and closed-bound eigenvalues which allow much faster calculation [8]. c) A comparison between a quantum-mechanical and a classical calculated electron concentration at different bias voltages for a DG-MOSFET.

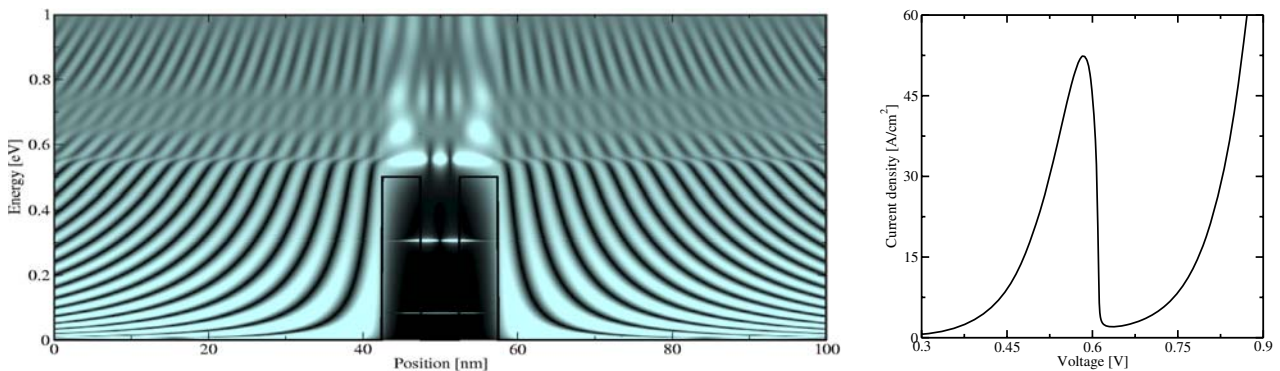


Fig. 3. a) Local density of states of a resonant tunneling diode (RTD) at zero bias. Quantized states are clearly shown in the well. b) IV characteristics of the RTD with open boundary conditions.

## REFERENCES

- [1] Semiconductor Industry Association, *International Technology Roadmap for Semiconductors - 2005 Update* (2005)
- [2] A. Trellakis et al., *J. Appl.Phys.*, vol. 81, no. 12, pp. 7880-7884 (1997)
- [3] M. Karner et al., *Proc. MSED 2005*, pp. 97-98 (2005)
- [4] A. Gehring et al., *IEEE Transactions on Device and Materials Reliability*, vol. 4, no. 3; pp. 306-319 (2004)
- [5] S. Datta, *Superlattices and Microstructures*, vol. 28, 253-278 (2000)
- [6] M. Pourfath et al., *Proc. MSED 2005*, pp. 95-96 (2005)
- [7] S. Holzer et al., *SNDT 2004, Symposium on Nano Devices Technology 2004*, pp. 113-116 (2004)
- [8] A. Gehring et al., *Proc. SISPAD 2004*, pp. 25-28 (2004)

# Self-Consistent Quantum Transport Theory: Applications and Assessment of Approximate Models

T. Kubis and P. Vogl

Walter Schottky Institute, TU München, Am Coulombwall 3, 85748 Garching, Germany  
e-mail: kubis@wsi.tum.de

In this paper, we present fully self-consistent non-equilibrium Green's function (NEGF) calculations of resonant tunneling diodes and quantum cascade laser structures and a careful assessment of commonly used approximations in the NEGF scheme [1,2].

## METHOD

In the present implementation of the NEGF formalism, we take into account acoustic and polar-optical phonon scattering as well as impurity scattering, both within the self-consistent Born approximation. The momentum and energy dependence of all scattering mechanisms is fully accounted for. The electron-electron scattering is incorporated self-consistently within the Hartree approximation. The coupling between the lesser and the retarded Green's function is fully taken into account. In this way, the scattering states, the transition probabilities between them, and their occupations are calculated self-consistently. The Ohmic leads supply electrons with a density of states that is matched to that of the device region near the interface to avoid quantum mechanical reflections. The occupancy of the lead states is represented by a drifted Fermi distribution such that device charge neutrality and current conservation is preserved.

## RESONANT TUNNELING DIODE

In Fig. 1, we depict a 40 nm GaAs/Al<sub>0.3</sub>Ga<sub>0.7</sub>As resonant tunneling diode with two 3 nm wide Al<sub>0.3</sub>Ga<sub>0.7</sub>As barriers and a 4 nm quantum well in the center. To the left and right of the barriers, there is a 3 nm intrinsic region and a 12 nm n-doped region with  $n=2 \times 10^{17} \text{ cm}^{-3}$ , respectively. In order to assess the adequacy of approximate quantum transport models, Fig. 2 shows a comparison of the full NEGF calculation (circles) with a simplified model

(diamonds) that neglects all inelastic and off-diagonal phonon scattering processes ( $\Sigma(z, z') \propto \delta_{z, z'}$ ) at 300 K. Computationally, the latter approach is orders of magnitudes faster. However, the strong inelastic scattering causes the triangular quasi-bound state in front of the left barrier to get filled with electrons. Then, the peak current occurs at a voltage where this quasi-bound state energy is in resonance with the resonant quantum well state [3]. This is a radically different physical situation as in the elastic model where artificial energy conservation prevents the electrons to occupy the quasi-bound state in front of the left barrier.

## QUANTUM CASCADE LASER STRUCTURE

In Fig. 3, we show the potential profile and the energy resolved electron density, defined by  $\rho(z, E) \propto \text{Im} \int d^2k G^<(z, z, k, E)$ , in the active region of a GaAs/Al<sub>0.15</sub>Ga<sub>0.85</sub>As quantum cascade laser structure. The geometry and doping of the structure has been taken from Ref. [4]. The results show clearly the necessity to treat coherent and incoherent quantum transport on an equal footing. The inverted occupation of the two resonance levels in the central double quantum well is clearly visible. The calculated photon emission energy is 17.5 meV (exp: 14.2 meV). The inelastic LO phonon emission (35 meV) across the last barrier on the right hand side efficiently empties the lower of the double quantum well levels, in accord with the data.

## ACKNOWLEDGEMENT

Financial support by Deutsche Forschungsgemeinschaft (SFB 631) is gratefully acknowledged.

## REFERENCES

- [1] S. Datta, *Electronic Transport in Mesoscopic Systems*, Cambridge University Press (1995).

- [2] R. Lake, Gerhard Klimeck, R. Bowen and D. Jovanoic, *Single and multiband modeling of quantum electron transport through layered semiconductor devices*, Journal of Applied Physics 81, 7845 (1997).
- [3] M. Fischetti, *Theory of electron transport in small semiconductor devices using the Pauli master equation*, Journal of Applied Physics 83, 270 (1998).
- [4] B. Williams, H. Callebaut, S. Kumar and Q. Hu, *3.4-THz quantum cascade laser based on longitudinal-optical phonon scattering for depopulation*, Applied Physics Letters 82, 1015 (2003).

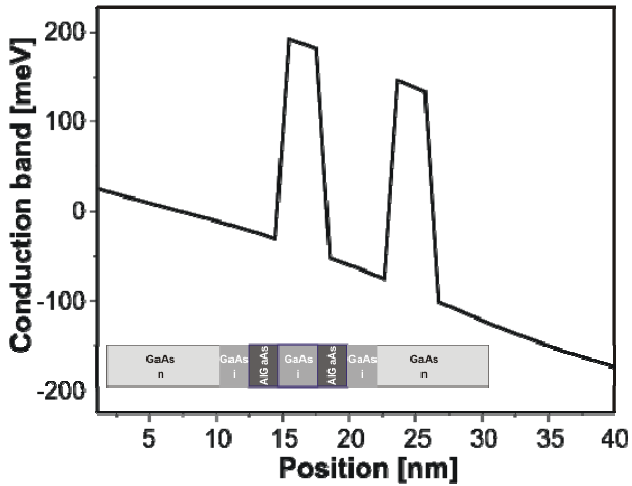


Fig. 1. Conduction band energy of the GaAs/Al<sub>3</sub>Ga<sub>7</sub>As resonant tunneling structure described in the text, at a bias voltage of 200 mV.

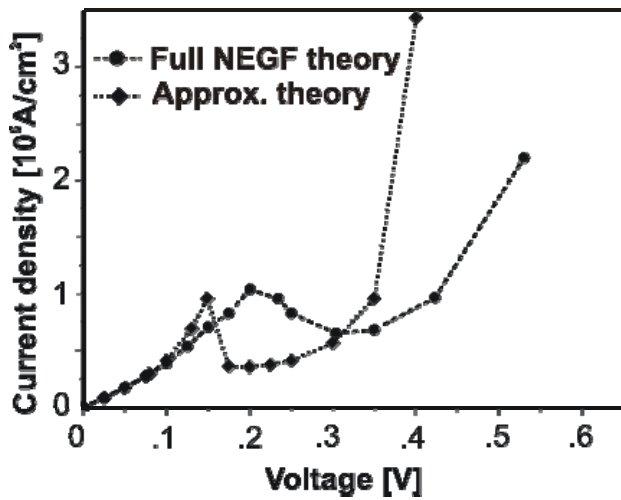


Fig 2. Calculated current density in the GaAs/Al<sub>3</sub>Ga<sub>7</sub>As resonant tunneling structure of Fig. 1 with (circles) and without (diamonds) off-diagonal inelastic scattering. The connecting lines are only meant to guide the eye.

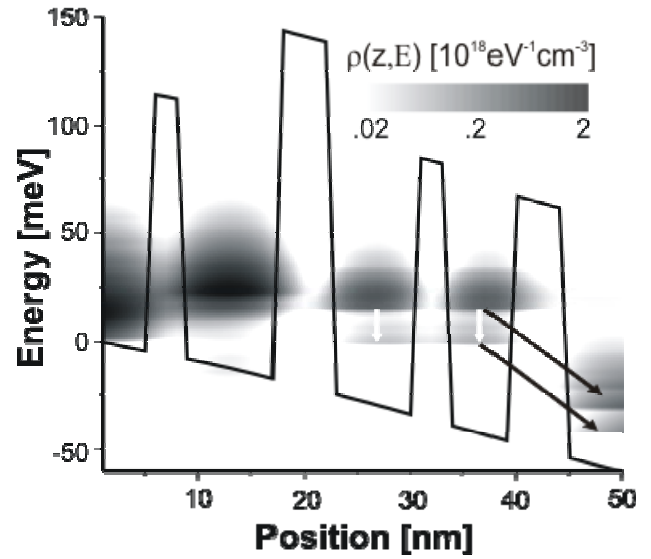


Fig. 3. Potential profile of 50 nm GaAs/Al<sub>15</sub>Ga<sub>85</sub>As quantum cascade laser structure from Ref. [4] at a bias voltage of 60 mV. The energy resolved electron density is shown as contour plot. The arrows are only meant to guide the eye and show the calculated emission energies (white = photons, black = phonons).

# Fast Inverse using Nested Dissection for the Non Equilibrium Green's Function

S. Li and E. Darve

Institute for Computational and Mathematical Engineering, Stanford University  
496 Lomita Mall, Durand building, Room 265, Stanford, CA 94305-4040, U.S.A.  
e-mail: darve@stanford.edu

## INTRODUCTION

In recent years, nanoscale MOS transistors as well as nanowires and molecular electronic devices have been actively studied [1]. It is now possible to manufacture transistors with channel lengths as small as 10 nm and below. At these scales, quantum effects such as tunneling are significant and have to be included in the simulation model. Despite the fact that transport issues for nano-transistors, nanowires and molecular electronic devices are very different from one another, they can be treated with the common formalism provided by the Non Equilibrium Green's Function. This approach is based on the coupled solution of the Schrödinger and Poisson equations. Our algorithm focuses on the computationally most expensive part which is the solution of the Schrödinger equation for the electron density, which is then used in the Poisson equation. After certain key simplifications [4], the problem is reduced to computing the diagonal elements of the matrix  $\mathbf{G} = [\mathbf{EI} - \mathbf{H} - \mathbf{\Sigma}]^{-1}$  (retarded Green's function) and  $\mathbf{G}^< = \mathbf{G}\mathbf{\Sigma}^<\mathbf{G}^\dagger$  (less-than Green's function), where the energy level  $E$ , Hamiltonian matrix  $\mathbf{H}$ , and self energies  $\mathbf{\Sigma}$  and  $\mathbf{\Sigma}^<$  (see Svizhenko [2] for those notations) are in this work considered to be given. ( $\dagger$  denotes the transpose conjugate of a matrix.) We now describe how to compute the diagonal of  $\mathbf{G}$  and  $\mathbf{G}^<$  efficiently. Our algorithm can be derived for devices of arbitrary geometry and for arbitrary boundary conditions; however for simplicity we will focus in this paper on 2D rectangular devices (a typical geometry used for modeling MOSFETs [2]).

## DESCRIPTION OF THE ALGORITHM

Let's first consider  $\mathbf{G}$  (the extension to  $\mathbf{G}^<$  is presented below). The basic idea of our algorithm is

to perform many LU factorizations on the given matrix to compute the diagonal elements of its inverse. By taking advantage of the sparsity of the given matrix, LU factorizations can be performed very efficiently. Once the LU factorization is complete, we can easily compute the last entry on the diagonal of the inverse: for the  $n \times n$  matrix  $\mathbf{G}^{-1} = \mathbf{LU}$ , we have  $G_{nn} = 1/U_{nn}$ . Although we can only compute  $G_{nn}$  in this way, we can choose any node and reorder  $\mathbf{G}^{-1}$  to make the node correspond to the  $(n, n)$  entry of the reordered matrix and thus compute all the diagonal elements of  $\mathbf{G}$ .

If we have to perform a full LU factorization for each of the  $n$  reordered matrices, the algorithm will not be computationally efficient even though each LU factorization is very fast. However, if we reorder those matrices properly, many partial factorizations for different reordered matrices turn out to be identical. We can store the results of those partial factorizations in a binary tree (its structure follows the nested dissection procedure of George [5]) and reuse them many times thereby reducing considerably the computational cost. As a result, the total cost of performing the LU factorizations on all the  $n$  reordered matrices is of the same order as performing the LU factorization on one matrix and thus computing all the diagonal elements of  $\mathbf{G}$  is very efficient. This is the main merit of our algorithm.

For a square mesh of size  $N \times N$ , the computational cost dominates at the top level of the binary tree. The cost of performing partial factorization at the top level is  $O(N^3)$  and we showed that the total cost turns out to be also  $O(N^3)$ . For rectangle meshes of size  $N_x \times N_y$  with  $N_x < N_y$ , the cost is  $O(N_x^2 N_y)$ .

We can also extend the above idea to computing

$\mathbf{G}^<$ . Define  $\mathbf{R} \stackrel{def}{=} \mathbf{L}^{-1} \mathbf{\Sigma}^< \mathbf{L}^{-\dagger} = \mathbf{U} \mathbf{G}^< \mathbf{U}^\dagger$ , then we have  $\mathbf{G}_{nn}^< = \mathbf{R}_{nn} / |\mathbf{U}_{nn}|^2$ . In principle,  $\mathbf{R}$  is a dense matrix which is very expensive to calculate. However, by taking advantage of the sparsity of  $\mathbf{\Sigma}^<$ , we created an algorithm to compute  $\mathbf{R}_{nn}$  whose cost is of the same order as computing  $\mathbf{U}_{nn}$ . By using a re-ordering strategy and storage of intermediate steps similar to the ones described above, we derived an algorithm to calculate the diagonal of  $\mathbf{G}^<$  in  $O(N_x^2 N_y)$  steps.

Unlike the computing cost that dominates at the top level, the memory cost is about the same ( $\propto N_x N_y$ ) at each level of the tree. We have  $\log(N_x N_y)$  levels and thus the total memory cost is  $O(N_x N_y \log(N_x N_y))$ . This is asymptotically better than the algorithm given by Svizhenko *et al.* [2] since the memory cost of their algorithm is  $O(N_x^2 N_y)$ .

## RESULTS

We made comparisons between our algorithms and the algorithm given by Svizhenko [2] (see Lake [3] for an earlier version in 1D). Their algorithm is based on computing all the diagonal blocks of  $\mathbf{G}$  and  $\mathbf{G}^<$  using a forward and backward recurrence along the  $y$  axis of the device. The cost of their algorithm is  $O(N_x^3 N_y)$  since the inverse of  $N_y$  matrices of size  $N_x$  needs to be computed. Fig. 1 shows a comparison of running time between the two algorithms. We can see that our algorithm uses much less time when the mesh size exceeds  $100 \times 100$  and scales much better overall. Fig. 2 shows the comparison of memory cost between the two algorithms. We can see that the memory cost of the two algorithms is about the same (because of the larger constant factor in our algorithm) but the memory cost of our algorithm increases slower than the other algorithm so it is asymptotically better.

## DISCUSSION

The constant factors in the running time and the memory cost of our algorithm are expected to improve by about 50%. This will be achieved by exploiting more efficiently the sparsity of  $\mathbf{G}^{-1}$ .

The algorithm described here can be extended to arbitrary geometries. It is applicable to a large class of devices including nanotubes and nanowires.

## REFERENCES

- [1] Y. Xue, S. Datta, and M. A. Ratner, "First-principles based matrix Green's function approach to molecular electronic devices: general formalism," *Chemical Physics* **281**(2/3), pp. 151-70, 2002
- [2] A. Svizhenko, M. P. Anantram, T.R. Govindan, B. Biegel and R. Venugopal, "Two-dimensional quantum mechanical modeling of nanotransistors," *Journal of Applied Physics* **91**(4), pp. 2343-2354, 2002
- [3] R. Lake, G. Klimeck, R.C. Bowen, and D. Jovanovic, "Single and multiband modeling of quantum electron transport through layered semiconductor devices," *Journal of Applied Physics* **81**(12), pp. 7845-69, 1997
- [4] S. Datta, "Nanoscale device modeling: the Green's function method," *Superlattices and microstructures* **28**(4), pp. 253-278, 2000
- [5] A. George, "Nested dissection of a regular finite element mesh," *SIAM Journal on Numerical Analysis* **10**(2), pp. 345-63, 1973

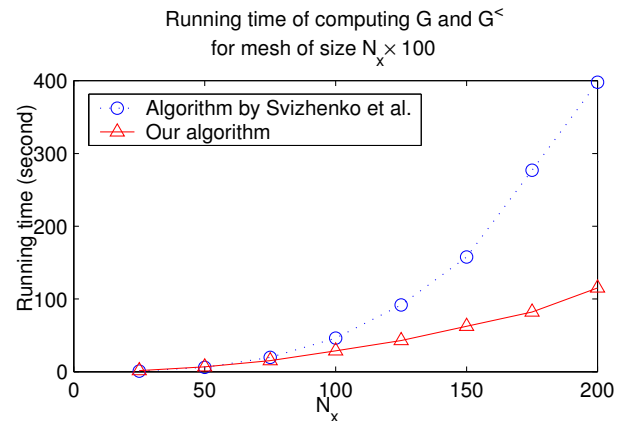


Fig. 1. Running time of our algorithm and the algorithm proposed by Svizhenko [2].

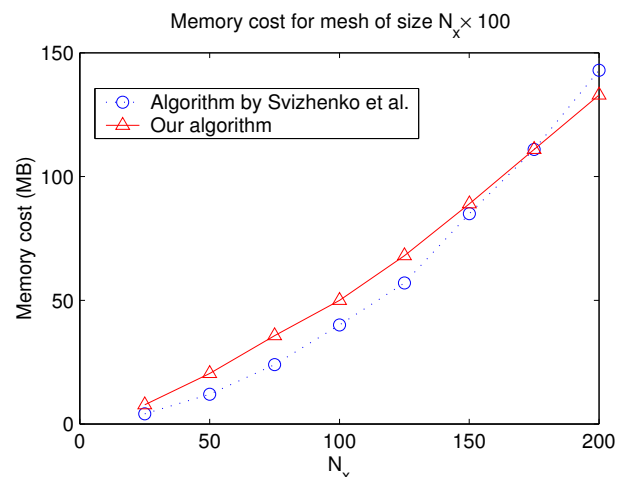


Fig. 2. Memory cost of our algorithm and the algorithm proposed by Svizhenko [2].

# 3D simulation of a silicon quantum dot in a magnetic field based on Current Spin Density Functional Theory

M. Lisieri, G. Fiori, and G. Iannaccone

Dipartimento di Ingegneria dell'Informazione, Università di Pisa,  
Via Caruso 16, I-56100 Pisa, Italy  
e-mail: michele.lisieri@iet.unipi.it

Recent research considers silicon a promising material for spintronic applications, because of its high spin coherence time and its mature technology [1], [2]. A detailed investigation of the spin properties of a quantum dot would require a suitable simulation tool, of which there are no examples in literature.

In this work, we present a numerical simulation of a silicon quantum dot in a magnetic field based on the solution of the many body Schrödinger equation, on the basis of Current Spin Density Functional Theory (CSDFT) [3], in the Local Density and Approximation (LDA), based on the formulation proposed by Koskinen et al. [4]. The effective mass approximation is used; mass anisotropy and degeneracy of conduction band minima are taken into account.

In Fig. 1, we show the flow chart of the simulation. Starting from an initial guess, the single particle Kohn-Sham equation is solved 6 times in the dot region, for each spin in each conduction band minimum (3 for silicon). Each single particle level is filled in the order of increasing energy, and the electrochemical potential  $\mu$  is calculated with Slater's rule.

Once spin up and spin down electron densities are computed, the nonlinear Poisson equation is solved in the three dimensional domain by means of the Newton-Raphson method. The algorithm is then repeated cyclically till convergence is achieved.

In Fig. 2 we show the 3D structure of the simulated device, which has a square transverse cross section. The dot is a  $4 \times 30 \times 30$  nm<sup>3</sup> silicon box embedded in SiO<sub>2</sub>. In Fig. 3, we show a cross

section of the electron density for 3 electrons in the dot for  $B = 0$  T and  $B = 4.75$  T.

In Fig. 4 we show the addition energy  $\Delta_2(N) = \mu(N+1) - \mu(N)$  of the dot, where  $N$  is the total number of electrons in the dot. The maxima are for multiples of four electrons in the dot, due to the double degeneracy of each conduction band minimum. In Fig. 5 we show the first seven eigenvalues as a function of the magnetic field for three electrons in the dot. As can be seen, for  $B = 2$  T there is a change of spin polarization.

In the final version of the paper, we discuss all the convergence issues and the behavior of spin polarization of the quantum dot as a function of the magnetic field, of the number of electrons, and of the dot geometry.

Authors gratefully acknowledge support from EU through the network of Excellence SINANO (EC contract n. 506844).

## REFERENCES

- [1] S. Das Sarma, R. de Sousa, X. Hu, B. Koiller, *Spin quantum computation in silicon nanostructures* Solid State Communications **133**, 737-746, (2005).
- [2] L. P. Rokhinson, L. J. Guo, S. Y. Chou, and D. C. Tsui, *Spin transitions in a small Si quantum dot*, Physical Review B **63**, 035321 (2001).
- [3] S. M. Reimann and M. Manninen *Electronic structure of quantum dots*, Review of Modern Physics, **74**, 1283-1342, (2002).
- [4] M. Koskinen, J. Kolehmainen, S. M. Reimann, J. Toivanen, and M. Manninen, *Quantum dots in magnetic fields: Unrestricted symmetries in the current spin-density functional formalism*, Eur. Phys. J. D, **9**, 487-490, (1999)

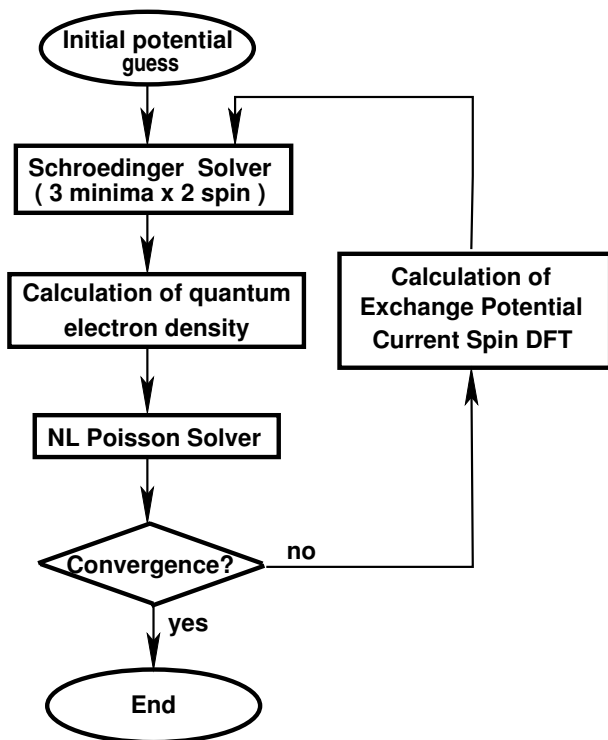


Fig. 1. Flow chart of the implemented 3D Poisson/Schrödinger solver.

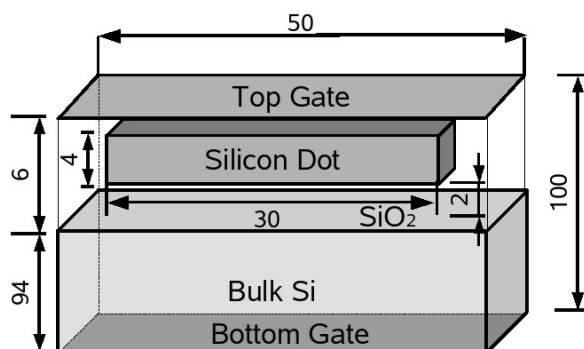


Fig. 2. Three dimensional simulated quantum dot structure: the silicon dot ( $4 \times 30 \times 30 \text{ nm}^3$ ) is embedded in  $\text{SiO}_2$ . The bulk is  $p$ -doped with  $N_A=10^{18} \text{ cm}^{-3}$ . Dimensions in the figure are in nanometers.

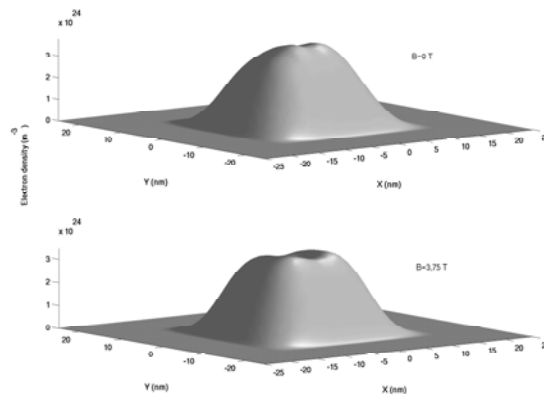


Fig. 3. Electron density for three electrons in the quantum dot for  $B = 0 \text{ T}$  (top) and  $B = 4.75 \text{ T}$  (bottom).

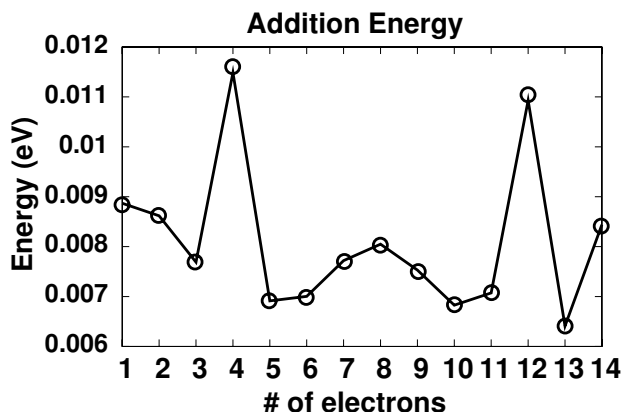


Fig. 4. Addition Energy as a function of the number of electrons in the dot.

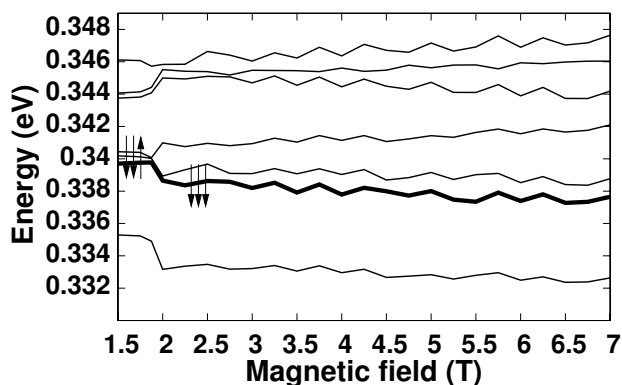


Fig. 5. First seven eigenvalues calculated when three electrons are in the dot as a function of the magnetic field. The bold line is the electrochemical potential, and the arrows indicate spin polarization.

# Comparing Models of Many Electron Quantum Dynamics

M. Lohwasser and N. J. Mauser\*  
 Wolfgang Pauli Institut c/o Fak. f. Math., Univ. Wien,  
 Nordbergstraße 15, 1090 Wien, Austria

e mail: michael.lohwasser@univie.ac.at  
 e mail: mauser@courant.nyu.edu

## INTRODUCTION

We are concerned with approximations of the many body problem of nonrelativistic quantum dynamics of  $N$  interacting electrons. One would ideally like to solve the  $N$  body time dependent linear Schrödinger equation (TDLSE) with Coulomb potential and a time dependent external potential  $V(\mathbf{r}_j, t)$  which reads,

$$i\frac{\partial}{\partial t}\Psi = \sum_{j=1}^N \left( -\frac{1}{2}\Delta_{\mathbf{r}_j}\Psi + V(\mathbf{r}_j, t)\Psi \right) \quad (1)$$

$$+ \sum_{1 \leq j < k \leq N} \frac{1}{|\mathbf{r}_j - \mathbf{r}_k|} \Psi$$

in atomic units. Here  $\mathbf{r}_j \in \mathbb{R}^3$  denotes the position coordinates of the  $j^{\text{th}}$  particle. Although (1) is a linear PDE, it scales quite unfavourable with increasing number of particles which makes it practically impossible to compute solutions directly for systems with more than a few electrons.

To avoid this problem, often coupled systems of nonlinear Schrödinger equations for several single electron “orbitals” are used in practice. One way to obtain such simplified models from (1) is by “variational approximation”. This technique produces the time dependent Hartree Fock (TDHF) or *multiconfiguration* time dependent Hartree Fock (MCTDHF) systems and a large variety of other possibilities [9]. A different approach is time dependent density functional theory (TDDFT) which produces the time dependent Kohn Sham system [10] and [1].

In this work we will focus on models derived by the “variational approximation” approach namely the TDHF and MCTDHF system.

## THE MCTDHF EQUATIONS

To illustrate the method we consider the 2 particle MCTDHF ansatz

$$\Psi(x_1, x_2) = \sum_{j,k=1}^n a_{jk} \phi_j(x_1) \phi_k(x_2), \quad (2)$$

where  $\{\phi_1, \phi_2, \dots, \phi_n\}$  is an orthonormal set of  $n \geq 2$  orbitals. The coefficients satisfy  $a_{jk} = -a_{kj}$  so that  $\Psi$  is antisymmetric, thus obeying Pauli’s exclusion principle, and  $\sum |a_{jk}|^2 = 1$  to ensure  $\|\Psi\| = 1$ .

The Dirac Frenkel variational principle yields a system of ordinary differential equations for the coefficients  $a_{jk}$ , coupled to a system of partial differential equations for the orbitals  $\phi_i$  which reads in vector notation for  $\vec{\phi} = (\phi_1, \phi_2, \dots, \phi_n)^T$

$$\frac{d}{dt} a_{jk} = -i \langle \phi_j(x_1) \phi_k(x_2), V \Psi(x_1, x_2) \rangle \quad \forall j, k \quad (3)$$

$$\frac{d}{dt} \vec{\phi} = \frac{i}{2} (\Delta \otimes I_n) \vec{\phi} - i((I - P) \otimes \Gamma^{-1} \bar{A}) V_{\vec{\phi}}(\Psi) \quad (4)$$

Here  $A$  is the antisymmetric coefficient matrix and  $\Gamma = \bar{A} A^T$ .  $P$  is the projection onto the subspace spanned by the orbitals  $\phi_i$ ,  $V_{\vec{\phi}}(\Psi)$  denotes the vector  $(V_{\phi_1}(\Psi), \dots, V_{\phi_n}(\Psi))^T$ , where  $V_{\phi_j}(\Psi)$  is defined by

$$\langle \xi, V_{\phi_j}(\Psi) \rangle = \int \overline{\xi(x_1) \phi_j(x_2)} V(x_1, x_2) \Psi(x_1, x_2) dx_1 dx_2$$

for all  $\xi \in \mathcal{H}$ .

## OUR GOALS AND (NUMERICAL) METHODS

We want to contribute to a better understanding of the derivation of these models (cf. [5], [3] and to understand their interrelationships as part of a model hierarchy.

We carry out numerical tests to study systematically how the (MC)TDHF models perform in the context of computationally feasible “toy” problems, compared to the linear  $N$  particle Schrödinger equation.

It is basically impossible to estimate “a priori” which of the models in the hierarchy is “better” for the calculation of a certain quantity – for example it is well known that sometimes the simple Hartree approximation gives better results than the more sophisticated Hartree Fock equation, especially when “correlation” effects play a role that are ignored by definition in the TDHF method. (cf e.g. [3] and [8]).

Clearly, MCTDHF is the canonical way to improve the TDHF method and should, with increasing number of configurations, converge to the solutions of the  $N$  body TDLSE.

However, the proof of convergence of solutions of MCTDHF to the solutions of the time dependent  $N$  body SE (in some appropriately defined trace norm, cf. [5], [3] is still completely open. Let us remark that for MCTDHF all basic mathematical questions are open, starting with existence of unique solutions (cf. [4]) up to questions of how going beyond the Born Oppenheimer approximation of “static ions” (cf. e.g. [7]).

We state recent results of mathematically oriented papers in a way that is understandable also for physicists and (quantum) electrical engineers and we study numerical convergence of certain physically interesting quantities, like charge densities or “correlation” according to the new definition [8].

To calculate numerical solutions of the MCTDHF equations is not trivial, since it requires the solution of a nonlinear system of ODEs for the coefficients  $a_{jk}(t)$  coupled to the evolution equations for the “orbitals”  $\phi_i(\mathbf{r}, t)$ .

In order to solve the MCTDHF equations (as well as the TDHF equations) we use a time splitting spectral scheme which was originally developed for the cubic NLS [2] and which has been proven to be a very efficient tool for very general classes of NLS (e.g. [1], [6]).

Using Born von Karman periodic boundary conditions on a sufficiently large domain of calculation fits well with the trigonometric spectral method for the free evolution that is split in time from the nonlinear potential part that yields an ODE that is solved by a fourth order Runge Kutta scheme.

We present simulations for a 2 electron system in 1 space dimension where all equations of the hierarchy, including the  $N$  body TDSE, can be solved relatively easily.

## ACKNOWLEDGMENT

This work was supported by the Austrian Ministry of Science (BM:BWK) via its grant for the Wolfgang Pauli Institute and by the Austrian Science Foundation (FWF) via the Wissenschaftkolleg “Differential equations” (W17) and the START Project (Y 137 TEC) of N. Mauser, and also by the European network HYKE funded by the EC as contract HPRN CT 2002 00282.

## REFERENCES

- [1] W. Bao, N.J. Mauser, H.P. Stimming, *Effective one particle quantum dynamics of electrons: a numerical study of the Schrödinger-Poisson- $X\alpha$  model*, Comm. Math. Sci., **1**(4), 809 (2003)
- [2] W. Bao, S. Jin, P.A. Markowich, *Numerical studies of time-splitting spectral discretisations of nonlinear Schrödinger equations in the semiclassical regime*, SIAM J. Sci. Comp., **25**(1), 27 (2003)
- [3] C. Bardos, F. Golse, A. Gottlieb, N.J. Mauser, *Accuracy of the time-dependent Hartree-Fock approximation for uncorrelated initial states*, J. Stat. Phys. **115**(3/4), 1037-1055 (2004)
- [4] C. Bardos, I. Catto, A. Gottlieb, N.J. Mauser and T. Saber, manuscript
- [5] C. Bardos, L. Erdős, F. Golse, N.J. Mauser and H.-T. Yau, *Derivation of the Schrödinger-Poisson equation from the quantum  $N$ -particle Coulomb problem*, C. R. Acad. Sci., **t 334**(6) Série I Math., 515-520 (2002)
- [6] C. Besse, N.J. Mauser, and H. P. Stimming, *Numerical study of the Davey-Stewartson system*, M2AN Math. Model. Numer. Anal. **38**(6), 1035-1054 (2004)
- [7] E. Cancès and C. Le Bris, *On the time-dependent Hartree-Fock equations coupled with a classical nuclear dynamics*, Math. Models Methods Appl. Sci. **9**, 963-990 (1999).
- [8] A.D. Gottlieb and N.J. Mauser, *A new definition of correlation for electron systems*, Phys.Rev.Lett. **95**(12) (2005) 213-217
- [9] C. Lubich, *On variational approximations in quantum molecular dynamics*, Mathematics of Computation, **74**, 765-779 (2005)
- [10] E. Runge, E.K.U. Gross, *Density functional theory for time-dependent systems*, Phys. Rev. Lett. **52**(12), 997-1000 (1984)

# Eigenstate fitting in the $\mathbf{k} \cdot \mathbf{p}$ method

H. López, A. N. Chantis\*, J. Suñé, and X. Cartoixa

Departament d'Enginyeria Electrònica, Universitat Autònoma de Barcelona, 08193 Bellaterra, Spain

\*Department of Chemical and Materials Engineering, Arizona State University, Tempe, AZ 85287, USA  
e-mail: Xavier.Cartoixa@uab.es

The  $\mathbf{k} \cdot \mathbf{p}$  method [1] is widely used in computational electronics for its ability to yield accurate band structures in the region of relevance for device operation. Several models can be constructed, based on the number of bands that are explicitly treated. Thus, it is common to talk about a single band (or two-band, with spin) model when only the conduction band (CB) is of interest, a four-band model describing heavy and light holes (HH, LH), or an eight-band for equal treatment of the CB, HH, LH and split-off (SO) bands. If nonparabolicity effects farther from the zone center need to be included, or the device operates under the action of a magnetic field, it may become necessary to venture into fourteen- [2] or even sixteen-band models [3], [4]. Of course, if the parametrization of these models is appropriately obtained, the obtained value for, say, the conduction band effective mass should be independent from the model choice. Thus, we can say that these  $\mathbf{k} \cdot \mathbf{p}$  models provide good fitting of the *eigenvalues* to experiment.

Then, the natural question arises to whether  $\mathbf{k} \cdot \mathbf{p}$  models can also provide good fittings to experimental *eigenstates*. The correct computation of these eigenstates is of great importance for optical transitions [5] or in interband tunneling [6], whose magnitude is given by the amount of coupling and, ultimately, by the overlap between different eigenstate components. These components also play a determinant role in some aspects of spin dynamics, such as the Elliot-Yafet [7], [8] spin relaxation mechanism. By eigenstate components we mean the coefficients  $c^{m,n}(\mathbf{k}) = \langle u_{\mathbf{k}_0}^m | u_{\mathbf{k}}^n \rangle$ , where  $u_{\mathbf{k}}^n(\mathbf{r})$  is the periodic part of the wavefunction of band  $n$  at a general  $\mathbf{k}$  point in the Brillouin zone, and  $u_{\mathbf{k}_0}^m(\mathbf{r})$  is the wavefunction for the preferred  $\mathbf{k}_0$  about which the  $\mathbf{k} \cdot \mathbf{p}$  development is made—the set of  $|u_{\mathbf{k}_0}^m\rangle$  for all  $m$  form a basis.

For some cases, the answer to the question in

the preceding paragraph is obviously not. Take, for example, a single band model. Far from the zone center, this model would be unaware that the true eigenstate acquires some hole component (and split-off, remote conduction band. . . components as well). Thus, we are interested in studying how big a model must be taken in order to ensure that the eigenstates have the correct mixing behavior.

Here we will present a systematic study with several  $\mathbf{k} \cdot \mathbf{p}$  models with increasing number of bands to determine the minimum number required to obtain realistic descriptions of the eigenstate behavior close to the Brillouin zone center for zincblende semiconductors. Because of the difficulty of finding experimental values for the eigenstate components, we will fit to eigenstates computed by more atomistic methods, such as a 40-band empirical tight binding model [9] and Quasiparticle self-consistent GW (QPscGW) [10], [11] calculations.

We will also show how the eigenstate fitting procedure can remove some of the uncertainties that the determination of  $\mathbf{k} \cdot \mathbf{p}$  parameters from the effective masses only has.

## ACKNOWLEDGMENT

This work is supported in part by the European Commission's Marie Curie International Reintegration Grant No. MIRG-CT-2005-017198 and by the Organization of Naval Research Contract No. N00014-02-1-1025. XC is a Spain's Ministry of Education and Science Ramón y Cajal fellow.

## REFERENCES

- [1] E. O. Kane, "The  $\mathbf{k} \cdot \mathbf{p}$  method," in *Semiconductors and Semimetals*, R. K. Willardson and A. C. Beer, Eds. New York: Academic, 1966, vol. 1, pp. 75–100.
- [2] U. Rössler, "Nonparabolicity and warping in the conduction-band of GaAs," *Solid State Commun.*, vol. 49, no. 10, pp. 943–947, 1984.

- [3] M. Cardona, N. E. Christensen, and G. Fasol, "Relativistic band structure and spin-orbit splitting of zinc-blende-type semiconductors," *Phys. Rev. B*, vol. 38, no. 3, pp. 1806–1827, 1988.
- [4] P. Pfeffer and W. Zawadzki, "Five-level k-p model for the conduction and valence bands of GaAs and InP," *Phys. Rev. B*, vol. 53, no. 19, pp. 12 813–12 828, 1996.
- [5] R. C. Miller, A. C. Gossard, G. D. Sanders, Y. C. Chang, and J. N. Schulman, "New evidence of extensive valence-band mixing in GaAs quantum wells through excitation photoluminescence studies," *Phys. Rev. B*, vol. 32, no. 12, pp. 8452–8454, 1985.
- [6] D. Z.-Y. Ting, E. T. Yu, and T. C. McGill, "Effect of band mixing on hole-tunneling times in GaAs/AlAs double-barrier heterostructures," *Phys. Rev. B*, vol. 45, no. 7, pp. 3576–3582, 1992.
- [7] R. J. Elliott, "Theory of the effect of spin-orbit coupling on magnetic resonance in some semiconductors," *Phys. Rev.*, vol. 96, no. 2, pp. 266–279, 1954.
- [8] Y. Yafet, in *Solid State Physics*, F. Seitz and D. Turnbull, Eds. New York: Academic Press, 1963, vol. 14, pp. 1–98.
- [9] J. M. Jancu, R. Scholz, F. Beltram, and F. Bassani, "Empirical sp<sup>3</sup>s\* tight-binding calculation for cubic semiconductors: General method and material parameters," *Phys. Rev. B*, vol. 57, no. 11, pp. 6493–6507, 1998.
- [10] M. van Schilfgaarde, T. Kotani, and S. Faleev, "Quasiparticle self-consistent gw theory," *cond-mat/0510408*, 2005.
- [11] A. N. Chantis, M. van Schilfgaarde, and T. Kotani, "Ab-initio prediction of conduction band spin splitting in zincblende semiconductors," *cond-mat/0508274*, 2005.

# Transport Calculation of Semiconductor Nanowires Coupled to Quantum Well Reservoirs

M. Luisier, G. Klimeck\*, A. Schenk, and W. Fichtner

Integrated Systems Laboratory, Gloriastrasse 35, ETH Zurich, 8092 Zurich, Switzerland

\*Network for Computational Nanotechnology, Purdue University, West Lafayette, IN 47907, USA  
e-mail: mluisier@iis.ee.ethz.ch

## INTRODUCTION

Semiconductor nanowires represent an attractive material system since they can be now produced with controlled material composition, physical dimensions, and electronic properties. Furthermore they can function at the same time as interconnects and as devices: with an individual nanowire, nanoscale field effect transistors (FETs) have already been realized [1].

On a simulation perspective, semiconductor nanowires are also very interesting because they exhibit electronic properties that can not be found in the usual MOSFET, like the 2D confinement of the electrons (or holes) in the channel. This implies that the widely spread effective-mass approximation can no more be used for transport calculation in devices with strong confinement, where the bandstructure plays a crucial role. In this work, therefore, an atomistic treatment of silicon nanowires is proposed with not only perfect contacts but also transitions from 1D (quantum well) to 2D (quantum wire) confined structures.

## RESULTS

To account for bandstructure effects in Si nanowires, the  $sp^3d^5s^*$  empirical tight-binding method is applied. Its parameters are optimized to reproduce the bulk bandstructure [2] and are assumed unchanged for nanostructures. The wire itself is constructed by translating the primitive unit cell of the semiconductor crystal, composed of two atoms. A small example with two additional quantum well reservoirs is shown in Fig. 1: the two different atoms of the primitive cell are plotted with different colors. Others than (100) growth directions can also be selected.

Any quantum transport problem requires appropriate open boundary conditions. The usual technique assumes semi-infinite reservoirs (Source and Drain) that are the prolongation of the device. In the present case this means a 2D electron confinement for the reservoirs. However, realistic devices have larger Source and Drain regions than the nanowire channel, leading to a transition from a 1D confined electron gas to a 2DEG one. This has a strong influence on the characteristics of the device, such as the transmission and the density of states, as shown in Fig. 2 and 3 but also on the computational effort.

The device is solved with an atomistic Green's function method whose boundary conditions are represented via self-energies. Their calculation can be accomplished via a recursive algorithm [3]. However 80% of the CPU time is still dedicated to that process. To improve the numerical efficiency a new algorithm was developed, based on the propagating waves in the reservoirs. It is 15-20 times faster than what is presented in Ref. [3] for this specific problem. The well established algorithm is labeled "Sancho-Rubio", the new one "injection" in Fig. 3.

## CONCLUSION

A more realistic treatment of Si nanowires is presented where perfect contacts are replaced by quantum wells. A new algorithm is used to solved the resulting problem.

## REFERENCES

- [1] Y. Cui, Z. Zhong, D. Wang, W.U. Wang, and C. Lieber, , *Nano Letters* **3**, 149 (2003).
- [2] T.B. Boykin, G. Klimeck, and F. Oyafuso, , *Phys. Rev. B* **69**, 115201 (2004).
- [3] M.P. Lopez Sancho, J.M.. Lopez Sancho, and J. Rubio, *J. Phys. F: Met. Phys.* **15**, 851 (1985).

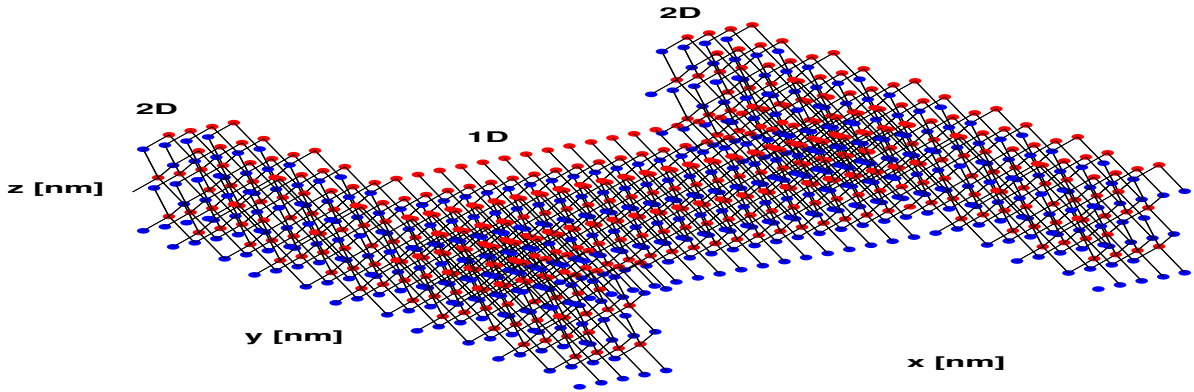


Fig. 1. Schematic view of a Si nanowire (1D electron gas) with quantum well Source and Drain (2D electron gas). Benchmark example for the wire:  $x=22$  nm,  $y=1.6$  nm,  $z=1.6$  nm. Source and Drain are assumed infinite in the  $x$  and  $y$  directions.

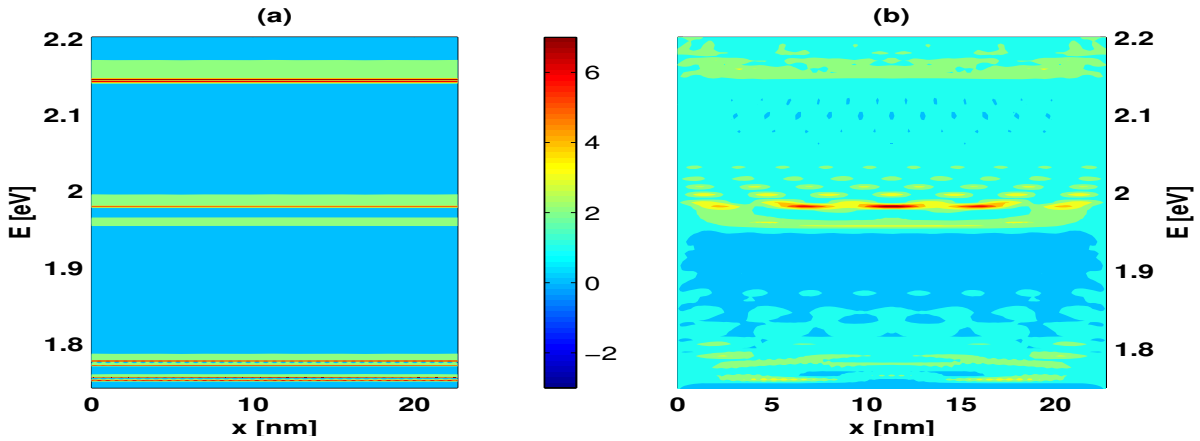


Fig. 2. Spectral density of states for the wire from Fig. 1, (a) with perfect boundary conditions (BC) where Source and Drain are the same as the Device, DOS is perfectly smooth in  $x$  and step-like in  $E$ , (b) with discontinuity in BC (2DEG-1DEG transition) inducing evident interference effects in the inhomogeneous DOS.

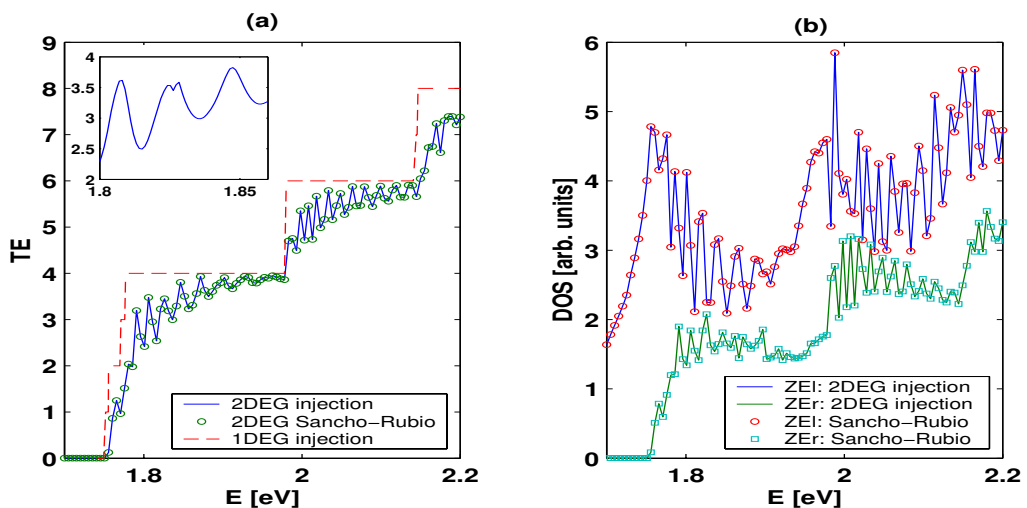


Fig. 3. (a) Transmission through the wire from Fig. 1 with quantum well (circled line + zoom) and perfect contacts (dashed line). “Injection” labels the new algorithm, “Sancho-Rubio” the usual one. (b) Density of state at  $x=0$  nm (Source) coming from left (Source, solid line with circles) and right (Drain, solid line with squares) quantum well reservoirs.

# Tunneling Enhancement through a Barrier Surrounded by a Mesoscopic Cavity

M. Macucci and P. Marconcini

Dipartimento di Ingegneria dell'Informazione, Università di Pisa, via Caruso 16, I-56122 Pisa, Italy

e-mail: macucci@mercurio.iet.unipi.it

## INTRODUCTION

We have studied the effect of a potential barrier included in a mesoscopic cavity, i.e. a region much wider than the Fermi wavelength of the electrons and delimited by constrictions that are of the order of such a wavelength. Mesoscopic cavities are usually obtained by means of two quantum point contacts that define constrictions with a width of a few tens or hundreds of nanometers in a mesa that is several microns wide [1]. Several interesting results have been obtained for the noise and conductance behavior of such structures [2], [3], [4].

Here we focus on an intriguing property of a cavity containing a relatively opaque (compared to the constrictions defining the cavity) barrier. In particular, we have observed that the overall conductance of the cavity is strongly dependent on the position of the barrier, with a maximum corresponding to the situation with the barrier exactly in the middle of the cavity. The most striking feature is that in this condition the overall transmission coefficient is much larger than that which would be associated with the isolated barrier.

## MODEL AND NUMERICAL RESULTS

We adopt a numerical approach based on the recursive Green's function technique and consider a mesoscopic cavity, sketched in Fig. 1, which is defined by hard walls, with a length of  $5 \mu\text{m}$ . Different values are considered for the width of the cavity and of the constrictions. In Fig. 2 we report the dependence of the overall transmission of the structure as a function of the position of an 11 nm thick and 40 meV high potential barrier in a cavity that is 500 nm wide and delimited by 50 nm constrictions. The transmission of the barrier alone at the value of the energy being considered (9.03 meV) is 0.195: it is apparent that when the barrier is

located exactly in the middle of the cavity, the transmission reaches a value (0.6) well above that for the cavity, thus exhibiting quite significant a tunneling enhancement. Enhanced tunneling is observed also for positions corresponding to  $1/4$  and  $3/4$  of the cavity and for other intermediate positions. In Fig. 3 we report data for a structure identical to the one just described, but with the right constriction 70 nm wide: constriction asymmetry does not destroy the effect. The tunneling enhancement gains in strength as the cavity is made wider, as shown in Fig. 4, where the transmission dependence is reported for a cavity width of  $4 \mu\text{m}$ , and a 15 nm thick barrier (with a transmission factor 0.244). In this case only a very strong peak for the barrier in the cavity center survives, while the others disappear.

This is not a simple resonance effect, because it can be observed over a large range of energies, as shown in Fig. 5, where the transmission of a cavity with a barrier in the middle is plotted (thick curve) as a function of the Fermi energy. We propose a preliminary explanation based on the fact that odd longitudinal modes in the cavity are not significantly affected by the presence of a barrier in the middle, where they have a node. The modes in the constriction couple to such modes in the cavity, which can propagate freely and reach the exit constriction.

## REFERENCES

- [1] S. Oberholzer, E. V. Sukhorukov, C. Strunk, C. Schönenberger, T. Heinzel, M. Holland, *Phys. Rev. Lett.* **86**, 2114 (2001).
- [2] R. A. Jalabert, J. L. Pichard, C. W. J. Beenakker, *Europhys. Lett.* **27**, 255 (1994).
- [3] S. A. van Langen and M. Büttiker, *Phys. Rev. B* **56**, R1680 (1997).
- [4] P. Marconcini, M. Macucci, G. Iannaccone, B. Pellegrini, and G. Marola, to be published in *Europhysics Letters*

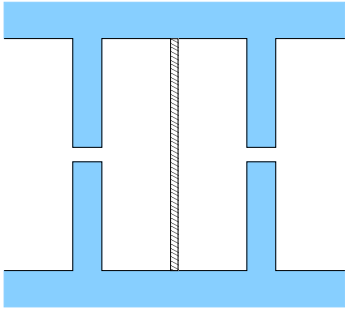


Fig. 1. Sketch of the cavity with the potential barrier.

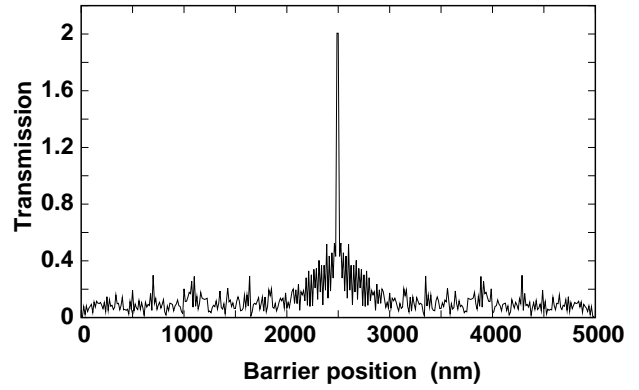


Fig. 4. Transmission vs. barrier position for a 4000 nm wide cavity.

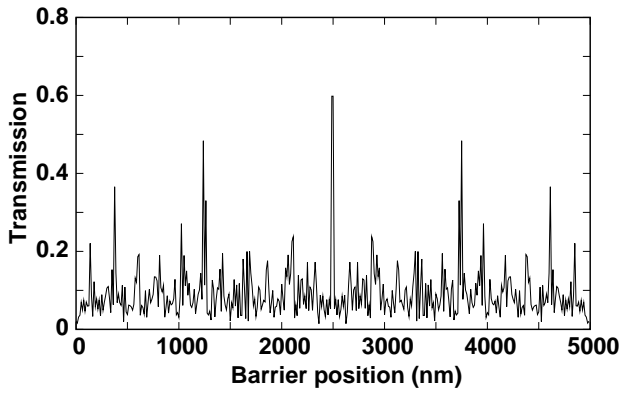


Fig. 2. Transmission vs. barrier position for a symmetric 500 nm wide cavity.

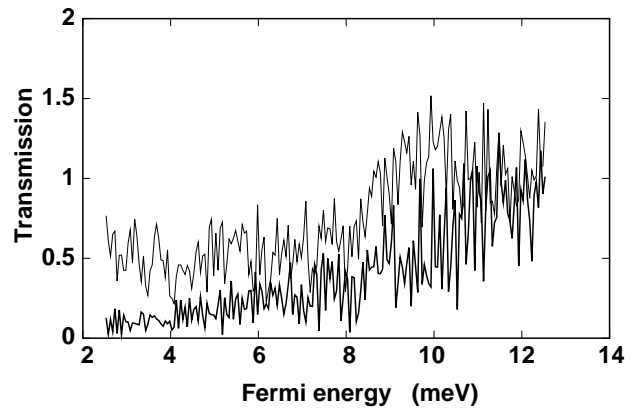


Fig. 5. Transmission vs. Fermi energy for a cavity with (thick line) and without (thin line) barrier.

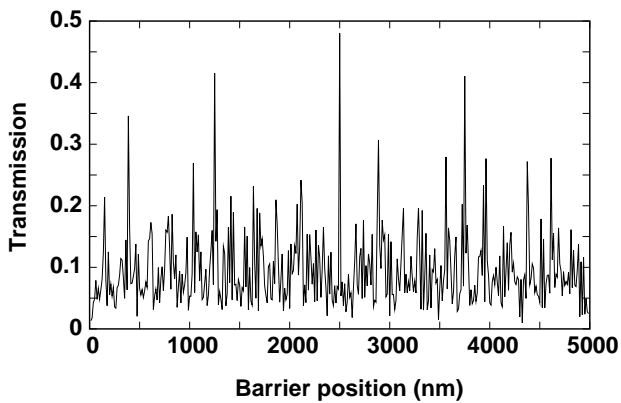


Fig. 3. Transmission vs. barrier position for an asymmetric 500 nm wide cavity.

# Modeling the Inelastic Scattering Effect on the Resonant Tunneling Current

B. Majkusiak

Institute of Microelectronics and Optoelectronics, Warsaw University of Technology,  
Koszykowa 75, 00-662 Warsaw, Poland  
e-mail: majkusiak@imio.pw.edu.pl

## INTRODUCTION

Since the double gate SiO<sub>2</sub>/Si/SiO<sub>2</sub> structure has been proposed as a resonant tunneling diode (RTD) [1] the first experimental observations [2] and theoretical models [3] have been reported. However, theoretical simulation of current flowing through the RTD structure wrestles with difficulties resulting from details of the device's physics and numerical procedure efficiency. This paper describes an implementation of the inelastic scattering into the steady-state model of the RTD.

## THEORETICAL MODEL

Fig. 1 shows the carrier flow paths in a biased RTD structure.  $J_{eCr}$  is a current of electrons, which successfully tunnel from the emitter to collector.  $S_{eE}$  is the current of electrons tunneling from the emitter to the base and then, on their way of multiply reflections between the barriers, are scattered by inelastic processes.  $J_{eEr}$  and  $S_{eC}$  denote similar fluxes for electrons tunneling from the collector. In the steady state the total scattering flux  $S_{eE} + S_{eC}$  charging the base must be equal to the flux of electrons leaving the quasi-bounded levels in the base  $E_{ij}$  by tunneling to the emitter  $I_{eE}$  and collector  $I_{eC}$  or recombining with holes  $S_{rg}$ . Similar fluxes and the steady-state condition can be defined for holes. Thus, the terminal electron and hole currents are:

$$J_e = I_{eRT} + S_{eE} - J_{eE} = J_{eRT} - S_{eC} + J_{eC} \quad (1)$$

$$J_h = J_{hRT} - S_{hE} + J_{hE} = J_{hrt} + S_{hC} - J_{hC} \quad (2)$$

where  $I_{eRT} = I_{eCr} - I_{eEr}$  and  $I_{hRT} = I_{hEr} - I_{hCr}$  are the net electron and hole resonant tunneling currents.

With the use of the transfer matrix method, the scattering matrix elements  $[S_E]$ ,  $[S_B]$  and  $[S_C]$  are determined, that tie  $(a_{out}, b_{in})$  to  $(a_{in}, b_{out})$  components of the wave functions in the appropriate regions (Fig. 2). It is assumed that due to scattering the  $t_B$  and  $t'_B$  transition factors through the base are

reduced by  $(1-P_{sc})^{1/2}$ , where  $P_{sc} = 1 - \exp(-t_T/\tau_{sc})$  is the scattering probability during the time  $t_T$  of one transit through the base between the subsequent reflections from the barriers. The resonant tunneling probability  $P_{eCr}$  to the collector is expressed as:

$$P_{eCr} = \frac{k_C m_{xE}}{k_E m_{xC}} \left| \frac{t_E t_B t_C}{(1 - r_E' r_B)(1 - r_B' r_C) - r_E' t_B t_B' r_C} \right|^2 \quad (3)$$

where the transmission  $t$  and reflection coefficients  $r$  are complex quantities. The scattering probability of electrons tunneling from the emitter is given by:

$$P_{sE} = P_E P_{sc} \frac{1 + P_B R_C}{1 - P_B^2 R_E R_C} \quad (4)$$

The resonant tunneling currents and the scattering fluxes are obtained by integrating products of the appropriate probabilities  $P_{eEr}$  or  $P_{sE}$  and the ' supply function  $N_E(E)$  in the emitter. The tunnel currents from discrete levels to the gate electrodes are calculated by summing the products of two-dimensional electron concentrations and escape rates to the electrodes.

## DISCUSSION

Fig. 3 shows the resonant tunneling probability to the collector without ( $P_{rt0}$ ) and with scattering ( $P_{rts}$ ) for a double polysilicon gate ( $N_D = 2 \times 10^{20} \text{ cm}^{-3}$ ) diode with a 3nm thick intrinsic silicon well and two SiO<sub>2</sub> layers of 1nm thickness. The assumed scattering time constant was  $t_{sc} = 3 \times 10^{-14} \text{ s}$  as an average of the scattering rates calculated for the obtained quasi-bounded level spectrum according to the perturbation approach. As can be seen, the scattering probability flux for a given energy can be approximated by probability of the sequential tunneling through the first barrier. Scattering damps the tunneling probability peaks. Fig. 4 shows the energy distribution of currents of electrons tunneling from the emitter with the transverse effective mass. The net resonant tunneling current

$J_{ert}$  is compared with the fluxes  $S_{eC}$  and  $I_{eC}$  affecting the terminal current according to (2). The resultant terminal current with and without scattering is shown in Fig. 5 in dependence on the voltage. Scattering suppresses the resonant current peak for the considered parameters of the DG MOS system and the total current in the plane of collector is dominated by current  $I_{eC}$  of non-coherent electrons.

### CONCLUSION

Modeling the inelastic scattering effect on the resonant tunneling current may be a key issue for developing a reliable RTD' s simulator.

### ACKNOWLEDGEMENT

This work has been carried out in the framework of the European NoE SINANO (IST-506884).

### REFERENCES

- [1] R. M. Wallace, A. C. Seabaugh, *Silicon oxide resonant tunneling diode structure*, U.S. Patent no. 5,606,177, 25 Feb. 1997.
- [2] Y. Ishikawa, T. Ishihara, M. Iwasaki, M. Tabe, *Negative differential conductance due to resonant tunneling through SiO<sub>2</sub>/single-crystalline-Si double barrier structure*, Electronics Letters, **37**, 1200 (2001).
- [3] B. Majkusiak, *Theoretical modeling of the double gate MOS resonant tunneling diode*, ULIS' 03, Udine, Italy, March 2003, Proceedings.

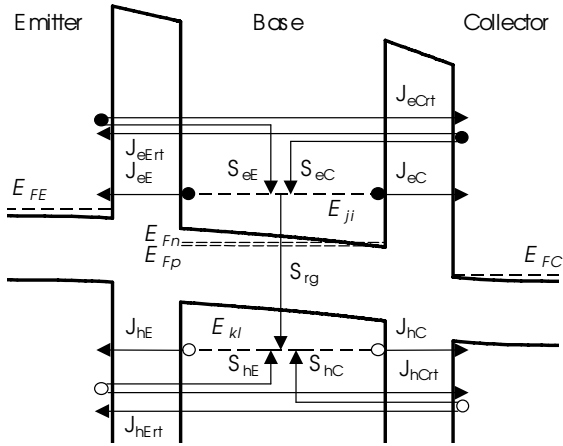


Fig. 1. Current fluxes in the biased DG MOS RTD structure.

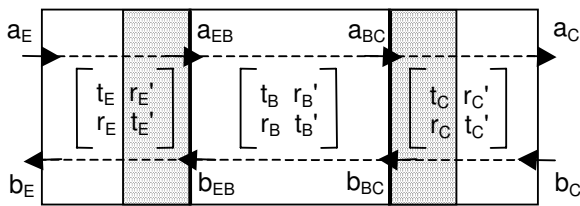


Fig. 2. Scattering matrix representation for considerations of the resonant transition of the wave function.

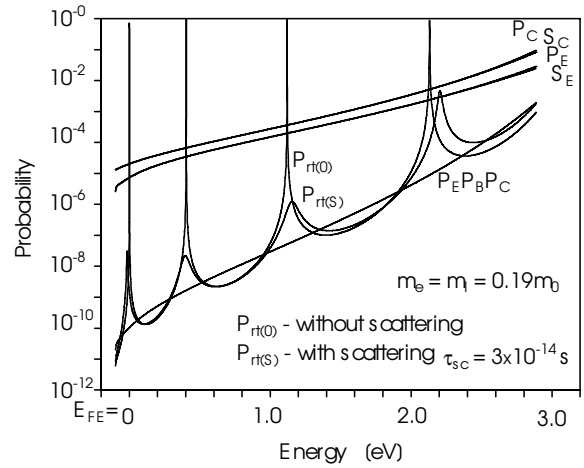


Fig. 3. Energy distribution of probabilities of the resonant tunneling  $P_{rt}$ , sequential tunneling  $P_E$  and  $P_C$ , and scattering  $P_{sE}$  and  $P_{sC}$  for RTD structure at  $V_{CE} = 0.5V$ .

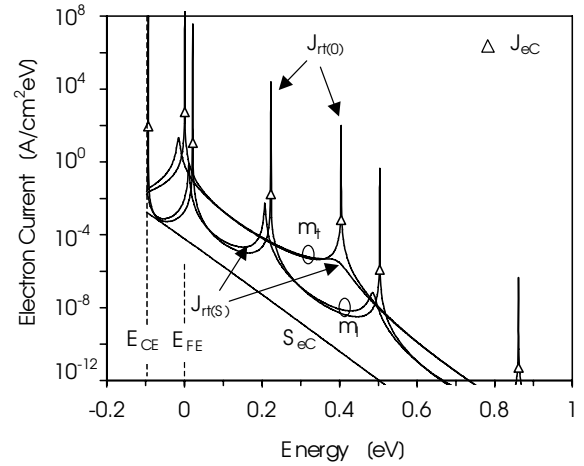


Fig. 4. Energy distribution of the electron resonant tunneling current  $J_{eCrt}$  and the scattering current  $S_{eE}$  at  $V_{CE} = 0.5V$ .

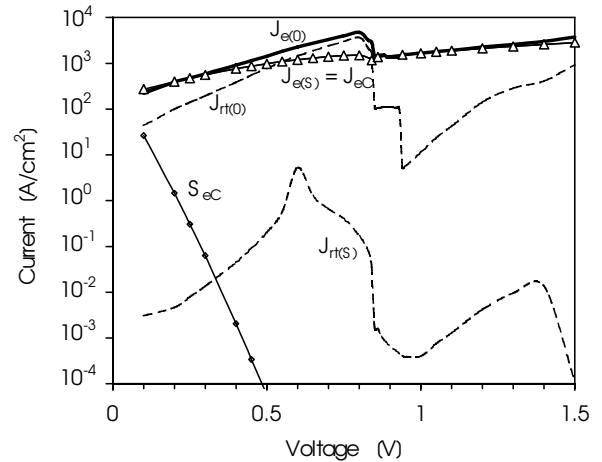


Fig. 5. Comparison of currents flowing through the collector junction and the total currents with and without scattering.

# Tight-binding and $\mathbf{k} \cdot \mathbf{p}$ Methods in Carbon Nanotubes: Comparison, Results, and Improvements

P. Marconcini and M. Macucci

Dipartimento di Ingegneria dell'Informazione, Università di Pisa, Via Caruso 16, I-56122 Pisa, Italy  
e-mail: macucci@mercurio.iet.unipi.it

## INTRODUCTION

Carbon nanotubes are a very promising material for nanoelectronic applications, due to their very small size and to their peculiar physical properties. A carbon nanotube can be described as a graphene sheet rolled into a cylindrical shape. Its dispersion relations can be found from those of 2D graphite by enforcing a closure boundary condition.

## METHODS

The graphene energy bands can be found either using global methods (such as tight-binding), which provide results over the whole  $k$ -space, or local methods (such as  $\mathbf{k} \cdot \mathbf{p}$ ), which yield the correct energy bands only near their extrema, but with less computational effort. In particular, using the tight-binding method [1] and considering only the effect of the  $2p_z$  atomic orbitals (the most relevant for transport) as well as only nearest-neighbor interaction, we find the graphene energy dispersion relations reported in Fig. 1. Alternatively, if we insert the slowly varying electronic envelope functions into the tight-binding equations, around the extrema we obtain a  $\mathbf{k} \cdot \mathbf{p}$  Hamiltonian matrix, the eigenvalues of which give the  $\mathbf{k} \cdot \mathbf{p}$  dispersion relations of graphene [2]. Enforcing closure periodic boundary condition for graphene corresponds to considering cross-sections of the graphene energy bands along parallel segments; if we replot the thus found cross-sections in the nanotube Brillouin zone, we obtain the nanotube dispersion relations (Fig. 2). By differentiating the thus computed dispersion relations, it is then possible to obtain the density of states (DOS).

## COMPARISON AND IMPROVEMENTS

In Figs. 3-6 we show the results obtained with the two methods, in terms of energy bands and DOS, for two nanotubes with different circumference. The  $\mathbf{k} \cdot \mathbf{p}$  method yields quite good results for the bands obtained by cross-sectioning the graphene dispersion relations near their extrema. In particular, for nanotubes with larger circumference, the bands closer to the graphene extrema are better reproduced, due to the smaller distance between the parallel segments on which we take the cross sections of the graphene energy bands. Analogously, the DOS obtained with the  $\mathbf{k} \cdot \mathbf{p}$  method is very close to the one computed with the tight-binding approach for small values of the energy, corresponding to the energies for which the  $\mathbf{k} \cdot \mathbf{p}$  method provides a good approximation of the graphene energy bands. In these calculations  $\mathbf{k} \cdot \mathbf{p}$  is faster than tight-binding, not only because of the reduced complexity of the calculations, but also because in the  $\mathbf{k} \cdot \mathbf{p}$  approach (in which calculations are made relatively to the graphene extrema points) we can eventually limit ourselves to the determination of only the bands closest to the graphene extrema (which are the most interesting for transport analysis), while with tight-binding this choice of bands can be much more difficult. We propose an innovative procedure that, adopting an unusual choice of unit vectors in the reciprocal space, allows to easily select such bands in the tight-binding method.

## REFERENCES

- [1] R. Saito, G. Dresselhaus, and M. S. Dresselhaus, *Physical Properties of Carbon Nanotubes* (Imperial College Press, London, 1998).
- [2] T. Ando, *Theory of Electronic States and Transport in Carbon Nanotubes*, J. Phys. Soc. Jpn. **74**, 777 (2005).

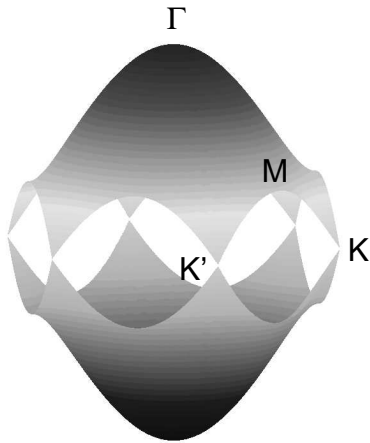


Fig. 1. Energy dispersion relations of the graphene within its Brillouin zone.

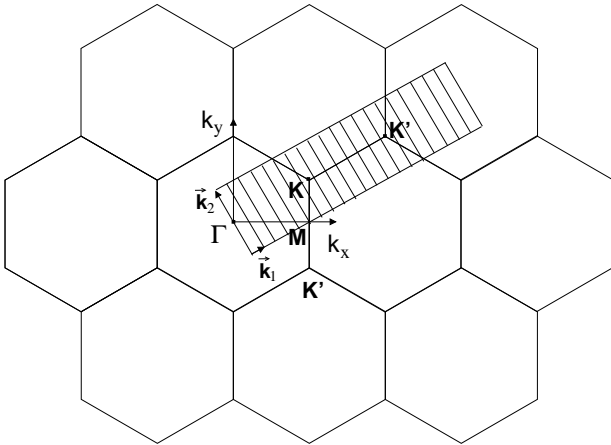


Fig. 2. The energy dispersion relations of the nanotube can be obtained from the ones of the graphene cross-sectioning them in correspondence of parallel segments.

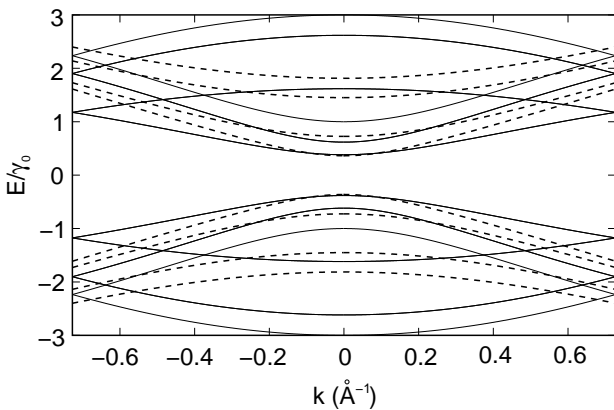


Fig. 3. Dispersion relations of the nanotube (5,0) computed with the tight-binding method (solid lines) and with the  $\mathbf{k} \cdot \mathbf{p}$  method (dashed lines);  $\gamma_0$  is the absolute value of the transfer integral between nearest-neighbor atomic orbitals.

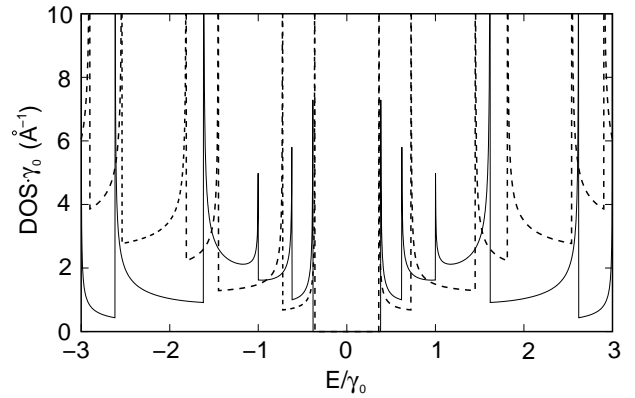


Fig. 4. Density of states of the nanotube (5,0) computed with the tight-binding method (solid lines) and with the  $\mathbf{k} \cdot \mathbf{p}$  method (dashed lines).

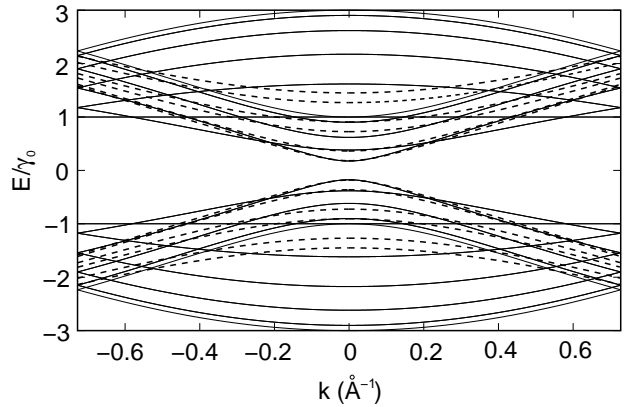


Fig. 5. Dispersion relations of the nanotube (10,0) (which has a circumference twice that of the nanotube (5,0)), computed with the tight-binding method (solid lines) and with the  $\mathbf{k} \cdot \mathbf{p}$  method (dashed lines).

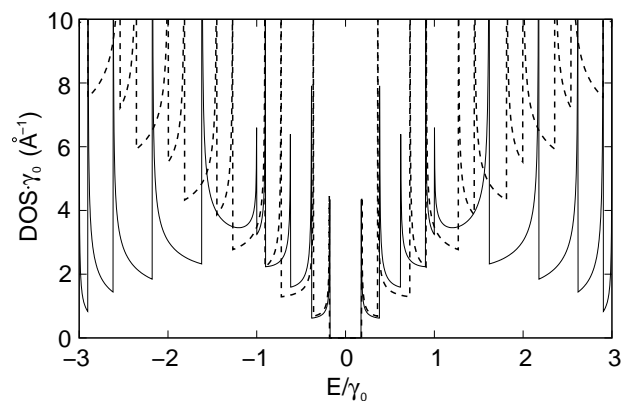


Fig. 6. Density of states of the nanotube (10,0) computed with the tight-binding method (solid lines) and with the  $\mathbf{k} \cdot \mathbf{p}$  method (dashed lines).

# Developing a Full 3D NEGF Simulator with Random Dopant and Interface Roughness

A. Martinez, J. R. Barker, M. P. Anantram\*, A. Svizhenko\* and A. Asenov  
Dept of Electronic and Electrical Engineering, University of Glasgow, Glasgow G128LT, UK  
\*NASA Ames research center, MS:229-1, Moffet Field, California 94035-1000, USA  
e-mail: antonio@elec.gla.ac.uk

The importance of discrete dopant in the source/drain, straight dopant in the channel, and imperfections in the Si/SiO<sub>2</sub> interface became very important at nanometer device dimensions. The effect of random dopants and surface roughness do not average on such small devices. Therefore the particular configuration of dopants from device to device produce fluctuations in the current and threshold voltage in an ensemble of technologically similar devices as show previously using 2D NEGF simulations [1]. Quantum phenomena are important for those small devices. One of the well established techniques for Nano-CMOS device simulation is the Non Equilibrium Green's Function (NEGF) approach to quantum transport. Two dimensional NEGF models produce reasonable qualitative results however the restrictions to the line charges and 1D interface roughness result in an overestimation of the effect of fluctuations, especially in very small devices. A more realistic situation can be achieved in 3D but unfortunately the 3D quantum mechanical NEGF description of the transport is very computationally expensive and memory consuming. This is because of the fine step energy integration and large matrix inversions requirements. Fortunately faster processors and larger memories are becoming available allowing the 3D NEGF technique to become a realistic choice for the simulation of in ballistic nanotransistors. Here we present the development of a full 3D NEGF simulator, which runs in parallels, and is able to compute electron density, current and transmission for different device configurations. The simulator allows the used of different boundary conditions in the cross section of the device including reflected, wrapped around, and zero density boundaries. A recursive algorithm, in order to calculate the density of states and electron density has been incorporated. This allows us to calculate

efficiently the diagonal terms of the  $G^r$  retarded green function and  $G^<$  the less than green function which are needed in order to compute the density of states and the electron density respectively. The calculation of the first off diagonal terms of  $G^<$  is needed in order to compute the current density. The self-energies are calculated following [2]. In this work we have concentrated on the sub threshold regime, where the coupling with the Poisson equation is not essential. Our main focus is the impact of the location of unintentional dopant, and their relative configuration on the transmission and electron density. The effect of the surface roughness on the electron density has also been studied for different randomly generated surface roughness configurations. A slab of 2nm x 2nm x 6nm undoped Si has been used in the simulations. Å mesh spacing is used for generating the space mesh. The energy mesh contains around 600 points. Fig 1 and Fig. 2 show the potential and current density landscapes for two transversal plane (y is the transport direction) in the case of 2 non aligned charges along the channel. Figs. 3, 4 show the same distribution in the case with interface roughness. The potential and electron density for two different cross sections are shown in fig. 5 in the presence of roughness. Fig. 6 shows the transmission as a function of energy for 5 different cases. Note than in the case of 3 impurities the transmission start early than in the case of 2 impurities showing a constructive interference.

## REFERENCES

- [1] A. Martinez, A. Svizhenko, M. P. Anantram, J. R. Barker, A.R. Brown and A. Asenov, IEDM Tech. Dig., 627 (2005).
- [2] R. Venugopal, Z. Ren, S. Datta and M. Lundstrom, *Simulating quantum transport in nanoscale transistors: Real versus mode-space approaches*, J. App. Phys. **92**, 3730-3739 (2002)

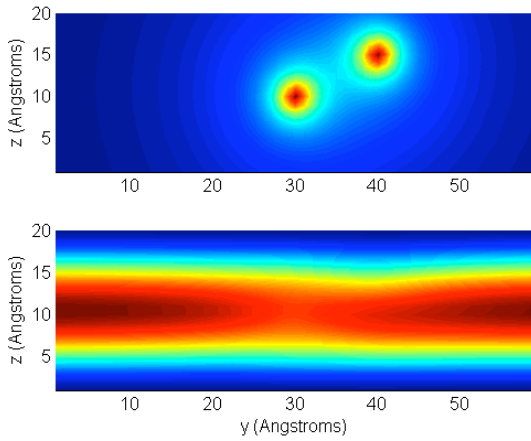


Fig. 1. upper and lower panels present the potential and current landscape respectively for the case of two non alignment charges for the zy plane

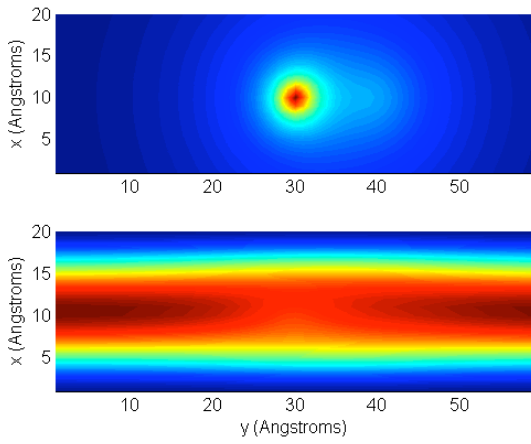


Fig. 2. Same as fig. 1 but for the xy-plane

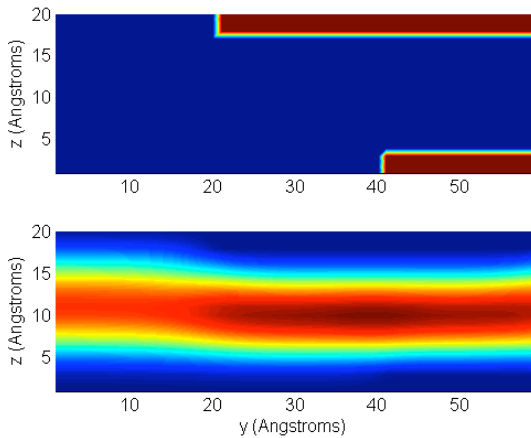


Fig. 3. Same as fig 1 but for the case with interface roughness

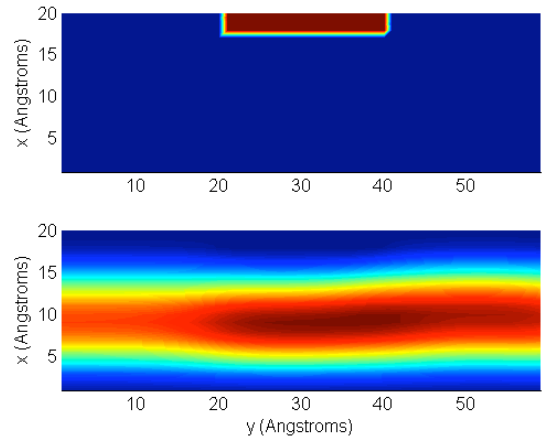


Fig. 4. The same as fig. 3 but in the xy-plane

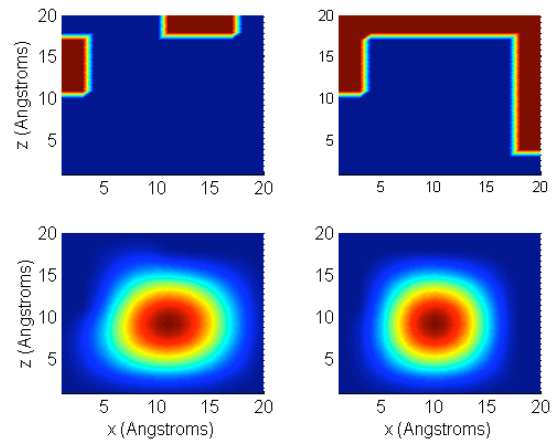


Fig. 5. The two upper panels show the interface roughness for two different cross sections and the lower panels stand for the corresponding electron densities

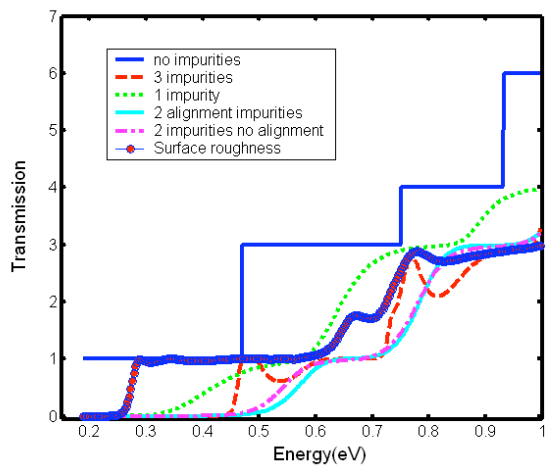


Fig. 6. The transmission function for some of the cases simulates. The case without impurities and surface roughness is also shown.

# Simulation of High-Field Magnetotransport in Non-Planar 2D Electron Systems

Gregory J. Meyer and Irena Knezevic

Department of Electrical and Computer Engineering, University of Wisconsin-Madison,  
Madison, WI 53706, USA

e-mail: gjmeyer@wisc.edu, knezevic@engr.wisc.edu

Non-planar two-dimensional (NP2D) electron systems have started to attract theoretical attention [1,2], as they can presently be reliably fabricated on both III-V thin-film heterostructures [3-5] and strained Si nanomembranes [6]. Curvature becomes another degree of freedom available for manipulating electronic properties of these systems (Fig. 1), which leads to novel basic physics and suggests NP2D application in NEMS as ultra-sensitive scales and sensors.

In this paper, we report the high-field magnetotransport calculations in a ballistic curved resonant quantum cavity (RQC). The NP2D electron system is formed at the junction of a GaAs/InGaAs heterostructure by creating two symmetric constrictions (of 40 nm width) in a 200 nm wide quantum wire (Fig. 2). Upon selective underetching of the sacrificial layer, strain relaxation causes the wings of the cavity to roll into a partial cylinder, while the central spine (also 40 nm wide) remains tethered to the substrate. (This design loosely follows that of Ref. [7], although those experiments dealt with pronouncedly scattering-limited transport at non-cryogenic temperatures.) Planar RQCs of similar construction have been studied extensively and their transport properties are well-known [8]. Cylindrical structures, however, display interesting physics on a number of levels. Their curvature induces an attractive geometric potential [9], inversely proportional to the radius of curvature squared. Moreover, their surfaces do not remain normal to the direction of the magnetic field, creating non-uniformities in the flux. The interplay of these factors has interesting effects on the transport properties of cylindrical RQCs, as seen in Fig. 1, which depicts the dependence of the conductance on the curvature and magnetic field (low-field regime).

Computationally efficient modeling of quantum-scale transport under *strong* ( $>1$  Tesla) magnetic fields has been a challenge. Recent enhancements to the well-known recursive Green's function method [10] have improved the feasibility of high-field magnetotransport simulations. This has been accomplished through the decomposition of complex geometries into multiple connected modules with symmetry-adapted gauges. Local gauge transformations are performed at the junctions between modules, and the final transmission matrix is transformed back to gauge-invariant form. We have expanded this method to incorporate non-planar (specifically cylindrical) geometries. Fig. 2 illustrates the evolution of the calculated electron density as the cavity rolls up in a homogeneous magnetic field of 10 T, applied perpendicular to the flat cavity (topmost left panel). Starting from the well-defined edge states in the flat cavity, the electron distribution throughout the cavity is altered with increasing curvature.

In summary, we present a comprehensive magnetotransport calculation on NP2D cylindrical systems. This work elucidates a signature of NP2Ds and a source of their large potential in NEMS and sensing applications: the interplay between electronics and geometry.

This work was funded by NSF through the University of Wisconsin MRSEC.

- [1] A.V. Chaplik *et al.*, *Superlatt. Microstruct.* **23**, 1227 (1998).
- [2] A. Marchi, S. Reggiani, M. Rudan, and A. Bertoni, *Phys. Rev. B* **72**, 035403 (2005).
- [3] V. Ya. Prinz *et al.*, *Physica E* **6**, 828-31 (2000).
- [4] A. Lorke *et al.*, *Superlatt. Microstruct.* **33**, 347 (2003).
- [5] S. Mendach *et al.*, *Physica E* **23**, 274-9 (2004).
- [6] M.M. Roberts *et al.* *Nature Materials*, submitted (2005).
- [7] N. Shaji *et al.*, *Physica E*, *in press*.
- [8] J.P. Bird *et al.*, *Rep. Prog. Phys.* **66**, 583 (2003).
- [9] R.T. DaCosta, *Phys. Rev. A* **34**, 1982 (1981).
- [10] S. Rotter *et al.*, *Phys. Rev. B* **68**, 165302 (2003).

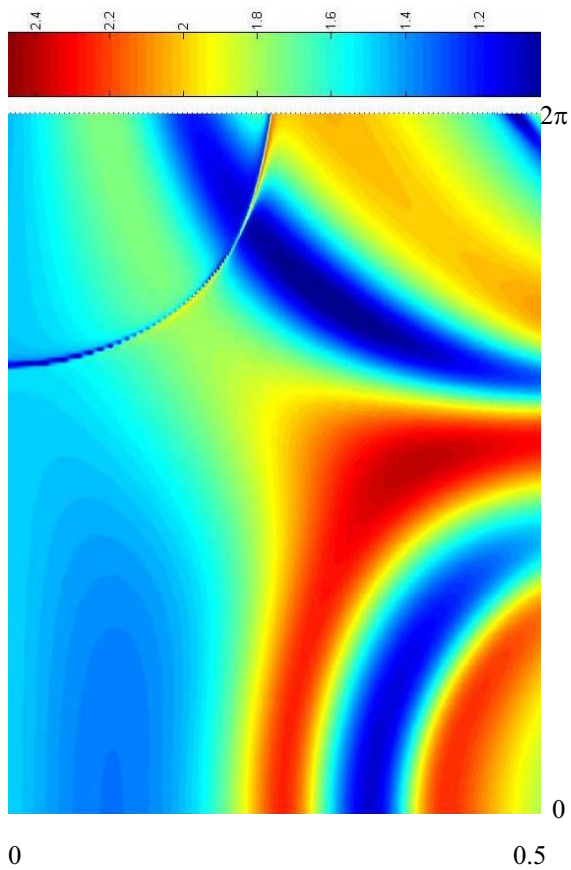


Fig. 1. Conductance, represented by color and given in the units of the conductance quantum  $2e^2/h$  (see color bar, top) as a function of the magnetic field (horizontal axis, in Tesla) and curvature (vertical axis, in units of width / radius of curvature). Electron density is  $4.5 \times 10^{11} \text{ cm}^{-2}$ .

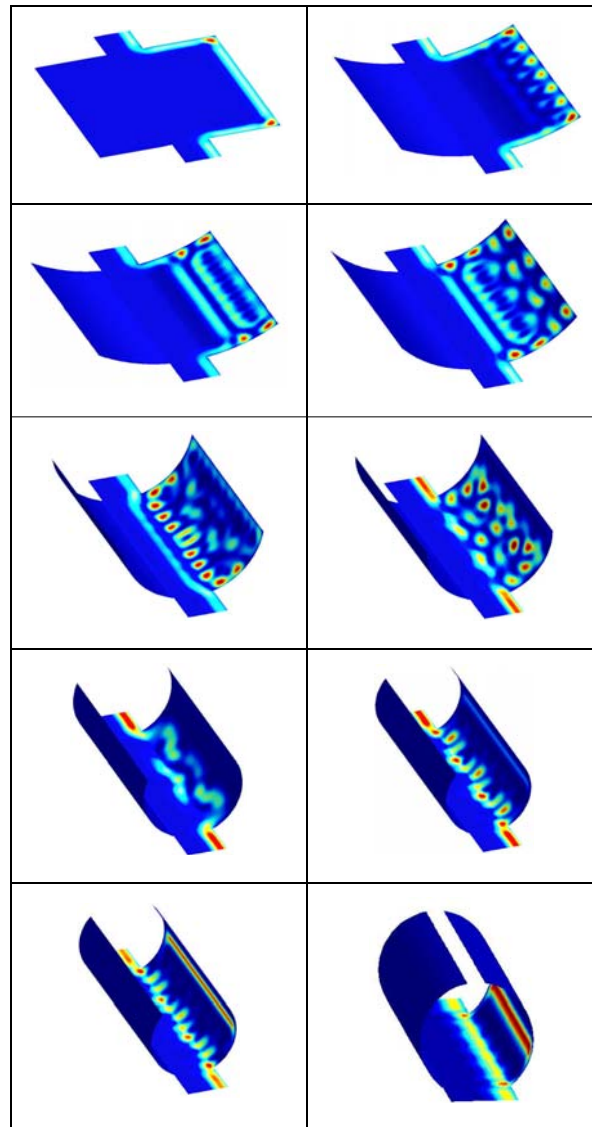


Fig. 2. Evolution of edge states under a 10 Tesla uniform magnetic field (perpendicular to the flat cavity), as the quantum cavity rolls up under strain.

# Numerical Simulation of Hole Transport in Silicon Nanostructures

H. Minari, H. Takeda, M. Okamoto, and N. Mori  
Department of Electronic Engineering, Osaka University  
2-1 Yamada-oka, Suita City, Osaka 565-0871, Japan  
e-mail: mitsunari@ele.eng.osaka-u.ac.jp

## INTRODUCTION

In ultra-small MOSFETs, quantum-mechanical effects, such as quantum confinement and source-drain direct tunneling, significantly affect device characteristics. To simulate electron transport in such devices, quantum-transport modeling is necessary. For CMOS application, quantum simulation of hole transport is also required. For hole transport modeling, it is desirable to include the valence-band structure using an accurate method, such as an empirical tight-binding method, since the valence-band structure is complex and makes the hole effective mass dependent on the axis orientation. Quantum simulation with the complex valence-band structure, however, requires expensive computational costs, which may restrict the device size that can be simulated. The tradeoff between accuracy and computational costs is one of important issues associated with the quantum simulation of hole transport. In order to address this issue, we have performed numerical simulation of hole transport in nanoscale Si structures within a nonequilibrium Green's function formalism combining with three different types of methods for band structure calculation; an empirical  $sp^3d^5s^*$  tight-binding method (TBM) [1],  $\mathbf{k}\cdot\mathbf{p}$  multi-band approximation (MBA) [2], and effective-mass approximation (EMA).

## METHOD

We consider a (100)-oriented  $p^+pp^+$  Si nanostructure whose schematic diagram is given in Fig. 1. The device structure is the same as that considered in Ref. [3] except for the type of doping. For the longitudinal direction ( $x$  direction), we use a discrete lattice in real space. For the transverse directions ( $y$ - $z$  directions), we assume periodic boundary conditions and use the eigenstate basis labeled by

two-dimensional wavevectors  $\mathbf{k} = (k_y, k_z)$ . We discretize the two-dimensional  $\mathbf{k}$ -space into triangular meshes and evaluate spectral functions,  $A(\mathbf{k}, E)$ , and transmission functions,  $T(\mathbf{k}, E)$ , at each mesh point. Hole density and the total transmission are then calculated by summing those functions over  $\mathbf{k}$ - and energy-spaces.

## RESULTS AND DISCUSSION

We used the parameters of Ref. [4] for TBM and those of Ref. [2] for MBA. For EMA, we adjust the heavy hole mass so as that the density of states agrees with that of TBM (see Fig. 2). Fig. 3 shows a density plot of  $A(\mathbf{k}, E)$  at  $\Gamma$ -point calculated with EMA for  $V_d = 50$  meV. The self-consistent potential profile is also plotted by solid line. Figs. 4 and 5 represent  $A(\mathbf{k}, E)$  at  $\Gamma$ -point calculated with MBA and TBM, respectively, for the same potential profile given in Fig. 3. Performing similar calculations for other  $\mathbf{k}$  mesh points, we obtain the hole density profile and current density. In Fig. 6, the calculated hole density profile is plotted for  $V_d = 50$  meV. We see that EMA is insufficient for an accurate modeling of hole transport in Si nanostructures.

## ACKNOWLEDGMENT

We would like to thank Semiconductor Technology Academic Research Center (STARC) for financial support.

## REFERENCES

- [1] J.-M. Jancu, R. Scholz, F. Beltram, and F. Bassani, *Phys. Rev. B*, **57**, 6493 (1998).
- [2] C. Hamaguchi, *Basic Semiconductor Physics*, (Springer-Verlag, Berlin Heidelberg, 2001).
- [3] S. Datta, *Superlatt. & Microstruct.*, **48**, 253 (2000).
- [4] T.B. Boykin, G. Klimeck and, F. Oyafuso, *Phys. Rev. B*, **69**, 115201 (2004).

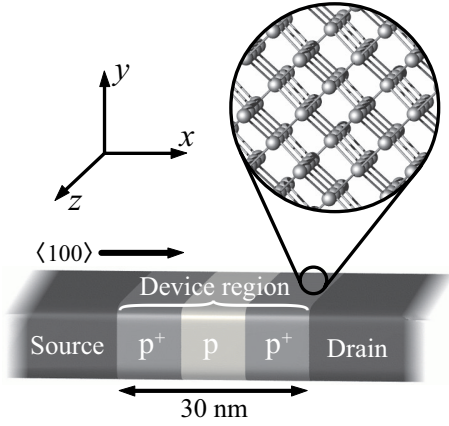


Fig. 1. Schematic diagram of the device structure together with the coordinate axis.

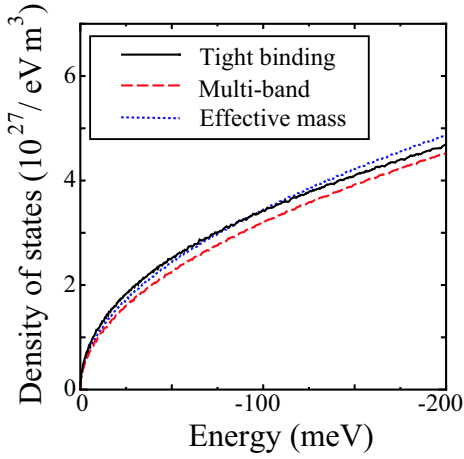


Fig. 2. Density of states calculated with the tight-binding method (solid line),  $k \cdot p$  perturbation (dashed line), and effective-mass approximation (dotted line).

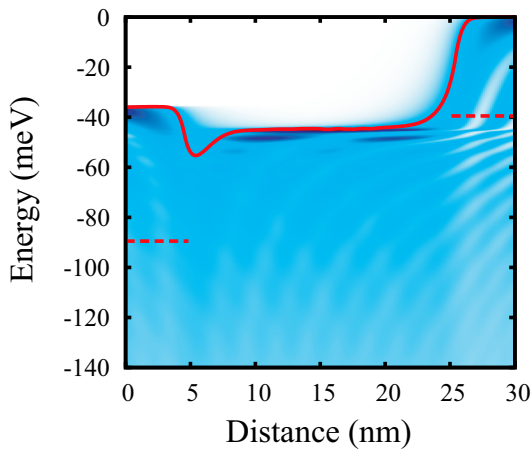


Fig. 3. Spectral function at  $\Gamma$ -point calculated with the effective-mass approximation. Solid line represents the self-consistent potential profile and dashed lines the Fermi levels.

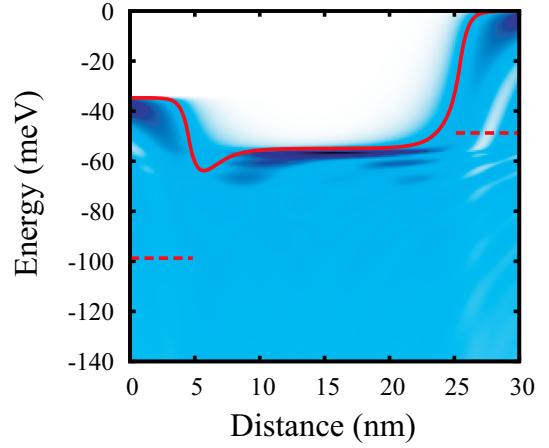


Fig. 4. The same as Fig. 3 but for the  $k \cdot p$  perturbation.

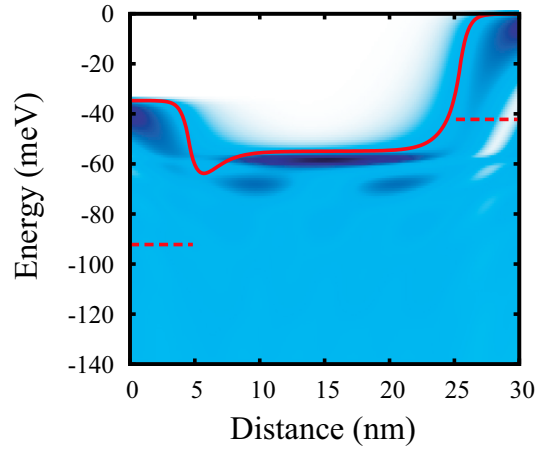


Fig. 5. The same as Fig. 3 but for the tight-binding method.

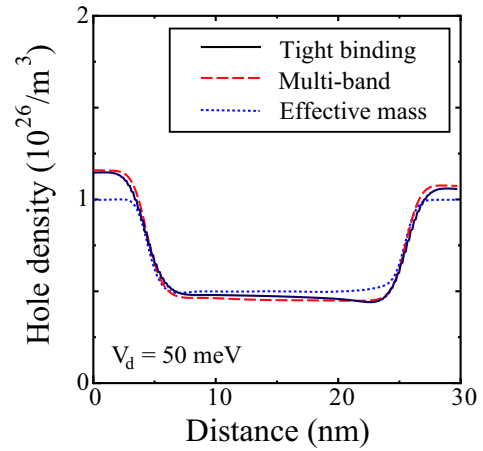


Fig. 6. Hole density profile calculated with the tight-binding method (solid line),  $k \cdot p$  perturbation (dashed line), and effective-mass approximation (dotted line).

# Energy Dispersion Relations for Holes in Silicon Quantum Wells and Quantum Wires

V. V. Mitin, N.Z. Vagidov, M. Luisier<sup>1</sup>, and Gerhard Klimeck<sup>2</sup>

University at Buffalo, SUNY, 332D Bonner Hall, Buffalo, NY 14260, USA

<sup>1</sup>Integrated Systems Laboratory, ETH Zurich, 8092 Zurich, Switzerland

<sup>2</sup>Network for Computational Nanotechnology, Purdue University, West Lafayette, IN 47907, USA  
e-mail: vmitin@buffalo.edu

## INTRODUCTION

Energy dispersion relations,  $E(\mathbf{k})$ , for holes in low-dimensional structures of silicon are substantially richer than those for electrons. In particular, there are extensive regions with negative effective masses (NEM) in  $E(\mathbf{k})$ , i.e. regions where second derivative of  $E$  upon  $\mathbf{k}$  changes its sign. Here an empirical  $sp^3d^5s^*$  tight-binding model which includes interaction of each atom with its nearest neighbors and takes into account ten of its atomic orbitals:  $s$ - and excited  $s^*$ -orbitals, three  $p$ -, and five  $d$ -orbitals is used. The inclusion of higher  $d$ -orbitals and spin-orbital coupling dramatically improves the precision of the calculated electron and hole dispersion relations [1]. Quantum wells (QW) and quantum wires (QWR) are considered.

## RESULTS AND DISCUSSION

$E(\mathbf{k}_{2D})$  for QWs for different orientations of the two-dimensional vector  $\mathbf{k}_{2D}$  in the plane of the well and for different QW growth directions  $\mathbf{n}$  are computed. The results obtained for a wide range of well thickness show that the dispersion relations strongly depend on the direction of  $\mathbf{k}_{2D}$  in the plane of the QW as well as on direction of  $\mathbf{n}$ . In particular, for a  $\mathbf{k}_{2D} \parallel [100]$  the dispersion relations have small values of NEM. For  $\mathbf{k}_{2D} \parallel [110]$  the NEM sections are well pronounced as it is shown in Fig. 1. Kramers' degeneracy is lifted for most of combinations of considered  $\mathbf{k}_{2D}$  and  $\mathbf{n}$ .

For QWRs grown in  $[100]$  direction ( $x$ -axis) and rectangular cross section (axes  $y$  and  $z$  are in  $[010]$  and  $[001]$  directions, respectively) the quantization energy is substantially larger than for QWRs of other growth directions, but the dispersion curves are almost flat with large effective masses and with

almost no regions with NEM as shown in Fig. 2(a). For wires grown in  $[110]$  direction ( $x$ -axis) and rectangular cross section (axes  $y$  and  $z$  are in  $[-110]$  and  $[001]$  directions, respectively) the dispersion curves have well pronounced regions with NEM. The Kramers' degeneracy for  $\mathbf{k}_{1D} \parallel [100]$  is not lifted, whereas for  $\mathbf{k}_{1D} \parallel [110]$  a lift of degeneracy is well pronounced.

Finally, Fig. 3 presents a discussion on the analytical analysis of obtaining  $E(\mathbf{k})$  of a QWR using  $E(\mathbf{k})$  of the QW. This approach provides insights into the general behavior of the expected  $E(\mathbf{k})$  in QWRs before the QWR simulations are performed.

## CONCLUSION

QWs as well as QWRs can exhibit well pronounced regions of NEM which may find significant applications in active components of circuits. The critical design parameters, such as splitting between the lowest and upper subbands,  $\Delta$ , as well as the magnitude of the wave vector,  $k_c$ , when the NEM occurs, and the energy interval with NEM, are sensitive to the directions of confinement as well as to the direction of  $\mathbf{k}$ .

## ACKNOWLEDGEMENT

This work was supported by Petroleum Research Fund Grant No. 41317-AC10, NSF Grant No. EEC-0228390, and the Indiana 21<sup>st</sup> Century Fund.

## REFERENCES

- [1] A. Rahman, G. Klimeck, M. Lundstrom, N. Vagidov, and T.B. Boykin, *Jap. J. of Applied Physics* **44**, 2187 (2005).
- [2] The  $sp^3d^5s^*$  model includes spin and spin-orbit coupling explicitly. These simulations do not include any external magnetic field that would provide spin selection. The splitting of the states is purely due to symmetry breaking and the two split states are a mixture of up and down spins.

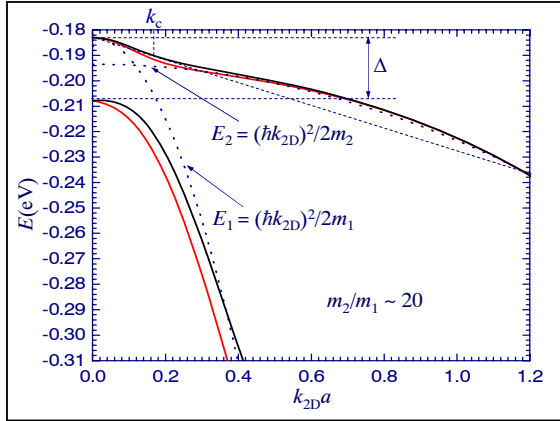


Fig. 1. Dispersion relations  $E(\mathbf{k}_{2D})$  for holes in a silicon QW for  $\mathbf{k}_{2D} \parallel [110]$ . The thickness of QW is 1.63 nm.  $\Delta$  is the energy gap between the lowest and next hole subbands,  $k_c$  is an inflection point where NEM region starts, and  $a$  is the Si lattice constant equal to 5.43 Å. Black and red curves relate to two different spins [2].

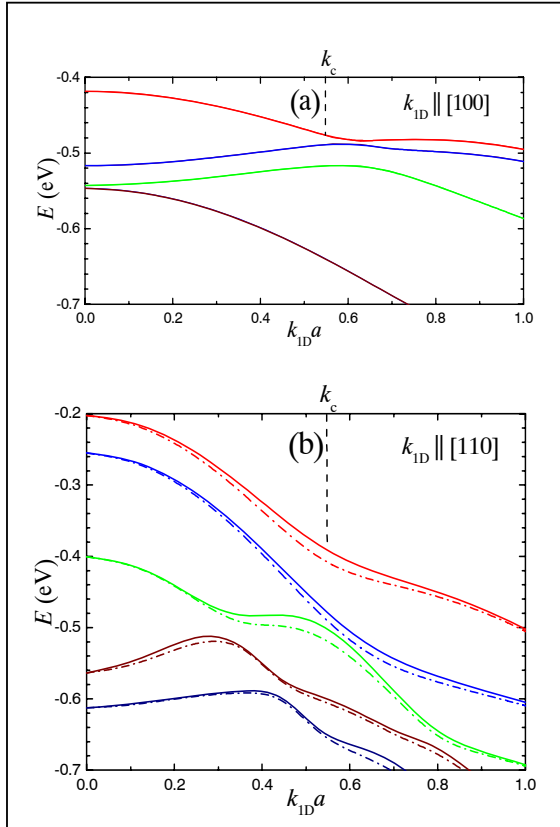


Fig. 2. Dispersion relations  $E(\mathbf{k}_{1D})$  for holes in a silicon QW: (a) in the direction [100] with cross section 1.63 nm in direction [001] and 1.63 nm in direction [010]; (b) in the direction [110] with cross section 1.63 nm in direction [001] and 1.73 nm in direction [-110]. Solid and dash-dotted curves correspond to different spins [2].

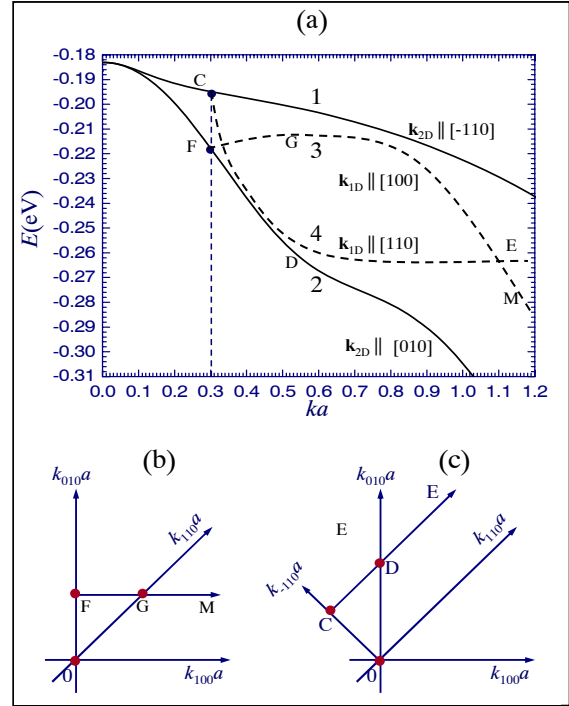


Fig. 3. (a) Solid curves show calculated  $E(\mathbf{k}_{2D})$  for a QW in a plane (001) and two directions of the two-dimensional vector,  $\mathbf{k}_{2D}$ , in the plane of the well:  $\mathbf{k}_{2D} \parallel [-110]$  (curve 1) and  $\mathbf{k}_{2D} \parallel [010]$  (curve 2). QW thickness is 1.63 nm.

Qualitative behavior of the dispersion relations in QWRs are shown by dashed curves and they are obtained using the following procedure. The qualitative curves,  $E(\mathbf{k}_{1D})$ , for a QWR can be presented as slices of the dispersion relations of thin films,  $E(\mathbf{k}_{2D})$ , assuming that  $\mathbf{k}_{2D} = \mathbf{k}_{1D} + \mathbf{k}_Q$  where  $k_Q \approx \pi/d$  corresponds to the quantized wave vector in the plane of the film perpendicular to the direction  $\mathbf{k}_{1D}$  and  $d$  is the wire thickness in that direction. For demonstration purposes we have chosen  $ka = 0.3$ .

For curve 3  $\mathbf{k}_{1D} \parallel [100]$ . As  $k_{1D}$  increases, the vector  $\mathbf{k}_{2D} = \mathbf{k}_{1D} + \mathbf{k}_Q$  deviates from the direction [010] (point F in Figs. 3(a) and 3(b)) towards the direction [110] and then towards [100]. At  $k_{1D} = k_Q$  vector  $\mathbf{k}_{2D}$  is parallel to [110] and this is why  $E(\mathbf{k}_{1D})$  tends first to point G (or curve 1) and with the further increase of  $k_{1D}$  it tends to curve 2 as  $k_{1D}$  becomes substantially larger than  $k_Q$  (point M on Figs. 3(a) and 3(b)).

For curve 4  $\mathbf{k}_{1D} \parallel [110]$ . As  $k_{1D}$  increases, the vector  $\mathbf{k}_{2D} = \mathbf{k}_{1D} + \mathbf{k}_Q$  deviates from the direction [-110] (point C in Figs. 3(a) and 3(c)) towards the direction [010] and then towards [110]. At  $k_{1D} = k_Q$  vector  $\mathbf{k}_{2D}$  is effectively parallel to [010] and this is why  $E(\mathbf{k}_{1D})$  tends first to point D (or curve 2) and with the further increase of  $k_{1D}$  it tends to curve 1 as  $k_{1D}$  becomes substantially larger than  $k_Q$  (point E on Figs. 3(a) and 3(c)).

We present this method of slicing because it allows one to get qualitative behavior of dispersion curves in QWRs and to identify the favorable directions of QWRs for more detailed calculations of  $E(\mathbf{k})$  (as presented in Fig.2) instead of running the time-consuming detailed QWR numerical calculations for all possible directions. Analogous analysis can be used to obtain qualitative  $E(\mathbf{k})$  in QWs by slicing  $E(\mathbf{k})$  of bulk silicon.

# Simulation of the Rashba Effect in a Multiband Quantum Structure

O. Morandi, L. Demeio\*

Dipartimento di Elettronica e Telecomunicazioni, Università degli Studi di Firenze  
Via S. Marta 3, I-50139 Firenze, Italy, e-mail: omar.morandi@unifi.it

\*Dipartimento di Scienze Matematiche, Università Politecnica delle Marche

## THE MULTI-BAND ENVELOPE FUNCTION MODEL

The aim of this work is to present an application of the “kp” multiband model, derived in [1], to some spin-sensitive devices. In recent years, much interest has been devoted to the investigation of spin phenomena in semiconductors with the aim of controlling not only the spatial degrees of freedom of the electrons, but also the spin. Various devices have already been proposed. These devices contain asymmetric quantum wells where quantized states are spin-split by the Rashba effect, and achieve spin filtering by exploiting the phenomenon that the spin of a resonantly transmitted electron aligns with that of the quasibound state traversed.

Several models have been proposed in order to analyze the properties of such devices from a theoretical point of view [2], [3]. The mixing of valence and conduction bands at the interfaces makes a many-band treatment necessary and, in particular, the investigation of the bands for  $k$  parallel to the layers requires a realistic description of the degenerate valence-band edge; furthermore, the occurrence of charge transfer requires self-consistent calculations. The envelope-function method, which is based on an expansion of the full wave function in a suitable orthonormal and complete  $L^2$  basis, is the most popular method for calculating the properties of electrons in semiconductor heterostructures.

In this work we propose a new model derived within the usual Bloch-Wannier formalism by a  $k$ -expansion. The effective-mass equations are based on an invariant expansion of the valence-band Hamiltonian, which is intimately related to the symmetry of the diamond lattice (point group  $\mathcal{O}_h$ ) [4]. The equations are restricted to the manifold of the uppermost ( $j = 3/2$ ) valence-band states,

coupled with the split-off and the conduction states. They are formulated in terms of a set of coupled equations for the electron envelope functions. Our approach allows us to obtain a very simple and direct interpretation of the phenomena involved in the electronic motion in heterostructure devices. The initial formalism is equivalent to the one-electron Schrödinger equation; approximations suitable to treat heterostructure devices are then introduced.

In this contribution, we present the eight-band version of our model which gives a full description of the coupling between the conduction and the valence band for the most common semiconductors.

## NUMERICAL RESULTS

Here, we apply our multiband envelope function model to an asymmetric resonant interband tunneling diode (a-RITD), and we present some numerical results showing the ability of our model to reproduce the spin-orbit splitting arising from the Rashba effect.

Figure 1 shows the band alignments of the *InAs/AlSb/GaSb/AlSb/InAs* double barrier structure (*p*-type-well resonant interband tunneling diode at room temperature) used in the simulation. The band offset between *InAs* and *GaSb* is such that the conduction-band edge of *InAs* lies 0.15 eV below the energy of the valence-band edge of *GaSb*. Transport through this system involves resonant tunneling of electrons from the *InAs* emitter, through unoccupied electron states in the subbands of the *GaSb* well, and subsequently back into the conduction band of the collector.

Figure 2 shows the calculated transmission coefficient for the resonant diode. The in-plane wave vector is  $k_{\parallel} = \frac{2\pi}{a}(0.03, 0, 0)$  where  $a$  is the lattice constant. The resonant peak is related only to

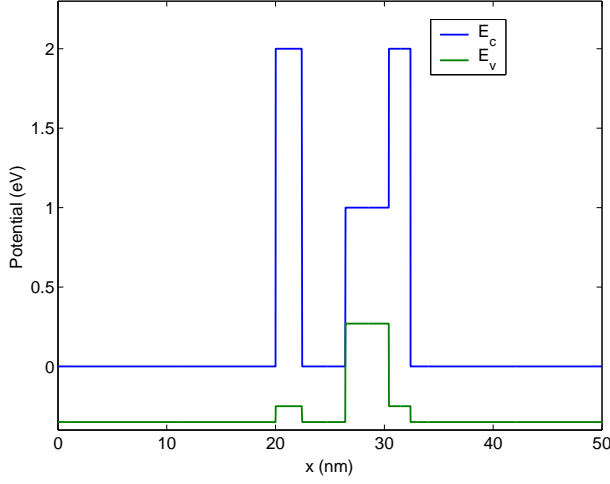


Fig. 1. Band alignments of the double barrier structure used in the simulations.

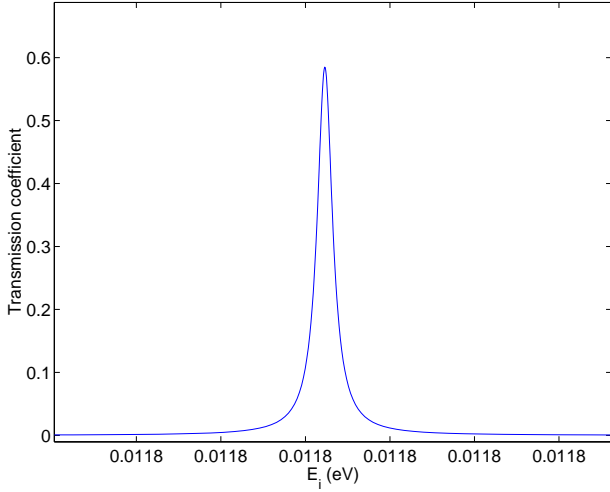


Fig. 2. Transmission coefficient spectra for the *InAs/GaSb/AlSb* diode of Fig. 1 related to the spin up conduction electrons.

the spin-up conduction electrons, and it disappears completely for the spin-down states. In this way, only conduction electrons injected into the device with resonant energy and with spin parallel to the direction of motion can travel from the emitter to the collector lead; electrons with anti-parallel spin are reflected.

Finally, in Figures 3 and 4 we show the conduction and valence envelope functions, for the spin-up and spin-down case respectively, in the two band approximation, calculated in the resonant energy case.

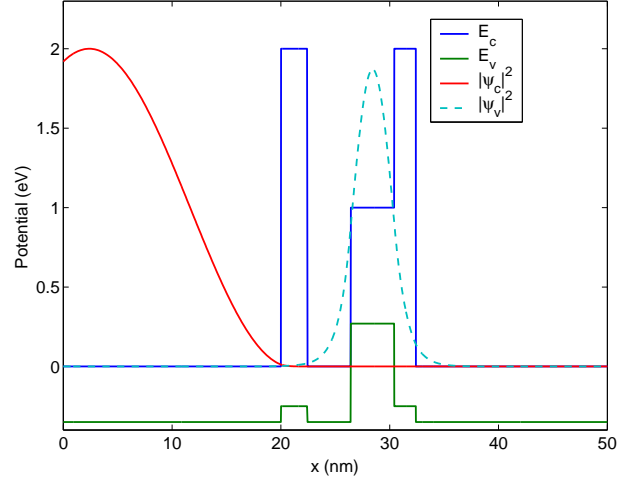


Fig. 3. Conduction and valence envelope functions,  $\psi_c$  and  $\psi_v$ , related to the resonant energy  $E = 1.18$  eV for the spin-up case.

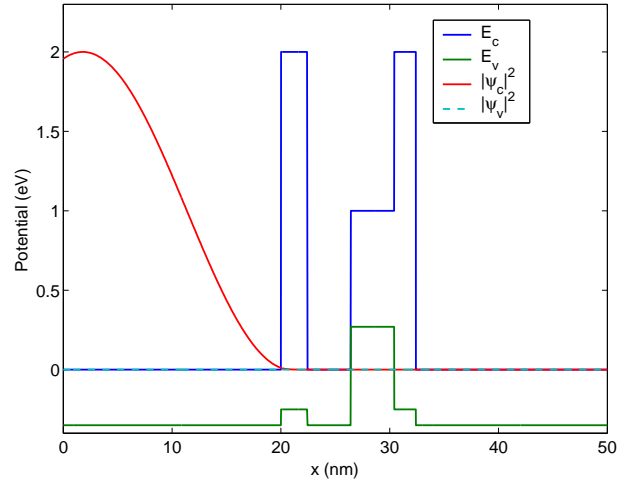


Fig. 4. Conduction and valence envelope functions,  $\psi_c$  and  $\psi_v$ , related to the resonant energy  $E = 1.18$  eV for the spin-down case.

## REFERENCES

- [1] O. Morandi and M. Modugno, A multiband envelope function model for quantum transport in a tunneling diode, *Phys. Rev. B* **71**, 235331 (2005).
- [2] M. Altarelli, Electronic structure and semiconductor-semimetal transition in InAs GaSb superlattices, *Phys. Rev. B* **28**, 842-845 (1983).
- [3] D. Z. Y. Ting, E. T. Yu, and T. C. McGill, Multiband treatment of quantum transport in interband tunnel devices, *Phys. Rev. B* **45**, 3583-3592 (1992).
- [4] H. R. Trebin, U. Rössler and R. Ranvaud, Quantum resonances in the valence bands of zinc-blende semiconductors. I. Theoretical aspects *Phys. Rev. B* **20**, 686-700 (1979).

# Ultrafast Wigner Transport in Quantum Wires

M. Nedjalkov, D. Vasileska\*, E. Atanassov†, V. Palankovski

AMADEA Group, Inst. for Microelectronics, TU Wien, Gußhausstr. 27–29/E360, 1040 Wien, Austria

\* Department of Electrical Engineering, Arizona State University, Tempe, 85287-5706 USA

† IPP, Bulgarian Academy of Sciences, 1113 Sofia, Bulgaria

e-mail: mixi@iue.tuwien.ac.at

## TRANSPORT MODELS

The early time dynamics of highly non-equilibrium confined carriers incorporates a number of quantum phenomena, which are subject of active investigations [1]. We explore two models of evolution of an initial distribution of carriers interacting with optical phonons in a quantum wire. The carriers can be injected or optically excited, an electric field  $E$  can be applied along the direction  $z$  of the wire. The models are introduced by the Boltzmann-like equation

$$\mathcal{L}f_w(z, k_z, t) = \int dk'_z \int_0^t dt' \{S'f'_w - Sf_w\} \quad (1)$$

Here  $\mathcal{L}$  is the Liouville operator, the Wigner function on the right  $f' = f_w(\mathcal{Z}(t'), k'_z(t'), t')$  depends on the Newton trajectory  $z(t'), k'_z(t')$  as follows:

$$\mathcal{Z}(t') = z(t') + \frac{\hbar(k_z - k'_z)}{2m} \Delta_c; \quad \Delta_c = t - t'. \quad (2)$$

$S(k_z, k'_z, t, t')$  is obtained from the Boltzmann scattering rate in the wire by replacing the energy conserving  $\delta$ -function by the real part of

$$\mathcal{D} = \frac{1}{2} e^{-\int_{t'}^t \Gamma \left( \frac{k_z(\tau) + k'_z(\tau)}{2} + i \frac{\epsilon(k_z(\tau)) - \epsilon(k'_z(\tau)) - \hbar\omega}{\hbar} d\tau \right)} \quad , \quad (3)$$

$\Gamma$  is the total Boltzmann out-scattering rate, and  $Sf_w$  is obtained from  $S'f'_w$  by the usual exchange of the primed and unprimed momentum variables. As suggested by the energy term in (3), a ground state is assumed in the plane of confinement. The two evolution models are counterparts of the Levinson (L),  $\Gamma = 0$ , and the Barker-Ferry (B-F),  $\Gamma \neq 0$  equations, now generalized to account for a space-dependent evolution. Derived [2] from the electron-phonon Wigner equation, (1) accounts for the finite time of the electron collisions.

## PHYSICAL FEATURES AND SIMULATIONS

The interval  $\Delta_c$  is identified as the collision duration time. The two models differ in the way of treatment of collisions with different  $\Delta_c$ . While in the L case all collisions are welcome, in the B-F case long correlation times are damped by  $\Gamma$  in (3).

A GaAs quantum wire with 10 nm square cross section has been considered in the numerical experiments. The choice  $T = 0\text{K}$  provides a clear reference picture, where classical electrons can only emit phonons and since the constant POP energy form replicas of the initial distribution. The later is chosen to be Gaussian in both energy and space. A backward Monte Carlo method is used to evaluate directly the Wigner function  $f_w$  and its first moments - the density  $n(z)$  and the wave vector distribution  $f(k_z)$ . To analyze certain numerical aspects the later are computed also from the values of  $f_w$ . We summarize the quantum effects revealed in the simulation results. The non-Markovian evolution gives rise to a retardation in the build-up of the replicas. The retardation is larger in the B-F model (Figs. 1 and 2). The lack of energy conservation causes broadening of the replicas and appearance of electrons in the classically forbidden energy region. Certain carriers reach larger distances than the classically fastest ballistic electrons (Fig. 3). The modification of the classical trajectory caused by  $\Delta_c$  in (2) has an important physical effect. The lack of this term leads to negative densities around the front of the fastest quantum electrons (Fig. 4).

## REFERENCES

- [1] M. Herbst, M. Glanemann, V. Axt, and T. Kuhn, *Electron-Phonon Quantum Kinetics for Spatially Inhomogeneous Excitations*, Physical Review B, **67**, 195305:1–18 (2003).
- [2] The derivation is due to a collaboration with groups from ASU and Modena Univ. and will be published elsewhere.

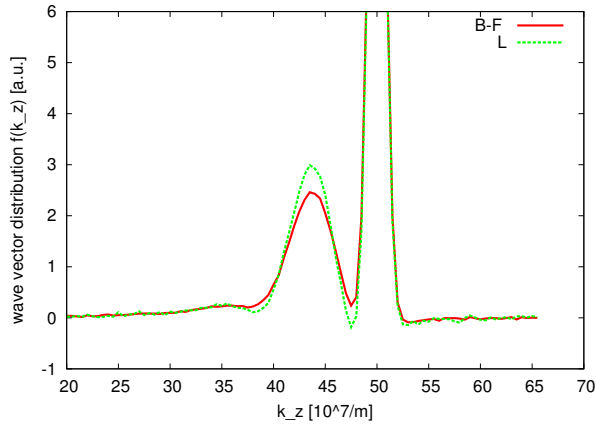


Fig. 1. Wave vector distribution  $f(k_z)$ , plotted in a window of positive  $k_z$ , after 150 femtoseconds evolution time.  $f(k_z)$  is computed from the values of the Wigner function which has been evaluated with a high precision in  $800 \times 260$   $z$  and  $k_z$  points and then numerically integrated on  $z$ . The initial peak is centered at  $5 \times 10^8 \text{ m}^{-1}$ . The classical evolution will form exact replicas of the initial peak shifted by the phonon energy to the left. The first quantum replicas are much broadened due to the lack of energy conservation. The peak-to-valley ratio of the L curve is more pronounced, in particular it touches the zero in the valley, which demonstrates the retardation of the B-F evolution. However the appearance of electrons above the initial distribution, which can be observed at smaller evolution times, is already missing. The reason is explained below.

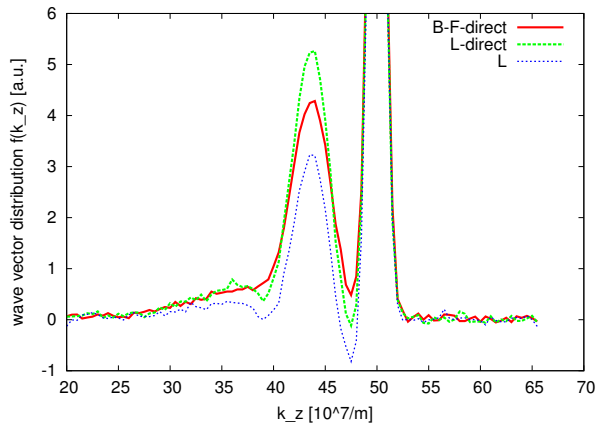


Fig. 2. Broadening and retardation effects after 175 femtoseconds evolution time. The L curve, computed from  $f_w$ , differs significantly from the directly computed with the Monte Carlo method counterpart and becomes unphysical. The reason is that with the increase of the evolution time  $f_w$  becomes less and less smooth function and thus more and more points are needed for a precise evaluation of the corresponding functionals. This suggests that a direct evaluation of any physical observable is necessary for larger evolution times.

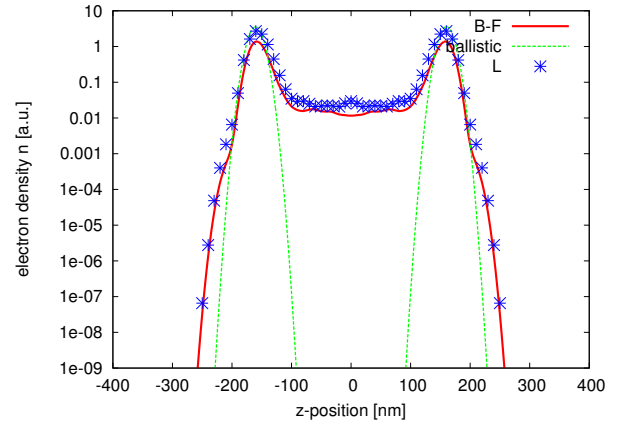


Fig. 3. Electron density after 175 femtoseconds of evolution presented in a logarithmic scale. The initial distribution centered at 0 splits in two peaks, which move in the positive and the negative directions of the wire. There are no ballistic electrons left around the center. On contrary, due to the electrons which lost energy from the collisions, the two quantum solutions demonstrate finite density in the central part. Above and below the ballistic front, at around 230 and  $-230$  nanometers, respectively, there are faster quantum electrons which gained energy during the finite collisions. The difference in the spatial behavior of the two models is due to the effects of retardation.

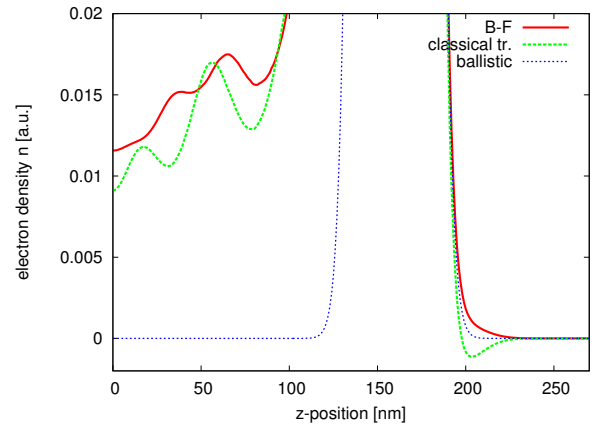


Fig. 4. Electron density obtained after 175 femtoseconds evolution from the B-F model plotted around the ballistic curve in the positive direction of the wire. The excess electron density above 200 nanometers is well demonstrated by the quantum solution. If the term accounting for the effect of the finite collision duration  $\Delta_c$  is neglected in (2),  $\mathcal{Z}(t')$  becomes equivalent to the classical trajectory  $z(t')$ . The third curve on the plot is obtained by using classical trajectories in the B-F model. This leads to a modification of the electron distribution and appearance of negative densities in the region around 200 nanometers. Thus, this term has an important role in maintaining the physical relevance of the quantum evolution process.

# A Many-Particle Quantum-Trajectory Approach for Modeling Electron Transport and its Correlations in Nanoscale Devices

X. Oriols

Departament d'Enginyeria Electrònica, Universitat Autònoma de Barcelona, Spain  
e-mail: Xavier.Oriols@uab.es

## ABSTRACT

A new approach for modeling quantum transport that explicitly takes into account the electron-electron interaction is presented. The approach is based on the computation of transport properties of many-particle systems using quantum trajectories.

## INTRODUCTION

The coulomb interaction (due to the charge of the electron) and the exchange interaction (due to its fermion nature) are always present in any electron device. The role of both interactions can be obtained by directly solving the many-particle Schrödinger equation. However, due to computational limitations, its direct solution is only possible for a very limited number ( $N < 5$ ) of electrons. Therefore, much of our understanding of electron transport is based on a single-particle (“mean field”) approximations [1]. In this conference, we will present a new approach for the modeling of quantum transport that overcomes this assumption by dealing with many-particle effects using quantum (Bohm) trajectories [2].

## MANY-PARTICLE TRANSPORT PROPERTIES IN TERMS OF QUANTUM TRAJECTORIES

It is well-known that Bohm trajectories exactly reproduce the results obtained from, either the single- or many-particle Schrödinger equation [3,4]. However, the application of such trajectories to transport has been quite limited because the computation of these trajectories needs, in general, the earlier knowledge of the full wave-function.

In this conference, we show that a Bohm trajectory associated to a many-particle Schrödinger equation can be computed from a wave-function,  $\Psi_b(\vec{r}_b, t)$ , solution of the single-particle Schrödinger equation (with a complex unknown potential) [2]. Thus, the practical computation of Bohm trajectories in a system of  $N$ -interacting electrons

can be greatly simplified. The electron-electron interaction is introduced in the computation of Bohm trajectories by taking into account the exact Coulomb force between pairs of electrons and the applied bias at the boundaries of the device. Thus, Identical bias with different lateral areas ( $L_y \cdot L_z$ ), provide different strength of the interaction. The exchange-interaction needs the simulation of  $N^2$  Bohm trajectories to assure the antisymmetrical behavior of the wave-function. Figs. 1, 2 and 3, show the accuracy of our approach (blue  $\square$ ) when compared to the exact two-particle Schrödinger solutions (red  $\Delta$ ).

## CURRENT AND NOISE OF INTERACTING-SYSTEMS

The computational viability of the previous many-particle Bohm-trajectories formalism for is shown in Figs. 4 and 5 where  $N \approx 50$  interacting-electrons are simulated. Since we are dealing with electron trajectories, most of the tools used in Monte-Carlo simulator can be directly adapted. In Fig. 4 and 5 we show how the (average) current and the (Fano factor) noise are sensible to electron-electron interactions. Such interactions provide correlations among electron dynamics that can not be simulated with independent-electron formalisms.

## CONCLUSION

A new approach for modeling quantum transport that explicitly takes into account the Coulomb and exchange interactions is presented. The approach opens a new path to provide a deeper understanding of nanoscale devices, since it can directly provides information on DC, AC and noise performances of interacting-electrons phase-coherent systems [5,6].

## REFERENCES

- [1] Ya. M. Blanter and M. Büttiker, Phys. Rep. 336, 1 (2000).
- [2] X. Oriols (submitted).
- [3] J. Suñé, X. Oriols, Physical Review Letters 85, 894 (2000).
- [4] X. Oriols, Physical Review A, 71, 017801 (2005).
- [5] X. Oriols, et al. Appl. Phys. Lett., 85 3596 (2004).
- [6] X. Oriols et al. Physical Review B, 71, 245322 (2005).

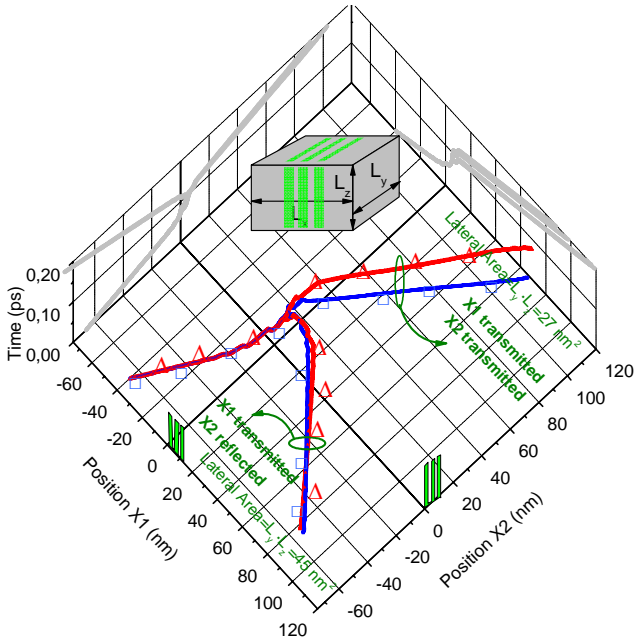


Fig. 1. Two Bohm trajectories in a two-particle configuration space ( $X_1, X_2, t$ ) with identical initial positions but different lateral area. Only the Coulomb interaction determines ( $X_1=\text{trans.}, X_2=\text{trans.}$ ) or ( $X_1=\text{trans.}, X_2=\text{reflc.}$ ). In red ( $\Delta$ ), exact Bohm trajectories from a two-particle Schrödinger equation and, in blue ( $\square$ ), our approach. Inset: 3D device dimensions (transport in x direction). The triple-barrier region is indicated.

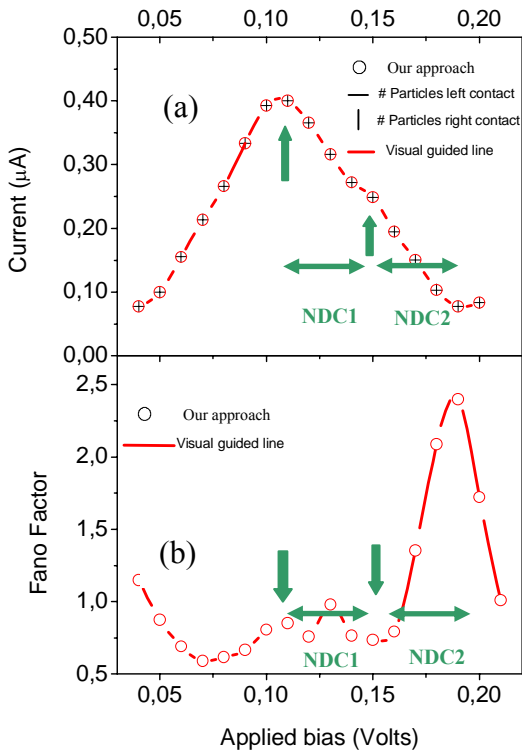


Fig. 4: Simulated (a) current and (b) noise (Fano factor) for a three barrier diode using our approach with the explicit consideration of interacting electrons. See Fig. 5. The results from our approach are obtained through the Ramo-Shockley theorem [6].

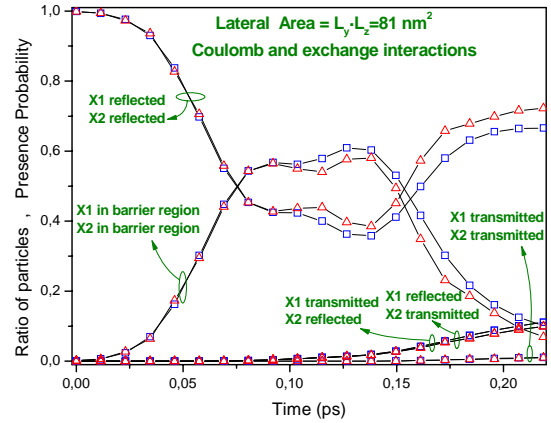


Fig. 2. In red ( $\Delta$ ), exact time-evolution of probability presence of a two-particle Schrödinger equation impinging in the double barrier where Coulomb and exchange interaction are considered. In blue ( $\square$ ), same scenario simulated with our approach.

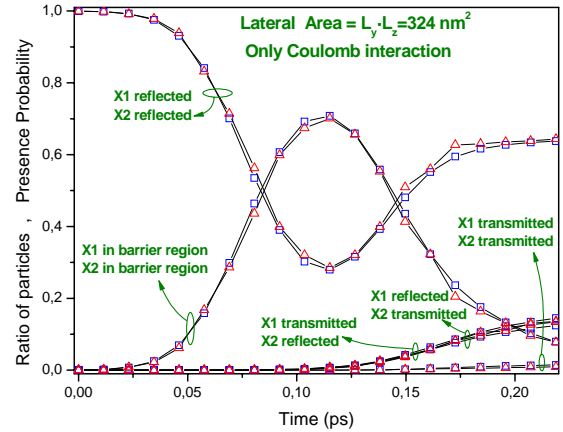


Fig. 3. Identical results of figure 2 without exchange interaction. Excellent agreement between our approach (in blue  $\square$ ) and two-particle Schrödinger equation (in red  $\Delta$ ).

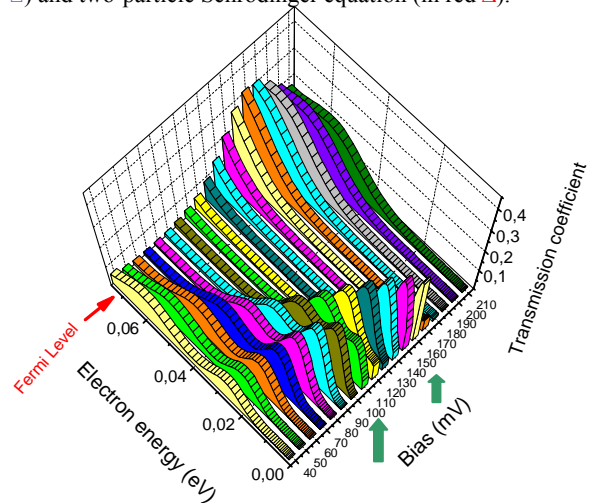


Fig. 5. The triple-barrier diode transmission coefficient of the device simulated in Fig. 4, showing the presence of two resonances ( $\uparrow$ ) at  $V=0.12$  V and  $V=0.15$  V (a richer phenomenology in three-barrier than in two-barrier diodes). The electron correlations explain the different noise behavior after such resonances (**NDC1** and **NDC2**) in Fig. 4(b).

# Computational Study of the Schottky Barrier at the Metal-Carbon Nanotube Contact

Noejung Park and Suklyun Hong\*

Department of Applied Physics, Dankook university, Seoul 140-714, Korea

\*Department of physics and Institute of fundamental physics, Sejong University, Seoul 143-747, Korea  
 e-mail: noejung@dankook.ac.kr

## INTRODUCTION

Nano scale electronic devices utilizing material properties of the carbon nanotube (CNT) have been widely investigated recent years [1]. In this field of study the Schottky barrier at the metal-carbon nanotube contact has been a prime issue [2]. Here we use *ab initio* density-functional method [3,4] to investigate the electronic structure and the Fermi level alignment at the metal-carbon nanotube contact. The dependency of the Schottky barrier on the metal work function as well as on the detailed atomic structures at the contact is addressed with an accurate electronic structure calculations [5,6]. We find that, in such a contact between metal and nano-sized semiconductor, the interface atomic geometry could be far more important than the simple electrostatic effect of the metal surfaces.

## CALCULATION AND DISCUSSION

We use the standard density-functional method to investigate the metal-nanotube contact [3]. The total energy of the system and the energy band structures are obtained by the self-consistent solution of the Kohn-Sham equation, as described in the Eq. (1) and (2). Throughout this work, the Vienna *Ab initio* Simulation Package is used [4].

$$E_{tot} = T_0[n(\mathbf{r})] + \frac{1}{2} \iint d\mathbf{r}d\mathbf{r}' \frac{n(\mathbf{r})n(\mathbf{r}')}{|\mathbf{r} - \mathbf{r}'|} + E_{xc}[n] + \int d\mathbf{r} v_{ext}(\mathbf{r})n(\mathbf{r}) + \frac{1}{2} \sum_{\mu\nu} \frac{z_\mu z_\nu}{|R_\mu - R_\nu|} \quad (1)$$

$$\left[ -\frac{1}{2} \nabla^2 + \hat{v}_{ion} + v_H + v_{xc} \right] \psi_i = \epsilon_i \psi_i \quad (2)$$

Figure 1 is an illustration of the prototypical back-gated carbon nanotube field effect transistor

(CNFET). Noting previous suggestions that the CNFET may operate as a Schottky barrier transistor (SBFET) [2] we focus on the metal-nanotube contact, as indicated by the arrow in Fig. 1.

We first investigate the effect of metal work function, calculating the projected densities of states (PDOS) for the semiconducting nanotube on the Al, oxidated Al, and Au surfaces, as shown in Figs. 2(a), 2(b), and 2(c), respectively. The Fermi level of the aluminum surface sits at the conduction band edge of the semiconducting (10,0) nanotube, while that of oxidized aluminum surface and that of gold surface are aligned at the valence band edge of the nanotube. This clearly indicates that, when the CNT is side-contacted without metal-carbon bond formation, the work function of the metal surface would be a governing factor whether the Schottky barrier favors either the hole transport or electron transport.

However, such Schottky barrier could not be solely determined by a simple difference between the metal work function and the electron affinity of the carbon nanotube. Here we show one example that a detailed local atomic structure substantially affect the Schottky barrier height. Following usual experimental procedure to form the source and drain electrode, there are likely to be a substantial pressure on the carbon nanotube surface imbedded under the metal layers [7]. Figure 3 shows that such a pressure between the metal layer and carbon nanotube surface could result in a significant modification in the Schottky barrier height. When the CNT is simply in contact with gold surface, as shown in Fig. 2(c), the Fermi level is aligned at the

valence band edge. However, as the CNT is compressed between the metal layers, the metal Fermi level is found to shift up toward the conduction band edge of the nanotube, as shown in Figs. 3(a) and 3(b). This means the simple Au-CNT contact favors the hole transport, while the compressed Au-CNT contact favors the electron transport.

### CONCLUSION

We investigated the Schottky barrier formation at the metal-carbon nanotube contact, with *ab initio* electronic structure calculations. We found that not only the metal work function but the local atomic configuration as well significantly affects the height of the Schottky barrier at the metal-CNT contact

### ACKNOWLEDGEMENT

We would like to acknowledge the support from KISTI under “Grand Challenge Support Program” with Dr. S. Lee as the technical supporter. The use of the computing system of the Supercomputing Center is also greatly appreciated.

### REFERENCES

- [1] V. Derycke, R. Martel, J. Appenzeller, and Ph. Avouris, *Carbon Nanotube Inter- and Intramolecular Logic Gates*, *Nano Letters* **1**, 453 (2001).
- [2] S. Heinze, J. Tersoff, R. Martel, V. Derycke, J. Appenzeller, and Ph. Avouris, *Carbon Nanotubes as Schottky Barrier Transistors*, *Physical Review Letters* **89**, 106801 (2002).
- [3] W. Kohn and L. J. Sham, *Physical Reviews* **140**, A1133 (1965); P. Hohenberg and W. Kohn, *Physical Reviews* **136**, B 864 (1964)
- [4] G. Kresse and J. Furthmüller, *Efficiency of ab-initio total energy calculations for metals and semiconductors using plane-wave basis*, *Computational Materials Science* **6**, 15 (1996).
- [5] N. Park and S. Hong, *Electronic structure calculations of metal-nanotube contacts with and without oxygen adsorption*, *Physical Review B* **72**, 045408 (2005).
- [6] N. Park, D. Kang, S. Hong, and S. Han, *Pressure-dependent Schottky barrier at the metal-nanotube contact*, *Applied Physics Letters* **87**, 013112 (2005).
- [7] B. Wei, P. K.-Redlich, U. Bäcker, B. Heiland, R. Spolenak, E. Arzt, and M. Rühle, *Selective specimen preparation for TEM observation of the cross-section of individual carbon nanotube/metal junctions*, *Ultramicroscopy* **85**, 93 (2000).

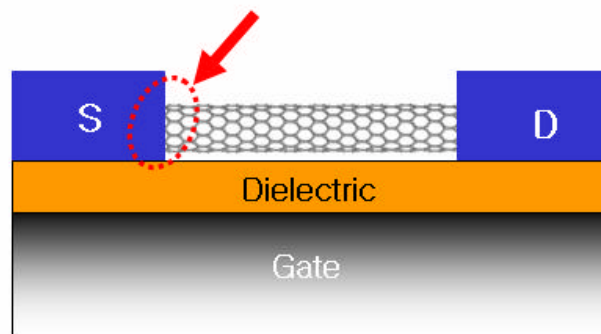


Fig. 1. Prototypical back-gated nanotube field effect transistor

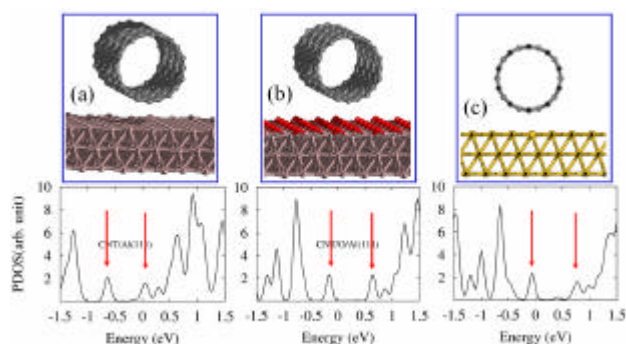


Fig. 2. Electronic structures of the carbon nanotube in contact with (a) Al, (b) oxidized Al, and (c) Au surfaces, respectively. Down-ward arrows in the lower panels indicate valence band and conduction band edges of the nanotube.

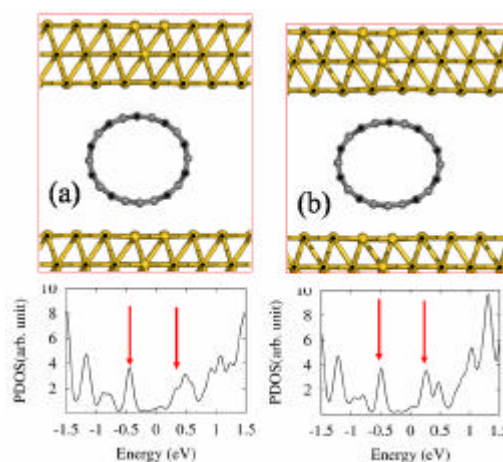


Fig. 3. Electronic structures of the semiconducting carbon nanotube compressed between two gold layers.

# Tunneling-CNTFETs

M. Pourfath, H. Kosina, and S. Selberherr

Institute for Microelectronics, TU Wien, Gußhausstraße 27–29/E360, 1040 Wien, Austria

e-mail: pourfath@iue.tuwien.ac.at

## INTRODUCTION

Exceptional electronic and mechanical properties together with nanoscale diameter make carbon nanotubes (CNTs) candidates for nanoscale field effect transistors (FETs). High performance CNTFETs were achieved recently [1, 2]. Metallic contacts can be directly connected to the gate-controlled CNT channel [1]. To reduce the parasitic capacitances the spacing between the gate-source and the gate-drain contacts can be increased. The extension region can be of n or p-type leading to n/i/n or p/i/p devices. Unlike conventional semiconductors, in which doping is introduced by implantation, doping of CNTs requires controlling the electrostatics of the CNT environment by additional gates [2], molecules [3], or metal ions [4]. The gate controls the thermionic emission current, therefore a sub-threshold slope of about 64 mV/dec can be achieved [2]. Aggressively scaled devices of this type suffer from charge pile-up in the channel [5], which deteriorates the off-current substantially and ultimately limits the achievable  $I_{on}/I_{off}$  ratio [5].

In order to overcome this obstacle a gate-controlled tunneling device (T-CNTFET) has been proposed [5]. In this type of device either a p/i/n or n/i/p doping profile can be used. The gate voltage controls the band bending at the junctions, which modulates the band to band tunneling current. The T-CNTFET benefits from a steep inverse sub-threshold slope and a better controlled off-current.

## SIMULATION RESULTS

In this work we present a numerical study of a T-CNTFET. Because of strong quantum effects, the non-equilibrium Green's function (NEGF) formalism has been chosen to investigate the behavior of these devices. Ballistic transport is assumed and the coupled transport and Poisson equations have

been solved. We studied the effect of the doping concentration on the device performance.

The operation of the device can be well understood by considering the spectrum of electrons along the device (Fig.3 and Fig.5). At high negative gate voltages, due to strong band bending near the source contact, band to band tunneling contributes greatly to the total current. By increasing the gate voltage to positive values the band bending near the source contact decreases, and as a result band to band tunneling decreases. On the other hand the increase of the gate voltage results in a strong band to band tunneling near the drain contact, see Fig.3 ( $V_{GS} = -0.6V$ ). As a result the total current increases in the off regime which has a detrimental effect on the device performance (Fig.2). In the device we discussed, the doping concentrations at the source and drain sides are assumed to be equal. By decreasing the doping of the drain side the band bending decreases for the same gate voltage (Fig.5) and the band to band tunneling current near the drain contact decreases greatly, see Fig.2 and Fig.4.

## CONCLUSION

We performed numerical investigation of a T-CNTFET. Due to strong quantum effects including band to band tunneling, the NEGF formalism along with complex band structure gives a suitable model for the analysis of these devices. Simulation results suggest that an asymmetric doping concentration reduces the parasitic carrier injection and increases the  $I_{on}/I_{off}$  ratio by several orders of magnitude.

## ACKNOWLEDGMENT

This work has been partly supported by the Austrian Science Fund FWF, project 17285-N02 and the National Program for Tera-level Nano-devices of the Korean Ministry of Science and Technology.

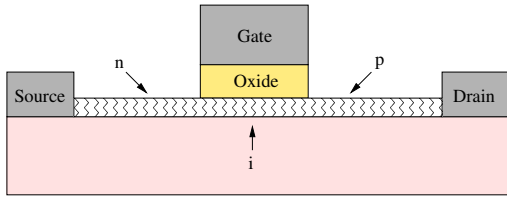


Fig. 1. T-CNTFET device with n/i/p doping profile.

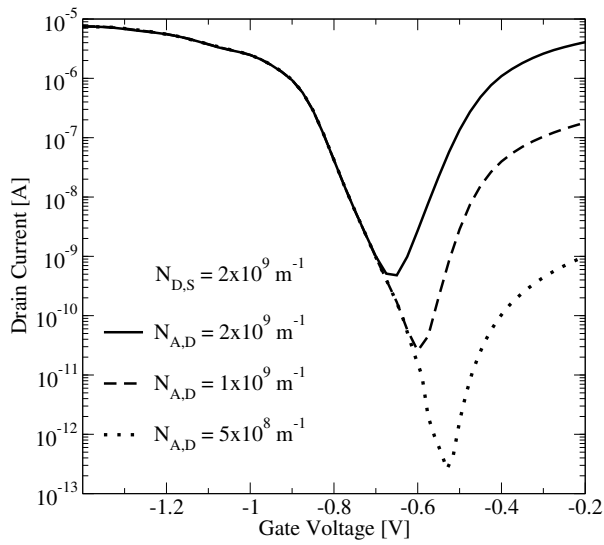


Fig. 2. Transfer characteristics for different doping profiles.

### REFERENCES

[1] A. Javey *et al.*, Nano Lett. **4**, 1319 (2004).  
 [2] Y.M. Lin *et al.*, IEEE Trans.Nanotechnology **4**, 481 (2005).  
 [3] J. Chen *et al.*, in *IEDM Tech.Dig.* 695 (2004)  
 [4] A. Javey *et al.*, Nano Lett. **5**, 345 (2005).  
 [5] J. Appenzeller *et al.*, **52**, 2568 (2005).  
 [6] R. Venugopal *et al.*, J.Appl.Phys. **92**, 3730 (2002).

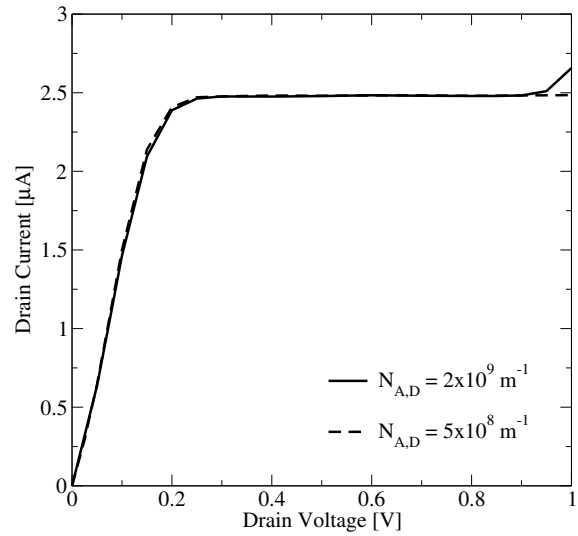


Fig. 4. Output characteristics for different doping profiles.

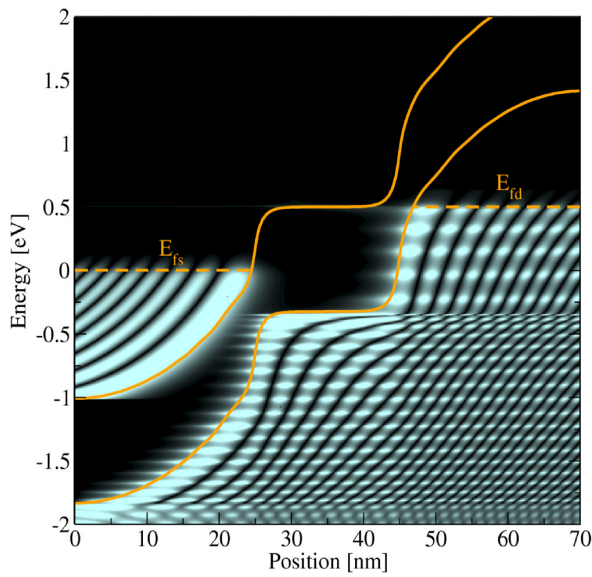


Fig. 3. The distribution of electrons in energy space along the device with  $N_{D,S} = 2 \times 10^9 \text{ m}^{-1}$  and  $N_{A,D} = 2 \times 10^9 \text{ m}^{-1}$ .

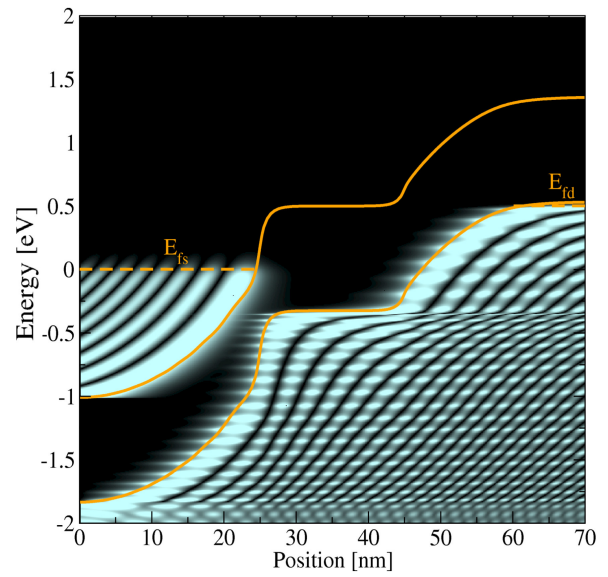


Fig. 5. The distribution of electrons in energy space along the device with  $N_{D,S} = 2 \times 10^9 \text{ m}^{-1}$  and  $N_{A,D} = 5 \times 10^8 \text{ m}^{-1}$ .

# Conductance of Nanowires

Amit Raichura, Michael A. Stroschio and Mitra Dutta

Nano Engineering Research Group, University of Illinois at Chicago, Chicago, IL, 60607 USA  
email: araich2@uic.edu

## INTRODUCTION

This paper examines the conductivity of a variety of nanowires within the Landauer formalism by taking into account phonon quantization in finite-length nanotubes.

## DISCUSSION

The elastic continuum model and dielectric continuum models have been applied to derive acoustic and optical phonon modes for both carbon nanotubes (CNTs) and solid-cylinder quantum wires fabricated of a variety of polar semiconductors. Phonon-confinement and geometrically-determined mode symmetries have taken into account to derive suitable phonon modes for such nanowires [1-4]. Using these confined and interface phonon modes, the Landauer formalism is used to evaluate the conductance of these nanowires in the presence of phonon scattering. For nanowires of finite length these results indicate the presence of phonon-bottleneck effects as a result of the phase space reductions of finite-length wires as compared with idealized nanowires of infinite length. Exemplary phase space reductions, leading to phonon bottleneck effects, in nanowires of finite length are shown Figure 1 and Figure 2 for a 7.0-nm-long (10,10) single-wall CNT clamped at the ends and 2 for a 16.0-nm-long (40,0) single-wall CNT clamped at the ends, respectively. Instead of a continuous wavevector down the axis of the nanowire, as is the case for a nanowire of infinite length, the wavevector is quantized as shown by the discrete normalized wavevectors depicted in Figures 1 and 2. For a variety of finite-length nanowires, such discrete phonon modes are used to demonstrate phonon bottleneck effects. In addition, these phase-space reductions are used in a Landauer formalism to evaluate conductance in finite-length nanotubes. These effects lead to conductivity enhancements as a result of the reduction in the number of scattering

channels. These results provide insights into the observed quasi-ballistic transport in nanowires.

## CONCLUSION

The conductivity of a variety of finite-length nanowires is modeled in this effort. Enhanced conductivity is attributed to discrete phonon modes that lead to phonon bottleneck effects associated with phase-space reductions for nanowires of finite length.

## ACKNOWLEDGEMENT

We would like to thank Profs. Supriyo Datta and Mark Lundstrom for helpful discussions.

## REFERENCES

- [1] Michael A. Stroschio and Mitra Dutta, *Phonons in Nanostructures*, Cambridge University Press, Cambridge, 2001.
- [2] Amit Raichura, Mitra Dutta, and Michael A. Stroschio, *Quantized Optical Vibrational Modes of Finite-Length Multi Wall Nanotubes: Optical Deformation Potential, Superlattices and Microstructures*, **35**, 147-153 (2004).
- [3] Amit Raichura, Mitra Dutta, and Michael A. Stroschio, *Deformation Potential and Acoustic Phonon Modes for Single-Wall Carbon Nanotubes of Finite Length quantized Optical Vibrational Modes of Finite-Length Multi Wall Nanotubes: Optical Deformation Potential*, *Journal of Applied Physics*, **94**, 4060 (2003); also in *Virtual Journal of Nanoscience and Technology*, September 8, 2003.
- [4] Amit Raichura, Mitra Dutta, and Michael A. Stroschio, *Elastic Continuum Models of Phonons in Carbon Nanotubes*, pp. 89-110, in *Applied Physics of Carbon Nanotubes : Fundamentals of Theory, Optics and Transport Devices*, edited by S. V. Rotkin and S. Subramoney, (Springer-Verlag Series in Nanoscience and Technology, Berlin, Heidelberg, 2005).

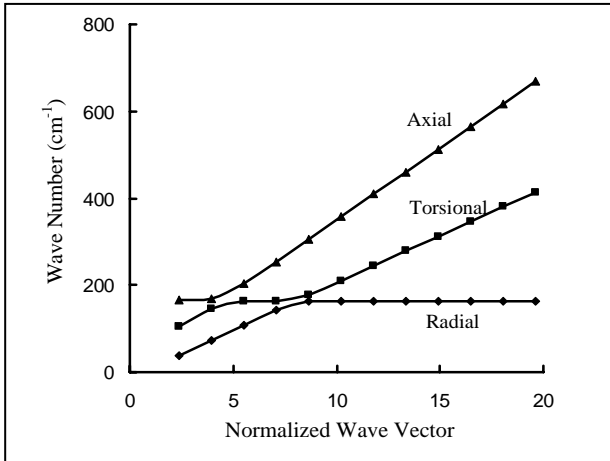


Fig. 1. Dispersion curves for (10,10) single-wall CNT with a length of 7 nanometers.

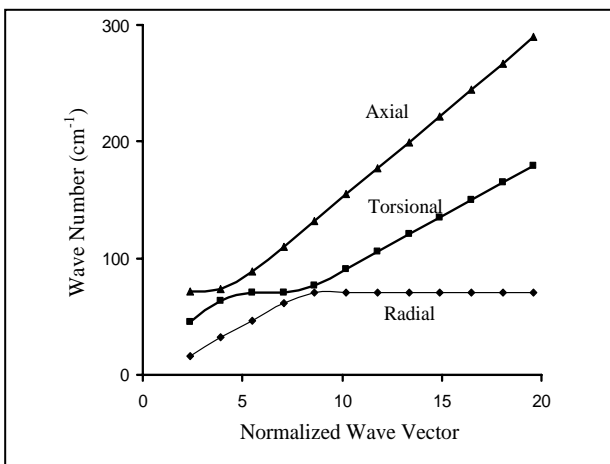


Fig. 2. Dispersion curves for (40,0) single-wall CNT with a length of 16 nanometers.

# Extension of the $R$ - $\Sigma$ Method to Any Order

M. Rudan, E. Gnani, S. Reggiani, and G. Baccarani

Advanced Research Center on Electronic Systems (ARCES), and Department of Electronics (DEIS)  
 University of Bologna, Viale Risorgimento 2, I-40136 Bologna, Italy  
 Tel. +39-051-20-93016, Fax. -93779, e-mail: mrudan@arces.unibo.it

## I. INTRODUCTION

In recent papers, a theory has been proposed that leads to a set of two Newton-like equations describing the single-particle dynamics. The dynamical variables are the expectation value  $x$  of the wave function  $\psi$  and its dispersion  $\sigma$  [1],[2]. The equations inherently account for the Heisenberg position-momentum uncertainty relation. The theory is part of an investigation that aims at consistently incorporating quantum corrections into the transport model, for applications to advanced solid-state devices. The task is carried out in two steps. The first one, which is of interest for the present paper, derives two equations in which the dynamics of the dispersion of the single-particle wave function is accounted for in addition to that of the expectation value of position. The model is founded on an approximate description of the wave function that eliminates the need of the Ehrenfest approximation. As the dynamical variables of the model are the position and dispersion of the particle, the resulting equations are also termed “ $R$ - $\Sigma$  equations” [3] to remind the symbols by which such variables are usually indicated in the literature.

The starting point of the method is the observation that the particle’s localization is provided at every time  $t$  by the squared modulus  $|\psi(\xi, t)|^2$ . Non-normalizable wave functions are not considered. Here,  $\xi \equiv (\xi_1, \xi_2, \xi_3)$  denotes the coordinates, while the symbol  $x \equiv (x_1, x_2, x_3)$  is reserved for the expectation value. As  $|\psi|^2$  can be reconstructed from its moments [1], the knowledge of the time evolution of the moments provides that of  $|\psi|^2$ . In turn, the moments’ dynamics is described by Newton-like equations, that lend themselves to a statistical extension. In this way, a set of transport equations coherently incorporating quantum features may be worked out [2].

## II. THEORY

The position and dispersion are first- and second-order moments of  $|\psi|^2$ . It is of interest to extend the model beyond the second order, to the purpose of improving the understanding of its formal aspects and extending its practical applicability. In this paper, the model will be worked out to any order. As the calculations are quite involved, the results will be presented with reference to the one-dimensional case only. Letting  $V(\xi, t)$  be the potential energy,  $m$  the particle mass,  $\mathcal{P} = -j\hbar d/d\xi$  the momentum operator, and

$$\langle \xi^r \rangle = \int |\psi|^2 \xi^r d\xi \quad (1)$$

the  $r$ -th moment of  $|\psi|^2$ ,  $r = 0, 1, \dots$ , the Newton equation for  $\langle \xi^r \rangle$  reads

$$m \frac{d^2 \langle \xi^r \rangle}{dt^2} = -r \int |\psi|^2 \xi^{r-1} \frac{dV}{d\xi} d\xi + a_r \int |\mathcal{P}\psi|^2 \xi^{r-2} d\xi - b_r \langle \xi^{r-4} \rangle, \quad (2)$$

where the normalization condition  $\int |\psi|^2 d\xi = 1$  is assumed, and  $a_r = r(r-1)/m$ ,  $b_r = \hbar^2 r(r-1)(r-2)(r-3)/(4m)$ . Equation (2) is found starting from the expression of the time derivative of the expectation value of a time-independent operator  $\mathcal{A}$ ,

$$\frac{d}{dt} \langle \mathcal{A} \rangle = \frac{j}{\hbar} \int \psi^* (\mathcal{H}\mathcal{A} - \mathcal{A}\mathcal{H}) \psi d\xi, \quad (3)$$

with  $\mathcal{H} = \mathcal{P}^2/(2m) + V$  the Hamiltonian operator, and by systematically applying suitable commutation rules involving quantum operators. Unfortunately, the possible commutation rules of Quantum Mechanics are many, whereas those useful for the purpose at hand are fewer. They are

$$\xi^r \mathcal{P} - \mathcal{P} \xi^r = r j \hbar \xi^{r-1}, \quad (4)$$

$$\mathcal{P} \mathcal{G}_r - \mathcal{G}_r \mathcal{P} = -r j \hbar \mathcal{G}_{r-1}. \quad (5)$$

with  $-j\hbar \mathcal{G}_r = m (\mathcal{H}\xi^r - \xi^r \mathcal{H})$ .

### III. DISCUSSION

A remarkable feature of (2) is that the second term at the right hand side does not contribute unless  $r \geq 2$ , and the third term does not contribute unless  $r \geq 4$ . Note that the dimensions of (2) are energy  $\times$  length $^{r-2}$ . As expected, the case  $r = 1$  provides the standard relation

$$m \frac{d^2 \langle \xi \rangle}{dt^2} = - \int |\psi|^2 \frac{dV}{d\xi} d\xi \quad (6)$$

which, after parametrizing  $|\psi|^2$  as  $\delta(\xi - x)$  with  $x = \langle \xi \rangle$ , yields the Ehrenfest approximation. Note that such a parametrization is equivalent to expanding  $dV/d\xi$  into a Taylor series around  $\xi = x$  and truncating the series to order zero. Instead, the expansion of  $dV/d\xi$  to the second order (still with  $r = 1$ ) yields, after letting  $\sigma = \langle \xi^2 \rangle - x^2$ ,

$$m \frac{d^2 x}{dt^2} = - \frac{dV}{d\xi} - \frac{\sigma}{2} \frac{d^3 V}{d\xi^3}, \quad (7)$$

namely, the first of the  $R$ - $\Sigma$  equations [1].

For the case  $r = 2$  it is useful to remind that  $m \dot{x} = \langle \mathcal{P} \rangle$  and  $\langle \mathcal{P}^2 \rangle = (\Delta p)^2 + m^2 \dot{x}^2$ , with  $(\Delta p)^2$  the momentum dispersion. In the second-order approximation of the  $R$ - $\Sigma$  model, such a dispersion is replaced with  $\hbar^2/(4\sigma)$  by assuming that  $\psi$  is a minimum-uncertainty wave function. Such an assumption may be viewed as the closure condition for the system of Newton equations built up by the first and second moment. Expanding  $\xi dV/d\xi$  to the second order around  $x$  yields, after some manipulation,

$$m \frac{d^2 \sigma}{dt^2} = \frac{\hbar^2}{2m\sigma} - 2\sigma \frac{d^2 V}{d\xi^2}, \quad (8)$$

namely, the second of the  $R$ - $\Sigma$  equations. About Eq. (8) it is worth adding that the factor 2 multiplying  $\sigma d^2 V/dx^2$  was missing in the corresponding equations of Refs. [1], [2], and [3]. However, none of the conclusions of such papers is affected, with the exception of the calculation of the frequency of  $\sigma$  in the harmonic-oscillator type of motion, which must be corrected by a factor  $\sqrt{2}$ .

It may be argued that using the moments of  $|\psi|^2$  may eventually lead to canceling the information carried by the phase of the wave function. Actually

this is not true. In fact, using the polar form  $\psi = \alpha \exp(j\beta)$ ,  $\alpha > 0$ , one finds

$$g_r \doteq m \frac{d \langle \xi^r \rangle}{dt} = r \langle \xi^{r-1} \hbar \beta' \rangle, \quad (9)$$

where the prime indicates the derivative with respect to  $\xi$ . In particular, the case  $r = 1$  of (9) is equivalent to  $m \dot{x} = \langle \mathcal{P} \rangle$ . As a consequence, the phase  $\beta$  also enters the second term at the right hand side of (2).

Another remark is that the external force  $-dV/d\xi$  enters only the first term at the right hand side of (2), while the other two terms are determined by the form of the wave function alone. If the force is absent, the evolution of the wave function is determined by the initial condition only. It follows that in this case the dynamics of the moments is determined solely by the initial conditions, as it should be. No matter what the force is, the initial conditions are determined by calculating (1) and (9) at  $t = 0$ . As  $|\psi|^2 = \alpha^2$ , one notices that the initial condition for the moment is determined by the wave function's modulus, whereas that for the moment's velocity is determined by the phase.

To bring the model beyond the second order it is necessary to add, say, the equation for  $r = 3$  and expand  $\xi^{r-1} dV/d\xi$  in (2) to the extent of making the third-order moment  $\langle \xi^3 \rangle$  to appear. The same scheme applies to the higher moments. Evidently, for  $r > 2$  the closure condition  $(\Delta p)^2 = \hbar^2/(4\sigma)$  of the second-order case becomes less sensible, because the modulus of the minimum-uncertainty wave function is Gaussian, which makes the odd moments of order  $r \geq 3$  to vanish due to symmetry. It follows that the closure condition must incorporate the moments of order higher than the second.

### REFERENCES

- [1] M. Rudan, E. Gnani, S. Reggiani, and G. Baccarani, *A Coherent Extension of the Transport Equations in Semiconductors Incorporating the Quantum Correction. Part I — Single-Particle Dynamics*, IEEE Trans. on Nanotechnology **4**, 495 (2005).
- [2] M. Rudan, S. Reggiani, E. Gnani, and G. Baccarani, *A Coherent Extension of the Transport Equations in Semiconductors Incorporating the Quantum Correction. Part II — Collective-Transport*, IEEE Trans. on Nanotechnology **4**, 503 (2005).
- [3] M. Rudan, *The R- $\Sigma$  Method for Nanoscale-Device Analysis* Proc. Simulation of Semiconductor Processes and Devices (SISPAD 2005), K. Taniguchi, M. Hane and N. Sano Eds., IEEE 05TH8826, ISBN 4-9902762-0-5, Tokyo, Sept. 1–3, p. 13–18 (2005).

# Quantum Simulation of Silicon Nanowire FETs: Ballistic Transport and Corner Effects

Mincheol Shin

Information and Communications University,  
119 Munji-ro, Yuseong, Daejeon 305-732, Rep. of Korea  
e-mail: mcshin@icu.ac.kr

In this work, the device characteristics of silicon nanowire field-effect transistor (SNWFET) have been investigated by solving the three-dimensional (3D) Poisson equation and the quantum ballistic transport equation self-consistently, using an efficient numerical algorithm to solve the 2D Schrödinger equations in the cross-sectional planes. The dependence of the device performance on the gate number, configuration, and shape has been examined in conjunction with the effect of the wave function confinement.

The simulated device is a three-dimensional (3D) structure which can have multiple gates around the silicon channel (Fig. 1). The source/drain doping concentration is heavily n-doped and the channel region is lightly p-doped or undoped. To simulate the device, we have adopted the uncoupled mode-space NEGF method, where the original 3D problem is split into 2D Schrödinger equation in the plane perpendicular to the transport direction and 1D NEGF equation in the transport direction ( $x$ ) [1], [2]. In such numerical simulations, most of the computing time is spent on solving the 2D Schrödinger equation in the cross-sectional planes, whether they are solved in the real-space or  $k$ -space.

In this work, we have developed an efficient way to solve the 2D Schrödinger equations in the cross-sectional planes, by transforming them into the “mode-space”, as follows. We expand the wavefunction  $\Psi(y, z)$  by a product of two 1D wavefunctions  $\chi_i(y)$  and  $\zeta_j(z)$  that are chosen appropriately:  $\Psi(y, z) = \sum_K a_K |K\rangle$ , where  $|K\rangle \equiv \chi_i(y)\zeta_j(z)$ . Then the problem reduces to solving  $M \times M$  eigenvalue problem of  $\sum_L \langle K | H_{2D} | L \rangle a_L = \epsilon_K a_K$ , where  $H_{2D}$  is the 2D Hamiltonian,  $\epsilon_K$  its  $K$ -th eigenvalue, and  $M$  the number of modes participating in the transport. Since  $M$  is  $10 \sim 200$  for

the nanowire transistors with a cross-sectional area  $S \lesssim 20\text{nm} \times 20\text{nm}$ , the computational burden can be greatly lifted.

Using the efficient numerical scheme, we have studied the scaling issues of the SNWFETs with the rectangular cross-section. Also we have investigated the effect of the corner rounding, starting with the rectangular cross-section and gradually rounding the corners until the cross-section becomes a circular one (Fig. 2).

Fig. 3 shows the  $I$ - $V$  characteristics when the silicon channel of the transistor of the gate-all-around (GAA) structure shrinks three-dimensionally: starting with  $L = T_{si} = W_{si} = 25$  nm,  $L$  is reduced gradually until  $L = 5$  nm ( $T_{si}$  and  $W_{si}$  are reduced by the same ratio). It can be seen in the figure that almost the same  $I$ - $V$  characteristics are maintained until  $L = 10$  nm.

Fig. 4 shows the effect of the corner rounding of a GAA transistor with  $L = T_{si} = W_{si} = 5$  nm; the degree of the corner rounding is given by  $2R/W_{si}$  where  $R$  is the radius of the curvature as shown in Fig. 2. The effect of the corner rounding becomes pronounced as the cross-section becomes closer to a circular shape. In Fig. 5, the dependence of the subthreshold swing (SS) on the curvature radius is shown for various transistor dimensions and gate configurations. It can be seen in the figure that, if the device performance of the transistor with the rectangular-shaped cross section is poor with greater SS values, the corner-rounding improves the device performance more greatly, and as the SS value approaches 60 mV/decade, the effect of the corner rounding becomes negligible. This can be understood by examining the quantum charge distributions in the cross-sectional planes, as shown in Fig. 6, where the current conduction

channels formed at the corners of the rectangular cross-section move toward the center as the corner rounding proceeds.

### REFERENCES

- [1] P.S. Damle et. al., in Molecular Electronics (ed. M. Reed and T. Lee, Amer. Sci. Pub., 2003.)
- [2] J. Wang, E. Polizzi, and M. Lundstrom, J. of Applied Physics, vol. 96, pp. 2192 - 2203, 2004.

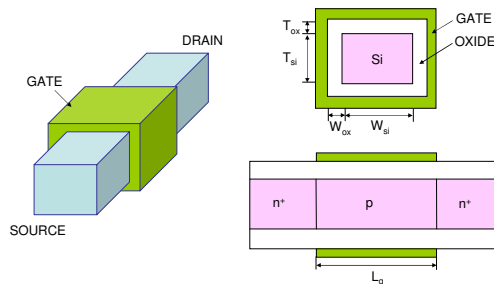


Fig. 1. Silicon nanowire field effect transistor

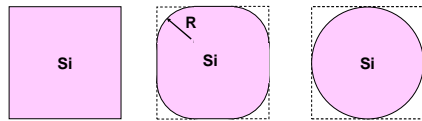


Fig. 2. Cross sections of SNWFETs with different radius of the curvature at the corners.

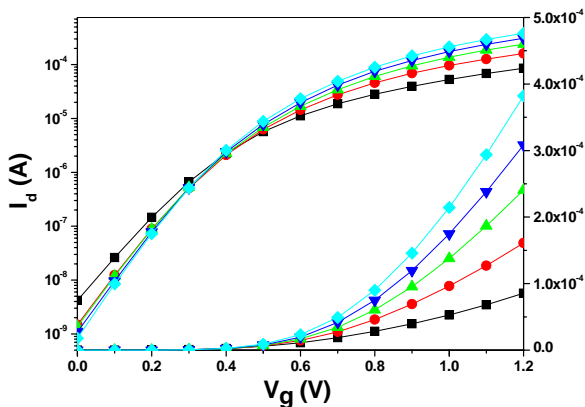


Fig. 3. I-V characteristics for  $L=25$  (diamonds),  $20$  (inverse triangles),  $15$  (triangles),  $10$  (circles), and  $5$  nm (squares), respectively ( $W_{si} = T_{si} = L$ ).

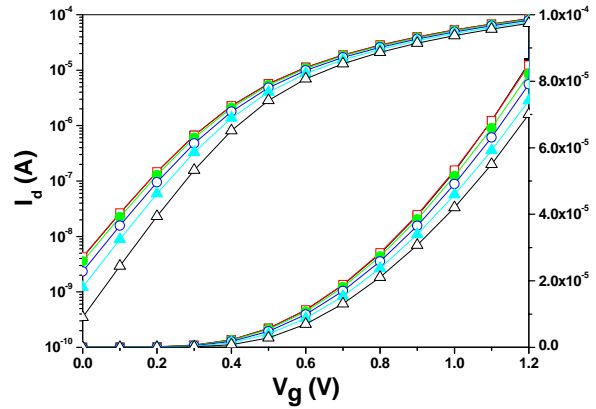


Fig. 4. Corner rounding effect for  $L = T_{si} = W_{si} = 5$  nm, for  $2R/W = 0.0$  (solid squares),  $0.2$  (open squares),  $0.4$  (solid circles),  $0.6$  (open diamonds),  $0.8$  (solid triangles), and  $1.0$  (open triangles).

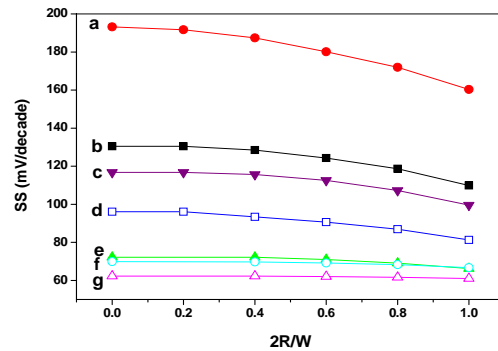


Fig. 5. Subthreshold swing values for different channel dimensions: GA (b,c,e,f,g), Tri (a,d),  $L = 5$  (a,b,d,e),  $L = 10$  (c,f,g),  $L_g = 5$  (a,b),  $L_g = 10$  (c,f),  $L_g = 15$  (d,e),  $L_g = 20$  (g),  $W = 5$  (a,b,d,e,f,g),  $W = 10$  (c) nm.

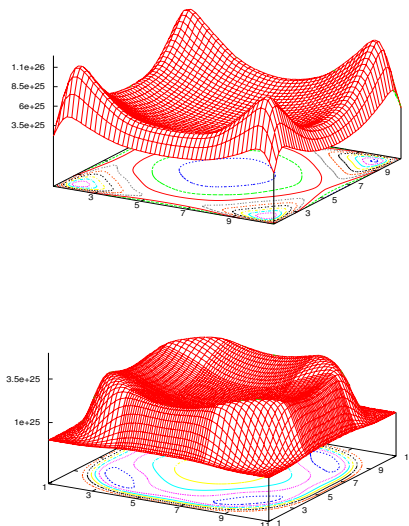


Fig. 6. Electron distributions in a cross-sectional plane of  $10\text{nm} \times 10\text{nm}$ :  $2R/W = 0.0$  (top) and  $2R/W = 0.6$  (bottom).

# Quantized Conductance Without Reservoirs: Method of the Non-Equilibrium Statistical Operator

B. Sorée and W. Magnus

Interuniversity Microelectronics Center (IMEC), Kapeldreef 75, B-3001 Leuven, Belgium  
e-mail: bart.soree@imec.be or wim.magnus@imec.be

## INTRODUCTION

We introduce a generalized time-dependent statistical operator to calculate nonequilibrium statistical averages of inhomogeneous current-carrying dissipative nanoscale conductors. We show that the method of the nonequilibrium statistical operator (NSO) [1] and the boosted statistical operator [2], [3] yield the same result for an appropriate choice of the thermodynamic parameters responsible for time-reversal breaking in homogeneous systems.

Next we demonstrate the method of the generalized statistical operator that also leads to a quantized conductance  $G_{\text{LB}} = 2e^2/h$  [6], [7] for a single-channel quantum point contact (QPC) and we infer that energy dissipation must be included to obtain a finite conductance.

Moreover a connection is made between our approach and the method of M.P. Das and F. Green [4] who have obtained the Landauer-Büttiker conductance without making the "Landauer assumptions".

## THE GENERALIZED NON-EQUILIBRIUM STATISTICAL OPERATOR

Within the framework of the NSO method of Zubarev our generalized non-equilibrium statistical operator corresponds the following form of the quasi-equilibrium statistical operator :

$$\hat{\rho}_t^{\text{B}} = \frac{1}{Z(t)} e^{-\beta_e(t)(\hat{H}_e^{\text{B}} - \mu(t)\hat{N})} e^{-\beta(t)\hat{H}_p} \quad (1)$$

with

$$\hat{H}_e^{\text{B}} = \hat{H}_e + \tau(t) \int_{\Omega} d\mathbf{r} \hat{\mathbf{J}} \cdot \mathbf{E} \quad (2)$$

where  $\hat{H}_e$  and  $\hat{\mathbf{J}}$  denote the Hamiltonian and current density operator of the unperturbed electron system and  $\hat{H}_p$  refers to the free phonon bath. Eq. (1) represents a current-carrying quasi-equilibrium statistical operator due to the presence of the time-reversal breaking term :

$$\hat{H}_B(t) = \tau(t) \int_{\Omega} d\mathbf{r} \hat{\mathbf{J}} \cdot \mathbf{E}. \quad (3)$$

It is possible to show that the generalized statistical operator can also be derived from the principle of maximum entropy under the constraint that it yields the correct total current  $\langle \hat{I} \rangle$ . In the steady-state regime where the quasi-equilibrium statistical operator becomes time-independent the integral containing the dot product of  $\hat{\mathbf{J}}$  and  $\mathbf{E}$  can be disentangled [5] and we obtain  $\hat{H}_B = \tau \hat{I} V_e$  where  $V_e$  is the applied electromotive force. The time-reversal breaking term  $\hat{H}_B(t)$  is a measure of the average energy increase of the electron ensemble at time  $t$  due to the power supplied by the nonconservative electric field  $\mathbf{E}$ .

## SELF-CONSISTENT SOLUTION OF POISSON AND BALANCE EQUATIONS IN THE STEADY-STATE

In the steady-state the parameters  $\beta_e$ ,  $\mu$  and  $\tau$  are obtained from a set of balance equations for energy and momentum [2] which are given by :

$$IV_e = \frac{i}{\hbar} \langle [\hat{H}_e, \hat{H}_{\text{ep}}] \rangle \quad (4)$$

$$\int d\tau \rho_e \mathbf{E} = \frac{i}{\hbar} \langle [\hat{\mathbf{P}}, \hat{H}_{\text{ep}}] \rangle + \frac{i}{\hbar} \langle [\hat{H}_e, \hat{H}_{\text{imp}}] \rangle. \quad (5)$$

Eqs. (4)-(5) are solved self-consistently together with Poisson's equation :

$$\nabla^2 \Phi = \frac{e}{\epsilon} [n(\mathbf{r}) - n_0]. \quad (6)$$

Due to the presence of the electron-phonon interaction Hamiltonian  $\hat{H}_{\text{ep}}$  in the balance equations (4)-(5) energy dissipation is explicitly included.

#### QUANTIZED CONDUCTANCE BEYOND THE RESERVOIR PICTURE

For the case of the QPC we show that the Poisson equation together with the requirement of charge neutrality in the asymptotic regions of the QPC yields  $\tau = L/2v_F$  where  $L$  is the operational length of the QPC, while  $v_F$  is the Fermi-velocity. Calculating the current  $I$  with this value for  $\tau$ , we obtain for a one-channel QPC at low temperature in the linear-response regime :

$$I = -2e \sum_k F(\epsilon_k + \tau V_\epsilon I_k) I_k \approx \frac{2e^2}{h} V_\epsilon \quad (7)$$

where

$$I_k = -\frac{e\hbar k}{mL} \quad (8)$$

is the one-particle current.

As a result we have obtained the Landauer-Büttiker quantized conductance through a self-consistent calculation without referring to the reservoir picture. For the particular case of the QPC this value of the corresponding total relaxation time  $\tau = L/2v_F$  was also obtained by Das and Green [4] from the Kubo-Greenwood formula for the conductance. In their case the requirement that  $\tau_{\text{in}} = \tau_{\text{el}} = L/v_F$  was necessary to obtain the quantized conductance. The total relaxation time  $\tau$  was then obtained through Matthiessen's rule :

$$\tau^{-1} = \tau_{\text{in}}^{-1} + \tau_{\text{el}}^{-1} = \frac{2v_F}{L}. \quad (9)$$

The corresponding total scattering length  $\lambda = v_F \tau = L/2$  is thus half the length  $L$  of the QPC and is due to both inelastic (phonons) and elastic scattering.

Finally, we also mention the result obtained by Kamenev and Kohn [8] who have also obtained the Landauer-Büttiker conductance without using the reservoir picture. Their calculation is based upon a self-consistent solution of the Schrödinger, Poisson and continuity equations.

#### CONCLUSION

The use of a generalized NSO allows us to obtain a self-consistent solution of the energy and momentum balance equations and Poisson equation. The self-consistent solution involves the Lagrange multipliers  $\tau(t)$ ,  $\mu(t)$  and  $T_e(t)$  which are in general time-dependent. Applying the generalized NSO method to a one-channel QPC in the low-temperature linear-response regime yields the Landauer-Büttiker conductance  $G_{\text{LB}}$ . The corresponding value of the Lagrange multiplier  $\tau$  is given by  $L/2v_F$  and is in agreement with the results obtained by [4]. Moreover we have corroborated the result of Green and Das, stating that inelastic scattering is essential for the Landauer-Büttiker conductance.

#### REFERENCES

- [1] D. N. Zubarev , *Nonequilibrium Statistical Thermodynamics*, Consultant bureau N.Y., 1974
- [2] Bart Sorée, Wim Magnus, Wim Schoenmaker, *Energy and momentum balance equations : a novel approach to quantum transport in closed circuits*, Phys.Rev.**B66** (2002) 035318
- [3] Bart Sorée, Wim Magnus, Wim Schoenmaker, *Conductance quantization and dissipation*, Phys.Lett.**A310** (2003) 322-328
- [4] M.P. Das and F. Green, *Landauer formula without Landauer's assumptions*, J.Phys. : Condens. Matter **12** (2003) L687-693
- [5] W. Magnus and W. Schoenmaker, *On the Use of a New Integral Theorem for the Quantum Mechanical Treatment of Electric Circuits*, J. Math. Phys.,**39** (1998) 6715
- [6] R. Landauer, IBM Journ. Res. Development **1** (1957) 223 and Philos. Mag. **21** (1970) 863
- [7] M. Büttiker and Y. Imry and R. Landauer and S. Pinhas , Phys.Rev. **B31** (1985) 6207
- [8] A. Kamenev and W. Kohn, *Landauer Conductance without Two Chemical Potentials*, Phys.Rev.**63** (2001) 155304

# Validity of the Effective Mass Approximation in Silicon and Germanium Inversion Layers

J.L. van der Steen, D.Esseni\*, P.Palestri\*, L.Selmi\*

MESA+ Institute for Nanotechnology, University of Twente, Enschede, The Netherlands

\* DIEGM, University of Udine, Via delle Scienze 208, 33100 Udine

## INTRODUCTION

The electron device community is actively investigating transistors realized in Ultra-Thin (UT) semiconductor films. The Effective Mass Approximation (EMA) is very frequently used to describe the nano-MOSFETs [1], however a comparison with more rigorous bandstructure calculations is highly demanded [2]. In this paper we use the method of the Linear Combination of Bulk Bands (LCBB) to calculate the band structure in UT silicon and germanium nano-transistors and compare the eigenvalues, energy dispersion and density of states (DOS) with the simplified EMA results

## LCBB AND EMA QUANTIZATION MODELS

In the LCBB quantization model the *unknown* wavefunction is expanded in terms of the Bloch functions  $\Phi_{n\mathbf{k}k_z}$  of the underlying crystal [3], [4], where  $n$  is the band of the Bloch function,  $\mathbf{k}$  denotes the in-plane wavevector, and  $z$  is the quantization direction. By selecting an appropriate set of  $k_z$  values it is possible to obtain a separated eigenvalue problem for each in-plane  $\mathbf{k}$  [4], the resulting energy dispersion for Si(111) is illustrated Fig.1.

In the EMA approach, a *single* Schrödinger-like equation in the real space is solved for each valley [5]. The set of EMA parameters used in this work are reported in Tab.I and are derived from [6].

## RESULTS AND DISCUSSION

The confining potential used for both EMA and LCBB calculations is a squared well with a width of  $T_{SCT}$  and a barrier of  $\Phi_B=3eV$ , hence the penetration of the wavefunction in the oxide is accounted for. Fig.2 reports the lowest eigenvalue versus  $T_{SCT}$  for the  $D_{0.916}$  and the  $D_{0.19}$  valleys of Si(100). The EMA tracks the LCBB results very well. With an infinite barrier, instead, the EMA

eigenvalues increase well above the LCBB values at the smallest  $T_{SCT}$ . Fig.3 reports the same comparison as in Fig.2 for the  $L_{0.219}$ , the  $D_{0.33}$  and the  $\Gamma$  valleys in Ge(110). Even in this case the EMA reproduces the absolute and relative position of the valleys indicated by the LCBB model.

Fig.4 reports the energy dispersion for Si(111) along the dashed line indicated in Fig.1. According to the position of the minima in the 3D Brillouin Zone (BZ), the EMA predicts a minimum at  $k_x=1.7/\sqrt{6}(2\pi/a_0)\simeq 0.6940(2\pi/a_0)$ . The LCBB results do exhibit such a minimum for relatively large  $T_{SCT}$  values (not shown). However, Fig.4 shows that for  $T_{SCT}=2nm$  the minimum of the LCBB bandstructure tends to move at the edge of the 2D BZ (i.e. at  $k_x=2.0/\sqrt{6}(2\pi/a_0)\simeq 0.8165(2\pi/a_0)$ ) thus creating a discrepancy between the EMA and LCBB results. The LCBB energy dispersion has a flat energy branch, whose effective mass is much larger than the  $m_{le}=0.674$  value reported in Tab.I. This feature of the LCBB calculations result in a large DOS at the very bottom of the conduction subbands (see Fig.5), that decreases with the increase of the energy.

As illustrated in Fig.4, we found that the LCBB and EMA 2D energy dispersion can be quite different at the smallest  $T_{SCT}$ . Thus, the LCBB method has been used to calculate  $T_{SCT}$  dependent transport masses, that will be discussed at the conference. **Acknowledgment:** This work was partially supported by the Italian MIUR (PRIN 2004) and by the EU (SINANO NoE, IST-506844).

## REFERENCES

- [1] S.E. Laux. in *IEDM Technical Digest*, p.135, 2004.
- [2] A.Rahman *et al.* in *IEDM Technical Digest*, p.139, 2004.
- [3] F.Chirico *et al.* in *Phys.Rev.B*, **64**, p.045314, 2001.
- [4] D.Esseni *et al.* in *Phys.Rev.B*, **72**, p.165342, 2005.
- [5] C.Jungemann *et al.* in *Solid State Electr.*, **36**, p.1529, 1993.
- [6] F.Stern *et al.*, *Physical Review* **163**, 816-835 (1967).

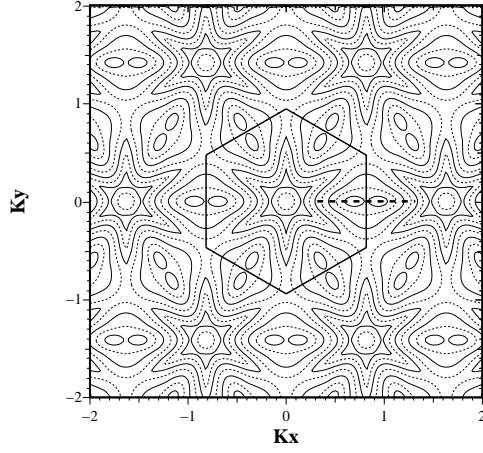


Fig. 1. Si(111),  $T_{SCT}=5nm$ . Lowest eigenvalue vs.  $\mathbf{k}$  obtained with the LCBB method. The six degenerate minima are in  $\mathbf{k}=(\pm 1.7/\sqrt{6}, 0)$  and in  $\mathbf{k}=(\pm 0.85/\sqrt{6}, \pm 0.85/\sqrt{2})$ . The hexagon indicates the 2D Brillouin zone [4].

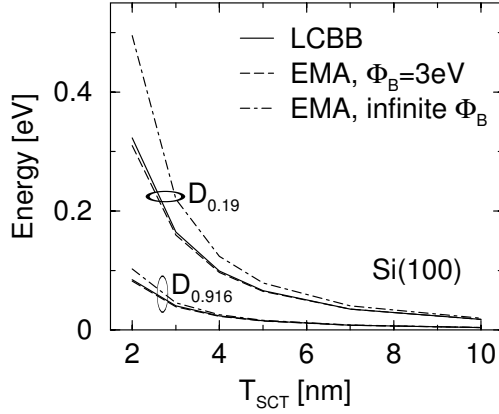


Fig. 2. Si(100). Lowest eigenvalue versus  $T_{SCT}$  for the  $D_{0.916}$  and  $D_{0.19}$  valleys calculated with either the LCBB or the EMA model. The infinite  $\Phi_B$  EMA results are obtained by setting the wavefunction to zero at the oxide interface.

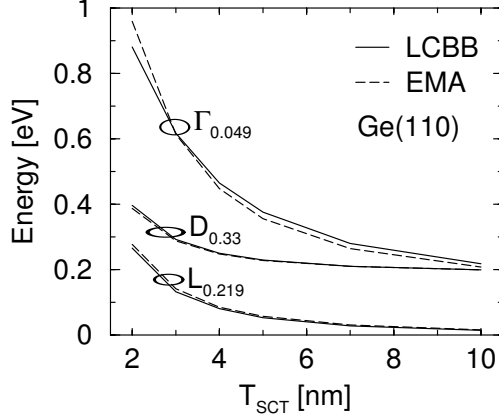


Fig. 3. Ge(110). Lowest eigenvalue versus  $T_{SCT}$  for the  $L_{0.219}$ ,  $D_{0.33}$  and  $\Gamma_{0.049}$  valleys calculated with either the LCBB or the EMA model. The energy offset of the  $D$  and  $\Gamma$  valleys with respect to the  $L$  valleys of bulk germanium is assumed to be  $189meV$  and  $145meV$ , respectively.

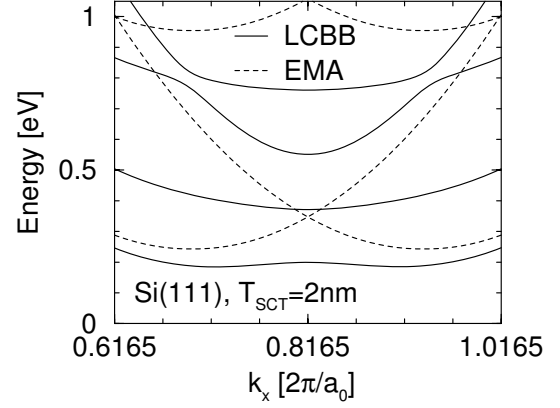


Fig. 4. Si(111),  $T_{SCT}=2nm$ . Energy dispersion along the dashed line indicated in Fig.1 obtained with either the LCBB or the EMA model. The minimum is at  $k_x=1.7/\sqrt{6}(2\pi/a_0)$  according to the EMA model. The minimum in the LCBB model has both a different position and a different value.

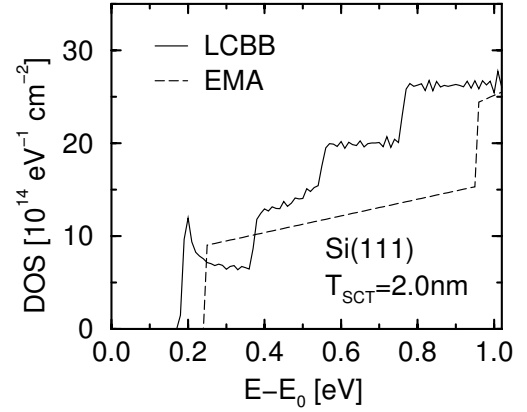


Fig. 5. Si(111),  $T_{SCT}=2nm$ . Density of states calculated with either the LCBB or the EMA model. A spike of DOS is observed in the LCBB results, which is produced by the flat energy branch in Fig.4. In the EMA model a non-parabolicity factor  $\alpha=0.5eV^{-1}$  is used.

Material	$m_{te}$	$m_{le}$	$m_z$	$n_\nu$	Label
Si(100)	0.190	0.190	0.916	2	$D_{0.916}$
	0.19	0.916	0.190	4	$D_{0.19}$
Si(111)	0.190	0.674	0.258	6	$D_{0.258}$
Ge(110)	0.080	0.600	0.219	2	$L_{0.219}$
	0.2	0.575	0.33	4	$D_{0.33}$
	0.049	0.049	0.049	1	$\Gamma_{0.049}$

TABLE I  
DEGENERACY  $n_\nu$ , QUANTIZATION MASS  $m_z$  AND EFFECTIVE MASSES  $m_{le}$  AND  $m_{te}$  ALONG THE PRINCIPAL AXES OF THE ELLIPSES THAT DESCRIBE THE IN-PLANE ENERGY DISPERSION IN THE EMA MODEL. THE PARAMETERS CORRESPOND TO THE DOMINANT VALLEYS FOR Si(100), Si(111) AND Ge(110) AND ARE CALCULATED AS EXPLAINED IN [6].

# Simulation of Magnetization Reversal and Domain-Wall Trapping in Submicron NiFe Wires with Different Wire Geometries

E. Varga, A. Imre\*, L. Ji\*, and W. Porod\*

Pázmány Péter Catholic University, Department of Information Technology, Práter utca 50/a, 1088  
Budapest, Hungary

\*University of Notre Dame, Department of Electrical Engineering, Notre Dame, IN 46556  
e-mail: vared@digitus.itk.ppke.hu

## INTRODUCTION

In recent years, there has been a surge of interest in current-induced magnetic domain-wall motion (CIDWM) and domain-wall trapping in submicron NiFe (permalloy) wires [1-3]. In these experiments, the domain wall is generated by an external magnetic field that induces magnetization reversal of the wire, and the location of domain-wall generation can be controlled by the wire geometry. The reversal process starts from the extended wire pads which inject domain walls into the wire [4-5]. These propagating domain walls then can be trapped in the wire, and they can be dragged by an applied electrical current due to spin-momentum transfer, i.e. CIDWM. This method is considered for novel memory devices [6]. In this work, we investigate the effect of different wire-pad geometries on magnetization reversal and domain-wall injection, and we report results for threshold magnetic field values required in these experiments. We also present a novel method of trapping domain wall in the magnetic wire without pinning. This method can be used in the above mentioned CIDWM studies, and in addition, it is a promising candidate as read-out structure for magnetic quantum-dot cellular automata (MQCA) [7].

## DISCUSSION

We performed micromagnetic simulations [8] in order to determine the switching-field values, i.e. the field thresholds for field-induced magnetization reversal, as a function of wire-pad geometry. Figure 1 shows a comparison of threshold fields for various pad shapes, such as square, triangular, diamond,

circular, and others. We find that the magnetic properties of these wire-pad structures strongly depend upon geometry, and we find switching-field variations of more than a factor of two. Our results have implications for magnetic-field-assisted CIDWM since these auxiliary fields need to be chosen below the switching field of the wire in order to avoid injection of additional domains and field-induced magnetization reversal. We also study wire structures with differently-shaped contact pads on either end, which can be used to preferentially nucleate domain walls on one end of the wire, or the other. The wire geometry between the pads can be further used to manipulate CIDWM. The effect of geometrical constrictions in wires was carefully studied by several groups [9-15], who demonstrated successful trapping of domain walls by pinning at the constrictions. Here we present a novel method to trap domain wall by placing two nanomagnets near the permalloy wire. We investigate this structure both theoretically and experimentally. The fabrication is done by electron-beam lithography and lift-off process. Figure 2.a shows one of our test patterns with a circular disk at one end and a pointed shape at the other end of the wire. The additional nanomagnets are placed in the close vicinity, in this case, about 40 nm away from the wire. These nanomagnets consist of only one domain, and their stray field penetrates the wire. The process of trapping a domain wall begins with applying a relatively large magnetic field parallel to the axis of the wire, such that the nanomagnets and the wire have a uniform magnetization pointing from the pointed end to the circular end. By applying a small, 210 Gauss magnetic field in the

opposite direction, the magnetization of the wire starts to reverse from the circular end, and a domain wall propagates toward the pointed end. When it reaches the region between the two nanomagnets, where a local magnetic field is generated, it is stopped, and thus a head to head domain wall is trapped (Figure 2.b).

#### SUMMARY

The magnetization reversal of submicron NiFe wires is largely dominated by the physical geometry. Domain walls that are nucleated at the end of the wires can be controlled by choosing appropriate pad-shape design. Using the stray field of additional nanomagnets the domain walls can be trapped as they propagate along the wire. This provides a novel method for CIDWM studies, since the critical value of required current density, that is capable of moving the domain wall, is expected to be different from those corresponding to experiments where the domain wall is pinned by geometrical constriction of the wire. This kind of domain wall trapping can be employed to serve as a signal detector and an interface to electronic circuits for MQCA.

#### REFERENCES

- [1] M. Tsoi et al., *Magnetic domain wall motion triggered by an electric current*, Appl. Phys. Lett. **83**, 2617 (2003).
- [2] A. Yamaguchi et al., *Real-space observation of current-driven domain wall motion in submicron magnetic wires*, Phys. Rev. Lett. **92**, 077205 (2004).
- [3] S. H. Florez et al., *Spin-current-induced magnetization reversal in magnetic nanowires with constrictions*, Journ. Appl. Phys. **97**, 10C705 (2005).
- [4] W. Y. Lee et al., *Magnetization reversal in mesoscopic NiFe wires: a magnetic domain launching device*, IEEE Trans. Magn. **36**, 3018 (2000).
- [5] C. C. Faulkner et al. *Controlled switching of ferromagnetic wire junctions by domain wall injection*, IEEE Trans. Magn. **39**, 2860 (2003).
- [6] S.Parkin, M.Oishi, *IBM's magnetic race-track memory*, Nikkei Electronics Asia, May, 48 (2005).
- [7] A.Imre et al, *Field-coupled nanomagnets for logic applications*, Proc. SPIE Int. Soc. Opt. Eng. 5838, 162 (2005).
- [8] M. J. Donahue and D. G. Porter, *OOMMF User's Guide, Version 1.0* Interagency Report NISTIR 6376, <http://math.nist.gov/oommf/>
- [9] R. D. McMichael et al., *Domain wall traps for low-field switching of submicron elements*, Journ. Appl. Phys. **87**, 7058 (2000).
- [10] A. Hirohata et al. *Domain wall trapping in controlled submicron ferromagnetic elements*, Journ. Appl. Phys. **87**, 4727 (2000).
- [11] A. Hirohata et al. *Domain-wall trapping in controlled mesoscopic ferromagnetic wire junctions*, Journ. Magn. Mat. **226-230**, 1845 (2001).

- [12] J. M. D. Coey et al. *Magnetic excitations in a nanocontact*, Phys. Rev. B. **64**, 020407 (2001).
- [13] Y. Labaye et al., *Domain walls in ferromagnetic nanoconstriction*, Journ. Appl. Phys. **91**, 5341 (2002).
- [14] C. C. Faulkner et al., *Artificial domain wall nanotraps in NiFe wires*, Journ. Appl. Phys. **95**, 6717 (2004).
- [15] K. Miyake et al., *Exchange biasing of a Neel wall in the nanocontact between NiFe wires*, Journ. Appl. Phys. **97**, 014309 (2005).

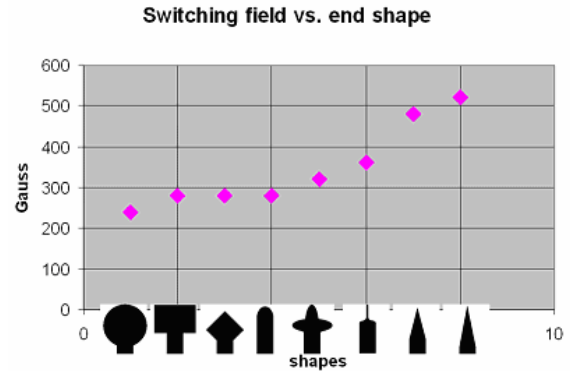


Fig. 1. Simulation results of switching-field dependence on different wire pad shapes (end shapes). All of the wires shown here were designed to be 4  $\mu\text{m}$  long, 180 nm wide, 10 nm thick and made of NiFe.

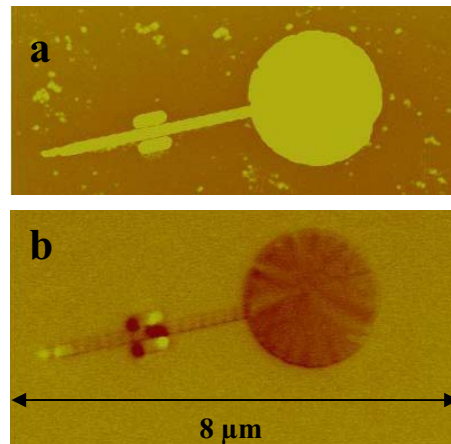


Fig. 2. Domain wall trapped in a permalloy wire by means of stray field of two nearby nanomagnets. a, Atomic force microscopy image of a test sample shows topographic information. b, Magnetic force microscopy image reveals the internal magnetization of the test sample.

# The NEGF Simulation of the RTD Bistability

J. Voves, T. Třebický and R. Jackiv

Department of Microelectronics, CTU FEE Prague, Technická 2, 16627 Praha 6, Czech Republic  
e-mail: voves@fel.cvut.cz

## INTRODUCTION

It is well known that the current-voltage (I-V) curves of the resonant tunneling diodes (RTD) exhibit a characteristic plateau-like behavior and hysteresis. Response times approach terahertz frequencies. Hence, the RTD offer advantages for terahertz electronic devices and components. A proper and complete interpretation of the I-V curves is still a controversial issue. Some groups [1-2] utilized self-consistent solutions of the time-dependent Wigner function equation (WFE) for a GaAs-AlGaAs RTD. These simulations revealed intrinsic high-frequency oscillations in the tunneling current. Plateau-like behavior in the I-V curves were obtained from the time-average of the current oscillations. The results showed that the formation of the emitter quantum well (EQW) and the coupling of its quasi-bound state to the state in the main quantum well (MQW) is the physical mechanism responsible for both the hysteresis and the plateau-like behavior. The relaxation time affects the width of the hysteresis and if it is smaller than 200 fs, the hysteresis will disappear. WFE approach is very complex and time consuming. Other approach is based on the non-equilibrium Green's functions (NEGF). Other group [3] performed numerical calculations by the program NEMO based on the NEGF approach. They found that scattering in the emitter reduces hysteresis by broadening the quasi-bound state formed in the emitter as well. Nevertheless, the plateau region did not appear in their results.

## EXPERIMENT AND SIMULATION

We simulated the same structure as in [1] and our AlAs-GaAs double barrier RTD grown by molecular beam epitaxy with two identical 3.4 nm AlAs barriers, 5.9nm GaAs well and 10 nm undoped GaAs spacer layers. We used the program Wingreen [4] based on the NEGF approach with the different values of scattering parameter "s". Our

results in Fig.1 and Fig.4 show the dependence of the current peak position and the with of the hysteresis on the scattering rate. No plateau region appeared on the I-V curve in the contrast to the experimental data. The bistable region is produced by the different charge distribution in the both RTDs (see Fig.2 and Fig.5). The evolution of the electron charge distribution during the increasing bias is on the Fig.3. Experimental results to be further analyzed are shown in Fig.6.

## CONCLUSION

We analyzed the reason why plateau region does not appear in the NEGF results. Full time-dependent Wigner-Poisson approach is able to retain necessary information about forming high frequency current oscillations and coupling of energy levels within EQW and MQW. On the other hand, NEGF approach implemented in Wingreen does not take into account a time evolution of such quantum effects and therefore is unable to involve plateau-like structure on I-V characteristics. Scattering rates have impact on the position and slope of hysteresis and therefore should be set appropriately.

## ACKNOWLEDGEMENT

The work was supported by the grant No. 102/06/0381 GACR and by the grant No. MSM 6840770014 The Ministry of Education CR.

## REFERENCES

- [1] B. A. Biegel, J. D. Plummer, *Applied Bias Slewing in Transient Wigner Function Simulation of Resonant Tunneling Diodes*, IEEE Trans. on El. Dev. **44**, 733 (1997)
- [2] P. Zhao, H. L. Cui, D. L. Woolard, K. L. Jensen, F. A. Buot, *Origin of Hysteresis and Plateau-Like Behavior of the I-V Characteristics of Resonant Tunneling Diodes*, Int. J. of Mod. Phys. **B14**, 411 (2000)
- [3] C.L. Gardner, G.Klimeck, Ch. Ringhofer, *Smooth Quantum Hydrodynamic Model vs. NEMO Simulation of a Resonant Tunneling Diode*, J. of Comp. Electronics **3**, 95 (2004)
- [4] K. M. Indlekofer, J. Malindretos, <http://www.fz-juelich.de/isg/mbe/software.html>

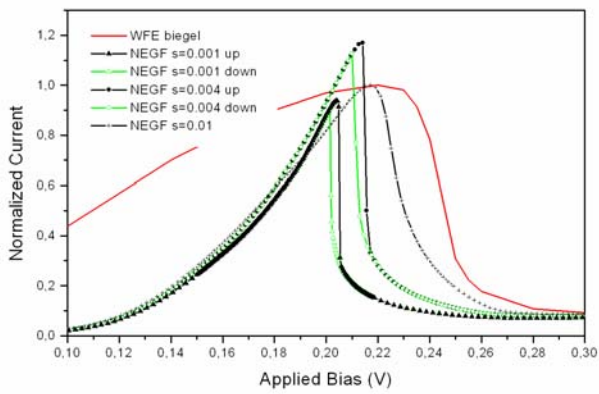


Fig. 1. I-V characteristics of RTD from [1] simulated by NEGF with different scattering parameter and WFE self-consistent time independent model [1]. (No hysteresis with  $s=0.01$ ).

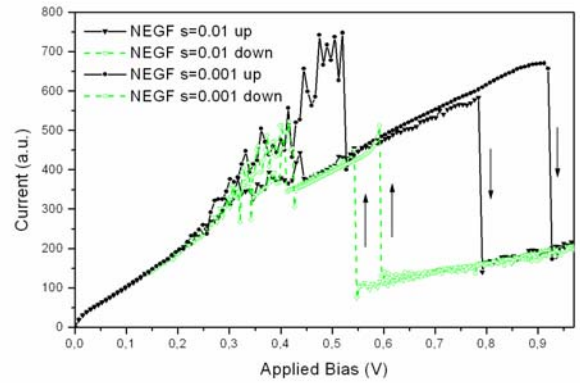


Fig. 4. I-V characteristics of GAAs/AlAs RTD simulated by NEGF with different scattering parameter.

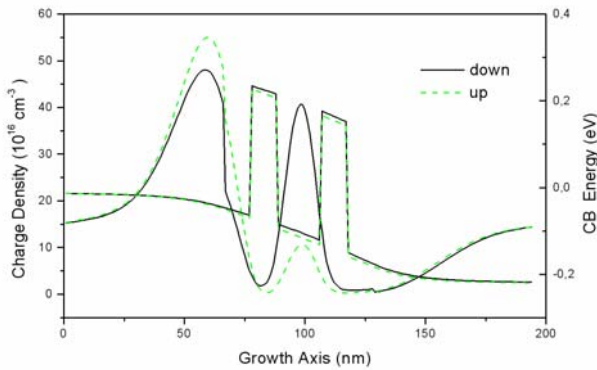


Fig. 2. Charge and potential distribution in RTD [1] in the bistable region at  $V=0.204V$  (NEGF simulation with  $s=0.001$ ).

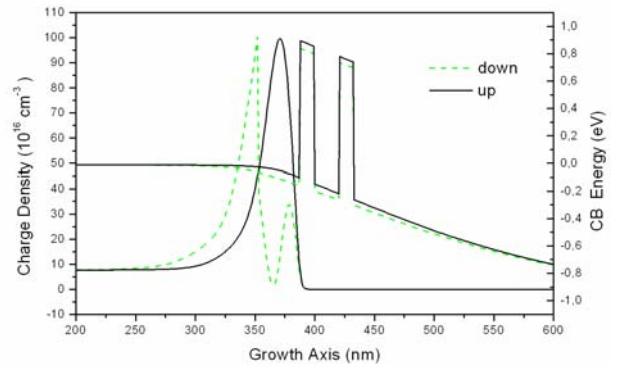


Fig. 5. Charge and potential distribution in GaAs/AlAs RTD [1] in the bistable region at  $V=0.88V$  (NEGF simulation with  $s=0.001$ ).

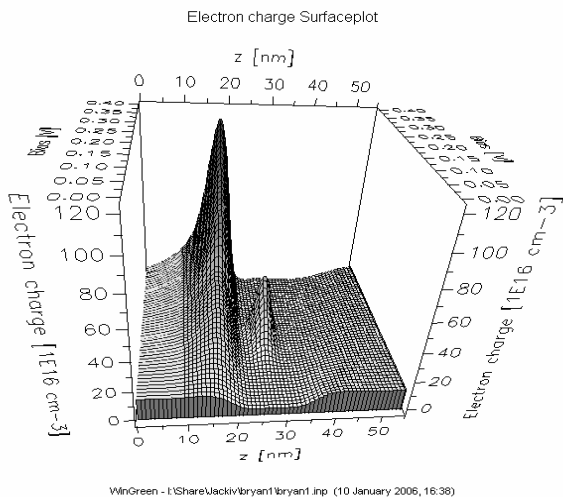


Fig. 3. Electron charge surface plot in RTD[1] (NEGF simulation with  $s=0.001$ ).

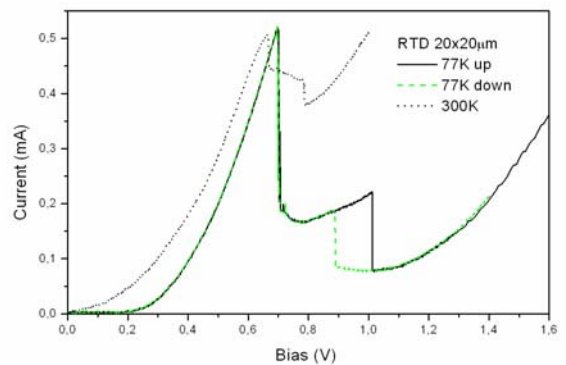


Fig. 6. Experimental I-V characteristics of the GaAs/AlAs RTD measured at the temperatures 300K and 77K.

# *I-V* Characteristics and Nonclassical Behavior in Networks of Small Metal Clusters

H. Zhang, D. Mautes, and U. Hartmann

Institute of Experimental Physics, University of Saarbruecken, P. O. Box 151150, D-66041 Saarbruecken, Germany

e-mail: h.zhang@mx.uni-saarland.de

## INTRUDUCTION

The miniaturization of electronic components approaches the limit at which the functionality of the components cannot be described solely by classical physics. Quantum phenomena, such as electron tunneling, play an important role for devices with functional structures at the nanometer scale. For an investigation of the electron-transport in such small structures scanning tunneling microscopy (STM) and spectroscopy provide an ideal access..

## EXPERIMENT

In this work monolayers of metal clusters of type  $\text{Au}_{55}[\text{P}(\text{C}_6\text{H}_5)_3]_{12}\text{Cl}_6$ , deposited on highly oriented pyrolytic graphite (HOPG) or Au(111) substrates were investigated with a low-temperature ultrahigh vacuum scanning tunneling microscope. The diameter of the cluster core is 1.4 nm. The ligand shell  $[\text{P}(\text{C}_6\text{H}_5)_3]_{12}\text{Cl}_6$  has a thickness of about 0.35 nm. It acts as dielectric spacer. Apart from the usual charge-quantization phenomena, such as Coulomb blockade and staircase, negative differential resistance (NDR) was observed by performing *I-V* measurements at distinct locations on the cluster layers (see Fig. 1).

## DISCUSSION

Surprising at first sight is the appearance of NDR if the tip is fairly close to a neighboring cluster (Fig. 1(c)). It is obvious that in this case one cannot neglect the capacitance between the tip and the neighboring cluster. This stray capacitance can evidently cause a significant change of the electrical potential of the neighboring cluster during the variation of the tunneling voltage which is applied between STM tip and substrate. The potential variation of the neighboring cluster in turn

influences the potential of the primary cluster through the capacitance between the two clusters. That leads to a Coulomb blockade in the main current path. The neighboring cluster ultimately acts as a "gate".

## SIMULATION

We performed a modeling of the resulting *I-V* curve using a Monte-Carlo method [1] based on the orthodox single-electron tunneling theory. A scheme of the corresponding cluster arrangement and the ersatz circuit together with the calculated behavior is shown in Fig. 2. In the case of Fig. 2(b) we found that NDR can only occur if the capacitance between the two neighboring clusters is larger than that between cluster and substrate. This situation is excluded in a treatment according to classical physics: The separation between the clusters ( $\sim 7 \text{ \AA}$ ) is larger than that between cluster and substrate ( $\sim 3.5 \text{ \AA}$ ).

We explain this phenomenon by a nonclassical capacitive behavior: For tunnel junctions electrons can overcome the dielectric or vacuum region through tunneling and this leads to a reduction in capacitance. As a consequence, the capacitance decreases with decreasing separation of the electrodes because the tunneling current increases.

Accordingly, we have chosen the proper values of capacitances and resistances for simulating all three cases. The results are in good agreement with the experimental findings.

## ACKNOWLEDGEMENT

This work is supported by the Deutsche Forschungsgemeinschaft .

## REFERENCES

- [1] Ch. Wasshuber, H. Kosina and S. Selberherr, IEEE Transactions on Computer- Aided Design of Integrated Circuits and Systems **16**, 937 (1997).

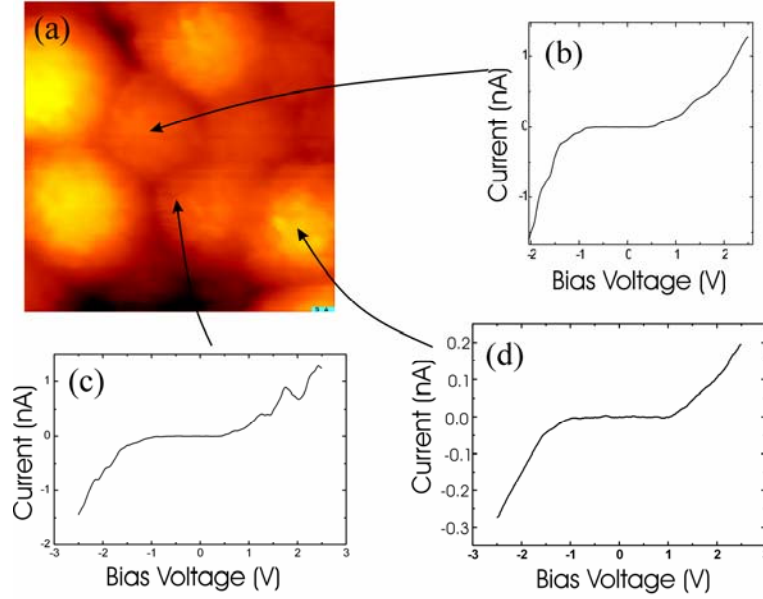


Fig. 1. (a) STM image of  $\text{Au}_{55}[\text{P}(\text{C}_6\text{H}_5)_3]_{12}\text{Cl}_6$  clusters deposited on HOPG, obtained at a bias of 2 V and a current of 100 pA at a scan range of 7 nm x 7 nm. (b)  $I$ - $V$  curve acquired above the center of a cluster, (c) away from the center and near a neighboring cluster, and (d) above a cluster which belongs to the second cluster layer, as marked in (a). Setpoint for (b) and (c):  $I_T = 0.7$  nA,  $V_T = 2$  V, for (d):  $I_T = 0.1$  nA,  $V_T = 2$  V

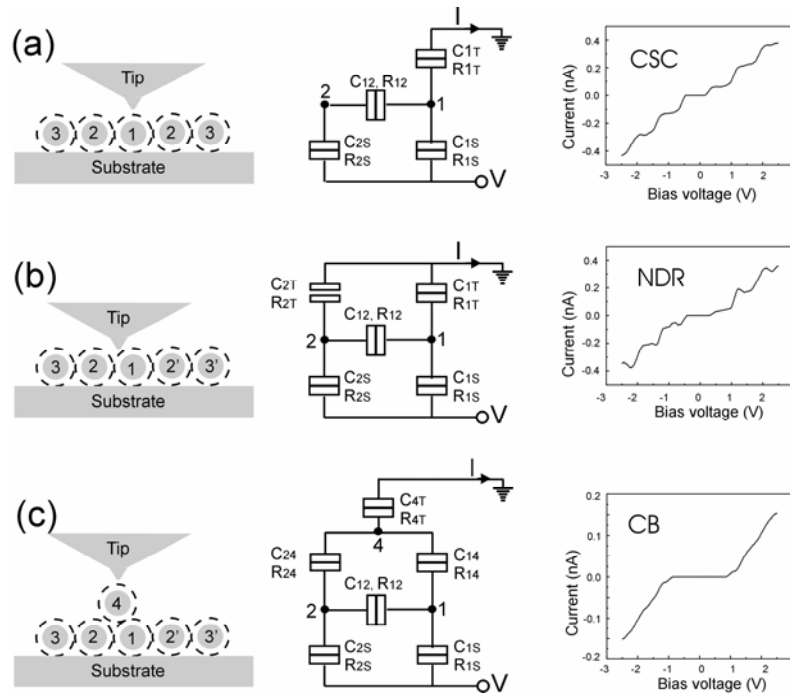


Fig. 2. Schematic diagrams of the different tip-cluster-substrate arrangements, the equivalent electrical circuits, and Monte-Carlo simulation of  $I$ - $V$  curves. (a), (b) and (c) correspond to the cases of (b), (c) and (d) in Fig. 1, respectively. The C and R values chosen for modeling are: (a)  $C_{1T} = 0.2$  aF,  $C_{1S} = C_{2S} = 0.05$  aF,  $C_{12} = 0.25$  aF,  $R_{1T} = 5$  G $\Omega$ ,  $R_{1S} = R_{2S} = 100$  M $\Omega$ ,  $R_{12} = 100$  G $\Omega$ ; (b)  $C_{1T} = 0.08$  aF,  $C_{1S} = C_{2S} = 0.03$  aF,  $C_{12} = 0.25$  aF,  $C_{2T} = 0.12$  aF,  $R_{1T} = 5$  G $\Omega$ ,  $R_{1S} = R_{2S} = 100$  M $\Omega$ ,  $R_{12} = 100$  G $\Omega$ ,  $R_{2T} = 1200$  G $\Omega$ ; (c)  $C_{4T} = 0.08$  aF,  $C_{1S} = C_{2S} = 0.05$  aF,  $C_{12} = 0.25$  aF,  $C_{14} = 0.25$  aF,  $C_{24} = 0.27$  aF,  $R_{4T} = 2$  G $\Omega$ ,  $R_{1S} = R_{2S} = 200$  M $\Omega$ ,  $R_{12} = 100$  G $\Omega$ ,  $R_{14} = 8$  G $\Omega$ ,  $R_{24} = 80$  G $\Omega$

# Perimeter Recombination in Thin Film Solar Cells

Abderrahmane BELGHACHI

Laboratory of Semiconductor Devices Physics

Physics Department, University of Béchar, POB 417, BECHAR 08000, ALGERIA

Tel: +213 49810324, Fax: +213 49815244

e-mail: [abelghachi@wissal.dz](mailto:abelghachi@wissal.dz)

## EXTENDED ABSTRACT

Surface recombination has a profound effect on the performance of a solar cell, at the illuminated surface reduces its photocurrent and along the cell's perimeter increases its dark current. The perimeter recombination increases considerably the dark current particularly for small area solar cells where the perimeter to area ratio is important. Perimeter recombination current has two components, the first is due to recombination at the surface that intersects the space-charge layer while the second originates recombination at the surface of quasi-neutral regions.

Recombination at the depleted layer surface has a  $2kT$  character and is treated in the present work in a similar way to that of the bulk, using the model of Sah, Noyce and Shockley. The electric field at the surface is different from that of the bulk because of the presence of surface states. The density of surface states at the GaAs surface is known to be very high and distributed across the entire forbidden energy band gap. However the Fermi level could be assumed pinned near mid gap throughout the structure. We suggested that at the surface the potential varies linearly and the electric field is uniform along the surface [1]. Using this simple model we were able to obtain an analytical form of the perimeter current that yielded values of the product of the characteristic length by the surface recombination velocity ( $L_s S_0$ ) that agreed well with reported experimental values, Fig.1.

The recombination current outside the space-region is of two-dimensional nature, it represents lateral diffusion of minority carriers at the boundary of the space-charge region close to the perimeter. This current is calculated by solving numerically the

two-dimensional continuity equation at the base, the contribution of the emitter is negligible. An effective surface recombination ( $S_e$ ) was introduced to account for intrinsic surface recombination along with the effect of the bend bending caused by the charged states. This current is of  $kT$  character at low biases but tends towards  $2kT$  behaviour at higher biases. A value of  $S_e = 1 \times 10^7$  cm/s is found to give better result, Fig.2.

We found that at low bias the ideality factor of the total perimeter (Fig.3) current is about 2, thus the recombination inside the depleted layer surface is dominant. Whereas at higher bias the ideality factor sharply decreases to around 1 that corresponds to the  $kT$  character of the perimeter current associated with recombination at the quasi-neutral base surface.

The calculation demonstrates that perimeter component of the dark current is very important, Fig.4. It affects seriously the performance of small area solar cells. As the ratio of perimeter to area ( $P/A$ ) is increased the perimeter current acquired significant proportions, thus the expected  $2kT$  current due to bulk deep levels existing in the depletion layer is two to three orders of magnitude too small to account for [1,2].

## REFERENCES

- [1] A. Belghachi, Modelling of perimeter recombination in GaAs solar cells, *Microelectronics Journal* **36** (2005) 115-124.
- [2] S. P. Tobin, S. M. Vernon, C. Bajgar, S. J. Wojtczuk, M. R. Melloch, M. S. Lundstrom, K. A. Emery, Assessment of MOCVD- and MBE- Grown GaAs for High-Efficiency Solar Cell Applications, *IEEE Trans. Electron Devices* **37** (2)(1990) 469-475

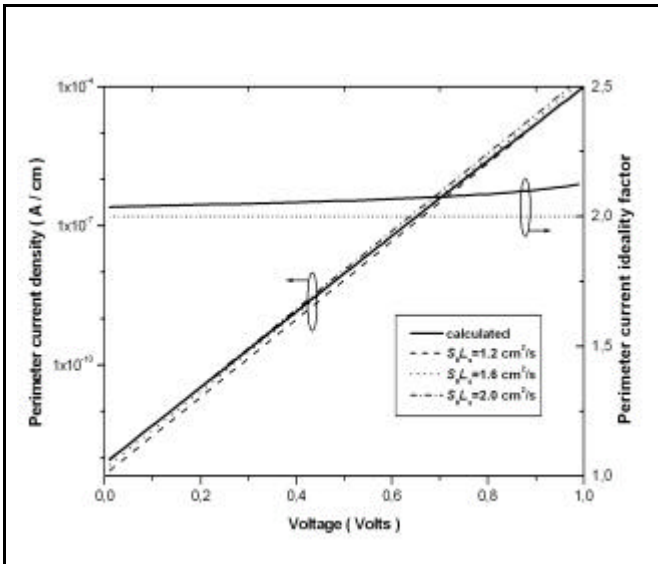


Fig. 1: current vs. voltage characteristics and current ideality factor of perimeter recombination current at the space-charge region surface. Comparison is made with the equation:

$$I_p = en_i S_0 P L_s \exp\left(\frac{eV}{2kT}\right)$$

using three values of the product  $S_0 L_s$ .

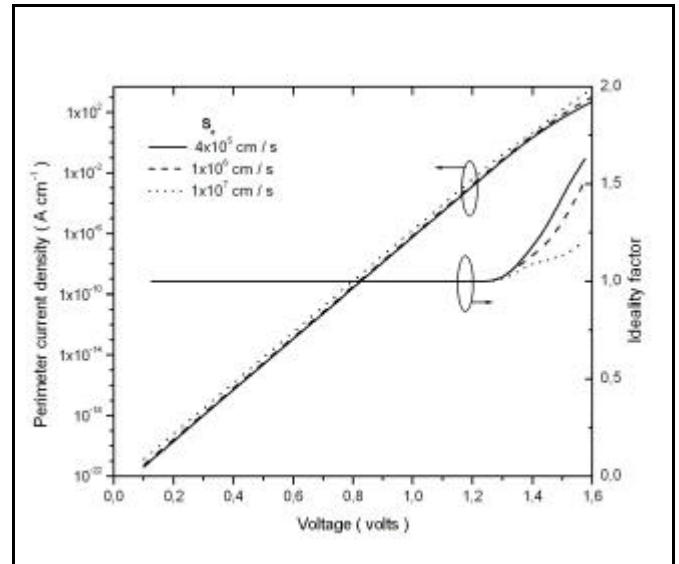


Fig. 2: current vs. voltage characteristics and current ideality factor of perimeter recombination current at the quasi-neutral base for different effective surface recombination velocities.

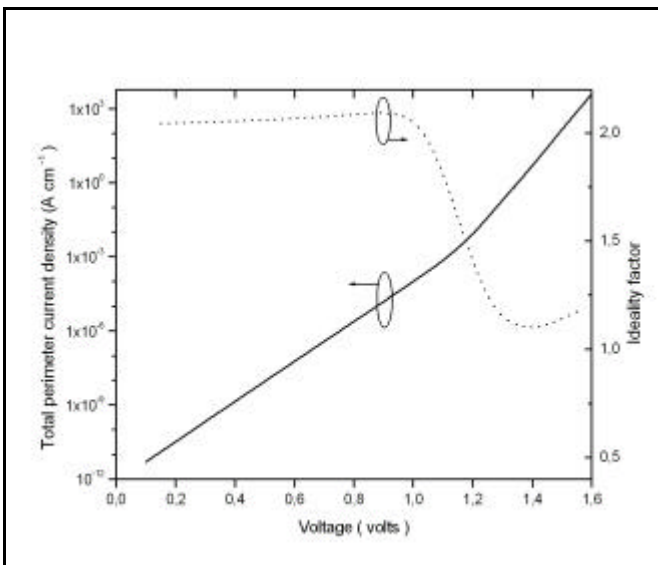


Fig. 3: current vs. voltage characteristics and ideality factor of the total perimeter recombination current. (Effective surface recombination velocity  $S_e = 10^7$  cm/s. at the quasi-neutral base).

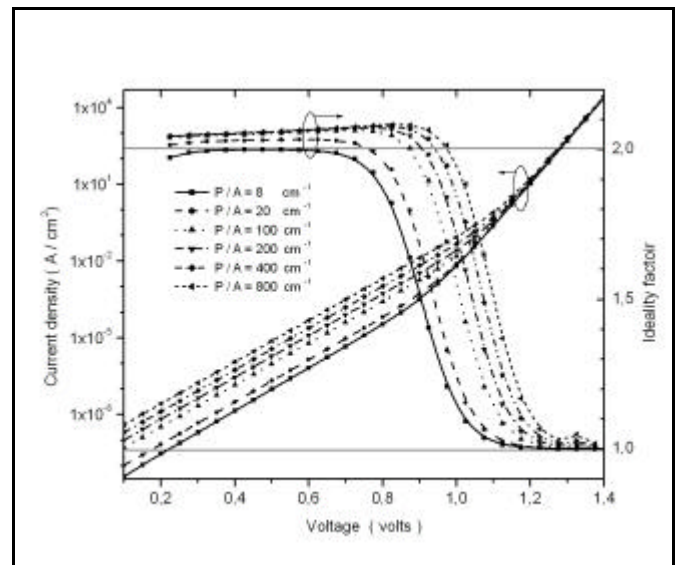


Fig. 4: dark current vs. voltage characteristics and current ideality factor of heteroface GaAs solar cell with different perimeter to area ratios ( $P/A$ ).  $P/A = 8$  cm<sup>-1</sup> corresponds to the fitted data of Tobin et al. [2].

# Study of the Light Intensity Threshold for Simulated PIN Photodiode under Proton Radiation

M.A. Cappelletti<sup>1</sup> and E.L. Peltzer y Blancá<sup>1,2</sup>

<sup>1</sup> Grupo de Estudio de Materiales y Dispositivos Electrónicos (GEMyDE), Depto. de Electrotecnia, Facultad de Ingeniería, Universidad Nacional de La Plata, 48 y 116, CC.91, La Plata (1900), Buenos Aires, Argentina

<sup>2</sup> Instituto de Física de Líquidos y Sistemas Biológicos (IFLYSIB) CONICET – UNLP – CIC,

La Plata, Buenos Aires, Argentina

e-mail: [mcappel7@yahoo.com.ar](mailto:mcappel7@yahoo.com.ar)

## INTRODUCTION

The knowledge of the space radiation environment is essential for predicting if a device will survive to the total radiation which will expect to encounter in a space mission.

The trapped proton fluxes are often the most important radiation consideration for devices especially designed to operate in spatial applications in low earth orbit (LEO), near 600 km altitude [1]. This illustrate why proton testing is important.

The PIN (p-intrinsic-n) photodiodes are every time more used in spatial applications. The PIN photodiodes are semiconductor devices that answer to high energy particles and photons generating a flow of current proportional to the incident power.

The effects of the radiation studied were the atomic displacement damages.

## PHYSICAL MODEL

The modelling and simulation of the PIN photodiodes were done solving the Poisson and continuity equations self consistently [2, 3]. This results were compared with experimental values.

## RESULTS AND DISCUSSION

In this work we present results of nine differently constructed PIN photodiodes exposed to spatial radiation. In Fig. 1 we show a simplified PIN photodiode. Table 1 gives the characteristic lengths of the nine simulated PIN photodiodes.

All the simulations considered the effects of 10 MeV proton radiation on the PIN photodiodes. The fluencies used were of  $1 \times 10^{13}$ ,  $5 \times 10^{13}$ ,  $1 \times 10^{14}$ ,  $2.5 \times 10^{14}$  p<sup>+</sup>/cm<sup>2</sup> and zero fluence (not irradiated photodiode). We included in our simulation the effects produced by the light illumination on the

photodiodes. The intensities used were ranged from 0 to 100 mW/cm<sup>2</sup>. The wavelength of the incident light was 900 nm (in the infrared band).

A comparison among the nine simulated PIN photodiodes irradiated with  $2.5 \times 10^{14}$  p<sup>+</sup>/cm<sup>2</sup> is shown in Fig. 2, where a lineal relation between the total reverse current and the light intensity can be seen for each PIN photodiode. We can also see in Fig. 2 that the slopes rise when the length of the intrinsic region increase, therefore, the efficiency in the detection of photons and protons is maximized. Similar results were obtained for the others fluencies simulated.

From these results we have obtained one expression that relates the total reverse current and the incident radiation.

The simulation results in Fig. 3 show the current increment when a PIN photodiode (PIN\_4) is exposed to several proton fluencies regarding to the not irradiated photodiode. For each set of curves of each PIN photodiode, the straight line of the total reverse currents in function of light intensities have a cross point called threshold.

The light intensity threshold (LIT) is not constant, it is variable for each PIN photodiode. The variation of the LIT with the length of the type p, intrinsic and type n regions is shown in Fig. 4. We have deduced an expression that reproduce the behaviour of the LIT. We can see that the LIT decreases when the length of the type p and type n regions are increased.

## CONCLUSION

With the codes generated we are able to reproduce very precisely the behaviour of the PIN photodiodes studied under proton radiation.

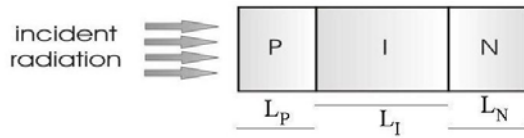


Fig. 1. Simplified scheme of a PIN photodiode, where  $L_p$ ,  $L_i$  and  $L_n$  are the length of the type p, intrinsic and type n regions respectively.

	$L_p$ [ $\mu\text{m}$ ]	$L_i$ [ $\mu\text{m}$ ]	$L_n$ [ $\mu\text{m}$ ]
PIN_1	0.9	28.2	0.9
PIN_2	1.35	27.3	1.35
PIN_3	1.8	26.4	1.8
PIN_4	2.25	25.5	2.25
PIN_5	2.7	24.6	2.7
PIN_6	3.6	22.8	3.6
PIN_7	4.5	21.0	4.5
PIN_8	4.95	20.1	4.95
PIN_9	5.4	19.2	5.4

Table 1. Characteristic lengths of the nine simulated PIN photodiodes. All the simulations were considered with  $L_p + L_i + L_n = 30 \mu\text{m}$  and  $L_p = L_n$ .

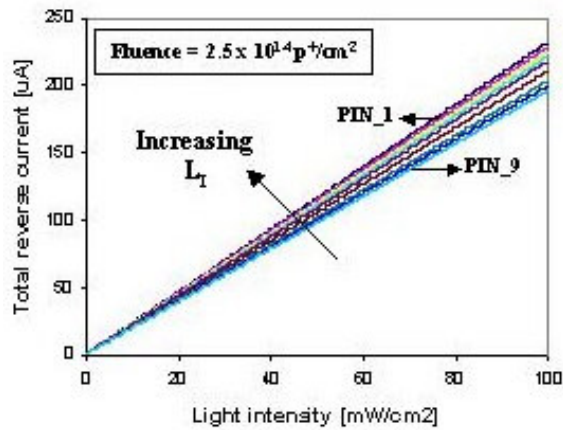


Fig. 2. Total reverse current in function of light intensity at 10V for the irradiated nine simulated PIN photodiodes at one proton fluence.

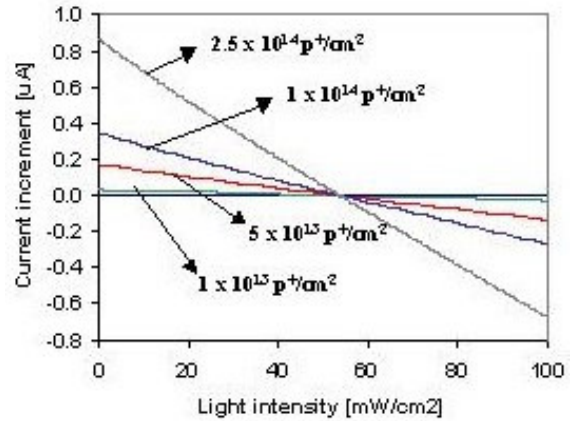


Fig. 3. Light intensity versus current increment for a irradiated PIN photodiode (PIN\_4) at several proton fluencies.

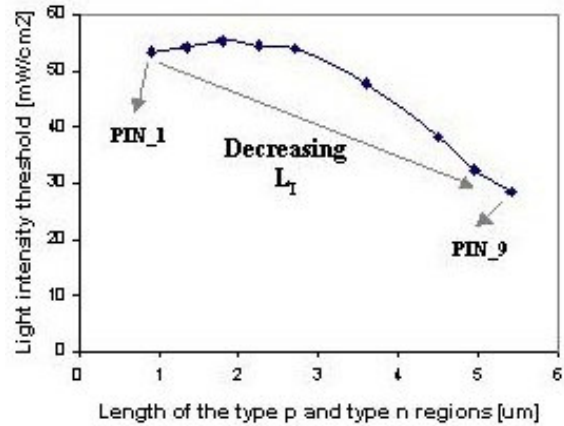


Fig. 4. Variation of the light intensity threshold (LIT) with the length of the type p and type n regions.

## REFERENCES

- [1] M. Xapsos, S. Huston, J. Barth and E. Stassinopoulos, *Probabilistic Model for Low-Altitude Trapped-Proton Fluxes*, IEEE Transactions on Nuclear Science, NS-49 (6), 2776 (2002).
- [2] D.G. Yagüez, D. Villaraza, M.A. Cappelletti and E.L. Peltzer y Blancá, *Study of semiconductor devices exposed to spatial radiation*, WSEAS Transactions on Systems, Issue 3, Vol 3, 1228 (2004).
- [3] D.G. Yagüez, D. Villaraza, M.A. Cappelletti and E.L. Peltzer y Blancá, *Simulation of PIN Photodiodes Exposed to Spatial Radiation*, WSEAS (World Scientific and Engineering Academy and Society) accepted publication (2004).

# Determination of Single Mode Condition in Dielectric Rib Waveguides with Large Cross Section by Finite Element Analysis

M. De Laurentis, A. Irace, G. Breglio

Dipartimento di Ingegneria Elettronica e delle Telecomunicazioni  
Università degli Studi di Napoli "Federico II"  
Via Claudio, 211-80125 Naples, ITALY  
e-mail: a.irace@unina.it

The single mode condition in large cross section rib waveguides is of great interest because almost every kind of active and passive integrated optoelectronic device or sensor, is designed to sustain only the fundamental mode of propagation for better matching with optical fibers.

In this paper we present a criterion to determine the single mode condition for a large cross section rib waveguides, by comparison between the numerical solutions found with Neumann boundary conditions and Dirichlet boundaries conditions applied when solving the eigenvalues problem.

## INTRODUCTION

The main issue when solving the Helmholtz equation with numerical techniques is that the numerical solver may find solutions that are not physical nor related to the geometries of the problem, but "inspired" by the boundaries conditions. Such solutions are usually caused by the unavoidable need to limit the inspection domain to save computational resources. Sometimes it can be difficult to distinguish between physical solution and these "spurious" solutions. Therefore, if we want to investigate the single-mode condition in rib waveguides, we have choose a robust criterium to understand weather a numerical solution is either a guided mode or it is leaking away from our guiding structure.

The rib waveguide guides modes are supposed to be well confined nearby the rib region and insensible of the lateral boundaries, so we suppose the non physical solutions having larger spatial extension and, for these reason, they are more sensible to lateral boundary conditions. Therefore, by changing the rib section geometrical dimensions, we expect a higher difference between the eigenvalue of first mode solution found with Dirichlet boundaries conditions the one found with Neumann boundaries conditions, when these solutions become not physical (i.e. the mode is not longer guided).

## SINGLE MODE CONDITION: FEM ANALYSIS

Along this line of argument, we have developed a numerical code based on FEMLAB and MATLAB which, keeping fixed the rib height  $H$ , studies the difference ( $|n_{\text{eff10D}} - n_{\text{eff10N}}|$ ) between the first higher order mode effective refractive index found with Dirichlet boundaries conditions ( $n_{\text{eff10D}}$ ) and first mode effective refractive index found with Neumann boundaries conditions ( $n_{\text{eff10N}}$ ), by changing etching value (i.e. changing the etching complement  $r$ , see Fig.1) for each width-height ratio value,  $w/H$ , chosen between 0.5 and 1.75. This has been done in order to compare our results with recently published literature data [1-3].

The typical outcome of this analysis is the plot reported in the Fig. 2 where we observe, for  $r < r^*$ , the quantity  $|n_{\text{eff10D}} - n_{\text{eff10N}}|$  being essentially negligible, while for  $r > r^*$ , the difference  $|n_{\text{eff10D}} - n_{\text{eff10N}}|$  increases as expected. The  $r^*$  value is what we expect to be the boundary between a single mode waveguide and a multimode one. In Fig. 3 we show the comparison between our results, Soref [1] and Pogossian [2] results.

The analysis, originally performed for TE polarization, can be extended to the TM case and to different cross sections in order to evaluate if field polarization or waveguide geometries affect the single mode condition as they become comparable to the wavelength of the propagating field.

## REFERENCES

- [1] R. A. Soref, J. Schmidtchen, K. Peterman, *Large single-mode rib waveguides in GeSi-Si and Si-on-SiO<sub>2</sub>*, Journal of Quantum electronics, **27**,8, 1971-1974 (1991)
- [2] S. P. Pogossian, L. Vescan, A. Vosonovici, *The single-mode condition for semiconductor rib waveguides with large cross section*, Journal of Lightwave technology, **16**,10, 1951-1955 (1998)
- [3] J. Lousteau, D. Furniss, A.B. Seddon, T. M. Benson, P. Sewell, *The single-mode condition for Silicon-on-Insulator optical rib waveguides with large cross section*, Journal of Lightwave technology, **22**,8, 1923 (2004)

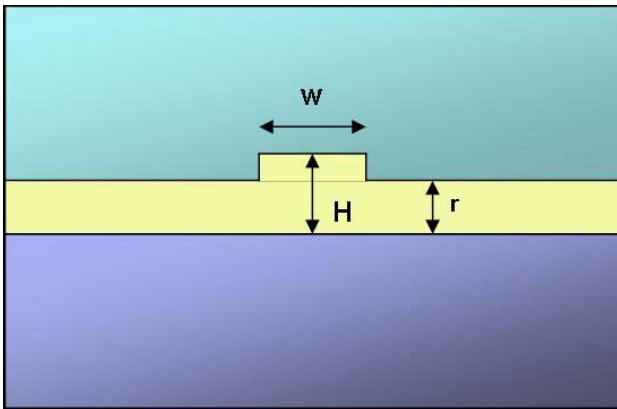


Fig. 1. Rib waveguide section.  $H$  is the rib height;  $w$  the rib width and  $r$  the etching complement.

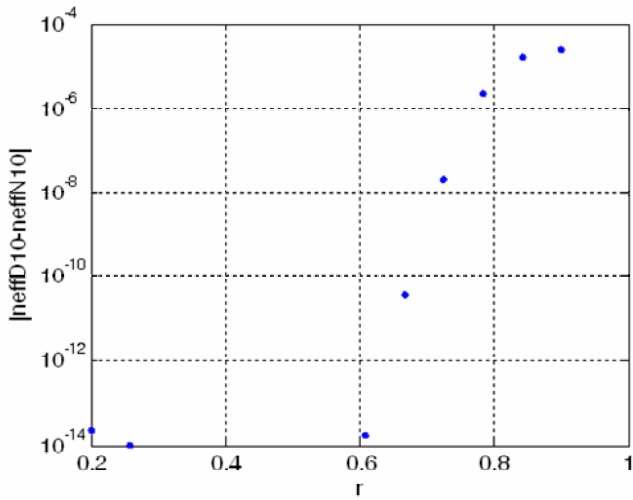


Fig. 2. Difference between first mode solution found with Dirichlet boundaries conditions and first mode solution found with Neumann boundaries conditions. Typically, when this solutions become not physical (i.e. the mode is not longer guided) the difference explodes, so we can observe a particular value of  $r$ ,  $r^*$ , so that for  $r < r^*$ , the quantity  $|neff10D - neff10N|$  being essentially negligible, while for  $r > r^*$ , the difference  $|neff10D - neff10N|$  increases. The  $r^*$  value is what we expect to be the boundary between a single mode waveguide and a multimode one.

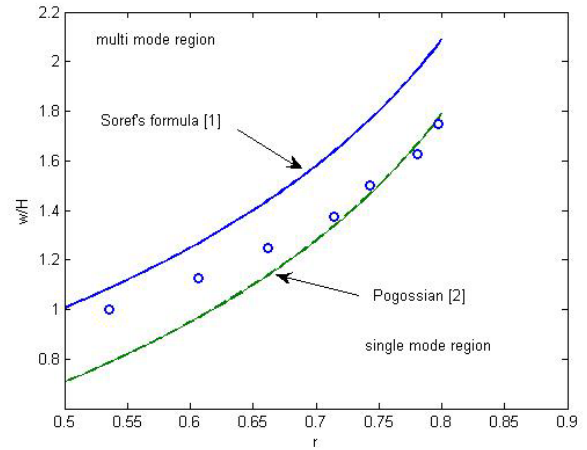


Fig. 3. Comparison between our FEM analysis results (circle), Soref's formula [1] and Pogossian et al. results [2]. Above the curves we define the multi mode region, while below the single mode region.

# Improved Simulation of VCSEL Distributed Bragg Reflectors

F. De Leonardis, V.M.N. Passaro\*, and F. Magno\*

Dipartimento di Ingegneria dell'Ambiente e per lo Sviluppo Sostenibile, Politecnico di Bari, Taranto, Italy

\*Dipartimento di Elettrotecnica ed Elettronica, Politecnico di Bari, via E. Orabona n.4, 70125 Bari, Italy  
e-mail: passaro@deemail.poliba.it

## INTRODUCTION

In this paper, the Floquet-Bloch theory (FBT) [1] has been applied to the accurate simulation of distributed Bragg reflectors (DBRs) in vertical cavity surface emitting lasers (VCSELs). A number of comparisons with other largely used methods are presented. Performance predictions for long-wavelength VCSELs with GaInAsP active region are derived.

## VCSEL STRUCTURE

The VCSEL structure (see Fig. 1) under investigation employs InP/Al<sub>0.05</sub>Ga<sub>0.42</sub>In<sub>0.53</sub>As DBRs, having a layer index difference  $\Delta n = 0.63$  [2]. The structure is optimized for lasing at the wavelength of 1546 nm. The calculations have been carried out for the bottom n-DBR, consisting of  $N = 22$  periods. DBRs with various refractive index profiles have been examined, i.e. step index (square), sinusoidal and trapezoidal. Accurate results by FBT have been found by using five space harmonics, as the best trade-off between accuracy and calculation time. Reflectivity calculations have been compared as obtained by FBT, modified transfer matrix method (TMM) [2], coupled mode theory (CMT) [3], *tanh* [4] and TMM [5].

## NUMERICAL RESULTS

Fig. 2 shows the DBR reflectivity spectra in case of abrupt interfaces (square profile). The central lobe is clearly similar for the three analysed methods, as they exhibit the same value of peak reflectivity. However, the 3dB stopbands are slightly different (207.5 nm for FBT, 210.8 nm for CMT and 210.5 nm for TMM, respectively) and centred at different wavelengths (1.5325  $\mu\text{m}$ , 1.5475  $\mu\text{m}$  and 1.5531  $\mu\text{m}$ , respectively), because of the rigorous evaluation of leaky modes by FBT, whose interference shifts the band a little. Other DBR

system compositions have been also considered, and results are summarized in Table I. It clearly shows the advantage of using FBT, including scattering losses, instead of other approaches [6]. Increasing approximations are given by CMT and TMM when the index profiles become more trapezoidal and the index contrast larger.

Finally, Tables II-IV show the comparison among various methods in terms of DBR reflectivity, VCSEL threshold gain, threshold current density and external quantum efficiency, being  $B = \Lambda/2$  and  $\Lambda$  the DBR layer period. Accurate predictions by FBT are clearly shown.

## CONCLUSION

Rigorous simulations of DBR reflectivity and VCSEL performance by Floquet-Bloch theory are presented in this work.

## ACKNOWLEDGEMENT

This work has been partially supported by the Italian National Fund for Basis Research (FIRB) with project n. RBAU01E8SS.

## REFERENCES

- [1] V.M.N. Passaro, *Optimal design of grating-assisted directional couplers*, J. Lightwave Technol. **18**, 973 (2000).
- [2] M. Linnik and A. Christou, *Effects of Bragg mirror interface grading and layer thickness variations on VCSEL performance at 1.55  $\mu\text{m}$* , Proc. SPIE **4286**, 162 (2001).
- [3] S. F. Yu, *Analysis and Design of Vertical Cavity Surface Emitting Lasers*, John Wiley & Sons, (2003).
- [4] B.-G. Kim and E. Garmire, *Comparison between the matrix method and the coupled-wave method in the analysis of Bragg reflector structures*, J. Opt. Soc. Am. **9**, 132 (1992).
- [5] S. W. Corzine, R. H. Yan, and L. A. Coldren, *A tanh substitution technique for the analysis of abrupt and graded interface multilayer dielectric stacks*, IEEE J. Quantum Electron. **27**, 2086 (1991).
- [6] A. Karim, J. Piprek, P. Abraham, D. Lofgreen, Y.-J. Chiu, and J. E. Bowers, *1.55  $\mu\text{m}$  Vertical-Cavity Laser Arrays for Wavelength-Division Multiplexing*, IEEE J. Sel. Top. in Quantum Electron. **7**, 178 (2001).

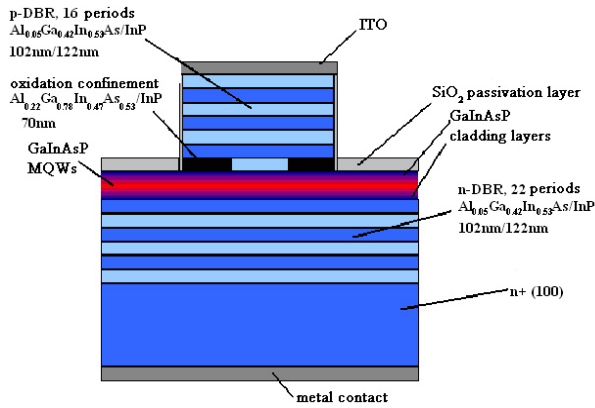


Fig. 1. VCSEL structure under investigation.

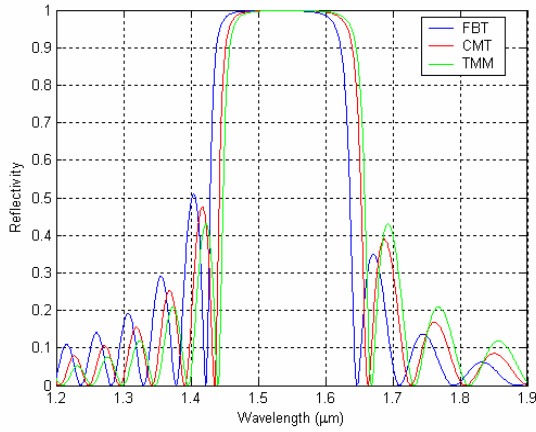


Fig. 2. Reflectivity spectra for 22 periods (square profile).

Table I. Number of periods for 99% reflectivity for various DBR system materials (square profile).

DBR composition	$n_2$	$n_1$	$\Delta n$	This work	Loss by FBT (dB/ $\mu\text{m}$ )	Ref. [6]
GaAs/AlAs	3.37	2.89	0.48	20	2.657	16
InGaAsP/InP	3.45	3.17	0.28	36	1.568	28
AlGaAsSb/AlAsSb	3.5	3.1	0.40	25	2.228	16
AllnGaAs/AllnAs	3.47	3.21	0.26	39	1.457	30
a-Si/SiO <sub>2</sub>	3.6	1.45	1.15	4	9.512	4
a-Si/Al <sub>2</sub> O <sub>3</sub>	3.6	1.74	1.86	4	9.457	5

Table II. Comparison of reflectivity and laser performance with various calculation methods (square profile,  $A = 0$ ).

Method	DBR Reflectivity (%)		VCSEL performance		
	$R_1$	$R_2$	$g_{th}$ (cm <sup>-1</sup> )	$J_{th}$ (A/cm <sup>2</sup> )	$\eta_d$ (%)
FBT (this work)	99.8338	98.6241	172.7136	694.3365	24.86
modified TMM [2]	92.3076	79.7471	481.5607	844.7579	76.58
CMT [3]	99.8685	98.8345	155.3526	686.7250	17.58
$\tanh$ [4]	99.8610	98.7899	140.7890	680.4043	18.15
TMM [5]	99.8639	98.8082	156.0793	687.0419	17.92

Table III. Comparison of reflectivity and laser performance for various calculation methods (“abrupt” trapezoidal,  $A=0.3B$ ).

Method	DBR Reflectivity (%)		VCSEL performance		
	$R_1$	$R_2$	$g_{th}$ (cm <sup>-1</sup> )	$J_{th}$ (A/cm <sup>2</sup> )	$\eta_d$ (%)
FBT (this work)	99.7974	98.4303	166.5497	691.6245	22.45
modified TMM [2]	91.1234	77.6109	528.1910	870.1422	77.92
CMT [3]	99.8237	98.5591	162.8924	690.0203	20.94
$\tanh$ [4]	99.8153	98.5165	144.5473	682.0298	21.44
TMM [5]	99.8639	98.8082	156.0781	687.0414	17.92

Table IV. Comparison of reflectivity and laser performance for various calculation methods (“smooth” trapezoidal,  $A=0.7B$ ).

Method	DBR Reflectivity (%)		VCSEL performance		
	$R_1$	$R_2$	$g_{th}$ (cm <sup>-1</sup> )	$J_{th}$ (A/cm <sup>2</sup> )	$\eta_d$ (%)
FBT (this work)	99.3225	96.2632	229.4754	719.8163	40.98
modified TMM [2]	85.1038	68.5485	752.2500	1003.1661	81.84
CMT [3]	99.3995	96.5180	221.5182	716.1888	39.21
$\tanh$ [4]	99.3942	96.5371	173.0909	694.5029	39.14
TMM [5]	99.8639	98.8082	156.0781	687.0414	17.92

# Scattering Effect in Optical Microring Resonators

F. De Leonardis and V.M.N. Passaro\*

Dipartimento di Ingegneria dell'Ambiente e per lo Sviluppo Sostenibile, Politecnico di Bari, Taranto, Italy

\*Dipartimento di Elettrotecnica ed Elettronica, Politecnico di Bari, via E. Orabona n.4, 70125 Bari, Italy

e-mail: [passaro@deemail.poliba.it](mailto:passaro@deemail.poliba.it)

## INTRODUCTION

Optical microring resonators are of great interest for monolithic and integrated optoelectronic applications. In fact, passive ring resonators side-coupled to signal waveguides provide compact, narrow band, and large free spectral range optical channel dropping filters [1]. On the other hand, active ring resonators lead to obtain small occupation area, high side-mode suppression ratio, and reduced sensitivity to feedback. Due to the fabrication advances, the performance limits of both passive and active microring resonators are mainly influenced by optical scattering effects.

## THEORY

In general, the ring resonator sidewall roughness or boundary imperfections can have two significant detrimental effects: 1) energy scattering towards the radiation field, reducing the total quality factor of the optical mode; 2) power redistribution between two counter-propagating modes. The backscattering coefficient and scattering losses have been calculated using the volume current method [2], by assuming that the sidewall imperfections can be described by a random function having a Gaussian distribution for its self-correlation function as:

$$\text{corr}(s-s') = \sigma_c^2 \exp\left[-(s-s')^2 / L_c^2\right] \quad (1)$$

being  $s$  the relevant curvilinear coordinate,  $L_c$  the correlation length and  $\sigma_c$  the standard deviation.

## NUMERICAL RESULTS

The numerical simulations for a passive ring resonator have been performed by considering a tightly confined GaAs-AlGaAs input waveguide at  $\lambda=1.55 \mu\text{m}$ , a microring with radius  $5 \mu\text{m}$ , and an output waveguide. Fig. 1 shows the normalized power at the end of input waveguide versus the wavelength detuning for different values of  $L_c$  with  $\sigma_c=4.7 \text{ nm}$ . Fig. 2 shows the detuning from the travelling-wave optimal condition (minimum

transmittivity) as influenced by roughness-induced scattering in terms of  $L_c$  and different values of  $\sigma_c$ . Fig. 3 plots the optimal coupling factor versus  $L_c$  for various  $\sigma_c$ . It is clear that the optimum travelling-wave condition cannot be met in the presence of strong scattering effects.

Numerical simulations for an active microring resonator have been performed by considering a standard GaAs-AlGaAs quantum well structure. Fig. 4 shows the stationary values of the two counter-propagating mode intensities (Modes 1 and 2) versus  $L_c$  for various  $\sigma_c$ , by assuming an injection current  $I=100\text{mA}$  (one well). The plot shows a critical value  $\sigma_{c,th}$  (4.7 nm in this case), depending of injection current, where the unidirectional changes to bidirectional regime. In Fig. 5, the mode intensities are sketched versus the ring radius for various injection currents with  $L_c=0.07 \mu\text{m}$  and  $\sigma_c=12 \text{ nm}$ . Thus, it is possible to observe that the operating regime of the active ring resonator is influenced by the ring cavity sizes. Finally, Fig. 6 describes the influence of the grating included in the output waveguide to induce an unidirectional behavior. The 3D plot shows the intensities of the Mode 1 (red surface) and Mode 2 (blue surface) versus the grating reflectivity and the output coupling coefficient ( $I=100 \text{ mA}$ ,  $L_c=0.07 \mu\text{m}$ ,  $\sigma_c=12 \text{ nm}$ ).

## CONCLUSION

In this paper we present an investigation of the detrimental effects due to roughness-induced scattering on the properties of both passive and active optical microring resonators.

## REFERENCES

- [1] C. Manolatu and H. A. Haus, *Passive components for dense optical integration*, Kluwer Acad. Publ., (2002).
- [2] M.N. Armenise, V.M.N. Passaro, F. De Leonardis, M. Armenise, *Modeling and design of a novel miniaturized integrated optical sensor for gyroscope systems*, J. Lightwave Technol., **19**, 1476 (2001).

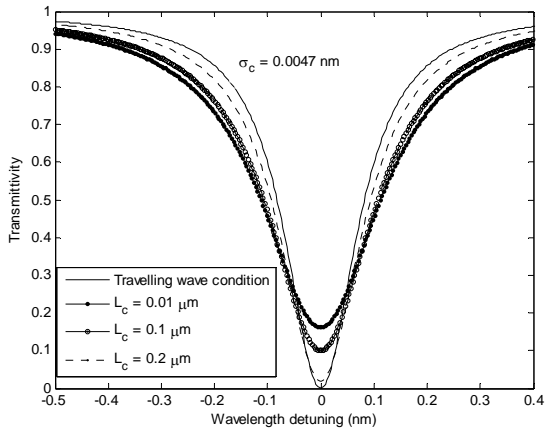


Fig. 1. Transmittivity versus wavelength detuning for different correlation lengths ( $\sigma_c = 4.7$  nm) in a passive ring.

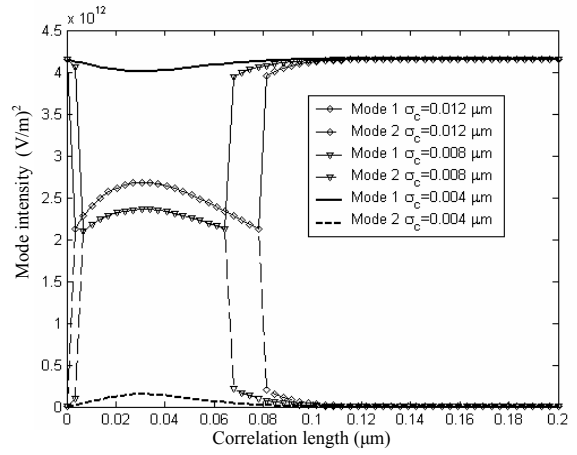


Fig. 4. Mode intensities versus correlation length for various standard deviations of the active ring roughness function.

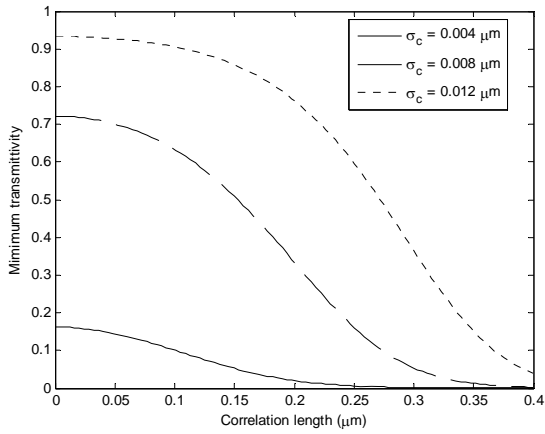


Fig. 2. Minimum transmittivity versus correlation length for various standard deviations of ring sidewall roughness function.

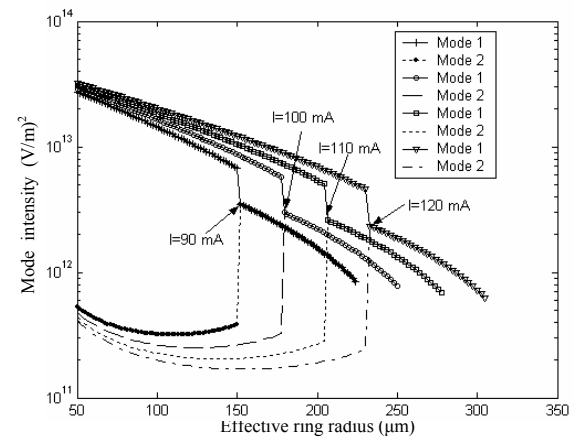


Fig. 5. Mode intensities versus effective ring radius for various injection currents.

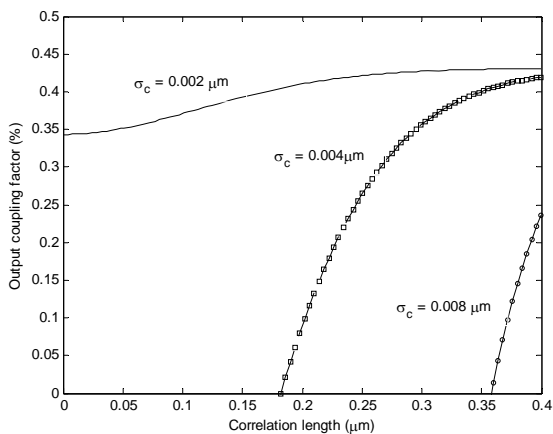


Fig. 3. Output coupling factor versus correlation length for different standard deviations in a passive microring.

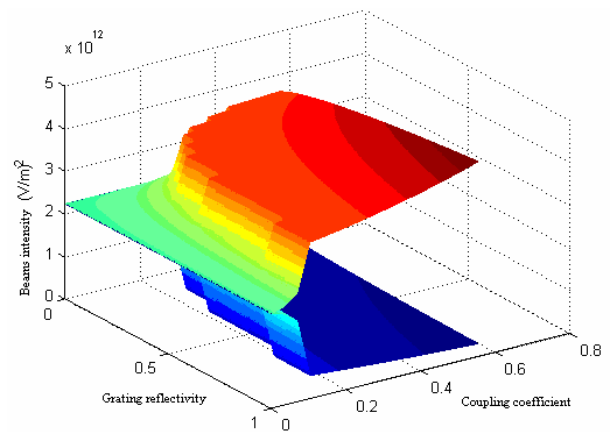


Fig. 6. Mode intensities versus grating reflectivity and output coupling coefficient in an active microring.

# Simulation of a High Speed Interferometer Optical Modulator in Polymer Materials

F. Dell'Olio, V.M.N. Passaro, and F. De Leonardis\*

Politecnico di Bari, Dipartimento di Elettrotecnica ed Elettronica, via E. Orabona n. 4, 70125 Bari, Italy

\*Politecnico di Bari, Dipartimento di Ingegneria dell'Ambiente e per lo Sviluppo Sostenibile,  
viale del Turismo, 74100 Taranto, Italy

e-mail: passaro@poliba.it

## ABSTRACT

In this work, the design and simulation of a high speed (300 GHz) electrooptic modulator operating at 1550-nm wavelength is presented. As electrooptic active material, a nonlinear optical polymer with highly nonlinear chromophores dispersed in an amorphous polycarbonate is used. Optimization of modulator geometrical structure and extraction of device performance parameters are obtained by 3D simulations.

## INTRODUCTION

The electro-optic (EO) polymer modulators have been investigated for more a decade, because of their low index dispersion at millimetre wave frequencies, low cost, large electro-optical coefficients, and easy integration with electronic circuits. Polymer based technology has allowed to demonstrate ultra-fast EO Mach-Zehnder modulators, having wideband frequency response to over 100 GHz and low driving voltage [1]. Guest-host polymers are used, consisting of highly nonlinear chromophore and amorphous polycarbonate (APC) or polymethylmethacrylate (PMMA) as active EO material. When doped into amorphous polycarbonate host (ACP), phenyltraene-bridged chromophore (CLD-1), gives an EO coefficient  $r_{33}$  of 90 pm/V (@1060 nm) and loss of 1.2 dB/cm (@1550 nm) [2].

In the proposed modulator, CLD-1/ACP is assumed for core layer, UV15 (an UV curable epoxy) and UFC17 (a polymer that doesn't contain any solvent) are used for lower and upper cladding, respectively.

## MODULATOR DESIGN AND SIMULATION

The interferometer optical modulator (whose

geometry is shown in Fig. 1) has been 3-D simulated using BPM [3]. The quasi-TM single-mode behaviour of its rib waveguide has the field profile shown in Fig. 2. To optimize the Y-branch power splitter geometry, composed by a parabolic taper and an arc cosine branch, we have simulated the modulator without any RF signal applied and examined its optical field at the output (Fig. 3).

Polymer modulator bandwidth is limited only by the conductor loss because the microstrip electrodes are engineered to achieve  $n_m \approx n_{opt}$  (being  $n_m$  and  $n_{opt}$  the microwave and optical effective index, respectively). Thus, modulator 3-dB bandwidth is:

$$f_{-3dB} \approx \left( \frac{3.2}{aL} \right)^2 \quad (1)$$

where L is the interaction length between RF and optical signals and  $a$  (0.48 dB/cm $\sqrt{\text{GHz}}$  for Au electrodes) is the loss coefficient of transmission lines. To obtain a 300 GHz 3-dB bandwidth, the interaction length (L) has to be 16 mm long (Fig. 4).

Simulating the modulator behaviour when a RF signal is applied to the electrodes, we have determined the half-wave voltage as  $V_\pi = 4$  V, and obtained the relative power versus propagation length diagram, as sketched in Fig. 5.

Finally, the DC characteristic of the proposed modulator has been obtained (see Fig. 6) and the extinction ratio calculated as ER = 28 dB.

## REFERENCES

- [1] M. Lee, H. E. Katz, C. Erben, D.M. Gill, et al., *Broadband Modulation of Light by Using an Electro-Optic Polymer*, Science **298**,1401 (2002).
- [2] M.C. Oh, H. Zhang, C. Zhang, et al., *Recent Advances in Electrooptic Polymer Modulators Incorporating Highly Nonlinear Chromophore*, IEEE J. Sel. Top. Quantum Electron. **7**, 826 (2001).
- [3] OptiBPM 7.0 User's Reference, by OPTIWAVE© (2005).

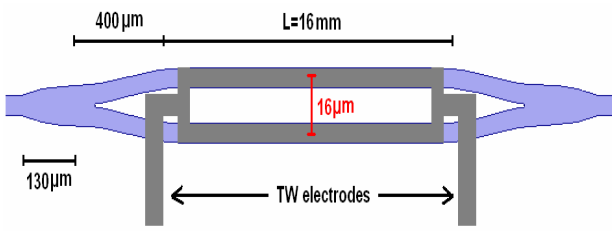


Fig. 1. Proposed EO modulator geometry.

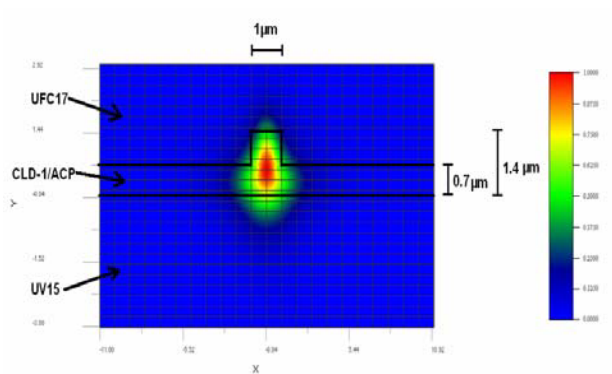


Fig. 2. Quasi-TM mode profile.

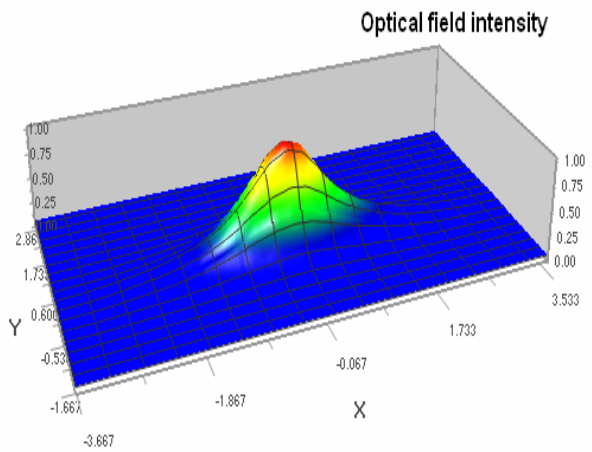


Fig. 3. Optical field intensity at the output cross section.

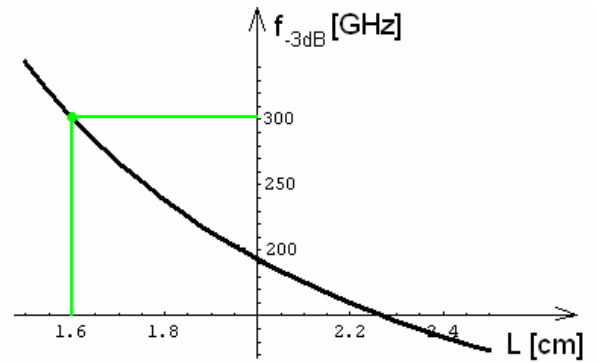


Fig. 4. Modulator 3-dB bandwidth versus interaction length between RF and optical signals (Au electrodes).

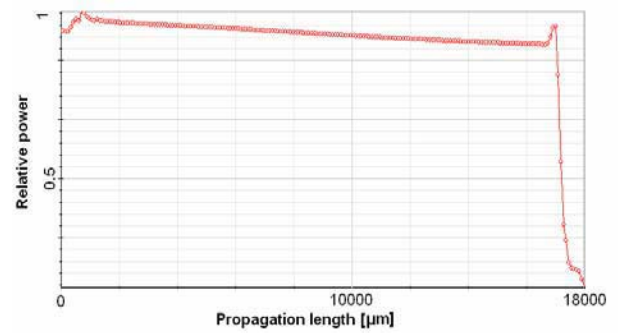


Fig. 5. Relative power versus device length when  $V_{\pi} = 4$  V is applied to the electrodes.

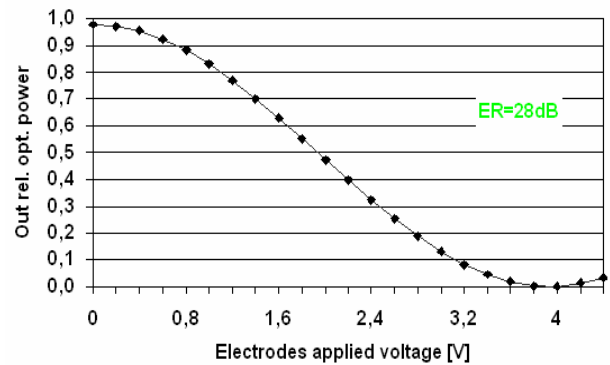


Fig. 6 EO modulator DC characteristic (extinction ratio 28 dB).

# Blinking of Colloidal Semiconductor Quantum Dots: Blinking Mechanisms

Mitra Dutta,<sup>1,2</sup> Michael A. Stroschio,<sup>1,2,3,\*</sup> and Bruce J. West<sup>4</sup>

<sup>1</sup>Dept. of Electrical and Computer Engineering, Univ. of Illinois, Chicago, Illinois, 60607

<sup>2</sup>Department of Bioengineering, University of Illinois at Chicago, Chicago, Illinois, 60607

<sup>3</sup>Department of Physics, University of Illinois at Chicago, Chicago, Illinois, 60607

<sup>4</sup>Army Research Office, PO Box 12211, RTP, NC 27709-2211 USA

\*stroschio@uic.edu

## INTRODUCTION

Colloidal semiconductor quantum dots are observed to blink on and off with a distribution of off times that obeys an inverse power law distribution. In this paper, a model describing mechanisms contributing to this blinking distribution is presented.

## DISCUSSION

Wurtzite semiconductor quantum dots in colloidal suspensions are now realizable for a variety of semiconducting materials as shown to Figure 1. These colloidal suspensions of nanoscale quantum dots contain ions that constitute an electrolytic environment for the colloidal quantum dots. The fact that individual quantum dots are charged is responsible for a repulsive interaction between colloidal dots that allows them to remain in suspension. Moreover, the surface charge on each quantum dot attracts ions of opposite charge to form a double layer near the surface of each quantum dot. Such colloidal quantum dots are observed to blink with off times,  $\tau$ , that obey an inverse-power-law distribution with the asymptotic form of a one-sided Lévy distribution:

$$p_{\tau}(\tau) = (k_B T / E_0) (\tau_0^{\mu} / \tau^{1+\mu}),$$

$\mu = k_B T / E_0$  and  $E_0$  is the energy associated with the barrier potential. In this work, different

mechanisms for blinking are considered and it is shown that thermally-induced fluctuations in the double layer potential are a mechanism contributing to the observed blinking. By relating the fluctuations in the double layer potential to fluctuations in the surface charge density on the quantum dot, it is shown that associated fluctuations in the barrier potential have exactly the functional form needed to result in an inverse-power-law distribution for off times [1]. In addition, analytical results show that the distribution of off times,  $\tau$ , scales as  $1/\tau^{3/2}$  just as previously observed.

## CONCLUSION

In this paper, the thermally-driven fluctuations in the double layer potential are related to the fluctuations in the surface charge density on the quantum dot. Moreover, it is shown that associated fluctuations in the barrier potential have exactly the functional form needed to explain the distribution of off times observed previously.

## ACKNOWLEDGEMENT

We would like to express our sincere thanks to Dr. Tijana Rajh of the Argonne National Laboratory.

## REFERENCES

- [1] Michael A. Stroschio and Mitra Dutta, *Biological Nanostructures and Applications of Nanostructures in Biology: Electrical, Mechanical & Optical Properties*, (Kluwer Academic Publishers, New York, 2001) provides a review of work on blinking of colloidal semiconductor quantum dots.

Compound Semicond.	Bandgap, (eV)	Spontaneous Polarization, (C/m <sup>2</sup> )
AlN	6.2	- 0.081
CdS	2.4 E <sub>g</sub> (A) 2.5 E <sub>g</sub> (B) 2.55 E <sub>g</sub> (C)	0.002
CdSe	1.76 E <sub>g</sub> (A) 1.771 E <sub>g</sub> (B) 2.17 E <sub>g</sub> (C)	0.006
GaN	3.36	- 0.029
ZnO	3.35	- 0.07

Fig. 1. Wurtzite bandgaps and spontaneous polarizations.

# Monte Carlo Modeling of the X-Valley Leakage in Quantum Cascade Lasers

X. Gao, D. Botez, and I. Knezevic

Department of Electrical and Computer Engineering, University of Wisconsin – Madison,  
1415 Engineering Dr, Madison, WI 53706-1691, USA  
e-mail: xujiaogao@wisc.edu, knezevic@engr.wisc.edu

Room-temperature, pulsed mode operation of a 9 $\mu$ m GaAs/AlGaAs quantum cascade laser (QCL) has been accomplished by increasing the Al content from 33% to 45% within the conventional three-well active region design [1]. This important milestone in the mid/far-infrared QCL technology was achieved due to the  $\sim$ 95 meV larger band offset in the 45% Al structure, which suppressed thermal leakage into the continuum states and significantly improved the temperature dependence of the threshold current. However, Al content of 45% or above is also expected to result in appreciable carrier leakage into the X-valley subbands [2, 3], but has not yet been accounted for in theoretical predictions [2-4].

In this paper, we present the first numerical simulation of X valley leakage in GaAs/AlGaAs QCLs [5]. The Monte Carlo QCL simulator we developed is based on solving the microscopic Boltzmann-like transport equation of Ref. [4], but also incorporates the X valley transport. The wavefunctions and energy levels in both  $\Gamma$  and X valleys are obtained by self-consistently solving the coupled 1D Schrödinger and Poisson equations. The Schrödinger equation for the  $\Gamma$  valley is solved using the 3-band  $\mathbf{k}\cdot\mathbf{p}$  method within the envelop function and effective mass approximations. For the X valley subbands, the usual effective mass equation for the conduction band is sufficient, since the X valleys are well above the valence bands. The self-consistent Schrödinger-Poisson solver results in the wavefunctions and energy levels of the conduction subbands in both valleys, which are then used as input for the 3D Monte Carlo transport kernel.

The Monte Carlo transport simulation is based on the technique introduced in [4], with both the  $\Gamma$  and X valley transport included. In addition to the

intersubband (including inter-stage and intra-stage) and intrasubband electron-LO and electron-electron scattering mechanisms within the  $\Gamma$  valley [2,3], we also include the  $\Gamma$ -X and X-X intervalley scattering, and the inter- and intra-subband electron-LO scattering mechanisms in the X valleys.

In Fig. 1, we present the calculated electric field vs. current density for the extensively simulated [2, 3], 36-stage GaAs/Al<sub>0.45</sub>Ga<sub>0.55</sub>As QCL structure introduced in Ref. [1]. The simulations were done at low (77 K) and high temperatures (300 K), both with and without the X valley transport included. At both temperatures, the results from our Monte Carlo simulator without the X valley transport agree with the data from Ref. [2]. At low temperature, the increase in current density due to X-valley leakage is small. At room temperature, however,  $\Gamma$ -X intervalley scattering becomes strong, and the parallel current path through the X valley leads to a significant increase in the current density for a given electric field.

In summary, we have presented the first Monte Carlo simulation incorporating the effects of the X-valley leakage on the operation of GaAs-based QCLs. This realistic simulator can also be adapted to account for the indirect valley leakage in InP-based structures, thereby becoming a versatile aid in the design of mid and far-infrared QCLs.

This work is supported by the Wisconsin Alumni Research Foundation (WARF).

- [1] H. Page, C. Becker, A. Robertson, G. Glastre, V. Ortiz, and C. Cirtori, *Appl. Phys. Lett.* **78**, 3529 (2001).
- [2] A. Mircetic, D. Indjin, Z. Ikonic, P. Harrison, V. Milanovic, and R. W. Kelsall, *J. Appl. Phys.* **97**, 084506 (2005).
- [3] D. Indjin, P. Harrison, R. W. Kelsall, and Z. Ikonic, *Appl. Phys. Lett.* **81**, 400 (2002).
- [4] R. C. Iotti, and F. Rossi, *Phys. Rev. Lett.* **87**, 146603 (2001).
- [5] X. Gao, D. Botez, and I. Knezevic, *in preparation*.

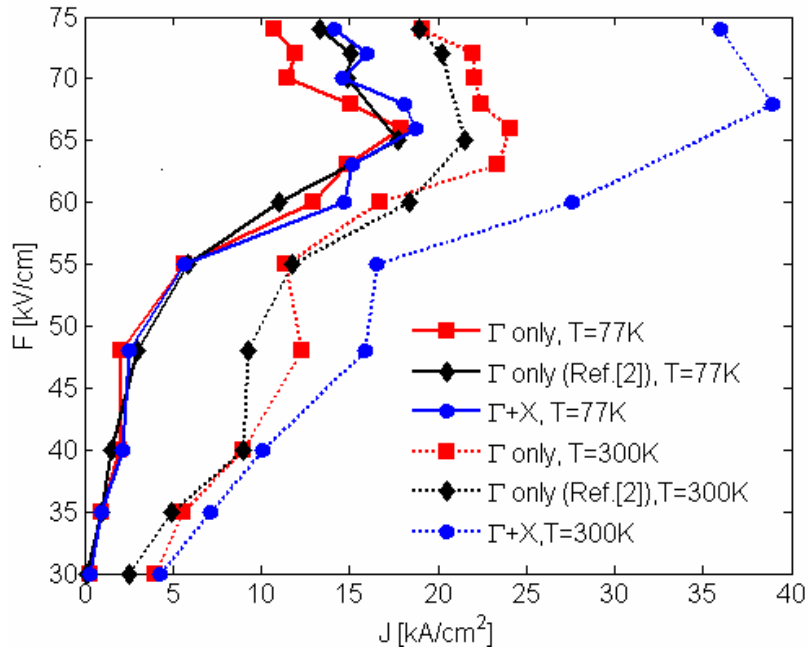


Fig. 1. Electric field vs. current density characteristics for the GaAs/Al<sub>0.45</sub>Ga<sub>0.55</sub>As structure introduced in Ref. [1], at T = 77 K and T = 300 K, with and without X valley transport included. The simulation results without the X-valley leakage agree with those previously obtained for the same structure by Mircetic *et al.* [2], who used a self-consistent solution of the rate equations. At low temperature, it is clear that X-valley leakage does not play a major effect in the QCL performance. Although the 45% Al content of this structure suppresses thermal leakage of carriers into the continuum states, we see that the X-valley leakage becomes appreciable at room temperature.

# A Parallel MCTDHF Code for Few-Electron Systems with Time-Dependent External Fields

G. Jordan, J. Caillat\*, V. Putz, C. Ede, and A. Scrinzi  
Vienna U. of Technology, Photonics Institute  
Gusshausstrasse 27/387, 1040 Wien, Austria/EU  
e-mail: scrinzi@tuwien.ac.at

## THE MCTDHF METHOD

In this paper we introduce an extension of the time-dependent Hartree-Fock to the Multi-Configuration Time-Dependent Hartree-Fock (MCTDHF) method, which in the limit of infinitely many configurations converges to the exact few-electron time-dependent Schrödinger equation. Denoting the spatial and spin coordinates collectively by  $q_i = (\vec{r}_i, s_i)$ , the MCTDHF ansatz for the wave function  $\Psi$  of  $f$  electrons reads

$$\Psi(q_1, \dots, q_f; t) = \sum_{j_1=1}^n \cdots \sum_{j_f=1}^n c_{j_1 \dots j_f}(t) \phi_{j_1}(q_1; t) \cdots \phi_{j_f}(q_f; t)$$

where the coefficients  $c_{j_1, \dots, j_f}$  are taken to be totally antisymmetric with respect to their indices, which leaves only  $\binom{n}{f}$  independent  $c$ 's. Increasing the number of orbitals  $n$  allows to systematically include correlation effects. The evolution equations for  $c_{j_1 \dots j_f}(t)$  and  $\phi_{j_i}(q_i; t)$  involve the non-linear and non-local mean-field operators and are given in Ref. [1].

For the implementation of the method on a parallel computer the spatial domain of  $\phi_{j_i}(q_i; t)$  is distributed over computing nodes. Communication is minimized by a finite-element discretization [2] and by low-rank approximations for the non-local operators. The block diagram of parallelization is given in Fig. 1. We found near linear scaling with the number of nodes. Interaction potentials of arbitrary, numerically defined shape allow application to atoms and molecules as well as quantum dots and nano-structures. Convergence of electron spectra for 1-d model systems is shown in Fig. 2.

## CORRELATION AND SPATIAL DIMENSION

Using MCTDHF we solve the time-dependent Schrödinger equation with a strong external laser field in 3 spatial dimensions with 3-d molecular model potentials and Coulomb repulsion between electrons. Laser and molecule parameters are chosen such that a large fraction of the molecules become ionized. Analogous 1-d model systems with the same ionization potentials and properly screened interactions were constructed.

We find pronounced differences between the 3-d system and the 1-d model (Fig. 3): (1) The importance of correlation is greatly overestimated in 1-d and (2) ionization increases with molecule size in 3-d, while the opposite is observed in 1-d.

## CONCLUSIONS

The newly developed MCTDHF method can be employed for solving the time-dependent Schrödinger equation for several interacting electrons with general 3-d potentials. We demonstrate favorable scaling in parallel computation and convergence of important observables such as electron spectra. Calculations in 3-d are mandatory, as lower-dimensional models were shown to generate severe artefacts.

*Acknowledgment:* The work was supported by the Austria Research Fund SFB016 and SFB011.

## REFERENCES

- [1] J. Caillat *et al.* Correlated multielectron systems in strong laser fields - an MCTDHF approach. *Phys. Rev. A*, 71:012712, 2005.
- [2] A. Scrinzi and N. Elander. A finite element implementation of exterior complex scaling. *J. Chem. Phys.*, 98:3866, 1993.

\*present address: Laboratoire de Chimie Physique-Matière et Rayonnement, Université Pierre et Marie Curie, 11, rue Pierre et Marie Curie, F-75231 Paris Cedex 05, France.

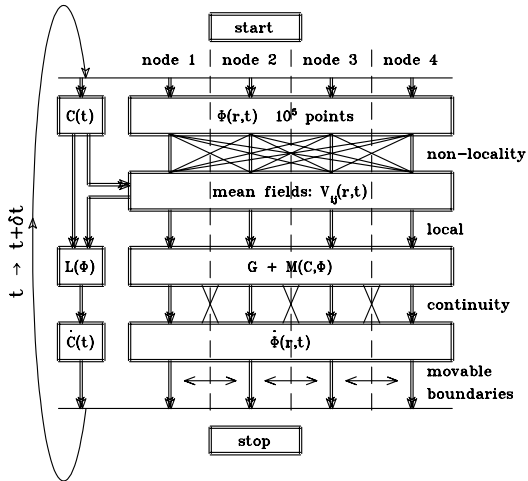


Fig. 1. Flow chart of the parallelization of MCTDHF. Orbitals are distributed over compute nodes. The calculation of mean-field operators requires all-to-all communication. Application of mean field operators is strictly local. Differential operators require minimal nearest-neighbor communication.

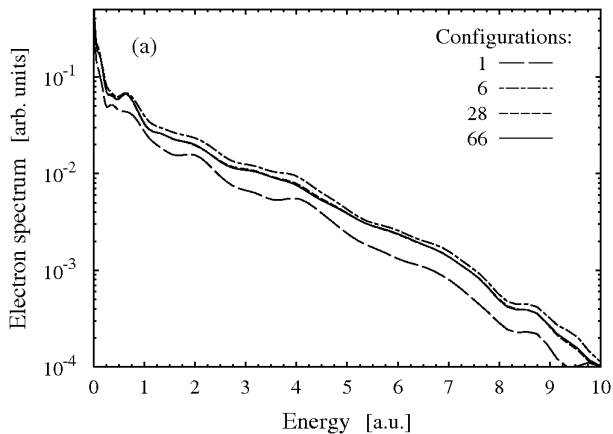


Fig. 2. Convergence of MCTDHF: the photoelectron spectrum from model He atom generated by an 800 nm laser pulse. Calculations with 28 and 66 configurations nearly coincide.

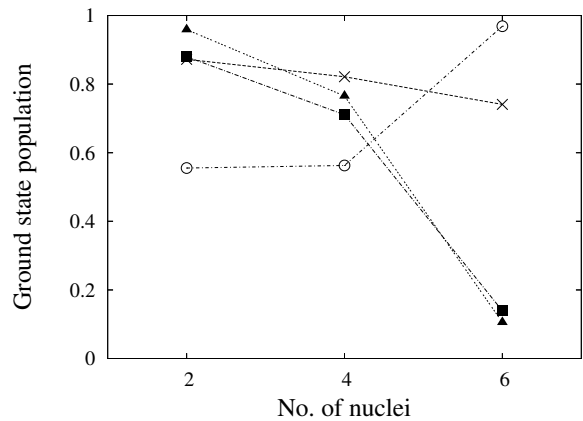


Fig. 3. Ground state depletion for 3-d and 1-d model molecules as a function of molecule size. In 3-d, depletion increases with molecule size for internuclear separations  $R = 1.4$  (crosses) and  $R = 3$  (full squares), and the Hartree-Fock result is similar to the correlated result (triangles,  $R = 3$ ). In contrast, 1-d models show an decrease of depletion with size (circles).

# Input and Intrinsic Device Modeling of VCSELs

K. Minoglou<sup>1</sup>, E. D. Kyriakis-Bitzaros<sup>2,1</sup>, D. Syvridis<sup>3</sup> and G. Halkias<sup>1</sup>

<sup>1</sup> Institute of Microelectronics, NCSR "Demokritos", 15310 Agia Paraskevi, Greece

<sup>2</sup> Department of Electronics, TEI of Pireaus, 12244 Egaleo, Greece

<sup>3</sup> Department of Informatics and Telecommunications, Univ. of Athens, 15784 Athens, Greece

## INTRODUCTION

In recent years the Vertical Cavity Surface Emitting Lasers (VCSELs), have emerged and threaten to supplant the standard laser technology in a variety of applications, such as short hull high speed networks and MOEMS. Thus, motivated by the fact that the ability to model VCSELs is critical to the design and analysis of optoelectronic microsystems, we propose a new model scheme that will combine the non-linear behavior of the input parasitics with the intrinsic fundamental device rate equations. A systematic methodology for the model parameter extraction from dc and ac, electrical and optical measurements is also presented and simulation results are compared with the experimental measurements. Simulation and extraction procedures are proved to be very fast while they preserve adequate accuracy.

## MODEL DESCRIPTION

The proposed circuit model for a packaged VCSEL is illustrated in Fig. 1.  $L_o$ ,  $R_o$  and  $C_o$ , model the connection to the measurement equipment and inductance  $L_p$  with capacitance  $C_p$  represent the parasitics of the package-leads as well as the wire-bonds of the package. The intrinsic VCSEL is modeled by a series resistance  $R_a$  in shunt with a non-linear capacitance  $C_j$  and the combination of a non-linear temperature-dependent current-controlled voltage-source  $E_{inp}$  with a series resistance  $R_{int}$  and an ideal diode  $D_{vcsel}$ . Intrinsic voltage drop  $E_{inp}$  and the intrinsic capacitance of the VCSEL are modeled according to the semi-empirical equation and to the junction diode's equation presented in [1]. The internal device temperature  $T$ , the carrier density and the photon density, which is equivalent to the output optical power are dynamically calculated using the respective rate equations [2]. Moreover non-linear gain and transparency number and temperature dependent leakage current are included in the model.

Since a circuit simulator is a differential equation solver, the rate equations can be solved with such a tool by mapping the dynamic quantities (i.e. the electron and photon populations) into node voltages, which are dynamically calculated. Working towards this direction, we have implemented all rate equations based on the analysis of Mena [2] in OPSIM<sup>TM</sup>. As an example in fig.2 is presented the equivalent circuit (with the expressions for the circuit elements) that corresponds to the following photon density equation:

$$\frac{dS}{dt} = -\frac{S}{\tau p} + \frac{\beta}{\tau n} N_o + \frac{Go \cdot zn(\gamma_o N_o - \gamma_1 N_1 - \gamma_o N_1 \cdot zn) S}{1 + \varepsilon S}$$

Where  $\tau p$ ,  $\tau n$ ,  $\beta$ ,  $N_o$ ,  $Go$ ,  $zn$ ,  $\gamma_o$ ,  $\gamma_1$  and  $\varepsilon$  are model parameters.

## PARAMETER EXTRACTION PROCEDURE

Due to the large number of the model parameters (16 for the input circuit and 24 for the rate equations) a three-step parameter extraction methodology is proposed to estimate them by dividing them into distinct groups. The parameter estimation is achieved by using I-L-V dc characteristics measured at four ambient temperatures and S11 and optical signal ac responses for various bias currents.

In the first step the dc dependent parameters of the input circuit (such as  $R_{in}$ ,  $R_{int}$  and  $R_a$ ) are estimated using as input to the optimization tool the dc current-light (I-L) characteristics and as targets the measured I-Vs. In the second step, using the previously calculated values, the optimization target is changed to  $S_{11}$  vector measurements and the remaining parameters of the input circuit, which influence its ac behavior (such as  $L_o$ ,  $R_o$ ,  $C_o$ ,  $L_p$ , and  $C_p$ ) are estimated. In the above procedures the rate equation that affects the results is only the thermal one, which is used to determine the internal device temperature. Thus, in the third step, the parameters of the carrier and photon rate equations as well as gain, transparency number and leakage current parameters are estimated using as optimi-

zation targets the dc I-L characteristics and the ac optical response.

As it is shown in Figures 3 and 4 satisfactory agreement between measured values and simulation results for a commercially available VCSEL is achieved using the proposed model and extraction methodology.

Unambiguously, the level of model complexity and the different nature of the parameters (physical, geometrical, fitting values), suggest that methods like sensitivity analysis, classification of the parameters, possible calculation or estimation based on published values can significantly improve the extraction methodology. Currently we are developing the parameter extraction procedure pursuing the goal to be robust and efficient. Up to now the two first steps of the parameter extraction methodology have been successfully completed while the third one needs further refinement due to the increased number of parameters.

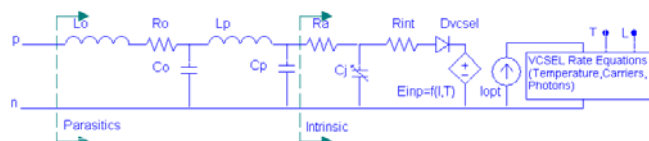


Figure 1 The proposed circuit model of the VCSEL.

$$g_{sp} = \frac{\tau p \cdot \beta \cdot k_f \cdot N_o}{\tau n \cdot (V(m) + \delta_m)}$$

$$g_{stm} = \tau p \cdot z n \cdot G_o \cdot \frac{(\gamma_o N_o - \gamma_i N_1 - \gamma_o N_i z n) \cdot (V(m) + \delta_m)}{1 + \varepsilon \frac{(V(m) + \delta_m)^2}{k_f}} - \delta_m$$

$$C_{ph} = 2 \cdot \tau p$$

$$R_{ph} = 1 \quad \text{and} \quad S = \frac{(V(m) + \delta_m)^2}{k_f}$$

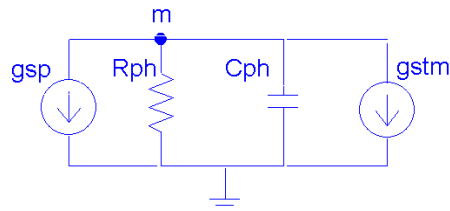


Figure 2 Equivalent circuit for the photon rate equation

## CONCLUSIONS

A compact and efficient VCSEL model for the VCSEL that models by means of equivalent circuits the fundamental device rate equations, the thermal effects, the non-linear gain and transparency number functions and the input parasitics elements has been presented. The parameter extraction is based on standard dc and ac measurements and it is achieved by a three-step procedure, which divides model parameters into distinct groups. Simulation results, using the proposed model, present satisfactory agreement with the measurements.

## REFERENCES

- [1] K.Minoglou,, E.D. Kyriakis-Bitzaros, D. Syvridis, G. Halkias, J.Lightwave Technol, vol. 22, No.12, , pp.2823-2827 Dec. 2004
- [2] P. V. Mena et al. J. Lightwave Technol., vol. 17, pp. 2612–2632, Dec. 1999.

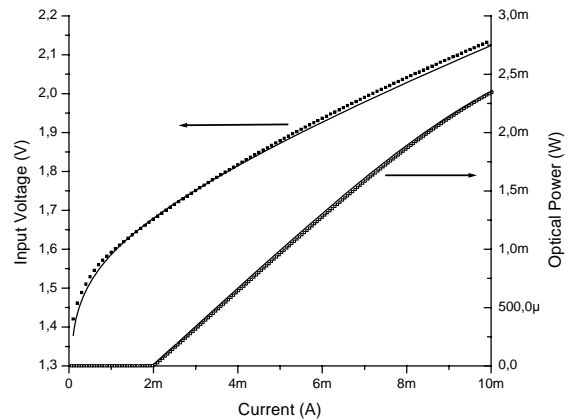


Figure 3 Measured values (dots) and simulated (continuous line) I-V and I-L characteristics at 20°C

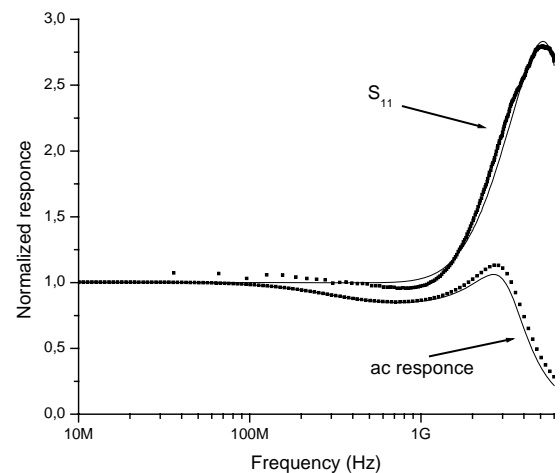


Figure 4 Measured (dots) and simulated (continuous line) S11 and optical ac responses at a bias of 6 mA

# A Two Dimensional Analytical Model for Finger Photodiodes

T. Naeve, and P. Seegebrecht

Chair for Semiconductor Electronics, CAU Kiel, Kaiserstr. 2, D-24143 Kiel, Germany  
e-mail: tn@tf.uni-kiel.de

## Introduction

In this work we present a new analytical 2D photodiode model. Our model is capable to predict the stationary as well as the dynamic behavior of different finger photodiode structures. The model is in very good agreement with the numerical results gained with the two dimensional device simulator Atlas/Silvaco. For all relevant carrier distributions within the diode we have found simple analytical expressions. Our model is suitable as circuit simulation model, e.g. for the simulation of high speed fiber-optic systems.

## Model

Because the illuminated part of the finger photodiode under consideration consists of a periodic topology, it is sufficient to consider only one of the periodic sections (see fig. (1)) of the structure to characterize the opto-electronic conversion of the diode. We have divided this structure into five quasi neutral regions I to V in addition to the space charge region (SCR). We assume that the minority carrier current within the neutral regions is a pure diffusion current. Therefore, for the calculation of the photocurrent we require the minority carrier distribution within the neutral regions. To this end we have to solve the diffusion equation

$$\frac{\partial^2 \delta c}{\partial x^2} + \frac{\partial^2 \delta c}{\partial y^2} - \frac{\partial \delta c}{D_c \partial t} - \frac{\delta c}{L_c^2} = - \frac{\tau_c g(x) \delta_0(t)}{L_c^2} \quad (1)$$

within the region I to V.  $c$  is the minority carrier density,  $\tau_c$ ,  $L_c$  and  $D_c$  the lifetime, diffusion length and diffusion coefficient, respectively, of the minority carriers. Applying Laplace-transformation on eq. (1) results in a partial differential equation in

$x$  and  $y$ . Due to the photo-generation rate and the boundary conditions of regions IV and V we expect no  $y$ -dependency of the carrier distributions in these regions. Therefore, we end up with a simple differential equation in these regions which easily can be solved.

To simplify the calculation of the minority carrier distribution within regions I, II, and III we first of all assume that the extension of these regions in the  $y$ -direction is large compared to the relevant diffusion length of the minority carriers.

Using the technique of separation of variables we find the minority carrier distribution by first solving the diffusion equation in a regime far away from the dashed vertical lines in fig. (1) which represent the boundary of the SCR. In this regime we again assume the carrier density to be a function of  $x$  only. Utilizing this solution we then solve the diffusion equation to come to the  $y$ -function of the carrier distribution. As an example fig. (2) gives a comparison of the hole distribution within region I calculated with our model and the simulator Atlas/Silvaco.

For the current contribution of each region to the photocurrent we have to integrate the gradient of the minority carrier concentration along the edges of the SCR.

To calculate the contribution of the SCR to the total current we neglect recombination and thermal generation processes within the SCR. Thus the current contribution of the SCR can be found by integrating the generation rate over the whole depletion region. The temporal variation of the drift current contribution is dominated by the RC time constant of the device. The bulk resistance and the depletion capacity of the diode can be calculated easily and implemented as a RC low-pass filter.

Due to the choice of the photo-generation rate the current contribution of a certain region corresponds to the transfer function of this region. Therefore, the transfer function of the photodiode is given by the sum of the transfer functions of each region multiplied by the transfer function of the RC low-pass filter

### Results

Fig. 3 shows the stationary photocurrent of the device calculated with our model in comparison with the results of the numerical device simulator. In one case we have contacted the substrate of the diode which results in a higher efficiency of the diode in the red and infrared spectra compared with the case of the floating substrate.

The frequency responses in fig. 4 presents the results of our model and the device simulator, respectively. The dynamic behaviour of the diode in this case is totally dominated by the RC time constant of the device. For other diode parameters (e.g. doping concentrations, dimensions) or other structures the diffusion in some of the diode regions may not follow the modulated signal resulting in different kinks (cut-off frequencies) of the transfer function.

### CONCLUSION

We have developed a two dimensional model of a photodiode which takes care on the transit-time effects due to carrier diffusion. This model is versatile and capable to predict the stationary as well as the dynamic performance of finger diodes of different types and parameters.

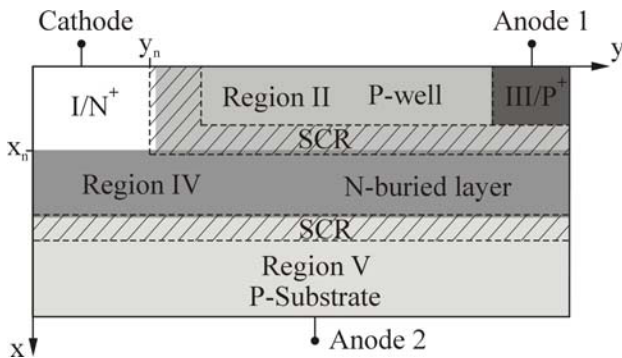


Fig. 1. Modeled section of a NCPWNBL – finger photodiode. The greyscales stand for the different doping concentrations.

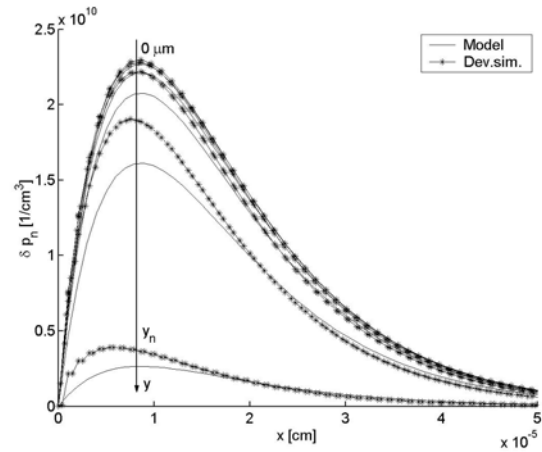


Fig. 2. Hole distribution within region I calculated with our model compared with numerical results.

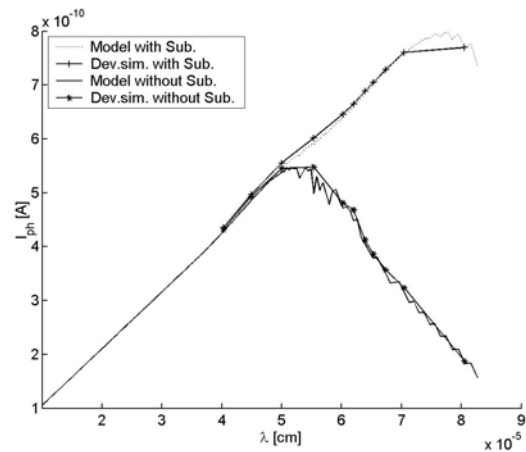


Fig. 3. Stationary photocurrent with and without contacted substrate. Model in comparison with the device simulator.

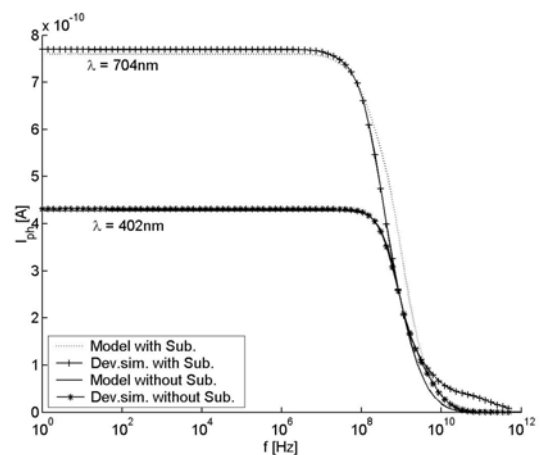


Fig. 4. Frequency responses of the device: model compared with numerical simulation.

# Atomistic Modeling of GaN Based Nanowires

L. Prokopova, M. Persson, M Povolotskyi, M. Auf Der Maur and A. Di Carlo\*  
Dept. Electronic Eng. University of Rome "Tor Vergata", via del Politecnico 1, 00133 Roma (Italy)  
\*e-mail: aldo.dicarlo@uniroma2.it

Recent progress in growth technology gives a possibility to produce high quality nitride nanostructures such as free-standing nanowires, quantum discs and quantum dots [1]. The growth of GaN nanotubes is of particular interest due to the large band gap of GaN. Potential applications of the structures are possible candidates for LEDs, Bragg reflectors, laser and photonic crystals, biochemical-sensing. The use of nanowires and possibly nanotubes as active components promise to enhance the performance of such devices due to increased charge localization and reduced defect density. We report a theoretical study of the electronic and optical properties of GaN wires and GaN/AlGaN heterostructures and of single crystalline semiconducting GaN nanotubes using an atomistic tight binding approach.

## MODEL AND RESULTS

We consider two different kinds of objects: strain-free homogeneous GaN nanowires and pseudomorphically grown GaN discs embedded into a AlGaN column.

The GaN nanowire is modeled as an infinitely long oriented along the [0001] direction, with a hexagonal cross-section and wurtzite crystal structure. Both solid nanowire and hollow nanowire (nanotube) are considered. The calculations are based on an sp<sup>3</sup>d<sup>5</sup>s\* nearest neighbor tight binding basis. The effect of introducing a hole in a nanowire is studied and we find that the charge in energy for the original nanowire states depends strongly on the state of the wave function. The first conduction band state increase in energy as the outer size of the nanotube is increased while keeping the tube wall constant. The order of the first two valence bands are reversed compared to the solid nanowire (Fig.1-2). For the optical properties we find that the transition between the first

conduction band and first valence band is weak and that the first strong transition is associated with the second or third valence band. The lowest conduction band state is found to increase in energy as the radius of nanotube is increased. The first strong transition has a strong polarization anisotropy with the dominating component along the nanotube axis. A typical band structure for a solid GaN wire is shown in figure 3

Tight-binding calculations are also extended to AlGaN/GaN nanowires (see Fig 4) forming confining quantum disc. These structures are similar to those analyzed in Ref. [1]. Here piezoelectric as well as pyroelectric polarization have been accounted for by using a continuum model solved via the finite element method. The atomic position are relaxed by minimizing the elastic energy and the strain of the structure is calculated (Fig 5). From the strain map, the polarization vector is extracted and the potential profile is then obtained by solving the Poisson equation. The potential profile is shown in Fig. 6. Relaxed atomic position and potential profile are then feed back in the tight-binding solver and both electronic and optical properties of the AlGaN/nanowire are calculated. A detailed comparison between theory and experiment will be shown

## ACKNOWLEDGEMENT

Support of the Marie Curie project "CLERMONT II" is acknowledge.

## REFERENCES

- [1] J. Ristic, E. Calleja, A. Trampert, S. Fernandez-Garrido, C. Rivera, U. Jahn, and K.H. Ploog "Columnar AlGaN/GaN Nanocavities with AlN/GaN Bragg Reflectors Grown by Molecular Beam Epitaxy on Si(111)", Physical Review Letters 94, 146102 (2005).

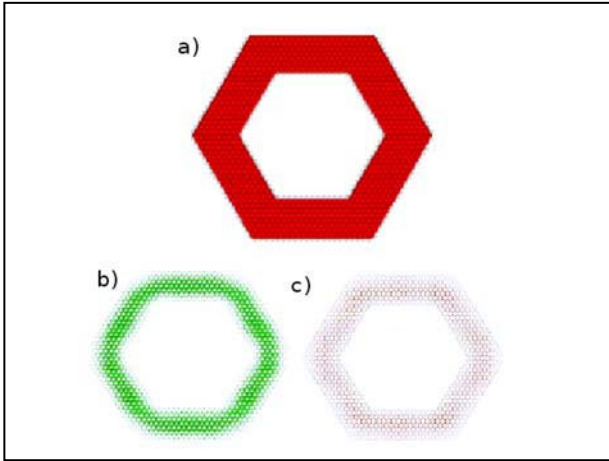


Fig. 1. (a) GaN nanotube (b) Second valence band state (c) First conduction band state

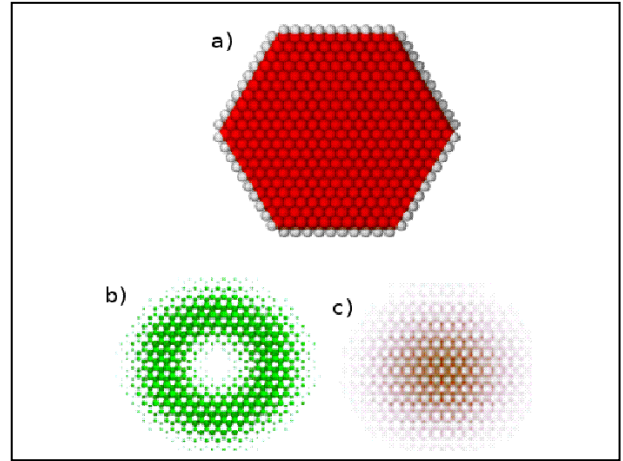


Fig. 2. (a) GaN nanowire (b) Second valence band state (c) First conduction band state

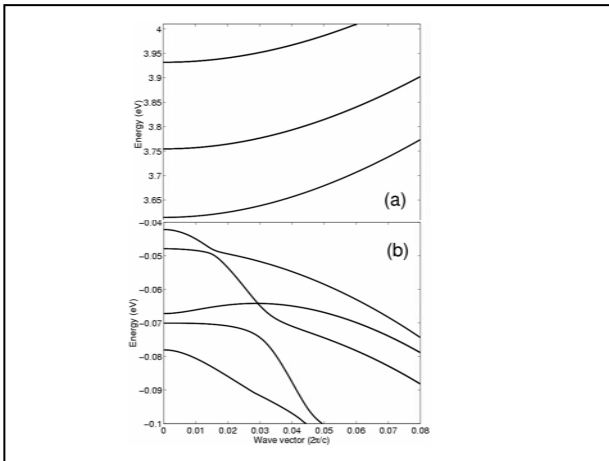


Fig. 3. Band structure of a solid GaN nanowire with 4.8 nm diameter. (a) conduction band (b) valence band

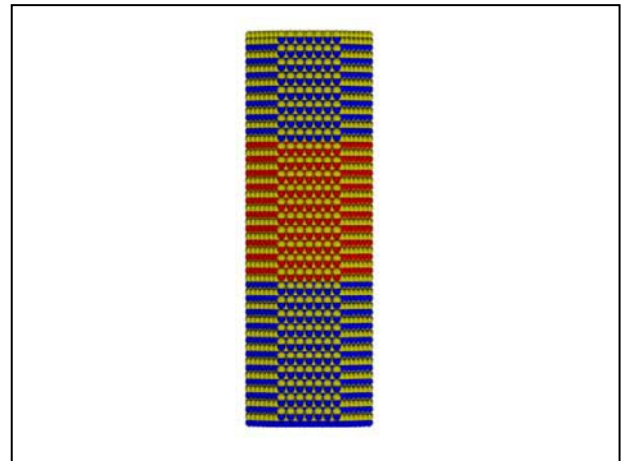


Fig. 4. Typical AlGaIn/GaN nanowire used in the simulations. (Red) Ga atoms, (Blue) Al atoms, (yellow) N atoms.

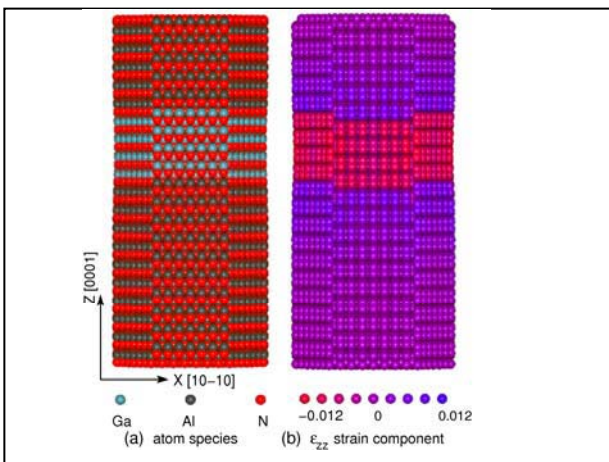


Fig. 5. Pseudomorphically grown AlN/GaN/AlN nanowire b) Strain component  $\epsilon_{zz}$  distribution over the nanowire.

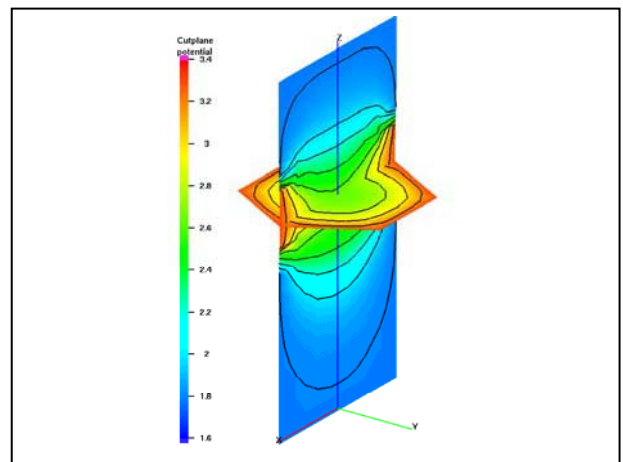


Fig. 6. Potential profile induced by the piezo and pyro polarizations in the AlGaIn/GaN nanowire

# Plasma Effects in Lateral Schottky Junction Terahertz Detector: Models and Characteristics

V. Ryzhii, A. Satou, and M. S. Shur\*

Computer Solid State Physics Laboratory, University of Aizu, Aizu-Wakamatsu 965-8580, Japan

\* Department of Electrical, Computer, and Systems Engineering,

Rensselaer Polytechnic Institute, Troy, NY 12180, USA

e-mail: v-ryzhii@u-aizu.ac.jp

## INTRODUCTION

Two-dimensional electron gas (2DEG) systems in both ungated and gated channels with sufficiently high mobility of electrons confined in the lateral directions can serve as resonant cavities for electron plasma waves in different devices. The resonant plasma effects in gated 2DEG systems similar to high-electron mobility transistors (HEMTs) can be used for detection, frequency multiplication and generation of terahertz (THz) radiation [1].

In this paper, we propose novel detectors of THz radiation based on heterostructures with a 2DEG channel and a lateral Schottky junction (LSJ), develop their device models, and calculate their characteristics (frequency-dependent detector responsivity as a function of the device structural parameters). The some devices utilizing lateral LSJs have been proposed and studied for more than decade for applications as detectors and varactors for frequency multiplication in the THz range. However, since the 2DEG channels with high electron mobility can exhibit pronounced resonant response at the plasma frequencies, LSJ resonant detectors (and some other devices, for example, such as frequency multipliers) can provide substantially higher detection responsivity at the signal frequencies coinciding with the resonant plasma frequencies. The proposed LSJ resonant detectors using nonlinearity of the LSJ current-voltage characteristic can also surpass the HEMT-like resonant detectors utilizing the hydrodynamic nonlinearity [1].

## DEVICE STRUCTURES AND OPERATION

The LSJ device structures with ungated and gated 2DEG channel schematically shown in Figs. 1(a) and 1(b), respectively. The band diagram of the

LSJ portion of the devices is shown in Fig. 1(c). These devices comprises an Ohmic contact serving as a source and a Schottky contact (drain or collector) forming LSJ. The latter plays the role of a nonlinear element providing the rectification of the THz signals (detection). The LSJ resonant detectors in question can be fabricated using heterostructures based on different III-V materials or nitrides.

It is assumed that apart from some biasing voltage  $V$ , an ac voltage  $V_{\omega} \cos \omega t$  (created by incoming THz signals, which are received by an antenna) is applied between the source and drain. This voltage stimulates the excitation of the plasma oscillations (self-consistent oscillations of the electron concentration in the 2DEG channel and the electric field around it). At the signal frequency  $\omega$  coinciding with or close to one of the plasma resonant frequency  $\Omega_n$  ( $n = 1, 2, 3, ..$  is the index of the plasma resonance), the amplitude of the ac potential drop across the depleted region of the 2DEG channel can be rather large. Due to a strong nonlinearity of the LSJ current-voltage characteristics, this can lead to large nonlinear (rectified) component of the net current.

## DEVICE MODELS

Due to a relatively large electron concentrations in the device channel and relatively low frequencies of electron collisions with impurity in phonons, 2DEG can be described by hydrodynamic electron transport model (Euler's equation and continuity equation). The hydrodynamic equations should be supplemented by the 2D Poisson equation for the self-consistent electric potential. In the case of the devices with the gated 2DEG channel, this equation can be replaced by its simplified ver-

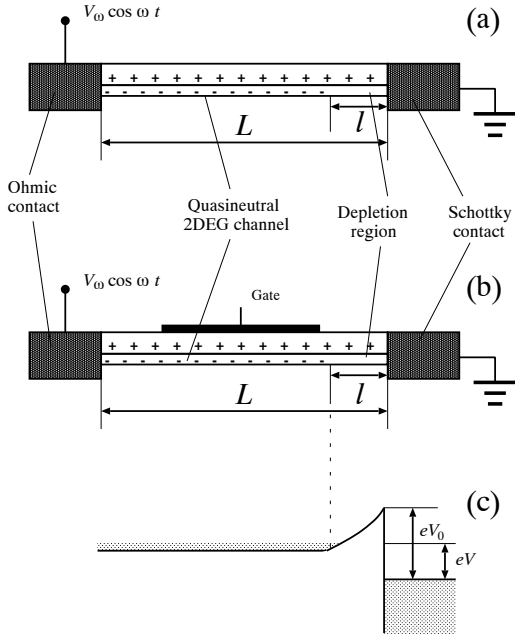


Fig. 1. Schematic view of LSJ resonant detectors with (a) ungated and (b) gated 2DEG channel; (c) band diagram of the device Schottky junction region with forward bias.

sion. The matching conditions at the point between the quasineutral and depletion regions in the 2DEG channel invoke simple expression for the LSJ current-voltage characteristic. Since the nonlinearity of the LSJ current-voltage characteristic is much stronger than that of the hydrodynamic equations, the linearized version of the latter can be used. More detailed models should account for hydrodynamic nonlinearities and specifics of nonequilibrium non-stationary transport in the high-electric field depletion region (combined hydrodynamic and ensemble Monte-Carlo particle models).

## RESULTS

Using the model based on a simplified description of the electron transport in the 2DEG channel, one can obtain the following equation for the LSJ resonant detector responsivity:

$$R_\omega = \frac{2R_\omega^{SJ}}{[\cosh(\pi\nu/2\Omega) + \cos(\pi\omega/\Omega)]}, \quad (1)$$

where  $R_\omega^{SJ}$  is the responsivity of LSJ without excitation of plasma oscillations in the 2DEG channel,  $\nu$  is the electron collision frequency. The frequency of fundamental plasma resonance is given by  $\Omega \propto$

$\sqrt{\Sigma_0/L}$  and  $\Omega \propto \sqrt{\Sigma_0 W_g/L_g^2}$  for ungated and gated 2DEG channels, respectively,  $\Sigma_0$  is the dc electron sheet concentration in the channel,  $L$  is the length of the channel,  $L_g < L$  and  $W_g \ll L$  are the gate length and the gate layer thickness. It is assumed that the length of the LSJ depletion region  $l \ll L_g, L$ . As seen from Eq. (1), the responsivity  $|R_\omega|$  reaches maxima at the plasma resonant frequencies:  $\omega = \Omega_n$ , where  $\Omega_n = (2n - 1)\Omega$ . The responsivity maxima are fairly high when  $\nu \ll \Omega$ :

$$\max \left| \frac{R_\omega}{R_\omega^{SJ}} \right| \simeq \left( \frac{8}{\pi^2} \right) \left( \frac{\Omega}{\nu} \right)^2 \gg 1. \quad (2)$$

The fundamental plasma frequencies for the devices with both ungated and gated 2DEG channels fall into the THz range at real device structural parameters. For fairly typical parameters  $\Omega/2\pi = 1$  THz and  $\nu = (5 - 10) \times 10^{11} \text{s}^{-1}$ , one obtains  $\max |R_\omega/R_\omega^{SJ}| \simeq 32 - 128$ . In the devices with the gated 2DEG channel, the gate-drain voltage  $V_g$  can be applied to control the electron concentration under the gate  $\Sigma_0 = \Sigma_0(V_g)$  and, hence, the resonant plasma frequencies.

The comparison of the responsivity of the LSJ resonant detector with the gated 2DEG channel under consideration ( $R_\omega$ ) with that based on the HEMT and utilizing the hydrodynamic nonlinearity ( $R_\omega^{HEMT}$ ) results in

$$\max \left| \frac{R_\omega}{R_\omega^{HEMT}} \right| \simeq \left( \frac{s}{v_T} \right)^2 \gg 1. \quad (3)$$

Here  $s \propto \sqrt{\Sigma_0 W_g}$  is the characteristic plasma wave velocity and  $v_T$  is the thermal electron velocity in the 2DEG channel. Usually,  $s/v_T \simeq 10$ , so that  $\max |R_\omega/R_\omega^{HEMT}| \simeq 10^2$ .

## CONCLUSION

We proposed novel THz detectors based on heterostructures with LSJ, developed their models and assessed the device characteristics. It was shown that the devices proposed can substantially surpass those studied previously. Numerical studies using more detailed and complex device models are necessary.

## REFERENCES

- [1] M. Dyakonov and M. Shur, *Detection, mixing, and frequency multiplication of terahertz radiation by two dimensional electronic fluid*, IEEE Trans. Electron Devices **43**, 1640 (1996).

# New Scales: Properties of Nanostructures in the Femtosecond Regime

A. Vernes and P. Weinberger

Center for Computational Materials Science, TU Vienna, Gumpendorferstr. 1a, 1060 Vienna, Austria  
 e-mail: av@cms.tuwien.ac.at

## INTRODUCTION

Many fundamental processes in matter like electron–electron or electron–phonon scattering in solids, occur on a time scale ranging from a few tenth of a femtosecond (1 fs =  $10^{-15}$  s) to a picosecond (1 ps =  $10^{-12}$  s). These ultrafast phenomena are experimentally accessed by monitoring the interaction of ultrashort light pulses with a given sample. Among the experimental techniques available nowadays, the so–called pump–probe methods are most frequently used. In such a pump–probe experiment one needs two ultrafast laser pulses: a pump pulse, which excites the investigated system and a probe pulse, delayed in time, which explores the relaxation of the excited system.

Based on the superposition principle of electromagnetic fields, within the Slowly Varying Envelope Approximation (SVEA) the total external electric field in a pump–probe experiment is given by

$$\begin{aligned} \vec{E}(\vec{r}, t) &= \vec{E}_{\text{pu}}(\vec{r}, t) + \vec{E}_{\text{pr}}(\vec{r}, t) \\ &= \vec{e}_{\text{pu}} \mathcal{E}_{\text{pu},0} \tilde{\mathcal{E}}_{\text{pu}}(t) \exp[i(\vec{q}_{\text{pu}} \vec{r} - \omega_{\text{pu}} t)] \\ &\quad + \vec{e}_{\text{pr}} \mathcal{E}_{\text{pr},0} \tilde{\mathcal{E}}_{\text{pr}}(t - \tau) \exp[i(\vec{q}_{\text{pr}} \vec{r} - \omega_{\text{pr}} t)] , \end{aligned} \quad (1)$$

where  $\tilde{\mathcal{E}}_{\text{pu}}(t)$  and  $\tilde{\mathcal{E}}_{\text{pr}}(t)$  are the time–dependent envelopes of the pump and the probe pulse propagating in the directions  $\vec{q}_{\text{pu}}$  and  $\vec{q}_{\text{pr}}$  with the carrier frequencies  $\omega_{\text{pu}}$  and  $\omega_{\text{pr}}$  and having the polarizations  $\vec{e}_{\text{pu}}$  and  $\vec{e}_{\text{pr}}$ . In considering an external electric field as defined in Eq. (1), it is assumed that no significant overlap in time exists between the pump and probe pulse, i.e., all coherence coupling effects can be neglected.

## GENERALIZED KUBO THEORY

Because in Eq. (1) a possible overlap between the pump and probe pulse is neglected, it can be considered that for  $t > \tau$  the probe pulse interacts

only with the pump–excited system. The problem to be solved reduces therefore in finding the dynamic linear response of the pump–excited system with respect to the probe pulse at times  $t > \tau$ . If within the interaction picture the only source of perturbation is the probe pulse then from the linearization of the density,

$$\rho_{\text{pr}}(t) \simeq \rho_{\text{pu}} + \frac{i}{\hbar} \int_{\tau}^t dt' [\vec{r}(t'), \rho_{\text{pu}}] \vec{E}_{\text{pr}}(t') , \quad (2)$$

where the density for the pump–excited state is written

$$\begin{aligned} \rho_{\text{pu}} &\simeq \rho_0 + \frac{i}{\hbar} \sum_{\kappa} \int_{-\infty}^{\tau} dt [\vec{r}(t), \rho_0] \vec{E}_{\text{pu}}(t) \\ &\equiv \rho_{\text{pu}}^{(0)} + \rho_{\text{pu}}^{(1)} . \end{aligned}$$

Accordingly the frequency–frequency representation of the generalized, strictly linear conductivity for the pump–probe experiments is given by [1]

$$\begin{aligned} \tilde{\sigma}_{\mu\nu}^{(0)}(\omega_{\text{pr}}, \omega; \tau) &= \frac{1}{2\pi} \exp[+i(\omega - \omega_{\text{pr}})\tau] \\ &\quad \times \mathcal{L} \left[ \tilde{\mathcal{E}}_{\text{pr}}(t) \right] \Big|_{i(\omega_{\text{pr}} - \omega)} \tilde{\sigma}_{\mu\nu}(\omega) , \end{aligned} \quad (3)$$

where in terms of  $\omega$  this quantity is now resolved with respect to the spectral components of the probe pulse. The first order conductivity, on the other hand, is resolved with respect to the spectral components of the pump pulse and hence is written

as [1]

$$\begin{aligned}
\tilde{\sigma}_{\mu\nu}^{(1)}(\omega_{\text{pr}}, \omega_{\text{pu}}, \omega; \tau) &= \frac{\beta}{2\pi} \exp[+i(\omega - \omega_{\text{pu}})\tau] \\
&\times \sum_{\kappa} \mathcal{E}_{\text{pu},0\kappa} \int_0^{\infty} dt \exp(+i\omega t) \\
&\int_0^t d\xi \tilde{\mathcal{E}}_{\text{pr}}(t - \xi) \exp(+i\omega_{\text{pr}}\xi) \\
&\int_0^{\infty} d\xi' \langle J_{\mu}(t); J_{\nu}(t - \xi); J_{\kappa}(-\xi') \rangle \\
&\times \tilde{\mathcal{E}}_{\text{pu}}(\tau - \xi') \exp(+i\omega_{\text{pu}}\xi') .
\end{aligned} \tag{4}$$

Although for this form one can also take advantage on the properties of Laplace transforms, for  $\tilde{\sigma}_{\mu\nu}^{(1)}(\omega_{\text{pr}}, \omega_{\text{pu}}, \omega; \tau)$  a similar expression to that in Eq. (3) cannot be deduced. The total and formally linear dynamic conductivity is finally obtained by combining the zeroth and first order conductivities as given by Eqs. (3) and (4),

$$\begin{aligned}
\tilde{\sigma}_{\mu\nu}(\omega_{\text{pr}}, \omega_{\text{pu}}, \omega; \tau) &= \tilde{\sigma}_{\mu\nu}^{(0)}(\omega_{\text{pr}}, \omega; \tau) \\
&+ \tilde{\sigma}_{\mu\nu}^{(1)}(\omega_{\text{pr}}, \omega_{\text{pu}}, \omega; \tau) .
\end{aligned}$$

#### SUMMARY

By linearizing the density of both the pump- and probe-excited states and neglecting the overlap between femtosecond laser pulses, the Kubo response theory has been extended to describe pump-probe experiments. The main advantages of this response scheme is that although second order responses are included, it formally remains a linear theory and therefore all obtained expressions can be implemented straightforwardly within any standard bandstructure method.

#### REFERENCES

- [1] A. Vernes and P. Weinberger, Phys. Rev. B **71**, 165108 (2005).

# Spontaneous Polarization Effects in Nanoscale Wurtzite Structures

Takayuki Yamanaka, Mitra Dutta, and Michael A. Strosio  
Nano Engineering Research Group, University of Illinois at Chicago, Chicago, IL, 60607.  
email: tyaman1@uic.edu

## INTRODUCTION

For nanoscale wurtzite structures such as quantum dots and nm-thick layers, the surfaces may terminate locally in different atoms; for example, GaN structures may terminate with Ga-surfaces or N-surfaces. In this paper, the spontaneous polarization is calculated and shown to be depend on these surface terminations.

## DISCUSSION

Fig. 1 shows the unit cell of wurtzite crystals. The left hand side of Fig. 1 shows the geometry for ideal wurtzite structures. The lattice constant along a-axis of GaN is  $3.189\text{\AA}$ , consequently, the ideal height of the unit cell is  $5.208\text{\AA}$ . However, the actual height of the unit cell is  $5.185\text{\AA}$ . This is caused by the polarization in the crystal. In the wurtzite unit cell, the number of atom is identical for each layer. This means that the sheet charge density of each layer is same and the only the sign is different. If the horizontal area is large, the horizontal polarization can be approximated as zero. In the following, the vertical polarization is evaluated from the sheet charge density. Now, the large white circle in Fig. 1 is assumed to be a nitride, on the other hand, the gray circle is assumed to be a gallium. Thus, the sheet charge density is as shown in the left hand side of Fig. 2. The bottom area of the GaN unit cell is  $(3.189\text{\AA})^2 \sin 60^\circ = 8.807\text{\AA}^2$ . As a result, the sheet charge density  $\sigma$  is,

$$\sigma = (1.6 \times 10^{-19} \text{ C}) / (8.8 \times 10^{-20} \text{ m}^2) = 1.8 \text{ C/m}^2$$

The contribution for polarization is half of the sheet density to consider both sides of the layer. The polarization  $P$  can be evaluated by averaging the total dipole moment of the unit cell with regard to

the volume. The right hand side of Fig. 2 describes the dipole moment of each layer. Assuming a given area  $S$ , the polarization is expressed by

$$P = \sigma (c_1 - c_2) / 2(c_1 + c_2)$$

At the same time, the height of the unit cell is  $2(c_1 + c_2) = 0.5185$  nanometer as mentioned above. The spontaneous polarization of bulk wurtzite GaN is taken to be  $-0.029 \text{ C/m}$ . From above equations and the spontaneous polarization, the thickness of layers in the equilibrium state is obtained as  $c_1 = 0.1256 \text{ nm}$  and as  $c_2 = 0.1338 \text{ nm}$ . Here, the polarization change from the spontaneous polarization is evaluated for four cases shown in Fig. 3. These two cases, 1 and 2, are possible arrangements to change the polarization. It is noted that there are two more cases, 3 and 4, that are simply turned upside down compared with cases 1 and 2, so, the polarization of the cases 3 and 4 will become the same value and the opposite direction of cases 1 and 2. Fig. 4 shows the polarization according to the number  $n$ , which is the number of the alternated units shown in Fig. 3. The two dotted lines in Fig. 4 represents  $0.029 \text{ C/m}^2$  and  $-0.029 \text{ C/m}^2$ , respectively. These spontaneous polarization effects are considered for different nanostructures.

## CONCLUSION

Spontaneous polarizations have been calculated for nanostructures and the sensitivity of the results on the surface termination have been determined.

## ACKNOWLEDGEMENT

We would like to express our sincere thanks to Prof. Umesh Mishra for useful insights.

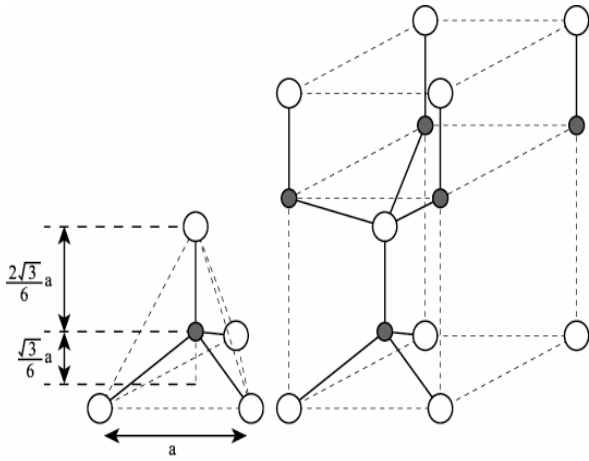


Figure 1. Wurtzite unit cell.

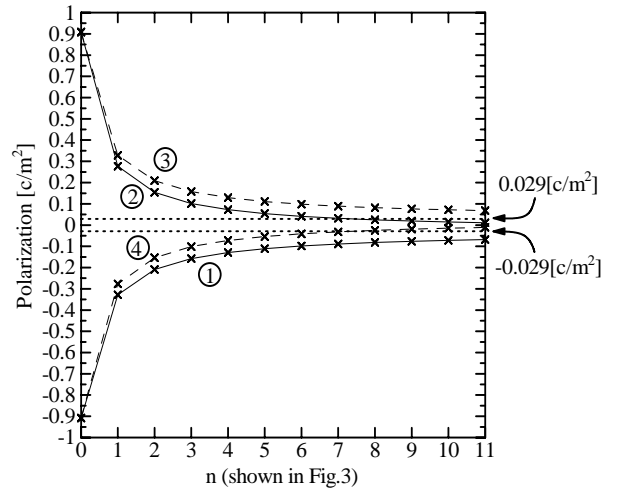


Fig. 4. Polarization change according to the number of layers.

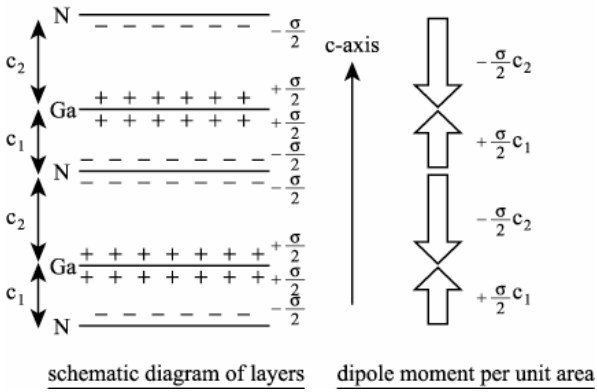


Figure 2. Sheet charge density and its dipole moment.

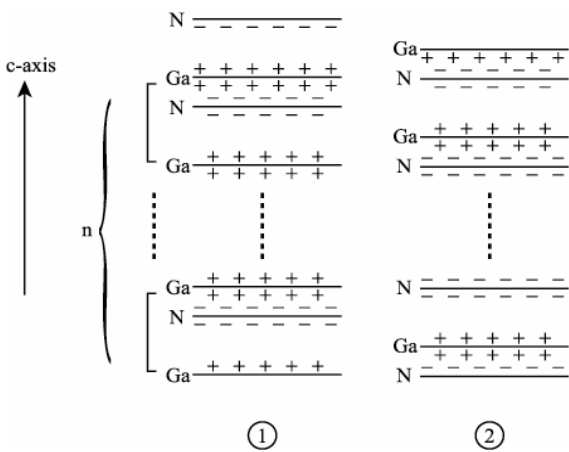


Figure 3. Arrangements to change the polarization.

# Modeling and Numerical Challenges in Nanoscale Device Engineering

E. Polizzi

University of Massachusetts,  
Department of Electrical and Computer Engineering,  
100 Natural Resources Road, Amherst, MA 01003, USA  
email: polizzi@ecs.umass.edu

In spite of considerable research effort and progress, high quality simulation-based design of nanoscale emerging devices still presents formidable modeling and computational challenges. Characterization of nanoscale emerging devices needs to be addressed via quantum simulations that need to account for: (i) information of the material at the atomistic level, (ii) multiscale aspects of electron transport modeling and electrostatics effects, (iii) high-fidelity treatment of the contact regions, and (iv) efficient methodology for dissipative scattering. For enhanced reliability and accuracy of the simulation of transport phenomena, one needs detailed knowledge of the electronic structure of the materials. Ab-initio calculations have been, so far, restricted to the simulations of small two-probe molecular systems, that does not consider the coupling with the surroundings such as electrostatics gate effects [1]. In practice to reduce the computational costs, one needs to use simplified electronic structure models such as effective mass type-models for semiconductors [2], or semi-empirical and tight-binding methods for molecules and nanotubes [3-4].

Given the advances in the state-of-art of computer architecture, processor and memory technology, underlying system software, and parallel algorithms, computational scientists and engineers can now expect to solve large-scale nanoelectronics problems using real-space mesh techniques for atomistic ab-initio simulations. These techniques that were thought to be intractable in the not-too-distant past, will result in fundamentally superior accuracy to address a combination of the two following challenging problems: (i) a comprehensive description of the transport problem, (ii) a fully atomistic description of the materials.

In material sciences, real-space mesh techniques such as the finite difference method (FDM) [5], and the finite element method (FEM) [6-7], were proposed in the early nineties, for the simulation of electronic structures. In contrast to the Linear Combinations of Atomic Orbitals (LCAO) methods (along with the dominant use of Gaussian basis sets), or plane waves expansion schemes, they offer significant advantages that have been summarized in [8]. They also produce very sparse matrices and can be cast as linear scaling electronic structure methods. These advantages, in turn, enable the use of multiscale and multilevel methods, and other sophisticated parallel numerical techniques on high-end computing platforms [9-10].

In principle, it is possible to extend the capabilities of an effective mass-based transport simulation code such as NESSIE (see Fig. 1), to account for higher degree of details of the electronic structure. The Kohn-Sham/DFT equation is then expected to replace the Schrödinger equation, and a pseudopotential approach may be used to remove the core electrons and the singularities in the discretization [11]. These simulations pose, however, significant challenges in developing robust and efficient large sparse linear system solvers and eigenvalue problem solvers resulting from the numerical handling of the transport problems [14-16].

This work aims to explore strategies that will result in fundamentally superior modeling accuracy and will enhance our ability to handle multiscales to achieve high-fidelity simulations of materials and transport problems. We propose to review the associated challenges in modeling, mathematical and numerical techniques, and the needed parallel algorithms.

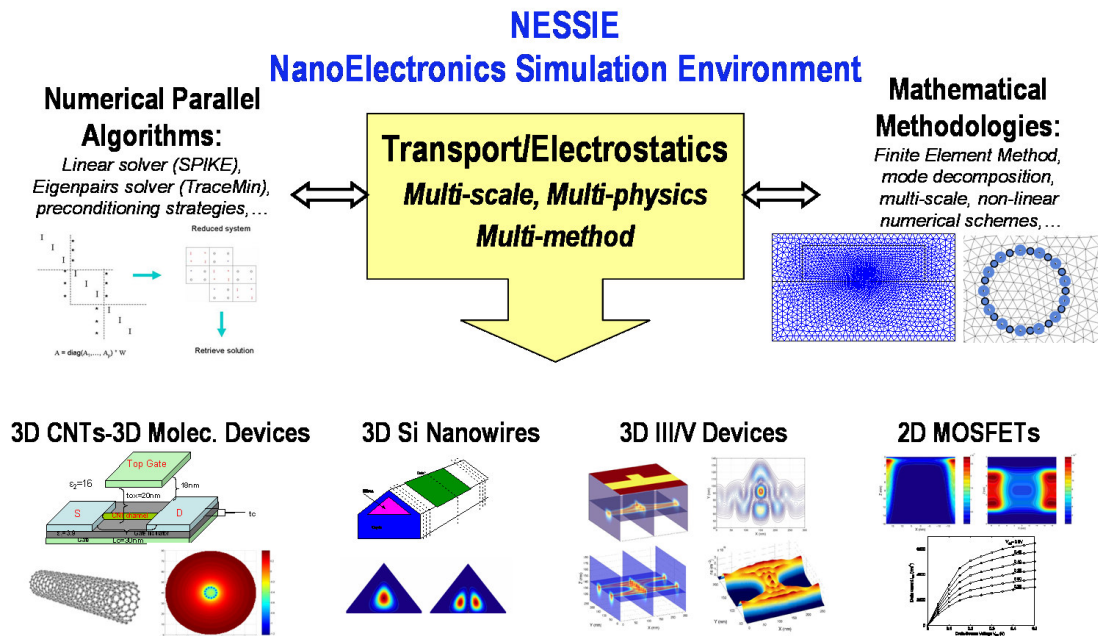


Fig. 1. This figure summarizes the capabilities of NESSIE (1998-2006), that is currently using real-space mesh techniques for performing nanoelectronics simulations on the following devices: 2D-MOSFET and 2-D DG MOSFET [12], 3-D Silicon Nanowire transistors [13], 3-D electron waveguide devices (III-V heterostructure) [2], and electrostatics calculations of molecular transistors and carbon nanotube devices [3], [4]. In carbon nanotube simulations, the transport phenomenon is localized in the nanotube while the coupling with the surroundings is achieved by considering only the electrostatics. Within our simulations, the atoms inside the device are considered as localized point charges, while FEM is needed for solving the Poisson equation in the overall transistor [3], [4].

## REFERENCES

- [1] M. Brandbyge, J-L. Mozos, P. Ordejón, J. Taylor and K. Stokbro, *Density functional method for nonequilibrium electron transport*, Phys. Rev. B 65, 165401 (2002).
- [2] E. Polizzi and N. Ben Abdallah. *Self-consistent three dimensional models for quantum ballistic transport in open systems*, Phys. Rev. B, 66, 245301, (2002).
- [3] F. Zahid, M. Paulsson, E. Polizzi, A. W. Ghosh, L. Siddiqui, and S. Datta. *A self-consistent transport model for molecular conduction based on extended Hckel theory with full three-dimensional electrostatics*, J. Chem. Phys., 123, 064707 (2005)
- [4] N. Neophytou, E. Polizzi, M. P. Anantram, D. Kienle, and M. Lundstrom. *Three-dimensional simulations of carbon nanotube transistors*, to be submitted (2006)
- [5] S. R. White, J. W. Wilkins, and M. P. Teter, *Finite Element method for electronic structure*, Phys. Rev. B, 39, 5819 (1989).
- [6] J. R. Chelikowsky, N. Troullier, and Y. Saad, *Finite-Difference-Pseudopotential method: electronic structure calculations without a basis*, Phys. Rev. Let. 72, 1240, (1994).
- [7] E. Tsuchida, and M. Tsukada, *Electronic-structure calculations based on finite-element method*, Phys. Rev. B, 52, 5573, (1995).
- [8] T. Beck, *Real-space mesh techniques in density-functional theory*, Rev. of Modern Phys., 72, 1041, (2000).
- [9] M. Heiskanen, T. Torsti, M. J. Puska, and R. M. Nieminen, *Multigrid method for electronic structure calculations*, Phys. Rev. B, 63, 245106, (2001).
- [10] S. Goedecker, *Linear scaling electronic structure methods*, Rev. of Modern Phys., 71, 1085, (1999).
- [11] J.R. Chelikowsky, *The pseudopotential-Density Functional method applied to nanostructures*, J. Phys. D 33, R33 (2000).
- [12] E. Polizzi and N. Ben Abdallah. *Subband decomposition approach for the simulation of quantum electron transport in nanostructures*, J. Comp. Phys. 202, 150, (2004).
- [13] J. Wang, E. Polizzi, and M. Lundstrom. *A three-dimensional quantum simulation of silicon nanowire transistors with the effective-mass approximation*, J. Appl. Phys. 96, 2192 (2004).
- [14] E. Polizzi, and A. Sameh. *A Parallel Hybrid Banded System Solver: The SPIKE Algorithm*, parallel computing, to appear (2004).
- [15] A. Sameh and J. Wisniewski. *A Trace Minimization Algorithm for the Generalized Eigenvalue Problem*, SIAM J. on Num. Anal., Vol. 19, No. 6, pp. 1243-1259, (1982).
- [16] E. Polizzi, A. Sameh *Numerical Parallel Algorithms for Large-Scale Nanoelectronics Simulations using NESSIE*, J. of Comput. Electronics, Vol. 3, N. 3-4, 363 (2005).

# Electronic Transport Properties of CNT Fibers

H. Mehrez and M. P. Anantram

Mail Stop: 229-1, Center for NanoTechnology and NASA Advanced Supercomputing Division,  
NASA Ames Research center, Moffett Field, CA 94035-1000, USA  
e-mail: hmehrez@mail.arc.nasa.gov, anant@mail.arc.nasa.gov

## INTRODUCTION

Carbon nanotube (CNT) fibers are promising in applications involving high strength and light weight conductors. Moreover, industrial-scale production of 30 m long fibers appears to be feasible [1]. The measured electrical resistivity of fibers are however considerably larger than that of individual CNTs. In fact, the fiber resistivity is  $10^{-4}\Omega\text{cm}$ , which is almost two orders of magnitude larger than that of copper. In this work we perform *first principles* calculations to determine the electronic and transport properties of defect free CNT fibers. This allows us to determine some underlying mechanism for such high resistivity and ways to decrease it so that CNT fibers compare better with copper.

## METHODOLOGY

Our procedure to calculate transport properties of a CNT fiber consists of the following steps: (i) Determine the equilibrium distance between nanotubes in a bundle using density functional theory (DFT). (ii) The inter-tube distance obtained in (i) is used to construct junctions of two tubes as well as single fiber trajectories which consist of a number ( $N$ ) of CNTs. (iii) We determine the inter-tube interaction Hamiltonian between two neighboring tubes by performing DFT calculations on a system of two adjacent tubes. (iv) The inter-tube Hamiltonian is treated as a perturbation to the ideal CNTs' Hamiltonians. (v) We calculate the conductance between two CNTs as a function of their overlap distance. (vi) We model transport through a single fiber trajectory in the phase decoherent limit by following reference [2]. (vii) We use the computed conductance in (vi) to derive the conductance through macroscopically large fibers and determine the limiting factors of fiber conductance.

## RESULTS

Our calculations demonstrate that fibers are more stable compared to CNTs. In Fig. 1-a, we show the total energy ( $E_T$ ) for an (8,8) CNT bundle as a function of inter-tube distance ( $d$ ) and orientation angle ( $\theta$ ) between CNTs. The lowest energy configuration is obtained for  $d = 3.07 \text{ \AA}$ , with very weak rotational barrier. In Fig. 1-b, we also show the band-gap ( $E_g$ ), which opens due to tube-tube interaction. At the equilibrium distance,  $E_g \sim 50 \text{ meV}$  and its effect on transport is expected to be small at room temperature.

The inter-tube conductance oscillates as a function of overlap distance. When mirror symmetry is preserved and for tubes with similar chiralities, the conductance oscillates between 0 and  $2G_o$ . In Fig. 2, we present the (8,8)x(7,7) inter-tube conductance as a dotted line. If the tubes have different chiralities, Fermi wave vectors of the two tubes are different and this results in substantial conductance reduction. The inter-tube conductance between (8,8) and (12,0) CNTs is  $\leq 0.01G_o$  as shown in Fig. 2. We also find that when mirror symmetry is broken, the conductance decreases. In Fig. 3, we show the inter-tube conductance between (8,8)x(8,8) CNTs, which undergoes damped oscillations. The zero-temperature conductance (transmission at  $E_F$ ) is shown in Fig. 3 as a continuous line, which vanishes for large overlap distance. This is due to  $E_g$  formation and is demonstrated in the insets.

Our model for transport through a fiber trajectory is shown in Fig. 4-a. For a given number of CNTs, the conductance is independent of overlap length ( $L_{ov}$ ) and bare CNT length ( $L_0$ ), as shown in Fig. 4-b,c. However, the conductance is inversely proportional to the number of tubes. In the phase decoherent limit we determine inter-tube transmission coefficient,  $T_a = \frac{(N-1)T}{1+0.5 \times (N-2)T}$ , where  $T$  is the

total transmission coefficient through the trajectory. The calculated  $T_a$  values from all simulations are shown in Fig. 4-d and result in  $T_a \sim 1.0$ . Within this model, the fiber resistivity is estimated to be,  $\rho \sim [\frac{1}{T_a} - 0.5] \times \frac{1}{l_0} \times 10^{-5} \Omega\text{cm}$ , where  $l_0$  is the average CNT length in  $\mu\text{m}$ . Using the computed value of  $T_a \sim 1.0$  found in Fig. 4-d, we find that if the fiber is composed of short nanotubes ( $0.5\mu\text{m}$ ) [1] the resistivity is  $\rho \sim 10^{-5} \Omega\text{cm}$ . This value is within the experimental range of Ref. [1]. However, if each CNT has a length of  $10\mu\text{m}$ , we find that the conductivity of an the fiber can be comparable to that of copper.

### REFERENCES

- [1] Lars M. Ericson, *et al.*, *Macroscopic, Neat, Single-Walled Carbon Nanotube Fibers*, *Science*, **305**, 1447-1450 (2004).
- [2] Y. Gefen and G. Schön, *Effect of inelastic processes on localization in one dimension* *Phys. Rev. B* **30**, 7323 (1984).

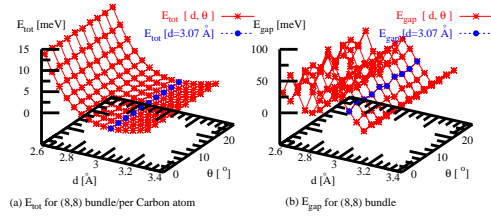


Fig. 1. (a) Total electronic energy ( $E_T$ ) per atom, and (b) band gap ( $E_g$ ) for an (8,8) CNT bundle as a function of inter-tube separation distance  $d$ , and orientation angle  $\theta$  between tubes. Lines represented with  $\bullet$  correspond to the results with the lowest  $E_T$ . Similar results have been obtained for other metallic tubes, (10,4) and (12,0) CNTs.

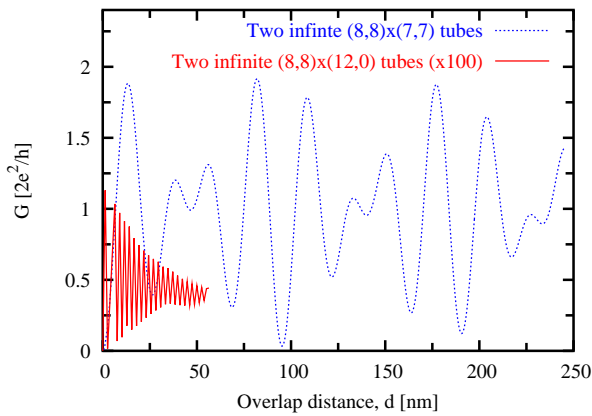


Fig. 2. Inter-tube conductance at  $T = 300K$  as a function of overlap distance between two CNTs. Results for (8,8)x(7,7) CNTs where mirror symmetry is preserved, are shown as a dotted line; and those of (8,8)x(12,0) CNTs are shown as a continuous line and multiplied by 100 for clarity.

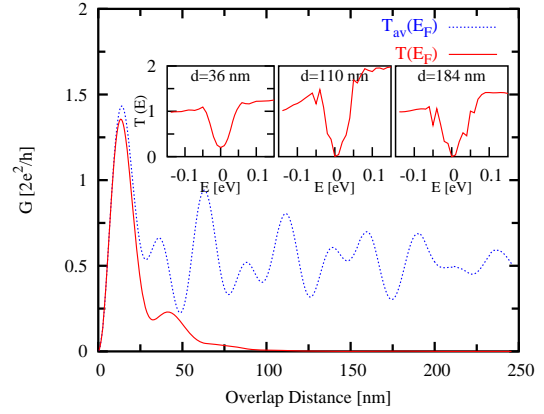


Fig. 3. Inter-tube conductance between (8,8)x(8,8) CNTs where mirror symmetry is broken by  $5^\circ$ . Dotted and continuous lines correspond to conductance at  $T = 300K$  and  $T = 0K$ , respectively. Insets represent inter-tube transmission coefficient in the vicinity of  $E_F$ , and indicate that  $T(E_F) = 0$  for  $d \geq 110$  nm. Atomic positions of the CNTs are also displayed.

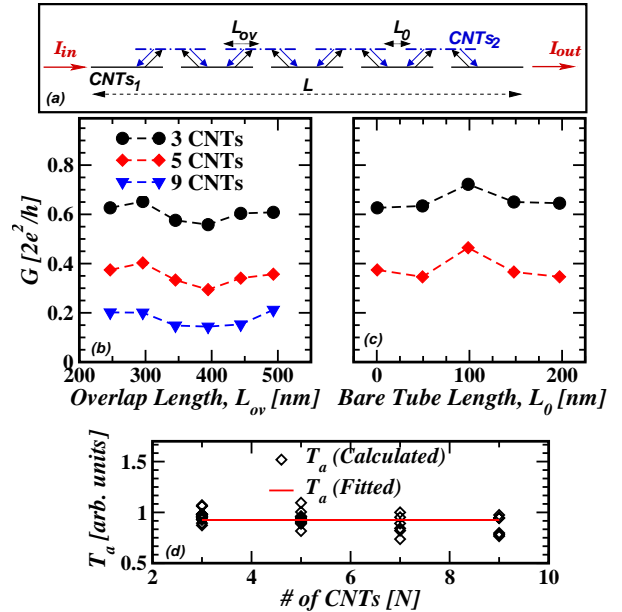


Fig. 4. (a) Single trajectory model through a fiber of length  $L$  with  $N$  tubes so that  $L_{av} = 2 \times L/N$  is the average length of each CNT.  $L_0$  and  $L_{ov}$  are the bare CNT length and overlap distance between the CNTs, respectively. We consider CNTs<sub>1</sub> and CNTs<sub>2</sub> as (8,8) CNTs with mirror symmetry broken by  $5^\circ$ . (b) Conductance as a function of  $L_{ov}$ , with  $L_0 \sim 5 \text{ \AA}$  and the number of CNTs in the trajectory are 3, 5, and 9. (c) Conductance as a function of  $L_0$ , with  $L_{ov} \sim 250 \text{ \AA}$  and the number of CNTs in the trajectory are 3 and 5. (d) Inter-tube transmission  $T_a$  (shown as open diamonds) for various configurations considered. Continuous line is an average fit of the computed  $T_a$  values and the results correspond to  $T_a = 0.924 \pm 0.095$ .

# Non-Equilibrium Green's Function (NEGF) Simulation of Metallic Carbon Nanotube Transistors: Impact of Vacancy Defect

Neophytos Neophytou, Shaikh Ahmed and Gerhard Klimeck  
School of Electrical and Computer Engineering, Purdue University, 465 Northwestern Ave.  
Network for Computational Nanotechnology  
West Lafayette, Indiana 47907-2035, USA.  
E-mail: [ssahmed@purdue.edu](mailto:ssahmed@purdue.edu), Phone: (765) 494 9034, Fax: (765) 494 6441

Carbon nanotube (CNT) based devices are promising structures for future electronic applications. An accurate treatment of quantum effects is necessary for short channel CNT devices. In this work, we describe a method to simulate realistic 3D CNT field effect transistors (CNTFETs) based on Finite Element Method (FEM) for the electrostatic treatment and nearest neighbour Tight-Binding (TB) method for electron transport, employing Non-Equilibrium Green's Function (NEGF) techniques.

The device geometry treated is shown in Fig. 1. The continuous grid includes the positions of the carbon atoms of the CNT and the charge distribution is treated as delta functions (point charges). The mesh created is fine enough to capture atomistic resolution for the potential on the shell of the CNT. The solution of the Poisson equation is self-consistently coupled to the transport part of the simulator where we employ three different techniques: (1) a semiclassical ballistic transport model, (2) an uncoupled mode space, and (3) a real space Nearest Neighbor Tight Binding (NNTB)  $p_z$  orbital model using the NEGF technique [1]. The simulator can treat both MOSFET-like devices using open boundary conditions, and Schottky-Barrier devices using a phenomenological model of metallic contacts. We have used two different algorithms in the computation of the Green's functions in the transport kernel of the simulator: (1) the LAPACK routines for solving a complex system of linear equations utilizing the LU decomposition with partial pivoting and row interchanges, and (2) the recursive Green's function (RGF) approach. Fig. 2 shows a comparison of the two approaches as a function of the Hamiltonian size (corresponding to

the total number of atoms in the nanotube as the length of the nanotube is changed) through non-self-consistent simulation experiments. Noticeable is the superior performance with the RGF algorithm as the system size increases.

The simulator has been used to study the effects of vacancies on the performance of metallic CNTFETs. The model device used is a (12,0) metallic CNT within a 3D geometry (Fig. 1). We introduce a single vacancy in the mid-region of the channel by raising the on-site energy of the vacancy and thus preventing any hopping of electrons to that particular site. Fig. 3 shows the local density of states (LDOS) in the vicinity of the vacancy and transmission ( $Tr$ ) calculated from non-self consistent simulations. For comparison, we also show the results for a device without a vacancy. We find that the presence of a single vacancy locally modulates the LDOS significantly. More importantly, regardless of the chirality of the nanotube, the transmission is reduced throughout the entire energy spectrum (note the reduction by one quantum unit in some regions) in agreement with [2, 3].

We also address the efforts and on-going activities on building and deploying community nanotechnology software tools on nanoHUB.org which currently provides the nanoscience research community with interactive on-line simulation and educational resources such as tutorials, seminars, and on-line courses. One such community tool is the CNTFET which is going to be publicly released and has recently been expanded in its capabilities through detailed numerical performance analysis. Fig. 4 shows the graphical user interfaces for this simulator used in an interactive session.

## REFERENCES

- [1] J. Guo, S. Datta, M. Lundstrom, and M. P. Anantram, *Multi-Scale Modeling of Carbon Nanotube Transistors*, The International Journal on Multiscale Computational Engineering, **2**, 257 (2004).
- [2] N. Neophytou, D. Kienle, E. Polizzi, M.P. Anantram, *Influence of Defects on nanotube transistor performance*, Appl. Phys. Lett., 2005 (submitted).
- [3] L. Chico, L. Benedict, S. Louie and M. Cohen, *Quantum conductance of carbon nanotubes with defects*, Phys. Rev. B **54**, 4 (1996).

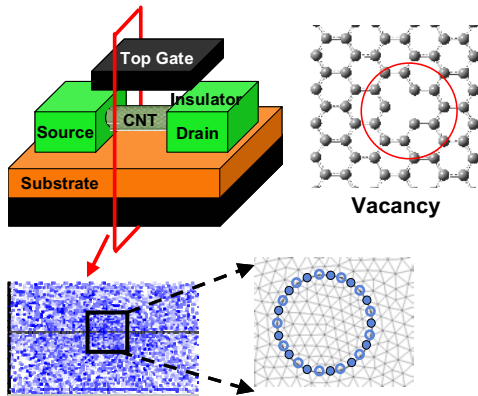


Fig. 1. The device structure and the creation of finite element mesh.

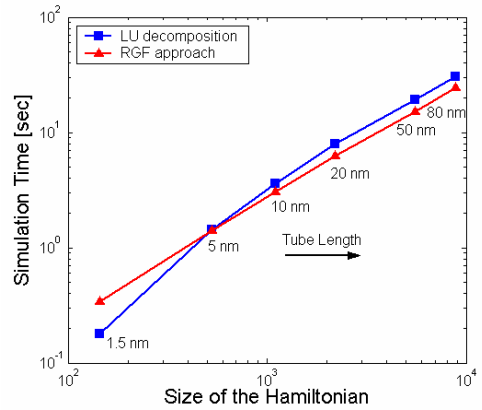


Fig. 2. Comparison between RGF and LU approaches.

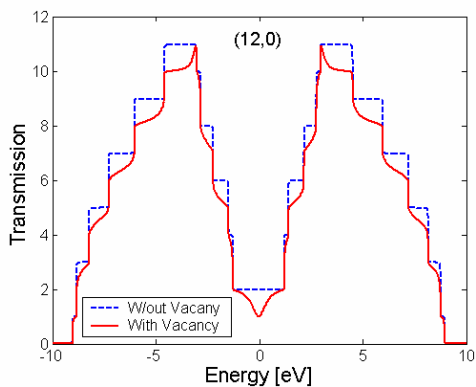
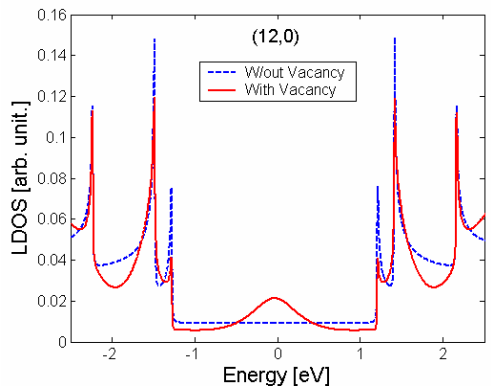


Fig. 3. (Left panels) Simulated local density of states (LDOS) in the vicinity of a vacancy and transmission for (12,0) metallic CNT.

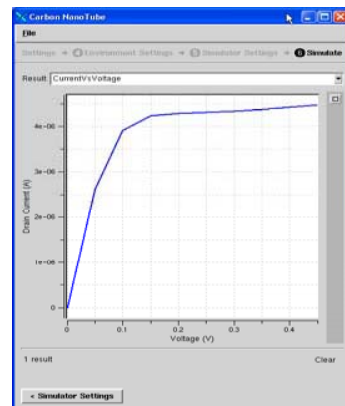
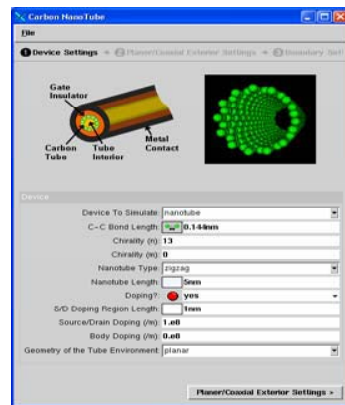


Fig. 4. (Right panels) The rappurturized graphical user interfaces for the CNTFET simulator.

# Dissipative Transport in CNTFETs

M. Pourfath, H. Kosina, and S. Selberherr

Institute for Microelectronics, TU Wien, Gußhausstraße 27–29/E360, 1040 Wien, Austria

e-mail: pourfath@iue.tuwien.ac.at

## INTRODUCTION

Exceptional electronic and mechanical properties together with nanoscale diameter make carbon nanotubes (CNTs) candidates for nanoscale field effect transistors (FETs). High performance CNTFETs were achieved recently [1, 2]. In this work we focus on an  $n/i/n$  device [2, 3]. Using the non-equilibrium Green's function (NEGF) formalism quantum phenomena like tunneling and scattering processes can be rigorously modeled. Recently a semiclassical Monte Carlo analysis of the effect of scattering on CNTFET characteristics has been reported [4, 5]. However, even with quantum corrections included, semiclassical methods cannot accurately predict the behavior of these devices because of the strong quantum effects. Therefore, in this work the NEGF formalism has been chosen to investigate transport phenomena in CNTFETs. Based on this method the performance of CNTFETs has been studied. The effects of elastic and inelastic scattering on the device performance have been investigated. The results indicate that elastic scattering has a more detrimental effect on the device characteristics than inelastic scattering. However, for short devices the performance is not affected because of the long mean free path for elastic scattering.

## APPROACH

We have solved the coupled transport and Poisson equations. In this work we assume bias conditions in which the first sub-band contributes mostly to the total current. In the mode-space approach [6] the transport equations for each sub-band can be written as:

$$G^R = [EI - H - \Sigma_{\text{el-ph}}^R - \Sigma_{\text{s,d}}^R]^{-1} \quad (1)$$

$$G^{<, >} = G^R [\Sigma_{\text{e-ph}}^{<, >}(E) + \Sigma_{\text{s,d}}^{<, >}(E)] [G^R]^\dagger \quad (2)$$

In (1) an effective mass Hamiltonian was assumed. All our calculations assume a CNT with

$E_g = 0.8$  eV, and  $m^* = 0.05m_0$  for both electrons and holes. A recursive Green's function method is used for solving (1) and (2) [7]. The self-energy due to electron-phonon interaction consists of the contribution of elastic and inelastic scattering mechanisms,  $\Sigma_{\text{e-ph}}^{<, >} = \Sigma_{\text{el}}^{<, >} + \Sigma_{\text{inel}}^{<, >}$ . Assuming a single sub-band the electron-phonon self-energies are simplified as (3)-(6).

$$\Sigma_{\text{el}}^{<, >}(E) = D_{\text{el}} G^{<, >}(E) \quad (3)$$

$$\Sigma_{\text{inel}}^{<}(E) = \sum_{\nu} D_{\text{inel}, \nu} [(n_B(\hbar\omega_{\nu}) + 1)G^{<}(E + \hbar\omega_{\nu}) + n_B(\hbar\omega_{\nu})G^{<}(E - \hbar\omega_{\nu})] \quad (4)$$

$$\Sigma_{\text{inel}}^{>}(E) = \sum_{\nu} D_{\text{inel}, \nu} [(n_B(\hbar\omega_{\nu}) + 1)G^{>}(E - \hbar\omega_{\nu}) + n_B(\hbar\omega_{\nu})G^{>}(E + \hbar\omega_{\nu})] \quad (5)$$

$$\Im m[\Sigma_{\text{e-ph}}^R(E)] = \frac{1}{2i} [\Sigma_{\text{e-ph}}^{>} - \Sigma_{\text{e-ph}}^{<}] \quad (6)$$

where  $n_B$  is given by the Bose-Einstein distribution function.  $D_{\text{el}}$ , and  $D_{\text{inel}}$  are related to the mean free path of the corresponding scattering mechanisms [8]. The transport equations are iterated to achieve convergence of the electron-phonon self-energies, resulting in a self-consistent Born approximation. The transport equations are iterated to achieve convergence of the electron-phonon self-energies, resulting in a self-consistent Born approximation. The carrier concentration and the current density at some point  $j$  of the device is calculated as (7) and (8).

$$n_j = -2i \int G_{j,j}^{<}(E) \frac{dE}{2\pi} \quad (7)$$

$$j_j = \frac{4q}{\hbar} \int 2\text{Re}\{G_{j,j+1}^{<}(E)H_{j+1,j}\} \frac{dE}{2\pi} \quad (8)$$

The coupled transport and Poisson system is solved iteratively.

## SIMULATION RESULTS

The mean free paths of carriers in semiconducting CNTs at high energies approach those in metallic CNTs [4]. Reported values are  $\lambda_{el} \approx 1.6 \mu\text{m}$  and  $\lambda_{inel} \approx 10 \text{ nm}$  for a metallic CNT with a diameter of 1.8 nm, [9]. Elastic scattering is due to acoustic phonons, and inelastic scattering due to zone boundary and optical phonon modes with energies of  $\hbar\omega_{op} = 160 \text{ meV}$  and  $200 \text{ meV}$ , respectively [9]. Elastic scattering conserves the energy of carriers as in the ballistic case, but the current decreases considerably due to the elastic back-scattering of carriers. On the other hand, with inelastic scattering the energy of carriers is not conserved. Carriers which acquire enough kinetic energy can emit phonons and scatter into lower energy states. This process does not decrease the current as much as elastic scattering does (Fig. 2), since scattered carriers lose their kinetic energy and the probability for back-scattering is low [4]. Due to a long mean free path for elastic scattering process, the performance of short devices (less than several hundred nano-meter) is only weakly affected. On the other hand, the mean free path for inelastic scattering in CNTs is quite short, but this process does not degrade device performance. Fig. 1 and Fig. 3 show the current spectrum in the absence and presence of scattering. In the presence of scattering the current decreases slightly and carriers at high energy states are scattered into lower energy states.

## CONCLUSION

We theoretically investigated the effect of scattering on the performance of CNTFETs. Because of

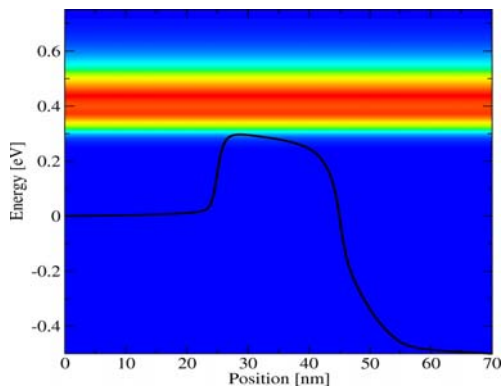


Fig. 1. The current spectrum for ballistic transport.

back-scattering, elastic scattering has a detrimental effect on the device performance. Our analysis shows that short CNTFETs can operate close to their ballistic limit.

## ACKNOWLEDGMENT

This work has been partly supported by the Austrian Science Fund FWF, project 17285-N02 and the National Program for Tera-level Nano-devices of the Korean Ministry of Science and Technology.

## REFERENCES

- [1] A. Javey *et al.*, Nano Lett. **4**, 1319 (2004).
- [2] Y.M. Lin *et al.*, IEEE Trans.Nanotechnology **4**, 481 (2005).
- [3] J. Chen *et al.*, in *IEDM Tech.Dig.* 695 (2004)
- [4] J. Guo *et al.*, Appl.Phys.Lett. **86**, 193103 (2005).
- [5] S. Hasan *et al.*, J.Comp.Electronics **3**, 333 (2005).
- [6] R. Venugopal *et al.*, J.Appl.Phys. **92**, 3730 (2002).
- [7] A. Svizhenko *et al.*, J.Appl.Phys. **91**, 2343 (2002).
- [8] A. Svizhenko *et al.*, Phys.Rev.B **72**, 085430 (2005).
- [9] J. Park *et al.*, Nano Lett. **4**, 517 (2004).

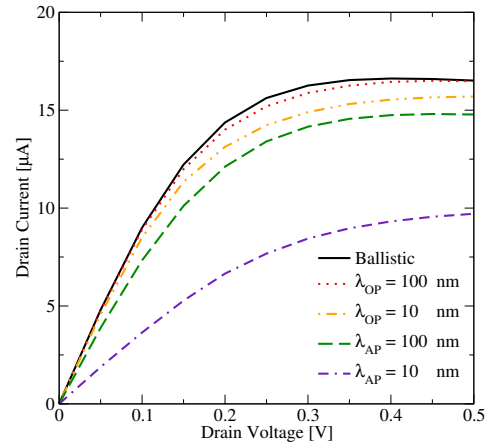


Fig. 2. The effect of scattering on the output characteristics.

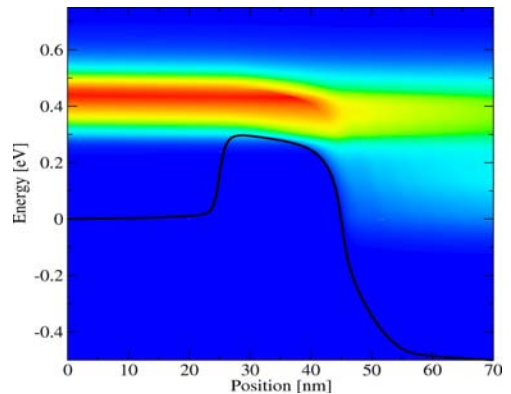


Fig. 3. Current spectrum in the presence of scattering.

# Influence of Hot Phonons on the Transport Properties of Single-Wall Carbon Nanotubes

Ch. Auer, C. Ertler, and F. Schürer

Institute of Theoretical and Computational Physics, TU Graz, Petersgasse 16, 8010 Graz, Austria  
 e-mail: auer@itp.tu-graz.ac.at, ertler@itp.tu-graz.ac.at, schuerer@itp.tu-graz.ac.at

Single-wall carbon nanotubes (SWCNTs) are promising candidates for future electronic applications. The development of high performance nanotube devices requires a thorough investigation of their fundamental transport properties. At high applied fields, the interactions of electrons with optical phonons are the dominant scattering mechanisms in SWCNTs. Calculations of the optical mean free path ( $l_{\text{op}}$ ) in metallic SWCNTs according to the density functional theory (DFT) [1] lead to values which strongly disagree with those obtained by fitting the results of transport simulations to measured IV-characteristics [2]. Very recently, it was suggested that this disagreement is due to a nonequilibrium behavior of the optical phonons [3].

In order to quantify the hot-phonon effect in metallic SWCNTs, we perform simulations of the electron transport by taking into account the full dynamics of optical  $\Gamma$ - and K-phonons. The considered kinetic model is based on the coupled set of semiclassical Boltzmann transport equations (BTEs)

$$[\partial_t \pm v_f \partial_z \mp eE v_F \partial_\varepsilon] f_{R/L} = \mathcal{C}_{R/L}, \quad (1)$$

$$\left[ \partial_t + \frac{\partial \omega_{\Gamma/K}}{\partial q} \partial_z \right] g_{\Gamma/K} = \mathcal{D}_{\Gamma/K} \quad (2)$$

for electrons and phonons. Linearly dispersive electrons which move right (R) and left (L) with the Fermi velocity  $v_F$  are characterized by the distribution functions  $f_{R/L}(z, \varepsilon, t)$  depending on position  $z$ , energy  $\varepsilon$  and time  $t$ . The distribution functions  $g_{\Gamma/K}(z, q, t)$  describe optical  $\Gamma$ -phonons and zone-boundary phonons with wave vector  $q$  and energy  $\hbar\omega_{\Gamma/K}$ . The electron and phonon BTEs (1) and (2) are coupled by the collision terms  $\mathcal{C}_{R/L}$  and  $\mathcal{D}_{\Gamma/K}$  which model backscattering processes of electrons via phonon absorptions and emissions.

A new deterministic numerical method is applied to solve the kinetic equations (1) and (2). This

method is based on fixed uniform discretizations of the phase-space variables  $z$ ,  $\varepsilon$  and  $q$ . The numerical grid is constructed so that the collision operators can be evaluated exactly at the grid points. A high-order conservative finite-difference scheme [4] is used to approximate the derivatives of the distribution functions with respect to the phase-space variables. The time integration of the discretized kinetic equations is performed with the help of total variation diminishing Runge-Kutta type schemes. The developed numerical method provides highly accurate results for the distribution functions without statistical noise (see Figs. 1-3). This is the main advantage over the usually applied Monte Carlo techniques.

The transport simulations performed for metallic SWCNTs with several lengths and diameters clearly show that the  $\Gamma$ - and K-phonons are driven far from equilibrium (see Figs. 1 and 3). We observe that these hot phonons have major influence on the electron transport. Comparisons of experimental data with results obtained by using DFT-values for the electron-phonon coupling strength exhibit very good agreement (see Fig. 4).

## ACKNOWLEDGMENT

This work has been supported by the Fond zur Förderung der wissenschaftlichen Forschung, Vienna, under contract number P17438-N08.

## REFERENCES

- [1] S. Piscanec et al., *Kohn anomalies and electron-phonon interactions in graphite*, Phys. Rev. Lett. **93**, 185503 (2004).
- [2] A. Javey et al., *High-field quasiballistic transport in short carbon nanotubes*, Phys. Rev. Lett. **92**, 106804 (2004).
- [3] M. Lazzeri et al., *Electron transport and hot phonons in carbon nanotubes*, cond-mat/0503278 (2005).
- [4] G. Jiang and C.-W. Shu, *Efficient implementation of weighted ENO schemes*, J. Comput. Phys. **126**, 202 (1996).

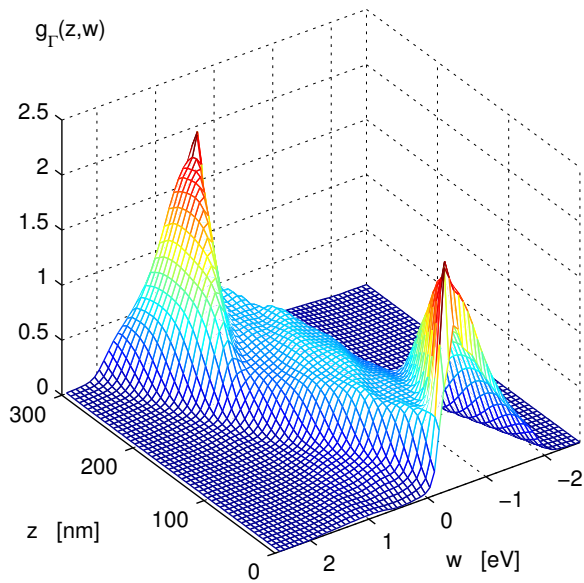


Fig. 1. Steady-state results for a 300 nm long SWCNT at 1 V bias: distribution of  $\Gamma$ -phonons as a function of position  $z$  and energy  $w = \hbar v_F q$ .

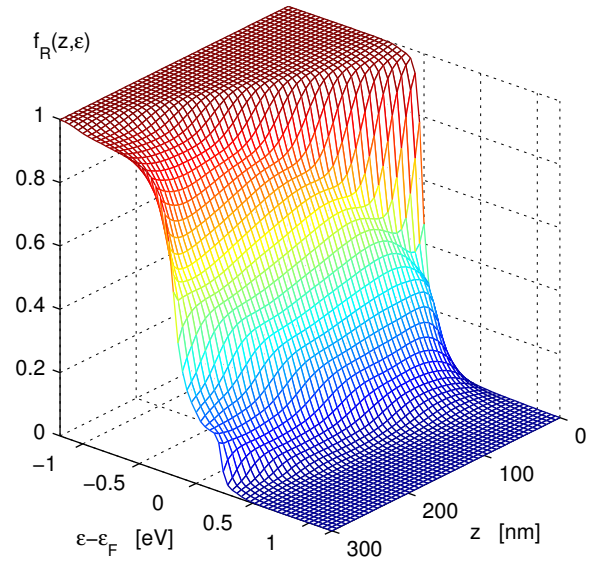


Fig. 3. Steady-state results for a 300 nm long SWCNT at 1 V bias: distribution of right moving electrons as a function of position  $z$  and energy  $\varepsilon$ .

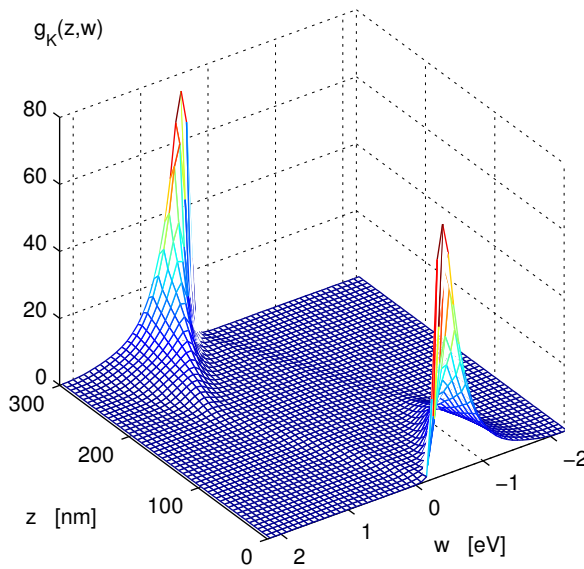


Fig. 2. Steady-state results for a 300 nm long SWCNT at 1 V bias: distribution of K-phonons as a function of position  $z$  and energy  $w = \hbar v_F q$ .

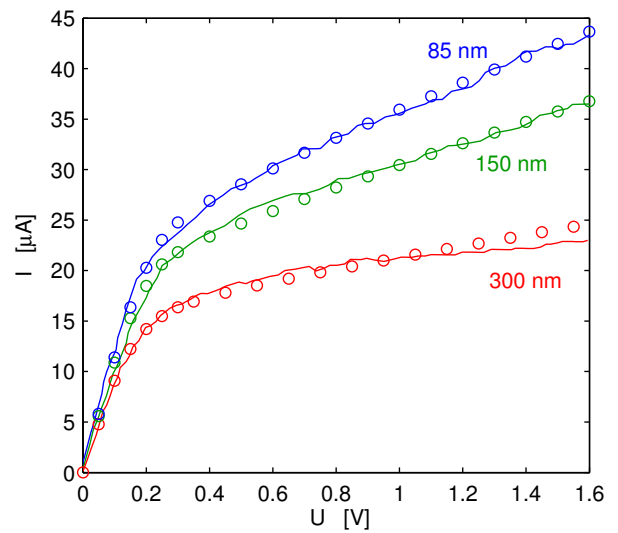


Fig. 4. Current-voltage (I-U) characteristics of SWCNTs with different lengths: solid lines refer to experimental data [2] and markers represent results of our transport simulations.

# Electronic and Transport Properties of Silicon Nanowires

F.Sacconi<sup>1</sup>, M. Persson<sup>1</sup>, M. Povolotskyi<sup>1</sup>, L. Latessa<sup>1</sup>, A.Pecchia<sup>1</sup>, A. Gagliardi<sup>2</sup>, B. Aradi<sup>2</sup>, T. Frauenheim<sup>2,3</sup>, A. Di Carlo<sup>1,\*</sup>

<sup>1</sup>Dept. Electronics Eng. , Univ. of Rome “Tor Vergata”, via Politecnico 1, 00133 Roma, Italy

<sup>2</sup>University of Paderborn, Warburger Str. 100, 33100 Paderborn, Germany

<sup>3</sup>on move to Center for Computational Material Science, University of Bremen, Germany, 28359 Bremen.

\*e-mail: aldo.dicarlo@uniroma2.it

## INTRODUCTION

The current process of scaling of semiconductor devices to the nanoscale size can lead to great improvements in the device performance, such as increased speed and low-voltage operation.

In Si metal-oxide-semiconductor field effect transistors (MOSFETs), the scaling of channel length requires that gate performs an effective control action. This can be achieved with new technology solutions such as silicon nanowires, which allows 3D control of the channel. Silicon nanowire structures can be obtained by using both a “top-down” approach, mainly based on etching techniques and a “bottom-up” approach, where silicon nanowires are directly synthesized. Both approaches are well suited for the realization of nanoMOSFET, however, structural and electronic properties of top-down and bottom-up nanowire are different. During nanowire synthesis atomic position are relaxed while in the top-down process the silicon nanowire maintains a typical bulk atomic structure.

This work present a detail investigation of structural, electronic and transport properties of silicon nanowires and silicon nanowire based nanoMOSFET

## METHODS AND RESULTS

Electronic properties of etched silicon nanowires are investigated with two different approaches, namely the Empirical Tight-Binding (ETB) model and the Linear Combination of Bulk Bands (LCBB) method. Within the ETB the system is described by using a nearest-neighbour  $sp^3d^5s^*$  parameterization for silicon. We consider both hydrogenated and  $SiO_2$  terminated silicon surface.  $SiO_2$  is wrapped around the Silicon cell, by means of an interface which avoids dangling bonds and surface states; we

use the  $\beta$ -cristobalite polytype of  $SiO_2$  which is described with a second-nearest-neighbour  $sp^3$  parameterization [1]. With this model, we have calculated electronic energies, dispersion, minimal gap and effective masses of silicon nanowires structures (see Figs.1-3). LCBB approach is based on an empirical pseudopotential description of the Si structure[2]. Single-particle eigenstates of electron and holes are obtained as a linear combination of conduction or valence bands states of bulk silicon. Here  $SiO_2$  is modelled as a potential barrier. Dispersion relation for two typical silicon nanowires as obtained with LCBB is shown in Fig. 4. A comparison between LCBB and ETB will be given.

The structure of synthesized Si nanowires (freestanding and functionalized) is obtained by minimizing the total energy by using an approximated DFT tight-binding method (DFTB). Figure 5 shows a calculation of the final geometry of a (110) oriented hydrogenated silicon nanowire.

Transport properties of nanowires are obtained by applying the Green function method to both empirical and DFT tight-binding description.[3] Figure 5 shows the calculated IV characteristics for the relaxed silicon nanowire. The non-equilibrium Green function (NEGF) approach has been considered to describe nanoMOSFET devices based on Silicon nanowires. Figure 6 shows the calculated potential profile and charge density for a silicon nanowire based nanoMOSFET.

## REFERENCES

- [1] F. Sacconi et al. IEEE Transactions on Electron Devices, 51 (5), 741-748, (2004).
- [2] F. Sacconi et al. Solid-State Electronics, 48 (2004), 575-580T.
- [3] A. Pecchia and A. Di Carlo, Rep. Prog. Phys. 67, 1497 (2004)

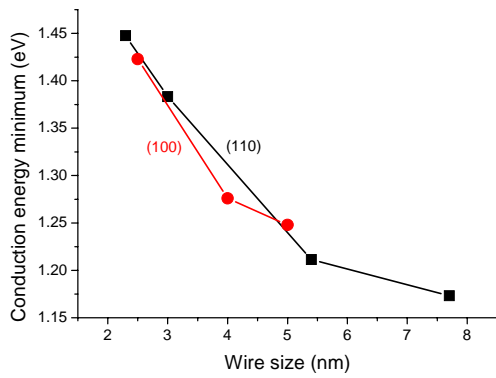


Fig. 1 Conduction band minimum as a function of silicon nanowire size for both (100) and (110) oriented nanowires. ETB results

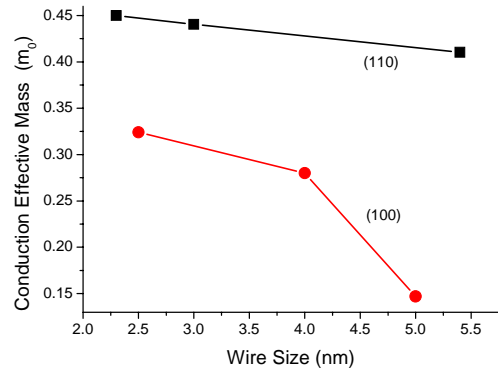


Fig. 2 Effective mass as a function of silicon nanowire size as obtained with ETB.

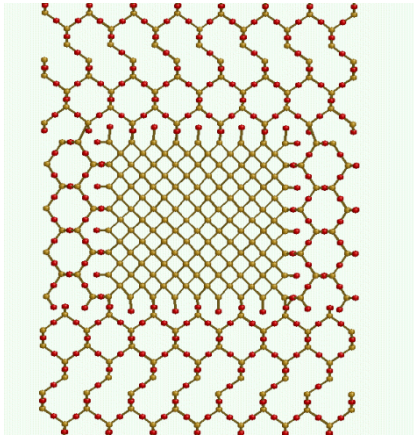


Fig. 3 Structure of the silicon nanowire surrounded by  $\text{SiO}_2$

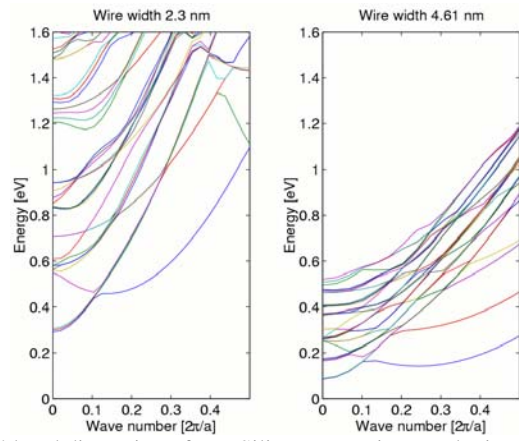


Fig. 4 band dispersion of two Silicon nanowires as obtained with LCBB.

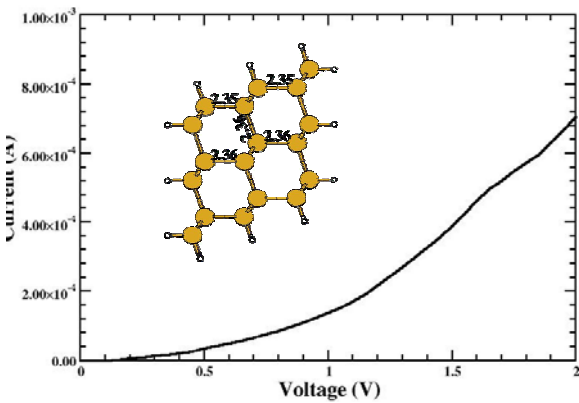


Fig. 5 Current flowing in a Silicon nanowire as a function of applied voltage (inset) Relaxed structure of the hydrogenated silicon nanowire.

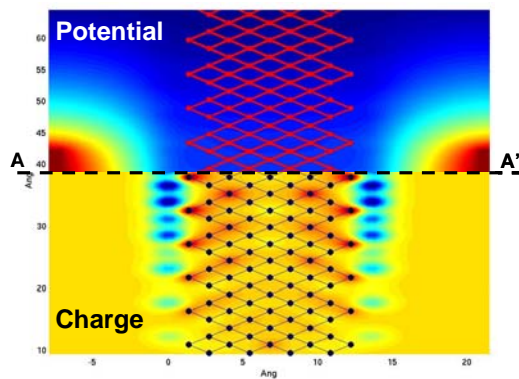


Fig. 6 NEGF results of a coaxially gated silicon nanowire. The system is symmetric with respect to AA' line. Gate bias is 0.5 V. Charge is referred as a difference with respect to zero bias condition.

# Beyond the Local Density Approximation

G. Kresse and J. Hafner

Institut für Materialphysik and Center for Computational Material Science, Universität Wien  
Sensengasse 8, A-1090, Wien, Austria  
e-mail: kresse@univie.ac.at

*Ab initio* density functional theory calculations have been widely successful in many fields, including bulk semiconductors, semiconductor-insulator interfaces, and semiconductor surfaces. For the modeling of semiconductor devices, the well known underestimation of band gaps, however, remains a yet unsolved problem; in some cases, the band structures are even qualitatively wrong. This makes prediction of effective masses, impurity levels or band alignments often unreliable or even impossible. The incorrect prediction of band gaps also possibly deteriorates the description of the energetics of defects.

Several remedies to this problem have been suggested over the last 10 years. Hybrid functionals, that include a fixed fraction of the exact non-local exchange operator, hold the promise to yield both, an improved description of the energetics of defects, as well an improved description of their energy levels. The drawback of this approach is that it is computationally more demanding than traditional semi-local density functionals, but with the rapid advances in computer performance, this has become less of an issue. The availability in widely used DFT codes, however, has been limited as well, with efficient implementations becoming available only very recently [1], [2].

Another approach, known even before the foundations of density functional theory were laid, is the *GW* method [3]. In this approach, the non-local exchange interaction is dynamically screened by the electrons, requiring the calculation of the frequency dependent non-local dielectric matrix  $\epsilon(\mathbf{r}, \mathbf{r}', \Omega)$ . The method is generally even more demanding than the aforementioned hybrid functionals, but should yield accurate band gaps and transport properties across all materials, including metals and wide gap insulators. Its application has yet been limited to very small systems, one major drawback being that

easy to use implementations were not available in standard DFT packages.

In the present lecture, hybrid functionals and the *GW* method will be briefly introduced and discussed. Systematic studies for a large variety of systems are presented (see Fig. 1 and Fig. 2). We show that the *GW* approximation indeed improves significantly upon DFT, but the often applied approximation that the *GW* wavefunctions equal the DFT groundstate wavefunctions—the so called  $G_0W_0$  approximation—can give unsatisfactory results. A novel hybrid scheme merging non-local exchange functionals with *GW* inspired screening is presented and discussed. It allows predictive band gap engineering, even in those cases, where the other two approaches fail.

Particular attention will be given to two case studies. The lead chalcogenides pose a critical test to any electronic structure method. Their band gaps are small and follow an usual trend with  $\text{PbS} > \text{PbSe} \approx \text{PbTe}$ . We show that, in this case, hybrid functionals as well as *GW* can recover the correct trend, if spin orbit coupling is properly included.

The second case study concentrates on ZnO, where the precise properties of native point defects are still a question of debate. We concentrate on native electron donors, such as oxygen vacancies, and address the question of their precise electronic structure by performing large scale density functional calculations with up to 700 atoms, and hybrid density functional studies for medium sized systems with more than 100 atoms.

## REFERENCES

- [1] J. Heyd, G. E. Scuseria, and M. Ernzerhof, *J. Chem. Phys.* **118**, 8207 (2003).
- [2] J. Paier, I.C. Gerber, J.G. Angyan, M. Marsman, and G. Kresse, *J. Chem. Phys.* accepted.
- [3] L. Hedin, *Phys. Rev.*, **139**, A796 (1965).

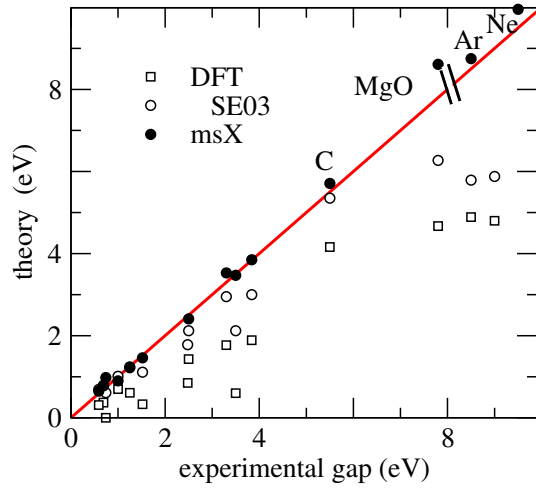


Fig. 1. Band gaps of 15 semiconductors and insulators using standard DFT, a hybrid functional with 25% non-local exchange (HSE03), and a  $G_0W_0$  inspired model screened exchange (msX) approach

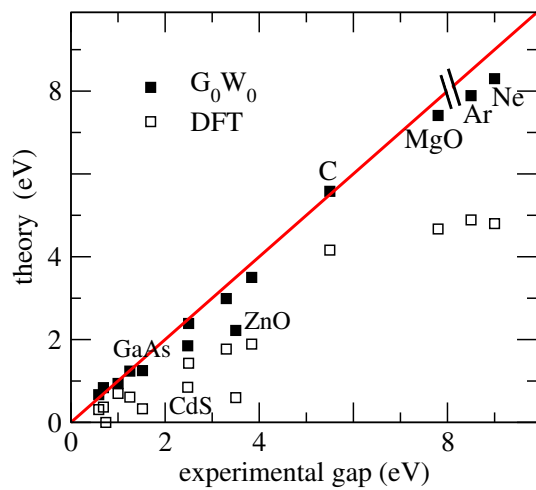


Fig. 2. Band gaps of 15 semiconductors and insulators using standard DFT and  $G_0W_0$ .

# Heat Dissipation and Non-Equilibrium Phonon Distributions in Molecular Devices

A. Pecchia\*, A. Gagliardi†, Th. Frauenheim†, A. Di Carlo\*

\*Dep. of Electronics Engineering, University of Rome 'Tor Vergata', Via del Politecnico 1, 00133, Roma, Italy

†Theoretische Physik, Universität Paderborn, D-33098 Paderborn, Germany

e-mail: pecchia@ing.uniroma2.it

## ABSTRACT

Using a density functional approach we compute vibrations of molecules adsorbed on metal and semiconducting substrates and the electron-phonon coupling of these modes. A non-equilibrium Green's function approach is used to compute the partially coherent transmission in molecular junctions due to electron-vibration scattering [1], [2]. The electronic power dissipated into molecular vibrations allows to set a rate equation for the phonon population in the vibrational degrees of freedom of the molecule. The rate equation includes the phonon emission rate and phonon decay due to absorption, electron-hole pair production and dissipation into the contacting leads, which are assumed to behave as reservoirs. The rate of phonon decay is computed using a microscopic approach which includes a first-principle calculation of the coupling of the molecular modes with the vibrations of the contacts. In turn, the calculated phonon lifetime is used to correct the phonon propagator. As the power dissipated in the molecular junction depends non-trivially on the phonon populations, the equilibrium distribution under bias condition is a complex issue.

A self consistent loop allows to compute the steady state non-equilibrium phonon population of the molecular junction under bias condition. We find that the resulting average population is far from the equilibrium thermal distribution, frequently assumed in such calculations, which allows to obtain a mean temperature of the junction. As expected the deviations increase with applied bias.

As molecular electronics is moving to semiconducting substrates, it is relevant to explore and understand thermal issues. Metallic substrates have

in fact a very efficient channel of phonon damping into electron-hole pairs, while vibrational coupling to the substrate may not be very efficient due to ionic mass mismatch and a weaker bond. On the other hand the the electron-hole generation is prevented on semiconducting substrates, where instead vibrational coupling is stronger. We compare thermal behavior of organic molecules adsorbed on Si with molecules adsorbed on metallic substrates (Au or Cu) and determine the molecular temperature as a function of applied bias and for different temperatures of the thermostats.

## PRELIMINARY RESULTS

While the electrons cross the system, they interact with the molecular ionic vibrations from which they can be inelastically scattered. The electron-phonon scattering within the leads is not considered. The electronic system is described via a single-particle tight-binding Hamiltonian derived from Density functional theory (DFTB) [3], [4]. The method has been extended to the non-equilibrium Green's function (NEGF) approach [?]. In order to study the electron-phonon coupling we consider the first order diagram in the expansion of the Green's functions [6], [7] as

$$\Sigma_{ph}^{<, >}(\omega) = i \sum_q \gamma_q^2 \int \frac{d\omega'}{2\pi} G^{<, >}(\omega - \omega') D_{0,q}^{<, >}(\omega'), \quad (1)$$

where the  $D_{0,q}^{<, >}$  are the correlation functions related to the vibrational modes. The power dissipation is obtained using the virtual contact concept [1].

In this illustrative example we consider a dithio-phenyl molecule bridging two metal contacts. The analysis is restricted to those vibrational modes which give non-negligible incoherent

electron-phonon scattering [8]. These have frequencies of  $w_q = 756 \text{ cm}^{-1}$ ,  $w_q = 1147 \text{ cm}^{-1}$ ,  $w_q = 1182 \text{ cm}^{-1}$  and  $w_q = 1754 \text{ cm}^{-1}$ , respectively. The molecule and its vibrational modes are represented in Figure 1.

The coupling of the vibrational modes with the reservoirs gives a phonon decay rate of the order of  $10^{-13}$  sec. The self-consistent solution of the steady-state phonon population of the different modes gives the results shown in Figures 2 and 3.

Figure 2 shows the power dissipated and the non-equilibrium equivalent temperature of each mode as a function of applied bias for a contact temperature of 300 K. Similarly, Figure 3 is computed for a contact temperature of 100 K. It is possible to see that the highest energy modes heat up considerably, reaching a temperature of almost 600 K, while low energy modes are less sensitive. This is related to the larger power emitted in such modes and the fact that the power emitted depends on the population itself. Since the lowest modes have an equilibrium population larger than  $N=1$  the absorption probability becomes similar to the emission, decreasing the net emission rate.

## REFERENCES

- [1] S. Datta, *Electronic Transport in Mesoscopic System*. -: Cambridge University Press, 1995.
- [2] M. Galperin, M. Ratner, and A. Nitzan, "On the line widths of vibrational features in inelastic electron tunneling spectroscopy," *Nano Lett.*, vol. 4, p. 1605, 2004.
- [3] M. Elstner, D. Prezag, G. Jugnickel, J. Elsner, M. Haugk, T. Frauenheim, S. Suhai, and G. Seifer, "Self-consistent charge density tight-binding method for simulation of complex materials properties," *Phys. Rev. B*, vol. 58, p. 7260, 1998.
- [4] D. Porezag, T. Frauenheim, T. Kohler, G. Seifert, and R. Kaschner, "Construction of tight-binding-like potentials on the basis of density-functional theory: Applications to carbon," *Phys. Rev. B*, vol. 51, p. 12947, 1995.
- [5] A. Pecchia and A. Di Carlo, "Atomistic theory of transport in organic and inorganic nanostructures," *Rep. Prog. Phys.*, vol. 67, p. 1497, 2004.
- [6] A. Pecchia, A. Gagliardi, S. Sanna, T. Frauenheim, and A. Di Carlo, "Incoherent electron-phonon scattering in octanethiols," *Nano Lett.*, vol. 4, p. 2109, 2004.
- [7] Y. C. Chen, M. Zwolak, and M. Di Ventra, "Local heating in nanoscale conductors," *Nano Lett.*, vol. 3, p. 1691, 2003.
- [8] A. Pecchia, M. Gheorghie, L. Latessa, and A. Di Carlo, "Coherent phonon scattering in molecular devices," *J. of Comp. Elec.*, vol. 2, p. 251, 2003.

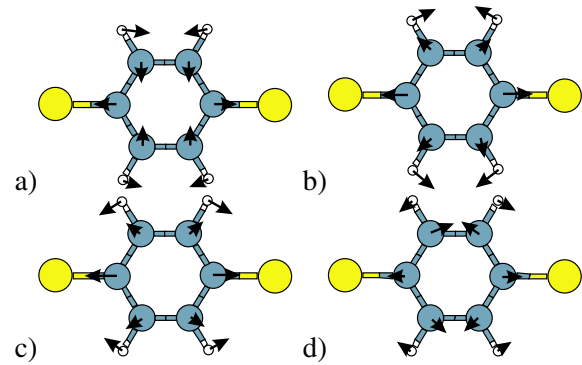


Fig. 1. Vibrational mode representation of the most important modes for incoherent electron-phonon scattering. a)  $756 \text{ cm}^{-1}$ , b)  $1147 \text{ cm}^{-1}$ , c)  $1182 \text{ cm}^{-1}$ , d)  $1754 \text{ cm}^{-1}$ .

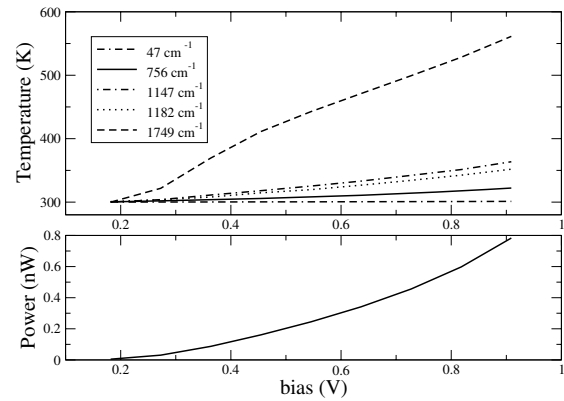


Fig. 2. Effective mode temperature and total power dissipated into the molecule as a function of bias for a reservoir temperature of 300 K.

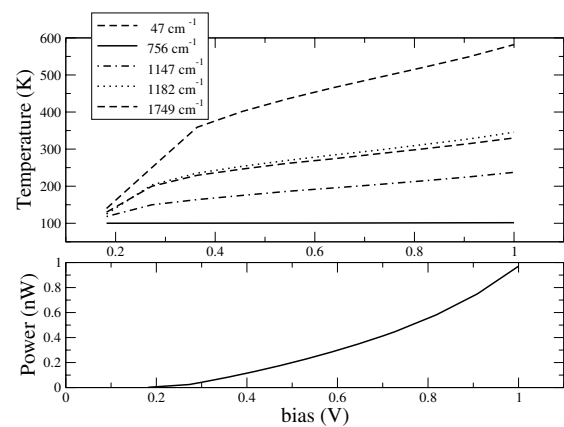


Fig. 3. Like figure 2 but for a reservoir temperature of 100 K

# Tight-Binding Calculations of Ge-nanowire Bandstructures

M. Bescond, N. Cavassilas\*, K. Nehari\*, M. Lannoo\*  
IMEP, UMR CNRS 5130 – 23, rue des Martyrs, BP 257, 38016 Grenoble Cedex, France  
\*L2MP, UMR CNRS 6137 – 13384 Marseille Cedex 20, France

e-mail: marc.bescond@enspg.inpg.fr

## INTRODUCTION

Recent development of CMOS industry has demonstrated the possibility to fabricate ultimate semiconductor nanowire MOSFET [1]. Since this device represents a promising candidate due to its better electrostatic control, it then becomes relevant to develop modeling tools based on atomistic and quantum methods capable to calculate nanowire bandstructures [2,3]. In this work, we study Ge nanowires using a tight-binding approach. We consider a  $sp^3$  model which includes the third-neighbor-interactions as well as the spin-orbit coupling. The present model was developed by Niquet *et al.* [4] and gave very good agreement with the  $sp^3d^5s^*$  [5] tight-binding approach and ab initio LDA calculations.

## RESULTS AND DISCUSSION

We investigate germanium nanowire bandstructures. The [100] orientation is first adopted as the wire axis and the square cross-section (size  $D$ ) is confined with four {100} faces (Fig. 1). The wire surfaces are saturated by hydrogen atoms in order to remove the dangling bonds. We consider the standard  $sp^3$  tight-binding scheme using a supercell periodically repeated along the nanowire axis and setting 4 orbitals (one  $s$  and three  $p$ ) on each Ge atom. In the  $sp^3$  model, each orbital interacts with the third neighbors whereas its  $sp^3d^5s^*$  counterpart, which has more orbitals per atom, only includes the nearest neighbor interactions. As a result, the number of orbitals and the number of neighbor-interactions compensate each other, and these two tight-binding models finally provide very close physical features. Figure 3 shows the energy bandstructures of the Ge nanowires previously described. For large cross-

sections ( $D > 4$  nm), the minimum of the conduction band is determined by four degenerated half-bands at the limits of the Brillouin zone ( $k_x \pm \pi/a$ , where  $a$  is lattice constant of the Ge) and represents the eight projected L-valleys of the bulk. When quantum confinement becomes stronger ( $D < 3$  nm) the L-valleys are lifted, showing that the effective mass approximation (EMA) is no longer valid. Figure 4 compares the energy bandgap for Ge and Si [2] nanowires (with the same surface configuration) as a function of the diameter  $D$ . For the two materials, the bandgap increases by reducing the cross-section as predicted by the EMA. Although the silicon bandgap is the largest, the increase of the Ge bandgap is more pronounced as expected from the transverse effective mass difference [6]. At the ultimate scaling, Ge nanowires have then a bandgap very close to the one of Si. We can note that such effect should have a beneficial impact on the leakage current of Ge nanowire-transistors. Figure 5 shows the hole effective mass of the valence band versus the diameter calculated from the  $E-k_x$  dispersion relations. Strong transverse confinement (*i.e.* diameters smaller than 4 nm) induces a significant variation of the hole effective mass from  $-0.20 \times m_0$  to  $-0.46 \times m_0$ .

Different wire orientations and confinement directions have also been studied. As a conclusion, we found that the physical properties of Ge (bandgap, effective masses) are more dependent to the quantum confinement than in Si and should have an important impact in the transport of ultimate Ge-nanowire MOSFETs.

## ACKNOWLEDGEMENT

This work is supported by the Network of Excellence SINANO founded by the European Commission under the EC Contract N° IST-506844.

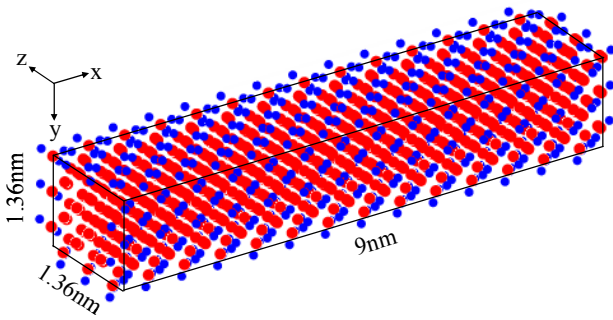


Fig. 1. Atomistic view of a Ge square nanowire [ $1.36\text{nm} \times 1.36\text{nm} \times 9\text{nm}$ ] playing the role of the conduction channel in the active region of the transistor. Germanium atoms are in red and the dangling bonds are saturated by hydrogen atoms (in blue).

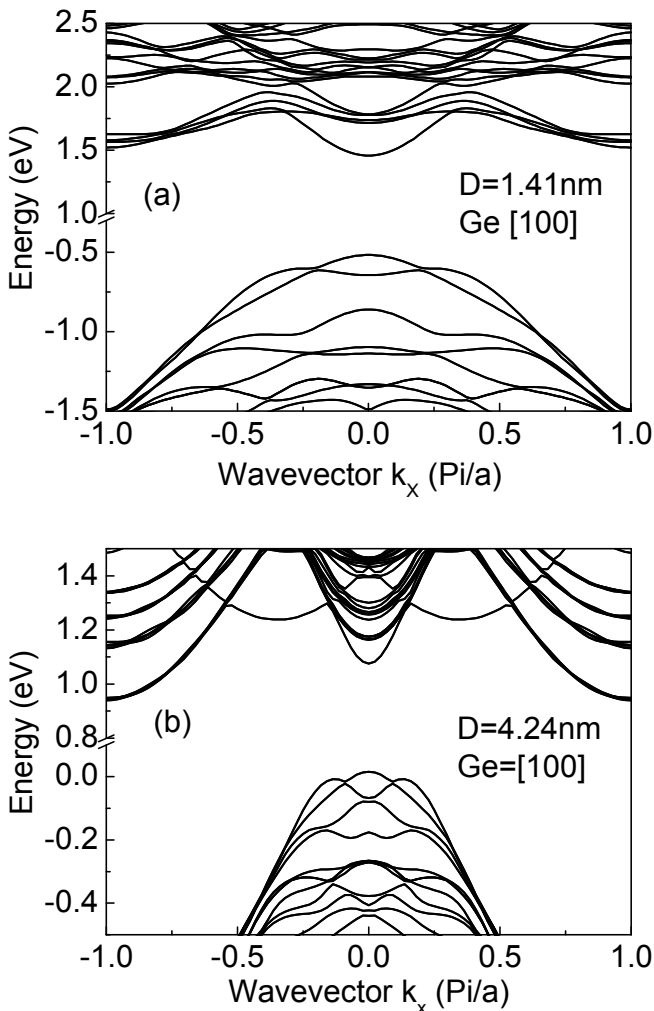


Fig. 2. Energy bandstructures of [100]-oriented Ge nanowires with two diameters: a) 1.41 nm and b) 4.24 nm. The transverse surfaces are  $\{100\}$  faces with dangling bonds pacified by hydrogen. The lattice constant  $a=0.5658$  nm and  $k_x$  is the wavevector along the nanowire axis.

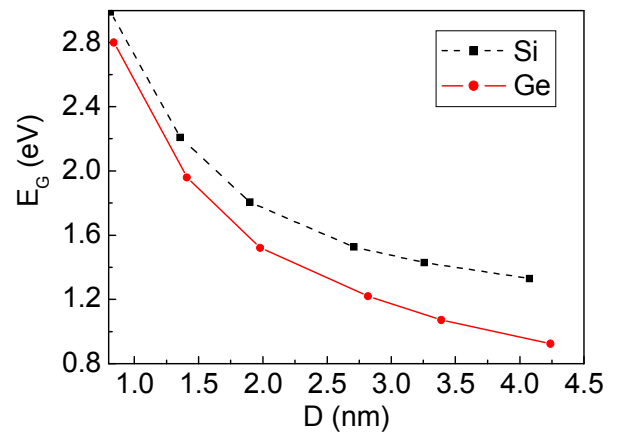


Fig. 3. Bandgap versus the diameter  $D$  of Ge and Si [2] nanowires with axis oriented along the [100] direction. The same surface configuration (orientation and boundary conditions) is considered for the both materials.

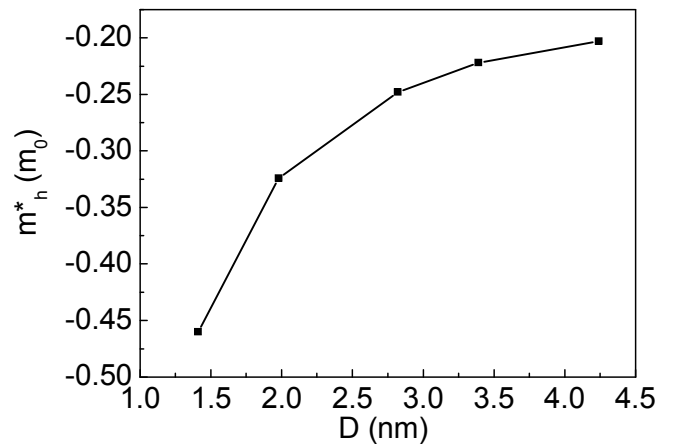


Fig. 4. Hole effective mass  $m_h^*$  at the  $\Gamma$  point in the valence band versus the wire diameter  $D$  for a [100]-oriented Ge nanowire.  $m_0$  is the free electron mass.

#### REFERENCES

- [1] D.D. Ma, D.S. Lee, F.C.K. Au, S.Y. Tong, S.T. Lee, *Small-diameter silicon nanowire surfaces*, Science **299**, 1874 (2003).
- [2] K. Nehari *et al.* *Influence of band-structure on electron ballistic transport in Silicon nanowire MOSFET's: an atomistic study*, Proc. ESSDERC, p. 225 (2005).
- [3] J. Wang, A. Rahman, G. Klimeck, and M. Lundstrom, *Bandstructure and orientation effects in ballistic Si and Ge nanowire FETs*, IEDM Tech. Dig., p. 537 (2005).
- [4] Y.M. Niquet, G. Allan, C. Delerue, and M. Lannoo, *Quantum confinement in germanium nanocrystals*, Applied Physics Letters **77**, 1182 (2000).
- [5] J.M. Jancu, R. Scholz, F. Beltram, and F. Bassani, *Empirical sp<sup>s</sup>\* tight-binding calculation for cubic semiconductors: general method and material parameters*, Physical Review B **57**, 6493 (1998).
- [6] M. Bescond *et al.*, *Ballistic transport in Si, Ge, and GaAs nanowire MOSFETs*, IEDM Tech. Dig., p. 533 (2005).

# GW Corrections of Energy Bandgaps for Coherent Transport Across Molecular Junctions

A. Pecchia\*, A. Gagliardi<sup>†</sup>, T. A. Niehaus<sup>†</sup>, Th. Frauenheim<sup>†</sup>, A. Di Carlo\*

\*Dep. of Electronics Engineering, University of Rome 'Tor Vergata', Via del Politecnico 1, 00133, Roma, Italy

<sup>†</sup>Theoretische Physik, Universitat Paderborn, D-33098 Paderborn, Germany

## ABSTRACT

Despite its mathematical complexity, the non-equilibrium Green's function method has gained a great popularity in recent years in the computation of transport across molecular junctions, mostly because of the elegant way in which, at least in principle, electron-phonon and electron-electron interactions can be treated in a unified and systematic way [1], [2], [3].

In most cases the system Hamiltonian is described within a single particle DFT approach. The advantage is the possibility to include several hundreds of atoms which are normally necessary in order to describe both contacts and molecule. The main problem of DFT is related to the description of the unknown exchange-correlation potential, usually approximated as that of a free electron gas. This tends to overestimate the metallic characteristics of the molecular states, producing among the others, an underestimation of the HOMO-LUMO gap, with relevant consequences to transport.

Therefore a better correlation potential is a central issue in order to achieve not only quantitative predictions of tunneling currents, but also correct qualitative trends. In order to improve this aspect many groups have tried to improve the DFT formalisms either using hybrid functionals, or including correlated transport [4], [5] and self-interaction corrections [6].

In this paper we present a different approach based on the GW approximation technique, related to Green's function theory [7], [8]. The system Hamiltonian is obtained within the spirit of a DFT-based tight-binding approach called DFTB [9]. The implementation of the GW method over DFTB in the plasmon-pole approximation is a fast and flex-

ible scheme [10]. This scheme is quite accurate in predicting correction to HOMO and LUMO states, in good agreement with the experimental workfunction and affinities. Unfortunately the quasiparticle energies degrade for energy levels of the molecule far from the gap. This is due to the approximations of our GW implementation and the use of a minimal basis set. However this lack of accuracy becomes problematic in transport calculations. Numerical artifacts have been observed, producing large broadening of the energy levels tailing in the energy gap considerably enlarging the transmission. We expect however the off-resonant transmission to be dominated by the position and broadening of the HOMO and the LUMO energies only, with little effect of the other levels. For these reasons we have worked around the problem by using the GW correction as a first step for the energy gap correction and implemented a simple scissor operator which rigidly shifts the valence and conduction set of molecular orbitals according to the GW prediction. This scheme was applied to calculations of various polymeric chains. Here we show results relative to poly-phenylene molecules represented in Figure 1.

Figure 2 shows the complex band structure calculated for an infinite poly-phenylene chain. The imaginary part of the complex bandstructure represents the tunneling decay for vanishing states and is related to off-resonant tunneling. The plot shows the difference between the full GW renormalization in comparison to the scissor operator.

Figure 3 shows the coherent tunneling across phenylene chains of varying lengths. The figure shows a significant increase of the HOMO-LUMO gap with a consequent decrease of tunneling probability at the Fermi level of the Cu-Molecule-Cu system used in our calculations.

## REFERENCES

- [1] S. Datta, *Electronic Transport in Mesoscopic System*. -: Cambridge University Press, 1995.
- [2] M. Galperin, M. Ratner, and A. Nitzan, *Nano Lett.*, vol. 4, p. 1605, 2004.
- [3] S. V. Faleev and M. I. Stockman, *Phys. Rev. B*, vol. 66, p. 085318, 2002.
- [4] A. Ferretti, A. Calzolari, R. D. Felice, F. Manghi, M. J. Caldas, M. B. Nardelli, and E. Molinari, *Phys. Rev. Lett.*, vol. 94, p. 116802, 2005.
- [5] N. Sai, M. Zwolak, G. Vignale, and M. Di Ventra, *Phys. Rev. Lett.*, vol. 94, p. 186810, 2005.
- [6] C. Toher, A. Filippetti, S. Sanvito, and K. Burke, *Phys. Rev. Lett.*, vol. 95, p. 146402, 2005.
- [7] F. Aryasetiawan and O. Gunnarsson, *Rep. Prog. Phys.*, vol. 61, pp. 237–312, 1998.
- [8] G. Onida, L. Reining, and A. Rubio, *Rev. Mod. Phys.*, vol. 74, p. 601, 2002.
- [9] T. Frauenheim, G. Seifert, M. Elstner, T. Niehaus, C. Kohler, M. Amkreutz, M. Sternberg, Z. Hajnal, A. Di Carlo, and S. Suhai, *J. Phys.: Condensed Matter*, vol. 14, p. 3015, 2002.
- [10] T. A. Niehaus, M. Rohlfing, F. Della Sala, A. Di Carlo, and T. Frauenheim, *Phys. Rev. A*, vol. 71, p. 022508, 2004.

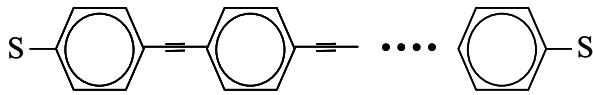


Fig. 1. Schematic representation of a poly-phenylene-dithiol molecule.

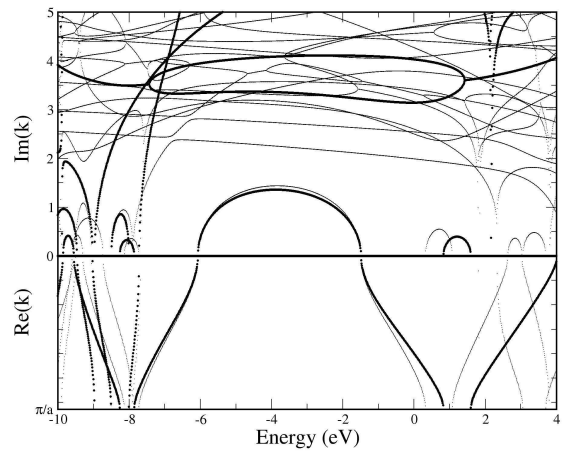


Fig. 2. Complex bandstructure of poly-phenylene. Thin curves correspond to a complete GW calculation, thick curves to the cut-shift operator based on the GW gap renormalization.

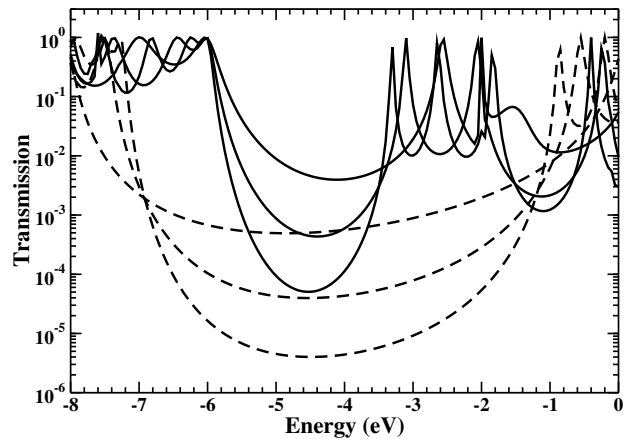


Fig. 3. Transmission across thio-phenylenes of increasing lengths (1 to 3 benzene rings). Solid lines correspond to DFT calculations, dashed lines to GW corrected results.

# Multi-Scale Approaches in Computational Materials Science

P. Weinberger

Center for Computational Materials Science, TU Vienna, Gumpendorferstr. 1a, 1060 Vienna, Austria  
e-mail: pw@cms.tuwien.ac.at

## INTRODUCTION

The term "multi-scale" is presently very much en vogue, one almost gets the impression that this term very often is simply used to emphasize the "importance" of a particular scheme or to impress an audience with a "buzz word". In the applied mathematics literature [1] it seems that essentially two types of multi-scale schemes are in discussion, namely "one shot" schemes in which one approach is combined in a consecutive manner with another one of different mathematical origin, and procedures by intertwining two such approaches "iteratively", or, to use a term more common in physics and chemistry, "selfconsistently".

Clearly enough the easiest way to define multi-scale procedures in particular in the realm of physics and chemistry would be to state that a combination of say two different kinds of differential equations is required. Although this in principle would be a valid definition it is too narrow, since, e.g., any use of density functional theory (DFT) requires already the application of two differential equations of different kind, namely the Kohn-Sham equations (effective Schrödinger or Dirac equation) and the Poisson equation, in an "iterative" manner. Surely enough nobody would call ab-initio type calculations in terms of the DFT a "multi-scale" procedure. This simple counter-example indicates that it is perhaps quite appropriate to discuss the concept of "multi-scale" only in the context of a particular field of research or discipline. In the present paper such a discussion is devoted to computational physics, in particular to computational materials science, since this is a well-established field of research in which many different types of computer simulations are performed.

## FORMAL DISTINCTIONS

Suppose multi-scale schemes refer to a combination of different levels in physics such as, e.g., by combining quantum mechanical approaches with phenomenological ones, or, phrased differently, by combining microscopical with macroscopical schemes. A "one shot" multi-scale procedure would then consist of a quantum mechanical calculation (e.g., within the framework of the DFT) followed by a phenomenological one, in which the results of the former are used; an "iterative" procedure combines both in a kind of selfconsistent manner [2 – 7]. In the latter case of course great care has to be taken that fundamental concepts are not violated (microcosmos versus macrocosmos), i.e., that only quantities can be varied that are well-defined on both "conceptual" levels.

Two typical situations will be discussed, namely augmenting a time-independent quantum mechanical scheme with (1) the concept of time (e.g., in terms of the phenomenological Landau-Lifshitz-Gilbert equation), and (2) with a method typical for statistical mechanics (e.g., Monte Carlo simulations based on ab-initio determined parameters), both schemes in fact can be operated in an iterative manner. Most frequently in computational materials science "one-shot" multi-scale procedures are used, in which typically physical properties of materials are calculated in terms of the results of ab-initio approaches. In order to be classified as a multi-scale approach the evaluation of these properties has to be based on a scheme, which by definition is different from a typical DFT method such as, e.g., the Kubo equation for evaluating electric and (magneto-) optical transport, i.e., by requiring "physically separate" computer program packages that in the end provide macroscopic quantities. Very

often also multiple combinations of "one shot" multi-scale procedures are used as for example in evaluating magnetic domain wall properties [8 – 10], the switching times (pico-second regime) in current induced switching [11 – 13], or, rotation and ellipticity angles in the magneto-optical Kerr-effect [14 – 16].

#### REFERENCES

[1] Multiscale Modelling and Simulation, Lecture Notes in Computational Science and Engineering, (Eds. S. Attinger and P. Koumoutsakos) Vol. 39, Springer-Verlag, 2004.

[2] B. Újfalussy, B. Lazarovits, L. Szunyogh, G. M. Stocks, and P. Weinberger, *Phys. Rev. B* 70, 1(R) (2004).

[3] J. Zabloudil, R. Hammerling, L. Szunyogh, P. Weinberger, *Electron Scattering in Solid Matter*, Springer Verlag, Heidelberg, 2004.

[4] V. Drchal, J. Kudrnovský, A. Pasturel, I. Turek, and P. Weinberger, *Phys. Rev. B* 54, 8202 (1996).

[5] F. Ducastelle, *Order and Phase Stability* (North-Holland, Amsterdam, 1991).

[6] I. Turek, V. Drchal, J. Kudrnovský, M. Šob and P. Weinberger, *Electronic Structure of Disordered Alloys, Surfaces and Interfaces*, Kluwer Academic Publishers, 1997.

[7] K. Binder and D.W. Heermann, *Monte Carlo Simulation in Statistical Physics* (Springer, Berlin, 1994).

[8] A. M. Kosevich, in *Modern Problems in Condensed Matter Sciences*, Vol. 17, edited by V. M. Agranovich and A. A. Maradudin (North Holland, Amsterdam, 1986), p. 495.

[9] J. Switalla, B. L. Gyorffy, and L. Szunyogh, *Phys. Rev. B* 63, 104423 (2001).

[10] S. Gallego, P. Weinberger, L. Szunyogh, P. M. Levy, and C. Sommers, *Phys. Rev. B* 68, 054406/1-8 (2003).

[11] P. Weinberger, *Physics Reports* 377, 281 - 387 (2003).

[12] P. Weinberger, A. Vernes, B. L. Gyorffy, and L. Szunyogh, *Phys. Rev. B* 70, 094401/1-13 (2004).

[13] A. Vernes, P. Weinberger, and L. Szunyogh, *Phys. Rev. B* 72, 054431/1-5 (2005).

[14] A. Vernes and P. Weinberger, *Phys. Rev. B* 70, 134411/1-11 (2004).

[15] I. Reichl, R. Hammerling, A. Vernes, C. Sommers, L. Szunyogh, and P. Weinberger, *Phys. Rev. B* 70, 214417/1-6 (2004).

[16] I. Reichl, A. Vernes, P. Weinberger, C. Sommers, and L. Szunyogh, *Phys. Rev. B* 71, 214416/1-5 (2005).

# Convergence of Density Functional Iterative Procedures with a Newton-Raphson Algorithm

J.W. Jerome\*, L.-H. Ye, P.R. Sievert, I.G. Kim, and A.J. Freeman

\* Department of Mathematics, Northwestern University, 2033 Sheridan Road, Evanston, IL 60208 USA  
 e-mail: jwj@math.northwestern.edu

Department of Physics, Northwestern University, 2145 Sheridan Road, Evanston, IL 60208 USA

## INTRODUCTION

State of the art first-principles calculations of electronic structures aim at finding the ground state electronic density distribution. The performance of such methodologies is determined by the effectiveness of the iterative solution of the nonlinear density functional equation. We present a novel approach based on the appropriate density mapping. We start with the simplest density functional model, i.e., the atomic Thomas-Fermi model.

Traditional mixing methods may not be appropriate for the larger complex systems of current technological interest. Mixing employs successive approximation iterates of a fixed point mapping. Such iterates are often found to converge very slowly or not at all. Attempting to resolve this, we have designed a quadratically convergent operator version of the Newton-Raphson method. From the minimization of the Thomas-Fermi functional, one obtains by variational methods a nonlinear integral mapping for which the ground state density function is a fixed point.

## THOMAS-FERMI MODEL

After the functional minimization, we obtain, for the atomic number  $Z$ , the following mapping for the nonnegative density  $\rho$  in SI units:

$$\frac{5\kappa}{3}\rho^{2/3}(\mathbf{r}) - \frac{e^2}{4\pi\epsilon_0} \frac{Z}{|\mathbf{r}|} + \frac{e^2}{4\pi\epsilon_0} \int d^3r' \frac{\rho(\mathbf{r}')}{|\mathbf{r} - \mathbf{r}'|} = 0, \quad (1)$$

where  $\kappa = 3^{5/3}\pi^{4/3}\hbar^2/(10m)$ . Here, the usual Lagrange multiplier  $\mu$ , which fixes the number of electrons, has been set to zero, as appropriate for the neutral atom [1]. After assuming spherical symmetry, we introduce a new variable  $Q(r) = r^{3/2}\rho(r)$  which regularizes the density at the origin. We then obtain the mapping in the form

$$Q^{\text{out}} = R \circ P [Q^{\text{in}}], \quad (2)$$

where

$$P[\bullet] \equiv \left[ \int_r^\infty dr' \bullet \left( \frac{r' - r}{\sqrt{r'}} \right) \right]^{3/2} \quad (3)$$

and

$$R[\bullet] = \frac{N}{4\pi \int_0^\infty dr' \bullet / \sqrt{r'}} \bullet, \quad (4)$$

where  $N$  is the number of electrons.

## OPERATOR NEWTON-RAPHSON METHOD

To apply the Newton-Raphson method, we introduce the mapping  $Y = I - R \circ P$ . In terms of this mapping, the iterates are given by  $Q^{\text{new}} = Q^{\text{old}} + \delta Q$ , where  $\delta Q$  is determined by the implicit relation

$$Y' [Q^{\text{old}}] \delta Q = -Y [Q^{\text{old}}]. \quad (5)$$

## DISCUSSION

We observed that  $\int_0^\infty dr \delta Q(r) \sqrt{r} = 0$ , which ensures the charge conservation for the Newton-Raphson algorithm. The figures are based upon simulations involving a damped Newton-Raphson implementation of Eq. (5) with simple integration rules. An iteration history is included. A discussion of the Thomas-Fermi model using the variable  $\chi = Q^{2/3}$  may be found in Ref. [2].

## ACKNOWLEDGMENT

This work was supported by the ONR (Grant No. N00014-05-C-0241) and NSF through its MRSEC program.

## REFERENCES

- [1] E. H. Lieb, *Reviews of Modern Physics* **54**, 603 (1981).
- [2] B. H. Bransden and C. J. Joachain, *Physics of Atoms and Molecules* (Prentice Hall, Harlow, 2003) Chap. 8.

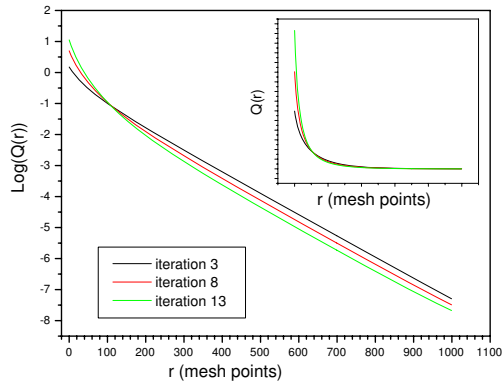


Fig. 1.  $Q(r)$  for the 3rd, 8th and 13th iterations in logarithmic scale. Inset represents the same data in linear scale.

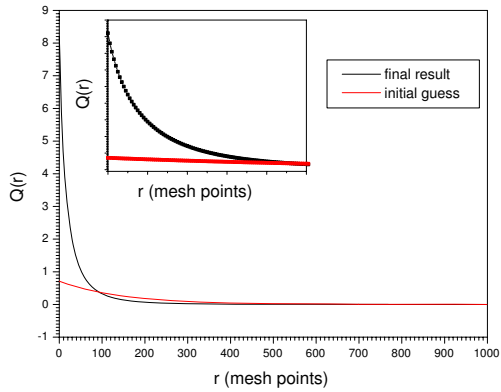


Fig. 2. Initial exponentially decreasing guess and the converged result. Inset magnifies the data around the origin.

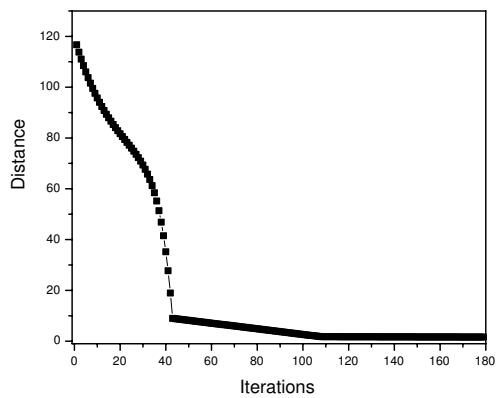


Fig. 3. Variation of successive iteration distances which is determined by  $\sum_m |Q^{(i)}(r_m) - Q^{(i-1)}(r_m)|$ .

# Simulating Biological Ion Channels using Computational Electronics Methods

Karl Hess

Beckman Institute, University of Illinois, Urbana, IL 61801  
e-mail: k-hess@uiuc.edu

In this presentation a review is given covering recent developments in the simulation of biological ion channels. Biological ion channels perform important functions ranging from the destruction of cancer cells to electrically enabling heart beat. Correspondingly a detailed understanding of ion channel function is desirable and the only way for this detailed understanding is offered by numerical simulation using a multi-scale simulation tool, for the processes that need to be understood range from the molecular dimensions of the constituting proteins to the macroscopic ion concentrations and membrane potentials. A multi-scale approach, as it is available for semiconductor devices in TCAD has not existed for ion channels in the past and is only now being developed in analogy to the TCAD tools. Ion channels have been treated in the past mainly by Molecular Dynamics as pioneered by K. Schulten and coworkers, a method very demanding with respect to computational resources. Alternatively the so called PNP method has been used that corresponds in essence to the drift diffusion approach (plus equation of Poisson) of semiconductor theory. In-between methods such as Brownian Dynamics have been applied by Jakobsson, Roux and others. Monte Carlo solutions of the Boltzmann transport equation have recently been developed by Ravaioli and his group.

The case that the methods of computational electronics may be used for ion channel simulation was mainly made by R. Eisenberg and is based on the fact that the ion transport properties in channels should be describable by the Boltzmann transport equation for a variety of reasons, including: (i) The large ion mass and corresponding small de Broglie wavelength around room temperature and (ii) the dilute ion concentrations and small ion numbers that are at any instance in a channel which permits one to think of an ion "gas". Counterarguments to the use of the Boltzmann transport equation center on the fact that chemical forces lead sometimes to ion localization and hopping and, more importantly on

the fact that the ions are mostly surrounded by water molecules. While treatments of ions in bulk water has been well researched and is largely understood, the case of a few water and ion molecules in narrow channels is not; except, of course, for the results of molecular dynamics methods that typically require large computational resources.

I will show in my review that the localization of ions in channels can be treated by the semiconductor methods developed by Shockley, Read and Hall. This method had not been applied by bio-physics researchers of ion channels and has been shown to expand the PNP method significantly for channels such as Gramicidin. Furthermore it will be shown that the Monte Carlo method as used in semiconductor electronics can be extended to include important ion properties such as their finite size and that this method may serve as a link between continuum methods and molecular dynamics. It will also be discussed that the question of how to treat water is still open and that interesting possibilities exist. On the molecular level a few examples will be given how other methods such as density functional theory are advantageously being used to understand natural and also certain artificial channels such as carbon nanotubes and how the knowledge of both types of channels currently expands through simulation.

In summary, this presentation will show the fruitfulness of an interdisciplinary approach to develop new simulation tools and to modify known tools from different research areas to achieve a more extensive and precise multi-scale simulation tool. A few insights will also be given on the interdisciplinary difficulties and the barriers that exist when such a broad subject is approached.



# Shockley-Ramo Theorem Measures Conformation Changes of Ion Channels and Proteins

Bob Eisenberg\* and W. Nonner

Dept of Molecular Biophysics, Rush University Medical Center, Chicago IL USA and

Mathematics and Computer Science Division, Argonne National Laboratory, Argonne IL USA

\*Dept of Physiology and Biophysics, Miller School of Medicine, University of Miami, Miami FL USA

\*e-mail: beisenbe@rush.edu

Theorems are rarely used in biology because they rarely help the descriptive experimentation to which biologists are devoted. A generalization of Kirchoff's current law—the Shockley-Ramo (SR) theorem [1-6]—seems an exception. SR allows interpretation of 'gating' currents associated with atomic scale charge movements within proteins.

Conformation currents have been measured in biology [7] and used to estimate atomic motions within proteins in hundreds of publications [8-14] since Hodgkin & Huxley [15] postulated their existence, and Schneider & Chandler observed them [16] with a clever algorithm that apparently has not been used in electrical engineering.

Despite this extensive experimentation, the relation of the currents recorded and underlying atomic motions within the protein was not understood. Energetic arguments have been used to link atomic motions to charge movements measured in an external circuit. Unfortunately, energetic considerations are best suited to isolated closed systems of classical thermodynamics where total energy (e.g., of the protein) is constant. Energetic considerations are difficult to use in open complex systems like a protein in a membrane, from which gating currents are measured. In such an open system, heat, matter, energy, and charge flow in unknown amounts in and out of proteins—and is stored in the protein on long time scales of inactivation, and desensitization. In open systems, electrical energy supplied to the electrodes for a few milliseconds is not easily related to the energy of the channel protein.

The Shockley-Ramo theorem replaces these energetic arguments and allows a new view of the conformation currents and internal dynamics of proteins in general. Fortunately, general conclusions of previous work are justified by the theorem, although specific molecular interpretations are not.

## SHOCKLEY-RAMO AND VOLTAGE CLAMP

The SR theorem relates the measured current to the atomic motion of charge

$$I = \frac{1}{1\text{volt}} \sum_j q_j \mathbf{W}(\mathbf{r}_j) \cdot \mathbf{v}_j \quad (1)$$

We follow Yoder et al (1997):  $\mathbf{v}_j$  and  $\mathbf{r}_j$  are the instantaneous velocity and position vectors, respectively, of the particle  $j$  with charge  $q_j$  when the clamped voltage  $E_m$  is applied.  $\mathbf{W}$  is the electric field that would be generated by removing *all* particle charges (mobile and fixed) from the domain and setting the clamped voltage to 1 volt. The only charges contributing to  $\mathbf{W}$  are (1) the charges needed to impose ground potential and 1 volt at the voltage electrodes and (2) the charges induced by the electrode charges on and in the dielectrics of the domain.  $\mathbf{W}$  is *not* the field that is present when the clamped voltage  $E_m$  is applied and the current is observed. The field resulting from the clamped voltage  $E_m$  enters the equation indirectly, through the positions  $\mathbf{r}_j$  and velocities  $\mathbf{v}_j$  that it imparts to mobile charged particles. The sum in Eq. (1) is over all mobile particle charges  $q_j$  in the domain; that is, it is the sum of all charges  $q_j$  moving with velocity  $\mathbf{v}_j$  at the time the sum is taken, including both those that belong to the channel protein and all ions in bath solutions and in the pore of the channel.

The measured current  $I$  of Eq. 1 is converted to the gating charge reported extensively in the biological literature by integrating over arbitrary trajectories that connect known starting locations  $\mathbf{r}_j$  of the particles to known ending locations  $\mathbf{r}_j$ . This integration yields the gating charge measured in an external circuit connected to the current electrodes:

$$Q = -\frac{1}{1\text{volt}} \sum_j q_j U(\mathbf{r}_j) - U(\mathbf{r}_j) \quad (2)$$

$U(\mathbf{r})$  is the potential of field  $\mathbf{W}$ , cf. Eq. (1).

An expression for external charge has been derived by Roux [17] for equilibriums systems without current flow with  $U = kT/e$ . Channel systems, however, function with large current flows and are usually nonlinear, often with  $U > kT/e$ .

Eq (1) & (2) can estimate charge movements in proteins from charge motions in any part of the system in series with the channel protein, provided that the movements of all charges (for example, all ions in the bathing solutions) are included in the summation. For a chosen domain (large or small), the SR theorem exactly computes the current measured in that geometry.

The optimal choice of domains for SR has not been determined. Optimizing the domain could be of considerable help. Simulations of channels are frustrating because most of computational effort concerns uninteresting ions in the baths, not the biologically and chemically important charges in the pore or channel protein. [10]

#### DISCUSSION

We include extensive literature references here because biological applications of SR [7, 18] are not well known to the electronics community.

The biological significance of ‘gating’ current perceived long ago is reinforced by our derivation using the SR theorem. Specific atomic interpretations are strongly affected, however, as discussed in detail in one case by [18]

Simulations of ionic current containing larger numbers of charged particles can be dramatically improved by use of eq. (1) to estimate current through a channel, instead of counting particles that cross boundaries. [10, 18-22]

We thank Marco Saraniti for reminding us of SR and showing us the modern references. We thank the community of computational electronics for its generous welcome to work on ions and channels.

#### REFERENCES

- [1] Yoder, P.D., K. Gärtner, U. Krumbein, and F. W., *Optimized terminal current calculation for Monte Carlo device simulation*. . IEEE Transactions on Computer-Aided Design, 1997. **16**: p. 1082-1087.
- [2] Yoder, P.D., K. Gärtner, and W. Fichtner, *A generalized Ramo-Shockley theorem for classical to quantum transport at arbitrary frequencies*. Journal of Applied Physics, 1996. **79**: p. 1951-1954.
- [3] Shockley, W *Currents to conductors induced by a moving point charge*. J of Applied Physics, 1938. **9**: p. 635-636.
- [4] Ramo, S., *Currents induced by electron motion*. Proc. IRE., 1939. **27**: p. 584-585.
- [5] Pellegrini, B., *Electric charge motion, induced current, energy balance, noise*. Phys Rev B 1986 **34**: p. 5921-5924.
- [6] Kim, H., H.S. Min, T.W. Tang, and Y.J. Park, *An extended proof of the Ramo-Shockley theorem*. Solid-State Electronics, 1991. **34**: p. 1251-1253.
- [7] Bottinger, E. and E. Furshpan, *Recording Flight Movements in Insects*. Science, 1952. **116**: p. 60-61.
- [8] Armstrong, C.M., *Sodium Channels and Gating Currents*. Physiological Reviews, 1981. **61**: p. 644-683.
- [9] Bezanilla, F., *The voltage sensor in voltage-dependent ion channels*. Physiol Rev, 2000. **80**(2): p. 555-92.
- [10] Chanda, B., O.K. Asamoah, R. Blunck, B. Roux, and F. Bezanilla, *Gating charge displacement in voltage-gated ion channels involves limited transmembrane movement*. Nature, 2005. **436**(7052): p. 852-6.
- [11] Nonner, W., *Effects of Leiurus scorpion venom on the "gating" current in myelinated nerve*. Adv Cytopharmacol, 1979. **3**: p. 345-52.
- [12] Roux, M.J., R. Olcese, L. Toro, F. Bezanilla, and E. Stefani, *Fast inactivation in Shaker K<sup>+</sup> channels. Properties of ionic and gating currents*. J Gen Physiol, 1998. **111**(5): p. 625-38.
- [13] Seoh, S.A., D. Sigg, D.M. Papazian, and F. Bezanilla, *Voltage-sensing residues in the S2 and S4 segments of the Shaker K<sup>+</sup> channel*. Neuron, 1996. **16**(6): p. 1159-67.
- [14] Sigworth, F., *Voltage gating of ion channels*. Quarterly Review of Biophysics, 1994. **27**: p. 1-40.
- [15] Hodgkin, A.L. and A.F. Huxley, *A quantitative description of membrane current and its application to conduction and excitation in nerve*. J. Physiol., 1952. **117**: p. 500-544.
- [16] Schneider, M. and W.K. Chandler, *Voltage-dependent charge movement in skeletal muscle*. Nature (London) 242:244-246, 1973.
- [17] Roux, B., *Influence of the membrane potential on the free energy of an intrinsic protein*. Biophysical Journal, 1997. **73**(December): p. 2980-2989.
- [18] Nonner, W., A. Peyser, D. Gillespie, and B. Eisenberg, *Relating microscopic charge movement to macroscopic currents: the Ramo-Shockley theorem applied to ion channels*. Biophys J, 2004. **87**(6): p. 3716-22.
- [19] Aboud, S., D. Marreiro, M. Saraniti, and R. Eisenberg, *A Poisson P3M Force Field Scheme for Particle-Based Simulations of Ionic Liquids*. J. Computational Electronics, 2004. **3**: p. 117-133.
- [20] Aksimentiev, A. and K. Schulten, *Imaging alpha-hemolysin with molecular dynamics: ionic conductance, osmotic permeability, and the electrostatic potential map*. Biophys J, 2005. **88**(6): p. 3745-61.
- [21] Saraniti, M., S. Aboud, and R. Eisenberg, *The Simulation of Ionic Charge Transport in Biological Ion Channels: an Introduction to Numerical Methods*. Reviews in Computational Chemistry (in press). 2005. **22**: p. 229-294.
- [22] van der Straaten, T.A., G. Kathawala, R.S. Eisenberg, and U. Ravaioli, *BioMOCA - a Boltzmann transport Monte Carlo model for ion channel simulation*. . Molecular Simulation, 2004. **31**: p. 151-171.

# Continuum versus Particle Simulation of Model Nano-Pores

C.Millar, S.Roy, O.Beckstein<sup>1</sup> and M.S.P.Sansom<sup>1</sup>, A.Asenov,  
Dept. Of Electronics and Electrical Engineering, University of Glasgow, Glasgow, U.K.  
<sup>1</sup>Dept. Of Biochemistry, University of Oxford, South Parks Road, Oxford, U.K.  
e-mail: c.millar@elec.gla.ac.uk

## INTRODUCTION

The class of biological macromolecules known as ion channels are becoming of great interest to physical scientists and engineers, as well as biophysicists and pharmacologists. Long term stability and the wide range of properties displayed by this large group of proteins, makes them one of the most popular contenders to bridge the gap between solid state and biological systems. However, many of the most basic properties of sub-nanometre pores are poorly understood.

We present a comparison between continuum and discrete simulation methods in model sub-nanometre pores. We demonstrate that continuous methods are not sufficient to model simple pore structures.

## SIMULATION METHODOLOGY

In order to make comparison as accurate as possible, all simulations were carried out on identical model structures (a 6Å square channel model pore is shown in Fig. 1). Materials are represented by blocks of either, ion accessible or inaccessible regions. In order to obviate effects from the geometry of the simulation domain, a single dielectric constant of 80 is applied to all regions of the simulation.

Continuous simulations have been performed using the commercial 3D Drift Diffusion (DD) simulator, Taurus [1]. Particle simulations were performed using the Glasgow self-consistent Brownian dynamics (BD) simulator [2]. Particle simulations with exact ions and ion splitting in micro particles (BDM) [3] were carried out to better compare with continuous methods. All simulations were performed using a bulk concentration of mobile Potassium ions of 1M and a continuous background charge density ensuing electro-neutrality of the solution.

## RESULTS

Due to the discrete nature of ions, the effect of inter-particle interactions becomes significant in channels with dimensions comparable to the characteristic length of the Coulomb interactions. Fig. 2 shows the single filing of ions in a model pore with 3Å cross-section. By comparing the temporal correlation in pore occupancy, we can attempt to quantify the impact of single filing on the permeation of ions through the pore.

Fig. 3 shows that the magnitude of the conduction mediated by single filing is strongly dependant on the diameter of the pore.

Single filing reduces the overall occupancy of the pore, which produces a drop in the conductivity when compared with continuous calculation. Fig. 5 shows a comparison between the calculated current using DD, BD and BDM. In a 3Å pore BD shows ~60% less current compared to DD. As expected the BDM simulations of the same structure show much closer agreement with DD. Fig. 5 and

Fig. 6 show the difference in average charge density through pores of 3Å and 12Å when compared to DD. Note that the BDM simulation compares well with DD but BD shows a very different charge distribution.

## CONCLUSIONS

While continuous methods are both efficient and accurate in many situations, great care must be taken when modelling particular transport through very small structures such as nano-pores. Due to the discrete nature of ionic transport continuum results can differ widely from discrete particle methods.

## REFERENCES

- [1] Synopsis Inc. <http://www.synopsis.com>
- [2] C.Millar, *3D Simulation Techniques for Biological Ion Channels*, PhD Thesis, University of Glasgow, 2004
- [3] C.Millar, A.Asenov and S.Roy, *Self-Consistent Particle Simulation of Ion Channels*, Journal of Theoretical and

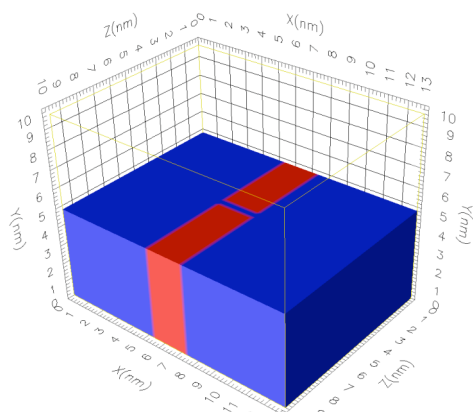


Fig. 1. The model pore simulation structure for a 6 Å square channel pore. Ion accessible water is shown in blue, inaccessible material is shown in red. Particle and electrostatic boundaries are applied at  $x=0\text{nm}$  and  $x=12.8\text{nm}$ .

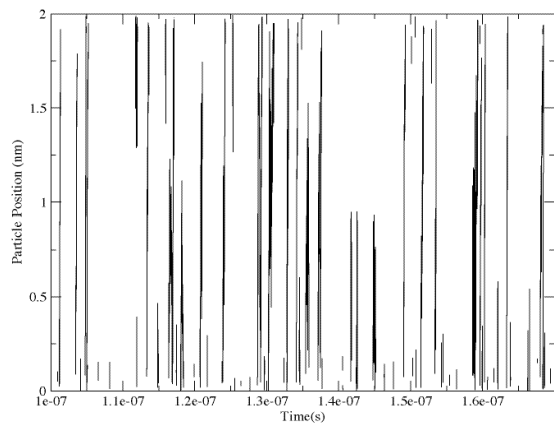


Fig. 2. Single filing of Potassium in a 3 Å pore

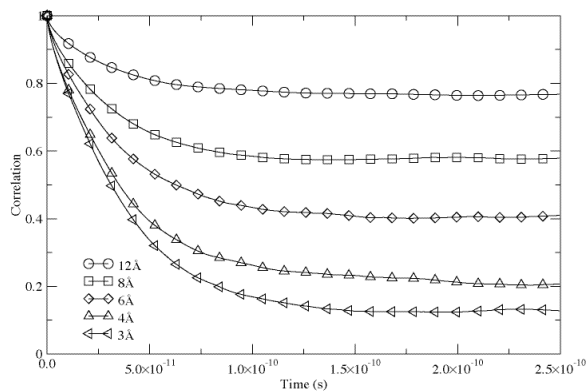


Fig. 3. Time correlation of model pore ion occupancies.

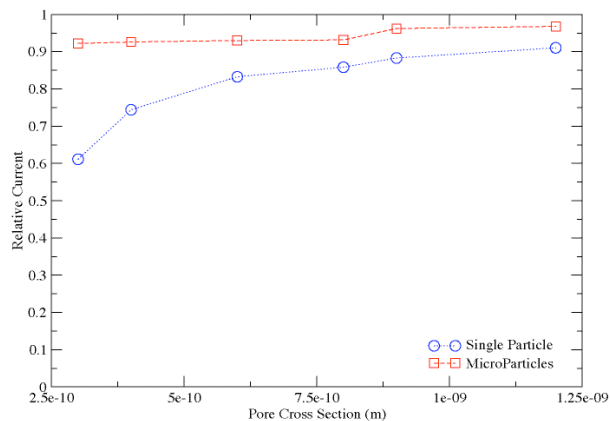


Fig. 4. Model pore current relative to Taurus drift diffusion simulation

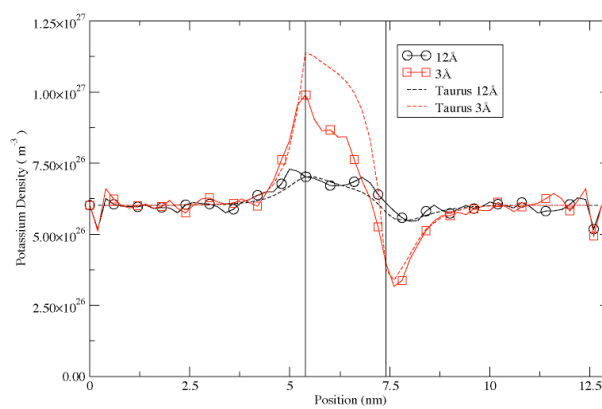


Fig. 5. Single particle Brownian simulation. Charge densities through the pore are compared to continuum simulation.

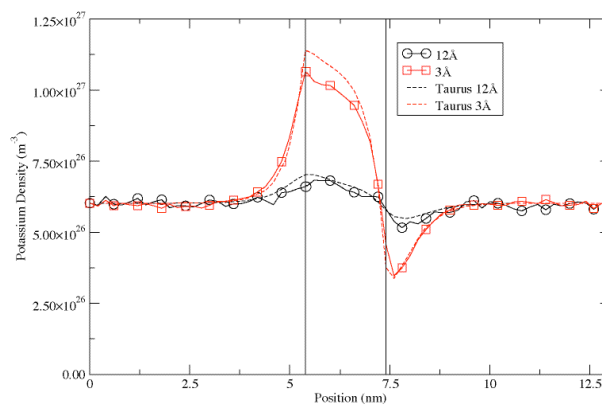


Fig. 6. Micro-particle simulation charge densities compared to continuum.

# Exploring Free Energy Profiles Through Ion Channels: Comparison on a Test Case

E. Piccinini, M. Ceccarelli\*, F. Affinito, R. Brunetti, and C. Jacoboni  
CNR-INFM S3 Research Center,  
via Campi 213/A, I-41100 Modena, Italy  
e-mail: piccinini.enrico@unimore.it

\*Dept. of Physics and Sardinian Laboratory for Computational Materials Science,  
University of Cagliari, Cittadella Universitaria, I-09042 Monserrato (CA), Italy

## ABSTRACT

The calculation of free energy profiles in proteins, and more specifically in ion channels, is a challenge in modern numerical simulations due to convergence problems associated with the electrostatics of the environment and to the modelisation of the fields acting on the permeating ions. The present study is aimed at comparing different simulation techniques, with the purpose of testing their capabilities and limits.

## INTRODUCTION

The translocation of single ions through cell membranes underlies many important physiological features, such as electrical signaling in neural and muscular systems [1], but despite of a large number of electrophysiological recordings many keypoints are still open questions.

Several steps forward to a deeper knowledge of these problems have been performed after the elucidation of the crystal structure of a bacterial potassium channel, KcsA from *Streptomyces Lividans* [2], when it became clear that only microscopic simulations can provide a detailed and quantitative description of many properties of such systems. From atomistic simulations an estimate of the potential of mean force (PMF) can be obtained and, from it, the energy profiles and barriers ruling the conduction process can be extracted.

## DISCUSSION

Different techniques aiming at the reconstruction of the PMF have been applied so far. We here show an application of three methods, namely Steered

Molecular Dynamics (SMD) [3], the most widely used Umbrella Sampling Method [4] and finally the recently appeared Metadynamics [5] to a test case, i.e. ions permeating the KcsA potassium channel. The purpose is to establish the degree of reliability and the convergence limitations of the three techniques through their application to the same system.

X-ray investigations, furtherly confirmed by molecular dynamics simulations, show that the conduction process in the KcsA channel involves a short and narrow region of the protein called selectivity filter. Two ions should always reside in this region in a stable conductive situation; at lower potassium concentrations the protein changes its conformation and switches to a non-conductive state. The conduction process involves the simultaneous and concerted movement of ions in a single-file, giving origin to a cycle of different occupancy configurations, as indicated in the sketch reported in Fig. 1. Each transition between different configurations is identified by a proper free energy barrier.

In this study we are interested in reconstructing the free energy profile associated to internal transitions, i.e. transitions not involving new ion entries or exits. Our simulation framework is composed by the KcsA atomic structure solved at 2.0 Å resolution [6], 8 potassium ions, 24 chlorine ions acting as counterions to keep the system electrically neutral, 500 octane molecules mimicking the cell membrane, and 8802 water molecules (SPC model), giving a total of approximately 35000 atoms. In the simulations we adopted the standard GROMACS force field, using the GROMACS [7] package for SMD and US and the ORAC [8] code for metady-

namics.

Preliminary results for SMD and US simulations are shown in Fig. 2 for a concerted motion of two ions where the energy profile has been reported to a comparable scale with a common reference. From both techniques an energy barrier of approximately  $2.5kT$  is found, which is consistent with analogous calculations available in the literature [9]. However the position of the minima obtained from independent implementations of the two methods is different, mainly for the situation after barrier crossing, which is higher for SMD. We address this problem to the intrinsic one-dimensional one-way forced motion of ions in SMD with respect to US. Some minor, but not less important differences due to the reduced set of coordinates used in the two simulations, are also present in trajectory analysis and can affect the final results.

The third proposed technique should be implemented to further validate the PMF reconstruction. Metadynamics, which is still under investigation at present time and whose results will be discussed at the Workshop, promises to be a more easily converging method and produces an estimate of the PMF without introducing artificial biases on ion dynamics. In fact once a set of appropriate coordinates is chosen, the dynamics is “driven” directly by the free energy profile of the system and it is biased only through the controlled summation of Gaussians centered on the particular trajectory followed. The sampled potential can provide directly quantitative informations on the original structure of the PMF.

## REFERENCES

- [1] B. Hille, *Ionic Channels of Excitable Membranes*, 2nd ed., Sinauer Assoc., Sunderland, MA, (1992).
- [2] D.A. Doyle, J. Cabral, et. al., *The structure of the potassium channel: molecular basis of  $K^+$  conduction and selectivity*, *Science* **280**, 69 (1998).
- [3] J. Gullingsrud, R. Braun, and K. Schulten, *Reconstructing potentials of mean force through time series analysis of steered molecular dynamics simulations*, *J. Comp. Phys.* **151**, 190 (1999).
- [4] B. Roux, *The calculation of the potential of mean force using computer simulations*, *Comput. Phys. Comm.*, **91**, 275 (1995).
- [5] A. Laio, and M. Parrinello, *Escaping free energy minima*, *Proc. Natl. Acad. Sci. USA*, **99**, 12562 (2002).
- [6] Y. Zhou, J. Morais-Cabral, A. Kaufman, and R. MacKinnon, *Chemistry of ion coordination and hydration revealed by a  $K^+$  channel-fab complex at 2.0 Å resolution*, *Nature*, **414**, 43 (2001).

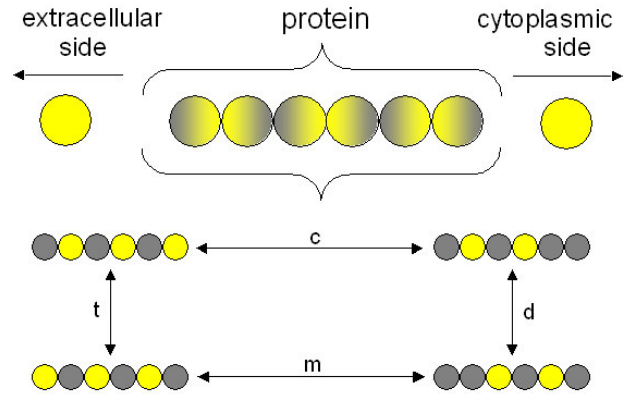


Fig. 1. Conduction cycle inside the channel. Ions move concertedly following a 4-step mechanism like entry (c), double movement (d), triple movement (t) and exit (m). Light grey balls represent potassium ions and dark grey balls stand for water molecules

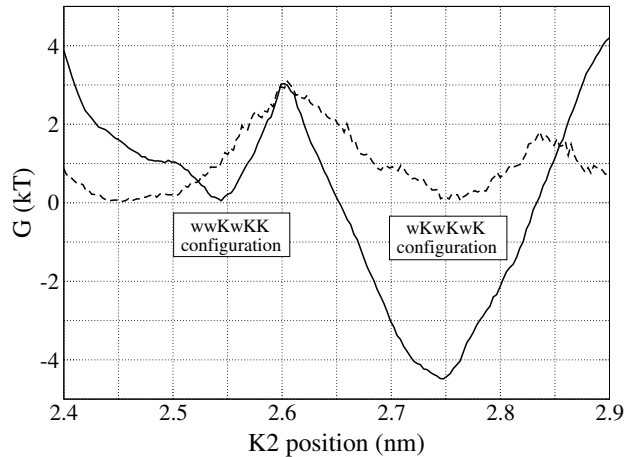


Fig. 2. Reconstructed PMF for internal double movement ( $wwKwKK$ ) $\rightarrow$ ( $wKwKwK$ ) Solid and dashed line refer to US and SMD, respectively.

- [7] E. Lindhal, B. Hess, and D. van der Spoel, *Gromacs 3.0: A package for molecular simulation and trajectory analysis*, *J. Mol. Mod.*, **7**, 306 (2001).
- [8] P. Procacci, E. Paci, T. Darden, and M. Marchi, *ORAC: A Molecular Dynamics Program to Simulate Complex Molecular Systems with Realistic Electrostatic Interactions*, *J. Comp. Chemistry*, **18**, 1848 (1997).
- [9] B. Roux, T.W. Allen, S. Bernèche, and W.Im, *Theoretical and computational models of biological ion channels*, *Q. Rev. Biophys.*, **37**, 15 (2004).

# Improving the Efficiency of BD Algorithms for Biological Systems Simulations

David Marreiro<sup>1</sup>, Yuzhou Tang<sup>2</sup>, Shela Aboud, Eric Jakobsson<sup>2,3</sup>, Marco Saraniti<sup>1,3</sup>

<sup>1</sup>Illinois Institute of Technology, Chicago, IL 60616

<sup>2</sup>University of Illinois, Urbana, IL 61801

<sup>3</sup>National Center for Design of Biomimetic Nanoconductors, Urbana, IL 61801

email: marrdav@iit.edu

## ABSTRACT

The simulation of complex biological systems such as ion channels require very efficient and accurate computer models. A Particle Particle Particle Mesh (P<sup>3</sup>M) force field scheme for molecular and Brownian dynamics simulations was developed to improve the original approach proposed by Hockney [1], allowing the simulation of non periodic systems by computing the Particle Mesh component in real space [2]. An assessment methodology for the error associated with the force computation within this framework was also developed in a previous work [3], together with the analysis of the accuracy and efficiency of the P<sup>3</sup>M approach.

In this work, this error analysis methodology is applied to the study of various integration schemes used in Brownian Dynamics algorithms. The duration of the timestep between two successive integrations of the particle motions governs the trade off between the accuracy of the particle trajectories and the time required for the simulation. Three algorithms have been compared for the integration of the full Langevin equation [4]. A first order Euler scheme [2], the Verlet like algorithm proposed by [5], and a novel Predictor Corrector scheme [6] have been implemented and analyzed using our assessment methodology. Our results, presented in Fig. 1 show the maximum value of the Radial Distribution Function (RDF) of K<sup>+</sup> and Cl<sup>-</sup> ions as a function of the timestep duration for the three integration schemes and an analytical calculation based on the Hypernetted Chain approximation [3]. It can be seen that a significant increase in the integration timestep, and a subsequent reduction in computational cost, is obtained with the Predictor

Corrector scheme, while maintaining an excellent accuracy for the description of both structure and dynamics of the electrolyte solution.

While the methodology discussed in [3] focuses on equilibrium properties of bulk electrolyte solutions, this work extends the analysis to dynamic properties of the solution as well as the structural aspects of inhomogeneous systems such as a lipid membrane. The conductivity of bulk KCl electrolyte solutions is computed with the Predictor Corrector integration scheme and compared to published data. Furthermore, the simulation of a dielectric membrane separating two electrolyte solutions and subjected to an applied potential is performed as well. The ionic distribution in this non periodic system, such as the KCl solution in Fig. 2 shows the predicted accumulation of ions of opposite signs on the membrane surfaces. This distribution is compared to the theoretical prediction of the double layer theory of Gouy and Chapman [7] to validate the highly efficient modeling scheme proposed here.

## REFERENCES

- [1] R.W. Hockney and J.W. Eastwood, *Computer Simulation Using Particles*, Adam Hilger, Bristol, (1988).
- [2] S. Aboud, D. Marreiro, M. Saraniti, and R. Eisenberg *Journal of Computational Electronics*, **3**, 117, (2004).
- [3] D. Marreiro, S. Aboud, M. Saraniti, and R. Eisenberg *Journal of Computational Electronics*, **4**, 179, (2005).
- [4] P. Turq, F. Lantelme, and H.L. Friedman *Journal of Chemical Physics*, **66**, 3039, (1977).
- [5] W.F. van Gunsteren and H.J.C. Berendsen *Molecular Physics*, **45**, 637, (1982).
- [6] Y. Tang, *1-D Brownian Dynamics Simulation with its Application in Study of Ion Channels*, Ph.D. thesis, University of Illinois at Urbana-Champaign, (2005).
- [7] R.S. Berry, S.A. Rice, and J. Ross, *Physical Chemistry*, Oxford University Press, (2000).

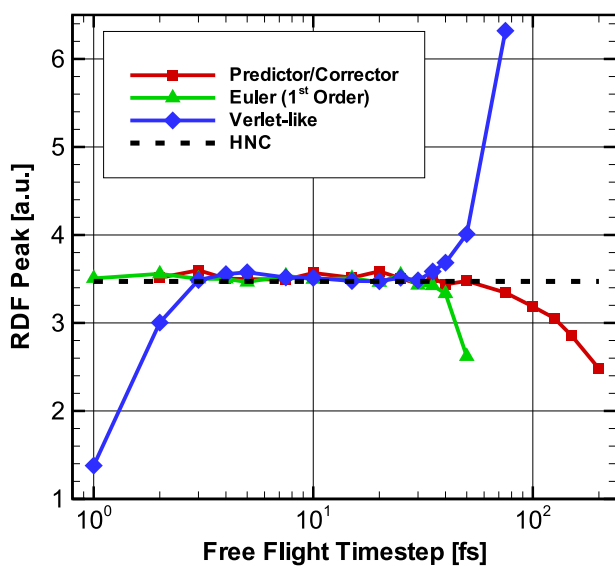


Fig. 1. Comparison of 3 different integration schemes for a range of integration timesteps. The RDF peak value for a bulk KCl solution of 0.30 M is used as a benchmark and compared to the analytical HNC result.

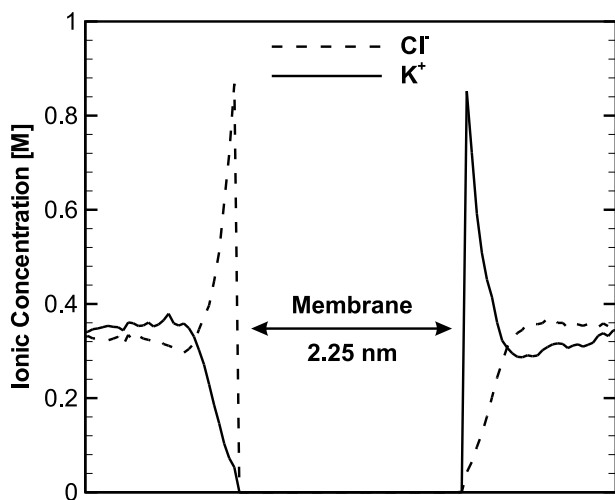


Fig. 2. Ionic distribution from a KCl 0.30 M solution in the vicinity of a dielectric membrane subjected to a potential of 1.0 V.

# Negative Bias Temperature Instability What Is It and Why Is It a Problem?

Dieter K. Schroder

Dept. of Electrical Engineering and Center for Solid State Electronics Research  
Arizona State University, Tempe, AZ 85287-5706, USA  
e-mail: schroder@asu.edu

## INTRODUCTION

Negative bias temperature instability (NBTI) commonly observed in *p*-MOSFETs, when stressed with negative gate voltages at elevated temperature, is a major reliability problem. We discuss the results of such stress on device and circuit performance and review interface traps and oxide charges, their origin, present understanding, and changes due to NBTI. Next we discuss the effects of varying parameters (hydrogen, deuterium, nitrogen, water, fluorine, and boron) on NBTI and conclude with the present understanding of NBTI and its minimization.

## NBTI MECHANISM

NBTI has been known since the very early days of MOS device development, having been observed as early as 1966 [1]. It occurs in *p*-channel MOS devices stressed with negative gate voltages at elevated temperatures and is the result of interface trap generation at the oxide/silicon interface and positive charge creation in the oxide. It manifests itself as absolute drain current and transconductance decrease and threshold voltage increase. The threshold voltage change typically exhibits the gate voltage, temperature, and time dependence

$$\Delta V_T = At^n \exp(\beta V_G) \exp(-E_A/kT) \quad (1)$$

NBTI is lower, in *n*-MOSFETs biased into accumulation. Typical stress temperatures lie in the 100-250°C range with oxide electric fields below 6 MV/cm, *i.e.*, fields below those that lead to hot carrier degradation. Such fields and temperatures are typically encountered during burn in, but are also approached in high-performance ICs during routine operation. Either negative gate voltages or elevated temperatures can produce NBTI, but a stronger and faster effect is produced by their combined action. In MOS circuits, it occurs most commonly during the “high” state of *p*-MOSFET inverter operation. It

leads to timing shifts and potential circuit failure due to increased spreads in signal arrival in logic circuits and matching problems in analog circuits. A fraction of NBTI degradation can be recovered by removing the stress voltage. Early MOS devices, containing only SiO<sub>2</sub> as the gate dielectric exhibited NBTI. Migration to nitrided oxides aggravated NBTI coinciding with a shift from research to production around 1999 after nitrided oxides became the industry standard in advanced CMOS.

NBTI-generated interface traps ( $D_{it}$ ) and oxide charges also have an adverse effect on 1/*f* noise, which is believed to be closely related to these charges. NBTI has also been reported for HfO<sub>2</sub> high-K insulators [2]. Figure 1 shows typical changes of threshold voltage and transconductance as a function of stress time [3]. Transconductance is related to mobility that is degraded during the stress.

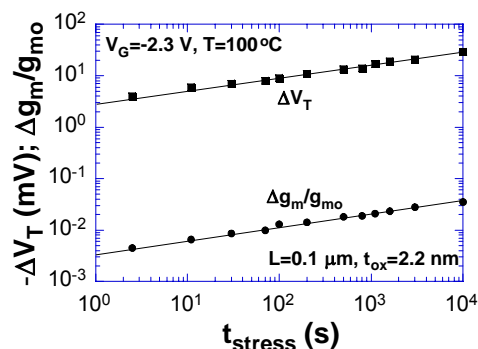
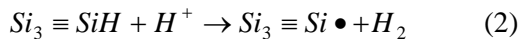


Fig. 1. Time-dependent threshold voltage and stress-induced transconductance increase. Data after Kimizuka et al. [3].

The exact model describing NBTI physics remains somewhat elusive at this time. One model assumes that *SiH* bonds at the SiO<sub>2</sub>/Si interface are broken by a combination of electric field, temperature, and holes. First-principles calculations show that positively-charged hydrogen or protons,  $H^+$ , react directly with the *SiH* to form an interface trap, according to the reaction [4]



where  $Si_3 \equiv SiH$  is a hydrogen-terminated interface trap and  $Si_3 \equiv Si \bullet$  is an interface trap with the dot representing the dangling bond. As shown in Fig. 2, the hydrogen is assumed to originate from phosphorus-hydrogen bonds in  $n$ -Si substrates. This model predicts reduced NBTI for  $n$ -channel devices due to the difficulty of breaking boron-hydrogen bonds in  $p$ -Si substrates.

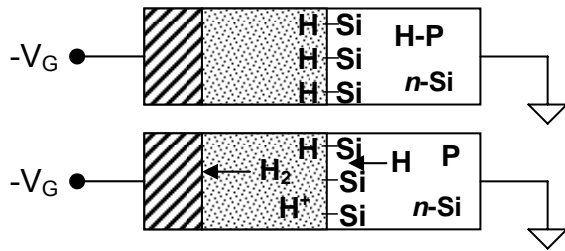


Fig. 2. Possible interface trap creation by hydrogen

The  $P-H$  bonds dissociate and the hydrogen on the way to the  $SiO_2/Si$  interface “picks up” a hole to become  $H^+$ , to react with the  $H$  from the  $SiH$  bond to form  $H_2$  leaving behind a positively charged Si dangling bond (or trapping center). The  $H_2$  diffuses from the interface into the oxide or poly-Si gate. It can later passivate a dangling bond by diffusing back to the interface when the stress voltage is interrupted. In another model, a hole, captured by a  $SiH$  bond, weakens the bond which then breaks to form an  $H_2$  molecule.

In the *reaction-diffusion model* the gate voltage initiates a field-dependent reaction at the  $SiO_2/Si$  interface that is initially limited by the  $SiH$  dissociation and  $D_{it}$  generation rate [5]. Later, the limiting rate is hydrogen diffusion from the interface into the  $SiO_2$ .

#### AMBIENT EFFECTS

*Hydrogen* is a common impurity in MOS oxides, being incorporated into the oxide during various phases of IC fabrication, *e.g.*, nitride deposition and forming gas anneal and is believed to be the main passivating species for Si dangling bonds. *Deuterium*, a hydrogen isotope, reduces NBTI due to its heavier mass or giant isotope effect. Deuterium can be introduced early or late in the device fabrication process. It is not clear yet, whether this improvement is enhanced at the low fields that are more typical of actual circuits. *Nitrogen*, commonly in-

corporated into gate oxides to reduce boron diffusion, improve hot carrier resistance, and increase the dielectric constant, can improve or degrade NBTI. It appears that low nitrogen densities in  $SiO_2$  improve NBTI due to strong  $SiN$  bonds at the  $SiO_2/Si$  interface. However, higher nitrogen density in the oxide degrades NBTI, possibly by trap formation. *Water* and *boron* in the oxide also degrade NBTI while *fluorine* improves it.

#### CONCLUSION

NBTI has become a significant reliability problem in today’s, thin-oxide integrated circuits. It degrades both digital (transconductance, delay time) and analog (current mirror, device matching) circuits. The type of circuit operation is important for NBTI, with ac degradation usually less than dc degradation because the gate voltage stress is interrupted for unipolar stress and reversed for bipolar stress. For sufficiently long dormant times, NBTI damage is totally healed. To minimize NBTI, one should start with low densities of electrically active defects at the  $SiO_2/Si$  interface, keep water out of the oxide, minimize stress and hydrogen content, and keep damage at the  $SiO_2/Si$  interface to a minimum during processing. Fluorine and deuterium improve NBTI, but it is important to ensure deuterium can get to the  $SiO_2/Si$  interface and passivate dangling bonds or replace the hydrogen with deuterium in  $SiH$  bonds.

#### REFERENCES

- [1] A. Goetzberger and H.E. Nigh, *Surface charge after annealing of Al-SiO<sub>2</sub>-Si structures under bias*, Proc. IEEE, **54**, 1454 (1966); Y. Miura and Y. Matukura, *Investigation of silicon-silicon dioxide interface using MOS structure*, Japan. J. Appl. Phys. **5**, 180 (1966); B.E. Deal, M. Sklar, A.S. Grove, and E.H. Snow, *Characteristics of the surface-state charge ( $Q_{ss}$ ) of thermally oxidized silicon*, J. Electrochem. Soc. **114**, 266 (1967).
- [2] K. Onishi, C. S. Kang, R. Choi, H.J. Cho, S. Gopalan, R. Nieh, E. Dharmarajan, and J.C. Lee, IEEE IEDM, 659 (2001).
- [3] N. Kimizuka, K. Yamaguchi, K. Imai, T. Iizuka, C.T. Liu, R.C. Keller, and T. Horiuchi, *NBTI enhancement by nitrogen incorporation into ultrathin gate oxide for 0.10  $\mu$ m gate CMOS generation*, IEEE 2000 VLSI Symp. 92 (2000).
- [4] L. Tsetseris, X.J. Zhou, D.M. Fleetwood, R.D. Schrimpf, and S.T. Pantelides, *Physical mechanism of negative-bias temperature instability*, Appl. Phys. Lett. **86**, 142103 (2005).
- [5] K.O. Jeppson and C.M. Svensson, *Negative bias stress of MOS devices at high electric fields and degradation of MNOS devices*, J. Appl. Phys. 2004 (1997); M.A. Alam and S. Mahapatra, *A comprehensive model of PMOS NBTI degradation*, Microelectron. Rel. **45**, 71 (2005).

# On Prospects of Computational Modeling of Reliability Phenomena

Muhammad A. Alam,  
Purdue University, West Lafayette, IN 47906, USA

Transistor design has been always been bracketed by the trade-off between performance and reliability. Yet, even a cursory review of the existing mainstream CAD tools shows that optimization of transistor performance (defined in terms of on current, on-off ratio, power dissipation, circuit delay, etc.) has been the primary focus on the CAD tools and reliability considerations have only been used to define a static guard-band (typically plus-minus 15%) for IC design. Although there have been a number of attempts to develop reliability simulators, these stand-alone reliability tools have never been integrated within the mainstream CAD software.

In recent years, however, the scenario is beginning to change. As scaling becomes difficult and design margin for high-performance IC becomes small, a static, worst-case guard-band limited design is both wasteful and unsustainable. Indeed, CAD tools that allow IC-specific optimization for both reliability and performance would allow additional design margin for a given technology node. In this presentation, I will review the development both TCAD models to predict performance degradation for specific operating conditions as well as IC-design approaches to optimize overall design in response to specific degradation. Below, we briefly discuss the status of modeling approaches to various degradation mechanisms.

*Negative Bias Temperature Instability* (NBTI) has been known to be an important degradation mechanism for PMOS transistors since 1970s. Jeppson et al. analyzed the NBTI phenomena within a Reaction-Diffusion (R-D) model and was able to explain the observed time-dependence ( $t^{0.25}$ ) during the stress phase as well as relaxation behavior when

the stress is removed. In this version of R-D theory, the negative gate bias on PMOS transistors allows a hole-assisted dissociation of Si-H bonds at the Si/SiO<sub>2</sub> interface. Atomic H diffuses away from the interface, leaving behind a depassivated, dangling Si bond that acts as interface trap. Recent refinement of the original R-D model have been able to interpret long term saturation characteristics, the relevance of measurement delay, frequency independence of AC lifetime, etc. The key feature of this refined R-D model is the realization that atomic H diffusion must be complemented by diffusion of molecular H<sub>2</sub> to interpret NBTI experiments consistently. The R-D model equations are now well defined and can be included in TCAD software. Finally, the R-D model is phenomenological and therefore the model parameters (e.g., forward and reverse dissociation rates, diffusion coefficients, etc.) must be extracted from experiments and/or first-principle theory. There have been considerable progress on both fronts in recent years.

There have also been some progress in translating the TCAD NBTI models to appropriate VLSI design algorithms such that the circuits can be optimized for a given power-delay product. Both logic as well as memory circuits have been considered. The Lagrangian-based transistor sizing, activity rebalancing, redundancy algorithms, etc. show considerable promise, although it is still too early to predict if the algorithms would be practical for large designs.

*Time-Dependent Dielectric Breakdown* is another important reliability consideration for modern IC design and has been particularly important since late 1990s as oxide thickness has scaled to sub

5nm regime. It is widely believed that under typical operating conditions, the dielectric breakdown is soft and the breakdowns only contribute to the total leakage current. This increase in gate leakage is a predictable function of operating conditions, oxide thickness, and area of the oxide and its implication on transistor performance can easily be analyzed with TCAD and SPICE models both for logic as well memory circuits. Many companies use in-house simulators to predict these performance characteristics, although there have been no academic or commercial software available for general use.

Although *Hot-Carrier Degradation* is no longer the dominant degradation mechanism for core technology it once was in late 1980s and early 1990s, the continued scaling of channel length makes HCI a relevant design consideration. In addition, HCI degradation remains an important design consideration for Flash memories as well high-voltage devices like LDMOS and DeMOS. The early models of HCI discussed the relative merits of hot electron and/or hot hole degradation and the research results were encapsulated in compact models suitable for TCAD analysis. The relatively compact form of the models helped define the SPICE model and have been used in HCI circuit simulator like BERT, RELY, and more recently GLACIER.

*Radiation Induced Single Event Upset (SEU)*, *Radiation Induced Gate Leakage (RILC)*, and *Radiation Induced Gate Rupture* are important design considerations for modern ICs and there have been consideration progress in modeling these radiation induced phenomena. For example, the accurate modeling of ion tracks have been demonstrated, the modeling of SEU with 3D device simulators now provides predictable estimates, and the RILC and radiation induced gate breakdown has been considered within the same framework as TDDB. In addition, the circuit implication of correlated multi-bit failure as well as development of appropriate error correction codes are active research areas, results from which can be translated to CAD models.

In short, the physics of many important reliability phenomena are now generally well understood

and therefore a systematic effort may allow development of a new generation of TCAD and CAD tools that can simultaneously optimize for performance and reliability of integrated circuits.

## REFERENCES

- [1] The original Reaction-Diffusion model was proposed by K. Jeppson and C. Svensson, JAP, 48(5), 2004, 1977. For more recent versions, see M. Alam and S. Mahapatra, Microelectronics Reliability, 45, 71, 2005. M. Alam, IRPS Tutorial, 2006, and S. Chakravarthi, Proc. of IRPS, 273, 2004. V. Reddy discusses TCAD and SPICE level models in IRPS 2002, p. 248 and NBTI tolerant VLSI design are discussed in B. Paul et al., EDL, 26(8), 560, 2005 and in S. Kumar et al., Int. Symp. Of Quality Electronic Design, 2006.
- [2] The model for gate leakage current due to soft breakdown is discussed in M. Alam and R. Smith, Proc. of IRPS, 406, 2003. B. Kaczer et al. IEDM p. 553, 2000 discusses the effects of soft-breakdown on logic circuits and Rodrigues et al. EDL, 23, 559, 2002 discusses the impact of soft-breakdown on SRAM circuit. The statistics of breakdown by percolation theory is analyzed in Degraeve et al., TED, 45, 904, 1998.
- [3] Early theoretical work on HCI degradation is due to C. Hu et al., Tran. Elec. Dev. 32, 375, 1985. Many of these models have been included in simulators like BERT, e.g., R. Tu et al., IEEE Trans. Comp. Aided Design, 12, 1524, 1993 and GLACIER, Symp. Of Quality Elec. Design, 73, 2000. New reliability issues involving Flash memory and their modeling by Monte Carlo simulation is discussed in P. Nair et al., IEDM, 403, 2004 and for HCI concerns of LDMOS devices, see P. Moens et al, ITED, 51, 623, 2004.
- [4] For a comprehensive review of TCAD analysis of SER, see P. Dodd et al., TDMR, 5(3), 343, 2005. The same issue contains a good model for circuit simulation by S. Walstra and C. Dai, p. 305. Multi-bit soft-error is discussed in J. Mai et al., Proc. of IEDM, p. 21.4.1, 2003.

# Probing Negative Bias Temperature Instability using a Continuum Numerical Framework: Physics to Real World Operation

Srinivasan Chakravarthi,  
Texas Instruments, USA

A quantitative model is developed that comprehends all the unique characteristics of NBTI degradation. Several models are critically examined to develop a reaction/diffusion based modeling framework for predicting interface state generation during NBTI stress. The model captures key NBTI features including recovery, experimental delay and frequency effects successfully.



# NBTI Product Level Reliability Challenges

H. Puchner

Technology R&D, Cypress Semiconductor, San Jose, CA95134, USA

e-mail: hrp@cypress.com

## INTRODUCTION

The gate dielectric has been the subject of constant improvement and innovation since the invention of the MOSFET transistor. The gate oxide is the major transistor component to control the transistor channel underneath with respect to leakage currents as well as saturation drive currents. The demand for higher drive currents and better performance has also pushed the gate oxide thickness towards its material limits, especially as we enter the 65nm technology node. The common candidate for the ultimate gate dielectric, silicon dioxide, is facing its structural boundaries and silicon dioxide/nitride stacks will become main stream for 65nm technologies and beyond. Since the introduction of heavily nitrated gate oxides the NBTI phenomena gained significantly on importance. Extensive work has been published on the NBTI reliability for standard DC test conditions ( $V_s, V_d, V_b=0.0V$ ) as well as under pulsed conditions. However, the role of hydrogen is still not fully understood [1]. Less work was published on the circuit level reliability degradation due to NBTI and the impact of relaxation. This work is analyzing all possible circuit level biasing conditions, maximum operating temperatures, and operating cycles to understand the impact on the circuit level. A simple analytical reliability model is referenced to estimate the threshold voltage shift during real operation conditions. This additional threshold voltage shift is counting against the design margin budget and, hence, has to be added to the SS corner at elevated temperature in order to evaluate the worst case circuit conditions.

## TRANSISTOR LEVEL RELIABILITY

Numerous transistor level reliability data and degradation curves have been published in the recent literature on NBTI. A typical threshold degradation plot for a 90nm PMOS transistor is shown in Fig.1. The same gate oxide measured in a package level testing system which has a relaxation between the stress and the measurement cycle of 700ms is shown in Fig.2. It can be clearly shown that relaxation gives false readings in the early phases of the stress experiment, whereas the

degradation curves converge at higher stress levels suggesting that recovery is limited at longer stress intervals. The recovery phenomenon has been reported extensively in the literature and was attributed to the re-passivation of the broken Si-H bonds at the Si-Gate oxide interface by molecular hydrogen [2]. Almost 40% of the damage recovers after 30min of relaxation (see Fig.3). Whether to achieve higher level of recovery depends on the local stress equilibrium at the gate oxide and the availability of hydrogen to passivate the Si-H bonds. Fig.4 gives a PMOS transistor which has been stressed up to a certain stress time at a constant bias and afterwards different stress bias conditions have been applied. It is worth noting that the new equilibrium established fairly quickly and in the case of a lower stress voltage a recovery of NBTI degradation occurred for the 1.35V stress condition. Recently, it has been shown that NBTI lifetime under low frequency stress can be enhanced by a factor of 10 as compared to the DC NBTI lifetime [3,4]. Similar results are given in Fig.5 and a comparison with simulation results using a reaction based diffusion model to predict the DC and AC degradation [5] is given.

## PRODUCT LEVEL RELIABILITY

Fig.6 shows the product level NBTI stress data for a low power asynchronous SRAM memory. We selected the access time as quality criterion to evaluate the NBTI lifetime. The memory is stressed at constant accelerated DC bias and temperature and different read points are acquired for the access time  $T_{aa}$  at 0.5, 1, 2, 3 and 4hours. The  $T_{aa}$  push out caused by NBTI stress is then used to extract the lifetime using a power law dependence.  $T_{aa}$  reflects well the NBTI related degradation behavior. The lifetime slope was correlated to single transistor data and showed good agreement.

## CONCLUSION

Transistor and product level reliability data have been presented and correlated. It is important to notice that product level reliability is at least an order of magnitude higher compared to the transistor level reliability lifetime.

## ACKNOWLEDGEMENT

We would like to thank the Device and Platform management of Cypress R&D for supporting this effort and for providing this excellent data especially O. Pohland, C.Cai, N.Mathur, D.Ho, and L. Hinh.

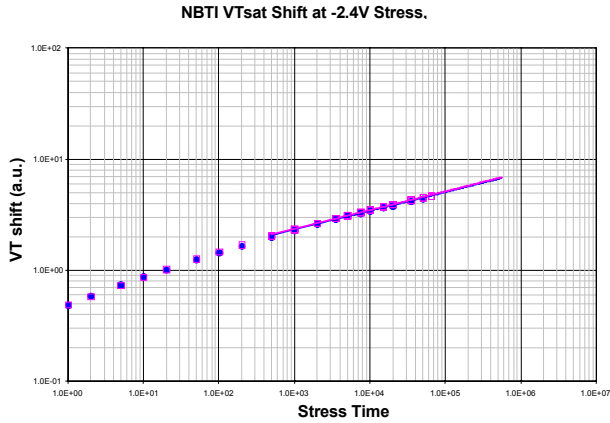


Fig. 1. Stress plot for extrapolation of NBTI lifetime for a 10/10 90nm PMOSFET device. The lifetime can be extrapolated for different Vtsat criteria.

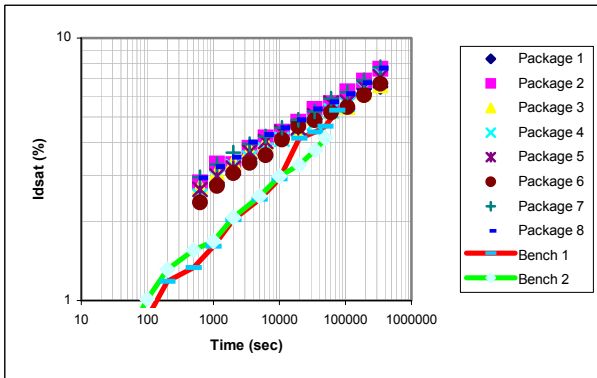


Fig. 2. NBTI Idsat degradation for different S-M-S methods. Package level (Symbols) and bench (lines) testing show the impact of relaxation at the early stress phases.

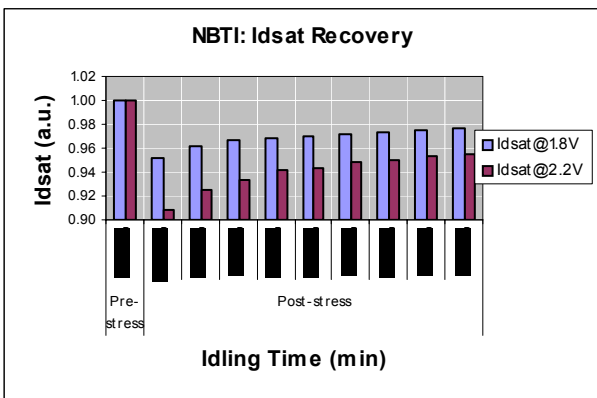


Fig. 3. Idsat recovery vs. relaxation time for 90nm PMOSFET. Almost 40% of the degradation recovers after 30min.

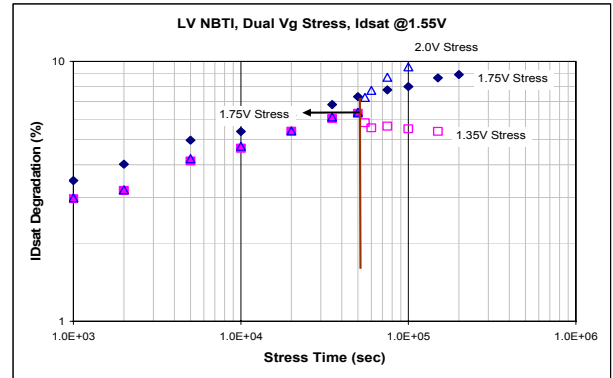


Fig. 4. NBTI degradation dependence on local stress equilibrium. Recovery can be found for switching to lower stress voltages.

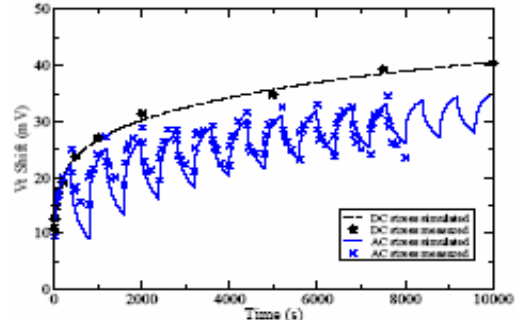


Fig. 5. NBTI degradation for a DC vs. 200kHz AC signal. Significant improvement is found for AC stressing.

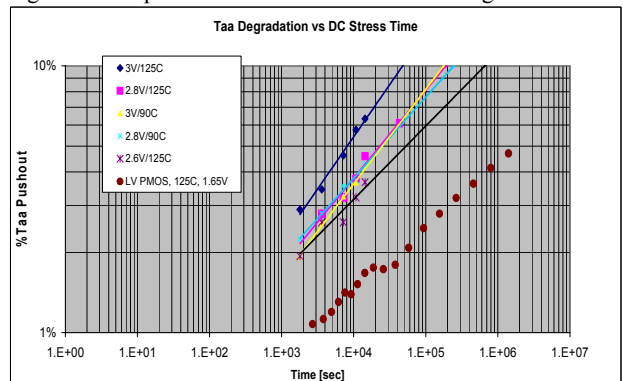


Fig. 6. Asyn SRAM memory Taa pushout due to NBTI stress for different temperatures and stress voltages .

## REFERENCES

- [1] V. Huard et al., "Evidence for hydrogen-related defects during NBTI stress in p-MOSFETs", IRPS 2003, pp.178-182, 2003
- [2] S. Mahapatra et al., "A predictive reliability model for PMOS bias temperature degradation", IEDM 2002 Technical Digest, pp.505-508, 2002.
- [3] Chen et al., "Dynamic NBTI of PMOS transistors and its impact on device lifetime", IRPS 2003, pp.196-202, 2003.
- [4] Abadeer et al., "Behavior of NBTI under AC dynamic circuit conditions", IRPS 2003, pp.17-22, 2003.
- [5] Wittman et al., "Simulation of Dynamic NBTI Degradation for a 90nm CMOS Technology", IRW 2005, pp.29-32, Lake Tahoe, 2005.

# Negative Bias Temperature Instabilities in HfSiO(N)-Based MOSFETs: Electrical Characterization and Modeling

M. Houssa<sup>1,2</sup>, M. Aoulaiche<sup>1,2</sup>, S. De Gendt<sup>1,3</sup>, G. Groeseneken<sup>1,2</sup>, and M.M. Heyns<sup>1,2</sup>

<sup>1</sup>IMEC, 75 Kapeldreef, B-3001 Leuven, Belgium

<sup>2</sup>Dept. of Electrical Engineering and <sup>3</sup>Dept. of Chemistry, University of Leuven, B-3001 Leuven, Belgium  
e-mail: houssa@imec.be

## INTRODUCTION

High- $\kappa$  gate dielectrics, in combination with metal gates, are extensively studied for the potential replacement of SiON/poly-Si stacks in advanced MOSFETs [1]. One of the most promising high- $\kappa$  gate oxides is HfSiON [1]. However, reliability issues concerning this material remain a challenge for CMOS devices scaling, in particular NBTI [2]. In this work, the impact of N incorporation in HfSiON layers on NBTI in SiO<sub>x</sub>/HfSiON/TaN pMOSFETs is investigated. Like in SiON-based devices, the presence of nitrogen is shown to strongly degrade NBTI immunity of the high- $\kappa$  gate stack. The enhanced degradation is shown to mainly arise from the generation of slow states in the gate stack. The kinetics, field and temperature dependence of fast and slow states generation are simulated, assuming the former defects to be Si dangling bonds at the Si/SiO<sub>x</sub> interface (so-called P<sub>b0</sub> centers) and the latter to be N-related traps present in the high- $\kappa$  stack.

## EXPERIMENTAL DETAILS

pMOSFETs with 1nm SiO<sub>x</sub>/2 nm HfSiO(N) gate stacks and TaN gates were fabricated using a conventional self-aligned flow. The gate stacks received post-deposition anneals in different ambient, i.e N<sub>2</sub>, O<sub>2</sub>, or NH<sub>3</sub>, or exposed to decoupled plasma nitridation (DPN).

## RESULTS AND DISCUSSION

The threshold voltage shifts of HfSiO(N)/TaN stacks are presented in Fig. 1 as a function of the electric field across the interfacial oxide, E<sub>ox</sub> (NBT stress performed at 125 °C). The nitrated stacks present a clear enhanced degradation, compared to the non-nitrated layers. The fraction of (fast) interface states generated during NBTI stress, estimated from charge-pumping measurements at 3 MHz, is presented in Fig. 2 for gate stacks annealed in N<sub>2</sub>, NH<sub>3</sub>, or exposed to DPN. The enhanced

degradation of the nitrated stacks is caused essentially by the generation of slow states, most likely resulting from the trapping of holes (injected from the channel) at N-related defects in the gate stack. The kinetics, electric field and temperature dependence of interface states (N<sub>it</sub>) generated in a typical HfSiON stack are presented in Fig. 3. These data can be reproduced (Fig. 4) by considering the generation of P<sub>b0</sub> centers during NBT stress, taking into account the dispersive transport of H<sup>+</sup> away from the Si/SiO<sub>x</sub> interface [3]. The kinetics, field and temperature dependence of the slow states (N<sub>ot</sub>) generated in a nitrated stack are presented in Fig. 5. The N<sub>ot</sub> generation probability, P<sub>gen</sub>=N<sub>ot</sub>/N<sub>inj</sub>, where N<sub>inj</sub> is the density of holes injected from the channel (assuming slow states are related to the trapping of holes in the gate stack) is shown in Fig 6 as a function of N<sub>inj</sub>, at different stress voltages. The increase of P<sub>gen</sub> with |V<sub>g</sub>| suggests that these defects are generated during the NBT stress, as opposed to filling of pre-existing traps. Considering the generation of N-related defects in the gate stack (like e.g. N dangling bonds), followed by hole-trapping at these defects, the kinetics and generation of N<sub>ot</sub> can be well reproduced [4], as shown in Fig. 7 and 8, respectively.

## CONCLUSIONS

NBTI degradation of HfSiON stacks was shown to be much enhanced when N was incorporated in these layers. The enhancement was correlated to generation of slow states, most likely related to hole trapping at N-related defects. The kinetics of fast and slow states was successfully simulated, taking into account the generation of P<sub>b0</sub> defects and N dangling bonds, respectively.

- [1] G. Wilk et al., J. Appl. Phys. **87**, 484 (2000).
- [2] M. Houssa et al., IEDM Tech. Dig. (2004), p. 121.
- [3] M. Houssa et al., Appl. Phys. Lett. **86**, 093506 (2005).
- [4] M. Aoulaiche et al., IRPS (IEEE, 2006), p.317.

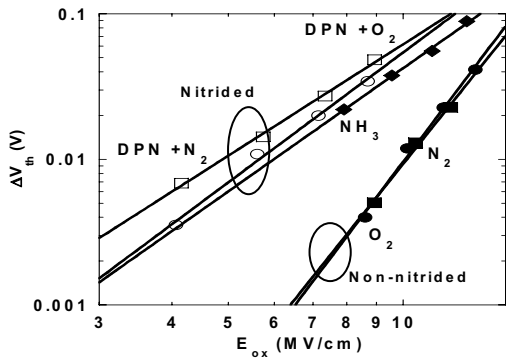


Fig. 1.  $V_{th}$  shifts as a function of oxide electric field of HfSiO(N)/TaN gate stacks.

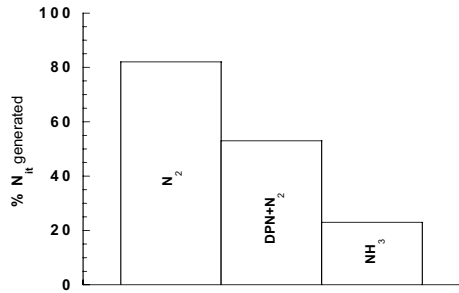


Fig. 2. Fraction of fast interface states,  $N_{it}$ , generated during NBT stress of HfSiO(N)-based gate stacks.

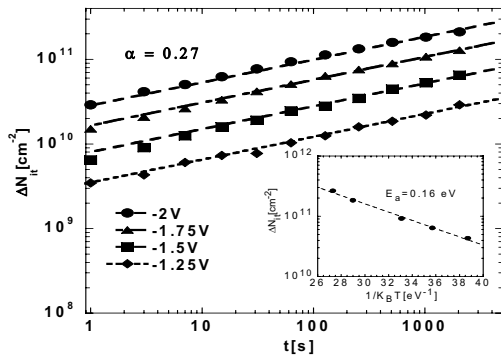


Fig. 3. Kinetics of fast interface states generation of a HfSiO(N)/TaN stack stressed at different  $V_g$ . Inset shows  $N_{it}$  as a function of inverse temperature.

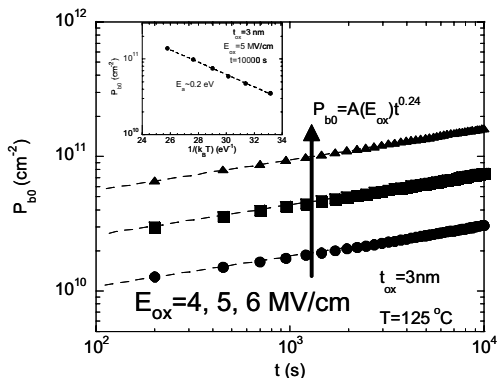


Fig. 4. Simulations of the kinetics and inverse temperature dependence (inset) of  $P_{b0}$  center generation within the dispersive  $H^+$  transport model [3].

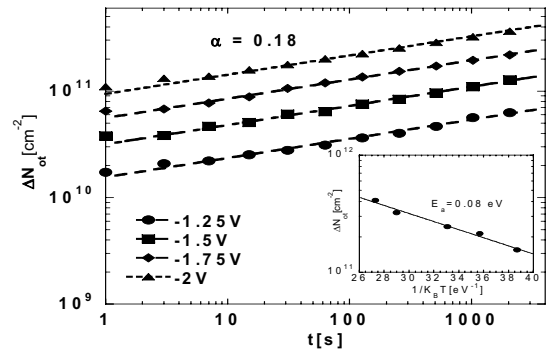


Fig. 5. Kinetics of slow states generation of a HfSiO(N)/TaN stack stressed at different  $V_g$ . Inset shows  $N_{ot}$  as a function of inverse temperature.

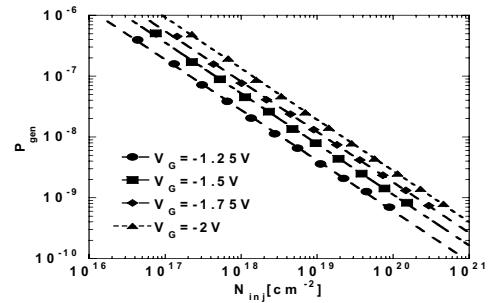


Fig. 6. Generation probability of slow states, as a function of the injected hole density during NBT stress, for different values of  $V_g$  stress.

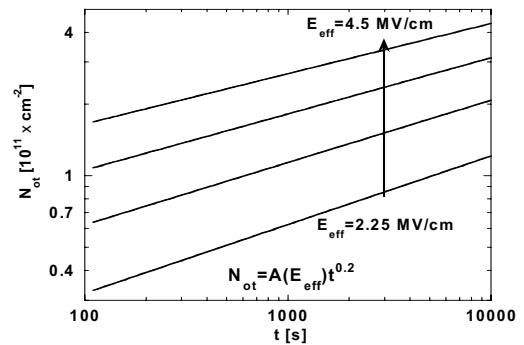


Fig. 7. Simulations of the kinetics of generation of slow states for different values of the electric field across the gate stack.

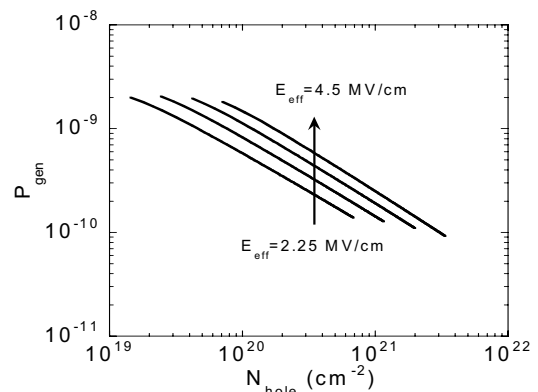


Fig. 8. Simulations of the generation probability of slow states, as a function of the injected hole density, for different values of the electric field across the gate stack.

# Physical Modeling of Negative Bias Temperature Instabilities for Predictive Extrapolation

Vincent Huard,  
Philips Semiconductors, Crolles, France

Based on recent developments in the analysis of the NBTI degradation, the emphasis will be put on three main topics. First, several measurement methodologies will be compared to figure out how to totally assess the degradation in spite of the presence of transient effects. Second, due to an optimized measurement approach, the consequences on the understanding of underlying physical mechanisms will be described. Finally, the consequences of the various contributions on extrapolation laws will be discussed.



# Reliability Issues in Power MOSFETs

M. Pölzl, M. Nelhiebel, S. Gamerith, J. Wissenwasser  
Infineon Technologies Austria, Siemensstr.2, 9500 Villach, Austria  
E-Mail: martin.poelzl@infineon.com

## ABSTRACT

Process influences on NBTI as observed on 30nm-GOX trench MOSFETs of two recent power technologies are presented. Both front end of line (FEOL) und backend of line (BEOL) processes are shown to have major effects on the interface quality. A p-channel device serves as demonstrator that nitrogen, introduced into the MOS system during a long-time, high-temperature diffusion step in FEOL processing, plays a major role in the NBTI characteristics. For a n-channel device, we discuss influences of the metallization/passivation BEOL stack on NBTI, but also on initial MOS characteristics and time dependent breakdown. Here, effects are attributed to the release of reactive hydrogen from PECVD deposited silicon-nitride layers.

## PROCESS EXPERIMENTS/RESULTS

In case of the p-channel Trench MOSFET a short summary of the different process experiments concentrating on the integration of a long-time, high temperature diffusion step is given in Table 1.

Our observations of parameter degradation of the investigated DMOS devices at NBTI are consistently explained by a diffusion-reaction model ([1], [2]) introduced by Jeppson and Svensson [1] in its basic form. Fig. 1 shows the power-law time dependence of the normalized changes of  $V_T$  for the different process experiments.

It is found that the degradation is less severe the better the gate oxide was sealed during the body-diffusion step (see fig.1). Actually the fabrication process influences the density of latent defects. As the sealing of the gate oxide during the body drive strongly influences the amount of latent defects we considered the possibility of an atmospheric species intruding into the MOS system during the drive, increasing the latent defect density. The model of varying latent defect density is supported by the long-term drift data in fig.1 as saturation is observed within stress time at different levels.

The device for the BEOL study is a n-channel trench MOS-FET with a 30 nm oxide. Over the trenches a pre-metal dielectric (PMD) is deposited and structured, isolating gate poly from the aluminum source metallization. The metallization stack is completed by inter-level dielectric (ILD) and power metal. For experiments, a PECVD-SNIT (silicon nitride) layer was integrated by different means to the BEOL stack, or the BEOL stack completely omitted (M1 control wafer).

There is a negative correlation between virgin-device interface quality and NBTI characteristics as illustrated in Figs. 2 and 3. The overall GOX-quality defined by TDDB performance is worse when the virgin interface state density is low (Fig. 2). The evolution of  $D_{it}$  upon NBTI stress is displayed in Fig. 3: The ILD/SNIT wafer starts on a very good  $D_{it}$  level, but its  $D_{it}$  rapidly increases and after 15000 s of stress amounts to roughly three times the  $D_{it}$  of the M1 wafer.

## DISCUSSION

For FEOL experiments the differences in the absolute values of the degradation are ascribed to different densities of latent defects at the Si-SiO<sub>2</sub> interface of virgin devices. A long-time high temperature body diffusion step in nitrogen was detected as the key process concerning NBTI degradation. Based on this observation the role of nitrogen intruding into the system and enhancing the formation of latent defects is discussed.

With the BEOL experiments we demonstrated that deposited silicon nitride layers act as a source of reactive hydrogen [3] with significant influence on the gate oxide of a trench MOS transistor. On the one hand, this reactive hydrogen is more efficient than standard forming-gas tempering and leads to well annealed Si-SiO<sub>2</sub> interfaces and good masking of positive bulk-oxide charge. On the other hand the reactive hydrogen has adverse effects on the reliability of the devices, both concerning drift behavior under negative bias temperature stress and

dielectric lifetime measured by TDDB tests. Therefore, backend of line processing must be carefully optimized in order to obtain technologies which show a correct device performance together with the required high reliability.

ACKNOWLEDGEMENTS

We would like to express our sincere thanks to all the contributors to the NBTI investigations (fab, characterisation, technology development and Q department).

REFERENCES

[1] Jeppson K. O., Svensson C. M. Negative bias stress of MOS devices at high electric fields and degradation of MNOS devices. J. Applied Physics, vol 48(5) 2004-14 (1977)  
 [2] Ogawa S., Shiono N.. Generalized diffusion-reaction model for low-field charge-build up Instability at the Si-SiO<sub>2</sub> Interface. Physical Review, vol, 51(7), 4218-30 (1995)  
 [3] H.K. Sii, J.F. Zhang, R. Degraeve and G.Groeseneken, Relation between hydrogen and the generation of interface state precursors, Microelectron. Eng. 48 (1999) 135

EXPERIMENT	LAYER ON GATE OXIDE DURING BODY DRIVE
body drive before poly deposition	none
body drive before poly deposition + nitride	7 nm CVD-Si <sub>3</sub> N <sub>4</sub>
standard	p+polysilicon in trench (recessed)
nitride on poly	p+polysilicon in trench + 7 nm CVD-Si <sub>3</sub> N <sub>4</sub> (recessed)
body drive after poly deposition	950 nm p+polysilicon

Table 1: overview of FEOL process experiments

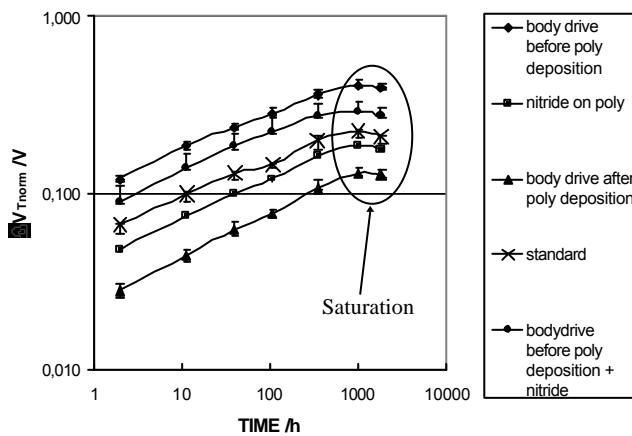


Fig. 1. Time dependence of  $\Delta V_{Tnorm}$  (shift to more negative values at  $I_d=1$  mA) after 4 MV/cm, 175°C NBTI.

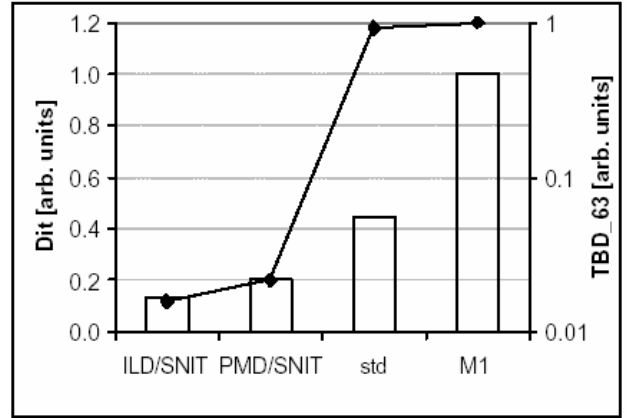


Fig. 2. D<sub>it</sub> of virgin device revealed by charge pumping measurements (bars) and characteristic TBD (diamond/line). Roughly, the higher the interface trap density on the virgin device, the better the TDDB performance.

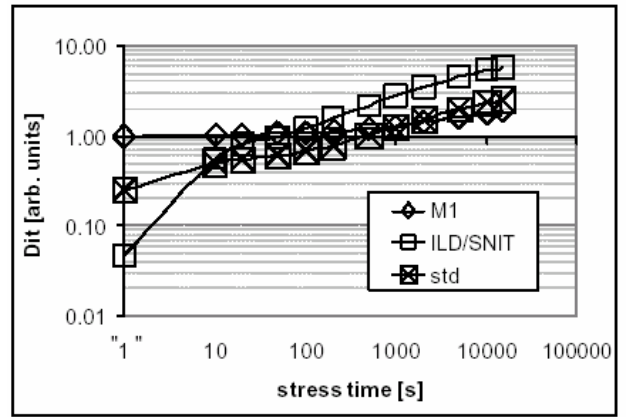


Fig. 3: Evolution of the D<sub>it</sub> during NBTI for M1-control (diamonds), ILD/SNIT (squares), and standard process (crossed squares) wafers, respectively. In contrast to the M1 wafer, the SNIT wafer starts from a good level, but traps are rapidly revealed and at the end it is worse than on the M1/std wafers. The values at time "1" are the D<sub>it</sub> values of the virgin devices.

# Deep Level Defects Involved in MOS Device Instabilities

P.M. Lenahan

Dept ESM, The Pennsylvania State University, University Park, PA 16802 USA  
e-mail: pmlesm@enr.psu.edu

## BACKGROUND

Several instabilities play important roles in limiting the reliability of metal-oxide-silicon field effect transistors (MOSFETs).<sup>1-7</sup> These instabilities almost always involve the creation of interface traps at the Si/dielectric boundary and also frequently involve deep level centers within the oxide. Important instabilities have involved the response of MOSFETs to ionizing radiation, hot carrier injection, high oxide field stressing, and the response of p-MOSFETs to moderately elevated temperature and negative gate bias, the negative bias temperature instability (NBTI).

The deep level defects involved in these instabilities can be observed by both conventional electron paramagnetic resonance (EPR)<sup>8-10</sup> and electrically detected magnetic resonance (EDMR) generally with spin dependent recombination (SDR).<sup>10-13</sup> The EDMR approach can allow studies of deep level defect structures in fully processed MOSFETs. Present day conventional EPR and SDR offer sensitivities close to that of standard MOS electrical characterization tools.

## THIS PRESENTATION

This presentation will include a very brief introduction to relevant magnetic resonance techniques with emphasis on SDR detected EDMR. The presentation will also include an introduction to trapping centers typically observed in technologically relevant instabilities.<sup>10,13-26</sup> This introduction will include the fairly well understood Si/dielectric interface  $P_b$  centers,  $\text{SiO}_2$  deep level defects called  $E'$  centers, several nitrogen related defects and some recently observed defects in  $\text{HfO}_2$  based MOSFETs. This introduction will include a brief description of defect structure and energy levels primarily though not exclusively obtained

through EPR studies. A major focus of this presentation will be recent magnetic resonance results on NBTI in conventional  $\text{SiO}_2$  and nitrated  $\text{SiO}_2$  based devices<sup>21-25</sup> as well as some preliminary results on negative bias stressing of  $\text{HfO}_2$  based metal gate transistors.<sup>26</sup>

The conventional  $\text{SiO}_2$  and nitrated  $\text{SiO}_2$  device NBTI studies indicate that several silicon "dangling bond" defects can clearly play dominating roles in this technologically important problem and further indicate that processing, in particular the introduction of nitrogen into the oxide, leads to gross differences in the structure of the performance limiting defects. Some very recent preliminary EDMR results on negative bias stressed metal gate  $\text{HfO}_2$  transistors<sup>26</sup> will also be included in this presentation.

In addition to the introduction to defect structure and electronic properties, a brief discussion of some relevant aspects of the statistical mechanics of the point defects will also be provided.<sup>27</sup>

## ACKNOWLEDGEMENT

The author is indebted to many collaborators but specifically wishes to thank the following for particularly useful contributions in preparation of this presentation: J.P. Campbell, C.J. Cochrane, J.T. Ryan, S. Krishnan, A.T. Krishnan, G. Bersuker, and J.F. Conley Jr.

## REFERENCES

- [1] T.P. Ma and P.V. Dressendorfer, *Ionizing Radiation Effects in MOS Devices and Circuits*, John Wiley and Sons, New York (1989).
- [2] T.R. Oldham, *Ionizing Radiation Effects in MOS Oxides*, World Scientific, Singapore, London (1999).

- [3] P. Heremans, R. Bellens, G. Groeseneeken, and H.E. Maes, *Consistent Model for the Hot Carrier Degradation in n-Channel and p-Channel MOSFETs*, IEEE Trans. Electron Devices **ED-35**, 2194-2209 (1988).
- [4] T.H. Ning, P.W. Cook, R.H. Dennard, C.M. Osburn, S.E. Schuster, and H.N. Ya, *1 $\mu$ m MOSFET VLSI Technology Part IV: Hot Electron Design Constraints*, IEEE Trans. Electron Devices **ED-26**, 346-353 (1979).
- [5] D.K. Schroder and J.A. Babcock, *Negative Bias Temperature Instability: Road to Cross in Deep Submicron Silicon Manufacturing*, J. Appl. Phys **94**, 1-18 (2003).
- [6] M.A. Alam and S. Mapahatra, *A Comprehensive Model of pMOS NBTI Degradation*, Microelectron. Reliability **45**, 71-81 (2005).
- [7] S. Chakravarti, A.T. Krishnan, V. Reddy, C.F. Machala, and S. Krishnan, *A Comprehensive Framework for Predictive Modelling of Negative Bias Temperature Instability*, IEEE International Reliability Physics Symposium Proceedings 273-282 (2004).
- [8] J.A. Weil, J.R. Bolton, and J.E. Wertz, *Electron Paramagnetic Resonance: Elementary Theory and Practical Applications*, Wiley Interscience, New York (1994).
- [9] C.P. Poole Jr., *Electron Spin Resonance: A Comprehensive Treatise on Experimental Techniques, Second Edition*, Wiley Interscience, New York (1983).
- [10] Application of ESR to MOS systems has been reviewed by P.M. Lenahan and J.F. Conley Jr.: *What Can Electron Paramagnetic Resonance Tell Us About the Si/SiO<sub>2</sub> System*, J. Vac. Sci. Technol. B **16**, 2139-2153 (1998).
- [11] D.J. Lepine, *Spin Dependent Recombination on a Silicon Surface*, Phys. Rev. B **6**, 436-441 (1972).
- [12] D. Kaplan, I. Solomon, and N.F. Mott, *Explanation of the Large Spin Dependent Recombination Effect in Semiconductors*, J. Phys. Lett. (Paris) **39**, L51-L54 (1978).
- [13] P.M. Lenahan and M.A. Jupina, *Spin Dependent Recombination at the Silicon-Silicon Dioxide Interface*, Colloids and Surfaces **45**, 191-211 (1990).
- [14] P.M. Lenahan and P.V. Dressendorfer, *Effects of Bias on Radiation Induced Paramagnetic Defects at the Silicon-Silicon Dioxide Interface*, Appl. Phys. Lett. **41**, 542,544 (1982).
- [15] P.M. Lenahan and P.V. Dressendorfer, *Holes Traps and Trivalent Silicon Centers in Metal/Oxide/Silicon Devices*, J. Appl. Phys. **55**, 3495-3499 (1984).
- [16] H. Miki, M. Naguchi, K. Yokogawa, B. Kim, K. Asada, and T. Sugano, *Electron and Hole Traps in SiO<sub>2</sub> Films Thermally Grown on Si Substrates in Ultra-Dry Oxygen*, IEEE Trans. Electron Devices **35**, 2245 (1998).
- [17] T. Takahashi, B.B. Triplett, K. Yokogawa, and T. Sugano, *Electron Spin Resonance Observations of the Creation, Annihilation and Charge State of the 74 Gauss Doublet in Device Oxides Dominated by Soft X-rays*, Appl. Phys. Lett. **51**, 1339 (1987).
- [18] L. Lipkin, L. Rowan, A. Reisma, and C.K. Williams, *Correlation of Fixed Positive Charge and E' gamma Centers via Electron Paramagnetic Resonance Techniques*, J. Electrochemical Society **138**, 2050 (1991).
- [19] J.T. Krick, P.M. Lenahan, and G.J. Dunn, *Direct Observation of Interfacial Point Defects Generated by Channel Hot Hole Injection in n-channel Metal Oxide Silicon Field Effect Transistors*, Appl. Phys. Lett. **59**, 3437-3439 (1991).
- [20] J.W. Gabrys, P.M. Lenahan, and W. Weber, *High Resolution Spin Dependent Recombination Study of Hot Carrier Damage in Short Channel MOSFETs: <sup>29</sup>Si Hyperfine Spectra*, Microelectronics Engineering **22**, 273-276 (1993).
- [21] S. Fujieda, Y. Miura, M. Saitoh, E. Hasegawa, S. Koyama, and K. Ando, *Interface Defects Responsible for Negative Bias Temperature Instability in Plasma Nitrided SiON/Si(100) Systems*, Appl. Phys. Lett. **82**, 3677-3679 (2003).
- [22] S. Fujieda, Y. Miura, M. Saitoh, Y. Yoshigoe, *Characterization of Interface Defects Related to Negative Bias Temperature Instability in Ultra Thin Plasma Nitrided SiON/Si(100) Systems*, Microelectronics Reliability **45**, 57-64 (2005).
- [23] J.P. Campbell, P.M. Lenahan, A.T. Krishnan, S. Krishnan, *Observations of NBTI-induced Atomic Scale Defects*, Accepted for Publication in IEEE Trans. Device and Materials Rel., (2/2006).
- [24] J.P. Campbell, P.M. Lenahan, A.T. Krishnan, S. Krishnan, *Direct Observation of the Structure of Defect Centers Involved in the Negative Bias Temperature Instability*, Appl. Phys. Lett., **87**, 204106 (2005).
- [25] J.P. Campbell, P.M. Lenahan, A.T. Krishnan, and S. Krishnan, *NBTI: An Atomic-Scale Defect Perspective*, Proceedings of the International Reliability Physics Symposium, 442-447 (2006).
- [26] C.J. Cochrane, P.M. Lenahan, J.P. Campbell, G. Bersuker, P. Lysaght, to be published.
- [27] P.M. Lenahan, *Atomic Scale Defects Involved in MOS Reliability Problems*, Microelectronic Engineering **69**, 173-181 (2003).

# Hydrogen Transport in Doped and Undoped Disordered Silicon

Norbert Nickel,  
Hahn-Meitner-Institut, Berlin, Germany

Hydrogen transport in amorphous, microcrystalline, and polycrystalline silicon has been studied intensively in the past due to its importance for understanding structure, growth, metastability, and defect passivation. Further substantial insight in the microscopic mechanism governing hydrogen diffusion can be obtained by comparing diffusion in doped material with H diffusion in undoped disordered silicon. Hydrogen migration was investigated by deuterium diffusion-experiments as a function of temperature, deuterium, phosphorous, and boron concentrations. At high D concentrations the diffusion is dispersive depending on the plasma exposure time. With increasing doping concentration the effective diffusion-coefficient,  $D_{\text{eff}}$ , increases. Poly-Si doped with a boron concentration of  $10^{18} \text{ cm}^{-3}$  exhibits an increase of  $D_{\text{eff}}$  by one order of magnitude compared to undoped poly-Si. On the other hand, phosphorous doped poly-Si shows only a 40% increase of  $D_{\text{eff}}$ . The diffusion activation energy, EA, depends significantly on the Fermi energy  $E_F$  and the hydrogen concentration. In polycrystalline silicon EA varies between 0.1 and 1.69 eV while in microcrystalline silicon the diffusion activation energy varies between 0.01 and 0.4 eV. This is accompanied by a variation of the diffusion prefactor by 15 orders of magnitude and is even consistent with results reported on H diffusion in hydrogenated amorphous silicon. Using the theoretical diffusion prefactor the energy EA required to yield the diffusion coefficient was calculated. EA reveals a Fermi energy dependence similar to that of the formation energy of  $\text{H}^+$  and  $\text{H}^-$  in c-Si. Based upon the experimental data a unified microscopic model for H diffusion in silicon is proposed.



# First-Principles Approach to the Reliability Issues of MOS Gate Oxides

T. Maruizumi, J. Ushio<sup>\*</sup>, I. Kitagawa<sup>\*</sup>, Y. Okuyama<sup>\*\*</sup>, and S. Ho<sup>\*</sup>

Musashi Institute of Technology, 1-28-1 Tamazutsumi, Setagaya-ku, Tokyo 158-8557, Japan

<sup>\*</sup>Advanced Research Laboratory, Hitachi Ltd., 1-280 Higashi-Koigakubo, Kokubunji-shi,  
Tokyo 185-8601, Japan

<sup>\*\*</sup>Central Research Laboratory, Hitachi Ltd., 1-280 Higashi-Koigakubo, Kokubunji-shi,  
Tokyo 185-8601, Japan

e-mail: marui@ee.musashi-tech.ac.jp

## INTRODUCTION

Negative-bias temperature instability (NBTI) is one of the important issues in reliability of metal-oxide-semiconductor (MOS) devices. Understanding the mechanism of the NBTI is demanded to design a higher-performance and more reliable device. Though the extensive studies have been done [1], the causes for some dependence of the NBTI on stress conditions have remained unknown. For example, the origin of the electric-field dependence is not established yet.

We have investigated the charged species that causes the electric field dependence of NBTI by a first-principles calculation.

## CALCULATIONAL METHOD

We took a hydrogen-originated NBTI and considered the specific role of hydrogen paying attention to the difference of the Si/SiO<sub>2</sub> and Si/SiO<sub>x</sub>N<sub>y</sub> interfaces. Hole-trapping energy (an energy required to trap a hole into the interface) and hydrogen-migration energy (an energy required to migrate a H atom from one place to another in the interface trapping a hole) were calculated for the two interfaces. We used the molecular models of the interfaces (Figures 1 and 2) and a first-principles density functional theory program, deMon [2].

## RESULTS AND DISCUSSION

The obtained hole-trapping and hydrogen-migration energies are listed in Tables I and II. The Si/SiO<sub>x</sub>N<sub>y</sub> interface needs less energy to trap a hole than the Si/SiO<sub>2</sub> interface does. This corresponds to the fact that the N incorporation into the Si/SiO<sub>2</sub> interface enhances the NBTI. The hole-trapping

energy at the O or N site in the interfaces is lower than that at the Si-H site or at the O or N vacancy, showing that hole trapping can occur most easily at the O or N site. On the other hand, the generation of a proton and a Si dangling bond from the hole-trapping Si-H site was calculated to be energetically less favorable to the generation of a H atom and a hole-trapping Si atom by 5.8 eV. We conclude that the hole trapping, an initial step of the NBTI, occurs at the O or N site in the interface, not at the Si-H site. The H atom should play a role in the following step of the NBTI.

The hydrogen migration from Si to O or an O vacancy trapping a hole destabilizes the hole-trapping state of the Si/SiO<sub>2</sub> interface by about 0.4 eV, while the migration from Si to N trapping a hole stabilizes the Si/SiO<sub>x</sub>N<sub>y</sub> interface by 0.1 eV. This difference in the hydrogen-migration energies is another reason for the enhancement of NBTI by the N incorporation into the interface.

Next, we investigated the possibility of reducing activation energy by electric field in the case of hydrogen migration by electric field in the case of hydrogen migration at a Si(100)/SiO<sub>2</sub> interface. The calculated energies of the interface along the assumed path (Fig. 3) of hydrogen migration are listed in Table III. The effect of electric field (either forward or backward) on the neutral state is negligible. The activation energy of the hole-trapping state, even without electric field, is significantly smaller than those of the neutral state. We conclude that the Si-H bond dipole is not the origin of the electric field dependence of the NBTI. A good correspondence between the hole-trapping energies and the NBTI tendencies of the dielectric materials implies that the rate-limiting step of the

NBTI is a hole trapping in the interface. So, the electric field dependence of NBTI may be explained by the hole-trapping rate under an applied electric field.

### CONCLUSION

Hole trapping, the initial step of the NBTI, occurs at the O or N atom in the Si/SiO<sub>2</sub> or Si/SiO<sub>x</sub>N<sub>y</sub> interface. The electric field dependence can be explained by the hole-trapping rate in the interface under the electric field.

### REFERENCES

- [1] S. Ogawa, M. Shimaya, and N. Shiono, *J. Appl. Phys.* **77**, 1137 (1995).  
 [2] D. R. Salahub, R. Fournier, P. Mlynarski, I. Papai, A. St-Amant, and J. Ushio, *Density Functional Methods in Chemistry*, edited by J. K. Labanowski and J. W. Andzelm (Springer-Verlag, New York, 1991) p. 77.

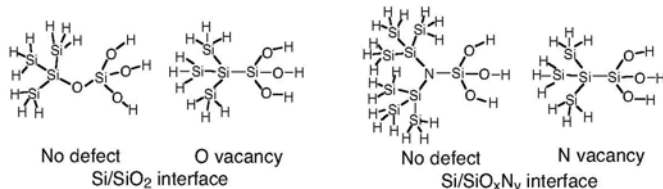


Fig. 1. Molecular models of Si/SiO<sub>2</sub> and Si/SiO<sub>x</sub>N<sub>y</sub> interfaces. The O-vacancy and N-vacancy structures are the same.

Table I. Hole-trapping reaction energies of Si/SiO<sub>2</sub> interfaces with and without hydrogen migration.

Hole-trapping site		Hole-trapping reaction	Reaction energy (eV)	Hydrogen-migration energy (eV)
Si-H bond		$\text{Si}-\text{Si}-\text{H} \xrightarrow{h^+} \text{Si}^{\ominus}-\text{Si}-\text{H}$	8.87	—
Si/SiO <sub>2</sub> interface	No defect	Without H migration $\text{Si}-\text{Si}-\text{O}-\text{Si}-\text{O} \xrightarrow{h^+} \text{Si}-\text{Si}^{\ominus}-\text{O}-\text{Si}-\text{O}$	8.14	0.39
		With H migration $\text{Si}-\text{Si}-\text{O}-\text{Si}-\text{O} \xrightarrow{h^+} \text{Si}-\text{Si}-\text{O}-\text{Si}-\text{O}^{\ominus}$	8.53	
	O vacancy	Without H migration $\text{Si}-\text{Si}-\text{O} \xrightarrow{h^+} \text{Si}-\text{Si}^{\ominus}-\text{O}$	8.39	0.38
		With H migration $\text{Si}-\text{Si}-\text{O} \xrightarrow{h^+} \text{Si}-\text{Si}-\text{O}^{\ominus}$	8.77	

Table II. Hole-trapping reaction energies of Si/SiO<sub>x</sub>N<sub>y</sub> interfaces with and without hydrogen migration.<sup>a</sup>

Hole-trapping site		Hole-trapping reaction	Reaction energy (eV)	Hydrogen-migration energy (eV)
Si/SiO <sub>x</sub> N <sub>y</sub> interface	No defect	Without H migration $\text{Si}-\text{Si}-\text{N}-\text{Si}-\text{O} \xrightarrow{h^+} \text{Si}-\text{Si}^{\ominus}-\text{N}-\text{Si}-\text{O}$	7.52	-0.10
		With H migration $\text{Si}-\text{Si}-\text{N}-\text{Si}-\text{O} \xrightarrow{h^+} \text{Si}-\text{Si}-\text{N}-\text{Si}-\text{O}^{\ominus}$	7.42	
	O vacancy	Without H migration $\text{Si}-\text{Si}-\text{O} \xrightarrow{h^+} \text{Si}-\text{Si}^{\ominus}-\text{O}$	8.39	0.38
		With H migration $\text{Si}-\text{Si}-\text{O} \xrightarrow{h^+} \text{Si}-\text{Si}-\text{O}^{\ominus}$	8.77	

<sup>a</sup>The energies for N vacancy are not shown, because the values are the same as those for O vacancy in Table I.

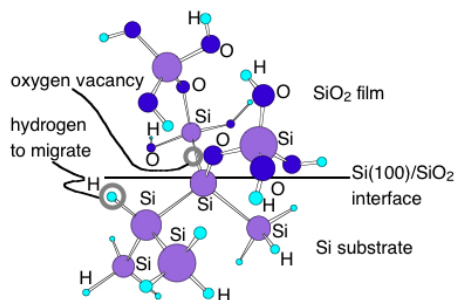


Fig. 2. Molecular model of the Si(100)/SiO<sub>2</sub> interface for the calculation of activation energy of hydrogen migration in an electric field.

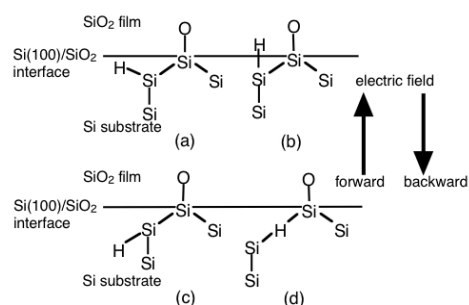


Fig. 3. Definitions of four hydrogen positions and directions of the electric field: (a) the equilibrium structure, (b) the Si-H bond perpendicular to the Si(100) surface, (c) the Si-H bond and the Si-Si bond on the same linear line, and (d) the H atom on the Si-Si bond.

Table III. The energies<sup>a</sup> of the three kinds<sup>b</sup> of H positions in neutral and hole-trapping states of the equilibrium structures and the large lattice distorted structures (LLDSs) under an electric field<sup>c</sup>.

charge state	base structure	electric field	energy (eV) <sup>a</sup>		
			H-position (b) <sup>b</sup>	H-position (c) <sup>b</sup>	H-position (d) <sup>b</sup>
neutral	equilibrium	none	0.93	2.23	—
		forward	0.88	2.15	—
		backward	0.87	2.19	—
	LLDS	none	0.91	2.36	1.21
		forward	0.93	2.32	1.20
		backward	0.89	2.39	1.22
hole trapping	equilibrium	none	0.42	1.17	—
	LLDS	none	0.09	1.30	0.03

<sup>a</sup>For the equilibrium base structure, the energy of the fully optimized structure in each charge state with or without an electric field was taken as zero of the energy. For the LLDS base structure in each charge state, the energy of the LLDS whose Si-Si bond length was 3.0 Å keeping the other part the same as the equilibrium structure was taken as zero.

<sup>b</sup>See Fig. 3 for the structures of H-positions (b), (c), and (d).

<sup>c</sup>The electric field strength was 10 MV/cm.

# Hydrogen in MOSFETs – The Good, the Bad, and the Ugly

Sokrates T. Pantelides<sup>1,2</sup>

L. Tsetseris,<sup>1</sup> S. N. Rashkeev,<sup>1,2</sup> X. J. Zhou,<sup>3</sup> D. M. Fleetwood<sup>3,1</sup> and R. D. Schrimpf<sup>3</sup>

<sup>1</sup>Department of Physics and Astronomy, Vanderbilt University, Nashville, Tennessee, USA

<sup>2</sup>Oak Ridge National Laboratory, Oak Ridge, Tennessee, USA

<sup>3</sup>Department of Electrical Engineering and Computer Science, Vanderbilt University,  
Nashville, Tennessee, USA

## INTRODUCTION

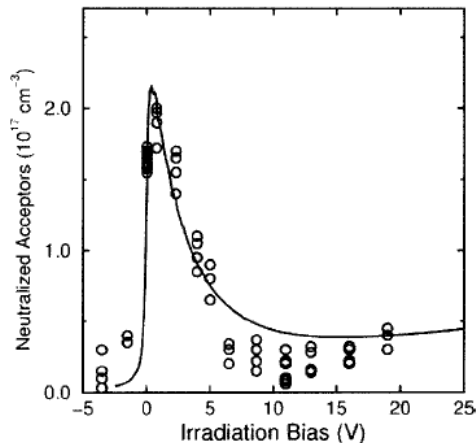
Hydrogen is intentionally introduced in metal-oxide-semiconductor field-effect transistors (MOSFETs) because of a highly beneficial effect at the Si-SiO<sub>2</sub> interface: it passivates the so-called dangling bonds, which results in high carrier mobilities in the channel. Over the years, many undesirable phenomena, observed in MOSFETs under different conditions and causing varying degrees of degradation, have gradually been attributed directly or indirectly to hydrogen. In the last several years, we pursued extensive first-principles calculations of hydrogen configurations and reactions in MOSFETs in the context of pertinent experimental data, both old and new. The calculations were based on density-functional theory, the local-density approximation for exchange-correlation, supercells, and plane-wave basis sets. The key questions were: where, in addition to passivated dangling bonds at the interface, does hydrogen reside? How is it released and in what charge state? How does it migrate? If H is released elsewhere and migrates to the Si-SiO<sub>2</sub> interface, how might it depassivate dangling bonds? Does it get through the interface in one or both directions and what are the consequences? As it migrates, can it induce the formation of other defects? The pertinent experimental data are the so-called bias temperature instability (BTI) and radiation-induced phenomena such as increase of interface trap density and pertinent annealing cycles, deactivation of dopants in Si, and combined radiation/BTI conditions. This talk will summarize a few of the key findings.

## DEPASSIVATION OF DANGLING BONDS

It has long been recognized that H is released as H<sup>+</sup> from various sites in the oxide under a variety of conditions (radiation, hot electrons, etc). Under suitable bias, it can travel to the interface, where it depassivates dangling bonds, and potentially crosses the interface, where it can deactivate dopants. It was believed that, in order to depassivate a dangling bond, H<sup>+</sup> must first capture an electron from the Si side and then, as neutral H, migrate until it finds its target, when the reaction Si-H + H → D + H<sub>2</sub> occurs (here D is a neutral dangling bond). Detailed density-functional calculations have demonstrated that H<sup>+</sup> can depassivate directly via the reaction Si-H + H<sup>+</sup> → D<sup>+</sup> + H<sub>2</sub>. The result has a significant consequence for modeling depassivation processes because they do not depend on the availability of excess electrons [1].

## DEACTIVATION OF DOPANTS IN Si

Dopant deactivation was also believed to require prior neutralization of H<sup>+</sup>. In fact, it has been shown that H in Si is a negative-U defect, meaning that neutral H is not the stable species at any value of the Fermi energy. We now have shown [2] that direct deactivation of boron impurities occurs by H<sup>+</sup>. We have modeled the process in the presence of bias using Monte-Carlo simulations and showed that the observed strong dependence of deactivation on electric field is due mainly to transport of H<sup>+</sup> in the depletion region. The dependence of the deactivated-boron concentration on irradiation bias, as



measured by Witzak et al. [3], was accounted by the model (see Figure above, taken from [2]).

#### NEGATIVE BIAS TEMPERATURE INSTABILITY

The interface trap density has long been known to increase under negative bias (2-6 MV/cm) at moderate temperatures (100-200°C). Small activation energies (~0.3 eV) are generally attributed to hydrogen-mediated depassivation of dangling bonds (larger activation energies are generally attributed to H<sub>2</sub>O-mediated processes). The effect is more pronounced in p-channel MOSFETs under negative bias. It is widely believed that, in the presence of the electric field and excess holes, Si-H at the interface undergoes direct dissociation, i.e., Si-H + h<sup>+</sup> → D + H<sup>+</sup>. We have shown with parameter-free density-functional calculations [4] that the direct dissociation activation energy in the absence of holes is 2.4 eV (in agreement with the experimental value of 2.6 eV) and that, in the presence of holes, the activation energy only drops to 2.1 eV. We proposed that deactivation must be mediated by H, which in this case, must originate on the Si side. Calculations of H release from dopants suggest that hydrogen attached to the dopant atoms is the likely source. The observed small activation energy, only ~0.3 eV, is the result of quasi-equilibrium that is established by the pertinent reactions. A diffusion-reaction theory developed by Jeppson and Svensson[5] in 1977 was applied. The activation energy is given by  $E_a = \frac{1}{2}\Delta E + \frac{1}{4}Q$ , where  $\Delta E$  is the reaction energy of depassivation by H<sup>+</sup>, as described earlier, and Q is the diffusion barrier of H<sup>+</sup>. Using

our calculated values for these energies ( $\Delta E = 0.5$  eV,  $Q = 0.45$  eV), we find  $E_a = 0.36$  eV. We have confirmed the experimental values with new experiments for both Si-SiO<sub>2</sub> and Si-SON-HfO<sub>2</sub> (an alternate dielectric) and found similar activation energies [6], establishing the generality of the phenomenon. We have also investigated the response of such structures to combined NBTI and radiation and found that the two phenomena can influence each other strongly, and often in surprising ways.

#### ACKNOWLEDGEMENTS

This work was supported in part by the Air Force Office of Scientific Research, and the U.S. Navy, and the McMinn Endowment at Vanderbilt University.

#### REFERENCES

- [1] S. N. Rashkeev, D. M. Fleetwood, R. D. Schrimpf, and S. T. Pantelides, "Defect generation by hydrogen at the Si-SiO<sub>2</sub> interface," *Phys. Rev. Lett.* **87**, 165506 (2001); L. Tsetseris and S. T. Pantelides, "Migration, incorporation and passivation reactions of molecular hydrogen at the Si-SiO<sub>2</sub> interface", *Phys. Rev. B* **70**, 245320 (2004).
- [2] S.N. Rashkeev, D.M. Fleetwood, R.D. Schrimpf, and S.T. Pantelides, "Radiation-induced acceptor deactivation in bipolar devices: effects of electric field," *Appl. Phys. Lett.* **83**, 4646-4648 (2003).
- [3] S. C. Witzak, P. S. Winokur, R. C. Laco, and D. C. Mayer, "Charge separation technique for MOS capacitors in the presence of hydrogen-deactivated dopants," *Appl. Phys. Lett.* **87**, 8206-8208 (2000).
- [4] L. Tsetseris, X. J. Zhou, D. M. Fleetwood, R. D. Schrimpf, and S. T. Pantelides, "Physical mechanisms of negative-bias temperature instability," *Appl. Phys. Lett.* **86**, 142103 (2005).
- [5] K. O. Jeppson and C. M. Svensson, "Negative bias stress of MOS devices at high electric fields and degradation of MNOS devices", *J. Appl. Phys.* **48**, 2004-2014 (1977).
- [6] X. Zhou, L. Tsetseris, S. N. Rashkeev, D. M. Fleetwood, R. D. Schrimpf, and S. T. Pantelides, "Negative Bias-Temperature Instabilities in Metal-Oxide-Silicon Devices with SiO<sub>2</sub> and Si-O<sub>x</sub>N<sub>y</sub>/HfO<sub>2</sub> Gate Dielectrics," *Appl. Phys. Lett.* **84**, 4394-4396 (2004).

# Author Index

Aboud, S.	11, 371	Birner, S.	173
Adessi, C.	151	Blakey, P.	47
Affinito, F.	171, 369	Blase, X.	151
Ahmed, S.	117, 343	Bloomfield, M.	45
Aigner, F.	207	Bordone, P.	187
Akis, R.	31, 189, 193	Born, M.	213
Aksamija, Z.	21, 93	Botez, D.	323
Al-Ahmadi, A.	35	Boudjella, A.	153
Alam, M.	375	Bourgade, J.	215
Aldegunde, M.	37	Bournel, A.	25, 107
Aleshkin, V.	135	Branlard, J.	109
Anantram, M.	275, 341	Breglio, G.	313
Ancona, M.	9	Bremer, J.	59
Andlauer, T.	173	Brown, A.	49
Andrei, P.	39	Brunetti, R.	171, 369
Aoulaiche, M.	381	Brunner, R.	189
Aradi, B.	349	Bufler, F.	101, 123
Asenov, A.	17, 37, 49, 81, 111, 275, 367	Burgdörfer, J.	207, 227
Ashizawa, Y.	41, 137	Burger, M.	51
Asokan, A.	95	Buscemi, F.	187
Atanassov, E.	285		
Auer, C.	347	Cabrera, S.	91
Auf der Maur, M.	43, 331	Cacelli, I.	155
Avouris, P.	197	Caceres, M.	103
Ayubi-Moak, J.	15	Caddemi, A.	53
		Caillat, J.	325
Bäcker, A.	227	Cale, T.	45
Baccarani, G.	295	Cancellieri, E.	175
Ballo, P.	97	Capizzo, M.	105, 125
Banerjee, S.	209, 231	Cappelletti, M.	311
Barker, J.	99, 111, 275	Carceller, F.	239
Barraud, S.	119	Carrillo, J.	103
Bastian, B.	223	Cartoixa, X.	67, 265
Basu, D.	209	Catalfamo, F.	53
Bates, S.	47	Caussanel, M.	183
Beckstein, O.	367	Cavassilas, N.	355
Begoin, M.	59	Ceccarelli, M.	369
Belghachi, A.	309	Chakravarthi, S.	377
Ben Abdallah, N.	211	Chantis, A.	265
Bentz, D.	45	Chassat, C.	25
Bersuker, G.	111	Chen, C.	69
Bertoni, A.	175, 185, 187	Chen, J.	243
Bescond, M.	355	Chen, W.	71
Bhuwalka, K.	213	Constantoudis, V.	55
Bird, J.	189	Csaba, G.	195, 217

Csurgay, A.	245	Fichtner, W.	267
Cui, H.	221	Fiebig, M.	57
Cummings, A.	193	Fiori, G.	229, 261
		Fischetti, M.	23, 181
Darve, E.	259	Fonseca, J.	167
De Gendt, S.	381	Frauenheim, T.	349, 353, 357
Degond, P.	215, 225	Freeman, A.	361
Delaney, P.	157		
De Laurentis, M.	313	Gärtner, K.	205
De Leonardis, F.	315, 317, 319	Gagliardi, A.	353, 357
Dell'Olio, F.	319	Gallego, S.	225
Demeio, L.	283	Gamba, I.	103
Dhar, S.	141	Gamiz, A.	133, 237
Di Carlo, A.	43, 331, 349, 353, 357	Gamerith, S.	385
Djuric, Z.	3	Ganguly, S.	231
Do, V.	27, 219	Gao, X.	323
Dollfus, P.	25, 27, 107, 119, 219	Garcia-Loureiro, A.	37, 81
Domaingo, A.	211	Garcia, A.	233
Donato, N.	53	Gehring, A.	255
Dong, B.	221	Gencer, A.	63
Donoval, D.	97	Gilbert, M.	177, 209, 235
Drouvelis, P.	223	Girlanda, M.	155
Du, G.	143, 243	Gnani, E.	295
Dubinov, A.	135	Godoy, A.	133, 237
Dutta, M.	293, 321, 337	Gogolides, E.	55
		Gomez-Campos, F.	239
Ede, C.	325	Goodnick, S.	11, 15, 109, 129
Eisele, I.	213	Grasser, T.	29, 87, 255
Eisenberg, B.	365	Greer, J.	157
Eitel, S.	199	Grimalsky, V.	233
Erdmann, A.	79	Groeseneken, G.	381
Erlebach, A.	101	Gruzinskis, V.	115, 135
Erlen, C.	57	Gutierrez, E.	233
Ertler, C.	347	Gutmann, R.	45
Eschermann, J.	33		
Esseni, D.	301	Hössinger, A.	3
Evans, M.	183	Hafner, J.	351
		Halkias, G.	327
Fühner, T.	61	Han, R.	143, 243
Fagas, G.	157	Harmatha, L.	97
Fahem, Z.	195	Harmer, M.	241
Faralli, N.	109	Hartmann, H.	79
Feist, J.	227	Hartmann, U.	307
Felgenhauer, F.	59	He, Y.	243
Fernandez-Diaz, E.	113	Hedin, E.	249
Ferrante, G.	127	Hegyí, B.	245
Ferrari, G.	17, 111, 175	Heigl, A.	191
Ferretti, A.	155	Heitzinger, C.	117, 169
Ferry, D.	31, 109, 189, 193	Heyns, M.	381

Herrmann, T.	159	Kitagawa, I.	391
Hess, K.	363	Kitamura, K.	65
Hjelm, M.	247	Klimeck, G.	169, 229, 267, 281, 343
Ho, S.	391	Klix, W.	159
Holzer, S.	255	Knezevic, I.	129, 277, 323
Hong, S.	289	Kobayashi, T.	89
Horio, K.	65	Kosina, H.	29, 87, 141, 161, 255, 291, 345
Hou, D.	243	Kresse, G.	351
Houssa, M.	381	Krishnan, S.	23
Huang, R.	147	Kubis, T.	257
Huard, V.	383	Kuchar, F.	189
Huckestein, B.	227	Kurosawa, N.	65
Hude, R.	101	Kyriakis-Bitaros, E.	327
Hwang, C.	165		
Iannaccone, G.	229, 261	Lannoo, M.	355
Ikarashi, A.	65	Latessa, L.	349
Imre, A.	303	Lebedev, A.	63
Irace, A.	313	Le Carval, G.	119
		Lenahan, P.	387
Jackiv, R.	305	Li, L.	161
Jacoboni, C.	17, 171, 175, 369	Li, S.	259
Jakobsson, E.	371	Li, W.	147
Jaouen, H.	1, 119	Li, Yiming	69, 71
Jaud, M.	119	Li, Yan	33
Jerome, J.	361	Lindfelt, M.	247
Ji, H.	147	Lisieri, M.	261
Ji, L.	217, 303	Liu, X.	243
Jimenez-Molinoz, F.	133	Lohwasser, M.	263
Jimenez, D.	67	Lopez, A.	265
Jirari, H.	251	Lu., J.-Q.	45
Jirauschek, C.	201	Lugli, P.	57, 195, 201, 217
Joe, Y.	249	Luisier, M.	267, 281
John, D.	253		
Jordan, G.	325	MacDonald, A.	231
Jung, T.	61	Macucci, M.	155, 269, 273
Jungemann, C.	13	Magno, F.	315
		Magnus, W.	299
Kalna, K.	37, 81	Maiti, C.	73
Kang, Y.	243	Majkusiak, B.	271
Karlowatz, G.	141	Majorana, A.	103
Karner, M.	87, 255	Mamaluy, D.	179
Kaya, S.	35, 167	Manenti, M.	201
Kelsall, R.	95, 131	Marconcini, P.	269, 273
Ketzmerick, R.	227	Marreiro, D.	371
Khan., H.	179	Martinez, A.	247, 275
Khmelevskiy, S.	163	Maruizumi, T.	391
Kim, I.	361	Mathis, W.	59
Kim, J.	121	Matsuo, K.	89

Mauser, N.	215, 263	Park, N.	289
Mautes, D.	307	Passaro, V.	315, 317, 319
May, C.	123	Pati, S.	77
Mehats, F.	225	Patsis, G.	55
Mehler, E.	159	Pavlov, B.	241
Mehrez, H.	341	Pecchia, A.	349, 353, 357
Meinerzhagen, B.	13	Peltzer y Blanca, E.	311
Meisels, R.	189	Peretti, F.	195
Meller, G.	161	Persano Adorno, D.	105, 125, 127
Meyer, G.	277	Persson, M.	331, 349
Millar, C.	367	Petrashenko, A.	79
Minari, H.	279	Pfäffli, P.	63
Minoglou, K.	327	Pham, A.	13
Miranda, E.	67	Piccinini, E.	171, 369
Mitin, V.	281	Pilgrim, N.	131
Mohn, P.	163	Polizzi, E.	339
Mokhtar, K.	153	Popp, S.	61
Monsef, F.	25	Porod, W.	217, 245, 303
Morandi, O.	283	Pourfath, M.	291, 331, 345
Mori, N.	279	Povolotskyi, M.	43, 349, 331
Morschl, R.	173	Pözl, M.	385
Mouis, M.	211	Pötz, W.	203, 251
Muscato, O.	75	Prokopova, L.	331
		Pulfrey, D.	253
Naeve, T.	329	Puchner, H.	379
Nakajima, K.	89	Putz, V.	325
Nedjalkov, M.	17, 285		
Negulescu, C.	211	Querlioz, D.	27
Nehari, K.	355		
Nelhiebel, S.	385	Raichura, A.	293
Neophytou, N.	343	Rakowski, R.	167
Nguyen, V.	27, 219	Ramayya, E.	129
Nickel, B.	57	Ravaioli, U.	21, 33, 93
Nickel, N.	389	Redinger, J.	163
Niehaus, T.	357	Reggiani, S.	295
Nilsson, H.	247	Register, L.	231
Nonner, W.	365	Richards, D.	5
		Ringhofer, C.	117, 215
O'Regan, T.	181	Roche, S.	67, 151
Odermatt, S.	199	Rodriguez-Bolivar, S.	239
Oka, H.	41, 137	Rosini, M.	175
Okada, T.	19	Rotter, S.	207, 227
Okamoto, M.	279	Roy, S.	111, 367
Okuyama, Y.	391	Rudan, M.	171, 295
Oriols, X.	113, 287	Ruiz-Gallardo, A.	237
		Ryzhii, V.	333
Palankovski, V.	285		
Palestri, P.	301	Sacconi, F.	43, 349
Pantelides, S.	183, 393	Sadi, T.	131

Saha, A.	73	Tang, Y.	371
Saint-Martin, J.	25	Tarik, K.	139
Saitoh, T.	89	Thornton, T.	139
Sampedro, C.	133, 237	Toyabe, T.	85
Samra, P.	7	Trebicky, T.	305
Sansom, M.	367	Trellakis, A.	173
Saraniti, J.	11, 15, 109, 371	Tripathy, P.	77
Satanin, A.	249		
Satou, A.	333	Ungersböck, E.	141
Scarpa, G.	201	Ushio, J.	391
Schürer, F.	347		
Schenk, A.	267	Vagidov, N.	281
Schindler, M.	213	Van der Steen, J.	301
Schmelcher, P.	223	Van der Straaten, T.	33
Schnattinger, T.	79	Varga, E.	303
Schrimpf, R.	183	Vasileska, D.	23, 117, 129, 139, 179, 285
Schroder, D.	373	Vauchelet, N.	211
Scrinzi, A.	325	Velazquez, J.	107
Seegebrecht, P.	329	Vernes, A.	335
Seidl, A.	79	Vogl, P.	173, 257
Selberherr, S.	29, 141, 255, 291, 345	Voves, J.	305
Selmi, L.	301		
Seoane, N.	81	Wachutka, G.	191
Shao, X.	83	Wagner, M.	87, 255
Shiktorov, P.	115, 135	Wang, G.	145
Shin, M.	297	Wang, J.	143
Shumway, J.	177	Wang, Y.	147
Shu, C.-W.	103	Watanabe, H.	89
Shur, M.	333	Watling, J.	49, 99, 111
Sieberer, M.	163	Weinberger, A.	335, 359
Sievert, P.	361	Wenin, M.	203
Skotnicki, T.	1	West, B.	321
Smith, K.	173	Wissenwasser, J.	385
Song, A.	145	Witzigmann, B.	199
Soree, B.	299	Won, T.	121, 165
Starikov, E.	115, 135		
Stenzel, R.	159	Xia, Z.	143
Strecker, N.	5	Xu, K.	145
Stroscio, M.	293, 321, 337		
Sune, J.	67, 265	Yafyasov, M.	241
Suvorov, V.	3	Yahya, U.	47
Sverdlov, V.	29	Yamanaka, T.	337
Svizhenko, A.	275	Yamasaki, T.	137
Syvridis, D.	327	Ye, L.	361
		Yoon, K.	165
Takani, T.	85	Yoshimura, H.	19
Takeda, H.	279	Yu, M.	147
Tanabe, R.	41, 137	Yu, S.	69
Tang, T.-W.	7	Yu, Z.	83, 149

Yuan, L.	147
Zarcone, M.	105, 127
Zeitoff, P.	111
Zemliak, A.	91
Zhan, K.	147
Zhang, H.	307
Zhang, X.	147
Zhao, J.	149
Zibold, T.	173
Zou, J.	149

ISBN 3-901578-16-1